

# REPORT DOCUMENTATION PAGE

AFRL-SR-AR-TR-02-

the data needed, and completing and reviewing this collection of information. Send comments regarding this burden estimate or any reducing this burden to Washington Headquarters Services, Directorate for Information Operations and Reports, 1215 Jefferson Davis Management and Budget, Paperwork Reduction Project (0704-0188), Washington, DC 20503

0245

<b>1. AGENCY USE ONLY (Leave blank)</b>		<b>2. REPORT DATE</b> May 1, 2002	<b>3. REPORT TYPE AND DATES COVERED</b> Final Report Sept. 1, 1996 - March 31, 2002	
<b>4. TITLE AND SUBTITLE</b> HIGH-CYCLE FATIGUE AND TIME-DEPENDENT FAILURE IN METALLIC ALLOYS FOR PROPULSION SYSTEMS			<b>5. FUNDING NUMBERS</b> AFOSR F49620-96-1-0478	
<b>6. AUTHOR(S)</b> R. O. RITCHIE, S. SURESH, J. W. HUTCHINSON, W. W. MILLIGAN				
<b>7. PERFORMING ORGANIZATION NAME(S) AND ADDRESS(ES)</b> Department of Materials Science and Engineering University of California, Berkeley CA 94720-1760			<b>8. PERFORMING ORGANIZATION REPORT NUMBER</b>	
<b>9. SPONSORING / MONITORING AGENCY NAME(S) AND ADDRESS(ES)</b> Air Force Office of Scientific Research AFOSR/NA 801 N. Randolph St., Arlington, VA 22203-1977			<b>10. SPONSORING / MONITORING AGENCY REPORT NUMBER</b>	
<b>11. SUPPLEMENTARY NOTES</b>				
<b>12a. DISTRIBUTION / AVAILABILITY STATEMENT</b>  Approved for public release; distribution unlimited.			<b>12b. DISTRIBUTION CODE</b>	
<b>13. ABSTRACT (Maximum 200 Words)</b>  The objective of the AFOSR-Multidisciplinary Research Initiative on <i>High-Cycle Fatigue</i> has been to characterize and performed physically-based modeling of the limiting damage states at the onset of high-cycle fatigue failure in blade and disk components in gas-turbine aircraft engines. The intent has been to facilitate mechanistic understanding as a basis for improved life prediction of such engine components. Efforts were focused on defining (i) the fatigue thresholds for high-cycle fatigue, specifically involving small crack and mixed-mode effects, (ii) the influence of foreign object damage (FOD) on such thresholds and on the subsequent life, and the role of fretting and fretting fatigue, in a Ti-6Al-4V blade alloy and a polycrystalline Ni-base disk alloy.				
<b>14. SUBJECT TERMS</b> High-cycle fatigue, fatigue thresholds, small cracks, mixed-mode, Foreign-object damage, fretting			<b>15. NUMBER OF PAGES</b> 524	
			<b>16. PRICE CODE</b>	
<b>17. SECURITY CLASSIFICATION OF REPORT</b> Unclassified	<b>18. SECURITY CLASSIFICATION OF THIS PAGE</b> Unclassified	<b>19. SECURITY CLASSIFICATION OF ABSTRACT</b> Unclassified	<b>20. LIMITATION OF ABSTRACT</b>	

20020816 049

JUL 19 2002

**FINAL REPORT**

**MULTIDISCIPLINARY UNIVERSITY RESEARCH INITIATIVE**

Grant No. AFOSR F49620-96-1-0478

September 1, 1966 – March 31, 2002

**HIGH-CYCLE FATIGUE AND TIME-DEPENDENT FAILURE  
IN METALLIC ALLOYS FOR PROPULSION SYSTEMS**

by

**R. O. Ritchie**

University of California at Berkeley

**S. Suresh**

Massachusetts Institute of Technology

**J. W. Hutchinson**

Harvard University

**W. W. Milligan**

Michigan Technological University

May 1, 2002

Sponsored by the U.S. Air Force Office of Scientific Research



Date 23/Jul/02

MEMORANDUM FOR PKC (Wendy) 703-696-7286

PROM: APOSR/NA

SUBJECT: Receipt of Final Report  
F49620-96-1-0478, UNIV OF CALIFORNIA, BERKELEY

Progress on subject report covering the period from 01-Oct-1996 to 31-Mar-2002

Received on 19-Jul-2002

Accepted on 24-Jul-2002

Non-acceptance-Contractor has been verbally informed of nonacceptance and a resubmission  
suspense date of \_\_\_\_\_ is recommended. Attached is Principal Contracting Officer (PCO) letter  
to the Business Office and PT detailing reasons for non-acceptance and establishing a resubmittal date.



Dr. Craig Hartley  
Program Manager

AEROSPACE & MATERIALS SCIENCE DIRECTORATE

## HIGH-CYCLE FATIGUE AND TIME-DEPENDENT FAILURE IN METALLIC ALLOYS FOR PROPULSION SYSTEMS

AFOSR F49620-96-1-0478

R. O. Ritchie,<sup>1</sup> S. Suresh,<sup>2</sup> J. W. Hutchinson,<sup>3</sup> W. W. Milligan,<sup>4</sup>

<sup>1</sup>University of California at Berkeley, <sup>2</sup>Massachusetts Institute of Technology

<sup>3</sup>Harvard University, <sup>4</sup>Michigan Technological University

### EXECUTIVE SUMMARY

The objective of the AFOSR-MURI High-Cycle Fatigue program has been to characterize and model the limiting damage states at the onset of high-cycle fatigue to facilitate mechanistic understanding as a basis for life prediction. Efforts were focused on the influence of foreign object damage (FOD) and fretting on a Ti-6Al-4V blade alloy and a polycrystalline Ni-base disk alloy. Accomplishments from the program are outlined below:

- Worst-case fatigue threshold stress intensities have been measured in STOA (bimodal) Ti-6Al-4V using large ( $> 5$  mm) cracks under representative HCF conditions ( $R > 0.95$ , 1000 Hz). Values provide a *practical*, frequency-independent (20 – 20,000 Hz) lower bound for the growth of naturally-initiated, physically-small ( $> 40$   $\mu\text{m}$ ) cracks.
- Stress-intensity solutions have been developed for small, semi-elliptical, surface cracks under mixed-mode loading. Such solutions are being used to experimentally measure (for the first time) small-crack, mixed-mode thresholds in Ti-6Al-4V.
- Mixed-mode thresholds, at mixities of  $K_{II}/K_I \sim 0.5$  to 8, for large, short and (for the first time) microstructurally-small cracks have been measured in Ti-6Al-4V, with both bimodal and lamellar microstructures. Mixed-mode short- and particularly small-crack thresholds are significantly lower than those for large cracks. Using a  $G$ -based approach, Mode I is found to be the worst-case threshold condition in the Ti-6Al-4V alloy.
- FOD, simulated with high velocity 200-300 m/s steel-shot impacts, has been found to severely reduce the smooth-bar fatigue life in Ti-6Al-4V microstructures. Whereas worst-case thresholds provide a lower-bound for high-cycle fatigue in the presence of continuum cracks, a modified Kitagawa-Takahashi is proposed where FOD-induced microstructurally-small cracks are formed in damaged regions.
- The local residual stress gradients surrounding FOD regions have been analyzed using quasi-static and dynamic numerical models; predictions have been verified using synchronous x-ray micro-diffraction techniques. X-ray studies have also focused on the cycle-dependent relaxation of such stress fields. Dynamic finite element simulations of FOD damage have also been correlated to such measurements. Evidence for relaxation of such stresses on fatigue cycling has been modeled and directly observed by *in situ* x-ray diffraction measurements.
- Large-crack threshold behavior in a polycrystalline Ni-base disk alloy has been characterized at 100 and 1000 Hz at 25°, 550° and 650°C, involving effects of microstructure, frequency

load ratio and temperature. Values of the measured fatigue thresholds have been correlated to the fracture surface roughness.

- Theoretical solutions for the crack-tip opening and crack-shear displacements controlling the growth of small fatigue cracks have been developed.
- New computational (finite-element) methods for 3-D simulations of fretting fatigue (*Fretting Fatigue Simulator*) have been developed using a ring-element approach.
- Through an analogy between the asymptotic fields at contact edges and ahead of a crack, a crack-analogue approach to contact fatigue (*Crack Analogue*) has been developed, and validated by experiment in Al and Ti alloys.
- A continuum level mechanics model (*Adhesion Model*), incorporating interfacial adhesion, material properties and contact loads, for predicting contact fatigue crack initiation for a variety of loading states and contact geometry, has been developed. The effect of roundness of a nominally sharp contact geometry on fretting fatigue crack initiation was investigated analytically and validated with experimental results on Ti-6Al-4V.
- Palliatives to fretting fatigue such as surface modifications through shot-peening, laser shock-peening and coatings on fretting fatigue damage are being explored.
- The influence of contact and bulk stresses, contact geometry, material microstructure and surface finish on the fretting fatigue behavior of Ti-6Al-4V has been investigated through controlled experiments, using the MURI-developed fretting fatigue device.
- A new framework for understanding the fundamentals of foreign object damage has been developed within the context of dynamic indentation.
- A new theoretical model for the fretting of coated metal surfaces has been developed which specifically addresses the role of plastic deformation of the metal substrate.

## RESEARCH OBJECTIVES

This program was centered on the definition, microstructural characterization and mechanism-based modeling of the limiting states of damage associated with the onset of high-cycle fatigue failure in Ti and Ni-base alloys for propulsion systems. Experimental and theoretical studies were aimed at three principal areas: high cycle/low cycle fatigue (HCF/LCF) interactions, the role of notches, foreign object damage and fretting. The approach was to combine the characterization of microstructural damage with detailed micro-mechanical evaluation and modeling of the salient micro-mechanisms to facilitate the prediction of the effects of such damage on HCF lifetimes.

Most efforts were focused at ambient temperatures on Ti-6Al-4V, with a bimodal processed blade microstructure, and at higher temperatures on a fine-grained poly-crystalline Ni-base disk alloy; additional studies were performed on Ti-6Al-4V with a lamellar microstructure. Specific objectives included: (a) systematic experimental studies to define crack formation and lower-bound fatigue thresholds for the growth of "small" and "large" cracks at high load ratios and high frequencies, in the presence of primary tensile and mixed-mode loading; (b) similar definition of lower-bound fatigue thresholds for crack formation in the presence of notches, fretting, or projectile damage, on surfaces with and without surface treatment (e.g., laser shock peened); (c) development of an understanding of the nature of projectile (foreign object) damage and its mechanistic and mechanical effect on initiating fatigue-crack growth under high-cycle fatigue conditions; (d) development of new three-dimensional computational and analytical modeling tools and detailed parametric analyses to identify the key variables responsible for fretting fatigue damage and failure in engine components, including the identification and optimization of microstructural parameters and geometrical factors and of surface modification

conditions to promote enhanced resistance to fretting fatigue; (e) development of a mechanistic understanding for the initiation and early growth of small cracks in order to characterize their role in HCF failure, with specific emphasis on initiation at microstructural damage sites and on subsequent interaction of the crack with characteristic microstructural barriers. The ultimate aim of the work was to provide quantitative physical/mechanism-based criteria for the evolution of critical states of HCF damage, enabling life-prediction schemes to be formulated for fatigue-critical components of the turbine engine.

#### A. Lower-Bound HCF Thresholds (Mode I and Mixed-Mode) in Ti-6Al-4V (UCB)

In view of the extremely high frequencies ( $>1$  kHz) involved, appropriate design against high cycle fatigue (HCF) failures invariably will be based on the concept of a threshold for fatigue-crack propagation, specifically characterized for HCF conditions, such as high load ratios, high frequencies and small crack sizes. In this study, the near-threshold crack-growth rate behavior of large ( $>5$  mm) cracks tested under both constant- $R$  and constant- $K_{\max}$  conditions was evaluated in the bimodal Ti-6Al-4V microstructure. Large crack behavior was compared to that of naturally-initiated small ( $\sim 45$ – $1000$   $\mu\text{m}$ ) cracks, and small ( $<500$   $\mu\text{m}$ ) surface cracks initiated from sites of simulated foreign object damage (FOD). The specific objective was to discern whether “worst-case” threshold values, measured for large cracks, can have any utility as a *practical* lower bound for the onset of small-crack growth under HCF conditions. The high load ratio, large-crack tests are designed to eliminate crack closure mechanisms, thereby simulating the behavior of small cracks that are larger than microstructural dimensions but do not have a developed wake, i.e., for “continuum-sized” cracks.

The alloy used for all experiments was a 6.30Al, 4.17V, 0.19Fe, 0.19O, 0.13N, bal. Ti (wt%) alloy, supplied as 20 mm thick forged plates from Teledyne Titanium after solution treating for 1 hr at  $925^\circ\text{C}$  and vacuum annealing for 2 hr at  $700^\circ\text{C}$ . The microstructure consisted of a bimodal distribution of  $\sim 60$  vol% primary- $\alpha$  and  $\sim 40$  vol% lamellar colonies of  $\alpha+\beta$ , with a UTS of 970 MPa, a yield strength of 930 MPa and a Young’s modulus of 116 GPa. To minimize residual machining stresses, all samples were low-stress ground and chemically milled.

*Effect of frequency:* A comparison of fatigue-crack growth behavior between 50 Hz and 20,000 Hz in ambient air, shown in Fig. 1, indicates no effect of frequency at near-threshold levels. Such frequency-independent growth rates in Ti alloys have also been reported for 0.1–50 Hz; the current work extends this observation to beyond 1000 Hz. This result is particularly interesting in light of the significant accelerating effect of ambient air on fatigue crack growth when compared to behavior in vacuum. Davidson *et al.* have shown that growth rates *in vacuo* ( $10^{-6}$  torr) are  $\sim 2$  orders of magnitude slower than in air at an equivalent  $\Delta K$ , although the threshold remains roughly the same. This apparent discrepancy is most likely an indication that the rate-limiting step of the environmental (air) effect goes to completion in  $<1$  ms.

*Effect of load ratio:* Constant- $R$  fatigue crack propagation at four load ratios (50 Hz) are compared to constant- $K_{\max}$  data at four  $K_{\max}$  values:  $K_{\max} = 26.5, 36.5, 46.5$ , and  $56.5$   $\text{MPa}\sqrt{\text{m}}$  (1000 Hz) in Fig. 2. As expected, higher load ratios induce lower  $\Delta K_{\text{th}}$  thresholds and faster growth rates at a given applied  $\Delta K$ . The role of load ratio is commonly attributed to crack closure. Based on compliance measurements, no closure was detected above  $R = 0.5$ ; however, at  $R = 0.1$ – $0.3$ ,  $K_{\text{cl}}$  values were roughly constant at  $\sim 2.0$   $\text{MPa}\sqrt{\text{m}}$ . The measured variation of  $\Delta K_{\text{th}}$  and  $K_{\max, \text{th}}$  values with  $R$  are compared in Figs. 3a,b and the variation of  $\Delta K_{\text{th}}$  with  $K_{\max, \text{th}}$  is shown in Fig. 3c. The transition apparent in Figs. 3a-c is consistent with the observed closure level  $\sim 2$   $\text{MPa}\sqrt{\text{m}}$ .

*Worst-case threshold concept:* To examine whether the very high load ratio thresholds, measured on large cracks in the apparent absence of crack closure effects, can be considered as “worst-case” thresholds for “continuum-sized” cracks, the high load-ratio fatigue-crack propagation data

are compared to fatigue behavior from naturally initiated small cracks ( $\sim 45\text{--}1000\ \mu\text{m}$ ) and small cracks ( $<500\ \mu\text{m}$ ) emanating from sites of foreign object damage; in both cases crack growth is not observed below  $\Delta K \sim 2.9\ \text{MPa}\sqrt{\text{m}}$  (Fig. 4). The present results show that with constant- $K_{\text{max}}$  cycling at 1 kHz, a "worst-case" threshold can be defined in Ti-6Al-4V at  $\Delta K_{\text{TH}} = 1.9\ \text{MPa}\sqrt{\text{m}}$  ( $R \sim 0.95$ ). Consequently, it is believed that the "worst-case" threshold concept can be used as a *practical* lower bound for the stress intensity required for the onset of small-crack growth under HCF conditions, provided crack sizes exceed microstructural dimensions.

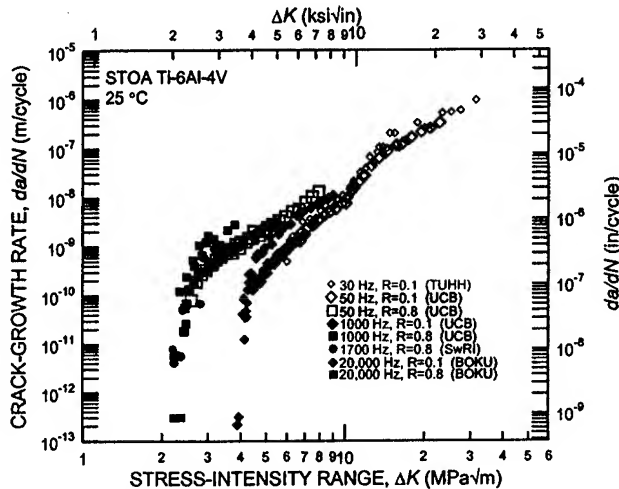


Fig. 1. Effect of frequency on fatigue-crack growth in bimodal Ti-6Al-4V in room air. Results at 50 to 1000 Hz at UCB are compared to data on the same material at 30 Hz collected by at TUHH, at 1500 Hz collected at SWRI, and at 20,000 Hz collected at BOKU.

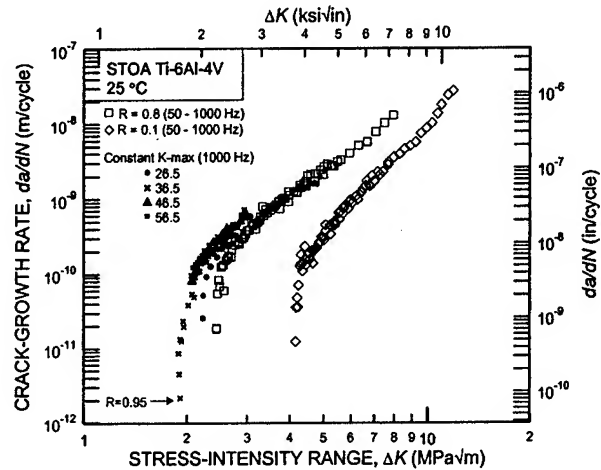


Fig. 2. Constant- $K_{\text{max}}$  fatigue-crack propagation behavior at four different  $K_{\text{max}}$  values:  $K_{\text{max}} = 26.5, 36.5, 46.5$ , and  $56.5\ \text{MPa}\sqrt{\text{m}}$  (1000 Hz) compared to constant- $R$  data at  $R = 0.1$  and  $0.8$  (50-1000 Hz), in bimodal Ti-6Al-4V, showing the definition of worst-case thresholds.

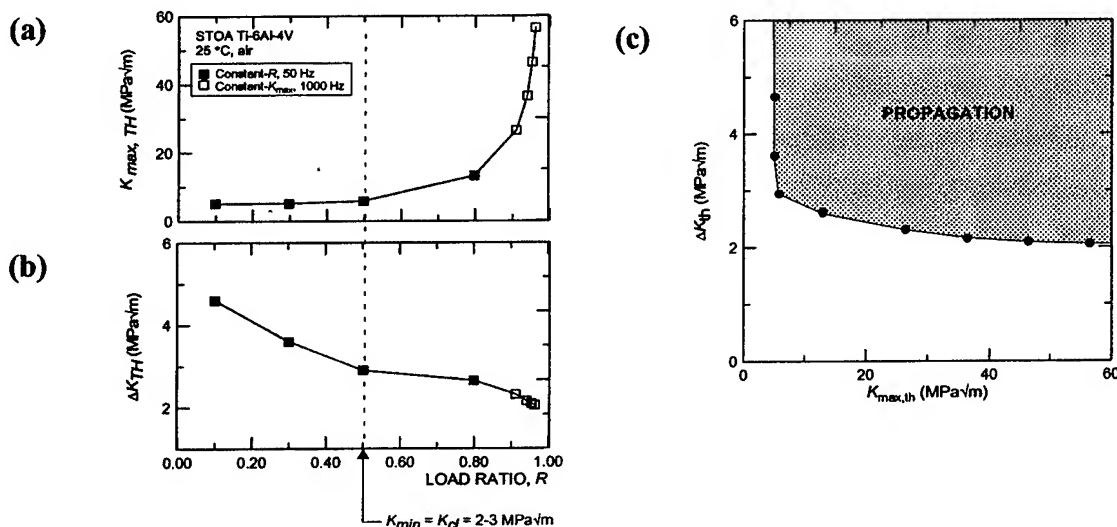


Fig. 3. Combinations of (a)  $K_{\text{max}}\text{--}R$ , (b)  $\Delta K\text{--}R$ , and (c)  $\Delta K\text{--}K_{\text{max}}$  required for "threshold": growth at  $10^{-10}\ \text{m/cycle}$ . As suggested by Schmidt and Paris [9], the closure mechanism would cause a transition from  $K_{\text{max}}$ -invariant growth to  $\Delta K$ -invariant growth at the load ratio at which  $K_{\text{min}} = K_{\text{cl}}$ . This transition is most apparent in (c) where the threshold envelope changes from nearly vertical to nearly horizontal. The continued downward slope of the threshold envelope at high  $K_{\text{max}}$  values is presumably independent of closure.

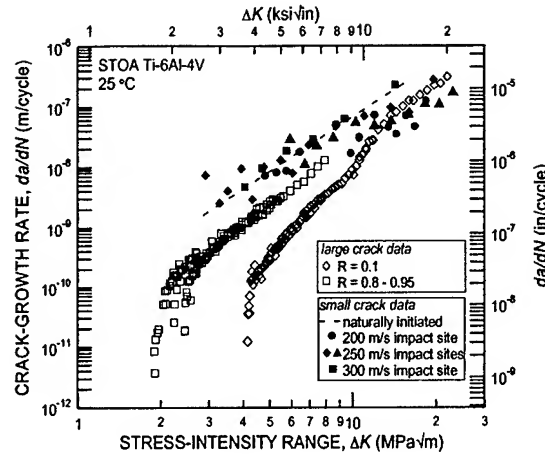


Fig. 4. Comparison of worst-case large-crack propagation data to fatigue growth from naturally initiated small cracks and small cracks originating from sites of foreign object damage.

## B. Mixed-Mode High-Cycle Fatigue Thresholds in Ti-6Al-4V (UCB)

The effect of mixed-mode (mode I+II) loading on the high-cycle fatigue thresholds was studied in Ti-6Al-4V primarily with a bimodal microstructure (~60% primary- $\alpha$ , ~40% lamellar  $\alpha$ + $\beta$ ). Specifically, the influence of crack size on such thresholds was investigated for large (> 5 mm) and short (~200  $\mu$ m) through-thickness cracks, and microstructurally-small (<50  $\mu$ m) surface cracks.

Large crack tests were conducted using the asymmetric four-point bend (AFPB) geometry [1], with load ratios,  $R$  of 0.1 to 0.8 being investigated for mode-mixities ranging from pure mode I (phase angle,  $\beta = 0^\circ$  or  $\Delta K_{II}/\Delta K_I = 0$ ) to nearly pure mode II ( $\beta = 82^\circ$  or  $\Delta K_{II}/\Delta K_I \sim 7.1$ ). Corresponding short crack thresholds were obtained using identical techniques, after carefully machining out the crack wake to within ~200  $\mu$ m of the crack tip [2]. Small crack thresholds were determined using an inclined crack technique. A small, semi-elliptical surface pre-crack was first obtained by standard mode I, three-point bend testing at  $R = 0.1$  (50 Hz) of wide (16.3 mm), 5 mm thick rectangular bars machined in the L-T orientation. Once a small crack had initiated, a bend bar was carefully machined from the original wide sample with the small crack inclined at the desired angle to the axis of the bar, which was then subjected to symmetric four-point bending for the threshold determination. Linear elastic solutions for the stress-intensity ranges for small semi-elliptical surface cracks in mode I and mixed-mode loading were obtained from the Newman-Raju [3] and He-Hutchinson [4] solutions, respectively.

**Large crack thresholds:** As observed previously in many metallic alloys (e.g., [5]), the fatigue threshold was seen to decrease with increasing load ratio (Fig. 5). In addition, a strong effect of mode-mixity was observed when the thresholds were characterized in terms of a single parameter, strain-energy release rate,  $\Delta G$  (incorporating both mode I and mode II contributions to the crack-driving force) (Fig. 6). Moreover, the mode I threshold was found to be the *worst-case* condition, implying that the presence of a mixed-mode loading component does not negate the possibility of a threshold-based design methodology. However, by “correcting” for crack-tip shielding using a compliance-based technique developed as part of this initiative [6], the marked influence of mode-mixity (and load ratio) was reduced, implying that the major influence of

mode-mixity in increasing the mixed-mode threshold is associated with mode II shielding by crack-surface interference, i.e., friction and interlock between crack-surface asperities [6].

*Short crack thresholds:* Short crack thresholds (Fig. 7), where the removal of the crack wake acts to markedly diminish the effect of crack-tip shielding, were found to be relatively independent of load ratio and mode-mixity, consistent with this reduced role of shielding. Indeed, the values of the short crack  $\Delta G$  thresholds were similar to the corresponding “shielding-corrected” large crack values.

*Small crack thresholds:*  $\Delta G$  thresholds for microstructurally-small surface cracks [7] were found to be substantially lower than thresholds for large cracks; in fact, up to 70-90 times lower (Fig. 8). In addition to the role of crack-tip shielding, biased sampling of “weak-links” in the microstructure by such small flaws becomes critical where their size is comparable to the scale of microstructure.

### C. Role of Foreign-Object Damage on HCF Thresholds in Ti-6Al-4V (UCB)

The objective of this study was specifically to examine the roles of residual stresses and foreign-object damage (FOD) induced microcracks ( $\sim 2$  to  $25\ \mu\text{m}$  in surface length) on the earliest stages of FOD-induced high-cycle fatigue (HCF) failures in the bimodal Ti-6Al-4V alloy,  $\alpha+\beta$  processed for typical turbine blade applications. This was achieved by defining the limiting conditions for crack initiation and early fatigue-crack growth in the presence of such microcracks, in comparison to the fatigue threshold behavior of naturally-initiated small ( $2c \sim 45\text{-}1000\ \mu\text{m}$ ) and large through-thickness ( $>5\ \text{mm}$ ) cracks in undamaged material.

Using high-velocity (200-300 m/s) impact of 1 or 3.2 mm steel spheres on the flat surface of fatigue test specimens (Fig. 9) to simulate FOD, it was found that the subsequent resistance to HCF was markedly reduced due to earlier crack initiation [8,9]. Premature crack initiation and subsequent near-threshold crack growth were primarily affected by the interplay of a number of factors, specifically (i) the stress concentration due to the FOD indentation, (ii) the creation (at highest impact velocities only) of microcracks at the crater rim of the damaged zone (Fig. 10), (iii) microstructural damage from FOD-induced plastic deformation, and (iv) the localized presence of tensile residual stresses [10,11] around the indent (Fig. 11).

Specifically, the magnitude of the residual stresses in the vicinity of the damage sites were computed numerically and experimentally measured using synchrotron x-ray micro-diffraction studies. Prior to fatigue cycling, peak tensile values of these residual stresses were of the order of 300 MPa and were located in the interior adjacent to the highly deformed region beneath the indentations [10,11] (Fig. 11).

Two groups of FOD-induced HCF failures could be identified. The first group involved fatigue crack initiation directly at the impact site and caused failures within  $10^5$  to  $10^6$  cycles. The proposed criteria for such failures was described by a modified Kitagawa-Takahashi approach, where the limiting threshold conditions are defined by the stress-concentration corrected smooth-bar fatigue limit (at microstructurally-small crack sizes) and a “worst-case” fatigue crack growth threshold (at larger “continuum-sized” crack sizes) as shown in Fig. 12 [9].

The second group of failures at  $10^7$  to  $10^8$  cycles was found to initiate at locations remote from impact damage in regions of high tensile residual stresses (Fig. 13). It was found that simple superposition of the initial tensile residual stresses onto the applied stresses provided a significant contribution to the reduction in fatigue strength by affecting the local mean stress and load ratio. Accordingly, the modified Kitagawa-Takahashi approach proposed above was corrected for the presence of tensile residual stresses to account for such failures (also shown in

Fig. 12). With this correction, the approach provides a rational basis for the effect of foreign-object damage on high cycle fatigue failures in Ti-6Al-4V [10].

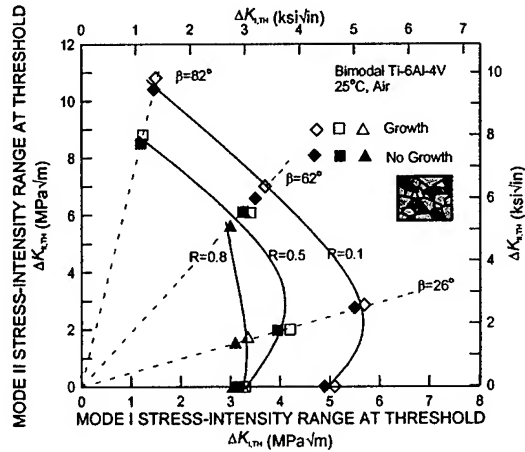


Fig. 5. Mixed-mode threshold envelopes for large ( $> 5$  mm) through-thickness cracks in the bimodal microstructure (schematic in inset), with the mode II stress-intensity range at threshold, as a function of the mode I stress-intensity range at threshold.

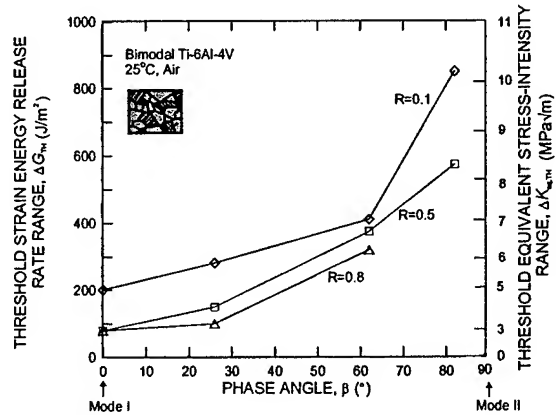


Fig. 6. The threshold strain-energy release rate,  $\Delta G_{TH}$ , and equivalent stress-intensity range,  $\Delta K_{eq,TH}$ , are plotted as a function of phase angle,  $\beta$ , for large cracks subjected to mixed-mode loading at  $R = 0.1, 0.5$  and  $0.8$ .

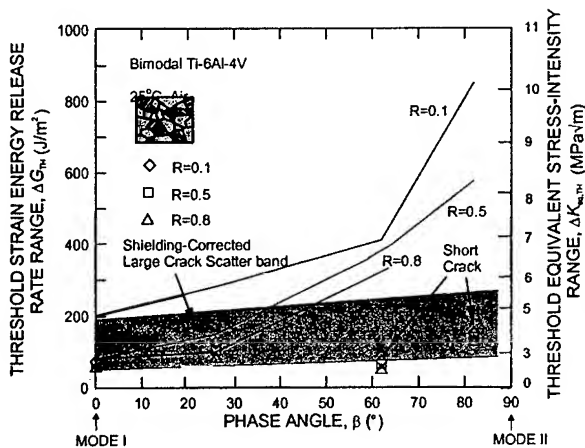


Fig. 7. Variation in the mixed-mode thresholds,  $\Delta G_{TH}$ , as a function of phase angle,  $\beta$ , in the bimodal structure. Shown are results for large ( $> 5$  mm) cracks, before and after "correcting" for crack-tip shielding, and for short ( $\sim 200$   $\mu$ m) through-thickness cracks.

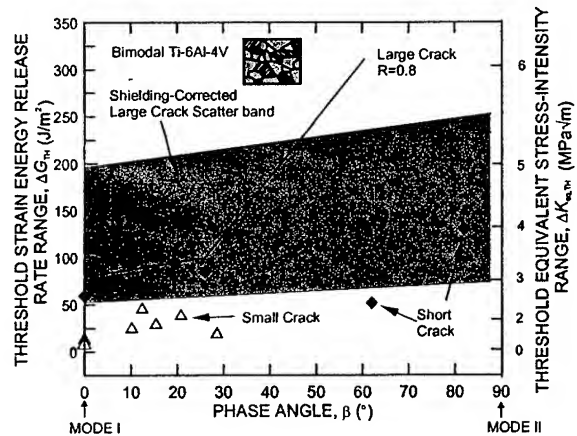


Fig. 8. Variation in the mixed-mode thresholds,  $\Delta G_{TH}$ , as a function of phase angle,  $\beta$ , for small ( $< 50$   $\mu$ m) surface cracks in the bimodal microstructure. Also shown are results for short ( $\sim 200$   $\mu$ m) through-thickness cracks and for large ( $> 5$  mm) cracks under worst-case, high  $R$  conditions.



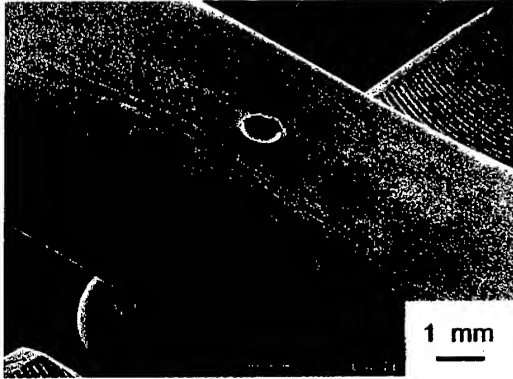


Fig. 9. Gauge section of modified  $K_B$  specimens for simulated FOD studies after high-velocity 300 m/s impact using 1.0 mm diameter steel sphere (normal impact angle)

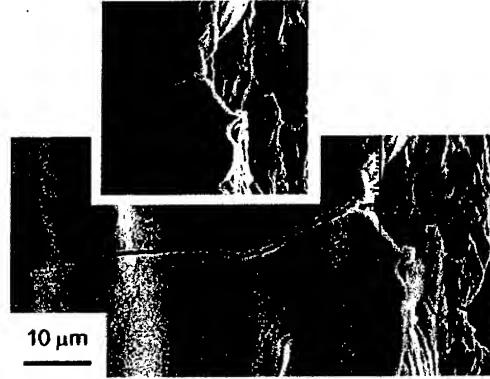


Fig. 10. SEM micrograph of fatigue crack that formed at FOD-induced microcrack (small inserts). 3.2 mm steel shot, 300 m/s impact velocity. Nominally applied  $\sigma_{\max} = 500$  MPa,  $R = 0.1$ ,  $N = 29,000$  cycles

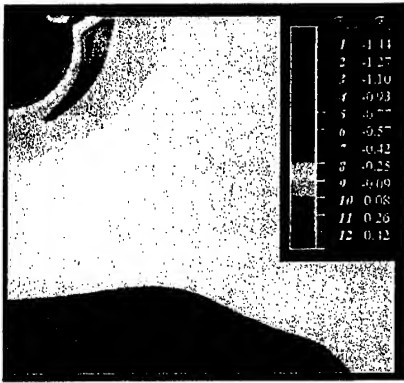


Fig. 11. Residual stress distribution in plane perpendicular to longitudinal axis of  $K_B$  specimen, after 300 m/s impact using 1 mm steel shot. After Chen and Hutchinson.  $\sigma_{33}$  = residual stress in longitudinal direction,  $\sigma_y$  = yield stress (915 MPa)

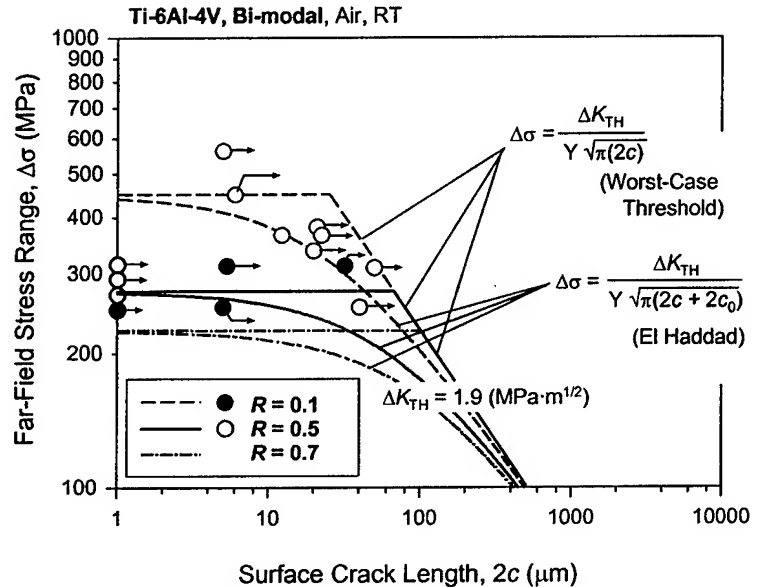


Fig. 12. Modified Kitagawa-Takahashi diagram representing the threshold crack-growth conditions ( $da/dN = 10^{-11}$ - $10^{-10}$  m/cycle) at  $R = 0.1$  and  $0.5$  for FOD-induced small-cracks in bimodal Ti-6Al-4V (300 m/s, 3.2 mm steel shots). Plotted is the threshold stress range as a function of surface crack length. Data points are corrected for the stress concentration of the FOD indents.

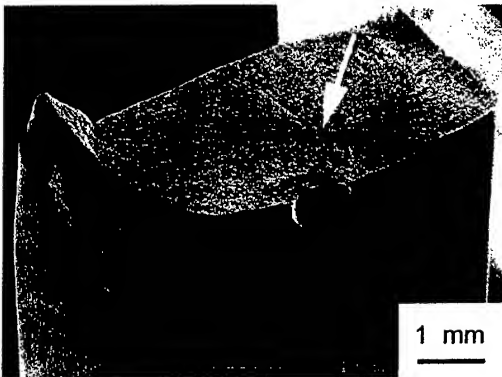


Fig. 13. Lower stress fatigue loading after 300 m/s impact using 1 mm diameter steel shot caused crack initiation away from the indent site (marked by arrow).  $\sigma_{\max} = 325$  MPa,  $R = 0.1$ ,  $N_F = 1.3 \times 10^8$  cycles.

#### D. Residual Stresses associated with FOD-Induced HCF Behavior in Ti-6Al-4V (UCB)

To better understand the driving force for fatigue-crack initiation and propagation associated with sites of foreign object damage, the residual stress and strain gradients were assessed using a synchrotron-based spatially-resolved polycrystalline x-ray diffraction technique. The spatial resolution of this technique was 300-500  $\mu\text{m}$ , limited at least in part by the size of the grains in the sample. The observed residual stress field was compared to both numerical predictions (by Chen and Hutchinson [10]) and experimental fatigue behavior (by Peters and Ritchie [8,9]). In all studies, foreign-object damage was simulated by firing a Cr-hardened steel sphere at velocities of 200-300 m/s onto the flat surface of a Ti-6Al-4V specimen in the bimodal (STOA) microstructure.

*Residual stresses at damage sites:* Consistent with the numerical predictions, spatially-resolved synchrotron x-ray diffraction measurements indicated the presence of a region of compression at the crater floor, and a region of tension und at the crater rim,. While the shape of the resulting strain gradients was qualitatively quite similar between the experimental observations and the numerical predictions, there were some notable discrepancies in the magnitude of the stresses [11]. Most specifically, the quasi-static analysis of Chen and Hutchinson [10] was insufficient to capture the observed residual stresses formed by dynamic impact, especially at the highest impact velocity of 300 m/s where the discrepancy was  $>500$  MPa at both the floor and rim of the crater. Modifications to the numerical model incorporated the dynamic effects of strain-rate sensitivity, the inertial effect, and elastic wave interactions. The results of the dynamic model were very similar to experimental observations. Remnant discrepancy at the crater rim of 300 MPa may be attributable to the presence of microcracking and inhomogeneous deformation that were not captured in the numerical model.

The spatially-resolved diffraction studies also revealed that the most substantial plasticity (as estimated by Bragg peak broadening) was present at the crater rim, and the crater floor showed a slightly lower degree of plasticity.

*Stability of the residual stress state during fatigue loading:* Using *in situ* x-ray diffraction studies during cyclic loading, it was found that there was as much as a 50% reduction in the residual stress component along the direction of loading during the first cycle at the smooth-bar fatigue limit, i.e., at  $\sigma_{\text{max}} = 500$  MPa (Fig. 14). The transverse stresses perpendicular to the load axis showed a  $\sim 20\%$  reduction during the first cycle. After the first cycle, there was no substantial decay of residual stresses as a function of the logarithm of the number of cycles (out to 1000 cycles). The threshold stress for first-cycle relaxation under the current conditions was between 325 and 500 MPa, as there was no observed relaxation at 325 MPa. The numerical model of Chen and Hutchinson was modified to incorporate the observed cycle-dependent reduction in the yield strength during reversed loading (Bauschinger effect). This model showed a  $\sim 40\%$  reduction in stresses at the crater floor during the first cycle and no subsequent relaxation, largely consistent with the observed behavior.

*Relevance to impact-induced fatigue failures:* In many of the cases considered in this study, the initial residual stress state was of little importance in assessing the location of crack formation due to fatigue loading. At high applied stresses, the initial residual stress state was reduced substantially during fatigue loading. But more importantly, the presence of microcracks at the crater rim, as well as the high stress concentration factor at the crater floor were the primary factors influencing the onset of failure. However, at low applied fatigue stresses ( $\sigma_{\text{max}}=325$  MPa), crack formation was often found to occur at the side of the  $K_B$  tensile specimens due to the presence of high tensile residual stresses (determined both experimentally and by numerical modeling) and the lack of crack-mitigating plasticity.

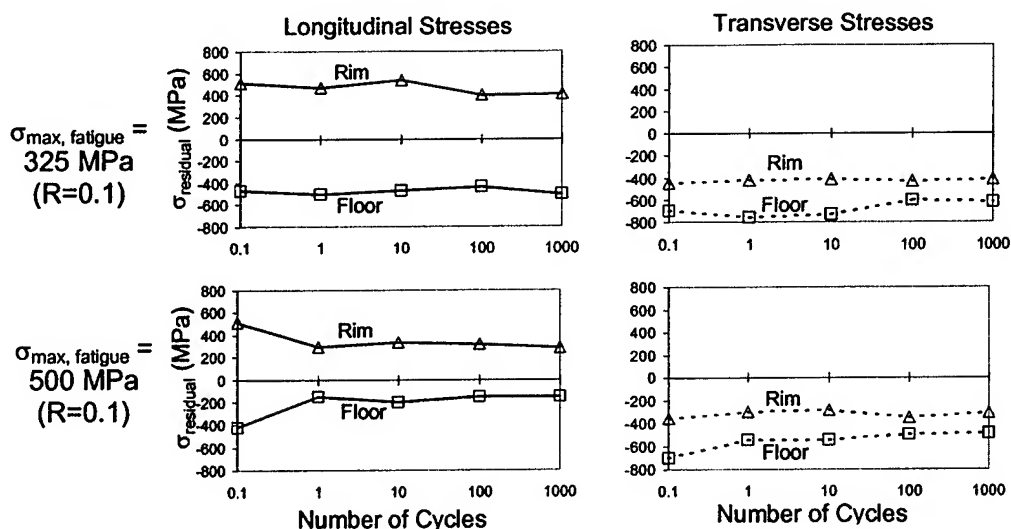


Fig. 14. Fatigue loading can cause a reduction in the residual stress state at the rim and base (floor) of a hemispherical damage site (quasi-static indentation loading, indenter diameter = 3.2 mm, crater diameter = 2.05 mm, crater depth = 0.30 mm). Longitudinal stresses are along the direction of loading and transverse stresses are perpendicular to the direction of loading. Based on the four graphs, relaxation occurs only at fatigue stresses  $\sigma_{\max} > 325 \text{ MPa}$ , and relaxation occurs almost entirely during the first cycle.

As noted above, the Kitigawa-Takahashi diagram proved to be a useful approach to predict the critical conditions for failure by incorporating both the fracture-mechanics based fatigue threshold (in the worst-case limit) and the stress-based fatigue limit. This approach can account for the contributions of both the stress concentration factor and the presence of microcracks. Moreover, in cases where residual stresses are significant, the alteration in stress ratio ( $\sigma_{\min}/\sigma_{\max}$ ) caused by the superposition of the residual stresses can also be captured to predict conditions of safe operation [10].

### E. Theoretical Modeling of High-Cycle Fatigue (Harvard)

**Fretting mechanics:** As a step towards the development of a mechanics of fretting damage, the work focused on the local plastic deformation accompanying fretting contact. Specifically, the study investigated plastic deformation in substrates that have been coated with a thin, soft metal layer for the purpose of reducing their fretting susceptibility. The substrate was fretted by a circular, flat-bottomed peg subject to a constant normal load and a fully reversed cyclic tangential load. The tangential load was assumed to be sufficiently large to cause the coating to undergo reversed yielding in shear in each cycle. Bulk cyclic stressing of the substrate was not considered. The role of the coating in the redistribution of the contact tractions was modeled. Two limiting boundary conditions for the peg-substrate interaction, as modified by the coating, were proposed and analyzed. It was found that plasticity in the substrate is generally limited to the immediate vicinity of the edge of the peg. This made possible the formulation of a small-scale yielding problem wherein the relevant load factors become amplitudes characterizing the elastic solution at the peg corner. The approach closely paralleled the small-scale yielding analysis of crack-tip plasticity, where the plastic zone is embedded within the elastic field whose amplitude is the stress intensity factor. Details of the cyclic plastic strain fields were obtained and their implications for initiation of fretting cracks discussed.

**Surface cracks and asymmetric four-point bend specimens:** Work was completed and published on the problem of semi-circular and semi-elliptical surface cracks subject to arbitrary loading, i.e., to mixed-mode loading conditions. The study was motivated by concerns that mixed-mode

loading may adversely affect threshold conditions for fatigue cracks. The aim was to provide a compendium of useful elastic crack solutions for the full range of possible loads, thereby extending the well known results of Newman and Raju to mixed-mode conditions.

Parallel studies on the asymmetric four-point bend specimens was prompted by a comparison by the Berkeley MURI group of published numerical solutions for the crack configuration, which showed discrepancies between the solutions as large as 25% within the parameter range of interest. A new fundamental reference solution was computed for an infinitely long cracked specimen subject to a constant shear force and associated bending moment distribution. The small corrections needed to apply this solution to the finite four-point loading geometry were also detailed.

*Foreign-object damage:* As noted above, extensive modeling was performed on various aspects of foreign object damage (FOD) as it relates to the fatigue life of turbine blades; this was coordinated with the experimental Berkeley effort described above [10,11]. Specific aspects of the problem that were investigated included (a) dynamic effects in FOD determination, (b) specimen size effects, (c) influence of inclined versus normal impacts, and (d) residual stress relaxation at FOD sites due to subsequent cyclic stressing.

Most of the discrepancy between the theoretical results for residual stress at FOD sites and the experimental data obtained by the Berkeley group could be accounted for by inclusion of dynamic effects (inertia and material strain-rate sensitivity), combined with a more realistic representation of the beam-like geometry of the Berkeley specimens. The major goal of the research of demonstrating the ability to predict indent geometry and residual stress due to prescribed FOD impacts was thus largely achieved. Under subsequent cyclic stressing, both the stress concentration due to the geometry change and the residual stresses influence fatigue-crack growth. The theoretical results from the FOD analysis were used to assess the effect of FOD level on critical crack size for threshold fatigue-crack growth. For sufficiently deep indents, it was shown that the stress concentration due to FOD is the dominant factor.

Another aspect where theory and experiment were brought into agreement was in connection with the role of residual stress relaxation at the bottom of the indent in the first few cycles of cyclic stressing following FOD. The Berkeley group obtained stress-strain data for cyclic stressing which provided quantitative constitutive input for the numerical simulation. The key to the relaxation is the Bauschinger effect under reversed loading. The computed relaxation results were in reasonably good agreement with the experimental measurements. The effect is significant because relaxation of the residual stress at the FOD site changes the effective  $R$ -value experienced by a putative fatigue crack at that location.

*Interactions associated with small fatigue-crack growth:* A study on the interactions of fatigue cracks with elastic obstacles, which grew out of the visit to Harvard of Dr. C. W. Wang of the Aeronautical Research Laboratory of Australia, was completed. This work extends the earlier work on small cracks by Hutchinson and Tvergaard [13].

## **F. High-Cycle Fatigue of Nickel-Base Superalloys (Mich. Tech.)**

The objective of the research at Michigan Tech was to study fatigue crack propagation thresholds in nickel-base superalloys at elevated temperatures and frequencies. Much of the work was conducted on an MTS 1,000 Hz servo-hydraulic machine (fitted with an induction heater for elevated temperature testing) on two different microstructures of KM4, a nickel-base turbine disk alloy, were studied. One microstructure contained coarse grains (on the order of 60  $\mu\text{m}$ ), while another contained fine grains (on the order of 6  $\mu\text{m}$ .) The yield strengths of the two microstructures were within 10% of each other. Fatigue-crack propagation thresholds were measured at 100 and 1,000 Hz, at room temperature, 550°C, and 650°C, and at load ratios

between 0.3 and 0.7. These conditions mimic those seen in turbine disks. An *in situ* study was also conducted on a single crystal superalloy at Southwest Research Institute in collaboration with D. L. Davidson. This study utilized the 2 kHz loading stage inside the SEM.

It was found that whereas in the Paris regime, the fatigue-crack propagation behavior at 100 and 1,000 Hz was quite similar to that observed by previous investigators at frequencies up to 50 Hz, i.e., coarser grains, lower load ratios, lower temperatures and higher frequencies are generally beneficial to elevated temperature crack-growth resistance, the near-threshold behavior in these alloys was an extremely complex function of frequency, microstructure, temperature, and load ratio. The only consistent trend in threshold behavior was found to be related to the load ratio, in that lower load ratios always resulted in higher thresholds. Fatigue crack closure, while measured in some cases, was not able to explain all the variations in the threshold values.

Fatigue crack closure in general, however, was determined to have a strong influence on threshold values, but only in the coarse-grain microstructure, and only at room temperature. A new model was developed to study the Mode II offsets (Fig. 15) required to observe significant closure. The model required finite element analysis of crack opening displacements and quantitative 3-D characterization of the fracture surfaces, both of which were accomplished. The model was in excellent agreement with closure load measurements, and with Mode II offsets observed in FCP specimens which were interrupted at threshold and then sectioned and studied in the SEM.

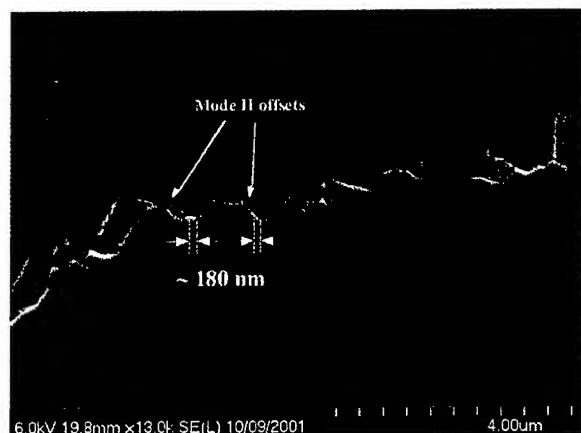
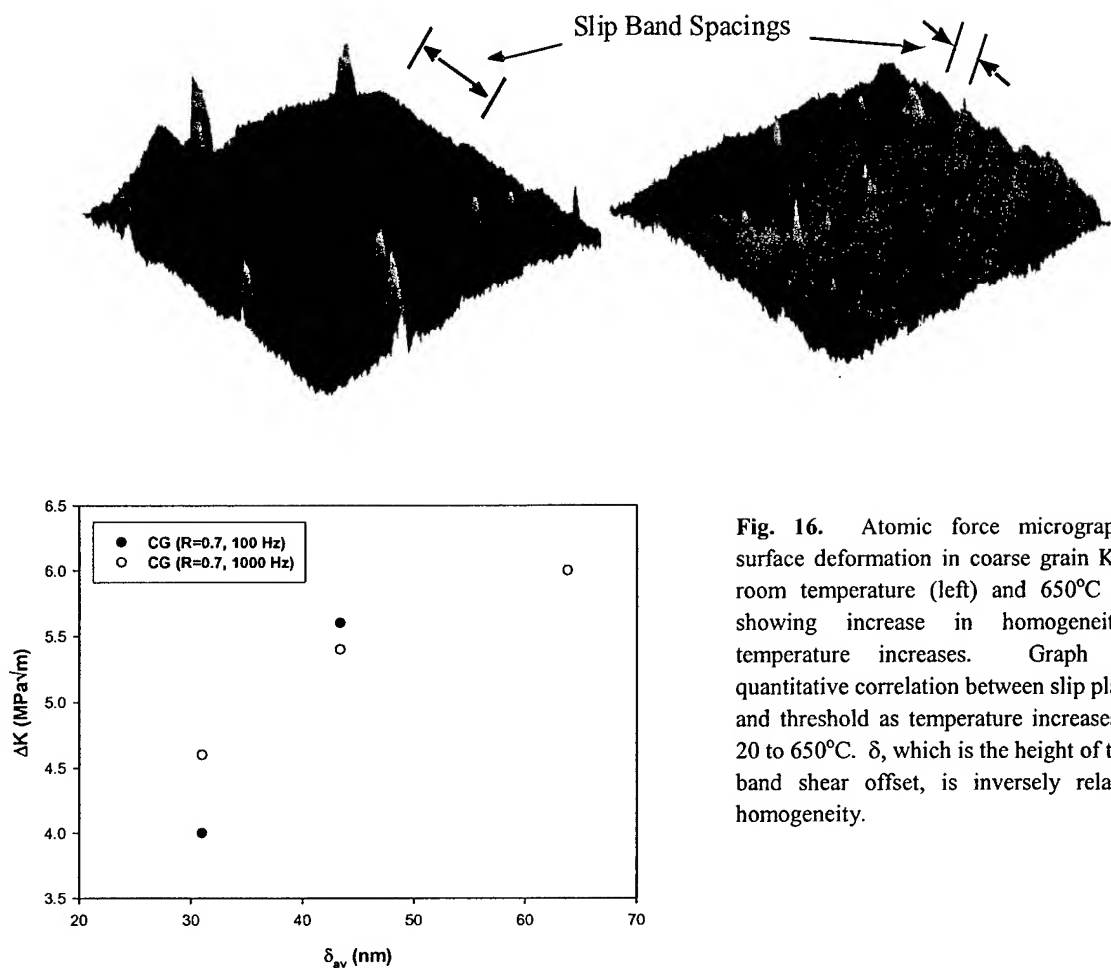


Fig. 10. Scanning electron micrograph of a crack tip in coarse-grain KM4 superalloy interrupted at threshold showing Mode II offsets. 180 nm offset is in excellent agreement with prediction of 150 nm from new closure model.

Atomic force microscopy and transmission electron microscopy (Fig. 16) were utilized to study slip homogeneity as a function of temperature, microstructure, and strain level. Results of these techniques were compared to quantitative fracture surface roughness, threshold values, fatigue-crack propagation behavior, and low-cycle fatigue behavior. The approach here has been to relate quantitatively slip homogeneity to the fatigue threshold; indeed, this is the first time that deformation behavior has been quantitatively linked to fatigue-crack propagation behavior in a superalloy.

Finally, AFM and TEM studies involving the planarity and homogeneity of slip have been performed to provide fundamental relationships between deformation and fatigue behavior in nickel-base superalloys.



**Fig. 16.** Atomic force micrographs of surface deformation in coarse grain KM4 at room temperature (left) and 650°C (right) showing increase in homogeneity as temperature increases. Graph shows quantitative correlation between slip planarity and threshold as temperature increases from 20 to 650°C.  $\delta$ , which is the height of the slip band shear offset, is inversely related to homogeneity.

## G. Modeling and Experimental Studies of Fretting Fatigue (MIT)

Through a combination of analytical modeling, numerical simulations and controlled experimentation, the overall objective of this part of the program has been to investigate fretting fatigue, a complex multi-stage, multi-axial, fatigue-fracture phenomenon involving fatigue crack initiation, initial small crack propagation and crack arrest or subsequent long crack propagation, ultimately leading to structural failure due to mechanical overload. Recognizing that fretting fatigue is strongly influenced by the contact conditions of which the contact geometry provides a natural metric for classification, two bounds were identified – the sharp-edged contact and the spherical contact. Sharp-edged contacts have been analyzed analytically using the crack analogue methodology [15], while the spherical contacts were modeled using finite elements [16] and investigated experimentally [17-19] and modeled analytically [20]. A notch-analogue model was developed to examine the influence of roundness of a nominally sharp contact geometry [21] and various approaches to combat fretting fatigue were investigated as well [22-24].

*“Crack analogue” model for contact fatigue* [15]: Aspects of quantitative equivalence between contact mechanics and fracture mechanics were identified via asymptotic matching. An analogy was invoked between the geometry of the near-tip regions of a cracked specimen and that of the sharp-edged contact region between two contacting surfaces. It was demonstrated that the

asymptotic elastic stress and strain fields around the rim of the contact region, as derived from classical contact mechanics analyses, were identical to those extracted from linear-elastic fracture mechanics solutions for analogous geometries. Conditions for crack initiation in the fretting fatigue problem were clearly identified through the application of the fracture mechanics of the crack analogue model.

*Adhesion model for fretting fatigue* [19]: By extending the crack analogue model that was previously developed for sharp contacts, the adhesion model presents a universal methodology that enables analysis of a variety of contact problems from those due to fretting fatigue in large-scale structures to contact fatigue in micro-scale devices, with adhesive or non-adhesive, sharp or rounded geometries. As the adhesion-induced, square-root singular stress fields are amenable for analysis within the "crack analogue" framework, the pre-existing long crack introduced by the contact circumvents "length scale" problems inherent in the modeling of crack initiation based on conventional fracture mechanics, or small crack growth based on initial dislocation distributions. Under conditions of small scale yielding, the effects of static and/or oscillatory bulk stresses (i.e. residual stresses induced by surface treatments such as shot-peening or laser shock-peening, or far-field applied stresses acting parallel to the contact surface) on contact fatigue crack initiation can also be analyzed by recognizing that these are analogous to the  $T$ -stresses present in a simple linear elastic fatigue-fracture formulation. All previous analyses which were based on stress-based approaches to fatigue at critical points (such as those using elastic stress fields of a sphere on a flat plane) in combination with a variety of fatigue strain-based, multiaxial criteria for endurance limits, predict contact fatigue cracking to initiate at the contact perimeter. This prediction is contrary to many experimental results which clearly indicate that cracking could initiate at either the contact perimeter or the stick-slip boundary. The present analysis, through an examination of the work of adhesion *vis-a-vis* the crack driving force arising from the contact loads, leads to a novel classification whereby cases of strong and weak adhesion are recognized unambiguously. Thus, the crack initiation location (contact perimeter for strong adhesion and the stick-slip boundary for weak adhesion) can be predicted without uncertainty.

*"Notch analogue" model for fretting fatigue* [20]: The effect of roundness of a nominally sharp contact geometry on fretting fatigue crack initiation was investigated. Using analytical and numerical finite element methods, the asymptotic forms for the stress fields in the vicinity of a rounded punch-on-flat substrate were derived for both normal and tangential contact loading conditions. By examining the similarities between the asymptotic stress fields for the sharply rounded flat punch contact and those around the tip of a blunt crack, a "notch analogue" model for fretting fatigue crack initiation was developed. The analysis showed that the maximum tensile stress that occurs at the edge of the contact is proportional the mode II stress-intensity factor of a sharp punch weighted by a geometric factor related to the roundness of the punch. Conditions for crack initiation were then derived through a comparison of the maximum tensile stress at the edge of the fretting contact and the plain fatigue endurance limit of the material.

*Fretting fatigue experiments* [17-19]: A systematic investigation of the fretting fatigue behavior of the titanium alloy Ti-6Al-4V in both the mill-annealed and the solution treated and overaged (STOA) microstructure, was carried out using a sphere-on-flat fretting fatigue device [17,18] that facilitated real-time, control and monitoring of all the relevant parameters such as the contact geometry, contact (normal and tangential) loads and the bulk alternating stress. While three sets of experiments were conducted to examine the influence of the bulk stress, the tangential load and the normal load, respectively, on fretting fatigue response, the effect of microstructure on fretting fatigue was explored briefly with experiments on acicular, Widmanstätten, and martensitic Ti-6Al-4V.

*Palliatives for fretting fatigue* [21-24]: Potential palliatives of fretting fatigue include surface modification and generation of compressive residual stresses through treatments such as shot-peening, laser shock-peening or coatings. The optimum depth for surface treatment to effectively



combat fretting fatigue was identified through a comprehensive simulation tool, for a variety of materials from their respective physical and mechanical properties [21]. The effect of coatings as fretting fatigue palliatives was investigated as well [22-24].

*Analysis of impact loading* [25]: A new method has been developed to analyze the impact of a sharp indenter at low impact velocities. A one-dimensional model is developed by assuming that the variation of indentation load as a function of depth under dynamic conditions has the same parabolic form (Kick's Law) as under static conditions. The motion of the indenter as it indents and rebounds from the target is described. Predictions are made of the peak indentation depth, residual indentation depth, contact time, and rebound velocity as functions of the impact velocity, indenter mass and target properties. Finite element simulations were carried out to assess the validity of the model for elasto-plastic materials. For rate-independent materials agreement with the model was good provided the impact velocity did not exceed certain critical values. For rate-dependent materials the relationship between load and depth in the impact problem is no longer parabolic and the model predictions cannot be applied to this case. The rate-dependent case can be solved by incorporating the relationship between the motion of the indenter and the dynamic properties of the material into the equation of motion for the indenter.

### Acknowledgement/Disclaimer

This work was sponsored by the U.S. Air Force Office of Scientific Research, Grant F49620-96-1-0478, under the auspices of the Multidisciplinary University Research Initiative on *High-Cycle Fatigue* to the University of California at Berkeley. The views and conclusions contained herein are those of the authors and should not be interpreted as necessarily representing the official policies or endorsements, either expressed or implied, of the Air Force Office of Scientific Research or the U.S. Government.

### References

1. S.Suresh, C.F.Shih, A.Morrone, N.P.O'Dowd, *J. Am. Ceram. Soc.*, **73**, 1257 (1990).
2. J.P.Campbell, R.O.Ritchie, *Eng. Fract. Mech.*, **67**, 209 (2000).
3. J.C.Newman, I.S.Raju, *Eng. Fract. Mech.*, **15**, 185 (1981).
4. M.Y.He, J.W.Hutchinson, *J. Appl. Mech.*, **67**, 207 (2000).
5. G.Hua, M.W.Brown, K.J.Miller, *Fat. Eng. Mater. Struct.*, **5**, 1 (1982).
6. J.P.Campbell, R.O.Ritchie, *Eng. Fract. Mech.*, **67**, 229 (2000).
7. R.K.Nalla, B.L.Boyce, J.P.Campbell, J.O.Peters, R.O.Ritchie, *Metall. Mater. Trans. A*, **33A**, 899 (2002).
8. J.O.Peters, O.Roder, B.L.Boyce, A.W.Thompson, R.O.Ritchie, *Metall. Mater. Trans. A*, **31A**, 1571 (2000).
9. J.O.Peters, R.O.Ritchie, *Eng. Fract. Mech.*, **67**, 193 (2000).
10. X.Chen, J.W.Hutchinson, *Int. J. Fract.*, **107**, 31 (2001).
11. B.L.Boyce, X.Chen, J.W.Hutchinson, R.O.Ritchie, *Mech. Mater.*, **33**, 441 (2001).
12. R.O.Ritchie, J.O.Peters, *Mater. Trans.*, **42**, 58 (2001).
13. V.Tvergaard, Y.Wei, J.W.Hutchinson, *Eur. J. Solids Mech.*, **20**, 731 (2001).
14. S.A.Padula II, A.Shyam, R.O.Ritchie, W.W.Milligan, *Int. J. Fat.*, **21**, 725 (1999).
15. A.E.Giannakopoulos, T.C.Lindley, S.Suresh, *Acta Mater.*, **46**, 2955 (1998).
16. A.E.Giannakopoulos, S.Suresh, *Acta Mater.*, **46**, 177 (1998).
17. B.U.Wittkowsky, P.R.Birch, J.Dominguez, S.Suresh, *Fat. Fract. Eng. Mater. Struct.*, **22**, 307 (1999).
18. B.U.Wittkowsky, P.R.Birch, J.Dominguez, S.Suresh *ASTM STP 1367*, ASTM (1999).
19. T.A.Venkatesh, B.P.Conner, C.S.Lee, A.E.Giannakopoulos, T.C.Lindley, S.Suresh, *Metall. Mater. Trans. A*, **32A**, 1131 (2001).
20. A.E.Giannakopoulos, T.A.Venkatesh, T.C.Lindley, S.Suresh, *Acta Mater.*, **47**, 4653 (1999).



21. A.E.Giannakopoulos, T.C.Lindley, S.Suresh, C.Chenut, *Fat. Fract. Eng. Mater. Struct.*, **23**, 561 (2000).
22. G.Kirkpatrick, M.S. Thesis, *Fretting Fatigue Analysis and Palliatives*, MIT, May 1999.
23. L.Chambon, M.S. Thesis. *A Unified Fracture Mechanics Approach to Fretting Fatigue Crack Growth*. MIT, May 2001.
24. B.P.Conner, M.S. Thesis. *Mechanical and Microstructural Effects of Fretting Fatigue of Ti-6Al-4V*. MIT, May 2000.
25. E.W.Andrews, A.E.Ginannkopoulos, E.Plisson, S.Suresh, *Int. J. Sol. Struct.*, **39**, 281 (2002).

## Personnel Supported

R. O. Ritchie	PI, Professor, University of California at Berkeley
S. Suresh	Co-PI, Professor, Massachusetts Institute of Technology
J. W. Hutchinson	Co-PI, Professor, Harvard University
W. W. Milligan	Co-PI, Professor, Michigan Technological University
A. W. Thompson	Lecturer, University of California at Berkeley
I. Altenberger	Post-doc, University of California at Berkeley
J. O. Peters	Post-doc, University of California at Berkeley
J. M. McNaney	Post-doc, University of California at Berkeley
O. Roder	Post-doc, University of California at Berkeley
T.A. Venkatesh	Post-doc, Massachusetts Institute of Technology
A. E. Giannakopoulos	Research Associate, Massachusetts Institute of Technology
S. Mukherjee	Research Associate, Michigan Technological University
B. L. Boyce	Graduate Student, University of California at Berkeley
R.K. Nalla	Graduate Student, University of California at Berkeley
L. Chambon	Graduate Student, Massachusetts Institute of Technology
B. Conner	Graduate Student, Massachusetts Institute of Technology
G. Kirkpatrick	Graduate Student, Massachusetts Institute of Technology
D. A. Johnson	Graduate Student, Harvard University
Xi Chen	Graduate Student, Harvard University
K. Kalaitzidou	Graduate Student, Michigan Technological University
S. Marras	Graduate Student, Michigan Technological University
A. Shyam	Graduate Student, Michigan Technological University
S. Padula, II	Graduate Student, Michigan Technological University
E. C. Aifantis	Collaborator, Michigan Technological University
D. L. Davidson	Collaborator, Southwest Research Institute
Ming He	Collaborator, University of California Santa Barbara
T. C. Lindley	Collaborator, Imperial College, London, UK
A. Solomonsson	Collaborator, Volvo Flygmotor AB, Trollhatten, Sweden.
S.E. Stanzl-Tschegg	Collaborator, BOKU, Vienna, Austria
V. Tvergaard	Collaborator, Technical University of Denmark, Lyngby, Denmark
C. H. Wang	Collaborator, Aeronautical Research Laboratory of Australia

## Publications

1. R.O. Ritchie, "Small Cracks and High-Cycle Fatigue", in *Proc. . ASME Aerospace Div.*, J. C. I. Chang, et al., eds., AMD-Vol. 52, ASME, New York, NY, 1996, pp. 321-33.
2. A.E. Giannakopoulos and S. Suresh, "A Three-Dimensional Analysis of Fretting Fatigue", *Acta Mater.*, vol. 46, 1997, pp. 177-92.
3. J.W. Hutchinson and V. Tvergaard, "Edge-Cracks in Single Crystals under Monotonic and Cyclic Loads", *Int. J. Fract.*, vol. 99, 1999, pp. 81-95.
4. J. M. Morgan and W.W. Milligan: "A 1 kHz Servohydraulic Fatigue Testing System", in *High Cycle Fatigue of Structural Materials*, W. O. Soboyejo and T. S. Srivatsan, eds, TMS, 1997, pp. 305-12.
5. A.J. McEvily and R.O. Ritchie: "Crack Closure and the Fatigue-Crack Propagation Threshold as a Function of Load Ratio", *Fatigue Fract. Engin. Mater. Struct.*, vol. 21, 1998, pp. 847-55.
6. A.E. Giannakopoulos, T.C. Lindley, and S. Suresh, "Aspects of Equivalence between Contact Mechanics and Fracture Mechanics: Theoretical Connections and a Life-Prediction Methodology for Fretting-Fatigue", *Acta Mater.*, vol. 46, 1998, pp. 2955-68.
7. R.O. Ritchie, B.L. Boyce, J.P. Campbell, and O. Roder, "High-Cycle Fatigue of Turbine Engine Alloys", *Proc. 24<sup>th</sup> Symp. on Fatigue*, The Society of Materials Science, Kyoto, Japan, 1998, pp. 1-6.
8. B.U. Wittkowsky, P.R. Birch, J. Dominguez, and S. Suresh, "An Apparatus for Quantitative Fretting Fatigue Testing", *Fatigue Fract. Engin. Mater. Struct.*, vol. 22 (4), 1999, pp. 307-20.
9. R.O. Ritchie, B.L. Boyce, J.P. Campbell, O. Roder, A.W. Thompson, and W.W. Milligan, "Thresholds for High-Cycle Fatigue in a Turbine Engine Ti-6Al-4V Alloy", *Int. J. Fat.*, vol. 21, 1999, pp. 653-62.
10. S.A. Padula II, A. Shyam, R.O. Ritchie, and W.W. Milligan, "High Frequency Fatigue Crack Propagation Behavior of a Nickel-Base Turbine Disk Alloy", *Int. J. Fat.*, vol. 21, 1999, pp. 725-31.
11. B.L. Boyce, J.P. Campbell, and O. Roder, A.W. Thompson, and R.O. Ritchie, "Aspects of High-Cycle Fatigue Performance in a Ti-6Al-4V Alloy", in *Fatigue Behavior of Titanium Alloys*, R. Boyer, D. Eylon, J. P. Gallagher, and G. Lütjering, eds., TMS, Warrendale, 1999, pp. 3-13.
12. A.W. Thompson, "Relations between Microstructure and Fatigue Properties of Alpha-Beta Titanium Alloys", *ibid.*, pp. 23-30.
13. R.O. Ritchie, D.L. Davidson, B.L. Boyce, J.P. Campbell, and O. Roder, "High-Cycle Fatigue of Ti-6Al-4V", *Fatigue Fract. Engin. Mater. Struct.*, vol. 22, 1999, pp. 621-31.
14. A.E. Giannakopoulos, T.C. Lindley, and S. Suresh, "Application of Fracture Mechanics in Fretting Fatigue Life Assessment", in *Fretting Fatigue: Current Technology and Practices*, ASTM STP 1367, D.W. Hoepfner, et al., eds., American Society for Testing and Materials, Philadelphia, 1999.
15. E.C. Aifantis, "Gradient Deformation Models at the Nano, Micro and Macro Scales", *J. Eng. Mater. Techn.*, vol. 121, 1999, pp. 189-202.
16. J.W. Hutchinson and M.R. Begley, "Plasticity in Fretting of Coated Surfaces", *Eng. Fract. Mech.*, vol. 62, 1999, pp. 145-64.
17. M.R. Begley, A.G. Evans, and J.W. Hutchinson, "Spherical Impressions on Thin Elastic Films on Elastic-Plastic Substrates", *Int. J. Solids Struct.*, vol. 36, 1999, pp. 2773-88.
18. R.O. Ritchie, "Small-Crack Growth and the Fatigue of Traditional and Advanced Materials", in *Fatigue '99, Proceedings of the Seventh International Fatigue Congress*, X.-R. Wu and Z. G. Wang, eds., Higher Education Press, Beijing, China/EMAS, Warley, U.K., vol. 1, 1999, pp. 1-14.
19. R.O. Ritchie, "The Importance of Small Crack Effects in the Microstructural Development of Advanced Materials", in *Small Fatigue Cracks: Mechanics, Mechanisms and*

- Applications*, K. S. Ravichandran, R. O. Ritchie, and Y. Murakami, eds., Elsevier, Oxford, U.K. 1999, pp. 233-46.
20. T.A. Venkatesh, A.E. Giannakopoulos, T.C. Lindley, and S. Suresh, "Modeling and Experimental Studies on Fretting Fatigue", *ibid.*, pp. 355-59.
  21. A.E. Giannakopoulos, T.A. Venkatesh, T.C. Lindley, and S. Suresh, "The Role of Adhesion in Contact Fatigue", *Acta Mater.*, vol. 47, 1999, pp. 4653-64.
  22. M.Y. He and J.W. Hutchinson, "Asymmetric Four-Point Crack Specimen", *J. Appl. Mech.*, vol. 67, 2000, pp. 207-09.
  23. M.Y. He and J.W. Hutchinson, "Surface Crack Subject to Mixed Mode Loading", *Eng. Fract. Mech.*, vol. 65, 2000, pp. 1-14.
  24. J.P. Campbell and R.O. Ritchie, "Mixed-Mode Fatigue-Crack Growth Thresholds in Bimodal Ti-6Al-4V", *Scripta Mater.*, vol. 41, 1999, pp. 1067-71.
  25. J.O. Peters, O. Roder, B.L. Boyce, A.W. Thompson, and R.O. Ritchie, "Role of Foreign Object Damage on Thresholds for High-Cycle Fatigue in Ti-6Al-4V", *Metall. Mater. Trans. A*, vol. 31A, 2000, pp. 1571-83.
  26. J.P. Campbell and R.O. Ritchie, "Mixed-Mode, High-Cycle Fatigue-Crack Growth Thresholds in Ti-6Al-4V: I – A Comparison of Large and Small Crack Behavior", *Eng. Fract. Mech.*, vol. 67, Oct. 2000, pp. 209-27.
  27. J.P. Campbell, R.O. Ritchie, "Mixed-Mode High-Cycle Fatigue-Crack Growth Thresholds in Ti-6Al-4V: II - Quantification of Crack-Tip Shielding", *Eng. Fract. Mech.*, vol. 67, 2000, pp. 227-49.
  28. J.O. Peters and R.O. Ritchie, "Influence of Foreign Object Damage on Crack Initiation and Early Fatigue-Crack Growth in Ti-6Al-4V", *Eng. Fract. Mech.*, vol. 67, 2000, pp. 193-207.
  29. A. Shyam, S.A. Padula and W.W. Milligan, "High Frequency Fatigue Crack Propagation in the Nickel-base Superalloy KM4 at High Temperatures", in *Fatigue and Fracture Behavior of High Temperature Materials*, P.K. Liaw ed., TMS, Warrendale, PA, 2000, pp. 9-15.
  30. S. Sinharoy, P. Virro-Nic and W. W. Milligan, "Deformation and Strength Behavior of Two Nickel-Base Turbine Disk Alloys at 650°C", *Metall. Mater. Trans. A*, vol. 32A, 2001, pp. 2021-32.
  31. B.L. Boyce and R.O. Ritchie, "Effect of Load Ratio and Maximum Stress Intensity on the Fatigue Threshold in Ti-6Al-4V", *Eng. Fract. Mech.*, vol. 68, 2001, pp. 129-47.
  32. R. O. Ritchie and J. O. Peters, "Fatigue Thresholds and Early Crack Growth: Applications to Design against High-Cycle Fatigue", in *Materials Science for the 21<sup>st</sup> Century (ISMS-21)*, The Society of Materials Science, Japan, vol. A, May 2001, pp. 29-35.
  33. J.P. Campbell and R.O. Ritchie, "High-Cycle Fatigue in Bimodal and Lamellar Ti-6Al-4V: Mixed-Mode Crack-Growth Thresholds", *Metall. Mater. Trans. A*, vol. 32A, 2001, pp. 497-503.
  34. J.O. Peters, B.L. Boyce, X.Chen, J.M. McNaney, J.W. Hutchinson, and R.O. Ritchie, "Role of Residual Stresses on High-Cycle Fatigue of Impact-Damaged Ti-6Al-4V: Surface vs. Subsurface Crack Initiation", in *Proceedings of the International Conference on Fatigue in the Very High Cycle Regime*, S. E. Stanzl-Tschegg and H. M. Mayer, eds., BOKU, Vienna, Austria, 2001, pp. 129-40.
  35. J.O. Peters and R.O. Ritchie, "Foreign Object Damage and High-Cycle Fatigue in Ti-6Al-4V", *Mater. Sci. Eng.*, vol. 319-21, 2001, pp. 597-601.
  36. J.O. Peters and R.O. Ritchie, "Foreign Object Damage and High-Cycle Fatigue: Role of Microstructure in Ti-6Al-4V", *Int. J. Fat.*, vol. 23, 2001, pp. S1413-21.
  37. R.O. Ritchie and J.O. Peters, "Small Fatigue Cracks: Mechanics, Mechanisms and Engineering Applications", *Mater. Trans.*, vol. 42, 2001, pp. 58-67.
  38. X. Chen and J.W. Hutchinson, "Foreign Object Damage and Fatigue Crack Threshold: Cracking Outside Shallow Indents", *Int. J. Fract.*, vol. 107, 2001, pp. 31-51.
  39. A.E. Giannakopoulos, T.C. Lindley, S. Suresh, and C. Chenut, "Similarities of Stress Concentration in Contact at Round Punches and Fatigue at Notches: Implication to Fretting Fatigue Crack Initiation", *Fatigue Fract. Engin. Mater. Struct.*, vol. 23, 2001, pp. 561-71.

40. T.A. Venkatesh, B.P. Conner, C.S. Lee, A.E. Giannakopoulos, T.C. Lindley, and S. Suresh, "An Experimental Investigation of Fretting Fatigue in Ti-6Al-4V: The Role of Contact Conditions and Microstructure", *Metall. Mater. Trans. A*, vol. 32A, 2001, pp. 1131-46.
41. V. Tvergaard, Y. Wei, and J.W. Hutchinson, "Edge Cracks in Plastically Deforming Surface Grains", *Eur. J. Solids Mech.*, vol. 20, 2001, pp. 731-38.
42. C.H. Wang and J.W. Hutchinson, "Interaction of Fatigue Cracks with Elastic Obstacles", *Int. J. Fract.*, vol. 109, 2001, pp. 263-83.
43. R.K. Nalla, J. P. Campbell, and R. O. Ritchie, "Mixed-Mode High-Cycle Fatigue Thresholds in Ti-6Al-4V: A Comparison of Large and Small Crack Behavior" in *Proceedings of the Sixth International Conference on Biaxial/Multiaxial Fatigue and Fracture*, Lisbon, Portugal, 2001.
44. B.L. Boyce, X. Chen, J.W. Hutchinson, and R.O. Ritchie, "The Residual Stress State due to a Spherical Hard-Body Impact", *Mech. Mater.*, vol. 33, 2001, pp. 441-45.
45. J.O. Peters, B.L. Boyce, J.M. McNaney, and R. O. Ritchie, "Foreign Object Damage and High-Cycle Fatigue Thresholds in Ti-6Al-4V", in *Advances in Fracture Research, Proceedings of the Tenth International Conference on Fracture*, K. Ravi-Chandar, B. L. Karihaloo, T. Kishi, R. O. Ritchie, A. T. Yokobori, Jr., and T. Yokobori, eds., Pergamon Press, Oxford, U.K., 2001, CD-Rom.
46. I. Altenberger, B. Scholtes, U. Noster, and R.O. Ritchie, "Characterization of Fatigue Crack Formation in Mechanically Surface Treated Austenitic Stainless Steels", *ibid.*
47. R. K. Nalla, J. P. Campbell and R. O. Ritchie, "Mixed-Mode, High-Cycle Fatigue in Ti-6Al-4V", in *The David L. Davidson Symposium on Fatigue*, K.S. Chan, P.K. Liaw, R.S. Bellows, T Zogas, and W.O. Soboyejo, TMS, Warrendale, PA, 2002, pp. 75-90.
48. S.A. Padula II, A. Shyam, D.L. Davidson and W.W. Milligan, "In Situ Study of High Frequency Fatigue Crack Propagation in a Single Crystal Superalloy", *ibid.*, pp. 183-89.
49. J. O. Peters, G. Lütjering, R. K. Nalla, I. Altenberger, and R. O. Ritchie, "High Cycle Fatigue of Beta Titanium Alloys", in *Fatigue 2002, Proceedings of the Eighth International Fatigue Congress*, A. F. Blom, ed., EMAS, Cradley Heath, West Midlands, UK, 2002, vol. 3, pp. 1763-72.
50. I. Altenberger, U. Noster, B. Scholtes, and R. O. Ritchie, "Fatigue of Mechanical Surface Treated Materials at Elevated Temperatures", *ibid.*, vol. 4, 2425-36.
51. R.K. Nalla, B.L. Boyce, J.P. Campbell, J.O. Peters, and R.O. Ritchie, "Influence of Microstructure on the High-Cycle Fatigue of Ti-6Al-4V: Bimodal vs. Lamellar Structures", *Metall. Mater. Trans. A*, vol. 33A, 2002, pp. 899-918.
52. R.K. Nalla, J.P. Campbell and R.O. Ritchie, "Effects of Microstructure on Mixed-Mode, High-Cycle Fatigue Crack Growth Thresholds in Ti-6Al-4V", *Fatigue Fract. Engin. Mater. Struct.*, vol. 25, 2002, pp. 587-606.
53. E. W. Andrews, A. E. Giannakopoulos, E. Plisson and S. Suresh, "Analysis of the Impact of a Sharp Indenter", *Int. J. Solids Struct.*, vol. 39, 2002, pp. 281-95.
54. A. Shyam, S.A. Padula II, S. Marras, and W.W. Milligan, "Fatigue Crack Propagation Thresholds in Nickel-Base Superalloys at High Frequencies and Temperatures", *Metall. Mater. Trans. A*, vol. 33A, 2002, in press.
55. J.O. Peters, B.L. Boyce, X. Chen, J.M. McNaney, J.W. Hutchinson, and R.O. Ritchie, "On the Application of the Kitagawa-Takahashi Diagram to Foreign-Object Damage and High-Cycle Fatigue", *Eng. Fract. Mech.*, 2002, in press.
56. R.K. Nalla, J.P. Campbell, and R.O. Ritchie, "Mixed-Mode High-Cycle Fatigue Crack Growth Thresholds in Ti-6Al-4V: Role of Small Cracks", *Int. J. Fat.*, 2002, in press.
57. B.L. Boyce, X. Chen, J.O. Peters, J.W. Hutchinson, R.O. Ritchie, "Mechanical Relaxation of Localized Residual Stresses Associated with Foreign Object Damage", *Mater. Sci. Eng. A*, 2002, in review.
58. X. Chen and J. W. Hutchinson, "Particle Impact on Metal Substrates with Application to Foreign Object Damage to Aircraft Engines", *J. Mech. Phys. Solids*, 2002, in review.

### Theses

59. P. Pallot, "Two Dimensional Studies of Contact", *Engineering Diplome Thesis*, Ecole Polytechnique, France, (completed at MIT), Sept. 1997 (co-supervisor: S. Suresh).
60. P. R. Birch, "A Study of Fretting Fatigue in Aircraft Components", *M.S. Thesis*, Department of Materials Science and Engineering, MIT, June 1998 (supervisor: S. Suresh).
61. C. Chenut, "Fretting Fatigue at Rounded Corners", *Engineering Diplome Thesis*, Ecole Polytechnique, France, (completed at MIT), Sept. 1998 (co-supervisor: S. Suresh).
62. B. L. Boyce, "High Cycle Fatigue Thresholds in a Turbine Engine Titanium Alloy", *M.S. Thesis*, Department of Materials Science and Mineral Engineering, University of California at Berkeley, Dec. 1998 (supervisor: R. O. Ritchie).
63. B. L. Boyce, "Understanding Impact-Induced Fatigue Failure", *Ph.D. Thesis*, Department of Materials Science and Engineering, University of California at Berkeley, Dec. 2001 (supervisor: R. O. Ritchie).
64. J. P. Campbell, "Mixed-Mode Fatigue-Crack Growth in Ti-6Al-4V", *Ph.D. Thesis*, Department of Materials Science and Mineral Engineering, University of California, Berkeley, Dec. 1999 (supervisor: R. O. Ritchie).
65. R. K. Nalla, "Effects of Microstructure on High Cycle Fatigue Thresholds in a Turbine Engine Titanium Alloy", *M.S. Thesis*, Department of Materials Science and Engineering, University of California at Berkeley, expected Dec. 2001 (supervisor: R. O. Ritchie).
66. G. Kirkpatrick, "Fretting Fatigue Analysis and Palliatives", *M.S. Thesis*, Department of Materials Science and Engineering, MIT, June 1999 (supervisor: S. Suresh).
67. B. P. Conner, "Mechanical and Microstructural Effects on Fretting Fatigue in Ti-6Al-4V", *M.S. Thesis*, Department of Materials Science and Engineering, MIT, May 2000 (supervisor: S. Suresh).
68. L. Chambon, "A Unified Fracture Mechanics Approach to Fretting Fatigue Crack Growth", *M.S. pending*, Department of Materials Science and Engineering, MIT, May 2001 (supervisor: S. Suresh).
69. Xi. Chen, "Foreign Object Damage and Fracture Cracking", *Ph.D. Thesis*, Division of Applied Sciences, Harvard University, June 2001 (supervisor: J. W. Hutchinson).
70. S. Marras, "On Some Experimental Aspects of High Cycle Fatigue", *M.S. Thesis*, Department of Mech. Engineering, Michigan Technological University, July 2001 (supervisor: W. W. Milligan).
71. S. A. Padula II, "Fatigue Crack Propagation Behavior of a Polycrystalline Nickel-Base Superalloy in the Near-Threshold Regime", *Ph.D. Thesis*, Department of Metallurgical and Materials Engineering, Michigan Technological University, April 2002 (supervisor: W. W. Milligan).
72. A. Shyam, "Failure Mechanisms in Nickel-Base Superalloys", *Ph.D. pending*, Department of Metallurgical and Materials Engineering, Michigan Technological University, expected August 2002 (supervisor: W. W. Milligan).

### Other Publications

73. B. L. Boyce and R. O. Ritchie, "Lower-Bound Thresholds for Fatigue-Crack Propagation under High-Cycle Fatigue Conditions in Ti-6Al-4V," in *Proceedings of the Third National Turbine Engine High Cycle Fatigue Conference*, W. A. Stange and J. Henderson, eds., Universal Technology Corp., Dayton, OH, CD-Rom, 1998, CD-Rom, session 5, pp. 11-18.
74. J. P. Campbell, A. W. Thompson, R. O. Ritchie, and D. L. Davidson, "Microstructural Effects on Small-Crack Propagation in Ti-6Al-4V under High-Cycle Fatigue Conditions," in *Proceedings of the Third National Turbine Engine High Cycle Fatigue Conference*, W. A. Stange and J. Henderson, eds., Universal Technology Corp., Dayton, OH, CD-Rom, 1998, CD-Rom, session 5, pp. 19-21.
75. S. A. Padula, A. Shyam, and W. W. Milligan, "High Cycle Fatigue of Nickel-Base Superalloys," in *Proceedings of the Third National Turbine Engine High Cycle Fatigue*

- Conference, W. A. Stange and J. Henderson, eds., Universal Technology Corp., Dayton, OH, CD-Rom, 1998, CD-Rom, session 5, pp. 22-28.
76. O. Roder, A. W. Thompson, and R. O. Ritchie, "Simulation of Foreign Object Damage of Ti-6Al-4V Gas-Turbine Blades," in *Proceedings of the Third National Turbine Engine High Cycle Fatigue Conference*, W. A. Stange and J. Henderson, eds., Universal Technology Corp., Dayton, OH, 1998, CD-Rom, session 10, pp. 6-12.
77. S. A. Padula II, A. Shyam, D.L. Davidson and W.W. Milligan, "High Frequency Fatigue of Nickel-Base Superalloys", in *Proceedings of the Fourth National Turbine Engine High Cycle Fatigue (HCF) Conference*, J. Henderson, ed., Universal Technology Corp., Dayton, OH, CD-Rom, 1999, CD-Rom, session 2, pp. 22-28.
78. B. L. Boyce and R. O. Ritchie, "On the Definition of Lower-Bound Fatigue-Crack Propagation Thresholds in Ti-6Al-4V under High-Cycle Fatigue Conditions", in *Proceedings of the Fourth National Turbine Engine High Cycle Fatigue (HCF) Conference*, J. Henderson, ed., Universal Technology Corp., Dayton, OH, CD-Rom, 1999, CD-Rom, session 2, pp. 29-40.
79. J. P. Campbell, A. W. Thompson and R. O. Ritchie, "Mixed-Mode Crack-Growth Threshold In Ti-6Al-4V under Turbine-Engine High-Cycle Fatigue Loading Conditions", in *Proceedings of the Fourth National Turbine Engine High Cycle Fatigue (HCF) Conference*, J. Henderson, ed., Universal Technology Corp., Dayton, OH, CD-Rom, 1999, CD-Rom, session 2, pp. 41-49.
80. S. Suresh, A. E. Giannakopoulos, T. C. Lindley, P. Birch, B. Wittkowsky, T. A. Venkatesh, and J. Dominguez, "A Review of Research on Fretting Fatigue in the Air Force MURI on High Cycle Fatigue", in *Proceedings of the Fourth National Turbine Engine High Cycle Fatigue (HCF) Conference*, J. Henderson, ed., Universal Technology Corp., Dayton, OH, CD-Rom, 1999, CD-Rom, session 5, pp. 41-76.
81. B. L. Boyce, O. Roder, A. W. Thompson, and R. O. Ritchie, "Measurement of Residual Stresses in Impact-Damaged Ti-6-4 Specimens", in *Proceedings of the Fourth National Turbine Engine High Cycle Fatigue (HCF) Conference*, J. Henderson, ed., Universal Technology Corp., Dayton, OH, CD-Rom, 1999, CD-Rom, session 10, pp. 28-40.
82. O. Roder, J. O. Peters, A. W. Thompson, and R. O. Ritchie, "Influence of Simulated Foreign Object Damage on the High Cycle Fatigue of a Ti-6Al-4V Alloy for Gas Turbine Blades", in *Proceedings of the Fourth National Turbine Engine High Cycle Fatigue (HCF) Conference*, J. Henderson, ed., Universal Technology Corp., Dayton, OH, CD-Rom, 1999, CD-Rom, session 10, pp. 41-50.
83. J. O. Peters, B. L. Boyce, A. W. Thompson, and R. O. Ritchie, "Role of Foreign-Object Damage on High-Cycle Fatigue Thresholds in Ti-6Al-4V", in *Proc. 5<sup>th</sup> National Turbine Engine High Cycle Fatigue Conf.*, M. J. Kinsella, ed., Universal Technology Corp., Dayton, OH, 2000, CD-Rom, session 1, pp. 28-37.
84. J. P. Campbell and R. O. Ritchie, "Mixed-Mode High-Cycle Fatigue Thresholds in Turbine Engine Ti-6Al-4V", in *Proc. 5<sup>th</sup> National Turbine Engine High Cycle Fatigue Conf.*, M. J. Kinsella, ed., Universal Technology Corp., Dayton, OH, 2000, CD-Rom, session 7, pp. 35-44.
85. S. A. Padula, II, A. Shyam, and W. W. Milligan, "High Temperature, High Cycle Fatigue of Nickel-Base Turbine Disk Alloy," in *Proc. 5<sup>th</sup> National Turbine Engine High Cycle Fatigue Conf.*, M. J. Kinsella, ed., Universal Technology Corp., Dayton, OH, 2000, CD-Rom, session 7, pp. 54-61.
86. S. Suresh,, A. E. Giannakopoulos, T. C. Lindley, T. A. Venkatesh, G. W. Kirkpatrick and B. P. Conner, "A Review of the Experimental and Modeling Studies on Fretting Fatigue at MIT," in *Proc. 5<sup>th</sup> National Turbine Engine High Cycle Fatigue Conf.*, M. J. Kinsella, ed., Universal Technology Corp., Dayton, OH, 2000, CD-Rom, session 13, pp. 1-6.
87. A. Shyam, S.A. Padula II and W.W. Milligan, "High Temperature, High Cycle Fatigue of a Nickel-Base Turbine Disk Alloy", in *Proc. 6<sup>th</sup> National Turbine Engine High Cycle Fatigue Conf.*, M. J. Kinsella, ed., Universal Technology Corp., Dayton, OH, 2001, CD-Rom, section 8.

88. J. O. Peters, B. L. Boyce, J. M. McNaney, X. Chen, J. W. Hutchinson, and R. O. Ritchie, "Foreign-Object Damage and High-Cycle Fatigue in Ti-6Al-4V", in *Proc. 6<sup>th</sup> National Turbine Engine High Cycle Fatigue Conf.*, M. J. Kinsella, ed., Universal Technology Corp., Dayton, OH, 2001, CD-Rom, section 8.
89. B. L. Boyce, X. Chen, J. W. Hutchinson, and R. O. Ritchie, "FOD Characterization by Mesoscale Synchrotron X-Ray Diffraction", in *Proc. 6<sup>th</sup> National Turbine Engine High Cycle Fatigue Conf.*, M. J. Kinsella, ed., Universal Technology Corp., Dayton, OH, 2001, CD-Rom, section 8.
90. I. Altenberger, R. K. Nalla, U. Noster, B. Scholtes, and R. O. Ritchie, "On the Fatigue Behavior and Associated Effect of Residual Stresses in Deep-Rolled and Laser Shock Peened Ti-6Al-4V Alloys at Ambient and Elevated Temperatures", in *Proc. 7<sup>th</sup> National Turbine Engine High Cycle Fatigue Conf.*, M. J. Kinsella, ed., Universal Technology Corp., Dayton, OH, 2002, CD-Rom.
91. R. K. Nalla and R. O. Ritchie, "Role of Crack Size and Microstructure in Influencing Mixed-Mode High-Cycle fatigue Thresholds in Ti-6Al-4V", in *Proc. 7<sup>th</sup> National Turbine Engine High Cycle Fatigue Conf.*, M. J. Kinsella, ed., Universal Technology Corp., Dayton, OH, 2002, CD-Rom.
92. I. Altenberger, U. Noster, B. L. Boyce, J. O. Peters, B. Scholtes, and R. O. Ritchie, "Effects of Mechanical Surface Treatment on Fatigue Failure in Ti-6Al-4V: Role of Residual Stresses and Foreign-Object Damage", in *Proc. 6<sup>th</sup> European Conf. on Residual Stresses*, Coimbra, Portugal, 2002.

#### Awards Received

- R. O. Ritchie, TMS 1996 Distinguished Materials Scientist/Engineer Award.
- S. Suresh, Fellow of the American Society of Mechanical Engineers, 1996.
- S. Suresh, Honorary Member of the Materials Research Society of India, 1996.
- R. O. Ritchie, Distinguished Van Horn Lectureship, Case Western Reserve University, 1996-97.
- S. Suresh, Swedish National Chair in Engineering (1996-98), Royal Institute of Technology, Stockholm.
- S. Suresh, Outstanding Alumnus Award, Indian Institute of Technology, Madras, Fall 1997.
- R. O. Ritchie, Southwest Mechanics Lectureship, 1997-1998.
- R. O. Ritchie, Most Outstanding Paper Award in 1998 from *ASTM Journal of Testing and Evaluation*.
- R. O. Ritchie C.J.Beevers Memorial Lecture at the 7<sup>th</sup> International Fatigue Congress, Beijing, June 1999.
- S. Suresh, Fellow of TMS, Fellow Class of 2000.
- S. Suresh, Clark Millikan Endowed Chair at Cal. Tech.- sabbatical leave 1999-2000.
- S. Suresh, TMS 2000 Distinguished Materials Scientist/Engineer Award.
- S. Suresh, Third Kelly Distinguished Lecture, Cambridge University, June 2001.
- R. O. Ritchie, National Academy of Engineering, 2001.
- J. W. Hutchinson Thurston Award from ASME, 2001.
- S. Suresh, Trull Distinguished Lecture in Engineering, University of Texas at Austin, 2002.
- S. Suresh, National Academy of Engineering, 2002.
- W. W. Milligan, Michigan Tech's *Research Award* for 2002.





## **Papers Published**

Reproduced below is a selection of papers published from the MURI Program on High-Cycle Fatigue. They are sub-divided into the following six categories:

1. Large and Small Crack High-Cycle Fatigue Thresholds in Ti-6Al-4V
2. Role of Mode-Mixity on High-Cycle Fatigue Thresholds in Ti-6Al-4V
3. Foreign-Object Damage in Ti-6Al-4V
4. High-Temperature High-Cycle Fatigue Thresholds in Nickel-Base Superalloys
5. Fretting
6. Miscellaneous Stress-Intensity Solutions

### Large and Small Crack High-Cycle Fatigue Thresholds in Ti-6Al-4V

- A.J. McEvily and R.O. Ritchie: "Crack Closure and the Fatigue-Crack Propagation Threshold as a Function of Load Ratio", *Fatigue Fract. Engin. Mater. Struct.*, vol. 21, 1998, pp. 847-55.
- R.O. Ritchie, B.L. Boyce, J.P. Campbell, O. Roder, A.W. Thompson, and W.W. Milligan, "Thresholds for High-Cycle Fatigue in a Turbine Engine Ti-6Al-4V Alloy", *Int. J. Fat.*, vol. 21, 1999, pp. 653-62.
- R.O. Ritchie, D.L. Davidson, B.L. Boyce, J.P. Campbell, and O. Roder, "High-Cycle Fatigue of Ti-6Al-4V", *Fatigue Fract. Engin. Mater. Struct.*, vol. 22, 1999, pp. 621-31.
- J.W. Hutchinson and V. Tvergaard, "Edge-Cracks in Single Crystals under Monotonic and Cyclic Loads", *Int. J. Fract.*, vol. 99, 1999, pp. 81-95.
- V. Tvergaard, Y. Wei, and J.W. Hutchinson, "Edge Cracks in Plastically Deforming Surface Grains", *Eur. J. Solids Mech.*, vol. 20, 2001, pp. 731-38.
- B.L. Boyce and R.O. Ritchie, "Effect of Load Ratio and Maximum Stress Intensity on the Fatigue Threshold in Ti-6Al-4V", *Eng. Fract. Mech.*, vol. 68, 2001, pp. 129-47.
- R.O. Ritchie and J.O. Peters, "Small Fatigue Cracks: Mechanics, Mechanisms and Engineering Applications", *Mater. Trans.*, vol. 42, 2001, pp. 58-67.
- R.K. Nalla, B.L. Boyce, J.P. Campbell, J.O. Peters, and R.O. Ritchie, "Influence of Microstructure on the High-Cycle Fatigue of Ti-6Al-4V: Bimodal vs. Lamellar Structures", *Metall. Mater. Trans. A*, vol. 33A, 2002, pp. 899-918.

### Role of Mode-Mixity on High-Cycle Fatigue Thresholds in Ti-6Al-4V

- J.P. Campbell and R.O. Ritchie, "Mixed-Mode, High-Cycle Fatigue-Crack Growth Thresholds in Ti-6Al-4V: I – A Comparison of Large and Small Crack Behavior", *Eng. Fract. Mech.*, vol. 67, Oct. 2000, pp. 209-27.
- J.P. Campbell, R.O. Ritchie, "Mixed-Mode High-Cycle Fatigue-Crack Growth Thresholds in Ti-6Al-4V: II - Quantification of Crack-Tip Shielding", *Eng. Fract. Mech.*, vol. 67, 2000, pp. 227-49.
- J.P. Campbell and R.O. Ritchie, "High-Cycle Fatigue in Bimodal and Lamellar Ti-6Al-4V: Mixed-Mode Crack-Growth Thresholds", *Metall. Mater. Trans. A*, vol. 32A, 2001, pp. 497-503.
- R.K. Nalla, J.P. Campbell and R.O. Ritchie, "Effects of Microstructure on Mixed-Mode, High-Cycle Fatigue Crack Growth Thresholds in Ti-6Al-4V", *Fatigue Fract. Engin. Mater. Struct.*, vol. 25, 2002, pp. 587-606.
- R.K. Nalla, J.P. Campbell, and R.O. Ritchie, "Mixed-Mode High-Cycle Fatigue Crack Growth Thresholds in Ti-6Al-4V: Role of Small Cracks", *Int. J. Fat.*, 2002, in press.

### Foreign-Object Damage in Ti-6Al-4V

- J.O. Peters, O. Roder, B.L. Boyce, A.W. Thompson, and R.O. Ritchie, "Role of Foreign Object Damage on Thresholds for High-Cycle Fatigue in Ti-6Al-4V", *Metall. Mater. Trans. A*, vol. 31A, 2000, pp. 1571-83.
- J.O. Peters and R.O. Ritchie, "Influence of Foreign Object Damage on Crack Initiation and Early Fatigue-Crack Growth in Ti-6Al-4V", *Eng. Fract. Mech.*, vol. 67, 2000, pp. 193-207.
- J.O. Peters and R.O. Ritchie, "Foreign Object Damage and High-Cycle Fatigue: Role of Microstructure in Ti-6Al-4V", *Int. J. Fat.*, vol. 23, 2001, pp. S1413-21.
- J.O. Peters and R.O. Ritchie, "Foreign Object Damage and High-Cycle Fatigue in Ti-6Al-4V", *Mater. Sci. Eng.*, vol. 319-21, 2001, pp. 597-601.
- X. Chen and J.W. Hutchinson, "Foreign Object Damage and Fatigue Crack Threshold: Cracking Outside Shallow Indents", *Int. J. Fract.*, vol. 107, 2001, pp. 31-51.
- B.L. Boyce, X. Chen, J.W. Hutchinson, and R.O. Ritchie, "The Residual Stress State due to a Spherical Hard-Body Impact", *Mech. Mater.*, vol. 33, 2001, pp. 441-45.
- B.L. Boyce, X. Chen, J.O. Peters, J.W. Hutchinson, R.O. Ritchie, "Mechanical Relaxation of Localized Residual Stresses Associated with Foreign Object Damage", *Mater. Sci. Eng. A*, 2002, in review.
- J.O. Peters, B.L. Boyce, X. Chen, J.M. McNaney, J.W. Hutchinson, and R.O. Ritchie, "On the Application of the Kitagawa-Takahashi Diagram to Foreign-Object Damage and High-Cycle Fatigue", *Eng. Fract. Mech.*, 2002, in press.

### High-Temperature High-Cycle Fatigue Thresholds in Nickel-Base Superalloys

- J. M. Morgan and W.W. Milligan: "A 1 kHz Servohydraulic Fatigue Testing System", in *High Cycle Fatigue of Structural Materials*, W. O. Soboyejo and T. S. Srivatsan, eds, TMS, 1997, pp. 305-12.
- S.A. Padula II, A. Shyam, R.O. Ritchie, and W.W. Milligan, "High Frequency Fatigue Crack Propagation Behavior of a Nickel-Base Turbine Disk Alloy", *Int. J. Fat.*, vol. 21, 1999, pp. 725-31.
- S. Sinharoy, P. Virro-Nic and W. W. Milligan, "Deformation and Strength Behavior of Two Nickel-Base Turbine Disk Alloys at 650°C", *Metall. Mater. Trans. A*, vol. 32A, 2001, pp. 2021-32.
- S.A. Padula II, A. Shyam, D.L. Davidson and W.W. Milligan, "In Situ Study of High Frequency Fatigue Crack Propagation in a Single Crystal Superalloy", in *The David L. Davidson Symposium on Fatigue*, K.S. Chan, P.K. Liaw, R.S. Bellows, T. Zogas, and W.O. Soboyejo, TMS, Warrendale, PA, 2002, pp. 183-89
- Shyam, S.A. Padula II, S. Marras, and W.W. Milligan, "Fatigue Crack Propagation Thresholds in Nickel-Base Superalloys at High Frequencies and Temperatures", *Metall. Mater. Trans. A*, vol. 33A, 2002, in press.

## Fretting

- A.E. Giannakopoulos and S. Suresh, "A Three-Dimensional Analysis of Fretting Fatigue", *Acta Mater.*, vol. 46, 1997, pp. 177-92.
- A.E. Giannakopoulos, T.C. Lindley, and S. Suresh, "Aspects of Equivalence between Contact Mechanics and Fracture Mechanics: Theoretical Connections and a Life-Prediction Methodology for Fretting-Fatigue", *Acta Mater.*, vol. 46, 1998, pp. 2955-68.
- A.E. Giannakopoulos, T.A. Venkatesh, T.C. Lindley, and S. Suresh, "The Role of Adhesion in Contact Fatigue", *Acta Mater.*, vol. 47, 1999, pp. 4653-64.
- J.W. Hutchinson and M.R. Begley, "Plasticity in Fretting of Coated Surfaces", *Eng. Fract. Mech.*, vol. 62, 1999, pp. 145-64.
- A.E. Giannakopoulos, T.C. Lindley, S. Suresh, and C. Chenut, "Similarities of Stress Concentration in Contact at Round Punches and Fatigue at Notches: Implication to Fretting Fatigue Crack Initiation", *Fatigue Fract. Engin. Mater. Struct.*, vol. 23, 2001, pp. 561-71.
- T.A. Venkatesh, B.P. Conner, C.S. Lee, A.E. Giannakopoulos, T.C. Lindley, and S. Suresh, "An Experimental Investigation of Fretting Fatigue in Ti-6Al-4V: The Role of Contact Conditions and Microstructure", *Metall. Mater. Trans. A*, vol. 32A, 2001, pp. 1131-46.
- E. W. Andrews, A. E. Giannakopoulos, E. Plisson and S. Suresh, "Analysis of the Impact of a Sharp Indenter", *Int. J. Solids Struct.*, vol. 39, 2002, pp. 281-95.

## Miscellaneous Stress-Intensity Solutions

- M.Y. He and J.W. Hutchinson, "Asymmetric Four-Point Crack Specimen", *J. Appl. Mech.*, vol. 67, 2000, pp. 207-09.
- M.Y. He and J.W. Hutchinson, "Surface Crack Subject to Mixed Mode Loading", *Eng. Fract. Mech.*, vol. 65, 2000, pp. 1-14.

## LARGE AND SMALL CRACK HIGH-CYCLE FATIGUE THRESHOLDS IN Ti-6Al-4V

- A.J. McEvily and R.O. Ritchie: "Crack Closure and the Fatigue-Crack Propagation Threshold as a Function of Load Ratio", *Fatigue Fract. Engin. Mater. Struct.*, vol. 21, 1998, pp. 847-55.
- R.O. Ritchie, B.L. Boyce, J.P. Campbell, O. Roder, A.W. Thompson, and W.W. Milligan, "Thresholds for High-Cycle Fatigue in a Turbine Engine Ti-6Al-4V Alloy", *Int. J. Fat.*, vol. 21, 1999, pp. 653-62.
- R.O. Ritchie, D.L. Davidson, B.L. Boyce, J.P. Campbell, and O. Roder, "High-Cycle Fatigue of Ti-6Al-4V", *Fatigue Fract. Engin. Mater. Struct.*, vol. 22, 1999, pp. 621-31.
- J.W. Hutchinson and V. Tvergaard, "Edge-Cracks in Single Crystals under Monotonic and Cyclic Loads", *Int. J. Fract.*, vol. 99, 1999, pp. 81-95.
- V. Tvergaard, Y. Wei, and J.W. Hutchinson, "Edge Cracks in Plastically Deforming Surface Grains", *Eur. J. Solids Mech.*, vol. 20, 2001, pp. 731-38.
- B.L. Boyce and R.O. Ritchie, "Effect of Load Ratio and Maximum Stress Intensity on the Fatigue Threshold in Ti-6Al-4V", *Eng. Fract. Mech.*, vol. 68, 2001, pp. 129-47.
- R.O. Ritchie and J.O. Peters, "Small Fatigue Cracks: Mechanics, Mechanisms and Engineering Applications", *Mater. Trans.*, vol. 42, 2001, pp. 58-67.
- R.K. Nalla, B.L. Boyce, J.P. Campbell, J.O. Peters, and R.O. Ritchie, "Influence of Microstructure on the High-Cycle Fatigue of Ti-6Al-4V: Bimodal vs. Lamellar Structures", *Metall. Mater. Trans. A*, vol. 33A, 2002, pp. 899-918.

## CRACK CLOSURE AND THE FATIGUE-CRACK PROPAGATION THRESHOLD AS A FUNCTION OF LOAD RATIO

A. J. McEvily<sup>1</sup> and R. O. Ritchie<sup>2</sup>

<sup>1</sup>Department of Metallurgy and Materials Engineering, University of Connecticut, Storrs, CT 06269–3136, USA

<sup>2</sup>Department of Materials Science and Mineral Engineering, University of California, Berkeley, CA 94720–1760, USA

Received in final form February 1998

**Abstract**—The phenomenon of crack closure, which involves the premature closing of fatigue cracks during the unloading portion of a fatigue cycle resulting in the development of crack-tip shielding due to crack wedging, has become widely accepted as a critical mechanism influencing many aspects of the behaviour of fatigue cracks in metallic materials; these include effects of load ratio, variable-amplitude loading, crack size, microstructure, environment and the magnitude of the fatigue threshold. Recently, however, the significance of crack closure has been questioned and alternative suggestions made for many of these phenomena, e.g. the effect of the load ratio (i.e. the ratio  $R$  of the minimum to maximum loads) on threshold behaviour. In the light of this, the present paper provides evidence to rebut the assertion that crack closure is an insignificant process. Particular attention is given to the effect of crack closure on the threshold level as a function of load ratio.

**Keywords**—Fatigue-crack growth; Crack closure; Load ratio.

### INTRODUCTION

Since its discovery by Elber [1,2] some 25 years ago, crack closure has been widely accepted as a significant mechanism affecting the crack-growth behaviour of fatigue cracks, particularly in metallic materials, as reviewed in Ref. [3]. Closure involves the premature contact and consequent wedging of the crack faces during the unloading portion of a fatigue cycle at a load above the minimum load, and as such acts as a crack-tip (contact) shielding mechanism [4] by reducing the local (near-tip) driving force for crack extension. From a continuum viewpoint, it is considered to result from cyclic plasticity which leaves a band of stretched material in the crack wake, a process which is promoted under plane-stress conditions. Mechanistic studies [5,6], however, have revealed other mechanisms of closure which are active under plane-strain conditions. Such mechanisms are illustrated schematically in Fig. 1, and most importantly are associated with crack wedging by corrosion debris (oxide-induced closure) and especially crack surface asperities (roughness-induced closure). Crack closure can also be associated with the hydrodynamic action of fluids inside the crack (viscous fluid-induced closure), and from residual compressive stresses resulting from the dilation associated with an *in situ* phase transformation (transformation-induced closure) [6]. The major types of closure are promoted at low  $R$  values and stress-intensity levels close to the fatigue threshold where the crack-tip opening displacements are comparable with the dimensions of the oxides or asperity wedges.

As a shielding mechanism, closure acts to increase the effective minimum stress intensity in a fatigue cycle, such that the local (near-tip) stress-intensity factor range is decreased from the nominal (applied) value of  $\Delta K = K_{\max} - K_{\min}$  to an effective value  $\Delta K_{\text{eff}} = K_{\max} - K_{\text{op}}$ , provided  $K_{\text{op}}$ , the stress-intensity factor required to open the crack, exceeds  $K_{\min}$ . Significant values of  $K_{\text{op}}$  have been estimated by a variety of experimental techniques, which include the use of:

- (i) displacement, near-crack tip, or back face strain gauges to determine the deviation from linearity on unloading of the elastic compliance curve [1,2].  $K_{\text{op}}$  values can be as much as

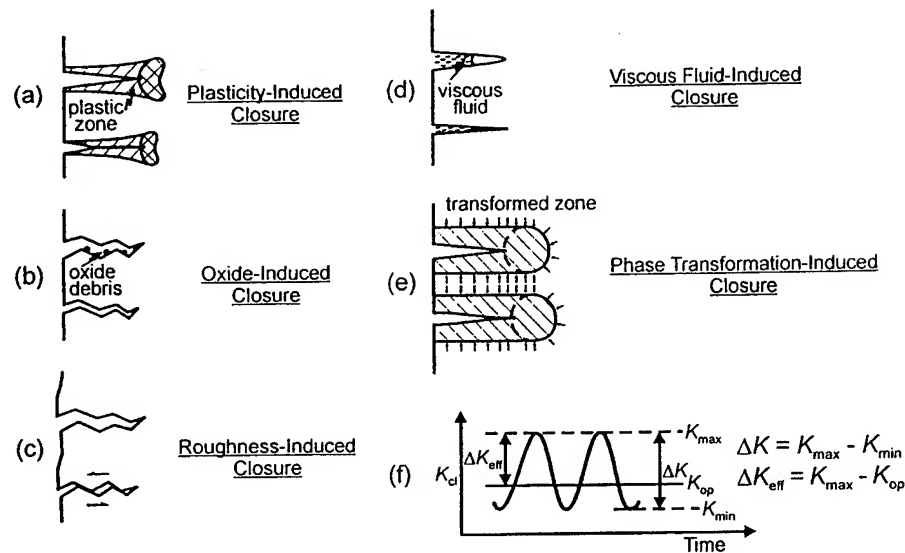


Fig. 1. Schematic illustration of the various mechanisms of crack closure [6].

90% of  $K_{max}$  as the threshold is approached, particularly in materials, e.g. aluminium–lithium alloys where extensive crack-path tortuosity leads to very rough fracture surfaces [7]. Load versus reduced-displacement plots have been used in a similar manner in an effort to determine the closure level more accurately, where the reduced displacement is the difference between the displacements of a linear (no-closure) curve and the actual load–displacement curve [8].

- (ii) replicas to determine the crack opening level at the specimen surface [9,10].
- (iii) laser interferometric gauges to determine the crack opening level at the surface [11].
- (iv) ultrasonics to determine the crack opening level through the specimen thickness [12].
- (v) acoustic emission to determine the crack-opening level, again through the specimen thickness [13].

Other investigators have attempted to avoid the influences of crack closure by testing at high  $R$  values or by using specialized techniques, e.g. constant  $K_{max}$ -increasing  $K_{min}$  procedures to approach a threshold free of closure,  $\Delta K_{eff,th}$  [14]. (Also see Ref. [15] for an analytical treatment of roughness-induced crack closure.)

Recently, Louat *et al.* [16] made use of a dislocation model to investigate plasticity-induced closure under plane-strain conditions, and found the crack-closure level to be minimal. Similarly, other investigators [17] have found that under plane-strain conditions, plane-strain plasticity-induced closure is quite low; indeed, the very existence of this type of closure in plane strain has been questioned [18]. However, Sadananda *et al.* [19] have also concluded that all forms of crack closure are of minimal significance in fatigue-crack growth, despite the wealth of experimental evidence to the contrary cited in the Introduction. It is with this generalization that we differ.

Specifically, Sadananda *et al.* claim that the actual magnitude of the closure effect is far less than typically measured, and offer alternative explanations for many of the fatigue phenomena which have been attributed in whole, or in part, to crack closure; these include the so-called anomalous growth of short cracks, overload effects and the influence of the load ratio on the rate

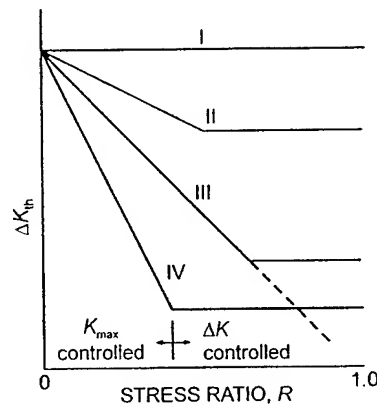


Fig. 2. Variation of  $\Delta K_{th}$  as a function of  $R$  [20].

of fatigue crack growth. In particular, they question how closure affects the value of the fatigue threshold,  $\Delta K_{th}$ , and the accompanying role of load ratio (ratio of minimum to maximum load in a fatigue cycle,  $R = K_{min}/K_{max}$ ).

Figure 2 shows schematically how the threshold  $\Delta K_{th}$  may vary with  $R$ . Vasudévan and Sadananda [20] have identified four classifications of material response for metals, which are labelled I, II, III and IV. They propose that the fatigue-crack growth process is intrinsically a two-parameter process that depends upon the material deformation characteristics, i.e. whether ductile or brittle, and on the crack-tip environment. The two parameters are associated with two regions of crack-growth behaviour; one being identified as  $K_{max}$  controlled, and the other as  $\Delta K$  controlled. In dealing with the threshold level for fatigue-crack growth, they identify the two parameters as  $\Delta K_{max,th}^*$  and  $\Delta K_{th}^*$ . Again, in reaching their conclusions they have minimized any contribution that crack closure might have on the threshold level. The purpose of this paper is to show that crack closure does indeed make an important contribution to the dependence of  $\Delta K_{th}$  on  $R$  by examining the behaviour for each of Vasudévan and Sadananda's four classifications. Furthermore, although it is reasonable to consider the cyclic crack-growth process in terms of  $\Delta K$  and  $K_{max}$  controlled contributions, it is incorrect to make use of a two-parameter explanation in the absence of closure to account for the observed behaviour.

### ROLE OF CRACK CLOSURE

The approach taken herein is that the rate of fatigue-crack growth, as well as the threshold level and its dependence on the load ratio,  $R$ , is controlled by a single parameter,  $\Delta K_{eff}$ , as proposed by Elber [1]. This notion has been substantiated by numerous subsequent investigators, most recently in a study by Hénaff and Petit [21]. The specific role of  $K_{max}$ , at least at near-threshold levels, is considered to provide a limit on the magnitude of the closure by its effect on the crack-tip opening displacements, as compared to the dimensions of the 'wedge', e.g. fracture-surface asperities (although at high growth rates it can become significant again as  $K_{max}$  approaches the instability condition and static fracture modes occur [22]). The basic quantities involved,  $K_{op}$ ,  $\Delta K$ ,  $\Delta K_{eff}$ ,  $K_{max}$  and  $K_{min}$ , are defined in Fig. 3.



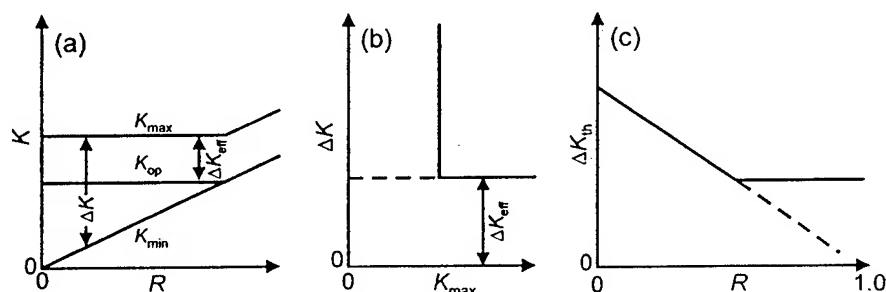


Fig. 3. Schematic illustration of Classification III-type behaviour.

### Classifications I and III

We consider the case where the crack-opening level,  $K_{op}$ , is taken to be independent of  $R$  [Fig. 3(a)]. This is naturally an approximation, although at near-threshold levels, i.e. typically for growth rates less than  $10^{-9}$  m/cycle, where roughness-induced crack closure is the dominant mechanism (except in severe oxidizing environments), experimental measurements in many materials have verified this behaviour [23]. This information, with the assumption of constant  $K_{op}$  level, is expressed in terms of a  $\Delta K$  versus  $K_{max}$  plot in Fig. 3(b). The variation in  $\Delta K_{th}$  with  $R$  is shown in Fig. 3(c); this figure indicates that between  $R = 0$  and  $R = K_{op}/K_{max}$ , the magnitude of  $\Delta K_{th}$  varies as

$$\Delta K_{th} = \Delta K_{th0}(1 - R) \quad (1)$$

where  $\Delta K_{th0}$  is the threshold value at  $R = 0$ . For the  $R$  values between  $K_{op}/K_{max}$  and  $(1 - \Delta K_{eff}/K_c)$ ,  $\Delta K_{th}$  is independent of  $R$ ; this corresponds to Vasudévan and Sadananda's [20] Classification III, and has been reported for many structural alloys, e.g. in 7090-T6 aluminium [23], where the opening stress intensity at the threshold,  $K_{op,th}$ , was measured as  $1.8 \text{ MPa}\sqrt{\text{m}}$  at both  $R = 0.05$  and  $R = 0.5$ . Note that the critical value of  $R$  at which the break occurs in Fig. 3(c) is a function of the level of crack closure. Indeed, to the first order, the critical value is achieved when  $K_{op} = K_{min}$ , if one assumes, as did Schmidt and Paris [24], that the effective stress intensity at the threshold,  $\Delta K_{eff,th}$ , is a constant and  $K_{op}$  is independent of  $R$ . Thus, as the level of crack closure decreases, the break point moves to lower  $R$  values to approach  $R = 0$  in the limit; this condition constitutes Vasudévan and Sadananda's [20] Classification I in Fig. 2, as, e.g. seen in the IN9021 alloy [23].

Vasudévan and co-workers [25,26] proposed that Classification I behaviour is obtained in vacuum and provide data from the literature to support the view [27,28]. This would indicate that the different behaviour observed in air is therefore due to an environmental effect. However, they also present  $\Delta K_{th}$  data as a function of  $R$  for 316 stainless obtained in air and in vacuum by Usami *et al.* [29]. These results clearly show behaviour much closer to Classification III behaviour than Classification I for both air and vacuum. In addition, in a recent study of the behaviour of three aluminium alloys tested in vacuum and air at  $R = 0.05$  and  $0.5$ , Classification II- (see below) or III-type behaviour has been seen, as indicated in Fig. 4 [30]. We also note that for a 9Cr-2Mo steel tested in vacuum at  $538^\circ\text{C}$ , no  $R$  effect was found, whereas there was one at  $20^\circ\text{C}$  [31]. In this case, the absence of an  $R$  effect at elevated temperature was ascribed to a loss of crack closure due to the compressive creep and flattening of asperities on unloading. It is possible that effects of a similar nature may have occurred at room temperature in vacuum in those cases where no  $R$  effect was observed, although precise explanation at this time is uncertain.

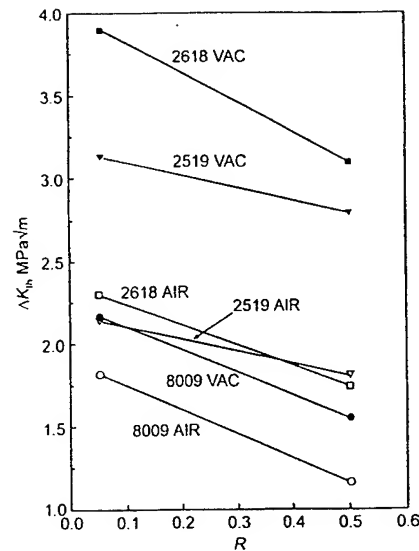


Fig. 4. Effect of  $R$  on  $\Delta K_{th}$  for three aluminium alloys tested in air and vacuum [30].

#### Classification II

Next, we consider the case where the crack-opening level increases with an increase in  $R$  [Fig. 5(a)], a situation which could occur as the result of a greater amount of wear of contacting asperities at the smaller crack-tip opening displacements associated with low load ratios compared to high. Figure 5(b) and (c) depicts the effect of this type of closure on plots similar to those shown in Fig. 3(a) and (b); such behaviour complies with Vasudévan and Sadananda's Classification II.

#### Classification IV

Classification IV is characterized by a decrease in  $K_{op}$  and  $K_{max}$  with an increase in  $\Delta K$ , as indicated in Fig. 6. It is noted that Vasudévan and Sadananda [20] have shown that at the threshold level, the behaviour of a ductile aluminium matrix composite tested by Shang and Ritchie [32] is of the type shown in Fig. 6(b).

It might be expected that this type of behaviour would occur in high-strength steels where oxide-induced closure is predominant. In such steels tested in moist air environments, fretting oxidation can markedly promote the formation of oxide debris at near-threshold stress intensities [33–35].

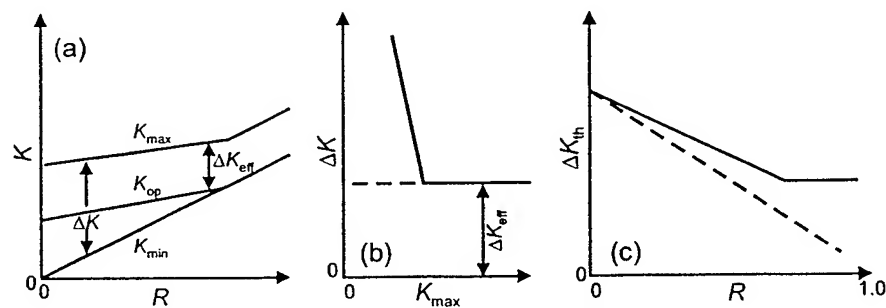


Fig. 5. Schematic illustration of Classification II-type behaviour.

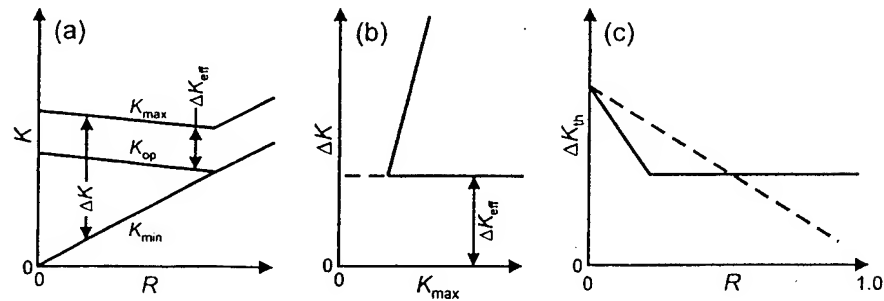


Fig. 6. Schematic illustration of Classification IV-type behaviour.

Since this process only occurs at low load ratios where the crack faces come in contact, the crack-opening level decreases with an increase in  $R$ . These excess oxide products, which constitute the crack wedge, can be up to 40 times thicker at  $R = 0.1$  than at  $R = 0.75$ , where the oxide forms as a natural limiting thickness. However, the  $K_{\max}$  threshold is fairly constant with  $\Delta K$  threshold decreasing with an increase in  $R$  (Fig. 7); with  $K_{\text{op}}$  constant, this corresponds to Classification III rather than Classification IV behaviour.

In a more oxidizing environment, e.g. distilled water, the growth of the oxide film is thermally induced at all  $R$  values. Since the crack wedge thickness is now comparable at  $R = 0.1$  and  $0.75$ ,

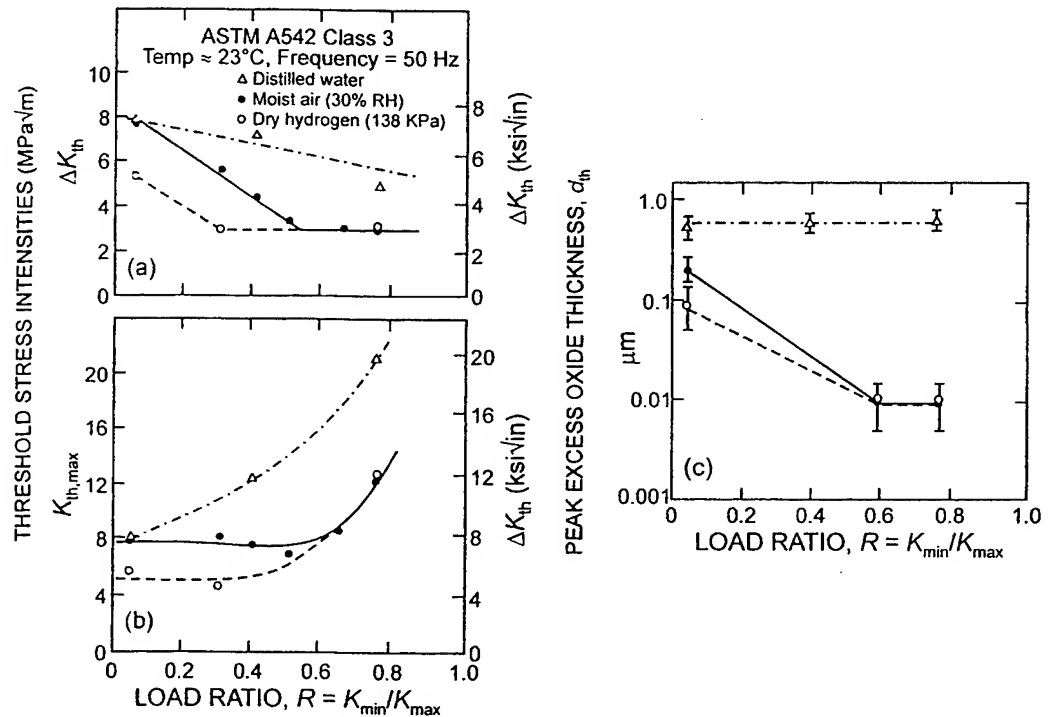


Fig. 7. Variation of alternating and maximum stress intensities at threshold ( $\Delta K_{\text{th}}$  and  $K_{\text{th,max}}$ , respectively) and the maximum excess oxide thickness ( $d_{\text{th}}$ ) with load ratio  $R$  for ASTM A542 Class 3 steel tested in ambient temperature environments of moist air, dry gaseous hydrogen and distilled water at 50 Hz [35].

the crack-opening load is essentially independent of  $R$  (Classification III behaviour), yet the resulting dependence of  $\Delta K_{th}$  on  $R$  conforms to Classification II (but with the break at a very high  $R$  value [35]). These examples serve to illustrate that it may be difficult to assign an appropriate classification *a priori*.

Finally, it should also be noted that the linear dependence of the crack-opening level on  $R$  is a simplifying assumption. Any deviation from linearity would of course have a corresponding effect on the shape of the plots described above.

## DISCUSSION

The conclusion to be drawn from this brief review is that in terms of the crack-advance process, there is no difference in the crack-growth controlling parameters above and below the break shown in Fig. 2. There is only one control parameter, i.e.  $\Delta K_{eff}$ , as has recently been demonstrated by Pippan [36], who showed that in the absence of crack closure the crack-growth rate was independent of  $R$ , over the range  $-2.0$  to  $0.1$ , and depended solely on  $\Delta K_{eff}$ .

Thus, in the absence of the static modes of rupture that may occur at high growth rates approaching instability, the role of  $\Delta K_{eff}$  is to advance the crack, and the corresponding role of  $K_{max}$  is in limiting the extent of crack closure behind the crack tip, as shown schematically in Fig. 8(a). These distinct contributions to the fatigue process are consistent with the crack growth rate ( $da/dN$ ) stress intensity relationship generally found in metals, where with a modified Paris-type relationship [37]:

$$da/dN \propto (\Delta K_{eff})^m (K_{max})^p \quad (2)$$

most ductile metallic materials are found to display a far higher dependency on  $\Delta K_{eff}$  than on

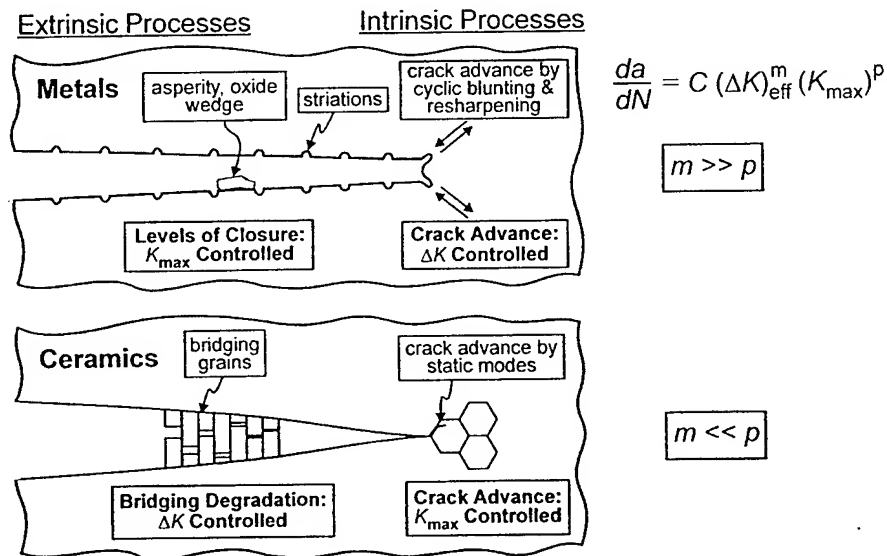


Fig. 8. Schematic illustrations of intrinsic and extrinsic mechanisms involved in cyclic fatigue crack growth in (a) metals and (b) ceramics, showing the relative dependencies of growth rates,  $da/dN$ , on the alternating,  $\Delta K$ , and the maximum  $K_{max}$  stress intensities [37].

$K_{\max}$ , e.g. for a Ni-base superalloy,  $n = 3.0$ ,  $p = 0.4$ . This is in stark contrast to brittle materials, e.g. ceramics, where the crack-advance process is  $K_{\max}$  controlled and  $p \gg n$  [Fig. 8(b)] [37,38].

### CONCLUSIONS

Whereas the role of plasticity-induced crack closure in plane strain may be quite low, other forms of closure, e.g. roughness induced, can play a major role in influencing fatigue-crack propagation in ductile materials.

The crack-growth controlling parameters do not change with load ratio. Except at high growth rates where static fracture modes occur as  $K_{\max}$  approaches instability, there is only one parameter,  $\Delta K_{\text{eff}}$ , controlling the rate of growth of fatigue cracks in ductile materials.

*Acknowledgements*—A.J.M. expresses his appreciation to the National Aeronautics and Space Administration for support provided during this study (Research Grant No. NAG 11382). Similarly, R.O.R. expresses his thanks to the Air Force Office of Scientific Research (MURI Grant No. F49620-96-1-0478 through the University of California, Berkeley).

### REFERENCES

1. W. Elber (1970) Fatigue crack closure under cyclic tension. *Engng Fracture Mech.* **2**, 37–45.
2. W. Elber (1971) The significance of crack closure. In: *Damage Tolerance in Aircraft Structures*, ASTM STP 486, American Society for Testing and Materials, Philadelphia, PA, pp. 230–242.
3. J. C. Newman Jr and W. Elber (eds) (1988) *Mechanics of Fatigue Crack Closure*, ASTM STP 982, American Society for Testing and Materials, Philadelphia, PA.
4. R. O. Ritchie (1988) Mechanisms of fatigue crack propagation in metals, ceramics and composites: role of crack tip shielding. *Mater. Sci. Engng* **103**, 15–28.
5. A. J. McEvily and K. Minakawa (1984) Crack closure and the conditions for fatigue crack propagation. In: *Fatigue Crack Growth Threshold Concepts*, TMS-AIME, Warrendale, PA, pp. 531–549.
6. S. Suresh and R. O. Ritchie (1984) Near-threshold fatigue crack propagation: a perspective on the role of crack closure. In: *Fatigue Crack Growth Threshold Concepts* (Edited by D. L. Davidson and S. Suresh), TMS-AIME, Warrendale, PA, pp. 227–261.
7. K. T. Venkateswara Rao, W. Yu and R. O. Ritchie (1988) Fatigue crack propagation in aluminum–lithium alloy 2090: Part I. Long crack behavior. *Metall. Trans. A* **9A**, 549–561.
8. M. Kikukawa, M. Jono and K. Tanaka (1976) Fatigue crack closure at low stress intensity level. In: *Proceedings of the 2nd International Conference on the Mechanical Behavior of Materials (ICM-2)*, American Society for Metals, Metals Park, OH, pp. 716–720.
9. J. E. Allison, R. C. Ku and M. A. Pompetzki (1988) A comparison of measurement methods and numerical procedures for the experimental characterization of fatigue crack closure. In: *Mechanics of Fatigue Crack Closure*, ASTM STP 982, American Society for Testing and Materials, Philadelphia, PA, pp. 171–185.
10. R. C. McClung and H. Sehitoglu (1988) Closure behavior of small cracks under high strain fatigue histories. In: *Mechanics of Fatigue Crack Closure*, ASTM STP 982, American Society for Testing and Materials, Philadelphia, PA, pp. 279–299.
11. J. Lee and W. N. Sharpe Jr (1988) Closure measurements on short fatigue cracks. In: *Mechanics of Fatigue Crack Closure*, ASTM STP 982, American Society for Testing and Materials, Philadelphia, PA, pp. 247–259.
12. D. De Vadder, Y. Park and D. Francois (1995) Apparatus for ultrasonic *in situ* accurate crack size measurement on laboratory test specimens. In: *Special Applications and Advanced Techniques for Crack Size Determination*, ASTM STP 1251, American Society for Testing and Materials, Philadelphia, PA, pp. 114–129.
13. A. Berkovits and D. Fang (1995) Study of fatigue crack characteristics by acoustic emission. *Engng Fracture Mech.* **51**, 401–416.
14. H. Döker, V. Bachmann and G. Marci (1982) A comparison of different methods of determination of the threshold of fatigue crack propagation. In: *Fatigue Thresholds: Fundamentals and Engineering Applications, Proceedings of the 1st International Conference on Fatigue Thresholds* (Edited by J. Bäcklund, A. F. Blom and C. J. Beevers), EMAS, UK, pp. 45–57.
15. A. M. García and H. Sehitoglu (1997) Contact of crack surfaces during fatigue: Part 1. Formulation of model. Part 2. Simulations. *Metall. Mater. Trans. A* **28A**, 2263–2289.

16. N. Louat, K. Sadananda, M. Duesbury and A. K. Vasudévan (1993) A theoretical evaluation of crack closure. *Metall. Trans. A* **24A**, 2225–2232.
17. N. A. Fleck and J. C. Newman Jr (1988) Analysis of crack closure under plane strain conditions. In: *Mechanics of Fatigue Crack Closure*, ASTM STP 982, American Society for Testing and Materials, Philadelphia, PA, pp. 319–341.
18. A. J. McEvily and Z. Yang (1988) On crack closure in fatigue crack growth. In: *Failure Analysis—Theory and Practice* (Edited by E. Czoboly), Vol. II, EMAS, Warley, UK, pp. 1231–1248.
19. K. Sadananda, A. K. Vasudévan and N. Louat (1997) Dislocation behavior under fatigue. In: *Recent Advances in Fracture*, TMS, Warrendale, PA, pp. 395–402.
20. A. K. Vasudévan and K. Sadananda (1996) Fatigue crack growth in advanced materials. In: *Fatigue'96, Proceedings of the 6th International Conference on Fatigue and Fatigue Thresholds* (Edited by G. Lütjering and H. Nowack), Vol. I, Pergamon Press, Oxford, UK, pp. 473–478.
21. G. Hénaff and J. Petit (1996) Environmentally-assisted fatigue crack propagation: some critical issues. In: *Fatigue'96, Proceedings of the 6th International Conference on Fatigue and Fatigue Thresholds* (Edited by G. Lütjering and H. Nowack), Vol. II, Pergamon Press, Oxford, UK, pp. 715–720.
22. R. O. Ritchie and J. F. Knott (1973) Mechanisms of fatigue crack growth in low alloy steel. *Acta Metall.* **21**, 639–648.
23. K. Minakawa, G. Levan and A. J. McEvily (1986) The influence of load ratio on fatigue crack growth in 7090-T6 and IN9021-T4 aluminum alloys. *Metall. Trans. A* **17A**, 1787–1795.
24. R. A. Schmidt and P. C. Paris (1973) Threshold for fatigue crack propagation and effects of load ratio and frequency. In: *Progress in Fatigue Crack Growth and Fracture Testing*, ASTM STP 536, American Society for Testing and Materials, Philadelphia, PA, pp. 79–94.
25. A. K. Vasudévan, K. Sadananda and N. Louat (1993) Critical evaluation of crack closure and related phenomena: I. Background and experimental analysis. In: *Fatigue'93, Proceedings of the 5th International Conference on Fatigue and Fatigue Thresholds* (Edited by J.-P. Baille and J. L. Dickson), EMAS, Warley, UK, pp. 565–570.
26. K. Sadananda, N. Louat and A. K. Vasudévan (1993) Critical evaluation of crack closure and related phenomena: II. Theoretical evaluation. In: *Fatigue'93, Proceedings of the 5th International Conference on Fatigue and Fatigue Thresholds* (Edited by J.-P. Baille and J. L. Dickson), EMAS, Warley, UK, pp. 571–576.
27. B. R. Kirby and C. J. Beevers (1979) Slow fatigue crack growth and threshold behaviour in air and vacuum of commercial aluminium alloys. *Fatigue Fract. Engng Mater. Struct.* **1**, 203–216.
28. J. Petit and J. L. Maillard (1980) Environment and load effects on fatigue crack propagation near threshold conditions. *Scripta Metall.* **14**, 163–166.
29. S. Usami, Y. Fukuda and S. Shida (1983) *Proceedings of the 4th National Congress on Pressure Vessel Technology*, American Society of Mechanical Engineers, New York, NY.
30. M. Renaud (1993) *Elevated Temperature, Near-Threshold Fatigue Crack Propagation in Aluminum Alloys*. M.Sc. thesis, University of Connecticut, Storrs, CT.
31. H. Nakamura, K. Murali, K. Minakawa and A. J. McEvily (1986) Fatigue crack growth in ferritic steels as influenced by elevated temperature and environment. In: *Microstructure and Mechanical Behaviour of Materials* (Edited by H. Gu and H. Jiawen), Vol. I, EMAS, Warley, UK, pp. 43–57.
32. J. K. Shang and R. O. Ritchie (1989) Crack bridging by uncracked ligaments during fatigue-crack growth in a SiC-reinforced aluminum alloy composite. *Metall. Trans. A* **20A**, 897–908.
33. R. O. Ritchie, S. Suresh and C. M. Moss (1980) New-threshold fatigue crack growth in 2¼Cr–1Mo steel in air and hydrogen. *J. Engng Mater. Technol., Trans. ASME Series H* **103**, 293–299.
34. S. Suresh, G. F. Zaminski and R. O. Ritchie (1981) Oxide induced crack closure: an explanation for near-threshold corrosion fatigue crack growth behavior. *Metall. Trans. A* **12A**, 1435–1443.
35. S. Suresh and R. O. Ritchie (1983) On the influence of environment on the load ratio dependence of fatigue thresholds in pressure vessel steel. *Engng Fracture Mech.* **18**, 785–800.
36. R. Pippan (1987) The growth of short cracks under cyclic compression. *Fatigue Fract. Engng Mater. Struct.* **9**, 319–328.
37. R. O. Ritchie and K. T. Venkateswara Rao (1996) Cyclic fatigue-crack growth in toughened ceramics and intermetallics at ambient to elevated temperatures. In: *ECF-11—Mechanisms and Mechanics of Damage and Failure, Proceedings of the Eleventh European Conference on Fracture* (Edited by J. Petit), Vol. I, EMAS, Warley, UK, pp. 53–69.
38. R. H. Dauskardt, M. R. James, J. R. Porter and R. O. Ritchie (1992) Cyclic fatigue-crack growth in SiC-whisker-reinforced alumina ceramic composite: long and small-crack behavior. *J. Am. Ceram. Soc.* **75**, 759–771.

## Thresholds for high-cycle fatigue in a turbine engine Ti–6Al–4V alloy

R.O. Ritchie <sup>a,\*</sup>, B.L. Boyce <sup>a</sup>, J.P. Campbell <sup>a</sup>, O. Roder <sup>a</sup>, A.W. Thompson <sup>a</sup>,  
W.W. Milligan <sup>b</sup>

<sup>a</sup> Department of Materials Science and Mineral Engineering, University of California, Berkeley, CA 94720-1760, USA

<sup>b</sup> Department of Metallurgical and Materials Engineering, Michigan Technological University, Houghton, MI 49931-0001, USA

Received 1 June 1998; received in revised form 1 December 1998

### Abstract

The characterization of critical levels of microstructural damage that can lead to fatigue-crack propagation under high-cycle fatigue loading conditions is a major concern for the aircraft industry with respect to the structural integrity of turbine engine components. The extremely high cyclic frequencies characteristic of in-flight loading spectra necessitate that a damage-tolerant design approach be based on a crack-propagation threshold,  $\Delta K_{TH}$ . The present study identifies a practical lower-bound large-crack threshold under high-cycle fatigue conditions in a Ti–6Al–4V blade alloy (with ~60% primary  $\alpha$  in a matrix of lamellar  $\alpha+\beta$ ). Lower-bound thresholds are measured by modifying standard large-crack propagation tests to simulate small-crack behavior. These techniques include high load-ratio testing under both constant- $R$  and constant- $K_{max}$  conditions, performed at cyclic loading frequencies up to 1 kHz and  $R$ -ratios up to 0.92. The results of these tests are compared to the near-threshold behavior of naturally-initiated small cracks, and to the crack initiation and early growth behavior of small cracks emanating from sites of simulated foreign object damage. © 1999 Elsevier Science Ltd. All rights reserved.

**Keywords:** Fatigue; Threshold; Titanium; High-cycle fatigue small cracks; Foreign object damage

### 1. Introduction

A 1992 study conducted by the Scientific Advisory Board of the US Air Force targeted high-cycle fatigue (HCF) as the single biggest cause of turbine engine failures in military aircraft [1]. HCF results in rapid, essentially unpredictable failures due to fatigue-crack propagation under ultrahigh frequency loading. Furthermore, cracking often initiates from small defects which are associated with damage caused by a variety of drivers, including fretting and impacts by foreign objects [2]. To prevent HCF failures, design methodologies are required that identify the critical levels of precursory microstructural damage which can lead to such failure. The current study, which is part of the US Air Force's Multidisciplinary University Research Initiative on 'High Cycle Fatigue,' is targeted at identifying these critical levels of

damage and characterizing fatigue behavior under representative operating conditions in a Ti–6Al–4V alloy. The Ti–6Al–4V alloy, typically used in the front, low-temperature, stages of the engine, was chosen as a prototypical material for study by the joint military–industry–academia HCF program.

While the exact forcing functions which cause HCF failure remain unknown, it has been established that engine components experience high frequency (>1 kHz) vibrational loading due to transient airflow dynamics [2, 3]. This vibratory loading is often superimposed on a high mean stress. Because of the very high frequency of loading, even cracks growing at slow per-cycle velocities (i.e.  $10^{-10}$  to  $10^{-9}$  m/cycle) propagate to failure in a short period of time. For example, a crack growing at a constant velocity of  $10^{-10}$  m/cycle would cause failure in a 20 mm thick turbine component in approximately 30 h of operation (at 1 kHz). In contrast, this same crack velocity in a 20 mm automobile piston rod would give 2000 h of continuous operation due to the low frequency of loading (~50 Hz). For this reason, it is necessary to

\* Corresponding author. Tel: (510)486-5798; fax: (510)486-4995.  
E-mail address: roritchie@lbl.gov (R.O. Ritchie)

operate HCF-critical turbine components below the fatigue-crack propagation threshold ( $\Delta K_{TH}$ ) such that crack propagation cannot occur (within  $\sim 10^9$  cycles).

Whereas an extensive database [4,5] exists for fatigue-crack propagation thresholds in metallic alloys, it has been largely derived from standard test geometries containing large ( $> \text{few mm}$ ) through-thickness cracks; such data are not necessarily relevant to the HCF problem where the flaws that cause failure are likely to be in the range of tens to hundred of micrometers [6]. Indeed, cracks with dimensions comparable to either characteristic microstructural size scales or to the crack-tip plastic-zone size can grow at velocities far faster than corresponding large cracks at the same *applied* driving force; and they can propagate at applied stress-intensity levels *below* the large-crack threshold,  $\Delta K_{TH}$  (Fig. 1). For this reason, design against HCF failure must be based on the notion of a small-crack threshold, measured under the representative conditions of high frequencies and high mean loads [7].

There are several reasons why small cracks can behave differently from large-cracks. Of these, the most important are associated with cracks of a size comparable to [8]:

- microstructural size scales, where biased statistical sampling of the microstructure leads to accelerated crack advance along ‘weak’ paths, i.e., microstructural features oriented for easy crack growth (a continuum or homogeneity limitation),
- the extent of local plasticity *ahead* of the crack tip, where the assumption of small-scale yielding implicit in the use of the stress intensity  $K$  is not strictly valid (a linear-elastic fracture mechanics limitation),
- the extent of crack-tip shielding (e.g. crack wedging

by crack closure) *behind* the crack tip, where the reduced role of shielding leads to a higher *local* driving force than the corresponding large crack at the same  $K$  levels (a similitude limitation).

Because of the experimental difficulties associated with conducting small-crack tests, one approach used in the present work is to develop, through a consideration of the mechanisms listed above, large-crack tests that simulate the behavior of small cracks, thereby yielding *lower-bound* threshold values. As small-scale yielding conditions, in terms of near-threshold cyclic plastic-zone sizes ( $\sim 0.2\text{--}1\text{ }\mu\text{m}$ ), clearly apply, the methods of determining lower-bound thresholds used in this study are focused on the similitude limitation, and are thus based on assuring that (i) minimal crack closure exists *behind* the crack tip, and (ii) minimal microstructural damage exists *ahead* of the tip. We recognize that such lower-bound large-crack techniques cannot also simulate the continuum limitation; however, the extent to which they do simulate true small-crack behavior will give some insight into the importance of this factor.

The techniques being employed are:

- conventional load-shedding to approach the threshold under high and *constant* load-ratio conditions [Fig. 2(a)], where the load ratio  $R$  is the ratio of minimum to maximum loads; this tends to minimize the role of crack closure by ensuring that crack-tip opening displacements (CTODs) are large enough to limit any premature contact of the crack surfaces on unloading (i.e. the minimum CTOD in the cycle is larger than the dimensions of the fracture surface asperities),
- load-shedding under variable  $R$  conditions, specifically involving a constant  $K_{max}$ /increasing  $K_{min}$  sequence to approach the threshold [9,10] [Fig. 2(b)], which ensures that the highest  $R$  values possible, and hence minimal closure loads, are achieved at  $\Delta K_{TH}$ ,
- pre-cracking in far-field compression to minimize microstructural damage ahead of the crack tip [6,11,12], followed by machining to remove the crack wake,
- ‘razor micro-notching’, where polishing with a razor blade at the root of a notch is used to produce a machined slot (i.e. with no crack closure and little damage ahead of the tip) with a root radius smaller than the characteristic microstructural dimensions ( $\sim 10\text{ }\mu\text{m}$ ).

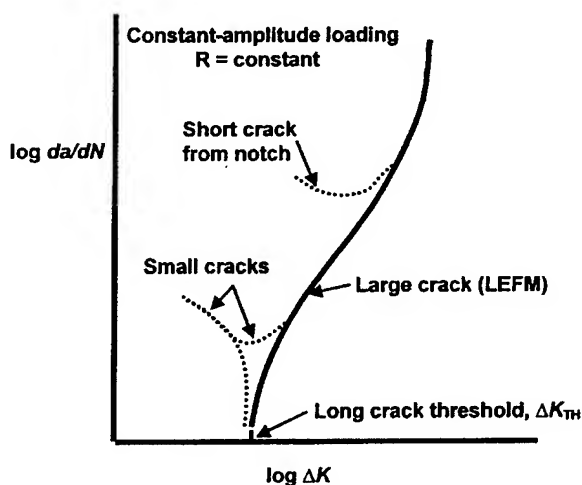


Fig. 1. A schematic comparison of typical growth-rate behavior for small cracks and large cracks. Small cracks are observed to grow below the large-crack threshold and at velocities greater than equivalently driven large cracks.

The current paper describes results using the first two techniques. In addition, as many engine components see the high frequency/high load-ratio (vibratory) cycling interrupted by large periodic unloading/loading (stop-start) cycles, we take a preliminary look at this effect of high-cycle/low-cycle fatigue (HCF/LCF) interactions on such thresholds. A secondary objective is to investigate



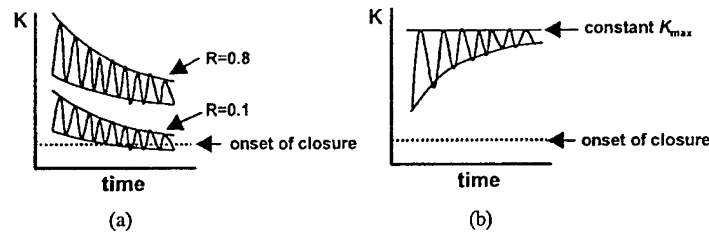


Fig. 2. Schematics illustrating the use of (a) high load ratio and (b) constant  $K_{max}$  cycling to minimize closure effects, thereby yielding lower-bound thresholds.

the effect of frequency on crack-growth behavior in Ti-6Al-4V; as many of the HCF data are measured at 1 kHz, comparisons are made with results at 'conventional' frequencies (e.g. 50 Hz). Finally, since foreign object damage represents a prime source of HCF failures, we also examine the fatigue-crack growth behavior of small cracks originating from foreign object damage sites that have been simulated by firing high-velocity hardened steel spheres onto the surface of test samples.

## 2. Experimental procedures

### 2.1. Material and microstructure

The Ti-6Al-4V alloy investigated in this study was supplied in a condition which has been termed 'solution-treated and overaged' (STOA), from a set of forgings produced specifically for the joint military-industry-academia HCF program. The chemical composition (in wt%) was 6.30% Al, 4.17% V, 0.19% Fe, 0.19% O, 0.013% N, bal. Ti. The bar-stock, originating from Teledyne Titanium, was forged into 40×15×2 cm plates and subsequently solution-treated at 925°C (1 h) and vacuum annealed at 700°C (2 h) for stabilization. The resulting microstructure consisted of a bimodal distribution of ~60 vol% primary- $\alpha$  and ~40 vol% lamellar colonies of  $\alpha$ + $\beta$  (Fig. 3). Studies of a separate forging from the same lot revealed a tensile strength of 970 MPa, a yield strength of 926–935 MPa and a Young's modulus of 116 GPa, based on tensile tests conducted along the longitudinal axis at a strain rate of  $5 \times 10^{-4} \text{ s}^{-1}$  [13].

### 2.2. Fatigue-crack propagation testing

Large-crack propagation studies were conducted on compact-tension C(T) specimens machined in the L-T orientation (with 8 mm thickness and 25 mm width) at  $R$  ratios (ratio of minimum to maximum loads) varying from 0.1 to 0.92 in a lab air environment (22°C, ~45% relative humidity). Crack lengths were monitored in situ using the back-face strain compliance technique, and were verified using periodic optical inspection. Crack closure was also monitored using back-face strain compliance; specifically, the closure stress intensity,  $K_{cl}$ , was

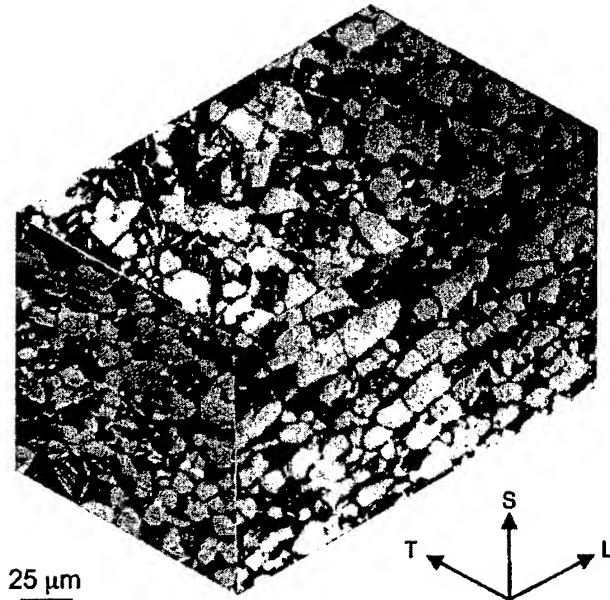


Fig. 3. Optical micrograph of the microstructure of the Ti-6Al-4V studied. The microstructure consists of approximately 60% primary  $\alpha$  and 40% lamellar  $\alpha$ + $\beta$  colonies. The grains were slightly elongated in along the L forging axis. All fatigue specimens were extracted in the L-T orientation (such that the crack surface was in the S-T plane and the crack propagated in the T direction). (Etched in Kroll's solution).

determined from the closure load,  $P_{cl}$ , measured at the point of first deviation from linearity in the elastic compliance curve upon unloading [14].

Fatigue tests were conducted largely in accordance with ASTM Standard E-647. For crack-growth threshold determination using constant  $R$  testing, loads were shed such that  $\Delta K = \Delta K_{initial} \exp[C(a - a_{initial})]$ , with the normalized  $K$ -gradient,  $C$ , set to  $-0.08 \text{ mm}^{-1}$ , as suggested in ASTM E-647 ( $\Delta K$  is the stress-intensity range and  $a$  is the crack length).<sup>1</sup> At 50–200 Hz, the fatigue thresholds,  $\Delta K_{TH}$  and  $K_{max,TH}$ , were defined as the minimum values of these parameters yielding a propagation rate

<sup>1</sup> Proprietary studies by industrial participants have found that gradients as high as  $C = -0.8 \text{ mm}^{-1}$  could be employed for this alloy without inducing observable effects on the measurement of the threshold.

of  $10^{-10}$  m/cycle; at 1 kHz, thresholds could be defined at a propagation rate of  $10^{-11}$  m/cycle.

Tests at 50–200 Hz (sine wave) were conducted on conventional MTS servo-hydraulic testing machines operating under automated closed-loop  $K$  control. Corresponding fatigue tests at 1 kHz were performed under load control on a newly developed MTS servohydraulic test frame using a voice-coil servovalve; details of this instrument are described elsewhere [15].

Results are presented in the form of the crack growth increment per cycle,  $da/dN$ , plotted as a function of the applied stress-intensity range,  $\Delta K = K_{\max} - K_{\min}$ ; after allowing for the effect of closure, growth rates are plotted as a function of the effective (near-tip) stress-intensity range,  $\Delta K_{\text{eff}} = K_{\max} - K_{\text{cl}}$ .

### 2.3. Simulation of foreign object damage

Foreign object damage (FOD) was simulated by firing chrome-hardened steel spheres onto a flat specimen surface using compressed gas. The specimen geometry chosen for this study has a rectangular gauge section with cylindrical buttonhead grip sections (Fig. 4), and is nearly identical to the  $K_b$  specimen used by GE Aircraft Engines for its similarity to the blade loading configuration [16]. To provide a consistent, nominally stress-free surface, gauge sections were prepared by standard stress relief and chemical-milling procedures. In this study, 3.2 mm diameter spheres were impacted onto the flat surface of a tensile specimen at velocities of ~200, 250, and 300 m/s. These velocities were chosen because (i) they represented typical in-service impact velocities on blades, and (ii) they provided different levels of damage (see below). All shots were fired at  $90^\circ$  to the specimen surface. After impacting, the tensile specimens were subsequently cycled at 20 Hz (sine wave) with a maximum nominal stress of 500 MPa at a load ratio of  $R=0.1$ . Periodically, the specimen was removed from the test frame and examined in a scanning electron microscope (SEM) to detect crack initiation. Once a crack had initiated, subsequent crack growth was similarly monitored using periodic SEM observations. As a preliminary assessment, residual stresses surrounding the indentation were ignored and the fatigue cracks were modeled as semi-elliptical surface cracks initiating at the bottom or rim of the impact crater. Stress intensities were com-

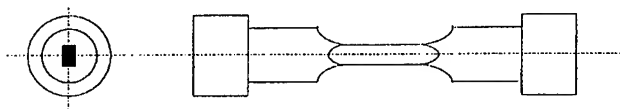


Fig. 4. Modified  $K_b$  geometry used for FOD studies. Gauge section is 3 mm  $\times$  5 mm. The specimen is based on a geometry used by General Electric to closely approximate the loading configuration of actual turbine blades. The FOD shot was fired at the 5 mm wide surface and created impact sites that were 2–2.6 mm in diameter.

puted from the Newman–Raju semi-elliptical surface crack solution [17], assuming a half-surface length to depth ratio ( $c/a$ ) of 0.9 (based on fractographic observations).

## 3. Results and discussion

### 3.1. Effect of load ratio

The effect of load ratio ( $R=0.1$ – $0.8$ ) on the fatigue-crack propagation rates of large ( $>5$  mm) cracks in the STOA Ti-6Al-4V at low frequencies (50 Hz) is shown in Fig. 5. As expected, higher load ratios induce lower  $\Delta K_{\text{TH}}$  thresholds and faster growth rates at a given applied  $\Delta K$  level. Threshold stress-intensity ranges were measured as 4.6, 2.9, and 2.6 MPa $\sqrt{\text{m}}$  at  $R=0.1$ , 0.5 and 0.8, respectively. A two-parameter fit of the Paris regime for the three load ratios yields a growth law of (units: m/cycle, MPa $\sqrt{\text{m}}$ ):

$$\frac{da}{dN} = 5.2 \times 10^{-12} \Delta K^{2.5} K_{\max}^{0.67} \quad (1)$$

While this law appears to work well at both of the higher load ratios, at  $R=0.1$  there is clearly a slight transition in slope at  $\Delta K \sim 10$  MPa $\sqrt{\text{m}}$  that cannot be captured in Eq. (1). This transition has been observed in similar Ti-6Al-4V alloys and has been attributed to a change in the crystallographic morphology of crack growth, from a ‘stage-I like’ fracture where all facets lie on the basal plane (0002) to a typical stage-II transgranular fracture resulting from slip alternating on nearly symmetrical slip systems [18].

The observed effect of load ratio is commonly attri-

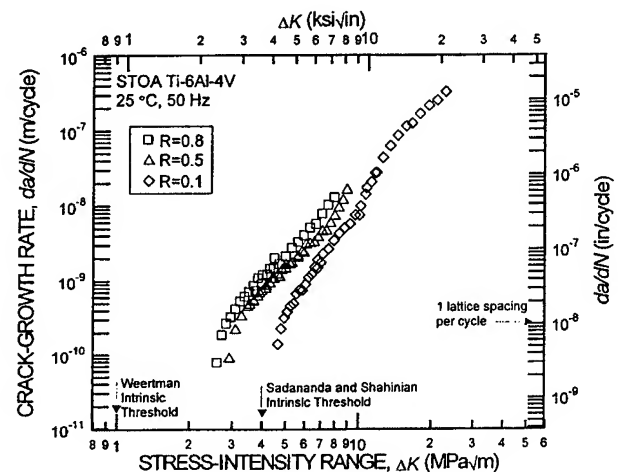


Fig. 5. Fatigue crack propagation data for  $R=0.1$ , 0.5, and 0.8 with thresholds at  $\Delta K_{\text{TH}}=4.6$ , 2.9, and 2.6 MPa $\sqrt{\text{m}}$ , respectively. Thresholds are compared to theoretical intrinsic thresholds based on analysis by Weertman [29], and Sadananda and Shahinian [28], as discussed in the text.

buted to the role of crack closure, which in Ti alloys is generally observed to be roughness induced (i.e. arising from the wedging of crack-surface asperities) [19–21]. To examine this, closure stress intensity values,  $K_{cl}$ , were measured at each load ratio. No detectable closure was observed at  $R=0.5$  and  $0.8$ . However, at  $R=0.1$ ,  $K_{cl}$  values were observed to be roughly constant at  $\sim 2.0 \text{ MPa}\sqrt{\text{m}}$  [Fig. 6(a)]. In Fig. 6(b), the results of Fig. 5 are replotted in terms of the effective stress-intensity range, after accounting for crack closure. It is apparent that, similar to previous studies in Ti–6Al–4V [22], characterizing growth rates in terms of  $\Delta K_{eff}$  reduces the disparity in crack-growth behavior between the three  $R$  ratios; this result is consistent with crack closure as a mechanism for the load ratio (or  $K_{max}$ ) effect.

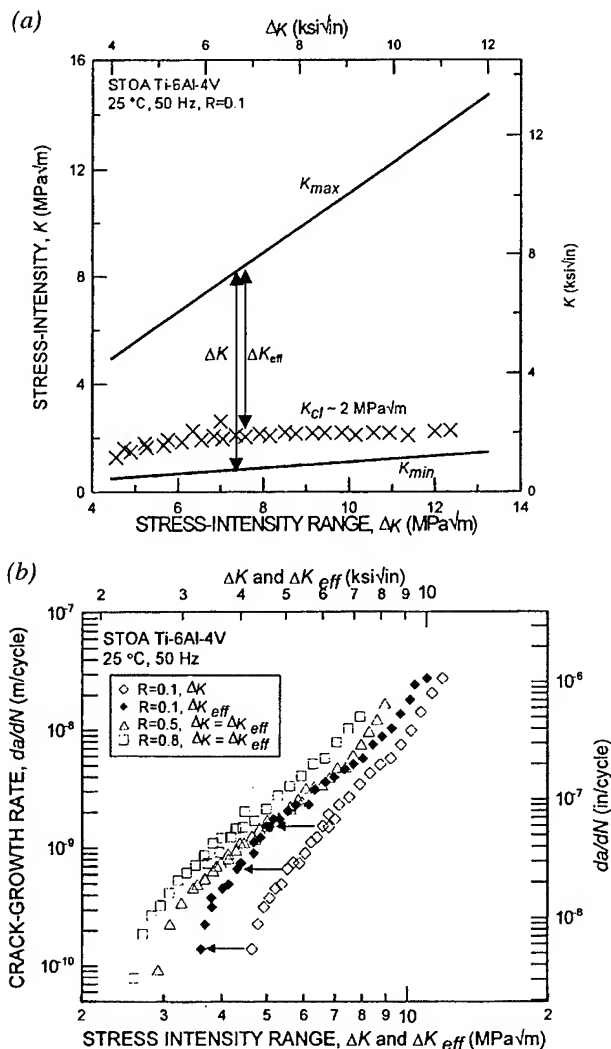


Fig. 6. (a) Crack closure, measured by unloading compliance, stays approximately constant at  $K_{cl} \sim 2 \text{ MPa}\sqrt{\text{m}}$ . (b) When crack closure is considered in  $\Delta K_{eff}$  ( $=K_{max} - K_{cl}$ ), the load ratio effect between  $R=0.1$  and  $R=0.5$  is negligible. At low growth rates, the apparent discrepancy is most likely due to imprecision in measuring the closure level.

The measured variation with load ratio of the threshold  $\Delta K_{TH}$  and  $K_{max,TH}$  values, plotted in Fig. 7, can be compared with the simple closure model of Schmidt and Paris [24]. This model is based on the notion that  $K_{cl}$  and the effective  $\Delta K$  threshold,  $\Delta K_{eff,TH}$ , are constant and independent of  $R$ ; it predicts that measured  $\Delta K_{TH}$  and  $K_{max,TH}$  thresholds will be load-ratio independent, respectively above and below a transition  $R$  at which point  $K_{min} = K_{cl}$ . Although clearly there are insufficient data to verify this simplified analysis, the present results

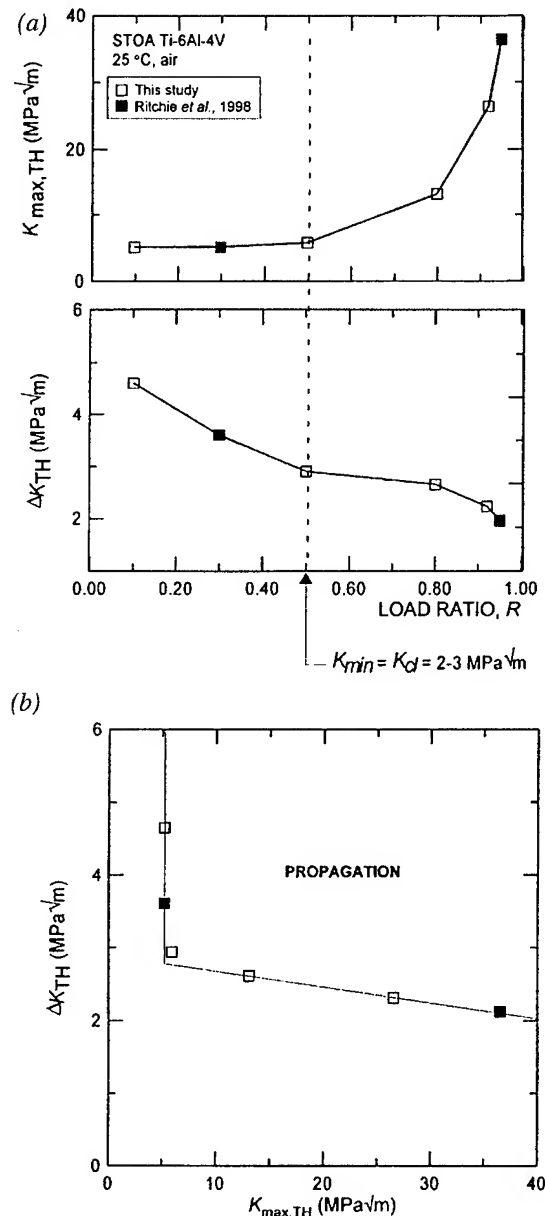


Fig. 7. Variation of  $K_{max,TH}$  and  $\Delta K_{TH}$  with load ratio appears to follow the Schmidt and Paris closure model [23]. Although more data are required to clearly establish a transition, the data presented here show a change in slope at  $R \approx 0.5$ , consistent with  $K_{cl} = 2-3 \text{ MPa}\sqrt{\text{m}}$  as observed.

are consistent with this model, and the transition  $R$ , above which closure is ineffective ( $K_{\min} > K_{cl}$ ), is observed at  $K_{\min}=K_{cl} \approx 2\text{--}3 \text{ MPa}\sqrt{\text{m}}$ . Such an estimate of  $K_{cl}$  is consistent with the experimentally measured values [Fig. 6(a)], determined from back-face strain compliance.

### 3.2. Effect of frequency

The role of cyclic frequency is shown in Fig. 8 where the growth rates at 50 Hz are compared with data collected at 1 kHz. It is clear that results at 1 kHz are not statistically distinguishable from the conventional frequency data. Cursory experiments performed at 200 Hz exhibited a similar result. This lack of a frequency effect on ambient-temperature growth-rate behavior in STOA Ti-6Al-4V is consistent with preliminary results at 2 kHz on the same material system [25]. In contrast, stress/life (S/N) fatigue tests conducted in another Ti-6Al-4V microstructure (consisting almost entirely of primary  $\alpha$ ) [26] showed an increase in fatigue strength (defined as the stress for failure within  $10^7$  cycles) as the frequency increased from 70 to 400 to 1800 Hz. These results suggest that the role of high frequencies on the fatigue of Ti-6Al-4V at ambient temperatures may be largely associated with crack initiation, rather than the propagation life per se.

Testing at 1 kHz permits thresholds to be readily obtained at much lower growth rates. Using the ASTM standard  $K$ -gradient of  $0.08 \text{ mm}^{-1}$ , measurements down to  $10^{-11} \text{ m/cycle}$  require several weeks at 50 Hz, whereas these same measurements can be obtained in a single day at 1 kHz. In the present study, thresholds measured at  $10^{-11} \text{ m/cycle}$  (at 1 kHz) were found to be  $\sim 0.1$

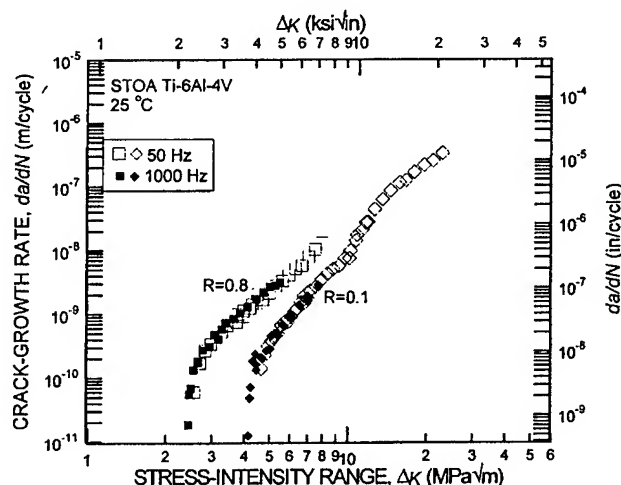


Fig. 8. Comparison of fatigue-crack propagation at 50 Hz and 1 kHz showing no statistically significant deviation in behavior. High frequency testing also enables collection of very low growth rate data (down to  $10^{-11} \text{ m/cycle}$ ) in a relatively short amount of time ( $\sim 1$  day).

$\text{MPa}\sqrt{\text{m}}$  lower than the  $10^{-10} \text{ m/cycle}$  thresholds (measured at either frequency).

### 3.3. Constant $K_{\max}$ /variable $R$ testing

Results at 1 kHz from the variable  $R$ , constant- $K_{\max}$ /increasing- $K_{\min}$  tests, which minimize the effect of crack closure, are shown in Fig. 9. Here, for a constant  $K_{\max}$  of  $26.5 \text{ MPa}\sqrt{\text{m}}$ , a final load ratio of  $R=0.92$  was achieved, yielding a threshold of  $2.2 \text{ MPa}\sqrt{\text{m}}$ , compared to a  $\Delta K_{TH}$  value of  $2.4 \text{ MPa}\sqrt{\text{m}}$  for constant  $R=0.8$  testing. These high load ratios result in an extremely large minimum crack-tip opening displacements<sup>2</sup> ( $\text{CTOD}_{\min} \approx 0.7 \mu\text{m}$  and  $4.3 \mu\text{m}$  for  $R=0.8$  and  $0.92$ , respectively) superimposed on a relatively small cyclic crack-tip opening displacement ( $\Delta\text{CTOD} \approx 20 \text{ nm}$  for both  $R=0.8$  and  $0.92$ ). With such large crack-tip opening displacements, crack closure from fracture-surface asperity wedging would be expected to be essentially non-existent, as the asperity sizes would need to exceed the  $\text{CTOD}_{\min}$  of several micrometers.

The  $\Delta K_{TH}$  threshold value of  $2.2 \text{ MPa}\sqrt{\text{m}}$  measured under constant- $K_{\max}$ /increasing  $K_{\min}$  cycling at  $R=0.92$  is considered to represent a practical lower-bound threshold for large cracks measured to date in STOA Ti-6Al-4V. It should be compared with measurements on naturally-initiated small cracks in the same microstructure, where small-crack growth ( $a \sim 45\text{--}1000 \mu\text{m}$ ) was not observed below a  $\Delta K$  of  $2.9 \text{ MPa}\sqrt{\text{m}}$  ( $R=0.1$ ) [28].

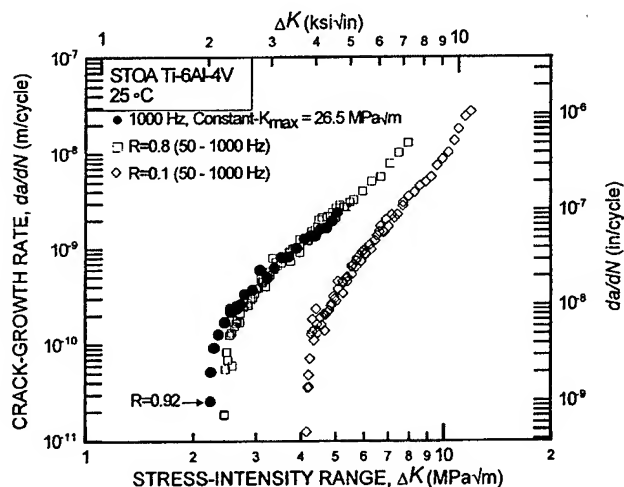


Fig. 9. A constant  $K_{\max}$  test at 1000 Hz was used to achieve  $R=0.92$  resulting in a lower-bound threshold of  $2.2 \text{ MPa}\sqrt{\text{m}}$ . Results are compared with constant  $R$  data at both 50 and 1000 Hz.

<sup>2</sup> Crack-tip opening displacements,  $\delta$ , were calculated in terms of the yield stress,  $\sigma_y$ , and appropriate Young's modulus,  $E'$ , from  $\delta \approx \beta(K^2/\sigma_y E')$ . The constant  $\beta$  is a function of the yield strain,  $\sigma_y/E'$ , the strain-hardening coefficient and whether plane-stress or plane-strain conditions are assumed; a value of 0.8 was used for Ti-6Al-4V, based on the numerical calculations of Shih [27].

### 3.4. Intrinsic thresholds

Since threshold values are experimentally measured at such high load ratios in the apparent total absence of an influence of crack closure, their magnitude should approach that of the so-called *intrinsic* threshold. Several estimates of this parameter have been theoretically calculated to represent the absolute lower-bound stress intensity for fatigue-crack growth.

The simplest approach to estimate the intrinsic threshold is to extrapolate the Paris law regime down to the point where the crack increment per cycle is on the order of a lattice spacing per cycle. In Ti–6Al–4V, this gives lower-bound  $\Delta K_{TH}$  thresholds of  $\sim 4.6$ ,  $3.0$ , and  $2.8$  MPa $\sqrt{m}$  at  $R$  values of  $0.1$ ,  $0.5$ , and  $0.8$ , respectively. Clearly, this approach is overly simplistic because near-threshold crack advance does not occur uniformly across the entire crack front; the measured  $da/dN$  values do not describe growth locally, but rather an average growth occurring over the entire crack front.

A more sound approach is to model the intrinsic threshold in terms of the applied driving force below which dislocations can no longer be emitted from the crack tip [29, 30]. In this regard, the approach of Sadananda and Shahinian [29] considers the total energy required to drive a dislocation from a crack tip as the sum of four components: the 'self' energy of the dislocation,  $U_s$ , the surface energy created by the slip step at the crack tip,  $U_p$ , the lattice frictional energy required to move a dislocation,  $U_f$ , and the energy from an image force,  $U_i$ , imparted by the presence of the nearby free surface (crack wake). This total energy  $U_T$  is then converted into a required shear stress and stress intensity:

$$U_T = U_s + U_p + U_f + U_i = \tau_{xy} b^2 \quad (2)$$

$$= \frac{Kb^2}{\sqrt{2\pi\rho}} \left( \cos \frac{\theta}{2} \sin \frac{\theta}{2} \cos \frac{3\theta}{2} \right)$$

where  $b$  is the Burgers vector,  $\rho$  is the distance between the dislocation and the crack tip (taken here to equal  $b$ ),  $\theta$  is the angle between the actual crack propagation direction and the pure Mode-I direction,  $\tau_{xy}$  is the shear stress required to drive the dislocation, and  $K$  is the corresponding stress intensity. The analysis predicts the threshold to occur when  $K_{max}$  is no longer sufficient to emit a dislocation, i.e. when:

$$K_{max,TH} \propto \tau_{xy}(b)^{\frac{1}{2}} \quad (3)$$

For Ti–6Al–4V, the predicted intrinsic threshold  $K_{max,TH}$  is  $4.3$  MPa $\sqrt{m}$  for all  $R$  values. This compares well to the experimentally measured values at  $R=0.1$  where  $K_{max,TH}=5.1$  MPa $\sqrt{m}$ ; however, at  $R=0.92$  where  $K_{max,TH}$  is held at  $26.5$  MPa $\sqrt{m}$ , the prediction is clearly questionable, possibly because the analysis is essentially based on static (monotonic) loading and makes no allow-

ance for reversed plasticity and enhanced crack-tip blunting at high  $R$  values.

The corresponding approach of Weertman [30] is also based on the limiting conditions for dislocation emission from an atomically sharp crack, in this case using the perfectly brittle Griffith solution modified by a parameter,  $g$ , which describes the degree of ductility:

$$\Delta K_{TH} = 2g \left[ \frac{2E\gamma}{1-\nu^2} \right]^{\frac{1}{2}} \quad (4)$$

Here  $E$  is the Young's modulus,  $\nu$  is Poisson's ratio, and  $\gamma$  is the true surface energy of the solid. The modifying parameter,  $g$ , is a function of the theoretical tensile strength normalized by the theoretical shear strength (typical values are taken between  $0.6$  and  $1$ , with unity representing the perfectly brittle case). Using this approach, the intrinsic threshold for Ti–6Al–4V is predicted to be on the order of  $1$  MPa $\sqrt{m}$ . Whereas this represents a better estimate of a theoretical lower bound for the fatigue threshold, it is a factor of  $2$  smaller than experimentally measured lower-bound values, possibly because the approach also does not taken into account cyclic plasticity, both in the form of crack-tip blunting and dislocation shielding arising from the presence of the plastic zone at the crack tip.

### 3.5. Effect of foreign object damage

As foreign object damage can be a prime source of cracks initiated in HCF, the role of simulated FOD on thresholds and early crack growth was examined using specimens previously impacted by steel shot at velocities between  $200$  and  $300$  m/s. An SEM micrograph of a typical impact site at  $300$  m/s is presented in Fig. 10 with a schematic illustration of the relevant features in the crater profile. While at  $300$  and  $250$  m/s, shear bands were seen emanating from the surface of the crater, such shear bands were not observed for  $200$  m/s impacts. In addition, the  $300$  m/s impact caused a piling-up of material along the crater rim; this feature was not seen for the lower velocity impacts.

The effect of these impact damage sites was to reduce the fatigue life markedly compared to that obtained with an un-impacted smooth-bar sample. At a maximum applied stress of  $500$  MPa ( $R=0.1$ ), single fatigue cracks in the  $200$  m/s impacted samples were initiated near the bottom of the crater within  $\sim 4.3 \times 10^4$  cycles, whereas in the  $300$  m/s FOD site, the crack initiated at the crater rim within  $\sim 2.9 \times 10^4$  cycles. In terms of total life, the  $200$  m/s impacted sample also resulted in a longer overall fatigue life of  $7.5 \times 10^4$  cycles, compared to  $4.6 \times 10^4$  cycles from the  $300$  m/s impacted sample. These lives are to be compared with corresponding behavior in a smooth bar, where initiation and total lives at this stress exceed  $10^7$  cycles (i.e.  $500$  MPa is below the  $10^7$ -cycle fatigue limit for this material).

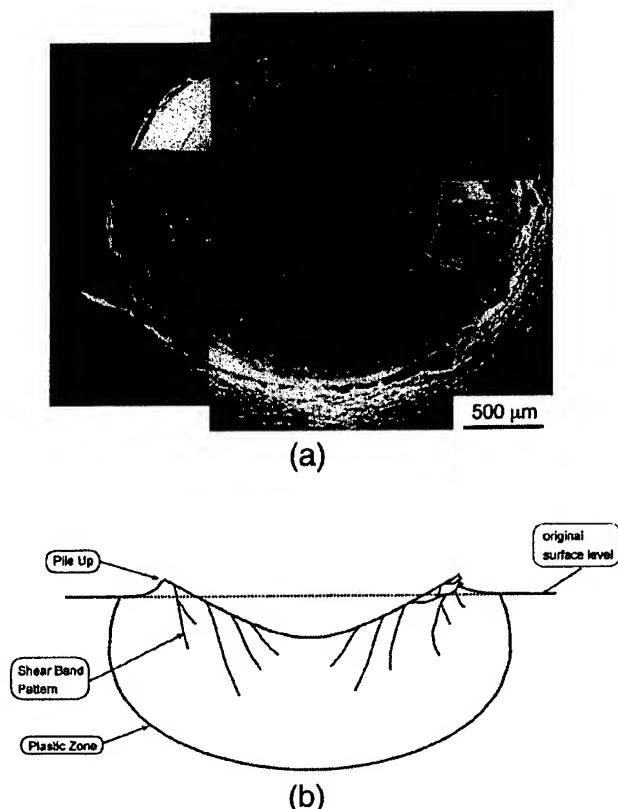


Fig. 10. (a) SEM micrograph of simulated foreign object damage resulting from an impact by a hardened steel sphere with an incident velocity of 300 m/s and (b) corresponding schematic illustrating features present at 300 and 250 m/s. At 200 m/s neither the shear bands nor the 'pile up' were observed.

Consistent with previous low-cycle fatigue results [31], the presence of the shear bands did not appear to play a significant role in the overall fatigue life, e.g. the initiation of the fatigue cracks at damage sites did not appear to be directly associated with them. It is possible, though, that shear banding will have an effect on fatigue behavior at lower applied stresses when lives exceed  $\sim 10^6$  cycles.

The growth rates of the small cracks originating from such impact sites are compared in Fig. 11 with growth-rate data for large ( $>5$  mm) and naturally-initiated small ( $\sim 45$ – $1000$   $\mu\text{m}$ ) cracks in this microstructure. Both the naturally-initiated and FOD-initiated small-crack velocities were within the same scatter band, initially up to an order of magnitude faster than corresponding large-crack results (although small-crack data tended to merge with large-crack results above  $\Delta K = \sim 10$   $\text{MPa}\sqrt{\text{m}}$  as the crack size increased). However, in the limited data collected to date, no FOD-initiated cracks have been observed in the STOA Ti-6Al-4V material below a  $\Delta K$  of  $\sim 2.9$   $\text{MPa}\sqrt{\text{m}}$ ; i.e. no FOD-initiated cracking was observed below the lower-bound (large-crack) threshold,  $\Delta K_{\text{TH}}$ .

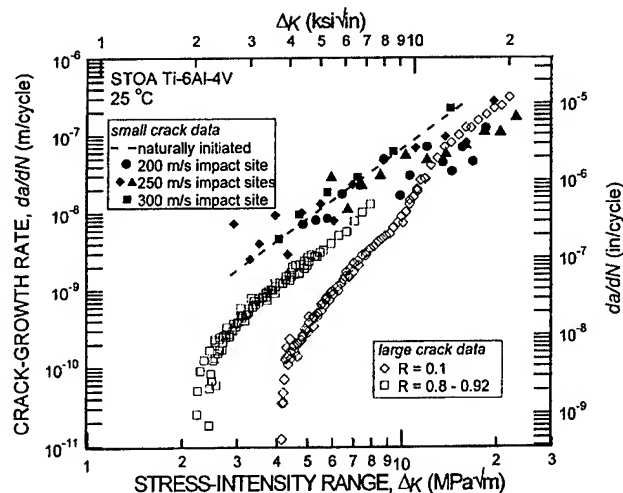


Fig. 11. Fatigue crack propagation rates of naturally-initiated small ( $45$ – $1000$   $\mu\text{m}$ ) cracks (dashed line) and small cracks emanating from a variety of FOD impact sites (closed symbols). These small crack results obtained at  $R=0.1$  are compared to large cracks at  $R=0.1$  and  $R=0.8$ – $0.92$  (open symbols).

#### 4. Summary

The problem of turbine engine high-cycle fatigue requires that design must be based on the notion of a threshold stress intensity for no crack growth under the appropriate conditions of high mean loads, ultrahigh frequency (vibratory) loading, and small crack sizes. Since the measurement of small-crack thresholds is experimentally tedious and complex, the approach used in the current work has been to simulate such thresholds with lower-bound large-crack measurements. Our preliminary results in Ti-6Al-4V show that using constant  $K_{\text{max}}$ /increasing  $K_{\text{min}}$  cycling, a  $\Delta K_{\text{TH}}$  threshold for large ( $>5$  mm) cracks can be measured at very high load ratios ( $R \sim 0.92$ ) and frequencies (1 kHz) which is a lower bound compared to that of naturally-initiated small ( $45$ – $1000$   $\mu\text{m}$ ) cracks and small cracks emanating from sites of foreign object damage.

#### 5. Conclusions

Based on a preliminary investigation into the high-cycle fatigue of a solution treated and overaged Ti-6Al-4V turbine engine alloy, the following conclusions can be made:

1. Ambient-temperature fatigue-crack propagation (over the range  $\sim 10^{-11}$  to  $10^{-6}$  m/cycle) and threshold  $\Delta K_{\text{TH}}$  values were found to be independent of test frequency (50–1000 Hz) for large ( $>5$  mm) through-thickness cracks.
2. A lower-bound threshold, measured for large cracks at  $R=0.92$  under constant- $K_{\text{max}}$ /increasing- $K_{\text{min}}$  con-

ditions, was found to be 2.2 MPa $\sqrt{m}$  for this alloy. This should be compared with measurements on naturally-initiated small cracks and FOD-initiated small cracks in the same microstructure, where small-crack growth was not reported below a  $\Delta K$  of 2.9 MPa $\sqrt{m}$ .

3. Foreign object damage, simulated by hardened steel spheres impacted at 200–300 m/s on a flat surface, provide sites for the initiation of small fatigue cracks. At applied stresses some 10% below the smooth-bar,  $10^7$ -cycles fatigue strength, crack-initiation lives were less than  $4 \times 10^4$  cycles, many orders of magnitude shorter than in un-impacted samples. Subsequent small-crack growth from the damage sites was found to occur at rates considerably faster than large cracks subjected to the same applied  $\Delta K$  level. No crack growth from FOD sites has been observed to date at  $\Delta K$  values less than 2.9 MPa $\sqrt{m}$ ; i.e. no FOD-initiated cracking was seen below the lower-bound  $\Delta K_{TH}$ .

### Acknowledgements

This work was supported by the US Air Force Office of Scientific Research under Grant No. F49620-96-1-0478 under the auspices of the Multidisciplinary University Research Initiative on *High Cycle Fatigue* to the University of California at Berkeley. B.L.B. would also like to acknowledge the support of the Hertz Foundation. Special thanks are due to Prof. G. Lütjering, Dr J.A. Hines and Dr J.O. Peters of the Technische Universität Hamburg-Harburg for providing us with their naturally-initiated small-crack results, and to Dr D.L. Davidson of the Southwest Research Institute for numerous helpful discussions.

### References

- [1] Report of the AdHoc Committee on Air Force Aircraft Jet Engine Manufacturing and Production Processes. The Pentagon, Washington (DC): United States Air Force Scientific Advisory Board, SAF/AQOS, 1992.
- [2] Cowles BA. High cycle fatigue in aircraft gas turbines—an industry perspective. *Int J Fract* 1996;80:147–63.
- [3] Chang JCI. An integrated research approach to attack engine HCF problems. Washington (DC): Air Force Office of Scientific Research, 1996.
- [4] Taylor D. A compendium of fatigue thresholds and crack growth rates. Warley (UK): EMAS Ltd, 1985.
- [5] Ritchie RO. Near-threshold fatigue crack propagation in steels. *Int Metals Rev* 1979;20(5–6):205–30.
- [6] Larsen JM, Worth BD, Annis CG, Haake FK. An assessment of the role of near-threshold crack growth in high-cycle-fatigue life prediction of aerospace titanium alloys under turbine engine spectra. *Int J Fract* 1996;80:237–55.
- [7] Ritchie RO. Small cracks and high-cycle fatigue. In: Chang JCI, Coulter J, Brei D, Martinez WHG, Friedmann PP, editors. Proceedings of the ASME Aerospace Division. New York: ASM, 1996:321–33.
- [8] Ritchie RO, Lankford J. Small fatigue cracks: a statement of the problem and potential solutions. *Mater Sci Engng* 1986;84:11–6.
- [9] Döker H, Bachmann V, Marci G. A comparison of different methods of determining the threshold for fatigue crack propagation. In: Bäcklund J, Blom AF, Beevers CJ, editors. Fatigue thresholds, Proceedings of the 1st International Conference. Warley (UK): EMAS Lt, 1982:45–57.
- [10] Herman WA, Hertzberg RW, Jaccard R. Influence of mean stress on fatigue in several aluminium alloys utilizing  $K_{max}$  threshold procedures. *Fat Fract Engng Mater Struct* 1988;11:303–20.
- [11] Pippin R, Plochl L, Klanner F, Stuwe HP. The use of fatigue specimens precracked in compression for measuring threshold values and crack growth. *J Test Eval* 1994;22(2):98–103.
- [12] Aswath PB, Suresh S, Holm DK, Blom AF. Load interaction effects on compression fatigue crack growth in ductile solids. *J Engng Mater Technol* 1988;110(3):275–85.
- [13] Eylon D. Summary of the available information on the processing of the Ti–6Al–4V HCF/LCF program plates. University of Dayton Report, Dayton (OH), 1998.
- [14] Ritchie RO, Yu W. Short crack effects in fatigue: a consequence of crack tip shielding. In: Ritchie RO, Lankford J, editors. Small fatigue cracks. Warrendale (PA): TMS-AIME, 1986:167–89.
- [15] Morgan JM, Milligan WW. A 1 kHz servohydraulic fatigue testing system. In: Soboyejo WO, Srivatsan TS, editors. High cycle fatigue of structural materials. Warrendale (PA): TMS, 1997:305–12.
- [16] Coles A, Johnson RE, Popp HG. Utility of surface-flawed tensile bars in cyclic life studies. *J Engng Mater Technol* 1976;98:305–15.
- [17] Newman JC Jr., Raju IS. An empirical stress-intensity factor equation for the surface crack. *Engng Fract Mech* 1981;15:185–92.
- [18] Sarrazin C, Chiron R, Lesterlin S, Petit J. Electron backscattering pattern identification of surface morphology of fatigue cracks in TA6V. *Fat Fract Engng Mater Struct* 1994;17(12):1383–9.
- [19] Halliday MD, Beevers CJ. Some aspects of fatigue crack closure in two contrasting titanium alloys. *J Test Eval* 1981;9(4):195–201.
- [20] Ravichandran KS. Near threshold fatigue crack growth behavior of a titanium alloy: Ti–6Al–4V. *Acta Metall Mater* 1991;39(3):401–10.
- [21] Ogawa T, Tokaji K, Ohya K. The effect of microstructure and fracture surface roughness on fatigue crack propagation in a Ti–6Al–4V alloy. *Fat Fract Engng Mater Struct* 1993;16(9):973–82.
- [22] Dubey S, Soboyejo ABO, Soboyejo WO. An investigation of the effects of stress ratio and crack closure on the micromechanisms of fatigue crack growth in Ti–6Al–4V. *Acta Mater* 1997;45(7):2777–87.
- [23] Schmidt RA, Paris PC. Threshold for fatigue crack propagation and effects of load ratio and frequency. In: Progress in fatigue crack growth and fracture testing. ASTM STP 536, 1973:79–94.
- [24] Ritchie RO, Boyce BL, Campbell JP, Roder O. High cycle fatigue of turbine engine alloys. In: Proceedings of the 24th Symposium on Fatigue, Japan. The Society of Materials Science (Committee on Fatigue, 1998:1–6.
- [25] Davidson DL. Southwest Research Institute, private communication, 1998.
- [26] Morrissey RJ, McDowell DL, Nicholas T. Frequency and stress ratio effects in high cycle fatigue of Ti–6Al–4V. In: Stange WA, Henderson J, editors. Proceedings of the Third National Turbine Engine High Cycle Fatigue Conference (session 1, CD-ROM). Dayton (OH): Universal Technology Cor, 1998:21–30.
- [27] Shih CF. Relationships between the  $J$ -integral and the crack opening displacement for stationary and extending cracks. *J Mech Phys Solids* 1981;29(4):305–26.
- [28] Lütjering G, Hines JA, Peters JO. Technische Universität Hamburg-Harburg, private communication, 1998.
- [29] Sadananda K, Shahinian PP. Prediction of threshold stress inten-

- sity for fatigue crack growth using a dislocation model. *Int J Fract* 1977;13(5):585–94.
- [30] Weertman J. Fatigue crack growth in ductile metals. In: Mura T, editor. *Mechanics of fatigue*. New York: ASME, 1982:11–9.
- [31] Timothy SP, Hutchings IM. Influence of adiabatic shear bands on the fatigue strength of a titanium alloy. *Fat Engng Mater Struct* 1984;7(3):223–7.



# High-cycle fatigue of Ti-6Al-4V

R. O. RITCHIE, D. L. DAVIDSON<sup>1</sup>, B. L. BOYCE, J. P. CAMPBELL and O. RÖDER

*Department of Materials Science and Mineral Engineering, University of California, Berkeley, CA 94720-1760, USA, <sup>1</sup>Southwest Research Institute, P.O. Drawer 28510, 6220 Culebra Road, San Antonio, TX 78228-0510, USA*

**ABSTRACT** The definition of the critical levels of microstructural damage that can lead to the propagation of fatigue cracks under high-cycle fatigue loading conditions is a major concern with respect to the structural integrity of turbine-engine components in military aircraft. The extremely high cyclic frequencies characteristic of in-flight loading spectra, coupled with the presence of small cracks resulting from fretting or foreign object damage (FOD), necessitate that a defect-tolerant design approach be based on a crack-propagation threshold. The present study is focused on characterizing such near-threshold fatigue-crack propagation behaviour in a Ti-6Al-4V blade alloy (with ~60% primary  $\alpha$  in a matrix of lamellar  $\alpha + \beta$ ), at high frequencies (20–1500 Hz) and load ratios (0.1–0.95) in both ambient temperature air and vacuum environments. Results indicate that 'worst-case' thresholds, measured on large cracks, may be used as a practical lower bound to describe the onset of naturally initiated small-crack growth and the initiation and early growth of small cracks emanating from sites of simulated FOD.

**Keywords** high-cycle fatigue; crack propagation; foreign object damage; fatigue thresholds; small cracks; titanium alloys.

## INTRODUCTION

High-cycle fatigue (HCF) has been identified as one of the prime causes of turbine-engine failure in military aircraft.<sup>1</sup> It can result in essentially unpredictable failures due to the propagation of fatigue cracks in blade and disk components under ultrahigh-frequency loading, where the cracking initiates from small defects often associated with microstructural damage caused by fretting or foreign object impacts.<sup>2</sup> To prevent HCF failures, design methodologies are required that identify the critical levels of microstructural damage which can lead to such failures. The current study is focused on identifying these critical levels of damage and in characterizing fatigue behaviour under representative operating conditions in a Ti-6Al-4V alloy, typically used in the front, low-temperature stages of the engine.

During HCF, engine components experience high-frequency (~1–2 kHz) vibrational loads due to resonant airflow dynamics, often superimposed on a high mean stress,<sup>2,3</sup> although the exact source and magnitude of the stresses remains uncertain. Because of the high frequencies, even cracks growing at slow per-cycle velocities (i.e.  $\sim 10^{-10}$ – $10^{-9}$  m/cycle) propagate to failure in a short period of time; consequently, HCF-critical turbine com-

ponents must be operated below the fatigue-crack propagation threshold ( $\Delta K_{TH}$ ) such that crack propagation cannot occur (within  $\sim 10^9$  cycles). An extensive database (e.g. Refs [4,5]) exists for such thresholds; however, it has been largely derived from standard test geometries containing large (> few mm) through-thickness cracks, often under loading conditions that may not be representative of turbine-engine HCF. Furthermore, except under specific loading conditions, e.g. at high mean loads, as discussed below, such tests are not necessarily relevant to the HCF problem, where the critical flaw sizes are much smaller, i.e.  $< 500 \mu\text{m}$ .<sup>6</sup> Because small cracks can grow at velocities faster than corresponding large cracks (at the same applied driving force) and can propagate below the large-crack  $\Delta K_{TH}$  threshold, design against HCF failure must be based on the notion of a practical small-crack threshold, measured under the representative conditions.<sup>7</sup>

The principal reasons why small cracks behave differently from large cracks are associated with crack sizes becoming comparable to: (i) microstructural size scales, where biased sampling of the microstructure leads to accelerated crack advance along 'weak' paths (a continuum limitation); (ii) the extent of local plasticity ahead of the crack tip, where the assumption of small-scale

yielding implicit in the use of the stress intensity,  $K$ , is not strictly valid (a linear-elastic fracture mechanics limitation); and (iii) the extent of crack-tip shielding (e.g. by crack closure) behind the crack tip, where the reduced role of shielding leads to a higher local driving force than the corresponding large crack at the same applied  $\Delta K$  (a similitude limitation).<sup>8</sup>

Of these three classes of small cracks, we believe that the latter (the physically small crack) is most important in the present case, as cyclic plastic-zone sizes will generally not exceed a few micrometres, and the crack sizes relevant to the aircraft HCF problem are invariably much larger than the characteristic microstructural dimensions. However, as it would be difficult to design engine components on the basis of small-crack results, simulating such results using a reproducible large-crack technique would appear to offer a feasible and practical solution. The philosophy here is that as the relevant crack sizes in HCF are not small compared to microstructural size-scales or the dimensions of local inelasticity, then the principal difference between large and small cracks lies in the degree of crack-tip shielding present in the crack wake. Thus, by performing large-crack tests where the extent of crack closure behind the crack tip is minimized, it is reasoned that a worse-case large-crack threshold can be measured which would reflect the behaviour of physically small cracks. It should be emphasized that such procedures will not work where crack sizes become small compared to microstructural dimensions.

Accordingly, in the present work, we compare fatigue threshold values and the near-threshold crack growth rate behaviour of large ( $>5$  mm) through-thickness cracks, naturally initiated small ( $\sim 45$ – $1000$   $\mu\text{m}$ ) cracks, and small ( $<500$   $\mu\text{m}$ ) surface cracks initiated from artificially induced notches and from sites of simulated foreign object damage (FOD), in a single microstructure of Ti-6Al-4V, tested at high frequencies ( $\sim 50$ – $1500$  Hz) and load ratios ( $R \sim 0.1$ – $0.95$ ) in both room air and vacuum environments. In addition to seeking insight into the mechanisms of crack growth under these conditions, we examine whether 'worst-case' threshold values, measured for the large cracks using standard test geometries subject to special loading conditions, can have any utility as a practical lower bound for the onset of small-crack growth under HCF conditions.

## EXPERIMENTAL PROCEDURES

### Material and microstructure

A Ti-6Al-4V alloy, with a composition (in wt%) of 6.30Al, 4.17V, 0.19Fe, 0.19O, 0.013N, bal. Ti, was supplied from a set of forgings produced specifically for

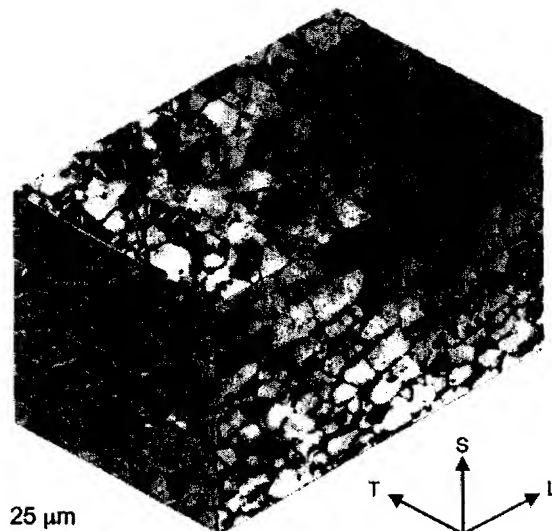


Fig. 1 Optical micrograph of the microstructure of the solution-treated and overaged Ti-6Al-4V studied. The microstructure consists of  $\approx 60\%$  primary  $\alpha$  and  $40\%$  lamellar  $\alpha + \beta$  colonies. The grains were slightly elongated along the L forging axis. All fatigue specimens were extracted in the L-T orientation (such that the crack surface was in the S-T plane and the crack propagated in the T direction). (Etched in Kroll's solution.)

the US Air Force sponsored program on HCF. The bar-stock, originating from Teledyne Titanium, was forged into  $400 \times 150 \times 20$  mm plates and subsequently solution-treated at  $925^\circ\text{C}$  (1 h) and vacuum-annealed at  $700^\circ\text{C}$  (2 h) for stabilization. The microstructure consisted of a bimodal distribution of  $\sim 60$  vol.% primary- $\alpha$  and  $\sim 40$  vol.% lamellar colonies of  $\alpha + \beta$  (Fig. 1), with a tensile strength of 970 MPa, a yield strength of 926–935 MPa and a Young's modulus of 116 GPa (based on tensile tests conducted along the longitudinal axis at a strain rate of  $5 \times 10^{-4} \text{ s}^{-1}$ ).<sup>9</sup>

To minimize residual stresses in this material, all small-crack test samples were machined using low-stress procedures, and chemically milled or electropolished to remove  $\sim 30$ – $100$   $\mu\text{m}$  of material.

### Fatigue-crack propagation testing

#### Large-crack testing

Large-crack propagation studies were conducted in ambient temperature air on compact-tension C(T) specimens machined in the L-T orientation (8 mm thick, 25 mm wide) at  $R$  ratios (ratio of minimum to maximum loads) varying from 0.10 to 0.95 in a lab air environment ( $22^\circ\text{C}$ ,  $\sim 45\%$  relative humidity). Crack lengths were monitored *in situ* using the back-face strain compliance

technique, and were verified periodically by optical inspection. Macroscopic levels of crack closure were also monitored using back-face strain compliance; specifically, the (global) closure stress intensity,  $K_{cl}$ , was approximated from the closure load, measured at the point of first deviation from linearity in the elastic compliance curve upon unloading.<sup>10</sup>

To approach the threshold, both constant and variable  $R$ -testing was employed. Under both conditions, loads were shed such that  $\Delta K = \Delta K_{initial} \exp[C(a - a_{initial})]$ , with the normalized  $K$ -gradient,  $C$ , set to  $-0.08 \text{ mm}^{-1}$ , as suggested in ASTM Standard E-647 ( $\Delta K$  is the stress-intensity range and  $a$  is the crack length). With variable  $R$ -testing, the threshold was approached under constant  $K_{max}$ /increasing  $K_{min}$  conditions to minimize the effect of crack closure.<sup>11,12</sup> At 50–200 Hz (sine wave), tests were conducted on conventional MTS servo-hydraulic testing machines operating under automated closed-loop  $K$  control, with the fatigue thresholds,  $\Delta K_{TH}$  and  $K_{max,TH}$ , defined as the minimum values of these parameters yielding a propagation rate of  $10^{-10} \text{ m/cycle}$ . Corresponding fatigue tests at 1000 Hz were performed under  $K$  control on a newly developed MTS servo-hydraulic test frame using a voice-coil servovalve; details of this instrument are described elsewhere.<sup>13</sup> At the higher frequencies, thresholds could be readily defined at a lower propagation rate of  $10^{-11} \text{ m/cycle}$ .

Results are presented in the form of the crack growth increment per cycle,  $da/dN$ , plotted as a function of the applied stress-intensity range,  $\Delta K = K_{max} - K_{min}$ . Where the effect of closure is considered, growth rates are alternatively plotted in terms of the effective (near-tip) stress-intensity range,  $\Delta K_{eff} = K_{max} - K_{cl}$ .

#### Small-crack testing

Specifically to investigate the mechanistic aspects of HCF cracking in this alloy, small ( $< 750 \mu\text{m}$ ) surface crack tests were performed *in vacuo* ( $\sim 10^{-6}$  torr) on tensile samples (44 mm long with a  $12.5 \times 3.2 \text{ mm}$  rectangular cross-section) at  $\sim 1.5 \text{ kHz}$  with load ratios between 0.20 and 0.85 in a specially designed magnetostrictive loading stage for the scanning electron microscope (SEM). Cracks were initiated in three-point bending at artificial notches, generated either using electro-discharge machining ( $\sim 250 \mu\text{m}$  in diameter,  $250 \mu\text{m}$  deep) or focused ion beam milling ( $\sim 30 \mu\text{m}$  long,  $5 \mu\text{m}$  wide,  $30 \mu\text{m}$  deep).

In addition, the growth rates of small surface cracks initiated from sites of simulated FOD were examined at an applied maximum stress of 500 MPa (at  $R = 0.1$  with a frequency of 20 Hz) using cylindrical (buttonhead) tensile specimens containing a rectangular gauge section. The damage was obtained by firing 3.2-mm-diameter,

chrome-hardened steel spheres, using compressed gas, onto the flat specimen surface, which had previously been stress relieved and chemically milled to give a nominally stress-free surface. In this study, normal impacts (i.e. incident path orthogonal to the sample surface) were performed at velocities between  $\sim 200$  and  $300 \text{ m/s}$ , representing typical in-service impact velocities on blades.

The initiation and growth of such small cracks was measured in the SEM, either *in situ* with the notched tensile specimens or periodically with the simulated FOD specimens. Stress intensities characterizing such crack growth were computed from the Newman-Raju semielliptical surface crack solution,<sup>14</sup> assuming a half-surface length to depth ratio of 0.9–1 (based on fractographic observations).

## RESULTS AND DISCUSSION

### Large-crack behaviour

#### Effect of load ratio

The effect of load ratio ( $R = 0.1$ – $0.8$ ) on the fatigue-crack propagation rates of large ( $> 5 \text{ mm}$ ) cracks, shown in Fig. 2 for Ti-6Al-4V at 50 Hz, indicates (as expected) that higher load ratios induce lower  $\Delta K_{TH}$  thresholds and faster growth rates at a given applied  $\Delta K$  level. Threshold stress intensity ranges varied from  $4.6 \text{ MPa}\sqrt{\text{m}}$  at  $R = 0.1$  to  $2.6 \text{ MPa}\sqrt{\text{m}}$  at  $R = 0.8$ . A two-parameter fit of the Paris regime yields a growth

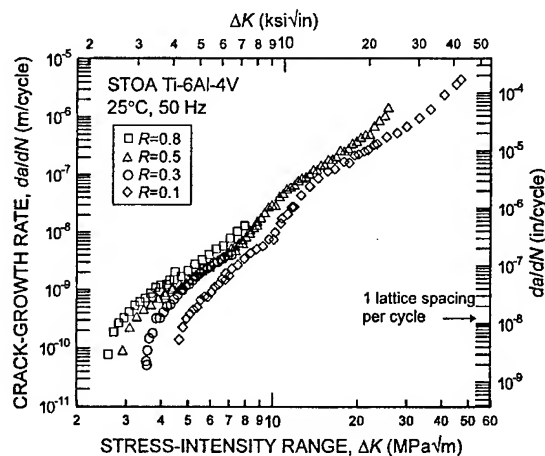


Fig. 2 Fatigue-crack propagation behaviour (large-crack), in the form of growth rates,  $da/dN$ , as a function of the applied stress intensity range,  $\Delta K$ , for a solution-treated and overaged Ti-6Al-4V in room air at  $R = 0.1, 0.3, 0.5$  and  $0.8$  (at 50 Hz frequency).  $\Delta K_{TH}$  fatigue thresholds, measured at growth rates of  $10^{-10} \text{ m/cycle}$ , were 4.6, 3.6, 2.9 and  $2.6 \text{ MPa}\sqrt{\text{m}}$ , respectively.

law of (units: m/cycle, MPa√m):

$$\frac{da}{dN} = 5.2 \times 10^{-12} \Delta K^{2.5} K_{\max}^{0.67} \quad (1)$$

The observed effect of load ratio is commonly attributed to the role of crack closure, which in Ti alloys is primarily associated with the roughness-induced mechanism (i.e. arising from the wedging of crack-surface asperities, e.g. Refs [15–17]). To examine this, closure stress intensity values,  $K_{cl}$ , were measured globally at each load ratio using back-face strain compliance. No detectable (global) closure was observed at  $R=0.5$  and  $0.8$ ; however, at  $R=0.1$ ,  $K_{cl}$  values were observed to be roughly constant at  $\sim 2.0$  MPa√m [Fig. 3(a)]. In Fig. 3(b), the results of Fig. 2 are replotted in terms of

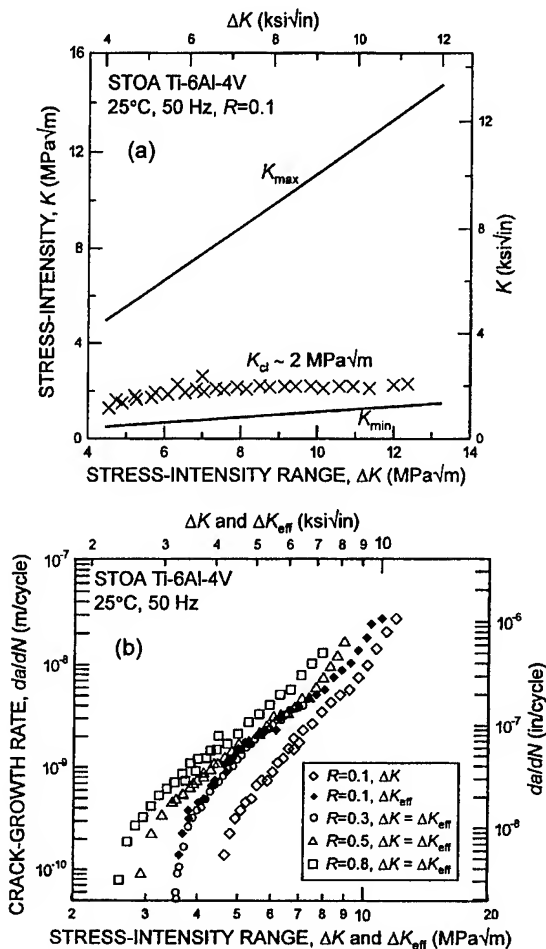


Fig. 3 Crack closure considerations: (a) closure, measured by unloading compliance, stays approximately constant at  $K_{cl} \sim 2$  MPa√m; (b) crack growth rates in terms of  $\Delta K_{eff}$  ( $= K_{\max} - K_{cl}$ ) showing the effect of load ratio between  $R=0.1$  and  $0.5$  is far less pronounced.

the effective stress-intensity range, after accounting for such closure. It is apparent that, similar to previous studies in this alloy,<sup>18</sup> characterizing growth rates in terms of  $\Delta K_{eff}$  reduces the disparity in crack-growth behaviour between the four  $R$  ratios, implying that an important origin of the load ratio effect is indeed crack closure. However, above  $R \sim 0.5$  where the role of closure is presumed to be minimal, near-threshold crack-growth rates continue to increase somewhat, and  $\Delta K_{TH}$  thresholds continue to decrease, with increasing  $R$  (see also Fig. 6). This indicates that there may be additional mechanisms, independent of global closure and apparently both  $K_{\max}$  and  $\Delta K$  related, which are responsible for the load ratio effect at very high  $R$ -values. Alternatively, the effect may be due to the presence of local (near-tip) crack closure which cannot be detected using global methods, e.g. back-face strain compliance. Indeed, such local closure has been detected in microscopy studies, as described below.

The measured variation with load ratio of the threshold  $\Delta K_{TH}$  and  $K_{\max,TH}$  values, plotted in Fig. 4, can be compared with the simple closure model of Schmidt and Paris.<sup>19</sup> This model is based on the notion that  $K_{cl}$  and the effective  $\Delta K$  threshold,  $\Delta K_{eff,TH}$ , are constant and independent of  $R$ ; it predicts that measured  $\Delta K_{TH}$

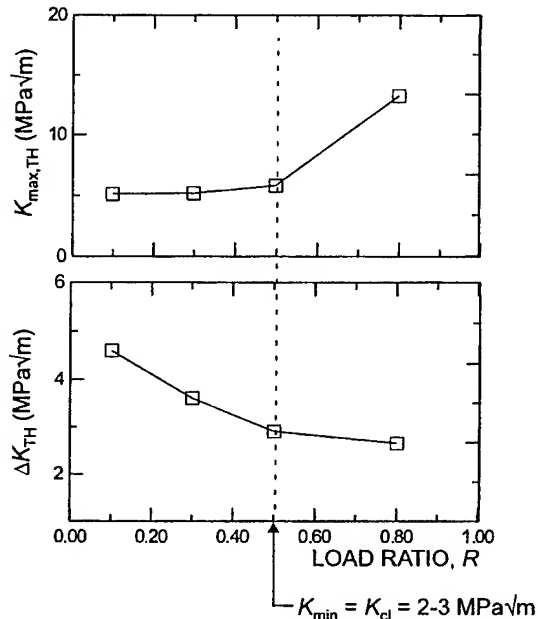


Fig. 4 The variation of  $K_{\max,TH}$  and  $\Delta K_{TH}$  with load ratio appears to follow the Schmidt and Paris closure model.<sup>19</sup> Although more data are required to clearly establish a transition, the results presented here show a change in slope at  $R \approx 0.5$ , consistent with a  $K_{cl}$  value of  $2-3$  MPa√m, similar to that measured directly from test samples using unloading compliance techniques.

and  $K_{\max,TH}$  thresholds will be load ratio independent, respectively, above and below a transition  $R$  at which point  $K_{\min} = K_{cl}$ . Although clearly there are insufficient data to verify this analysis, the present constant- $R$  results are consistent with this model, and the transition  $R$ , above which closure is ineffective ( $K_{\min} > K_{cl}$ ), is observed at  $K_{\min} = K_{cl} \approx 2-3 \text{ MPa}\sqrt{\text{m}}$ . Such an estimate of  $K_{cl}$  is consistent with the experimentally measured values [Fig. 3(a)] determined from back-face strain compliance.

#### Effect of frequency

The role of cyclic frequency is shown in Fig. 5, where the growth rates at 50 Hz are compared with data collected at 1000 Hz (at UCB) and 1100–1500 Hz (at SWRI). It is clear that the high-frequency results are not statistically distinguishable from the conventional frequency data. Additional limited experiments at 200 Hz (performed on a conventional servohydraulic machine) and 20 000 Hz (performed by Bathias and co-workers<sup>20</sup> using ultrasonic fatigue testing on a similar microstructure) confirmed this lack of a frequency effect on ambient temperature growth rate behaviour in Ti-6Al-4V. The absence of frequency-dependent growth rates for titanium alloys tested in air over the range 0.1–50 Hz has been reported previously in the literature;<sup>21,22</sup> the current work extends this observation for Ti-6Al-4V to beyond 1000 Hz.

Testing at high frequencies permits thresholds to be defined at lower growth rates. Using the ASTM standard  $K$ -gradient of  $0.08 \text{ mm}^{-1}$ , measurements down to  $10^{-11}$

m/cycle may require several weeks at 50 Hz, whereas these same measurements can be obtained in a single day at 1000 Hz and within a few hours at 20 000 Hz. In the present study, thresholds measured at  $\sim 10^{-11}$ – $10^{-12}$  m/cycle (at 1000 Hz or above) were found to be  $\sim 0.1$ – $0.2 \text{ MPa}\sqrt{\text{m}}$  lower than the  $10^{-10}$  m/cycle thresholds measured at any frequency.

#### Effect of loading sequence

In an attempt to measure 'lower-bound' thresholds, i.e. at very high  $R$ -values where the effect of crack closure is minimized, additional variable  $R$  testing was performed at 1000 Hz using constant  $K_{\max}$ /increasing  $K_{\min}$  loading sequences (Fig. 6). Here, at a constant  $K_{\max}$  of  $26.5 \text{ MPa}\sqrt{\text{m}}$ , a final load ratio of  $R = 0.92$  was achieved, yielding a threshold of  $2.2 \text{ MPa}\sqrt{\text{m}}$ ; with a constant  $K_{\max}$  of  $36.5 \text{ MPa}\sqrt{\text{m}}$ , a threshold of  $\Delta K_{TH} = 1.9 \text{ MPa}\sqrt{\text{m}}$  was achieved with a final load ratio of  $R = 0.95$ . These values should be compared to a  $\Delta K_{TH}$  value of  $2.6 \text{ MPa}\sqrt{\text{m}}$  for constant  $R = 0.8$  testing. It should be noted that the effect of closure is expected to be minimal here as the high load ratios result in an extremely large minimum crack-tip opening displacement ( $\text{CTOD}_{\min} \approx 0.6$  and  $8.0 \mu\text{m}$  for  $R = 0.8$  and  $0.95$ , respectively), as computed from the numerical analysis of Shih.<sup>23</sup>

The  $\Delta K_{TH}$  threshold value of  $1.9 \text{ MPa}\sqrt{\text{m}}$  measured under constant  $K_{\max}$ /increasing  $K_{\min}$  cycling at  $R = 0.95$  is considered to represent the lowest threshold for large cracks measured to date in Ti-6Al-4V. It should be compared with measurements on naturally initiated small

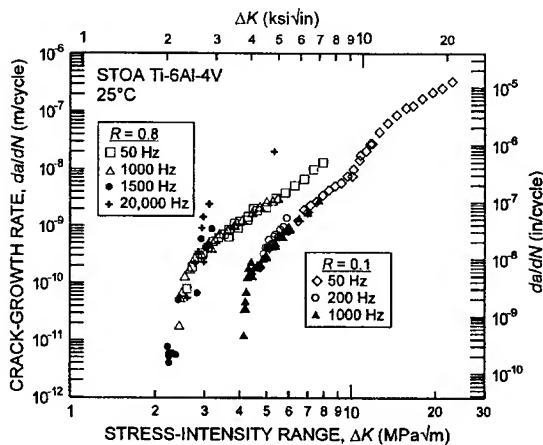


Fig. 5 Effect of test frequency on fatigue-crack propagation in Ti-6Al-4V in room air. Results from (large-crack) compact-tension tests at 50, 200 and 1000 Hz, notched tensile tests at 1500 Hz, and ultrasonic fatigue tests<sup>20</sup> at 20 000 Hz, show no statistically significant deviation in near-threshold behaviour.

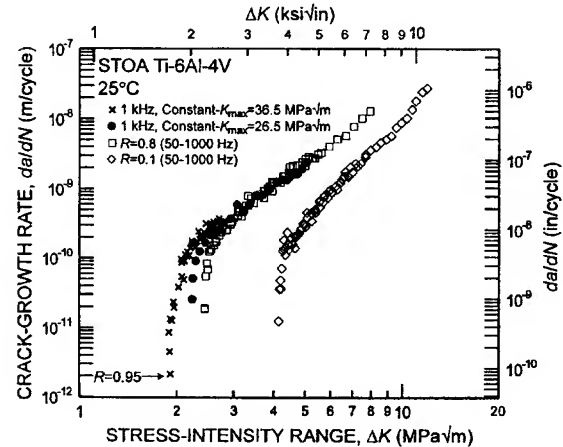


Fig. 6 Large-crack constant  $K_{\max}$ /increasing  $K_{\min}$  testing at 1000 Hz in room air on the solution-treated and overaged Ti-6Al-4V alloy was used to achieve  $R = 0.95$ , resulting in a lower-bound threshold of  $1.9 \text{ MPa}\sqrt{\text{m}}$ . Results are compared with constant  $R$  data at both 50 and 1000 Hz.

cracks in the same microstructure (see below), where small-crack growth was not observed below a  $\Delta K$  of  $2.9 \text{ MPa}\sqrt{\text{m}}$  ( $R = 0.1$ ).<sup>24</sup>

### Small-crack behaviour

Naturally initiated small-crack growth ( $a \sim 45\text{--}1000 \mu\text{m}$ ) behaviour has been measured in this microstructure by Lütjering and co-workers using cylindrical tensile samples.<sup>24</sup> Results at  $R = 0.1$  (with an applied maximum stress of 550 MPa and a frequency of 85 Hz) are compared in Fig. 7 with the present large-crack data at  $R = 0.1$  and  $0.8\text{--}0.95$ . Although the growth rates of the small cracks generally exceed those of the large cracks at the same applied  $\Delta K$  level, no small-crack growth has been reported to date below  $\Delta K \sim 2.9 \text{ MPa}\sqrt{\text{m}}$ . This value is 45% larger than the 'worst-case'  $\Delta K_{\text{TH}}$  value of  $1.9 \text{ MPa}\sqrt{\text{m}}$ , measured with large cracks in this alloy at  $R = 0.95$  using constant  $K_{\text{max}}$ /increasing  $K_{\text{min}}$  cycling.

Small-crack growth from simulated foreign object damage sites was also examined. A SEM micrograph of a typical impact site at 300 m/s is shown in Fig. 8 with a schematic illustration of the relevant features in the crater profile (for a more complete characterization of the damage, see Ref. [25]). The effect of the damage was to markedly reduce the fatigue life from that obtained with an undamaged sample, as shown in Table 1. Specifically, fatigue lives were reduced by over two orders of magnitude following 200 and 300 m/s impacts, with cracks tending to initiate at the bottom of the indent for

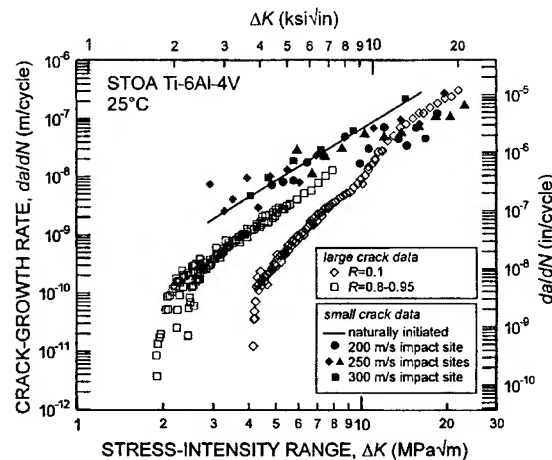


Fig. 7 Fatigue-crack propagation results for naturally initiated small ( $\sim 45\text{--}1000 \mu\text{m}$ ) surface cracks at  $R = 0.1$  (line)<sup>24</sup> and for small cracks emanating from a variety of FOD impact sites (closed symbols) in the solution-treated and overaged Ti-6Al-4V alloy, as compared to through-thickness, large cracks ( $> 5 \text{ mm}$ ) at  $R = 0.1$  and  $0.8\text{--}0.95$ . All measurements were made in room air.

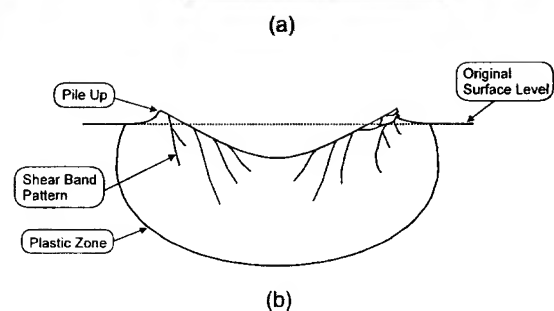
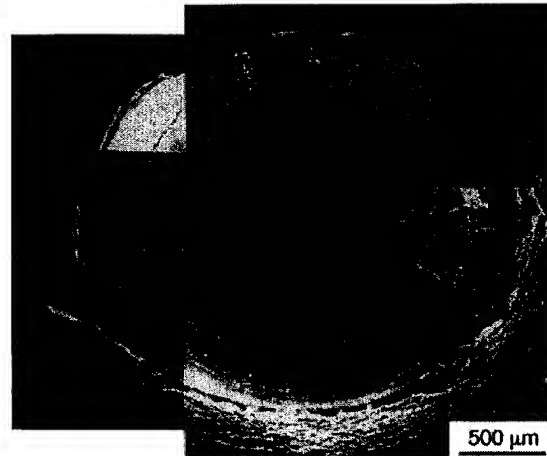


Fig. 8 Characteristics of surface damage due to impact: (a) SEM micrograph of simulated foreign object damage resulting from  $90^\circ$  impact by a hardened steel sphere with an incident velocity of 300 m/s; and (b) corresponding schematic illustrating features present at both 300 and 250 m/s. At 200 m/s, neither the shear bands nor the 'pile up' were observed.

Table 1 Summary of fatigue lives following simulated foreign object damage ( $\sigma_{\text{max}} = 500 \text{ MPa}$ ,  $R = 0.1$ , 20 Hz frequency)

	After 200 m/s FOD	After 300 m/s FOD	Smooth-bar undamaged sample
Initiation life	$4.3 \times 10^4$	$2.9 \times 10^4$	—
Total life	$7.5 \times 10^4$	$4.6 \times 10^4$	$> 10^7$

the lower velocity impacts and at the crater rim for the higher velocity impacts.

The growth rates of the small cracks originating from such impact sites are also compared in Fig. 7 with growth rate data for large ( $> 5 \text{ mm}$ ) and naturally initiated small ( $\sim 45\text{--}1000 \mu\text{m}$ ) cracks in this microstructure. Both the naturally initiated and FOD-initiated small-crack velocities were within the same scatter band, initially up to an order of magnitude faster than corresponding large-crack results (although small-crack data tended to merge with large-crack results above  $\Delta K \approx 10 \text{ MPa}\sqrt{\text{m}}$  as crack

sizes increased). However, in the limited data collected to date, no FOD-initiated cracks have been observed in the Ti-6Al-4V below a  $\Delta K$  of  $\sim 2.9 \text{ MPa}\sqrt{\text{m}}$ ; i.e. at a stress-intensity range above that of the 'worst-case', large-crack  $\Delta K_{\text{TH}}$  threshold. It should be noted, however, that the residual stresses locally surrounding the FOD sites were not taken into account in plotting the FOD-initiated small-crack results. Such residual stresses are currently being analysed using synchrotron X-ray microdiffraction techniques.

### Effect of environment

A comparison of fatigue-crack growth in Ti-6Al-4V at high frequencies (1–1.5 kHz) in ambient temperature air and vacuum ( $\sim 10^{-6}$  torr) is shown in Fig. 9 at  $R$  ratios between 0.6 and 0.8. Although the threshold values are essentially unchanged ( $\Delta K_{\text{TH}} \sim 2.6 \text{ MPa}\sqrt{\text{m}}$  in air versus  $2.7 \text{ MPa}\sqrt{\text{m}}$  *in vacuo*), crack growth rates are some three orders of magnitude faster in air than *in vacuo*. In view of the observed absence of a frequency effect on growth rates between 50 and 20 000 Hz, the magnitude of the disparity in growth rates in air and vacuum is quite surprising. The origin of the apparent environmental contribution to crack growth is unclear at this time, but it may be associated with embrittlement due to hydrogen released by the reaction of the Ti with water vapour in the air,<sup>26–28</sup> or more probably with the role of oxygen in delocalizing plastic deformation, specifically by limiting the degree of slip reversibility at the crack

tip.<sup>29</sup> The latter explanation is consistent with the rougher (macroscale) morphology of fatigue fracture surfaces in vacuum, as discussed below. However, as there is no effect of frequency on crack growth rates in air (between  $\sim 20$  and 20 000 Hz), the environmental mechanism responsible for faster growth rates in air compared to vacuum must be extremely rapid. Along these lines, Gao *et al.*<sup>28</sup> have demonstrated that the rate of oxidation of Ti-5Al-2.5Sn in the presence of small amounts of water vapour ( $10^{-6}$  torr) is extremely rapid. Applying the derived oxidation reaction kinetics to the equilibrium partial pressure of water vapour at 25 °C ( $p_{\text{water}} = 23.75$  torr), a clean surface of Ti-5Al-2.5Sn would be  $\sim 90\%$  covered in oxide in  $2.6 \times 10^{-7}$  s. Thus, if slip-step oxidation was responsible for the observed dependence of fatigue-crack growth rates on the environment, one would not expect to see an effect of cyclic loading frequency on crack-propagation rates in air for all frequencies less than  $\sim 3.9$  MHz, consistent with the current experimental results. However, given the fast nature of the oxidation process, it is likely that the surface reaction with  $\text{H}_2\text{O}$  is not the rate-limiting step. In fact, Gao *et al.*<sup>28</sup> suggest that the transport of the gas phase to the crack tip is rate limiting. Thus, a more realistic estimate of the critical frequency, above which slip-step oxidation will be suppressed in ambient air, requires a more detailed knowledge of the rate of water vapour transport to the crack tip.

### Mechanisms

There has been very little, if any, investigation of fatigue cracks growing below  $10^{-9}$  m/cycle and at high load ratios. Therefore, fatigue-crack growth at rates in the range of  $10^{-10}$ – $10^{-12}$  m/cycle were observed *in situ* using a 1.5-kHz loading stage for a scanning electron microscope. Cracks were cycled in increments of between 200 000 cycles and 1 million cycles between measurements of crack length, depending on the loading variables.

At these low rates of propagation, fatigue cracks did not grow during every cycle, but rather would alternate between propagation and local arrest. With decreasing applied load, propagation became more intermittent until finally ceasing at the threshold. The criteria used for establishing this threshold was no growth at either end of a surface crack in 5 million cycles. When the fraction of increments in which growth was measured was correlated to  $\Delta K$ , it was found that there was a transition period between a condition of no growth, presumably below  $\Delta K_{\text{TH}}$ , and growth on each cyclic increment, which may be termed  $\Delta K_{\text{ss}}$ . A fairly careful study of crack growth at two load ratios indicated that at  $R = 0.85$ , the transition period was over a small range

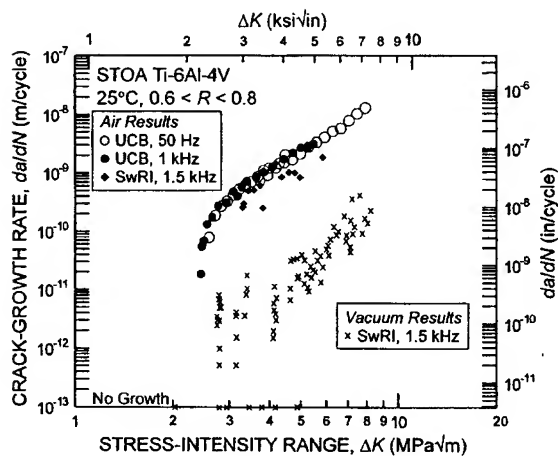


Fig. 9 Comparison of rates of fatigue-crack propagation in the solution-treated and overaged Ti-6Al-4V alloy at  $R = 0.6$ – $0.8$  and 1–1.5 kHz frequency in room air and vacuum ( $\sim 10^{-6}$  torr). Note that although  $\Delta K_{\text{TH}}$  threshold values are essentially unchanged, growth rates *in vacuo* are some three orders of magnitude slower than in air.

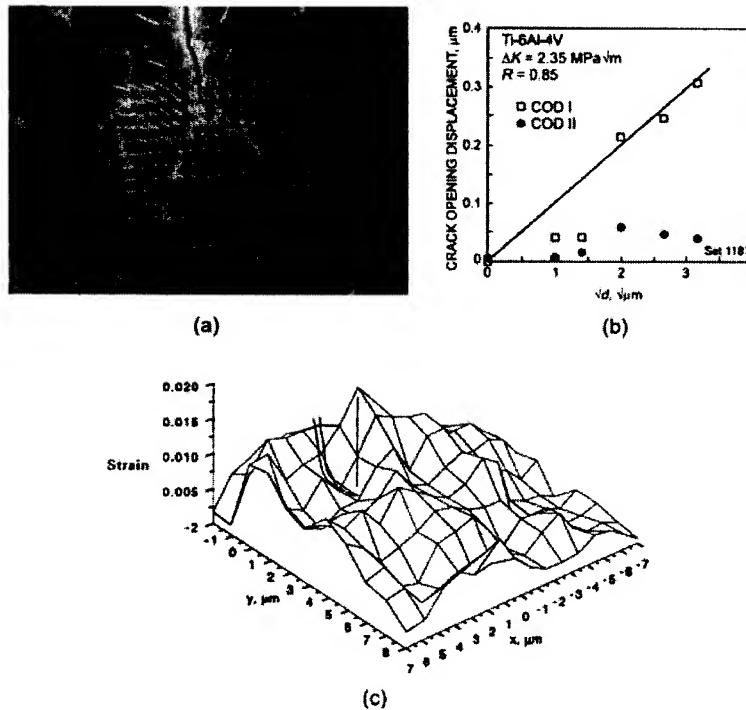


Fig. 10 (a) Crack-tip micromechanics are examined in a photograph of a crack growing at  $R = 0.85$  at a rate of  $\sim 10^{-11}$  m/cycle with displacements measured between minimum and maximum cyclic loads. (b) Crack-opening displacements (COD) in mode I and II measured from (a) (where the displacement interval is  $1 \mu\text{m}$  and the displacements are magnified 15 times), as a function of the square root of the distance,  $d$ , behind the crack tip. (c) Maximum shear strain distribution in the region covered by the displacements. Strain is a maximum at the crack tip and the estimated size of the plastic zone is  $2 \mu\text{m}$ .

of  $\Delta K$ , while at  $R = 0.5$ , the range in  $\Delta K$  over which growth was intermittent was larger.

The existence of a transition in  $\Delta K$  between no growth and growth on each cyclic increment is similar to the change in slope of the  $da/dN$ - $\Delta K$  curve as  $\Delta K$  is increased above  $\Delta K_{TH}$ . At  $\Delta K_{TH}$ , the slope of the curve is very steep. With increasing  $\Delta K$ , the slope slightly decreases, and when  $\Delta K_{ss}$  is reached, the curve assumes the slope of the Paris region, or the steady-state crack growth region.

Crack-tip micromechanics measurements were made for cracks growing at the low growth rates being studied. Only cracks growing *in vacuo* are discussed here because of the very large influence of an air environment on crack growth kinetics, and therefore on the mechanisms of crack growth.

Fatigue cracks were consistently found to be closed at the tip at the minimum cyclic load, although this closure in some of the observations extended only a few tens of micrometres. Crack-opening loads were found to be approximately half the cyclic load, even at  $R = 0.85$ . These observations are apparently inconsistent with the compliance-based closure measurements on large cracks in compact-tension samples, where no closure was detected above an  $R$ -ratio of  $\sim 0.5$ . However, compliance measurements are macroscopic and yield a global measure of crack-surface contact; it is unlikely that they

would detect such local closure within  $10 \mu\text{m}$  or so of the crack tip.

Photographs made at the minimum and maximum cyclic loads were analysed to determine the crack-opening displacement (COD) and crack-tip strain levels using the automated stereomaging technique. An example of these measurements is shown in Fig. 10. This figure shows a photograph of the crack-tip region with the displacements overlaid. COD is shown in the upper right of the figure as a function of the square root of  $d$ , the distance behind the crack tip. From this relationship, the crack-tip opening displacement (CTOD) may be defined at  $1 \mu\text{m}$  behind the tip.

The distribution of strain for crack tips at this high  $R$  does not seem to be much affected by the grain structure, although this point has not been extensively investigated. The plastic-zone size was determined by subtracting the elastic strain (twice the yield stress/modulus) from the total strain. The plastic-zone size for the crack tip shown in Fig. 10 extends  $\approx 2 \mu\text{m}$  ahead of the crack tip. Plastic-zone sizes are of the order of the  $\alpha$  particle size. Strains near the crack tip did not appear to be affected by the presence of  $\alpha/\alpha$  or  $\alpha/\beta$  boundaries.

The correlation between CTOD (defined at  $1 \mu\text{m}$  behind the crack tip) and crack-tip strain that has been found at lower  $R$  ratio<sup>30</sup> continues for high  $R$ , as shown in Fig. 11. The magnitude of the crack-tip strains under



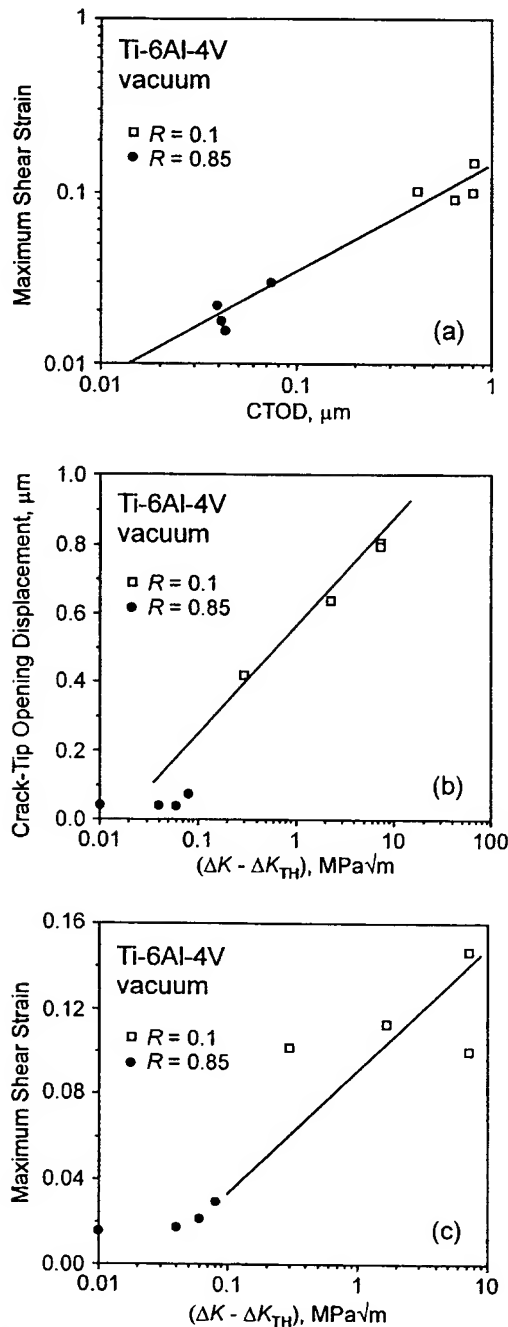


Fig. 11 Correlations between micromechanics and loading parameters are shown in the results obtained under HCF conditions ( $R = 0.85$ ); these are compared with those previously obtained at low  $R$ .<sup>30</sup> (a) Maximum shear strain at the crack tip correlated with CTOD. (b) CTOD correlated with  $(\Delta K - \Delta K_{TH})$ . (c) Maximum crack-tip shear strain correlated with  $(\Delta K - \Delta K_{TH})$ .

these conditions was not always found to be above the elastic limit. This condition probably resulted from the fact that cracks were not growing during some increments of cycling. Also shown in Fig. 11 are the correlations between crack-tip strain and CTOD and the term  $(\Delta K - \Delta K_{TH})$ .

### Fractography

Investigations of the fracture surfaces in the tensile fatigue samples indicated that the surface-crack profiles were approximately semicircular ( $c/a \sim 1$ ), meaning that crack growth rates on the surface and interiors of the material were approximately the same. The surface topography produced at the very low crack growth rates investigated was examined using a field emission SEM. The high resolution and low beam voltage of the field emission SEM was necessary to reveal the very low level of topography existent on individual primary  $\alpha$  grains and within individual lamellar colonies present at the fracture surfaces produced *in vacuo*; however, on a more macroscale, fracture surfaces in vacuum were distinctly rougher. Using this technique, some evidence of an incremental mechanism of fatigue-crack growth (striations) was found on the  $\alpha$  grains. At a growth rate of  $10^{-12}$  m/cycles, the average striation spacing on the surfaces of  $\alpha$  particles was  $\approx 50$  nm, or there were 20 striations in  $1 \mu\text{m}$  of growth. This means that under vacuum conditions, it required an average of 40 000 cycles to produce one striation. Clearly, *in vacuo*, the crack is not making one striation per loading cycle.

With a plastic-zone size of  $\approx 2 \mu\text{m}$  ( $\sim 100$  times larger than the observed striation spacing),  $\sim 2 \times 10^6$  cycles were needed for the crack to traverse the plastic zone when the average crack growth rate was  $10^{-12}$  m/cycle. The volume of material in the plastic zone would therefore experience  $\approx 2 \times 10^6$  cycles of loading, and it is likely that dislocation subcells would be formed during this large number of cycles near the crack plane, as has previously been found at higher  $\Delta K$  in these alloys.

### Worst-case threshold concept

The problem of turbine-engine high-cycle fatigue requires that design must be based on the notion of a threshold stress intensity for no crack growth under the appropriate conditions of high mean loads, ultrahigh frequency (vibratory) loading, and small-crack sizes. Because the measurement of small-crack thresholds is experimentally tedious and complex, one approach used in the current work has been to simulate the mechanistic origins of the small-crack effect using 'worst-case' large-cracks, i.e. the measurement of thresholds under conditions which simulate the similitude limitation of small

cracks by minimizing crack closure in the wake. Whereas this approach to simulate small-crack behaviour with large cracks might not be appropriate for truly microstructurally small cracks, where essentially any continuum measure of behaviour would be questionable, the crack sizes relevant to the Air Force HCF problem are expected to be somewhat larger, of the order of 50–100  $\mu\text{m}$  and above. As described above, using constant  $K_{\text{max}}$ /increasing  $K_{\text{min}}$  cycling, the present results show the 'worst-case' threshold in Ti-6Al-4V, measured with large ( $>5\text{ mm}$ ) cracks at very high load ratios ( $R \sim 0.95$ ) and representative frequencies (1 kHz), to be  $\Delta K_{\text{TH}} = 1.9\text{ MPa}\sqrt{\text{m}}$ .  $\Delta K_{\text{TH}}$  thresholds tend to approach zero as  $R \rightarrow 1$ ;<sup>31</sup> however, as the current value at  $R = 0.95$  is defined as  $K_{\text{max}} \rightarrow K_{\text{IC}}$ , in the apparent absence of global closure and below the stress intensities for the growth of naturally initiated small ( $\sim 45\text{--}1000\text{ }\mu\text{m}$ ) cracks and small cracks emanating from sites of foreign object damage, it is believed that the 'worst-case' threshold concept can be used as a practical lower-bound threshold for the stress intensity required for the onset of small-crack growth under HCF conditions.

## CONCLUSIONS

Based on a preliminary investigation into the high-cycle fatigue of a solution-treated and overaged Ti-6Al-4V turbine-engine alloy tested in ambient temperature air and vacuum, the following conclusions can be made.

- 1 Ambient temperature fatigue-crack propagation (over the range  $\sim 10^{-12}\text{--}10^{-6}\text{ m/cycle}$ ) and threshold  $\Delta K_{\text{TH}}$  values were found to be independent of test frequency over the range 50–1500 Hz, based on tests on servohydraulic and *in situ* SEM testing machines. Moreover, comparisons to the published results on a similar microstructure in Ti-6Al-4V strongly suggest that the frequency-independent behaviour extends out to 20 000 Hz, at least at near-threshold levels.
- 2 A 'worst-case' fatigue threshold, measured for large cracks at  $R = 0.95$  under constant  $K_{\text{max}}$ /increasing  $K_{\text{min}}$  conditions was found to be  $1.9\text{ MPa}\sqrt{\text{m}}$  for this alloy. This should be compared with measurements on naturally initiated small cracks and FOD-initiated small cracks in the same microstructure, where small-crack growth was not reported below a  $\Delta K$  value of  $2.9\text{ MPa}\sqrt{\text{m}}$ .
- 3 Foreign object damage, simulated by hardened steel spheres impacted at 200–300 m/s on a flat surface, provides sites for the initiation of small fatigue cracks. At applied stresses some 10% below the smooth-bar, fatigue strength (at  $10^7$  cycles), crack-initiation lives were less than  $4 \times 10^4$  cycles, many orders of magni-

tude shorter than in unimpacted samples. Subsequent small-crack growth from the damage sites was found to occur at rates considerably faster than large cracks subjected to the same applied  $\Delta K$  level. No crack growth from FOD sites has been observed to date at  $\Delta K$  values less than  $2.9\text{ MPa}\sqrt{\text{m}}$ .

- 4 Fatigue-crack growth rates *in vacuo*, over the range  $\sim 10^{-12}\text{--}10^{-9}\text{ m/cycle}$ , were found to be approximately three orders of magnitude slower than corresponding rates in room air;  $\Delta K_{\text{TH}}$  threshold values, conversely, were essentially unchanged.
- 5 Fractographically, fatigue-crack growth at  $\sim 10^{-11}\text{--}10^{-12}\text{ m/cycle}$  was found to be clearly intermittent, with evidence of near-tip crack-surface contact (i.e. within  $\sim 10\text{ }\mu\text{m}$  or so of the crack tip) at load ratios as high as 0.85. Measured crack-tip strain distributions were essentially unaffected by the microstructure (e.g. by the grain structure and  $\alpha/\alpha$  and  $\alpha/\beta$  boundaries).
- 6 The 'worst-case' fatigue threshold of  $1.9\text{ MPa}\sqrt{\text{m}}$ , measured for large cracks at  $R = 0.95$ , was found to provide a practical lower bound to describe the onset of growth of small cracks ( $a \sim 45\text{--}1000\text{ }\mu\text{m}$ ), initiated naturally or from sites of foreign object damage, under HCF conditions in this alloy.

## Acknowledgements

This work was supported by the US Air Force Office of Scientific Research under the auspices of the Multidisciplinary University Research Initiative on *High Cycle Fatigue* to the University of California at Berkeley under Grant no. F49620-96-1-0478; in addition, D.L.D. was supported by AFOSR Grant no. F49620-96-C-0037. B.L.B. would also like to acknowledge the support of the Hertz Foundation. Thanks are due to Prof. Dr G. Lütjering, Dr J. A. Hines and Dr J. O. Peters of the Technische Universität Hamburg-Harburg for their results on naturally initiated small cracks, and to Dr A. W. Thompson for several helpful discussions.

## REFERENCES

- 1 Report of the AdHoc Committee on Air Force Aircraft Jet Engine Manufacturing and Production Processes (1992) United States Air Force Scientific Advisory Board, SAF/AQSS: the Pentagon, Washington, D.C.
- 2 B. A. Cowles (1996) High cycle fatigue in aircraft gas turbines—an industry perspective. *Int. J. Fracture* **80**, 147–163.
- 3 J. C. I. Chang (1996) An integrated research approach to attack engine HCF problems. Air Force Office of Scientific Research, Bolling AFB, Washington, D.C.
- 4 D. Taylor (1985) *A Compendium of Fatigue Thresholds and Crack Growth Rates*, EMAS, Warley, UK.

- 5 J. K. Gregory (1994) Fatigue crack propagation in titanium alloys. In: *Handbook of Fatigue Crack Propagation in Metallic Structures* (Edited by A. Carpinteri), Elsevier Science, Oxford, U.K., pp. 281–322.
- 6 J. M. Larsen, B. D. Worth, C. G. Annis and F. K. Haake (1996) An assessment of the role of near-threshold crack growth in high-cycle-fatigue life prediction of aerospace titanium alloys under turbine engine spectra. *Int. J. Fracture* **80**, 237–255.
- 7 R. O. Ritchie (1996) Small cracks and high-cycle fatigue. In: *Proceedings of the ASME Aerospace Division* (Edited by J. C. I. Chang, J. Coulter, D. Brei, D. Martinez, W. Hg and P. P. Freidmann), ASME, New York, NY, AMD, Vol. 52, pp. 321–333.
- 8 R. O. Ritchie and J. Lankford (1986) Small fatigue cracks: a statement of the problem and potential solutions. *Materials Sci. Engineering* **84**, 11–16.
- 9 D. Eylon (1998) Summary of the available information on the processing of the Ti-6Al-4V HCF/LCF program plates. University of Dayton Report, Dayton, OH, USA.
- 10 R. O. Ritchie and W. Yu (1986) Short crack effects in fatigue: a consequence of crack tip shielding. In: *Small Fatigue Cracks* (Edited by R. O. Ritchie and J. Lankford), TMS-AIME, Warrendale, PA, USA, pp. 167–189.
- 11 H. Döker, V. Bachmann and G. Marci (1982) A comparison of different methods of determining the threshold for fatigue crack propagation. In: *Fatigue Thresholds, Proceedings of the 1st International Conference* (Edited by J. Bäcklund, A. F. Blom and C. J. Beevers), EMAS, Warley, UK, Vol. 1, pp. 45–57.
- 12 W. A. Herman, R. W. Hertzberg and R. Jaccard (1988) Influence of mean stress on fatigue in several aluminium alloys utilizing  $K_{\max}^c$  threshold procedures. *Fatigue Fract. Engng Mater. Struct.* **11**, 303–320.
- 13 J. M. Morgan and W. W. Milligan (1997) A 1 kHz servohydraulic fatigue testing system. In: *High Cycle Fatigue of Structural Materials* (Edited by W. O. Soboyejo and T. S. Srivatsan), TMS, Warrendale, PA, USA, pp. 305–312.
- 14 J. C. Newman, Jr and I. S. Raju (1981) An empirical stress-intensity factor equation for the surface crack. *Engng Fracture Mech.* **15**, 185–192.
- 15 M. D. Halliday and C. J. Beevers (1981) Some aspects of fatigue crack closure in two contrasting titanium alloys. *J. Testing Evaluation* **9**, 195–201.
- 16 K. S. Ravichandran (1991) Near threshold fatigue crack growth behavior of a titanium alloy: Ti-6Al-4V. *Acta Metall. Mater.* **39**, 401–410.
- 17 T. Ogawa, K. Tokaji and K. Ohya (1993) The effect of microstructure and fracture surface roughness on fatigue crack propagation in a Ti-6Al-4V alloy. *Fatigue Fract. Engng Mater. Struct.* **16**, 973–982.
- 18 S. Dubey, A. B. O. Soboyejo and W. O. Soboyejo (1997) An investigation of the effects of stress ratio and crack closure on the micromechanisms of fatigue crack growth in Ti-6Al-4V. *Acta Mater.* **45**, 2777–2787.
- 19 R. A. Schmidt and P. C. Paris (1973) Threshold for fatigue crack propagation and effects of load ratio and frequency. In: *Progress in Fatigue Crack Growth and Fracture Testing. ASTM STP 536*, pp. 79–94.
- 20 C. Bathias, K. El Alami and T. Y. Wu (1997) Influence of mean stress on Ti-6Al-4V fatigue crack growth at very high frequency. *Engng Fracture Mech.* **56**, 255–264.
- 21 R. J. H. Wanhill (1974) Environment and frequency effects during fatigue crack propagation in Ti-2.5Cu (IMI 230) sheet at room temperature. *Corrosion-NACE* **30**, 28–35.
- 22 D. B. Dawson and R. M. N. Pelloux (1974) Corrosion fatigue crack growth of titanium alloys in aqueous environments. *Metallurg. Trans.* **5**, 723–731.
- 23 C. F. Shih (1981) Relationships between the  $J$ -integral and the crack opening displacement for stationary and extending cracks. *J. Mech. Phys. Solids* **29**, 305–326.
- 24 J. A. Hines, J. O. Peters and G. Lütjering (1999) Microcrack propagation in Ti-6Al-4V. In: *Fatigue Behavior of Titanium Alloys* (Edited by R. Boyer, D. Eylon, J. P. Gallagher and G. Lütjering), TMS, Warrendale, PA, USA.
- 25 O. Roder, A. W. Thompson and R. O. Ritchie (1998) Simulation of foreign object damage of Ti-6Al-4V gas-turbine blades. In: *Proceedings of the Third National Turbine Engine High Cycle Fatigue Conference* (Edited by W. A. Stange and J. Henderson), Universal Technology, Dayton, OH, USA, CD-Rom, session 10, pp. 6–12.
- 26 D. A. Meyn (1971) An analysis of frequency and amplitude effects on corrosion-fatigue crack propagation in Ti-8Al-1Mo-1V. *Metallurg. Trans.* **2**, 853–865.
- 27 H. Döker and D. Munz (1977) Influence of environment on the fatigue crack propagation of two titanium alloys. In: *The Influence of Environment on Fatigue*, Mechanical Engineering Publications, London, UK, pp. 123–130.
- 28 S. J. Gao, G. W. Simmons and R. P. Wei (1984) Fatigue crack growth and surface reactions for titanium alloys exposed to water vapor. *Mater. Sci. Engng* **62**, 65–78.
- 29 M. Sugano, S. Kanno and T. Satake (1989) Fatigue behavior of titanium in vacuum. *Acta Metall.* **37**, 1811–1820.
- 30 D. L. Davidson and J. Lankford (1984) Fatigue crack growth mechanics for Ti-6Al-4V (RA) in vacuum and humid air. *Metallurg. Trans. A* **15A**, 1931–1940.
- 31 H. Döker (1997) Fatigue crack growth threshold: implications, determination and data evaluation. *Int. J. Fatigue* **19**, 5145–5149.



PERGAMON

Engineering Fracture Mechanics 68 (2001) 129–147

Engineering  
Fracture  
Mechanics

www.elsevier.com/locate/engfracmech

## Effect of load ratio and maximum stress intensity on the fatigue threshold in Ti–6Al–4V

B.L. Boyce, R.O. Ritchie \*

*Department of Materials Science and Engineering, University of California, Berkeley, CA 94720-1760, USA*

Received 14 February 2000; received in revised form 30 September 2000; accepted 2 October 2000

### Abstract

There has been a renewed interest of late in the mechanisms responsible for the influence of the load ratio,  $R$ , and the maximum stress intensity,  $K_{\max}$ , on the threshold for fatigue-crack growth,  $\Delta K_{\text{th}}$ . While mechanistic explanations in the past have largely focused on the role of crack closure, it is certainly not the only mechanism by which  $K_{\max}$  influences  $\Delta K_{\text{th}}$ . In this work, we examine the effect of a wide range of loading frequencies ( $\nu = 50\text{--}1000$  Hz) and load ratios ( $R = 0.10\text{--}0.95$ ) on fatigue-crack propagation and threshold behavior in a Ti–6Al–4V turbine blade alloy consisting of  $\sim 60$  vol% primary- $\alpha$  and  $\sim 40$  vol% lamellar  $\alpha + \beta$ . The data presented in this paper indicate that at  $K_{\max}$  values above 6 MPa $\sqrt{\text{m}}$  ( $R > 0.5$ ), where macroscopic crack closure is no longer detected in this alloy,  $\Delta K_{\text{th}}$  decreases approximately linearly with increasing  $K_{\max}$ . This result is discussed in terms of possible mechanistic explanations, including sustained-load cracking, microscopic near-tip closure, and static fracture modes, based on considerations of experimental evidence from both the current study and the literature. © 2000 Published by Elsevier Science Ltd.

**Keywords:** Titanium alloys; Ti–6Al–4V; Fatigue threshold; Load ratio; Crack closure; Sustained-load cracking

### 1. Introduction

The influence of load ratio,  $R$ , on fatigue-crack propagation rates has been widely studied from both experimental (e.g. Refs. [1–6]) and analytical (e.g. Refs. [7,8]) viewpoints. Almost without exception, an increase in load ratio results in an increase in fatigue-crack propagation rate at a given applied cyclic stress-intensity,  $\Delta K$ . Equivalently, the observed threshold stress-intensity range for fatigue-crack propagation,  $\Delta K_{\text{th}}$ , decreases as the (positive) load ratio is increased. Mechanistic explanations for such behavior have focused on (a) the presence of crack closure at low values of the minimum stress intensity,  $K_{\min}$  [1] or (b) the presence of static fracture modes as the maximum stress intensity,  $K_{\max}$ , approaches the fracture toughness,  $K_{\text{Ic}}$  [9].

\* Corresponding author. Tel.: +1-510-486-5798; fax: +1-510-486-4995.

E-mail address: roritchie@lbl.gov (R.O. Ritchie).

<sup>1</sup> Load ratio,  $R$ , is defined under fatigue loading conditions as the minimum applied load divided by the maximum applied load for any given loading cycle.

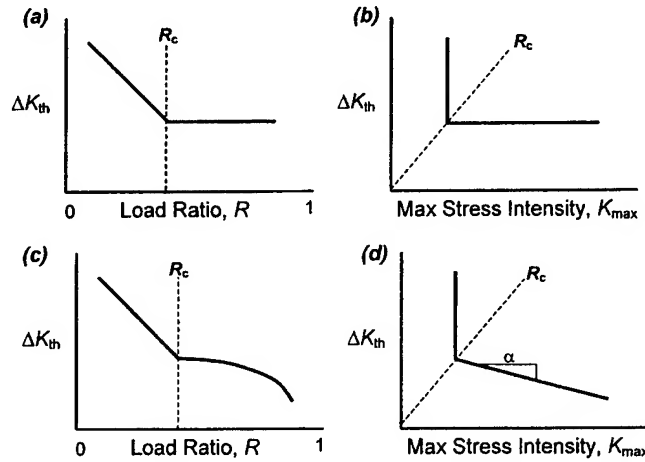


Fig. 1. (a) A “classic” representation of the influence of the load ratio,  $R$ , on the fatigue threshold,  $\Delta K_{th}$ . (b) A transformation into coordinates of  $(K_{max}, \Delta K_{th})$ . (c) Many data sets, however, exhibit decreasing threshold even beyond the transition,  $R > R_c$ . (d) The variation of  $\Delta K_{th}$  with  $K_{max}$  is shown here as approximately linear with slope,  $\alpha$ .

A common conception of the variation in the fatigue threshold with load ratio is shown in Fig. 1a. Schmidt and Paris [1] rationalized this behavior solely on the basis of the crack closure concept. Assuming that both the closure-corrected effective fatigue threshold,  $\Delta K_{eff,th}$  and the closure stress intensity,  $K_{cl}$ , are *not* affected by load ratio, then there exists some critical load ratio,  $R_c$  at which  $K_{min} = K_{cl}$ , such that:

$$\Delta K_{eff,th} = \begin{cases} K_{max,th} - K_{cl} < \Delta K_{th}, & \text{if } R < R_c \text{ } (K_{min,th} < K_{cl}), \\ K_{max,th} - K_{min,th} = \Delta K_{th}, & \text{if } R > R_c \text{ } (K_{min,th} > K_{cl}). \end{cases} \quad (1)$$

Under these conditions, the maximum stress intensity at threshold,  $K_{max,th}$ , is independent of  $R$  below  $R_c$  and the threshold stress-intensity range,  $\Delta K_{th}$ , is independent of  $R$  above  $R_c$ . Plotted as  $K_{max,th}$  versus  $\Delta K_{th}$ , this transition manifests itself as a distinct ‘L’ shape, as shown in Fig. 1b, highlighting that the value of  $\Delta K_{th}$  is independent of  $K_{max}$  when  $R > R_c$  where global closure is no longer effective. As a first approximation, the Schmidt and Paris analysis seems to work moderately well, with many data sets showing this transition at load ratios similar to the critical load ratio condition,  $R_c$ , at which point  $K_{min} = K_{cl}$ .

This behavior, however, is not universal, as shown by the compilation of data presented in Fig. 2. In most cases, the value of  $\Delta K_{th}$  is *not* invariant at  $R > R_c$ , but rather  $\Delta K_{th}$  decreases with increasing  $R$  (Fig. 1c and d), implying that either the Schmidt and Paris model is not properly described at  $R > R_c$ , or that there are additional mechanisms acting *in concert*. It is this variation in  $\Delta K_{th}$  with increasing  $R > R_c$ , that is apparently independent of crack closure, which is the focus of the current work. We examine this behavior in a Ti-6Al-4V alloy processed for turbine blade applications, and consider possible mechanistic explanations.

## 2. Background

The progressive downward trend of the threshold  $\Delta K_{th}$  with increasing load ratio at  $R > R_c$  was noted by Döker [12] based on the fatigue study of Huthmann and Gossmann [13] on a high-temperature steel at 550°C. Döker chose to characterize this behavior with an empirical relationship, which varied linearly with  $K_{max}$ :

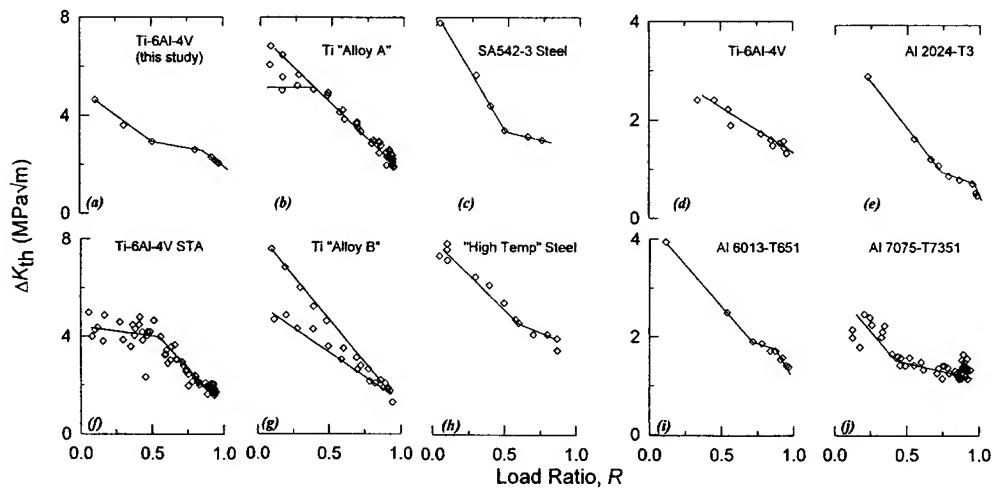


Fig. 2. A representative sampling of large data sets on the influence of load ratio on the fatigue threshold,  $\Delta K_{th}$ . Rather arbitrary lines are drawn through the data as a guide to interpretation. The only consistent trend among the various curves is that all slopes tend to be  $\leq 0$ . The slopes continue to be  $\leq 0$  even at high load ratios, where closure has presumably been eliminated. These data sets are taken from (clockwise from upper left): this study, Refs. [1], [10,11], [13–17].

$$\Delta K_{th} = \Delta K_{th,0} + \alpha K_{max}, \quad \text{if } R > R_c, \quad (2)$$

where  $\Delta K_{th,0}$  is the  $\Delta K_{th}$ -intercept extrapolated to  $K_{max} = 0$  and  $\alpha$  is the slope of the decrease in threshold with increasing  $K_{max}$ . The work of Bray and Donald [14] on Al alloys also noted a decrease in  $\Delta K_{th}$  which is apparently independent of crack closure, although in this case the behavior was parameterized by a power-law relationship:

$$\Delta K_{th} = c(K_{max})^d, \quad \text{if } R > R_c. \quad (3)$$

Whereas only a few studies have parameterized (or even noted) this behavior, many published data sets exhibit a similar trend (for examples, see Refs. [1,11,13–19]), most notably the actual data of Schmidt and Paris (Fig. 2e). To examine this effect further, a literature survey was conducted to identify published data sets on steels, aluminum and titanium alloys that contain high load-ratio threshold data. Data sets containing at least three threshold conditions where  $K_{max} \geq 10$  MPa√m were regressed according to a normal linear model. To exclude the effects of crack closure, the regression was only performed on those data points where  $K_{max} \geq 10$  MPa√m. The results of this analysis are presented in Table 1.

In Table 1, all titanium alloys have a negative value for  $\alpha$  in the range of  $-0.01$  to  $-0.07$  (this excludes the value of  $\alpha$  of  $-0.386$  that is presumably skewed due to the small number of data points and has a large standard deviation of 0.239). Furthermore, for eight of the 10 titanium data sets, a hypothesis that  $\alpha = 0$  is rejected based on a 99% confidence interval. This is not the case for all of the steel data sets and two of the three aluminum data sets, where the hypothesis that  $\alpha = 0$  is not rejected based on a 99% confidence interval. This indicates that in the case of aluminum or steels, there is not enough statistical evidence to determine that the threshold changes with increasing  $K_{max}$ . However, in the case of the titanium data sets, the decrease in threshold with increasing  $K_{max}$  is statistically significant. Such behavior is inconsistent with the notion that (global) crack closure is the only mechanism responsible for the  $R$  and  $K_{max}$  effects on  $\Delta K_{th}$ .

Table 1

Values for the slope,  $\alpha$ , of  $\Delta K_{th}$  versus  $K_{max}$  when  $K_{max} \geq 10 \text{ MPa}\sqrt{\text{m}}$ 

Material	Temp. (°C)	Method	$N^a$	$K_{max}$ range (MPa $\sqrt{\text{m}}$ )	$\alpha$	SD( $\alpha$ ) <sup>b</sup>	References
<i>Steels:</i>							
High-temp steel	550°C	Const- $R$	4	10–21	−0.141	0.091	[13]
		Const- $K_{max}$	4	11–30	−0.044	0.029	[13]
Steel 42CrMo4	RT <sup>c</sup>	Const- $K_{max}$	8	13–50	−0.005	0.007	[16]
		Jump III <sup>d</sup>	21	12–35	−0.001	0.006	[16]
<i>Aluminum Alloys:</i>							
Al 2024 T3	RT <sup>c</sup>	Const- $R$	3	15–31	−0.016	0.010	[1]
Al 6013-T651	RT <sup>c</sup>	Const- $K_{max}$	6	10–38	−0.013	0.006	[14]
Al 7075-T7351	RT <sup>c</sup>	Const- $K_{max}$	10	12–21	+0.017	0.019	[17]
<i>Titanium Alloys:</i>							
Ti Alloy A	RT <sup>c</sup>	Const- $R$	12	10–32	−0.063	0.027	[18]
		Const- $K_{max}$	17	12–40	−0.043	0.012	[18]
Ti Alloy B	RT <sup>c</sup>	Const- $K_{max}$	11	10–24	−0.062	0.023	[18]
Ti-6Al-4V STA	RT <sup>c</sup>	Const- $R$	4	10–14	−0.386	0.239	[17]
		Const- $K_{max}$	18	10–32	−0.024	0.009	[17]
Ti-6Al-4V	RT <sup>c</sup>	Const- $K_{max}$	3	13–25	−0.050	0.025	[16]
		Jump III <sup>d</sup>	3	13–25	−0.069	0.035	[16]
		Jump IV <sup>d</sup>	3	13–25	−0.063	0.032	[16]
Ti-6Al-4V	RT <sup>c</sup>	Const- $K_{max}$	4	10–25	−0.011	0.007	[19]
Ti-6Al-4V STOA	RT <sup>c</sup>	Const- $R$ , $K_{max}$	5	13–57	−0.013	0.006	This study

<sup>a</sup> Number of data points used for regression.<sup>b</sup> Standard deviation of the slope parameter,  $\alpha$ .<sup>c</sup> Room temperature.<sup>d</sup> For an explanation of these “jump-in” threshold-determination methods, see Ref. [16].

In the absence of closure, possible alternative mechanisms for this behavior include the presence of sustained-load cracking (SLC) mechanisms, such as creep or hydride-assisted cracking, or the occurrence of the so-called “Marci effect”, as described below. Both of these phenomena have been observed in titanium alloys at ambient temperatures.

*Sustained-load cracking:* It is well established that many titanium alloys exhibit stable crack growth under monotonic loading when the applied  $K$  exceeds a sustained-load cracking (SLC) threshold yet is less than  $K_{Ic}$  (for a review, see Ref. [20]). In Ti-6Al-4V, it has been noted that such SLC rates increase with increasing internal hydrogen content. Furthermore, SLC rates have been found to vary with temperature. For an alloy containing 50–70 ppm H, crack velocities were at a maximum at  $\sim 0^\circ\text{C}$  ( $da/dt \sim 5 \times 10^{-10} \text{ m/s}$ ) whereas below  $-10^\circ\text{C}$  or above  $25^\circ\text{C}$ , crack velocities were much slower ( $da/dt < 1 \times 10^{-11} \text{ m/s}$ ) [21]. The occurrence of such mechanisms during near-threshold fatigue-crack growth would impart an influence of  $K_{max}$  on the threshold and growth-rate behavior as they are primarily controlled by the static, rather than cyclic, loads.

*The Marci effect:* Some titanium alloys exhibit the so-called “Marci effect” at very high  $K_{max}$  levels. In these instances, the fatigue threshold ceases to exist and at all applied  $\Delta K$  levels (including static loading, where  $\Delta K = 0$ ), the crack advances with a substantial velocity, typically  $> 10^{-8} \text{ m/cycle}$  (Fig. 3). This behavior has been observed by Marci on Ti-6Al-6V-2Sn, IMI 834, IMI 685 [22,23], and by Lang on Ti-6Al-2Sn-4Zr-6Mo [24], and is likely associated with SLC. It is possible that this effect is a more aggressive example of the current observations, although there is no evidence to date that conclusively connects these two phenomena.

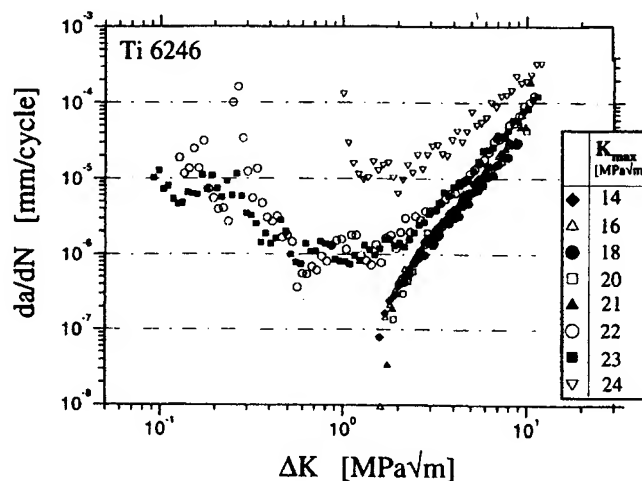


Fig. 3. Fatigue-crack growth behavior typical of the “Marci” effect in Ti–6Al–2Sn–4Zr–6Mo. In some titanium alloys, when  $K_{\max}$  is greater than some critical value (21 MPa $\sqrt{\text{m}}$  in this particular alloy), the fatigue threshold ceases to exist and all applied  $\Delta K$  values lead to an appreciable growth rates  $>10^{-10}$  m/cycle (after Ref. [24]).

### 3. Experimental procedures

#### 3.1. Material

The material under investigation was a Ti–6Al–4V alloy with a composition (in wt.%) of 6.30Al, 4.17V, 0.19Fe, 0.19O, 0.013N, 0.0035H, balance Ti. It was received as 20 mm thick forged plates from Teledyne Titanium after solution treating 1 h at 925°C and vacuum annealing for 2 h at 700°C. This alloy, which has been chosen as the basis of a comprehensive military/industry/university program on *High Cycle Fatigue*, has a microstructure consisting of a bimodal distribution of  $\sim 60$  vol% primary- $\alpha$  and  $\sim 40$  vol% lamellar colonies of  $\alpha + \beta$  (Fig. 4).<sup>2</sup> This microstructure displays room temperature yield and tensile strengths of 930 and 970 MPa, respectively, and a Young's modulus of 116 GPa [25]. The fracture toughness,  $K_{Ic}$ , was measured to be  $\sim 67$  MPa $\sqrt{\text{m}}$ .

#### 3.2. Crack-propagation testing

##### 3.2.1. Cyclic fatigue

Fatigue-crack propagation studies were conducted on large ( $>10$  mm) through-thickness cracks in compact-tension  $C(T)$  specimens ( $L$ – $T$  orientation; 8 mm thick, 25 mm wide) cycled at load ratios varying from 0.10 to 0.95 in a laboratory air environment (22–32°C,<sup>3</sup>  $\sim 45\%$  relative humidity). To approach the threshold, both constant- $R$  and constant- $K_{\max}$  loading regimens were employed. Under both conditions, the cyclic stress intensity was varied according to the relationship:

<sup>2</sup> In the context of the Air Force *High Cycle Fatigue* program, this microstructure in Ti–6Al–4V has been referred to as “solution treated and overaged” (STOA).

<sup>3</sup> For fatigue testing at 1000 Hz, the average temperature of the sample rises  $\sim 10^\circ\text{C}$  over ambient conditions.



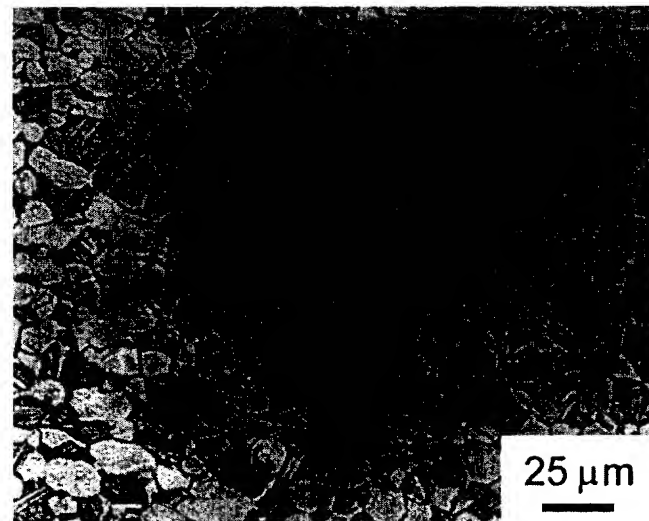


Fig. 4. Ti-6Al-4V in the "STOA" microstructure consisting of a bimodal distribution of  $\sim 60$  vol% primary- $\alpha$  and  $\sim 40$  vol% lamellar  $\alpha + \beta$ . This microstructure was chosen as the basis for a joint military/industry/university program on high cycle fatigue.

$$\Delta K = \Delta K_{\text{initial}} \exp[C(a - a_{\text{initial}})], \quad (4)$$

where  $a_{\text{initial}}$  and  $a$  are the initial and current values of the crack length, respectively,  $\Delta K_{\text{initial}}$  is the initial value of  $\Delta K$ , and  $C$  is the normalized  $K$ -gradient, set to a value of  $C = -0.08 \text{ mm}^{-1}$  (as suggested in ASTM Standard E-647). Constant- $K_{\text{max}}$  tests were employed to achieve threshold values at very high load ratios, i.e.,  $R > 0.8$ , thereby minimizing the effects of crack closure and representing worst-case *in-service* load ratios [26,27]. Loading frequencies were varied between 50 and 1000 Hz (sine wave). At 50–200 Hz, testing was conducted on conventional servo-hydraulic testing machines operating under automated closed-loop  $K$  control; corresponding tests at 1000 Hz were performed under  $K$  control on newly developed MTS servo-hydraulic test frames using voice-coil servovalves. The values of the fatigue thresholds,  $\Delta K_{\text{th}}$  and  $K_{\text{max,th}}$ , were defined as the minimum values of these parameters yielding a propagation rate of  $10^{-10} \text{ m/cycle}$ . Crack lengths were monitored in situ using back-face strain compliance techniques, with measurements verified periodically by optical inspection. Crack closure was also monitored using back-face strain compliance; specifically, the global closure stress intensity,  $K_{\text{cl}}$ , was obtained from the closure load,  $P_{\text{cl}}$ , which was approximated as the point of first deviation from linearity in the elastic compliance curve upon unloading [28], similar to the method described by Elber [29]. Based on such measurements, an effective (near-tip) stress-intensity range,  $\Delta K_{\text{eff}} = K_{\text{max}} - K_{\text{cl}}$ , was estimated.

### 3.2.2. Sustained-load cracking

SLC experiments were conducted using similar methodology to that for fatigue-crack growth. A pre-crack was grown under constant- $K_{\text{max}}$  fatigue loading conditions, with the  $K_{\text{max}}$  of the fatigue precrack chosen to equal the post-fatigue sustained- $K$ ,  $K_{\text{SLC}}$ . During precracking,  $\Delta K$  was shed according to Eq. (4) until a threshold growth rate of  $\sim 10^{-10} \text{ m/cycle}$  was reached. The  $\Delta K$  level was then reduced to 0.3–0.5  $\text{MPa}\sqrt{\text{m}}$  while holding  $K_{\text{max}}$  constant. This small  $\Delta K$ -cycle was chosen to be considerably smaller than the fatigue threshold ( $\sim 2 \text{ MPa}\sqrt{\text{m}}$ ) while retaining sufficient amplitude to facilitate "sustained-load" growth monitoring via back-face strain compliance, as had been used in the prior fatigue loading.

## 4. Results

### 4.1. Effect of loading frequency

A comparison of fatigue-crack propagation behavior at 50 and 1000 Hz is shown in Fig. 5 for load ratios of  $R = 0.1$  and  $0.8$ . Similar observations were made under constant- $K_{\max}$  loading conditions at  $K_{\max} = 36.5$  and  $56.5 \text{ MPa}\sqrt{\text{m}}$  ( $R \approx 0.9$  and  $0.95$  respectively). At all observed load ratios, a change in frequency induced a negligible (typically  $< 0.1 \text{ MPa}\sqrt{\text{m}}$ ) change in the  $\Delta K$  level for a given growth rate, well within the experimental scatter and specimen-to-specimen variation. Additional data obtained on the same alloy and microstructure at  $\sim 1700$  [30] and  $20,000$  Hz [31] also shows no significant frequency effect on the near-threshold fatigue behavior (Fig. 6). Such frequency-independent growth rates for titanium alloys tested in air have also been reported for the  $0.1$ – $50$  Hz range [33,34]; the current work extends this observation beyond  $1000$  Hz.

### 4.2. Effect of load ratio

Fatigue-crack propagation data collected under constant- $R$  loading conditions are shown in Fig. 7 at four load ratios:  $R = 0.1, 0.3, 0.5$ , and  $0.8$  ( $50$  Hz). These results are compared to constant- $K_{\max}$  fatigue-crack propagation at four  $K_{\max}$  values:  $K_{\max} = 26.5, 36.5, 46.5$ , and  $56.5 \text{ MPa}\sqrt{\text{m}}$  ( $1000$  Hz) in Fig. 8. As expected, higher load ratios result in lower  $\Delta K_{\text{th}}$  thresholds and faster growth rates at a given applied  $\Delta K$  value. Furthermore, this particular alloy does not exhibit the “Marci” effect as described previously. In Table 2, a comparison is given of the  $\Delta K$  levels required to achieve a growth rate ( $da/dN$ ) of  $10^{-9}$  and  $10^{-10}$  m/cycle (the latter representing the threshold  $\Delta K_{\text{th}}$ ) for all eight loading conditions. These results are compiled in Fig. 9a and b where the measured variation of the  $\Delta K_{\text{th}}$  and  $K_{\max, \text{th}}$  thresholds with positive  $R$  are compared.

The role of load ratio at near-threshold levels is generally attributed to crack closure, which is typically associated with the roughness-induced mechanism in titanium alloys [35–37]. In the current experiments,

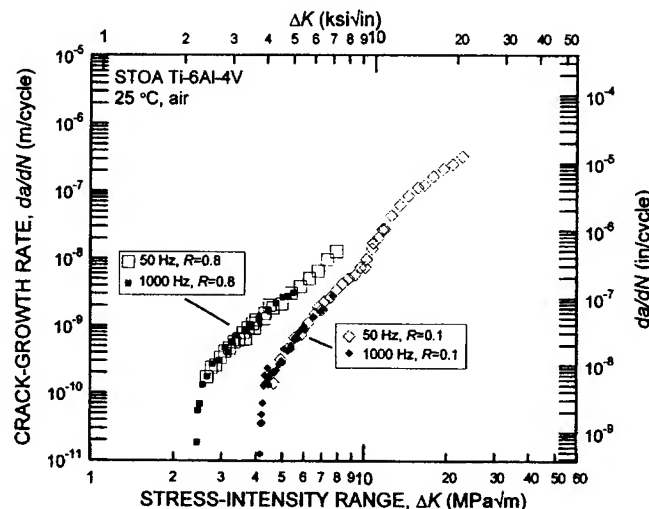


Fig. 5. Fatigue crack growth behavior of bimodal Ti-6Al-4V at two load ratios ( $R = 0.1$  and  $0.8$ ) and two frequencies ( $\nu = 50$  and  $1000$  Hz) suggesting that there is negligible influence of frequency in near-threshold growth behavior. Similar observations were made under constant- $K_{\max}$  loading conditions of  $K_{\max} = 36.5$  and  $56.5 \text{ MPa}\sqrt{\text{m}}$ .

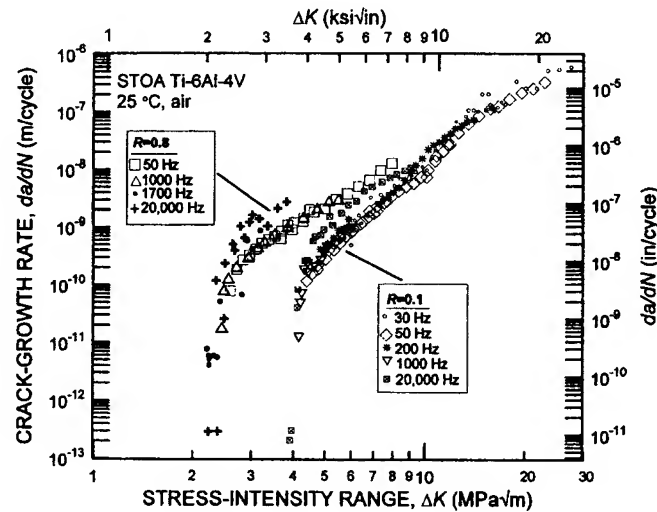


Fig. 6. Fatigue crack growth behavior of bimodal Ti-6Al-4V in the frequency range of 50–20,000 Hz indicating no obvious frequency effect in the near-threshold regime. Data at 1700 Hz were collected using a magnetostrictive fatigue loading stage by Davidson [30]. Data at 20,000 Hz were collected using ultrasonic fatigue by Mayer and Stanzl-Tschegg [31]. Data at 30 Hz was collected by Hines and Lütjering [32].

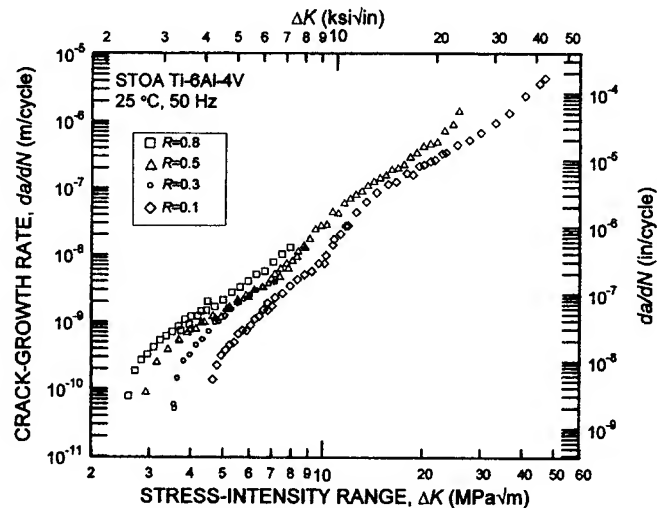


Fig. 7. Effect of load ratio,  $R$ , on fatigue crack propagation under constant- $R$  loading. As the load ratio is increased, the growth rates at a given  $\Delta K$  increase and the fatigue threshold decreases.

closure was approximated from the deviation from linearity in the unloading compliance curve. At low load ratios,  $R < 0.5$ , closure values were found to be approximately constant at  $K_{cl} \sim 2.0 \text{ MPa}\sqrt{\text{m}}$ , however, no closure was detected at  $R > 0.5$ . This closure value was essentially identical for  $R = 0.1$  and  $0.3$ ; moreover, the closure value did not change substantially as  $\Delta K$  was shed towards threshold. The variation of thresholds,  $\Delta K_{th}$  and  $K_{max,th}$ , with load ratio (Fig. 9a and b) show an apparent transition at  $R \sim 0.5$ , consistent with the Schmidt and Paris [1] analysis (Eq. (1)) which would predict a transition at  $R \sim 0.3\text{--}0.5$  based on the measured closure value of  $2 \text{ MPa}\sqrt{\text{m}}$ . Perhaps the most convincing representation of this

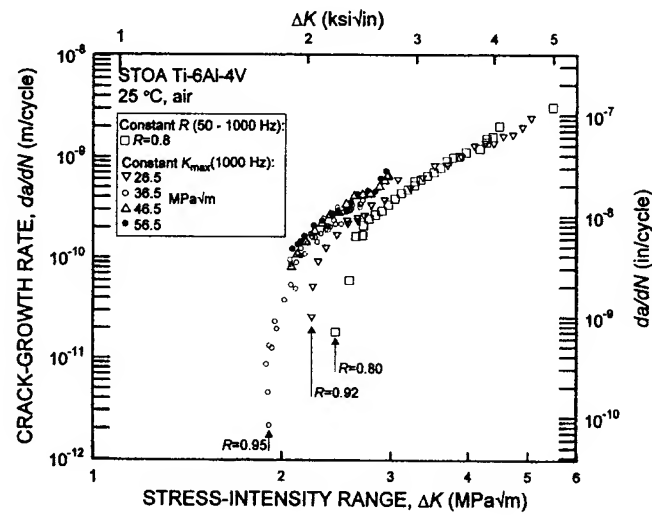


Fig. 8. Fatigue crack propagation data collected under constant- $K_{\max}$  conditions compared to  $R = 0.8$  data (squares) collected under constant- $R$  conditions. As  $K_{\max}$  was increased such that the load ratios exceed  $R = 0.8$ , the value of the fatigue threshold continued to decrease. This decrease in the fatigue threshold with increasing  $K_{\max}$  is observed in the apparent absence of crack closure, as detected by back-face strain compliance.

Table 2

$\Delta K$  levels required for growth rates of  $10^{-9}$  and  $10^{-10}$  m/cycle

$R$	$K_{\max}$ (MPa√m)	$\Delta K$ (MPa√m)
Growth rate, $da/dN = 10^{-9}$ m/cycle		
0.1 <sup>a</sup>	6.47–6.92	5.82–6.23
0.3 <sup>a</sup>	6.77–6.83	4.74–4.78
0.5 <sup>a</sup>	8.66–9.26	4.33–4.63
0.8 <sup>a</sup>	18.6–20.2	3.72–4.03
0.85	26.5 <sup>a</sup>	3.85
0.90	36.5 <sup>a</sup>	~3.6
0.93	46.5 <sup>a</sup>	~3.4
0.94	56.5 <sup>a</sup>	~3.15
Growth rate, $da/dN = 10^{-10}$ m/cycle		
0.1 <sup>a</sup>	4.72–4.78	4.25–4.30
0.3 <sup>a</sup>	5.16	3.61
0.5 <sup>a</sup>	5.86	2.93
0.8 <sup>a</sup>	12.5–13.1	2.50–2.61
0.91	26.5 <sup>a</sup>	2.33
0.94	36.5 <sup>a</sup>	2.11–2.15
0.955	46.5 <sup>a</sup>	2.09
0.954	56.5 <sup>a</sup>	~2.04

<sup>a</sup> This value was held constant during the fatigue test.

transition from a “closure-affected” to a “closure-free” threshold is shown in a plot of  $\Delta K_{th}$  versus  $K_{\max,th}$  in Fig. 9c, which is simply a coordinate transformation of Fig. 9a and b. The distinct change in slope in Fig. 9c is surely associated with some change in governing mechanism, and is, in this case, coincident with the elimination of global crack closure.

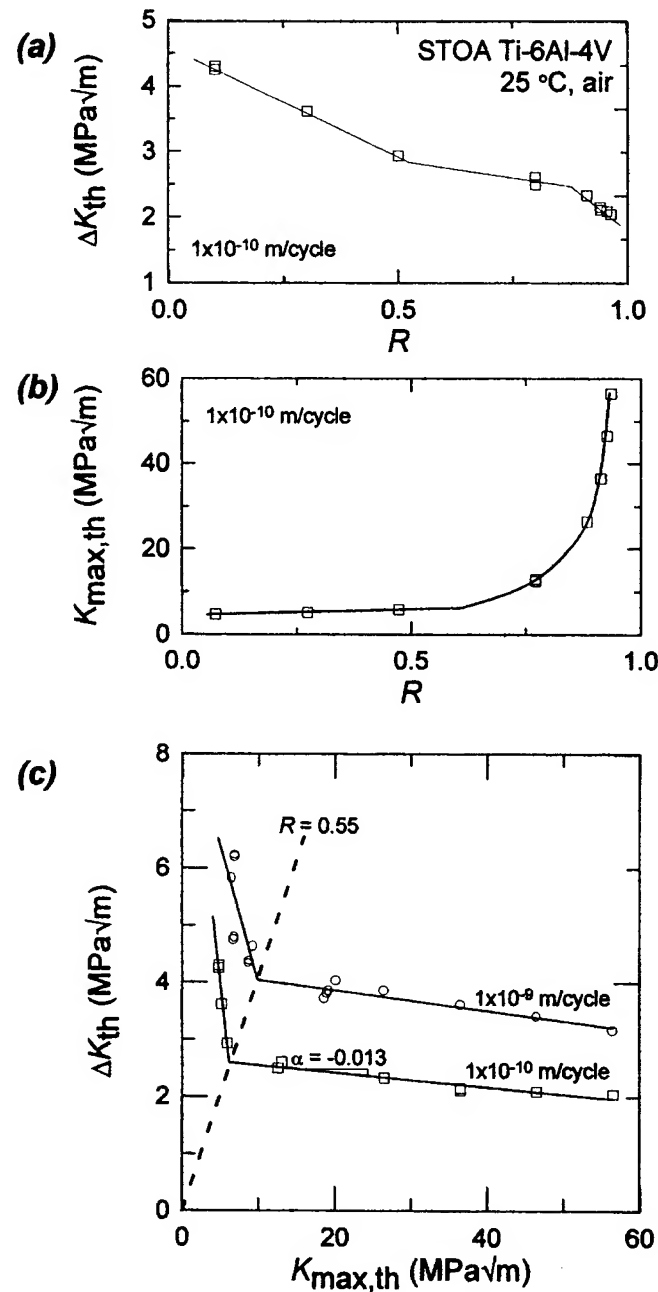


Fig. 9. Loading conditions for a threshold growth rate of  $10^{-10}$  m/cycle in bimodal Ti-6Al-4V (50 Hz and 1000 Hz). (a) Cyclic stress intensity at threshold,  $\Delta K_{th}$ , as a function of load ratio,  $R$  (b) the maximum stress intensity at threshold,  $K_{max,th}$ , as a function of  $R$ . (c)  $\Delta K_{th}$  as a function of  $K_{max,th}$  (along with data collected for a growth rate of  $10^{-9}$  m/cycle). Of the three parameters,  $\Delta K_{th}$ ,  $K_{max,th}$ , and  $R$ , only two are unique.

In the case where crack closure is the only mechanism responsible for the load ratio effect, one might expect that a closure-corrected stress-intensity range,  $\Delta K_{eff}$ , would yield a crack-propagation curve which is

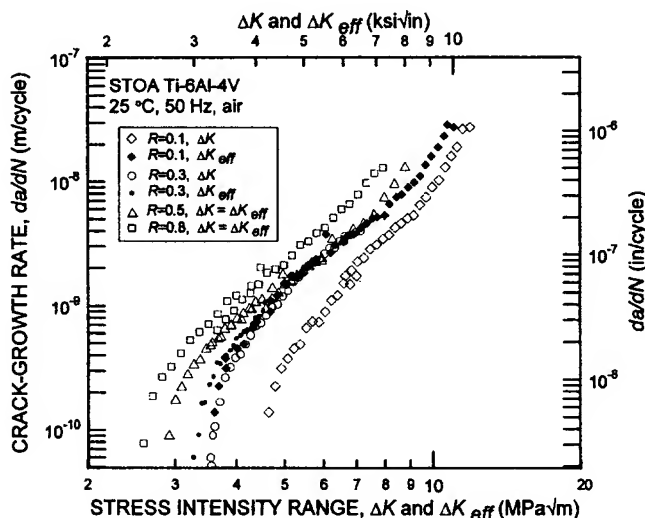


Fig. 10. Considering only 50 Hz, constant- $R$  data, raw growth data (open symbols) is compared to closure corrected data (closed symbols) where closure is assessed by determining the effective stress intensity range:  $\Delta K_{eff} = K_{max} - K_{cl}$ .

unaffected by load ratio. Indeed, in the current study,  $\Delta K_{eff}$  does tend to normalize the low load ratio data ( $R < 0.5$ ) onto a single curve (Fig. 10) (see also Ref. [5]). However, above  $R \sim 0.5$  where (global) closure was not experimentally detected,  $\Delta K_{th}$  values continue to decrease with increasing  $R$ . This is also apparent in the plot of  $\Delta K_{th}$  versus  $K_{max,th}$  in Fig. 9c; in the region where threshold is  $K_{max}$ -controlled,  $\Delta K_{th}$  is not invariant and decreases approximately linearly with increasing  $K_{max}$ . The slope of this decrease can be quantified in terms of Eq. (2) as  $\alpha = -0.013$ , implying that an increase in the  $K_{max}$  value of 10  $MPa\sqrt{m}$  is associated with a 0.13  $MPa\sqrt{m}$  decrease in  $\Delta K_{th}$  threshold.

#### 4.3. Fractography and crack profiles

Fractography (from scanning electron microscopy) and crack profiles (from optical microscopy) corresponding to the threshold growth rate of  $10^{-10}$  m/cycle at three load ratios,  $R = 0.1, 0.5$ , and  $0.95$ , are compared to the static overload condition in Fig. 11. The crack profiles for the three load ratios show a decrease in crack-path tortuosity as  $R$  or  $K_{max}$  is increased. Nevertheless, there are only minimal differences in the fractography for the three different load ratios, even though they span more than an order of magnitude in  $K_{max}$  and two orders of magnitude in the plastic-zone size. There is a clear distinction, however, in the morphology of the fatigue surfaces compared to that of the overload fracture condition where microvoid coalescence can be seen. Thus, it can be concluded that, even at  $R = 0.95$  where  $K_{max} = 57$   $MPa\sqrt{m}$  ( $K_{max}/K_{Ic} \cong 0.85$ ), there is no clear evidence of static fracture modes, in this case due to microvoid coalescence, in the fractography of fatigue-crack growth in this alloy.

#### 4.4. Effect of internal hydrogen content

To study the effects of internal hydrogen content, several samples were heat treated in high vacuum at 700°C for 24 h thereby reducing the hydrogen content from an as-received value of  $\sim 35$  to  $\sim 5$  ppm with no apparent microstructural changes. The low-hydrogen specimens were subsequently tested under fatigue loading conditions at constant  $R = 0.5$  and constant  $K_{max} = 28$   $MPa\sqrt{m}$ . A comparison of the near-threshold fatigue-crack growth behavior for the as-received and low internal hydrogen conditions is

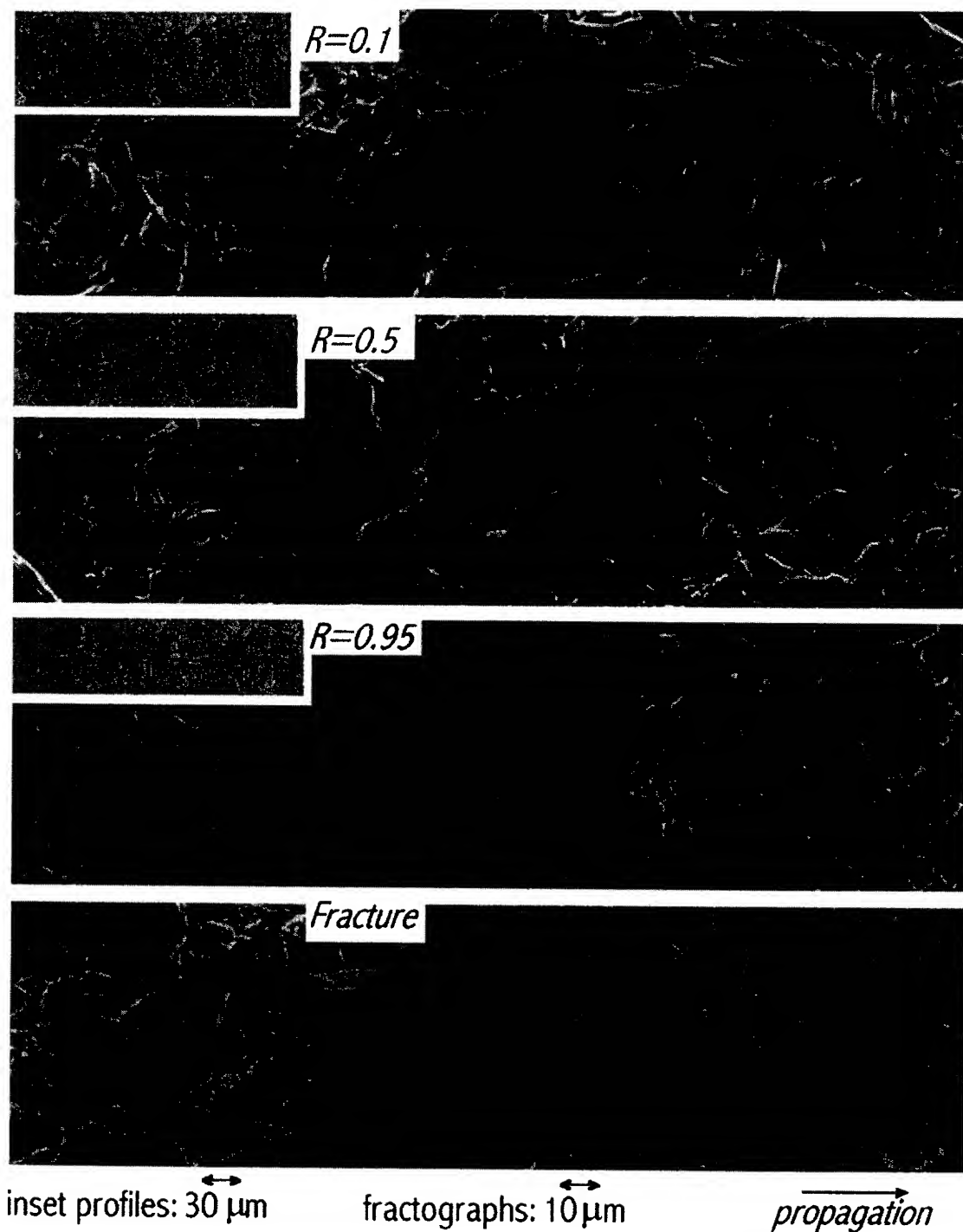


Fig. 11. A comparison of fractography and crack profiles under fatigue (observing a threshold growth rate  $\sim 10^{-10}$  m/cycle at three load ratios,  $R = 0.1$ ,  $0.5$ , and  $0.95$ ) and static overload fracture condition. While microvoid coalescence is apparent in the overload fracture, there is no clear evidence of this mode in the fatigue fractographs, even at  $R = 0.95$  where  $K_{\max} = 57 \text{ MPa}\sqrt{\text{m}}$ .

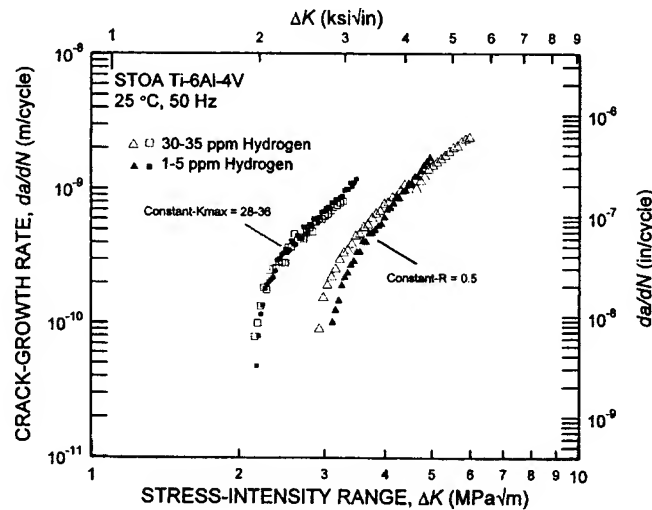


Fig. 12. The effect of internal hydrogen on near-threshold fatigue-crack propagation behavior in bimodal Ti-6Al-4V. Although the hydrogen content was reduced by a factor of six or more, the  $\Delta K_{th}$  threshold is still significantly affected by load ratios in excess of the “closure-free” transition,  $R \sim 0.5$ .

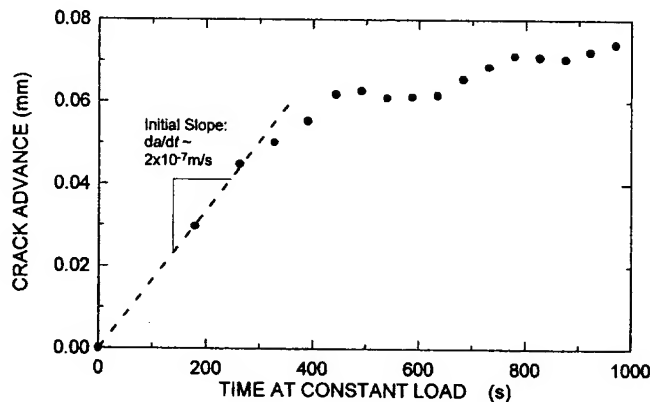


Fig. 13. Transient SLC observed at  $K = 36.5 \text{ MPa}\sqrt{\text{m}}$ . The initial SLC growth-rate of  $2 \times 10^{-7} \text{ m/s}$  is similar to the difference in the fatigue-crack growth rates between  $R = 0.8$  and  $K_{max} = 36.5 \text{ MPa}\sqrt{\text{m}}$  (Fig. 8).

presented in Fig. 12, where it is apparent that there is little effect of hydrogen content ( $\sim 5\text{--}35 \text{ ppm}$ ) in this alloy. Most specifically, we see that the threshold was still affected by load ratios in excess of the “closure-free” transition ( $R > 0.5$ ), in spite of the very low hydrogen content, and that the extent of this effect appears to be independent of hydrogen content over this range.

#### 4.5. Sustained-load cracking

The results of sustained-load tests on the Ti-6Al-4V alloy at a constant applied stress intensity of  $K = 36.5 \text{ MPa}\sqrt{\text{m}}$ , shown in Fig. 13, indicate approximately  $80 \mu\text{m}$  of slow crack growth over the first 1000 s following initiation from the fatigue pre-crack. The initial growth rate of  $\sim 2 \times 10^{-7} \text{ m/s}$  was seen to decay until crack arrest ( $< 1 \times 10^{-11} \text{ m/cycle}$ ) within 1000 s. This transient behavior indicates that for



near-threshold fatigue-crack growth to be affected by SLC, then the SLC mechanism must be “restarted” by each fatigue cycle. Without “restarting” on each fatigue cycle, the SLC growth-rate would decay to arrest within the first several minutes of a constant- $K_{\max}$  fatigue test, and thus would have little or no effect on the value of the fatigue threshold.

## 5. Discussion

Crack closure is generally considered to be the primary reason for the effect of load ratio on the  $\Delta K_{th}$  fatigue threshold in metallic materials. Indeed, at low load ratios such that  $R < R_c$ , the closure-based analysis describes threshold behavior reasonably well in most cases, including the data presented in this paper. However, based on the closure argument, at load ratios where  $K_{min}$  exceeds  $K_{cl}$ , (i.e.  $R > R_c$ ) such that the influence of (global) closure is minimized, the value of  $\Delta K_{th}$  would be expected to become independent of  $R$ . This is the generally anticipated behavior, however, in the current Ti–6Al–4V alloy, we have observed a progressive reduction in  $\Delta K_{th}$  from  $R = 0.5$  (the “closure-free” condition) to  $R = 0.95$ ; specifically, a  $\sim 1$  MPa $\sqrt{m}$  decrease in  $\Delta K_{th}$  is found as  $K_{\max}$  increases from  $\sim 6$  MPa $\sqrt{m}$  (at  $R = 0.5$ ) to 57 MPa $\sqrt{m}$  (at  $R = 0.95$ ). Furthermore, examples have been given (Table 1) of several other Ti-alloys that also exhibit a  $K_{\max}$ -sensitivity on the threshold at high load ratios ( $R > R_c$ ).

As noted previously, one possible explanation for this effect is the occurrence of SLC mechanisms during fatigue-crack growth at high load ratios, where the high values of  $K_{\max}$  exceed some SLC threshold. This being the case, the measured fatigue-crack growth rates would result from contributions from both mechanical fatigue cracking,  $(da/dN)_{fatigue}$ , and that due to SLC  $(da/dt)_{SLC}$ , as modeled using a process competition [38] or, as indicated in Eq. (5), a superposition [39] model:<sup>4</sup>

$$\left. \frac{da}{dN} \right|_{total} = \left. \frac{da}{dN} \right|_{fatigue} + \frac{1}{v} \left. \frac{da}{dt} \right|_{SLC} \quad (5)$$

Support for this notion comes from the observation that the measured sustained-crack growth rate of  $\sim 2 \times 10^{-7}$  m/s at a sustained  $K$  of 36.5 MPa $\sqrt{m}$  corresponds to a growth rate per cycle at 1000 Hz of  $\sim 2 \times 10^{-10}$  m/cycle, which is similar to the difference in the fatigue-growth rates at a given applied  $\Delta K$  for  $R = 0.5$  compared to 0.95. Two possible mechanisms for such SLC are described below:

(i) *Stress-assisted hydride formation.* Several independent studies in titanium alloys have concluded that under sufficient triaxial stress, internal hydrogen can precipitate as metal hydrides at  $\alpha/\beta$  [40] or  $\alpha/\alpha$  [41] interfaces, or within  $\alpha$ -grains [20] leading to brittle fracture of the hydrides. This phenomenon has been used to explain both sustained-load cracking [20,21,42], where crack advance is observed under monotonic load, and accelerated fatigue-crack propagation at high load ratios [40,43].

(ii) *Creep-assisted crack growth.* Alternatively, since room-temperature creep can occur in titanium alloys, it has been suggested that the role of hydrogen is to accelerate SLC by creep rather than through hydride formation. Williams [44], for example, observed in Ti–6Al–4V that the threshold stress intensity for failure by SLC,  $K_{SLC,th}$ , increased with increasing hydrogen content, which is apparently counterintuitive to the hydride formation mechanism. Furthermore, second-stage creep rate was observed to decrease significantly with increasing hydrogen content; at 95% of the yield strength, the creep rate decreased from  $120 \times 10^{-6}$  %/h for 7 ppm H to  $36 \times 10^{-6}$  %/h for 60 ppm H. From these or similar observations, some authors [44,45] have concluded that the role of hydrogen in sustained load crack stems from creep behavior rather than the formation and failure of brittle hydrides.

<sup>4</sup> One might argue that these models may be overly simplistic. Nevertheless, the rather basic notion that mechanical fatigue and SLC should somehow act in concert is what is most important for the ensuing arguments.

Both of the aforementioned mechanisms suggest that the degree and extent of SLC is related to the internal hydrogen content, although the exact role of hydrogen is still controversial. Nevertheless, if SLC growth was a significant contribution to the observed fatigue crack-growth rates at high load ratios, one may expect that the high- $R$  behavior could be altered by changing the internal hydrogen content. Alternatively, if hydrogen could (hypothetically) be entirely removed, the SLC mechanism should be entirely eliminated, thereby yielding an invariant  $\Delta K_{th}$  threshold above the “closure-free” transition ( $R > 0.5$ ), assuming that there are no *additional* mechanisms present. However, as illustrated in Fig. 12, a reduction in the hydrogen content by more than a factor of six has essentially no effect on the fatigue thresholds in this alloy. Moreover, the  $K_{max}$ -sensitivity of the fatigue threshold at high load ratios remains essentially unchanged by the reduction in internal hydrogen.

Furthermore, setting the hydrogen observations aside, it seems unlikely that any SLC mechanism could provide a major contribution to fatigue in this alloy in light of the observed frequency independence ( $\nu = 50$ –1000 Hz) of fatigue-crack propagation that is observed at all load ratios (Fig. 6). Indeed, the observed frequency independence indicates that if a chemically- or electrochemically-controlled mechanism was related to the observed high- $R$  load ratio effect, then the time-dependent processes must go to completion within 1 ms (the time for one cycle at 1000 Hz).

Finally, any thermally-activated mechanism such as SLC, would be expected to manifest itself in the temperature dependence of fatigue behavior. Thomas [46] has observed the SLC and fatigue-crack growth at three temperatures ( $-30^{\circ}\text{C}$ ,  $22^{\circ}\text{C}$  and  $140^{\circ}\text{C}$ ) in the same alloy and microstructure considered in this study. He found that the extent of SLC transient growth decreased with increasing temperature, obeying an Arrhenius relationship. At a sustained  $K$  of  $60 \text{ MPa}\sqrt{\text{m}}$ , there was  $\sim 500 \mu\text{m}$  of transient growth at  $-30^{\circ}\text{C}$ , but only  $\sim 45 \mu\text{m}$  of such growth at  $140^{\circ}\text{C}$ . Therefore, for SLC to be an important component of this alloy's fatigue behavior, one may expect the fatigue behavior to also be temperature-dependent. However, over this same range in temperature, the fatigue behavior of this alloy remained invariant (observed at  $K_{max} = 60 \text{ MPa}\sqrt{\text{m}}$ ).

While there is no doubt that SLC does occur in many titanium alloys, the observed lack of an effect of frequency, temperature, or hydrogen content on fatigue behavior strongly suggest that SLC does not contribute significantly to the  $K_{max}$ -sensitive fatigue behavior at high load ratios in this particular alloy and microstructure. However, since the slopes,  $\alpha$ , of  $\Delta K_{th}$  versus  $K_{max}$  (for  $R > R_c$ ) relationship (Eq. (1)) vary by a factor of roughly seven in titanium alloys and the current alloy/microstructure is at the shallow end of this range, it is conceivable that SLC does contribute to fatigue-crack growth behavior in certain other Ti alloy microstructures, particularly those with higher internal hydrogen content. Indeed, there is some evidence in the literature that SLC may be an important component in the high- $R$  fatigue behavior of *other* titanium alloys. For example, Pao et al. [40] studied the effect of hydrogen content on the fatigue threshold of a  $\beta$  titanium alloy at  $R = 0.9$ . As might be expected from a SLC contribution, they observed the fatigue threshold to decrease with increasing hydrogen content. Specifically, when the hydrogen content was changed from 40 to 1000 ppm, the threshold was reduced from 2.7 to 2.0  $\text{MPa}\sqrt{\text{m}}$ . This is in contrast to the behavior currently observed in the  $\alpha + \beta$  alloy in this study where an increase in hydrogen content from  $\sim 5$  to  $\sim 35$  ppm did not alter the threshold (Fig. 12), albeit these two observations were over different ranges of hydrogen content.

As the observed lack of a significant frequency or temperature effect on fatigue-crack propagation in this alloy largely negates a major role of environmentally-assisted mechanisms in influencing the  $K_{max}$  dependence of the  $\Delta K_{th}$  threshold, other purely mechanical mechanisms may be considered, as described below.

(i) *Microscopic near-tip closure.* During in situ studies in the scanning electron microscope of fatigue-crack propagation behavior in the same titanium alloy and microstructure at  $>1000 \text{ Hz}$ , Davidson reported that he detected crack closure in the local region (within  $\sim 10 \mu\text{m}$ ) behind the crack tip, despite being at  $R$

values of 0.8–0.9, i.e., well above the (global) “closure-free” load ratio,  $R_c$  [30]. While this near-tip (or local) closure is essentially undetectable by the macroscopic techniques such as unloading compliance, it could nevertheless significantly affect the effective stress intensity experienced at the crack tip. In this way, closure would exist at all load ratios; however, the extent of the crack flank over which it operates would be a function of the load ratio (or more specifically, the minimum stress intensity). However, what detracts from this explanation is the marked transition at  $R = 0.5$ . As shown in Fig. 9c, there is a distinct transition from  $\Delta K$ -controlled to  $K_{\max}$ -controlled thresholds at  $R = 0.5$ . It is difficult to reconcile this observation with a near-tip closure model, which would presumably manifest itself in a smooth transition from global- to near-tip closure as the extent of the closure wake grew smaller.

(ii) *Static fracture modes.* As  $K_{\max}$  values approach the point of instability, as characterized by  $K_{Ic}$ , additional static fracture modes, specifically cleavage, intergranular fracture or void coalescence, can occur during fatigue-crack growth and lead to accelerated growth rates and a strong sensitivity to both load ratio and  $K_{\max}$  [9]. Such behavior is most often observed at lower load ratios and high growth rates, e.g.  $>10^{-5}$  m/cycle, where the  $\Delta K$  level is large such that  $K_{\max} \rightarrow K_{Ic}$ ; in the present work at high load ratios where  $K_{\max}$  is held near  $K_{Ic}$ , static fracture modes could presumably occur even at near-threshold growth rates. The occurrence of such static modes provides a very feasible explanation of the continued  $K_{\max}$ -dependency of fatigue behavior at load ratios above the “closure-free” condition,  $R_c$ . However, scanning electron micrographs of the fatigue fracture surfaces, shown in Fig. 11, reveal no such differences in the near-threshold fracture morphology at  $R = 0.5$  and 0.95, despite the order of magnitude increase in  $K_{\max}$  (threshold  $K_{\max}$  values are 5.9 and 56.5 MPa $\sqrt{m}$  at  $R = 0.5$  and 0.95, respectively). Furthermore, the mechanism responsible for the downward trend in  $\Delta K_{th}$  with increasing  $R$  (or  $K_{\max}$ ) appears to active at even moderate “closure-free” load ratios ( $R = 0.8$ ), where  $K_{\max}$  is much less than  $K_{Ic}$ . Based on the lack of apparent static modes in the high- $K_{\max}$  fractography, and the observed  $K_{\max}$ -sensitivity at even moderate load ratios, the static mode argument can be discounted as a potential explanation in this alloy.

(iii)  *$K_{\max}$ -dependence on intrinsic near-threshold fatigue.* As noted above, the mechanistic role of  $R$  or  $K_{\max}$  on fatigue-crack growth is traditionally associated with crack closure and/or the occurrence of additional  $K_{\max}$ -controlled mechanisms, such as environmentally-assisted cracking or static modes. However, these mechanisms do not appear to be the controlling factors in the present alloy at  $R > R_c$ . Therefore, we must consider whether the magnitude of  $K_{\max}$  can also affect the *intrinsic* mechanism of fatigue-crack growth, particularly since between  $R = 0.5$  and 0.95 where the  $\Delta K_{th}$  threshold is reduced by  $\sim 1$  MPa $\sqrt{m}$ , the maximum plane-strain plastic-zone size varies by some two orders of magnitude, from  $\sim 2$  to 200  $\mu m$ , as  $K_{\max}$  increases from  $\sim 6$  to 57 MPa $\sqrt{m}$ . Based on this significant change in the local plasticity, it would seem likely that there would be an effect on the fatigue-crack growth behavior and the value of the threshold. However, a majority of the existing *mechanism-based* intrinsic threshold models [47–52], which are most often based on the critical conditions for dislocation emission at the crack-tip, do not explicitly describe the mechanistic nature of a  $K_{\max}$ -dependent component. The evidence presented here strongly implies that  $K_{\max}$  does indeed influence the threshold for fatigue-crack growth, independent of crack closure, presumably by its effect on intrinsic crack growth. The precise mechanism of this  $K_{\max}$  contribution, however, is presently unclear, although mechanisms associated with the spread of local plasticity would appear to be influential. An understanding of this mechanism would greatly enhance our knowledge of the fundamental fatigue process.

## 6. Conclusions

A study has been made of the role of the maximum stress intensity ( $K_{\max}$ ) and the load ratio (over the range  $R = 0.1$ –0.95) in influencing fatigue-crack propagation and specifically threshold behavior in a

Ti–6Al–4V alloy, tested over a range of loading frequencies (50–1000 Hz) and in room temperature air (22–32°C, 45% relative humidity). Based on this work, which was focused on an alloy with a bimodal (STOA) microstructure ( $\sim 60$  vol% primary- $\alpha$ ,  $\sim 40$  vol% lamellar  $\alpha + \beta$ ), the following conclusions can be made:

1. Room temperature fatigue-crack growth ( $\sim 10^{-12}$ – $10^{-6}$  m/cycle) and threshold  $\Delta K_{th}$  values were found to be independent of loading frequency over the range 50–1000 Hz; companion studies at 20,000 Hz on the same alloy/microstructure, together with previous results in the literature, suggest that such frequency-independent growth rate behavior at near-threshold levels extends over five orders of magnitude from 0.1 to 20,000 Hz.

2. The fatigue thresholds,  $\Delta K_{th}$  and  $K_{max,th}$ , were found to vary significantly with positive load ratio ( $R = 0.1$ – $0.95$ ). Consistent with the description of Schmidt and Paris, below a critical load ratio,  $R_c$  ( $\sim 0.5$ ), the  $K_{max,th}$  threshold was seen to be independent of  $R$ , and the  $\Delta K_{th}$  decreased with increasing  $R$ . By measuring (global) crack closure loads, using unloading compliance techniques, this behavior was found to be consistent with the traditional explanation of load ratio effects on the fatigue threshold involving closure, with  $R_c$  defining the condition at which the closure stress intensity,  $K_{cl} = K_{min}$ .

3. At load ratios larger than  $R_c$ , i.e.,  $R \sim 0.5$ – $0.95$ , where (global) crack closure could no longer be detected, a different dependence of the  $\Delta K_{th}$  threshold on load ratio was seen, with  $\Delta K_{th} \rightarrow 0$  as  $R \rightarrow 1$ . Such behavior is contrary to conventional explanations of the near-threshold load-ratio effect, which are based on crack closure and imply that  $\Delta K_{th}$  is independent of load ratio for  $R > R_c$ . The decrease in  $\Delta K_{th}$  threshold is approximately linear with increase in  $K_{max}$ , decaying at a rate of  $-0.013$ . A survey of literature indicated that this effect was seen by several titanium alloys, with slopes varying between  $-0.01$  to  $-0.07$ .

4. Explanations for this effect are suggested, based on the occurrence of (i) SLC due to internal hydrogen, (ii) static ( $K_{max}$ -controlled) fracture modes, (iii) near-tip crack closure, and (iv) an effect of  $K_{max}$  on the intrinsic mechanism of fatigue-crack growth. In the present alloy/microstructure, the effect could not be ascribed to hydrogen-assisted SLC, as fatigue thresholds were unaffected by changes in hydrogen content, frequency, or temperature. Nor was the effect ascribed to the occurrence of static modes, as the morphology of the near-threshold fatigue fracture surfaces was essentially unchanged between load ratios of  $0.5$ – $0.95$ . While near-tip closure may be a source for this effect, it seems most likely that the intrinsic fatigue-crack growth process is itself  $K_{max}$  dependent. The  $K_{max}$ -sensitivity should be considered in developing mechanistic *intrinsic* threshold models.

## Acknowledgements

This work was supported by the US Air Force Office of Scientific Research under Grant No. F49620-96-1-0478 under the auspices of the Multidisciplinary University Research Initiative on *High-Cycle Fatigue* to the University of California. Thanks are due to the Hertz Foundation for a graduate fellowship for B.L.B., to Drs. H.R. Mayer and S.E. Stanzl-Tschegg for performing the ultrasonic fatigue experiments, and to Dr. J.P. Campbell and Z. Bell for experimental assistance.

## References

- [1] Schmidt RA, Paris PC. Threshold for fatigue crack propagation and the effects of load ratio and frequency. *Progress in Flaw Growth and Fracture Toughness Testing*, ASTM STP 536, ASTM, Philadelphia, 1973. p. 79–94.
- [2] Ritchie RO. Near-threshold fatigue crack propagation in ultra-high strength steel: influence of load ratio and cyclic strength. *J Engng Mat Tech ASME Series H* 1977;99:195–204.

- [3] Liaw PK, Leax TR, Logsdon WA. Near-threshold fatigue crack growth behavior in metals. *Acta Metall* 1983;31:1581–7.
- [4] Taylor D. A compendium of fatigue thresholds and growth rates. Engineering Materials Advisory Services Ltd., West Midlands, UK, 1985.
- [5] Dubey S, Soboyejo ABO, Soboyejo WO. An investigation of the effects of stress ratio and crack closure on the micromechanisms of fatigue crack growth in Ti–6Al–4V. *Acta Materialia* 1997;45:2777–87.
- [6] Ritchie RO, Boyce BL, Campbell JP, Roder O, Thompson AW, Milligan WW. Thresholds for high cycle fatigue in a turbine engine Ti–6Al–4V alloy. *Int J Fatigue* 1999;22:621–31.
- [7] Kardomateas GA, Carlson RL. Predicting the effects of load ratio on the fatigue crack growth rate and fatigue threshold. *Fatigue Fract Engng Mat Struct* 1998;21:411–23.
- [8] Chiang CR. Threshold stress intensity factor of fatigue cracks. *Engng Fract Mech* 1994;49:29–33.
- [9] Ritchie RO, Knott JF. Mechanisms of fatigue crack growth in low alloy steel. *Acta Metall* 1973;21:639–48.
- [10] Suresh S, Ritchie RO. On the influence of environment on the load ratio dependence of fatigue threshold in pressure vessel steel. *Engng Fract Mech* 1983;18:785–800.
- [11] Lenets YN, Nicholas T. Load history dependence of fatigue crack growth thresholds for a Ti alloy. *Engng Fract Mech* 1998;60:187–203.
- [12] Döker H. Fatigue crack growth threshold: implications, determination and data evaluation. *Int J Fatigue* 1997;19:S145–149.
- [13] Huthmann H, Gossmann O. Verband für Materialforschung und – prüfung. in 23. Vortragsveranstaltung des DVM-Arbeitskreises Bruchvorgänge, Deutscher, Berlin, 1981. p. 271–84.
- [14] Bray GH, Donald JK. Separating the influence of  $K_{max}$  from closure-related stress ratio effects using the adjusted compliance ratio technique. In: McClung RC, Newman Jr JC, editors. *Advances in fatigue crack closure measurement and analysis: second volume*. ASTM STP 1343, American Society for Testing and Materials, Philadelphia, PA, 1997.
- [15] Smith SW, Piascik RS. An indirect technique for determining closure free fatigue crack growth behavior. In: Newman JC, Piascik RS, editors. *Fatigue crack growth thresholds, endurance limits and design*, ASTM STP 1372, American Society for Testing and Materials, Philadelphia, 2000. p. 109–22.
- [16] Marci G. A fatigue crack growth threshold. *Engng Fract Mech* 1992;41:367–85.
- [17] Marci G. Non-propagation conditions ( $\Delta K_{th}$ ) and fatigue crack propagation threshold ( $\Delta K_T$ ). *Fatigue Fract Engng Mater Struct* 1994;17:891–907.
- [18] Marci G. Comparison of fatigue crack propagation thresholds of two Ti turbine-disk materials. *Fatigue* 1994;16:409–12.
- [19] Marci G, Castro DE, Bachmann V. Fatigue crack propagation threshold. *J Test Eval* 1989;17:28–39.
- [20] Moody NR, Costa JE. A review of microstructure effects on hydrogen-induced sustained load cracking in structural titanium alloys. In: Kim Y-W, Bloyer RR, editors. *Microstructure/property relationships in titanium aluminides and alloys*. The Minerals, Metals, and Materials Society, Warrendale, PA, 1991.
- [21] Boyer RR, Spurr WF. Characteristics of sustained-load cracking and hydrogen effects in Ti–6Al–4V. *Metall Trans A* 1978;9A:23–9.
- [22] Marci G. Failure mode below 390 K with IMI 834. In: Lütjering G, Newack H, editors. *Fatigue '96*. Proceedings of the Sixth International Fatigue Conference, Berlin, Germany, vol. 1, Pergamon, Oxford, 1996. p. 493–8.
- [23] Marci G. *Werkstofftech. Mat.-wiss* 1997;28:51.
- [24] Lang M, Hartman GA, Larsen JM. Investigation of an abnormality in fatigue crack growth curves – the Marci effect. *Scripta Materialia* 1998;38:1803–10.
- [25] Eylon D. Summary of the available information on the processing of the Ti–6Al–4V HCF/LCF program plates. University of Dayton Report, Dayton, OH, 1998.
- [26] Döker H, Bachmann V, Marci G. A comparison of different methods of determination of the threshold for fatigue crack propagation. In: Bäcklund J, Blom AF, Beevers CJ, editors. *Fatigue Thresholds*, vol. 1. EMAS, Warley, UK, 1982. p. 45–58.
- [27] Herman WA, Hertzberg RW, Jaccard R. A simplified laboratory approach for the prediction of short crack behavior in engineering structures. *Fatigue Fract Engng Mater Struct* 1988;11:303–20.
- [28] Ritchie RO, Yu W. Short crack effects in fatigue: a consequence of crack tip shielding. In: Ritchie RO, Lankford J, editors. *Short Fatigue Cracks*, TMS, Warrendale, PA, 1986. p. 167–89.
- [29] Elber W. Fatigue crack closure under cyclic tension. *Engng Fract Mech* 1970;2:37–45.
- [30] Davidson D. Damage mechanisms in high cycle fatigue. AFOSR Final Report, Project 06–8243. Southwest Research Institute, San Antonio, TX, 1998.
- [31] Mayer HR, Stanzl-Tschegg SE. Universität für Bodenkultur, private communication, 1998.
- [32] Hines JA, Lütjering G. Propagation of microcracks at stress amplitudes below the conventional fatigue limit in Ti–6Al–4V. *Fatigue Fract Engng Mater Struct* 1999;22:657–65.
- [33] Wanhill RJH. Environment and frequency effects during fatigue crack propagation in Ti–2.5 Cu (IMI 230) sheet at room temperature. *Corrosion-NACE* 1974;30:28–35.
- [34] Dawson DB, Pelloux RMN. Corrosion fatigue crack growth of titanium alloys in aqueous environments. *Metall Trans* 1974;5:723–31.

- [35] Halliday MD, Beevers CJ. Some aspects of fatigue crack closure in two contrasting titanium alloys. *J Test Eval* 1981;9: 195–201.
- [36] Ravichandran KS. Near threshold fatigue crack growth behavior of a titanium alloy: Ti–6Al–4V. *Acta Metallurgica et Materialia* 1991;39:401–10.
- [37] Ogawa T, Tokaji K, Ohya K. The effect of microstructure and fracture surface roughness on fatigue crack propagation in a Ti–6Al–4V alloy. *Fatigue Fract Engng Mater Struct* 1993;16:973–82.
- [38] Austen IM, McIntyre P. Corrosion fatigue of high-strength steel in low-pressure hydrogen gas. *Metal Sci* 1979;13:420–8.
- [39] Wei RP, Landes JD. Correlation between sustained-load and fatigue crack growth in high strength steels. *Mater Res Standard* 1970;9:25–46.
- [40] Pao PS, Feng CR, Gill SJ. Hydrogen-assisted fatigue crack growth in beta-annealed Ti–6Al–4V. *Scripta Materialia* 1998;40:19–26.
- [41] Peterson KA, Schwanebeck JC, Gerberich WW. In situ scanning Auger analysis of hydrogen-induced fracture in Ti–6Al–6V–2Sn. *Metall Trans A* 1978;9A:1169–72.
- [42] Sastry SM, Lederich RJ, Rath BB. Subcritical crack-growth under sustained load in Ti–6Al–6V–2Sn. *Metall Trans A* 1981;12A:83–94.
- [43] Pao PS, O'Neal JE. Hydrogen-enhanced fatigue crack growth in Ti–6242S. *J Nucl Mater* 1984;123:1587–91.
- [44] Williams DN. Effects of hydrogen in titanium alloys on subcritical crack growth under sustained load. *Mater Sci Engng* 1976;24:53–63.
- [45] Freed AD, Sandor BI. Localised time-dependent and cycle dependent creep in notched plates. In: Gittus J, editor. *Cavities and cracks in creep and fatigue*. Applied Science, UK, 1981. p. 89–108.
- [46] Thomas JP. Subcritical crack growth of Ti–6Al–4V in the ripple-loading regime. In: Warren JR, Henderson J, editors. *Proceedings of the 4th National Turbine Engine High Cycle Fatigue Conference*, Monterey, CA, Universal Technology Corp., Dayton, OH, CD-Rom, session 2, 1999. p. 50–60.
- [47] Weiss V, Lal DN. A note on the threshold condition for fatigue crack propagation. *Metall Trans* 1974;5:1946–9.
- [48] Sandananda K, Shahinian PP. Prediction of threshold stress intensity for fatigue crack growth using a dislocation model. *Int J Fract* 1977;13:585–94.
- [49] Fine ME. Fatigue resistance of metals. *Metall Trans* 1980;11A:365–79.
- [50] Liu HW, Liu D. Near threshold fatigue crack growth behavior. *Scripta Metall* 1982;16:595–600.
- [51] Weertman J. Fatigue crack growth in ductile metals. In: Mura T, editor. *Mechanics of fatigue*, AMD-vol. 47. New York: ASME; 1982. p. 11–9.
- [52] Davidson DL. A model for fatigue crack advance based on crack tip metallurgical and mechanics parameters. *Acta Metall* 1984;32:707–14.

## Edge cracks in plastically deforming surface grains

Viggo Tvergaard<sup>a</sup>, Y. Wei<sup>b</sup>, J.W. Hutchinson<sup>b,\*</sup>

<sup>a</sup> *Department of Solid Mechanics, Technical University of Denmark, DK-2800 Lyngby, Denmark*

<sup>b</sup> *Division of Engineering and Applied Sciences, Harvard University, Cambridge, MA 02138, USA*

(Received 16 August 2000; revised and accepted 22 March 2001)

**Abstract** – A selection of surface crack problems is presented to provide insights into Stage I and early Stage II fatigue crack growth. Edge cracks at 45° and 90° to the surface are considered for cracks growing in single crystals. Both single crystal slip and conventional plasticity are employed as constitutive models. Edge cracks at 45° to the surface are considered that either (i) kink in the direction perpendicular to the surface, or (ii) approach a grain boundary across which only elastic deformations occur. © 2001 Éditions scientifiques et médicales Elsevier SAS

### 1. Introduction

For some rather pure metals, persistent slip bands (PSBs) develop in single crystals when they are subjected to cyclic loading (Ma and Laird, 1989; Pedersen, 1990). In such cases the development of small fatigue cracks is observed at the PSBs, usually along one of interfaces between the band and the surrounding crystal. Nucleation of these cracks is thought to be connected with the build-up of local stress concentrations, resulting from the development of extrusions and intrusions where the PSB intersects the surface of the crystal. The density of these small cracks is comparable to that of the PSBs, which may be as large as hundreds per centimeter (Ma and Laird, 1989). Most of the cracks appear to arrest and remain innocuous, while a few may grow large enough to become full fledged fatigue cracks. Structural polycrystalline metal alloys generally do not form PSBs, nevertheless, the early stage of fatigue crack initiation is thought to be qualitatively similar in that it is driven by highly localized irreversible plasticity. Thus, small cracks undergo Stage I growth along favorably oriented primary slip planes or microstructural features at approximately 45° to the surface. Most of these small cracks arrest, but a few continue into Stage II, change growth direction, and become small dominantly mode I cracks (Miller, 1993; McDowell, 1996).

In a recent paper Hutchinson and Tvergaard (1999) have investigated edge cracks in single crystals in order to study Stage I fatigue cracks, where the crack orientation is controlled by the slip direction. In that study slip was assumed to occur along planes inclined at 45° to the surface, and slip was modeled as elastic-perfectly plastic. In some cases slip was limited to a persistent slip band on one side of the crack, while in other cases slip was not confined. Studies were carried out for mixed mode conditions of small and large scale yielding. In small scale yielding, mixed mode elastic K-field displacements were prescribed as boundary conditions at an outer circular boundary of the region analyzed, while the full edge crack geometry was analyzed in large scale yielding. In these studies the focus was on crack tip opening and sliding displacements, as these measures are likely to be central in any extension of fatigue crack growth to small cracks and to formulations more

\* Correspondence and reprints.

E-mail address: hutchinson@husm.harvard.edu (J.W. Hutchinson).

fundamental than those based on elastic stress intensity factors. The analyses were used to obtain a parametric understanding of the effect of crack length relative to PSB width, as well as the effects of barriers to slip. Both monotonic loading and cyclic loading were analyzed. For the case where the assumption of small scale yielding applies and where slip in the crystal is not confined, a very useful, simple conversion from monotonic to cyclic loading results was discussed.

The present paper continues the study initiated in the earlier paper. First, results are presented for edge cracks in single crystal grains oriented at both 45° and 90° to the surface using constitutive models based on slip in single crystals. The importance of crystal orientation is explored and so is the efficacy of modeling the crystal using isotropic plasticity. The transition from Stage I to Stage II is investigated by considering the kinking of the 45° crack in a direction perpendicular to the surface. The second part of the paper concerns a fatigue crack approaching a grain boundary which constrains the zone of plasticity at the tip. The focus is on structural alloys where PSBs are not observed, but where Stage I fatigue cracks tend to initiate in surface grains with favorably oriented slip planes. A specimen under cyclic loading is analyzed, with an edge crack penetrating into a surface grain. This surface grain is elastic-plastic, while the surrounding grains in the specimen are assumed to remain elastic. The constraint as the crack tip approaches the grain boundary is thus likely to overestimate the effect of misorientation, but it should nevertheless indicate the effect such a barrier has to small crack growth. The surface grain slip is represented by two sets of slip planes, each inclined at 45° to the surface. The grain contains a single surface crack parallel to one of the sets of slip planes. For sufficiently small cyclic stress levels with no interaction between the plastic zone and the grain boundary, this model problem reduces to conditions of small scale yielding analyzed earlier (Hutchinson and Tvergaard, 1999). The main interest here is in cases where the cyclic stress levels are sufficiently high, or the crack tip is sufficiently close to the grain boundary, so that the active cyclic plastic zone at the crack tip shows significant interaction with the elastic material surrounding the grain at the other side of the grain boundary.

## 2. Edge cracks: sensitivity to choice of plasticity model

In this section a selection of solutions for edge cracks envisioned to be in Stage I or early Stage II will be presented. The sensitivity of the crack tip displacements to slip orientation and other modeling options will be illustrated. The computations employ a two-dimensional finite element representation of the solid, which is assumed to be in a state of plane strain. The first of the edge crack geometries (see *figure 1*) consists of an edge crack of length  $a$  oriented at either 45° or 90° to the surface and stressed remotely by a tensile component  $\sigma$  acting parallel to the surface. The finite element model employs a square region with dimension which is many times the crack length and the normal traction is applied to the top and bottom faces of this region.

Two elastic-perfectly plastic constitutive laws are used to characterize the solid: single crystal slip and isotropic plasticity. Both versions assume isotropic elasticity with Young's modulus  $E$  and Poisson's ratio  $\nu$ . For single crystal slip, a slip system is assumed to be oriented at angle  $\beta$  to the free surface (see *figure 1*). In small strain plasticity, which is assumed in this study, slip on this one system is equivalent to the existence of two sets of slip planes, one with the orientation  $\beta$  and the other perpendicular to it. With  $\tau_Y$  as the critical shear stress required to cause yielding on the slip plane and with  $\tau$  as the resolved shear stress acting on the plane, the constitutive limitations on the slip increments  $\dot{\gamma}$  for a perfectly plastic crystal are:

$$\dot{\gamma} = 0 \quad \text{for } |\tau| < \tau_Y, \quad \dot{\gamma} \geq 0 \quad \text{for } \tau = \tau_Y, \quad \dot{\gamma} \leq 0 \quad \text{for } \tau = -\tau_Y. \quad (1)$$

Calculations will also be presented based on an isotropic plasticity model which uses the von Mises yield surface normalized such that under a pure shear stress  $\tau$  yield occurs when  $\tau = \tau_Y$  (i.e. the tensile yield stress is  $\sigma_Y = \sqrt{3}\tau_Y$ ).



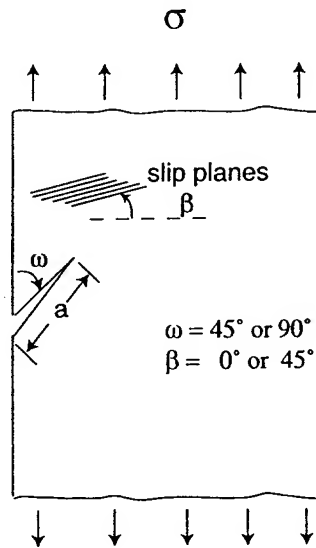


Figure 1. Edge cracks at  $\omega = 45^\circ$  and  $90^\circ$  under remote stressing. In the case of single crystal slip, the slip plane has orientation  $\beta = 0^\circ$  and  $45^\circ$ . Calculations for isotropic plasticity are also reported.

As in the earlier study, the emphasis will be on the opening and tangential displacements of the crack faces at the crack tip. These quantities seem to be the most obvious quantities to measure the intensity of deformation in the immediate vicinity of the crack tip and the most promising candidates for extending the current limitations of fatigue crack growth characterization. Let  $(\delta_n, \delta_t)$  denote the normal opening and tangential face displacements at the tip under monotonic loading and, similarly, let  $(\Delta\delta_n, \Delta\delta_t)$  denote the corresponding displacement changes under cyclic loading. The relative crack face displacements vary rather steeply as the crack tip is approached, and care must be taken to ensure the computed results are accurate. Here, the extrapolation scheme suggested by Hutchinson and Tvergaard (1999) has been used. With  $r$  as the distance to the tip at a point behind the tip, the equation for describing the variation of either of the relative face displacements is taken as:

$$\delta = Ar - B(r \ln r - r) + \delta(0), \quad (2)$$

where  $A$  and  $B$  are constants to be determined. The form (2) emerged from an analytic study of the near-tip behavior of cracks in single crystals by Saeedvafa and Rice (1992). It also pertains to the opening immediately behind the crack tip for the Dugdale model. While the general applicability of (2) has not been established, it does reflect the steep rate of change of the relative displacements found for the present models. To obtain the value at the tip,  $\delta(0)$ , three pairs of values of  $(r, \delta)$  from just behind the tip from the finite element calculation are used in (2) to evaluate  $A$ ,  $B$  and  $\delta(0)$ .

### 2.1. Cracks under monotonic and cyclic loads

Six cases are collected in figure 2, three for cracks at  $45^\circ$  to the surface and three for cracks perpendicular to the surface. For each crack orientation, three constitutive cases are considered: single crystal slip with systems oriented with  $\beta = 0^\circ$  and  $45^\circ$ , and isotropic plasticity. Moreover, results for both monotonic and cyclic loading have been presented. The emphasis in this section is not on large scale yielding effects (cf. Hutchinson and Tvergaard, 1999). The maximum stress applied under the monotonic history is  $\sigma_{\max}/(2\tau_Y) = 1/2$  such that the remote stress reaches exactly one half of the stress at yield and the crack remains just within the small scale



	$\beta=0^\circ$	$\beta=45^\circ$	Isotropic Plasticity
$\omega = 90^\circ$ 	$C_n = 1.30, C_t = 0$ $\Delta C_n = 0.63, \Delta C_t = 0$	$C_n = 0.60, C_t = 0$ $\Delta C_n = 0.32, \Delta C_t = 0$	$C_n = 1.31, C_t = 0$ $\Delta C_n = 0.66, \Delta C_t = 0$
$\omega = 45^\circ$ 	$C_n = 0.43, C_t = 0.27$ $\Delta C_n = 0.25, \Delta C_t = 0.13$	$C_n = 0.54, C_t = 0.24$ $\Delta C_n = 0.30, \Delta C_t = 0.13$	$C_n = 0.54, C_t = 0.29$ $\Delta C_n = 0.34, \Delta C_t = 0.15$

Figure 2. Numerical results for six cases – two crack orientations, each for three constitutive models.

yielding regime. The cyclic history applied to the specimen has the same maximum stress,  $\sigma_{\max}/(2\tau_Y) = 1/2$ , and zero minimum stress, such that  $\Delta\sigma/(2\tau_Y) = 1/2$ . It is important to mention that crack closure effects have not been emphasized in the present study. Under the cyclic history considered, the crack faces remain open over the entire cycle. Closure due to extrinsic effects such as crack face roughness, fatigue debris or plastic stretch left behind an advancing fatigue crack tip would affect the cyclic crack tip displacements.

For the monotonic cases, the crack tip displacements have been expressed as:

$$(\delta_n, \delta_t) = (C_n, C_t) \left( \frac{\sigma^2 a}{E\tau_Y} \right), \quad (3)$$

where the coefficients  $(C_n, C_t)$  calculated for the respective cases are included in figure 2. These are independent of the applied stress  $\sigma$  within the small scale yielding range. The corresponding expression for the changes in the crack tip displacements over a complete load cycle is:

$$(\Delta\delta_n, \Delta\delta_t) = (\Delta C_n, \Delta C_t) \left( \frac{\Delta\sigma^2 a}{E\tau_Y} \right), \quad (4)$$

where the  $(\Delta C_n, \Delta C_t)$  are also included in the figure. The behavior under the constant amplitude cyclic loading settles down to a "steady-state" after only several cycles in which the stress and crack face displacements no longer change from cycle to cycle at any given point in the cycle. Because the plastic zone size is much smaller under cyclic amplitude than that of the monotonic crack loaded to the same amplitude (by about a factor of four), the cyclic cases are well within the small scale yielding regime for the conditions under which the calculations have been carried out, i.e.  $\Delta\sigma/(2\tau_Y) = 1/2$ . It can be noted in figure 2 that  $(\Delta C_n, \Delta C_t)$  are approximately 1/2 the respective values of  $(C_n, C_t)$ . This is a consequence of both the cyclic and the monotonic cases being within small scale yielding. In mode III, and also for the Dugdale model in mode I, the cyclic coefficients are exactly 1/2 their monotonic counterparts in small scale yielding (Rice, 1967). In these two problems the cyclic problem can be put into correspondence with the monotonic problem by doubling the yield stress,  $\tau_Y$ , reflecting that fact that the stress state traverses from one side of the yield surface to exactly the opposite side on a trajectory through the stress space wherever cyclic plastic deformation occurs. In plane strain, the trajectory is not expected to be as simple and ratio should not be precisely 1/2. Nevertheless, the present results indicate that this ratio is nearly 1/2, within the accuracy of the numerical evaluation of the coefficients.

Several observations can be made from the results collected in figure 2:

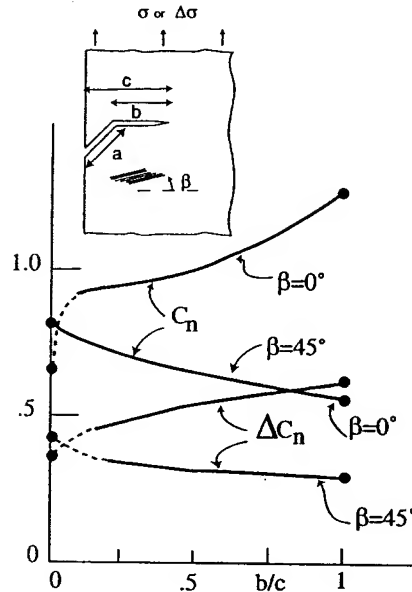


Figure 3. Coefficient specifying the opening crack tip displacements,  $\delta_n$  and  $\Delta\delta_n$ , for a kinked edge crack. The tangential components of the crack tip displacement are very small compared to the corresponding opening components and have not been presented.

(i) For cracks at  $90^\circ$  to the surface, the orientation of the slip system has a large effect on the crack tip opening. The system aligned at  $0^\circ$  (and therefore also at  $90^\circ$ ) is much more favorable to slip near the tip than that aligned at  $45^\circ$  (and also at  $-45^\circ$ ), and the coefficients  $C_n$  and  $\Delta C_n$  are correspondingly about twice as large. The coefficients from the isotropic plasticity model are very close to those for the slip system at  $0^\circ$ .

(ii) For cracks at  $45^\circ$  to the surface there are relatively small differences among the three constitutive models, although the normal opening component is about 20% smaller for the slip system oriented at  $0^\circ$  than as predicted for the other two models.

(iii) The behavior at the tip of the cracks at  $45^\circ$  is mixed mode with the opening component almost twice the tangential component. Moreover, the opening component is nearly as large as that for the mode I crack with the unfavorably oriented slip system (at  $45^\circ$ ), but it is less than one half the opening for the other two cases.

The results above are within the small scale yielding range. They may be re expressed in terms of stress intensity factors using:

$$K_I = 1.122\sigma\sqrt{\pi a}, \quad K_{II} = 0, \quad (5)$$

for the crack perpendicular to the edge, and by:

$$K_I = 0.705\sigma\sqrt{\pi a}, \quad K_{II} = 0.364\sigma\sqrt{\pi a}, \quad (6)$$

for the crack at  $45^\circ$  to the edge (Isida, 1979).

## 2.2. A $45^\circ$ edge crack transitioning to a $90^\circ$ mode I crack

Stage I cracks inclined to the surface transition to mode I, Stage II cracks as they grow longer. Here, an example will be presented which illustrates some features of this transition. The  $45^\circ$  edge-crack shown in the insert in figure 3 has kinked with the segment at its end oriented at  $90^\circ$  to the applied stress. Now, the total

penetration of the crack perpendicular to the surface is denoted by  $c$ , the length of the kinked segment by  $b$ , and the length of the inclined segment by  $a$ . Two cases are shown in *figure 3*. One has the slip system oriented at  $45^\circ$  (and  $-45^\circ$ ) to the surface while the other has the system at  $0^\circ$  (and  $90^\circ$ ) to the surface. Plotted as a function of  $b/c$  in *figure 3* are the coefficients for the opening displacement,  $C_n$  and  $\Delta C_n$ , now defined as:

$$\delta_n = C_n \left( \frac{\sigma^2 c}{E \tau_Y} \right), \quad \Delta \delta_n = \Delta C_n \left( \frac{\Delta \sigma^2 c}{E \tau_Y} \right). \quad (7)$$

The coefficients for the tangential crack face displacements are not shown because they are extremely small over the entire range of  $b/c$  shown, except when  $b/c$  is very small. Thus, the transition to mode I following kinking takes place remarkably quickly. This suggests that microstructural features may readily overcome the small barrier to the transition to Stage I cracks. Included as solid end points for each of the curves in *figure 3* are the results for the appropriate limits from *figure 2*. The limit at  $b/c = 1$  pertains to the perpendicular edge-crack with the corresponding slip plane orientation. The limit when  $b/c = 0$  must coincide with results from *figure 2*, taking into account that  $c = a/\sqrt{2}$  when  $b = 0$ . The dashed segments of the curves in *figure 3* near  $b/c = 0$  indicate segments which are not resolved numerically.

### 3. An edge crack approaching a boundary surrounded by elastic grains

Grain boundaries can block incipient surface fatigue cracks such that their further growth is arrested, rendering them impotent. The misorientation of the slip systems across the boundary impedes plastic deformation ahead of the advancing crack. Here we model the limit where plasticity is confined to the grain containing a  $45^\circ$  edge crack. The slip system within the grain is also at  $45^\circ$ , with one slip plane parallel to the crack (and another perpendicular to the crack), providing the most favorable orientation for plasticity within the grain whether induced by the applied stress or by the crack. As sketched in *figure 4*, the surface grain is half-circular with radius  $R$ , and the crack emerges from the center point of the grain at the edge, and extends a distance  $a$  into the grain. The distance from the crack tip to the boundary is  $b = R - a$ . Elastic anisotropy mismatch may also impede the growth of a crack from one grain into another, but in this study elastic mismatch is not considered. A common Young's modulus  $E$  and Poisson's ratio  $\nu$  are assumed.

Cyclic stressing  $\sigma(t)$  is assumed to have minimum stress  $\sigma_{\min} = 0$  and maximum stress  $\sigma_{\max}$ . The emphasis here will be on small scale yielding conditions in the sense that the plastic zone is small compared to the crack length, but not necessarily small compared to the distance  $b$  separating the tip from the grain boundary. While there is general interest in small crack effects attributed to large scale yielding, small scale yielding covers a highly important range of cyclic loading. It applies, to a good approximation, to stress amplitudes satisfying  $\sigma_{\max} \leq 2\tau_Y$  corresponding to the onset of general yielding in the polycrystal (Hutchinson and Tvergaard, 1999). At any stage in the cycle, the mode I and II elastic stress intensity factors for the crack are given by (6).

By dimensional analysis, the two components of the crack tip displacement amplitudes can be written as:

$$\Delta \delta_n = \frac{\Delta K_I^2}{E \tau_Y} f_n \left( \frac{b}{R_p}, \frac{\tau_Y}{E} \right) \quad \text{and} \quad \Delta \delta_t = \frac{\Delta K_{II}^2}{E \tau_Y} f_t \left( \frac{b}{R_p}, \frac{\tau_Y}{E} \right). \quad (8)$$

Here,

$$R_p = \frac{1}{3\pi} \left( \frac{\Delta K_I}{4\tau_Y} \right)^2 \quad (9)$$

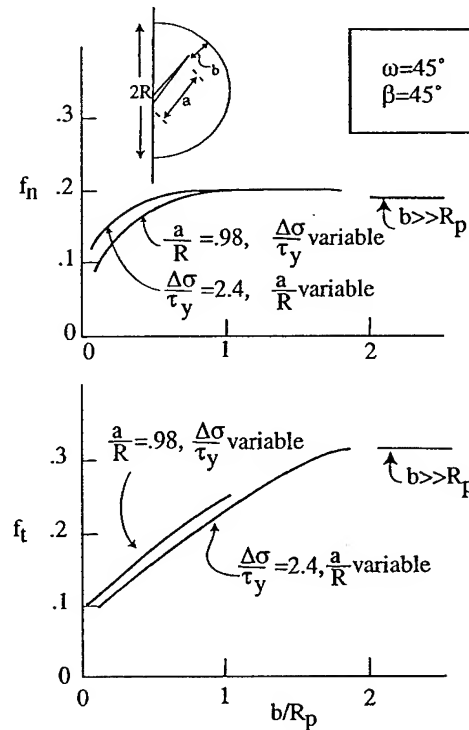


Figure 4. Edge crack at  $45^\circ$  contained within an elastic perfectly plastic grain surrounded by elastic grains. The slip system within the grain is oriented parallel to the crack (i.e. at  $45^\circ$  to the surface). Functions defining the crack tip displacements for the edge crack approaching the grain boundary.

is the reference length which scales with the active plastic zone size of the crack before it interacts with the boundary. The dependence on  $\tau_Y/E$  is weak, and  $\tau_Y/E = 0.002$  was used in all the calculations. Plots of  $f_n$  and  $f_t$  are given in figure 4. When the plastic zone does not reach the boundary (roughly  $b/R_p > 2$ ), the problem is the same as one addressed in Section 3.1. Then, by (7),  $f_n = 0.19$  and  $f_t = 0.31$ , strictly independent of  $b/R_p$  and  $\tau_Y/E$ . These limits are indicated in figure 4. The region outside the grain boundary constrains plastic deformation when  $b/R_p < 2$ , and the crack tip displacements are reduced relative to the unconstrained values. Two sets of calculations have been carried out producing the two sets of curves in figure 4. One was computed with  $a/R$  fixed at 0.98 by varying  $\Delta\sigma/\tau_Y$ , while the other set fixed  $\Delta\sigma/\tau_Y$  at 2.4 and varied  $a/R$ . The small differences between the two sets of curves, which should coincide, reflects inaccuracy in the numerical method. The drop off in the cyclic crack tip displacements becomes significant when  $b/R_p$  is reduced to  $1/2$ . The limiting behavior of  $f_n$  and  $f_t$  as  $b/R_p$  approaches zero is not entirely clear. A finite opening displacement should be possible even with  $b = 0$ , since slip perpendicular to the tip is possible. However, the tangential component of opening at the tip is blocked by the grain boundary, and thus  $f_t$  is expected to approach zero as  $b/R_p$  approaches zero. The present numerical results are unable to resolve these two limits more accurately than displayed in figure 4.

#### 4. Concluding remarks

The results in the present paper provide trends in crack tip opening displacements for small Stage I and beginning Stage II cracks. Furthermore, they give some insight into the sensitivity of the predictions to the factors such as crystal orientation and constitutive modeling of the crystal. Characterization of growth under

cyclic loading for small cracks is likely to involve criteria making use of the cyclic crack tip displacements,  $\Delta\delta_n$  and  $\Delta\delta_t$ . Under mixed mode conditions both components will influence growth. For the 45° edge-crack the tangential component is approximately one half the amplitude of the opening component. Thus, while the mode I component is dominant, it seems likely that the superposition of the mode II component will be important in growth along a slip plane. In the case of the kinked 45° edge crack discussed in Section 3.2, it is remarkable that the crack tip is dominated by mode I behavior after only an exceptionally small kink (i.e.  $b/c \cong 0.1$ ). This suggests that it is microstructural features that probably determine the transition from Stage I to II. Finally, the 45° edge crack approaching a grain boundary across which no plasticity occurs provides an effective barrier for the termination of growth of a small Stage I crack. Crystal misorientation will have a similar, albeit a somewhat weaker, effect.

### Acknowledgments

The work of J.W.H. and Y.W. was supported in part by the AFSOR under Grant No. SA1542-22500 PG and in part by the Division of Engineering and Applied Sciences, Harvard University. In addition, Y.W. acknowledges support from the Chinese National Science Foundation.

### References

- Hutchinson, J.W., Tvergaard, V.T., 1999. Edge-cracks in single crystals under monotonic and cyclic loads. *Int. J. Fracture* 99, 81–95.
- Isida, M., 1979. Tension of a half space containing array cracks, branched cracks and cracks emanating from sharp notches. *T. Jpn. Soc. Mech. Eng.* 45, 306–317.
- Ma, B.T., Laird, C., 1989. Overview of fatigue behavior in copper single crystals: I, II and III. *Acta Metall.* 37, 325–336, 337–348, 349–355.
- McDowell, D.L., 1996. Basic issues in the mechanics of high cycle fatigue. *Int. J. Fracture* 80, 103–145.
- Miller, K.J., 1993. Materials science perspective of metal fatigue resistance. *Mater. Sci. Tech.* 9, 453–462.
- Pedersen, O.B., 1990. Mechanism maps for cyclic plasticity and fatigue of single phase materials. *Acta Metall. Mater.* 38, 1221–1239.
- Rice, J.R., 1967. Mechanics of crack tip deformation and extension by fatigue. *American Society of Testing Materials ASTM STP* 415, 247–309.
- Saeedvafa, M., Rice, J.R., 1992. Crack tip fields in a material with three independent slip systems: NiAl single crystal. *Modelling and Simulation in Materials Science and Engineering* 1, 53–71.



## Edge-cracks in single crystals under monotonic and cyclic loads

JOHN W. HUTCHINSON<sup>1</sup> and VIGGO TVERGAARD<sup>2</sup>

<sup>1</sup>*Division of Engineering and Applied Sciences, Harvard University, Cambridge, MA 02138, U.S.A.*

<sup>2</sup>*Department of Solid Mechanics, Technical University of Denmark, DK-2800 Lyngby, Denmark*

Received 5 June 1997; accepted in revised form 27 January 1998

**Abstract.** Basic solutions are obtained for edge-cracks lying along the primary slip plane in a single crystal. The study is motivated by Stage I fatigue crack growth wherein crack orientation is controlled by the slip direction and continued growth is dependent on the crack overcoming barriers to slip. Plasticity is assumed to occur as slip along planes inclined at  $45^\circ$  to the surface. Problems where slip is limited to persistent slip bands are considered side-by-side with the problem where slip is not confined. Results for both monotonic and cyclic loadings are presented, with emphasis on the crack tip opening and sliding displacements. Both small and large scale yielding are considered. Preliminary results are given for interaction with barriers to slip, such as a grain boundary.

**Key words:** Edge-cracks, fatigue, single crystals, large scale yielding.

### 1. Introduction

Under cyclic loading, single crystals of certain metals are observed to develop small fatigue cracks parallel to persistent slip bands (PSBs), usually along one of the boundaries between the band and the surrounding crystal (Ma and Laird, 1989). Cracks are nucleated with densities comparable to the density of the PSBs (e.g., as many as hundreds per centimeter (Ma and Laird, 1989)). Nucleation of these cracks is thought to be connected with the build-up of local stresses and extruded material where the PSB intersects the surface of the crystal (see Repetto and Ortiz (1997) for recent developments and relevant references). Under continuing cyclic loading, a few of the cracks grow large enough to become full fledged fatigue cracks, but the vast majority appear to arrest and remain innocuous. In the observations of the copper single crystal by Ma and Laird, the width of a PSB is on the order of one micron, while the typical arrested crack extends several microns or more into the crystal from the surface. Those that become full fledged fatigue cracks continue growing beyond this length. The early stages of cracking for crystals and for structural polycrystalline metal alloys which do not form persistent slip bands is thought to be qualitatively similar to that just described. Small cracks undergo Stage I growth along favorably oriented primary slip planes at approximately  $45^\circ$  to the surface and either arrest at some barrier or succeed in transitioning to Stage II and become a small mode I crack (Miller, 1993; McDowell, 1996).

The aim of the present study is to provide some basic results for  $45^\circ$  edge-cracks that will be useful in formulating a mechanics of Stage I fatigue crack growth. Three situations are depicted in Figure 1: a crack lying along the direction of the slip plane where slip is not confined in (a), and a crack lying along one side or the other of a PSB in (b) and (c). The slip planes and the band are oriented at  $45^\circ$  measured from the surface of the crystal, corresponding to the plane of maximum shear stress magnitude for inplane stressing parallel to the edge. The crack has length  $a$ . The band width is  $w$  for the PSB models. Two-dimensional, plane strain

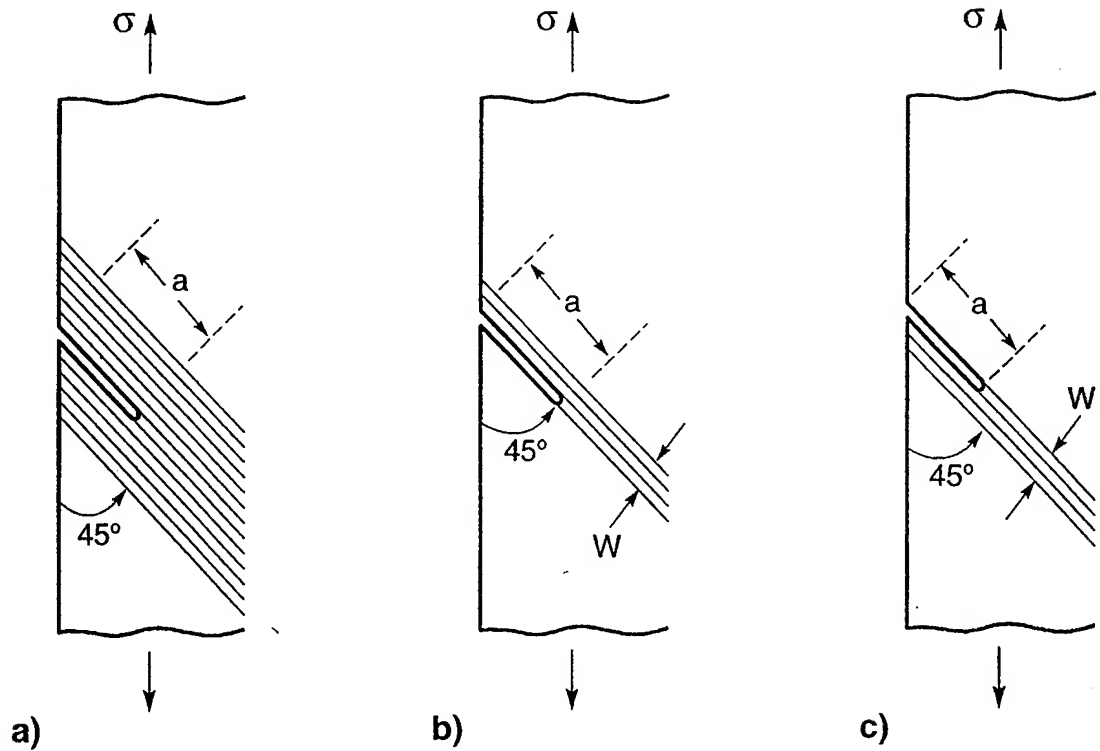


Figure 1. A 45° edge-crack aligned with the slip plane in a single crystal and subject to inplane tensile stress  $\sigma$ . (a) Unconfined slip. (b) and (c) Slip confined to a band of width  $w$  above or below the crack.

conditions are assumed with a remote tensile stress  $\sigma$  acting parallel to the free surface of the crystal. The elastic properties of the crystal are taken to be isotropic with Young's modulus  $E$  and Poisson's ratio  $\nu$ . The model will be investigated under monotonically increasing  $\sigma$  and under tensile loadings where  $\sigma$  is cycled between minimum and maximum values. In the last part of the paper, barriers to slip will be modeled to assess their effect on deformation at the crack tip.

When plasticity is completely suppressed, the elastic stress intensity factors  $K_I$  and  $K_{II}$  for an inclined edge-crack have been given by Isida (1979). For an edge-crack of length  $a$  at 45° to the free edge of a semi-infinite plane, slanted downward as in Figure 1,

$$K_I = 0.705\sigma\sqrt{\pi a} \quad \text{and} \quad K_{II} = -0.364\sigma\sqrt{\pi a}. \quad (1.1)$$

Thus the mode ratio,  $K_{II}/K_I \cong -1/2$ , pertains approximately for this crack when the stress is such that small scale yielding applies.

Only slip on the primary slip system is allowed. The mutually orthogonal slip direction and slip plane normal are designated by  $(\mathbf{t}, \mathbf{n})$ . The slip system is modeled as elastic-perfectly plastic with slip activated by a critical resolved shear stress  $\tau_Y$ . For the PSB problems, slip is confined to a band, whereas in the other case slip is free to occur where the resolved shear stress exceeds  $\tau_Y$ . The nonzero plastic strain rate component is

$$\dot{\epsilon}_{nt}^p = \dot{\epsilon}_{tn}^p = \frac{1}{2}\dot{\gamma}, \quad (1.2)$$



where the slip rate  $\dot{\gamma}$  must be consistent with

$$\begin{aligned} \dot{\gamma} &\geq 0 \quad \text{for} \quad \sigma_{nt} = \tau_Y, & \dot{\gamma} &\leq 0 \quad \text{for} \quad \sigma_{nt} = -\tau_Y, \quad \text{and} \\ \dot{\gamma} &= 0 \quad \text{for} \quad |\sigma_{nt}| < \tau_Y, \end{aligned} \quad (1.3)$$

where  $\sigma_{nt} = \sigma_{ij}n_i t_j$ .

The components of the crack tip displacement are denoted by  $(\delta_t, \delta_n)$ , corresponding to tangential sliding and a normal opening components. Amplitudes of the changes in these components in steady cycling between  $\sigma_{\min}$  and  $\sigma_{\max}$  are denoted by  $(\Delta\delta_t, \Delta\delta_n)$ . The range of the cyclic applied stress is assumed to be such that crack closure does not occur. Crack tip displacements are featured in this study. At the level of the continuum modeling pursued here, these measures of crack tip deformation are likely to be the most useful for correlating fatigue crack growth. The magnitudes of the two tip components change relative to one another as the scale of yielding changes and as the tip encounters obstacles. It remains an important open task to identify crack growth criteria under mixed mode conditions.

## 2. Numerical models

Two types of numerical models have been employed to analyze the various problems posed in this paper. Primary emphasis has been put on obtaining relationships between the components of crack tip displacement and the loading history. A finite element model with a grid specially designed for single slip plasticity has served as the primary numerical method. Features of the solution brought out by the finite element results reveal that in some instances an extended Dugdale (1960) – Barenblatt (1959a, 1959b, 1962) model can provide an effective approximation. When applicable, the double slip zone model has certain numerical advantages over the finite element model.

### 2.1. FINITE ELEMENT MODEL

In the elastic-plastic material with single slip specified by (1.3), the total strain rate is taken to be the sum of an elastic part and a plastic part,  $\dot{\epsilon}_{ij} = \dot{\epsilon}_{ij}^e + \dot{\epsilon}_{ij}^p$ . The elastic part satisfies Hooke's law,  $\dot{\sigma} = \ell_{ijkl}\dot{\epsilon}_{kl}^e$ , where  $\ell_{ijkl}$  are the elastic instantaneous moduli. The plastic part satisfies  $\dot{\epsilon}_{ij}^p = \dot{\gamma}\alpha_{ij}$  (see also (1.2)), where  $\alpha_{ij} = \frac{1}{2}(s_i n_j + s_j n_i)$  in terms of the slip direction  $s_i$  and the slip plane normal  $n_i$ . Then, the elastic-plastic incremental constitutive relation is of the form

$$\dot{\sigma}_{ij} = L_{ijkl}\dot{\epsilon}_{kl}, \quad L_{ijkl} = \ell_{ijkl} - \mu M_{ij}M_{kl} \quad (2.1)$$

where  $\mu = 1/(\alpha_{mn}M_{mn})$  for plastic yielding and  $\mu = 0$  for elastic unloading. Furthermore,  $M_{ij} = E\alpha_{ij}/(1 + \nu)$ , in terms of Young's modulus  $E$  and Poisson's ratio  $\nu$ .

The requirement of equilibrium is specified in terms of the incremental principle of virtual work. Approximate solutions are obtained by the finite element method, using the incremental constitutive relation (2.1) in the principle of virtual work. The element approximation of the displacement components is based on eight-noded isoparametric elements, and the integrations within each element, needed to compute the incremental stiffness matrix, are carried out using  $2 \times 2$ -point Gaussian quadrature.

Two types of boundary conditions are used in the present analyses. When conditions of small scale yielding are considered, a circular region is analyzed with displacement boundary

conditions prescribed on the outer edge in agreement with the mixed-mode singular elastic crack tip fields. When an edge-crack in a specimen under uniaxial plane strain tension is considered, a rectangular region is analyzed with uniform axial displacements and zero shear stress prescribed on the ends. The lateral sides are traction-free. The traction-free edge-crack inclined to the tensile direction is located at the middle of one of these traction-free sides.

The grid near the crack tip is particularly chosen to represent the characteristic near-tip strain fields. There is a tendency for plastic slip to concentrate in a narrow band along the extended crack plane ahead of the crack tip. In case of a finite size specimen, this narrow band eventually develops into a slip band which extends across the specimen. Some of the present computations have been continued until this stage, where the overall tensile load approaches the limit load for the cracked crystal. With the deformation mechanism allowing for single slip in directions parallel to the crack plane there is also a tendency for concentrated plastic shearing to develop from the crack tip in a direction perpendicular to the crack plane (and thus perpendicular to the slip planes). As discussed by Saeedvafa and Rice (1992), the slip system (1.2) allows concentrated shearing along planes perpendicular to the slip plane (interpretable in dislocation terms as a kink band), as well as in directions parallel to the slip plane. To represent localized yielding in these two characteristic directions, the near tip mesh has been specially designed with narrow element bands of constant width along these directions, as seen in Figure 2. Comparison with analyses for a standard mesh at a crack tip, with the mesh defined by radial lines focused on the tip, has shown that the narrow bands of uniform elements near the crack tip in Figure 2 are important for the accuracy.

Examples of plastic zones are illustrated in Figure 2 in terms of dots in deformed meshes, where a dot is drawn at integration points currently undergoing plastic yielding. Figures 2(a) and (b) are obtained for  $K_{II}/K_I = -1/2$  under small scale yielding (full details of the models are given in the next section), in one case for the PSB above the crack plane and in the other with the band below. Figure 2c, shows a portion of the mesh and yielded elements for large scale yielding of the full edge-cracked geometry, in this instance for the case where slip can occur wherever the critical shear stress is attained on a slip plane. Concentrated plastic shearing on the extended crack plane and perpendicular to the crack plane emerging from above the tip is clearly seen in Figure 2. The concentrated shearing is accompanied by diffuse plastic shearing, usually in one of the two directions but not the other.

Crack tip displacements ( $\delta_t$ ,  $\delta_n$ ) are sensitive to near tip mesh layout. The opening and sliding displacements behind the tip have a fairly steep variation with distance  $r$  back from the tip (Saeedvafa and Rice, 1992), such that the derivative of these quantities with respect to  $r$  can be logarithmically singular at the tip. To accurately compute ( $\delta_t$ ,  $\delta_n$ ), it is best to use crack face displacements at points behind the tip and extrapolate to the tip. If  $d\delta/dr = A - B \ln(r)$ , then near the tip,

$$\delta = Ar - B(r \ln r - r) + \delta(0), \quad (2.2)$$

where  $\delta(0)$  is the desired value at the tip. One method which has been employed here is to fit (2.2) to sets of values at three points  $r$  behind the tip, providing the extrapolation for ( $\delta_t$ ,  $\delta_n$ ).

## 2.2. DOUBLE SLIP ZONE MODELS

As evident in Figure 2, much of the plastic deformation occurs by concentrated shearing on the extended crack plane and on the plane perpendicular to it that emerges from the crack tip. If one is willing to neglect the contribution of diffuse plastic deformation in regions off

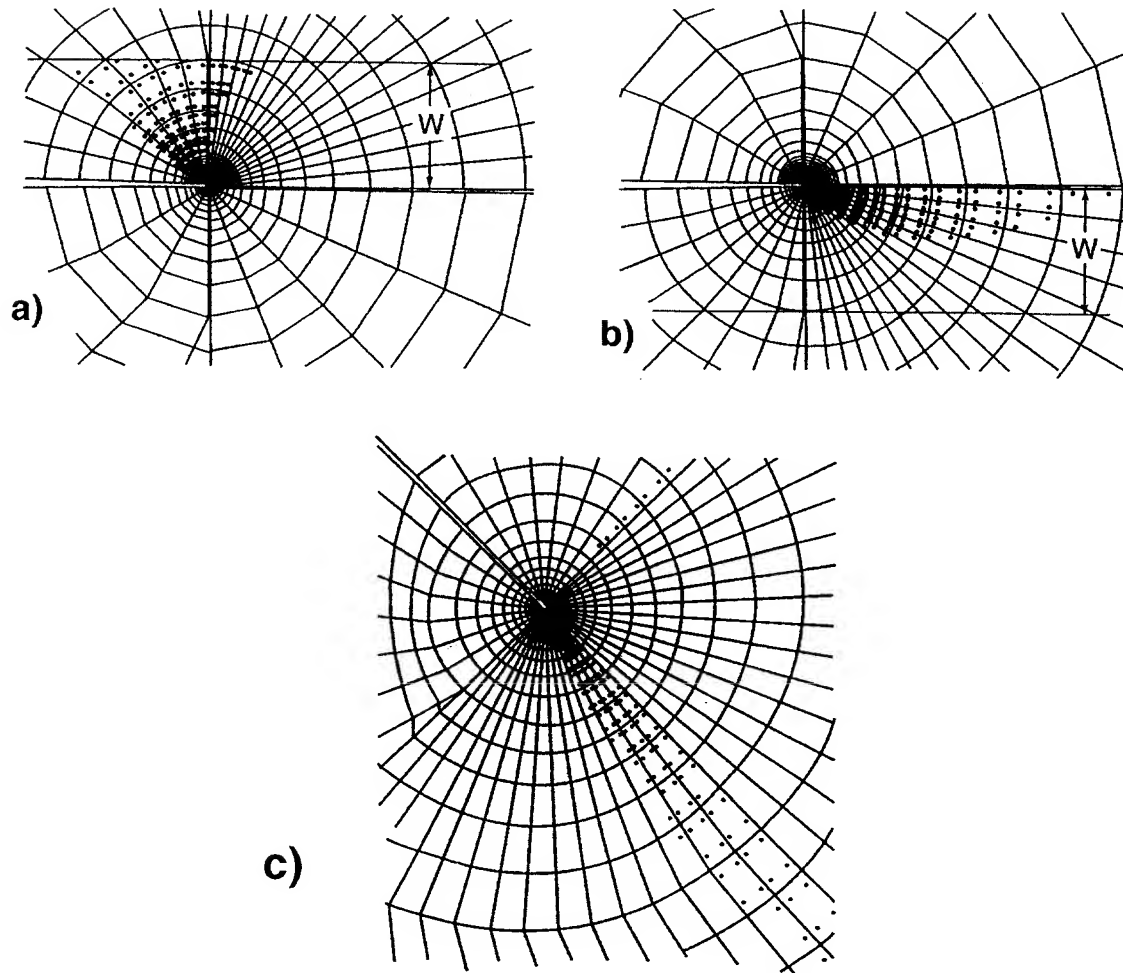


Figure 2. Examples of the near tip finite element mesh and zones of plastic yielding, as indicated by dots at integration points where the yield condition is met. Strips of narrow elements of uniform width are incorporated in the mesh on the extended crack plane and emerging from the tip at  $90^\circ$  to the crack plane. These are required to represent the localized slip along the slip plane and perpendicular to it. Cases (a) and (b) are for small scale yielding with slip confined to a band either above or below the crack plane. Case (c) is an example of large scale yielding where slip is unconfined.

these two planes, one can employ a double slip zone model akin to the Dugdale–Barenblatt Model. In the present plane strain model for the single crystal, the tangential displacement is allowed to be discontinuous across the slip zone when the resolved shear stress attains  $\tau_Y$ . One advantage of the double slip zone approximation is there exist efficient numerical methods for solving the integral equations for the distributions of the ‘dislocations’,  $d\delta/dr$ , that become the unknowns in these formulations. Several such examples are solved in this paper for the purposes of illustrating the approach. Another advantage of these models is that the two crack tip displacements ( $\delta_I$ ,  $\delta_n$ ) are readily expressed and computed in terms of the dislocation distributions. As is standard in such models, the extent of the zone is determined by the condition that the stresses are bounded at the end of the zone, assuming it is not blocked.

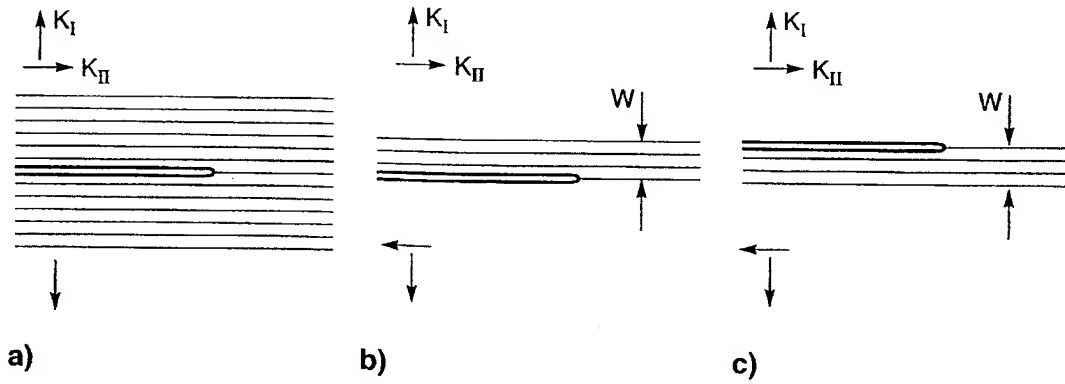


Figure 3. Conventions in small scale yielding. Slip is unconfined in (a), while it is confined to a band of width  $w$  above or below the crack plane in (b) and (c). The slip planes are parallel to the crack plane.

### 3. Small scale yielding

#### 3.1. PURE MODE REFERENCE CASES

Two small scale yielding results will serve as useful references in the present study. In *pure mode II* ( $K_I = 0$ , with monotonically increasing  $K_{II}$  in Figure 3) the analog of the Dugdale-Barenblatt Model applies with slip confined to the single plane coincident with the extended crack plane directly ahead of the tip. The normal component of the crack tip opening displacement,  $\delta_n$ , is zero and the tangential component,  $\delta_t$ , is given by

$$\delta_t = (1 - \nu^2) \frac{K_{II}^2}{E\tau_Y}. \quad (3.1)$$

The extent of the plastic slip zone ahead of the tip is  $R_t = (\pi/8)(K_{II}/\tau_Y)^2$ . If frictional effects between the crack faces are ignored, the amplitude of the change in  $\delta_t$  in each cycle under a *steady cyclic loading history* with the mode II stress intensity factor varying between  $K_{II}^{\min}$  and  $K_{II}^{\max}$  is

$$\Delta\delta_t = \frac{1}{2}(1 - \nu^2) \frac{\Delta K_{II}^2}{E\tau_Y}, \quad (3.2)$$

where  $\Delta K_{II} = K_{II}^{\max} - K_{II}^{\min}$ .

When the small scale yielding conditions are *pure mode I* ( $K_{II} = 0$  in Figure 3a), the solution for monotonically increasing  $K_I$  has been given by Saeedvafa and Rice (1992) for the case where slip on any plane parallel to the crack is possible. The tangential sliding displacement is zero while the opening displacement at the tip is

$$\delta_n \cong 0.26 \frac{K_I^2}{E\tau_Y} \quad (\text{for } \nu = 0.3). \quad (3.3)$$

The amplitude of the tip opening displacement under steady cyclic loading between  $K_I^{\min}$  and  $K_I^{\max}$  is

$$\Delta\delta_n \cong 0.13 \frac{\Delta K_I^2}{E\tau_Y} \quad (\text{for } \nu = 0.3), \quad (3.4)$$

where  $\Delta K_I = K_I^{\max} - K_I^{\min}$ , assuming no contact occurs between the crack faces.

### 3.2. MONOTONIC LOADING WITH $K_{II}/K_I = -1/2$

Under monotonic stressing, the edge-crack in Figure 1 satisfies small scale yielding for applied stresses  $\sigma$  up to approximately one half of the tensile yield stress of the uncracked crystal, i.e. for  $\sigma$  as large as about  $\tau_Y$ . Under steady cyclic loading, the range of applicability of small scale yielding is considerably larger (i.e.,  $\Delta\sigma$  as large as about  $2\tau_Y$ ), as will be discussed later. Thus, with reference to Figure 3, consider the small scale yielding limits of the three problems of Figure 1 where a semi-infinite crack is remotely subject to a mixed mode elastic field with amplitudes  $(K_I, K_{II})$ . For monotonic loading, the solution will be presented in the form

$$\delta_n = c_n \frac{K_I^2}{E\tau_Y} \quad \text{and} \quad \delta_t = c_t \frac{K_{II}^2}{E\tau_Y}. \quad (3.5)$$

For the problem in Figure 3(a) where plasticity is not confined to a band, the coefficients  $(c_t, c_n)$  are independent of the stress intensities, assuming  $K_{II}/K_I$  is fixed at  $-1/2$ . A crude estimate of the extent of the plastic zone perpendicular to the crack line is

$$R_n \equiv \frac{1}{9\pi} \left( \frac{K_I}{\tau_Y} \right)^2 \quad (3.6)$$

This quantity serves as a useful scaling length for presenting the solution. For the two PSB problems in Figures 3(b) and 3(c), the coefficients  $(c_t, c_n)$  will depend on  $R_n/w$  when the plastic zone is large enough such that it reaches across the PSB. Small scale yielding in the present context only requires that the maximum extent of the plastic zone be sufficiently small compared to the crack length. No restriction is placed on its interaction with the boundaries of the PSB.

The coefficients in (3.5) for the problem in Figure 3a where slip is not confined are

$$c_n = 0.35 \quad \text{and} \quad c_t = -0.64. \quad (3.7)$$

Comparison with the pure mode cases in (3.1) and (3.3) reveals that the nonlinear interaction between the modes under mixed mode loading is not exceptionally strong. At comparable stress intensities, the opening displacement is increased by about 20 percent in the presence of the mode II component, while the tangential sliding displacement is lowered by about 30 percent when coupled with the mode I component. Plots of  $(c_t, c_n)$  as a function of  $R_n/w$  for the two PSB crack problems are shown in Figure 4, together with the values (3.7). (In small scale yielding, the difference between a crack located on one side of the PSB versus the other can be captured by changing the sign of  $K_{II}$  without changing the location of the crack relative to the band. However, the PSB results in Figure 4 all have  $K_{II} < 0$  with the crack on top of the band in one case and below it in the other.)

### 3.3. CYCLIC LOADING WITH $K_{II}/K_I = -1/2$

The solution for steady cyclic loading between maximum and minimum stress intensities (with  $K_{II}/K_I$  fixed at  $-1/2$ ) follows immediately from (3.5) for the case in Figure 3(a) where slip is not confined to lie within a band. With  $\Delta K_I = K_I^{\max} - K_I^{\min}$  and  $\Delta K_{II} = K_{II}^{\max} - K_{II}^{\min}$ ,

$$\Delta\delta_n = \frac{1}{2}c_n \frac{\Delta K_I^2}{E\tau_Y} \quad \text{and} \quad \Delta\delta_t = \frac{1}{2}c_t \frac{\Delta K_{II}^2}{E\tau_Y}, \quad (3.8)$$

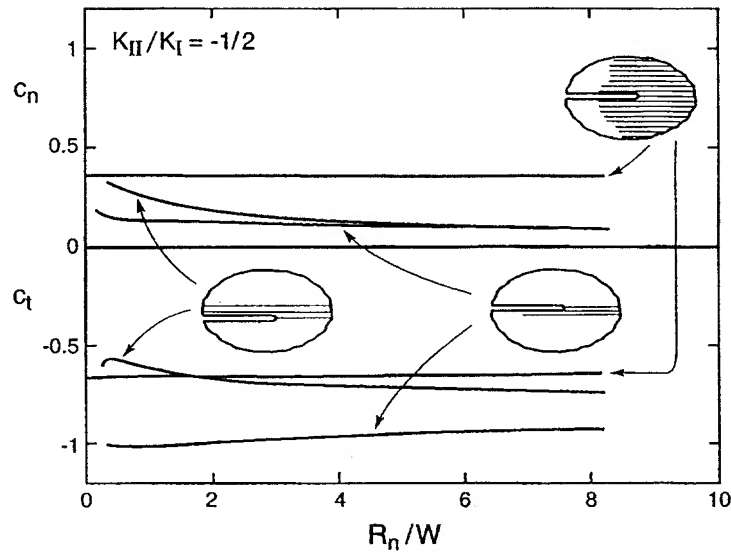


Figure 4. The coefficients specifying the crack tip displacement components in (3.5) for monotonic stressing of the  $45^\circ$  edge-crack under small scale yielding. The length quantity  $R_n$  is defined in (3.6), and  $w$  is the width of the band of confined slip in two of the three cases shown. In the third case, slip is not confined.

where  $c_n$  and  $c_t$  have been given (3.7). The argument for the validity of this simple conversion of the monotonic solution to the cyclic solution is essentially the same as that put forward by Rice (1967) in his analysis of Mode III cracks in elastic-perfectly plastic solids. In small scale yielding, the monotonic solution necessarily has the property that once slip starts at any point it continues with the magnitude of the resolved shear stress unchanging at  $\tau_Y$ . Yielding spreads in a self-similar manner. When the applied stress intensity factors decrease from their maximum values, the *changes* in the stresses, strains and displacements are related to the *changes* in stress intensities precisely by the monotonic solution (with due regard for sign changes) if  $\tau_Y$  is replaced by  $2\tau_Y$ . Any point which undergoes reversed yield will have experienced a change in shear stress from  $\pm\tau_Y$  to  $\mp\tau_Y$ , and the superposition of the changes calculated with a yield stress  $2\tau_Y$  exactly represents the behavior. The portion of the steady cycle wherein the stress intensities are reversed once more and brought back to their former maximum values is again characterized by changes computed from the monotonic solution with a yield stress of  $2\tau_Y$ . At the top of the cycle, the stresses and the crack tip displacements return to the values they had before any load reversal occurred.

The shape of the active zone which experiences cyclic plastic strains under steady cyclic loading in small scale yielding is precisely the same as that of the zone under monotonic loading, but the size scales with  $(\Delta K/2\tau_Y)^2$  rather than  $(K_{\max}/\tau_Y)^2$ . It follows that the size of zone of cyclic plastic strains is exactly  $(1/4)(\Delta K/K_{\max})^2$  times the size of the monotonic plastic zone at  $K_{\max}$ . In particular, for cycling between  $K_{\max}$  and  $K_{\min} = 0$ , the cyclic zone is one quarter the size of the monotonic zone, neglecting any possible effects of crack closure. The relatively small size of the cyclic plastic zone has important implications for the relevance of the small scale yielding results. Even when the maximum applied stress drives the monotonic problem well into the large scale yielding range, the cyclic problem may still satisfy small scale yielding. Specifically, cyclic problems for the finite edge-crack geometries posed in Figure 1 remain within the small scale yielding range for cyclic stress amplitudes,

$\Delta\sigma$ , less than about  $2\tau_Y$ . Thus, for example, steady cycling between zero stress and a stress level approaching overall yield at  $\sigma = 2\tau_Y$  is still governed by small scale yielding. These considerations highlight the importance of small scale yielding under cyclic loading.

Conversion of the results for monotonic loading to cyclic loading somewhat less straight forward for the PSB cracks because of the dependence on the band width through the parameter  $R_n/w$ . Inspection of the numerical solution to the monotonic problem has indicated that it has the property that points which yield undergo no subsequent elastic unloading. This is the necessary condition such that the solution for steady cyclic loading between  $K_{\max} - \Delta K$  and  $K_{\max}$  can be constructed by the procedure described above using the monotonic solution with  $\tau_Y$  replaced by  $2\tau_Y$ . The construction is as follows. Display the dependence of  $c_n$  and  $c_t$  on  $R_n/w$  shown in Figure 4 explicitly by writing  $c_n(R_n/w)$  and  $c_t(R_n/w)$ . Define a quantity for the cyclic problem analogous to  $R_n$  in (3.6) as

$$\Delta R_n = \frac{1}{9\pi} \left( \frac{\Delta K_I}{2\tau_Y} \right)^2. \quad (3.9)$$

Then, the cyclic crack tip displacements are given by

$$\Delta\delta_n = \frac{1}{2}c_n(\Delta R_n/w) \frac{\Delta K_I^2}{E\tau_Y} \quad \text{and} \quad \Delta\delta_t = \frac{1}{2}c_t(\Delta R_n/w) \frac{\Delta K_{II}^2}{E\tau_Y}, \quad (3.10)$$

where, as before, attention is limited to  $\Delta K_{II} = -\Delta K_I/2$ . The condition that no elastic unloading occurs in solution for monotonic loading ensures that the superposition employed in constructing the cyclic solution is valid. For single slip plasticity there are no additional complexities associated with nonproportional plastic deformation.

It can be seen from the plots in Figure 4 that the dependence of  $c_n$  and  $c_t$  on  $\Delta R_n/w$  is quite weak for  $\Delta R_n/w$  greater than about 2. For  $\Delta R_n/w$  less than 2, the dependence can become important. For example, in the case where the PSB lies above the crack, the fact that  $c_n$  decreases with increasing  $\Delta R_n/w$  while  $c_t$  increases in magnitude means that there is a range where  $\Delta\delta_n$  becomes larger than  $\Delta\delta_t$ .

#### 4. Edge-crack in large scale yielding

The three 45° edge-crack problems in Figure 1 are now considered for monotonically increasing  $\sigma$ . The results are presented as the stress dependent coefficients  $C_n$  and  $C_t$  in

$$\delta_n = C_n \left( \frac{\sigma}{2\tau_Y} \right) \frac{\sigma^2 a}{E\tau_Y} \quad \text{and} \quad \delta_t = C_t \left( \frac{\sigma}{2\tau_Y} \right) \frac{\sigma^2 a}{E\tau_Y}. \quad (4.1)$$

For the two PSB problems the coefficients also depend on  $w/a$ . Within the small scale yielding range, coinciding approximately with  $\sigma/(2\tau_Y) < 1/2$ , the two sets of coefficients in (3.5) and (4.1) are related by

$$C_n = 1.561c_n \quad \text{and} \quad C_t = 0.416c_t. \quad (4.2)$$

The coefficients are plotted in Figure 5. The small scale yielding limit as given by (4.2) with (3.7) is included in Figure 5(a) for the problem with no restrictions on the zone of plastic yielding ( $C_n = 0.55$  and  $C_t = -0.27$ ). Both components of the crack tip displacement

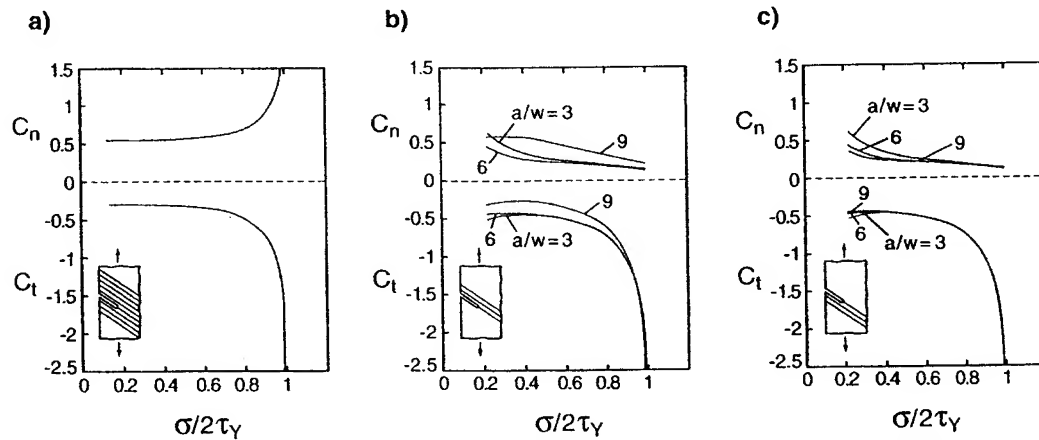


Figure 5. The coefficients specifying the crack tip displacement components in (4.1) for monotonic stressing of the  $45^\circ$  edge-crack under large scale yielding. (a) Unconfined slip. (b) Slip confined to a band of width  $w$  above the crack plane. (c) Slip confined to a band of width  $w$  below the crack plane.

experience large amplification due to large scale yielding, in the range  $\sigma/(2\tau_Y) > 1/2$ . The PSB problems display some dependence on  $a/w$ , but surprisingly little over the range of values of  $a/w$  chosen in Figure 5. The tangential component of the tip displacement follows the behavior of the problem with unconstrained yield. On the other hand, the band severely constrains the magnitude of the opening component in the large scale yielding range compared to the case where slip is not confined. An unexpected trend is noted in Figure 5(b) for the case where the PSB lies on the upper side of the crack. The normal component of the crack tip displacement is larger for the narrowest band ( $a/w = 9$ ) than for the wider bands ( $a/w = 6$  and  $3$ ). This trend is a consequence of the nonlinear coupling between the opening and tangential tip displacements under the mixed mode loading. Note that the tangential component is diminished by the narrowness of the band. These same trends can be inferred from the small scale yielding results in Figure 4, although they are obscured by the nondimensional variables used in that figure.

The double slip zone model discussed in Section 2.2 can be used to approximate the problems in Figures 1 and 3. As mentioned in Section 2.2, well established numerical methods for integral equations can be employed to generate results, and crack tip displacement components are readily extracted. A set of results for  $C_n$  and  $C_t$  in (4.1) for the two PSB problems is given in Figure 6. Included is the result for  $\delta_t$  for the limit of a band of zero width ( $w/a = 0$  such that  $\delta_n = 0$ ), and results for bands of small width,  $w/a = 0.05$ , located on one side of the crack or the other. These numerical results are in reasonable agreement with the finite element results for the unapproximated model, and the general trends are in close accord.

As has already been emphasized, the responses under steady cyclic loading should be well characterized by the small scale yielding results given in the previous section, assuming that  $\Delta\sigma$  is less than about  $2\tau_Y$ .

## 5. Barriers to slip

To obtain some insight into the effect of barriers to slip such as a grain boundary, two variations of the  $45^\circ$  edge-crack problem have been analyzed. The first imposes a boundary a distance  $D$  along the crack plane from the edge, across which slip is completely blocked.



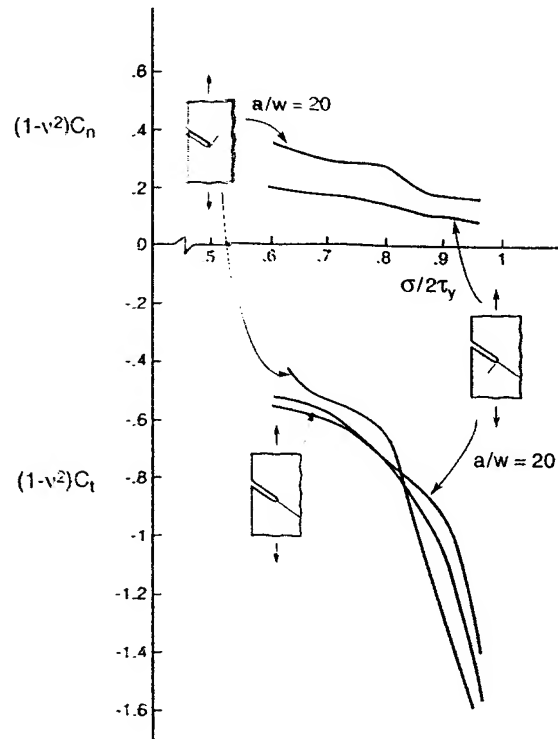


Figure 6. The coefficients specifying the crack tip displacement components in (4.1) for monotonic stressing of the  $45^\circ$  edge-crack under large scale yielding as computed using the double slip zone model of Section 2.2. Three cases are shown: a single slip zone on the extended crack plane for which  $C_n = 0$ , and double slip zones with  $a/w = 20$  modeling bands above and below the crack plane.

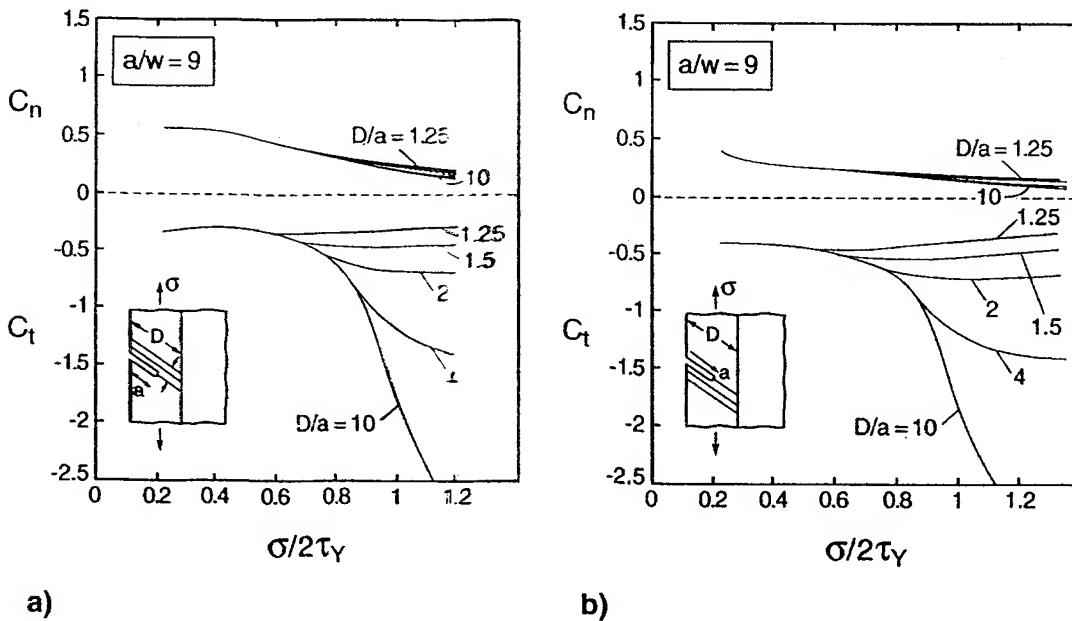


Figure 7. The coefficients specifying the crack tip displacement components in (4.1) for monotonic stressing of the  $45^\circ$  edge-crack under large scale yielding where slip is blocked a distance  $D$  from the edge in the slip direction. Slip confined to a band of width  $w$  above the crack in (a) and below the crack in (b), in both cases with  $a/w = 9$ .

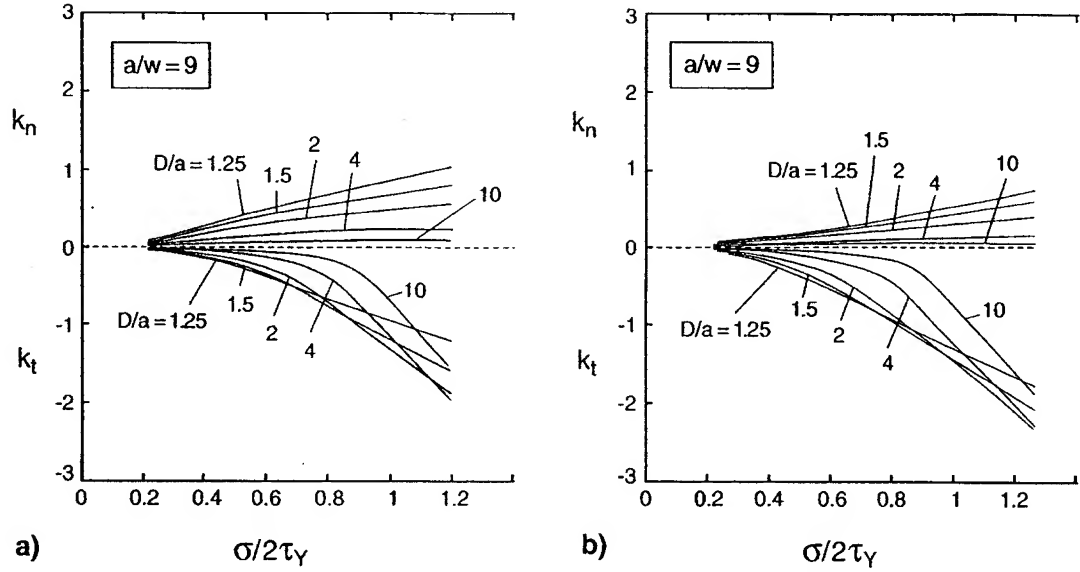


Figure 8. The coefficients specifying the crack tip displacement components in (5.1) for monotonic stressing of the  $45^\circ$  edge-crack under large scale yielding where slip is blocked a distance  $D$  from the edge in the slip direction. Slip confined to a band of width  $w$  above the crack in (a) and below the crack in (b), in both cases with  $a/w = 9$ . These are the same results shown in Figure 7, but here another normalization is employed to better reveal the influence of crack length at different positions of the crack relative to the slip barrier.

Only elastic deformations occur across the boundary. The second variation permits slip across the boundary, activated by the same critical shear stress  $\tau_Y$ , but on a plane oriented at an angle  $\omega$  relative to the slip plane in the cracked crystal. In both instances, monotonic loading is considered, but the effects are expected to carry over to cyclically loaded cracks as they approach slip barriers and their plastic zones are restricted.

### 5.1. BLOCKED SLIP

Plots of  $C_n$  and  $C_t$  as defined in (4.1) are given in Figure 7 for five values of  $D/a$ . The values for the largest value,  $D/a = 10$ , essentially coincide with the limiting case  $D/a = \infty$  presented earlier in Figure 5. For values of  $\sigma/(2\tau_Y)$  less than  $1/2$ , there is no effect of the barrier even when  $D/a = 1.25$  because the plastic zone has not yet reached the boundary. For larger applied stresses, the plastic zone is blocked by the boundary, depending on  $D/a$ , and the tangential component of the tip displacement,  $\delta_t$ , becomes substantially reduced. The opening tip displacement is much less affected. The magnitude of the opening displacement becomes comparable to the tangential component when  $D/a$  is about 1.25.

The normalization (4.1) used for the tip displacements in Figure 7 is not convenient for seeing the influence of the boundary on an approaching crack. This same set of numerical data is replotted in Figure 8 using the following normalization which employs the boundary distance in the normalization rather than the crack length:

$$\delta_n = k_n \frac{\tau_Y D}{E} \quad \text{and} \quad \delta_t = k_t \frac{\tau_Y D}{E}. \quad (4.2)$$

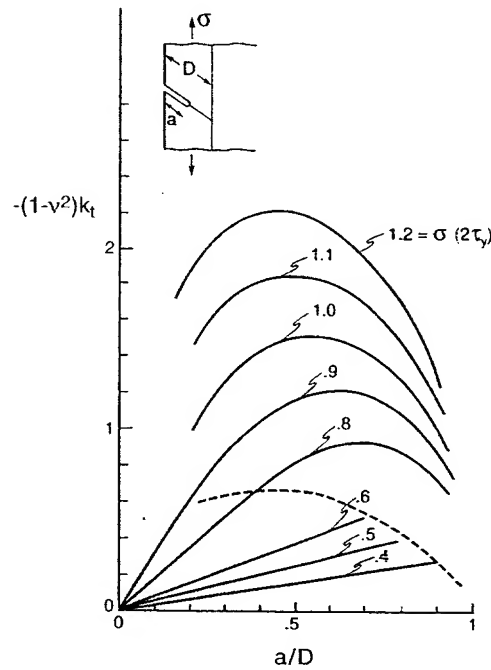


Figure 9. The coefficient  $k_t$  in (5.1) governing the tangential tip displacement as predicted by a single slip zone model with slip confined to the plane ahead of the crack tip. Slip is blocked a distance  $D$  along the plane from the edge. The straight line segments emanating from the origin correspond to the region where the slip zone has not yet reached the barrier.

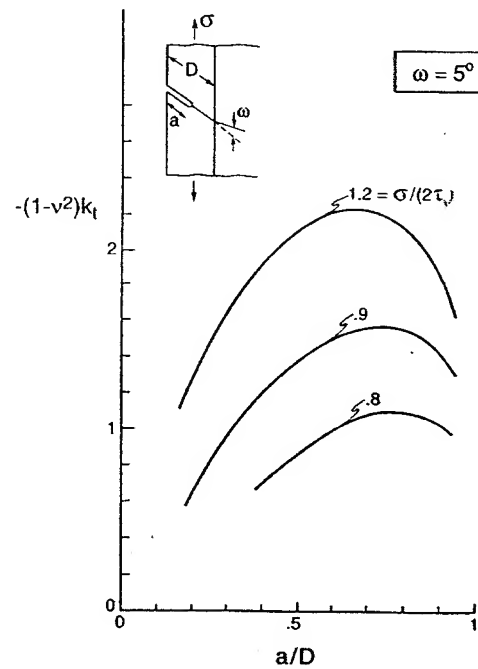


Figure 10. The coefficient  $k_t$  in (5.1) governing the tangential tip displacement as predicted by a single slip zone model with slip confined to the plane ahead of the crack tip. Slip is partially blocked a distance  $D$  along the plane from the edge. Beyond this boundary, the orientation of the slip plane changes. The results were obtained with a model which permits slip only on the single planes shown in the insert.

In this plot is evident that the crack tip displacements are larger as the crack travels across the crystal at a given applied stress, but the boundary holds down the magnitudes at the higher applied stress levels. In particular, the tangential tip displacement component peaks at a value of  $D/a$  below 1.25 at the higher applied stress levels. Predictions for  $k_t$  for the tangential component of the tip displacement from a single slip zone model with slip blocked at the boundary are plotted in Figure 9 against  $a/D$ . The straight line segments of the curves emanating from the origin within the dashed-line curve correspond to the regime where the yielding zone has not reached the boundary. Beyond the dashed-line curve, the boundary interferes with slip, and the crack tip displacement is significantly reduced.

## 5.2. PARTIALLY BLOCKED SLIP

The model of Figure 9 is modified by allowing slip to occur across the boundary, but on a slip system oriented at an angle other than  $45^\circ$ . The model depicted in Figure 10 permits slip at a critical stress  $\tau_Y$ , consistent with (1.3), on a single plane intersecting the primary  $45^\circ$  slip plane at an angle  $\omega$ . The results in Figure 10 have been obtained for a small misorientation of the slip planes,  $\omega = 5^\circ$ . Comparison of Figures 9 and 10, reveals that slip across the boundary does have some influence on the tangential tip displacement, but even with a small misorientation of the slip direction, the boundary serves as an effective block to the slip zone of the edge crack.

## 6. Concluding remarks

The small scale yielding solution describes cyclic crack tip behavior under steady cycling for a fairly wide range of stress because the cyclic plastic zone size is a small fraction of the monotonic zone size. Under the assumption that small scale yielding does apply, the  $45^\circ$  edge-crack subject to steady cyclic stressing between  $\sigma_{\min}$  and  $\sigma_{\max}$  experiences cyclic tip displacements which can be obtained from (1.1), (3.1) and (3.3) (by replacing  $\tau_Y$  by  $2\tau_Y$  as discussed in Section 3.3) as

$$\Delta\delta_n = 0.275 \frac{\Delta\sigma^2 a}{E\tau_Y} \quad \text{and} \quad \Delta\delta_t = 0.135 \frac{\Delta\sigma^2 a}{E\tau_Y}, \quad (6.1)$$

where  $\Delta\sigma = \sigma_{\max} - \sigma_{\min}$ . This result applies to the case where slip in the crystal is unconfined, and there is no crack face contact. When an obstacle or grain boundary is sufficiently close to the crack tip such that it interacts with the cyclic plastic zone, that interaction must be taken into account. The solutions in the present paper provide some insight into such interactions, but further studies will be needed to provide results which are applicable under cyclic loadings. Most Stage I fatigue cracks appear to be arrested by obstacles or barriers (Miller, 1993), and quantitative results for these interactions are needed to understand condition under which arrest occurs.

Attention here has been limited to applied stress levels such that the crystal itself does not experience overall yielding. In the range of cyclic stressing causing fatigue in a polycrystal, a small fraction of surface crystals favorably oriented for slip are expected to experience overall reversed plastic straining in each cycle. Were this not the case, it is unlikely fatigue crack nucleation would occur. Thus, an important extension of the present study will be to consider Stage I edge cracks lodged within favorably oriented crystals which experience reversed plastic straining each cycle even when no crack is present.

Components of the crack tip displacements have been featured in this study under the assumption that these quantities provide average measures of crack tip deformation which should provide a means of correlating crack growth rates. Further experimentation and more fundamental modeling are needed to relate crack growth per cycle to the amplitudes of the crack tip displacements under Stage I, when cracks tend to grow along the favorably oriented slip directions. In particular, the effect on the growth rate of the ratio of the normal to tangential tip displacements must be determined since the relative amplitude appears to vary considerably, depending on the cyclic stress level and on proximity to obstacles to slip.

### Acknowledgment

The work of J.W.H. was supported in part by the MURI on High Cycle Fatigue from AFOSR and in part by the Division of Engineering and Applied Sciences, Harvard University. The work of V.T. is partly supported by the MUP2 Center for Materials Processing, Properties and Modelling, financed by the Danish Agency for Development of Trade and Industry, the Danish natural Science Research Council, and the Danish Technical Research Council.

### References

- Barenblatt, G.I. (1959a). The formulation of equilibrium cracks during brittle fracture. General ideas and hypotheses. Axially-symmetric cracks. *Journal of Applied Mathematics and Mechanics* **23**, 622–636. (Translation from Russian: PMM **23** (1959a), 434–444).
- Barenblatt, G.I. (1959b). The formulation of equilibrium cracks during brittle fracture. Rectilinear cracks in plane plates. *Journal of Applied Mathematics and Mechanics* **23**, 1009–1029. (Translation from Russian: PMM **23** (1959b), 706–721).
- Barenblatt, G.I. (1962). The mathematical theory of equilibrium cracks in brittle fracture. *Advances in Applied Mechanics* **7**, 55–129.
- Dugdale, D.S. (1960). Yielding of steel sheets containing slits. *Journal of the Mechanics and Physics of Solids* **8**, 100–108.
- Isida, M. (1979). Tension of a half plane containing array cracks, branched cracks and cracks emanating from sharp notches. *Transaction of the Japan Society for Mechanical Engineers* **45**, 306–317.
- Ma, B.-T. and Laird, C. (1989). Overview of fatigue behavior in copper single crystals: I, II & III. *Acta Metallurgica* **37**, 325–336, 337–348, 349–355.
- McDowell, D.L. (1996). Basic issues in the mechanics of high cycle metal fatigue. *International Journal of Fracture* **80**, 103–145.
- Miller, K.J. (1993). Materials science perspective of metal fatigue resistance. *Materials Science and Technology* **9**, 453–462.
- Repetto, E.A. and Ortiz, M. (1977). A micromechanical model of fatigue crack nucleation in FCC metals. *Acta Materialia* **45**, 2577–2595.
- Rice, J.R. (1967). *Mechanics of Crack Tip Deformation and Extension by Fatigue*. ASTM STP 415, American Society of Testing Materials, 247–309.
- Saeedvafa, M. and Rice, J.R. (1992). Crack tip fields in a material with three independent slip systems: NiAl single crystal. *Modelling and Simulation in Materials Science and Engineering* **1**, 53–71.

# Small Fatigue Cracks: Mechanics, Mechanisms and Engineering Applications

R. O. Ritchie and J. O. Peters

Materials Sciences Division, Lawrence Berkeley National Laboratory, and Department of Materials Science and Engineering, University of California, Berkeley, CA 94720, USA

Damage-tolerant design and life-prediction methodologies have been practiced for metallic structures for decades, although their application to brittle materials, such as ceramics and intermetallic alloys, still poses particular problems, primarily because of their extreme flaw-sensitivity. Moreover, like metals, they are susceptible to premature failure by cyclic fatigue, which provides a prominent mechanism for subcritical crack growth that further limits life. One specific problem involves the large dependency of growth rates on the applied stress intensity, which necessitates that design is based on the concept of a fatigue threshold, particularly in the presence of small cracks. In this paper, studies on the role of small cracks in influencing thresholds and near-threshold growth rates are described for both brittle and ductile materials. Examples are given from the military engine "High-Cycle Fatigue" initiative, which represents an important problem where information on the behavior of small fatigue cracks is critical.

(Received August 7, 2000; Accepted September 18, 2000)

**Keywords:** high-cycle fatigue, fatigue-crack propagation, fatigue thresholds, small cracks, crack-tip shielding, foreign object damage, ceramics, intermetallics, Ti-6Al-4V

## 1. Introduction

The problem of small cracks remains one of the most critical, yet least understood, topics in fatigue research, despite the fact that 25 years have elapsed since the so-called anomalous behavior of small fatigue cracks was first reported for age-hardened aluminum alloys by Pearson.<sup>1)</sup> Since that time, innumerable papers, reviews and books have been published on the subject [e.g., Ref. 2–9)] indicating that the "small-crack effect" is associated with the fact that the growth rates of small cracks can exceed those of large cracks at the same *applied* stress-intensity range  $\Delta K$ , and that small cracks can propagate at applied stress intensities less than the fatigue threshold,  $\Delta K_{TH}$ , below which large-crack growth is presumed dormant. In general, these effects occur when crack sizes become comparable with (Fig. 1):

- *microstructural size scales*, where biased statistical sampling of the microstructure leads to accelerated crack growth along "weak paths" and local retardation or arrest can occur at microstructural "barriers" such as grain or phase boundaries (a continuum or homogeneity limitation)-*microstructurally-small cracks*,
- *the extent of local inelasticity*, e.g., the plastic-zone size, ahead of the crack tip, where the assumption of small-scale yielding implicit in the use of the stress intensity  $K$  is not strictly valid (a linear-elastic fracture mechanics limitation)-*mechanically-small cracks*,
- *the extent of crack-tip shielding*, e.g., crack wedging by crack closure, behind the crack tip, where the reduced role of shielding leads to a higher *local* driving force than the corresponding large crack at the same applied (global) stress intensity (a similitude limitation)-*physically-small cracks*.<sup>10)</sup>

Whereas the small-crack effect has always been of prime importance since it can result in gross overestimates of the damage-tolerant life of a structure, the problem has come into greater prominence of late due to (i) the *Aging Aircraft Initiative*, where the residual strength and remaining life of many

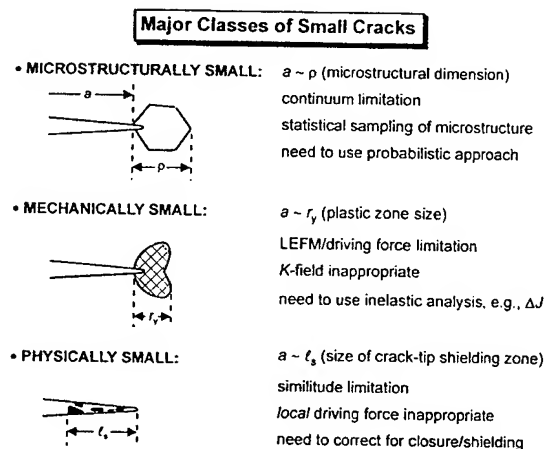


Fig. 1 Schematic illustration of the three major classes of small fatigue cracks.

sections of the fuselage of older aircraft is compromised by numerous small defects *i.e.*, multi-site damage, (ii) the *High-Cycle Fatigue Initiative*, where the failure of blades and disks in aircraft gas-turbine engines results from the rapid propagation of small cracks under high-frequency vibratory loading,<sup>9,11–13)</sup> (iii) an increasing emphasis on *durability*, particularly for the economically feasible life of aircraft structures, based on the statistical modeling of small flaw populations,<sup>14)</sup> and (iv) the potential *structural use of ceramics and intermetallic materials*, especially for engine and aerospace applications, where due to their highly restricted growth-rate curves, *i.e.*, very high Paris-law exponents, design must be based on the concept of a threshold, ideally defined for small cracks.<sup>15,16)</sup>

Although the behavior of small cracks is now quite well documented for metallic materials, far less information is available for advanced materials. Moreover, a major difficulty with small cracks has always been the difficulty of experimentally determining small-crack data, particularly for design purposes. Accordingly, we describe how in *limited*

cases worst-case large-crack data can be used to estimate small-crack growth rates and threshold behavior in both traditional and advanced materials. However, this approach is only viable for cracks larger than the scale of microstructure ("continuum-sized cracks"); it is not appropriate where cracks are of a size that they interact with microstructural features of comparable dimensions (microstructurally-small cracks), due to biased "sampling" of the microstructure.

In general, the behavior of small cracks is seen to be remarkably similar in traditional and advanced materials; specifically the behavior of cracks of a size comparable with the extent of shielding can be readily estimated from worst-case (shielding-corrected) large-crack results. This occurs despite the fact that the salient shielding mechanisms in the fatigue of ceramics and intermetallics are not simply crack closure but additionally involve other mechanisms including *in situ* phase transformations and mostly crack-bridging processes.<sup>15,16</sup> However, when cracks are small compared to microstructural dimensions, this approach cannot work. Moreover, it is shown that the optimal microstructures for small-crack resistance are rarely similar to those optimized for large-crack fracture toughness and fatigue resistance, as shown by recent results in  $\alpha + \beta$ <sup>17</sup> and  $\beta$  titanium alloys<sup>18</sup> and for  $\gamma$ -based TiAl alloys.<sup>19</sup>

Finally, the problem of foreign-object damage on jet engine fan blades<sup>9,11-13,20</sup> is shown as an engineering example where the critical conditions for fatigue failure must be defined in the presence of microstructurally-small cracks. In this example, simple worst-case large-crack data cannot be used to estimate small-crack growth rates and threshold behavior. Instead, a modified Kitagawa-Takahashi approach is presented, where the limiting conditions of fatigue failure are determined by the stress-concentration corrected ( $S$ - $N$ ) fatigue limit (at microstructurally-small crack sizes) and worst-case large-crack fatigue threshold (at larger, "continuum-sized" crack sizes).

## 2. Traditional Materials

### 2.1 Titanium alloys

High-cycle fatigue (HCF) has been identified as one of the prime causes of turbine engine failure in military aircraft. It can result in essentially unpredictable failures due to the propagation of fatigue cracks in blade and disk components under ultrahigh frequency loading, with failure resulting from the rapid growth of small cracks often initiated at microstructural damage caused by fretting or foreign object impacts.<sup>11-13</sup> To prevent HCF failures, design methodologies are required that identify the critical levels of microstructural damage which can lead to such failures. Since the engine components experience high frequency ( $\sim 1$ – $2$  kHz) vibrational loads due to resonant airflow dynamics, often with high mean stresses, even cracks growing at slow per-cycle velocities of  $\sim 10^{-10}$  m/cycle can propagate to failure in a short time period. Consequently, HCF-critical turbine components must be operated below a fatigue threshold, appropriate for flaw sizes typically smaller than  $\sim 500$   $\mu\text{m}$ . Since such small cracks are known to propagate below the large-crack threshold ( $\Delta K_{\text{TH}}$ ), design against HCF failure must be based on the notion of a practical small-crack threshold, measured under

the representative HCF conditions.

As small-crack testing is tedious and prone to excessive scatter, for design purposes one practical approach is to estimate the physically-small crack thresholds from "worst-case" large-crack threshold tests by attempting to minimize any crack-tip shielding in the crack wake.<sup>21</sup> This approach was evaluated for a Ti-6Al-4V alloy (Fig. 2),  $\alpha + \beta$  processed (solution treated and overaged, STOA<sup>22</sup>) for typical fan blade application. Large through-thickness cracks ( $> 10$  mm) in compact-tension specimens were measured at high mean stresses using at, above and below the representative frequencies ( $\sim 1,000$  Hz) using constant- $K_{\text{max}}$ /increasing- $K_{\text{min}}$  cycling<sup>23</sup> to approach the threshold at extremely high load ratios, i.e., at  $R (=K_{\text{min}}/K_{\text{max}})$  values approaching unity. Results, shown in Fig. 3 for both (a) constant- $R$  (at  $R = 0.1$  to  $0.8$ ) and (b) constant- $K_{\text{max}}$ /varying  $R$  tests, were found to be independent of frequency for the Ti-6Al-4V alloy in question, over the wide range of 50 to 20,000 Hz for tests in ambient temperature air.<sup>21</sup> Moreover, they indicate that whereas constant- $R$  cycling at  $R = 0.8$  gives a  $\Delta K_{\text{TH}}$  value of  $2.6 \text{ MPa}\sqrt{\text{m}}$  (compared to  $4.6 \text{ MPa}\sqrt{\text{m}}$  at  $R = 0.1$ ), even lower values are obtained with constant- $K_{\text{max}}$  cycling, a worst-case value of  $\Delta K_{\text{TH}} = 1.9 \text{ MPa}\sqrt{\text{m}}$  being achieved with  $K_{\text{max}} = 36.5 \text{ MPa}\sqrt{\text{m}}$  at  $R = 0.95$ . Crack closure could not be detected above  $R \sim 0.5$ .

Whereas even lower values can probably be obtained by using higher  $K_{\text{max}}$  values approaching  $K_{\text{IC}}$ , the measured worst-case value of  $1.9 \text{ MPa}\sqrt{\text{m}}$  at  $R = 0.95$  was found to provide a lower bound to thresholds for the onset of the growth of naturally-initiated small cracks ( $a \sim 45$ – $1000$   $\mu\text{m}$ ), shown in Fig. 4 for the Ti-6Al-4V material under study. Although small-crack growth rates are  $\sim 0.5$ – $1$  orders of magnitude faster than corresponding large-crack data, no small-crack growth was reported below  $\Delta K = 2.9 \text{ MPa}\sqrt{\text{m}}$ , i.e., well above the worst-case large-crack threshold.<sup>21</sup>

The higher growth rates of the naturally-initiated small-cracks, compared to the "closure-free" large cracks, are presumed to be associated with biased statistical sampling of the microstructure. The natural crack initiation process allows for sampling of a very large area of the specimen for more favor-

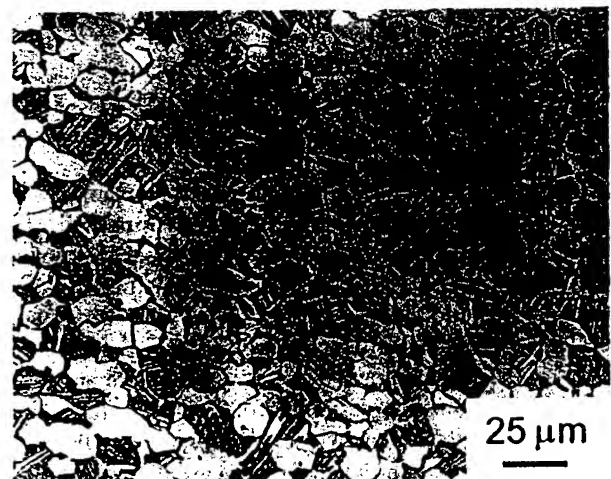


Fig. 2 Bimodal (solution treated and overaged, STOA) microstructure of Ti-6Al-4V.

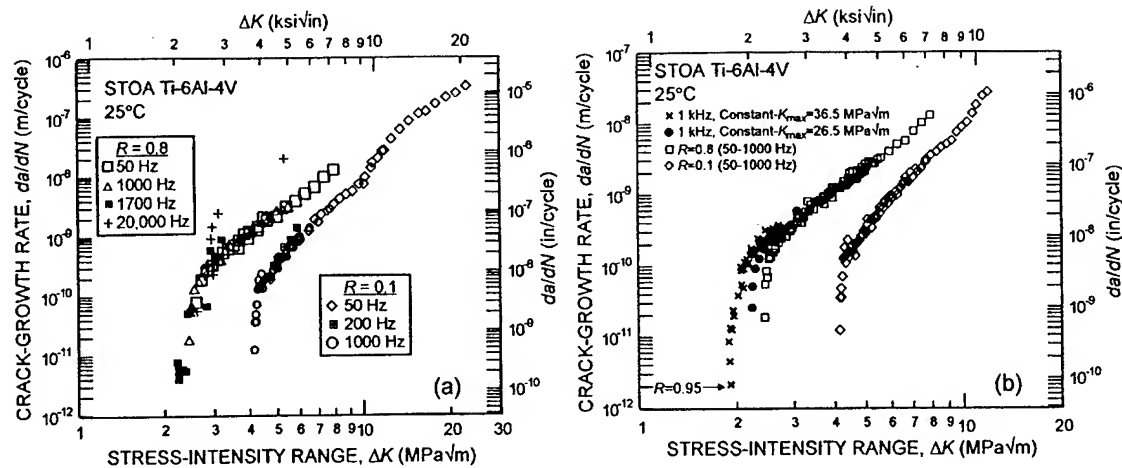


Fig. 3 High-cycle fatigue-crack growth behavior of through-thickness large cracks ( $> 10$  mm) in a bimodal (STOA) Ti-6Al-4V alloy in room air, showing (a) constant- $R$  cycling between 50 and 20,000 Hz for  $R = 0.1$  and 0.8, and (b) constant- $K_{max}$ /increasing- $K_{min}$  cycling at 1000 Hz to achieve final  $R$  values (at  $\Delta K_{TH}$ ) of 0.92 and 0.95.<sup>21)</sup>

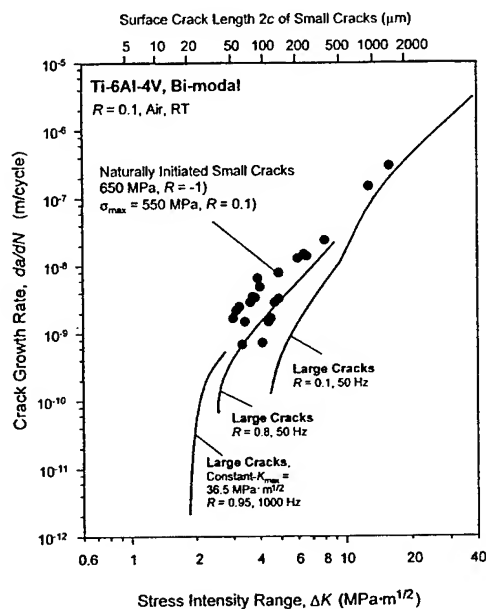


Fig. 4 Fatigue-crack growth results in bimodal Ti-6Al-4V for naturally-initiated small ( $\sim 45$ – $1000 \mu\text{m}$ ) surface cracks,<sup>17)</sup> as compared to the large-crack data shown in Fig. 3(b).<sup>21)</sup>

able microstructural orientations with respect to crack initiation and growth, compared to that of the large cracks which essentially sample an average of all microstructural orientations [e.g., Ref. 9)].

High-cycle fatigue thus provides a notable example of the importance of small cracks and thresholds for small cracks in traditional materials. Moreover, the approach of defining the type of small cracks, i.e., physically-small cracks in the example of Ti alloy turbine blades, permits the use of worst-case large-crack thresholds (measured under very high  $R$  conditions with minimal crack closure) as a feasible and practical solution of obtaining estimates of the small-crack thresholds. However, the use of "worst-case" large-crack thresholds is only feasible in cases where crack sizes are larger than the characteristic microstructural dimensions (and cyclic plastic-zone sizes). In the presence of microstructurally-small cracks,

alternative approaches must be sought. One, especially relevant to the high-cycle fatigue problem, involves the Kitagawa-Takahashi approach, as discussed in detail below.

### 3. Advanced Materials

The importance of small fatigue cracks with advanced materials, such as intermetallics and ceramics, is caused principally by the sensitivity of their crack-growth rates to the applied stress intensity; specifically this results in Paris power-law exponents (i.e.,  $m$  in relationships derived from  $da/dN \propto \Delta K^m$ ) often well in excess of 10, compared to metallic materials where typically  $m \sim 2$  to 4 (in the mid-range of growth rates) (Fig. 5) [e.g., Ref. 16)]. Since the projected damage-tolerant life is proportional to the reciprocal of the applied stress raised to the power of  $m$ , a factor of two change in this stress can lead to life projections of a ceramic component (where  $m$  can be as high as 15–20 or more) to vary by more than six orders of magnitude. Essentially, because of the high exponents, the life spent in crack propagation in advanced materials is extremely limited; accordingly, rather than basing lifetime calculations on the integration of crack-propagation data, as is typically done with metallic structures, design must be based on the concept of a fatigue threshold, invariably defined for small cracks due to the inherently low tolerance of brittle materials to flaws.

In light of this, an appreciation of the small-crack effect and the documentation of fatigue thresholds for small cracks are, if anything, more important for advanced materials than for traditional alloys. However, there are only a few published results on small fatigue crack-growth behavior in these materials.

#### 3.1 Ceramic materials

Unlike ductile materials where crack advance is motivated by *intrinsic* cyclic damage mechanisms *ahead* of the tip, e.g., crack-tip blunting and re-sharpening, the cyclic fatigue process in monolithic ceramics, e.g.,  $\text{Si}_3\text{N}_4$ ,  $\text{SiC}$ , involves the cyclically-induced suppression of *extrinsic* crack-tip shielding, primarily crack bridging, *behind* the crack tip; at ambi-



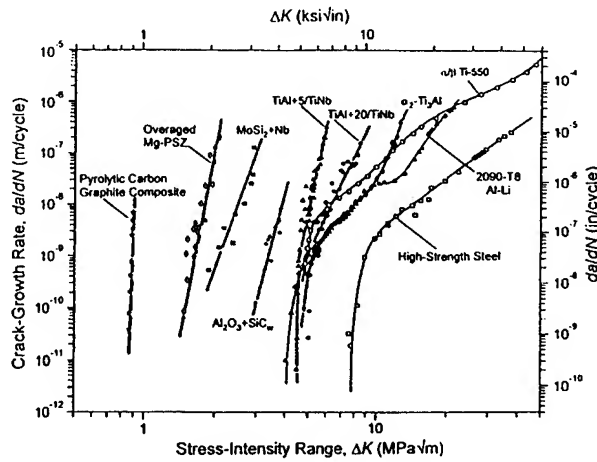


Fig. 5 Schematic illustration of the typical variation in fatigue-crack growth rates,  $da/dN$ , as a function of the applied stress-intensity range,  $\Delta K$ , in metallic, intermetallic and ceramic materials.<sup>16)</sup>

ent temperatures, the crack-advance mechanism itself is typically identical to that for crack growth under static loading (Fig. 6).<sup>16,24,25)</sup> With this approach, it is apparent that the high Paris exponents  $m$  seen in ceramics result primarily from an increased dependency upon the maximum stress intensity,  $K_{max}$ , rather than on  $\Delta K$  *per se*. Indeed, using a modified form of the Paris relationship:<sup>16,26)</sup>

$$da/dN \propto \Delta K^p K_{max}^n, \quad (1)$$

where  $(n + p) = m$ , the exponents  $n$  and  $p$  are  $\sim 36$  and  $1.9$  in a typical ceramic, *e.g.*, *in situ* toughened SiC, respectively;<sup>27)</sup> this is to be compared with values of  $n = 0.5$  and  $p = 3$  for metal fatigue of a nickel-base superalloy.<sup>28)</sup>

Since there is no apparent intrinsic damage process unique to cyclic loading, fatigue-crack initiation always occurs at pre-existing defects, *i.e.*, unlike crack formation in persistent slip bands in metals, natural crack initiation does not occur. The exception to this is ceramics toughened by *in situ* phase transformations, *e.g.*, MgO partially-stabilized zirconia (Mg-PSZ), where natural initiation can occur and is apparently associated with sites of local transformation.<sup>29)</sup> Behavior in both classes of ceramics is briefly described below.

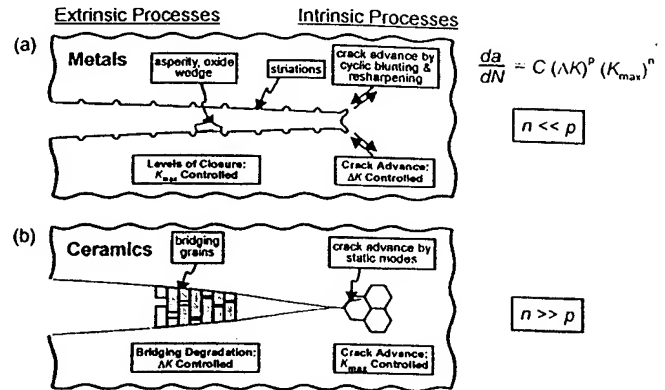


Fig. 6 Schematic illustrations of the intrinsic and extrinsic mechanisms involved in cyclic fatigue-crack propagation in (a) metals and (b) ceramics, showing the relative dependencies of growth rates,  $da/dN$ , on the alternating  $\Delta K$  and maximum  $K_{max}$  stress intensities.<sup>16)</sup>

### 3.1.1 Phase-transforming ceramics

The growth-rate behavior of microstructurally-small surface cracks ( $< 100 \mu\text{m}$ ), naturally initiated on the surface of cantilever bend bars of Mg-PSZ, is compared to the corresponding behavior of large, through-thickness cracks ( $> 3 \text{ mm}$ ) in compact-tension specimens in Fig. 7.<sup>29)</sup> Small cracks can be seen to propagate below the long-crack threshold, yet individual cracks grow at decreasing growth rates with increasing applied stress intensity, sometimes to arrest. Such behavior is similar to that reported for physically-small cracks in metallic materials where the primary shielding mechanism is crack closure [*e.g.*, Ref. 3)]; in PSZ, however, the effect results from shielding by transformation toughening.<sup>30)</sup>

Resistance to crack growth in PSZ is afforded by an *in situ* stress-controlled transformation of tetragonal  $\text{ZrO}_2$  precipitates to the monoclinic phase, which results in a zone of compressive material surrounding the crack wake due to an associated dilation of  $\epsilon_T \sim 6\%$  (there is also some degree of shear). Analogous to crack closure in metals, the effective (near-tip) stress intensity,  $\Delta K_{tip}$ , for large cracks is reduced from the applied value by shielding due to transformation toughening in the crack wake, *i.e.*,  $\Delta K_{tip} = K_{max} - K_s$ .

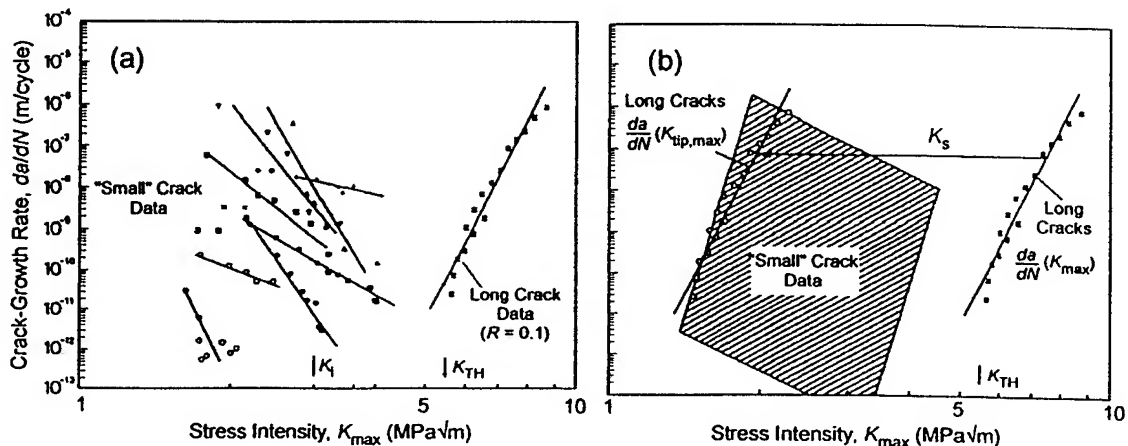


Fig. 7 (a) Comparison of the growth-rate behavior of naturally-initiated small ( $\sim 1$ – $100 \mu\text{m}$ ) surface cracks and through-thickness large ( $> 3 \text{ mm}$ ) cracks in transformation-toughened (MS-grade) Mg-PSZ ceramic, as a function of the applied  $K_{max}$ . Note how in (b) the initial growth of the small cracks occurs at stress intensities typical of unshielded large cracks.<sup>29)</sup>

At steady-state, the shielding stress intensity reaches a value given approximately by:<sup>31)</sup>

$$K_s \sim 0.2E'\varepsilon_T f \sqrt{h}, \quad (2)$$

where  $E'$  is the effective elastic modulus in plane stress or plane strain,  $f$  is the volume fraction of tetragonal precipitates, and  $h$  is the transformation-zone width. The steady-state condition is reached once there is a wake of transformed material extending at least five times  $h$ , i.e., the crack has penetrated the zone more than a distance of  $5h$ .<sup>31)</sup> Since the transformation-zone size is on the order of tens to hundreds of micrometers (depending upon the heat-treated condition of the PSZ), any crack of a length less than roughly five times this dimension would experience a diminished effect of the shielding; this in turn results in an enhanced near-tip stress intensity, compared to a large crack at the same applied  $K$ , such that the small cracks can propagate at lower applied  $K$  values.<sup>29)</sup> The decelerating growth rates result from the mutual competition of the applied  $K$ , which increases with increase in crack length, and the shielding  $K$  which also increases until a steady-state wake zone has been established.<sup>29)</sup>

Consistent with this explanation, a "worst-case" crack-growth relationship can be determined for the small-crack data by correcting the large-crack results for the maximum extent of transformation shielding,  $K_s$ , computed from eq. (2). This is shown in Fig. 7(b), where it is clear that the large-crack  $da/dN$  vs.  $\Delta K_{tip}$  relationship, which can be readily measured experimentally, can be utilized as a conservative representation of small-crack behavior.<sup>29)</sup> However, this practical solution to the physically-small crack problem is only feasible when i) the prevailing mechanism of shielding is known, and ii) the magnitude of its influence can be either measured or, as in the present case, computed theoretically.

### 3.1.2 Non phase-transforming ceramics

Although PSZ is perhaps the highest toughness ceramic, the absence of the transformation at elevated temperatures severely limits its use. For high temperature applications at 1000°C or above, silicon nitride and silicon carbide are currently the preferred ceramics. Both materials can be extrinsically toughened above their intrinsic toughness of  $\sim 2\text{--}3 \text{ MPa}\sqrt{\text{m}}$  to  $\sim 8\text{--}10 \text{ MPa}\sqrt{\text{m}}$  by promoting shielding by interlocking grain bridging in the crack wake [e.g., Ref. 27)]. This is generally achieved by elongating the grain structure and weakening the grain boundaries (through the presence of the glassy grain-boundary phase) to promote intergranular fracture.<sup>32)</sup>

Under cyclic loading, such grain bridging is degraded by frictional wear along the boundaries; indeed, as depicted schematically in Fig. 6(b), this is the primary mechanism for fatigue-crack growth in most ceramics at ambient temperatures.<sup>16,24,25)</sup> Since the bridging zones can traverse several grains, there is again a potential for small-crack effects where crack sizes are comparable to the size of this zone, i.e., on the order of the grain size.

To date, very few studies [e.g., Ref. 33)] have focused on the fatigue behavior of cracks of microstructural dimensions in ceramics. As natural initiation cannot occur in these materials, hardness indents have generally been used to initiate cracking such that the typical small cracks studied generally are larger than  $\sim 100 \mu\text{m}$  or so. Two examples are shown in

Figs. 8 and 9, respectively, for small surface cracks initiated at indents in cantilever bend samples of an *in situ* toughened monolithic SiC<sup>34)</sup> and a SiC-whisker reinforced alumina composite.<sup>26)</sup> As before, the small cracks propagate below the large-crack threshold at decreasing rates until they arrest or merge with the large-crack curve. In these cases, the decreasing growth rates are a result of the crack growing out of the residual tensile stress field of the indent. In fact, by determining an effective stress intensity by superposing the stress intensity resulting from this residual field,  $K_{RD}$ , and the globally applied stress intensity, the large and small crack data can be brought into correspondence. Similar results have been reported for several ceramics, including Si<sub>3</sub>N<sub>4</sub>,<sup>35)</sup> pyrolytic carbon,<sup>36,37)</sup> and several other grades of toughened SiC.<sup>34)</sup>

These examples for brittle ceramics serve to illustrate that for small cracks *larger than* the scale of the microstructure, discrepancies between large and small crack growth rates can be reconciled by a worst-case threshold approach by fully accounting for the various contributions to the local driving force, namely from the globally applied  $K$ , any residual stress fields, and the magnitude of the relevant shielding in the crack wake.

### 3.2 Ordered intermetallic alloys

Due to their complex and ordered crystal structures, intermetallics (like ceramics) generally display only very limited mobile dislocation activity at low homologous temperatures (below their brittle-to-ductile transition temperature), and are

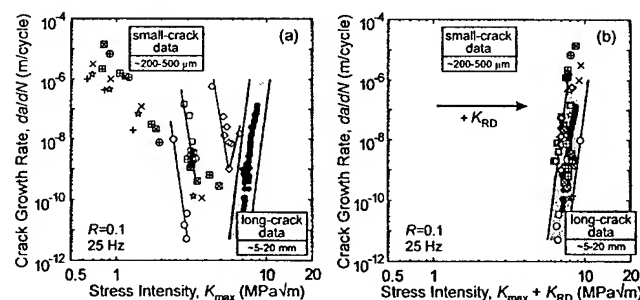


Fig. 8 Comparison of the growth-rate behavior of small ( $\sim 200\text{--}500 \mu\text{m}$ ) surface cracks, initiated at hardness indents, and through-thickness large ( $5\text{--}20 \text{ mm}$ ) cracks in an *in situ* toughened monolithic SiC ceramic, as a function of (a) the applied  $K_{max}$ , and (b) the total stress intensity from the applied  $K_{max}$  and residual stress field surrounding the indent  $K_{RD}$ .<sup>34)</sup>

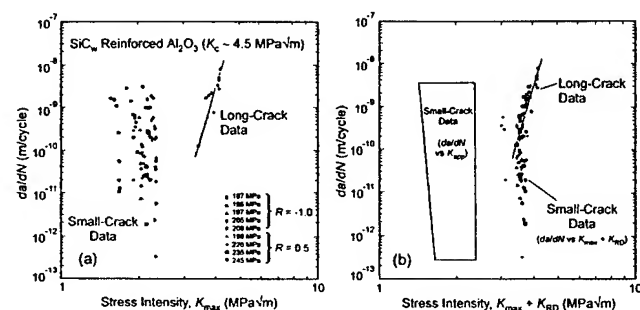


Fig. 9 Comparison of the growth-rate behavior of small ( $< 300 \mu\text{m}$ ) surface cracks, initiated at microhardness indents, and through-thickness large ( $> 3 \text{ mm}$ ) cracks in a 15 vol% SiC-whisker reinforced alumina composite, as a function of (a) the applied  $K_{max}$ , and (b) the total stress intensity from the applied  $K_{max}$  and residual stress field surrounding the indent  $K_{RD}$ .<sup>26)</sup>

thus often highly restricted in ductility and toughness. However, unlike ceramics, they can be toughened both intrinsically and extrinsically, although the former is far more difficult.<sup>38)</sup> Whereas intrinsic mechanisms, such as the activation of additional slip systems, do not degrade under cyclic loading, extrinsic toughening mechanisms such as crack bridging can suffer severe cyclic degradation, similar to behavior in ceramics. A notable example of this is ductile-phase reinforced intermetallic-matrix composites, such as  $\beta$ -TiNb-reinforced  $\gamma$ -TiAl, which due to extensive wake bridging by the uncracked ductile phase can display significantly higher toughness (*i.e.*, by a factor of 3 or greater) than the constituent matrix.<sup>39)</sup> However, the improvement in crack-growth resistance is far less obvious in fatigue simply because the ductile phase fails prematurely (by fatigue); indeed, the fatigue-crack growth properties are rarely any better than that of the unreinforced matrix.

Nevertheless, as the extrinsic toughening mechanisms act in the crack wake, *e.g.*, in TiNb-TiAl over a bridging zone of several millimeters, fatigue cracks smaller than this dimension will not develop the full magnitude of shielding and as such will behave as physically-small cracks. In addition, the microstructurally-small crack problem is prevalent in certain intermetallic alloys; as discussed below, coarse lamellar microstructures in  $\gamma$ -based TiAl alloys are a good example of this as colony and grain sizes in some alloys can approach and exceed millimeter dimensions.<sup>40)</sup>

### 3.2.1 Gamma-based TiAl alloys

Of the various intermetallic alloys considered for structural application,  $\gamma$ -based TiAl has received by far the most attention as possible low-pressure gas-turbine blades. Based on the composition (at%) of Ti-47Al with small additions of elements such as Nb, Cr, V and B, two microstructures have been most studied (Figs. 10(a), (b)): a *duplex* microstructure, consisting of  $\sim 15$ – $40\ \mu\text{m}$  sized equiaxed grains of  $\gamma$  (TiAl) with small amounts of  $\alpha_2$  ( $\text{Ti}_3\text{Al}$ ), and a *lamellar* microstructure, consisting of lamellar colonies (several hundred of micrometers in diameter) containing alternating  $\gamma/\gamma$  and  $\gamma/\alpha_2$  platelets.<sup>40)</sup> In general, duplex structures display better elongation and strength, whereas lamellar structures show better creep resistance, toughness and (large-crack) fatigue properties.

It is well documented that lamellar microstructures possess the far superior fracture toughness and R-curve behavior [*e.g.*, Refs. 40, 41)]. This arises primarily from intra- and inter-lamellar microcracking ahead of the crack tip, which results in the formation of uncracked (shear) ligament bridges.<sup>41)</sup> Such bridging degrades somewhat under cyclic loading,<sup>42)</sup> but is still sufficiently potent to give lamellar structures the far superior fatigue-crack growth resistance.<sup>42,43)</sup> As shown by the results for a Ti-47Al-2Nb-2Cr-0.2B (at%) alloy in Fig. 10(c),<sup>42)</sup> at a given applied  $\Delta K$ , growth rates are up to five orders of magnitude slower, and  $\Delta K_{\text{TH}}$  thresholds some 50% higher, than in the duplex structure. These properties are only realized, however, for large cracks of dimensions larger than the bridging zones. Corresponding results for small surface cracks, with half-surface lengths  $c \sim 25$ – $300\ \mu\text{m}$ , shown for the same microstructures in Fig. 10(c), indicate that growth rates in the two structures are comparable, although there is clearly more scatter in the data for the coarser lamellar

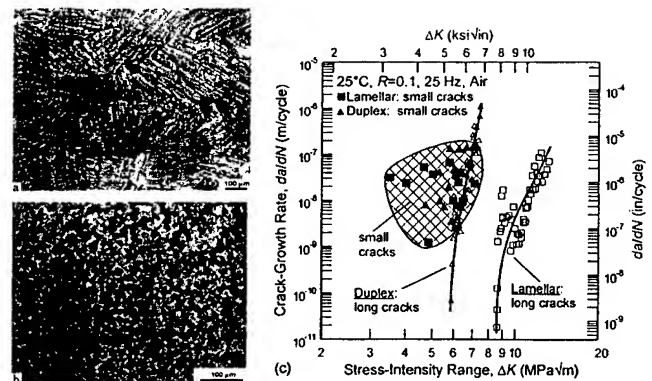


Fig. 10 Optical micrographs of the (a) fully lamellar and (b) duplex microstructures in a Ti-47Al-2Nb-2Cr-0.2B (at%) titanium aluminide intermetallic alloy, and (c) comparison of the growth-rate behavior of small ( $c \sim 25$ – $300\ \mu\text{m}$ ) surface cracks and through-thickness large ( $> 5\ \text{mm}$ ) cracks in these microstructures, as a function of the applied  $\Delta K$ .<sup>19,42)</sup>

lar structure.<sup>19,42)</sup> At the same applied  $\Delta K$  levels, the growth rates of the small cracks exceed those of corresponding large cracks by several orders of magnitude; moreover, the small cracks once more propagate below the large-crack thresholds.

If the small-crack data in Fig. 10(c) are compared with the shielding-corrected large-crack results, where the  $da/dN$  vs.  $\Delta K_{\text{tip}}$  relationship is derived by measuring the shielding contributions from both crack bridging ( $K_{\text{br}}$ ) (in lamellar structures only) and crack closure ( $K_{\text{cl}}$ ), *i.e.*,  $\Delta K_{\text{eff}} \equiv \Delta K_{\text{tip}} = (K_{\text{max}} - K_{\text{br}}) - K_{\text{cl}}$ , the large and small crack data come into normalization (Fig. 11), but only for the duplex microstructure.<sup>42)</sup> In this much finer-scale microstructure, the small cracks studied are only comparable in size to the wake shielding zones; thus, as for similar physically-small cracks in the metallic and ceramic materials, their behavior can be described by shielding-corrected large-crack data. In contrast, small cracks in the coarser lamellar microstructure are seen grow at applied stress intensities *below* the large-crack  $\Delta K_{\text{TH}}$  (Fig. 11(b)), such that a limited equilibrium shielding zone cannot be the sole cause of the small-crack effect in this structure.<sup>19)</sup> In fact, cracks in this structure are comparable to microstructural dimensions as average colony sizes ( $\sim 145\ \mu\text{m}$ ) are on the same order of magnitude as the cracks under study ( $c \sim 25$ – $300\ \mu\text{m}$ ). The influence of the coarser lamellar structure on small-crack behavior is apparent in Fig. 11(b), where the small-crack data are divided into cracks with initial surface crack lengths smaller and larger than the average colony size.<sup>19)</sup> From this comparison, it is apparent that all the small cracks that were observed to propagate below the “shielding-corrected” large-crack threshold had initial crack lengths smaller than the average colony size, while no small cracks with initial crack lengths larger than the average colony size grew below this threshold. Although using the colony size as the critical microstructural dimension is somewhat arbitrary, it does show that for cracks contained within one or two lamellar colonies, the growth behavior is quite different from that observed when a larger crack can “sample” the continuum microstructure.

Thus, duplex microstructures may offer far better HCF properties than lamellar microstructures for use in many applications such as turbine blades, despite the fact that the latter

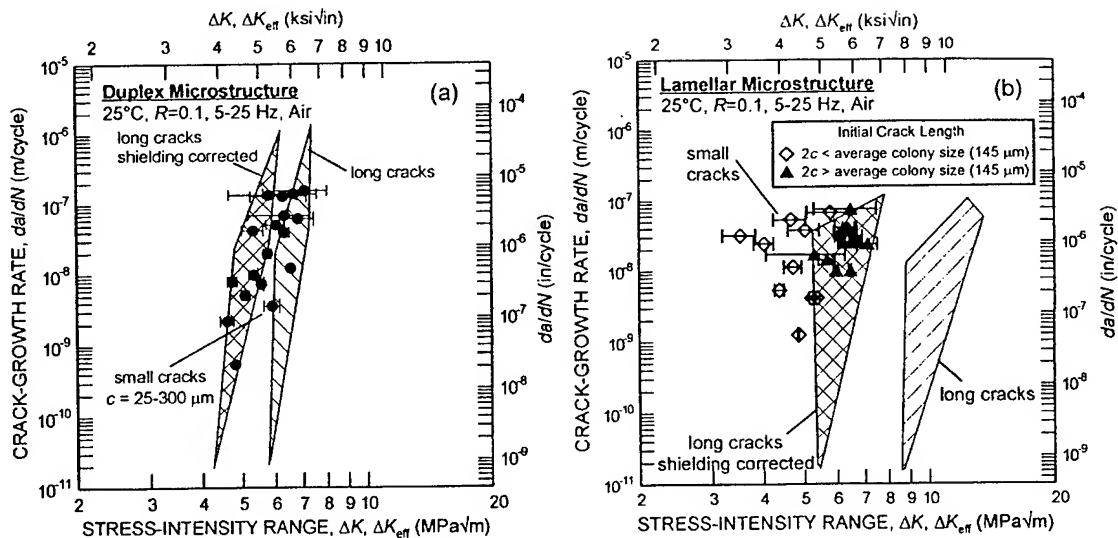


Fig. 11 Comparison of the growth-rate behavior of small ( $c \sim 25\text{--}300 \mu m$ ) surface cracks and through-thickness large ( $> 5 \text{ mm}$ ) cracks in (a) duplex and (b) lamellar microstructures in the Ti-47Al-2Nb-2Cr-0.2B (at%) alloy. The large-crack data (hatched areas) are plotted as a function of the applied  $\Delta K$  and, after correcting for both crack bridging ( $K_{br}$ ) and crack closure ( $K_{cl}$ ), the effective (near-tip) stress intensity,  $\Delta K_{eff} = (K_{max} - K_{br}) - K_{cl}$ . Error bars represent the range of  $\Delta K$  over measured growth increments.<sup>19)</sup>

structure displays markedly higher toughness and large-crack growth resistance. In addition to having higher strength and ductility, the definition of a worst-case (shielding-corrected) large-crack threshold, for both large and relevant small cracks, appears to be feasible in the duplex structure, whereas such an approach is far less certain for lamellar structures where relevant crack sizes are microstructurally small.

#### 4. Engineering Applications

An essential theme in this paper has been the use of worst-case large-crack thresholds to estimate the near-threshold behavior of "continuum-sized" small cracks. However, it has also been noted that this approach will not work where crack sizes approach microstructural dimensions, *i.e.*, in the presence of microstructurally-small cracks. An excellent example of this is the problem of foreign-object damage (FOD) in inducing high-cycle fatigue (HCF) failures of fan blades in aircraft gas-turbine engines.

Because of an increasing number of recent incidents of HCF-related military engine failures, currently used HCF design methodologies, based on stress-life ( $S-N$ ) curves and the Goodman diagram, are being re-evaluated.<sup>11-13)</sup> Both FOD and fretting, particularly in the blade dovetail/disk sections, are identified as critical problems,<sup>12,44)</sup> which can lead to premature fatigue crack initiation and growth; this in turn can result in seemingly unpredictable *in service* failures, due to the high-frequency vibratory loading ( $> 1 \text{ kHz}$ ) involved.<sup>12)</sup> In light of this, design against HCF based on the damage-tolerant concept of a fatigue-crack growth threshold ( $\Delta K_{TH}$ ) for no crack growth would appear to offer a preferred approach; however, such thresholds must reflect representative HCF conditions of small crack sizes, high frequencies and high mean stress levels (depending on the blade span location).<sup>11-13,45)</sup>

As a basis for such an approach, studies have been focused on the role of FOD in affecting the initiation and early growth

of small surface fatigue cracks in the STOA Ti-6Al-4V alloy (Fig. 2) under HCF conditions. The prime effect of FOD in markedly lowering resistance to HCF was found to be due to earlier crack initiation. Specifically, premature crack initiation and subsequent near-threshold crack growth is promoted by the stress concentration associated with the FOD indentation<sup>9,20,44,46,47)</sup> and the presence of small (micro)cracks<sup>20)</sup> in the damaged zone; in addition, residual stress gradients<sup>9,20,47)</sup> and microstructural changes<sup>9,20)</sup> due to FOD-induced plastic deformation can play an important role.

To simulate FOD, the flat surface of fatigue test specimens was subjected to high-velocity (300 m/s) impacts of 3.2 mm dia. hardened steel spheres;<sup>9,20)</sup> a typical damage site from a normal ( $90^\circ$ ) ballistic impact is shown in Fig. 12. Characteristic of such damage in titanium alloys,<sup>48,49)</sup> intense so-called adiabatic shear bands can be seen at the surface of the impact crater; moreover, a pronounced pile-up of material, some of it detached, is evident at the crater rim. However, of particular note is that plastic flow of material at the crater rim results in multiple notches and the occurrence of microcracks (insert in Fig. 13). These microcracks are quite small, *i.e.*, between  $\sim 2$  to  $50 \mu m$  in surface length, but when favorably oriented with respect to the subsequently applied fatigue stresses, they clearly provided the prime sites for premature crack nucleation and growth in high-cycle fatigue (Fig. 13).

Because of such phenomena, the  $S-N$  fatigue life of undamaged smooth-bar specimens is significantly affected by prior high-velocity impact damage (Fig. 14). Shown in this figure are the surface crack lengths of the FOD-induced microcracks, which are all comparable with microstructural size-scales. Although the presence of these small cracks represents the primary feature responsible for the FOD-induced reduction in fatigue resistance, tensile residual stresses (estimated in Ref. 50)), the highly deformed microstructure beneath the indent,<sup>9,19)</sup> and the stress-concentration factors associated with the indent ( $k_t \sim 1.25$ ) are all contributing factors.

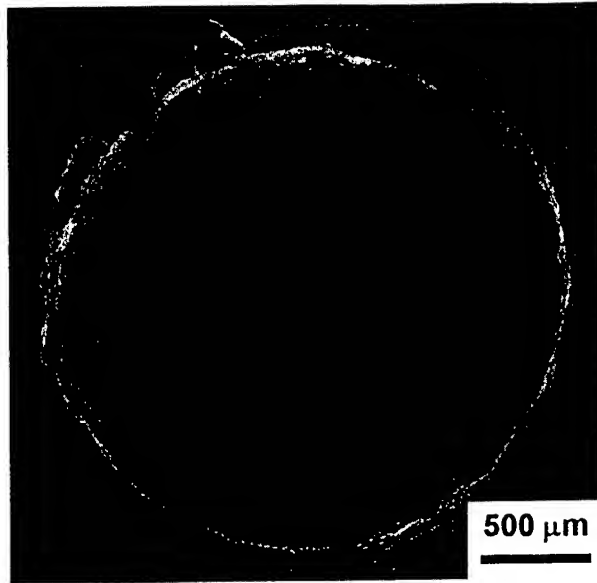


Fig. 12 SEM micrograph of 300 m/s impact crater.

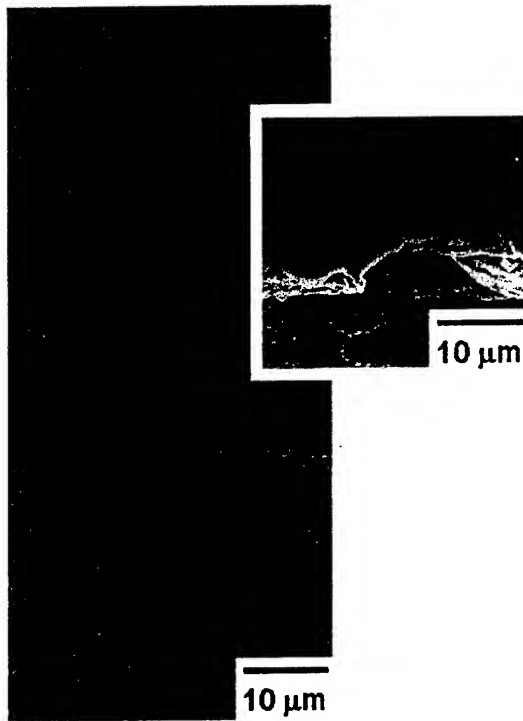


Fig. 13 SEM micrograph of FOD-induced microcracking at crater rim (insert) and subsequent fatigue-crack growth at such microcracks after 29,000 cycles ( $\sigma_{\max} = 500$  MPa,  $R = 0.1$ ).

Thresholds for fatigue-crack growth and the subsequent near-threshold fatigue-crack growth rates for the extension of the small (micro)cracks were measured<sup>20</sup> on all FOD-damaged samples; results are compared in Fig. 15 with previous results on this alloy for the behavior of naturally-initiated small ( $\sim 45$ – $1000$   $\mu\text{m}$ ) cracks<sup>17</sup>) and through-thickness large ( $> 5$  mm) cracks<sup>21</sup>) in undamaged material. The small crack growth-rate data are shown as a function of surface crack length,  $2c$ , and of the applied stress-intensity range. Approximate local stress intensities for small cracks at the indentation

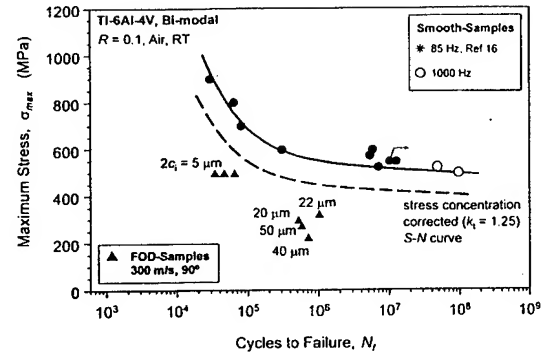


Fig. 14 S-N data show reduced fatigue life due to simulated FOD as compared to smooth-bar specimens<sup>17)</sup> in bimodal Ti-6Al-4V.  $2c_1$ : Surface crack length of FOD-induced microcracks.

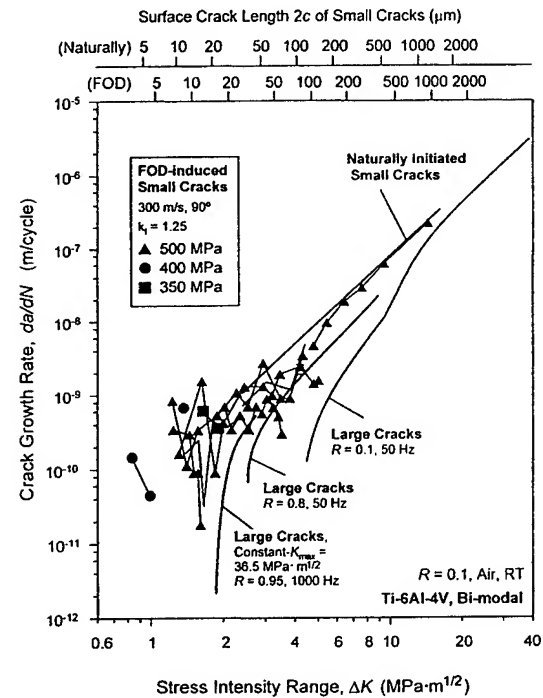


Fig. 15 Crack-growth rates as a function of applied stress-intensity range of FOD- and naturally-initiated small cracks and through-thickness large cracks in bimodal Ti-6Al-4V. Small-cracks were initiated at  $\sigma_{\max} = 650$  MPa ( $R = -1$ ).<sup>17)</sup> Large-crack growth data for  $R \leq 0.8$  were derived from constant load-ratio tests, whereas for  $R \geq 0.8$ , constant- $K_{\max}$ /increasing- $K_{\min}$  testing was used.<sup>21)</sup>

rim were calculated from Lukáš' solution<sup>51)</sup> for small cracks at notches (which includes indentation geometry and stress concentration effects), in terms of the crack depth  $a$ , indentation radius  $\rho$ , stress range  $\Delta\sigma$  and elastic stress-concentration factor  $k_t = 1.25$ .<sup>52)</sup>

$$\Delta K = \frac{0.7k_t}{\sqrt{1 + 4.5(a/\rho)}} \Delta\sigma \sqrt{\pi a}. \quad (3)$$

The factor of 0.7 is based on the stress-intensity boundary correction and the crack-shape correction factors.<sup>53)</sup> It should be noted that eq. (3) does not take into account the presence of residual stresses in the vicinity of the indents. To the first approximation, however, they do not change the value of the stress-intensity range ( $\Delta K$ ); they merely affect the mean stress and hence alter the local load ratio. Moreover, their ef-

fect of may not be that critical, as *in situ* synchronous X-ray micro-diffraction measurements,<sup>54)</sup> coupled with quasi-static numerical modeling,<sup>50)</sup> show a significant relaxation in their magnitude on fatigue loading, even within a few cycles.

The FOD-initiated small-crack growth rates in Fig. 15 are positioned roughly between the large-crack data (as a lower bound) and naturally-initiated crack data (as an upper bound). Typical for the small-crack effect [e.g., Ref. 7)], most small-crack growth rates are roughly an order of magnitude faster than corresponding large-crack results at near-threshold levels. Above a  $\Delta K$  of  $\sim 10 \text{ MPa}\sqrt{\text{m}}$ , however, the large and small crack results tend to merge, consistent with the development of a steady-state shielding zone in the wake of the small cracks.

As discussed previously, the large-crack results in Fig. 15 were determined up to the highest load ratios ( $R \sim 0.1\text{--}0.95$ ) under conditions (constant- $K_{\text{max}}$ /increasing- $K_{\text{min}}$ ) chosen to minimize the effect of crack closure; the threshold of  $\sim 1.9 \text{ MPa}\sqrt{\text{m}}$  at  $R = 0.95$  was thus considered to be a "worst-case threshold" for large or physically-small cracks of dimensions large compared to the scale of the microstructure, *i.e.*, for "continuum-sized" cracks.<sup>21)</sup> Of significance in the present results is that the smallest FOD-initiated cracks have dimensions of  $\sim 2$  to  $25 \mu\text{m}$ , which are comparable with microstructural size-scales in Ti-6Al-4V. These microstructurally-small cracks propagate at stress intensities well below this "worst-case" threshold, specifically at applied stress intensities as low as  $\Delta K \sim 1 \text{ MPa}\sqrt{\text{m}}$ .<sup>55)</sup> The implication of this result is that although there is a definitive lower-bound  $\Delta K_{\text{TH}}$  threshold ( $\sim 1.9 \text{ MPa}\sqrt{\text{m}}$ ) for "continuum-sized" cracks in the STOA Ti-6Al-4V alloy, when crack sizes approach microstructural size-scales, as in the case of the FOD-induced microcracks, crack growth is possible at applied stress intensities considerably less than this threshold, presumably due to biased sampling of the "weak links" in the microstructure. However, by coupling the notion of the worst-case threshold stress intensity with the fatigue limit, as in the Kitagawa-Takahashi diagram,<sup>56)</sup> an alternative formulation can be developed for defining the limiting conditions for HCF and FOD-related damage, as described below.

As an alternative HCF-design approach against FOD, which takes into account the presence of microstructurally-small cracks,<sup>20)</sup> Fig. 16 shows the influence of crack size on the worst-case fatigue thresholds in the form of a modified Kitagawa-Takahashi diagram,<sup>56)</sup> where the stress range for a corresponding crack-growth threshold condition ( $da/dN = 10^{-11}\text{--}10^{-10} \text{ m/cycle}$ ) is plotted versus the crack length. According to the Kitagawa-Takahashi approach (solid lines), the stress range  $\Delta\sigma$  for crack arrest is defined by the  $10^7$ -cycle fatigue limit ( $\Delta\sigma_{\text{HCF}} = 450 \text{ MPa}$ ) with the fatigue-crack growth threshold ( $\Delta K_{\text{TH}}$ ) measured on "continuum-sized" cracks. El Haddad *et al.*<sup>57)</sup> empirically quantified this approach by introducing a constant (intrinsic) crack length  $2c_0$ , such that the stress intensity is defined as  $Y\Delta\sigma\sqrt{\pi(2c+2c_0)}$ , where  $Y$  is the geometry factor (curved dashed line). The present results, plotted in this format in Fig. 16, show that the threshold conditions for crack growth from FOD-induced microstructurally-small cracks can be defined, in terms of stress concentration corrected stress ranges, from the "El

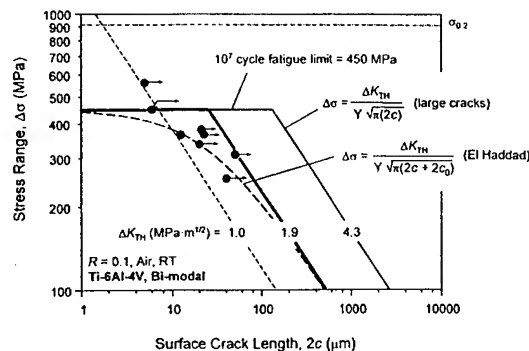


Fig. 16 Modified Kitagawa-Takahashi diagram representing the threshold crack-growth conditions ( $da/dN = 10^{-11}\text{--}10^{-10} \text{ m/cycle}$ ) for FOD-induced small-cracks in Ti-6Al-4V. Plotted is the threshold stress range as a function of surface crack length. Data points are corrected for the stress concentration of the FOD indents.

Haddad" line in the Kitagawa-Takahashi diagram, provided the limiting conditions are described in terms of the  $10^7$ -cycle (smooth-bar) fatigue limit (at microstructurally-small crack sizes) and worst-case large-crack fatigue threshold (at larger, "continuum-sized", crack sizes).

## 5. Concluding Remarks

The question of small fatigue cracks in metallic components remains a critical issue in the application of damage/fracture mechanics to the design, durability and damage tolerance of many structures, particularly for aircraft and gas-turbine applications. This has been highlighted for the problem of military engine high-cycle fatigue, especially in the presence of foreign-object damage. The problem of small fatigue cracks is similar in ceramic and intermetallic materials, although the micro-mechanisms of crack-tip damage and shielding are quite different. In all cases, failure to address this issue can lead to severely non-conservative lifetime predictions. Due to the difficulty of obtaining small-crack data, particularly at crucial near-threshold levels, worst-case large-crack data, where the effect of the predominant shielding mechanisms on the *local* driving force has been minimized or accounted for, can be used to estimate small-crack growth rates and threshold values, provided the cracks are small with respect to the extent of the wake shielding, *i.e.*, physically small. Whereas this approach is feasible for most structural materials for crack sizes down to  $\sim 50\text{--}100 \mu\text{m}$ , it will not work where relevant crack sizes approach the characteristic microstructural dimensions. Due to their biased sampling of the microstructure, thresholds for the onset of crack-ing and the subsequent near-threshold crack-growth rates for such microstructurally-small cracks must be determined as a function of crack size. In these instances, a modified Kitagawa-Takahashi approach, with the limiting conditions of the *S/N* fatigue limit at microstructurally-small crack sizes and the worst-case, large-crack, fatigue threshold at larger, "continuum-sized", crack sizes, provides a viable alternative.

## Acknowledgements

This work was supported by the U.S. Air Force Office of



Scientific Research under Grant No. F49620-96-1-0478 under the auspices of the Multidisciplinary University Research Initiative on High Cycle Fatigue to the University of California at Berkeley (for studies on Ti-6Al-4V), and the Office of Energy Research, Office of Basic Energy Sciences, Materials Sciences Division of the U.S. Department of Energy under Contract No. DE-AC03-76SF00098 (for studies on ceramics). Thanks are due to B. L. Boyce, J. C. Campbell, R. H. Dauskardt, C. J. Gilbert, J. J. Kruzic, J. M. McNaney, O. Roder, A. A. Steffen (Mayer) and K. T. Venkateswara Rao for their contributions to this study.

## REFERENCES

- 1) S. Pearson: *Eng. Fract. Mech.* **7** (1975) 235.
- 2) K. J. Miller: *Fat. Eng. Mater. Struct.* **5** (1982) 223.
- 3) S. Suresh and R. O. Ritchie: *Int. Metals Reviews* **29** (1984) 445.
- 4) R. P. Gangloff and R. O. Ritchie: In *Fundamentals of Deformation and Fracture* (Eshelby Memorial Symp., 1985) B. A. Bilby, K. J. Miller and J. R. Willis (Eds.) (Cambridge Univ. Press, Cambridge, U.K.) pp. 529–558.
- 5) K. J. Miller and E. R. de los Rios (Eds.): *The Behaviour of Short Fatigue Cracks* (Mech. Eng. Publ. London, U.K., 1986).
- 6) R. O. Ritchie and J. Lankford (Eds.): *Small Fatigue Cracks* (TMS-AIME, Warrendale, PA, 1986).
- 7) R. O. Ritchie and J. Lankford: *Mater. Sci. Eng.* **84** (1986) 11.
- 8) K. S. Ravichandran, R. O. Ritchie and Y. Murakami (Eds.): *Small Fatigue Cracks: Mechanics, Mechanisms and Applications* (Elsevier, Oxford, U.K.).
- 9) J. O. Peters, O. Roder, B. L. Boyce, A. W. Thompson and R. O. Ritchie: *Metall. Mater. Trans. A* **31A** (2000) 1571–83.
- 10) There is also the *chemically-small crack* which, unlike a corresponding longer crack, has a local crack-tip environment similar to that of the bulk environment, e.g., due to easier solution renewal.<sup>4)</sup>
- 11) B. A. Cowles: *Int. J. Fract.* **80** (1996) 147.
- 12) J. M. Larsen, B. D. Worth, C. G. Annis and F. K. Haake: *Int. J. Fract.* **80** (1996) 237.
- 13) T. Nicholas and J. R. Zuiker: *Int. J. Fract.* **80** (1996) 219–35.
- 14) A. F. Blom: In: *Small Fatigue Cracks*, R. O. Ritchie and J. Lankford (Eds.) (TMS-AIME, Warrendale, PA., 1986) pp. 623–638.
- 15) R. O. Ritchie: *Mater. Sci. Eng.* **103** (1988) 15.
- 16) R. O. Ritchie: *Int. J. Fract.* **100** (1999) 55–83.
- 17) J. A. Hines, J. O. Peters and G. Lütjering: In: *Fatigue Behavior of Titanium Alloys*, R. Boyer, D. Eylon and G. Lütjering (Eds.) (TMS, Warrendale, PA., 1999) pp. 15–22.
- 18) J. O. Peters and G. Lütjering: *Z. Metallkd.* **89** (1998) 464–73.
- 19) J. J. Kruzic, J. P. Campbell and R. O. Ritchie: *Acta Mater.* **47** (3) (1999) 801.
- 20) J. O. Peters and R. O. Ritchie: *Eng. Fract. Mech.* **67** (2000) 193–207.
- 21) R. O. Ritchie, D. L. Davidson, B. L. Boyce, J. P. Campbell and O. Roder: *Fat. Fract. Eng. Mater. Struct.* **22** (1999) 621–31.
- 22) This microstructural condition is also known as a *bimodal* microstructure.
- 23) H. Döker, V. Bachmann and G. Marci: In: *Fatigue Thresholds*, Proc. 1<sup>st</sup> Intl. Conf. on Fatigue, J. Bäcklund, A. F. Blom and C. J. Beevers (Eds.) (EMAS, Warley, U.K., 1982) Vol. 1, pp. 45–57.
- 24) S. Lathabai, J. Rödel and B. R. Lawn: *J. Am. Ceram. Soc.* **74** (1991) 1340.
- 25) R. H. Dauskardt: *Acta Metall. Mater.* **41** (1993) 2765.
- 26) R. H. Dauskardt, M. R. James, J. R. Porter and R. O. Ritchie: *J. Am. Ceram. Soc.* **75** (1992) 759.
- 27) C. J. Gilbert, J. J. Cao, W. J. MoberlyChan, L. C. DeJonghe and R. O. Ritchie: *Acta Metall. Mater.* **44** (1996) 3199.
- 28) R. H. Van Stone: *Mater. Sci. Eng. A* **103** (1988) 49.
- 29) A. A. Steffen, R. H. Dauskardt and R. O. Ritchie: *J. Am. Ceram. Soc.* **74** (1991) 1259.
- 30) R. H. Dauskardt, D. B. Marshall and R. O. Ritchie: *J. Am. Ceram. Soc.* **73** (1990) 893.
- 31) R. M. McMeeking and A. G. Evans: *J. Am. Ceram. Soc.* **65** (1982) 242.
- 32) P. F. Becher: *J. Am. Ceram. Soc.* **74** (1991) 255.
- 33) H. Kishimoto and A. Ueno: In: *Small Fatigue Cracks: Mechanics, Mechanisms and Applications*, K. S. Ravichandran, R. O. Ritchie and Y. Murakami (Eds.) (Elsevier, Oxford, U.K., 1999) pp. 247–58.
- 34) C. J. Gilbert, Y. S. Han, D. K. Kim and R. O. Ritchie: In: *Proc. 9<sup>th</sup> CIMTEC-World Ceramics Congress and Forum on New Materials*, P. Vincenzini (Ed.) (Techna Publishers S.r.l. Faenza, Italy, 1998).
- 35) Y. Mutoh, M. Takahashi, T. Oikawa and H. Okamoto: In: *Fatigue of Advanced Materials*, R. O. Ritchie, R. H. Dauskardt and B. N. Cox (Eds.) (MCEP, Edgbaston/EMAS, Warley, U.K., 1991) pp. 211–225.
- 36) R. H. Dauskardt, R. O. Ritchie, J. K. Takemoto and A. M. Brendzel: *J. Biomed. Mater. Res.* **28** (1994) 791.
- 37) R. O. Ritchie: *J. Heart Valve Disease* **5** (1996) Suppl. 1, S9.
- 38) D. P. Pope, C. T. Liu and S. H. Whang: (Eds.) *High Temperature Intermetallics—Parts 1 & 2* (Elsevier, Lausanne, Switzerland, 1995).
- 39) K. T. Venkateswara Rao, G. R. Odette and R. O. Ritchie: *Acta Metall. Mater.* **42** (1994) 893.
- 40) Y. W. Kim: *J. Metals* **46** (7) (1994) 30.
- 41) K. S. Chan: *Metall. Mater. Trans. A* **26A** (1995) 1407.
- 42) J. P. Campbell, K. T. Venkateswara Rao and R. O. Ritchie: *Metall. Mater. Trans. A* **30A** (3) (1999) 563.
- 43) J. M. Larsen, B. D. Worth, S. J. Balsone and J. W. Jones: In: *Gamma Titanium Aluminides*, Y.-W. Kim, R. Wagner and M. Yamaguchi (Eds.) (TMS, Warrendale, PA., 1995) pp. 821–834.
- 44) *Erosion, Corrosion and Foreign Object Damage Effects in Gas Turbines*, AGARD Conference Proceedings No. 558, North Atlantic Treaty Organization. Advisory Group for Aerospace Research and Development, Propulsion and Energetics Panel, Neuilly-sur-Seine, France. (1994).
- 45) R. O. Ritchie: In: *Proc. ASME Aerospace Division*, AD-Vol. 52, J. C. I. Chang, J. Coulter, D. Brei, W. H. G. Martinez, P. P. Friedmann, (Eds.) (ASME, Warrendale, PA., 1996) pp. 321–333.
- 46) T. Nicholas, J. R. Barber, R. S. Bertke: *Experimental Mechanics*, October 1980 (1980) 357–64.
- 47) S. J. Hudak, K. S. Chan, R. C. McClung, G. G. Chell, Y.-D. Lee and D. L. Davidson: *High Cycle Fatigue of Turbine Blade Materials*, Final Technical Report UDRI Subcontract No. RI 40098X SwRI Project No. 18–8653 (1999).
- 48) I. M. Hutchings: In: *Materials Behavior under High Stress and Ultra High Loading Rates*, J. Mescall, V. Weiss, (Eds.) (Plenum Press, NY., 1983) pp. 161–96.
- 49) S. P. Timothy and I. M. Hutchings: *Eng. Fract. Mech.* **7** (1984) 223–27.
- 50) X. Chen and J. W. Hutchinson: Foreign object damage and fatigue cracking: on the shallow indentation. *Int. J. Fract.* (1999) in review (Harvard University Report No. ME 358, Nov. 1999).
- 51) P. Lukáš: *Eng. Fract. Mech.* **26** (1987) 471–73.
- 52) M. Nisida and P. Kim: In: *Proc. Twelfth Nat. Cong. Applied Mechanics* (1962) pp. 69–74.
- 53) J. C. Newman, Jr. and I. S. Raju: *Eng. Fract. Mech.* **15** (1981) 185–92.
- 54) B. L. Boyce, A. W. Thompson, O. Roder, R. O. Ritchie: In: *Proc. Fourth National Turbine Engine High Cycle Fatigue (HCF) Conference*, J. Henderson, (Ed.) (University Technology Corp. Dayton, OH, CD-Rom, session 10, 1999) pp. 28–40.
- 55) It is believed that a  $\Delta K$  of 1 MPa $\sqrt{m}$  is the lowest stress-intensity range ever measured for crack growth in Ti–6Al–4V, representing a  $\Delta K$  value roughly a factor of two smaller than the lowest measured fatigue threshold for a “continuum-sized” crack.
- 56) H. Kitagawa and S. Takahashi: In: *Proc. Second Intl. Conf. on Mechanical Behavior of Materials* (ASM, Metals Park, OH, 1976) pp. 627–31.
- 57) M. H. Haddad, T. H. Topper and K. N. Smith: *Eng. Fract. Mech.* **11** (1979) 573–84.

# Influence of Microstructure on High-Cycle Fatigue of Ti-6Al-4V: Bimodal vs. Lamellar Structures

R.K. NALLA, B.L. BOYCE, J.P. CAMPBELL, J.O. PETERS, and R.O. RITCHIE

The high-cycle fatigue (HCF) of titanium alloy turbine engine components remains a principal cause of failures in military aircraft engines. A recent initiative sponsored by the United States Air Force has focused on the major drivers for such failures in Ti-6Al-4V, a commonly used turbine blade alloy, specifically for fan and compressor blades. However, as most of this research has been directed toward a single processing/heat-treated condition, the bimodal (solution-treated and overaged (STOA)) microstructure, there have been few studies to examine the role of microstructure. Accordingly, the present work examines how the overall resistance to high-cycle fatigue in Ti-6Al-4V compares between the bimodal microstructure and a coarser lamellar ( $\beta$ -annealed) microstructure. Several aspects of the HCF problem are examined. These include the question of fatigue thresholds for through-thickness large and short cracks; microstructurally small, semi-elliptical surface cracks; and cracks subjected to pure tensile (mode I) and mixed-mode (mode I + II) loading over a range of load ratios (ratio of minimum to maximum load) from 0.1 to 0.98, together with the role of prior damage due to sub-ballistic impacts (foreign-object damage (FOD)). Although differences are not large, it appears that the coarse lamellar microstructure has improved smooth-bar stress-life (S-N) properties in the HCF regime and superior resistance to fatigue-crack propagation (in pure mode I loading) in the presence of cracks that are large compared to the scale of the microstructure; however, this increased resistance to crack growth compared to the bimodal structure is eliminated at extremely high load ratios. Similarly, under mixed-mode loading, the lamellar microstructure is generally superior. In contrast, in the presence of microstructurally small cracks, there is little difference in the HCF properties of the two microstructures. Similarly, resistance to HCF failure following FOD is comparable in the two microstructures, although a higher proportion of FOD-induced microcracks are formed in the lamellar structure following high-velocity impact damage.

## I. INTRODUCTION

A 1992 study conducted by the Scientific Advisory Board of the United States Air Force targeted high-cycle fatigue (HCF) as the single largest cause of turbine engine failures in military aircraft.<sup>[1]</sup> HCF can result in essentially unpredictable failures of engine components, particularly turbine blades, due to the premature initiation of fatigue cracks at small defects and their rapid propagation under high-frequency vibratory loading. To address this problem, a consortium of industrial, government, and academic programs was charged

with the overall task of modifying existing design methodologies for improved HCF reliability. These programs have largely focused on a single alloy, Ti-6Al-4V, in a single microstructural condition, namely, the solution-treated and overaged (STOA) or bimodal condition, which is typically used for blade and disk applications in the front (low-temperature) stages of the engine. The current study seeks to extend these observations for the standard bimodal Ti-6Al-4V microstructure to a fully lamellar  $\beta$ -annealed microstructure in the same alloy and to specifically compare the relative merits of these two microstructures for HCF applications.

## II. BACKGROUND

The problem of HCF in turbine components is typically associated with a variety of drivers,<sup>[2]</sup> which vary with the location of interest (Figure 1). In general, components such as blades and disks are subjected to HCF loading associated with the high-frequency ( $>1$  kHz) vibrations in the engine, superimposed onto a low-cycle fatigue component associated with the start-to-stop cycles.<sup>[2,3]</sup> In the case of blades, this leads to a large variation in load ratios (the ratio ( $R$ ) of minimum to maximum loads) throughout the component; in particular, the superposition of centrifugal loading on the HCF vibrations can lead to very high  $R$ -values which approach unity. On the airfoil section of the blade, HCF cracks can initiate at sites of foreign-object damage (FOD) caused by the ingestion of debris into the engine;<sup>[4]</sup> here, the problem involves impact-induced residual stresses, microstructural distortion, incipient microcrack formation,

---

R.K. NALLA, Graduate Student, and R.O. RITCHIE, Professor, are with the Department of Materials Science and Engineering, University of California, Berkeley, CA 94720-1760. B.L. BOYCE, formerly Graduate Student with the Department of Materials Science and Engineering, University of California, is Senior Member, Technical Staff, Sandia National Laboratories, Albuquerque, NM 87185-1411. J.P. CAMPBELL, formerly Graduate Student with the Department of Materials Science and Engineering, University of California, is Senior Manufacturing Engineer, Metals Fabrication Division, General Motors, Troy, MI 48084. J.O. PETERS, formerly Post-doctoral Researcher with the Department of Materials Science and Engineering, University of California, is Research Associate, Technische Universität Hamburg-Harburg, D-21073 Hamburg, Germany.

This article is based on a presentation made in the symposium entitled "Defect Properties and Mechanical Behavior of HCP Metals and Alloys" at the TMS Annual Meeting, February 11-15, 2001, in New Orleans, Louisiana, under the auspices of the following ASM committees: Materials Science Critical Technology Sector, Structural Materials Division, Electronic, Magnetic & Photonic Materials Division, Chemistry & Physics of Materials Committee, Joint Nuclear Materials Committee, and Titanium Committee.



### HCF/LCF Interactions

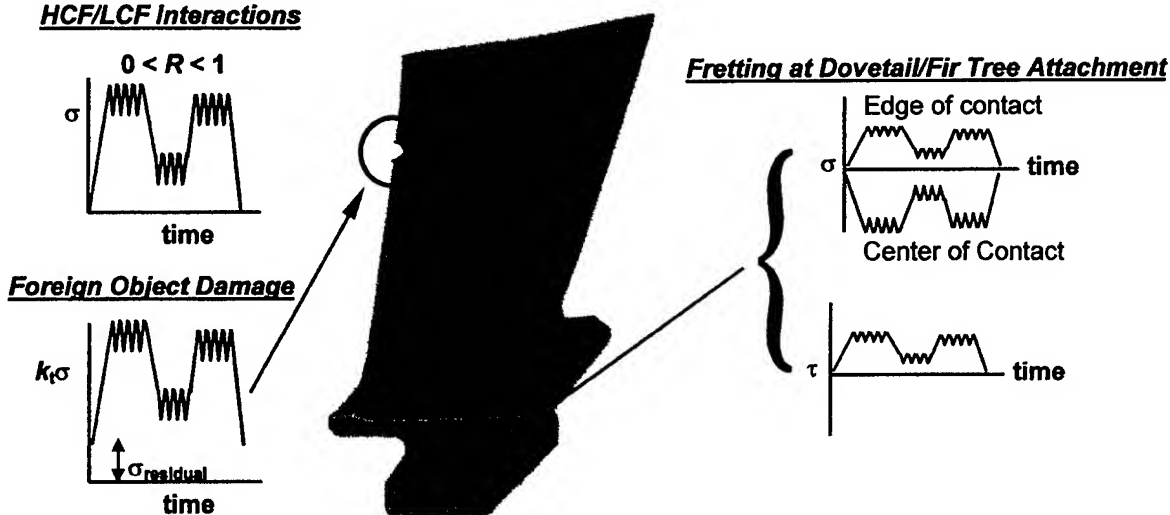


Fig. 1—Diagram illustrating the variety and range of factors involved in HCF failure.

and a geometric stress concentration. Another critical site for crack initiation is in the attachment section of the blade, where contact between the blade dovetail and disk can lead to the formation of fretting fatigue cracks;<sup>[5]</sup> this problem involves complex multiaxial loading conditions, surface damage, and associated residual stresses.

Current design methodologies for HCF utilize traditional stress-life (S-N) and Goodman diagram approaches, often applied with large safety factors to account for uncertainties in the understanding of the problem. However, because of the extremely high frequencies involved (*i.e.*, parts can experience  $10^6$  cycles in much less than 1 hour), once a crack starts propagating, failure can ensue rapidly, sometimes within a single flight. Consequently, alternative fracture-mechanics design methodologies, based on the concept of a threshold stress intensity for no crack growth, may offer a preferred approach, provided such thresholds are defined under representative HCF conditions involving small defects subjected to high-frequency, high-load-ratio loading.

Because of the wide range of drivers associated with HCF, selection of a HCF-resistant microstructure in Ti-6Al-4V is not a straightforward task. Indeed, a microstructure that is superior in one region or under one set of HCF conditions may well be deleterious in another region or set of conditions. For example, coarse lamellar microstructures in some titanium alloys often show superior toughness and fatigue-crack growth behavior in the presence of large cracks compared to finer equiaxed microstructures, yet at the same time display inferior fatigue endurance strengths and small-crack behavior (*e.g.*, Reference 6). There is indeed extensive literature on the role of microstructure in influencing the fatigue-crack growth of  $\alpha + \beta$  titanium alloys (*e.g.*, References 7 through 17). For example, recent reviews by Lütjering<sup>[7]</sup> and Thompson<sup>[8]</sup> summarized the effects of scale and arrangement of  $\alpha$  and  $\beta$  phases on the fatigue properties of  $\alpha + \beta$  titanium alloys.

Basically, coarse grained, so-called lamellar microstructures with large  $\beta$  grains ( $\sim 1$  mm) and a lamellar matrix of alternating  $\alpha$  and  $\beta$  plates can be produced by heat treatment in the high-temperature  $\beta$ -phase field and subsequent slow

cooling into the  $\alpha + \beta$ -phase field. The characteristic microstructural feature of slow-cooled lamellar microstructures is the  $\alpha$  colony ( $\sim 200$  to  $400 \mu\text{m}$ ), a packet of aligned  $\alpha$  plates with the same crystallographic orientation. Finer-scaled microstructures can be processed by faster cooling rates from the  $\beta$ -phase field, resulting in a martensitic type of microstructure with individual oriented  $\alpha$  plates (plate width  $\sim 1 \mu\text{m}$ ), or by deformation and recrystallization procedures in the  $\alpha + \beta$ -phase field, where the recrystallization temperature determines the volume fraction and size of equiaxed primary  $\alpha$  phase. So-called bimodal microstructures consist of a low volume fraction of primary  $\alpha$  grains ( $\sim 15$  to 30 pct,  $\sim 20 \mu\text{m}$ ) with a colony-type lamellar matrix of alternating  $\alpha$  and  $\beta$  plates within small  $\beta$  grains (20 to  $40 \mu\text{m}$ ).

The most critical parameter to increase the HCF strength (resistance against fatigue-crack nucleation) is to reduce the maximum dislocation slip length in the microstructure.<sup>[9]</sup> Generally, fatigue cracks nucleate due to irreversible slip within the longest crystallographic slip bands (*i.e.*, maximum slip length) available in the microstructure. Consequently, coarse lamellar microstructures with colonies of aligned  $\alpha$  and extended planar slip across these colonies often have a lower HCF strength as compared to fine-grained equiaxed and martensitic  $\alpha$ -plate-type microstructures with concomitant reduced effective slip lengths.<sup>[10,11]</sup>

The preference for propagation of naturally initiated small surface cracks along specific crystallographic planes combined with an aligned orientation of  $\alpha$  plates into colonies allows the crack to cross an entire colony as if it were a single microstructural unit. This propagation mechanism along planar slip bands is very fast in coarse lamellar microstructures because of the much larger slip length as compared to finer-scaled microstructures. Fine-grained and martensitic microstructures tend to slow the propagation rates of small cracks due to the higher density of grain boundaries or individual  $\alpha$  plates acting as obstacle points.<sup>[12,13,14]</sup>

However, this ranking between coarse lamellar and fine-grained microstructures is reversed with increasing crack length.<sup>[12,14-16]</sup> Lamellar microstructures in  $\alpha + \beta$  titanium

**Table I. Chemical Composition of Ti-6Al-4V Bar Stock (in Weight Percent)<sup>[28]</sup>**

Bar Location	Ti	Al	V	Fe	O	N	H
Top	bal	6.27	4.19	0.20	0.18	0.012	0.0041
Bottom	bal	6.32	4.15	0.18	0.19	0.014	0.0041

alloys exhibit superior fatigue-crack growth resistance compared to fine-grained microstructures when these properties are measured using large cracks, which are on the order of several millimeters (or at least many times the microstructural unit size). It is found that crack growth into adjoining, but differently oriented,  $\alpha$  colonies involves pronounced crack deflection, crack bifurcation, and secondary crack formation, because of the limited number of slip systems available within the hcp  $\alpha$  phase. Therefore, the superior crack-growth resistance in a colony-type lamellar microstructure is attributed to a crack path characterized by a high degree of crack deflection, bifurcation, and secondary cracking and, at low load ratios, also by a high degree of (roughness-induced) crack closure.<sup>[12,16–18]</sup> Indeed, Yoder *et al.*<sup>[17]</sup> pointed out that lamellar microstructures with reduced colony sizes had less resistance against crack propagation. Also, crack growth in fine equiaxed microstructures did not cause large crack deflections because of the smaller-sized microstructural features.<sup>[12,14]</sup>

It should be noted that most of these data, specifically for Ti-6Al-4V, pertain to lower frequencies and large (>5 mm), through-thickness cracks (e.g., References 18 through 26), which are not necessarily appropriate for the present HCF scenario, where frequencies are in excess of 1 to 2 kHz and the relevant crack sizes are on the order of fractions of a millimeter and can grow at stress intensities well below the established large-crack fatigue thresholds for the material.<sup>[27]</sup> Consequently, to evaluate the general susceptibility of Ti-6Al-4V alloys to HCF, in the present article, the HCF properties of the bimodal and lamellar microstructures are compared. In view of the complexity of the problem, many facets of HCF behavior are examined, including the effect of load ratio, mode-mixity, crack size, and pre-existing impact damage.

### III. MATERIALS AND EXPERIMENTAL PROCEDURES

#### A. Materials and Microstructures

The Ti-6Al-4V alloy used in this study originated as double vacuum-arc remelted forging stock produced by Teddyne Titanium (Pittsburgh PA) specifically for the joint government-industry-academia HCF program. The chemical composition of this alloy is given in Table I.<sup>[28]</sup>

##### 1. Bimodal microstructure

The original bar stock (63.5 mm in diameter) was sectioned into segments 400-mm long, preheated to 940 °C for 30 minutes, and forged as glass-lubricant-coated bars at this temperature into 400 × 150 × 20 mm plates.<sup>[28]</sup> These plates were solution treated at 925 °C for 1 hour, fan air cooled, and then stabilized at 700 °C for 2 hours. The microstructure of the STOA condition consisted of a bimodal distribution of interconnected equiaxed primary  $\alpha$  grains and lamellar  $\alpha + \beta$  colonies (transformed  $\beta$ ) (Figure 2(a)). A careful

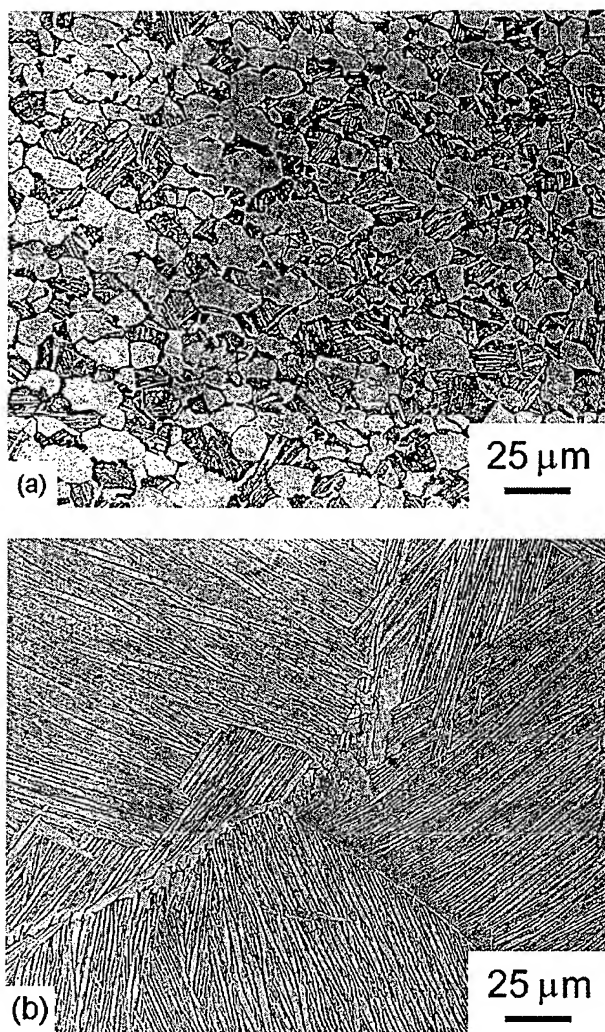


**Fig. 2—Optical micrographs of the microstructures of Ti-6Al-4V: (a) bimodal (solution treated and overaged, STOA) and (b) lamellar ( $\beta$  annealed). Etched for ~10 s in 5 parts 70 pct HNO<sub>3</sub>, 10 parts 50 pct HF, and 85 parts of H<sub>2</sub>O.**

investigation of the relative distribution of phases indicated an overall primary  $\alpha$  content of 64 pct. The average grain size obtained was ~20  $\mu$ m, with a slight grain elongation observed in the longitudinal (L) direction of the forging. Using differential thermal analysis, the  $\beta$ -transus temperature was measured to be 990 °C to 1005 °C.

##### 2. Lamellar microstructure

To compare with the bimodal Ti-6Al-4V structure, a fully lamellar microstructure was also examined. This microstructure (Figure 2(b)) was obtained by solution treating in a vacuum of 10<sup>-5</sup> to 10<sup>-6</sup> mbar at 1005 °C (slightly above the  $\beta$ -transus temperature) for 10 to 30 minutes (depending on the cross section), followed by a rapid quench (~100 °C/min)\* in high-purity helium gas. The microstructure thus

\*This quench rate was chosen to achieve a similar lath spacing of the transformed  $\beta$  in the two microstructures.

obtained was stabilized at 700 °C for 2 hours *in vacuo*, before slow furnace cooling to room temperature. The resulting Widmanstätten microstructure had an average prior- $\beta$  grain

**Table II. Uniaxial Tensile and Toughness Properties of Ti-6Al-4V**

Microstructure	Yield Strength (MPa)	Ultimate Tensile Strength (MPa)	Reduction in Area (Pct)	Fracture Toughness $K_{Ic}$ (MPa $\sqrt{m}$ )
Bimodal	930	978	45	64
Lamellar	975	1055	10	100

size of  $\sim 1$  mm, a colony size (parallel-oriented  $\alpha$ -phase lamellae) of 500  $\mu\text{m}$ , and an average  $\alpha$  lamellae lath width of 1 to 2  $\mu\text{m}$ , similar to the interlamellar spacing of the transformed  $\beta$  in the bimodal microstructure.

## B. Mechanical Testing

### 1. Uniaxial tensile and toughness properties

Uniaxial tensile tests were conducted in both microstructures in the L-orientation using strain rates of  $5 \times 10^{-4} \text{ s}^{-1}$ ; additional data for the bimodal microstructure were taken from Reference 28. Results in terms of the strength, ductility, and toughness are given in Table II. The lamellar structure exhibited somewhat higher strength levels, whereas the bimodal structure exhibited over a factor-of-4 higher ductility, due to its smaller grain size, which limited the effective slip length. Despite its lower ductility, plane-strain fracture toughness values, measured using 25-mm-thick, precracked compact-tension specimens, were over 50 pct higher in the lamellar microstructure; similar observations have been made in previous studies (e.g., Reference 29).

### 2. Smooth-bar stress-life (S-N) fatigue testing

To evaluate the smooth-bar stress-life (S-N) fatigue properties of both microstructures, fatigue tests were performed in room-temperature air (25 °C, 35 to 45 pct relative humidity) under load control at positive load ratios of  $R = 0.1$  and 0.5, on servohydraulic testing machines cycling at 25 Hz (for lives  $< 10^6$  cycles) and at 1000 Hz (for lives  $> 10^6$  cycles) on unnotched hourglass specimens with threaded grip sections and minimum gage diameters of 3.0 mm (25 Hz) and 5.4 mm (1000 Hz).\* The specimen axis was aligned

\*Based on a comparison of results performed at frequencies up to 1000 Hz by Ritchie *et al.*<sup>[30]</sup> and ultrasonic fatigue-threshold measurements by Meyer and Stanz-Tschegg, no effect of cyclic frequency has been found in this alloy for fatigue tests between 50 and 20,000 Hz, conducted in ambient-air environments.<sup>[31]</sup>

parallel to the length of the plate (L-orientation). For the bimodal microstructure, results were supplemented with 85 Hz S-N data from Reference 14 on the same material.

To achieve a nominally stress-free surface prior to fatigue testing, samples in both microstructures were stress relieved *in vacuo* for 2 hours at 705 °C prior to chemically milling in a solution of 50 mL HF, 500 mL HNO<sub>3</sub> and 1500 mL H<sub>2</sub>O. Similar procedures were used for the small-crack and FOD test samples.

### 3. Fatigue-crack growth testing in pure mode I

**Large-crack tests:** Mode I fatigue-crack propagation studies, on through-thickness cracks which were large compared to the scale of the microstructure ( $> 4$  mm), were carried out for both microstructures using 8-mm-thick compact-tension specimens (of 25.4-mm width) machined in the L-T orientation. To facilitate observation of crack propagation,

after machining the specimen sides were ground to a 1200-grit finish before chemically polishing to a finish of 0.05  $\mu\text{m}$ . Samples were first fatigue precracked for a minimum of  $\sim 2$  mm from the notch tip using initial  $\Delta K$  levels of 8 to 15 MPa $\sqrt{m}$ . This was carried out at the same load-shedding rate and load ratio as was subsequently used for the actual test, as described subsequently.

Fatigue-crack growth testing was performed in accordance with ASTM Standard E 647 in room-temperature air under load control, with crack lengths monitored *in situ* using back-face strain (BFS) compliance techniques. Two techniques were used to determine the alternating and maximum stress intensities at the threshold, ( $\Delta K_{TH}$  and  $K_{max,TH}$ , respectively), which were defined at a propagation rate of  $10^{-10}$  to  $10^{-11}$  m/cycle. Standard constant- $R$  testing for load ratios between 0.1 and 0.8 was performed by load shedding toward the threshold using the scheme  $\Delta K = \Delta K_{initial} \exp(C(a - a_{initial}))$ , with the  $K$ -gradient ( $C$ ) set at  $-0.08 \text{ mm}^{-1}$  ( $\Delta K$  and  $a$  are the stress-intensity range and crack length, respectively). In addition, constant- $K_{max}$ /increasing- $K_{min}$  testing\* was performed to achieve load ratios approaching

\*The constant- $K_{max}$ /increasing- $K_{min}$  test for threshold measurements was first developed by Döcker *et al.*<sup>[32]</sup> It was subsequently used by Hertzberg and co-workers to provide a simulation of short-crack growth behavior.<sup>[33]</sup>

unity, using  $K_{max}$  values from 26 to 57 MPa $\sqrt{m}$  for the bimodal microstructure and 27 to 87 MPa $\sqrt{m}$  for the lamellar microstructure. These procedures, which act to minimize the effect of crack closure, gave thresholds at very high load ratios between 0.89 and 0.98.

A range of frequencies between 50 and 1000 Hz was examined; additional ultrasonic fatigue tests at 20,000 Hz<sup>[34]</sup> were performed on the bimodal microstructure only. Tests at 50 Hz were performed on a standard MTS servohydraulic testing machine; corresponding tests at 200 to 1000 Hz were performed on a newly developed MTS servohydraulic test frame incorporating a voice-coil servovalve. Thresholds were determined using the same procedure described for the constant- $R$  tests. Data are presented in terms of the crack growth rate per cycle ( $da/dN$ ) as a function of the stress-intensity range ( $\Delta K = K_{max} - K_{min}$ ).\*

\*Note that for simplicity, the mode I stress intensity is referred to as  $\Delta K$ . However, in sections relevant to the mixed-mode behavior,  $\Delta K_I$  is used to distinguish the mode I stress intensity from the mode II stress intensity ( $\Delta K_{II}$ ).

The magnitude of crack closure was monitored using BFS compliance; specifically, the global closure stress intensity ( $K_{cl}$ ) was approximated from the point of first deviation from linearity in the elastic compliance curve on unloading.<sup>[35]</sup> Based on such measurements, an effective (near-tip) stress intensity ( $\Delta K_{eff} = K_{max} - K_{cl}$ ) was estimated.

**Small-crack tests:** Corresponding mode I fatigue-crack-propagation testing on microstructurally small ( $\sim 1$  to 50  $\mu\text{m}$ ) surface cracks was performed by periodic scanning electron microscopy monitoring of so-called  $K_B$  tensile samples, where cracking was initiated at sites of impact damage, as described in Section III-B-5. These samples had a rectangular cross section of 3.2 by 7.2 mm, a gage length of 20 mm, and cylindrical buttonhead ends and were cycled at 25 Hz (for lives  $< 10^6$  cycles) and 1000 Hz (for lives  $> 10^6$  cycles) at  $R = 0.1$  and 0.5.

Approximate local stress intensities for small cracks

formed at the base and crater rim of the damaged sites were calculated from the relationship<sup>[36]</sup>

$$\Delta K = \frac{0.7 k_t}{\sqrt{1 + 4.5 (a/\rho)}} \Delta \sigma \sqrt{\pi a} \quad (1)$$

where  $k_t$  is the elastic-stress-concentration factor,  $a$  is the crack depth, and  $\rho$  is the indentation radius. The factor of 0.7 is based on the stress-intensity boundary correction and the crack-shape correction factor,<sup>[37]</sup> the crack shape being determined from fractographic observations as  $a/2c \sim 0.45$  ( $a$  is the crack depth and  $2c$  is the surface-crack length).\*

\*The exact shape of such small surface cracks and the variation in this aspect ratio with crack extension clearly can have an important effect on the crack driving force and, hence, the crack-growth behavior.<sup>[38,39]</sup> In the current work, for small-crack threshold determination, the exact aspect ratios were obtained by postfractographic observations. For crack-growth-rate studies, a constant aspect ratio was assumed, although our crack-shape studies, described in Reference 40, did indicate that this was a reasonable assumption.

Despite the physically small size of the cracks, the use of the stress intensity was justified here, as maximum plastic zone sizes were only  $\sim 0.2$  to  $1 \mu\text{m}$  for 1 to  $10\text{-}\mu\text{m}$  sized cracks at  $\Delta K \sim 1$  to  $2 \text{ MPa}\sqrt{\text{m}}$  conditions were, thus, close to that of small-scale yielding. However, it should be noted that Eq. [1] does not take into account the presence of the impact-induced residual stresses, although these stresses will not change the value of the stress-intensity range. Moreover, recent X-ray diffraction studies<sup>[41]</sup> have shown that at the higher applied stresses, such residual stresses at the base and rim of the damage site tend to relax within the first few fatigue cycles.

#### 4. Fatigue-crack growth testing under mixed-mode loading

The corresponding fatigue-crack growth testing under mixed-mode conditions was performed using the asymmetric four-point-bend (AFPB) sample (e.g., Reference 42). This specimen can achieve a range of mode-mixities, essentially from pure mode I to mode II, by changing the crack offset from the load line. Specimens, 11.3-mm wide and 4.5-mm thick, were machined in the L-T orientation. For comparison, pure mode I tests were conducted using symmetric four-point bending, with inner and outer spans of 12.7 and 25.4 mm, respectively. For all samples, the surfaces required for crack-length observation were polished to a  $0.05 \mu\text{m}$  finish, whereas the sides to be used to carry the load-bearing pins were ground down to a 600-grit finish.

##### a. Large-crack tests

Mixed-mode thresholds were determined on the basis of crack initiation from a carefully prescribed precrack, as described in detail elsewhere.<sup>[43,44,45]</sup> Fatigue precracks were grown from 2-mm-deep electro discharge-machined notches in symmetric four-point bending at  $R = 0.1$ ; the final precrack length was  $4.50 \pm 0.25 \text{ mm}$ , achieved at final  $\Delta K_I$  values of  $4.8 \pm 0.5$  and  $6.8 \pm 0.5 \text{ MPa}\sqrt{\text{m}}$ , respectively, for the bimodal and lamellar microstructures. Using recently developed solutions<sup>[42]</sup> for the values of  $\Delta K_I$  and  $\Delta K_{II}$  for the AFPB geometry, mixed-mode tests for large ( $>4 \text{ mm}$ ) through-thickness cracks were performed at load ratios from 0.1 to 0.8 for mode-mixities varying from pure mode I ( $\Delta K_{II}/\Delta K_I = 0$ ) to nearly pure mode II ( $\Delta K_{II}/\Delta K_I = 7.1$ ), corresponding to phase angles ( $\beta = \tan^{-1}(\Delta K_{II}/\Delta K_I)$ ) of 0

deg, respectively. Each test involved cycling the precracked specimen at the desired mode-mixity, if no crack growth was observed using an optical microscope after  $2 \times 10^6$  to  $5 \times 10^6$  cycles, either  $\Delta K_I$  or  $\Delta K_{II}$  was increased by  $\sim 0.25 \text{ MPa}\sqrt{\text{m}}$  and the same testing procedure was repeated. In this way, a "growth/no growth" condition bounding the threshold was obtained, with growth being defined to be crack extension on the order of the microstructural dimension ( $\sim 20 \mu\text{m}$  for a bimodal and  $\sim 500 \mu\text{m}$  for a lamellar microstructure). Estimates of the extent of crack-tip shielding in both modes I and II were made using a compliance-based technique; as described in Reference 44, this technique involved determining the mode I and mode II compliance curves *in situ* using a crack-opening displacement gage.\*

\*As described in detail in Reference 44, the distinction between the contributions to shielding in modes I and II is achieved by examining separate load-displacement curves using two gages mounted near the crack tip; these gages are used to measure opening and shear displacements. Mode I shielding, in the form of crack closure, is determined from the compliance curve for the opening displacements, whereas mode II shielding, in the form of asperity rubbing and interlock, is determined in an analogous fashion from the compliance curve for shear displacements.

##### b. Short-crack tests\*

\*Short cracks are defined here as being small in all but one dimension, compared to small cracks, which are small in all dimensions. Further details on the distinction between, and relevance of large, short, and small cracks are given in the Appendix.

Corresponding mixed-mode thresholds for through-thickness short ( $\sim 200 \mu\text{m}$ ) cracks were obtained in an identical fashion, except that the wake of the precrack was carefully machined away to within  $\sim 200 \mu\text{m}$  of the crack tip using a slow-speed diamond saw. The intent of this procedure was to minimize the extent of crack-tip shielding by reducing the degree of surface contact in the crack wake.

##### c. Small-crack tests

Corresponding mixed-mode thresholds tests for microstructurally small ( $<50 \mu\text{m}$ ), semi-elliptical surface cracks were performed using an inclined crack technique. A small, semielliptical surface precrack ( $\sim 10$  to  $50 \mu\text{m}$ ) was first obtained by standard mode I, three-point bend testing at  $R = 0.1$  (50 Hz) of wide (16.3 mm), 5-mm-thick rectangular bars machined in the L-T orientation. Prior to testing, samples were stress-relieved for 2 hours at  $675^\circ\text{C}$  *in vacuo*, and surfaces necessary for observation were polished to a  $0.05 \mu\text{m}$  finish. Once a small crack had initiated, a bend bar was carefully machined from the original wide sample, with the small crack inclined at the desired angle to the axis of the bar. This bar was then subjected to symmetric four-point bending, and the threshold for crack initiation from the inclined crack was determined in a similar manner to that described previously for mixed-mode large-crack testing. Linear-elastic solutions for the stress-intensity ranges for small semielliptical surface cracks in mode I and mixed-mode loading were obtained from References 37 and 46. Exact crack shapes ( $a/2c$ ) were determined following threshold determination by fractographic observations.

##### 5. Foreign-object damage

The effect of FOD on the fatigue behavior of Ti-6Al-4V was examined using modified  $K_B$  tensile specimens.<sup>[40,47,48]</sup> The FOD was simulated by firing 3.2-mm-diameter

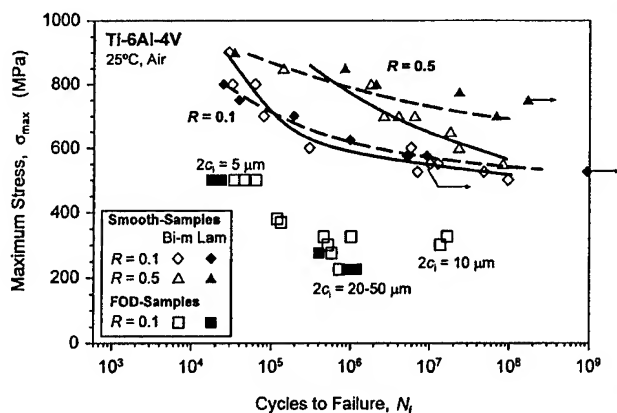


Fig. 3—Smooth-bar stress-life (S-N) data at  $R = 0.1$  and  $0.5$  for the bimodal and lamellar microstructures in Ti-6Al-4V. Data points refer to samples following simulated FOD and clearly show a severely reduced fatigue life due to such damage; numbers adjacent to data points indicate the surface crack length,  $2c_i$ , of the FOD-induced microcracks.

chrome-hardened steel spheres at velocities between 200 and 300 m/s onto the flat surface of the  $K_B$  specimens at an angle of 90 deg, using a compressed-gas gun facility. These velocities represent typical in-service impact velocities on aircraft engine fan blades. The resulting damage craters are also typical of those seen in service, with root radii similar to those of actual damage sites. After impacting, specimens were cycled at 1000 Hz at a stress range ( $\Delta\sigma$ ) between 225 and 500 MPa ( $R = 0.1$  and  $0.5$ ), and results were compared to the unimpacted smooth-bar S-N data. Throughout the fatigue testing, specimens were periodically removed and examined in a high-resolution field-emission scanning electron microscope in order to monitor crack-initiation and growth in the vicinity of the damage site. Resulting small-crack data are presented in terms of their growth rates as a function of both crack size ( $a$ ) and the stress-intensity range ( $\Delta K$ ).

Residual stresses surrounding the damage sites were both numerically computed and experimentally measured using synchronous X-ray diffraction.<sup>[49]</sup> However, relaxation of a significant portion of these stresses was found (from *in-situ* X-ray studies) at the higher applied stresses utilized for these tests.

#### IV. RESULTS AND DISCUSSION

##### A. Smooth-Bar Stress-Life Fatigue

Smooth-bar S-N curves for the bimodal and lamellar microstructures are shown in Figure 3 for load ratios of 0.1 and 0.5. (The numbers next to individual data points refer to microcrack sizes following FOD, as discussed in Section IV-D). In the high-cycle regime, in this case for lives exceeding  $\sim 10^5$  cycles at  $R = 0.1$  and  $10^6$  at  $R = 0.5$ , the lamellar structure appears to display the superior fatigue properties, with a higher  $10^8$  cycle endurance strength, particularly at  $R = 0.5$ . This is consistent with the higher tensile strength of this microstructure. It should be noted, however, that at shorter lifetimes in the low-cycle fatigue regime, it is the bimodal microstructure that appears to show the better fatigue properties, consistent with the higher ductility exhibited by this structure, although in the present study only limited data were collected in this regime. The fact that the

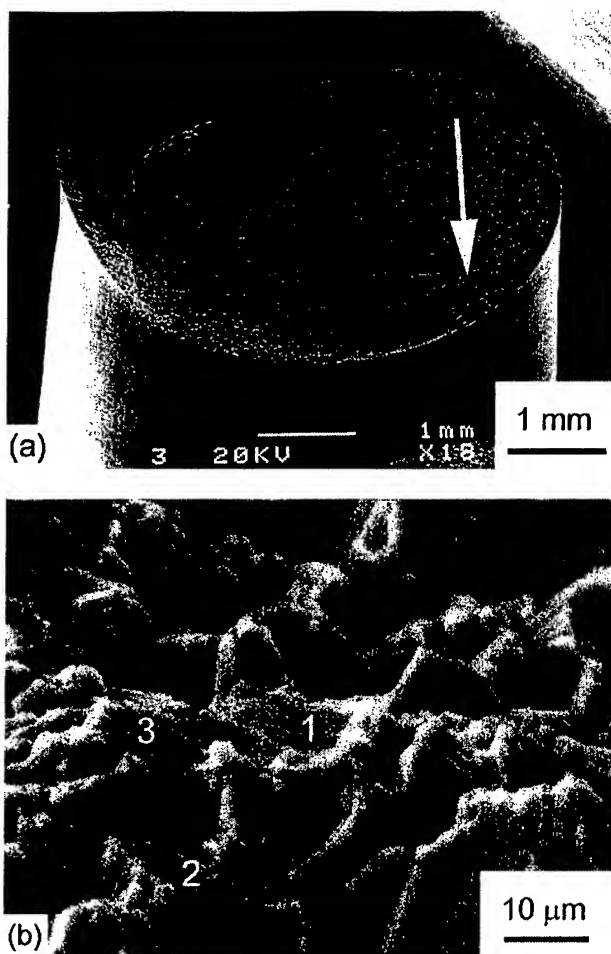


Fig. 4—(a) Subsurface fatigue crack, initiation site (arrow) in bimodal Ti-6Al-4V ( $R = 0.1$ ,  $\sigma_{\max} = 500$  MPa, and  $N_f = 9.6 \times 10^7$  cycles), showing (b) crack initiation and early growth along planar slip bands leading to facet-type fracture surface (specimen tilt: 70 deg). The EBSD analysis of fractured  $\alpha$  grains 1 through 3 revealed near-basal orientation of fracture plane.

lamellar structure appears to show better S/N properties in the HCF regime is somewhat unusual, but may be related to the fact that the bimodal structure studied in this work has a very high percentage ( $\sim 64$  pct) of interconnected primary  $\alpha$ , which leads to a large effective slip length; typical bimodal microstructures in Ti-6Al-4V usually consist of only  $\sim 30$  pct of primary  $\alpha$ .

Crack initiation, which is generally the dominant stage in smooth-bar HCF, was found to occur both at the surface and subsurface regions of the specimens. Although prior studies<sup>[14]</sup> in bimodal and lamellar Ti-6Al-4V under tension-compression ( $R = -1$ ) loading showed fatigue cracks to initiate at the surface, for the present work at positive load ratios ( $R = 0.1$  and  $0.5$ ), crack initiation was often seen in regions close to the surface. For example, crack initiation occurred at  $\sim 40$  to  $100 \mu\text{m}$  below the surface and extended farther into the interior, some  $\sim 250$  to  $450 \mu\text{m}$  for the bimodal structure and as deep as  $\sim 1$  to  $2$  mm for the lamellar structure.

Typical subsurface initiation sites in the bimodal microstructure were characterized by a faceted fracture surface (Figure 4), caused by the cracking of suitably oriented  $\alpha$



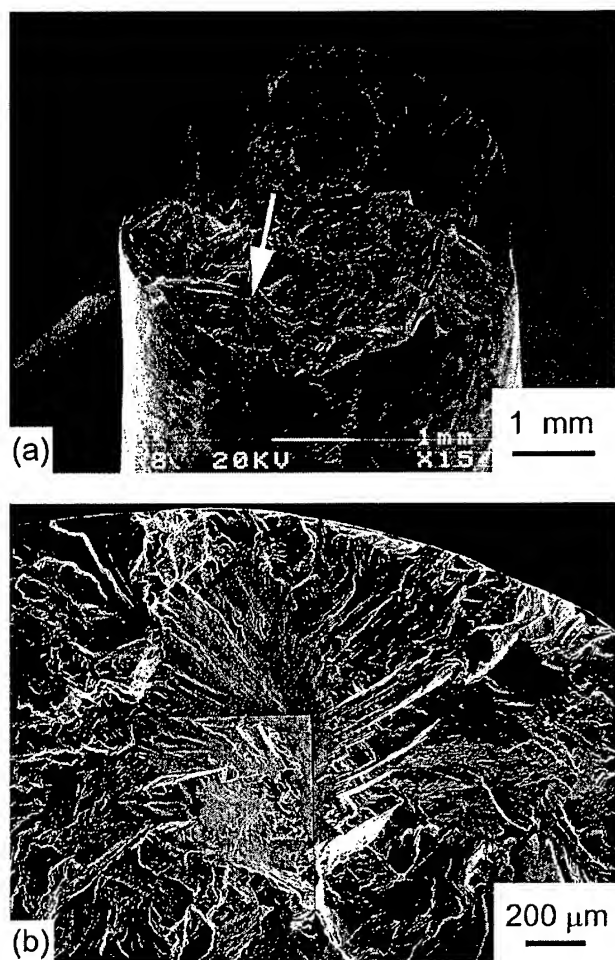


Fig. 5—Subsurface fatigue crack initiation site (arrow) in lamellar Ti-6Al-4V ( $R = 0.5$ ,  $\sigma_{\max} = 700$  MPa, and  $N_f = 6.8 \times 10^7$  cycles), showing (b) cross-colony slip band crack initiation and early growth along macroscopically planar facets of colony width dimensions ( $\sim 500 \mu\text{m}$ ).

grains and subsequent growth along planar slip bands within interconnected  $\alpha$  grains (Figure 4(a)). Electron back scattered diffraction (EBSD) analysis revealed that many of these  $\alpha$  grains were aligned with a near-basal orientation perpendicular to the stress axis (Figure 4(b)). Subsurface crack-initiation sites in fully lamellar Ti-6Al-4V were characterized by cross-colony slip-band fracture (Figure 5), typically of colony-width dimensions ( $\sim 500 \mu\text{m}$ ). Such slip bands can form across an entire colony where the laths are of similar orientation and the surrounding  $\beta$  layers are extremely thin.<sup>[8]</sup> Current studies are focused on crystallographic analysis of cross-colony fracture facets, which are also associated with a near-basal orientation,<sup>[50,51]</sup> as shown by the cracked  $\alpha$  grains of the bimodal microstructure.

Such subsurface crack initiation is not common in fatigue, but has become increasingly reported of late for fatigue failures under very-long-life conditions in steels (e.g., Reference 52); however, it is more frequently encountered in titanium alloys.<sup>[51,53–55]</sup> Most traditional explanations for this phenomenon rely on the presence of processing-induced, surface compressive residual stresses, i.e., due to heat treatment, case-hardening, or shot-peening procedures. Other explanations include the formation of such compressive

residual stresses due to preferential plastic deformation at the surface under tension-tension loading<sup>[54]</sup> and the higher probability of finding a stress-raising defect (e.g., inclusions in steels) or a weak microstructural orientation or “hard”  $\alpha$  particle (in titanium alloys) in the bulk of the material compared to the surface. As nominally stress-free surfaces were employed in the present study, it is believed that the subsurface initiation is the result of the latter effect. In particular, the high fatigue strength of lamellar Ti-6Al-4V may be due to the coarse microstructure, which has characteristic dimensions comparable to the size of the hourglass S-N sample geometry; this permits only a small number of colonies to be sampled for any weak orientation. Bache and Evans<sup>[55]</sup> have recently pointed out the significance of such weak microstructural orientations, and the related stress redistribution between individual grains, in causing premature crack initiation in titanium alloys.

## B. Mode I Fatigue-Crack Propagation

### 1. Large-crack behavior

The variation in (mode I) fatigue-crack growth rates for large ( $>4$  mm) through-thickness cracks in the bimodal<sup>[30,31]</sup> and lamellar microstructures is shown in Figure 6 for constant-load-ratio tests at  $R = 0.1, 0.5$ , and  $0.8$ . Corresponding average threshold values are listed in Table III. These results, which were collected at a frequency of 50 Hz, clearly show the expected trend of faster crack growth rates and lower  $\Delta K_{TH}$  thresholds with increasing  $R$ -value. More importantly, in the coarser lamellar structure, growth rates were consistently lower, by roughly one order of magnitude at comparable  $\Delta K$  levels, and thresholds higher, by more than 20 pct, at comparable load ratios, although there was considerably more scatter in the data for the lamellar microstructure. Specifically, between  $R = 0.1$  and  $0.8$ , (mode I)  $\Delta K_{TH}$  thresholds varied, respectively, from 5.7 to 3.9 MPa $\sqrt{\text{m}}$  in the lamellar structure compared to 4.6 to 2.6 MPa $\sqrt{\text{m}}$  in the bimodal structure; corresponding two-parameter fits of the growth rates in the Paris regime give (in units of m/cycle, MPa $\sqrt{\text{m}}$ ):

$$\frac{da}{dN} = 5.2 \times 10^{-12} \Delta K^{2.5} K_{\max}^{0.67} \quad (\text{bimodal structure})$$

$$\frac{da}{dN} = 1.25 \times 10^{-14} \Delta K^{4.5} K_{\max}^{0.67} \quad (\text{lamellar structure})$$

The variation in the fatigue thresholds, plotted as the  $\Delta K_{TH}$  threshold as a function of the  $K_{\max, TH}$  threshold, is shown in Figure 7 for a wider range of  $R$ -ratios up to 0.98, the latter results being obtained using constant- $K_{\max}$  tests conducted at high values of  $K_{\max}$ . It is apparent that neither structure showed evidence of the Marci effect,<sup>[56]</sup> where near-threshold growth rates start to increase with decreasing  $\Delta K$  levels at very high load ratios, most probably due to the superposition of a sustained-load (e.g., environmentally induced) cracking mechanism. Indeed, at these extremely high  $K_{\max}$  values, essentially as  $K_{\max} \rightarrow K_{Ic}$  ( $R \rightarrow 1$ ), the difference in  $\Delta K_{TH}$  thresholds between the two structures is lost, with both microstructural conditions showing a so-called “worst-case”  $\Delta K_{TH}$  threshold of 1.9 MPa $\sqrt{\text{m}}$ .\*

\*The worst-case threshold<sup>[30]</sup> is a term given to the lowest value of  $\Delta K_{TH}$  measured with large cracks at load ratios that approach unity (specifically, where  $K_{\max} \rightarrow K_{Ic}$ ), such that the extent of crack-tip shielding, e.g., by

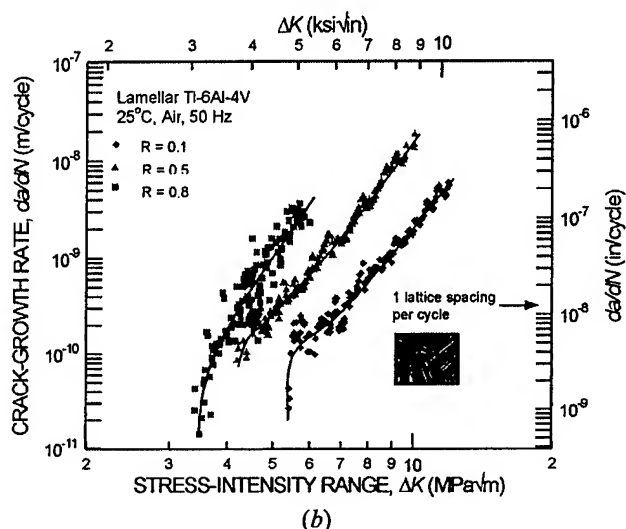
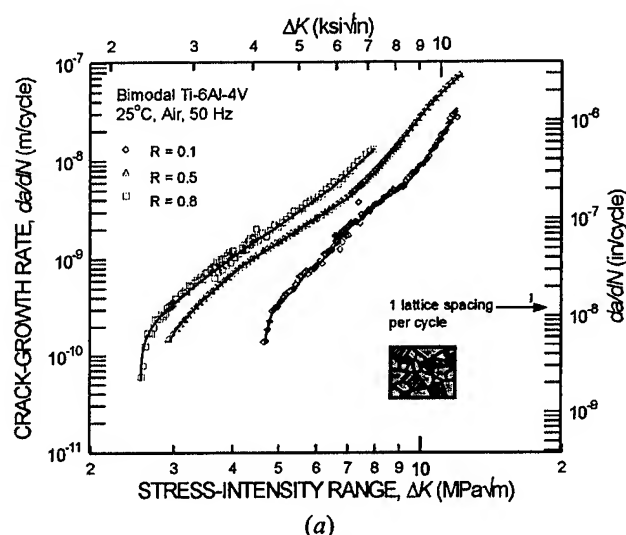


Fig. 6—Mode I fatigue-crack propagation (large crack) behavior of (a) bimodal Ti-6Al-4V in terms of the crack-growth rates,  $da/dN$ , as a function of the applied stress-intensity range,  $\Delta K$ , at various load ratios ( $R = 0.1, 0.5$  and  $0.8$ ), all at a frequency of 50 Hz. Fatigue thresholds measured at  $da/dN = 1 \times 10^{-10}$  m/cycle were 4.6, 3.6, and 2.9 MPa $\sqrt{m}$ , respectively.<sup>[30,31]</sup> (b) For the lamellar microstructure, fatigue thresholds measured at  $da/dN = 1 \times 10^{-10}$  m/cycle were 5.7, 4.4, and 3.9 MPa $\sqrt{m}$ , respectively.

crack closure, is minimized. Such thresholds, which are generally measured under constant- $K_{max}$ /increasing- $K_{min}$  cycling, represent a lower-bound threshold for the alloy/microstructure in question in the presence of "continuum-sized" cracks, *i.e.*, in the presence of physically large or small cracks which have dimensions specifically larger than the characteristic scale of the microstructure.

It should be noted that although the data shown in Figure 6 were collected at a loading frequency of 50 Hz, the growth-rate behavior of the bimodal microstructure over the range from 50 to 20,000 Hz and of the lamellar microstructure between 50 and 1000 Hz was examined. In ambient-temperature air, no effect of frequency on the (mode I)  $\Delta K_{TH}$  thresholds was seen in either microstructure.<sup>[30,31,34]</sup> Previous investigations have reported frequency-independent growth rates for titanium alloys in the 0.1 to 50 Hz range;<sup>[57,58]</sup> the current results significantly extend these observations.

Thus, the lamellar structure clearly provides superior

Table III. Average Threshold Values for Ti-6Al-4V

Load Ratio $R$	Bimodal Microstructure		Lamellar Microstructure	
	$\Delta K_{TH}$ (MPa $\sqrt{m}$ )	$K_{max, TH}$ (MPa $\sqrt{m}$ )	$\Delta K_{TH}$ (MPa $\sqrt{m}$ )	$K_{max, TH}$ (MPa $\sqrt{m}$ )
0.10*	4.3	4.8	5.7	6.3
0.30*	3.6	5.2	5.0	7.1
0.50*	2.9	5.9	4.4	8.8
0.80*	2.5	12.5	3.9	19.5
0.88**	—	—	3.2	26.5
0.91**	2.3	26.5	—	—
0.92**	—	—	3.0	36.5
0.94**	2.2	36.5	2.8	46.5
0.952**	—	—	2.7	56.5
0.955**	2.1	46.5	—	—
0.965**	2.0	56.5	2.4	66.5
0.973**	—	—	2.0	76.5
0.978**	—	—	1.9	86.5

\*Determined under constant  $R$  conditions.

\*\*Determined under constant  $K_{max}$  conditions.

mode I fatigue-crack-propagation resistance to the bimodal structure in the large-crack regime, an observation that can primarily be traced to the increased tortuosity in the crack path and resulting crack closure in the lamellar structure, as discussed in Section IV-B-3. However, this beneficial aspect of the lamellar structure is progressively diminished with increasing load ratio, again consistent with the diminishing role of crack closure, such that for  $R > 0.8$ ,  $\Delta K_{TH}$  thresholds in the two microstructures are essentially the same.

## 2. Crack closure

Crack-tip shielding from crack closure in titanium alloys has been primarily attributed to the roughness of the crack surfaces, *i.e.*, to the wedging of crack-face asperities; indeed, load-ratio effects in these alloys are generally presumed to result from such closure.<sup>[59,60,61]</sup> In the present study, significant closure was observed at the low  $R$ -ratios of 0.1 and 0.3 for both microstructures; none could be detected at  $R \geq 0.8$ . The magnitude of such closure, in terms of the variation in  $K_{cl}$ , and, hence  $\Delta K_{eff}$ , with  $\Delta K$  is shown in Figure 8. Unlike the bimodal structure, closure levels in the lamellar structure can be seen to vary with  $\Delta K$  level at low growth rates, consistent with previous studies.<sup>[60]</sup> However, more importantly, the overall magnitude of the closure effect is definitively higher in the coarser lamellar structure. As discussed in Section IV-B-3, this undoubtedly results from the increased tortuosity in the crack path and, hence, in the fracture-surface roughness associated with this microstructure.

## 3. Crack-path and fracture-surface morphologies

As shown in Figure 9, the coarser lamellar microstructure displayed a more tortuous and deflected crack path than the finer-scale bimodal microstructure. Whereas the controlling microstructural unit in the bimodal structure is the grain size, which is  $\sim 20 \mu m$ , it is clearly the entire lamellar colony size in the lamellar structure, which is more than one order of magnitude larger; furthermore, the deflection of the crack path across such boundaries in the latter structure can be seen to be strongly influenced by the orientation of neighboring colonies. Such increased crack-path tortuosity is a major contributor to the higher toughness of the lamellar microstructure.<sup>[8]</sup> Moreover, as noted previously, the enhanced

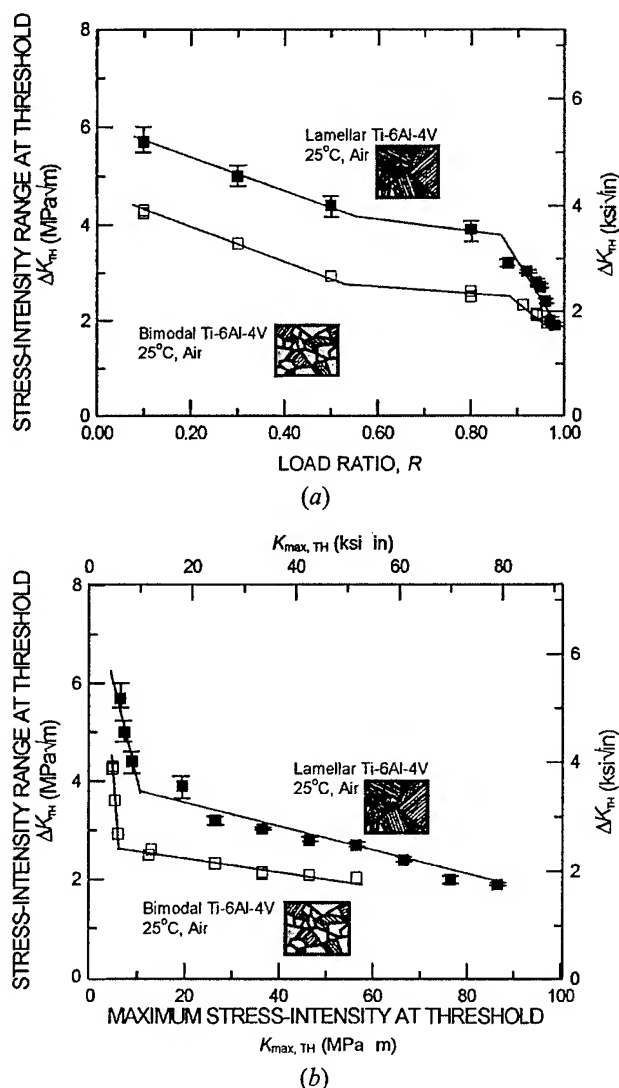


Fig. 7—(a) The mode I large-crack  $\Delta K_{TH}$  thresholds obtained for both bimodal and lamellar microstructures are shown as a function of the load ratio,  $R$ . The data include both constant- $R$  and constant- $K_{max}$  test results. At very high  $R$ -ratios ( $>0.9$ ),  $\Delta K_{TH}$  thresholds for both microstructures tend to converge. (b) The same data are plotted as a function of the  $K_{max}$  at threshold.

crack deflection and resulting roughness-induced crack closure both act to increase the fatigue-crack-growth resistance of this structure in the presence of large cracks and to increase the degree of scatter in the crack-growth data (Figure 6). At high  $R$ -values, where both microstructures show a decrease in such tortuosity, the difference between the cyclic crack-growth resistance of the two structures becomes essentially nonexistent. The less-deflected crack paths here may be associated with the much larger maximum plastic zone sizes as  $K_{max} \rightarrow K_{Ic}$  ( $R \rightarrow 1$ ); this markedly increases the number of slip systems available, which can change single-slip planar crack growth (in the form of deflected, crystallographic, crack paths) to multiple-slip crack growth (where the crack path is more straight).

The more tortuous crack path in the lamellar structure results in a far-rougher fracture surface, as shown by the scanning electron micrographs in Figures 10 and 11 for the

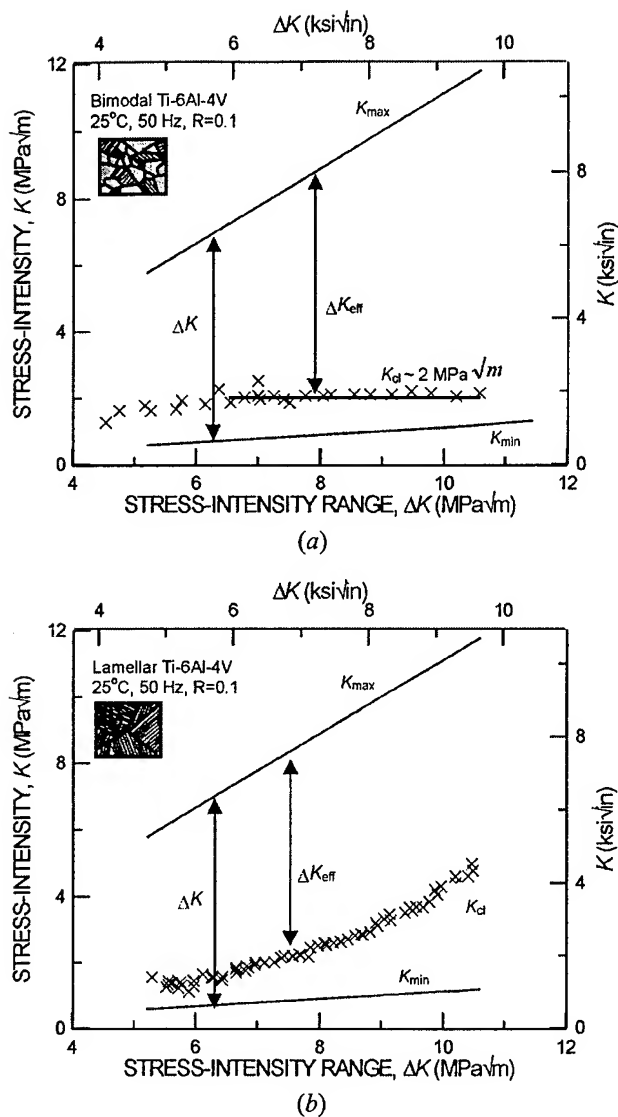


Fig. 8—Crack closure, measured at  $R = 0.1$ , using unloading compliance techniques on C(T) specimens for the (a) bimodal and (b) lamellar microstructures.

bimodal and lamellar structures, respectively, at load ratios of 0.1, 0.5, and  $>0.9$ . The  $\Delta K$  levels associated with the fracture surfaces are  $\sim 4.3$ , 2.9, and 1.9 MPa $\sqrt{m}$ , respectively, at  $R = 0.1$ , 0.5, and 0.96 for the bimodal structure (Figure 10) and  $\sim 5.7$ , 4.4, and 3.0 MPa $\sqrt{m}$ , respectively, at  $R = 0.1$ , 0.5, and 0.92 for the lamellar microstructure (Figure 11). The highly crystallographic nature of the crack paths in the lamellar structure is particularly evident in Figure 11. Also shown is the overload fracture region for both microstructures, which occurs by microvoid coalescence.

#### 4. Short-crack behavior

(Mode I)  $\Delta K_{TH}$  thresholds for short cracks, where the crack wakes have been machined away to within  $\sim 200 \mu m$  of the crack tip, are compared with the large-crack thresholds as a function of  $R$  in Figure 12. Whereas large- and short-crack thresholds are essentially identical above approximately  $R = 0.5$ , at lower load ratios where crack closure



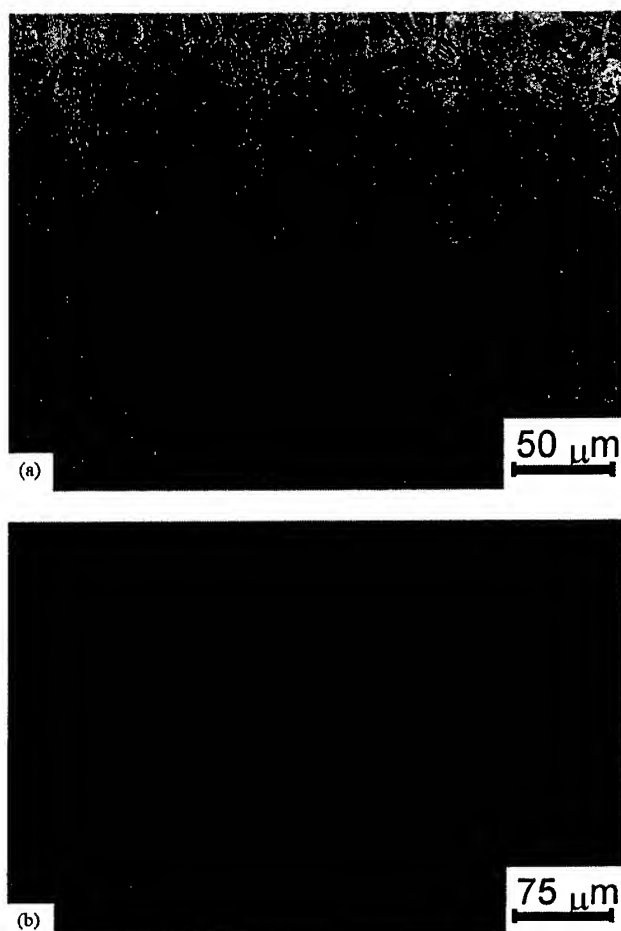


Fig. 9—A typical near-threshold crack profile observed for the (a) bimodal and (b) lamellar microstructure ( $R = 0.1$ , and  $da/dN \sim 10^{-10}$  m/cycle). The nominal crack propagation direction is indicated by the arrow. The structure-sensitivity of fatigue-crack growth is clearly stronger for the lamellar microstructure.

was observed, thresholds are much smaller for the short cracks due to the restricted role of such closure for cracks of limited wake. Indeed, by correcting the large-crack  $\Delta K_{TH}$  thresholds for closure, in the form of  $\Delta K_{TH,eff}$  thresholds, threshold values for large and short cracks are the same, similar to previous observations in Ti-6Al-4V.<sup>[62]</sup>

##### 5. Small-crack behavior

The fatigue-crack propagation behavior (at  $R = 0.1$ ) of the microstructurally small surface cracks, where crack sizes were in the range of  $\sim 1$  to  $50 \mu\text{m}$ , are plotted as a function of both  $\Delta K$  and surface-crack length,  $2c$ , for both microstructures in Figure 13; results are compared with corresponding data for through-thickness large ( $>4 \text{ mm}$ ) cracks at both  $R = 0.1$  (from constant- $R$  testing) and  $R = 0.91$  to  $0.95$  (from constant- $K_{max}$  testing). Several points are worthy of note:

- (1) Growth rates for the microstructurally small cracks were, in general, far in excess of those of corresponding large cracks at equivalent  $\Delta K$  levels. In both structures, the smallest cracks, with dimensions in the range  $\sim 2$  to  $20 \mu\text{m}$ , propagated at stress intensities well below the worst-case ("closure-free") thresholds for large cracks. Indeed, thresholds for such small cracks were below

$\Delta K \sim 1 \text{ MPa}\sqrt{\text{m}}$ , presumably due to biased sampling by the small flaw of the "weak links" in the microstructure.

- (2) With increasing crack size, growth rates for the small cracks merge first with the high- $R$  (closure-free) large-crack data (at  $2c \sim 50$  to  $100 \mu\text{m}$ ) and eventually with the low- $R$  data at larger crack sizes.
- (3) Although the lamellar structure shows superior fatigue-crack-growth properties in the presence of large ("continuum-sized") cracks (Figure 6), in the presence of the microstructurally small cracks, the fatigue-crack-growth resistance of the two structures is very similar, although the data are subject to considerably more scatter. This implies, though, that a primary difference in the fatigue-crack-growth properties of the bimodal and lamellar microstructures arises more from the extrinsic role of crack-path tortuosity and resultant crack closure, rather than any distinction in their respective intrinsic resistance to cyclic crack growth. Similar effects have been observed for other material systems (e.g., Reference 63).

From the perspective of defining thresholds for HCF, however, the results in Figure 13 clearly demonstrate that the concept of a worst-case threshold (determined under  $R \rightarrow 1$  conditions that minimize crack closure) applies strictly for continuum-sized cracks; such thresholds do not provide a lower-bound threshold stress intensity for cracks on the scale of microstructural dimensions. As discussed in Section IV-D, this is particularly pertinent for the early stages of FOD-induced fatigue failures.

It is interesting to note that the small-crack growth rates do not vary that much with microstructure, whereas the crack initiation mechanisms are strongly influenced by microstructure, as noted previously. Such initiation is often controlled by strain accumulation at the tips of the longest slip band, which leads to preferential nucleation and initial growth within the interconnected primary  $\alpha$  grains in the bimodal microstructure. In the lamellar microstructure, cross-colony slip-band crack initiation is observed, with subsequent small-crack growth generally occurring along the planar-slip bands into adjoining, but differently oriented, colonies. The coarser microstructure provides a longer path for the small crack to propagate before it encounters a serious microstructural "barrier" such as differently oriented neighboring colonies.

Thus, in general, whereas the lamellar structure offers better resistance to large-crack fatigue-crack growth than the bimodal structure, there is little difference in the resistance of the two microstructures to small-crack growth.

#### C. Mixed-Mode Fatigue Thresholds

##### 1. Large-crack behavior

Results for the large-crack threshold behavior of the bimodal and lamellar microstructures under mode I + II loading are shown in Figure 14 in the form of mixed-mode threshold envelopes, where the mode II threshold stress-intensity range ( $\Delta K_{II,TH}$ ) is plotted as a function of the corresponding mode I threshold ( $\Delta K_{I,TH}$ ). Once more, several points are worthy of note:

- (1) Similar to the behavior in other materials,<sup>[64-67]</sup> a clear reduction in threshold values with increasing  $R$ -value is evident. The slight increase in the  $\Delta K_{I,TH}$  threshold with increasing mode-mixity at low phase angles, observed

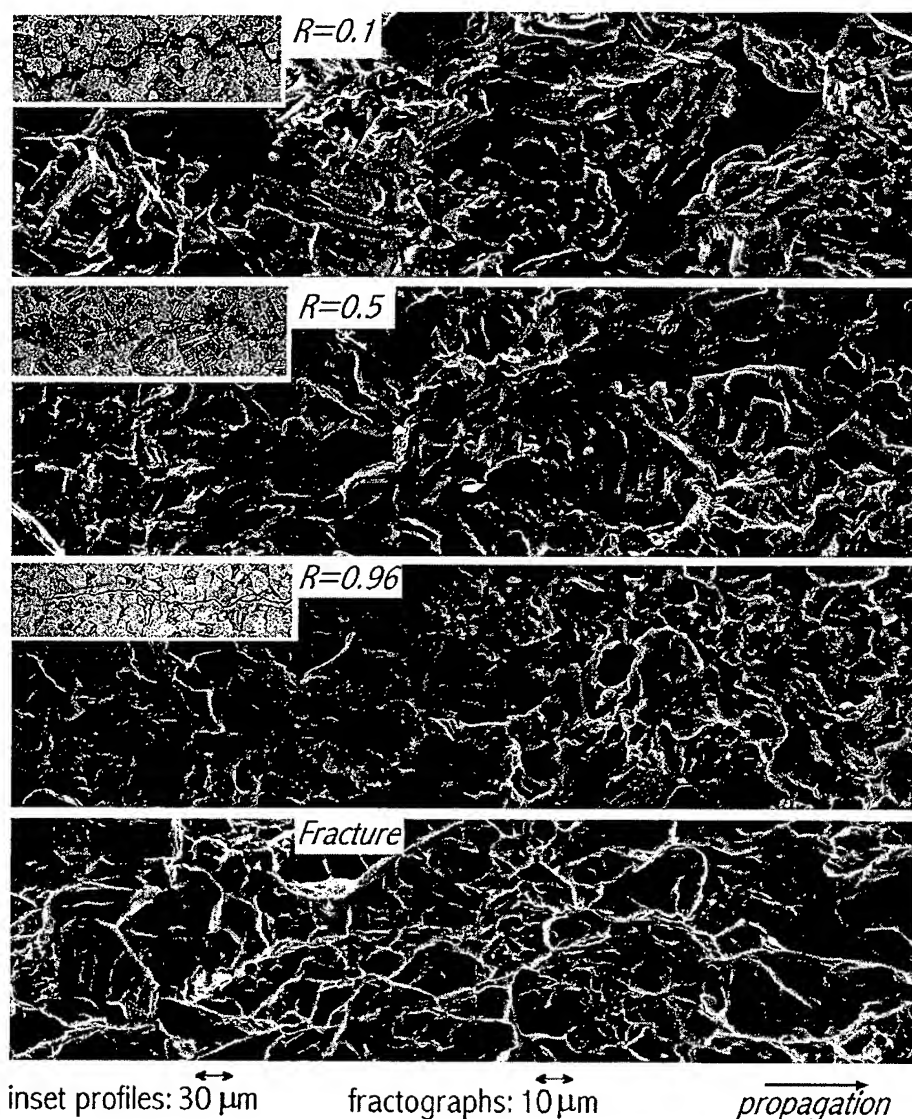


Fig. 10—A comparison of the fractography and crack profiles (inset) observed at near-threshold growth rates of  $\sim 10^{-10}$  m/cycle in the bimodal microstructure. Whereas microvoid coalescence can be seen in overload fracture, no such static modes are evident in fatigue, even at  $R = 0.96$ .

in the present data at phase angles between 0 and 26 deg, has been attributed to an effect of mode I/mode II crack-tip shielding.<sup>[43,44]</sup>

- (2) Although the mode I threshold decreases with increasing mode-mixity, if a more appropriate measure of the mixed-mode driving force is used, specifically the range in strain-energy release rate ( $\Delta G = (\Delta K_I^2 + \Delta K_{II}^2)/E'$ , where  $E' = E$  (Young's modulus) in plane stress and  $E/(1 - \nu^2)$  in plane strain ( $\nu$  being the Poisson's ratio), then there is a progressive increase in the mixed-mode threshold ( $\Delta G_{TH}$ ) with increasing mode-mixity in both microstructures for all load ratios studied (Figure 15). From the perspective of thresholds for high-cycle fatigue, this implies that, in terms of mixed-mode loading, the mode I threshold, defined in terms of  $\Delta G$ , represents a *worst-case* condition. Naturally, this is also evident when the equivalent stress-intensity factor range,  $\Delta K_{eq,TH} = (\Delta G_{TH} E')^{1/2}$ , is used to characterize the threshold (Figure 15).

- (3) As discussed in detail elsewhere,<sup>[43,44]</sup> the increase in the large-crack mixed-mode threshold with increasing mode-mixity can be related in these microstructures to an increased role in mode I and mode II crack-tip shielding, associated with, respectively, crack closure and sliding-crack interference (*i.e.*, friction and interlock of crack-surface asperities). Indeed, if such data are "corrected" for this shielding by characterizing the driving force in terms of a mixed-mode  $\Delta G_{eff}$ ,<sup>[43]</sup> then the effect of the mode-mixity on the threshold is greatly reduced (shown by the hatched regions in Figure 16).\*

\*The term  $\Delta G_{eff}$  is defined as  $(\Delta K_{I,eff}^2 + \Delta K_{II,eff}^2)/E'$ , where  $\Delta K_{I,eff}$  is the effective stress-intensity range in mode I, and  $\Delta K_{II,eff}$  is the corresponding effective stress-intensity range in mode II. The value of  $\Delta K_{I,eff}$  is determined in the usual way, in terms of  $K_{I,max} - K_{I,min}$ . The value of  $\Delta K_{II,eff}$ , on the other hand, is equal to the difference between the near-tip maximum and minimum mode II stress intensities in the fatigue cycle. The near-tip mode II stress-intensity range differs from the applied driving force due to the presence of shear-induced fracture-surface asperity contact and interlock.

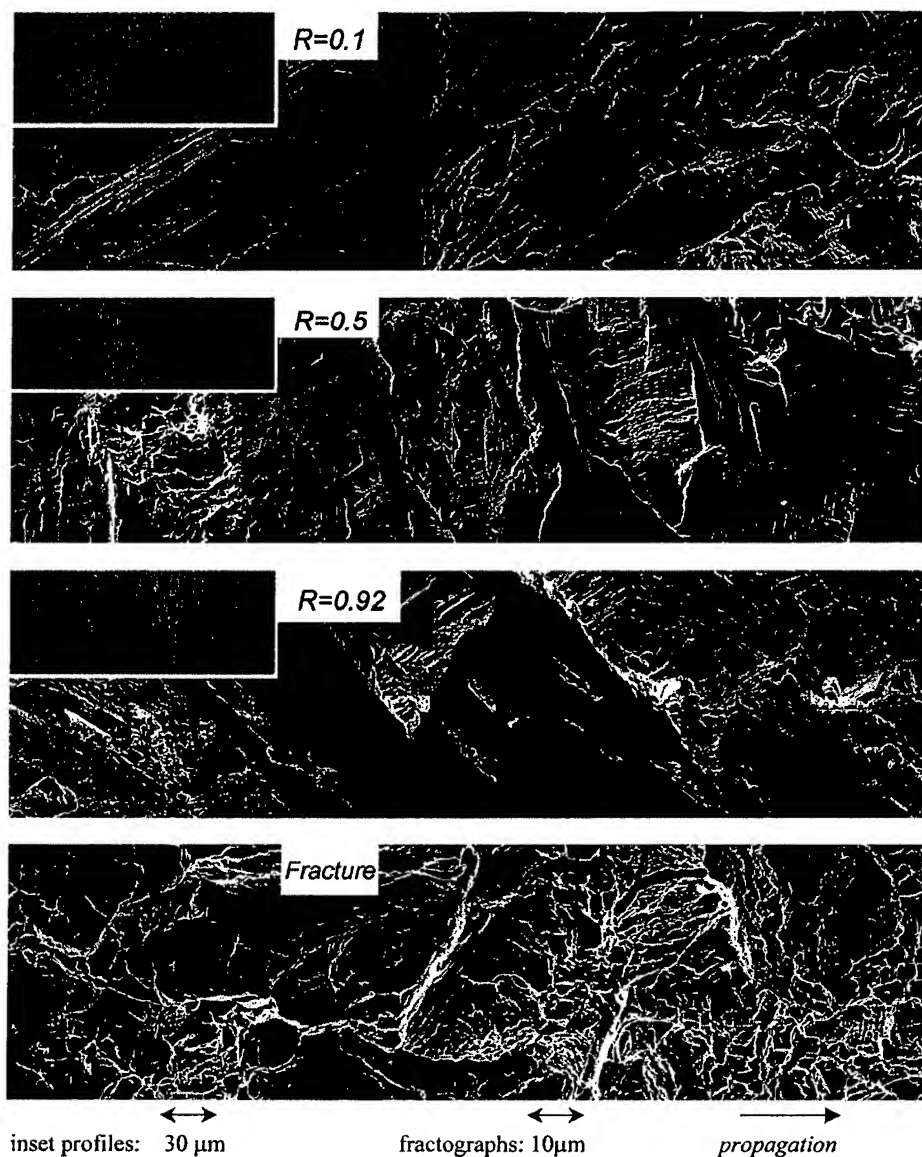


Fig. 11—A comparison of the fractography and crack profiles (inset) observed at near-threshold growth rates of  $\sim 10^{-10}$  m/cycle in the lamellar microstructure. The lamellar microstructure generally exhibits greater crack path tortuosity and fracture surface roughness.

Further details on the determination of  $\Delta K_{I,eff}$  and the estimation of  $\Delta K_{II,eff}$  using compliance-based techniques can be found in Reference 44.

(The shielding correction was based on compliance-based measurements of the mode I crack closure and mode II crack-surface interference and is described in Reference 44). Similarly, as discussed subsequently for short and small cracks, where such shielding is highly diminished due to the restricted crack wake, the mixed-mode threshold shows very little sensitivity to the mode-mixity.

- (4) Akin to pure mode I behavior, in the presence of large cracks, the lamellar structure displays superior mixed-mode crack-growth resistance to the bimodal structure. This is attributable to the large degree of crack deflection, bifurcation, and secondary crack formation associated with crack growth in the lamellar structure, as shown in Figure 17; all these factors result in rougher

fracture surfaces which, under sliding conditions (even more so than with tensile opening), can significantly promote crack-tip shielding (by sliding crack-surface interference) in large cracks. This difference in crack-growth resistance between the microstructures is considerably reduced at phase angles approaching 90 deg, although the reason for this is, as yet, unclear.

## 2. Short-crack behavior

The mixed-mode thresholds for short ( $\sim 200 \mu\text{m}$ ) cracks in the bimodal and lamellar structures are plotted in Figure 16 as a function of the phase angle; results are compared with the corresponding thresholds for large cracks from Figure 15. As noted previously, the effect of crack-tip shielding in the crack wake is particularly significant in the presence of shear loading, due to crack-surface friction and interlocking of asperities.<sup>[44,66-70]</sup> Consequently, due to the minimal role of crack-tip shielding with cracks of limited wake, short-crack

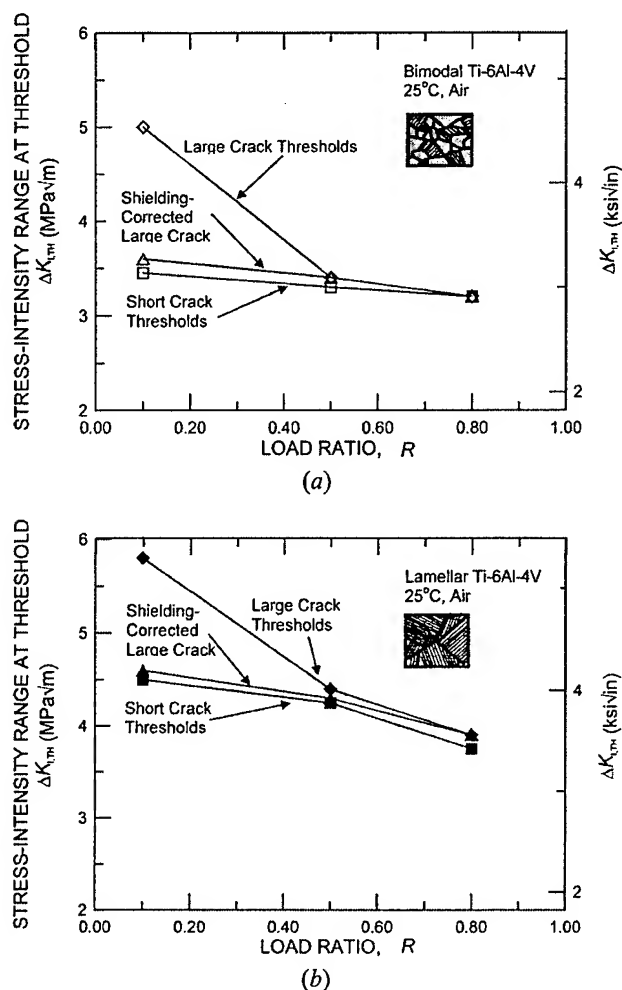


Fig. 12—(a) and (b) Mode I large-crack  $\Delta K_{TH}$  threshold values obtained for the bimodal and lamellar microstructures using symmetric four-point bending tests are shown, together with the corresponding values "corrected" for crack closure. Thresholds for short ( $\sim 200 \mu\text{m}$ ) through-thickness cracks are also shown for reference.

thresholds can be seen to be (1) far smaller than the large-crack values, (2) relatively insensitive to mode-mixity, in contrast to the large-crack thresholds, and (3) insensitive to the load ratio, again in contrast to large-crack results. Moreover, the short-crack threshold values were observed to lie within the scatter band for shielding-corrected large cracks,<sup>[43,44]</sup> again indicating that, similar to mode I conditions, the limited effect of shielding for short cracks is responsible for their lower threshold values. It should be noted here that, in addition to errors from varying precrack lengths, these tests (akin to large-crack tests<sup>[43]</sup>) are subject to errors caused by small variations in the offset of the crack from the load line of the AFB geometry. The root-mean-square error in this offset has been determined to be  $0.081 \text{ mm}$ .<sup>[43]</sup> At a phase angle of  $82^\circ$  and a load ratio of  $0.1$ , this translates into typical errors of  $\sim \pm 2.6^\circ$  in  $\beta$  and  $\sim \pm 2 \text{ J/m}^2$  in the threshold values; such uncertainties in  $\Delta G_{TH}$  values are typical for the entire range of  $R$  and  $\beta$  values studied.

With respect to microstructural effects, the distinction between the bimodal and lamellar microstructures in terms of the mixed-mode crack-growth resistance is substantially

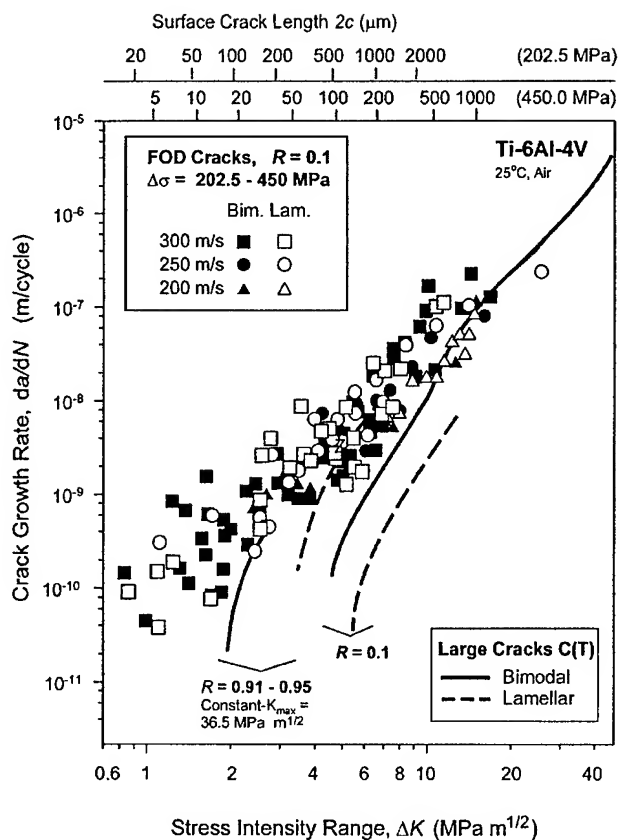


Fig. 13—Fatigue-crack growth rates as a function of applied stress-intensity range at  $R = 0.1$  for FOD-induced small ( $\sim 2$  to  $50 \mu\text{m}$ ) surface cracks in the bimodal and lamellar microstructures. Large-crack growth data at  $R = 0.1$  were obtained from constant load-ratio tests, whereas corresponding data at  $R = 0.91$  to  $0.95$  were obtained using constant- $K_{max}$ /increasing- $K_{min}$  testing.

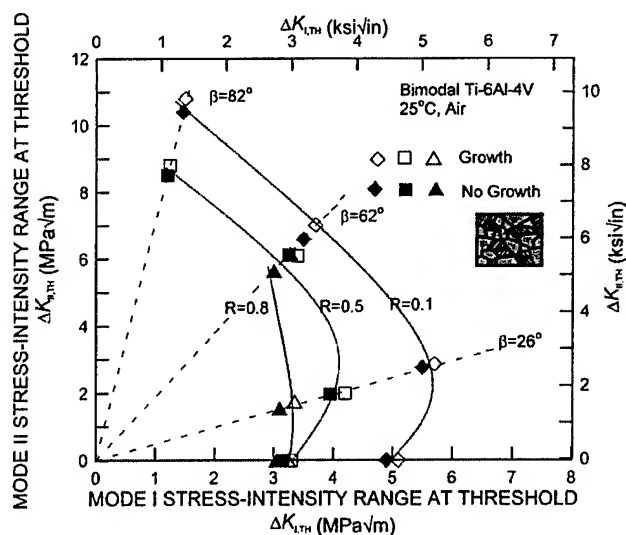
reduced for short cracks, compared to that for large cracks; however, the lamellar structure still displays somewhat higher  $\Delta G_{TH}$  thresholds, particularly at the lower  $R$ -values.

### 3. Small-crack behavior

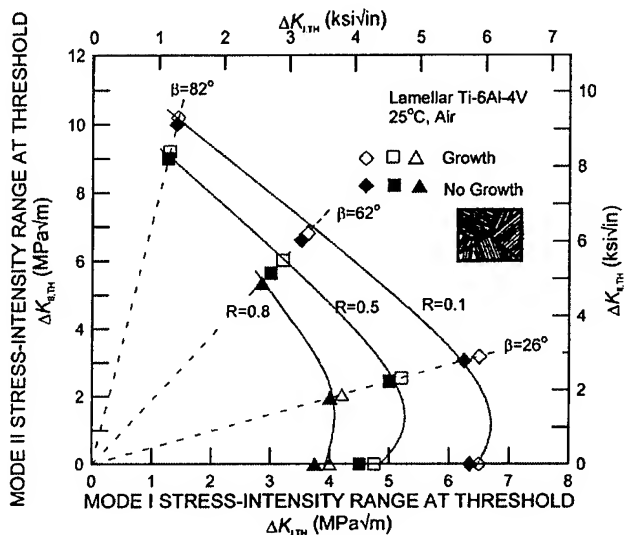
The results presented in Figure 16 show a marked effect of crack size on the mixed-mode thresholds, which we have attributed to a difference in the magnitude of the crack-tip shielding. However, even lower mixed-mode thresholds have been measured for microstructurally small ( $< 50 \mu\text{m}$ ) surface cracks, where there is the additional factor of the biased sampling of the weak links in the microstructure by the small flaw. As shown in Figure 18 for the bimodal structure, the large-crack  $\Delta G_{TH}$  mixed-mode thresholds at  $\Delta K_I/\Delta K_I = 7.1$  ( $R = 0.1$ ) are some 70 to 90 times larger than such measured small-crack thresholds. As there is little to no information in the literature concerning the mixed-mode behavior of such small flaws, this would appear to be an important topic for further investigation.

### D. Thresholds for FOD

High-velocity impacts of hardened steel spheres simulating FOD resulted in a dramatic reduction in the fatigue life in both microstructures, as shown by the  $S$ - $N$  data in Figure 3. Lifetimes are reduced by a minimum of two orders of



(a)

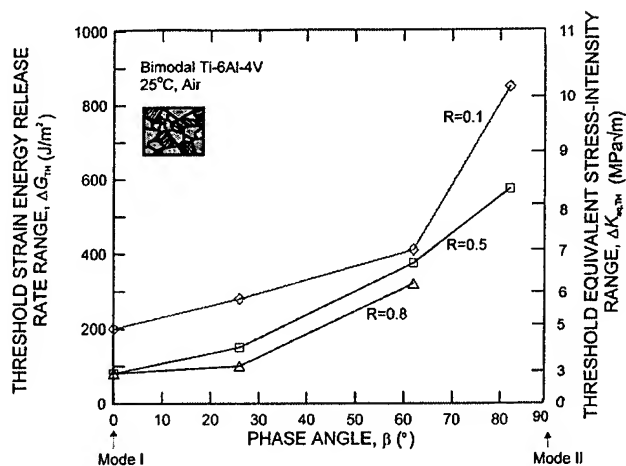


(b)

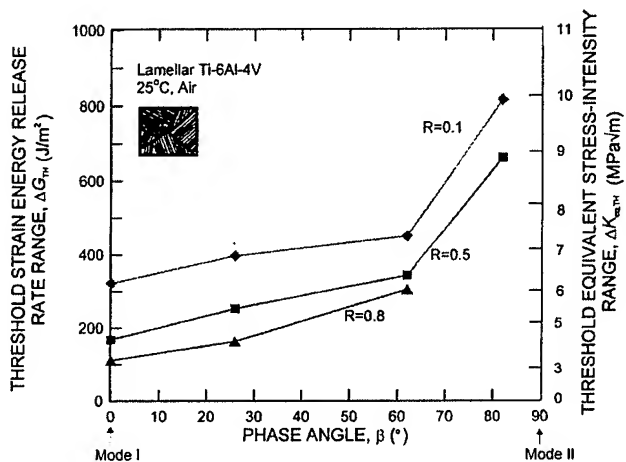
Fig. 14—Mixed-mode threshold envelopes for large (>4 mm) through-thickness cracks in the (a) bimodal and (b) lamellar microstructures. Note that the lamellar structure shows superior resistance to crack propagation, particularly at the lower phase angles.

magnitude, and FOD-induced failures can be seen to occur in as little as  $2 \times 10^4$  cycles at stresses below the smooth-bar fatigue limit. Corresponding images of the typical damage sites, following 300 m/s impacts on the flat surface of the fatigue samples, are shown in Figure 19 for both microstructures.

As discussed in detail elsewhere,<sup>[40,47]</sup> the mechanistic effect of such FOD can be considered in terms of (1) the possibility of forming microcracks in the damage zone, (2) the stress concentration associated with the FOD-induced notches, (3) microstructural damage from FOD-induced plastic deformation, and (4) the localized presence of tensile residual hoop stresses in the vicinity of the impact site. Although all these factors play an important role, a pivotal effect of FOD in reducing fatigue life in Ti-6Al-4V appears



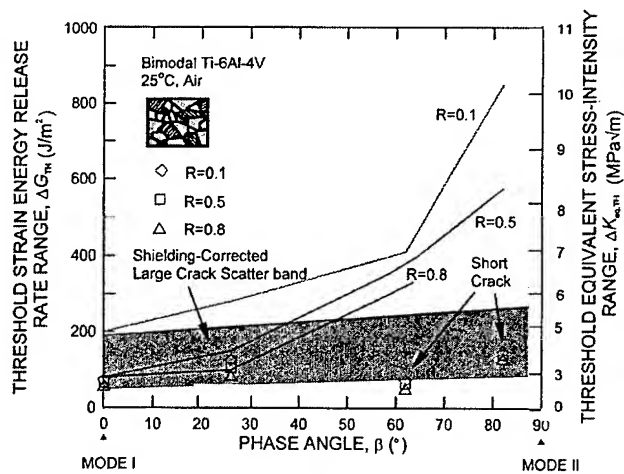
(a)



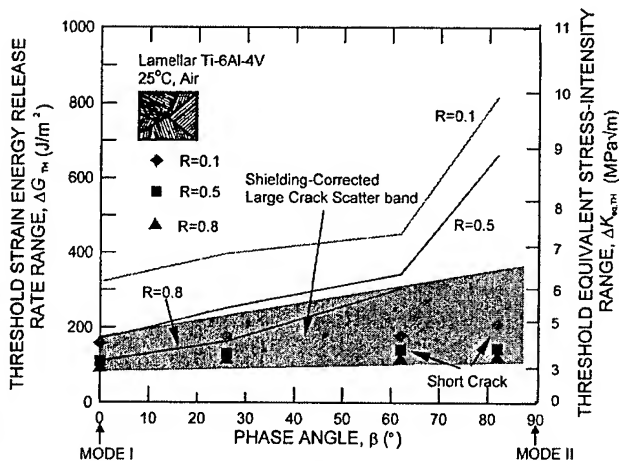
(b)

Fig. 15—The threshold strain-energy release rate,  $\Delta G_{TH}$ , is plotted as a function of phase angle,  $\beta$ , for both microstructures for large cracks subjected to mixed-mode loading at  $R = 0.1, 0.5$ , and  $0.8$ . Equivalent stress-intensity ranges at threshold for both microstructures are also shown. The lamellar microstructure generally displays superior resistance to fatigue-crack propagation.

to be the formation, at high impact velocities, of damage-induced microcracks; on subsequent cycling, these can act preferred sites for the premature initiation of fatigue cracks in the pileup of material around the rim of the impact crater, depending upon the relative magnitude of the residual stresses in the vicinity of the impact.<sup>[71]</sup> This pile-up of material at the crater rim can be seen in Figure 19; within this region, numerous microcracks ( $\sim 1$  to  $50 \mu\text{m}$  in size) are formed, which (when favorably oriented to the applied stress axis) serve as the starting point for fatigue cracking during subsequent cycling. Moreover, circumferentially oriented intense shear bands are formed at the higher impact velocities; these emanate from the surface of the impact crater and can be seen as concentric rings on the surface of the crater. The development of the pileup of material at the crater rim and the presence of shear banding and microcracking was more severe for the lamellar microstructure; however, although the microcrack density was increased, the size of the individual microcracks (*i.e.*,  $\sim 2$  to  $50 \mu\text{m}$ ) was comparable to that seen in the bimodal microstructure.<sup>[48]</sup>



(a)

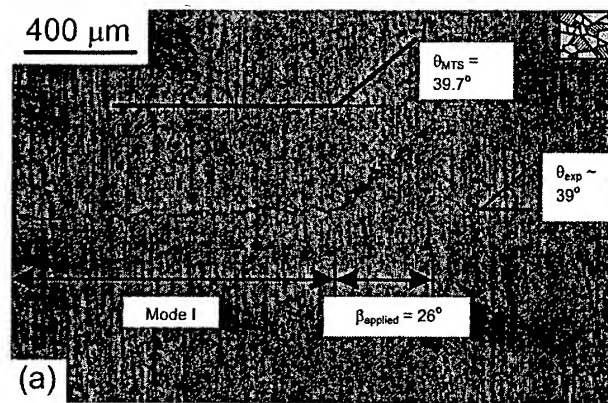


(b)

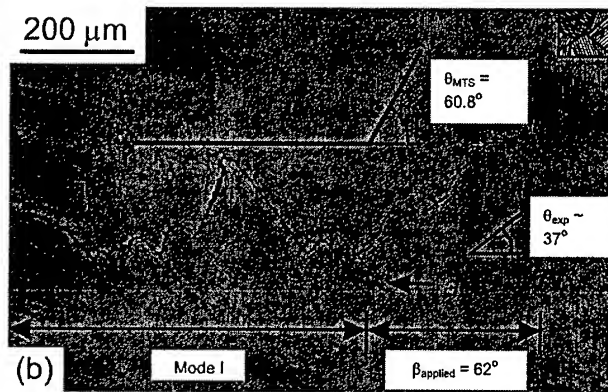
Fig. 16—Variation in mixed-mode thresholds,  $\Delta G_{TH}$ , as a function of phase angle,  $\beta$ , in (a) and bimodal and (b) lamellar structures. Shown are results at three load ratios for large ( $>4$  mm) cracks, before and after “correcting” for crack-tip shielding, and for short ( $\sim 200$   $\mu\text{m}$ ) through-thickness cracks.

The growth rates of the microstructurally small cracks that are initiated at, or near, such damage sites are shown in Figure 13. As discussed in Section IV-B-5, there is apparently little difference between the early growth of such FOD-initiated cracks in the two microstructures. However, it can be seen that the growth of  $<5$ - $\mu\text{m}$ -sized microcracks commences at  $\Delta K$  levels of  $\sim 1$  MPa $\sqrt{\text{m}}$ ; as this is far below the worst-case thresholds for continuum-sized cracks, an alternative approach must be found to describe the threshold conditions for HCF in the presence of FOD.

In light of the vanishingly low thresholds for microstructurally small cracks in Ti-6Al-4V, an alternative approach to describe the threshold conditions HCF failures can be found using modified Kitawaga-Takahashi diagrams,<sup>[72]</sup> where the threshold-stress range for fatigue failure ( $\Delta\sigma$ ) is plotted as a function of the surface-crack size,  $2c$ , as shown in Figure 20. For the present case of FOD-initiated HCF, we have proposed coupling the worst-case threshold stress intensity with the  $10^7$ -cycle smooth-bar fatigue limit to describe the HCF failure envelope, which is plotted for the bimodal and lamellar microstructures in Figures 20(a) and (b) at  $R = 0.1$  and  $0.5$ , respectively.<sup>[47]</sup>



(a)



(b)

Fig. 17—Fatigue crack profiles are compared for the (a) bimodal ( $R = 0.8$ , and  $\beta = 26$  deg) and (b) lamellar ( $R = 0.1$ , and  $\beta = 62$  deg) microstructures. Optical micrographs show both the mode I fatigue precrack and the region of deflected crack growth following the application of cyclic mixed-mode loading. Measured crack deflection angles,  $\theta_{exp}$ , are compared with those predicted by the path of maximum tangential stress,  $\theta_{MTS}$  (References 43 and 44).

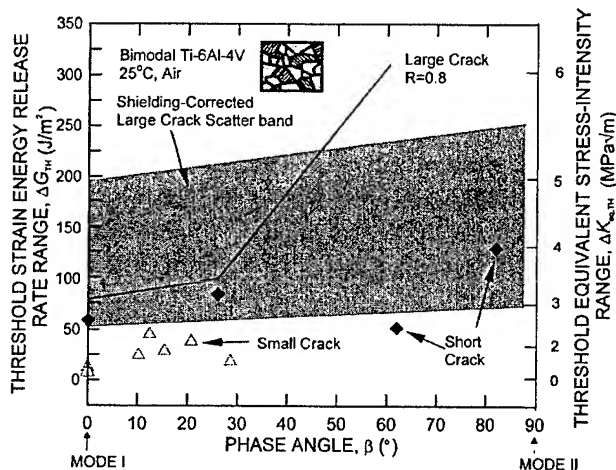


Fig. 18—Variation in mixed-mode thresholds,  $\Delta G_{TH}$ , as a function of phase angle,  $\beta$ , for small ( $<50$   $\mu\text{m}$ ) surface cracks in the bimodal microstructure. Shown for comparison are results for short ( $\sim 200$   $\mu\text{m}$ ) through-thickness cracks and for large ( $>4$  mm) cracks under worst-case, high  $R$  conditions.

Results for the bimodal microstructure (closed symbols, solid lines) show that crack growth at both load ratios from FOD-induced microstructurally small cracks can be adequately described by the fatigue limit, corrected for the stress



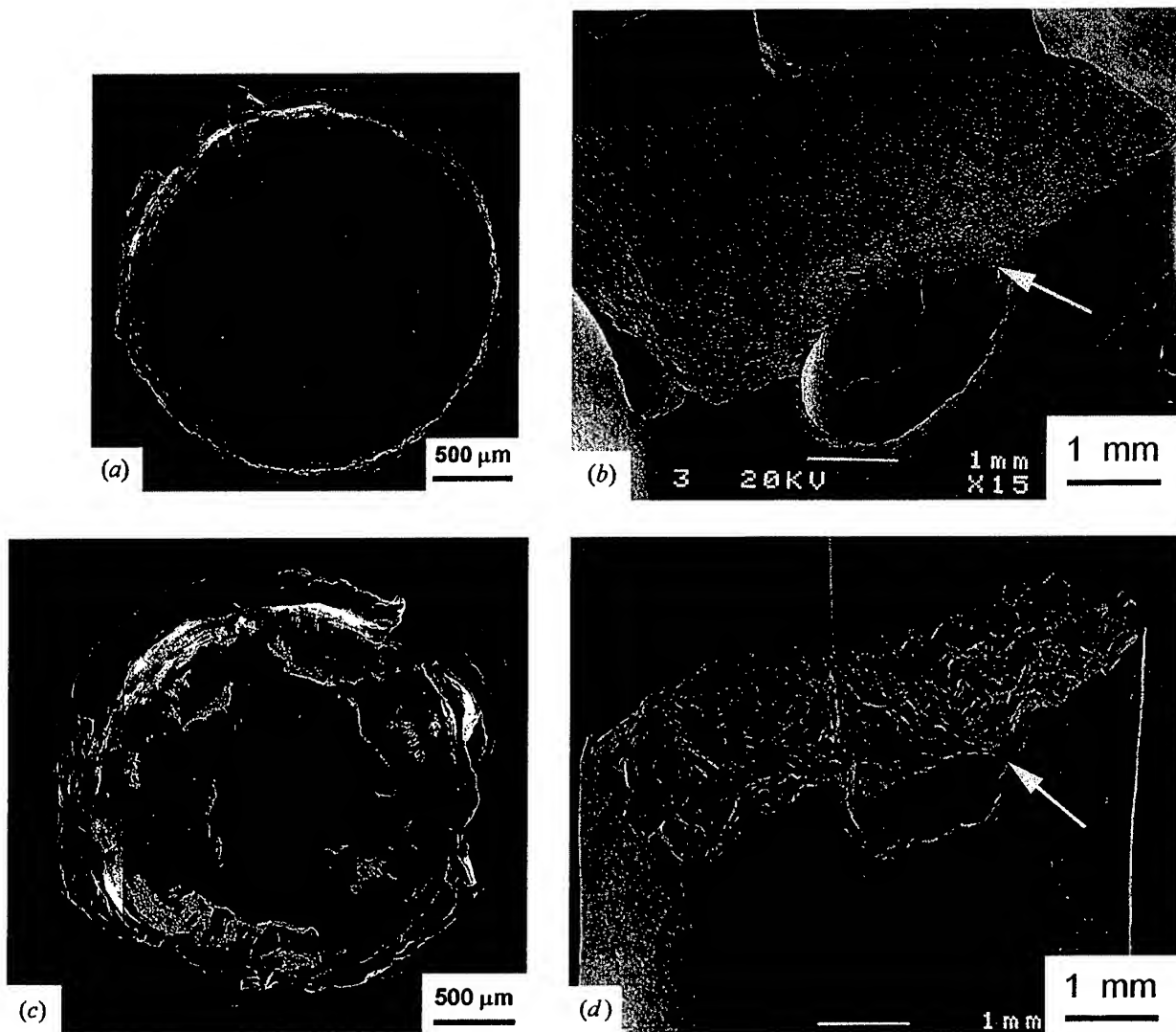


Fig. 19—FOD-induced craters formed following high velocity (300 m/s) impacts in the (a) bimodal and (c) lamellar microstructures. Note the extensive pileup observed at the impact crater rim, particularly for the lamellar microstructure. Failures initiated from impact-induced cracks at the crater rim (marked by arrows) in the (b) bimodal microstructure (nominally applied  $\sigma_{\max} = 500$  MPa,  $R = 0.1$ , and  $N_F = 65,000$  cycles) and (d) lamellar microstructure (nominally applied  $\sigma_{\max} = 500$  MPa,  $R = 0.1$ , and  $N_F = 23,000$  cycles).

concentration of the FOD indent, at small crack sizes, and the worst-case threshold stress intensity at larger continuum-sized crack sizes.\* The failure envelopes in Figure 20 can

\*An additional correction is required for the case of low applied stresses (relative to the magnitude of residual tensile stresses in the vicinity of the damage sites ( $\sim 300$  MPa)). As described in detail elsewhere,<sup>[71]</sup> the effective load ratio in the Kitagawa–Takahashi plots needs to be corrected by superimposing the tensile residual stress as a mean stress. This approach is often unnecessary for higher applied stresses, due to relaxation of the residual stresses at the base and rim of the damage sites during initial fatigue cycling.<sup>[41]</sup>

be somewhat better represented by the El Haddad *et al.*<sup>[73]</sup> empirical quantification of the Kitagawa–Takahashi diagram, as shown. This approach introduces a constant, termed the “intrinsic crack size.”\* ( $2c_0$ ), such that the stress inten-

\*Although called the intrinsic crack size, this term is a fitting parameter and has no physical significance.

sity is defined as  $\Delta K = Y\Delta\sigma (\pi(2c + 2c_0))^{1/2}$ , where  $Y$  is the geometry factor.

With respect to the lamellar microstructure, shown by the open symbols and dashed lines in Figure 20, the Kitagawa–Takahashi approach is less suited. This structure does possess significantly better resistance to large-crack growth in the form of higher fatigue thresholds, and it possesses higher resistance to crack initiation in the form of a higher smooth-bar fatigue limit; however, it is more prone to the formation of FOD-induced microcracks, and such microstructurally small cracks exhibit a low resistance to propagation, even at stress-concentration-corrected stress ranges well below the fatigue limit.

## V. CONCLUDING REMARKS

The selection of an ideal microstructure for optimal HCF properties in an alloy represents a complex task, particularly

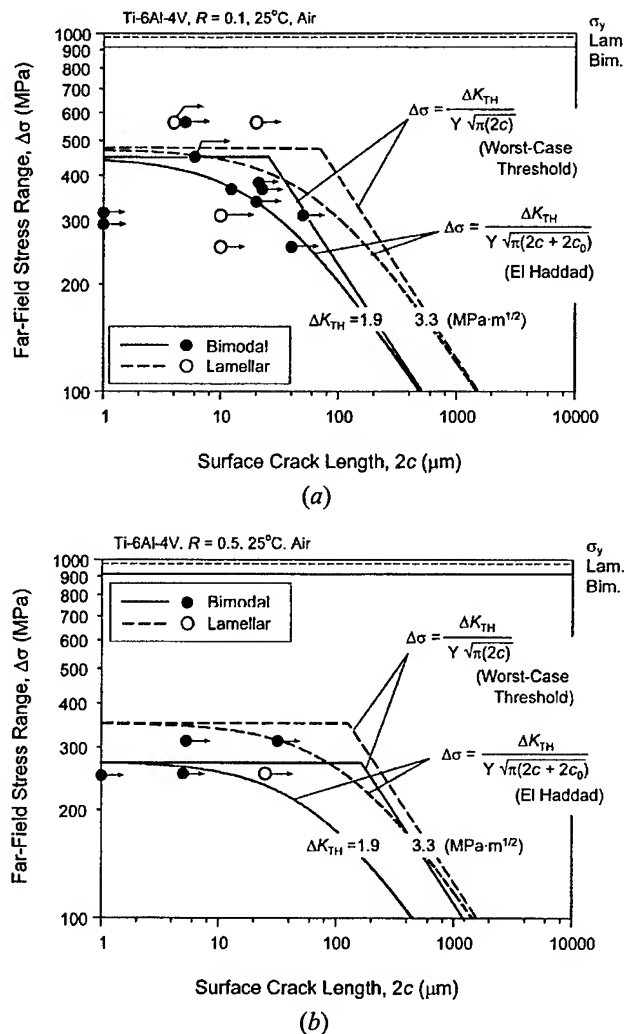


Fig. 20—Modified Kitagawa-Takahashi diagrams representing the threshold crack-growth conditions ( $da/dN = 10^{-10}$  to  $10^{-11}$  m/cycle) at (a)  $R = 0.1$  and (b)  $R = 0.5$  for FOD-induced small cracks in bimodal and lamellar Ti-6Al-4V. The threshold stress range as a function of the surface crack length is plotted, with the limiting conditions of the worst-case thresholds stress-intensity range at large crack lengths and the stress-concentration corrected  $10^7$ -cycle smooth-bar fatigue limit at small crack lengths.

in view of the conflicting requirements of developing a high resistance to large-crack growth, which is generally referred to as the *damage tolerance*, together with similar resistance to crack initiation and small-crack growth, which generally determines the *durability*. Whereas large-crack growth resistance is often controlled by extrinsic factors, such as crack closure, which generally are promoted by coarse microstructures, resistance to crack initiation and small-crack growth is more of an intrinsic property of the microstructure and is promoted by finer-scale microstructures.

In the present case of Ti-6Al-4V alloys for turbine engine applications, the coarse  $\beta$ -annealed lamellar structure, which has a characteristic microstructural dimension over one order of magnitude larger than the equiaxed bimodal (STOA) structure, clearly has the better damage tolerance. It is a higher-strength, higher-toughness microstructural condition that develops higher levels of crack-tip shielding in both mode I and mode II from its more deflected crack paths

and resulting rougher fracture surfaces; correspondingly, its large-crack fatigue-crack growth properties, in terms of mode I and mixed-mode fatigue thresholds, are definitely superior to those for the bimodal microstructure. However, at high load ratios where the effect of such shielding is diminished, the finer bimodal microstructure has comparable properties. Similarly, for the growth of microstructurally small cracks, specifically following FOD, again, where the role of shielding is minimized, the HCF resistance of the two microstructures is comparable. The problem with the lamellar structure is that it has a factor-of-4 lower ductility and, thus, is more prone to the formation of microcracks following impact damage. More importantly, cracks as large as  $\sim 500 \mu\text{m}$  (the average colony size) may be considered as microstructurally small in the lamellar condition. As such cracks are prone to biased sampling of the microstructure, properties are subject to more scatter and often do not conform to measurements from larger samples, which reflect continuum behavior. Consequently, it may be much more difficult in practice to define *reliable* HCF threshold properties in the lamellar microstructure that will prevent the occurrence of HCF failures in service. A probabilistic framework for such modeling and predictions may be required in these instances.

## VI. CONCLUSIONS

Based on a comparative study of the HCF properties of fine bimodal and coarse lamellar microstructures in Ti-6Al-4V, involving S-N behavior, mode I fatigue-crack propagation, and threshold behavior (as a function of load ratio and frequency) for large and small cracks, the corresponding fatigue-threshold behavior for large and small cracks under mixed-mode loading, and the role of FOD, the following conclusions can be made.

1. Although the differences are not large, the lamellar microstructure appears to display superior smooth-bar S-N cycle fatigue properties for lifetimes from  $\sim 10^5$  to  $> 10^8$  cycles at load ratios of 0.1 and 0.5, due to its roughly 10 pct higher tensile strength and coarser microstructural dimensions (which limited the number of colonies to be sampled for weak orientations). In contrast, at shorter lifetimes in the low-cycle regime, the bimodal microstructure exhibits the slightly better fatigue properties, presumably because of the much higher ductility of this microstructure.
2. Similarly, the lamellar microstructure displayed better (mode I) fatigue-crack-propagation properties than the bimodal microstructure in the presence of large ( $> 4 \text{ mm}$ ) cracks. This was associated with the more tortuous crack paths in the coarser microstructure, which promoted higher levels of crack-tip shielding primarily by roughness-induced crack closure. Consequently, at high load ratios where the effect of such closure was minimal, the HCF threshold properties of the two microstructures were comparable. Indeed, worst-case mode I thresholds, defined at constant  $K_{\text{max}}$ /increasing  $K_{\text{min}}$  conditions to give very high load ratios ( $R > 0.92$ ) and, hence, minimize the role of closure, were found to be  $1.9 \text{ MPa}\sqrt{\text{m}}$  in both microstructures; these values can be regarded as lower-bound HCF threshold values for continuum-sized cracks.



3. In the presence of microstructurally small ( $\sim 2$  to  $50 \mu\text{m}$ ) cracks, as, for example, are formed following high-velocity impact damage, thresholds for fatigue-crack propagation were observed to be far less than the worst-case thresholds and approach  $\sim 1 \text{ MPa}\sqrt{\text{m}}$ . The behavior in this regime was similar in both microstructures.
4. Mixed-mode large-crack measurements for both microstructures indicate that mixed-mode thresholds, characterized in terms of the strain-energy release rate,  $\Delta G_{TH}$ , or the equivalent stress intensity,  $\Delta K_{eq,TH}$ , are increased with increasing mode-mixity; correspondingly, pure mode I  $\Delta G_{TH}$  thresholds can be used as a conservative worst-case estimate. The larger threshold values with increasing mode-mixity can be attributed to an increased role of crack-tip shielding in mode I (crack closure) and mode II (crack-surface interference).
5. The lamellar microstructure displayed superior resistance to mixed-mode fatigue-crack propagation in the presence of large cracks; at very high mode-mixities, approaching pure mode II conditions ( $\beta = 82 \text{ deg}$ ), however, the properties of the bimodal and lamellar microstructure were similar.
6. Due to the limited effect of such shielding, mixed-mode thresholds for short ( $\sim 200 \mu\text{m}$ ) through-thickness and small ( $2$  to  $50 \mu\text{m}$ ) surface cracks were found to be substantially less than the large-crack values and to be essentially insensitive to the mode-mixity. Short-crack thresholds were seen to be comparable to the large-crack threshold values after correcting for crack-tip shielding. The lamellar microstructure exhibited somewhat higher short-crack thresholds compared to the bimodal microstructure.
7. The FOD simulated by high-velocity impacts by hardened steel shot, was found to markedly reduce the fatigue life; this effect was attributed to impact-induced residual stresses, microstructural distortion, geometric stress concentrations, and, most importantly, incipient microcrack formation. Threshold conditions for HCF failures following FOD can be described in terms of a modified Kitagawa-Takahashi approach, in terms of the smooth-bar fatigue limit, corrected for the stress concentration of the FOD indent and residual stresses, at small crack sizes and the worst-case threshold-stress intensity at larger continuum-sized crack sizes. Resistance to FOD-induced HCF failures was comparable in the bimodal and lamellar microstructures, although the lamellar microstructure was more prone to the formation of microcracks following high-velocity impact damage.

#### ACKNOWLEDGMENTS

This work was supported by the United States Air Force Office of Scientific Research under Grant No. F49620-96-1-0478 under the auspices of the Multidisciplinary University Research Initiative on *High Cycle Fatigue* to the University of California at Berkeley. One of the authors (BLB) acknowledges the support of the Hertz Foundation. Special thanks are due to Professor Werner Goldsmith for providing the compressed-gas gun facility, to Professor J.W. Hutchinson and Drs. J.M. McNaney, O. Roder, I. Altenberger, X. Chen, and A.W. Thompson for helpful discussions, and to Z. Bell, J.L. Hendricks, and C.K. Lau for their experimental assistance.

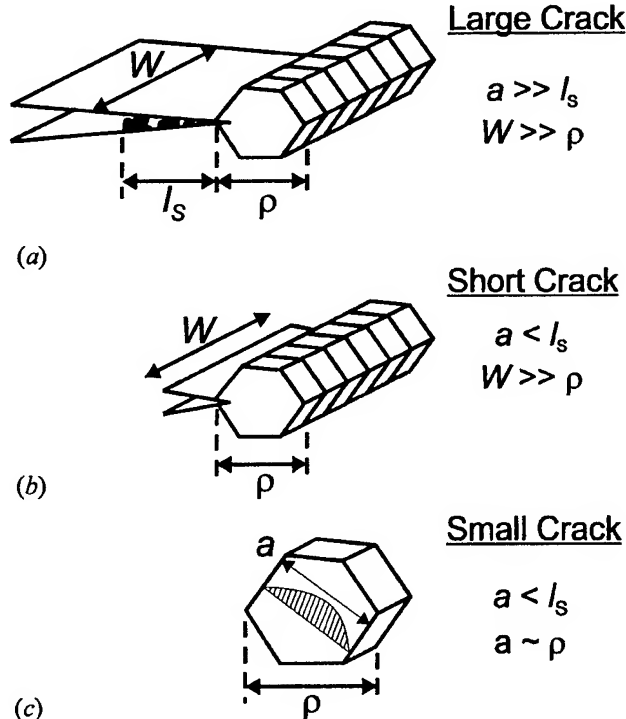


Fig. A1—Schematic illustrations highlighting the key distinctions between large, short, and small fatigue cracks. (a) Large cracks have length,  $a$ , and width,  $W$ , which are large both with respect to the equilibrium shielding-zone length,  $l_s$  (indicated here as a region of debris in the crack wake which produces crack closure), and the characteristic microstructural size scale,  $\rho$ , e.g., the grain size. In contrast to this, (b) short fatigue cracks are characterized by  $a < l_s$ , but  $W \gg \rho$ . The reduced crack-wake length results in a lower level of crack-tip shielding. (c) for small cracks, the fracture surface is reduced in both dimensions, with  $a$  (and  $W$ ) being small with respect to both  $l_s$  and  $\rho$ . The fact that  $a \sim \rho$  implies that the crack front samples only a few microstructural entities, leading to a biased sampling of the microstructure. It should be noted here that owing to the coarser microstructure in the lamellar case, a crack belonging to class (c) for this microstructural condition can be over an order of magnitude larger than similar cracks in the bimodal case.

#### APPENDIX

##### Distinction between large, short, and small cracks

A key component of the present work is a comparison of the crack-growth behavior for fatigue cracks of varying dimension, which are classified here as *large*, *short*, and *small* cracks. For the sake of clarity, the salient differences between such cracks are briefly reviewed here. Large fatigue cracks (Figure A1(a)) have fracture surface dimensions that are large compared to the scale of the microstructure in both directions. Therefore, they generally have a fully developed\*

\*For mixed-mode loading conditions, the shearing of the fracture surfaces with respect to one another can produce crack-wake contact via sliding interference over dimensions that are much larger than for mode I loading, perhaps over the entire wake of a large fatigue crack.<sup>[68,70]</sup> Thus, the notion of a "fully developed" shielding zone is somewhat unclear for mixed-mode loading conditions. At the least, one would expect the equilibrium shielding-zone length to be a function of the applied ratio of shear to tension.

crack-tip shielding zone and can "sample" the microstructure in a statistical (continuum) manner.<sup>[63]</sup> With respect to large cracks, small cracks are generally described as being comparable in size to the following:<sup>[74]</sup>

- microstructural dimensions, where biased statistical sampling of the microstructure can lead to accelerated crack advance along "weak" paths, *i.e.*, microstructural features oriented for easy crack growth (a continuum limitation);
- the extent of local inelasticity *ahead* of the crack tip, where the assumption of small-scale yielding implicit in the use of the stress intensity,  $K$ , is not strictly valid (a linear-elastic fracture mechanics limitation); and
- the extent of crack-tip shielding (*e.g.*, crack closure) *behind* the crack tip, where the reduced role of shielding leads to a higher local driving force than the corresponding large crack at the same applied  $K$  level (a similitude limitation).

However, a further important distinction can be made, namely, that of a short vs. small crack, as shown schematically in Figure A1. This distinction alludes not simply to physical size but the extent to which a fatigue crack is subjected to the first and third factors listed previously. Short fatigue cracks (Figure A1(b)) are physically short in only one dimension, a condition that is often realized experimentally by machining away the wake of a large crack. This type of fatigue flaw experiences limited crack-tip shielding due to its reduced length<sup>[35]</sup> yet still samples the microstructure as a continuum because of its extensive crack front. In contrast, small fatigue cracks (Figure A1(c)) are small and comparable to the microstructural size scale in all dimensions, as typified by the small, semielliptical surface flaw (*e.g.*, Reference 74). With such cracks, crack-tip shielding is significantly reduced (*e.g.*, Reference 63), and, since the crack front samples only few microstructural entities, this allows for a biased sampling of microstructurally weak paths. Because of this restriction in shielding and the biased microstructural sampling, fatigue-crack growth resistance in the presence of small cracks tends to be lowest.

## REFERENCES

1. Report of the AdHoc Committee on Air Force Aircraft Jet Engine Manufacturing and Production Processes, United States Air Force Scientific Advisory Board, SAF/AQOS: the Pentagon, Washington, DC, 1992.
2. B.A. Cowles: *Int. J. Fracture*, 1996, vol. 80, pp. 147-63.
3. J.C.I. Chang: Air Force Office of Scientific Research, Bolling AFB, Washington, DC, 1996.
4. T. Nicholas, J.R. Barber, and R.S. Bertke: *Exp. Mech.*, 1980, vol. 20, pp. 357-64.
5. *Fretting Fatigue*, European Structural Integrity Society Publication No. 18, R.B. Waterhouse and T.C. Lindley, eds., Mechanical Engineering Publications Ltd., London, 1994.
6. J.J. Kruzic, J.P. Campbell, and R.O. Ritchie: *Acta Mater.*, 1999, vol. 47, pp. 801-16.
7. G. Lütjering: *Mater. Sci. Eng.*, 1998, vol. A243, pp. 32-45.
8. A.W. Thompson: in *Fatigue Behavior of Titanium Alloys*, R.R. Boyer, D. Eylon, and G. Lütjering, eds., TMS, Warrendale, PA, 1999, pp. 23-30.
9. J.C. Williams and G. Lütjering: in *Titanium '80, Science and Technology*, H. Kimura and O. Izumi, eds., TMS-AIME, Warrendale, PA, 1981, vol. 1, pp. 671-81.
10. J.J. Lucas: in *Titanium Science and Technology*, R.I. Jaffee and H.M. Burte, eds., Plenum Press, New York, NY, 1973, vol. 3, pp. 2081-95.
11. M. Peters, A. Gysler, and G. Lütjering: *Metall. Trans. A*, 1984, vol. 15A, pp. 1597-1605.
12. G. Lütjering, J. Albrecht, and A. Gysler: in *Titanium '92: Science and Technology*, F.H. Froes and I. Caplan, eds., TMS, Warrendale, PA, 1993, pp. 1635-46.
13. C.W. Brown and M.A. Hicks: *Fatigue Eng. Mater. Struct.*, 1983, vol. 6, pp. 67-76.
14. J.A. Hines, J.O. Peters, and G. Lütjering: in *Fatigue Behavior of Titanium Alloys*, R.R. Boyer, D. Eylon, and G. Lütjering, eds., TMS, Warrendale, PA, 1999, pp. 15-22.
15. J.C. Chesnutt, A.W. Thompson, and J.C. Williams: in *Titanium '80, Science and Technology*, H. Kimura and O. Izumi, eds., TMS-AIME, Warrendale, PA, 1981, vol. 2, pp. 1875-82.
16. G.R. Yoder, L.A. Cooley, and T.W. Crooker: *Eng. Fract. Mech.*, 1983, vol. 17, pp. 185-88.
17. G.R. Yoder, L.A. Cooley, and T.W. Crooker: *Metall. Trans. A*, 1977, vol. 8A, pp. 1737-43.
18. K.S. Ravichandran: *Acta Mater.*, 1991, vol. 39, pp. 401-10.
19. P.E. Irving and C.J. Beevers: *Mater. Sci. Eng.*, 1974, vol. 14, pp. 229-38.
20. G.R. Yoder, L.A. Cooley, and T.W. Crooker: *Eng. Fract. Mech.*, 1979, vol. 11, pp. 805-16.
21. D. Taylor: *A Compendium of Fatigue Thresholds and Crack Growth Rates*, EMAS Ltd., Warley, United Kingdom, 1985.
22. J.K. Gregory: in *Handbook of Fatigue Crack Propagation in Metallic Structures*, A. Carpinteri, ed., Elsevier Science B.V., Amsterdam, The Netherlands, 1994, pp. 281-21.
23. M.R. Bache, W.J. Evans, and M. McElhone: *Mater. Sci. Eng.*, 1997, vols. A234-A236, pp. 918-22.
24. J.P. Thomas: *Scripta Mater.*, 1998, vol. 39, pp. 1647-52.
25. J.W. Sheldon, K.R. Bain, and J.K. Donald: *Int. J. Fatigue*, 1999, vol. 21, pp. 733-41.
26. Y.N. Lenets and R.S. Bellows: *Int. J. Fatigue*, 2000, vol. 22, pp. 521-29.
27. R.O. Ritchie: in *Proc. ASME Aerospace Division*, J.C.I. Chang, J. Coulter, D. Brei, D. Martinez, W. Hg, and P.P. Freidmann, eds., ASME, New York, NY, 1996, AMD vol. 52, pp. 321-33.
28. D. Eylon: *Summary of Available Information on the Processing of the Ti-6Al-4V HCF/LCF Program Plates*, University of Dayton Report, Dayton, OH, 1998.
29. J.C. Chesnutt, A.W. Thompson, and J.C. Williams: *Technical Report No. AFML-TR-78-68*, Air Force Materials Laboratory, Wright-Patterson Air Force Base, OH, 1978.
30. R.O. Ritchie, D.L. Davidson, B.L. Boyce, J.P. Campbell, and O. Roder: *Fat. Fract. Eng. Mater. Struct.*, 1999, vol. 22, pp. 621-31.
31. B.L. Boyce and R.O. Ritchie: *Eng. Fract. Mech.*, 2001, vol. 68, pp. 129-47.
32. H. Döker, V. Bachmann, and G. Marci: in *Fatigue Thresholds*, J. Bäcklund, A.F. Blom and C.J. Beevers, eds., EMAS, Warley, United Kingdom, 1982, vol. 1, pp. 45-58.
33. W.A. Herman, R.W. Hertzberg, and R. Jaccard: *Fatigue Fract. Eng. Mater. Struct.*, 1988, vol. 11, pp. 303-20.
34. H.R. Mayer and S.E. Stanzl-Tschegg: BOKU, Vienna, Austria, unpublished research, 1998.
35. R.O. Ritchie and W. Yu: in *Small Fatigue Cracks*, R.O. Ritchie and J. Lankford, eds., TMS-AIME, Warrendale, PA, 1986, pp. 167-89.
36. P. Lukáš: *Eng. Fract. Mech.*, 1987, vol. 26, pp. 471-73.
37. J.C. Newmann and I.S. Raju: *Eng. Fract. Mech.*, 1981, vol. 15, pp. 185-92.
38. K.S. Ravichandran: *Metall. Mater. Trans. A*, 1997, vol. 28A, pp. 149-56.
39. K.S. Ravichandran and J.M. Larsen: *Metall. Mater. Trans. A*, 1997, vol. 28A, pp. 157-69.
40. J.O. Peters, O. Roder, B.L. Boyce, A.W. Thompson, and R.O. Ritchie: *Metall. Mater. Trans. A*, 2000, vol. 31A, pp. 1571-83.
41. B.L. Boyce: Ph.D. Thesis, R.O. Ritchie, advisor, University of California, Berkeley, CA, Dec. 2001.
42. M.Y. He and J.W. Hutchinson: *J. Appl. Mech.*, 2000, vol. 67, pp. 207-09.
43. J.P. Campbell and R.O. Ritchie: *Eng. Fract. Mech.*, 2000, vol. 67, pp. 209-27.
44. J.P. Campbell and R.O. Ritchie: *Eng. Fract. Mech.*, 2000, vol. 67, pp. 229-49.
45. J.P. Campbell and R.O. Ritchie: *Metall. Mater. Trans. A*, 2001, vol. 32A, pp. 497-503.
46. M.Y. He and J.W. Hutchinson: *Eng. Fract. Mech.*, 2000, vol. 65, pp. 1-14.
47. J.O. Peters and R.O. Ritchie: *Eng. Fract. Mech.*, 2000, vol. 67, pp. 193-207.
48. J.O. Peters and R.O. Ritchie: *Int. J. Fatigue*, 2001, in press.
49. B.L. Boyce, X. Chen, J.W. Hutchinson, and R.O. Ritchie: *Mech. Mater.*, 2001, vol. 33, pp. 441-54.
50. D.L. Davidson and D. Eylon: *Metall. Trans. A*, 1980, vol. 11A, pp. 837-43.

51. M.R. Bache, W.J. Evans, and H.M. Davies: *J. Mater. Sci.*, 1997, vol. 32, pp. 3435-42.
52. Y. Murakami, T. Nomoto, and T. Ueda: *Fatigue Fract. Eng. Mater. Struct.*, 1999, vol. 22, pp. 581-90.
53. L. Wagner and G. Lütjering: *Proc. 2nd Int. Conf. Shot Peening*, H.O. Fuchs, ed., American Shot Peening Society, Paramus, NJ, 1984, pp. 194-200.
54. S. Adachi, L. Wagner, and G. Lütjering: *Titanium Science and Technology. Proc. 5th Int. Conf. on Titanium*, G. Lütjering, V. Zwickler, and W. Bunk, eds., DGM, Oberursel, Germany, 1985, p. 2139.
55. W.J. Evans and M.R. Bache: *Int. J. Fatigue*, 1994, vol. 16, pp. 443-52.
56. G. Marci: in *Fatigue '96, Proc. 6th Int. Congr. on Fatigue*, G. Lütjering and H. Nowack, eds., Pergamon Press, Oxford, United Kingdom, 1996, vol. 1, p. 493.
57. R.J.H. Wanhill: *Corrosion-NACE*, 1974, vol. 30, pp. 28-35.
58. D.B. Dawson and R.M.N. Pelloux, *Metall. Trans.*, 1974, vol. 5, pp. 723-31.
59. M.D. Halliday and C.J. Beevers: *J. Testing Eval.*, 1981, vol. 9, pp. 195-201.
60. K.S. Ravichandran: *Scripta Metall. Mater.*, 1990, vol. 24, pp. 1559-63.
61. T. Ogawa, K. Tokaji, and K. Ohya: *Fatigue Fract. Eng. Mater. Struct.*, 1993, vol. 16, pp. 973-82.
62. V. Sinha, C. Mercer, and W.O. Soboyejo: *Mater. Sci. Eng.*, 2000, vol. A287, pp. 30-42.
63. S. Suresh and R.O. Ritchie: *Int. Met. Rev.*, 1984, vol. 29, pp. 445-76.
64. M.A. Pustejovsky: *Eng. Fract. Mech.*, 1979, vol. 11(1), pp. 9-15.
65. M.A. Pustejovsky: *Eng. Fract. Mech.*, 1979, vol. 11(1), pp. 17-31.
66. H. Gao, M.W. Brown, and K.J. Miller: *Fat. Eng. Mater. Struct.*, 1982, vol. 5, pp. 1-17.
67. J. Tong, J.R. Yates, and M.W. Brown: *Fat. Eng. Mater. Struct.*, 1994, vol. 17, pp. 829-38.
68. H. Nayeib-Hashemi, F.A. McClintock, and R.O. Ritchie: *Metall. Trans. A*, 1982, vol. 13A, pp. 2197-204.
69. M.C. Smith and R.A. Smith: in *Basic Question in Fatigue: vol. 1, ASTM STP 924*, J.T. Fong and R.J. Fields, eds., ASTM, Philadelphia, PA, 1988, pp. 260-80.
70. E.K. Tschegg: *Acta Metall.*, 1983, vol. 31, pp. 1323-30.
71. J.O. Peters, B.L. Boyce, X. Chen, J.M. McNaney, J.W. Hutchinson, and R.O. Ritchie: *Proc. Int. Conf. Fatigue in the Very High Cycle Regime*, S. Stanzl-Tschegg and H. Mayer, eds., BOKU, Vienna, Austria, 2001, pp. 129-40.
72. H. Kitagawa and S. Takahashi: *Proc. 2nd Intl. Conf. on Mechanical Behavior of Materials*, ASM, Metals Park, OH, 1976, pp. 627-31.
73. M.H. El Haddad, T.H. Topper, and K.N. Smith: *Eng. Fract. Mech.*, 1979, vol. 11, pp. 573-84.
74. R.O. Ritchie and J. Lankford: *Mater. Sci. Eng.*, 1986, vol. 84, pp. 11-16.

## ROLE OF MODE-MIXITY ON HIGH-CYCLE FATIGUE THRESHOLDS IN Ti-6Al-4V

- J.P. Campbell and R.O. Ritchie, "Mixed-Mode, High-Cycle Fatigue-Crack Growth Thresholds in Ti-6Al-4V: I – A Comparison of Large and Small Crack Behavior", *Eng. Fract. Mech.*, vol. 67, Oct. 2000, pp. 209-27.
- J.P. Campbell, R.O. Ritchie, "Mixed-Mode High-Cycle Fatigue-Crack Growth Thresholds in Ti-6Al-4V: II - Quantification of Crack-Tip Shielding", *Eng. Fract. Mech.*, vol. 67, 2000, pp. 227-49.
- J.P. Campbell and R.O. Ritchie, "High-Cycle Fatigue in Bimodal and Lamellar Ti-6Al-4V: Mixed-Mode Crack-Growth Thresholds", *Metall. Mater. Trans. A*, vol. 32A, 2001, pp. 497-503.
- R.K. Nalla, J.P. Campbell and R.O. Ritchie, "Effects of Microstructure on Mixed-Mode, High-Cycle Fatigue Crack Growth Thresholds in Ti-6Al-4V", *Fatigue Fract. Engin. Mater. Struct.*, vol. 25, 2002, pp. 587-606.
- R.K. Nalla, J.P. Campbell, and R.O. Ritchie, "Mixed-Mode High-Cycle Fatigue Crack Growth Thresholds in Ti-6Al-4V: Role of Small Cracks", *Int. J. Fat.*, 2002, in press.



PERGAMON

Engineering Fracture Mechanics 67 (2000) 209–227

Engineering  
Fracture  
Mechanics

www.elsevier.com/locate/engfracmech

# Mixed-mode, high-cycle fatigue-crack growth thresholds in Ti–6Al–4V

## I. A comparison of large- and short-crack behavior

J.P. Campbell, R.O. Ritchie \*

Department of Materials Science and Mineral Engineering, University of California, 463 Evans Hall, Berkeley, CA 94720-1760, USA

Received 27 December 1999; received in revised form 4 May 2000; accepted 11 May 2000

### Abstract

Mixed-mode, high-cycle fatigue-crack growth thresholds are reported for through-thickness cracks (large compared to microstructural dimensions) in a Ti–6Al–4V turbine blade alloy with a bimodal microstructure. Specifically, the effect of combined mode I and mode II loading, over a range of phase angles  $\beta = \tan^{-1}(\Delta K_{II}/\Delta K_I)$  from  $0^\circ$  to  $82^\circ$  ( $\Delta K_{II}/\Delta K_I \sim 0-7$ ), is examined for load ratios (ratio of minimum to maximum loads) ranging from  $R = 0.1$  to  $0.8$  at a cyclic loading frequency of  $1000$  Hz in ambient temperature air. Although the general trend for the mode I stress-intensity range at the threshold,  $\Delta K_{I,TH}$ , is to decrease with increasing mode mixity,  $\Delta K_{II}/\Delta K_I$ , and load ratio,  $R$ , if the crack-driving force is alternatively characterized in terms of the strain-energy release rate,  $\Delta G$ , incorporating contributions from both the applied tensile and shear loading, the threshold fatigue-crack growth resistance increases significantly with the applied ratio of  $\Delta K_{II}/\Delta K_I$ . The pure mode I threshold, in terms of  $\Delta G_{TH}$ , is observed to be a lower bound (worst case) with respect to mixed-mode (I + II) behavior. These results are compared with mixed-mode fatigue thresholds for short cracks, where the precrack wake has been machined to within  $\sim 200$   $\mu\text{m}$  of the precrack tip. For such short cracks, wherein the magnitude of crack-tip shielding which can develop is greatly reduced, the measured mixed-mode fatigue-crack growth thresholds are observed to be markedly lower. Moreover, the dependence of the mixed-mode fatigue-crack growth resistance on the applied phase angle is significantly reduced. Comparison of the large- and short-crack data suggests that the increase in the large-crack fatigue threshold,  $\Delta G_{TH}$ , with an increasing mode mixity ( $\Delta K_{II}/\Delta K_I$ ) is largely due to shielding from shear-induced crack-surface contact, which reduces the local crack-driving force actually experienced at the crack tip. Quantification of such shielding is described in Part II of this paper. © 2000 Elsevier Science Ltd. All rights reserved.

**Keywords:** High-cycle fatigue; Mixed mode; Fatigue thresholds; Load ratio effects; Short crack effects; Crack-tip shielding

\* Corresponding author. Tel.: +510-486-5798; fax: +510-486-4995.

E-mail address: roritchie@lbl.gov (R.O. Ritchie).

## 1. Introduction

One of the principal challenges currently associated with the safety and readiness of military aircraft fleets is the susceptibility of turbine engine components to failure from high-cycle fatigue (HCF), i.e., the rapid propagation of fatigue cracks under high frequency vibratory loading [1,2]. Such failures are extremely costly, leading to severe engine damage, loss of aircraft, and even loss of human life. Multiaxial loading conditions are known to exist at specific fatigue-critical locations within the turbine engine components, particularly in association with fretting fatigue in the blade dovetail/disk contact section [3]. For fatigue-crack growth in such situations, the resultant crack-driving force may be a combination of the influence of a mode I (tensile opening) stress-intensity range,  $\Delta K_I$ , as well as mode II (in-plane shear) and/or mode III (anti-plane shear) stress-intensity ranges,  $\Delta K_{II}$  and  $\Delta K_{III}$ , respectively. While the vast majority of the published fatigue-crack growth data is measured for mode I loading only, it has been observed that the superposition of cyclic shear ( $\Delta K_{II}$  or  $\Delta K_{III} > 0$ ) to cyclic tension can lower the mode I threshold stress-intensity range,  $\Delta K_I$ , below which crack growth is presumed dormant [4–12]. Recent studies in single crystal Ni-based superalloys show that this effect can be severe [13].

For the high-cycle fatigue of turbine engine alloys, it is clearly critical to quantify the effect of combined tension and shear loading on the fatigue-crack growth threshold, as the extremely high cyclic loading frequencies ( $\sim 1$ – $2$  kHz) and correspondingly short times to failure may necessitate a threshold-based design methodology [14]. Given this, as well as the knowledge of the existence of such loading conditions in fatigue-critical components, the paucity of mixed-mode fatigue-crack propagation data in aerospace titanium alloys [5–7] is of some concern. Of further concern is the almost total lack of information on mixed-mode thresholds for cracks of limited dimensions, i.e., compared to the scale of microstructure or extent of crack-tip shielding; extensive results for behavior under nominal mode I loading indicate that the fatigue thresholds for the so-called small or short cracks can be significantly smaller than those measured for corresponding large cracks [15–22].<sup>1</sup>

Accordingly, in the present work, mixed-mode fatigue-crack growth thresholds for combined mode I + II loading are examined in a Ti–6Al–4V alloy with a typical turbine blade microstructure. The influence of various degrees of mode-mixity, ranging from  $\Delta K_{II}/\Delta K_I = 0$  (mode I loading) to  $\sim 7$ , on the crack-growth threshold condition is investigated for loading conditions characteristic of turbine engine HCF, i.e. high mean stresses (up to load ratios of  $R = 0.8$ ) and high cyclic loading frequencies (1000 Hz). Experiments are performed using an asymmetric bend geometry for both large ( $> 4$  mm) and short ( $\sim 150$ – $250$   $\mu\text{m}$ ) cracks; the latter is achieved by machining out the wake of larger cracks to within  $\sim 200$   $\mu\text{m}$  of the crack tip. Since both types of flaws are through thickness ( $\sim 5$  mm) and large compared to microstructural size scales (i.e., the grain size) in this dimension, in both cases, their crack fronts are able to “sample” many microstructural entities; such flaws may be termed “continuum-sized” cracks. However, the capacity for crack-tip shielding is significantly reduced with the short crack due to the restricted crack wake in which fracture surface contact mechanisms can operate.

It is found that, although the value of the mode I stress-intensity range at threshold,  $\Delta K_{I,TH}$ , can be *decreased* for a sufficiently high ratio  $\Delta K_{II}/\Delta K_I$ , provided the mixed-mode crack-driving force is characterized in terms of the strain-energy release rate,  $\Delta G_{TH}$ , (incorporating both tensile and shear contributions), the (large-crack) fatigue-crack growth threshold actually *increases* with increasing mode-mixity. Thus, the mode I fatigue-crack growth threshold, *expressed in terms of*  $\Delta G_{TH}$ , is the worst-case (at least for continuum-sized cracks). This strong dependence of  $\Delta G_{TH}$  on mode mixity is found to be reduced for short cracks, primarily due to a reduced role of crack-tip shielding; moreover, the magnitude of the  $\Delta G_{TH}$

<sup>1</sup> A brief description of the salient distinctions between large, short and small fatigue cracks can be found in Appendix A.

threshold for such short cracks is found to be lower than that exhibited by the large cracks for all values of  $\Delta K_{II}/\Delta K_I$  studied.

## 2. Materials and experimental methods

### 2.1. Material

The material investigated was a forged Ti–6Al–4V turbine engine alloy received with a bimodal microstructure<sup>2</sup> consisting of nearly equiaxed primary  $\alpha$  and lamellar  $\alpha + \beta$  colonies (Fig. 1). This alloy was processed specifically for the joint military–industry–university HCF program by Teledyne Titanium as mill-annealed, forging bar-stock material (diameter: 63.5 mm); its chemical composition is given in Table 1. The  $\beta$ -transus temperature, measured using differential thermal analysis, ranged from 990°C to 1005°C.

The bar stock was sectioned into 400 mm long segments, preheated to 940°C (30 min), and forged into 400 × 150 × 20 mm<sup>3</sup> plates. The forged plates were then solution treated at 925°C (1 h) in air, followed by fan air cooling, and a subsequent stabilization was performed at 700°C (2 h) in vacuo. Based on the measurements in each of the four random forging locations [24], the microstructure was found to consist of 64.1 vol.% (standard deviation: 6.6%) primary  $\alpha$  with an average grain diameter of  $\sim 20 \mu\text{m}$  (slightly elongated in the longitudinal ( $L$ ) direction) and lamellar  $\alpha + \beta$  colonies (Fig. 1); the lamellar spacing (center-to-center

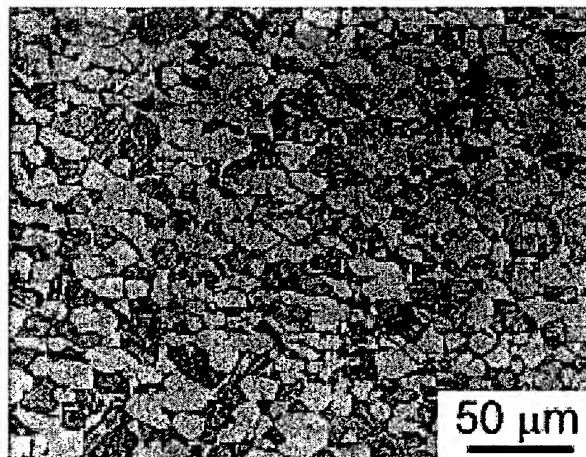


Fig. 1. Optical photomicrograph of the bimodal (STOA) Ti–6Al–4V. The bimodal structure consists of nearly equiaxed grains of primary  $\alpha$  phase ( $\sim 20 \mu\text{m}$  in diameter) and regions of lamellar  $\alpha + \beta$ . Etchant: aqueous 3.5%  $\text{HNO}_3$ , and 5%  $\text{HF}$ .

Table 1  
Chemical composition of Ti–6Al–4V bar stock (in wt.%) [23]

Bar location	Ti	Al	V	Fe	O	N	H
Top	Balance	6.27	4.19	0.20	0.18	0.012	0.0041
Bottom	Balance	6.32	4.15	0.18	0.19	0.014	0.0041

<sup>2</sup> This microstructural condition is often referred to as solution treated and overaged (STOA) by the HCF community.

distance for the  $\beta$  phase) was measured from phase contrast (backscattered electron imaging) scanning electron micrographs to be  $\sim 1 \mu\text{m}$ .

Tensile tests, conducted at initial strain rates of  $5 \times 10^{-4} \text{ s}^{-1}$  in the longitudinal ( $L$ ) orientation [23], indicated a yield strength of 930 MPa (range: 926–935 MPa) and an ultimate tensile strength of 978 MPa (range: 970–985 MPa).

## 2.2. Experimental methods

Thresholds for large fatigue cracks were measured using the asymmetric four-point bend (AFPB) specimen [4,25–27]. For this test geometry, the bending moment,  $M_z$ , varies linearly between the inner loading points, while the shear force,  $F_{xy}$ , is constant in this region (Fig. 2). Thus, a cracked sample may be subjected to loading conditions ranging from pure mode II to mode I dominant (i.e., a small value of  $\Delta K_{II}/\Delta K_I$ ) by careful control of the distance by which the crack is offset from the load line,  $s$ . Pure mode I tests were conducted using standard, symmetric four-point bend. Inner and outer loading spans (from load line to loading point) of 12.7 and 25.4 mm, respectively, were utilized. A high pressure  $\text{MoS}_2$  grease was applied at the loading points to minimize the effects of friction. Mixed-mode loading conditions were quantified both in terms of the ratio of  $\Delta K_{II}/\Delta K_I$ , which was varied from 0 (pure mode I) to 7.1, and the phase angle,  $\beta = \tan^{-1}(\Delta K_{II}/\Delta K_I)$ , which correspondingly varied from  $0^\circ$  to  $82^\circ$ . Positive load ratios ( $R = K_{\min}/K_{\max}$ ) were varied between 0.1 and 0.8.

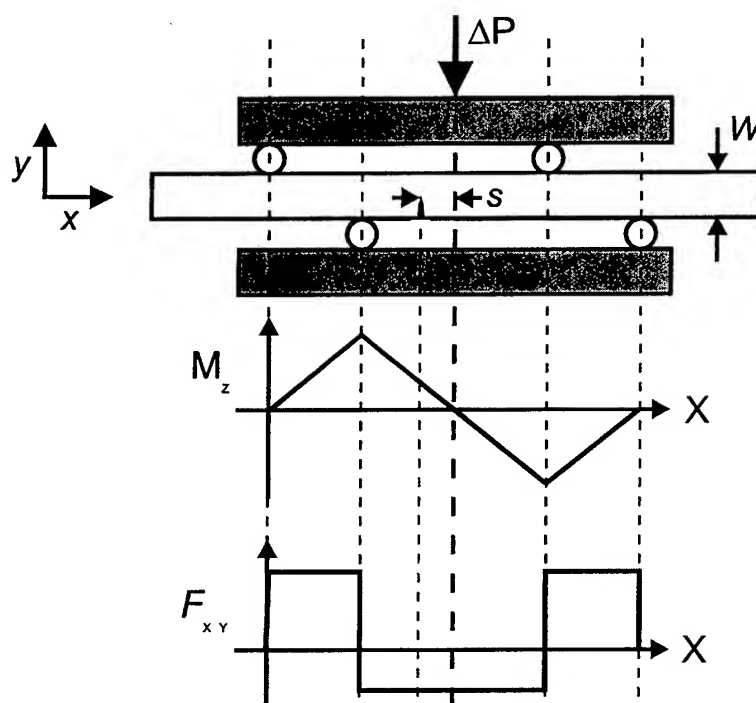


Fig. 2. The asymmetric, four-point-bend, crack-growth sample and the associated shear force,  $F_{xy}$ , and bending moment,  $M_z$ , diagrams are shown. When the crack is offset from the load line by an amount  $s$ , the value of  $s/W$  (where  $W$  is the beam height) dictates the ratio of  $\Delta K_{II}$  to  $\Delta K_I$ .



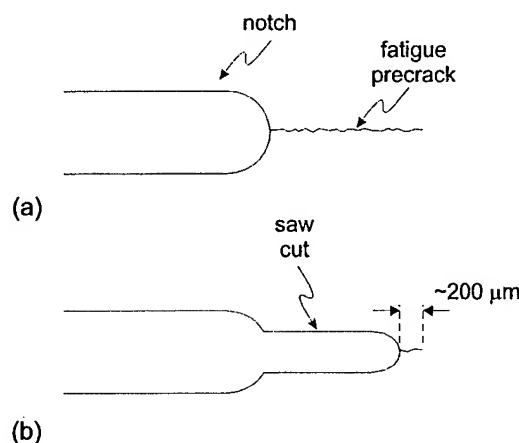


Fig. 3. The first step of fatigue precracking for short-crack threshold measurements was conducted in the same manner as for large-crack threshold measurements, as shown in (a). Following this procedure, the precrack wake was machined out using a slow speed diamond saw (b) to within  $\sim 200 \mu\text{m}$  of the precrack tip. Mixed-mode thresholds for short fatigue cracks were then measured by the same methods employed for large fatigue cracks.

Because of the potentially strong influence on mixed-mode crack-growth behavior of precracking technique [9] and crack-wake shielding effects [4,28–31], a very specific fatigue precracking regimen was employed to ensure a standard and reproducible precrack condition for all the threshold measurements. Fatigue precracks were grown, using computer-automated stress-intensity control, from a 2 mm deep electrical discharge machined notch under mode I loading in four-point bending, with a load ratio,  $R = K_{\min}/K_{\max}$ , of 0.1, and a cyclic loading frequency of 125 Hz (sine wave). Loads were shed at a  $K$ -gradient,  $^3 C$ , of  $-0.15 \text{ mm}^{-1}$  such that a final precrack length of  $4.50 \pm 0.25 \text{ mm}$  was achieved at a near threshold stress intensity range of  $4.8 \pm 0.3 \text{ MPa } \sqrt{\text{m}}$ .

To determine fatigue thresholds, tests were performed on an MTS servo-hydraulic high-frequency testing machine incorporating a voice-coil servovalve [32]. AFBP samples were loaded with the precrack tip offset from the load line to achieve the desired ratio  $\Delta K_{II}/\Delta K_I$ . The necessary offset and values of  $\Delta K_I$  and  $\Delta K_{II}$  corresponding to the applied load amplitude were determined using a recently updated stress-intensity solution for the AFBP geometry by He and Hutchinson [26]. Samples were then subjected to two million cycles at 1000 Hz (sine wave). If no crack growth was observed (via an optical microscope),  $\Delta K_I$  or  $\Delta K_{II}$  was increased by approximately  $0.25 \text{ MPa } \sqrt{\text{m}}$  and the test was repeated. In this way, the threshold for the onset of crack growth (defined as crack growth rates less than  $10^{-11} \text{ m/cycle}$ ) was measured as a “growth/no growth” set of loading conditions bounding the true threshold.

Fatigue precracks for short-crack threshold measurements were generated as described above. Following this procedure, the precrack wake was machined out using a slow speed diamond saw to within  $\sim 200 \mu\text{m}$  of the precrack tip, as illustrated in Fig. 3. This technique significantly restricts the degree of crack wake contact during subsequent mixed-mode loading and, hence, markedly reduces the magnitude of crack-tip shielding. Mixed-mode fatigue-crack growth thresholds were then measured by the same methods employed for large fatigue cracks.

<sup>3</sup> The  $K$ -gradient,  $C$ , is defined by the equation  $\Delta K_0 = \Delta K_i \exp(C(a_0 - a_i))$ , where subscripts “0” and “i” indicate current and initial parameter values.

### 3. Results and discussion

#### 3.1. Mixed-mode threshold envelopes

Mixed-mode fatigue-crack growth threshold envelopes, plotted as the mode II stress-intensity range at threshold,  $\Delta K_{II,TH}$ , as a function of the corresponding mode I threshold,  $\Delta K_{I,TH}$ , are shown in Fig. 4. The thresholds for the onset of crack extension are presented for  $\Delta K_{II}/\Delta K_I$  values of 0, 0.5, 1.9 and 7.1 ( $\beta = 0^\circ, 26^\circ, 62^\circ$  and  $82^\circ$ , respectively) at load ratios of 0.1, 0.5 and 0.8. Closed and open symbols represent the loading conditions that produced, respectively, no crack growth and crack growth; these loading conditions bound the true threshold for the onset of crack extension. An error analysis for these threshold data is presented in Appendix B; uncertainty in the position of the crack with respect to the mechanical test frame load line and the associated uncertainty in  $\Delta K_{I,TH}$  and the applied phase angle are considered.

Comparison of the three load ratios investigated reveals that the fatigue-crack growth resistance is degraded by increasing  $R$ , as evidenced by a shifting of the threshold envelope towards lower values of  $\Delta K_{I,TH}$  and  $\Delta K_{II,TH}$ . These findings are consistent with the previous reports regarding the influence of load ratio on mixed-mode fatigue-crack growth thresholds in other material systems [4,10]. Further discussion of the influence of load ratio on mixed-mode thresholds is presented below.

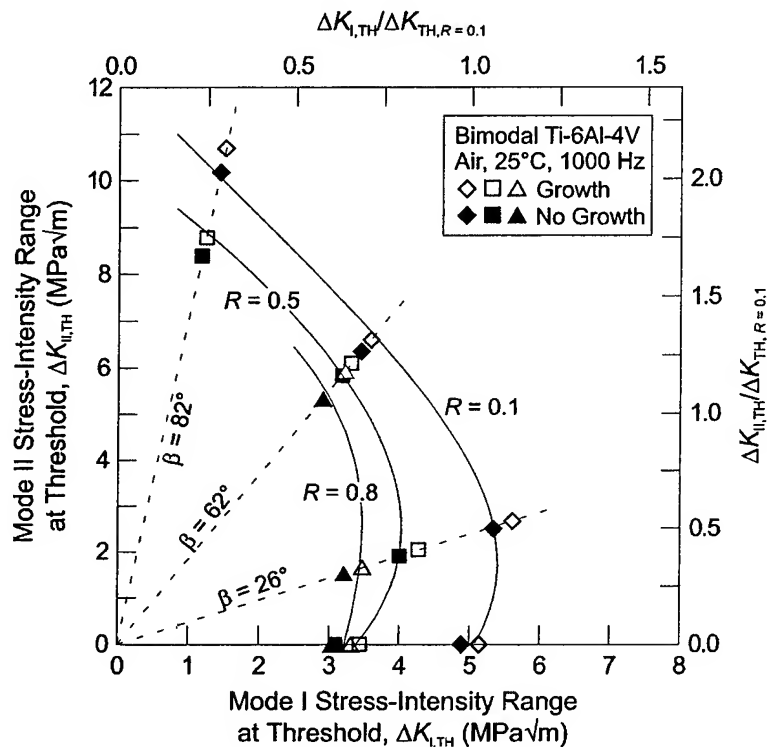


Fig. 4. Mixed-mode fatigue-crack growth threshold envelopes for bimodal Ti-6Al-4V at load ratios,  $R$ , of 0.1, 0.5 and 0.8 and a cyclic loading frequency of 1000 Hz in ambient temperature air. Closed and open symbols represent the loading conditions that produced, respectively, no crack growth and crack growth; these loading conditions bound the true threshold for the onset of crack extension. On the upper and right-hand axes,  $\Delta K_{I,TH}$  and  $\Delta K_{II,TH}$  are normalized by the pure mode I threshold at  $R = 0.1$ ,  $\Delta K_{TH,R=0.1}$ .

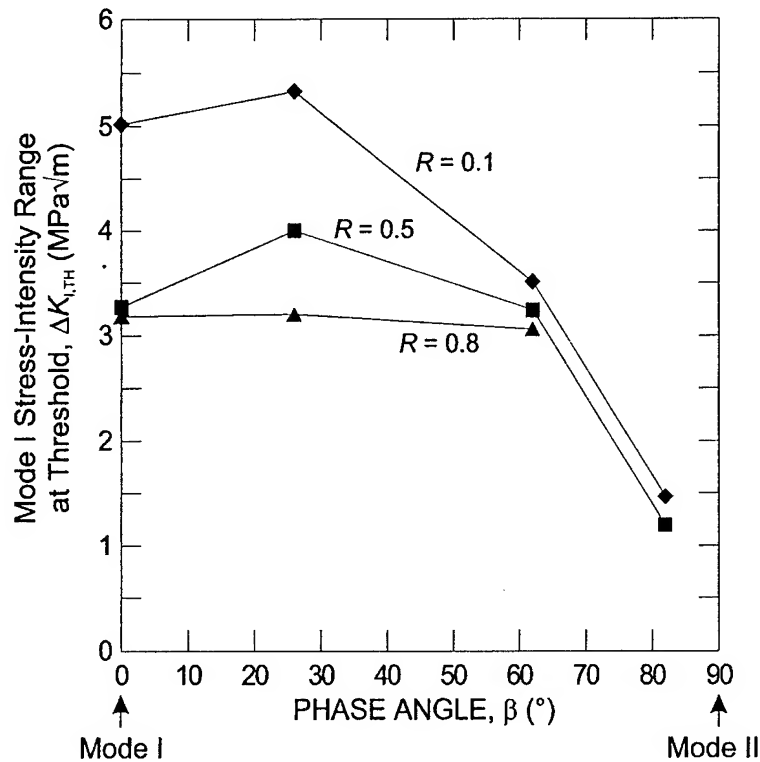


Fig. 5. For the mixed-mode fatigue-crack growth threshold data presented in Fig. 4, the mode I stress-intensity range at threshold,  $\Delta K_{I,TH}$ , is plotted as a function of the applied phase angle,  $\beta = \tan^{-1}(\Delta K_{II}/\Delta K_I)$ .  $\Delta K_{I,TH}$  is observed to increase slightly as  $\beta$  increases from  $0^\circ$  to  $26^\circ$  ( $\Delta K_{II}/\Delta K_I = 0$  and  $0.5$ , respectively) and then decrease for  $\beta = 62^\circ$  and  $82^\circ$  ( $\Delta K_{II}/\Delta K_I = 1.9$  and  $7.1$ ).

While the value of the mode I threshold,  $\Delta K_{I,TH}$ , is substantially reduced at high phase angles, a conspicuous feature of the mixed-mode threshold envelopes in Fig. 4 is that the value of  $\Delta K_{I,TH}$  does not necessarily decrease monotonically with increasing mode-mixity. Its value is actually nominally unchanged (indeed, it is slightly increased) as  $\beta$  is increased from  $0^\circ$  to  $26^\circ$  ( $\Delta K_{II}/\Delta K_I = 0$  and  $0.5$ , respectively), for all load ratios investigated. This variation of  $\Delta K_{I,TH}$  with phase angle,  $\beta$ , (plotted in Fig. 5) gives rise to the appearance of a “nose” in the threshold envelope. Such a feature in the mixed-mode fatigue-crack growth threshold envelope has not been previously reported in the literature and is contrary to the previous reports of fatigue-crack growth behavior in other material systems [5,8,11,33–35], where the mode I threshold,  $\Delta K_{I,TH}$ , has been reported to decrease monotonically due to the superposition of shear loading. Furthermore, for the present data, as  $\beta$  is increased to  $62^\circ$  ( $\Delta K_{II}/\Delta K_I = 1.9$ ), the value of  $\Delta K_{I,TH}$  does not necessarily decrease substantially relative to its value at  $\beta = 0^\circ$ , particularly at  $R = 0.5$  and  $0.8$ . For  $\beta = 82^\circ$  ( $\Delta K_{II}/\Delta K_I = 7.1$ ), however, the mode I threshold stress-intensity range does decrease substantially. As discussed in detail in Part II [36], quantification of crack-tip shielding with respect to the applied mode I stress-intensity range indicates that this insensitivity of  $\Delta K_{I,TH}$  to superimposed shear loading can be attributed largely to a shear-induced enhancement of mode I fatigue-crack closure.

### 3.2. Mixed-mode crack path

Contrary to the previous reports of transient self-similar crack extension during mixed-mode loading in Ti-6Al-4V [5] and other material systems [4,37], such coplanar crack extension was not observed in the

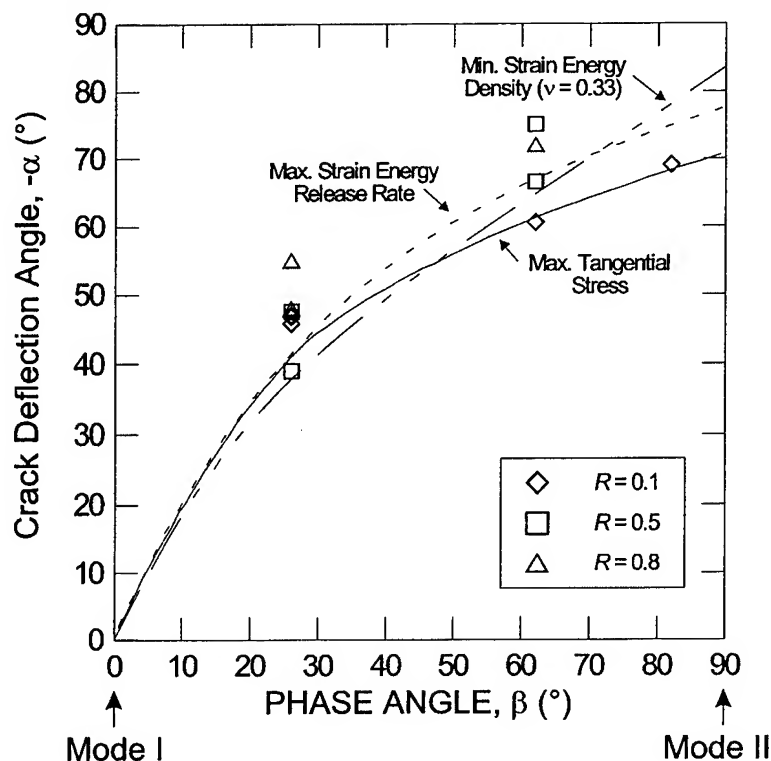


Fig. 6. Measured crack deflection angles,  $\alpha$ , are plotted as a function of the applied phase angle,  $\beta$ , for  $R = 0.1, 0.5$  and  $0.8$ . These data are compared with the crack deflection angles predicted by the three most prominent theories describing crack propagation under mixed-mode loading conditions: the maximum tangential stress criterion [38], the minimum strain energy density criterion [39], and the maximum strain energy release rate criterion [40].

present study. In all cases, the onset of crack propagation was deflected with respect to the precrack orientation. In Fig. 6, the measured crack deflection angles,  $\alpha$ , are plotted as a function of the applied phase angle,  $\beta$ , for  $R = 0.1, 0.5$  and  $0.8$ . Note that the length of the deflected cracks used to identify the crack deflection angles were large compared to the microstructural size scales, i.e.,  $\sim 25$  grain diameters. These data are compared with the crack deflection angles predicted by the three most prominent theories describing crack propagation under mixed-mode loading conditions: the maximum tangential stress criterion [38], the minimum strain energy density criterion [39], and the maximum strain energy release rate criterion [40]. Despite the experimental scatter in these data, the present results are generally consistent with any one of these theories, although there is a slight trend of higher crack deflection angles than that predicted by the theory. It has been reported previously for BS4360 50D structural steel [10] that the angle of crack deflection due to an applied mixed-mode loading is not a function of load ratio; the present results do not refute this finding.

### 3.3. Single-parameter characterization of the mixed-mode threshold

While it is instructive to examine the variation of fatigue-crack growth threshold as a function of mode mixity and load ratio using the threshold envelopes shown in Fig. 4, additional information can be obtained by replotting these same data using a single-parameter characterization of the mixed-mode, crack-driving

force which incorporates both  $\Delta K_I$  and  $\Delta K_{II}$ . In Fig. 7a, the mixed-mode fatigue thresholds are presented in terms of the range in strain energy release rate,  $\Delta G$ :<sup>4</sup>

$$\Delta G_{TH} = (\Delta K_{I,TH}^2 + \Delta K_{II,TH}^2)/E'. \quad (1)$$

Here,  $\Delta K_{I,TH}$  and  $\Delta K_{II,TH}$  are values of these parameters applied to the precrack tip,  $E' = E$  (the elastic modulus) for plane stress, and  $E' = E/(1 - \nu^2)$  for plane strain ( $\nu$  is Poisson's ratio). Alternatively, the results can be plotted in terms of an equivalent stress-intensity range,  $\Delta K_{eq}$  (Fig. 7b), where the equivalent (mixed-mode) stress-intensity threshold is given by

$$\Delta K_{eq,TH} = (\Delta G_{TH} E')^{1/2}. \quad (2)$$

Using this single-parameter characterization of the fatigue-crack growth resistance (Fig. 7), it is apparent that the crack-growth threshold,  $\Delta G_{TH}$  or  $\Delta K_{eq,TH}$ , increases monotonically with phase angle,  $\beta$ , for each load ratio investigated. For the highest phase angles investigated ( $\beta = 82^\circ$  for  $R = 0.1$  and  $0.5$  and  $\beta = 62^\circ$  for  $R = 0.8$ ),  $\Delta G_{TH}$  is 4.4, 7.0 and 4.1 times the mode I threshold value, respectively, for  $R = 0.1$ ,  $0.5$  and  $0.8$ . From the perspective of high-cycle fatigue in turbine engine components, the results presented in Fig. 7 indicate that for bimodal Ti-6Al-4V, the mode I  $\Delta G_{TH}$  fatigue threshold (measured at the appropriate load ratio) represents the worst-case condition for all phase angles measured. Thus, the presence of mixed-mode loading does not preclude the application of a threshold-based design methodology. In fact, a conservative estimate of the mixed-mode threshold can be attained simply by expressing the pure mode I threshold in terms of  $\Delta G$ . Alternatively, in terms of stress intensities, the lower-bound, mixed-mode threshold condition can be stated as the equivalent stress-intensity range equal to the mode I threshold  $\Delta K$  measured under pure mode I loading conditions, i.e.,  $\Delta K_{eq,TH} = \Delta K_{I,TH}$  at  $\beta = 0^\circ$ . Other examples of the crack-growth resistance increasing with increasing mode-mixity have been reported for monotonic fracture at interfaces [41,42], cyclic-loading induced delamination of Cu/Sn-Pb solder joints [43], and the fatigue of dual-phase steels [11].

### 3.4. Influence of load ratio

Although the influence of load ratio has been noted above with reference to the mixed-mode threshold envelopes shown in Fig. 4, the relationship between the mixed-mode threshold and  $R$  for each phase angle investigated can be more clearly observed in Fig. 8, where  $\Delta G_{TH}$  is plotted as a function of  $R$  for phase angles of  $\beta = 0^\circ$ ,  $26^\circ$ ,  $62^\circ$  and  $82^\circ$  ( $\Delta K_{II}/\Delta K_I = 0$ ,  $0.5$ ,  $1.9$  and  $7.1$ , respectively). For each value of  $\beta$ , the fatigue-crack growth threshold decreases as load ratio increases. For the case of mode I loading, a transition is observed between a region where  $\Delta G_{TH}$  is relatively strongly dependent on load ratio ( $R < 0.5$ ) and a region of significantly reduced load ratio dependence ( $R > 0.5$ ); this behavior is consistent with the model developed by Schmidt and Paris [44] to describe the variation of the mode I fatigue threshold with load ratio. On the assumption that the stress intensity for crack closure,  $K_{cl}$ , and the effective (near-tip) threshold stress-intensity range,  $\Delta K_{eff,TH}$ , are both independent of  $R$ , this model predicts that the  $\Delta K_{I,TH}$  threshold should be constant with  $R$  above a critical load ratio where  $K_{min}$  first exceeds  $K_{cl}$  (such that closure effects are minimal). Indeed, this relationship between the mode I fatigue-crack growth threshold and  $R$  has been documented previously for the same bimodal Ti-6Al-4V investigated in this study [14,24,25], and these findings were consistent with the current results.

<sup>4</sup> It should be noted that  $\Delta G$  defined this way is not exactly equal to  $G_{max} - G_{min}$ , where  $G_{max}$  and  $G_{min}$  are, respectively, the values of  $G$  determined at the maximum and minimum loads of the fatigue cycle.

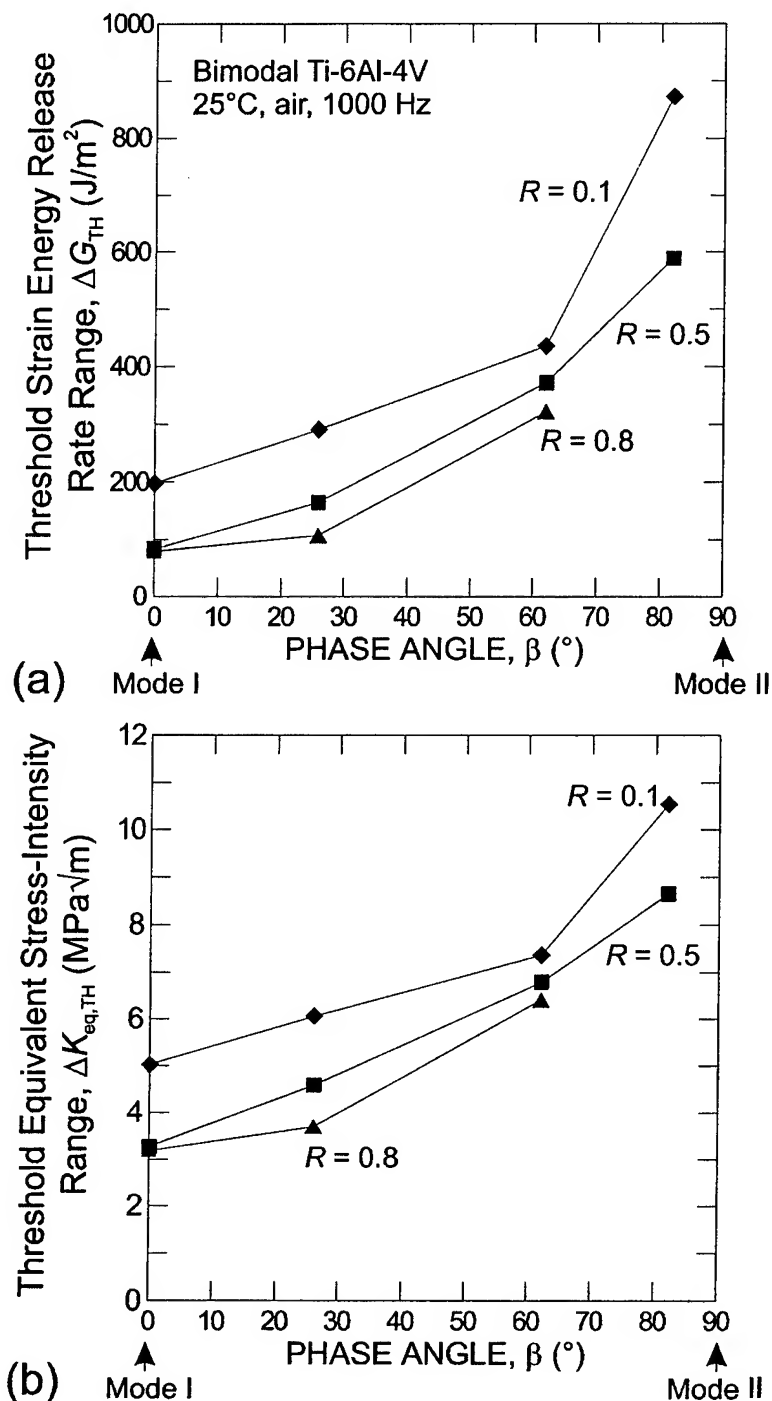


Fig. 7. Mixed-mode fatigue-crack growth thresholds in bimodal Ti-6Al-4V are plotted in terms of (a) the range in strain energy release rate at threshold,  $\Delta G_{TH}$ , and (b) the equivalent stress-intensity range,  $\Delta K_{eq,TH} = (\Delta G_{TH} E')^{1/2}$ , as a function of the applied phase angle,  $\beta = \tan^{-1}(\Delta K_{II}/\Delta K_I)$ , for load ratios of 0.1, 0.5 and 0.8.  $\Delta G_{TH}$  is observed to increase substantially with  $\beta$ .

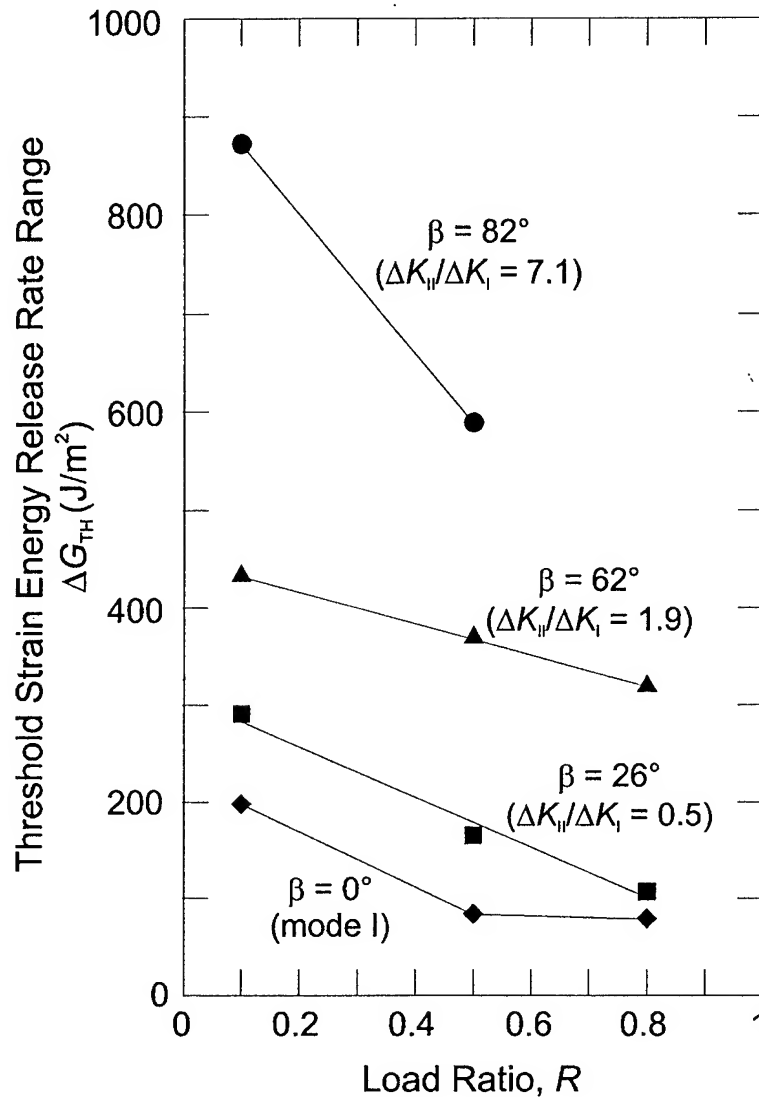


Fig. 8. The threshold range in strain energy release rate,  $\Delta G_{TH}$ , is plotted as a function of load ratio,  $R$ , for  $\beta = 0^\circ$ ,  $26^\circ$ ,  $62^\circ$  and  $82^\circ$  ( $\Delta K_{II}/\Delta K_I = 0$ ,  $0.5$ ,  $1.9$  and  $7.1$ , respectively). For each value of  $\beta$ , the fatigue-crack growth threshold decreases as load ratio increases.

For the mixed-mode loading conditions investigated ( $\beta = 26^\circ$ ,  $62^\circ$ , and  $82^\circ$ ), the relationship between  $\Delta G_{TH}$  and  $R$  is distinctly different from the behavior exhibited for mode I loading ( $\beta = 0^\circ$ ). Specifically, the fatigue threshold is observed to decrease at a nearly constant rate with increasing load ratio, i.e., there is no transition between regimes of relatively strong and weak load ratio dependence. Quantification of mixed-mode crack-tip shielding (reported in Part II [36]) suggests that the absence of such a transition may be attributed to enhanced crack-tip shielding under mixed-mode loading (where shielding is not fully suppressed even at  $R = 0.8$ ). A constant rate of decrease of mixed-mode fatigue-crack growth thresholds with increasing  $R$  has previously been observed in BS4360 50D structural steel by Tong et al. [10]. However, in that study, the rate of decrease in the threshold was reported to be the same for all phase angles investigated

and equal to the initial slope of the mode I threshold versus  $R$  data. Here, the slope of  $\Delta G_{TH}$  versus  $R$  for  $\beta = 26^\circ$  and  $62^\circ$  are similar to that of the strongly  $R$ -dependent regime of the mode I threshold data, but each of these slopes is indeed slightly different.

For  $\beta = 82^\circ$  ( $\Delta K_{II}/\Delta K_I = 7.1$ ), it appears that the threshold is much more strongly dependent on load ratio than for any other phase angle investigated. This finding must be questioned, however, because for fatigue loading with  $\beta = 82^\circ$  and  $R = 0.5$ , crack extension was observed to occur by the formation of a branch crack which deflected off the precrack wake approximately 275  $\mu\text{m}$  behind the crack tip (this result was reproducible in more than one sample). At this point in the crack wake,  $\Delta K_{II}/\Delta K_I$  is not equal to 7.1. Hence, the fatigue-crack growth threshold reported here for  $\beta = 82^\circ$ ,  $R = 0.5$  should be viewed as a conservative estimate and the dependence of the threshold on load ratio for  $\beta = 82^\circ$  may not be as strong as suggested in Fig. 8.

### 3.5. Short-crack fatigue thresholds for mixed-mode loading conditions

Mixed-mode fatigue-crack thresholds for short cracks in bimodal Ti-6Al-4V are compared with the threshold data for large cracks at  $R = 0.1$  and  $0.8$  in Fig. 9. Short-crack threshold measurements were performed at  $R = 0.1$  and 1000 Hz cyclic loading frequency in ambient temperature air. Threshold data for applied phase angles,  $\beta = \tan^{-1}(\Delta K_{II}/\Delta K_I)$ , of  $26^\circ$ ,  $62^\circ$  and  $82^\circ$  ( $\Delta K_{II}/\Delta K_I = 0.5$ ,  $1.9$  and  $7.1$ , respectively) are presented in terms of the threshold mode II stress-intensity range,  $\Delta K_{II,TH}$ , as a function of the corresponding mode I value,  $\Delta K_{I,TH}$ , in Fig. 9a. In Fig. 9b, the mixed-mode threshold, in terms of  $\Delta G_{TH}$ , is plotted as a function of the phase angle,  $\beta$ .

For each phase angle investigated, the short-crack fatigue threshold is considerably lower than that of the corresponding large crack at  $R = 0.1$ . This is particularly clear under shear-dominant loading conditions at  $\beta = 62^\circ$  and  $82^\circ$ . The reduction in the threshold for fatigue-crack growth with cracks of restricted wake is believed to arise from the limited extent of crack-tip shielding that can develop for short fatigue cracks. Also, the dependence on mode-mixity of the  $\Delta G_{TH}$  threshold for the short fatigue cracks is markedly reduced compared to the  $\Delta G_{TH}$  dependence on  $\beta$  for large cracks. Whereas, the large-crack  $\Delta G_{TH}$  threshold increases by as much as a factor of 7 with superimposed shear, the short-crack threshold at  $R = 0.1$  increases by only a factor of  $\sim 2.5$ . If it is assumed that the primary difference between the large and short fatigue cracks is the magnitude of crack-tip shielding [15], the present results suggest that such shielding contributes significantly to the magnitude of the large-crack mixed-mode thresholds, and is largely responsible for the elevation in the  $\Delta G_{TH}$  threshold as  $\beta$  is increased. Moreover, the mixed-mode fatigue-crack growth resistance may be even worse for incipient surface cracks that are of dimensions equivalent or less than the microstructural size scales. For such microstructurally-small cracks, in addition to a biased sampling of the microstructure, the magnitude of crack-tip shielding would likely be even less than that which exists for the short fatigue cracks investigated here (where crack lengths are  $\sim 10$  times the average grain size). This point is discussed in more detail in Section 3.6.

It is noted that, as no measurement of the pure mode I, short-crack threshold was made, the large-crack value of  $\Delta G_{TH}$  at  $R = 0.8$  is used as an estimate of this data point in Fig. 9b for purposes of illustrating the variation of  $\Delta G_{TH}$  with  $\beta$  for short fatigue cracks at  $R = 0.1$ . For mode I fatigue-crack growth in the bimodal Ti-6Al-4V of interest here, it has been shown that (global) crack-tip shielding (i.e., crack closure) is completely suppressed at  $R = 0.8$  [45]. Thus, it is expected that the large-crack threshold measured at  $R = 0.8$  would be comparable to a threshold measured from a short fatigue crack at  $R = 0.1$ , where closure is now largely suppressed by the limited crack wake length. Although, in general, mean stress may influence the fatigue-crack growth threshold independent of crack closure [46–48], this effect is not significant in the present material for load ratios between that necessary to fully suppress closure ( $R = 0.5$ ) and  $R = 0.8$ ; specifically, only a  $0.3 \text{ MPa } \sqrt{\text{m}}$  reduction in  $\Delta K_{I,TH}$  is observed between these  $R$  ratios [45].



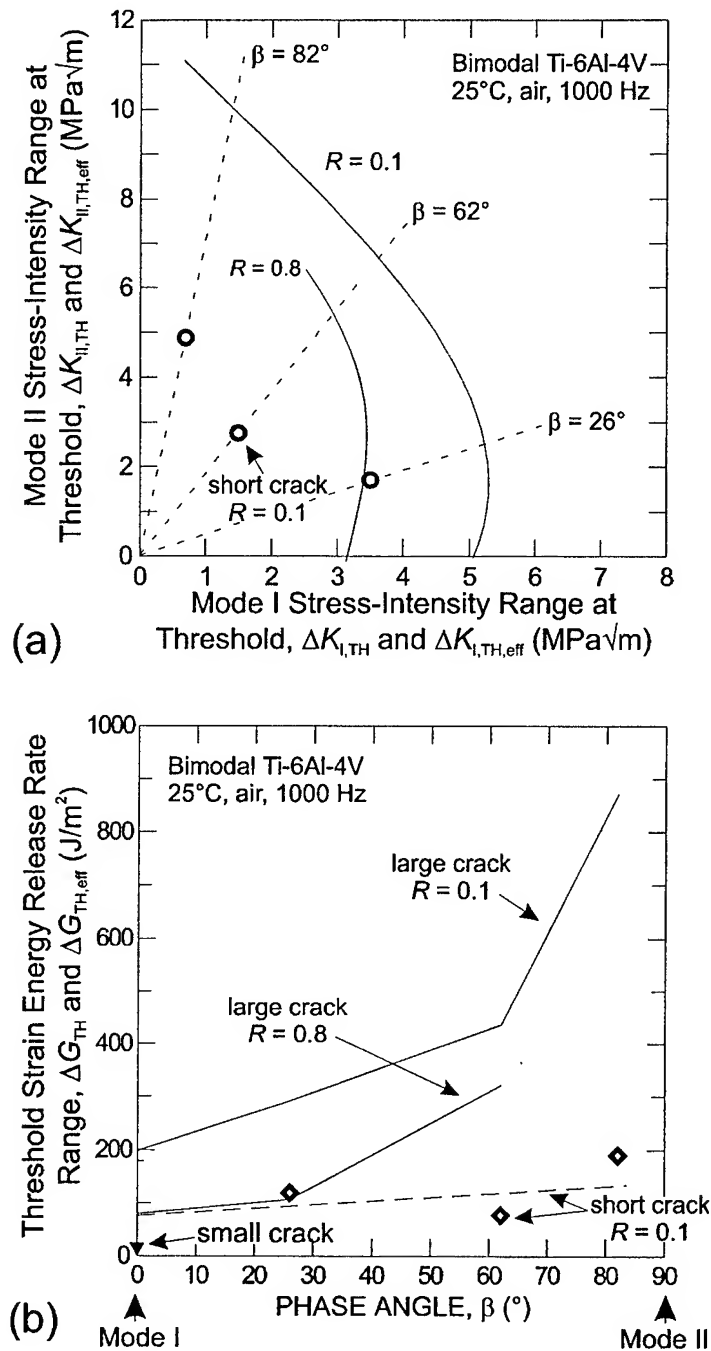


Fig. 9. Mixed-mode fatigue-crack growth thresholds for short cracks in bimodal Ti-6Al-4V ( $R = 0.1$ , 1000 Hz cyclic loading frequency) are compared with threshold data for large fatigue cracks at  $R = 0.1$  and 0.8. Threshold data are presented both in terms of (a) the threshold mode II stress-intensity range,  $\Delta K_{II,TH}$ , as a function of the corresponding mode I value,  $\Delta K_{I,TH}$ , and (b) the threshold range in strain energy release rate,  $\Delta G_{TH}$ , as a function of the applied phase angle,  $\beta = \tan^{-1}(\Delta K_{II}/\Delta K_I)$ . Also shown in (b) is an estimate of the mode I fatigue-crack growth threshold for a microstructurally small crack [49].

### 3.6. Fatigue-crack growth thresholds in the presence of microstructurally small cracks

While consideration has already been given to the manner in which the mixed-mode fatigue-crack growth threshold varies with the applied ratio  $\Delta K_{II}/\Delta K_I$  in the absence of crack-tip shielding, it is important to remember that fatigue-crack growth resistance can also be significantly altered when the crack front samples a limited number of microstructural entities. In Fig. 9, a mode I fatigue-crack growth threshold ( $R = 0.1$ ) is presented for a naturally initiated small crack in bimodal Ti-6Al-4V, which is on the order of the grain size of this material ( $\sim 20 \mu\text{m}$ ). This data point, measured by Peters and Ritchie [49], indicates that fatigue-crack growth can occur at applied driving forces as low as  $\Delta K_{I,TH} = 1 \text{ MPa } \sqrt{\text{m}}$  ( $\Delta G_{TH} = 9.5 \text{ J/m}^2$ ). This microstructurally small-crack threshold illustrates the marked influence which the biased microstructural sampling can have on the fatigue-crack growth threshold. Such behavior has been well documented for mode I fatigue loading [16–22], but has never been examined in terms of mixed-mode loading. Comparison of this small-crack threshold with a crack-tip shielding free, large-crack threshold ( $R = 0.8$ ,  $\Delta K_{I,TH} = 3.2 \text{ MPa } \sqrt{\text{m}}$  and  $\Delta G_{TH} = 79 \text{ J/m}^2$ ) subjected to an equivalent phase angle ( $\beta = 0^\circ$ ) indicates that such restricted sampling of the microstructure can reduce the fatigue-crack growth threshold by factors of  $\sim 3$  and  $8$ , respectively, in terms of  $\Delta K_{I,TH}$  and  $\Delta G_{TH}$ . It is also interesting to note the full range in fatigue-crack growth threshold that can be exhibited in bimodal Ti-6Al-4V due to variations in applied phase angle, crack size, and microstructural sampling. For  $R = 0.1$  and  $\beta = 82^\circ$  ( $\Delta K_{II}/\Delta K_I = 7.1$ ), the measured large-crack threshold,  $\Delta G_{TH} = 872 \text{ J/m}^2$ , is a factor 90 times higher than this mode I small crack threshold.<sup>5</sup> Clearly, further work is needed to determine the small-crack thresholds under mixed-mode loading conditions in order to complete the understanding of mixed-mode fatigue-crack growth resistance.

## 4. Conclusions

Based on a study of the high-cycle, fatigue-crack growth threshold for both large ( $>4 \text{ mm}$ ) and short ( $\sim 200 \mu\text{m}$ ) cracks under combined mode I and mode II loading (mode-mixities varying from  $\Delta K_{II}/\Delta K_I = 0$  to  $\sim 7$ ; phase angles from  $0^\circ$  to  $82^\circ$ ) in a Ti-6Al-4V turbine blade alloy with a bimodal (STOA) microstructure, tested in room temperature air at a loading frequency of  $1000 \text{ Hz}$  (sine wave), the following conclusions are made:

(1) Although the large-crack, mode I fatigue threshold stress-intensity range,  $\Delta K_{I,TH}$ , is found to decrease for sufficiently high mode-mixity ( $\Delta K_{II}/\Delta K_I$ ), more appropriate quantification of the crack driving force in terms of the range in strain-energy release rate reveals that the mixed-mode threshold,  $\Delta G_{TH}$ , actually increases; indeed, for an increase in mode-mixity from  $\Delta K_{II}/\Delta K_I = 0$  to  $\sim 7$ , a sevenfold increase in  $\Delta G_{TH}$  has been observed. Thus, for “continuum-sized” cracks (i.e., large compared to microstructural dimensions) in this alloy, the pure mode I threshold, defined in terms of  $\Delta G_{TH}$ , may be used as a conservative, lower-bound estimate of the mixed-mode fatigue-crack growth threshold.

(2) Measurements of short-crack fatigue thresholds, where the wake shielding zone is restricted to  $\sim 200 \mu\text{m}$ , suggest that this significant increase in the large-crack, mixed-mode  $\Delta G_{TH}$  threshold with increasing mode-mixity is primarily due to a shear-induced enhancement of crack-tip shielding. For the short fatigue cracks, where such shielding is minimal, the measured  $\Delta G_{TH}$  thresholds are significantly lower (relative to the large-crack threshold) for all values of  $\Delta K_{II}/\Delta K_I$  investigated. Moreover, the increase in  $\Delta G_{TH}$  with increasing mode-mixity is markedly reduced.

<sup>5</sup> When the thresholds are compared in terms of an equivalent stress-intensity range,  $\Delta K_{eq,TH}$ , the mixed-mode large-crack threshold at  $R = 0.1$  and  $\beta = 82^\circ$  is still a factor of  $\sim 9.5$  higher than the mode I small-crack threshold ( $\Delta K_{eq,TH} = 10.5$  and  $1.1 \text{ MPa } \sqrt{\text{m}}$ , respectively).

(3) For both mode I and mixed-mode loading conditions, the threshold for fatigue-crack growth decreases with increasing positive load ratio ( $R=0.1-0.8$ ). For mode I loading, at a critical load ratio ( $R_{cr} \sim 0.5$ ) above which crack closure effects are minimal (i.e.,  $K_{min} > K_{cl}$ ), a transition is observed between regimes of relatively strong load-ratio dependence (for  $R < R_{cr}$ ) and relatively weak load-ratio dependence (for  $R > R_{cr}$ ). Conversely, for mixed-mode loading conditions, no such transition is observed; the rate of decrease in mixed-mode  $\Delta G_{TH}$  threshold with increasing  $R$  is relatively constant over the range of  $R=0.1-0.8$ . Such behavior is reasoned to result from an increase in crack-tip shielding with increasing mode-mixity due to shear-induced crack-surface interference.

### Acknowledgements

This work was supported by the US Air Force Office of Scientific Research under Grant No. F49620-96-1-0478 under the auspices of the Multidisciplinary University Research Initiative on *High Cycle Fatigue* to the University of California.

### Appendix A. Distinction between large, short and small cracks

A key component of the present work is a comparison of the mixed-mode crack-growth behavior for fatigue cracks of varying dimension, which are classified here as *large*, *short* and *small* cracks. For the sake of clarity, the salient differences between such cracks are briefly reviewed here. Large fatigue cracks (Fig. 10a) have fracture surface dimensions that are large compared to the scale of the microstructure in both directions. They therefore generally have a fully developed<sup>6</sup> crack-tip shielding zone and can “sample” the microstructure in a statistical (continuum) manner [21]. With respect to large cracks, small cracks are generally described as being comparable in size to [20]:

- (i) microstructural dimensions, where biased statistical sampling of the microstructure can lead to accelerated crack advance along “weak” paths, i.e., microstructural features oriented for easy crack growth (a continuum limitation);
- (ii) the extent of local inelasticity *ahead* of the crack tip, where the assumption of small-scale yielding implicit in the use of the stress intensity,  $K$ , is not strictly valid (a linear-elastic fracture mechanics limitation);
- (iii) the extent of crack-tip shielding (e.g., crack closure) *behind* the crack tip, where the reduced role of shielding leads to a higher local driving force than the corresponding large crack at the same applied  $K$  level (a similitude limitation).

However, a further important distinction can be made, namely that of a short vs. small crack, as schematically shown in Fig. 10. This distinction alludes not simply to physical size but the extent to which a fatigue crack is subjected to the first and third factors listed above. Short fatigue cracks (Fig. 10b) are physically short in only one dimension, a condition that is often realized experimentally by machining away the wake of a large crack. This type of fatigue flaw experiences limited crack-tip shielding due to its reduced length [15], yet still samples the microstructure as a continuum because of its extensive crack front. In contrast, small fatigue cracks (Fig. 10c) are small and comparable to the microstructural size scale in all dimensions, as typified by the small, semi-elliptical surface flaw [19,20,22]. With such cracks, crack-tip

<sup>6</sup> For mixed-mode loading conditions, the shearing of the fracture surfaces with respect to one another can produce crack-wake contact via sliding interference over dimensions which are much larger than for mode I loading, perhaps over the entire wake of a large fatigue crack [28,50]. Thus, the notion of a “fully developed” shielding zone is somewhat unclear for mixed-mode loading conditions. At the least, one would expect the equilibrium shielding-zone length to be a function of the applied ratio of shear to tension.

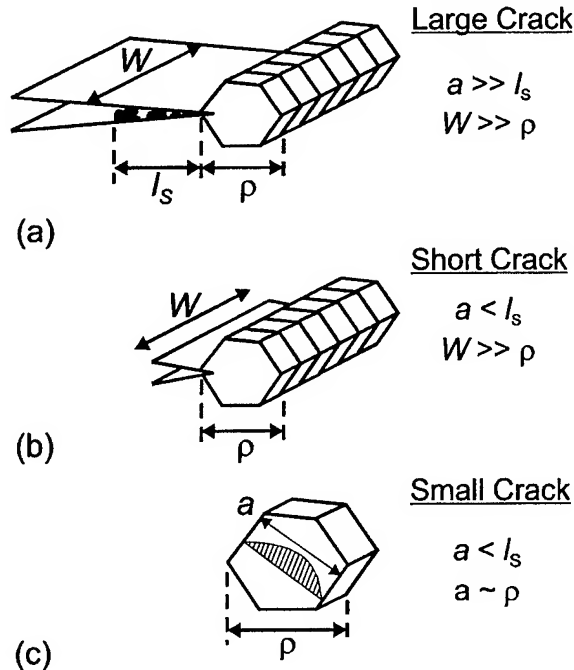


Fig. 10. These schematic illustrations highlight the key distinctions between large, short and small fatigue cracks. Large cracks (a) have length,  $a$ , and width,  $W$ , which are large both with respect to the equilibrium shielding-zone length,  $l_s$  (indicated here as a region of debris in the crack wake which produces crack closure), and the characteristic microstructural size scale,  $\rho$ , e.g., the grain size. In contrast to this, short fatigue cracks (b) are characterized by  $a < l_s$ , but  $W \gg \rho$ . The reduced crack-wake length results in a lower level of crack-tip shielding. For small cracks (c), the fracture surface is reduced in both dimensions, with  $a$  (and  $W$ ) being small with respect to both  $l_s$  and  $\rho$ . The fact that  $a \sim \rho$  implies that the crack front samples only a few microstructural entities, leading to a biased sampling of the microstructure.

shielding is significantly reduced [17,21], and since the crack front samples only few microstructural entities, this allows a biased sampling of microstructurally weak paths [18]. Because of this restriction in shielding and the biased microstructural sampling, fatigue-crack growth resistance in the presence of small cracks tends to be lowest.

## Appendix B. Error analysis

The attainment of the desired phase angle,  $\beta = \tan^{-1}(\Delta K_{II}/\Delta K_I)$ , using the asymmetric four-point bend loading geometry (Fig. 2) [26], requires that the crack be offset from the load line of the mechanical testing frame by a specific amount. Errors in the value of this offset,  $s$ , can lead to significant errors in  $\beta$  and  $\Delta K_I$ . This is particularly true when trying to achieve strongly shear-dominant loading conditions, as the value of  $\Delta K_{II}/\Delta K_I$  approaches infinity as  $s \rightarrow 0$ . As shown in Fig. 2, for the asymmetric four-point bend test, the bending moment,  $M_z$ , varies linearly between the inner loading points, while the shear force,  $F_{xy}$ , is constant in this region. As a result, uncertainty in  $s$  leads to uncertainty in  $\Delta K_I$  and, hence, in the phase angle;  $\Delta K_{II}$  is unaffected.

For the mixed-mode fatigue-crack growth threshold measurements made in the present study, the error in  $s$  was quantified by comparing the expected position of the crack with respect to the load line (based on a positioning of the sample using a micrometer) and to the true value of  $s$  (determined by measuring the

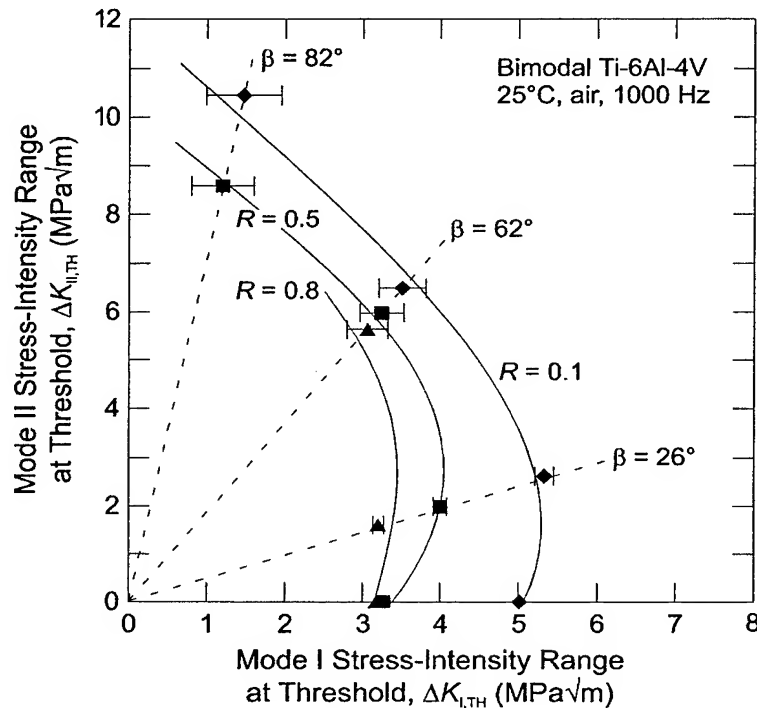


Fig. 11. The root mean squared error in the crack offset from the load line,  $s$ , was determined to be 0.081 mm. The uncertainty in  $\Delta K_{I,TH}$ , which arises because of this uncertainty in  $s$ , is indicated in the mixed-mode fatigue-crack growth threshold envelopes by error bars. These error bars span the range in  $\Delta K_{I,TH}$  corresponding to the desired value of  $s \pm 0.081$  mm.

Table 2  
Uncertainty in applied phase angle,  $\beta$ , for bimodal Ti-6Al-4V

Prescribed phase angle $\beta$ (deg)	Actual range in $\beta$ (deg)		
	$R = 0.1$	$R = 0.5$	$R = 0.8$
0	0	0	0
26	25.6–26.6	25.8–26.9	26.1–27.1
62	59.5–63.6	59.5–63.6	59.5–63.6
82	79.4–84.6	79.4–84.7	–

distance from the load line to the crack tip using an optical telescope). The root mean squared error in  $s$  was determined to be only 0.081 mm. The resultant uncertainty in the mixed-mode fatigue-crack growth threshold data for bimodal Ti-6Al-4V is presented in Fig. 11, where error bars indicate the range in  $\Delta K_{I,TH}$  corresponding to  $\pm 0.081$  mm with respect to the desired value of  $s$ . In accordance with the discussion above, the uncertainty in  $\Delta K_{I,TH}$  is larger for the higher phase angle loading conditions. The uncertainty in  $\beta$  is presented in Table 2 in terms of ranges in  $\beta$  (corresponding to the ranges in  $\Delta K_{I,TH}$  shown in Fig. 11).

## References

- [1] Cowles BA. High cycle fatigue in aircraft gas turbines – an industry perspective. *Int J Fract* 1996;80:147–63.
- [2] Nicholas T, Zuiker JR. On the use of the Goodman diagram for high cycle fatigue design. *Int J Fract* 1996;80:219–35.

- [3] Waterhouse RB, Lindley TC, editors. *Fretting Fatigue*, European Structural Integrity Society Publication No. 18, London: Mechanical Engineering Publications, 1994.
- [4] Gao H, Brown MW, Miller KJ. Mixed-mode fatigue thresholds. *Fatigue Engng Mater Struct* 1982;5:1–17.
- [5] Gao H, Alagok N, Brown MW, Miller KJ. Growth of fatigue cracks under combined mode I and mode II loads. In: Miller KJ, Brown MW, editors. *Multiaxial fatigue*, ASTM STP 853. ASTM, Philadelphia, PA, 1985. p. 184–202.
- [6] Pustejovsky MA. Fatigue crack propagation in titanium under general in-plane loading – I. Experiments. *Engng Fract Mech* 1979;11:9–15.
- [7] Pustejovsky MA. Fatigue crack propagation in titanium under general in-plane loading – II. Analysis. *Engng Fract Mech* 1979;11:17–31.
- [8] Tanaka K. Fatigue crack propagation from a crack inclined to the cyclic tensile axis. *Engng Fract Mech* 1974;6:493–507.
- [9] Tong J, Yates JR, Brown MW. The influence of precracking techniques on fatigue crack growth thresholds under mixed mode I/II loading conditions. *Fatigue Fract Engng Mater Struct* 1994;17:1261–9.
- [10] Tong J, Yates JR, Brown MW. The significance of mean stress on the fatigue crack growth threshold for mixed mode I + II loading. *Fatigue Fract Engng Mater Struct* 1994;17:829–38.
- [11] Zheng YS, Wang ZG, Ai SH. Mixed-mode I and II fatigue threshold and crack closure in dual-phase steels. *Metall Mater Trans A* 1994;25A:1713–23.
- [12] Iida S, Kobayashi AS. Crack-propagation rate in 7075-T6 plates under cyclic tensile and transverse shear loading. *J Bas Engng* 1969;91:764–9.
- [13] John R, DeLuca D, Nicholas T, Porter J. Near-threshold crack growth behavior of a single crystal Ni-base superalloy subjected to mixed mode loading. In: Miller KJ, McDowell DL, editors. *Mixed-mode crack behavior*, ASTM STP 1359. ASTM, West Conshohocken, PA, 1999. p. 312.
- [14] Ritchie RO, Davidson DL, Boyce BL, Campbell JP, Roder O. High-cycle fatigue of Ti–6Al–4V. *Fatigue Fract Engng Mater Struct* 1999;22:621–31.
- [15] Ritchie RO, Yu W. Short crack effects in fatigue: a consequence of crack tip shielding. In: Ritchie RO, Lankford J, editors. *Small fatigue cracks*, TMS-AIME, Warrendale, PA, 1986. p. 167–189.
- [16] Campbell JP, Kruzic JJ, Lillibridge S, Venkateswara Rao KT, Ritchie RO. On the growth of small fatigue cracks in  $\gamma$ -based titanium aluminides. *Scripta Mater* 1997;37:707–12.
- [17] Campbell JP, Venkateswara Rao KT, Ritchie RO. The effect of microstructure on fracture toughness and fatigue crack growth behavior in  $\gamma$ -titanium aluminide based intermetallics. *Metall Mater Trans A* 1999;30A:563–77.
- [18] Kruzic JJ, Campbell JP, Ritchie RO. On the fatigue behavior of  $\gamma$ -based titanium aluminides: role of small cracks. *Acta Mater* 1999;47:801–16.
- [19] Davidson DL, Campbell JB, Page RA. The initiation and growth of fatigue cracks in a titanium aluminide alloy. *Metall Trans A* 1991;22A:377–91.
- [20] Ritchie RO, Lankford J. Small fatigue cracks: a statement of the problem and potential solutions. *Mater Sci Engng* 1986;A84:11–6.
- [21] Suresh S, Ritchie RO. Propagation of short fatigue cracks. *Int Metals Rev* 1984;29:445–76.
- [22] Venkateswara Rao KT, Yu W, Ritchie RO. On the behavior of small fatigue cracks in commercial aluminum-lithium alloys. *Fract Engng Mech* 1988;31:623–35.
- [23] Eylon D. Summary of the available information on the processing of the Ti–6Al–4V HCF/LCF program plates, University of Dayton Report, 1998.
- [24] Boyce BL. MS Thesis, University of California at Berkeley, 1998.
- [25] He MY, Cao HC, Evans AG. Mixed-mode fracture: the four-point shear specimen. *Acta Metall Mater* 1990;38:839–46.
- [26] He MY, Hutchinson JW. Asymmetric four-point crack specimen. *J Appl Mech* 2000;67:207–9.
- [27] Suresh S, Shih CF, Morrone A, O'Dowd NP. Mixed-mode fracture toughness of ceramic materials. *J Am Ceram Soc* 1990;73:1257–67.
- [28] Nayeib-Hashemi H, McClintock FA, Ritchie RO. Effects of friction and high torque on fatigue crack propagation in mode III. *Metall Trans A* 1982;13A:2197–204.
- [29] Smith MC, Smith RA. Toward an understanding of mode II fatigue crack growth. In: Fong JT, Fields RJ, editors. *Basic questions in fatigue*, vol. I, ASTM STP 924, ASTM, Philadelphia, PA, 1988. p. 260–280.
- [30] Tong J, Yates JR, Brown MW. A model for sliding mode crack closure. I: theory for pure mode II loading. *Fract Engng Mech* 1995;52:599–611.
- [31] Tong J, Yates JR, Brown MW. A model for sliding mode crack closure. II: mixed mode I and II loading and application. *Engng Fract Mech* 1995;52:613–23.
- [32] Morgan JM, Milligan WW. A 1 kHz servohydraulic fatigue testing system. In: Soboyejo WO, Srivatsan TS, editors. *High cycle fatigue of structural materials*, TMS, Warrendale, PA, 1997. p. 305–12.
- [33] Pook LP. An observation on mode II fatigue crack growth threshold behavior. *Int J Fract* 1977;13:867–9.
- [34] Tong J, Yates JR, Brown MW. The formation and propagation of mode I branch cracks in mixed mode fatigue failure. *Engng Fract Mech* 1997;56:213–31.

- [35] Liu P, Wang Z. Mixed-mode I and II fatigue threshold and crack deflection angle in SiCp/2024Al composite. *Scripta Mater* 1996;34:1323–30.
- [36] Campbell JP, Ritchie RO. Mixed-mode, high-cycle, fatigue-crack growth thresholds in Ti–6Al–4V: Part II – quantification of crack-tip shielding. *Engng Fract Mech* 2000;67:229–49.
- [37] Otsuka A, Tohgo K, Matsuyama H. Fatigue crack initiation and growth under mixed mode loading in aluminum alloys 2017-T3 and 7075-T6. *Engng Fract Mech* 1987;28:721–32.
- [38] Erdogan F, Sih GC. On the crack extension in plates under plane loading and transverse shear. *J Bas Engng* 1963;85: 519–25.
- [39] Sih GC. Strain energy density factor applied to mixed mode crack problems. *Int J Fract* 1974;10:305–21.
- [40] Cotterell B. On brittle fracture paths. *Int J Fract Mech* 1965;1:96–103.
- [41] Thouless MD. Fracture of a model interface under mixed-mode loading. *Acta Metall Mater* 1990;38:1135–40.
- [42] O'Dowd NP, Stout MG, Shih CF. Fracture toughness of alumina-niobium interfaces: experiments and analyses. *Philos Mag A* 1992;66:1037–64.
- [43] Yao D, Shang JK. Effect of load-mix on fatigue crack growth in 63Sn–37Pb solder joints. *Trans ASME J Electron Packag* 1997;119:114–8.
- [44] Schmidt RA, Paris PC. Threshold for fatigue crack propagation and effects of load ratio and frequency. Progress in flaw growth and fracture toughness testing, ASTM STP 536. ASTM, Philadelphia, PA, 1973. p. 79–94.
- [45] Ritchie RO, Boyce BL, Campbell JP, Roder O, Thompson AW, Milligan WW. Thresholds for high-cycle fatigue in a turbine engine Ti–6Al–4V alloy. *Int J Fatigue* 1999;21:653–62.
- [46] Boyce BL, Ritchie RO. Effect of load ratio and maximum stress intensity on the fatigue threshold in Ti–6Al–4V, *Engng Fract Mech* 2000, submitted for publication.
- [47] Döker H. Fatigue crack growth threshold: implications, determination and data evaluation. *Int J Fatigue* 1997;19:S145–9.
- [48] Huthmann H, Gossmann O. Verband für Materialforschung und –prüfung. Vortragsveranstaltung des DVM-Arbeitskreises Bruchvorgänge, Deutscher 1981. p. 271–4.
- [49] Peters JO, Ritchie RO. Influence of foreign-object damage on crack initiation and early crack growth during high-cycle fatigue of Ti–6Al–4V. *Engng Fract Mech* 2000;67:193–207.
- [50] Tschegg EK. Sliding mode crack closure and mode III fatigue crack growth in mild steel. *Acta Metall* 1983;31:1323–30.



PERGAMON

Engineering Fracture Mechanics 67 (2000) 229–249

Engineering  
Fracture  
Mechanics

www.elsevier.com/locate/engfracmech

# Mixed-mode, high-cycle fatigue-crack growth thresholds in Ti–6Al–4V

## II. Quantification of crack-tip shielding

J.P. Campbell, R.O. Ritchie \*

*Department of Materials Science and Mineral Engineering, University of California, 463 Evans Hall, Berkeley, CA 94720, USA*

Received 27 December 1999; received in revised form 4 May 2000; accepted 11 May 2000

### Abstract

The role of crack-tip shielding in influencing mixed-mode (mode I + II) fatigue-crack growth thresholds for large, through-thickness cracks in a Ti–6Al–4V turbine blade alloy is examined under high-cycle fatigue loading conditions, i.e., at a loading frequency of 1000 Hz in ambient temperature air for load ratios ( $K_{\min}/K_{\max}$ ) of  $R = 0.1$ – $0.8$ . Techniques are developed to quantify crack-tip shielding with respect to both the mode I and mode II applied loading, enabling an estimation of the shielding-corrected, crack-driving forces actually experienced at the crack tip ( $\Delta K_{I,TH,eff}$  and  $\Delta K_{II,TH,eff}$  or  $\Delta G_{TH,eff}$ ). In Part I, it was shown that when the crack-driving force is characterized in terms of the range in strain-energy release rate,  $\Delta G$ , which incorporates contributions from both the applied tensile and shear loading, the mixed-mode (I + II) fatigue-crack growth resistance increases monotonically with the ratio  $\Delta K_{II}/\Delta K_I$ . When the fatigue-crack growth thresholds are expressed in terms of the near-tip (shielding-corrected) crack-driving force, this increase in crack-growth resistance with increasing mode mixity is markedly reduced. Moreover, for all mode mixities investigated, the near-tip mixed-mode fatigue threshold is lower than the applied (global) value, with the effect being particularly pronounced under shear-dominant loading conditions. These observations illustrate the prominent role of crack-tip shielding for the mixed-mode loading of fatigue cracks with crack-wake dimensions large compared with microstructural size scales; specifically, they indicate that the elevation of the  $\Delta G_{TH}$  fatigue-crack growth threshold with increasing applied mode mixity is largely due to a shear-induced enhancement of crack-tip shielding. © 2000 Elsevier Science Ltd. All rights reserved.

**Keywords:** High-cycle fatigue; Fatigue thresholds; Mixed mode; Crack-tip shielding

### 1. Introduction

The unexpected failure of turbine engine components due to high-cycle fatigue (HCF) loading conditions [1,2] currently represents one of the primary threats to the safety and readiness of US military aircraft fleets. The occurrence of such failures is extremely costly; moreover, attempts to control the problem substantially

\* Corresponding author. Tel.: +510-486-5798; fax: +510-486-4995.

E-mail address: roritchie@lbl.gov (R.O. Ritchie).



increase the cost associated with this phenomenon, both in terms of equipment “down-time” and expenses associated with component inspection. Multiaxial loading conditions are known to exist at some fatigue-critical locations within turbine engine components, particularly in association with fretting fatigue in the blade dovetail/disk contact section [3]. In the presence of cyclic multiaxial loading, the resultant crack-driving force may be a combination of the influence of a mode I (tensile opening) stress-intensity range,  $\Delta K_I$ , as well as mode II (in-plane shear) and/or mode III (anti-plane shear) stress-intensity ranges,  $\Delta K_{II}$  and  $\Delta K_{III}$ , respectively. Whereas most published fatigue thresholds are reported for (nominally) pure mode I loading, several studies have demonstrated that superimposed cyclic shear ( $\Delta K_{II}$  or  $\Delta K_{III} > 0$ ) can lower the value of  $\Delta K_I$  at threshold [4–12], sometimes markedly [13].

Since the high loading frequencies ( $\sim 1\text{--}2$  kHz) and correspondingly short failure times associated with HCF may necessitate a threshold-based design methodology [14], it is important that the effect of mode mixity (i.e., the applied ratio of shear to tensile loading) on fatigue-crack growth resistance is characterized for aircraft engine materials. For the Ti–6Al–4V blade alloy of interest here, it has been shown in Part I of this paper [15] that the presence of mixed-mode cyclic loading conditions does not preclude the application of such a threshold-based design criterion. Indeed, the threshold fatigue-crack growth resistance is observed to increase monotonically with the applied ratio of  $\Delta K_{II}$  to  $\Delta K_I$ , such that the pure mode I threshold (expressed in terms of the range in strain energy release rate,  $\Delta G$ ) may be used as a conservative estimate of the mixed-mode (I + II) fatigue-crack growth threshold for  $\Delta K_{II}/\Delta K_I > 0$ .

In the present work, mixed-mode, fatigue-crack growth thresholds for combined mode I + II loading are investigated for a Ti–6Al–4V alloy in the bimodal (STOA) microstructural condition (a typical turbine engine blade microstructure). The influence of various combinations of shear and tensile loading, ranging from  $\Delta K_{II}/\Delta K_I = 0$  (mode I loading) to  $\sim 7$  on the crack-growth threshold condition is reported for loading conditions characteristic of turbine engine HCF, i.e., high mean stresses (up to  $R = 0.8$ ) and high cyclic loading frequencies (1000 Hz). The mechanistic origins of the measured increase in the fatigue-crack growth threshold,  $\Delta G_{TH}$ , with increasing applied phase angle,  $\beta$  ( $= \tan^{-1}(\Delta K_{II}/\Delta K_I)$ ), described in Part I [15], are investigated through the development of sample-compliance-based techniques to quantify crack-tip shielding with respect to the applied mode I and mode II crack-driving forces,  $\Delta K_{II}$  and  $\Delta K_I$ , respectively. Such shielding is considered to occur by crack wedging (i.e., crack closure) in mode I and additionally by sliding crack-surface interference when mode II is superimposed. More specifically, when fatigue fracture surfaces are sheared with respect to one another, the transmission of the applied shear loading to the crack tip can be mitigated both by the development of frictional stress in the crack wake and by the interlocking of fracture surface asperities. Using the compliance-based techniques, quantitative estimates are made of the shielding-corrected crack-driving forces actually experienced at the crack tip ( $\Delta K_{I,TH,eff}$  and  $\Delta K_{II,TH,eff}$  or  $\Delta G_{TH,eff}$ ). When the fatigue thresholds are expressed in terms of the near-tip (shielding-corrected) driving force, threshold values are decreased and the increase in crack-growth resistance with increasing mode mixity is markedly reduced. This implies that the elevation of the mixed-mode, large-crack threshold (in terms of  $\Delta G_{TH}$ ) with increasing mode mixity can be attributed primarily to a shear-induced enhancement in crack-tip shielding.

## 2. Experimental procedures

### 2.1. Material

The material investigated was a forged Ti–6Al–4V turbine engine alloy received in a bimodal microstructural condition (nearly equiaxed primary  $\alpha$  with lamellar  $\alpha + \beta$  colonies). Full details of the composition, processing, heat treatment, section sizes and microstructural features are given in Part I of this paper

[15]. In the longitudinal orientation, the material displays mean yield and tensile strengths of 930 and 978 MPa, respectively [16].

## 2.2. Experimental methods

As described in Part I of this paper [15], mixed-mode thresholds for fatigue cracks, large compared to microstructural dimensions, were measured using the asymmetric four point bend (AFPB) specimen [4,17–19]. Mixed-mode loading conditions (applied to a mode I fatigue pre-crack) were quantified both in terms of the ratio  $\Delta K_{II}/\Delta K_I$ , which was varied from 0 (pure mode I) to 7.1, and the phase angle,  $\beta$  ( $= \tan^{-1}(\Delta K_{II}/\Delta K_I)$ ), which correspondingly varied from  $0^\circ$  to  $82^\circ$ . Positive load ratios ( $R = K_{min}/K_{max}$ ) were varied between 0.1 and 0.8. Fatigue testing was performed at 1000 Hz (sine wave) on a MTS servo-hydraulic, high-frequency testing machine incorporating a voice-coil servovalve [20]. Procedures for determining the fatigue thresholds, and for the prior pre-cracking of the AFPB samples, can also be found in Part I [15].

The extent of crack-tip shielding caused by crack-surface contact was evaluated using in situ measurements of the mode I and mode II compliance curves of the test sample (i.e., applied load as a function of mode I and mode II crack-opening displacement) during cyclic loading at the fatigue-crack growth threshold condition. Compliance curves were recorded using a crack-opening displacement (COD) gauge mounted on the side surface of the sample, approximately 1 mm behind the crack tip. For measurement of the mode I compliance, the COD gauge was bonded directly to the side of the sample, as indicated in Fig. 1a. Measurement of the mode II compliance curve required that the fixture shown in Fig. 1b be placed between the sample and the COD gauge. Compliance curves were recorded at a cyclic loading frequency of 1 Hz and applied values of  $\Delta K_I$  and  $\Delta K_{II}$  corresponding to the fatigue-crack growth threshold for the load ratio and phase angle,  $\beta$ , of interest. Such measurements were made following the application of 1 million

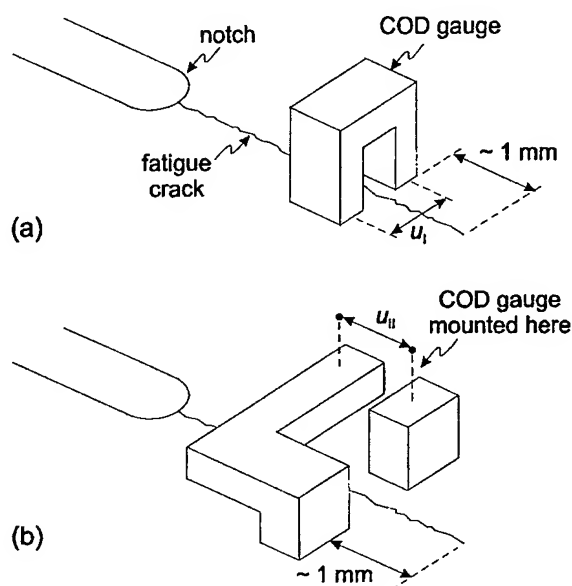


Fig. 1. Compliance curves were recorded using a COD gauge mounted on the side surface of the sample approximately 1 mm behind the crack tip. For measurement of the mode I compliance, (a) the COD gauge was bonded directly to the side of the sample. Measurement of the mode II compliance curve required that a fixture (b) be placed between the sample and the COD gauge. The COD gauge shown in (a) was then bonded to the surface of this fixture, at the location indicated in (b).

cycles at 1000 Hz cyclic loading frequency and this same loading amplitude. This pre-measurement cycling was intended to allow any cycle-dependent degradation of crack-wake contact due to fracture surface wear and abrasion to occur and (presumably) to reach steady state.

The mode I closure stress intensity,  $K_{cl}$ , was estimated using the known pre-crack length and the load,  $P_{cl}$ , corresponding to the onset of fracture surface contact (i.e., wedging) during unloading.  $P_{cl}$  was taken at the first deviation from linearity in the mode I unloading compliance curve [21,22]. The effective, threshold, mode I, stress-intensity range experienced at the crack tip was then defined as

$$\Delta K_{I,TH,eff} = K_{I,max} - K_{cl}, \quad (1)$$

where  $K_{I,max}$  is the maximum applied value of the mode I stress intensity.

The technique, which was developed for estimating the magnitude of shielding with respect to the applied value of  $\Delta K_{II}$ , is considered to be a significant result of the present work. For this reason, a detailed description of this technique will be deferred to the results and discussion section of this paper. As will be shown, it was possible to infer the maximum and minimum (local) values of  $K_{II}$  actually experienced at the crack tip,  $K_{II,max}^{tip}$  and  $K_{II,min}^{tip}$  respectively, using the mode II loading and unloading compliance curves. The effective, threshold, mode II, stress-intensity range experienced at the crack tip was then defined according to the following relationship:

$$\Delta K_{II,TH,eff} = K_{II,max}^{tip} - K_{II,min}^{tip}. \quad (2)$$

Using the techniques described above, the measured mixed-mode, fatigue-crack growth thresholds were compared in terms of both the applied crack-driving force and the near-tip, shielding-corrected driving force.

### 3. Results and discussion

#### 3.1. Mixed-mode fatigue-crack growth thresholds

The mixed-mode fatigue-crack growth thresholds for bimodal Ti-6Al-4V, in terms of the mode II stress-intensity range at threshold,  $\Delta K_{II,TH}$ , as a function of the corresponding mode I threshold,  $\Delta K_{I,TH}$ , are shown in Fig. 2 for mode mixities of  $\Delta K_{II}/\Delta K_I = 0, 0.5, 1.9$  and  $7.1$  ( $\beta = 0^\circ, 26^\circ, 62^\circ$  and  $82^\circ$ , respectively) and load ratios of 0.1, 0.5 and 0.8. Closed and open symbols represent the loading conditions that produced, respectively, no crack growth and crack growth; these loading conditions bound the true threshold for the onset of crack extension. While these data are in general agreement with mixed-mode fatigue-crack growth behavior reported in other material systems [4,8–11,23,24], as noted in Part I [15], an interesting feature is present which has not been previously reported for mixed-mode fatigue thresholds. Specifically, the value of mode I threshold,  $\Delta K_{I,TH}$ , is slightly increased as  $\beta$  is increased from  $0^\circ$  to  $26^\circ$ , which gives rise to the appearance of a “nose” in the threshold envelope. As discussed below, this insensitivity of  $\Delta K_{I,TH}$  to superimposed shear loading at phase angles below  $\sim 60^\circ$  can be attributed largely to a shear-induced enhancement of the mode I fatigue-crack closure. Over the wider range of mode mixities though, the mode I  $\Delta K_{I,TH}$  threshold decreases with increasing  $\beta$ . However, as noted in Part I, when threshold data are plotted in terms of the range in strain energy release rate,  $\Delta G$ , or the equivalent stress intensity,  $\Delta K_{eq}$  (Fig. 3), viz,

$$\Delta G_{TH} = (\Delta K_{I,TH}^2 + \Delta K_{II,TH}^2)/E' = \Delta K_{eq,TH}^2/E', \quad (3)$$

the pure mode I threshold ( $\beta = 0^\circ$ ), in terms of  $\Delta G_{TH}$  or  $\Delta K_{eq,TH}$ , is the worst case [15]. In Eq. (3),  $E' = E/(1 - \nu^2)$  in plane strain and  $E$  in plane stress, where  $E$  is Young's modulus and  $\nu$  is Poisson's ratio.

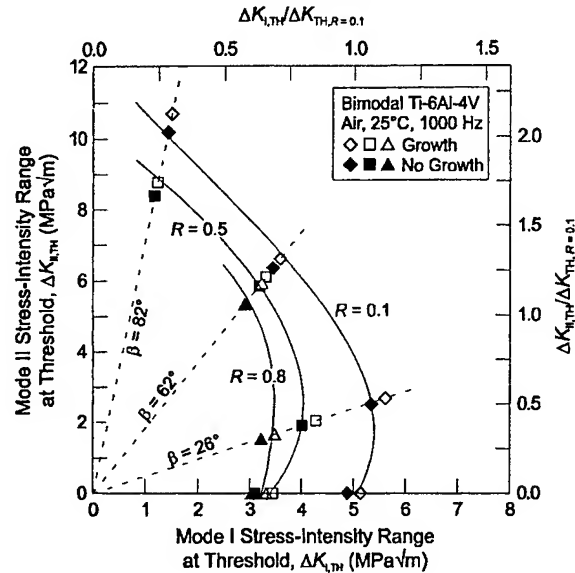


Fig. 2. Mixed-mode, fatigue-crack growth threshold envelopes for bimodal Ti-6Al-4V at load ratios,  $R$ , of 0.1, 0.5 and 0.8 and a cyclic loading frequency of 1000 Hz in ambient temperature air. Closed and open symbols represent the loading conditions that produced, respectively, no crack growth and crack growth; these loading conditions bound the true threshold for the onset of crack extension. On the upper and right-hand axes,  $\Delta K_{I,TH}$  and  $\Delta K_{II,TH}$  are normalized by the pure mode I threshold at  $R = 0.1$ ,  $\Delta K_{TH,R=0.1}$ .

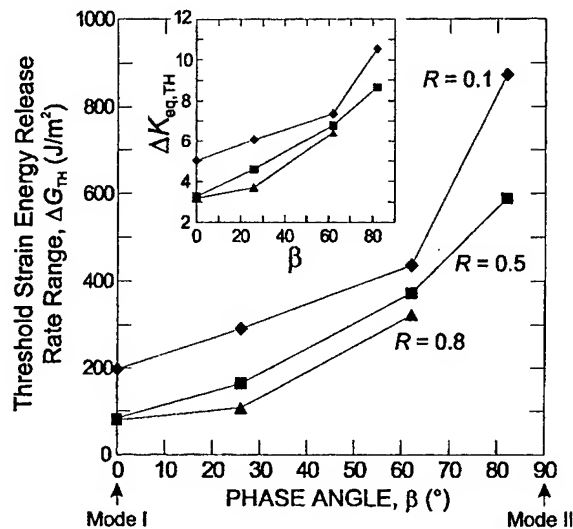


Fig. 3. Mixed-mode, fatigue-crack growth thresholds in bimodal Ti-6Al-4V are plotted in terms of the range in strain energy release rate at threshold,  $\Delta G_{TH}$ , as a function of the applied phase angle,  $\beta (= \tan^{-1}(\Delta K_{II}/\Delta K_I))$ , for load ratios of 0.1, 0.5 and 0.8.  $\Delta G_{TH}$  is observed to increase substantially with  $\beta$ . Inset: the equivalent stress-intensity range,  $\Delta K_{eq,TH} (= (\Delta G_{TH} E')^{1/2})$ , is plotted as a function of  $\beta$ .

### 3.2. Mixed-mode crack-tip shielding

The important role of wake interference in mixed-mode fatigue-crack growth has been well documented in the literature. There have been numerous experimental observations about the effects of crack-wake interference [4,11,24–28] and attempts to model this fracture surface interaction and the associated crack-tip shielding [25,29–31]. However, there does not yet exist a simple experimental technique for quantifying crack-tip shielding with respect to an applied mode II loading, akin to the well developed techniques for quantifying such crack-wake effects during pure mode I fatigue. For mode I loading, crack closure is routinely quantified using a rather simple in situ unloading compliance curve measurement on the fatigue test sample [22]. Using the same compliance curve, it is also possible to quantify [32,33] any crack bridging [34–36] which might be present. In the following paragraphs, simple experimental techniques (based upon the measurement of sample compliance curves) for quantifying crack-tip shielding with respect to both mode I and mode II loading in the presence of superimposed shear and tensile loading are described. Using these techniques, the magnitude of crack-tip shielding is measured for bimodal Ti–6Al–4V, and these shielding measurements are used to present the mixed-mode fatigue-crack growth threshold data shown in Figs. 2 and 3 in terms of the crack-driving force actually experienced at the crack tip.

Fatigue-sample compliance curves (loading and unloading) were determined for both mode I and mode II displacements, using the near-tip COD gauge described above. The general form of these curves is shown schematically in Fig. 4. Note that the mode I compliance curve measured during mixed-mode loading (Fig. 4a) is essentially identical to that measured for pure mode I fatigue. The form of the mode II compliance curve shown in Fig. 4b (actual experimental data are shown in Fig. 4c) is a generalization which captures all of the essential features observed for such curves at different values of  $\beta$  and  $R$ ; these features are discussed below.

At this point, it should be noted that the measured compliance curves for a subordinate loading mode<sup>1</sup> were not interpretable in the manner which will be described in the following sections. In other words, the features of the compliance curves which are used here to aid in quantification of crack-tip shielding were not discernable in these compliance curves. Thus, measurements of crack-tip shielding with respect to the applied mode II loading were only made for shear-dominant loading conditions ( $\Delta K_{II}/\Delta K_I > 1$ ), and mode I crack-tip shielding was quantified only for tensile dominant conditions ( $\Delta K_{II}/\Delta K_I < 1$ ). The distortion of the subordinate mode compliance curves is attributed to the large displacement imposed on the COD gauge (by the dominant loading mode) in a direction orthogonal to that in which the gauge is designed to make measurements. Such effects could be magnified by any misalignment of the gauge.

#### 3.2.1. Mode I crack-tip shielding

Mode I crack-tip shielding, i.e., crack closure, was quantified for tensile-dominant mixed-mode loading ( $\Delta K_{II}/\Delta K_I = 0.5$ ,  $\beta = 26^\circ$ ) and pure mode I loading ( $\Delta K_{II}/\Delta K_I = 0$ ,  $\beta = 0^\circ$ ) using the well established technique of defining the closure load,  $P_{cl}$ , as the load corresponding to the first deviation from linearity in the mode I unloading compliance curve. The mode I closure stress intensity,  $K_{cl}$ , was then calculated using  $P_{cl}$ , the known crack length, and a mode I stress-intensity solution for bending [37]. Measured values of  $K_{cl}$  are presented in Fig. 5 in terms of  $K_{cl}/K_{I,max}$  (where  $K_{I,max}$  is the maximum mode I stress intensity) as a function of  $R$  for  $\beta = 0^\circ$  and  $26^\circ$ . Note that the absolute values of  $K_{cl}$  are indicated adjacent to the data points.

<sup>1</sup> The term “subordinate loading mode” is most easily defined by the use of the following examples. For  $\Delta K_{II}/\Delta K_I = 0.5$  ( $\beta = 26^\circ$ ), the shear loading mode is subordinate while the tensile loading mode is dominant, i.e.,  $\Delta K_I > \Delta K_{II}$ . Conversely, for  $\Delta K_{II}/\Delta K_I = 1.9$  and  $7.1$  ( $\beta = 62^\circ$  and  $82^\circ$ , respectively), the shear loading mode is dominant and the tensile mode is subordinate.

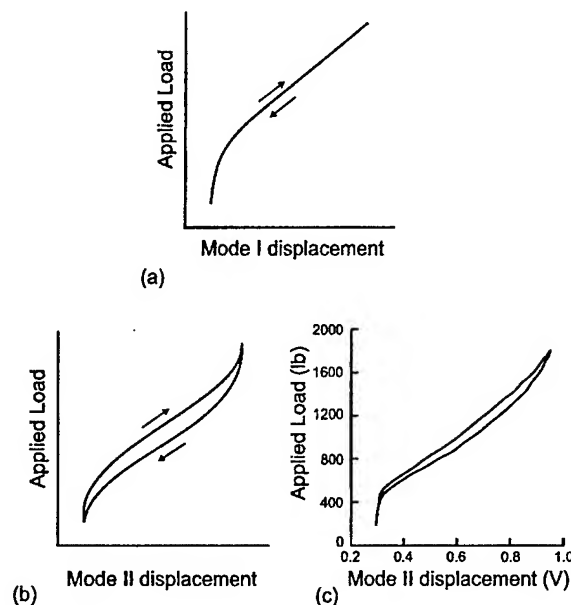


Fig. 4. Representation of the general form observed for, (a) mode I and (b) mode II compliance curves measured using a side-mounted, near-tip COD gauge. Actual experimental data for the mode II compliance behavior are shown in (c).

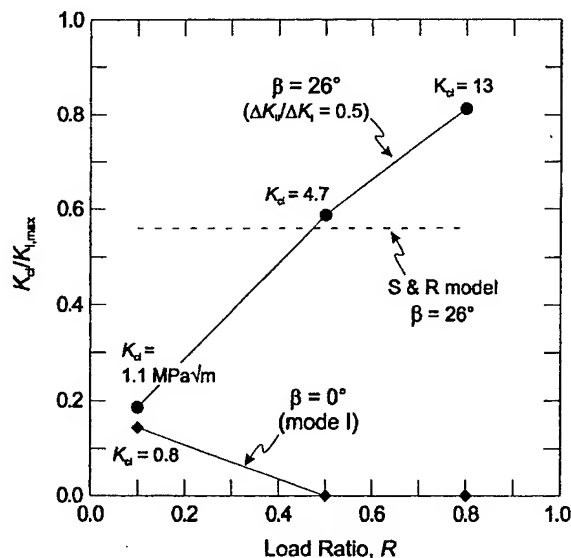


Fig. 5. Measured values of the mode I closure stress intensity,  $K_{cl}$ , (normalized by the maximum mode I stress intensity,  $K_{I,max}$ ) are presented as a function of load ratio,  $R$ , for  $\beta = 0^\circ$  and  $26^\circ$ . Note that values of  $K_{cl}$  (not normalized by  $K_{I,max}$ ) are indicated adjacent to the data points. While fatigue crack closure is observed to be suppressed by increasing load ratio for mode I loading ( $\beta = 0^\circ$ ),  $K_{cl}$  increases rather dramatically with load ratio when a small amount of shear loading is superimposed ( $\beta = 26^\circ$ ,  $\Delta K_{II}/\Delta K_I = 0.5$ ). Experimental results are compared with a prediction based upon the model of Suresh and Ritchie ("S and R" model [41]).

In Fig. 5, it is apparent that, for mode I loading ( $\beta = 0^\circ$ ), crack closure is suppressed as load ratio increases. In fact, closure appears to be completely eliminated at  $R = 0.5$  and  $0.8$ . It should be noted that these values of  $K_{cl}$  for  $\beta = 0^\circ$  are somewhat lower than previous reports of mode I crack closure in this same

material [38]. This small disparity may be due to differences in the technique employed to measure the unloading compliance curve (side-mounted, near-tip COD gauge in the current study; back-face-strain compliance in Ref. [38]).

In stark contrast to the behavior exhibited for  $\beta = 0^\circ$ , the mode I closure stress intensity for  $\beta = 26^\circ$  ( $\Delta K_{II}/\Delta K_I = 0.5$ ) is observed to increase markedly as load ratio increases from 0.1 to 0.8. Measured values of  $K_{cl}$  are 1.1, 4.7 and 13.0 MPa  $\sqrt{\text{m}}$ , respectively, at  $R = 0.1$ , 0.5 and 0.8; corresponding values of  $K_{cl}/K_{I,\text{max}}$  are 0.19, 0.59 and 0.81. While the assertion that crack closure is operative at  $R = 0.8$  may be surprising, supporting fractographic evidence can be seen in Fig. 6, which shows scanning electron photomicrographs of the fatigue surfaces in the near-tip crack wake for  $R = 0.1$  and 0.8 at  $\beta = 26^\circ$ . In both images, evidence of fracture surface contact is present in the form of “wear scars” produced by the relative shear displacements of the fracture surfaces. These wear scars are characterized by flat regions with parallel surface markings oriented exactly in the direction of the relative shear displacement between the fracture surfaces during cyclic loading. At  $R = 0.1$ , these markings tend to be larger in size, occupy more area on the fracture surface, and have more wear debris surrounding them than at  $R = 0.8$ . This suggests more extensive

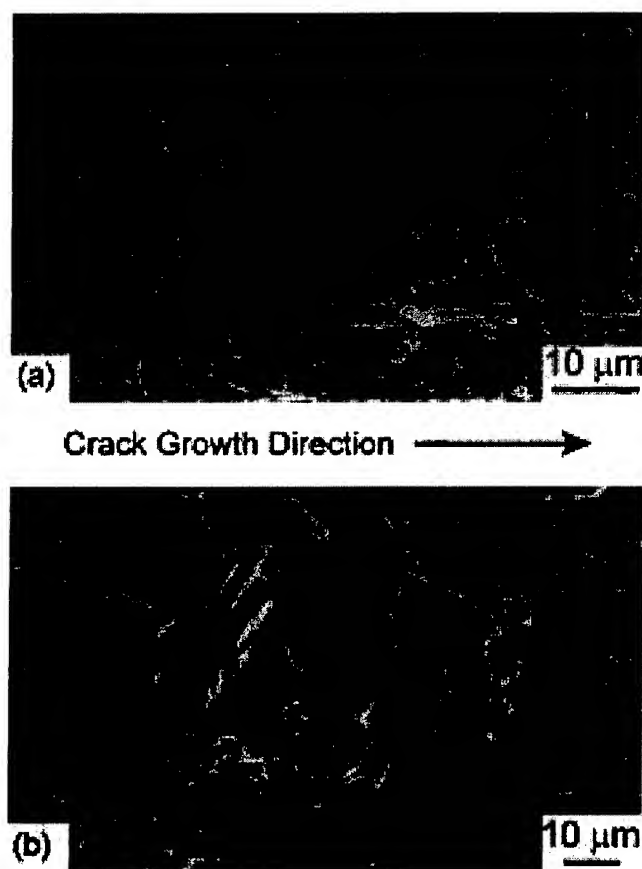


Fig. 6. Scanning electron photomicrographs of the fatigue fracture surfaces in the near-tip crack wake are shown for (a)  $R = 0.1$  and (b)  $R = 0.8$  at  $\beta = 26^\circ$ . In both images, evidence of fracture surface contact is present in the form of “wear scars” (indicated by arrows) produced by the relative shear displacements of the fracture surfaces; these wear scars are characterized by flat regions with parallel surface markings oriented exactly in the direction of the relative shear displacement (left to right) between the fracture surfaces during cyclic loading. At  $R = 0.1$ , considerable debris is observed around the wear scar.

fracture surface contact for  $R = 0.1$ ; nonetheless, the presence of these features at  $R = 0.8$  indicates that fracture surface contact does occur at this high value of load ratio.

The dramatic increase in  $K_{cl}$  with increasing load ratio for  $\beta = 26^\circ$  is believed to result from a shear-induced offsetting of the fracture surface asperities. While it is known that some amount of mode II crack opening generally occurs even for nominally mode I loading [39], clearly the amount of mode II displacement in the crack wake is increased when  $\beta > 0^\circ$ . An increase in the level of crack closure under mixed-mode loading conditions has previously been reported in a 2024-T3 aluminum alloy [40]. Such shear-induced enhancement of mode I closure has been modeled by Suresh and Ritchie [41]. Using a very simple idealization of a rough fatigue fracture surface, with asperities of high  $h$  and width  $W$ , and a geometrical consideration of crack surface contact, they derive an expression for  $K_{cl}$  as

$$K_{cl}/K_{I,max} = \{2\gamma x/(1 + 2\gamma x)\}^{1/2}, \quad (4)$$

where  $x = u_{II}/u_I$  is the ratio of mode II to mode I displacements in the crack wake and  $\gamma = h/W$ , the ratio of fracture surface asperity height to width. Characterization of the fatigue pre-crack fracture surfaces in the present study indicates that  $\gamma = 0.46$ . Using this value of  $\gamma$  and assuming that  $u_{II}/u_I = \Delta K_{II}/\Delta K_I = 0.5$  for  $\beta = 26^\circ$ , Eq. (4) predicts  $K_{cl}/K_{I,max} = 0.56$ . In contrast to the experimental data, this predicted value of  $K_{cl}/K_{I,max}$  is independent of load ratio (Fig. 5), a contradiction that is believed to be an artifact of the perfectly periodic fracture surface modeled by Suresh and Ritchie. In reality, fracture surfaces are not so regular, and it is likely that the maximum height differential of fracture surface asperities which may come into contact during mode I unloading will increase as the magnitude of shear offset of the fracture surfaces increases. This would explain the observed increase in  $K_{cl}/K_{I,max}$  with load ratio. For the measured fatigue-crack growth thresholds at  $\beta = 26^\circ$ , the mean value of  $K_{II}$  increases from  $\sim 1.6$  to  $7.2$  MPa  $\sqrt{m}$  as  $R$  increases from 0.1 to 0.8. In addition, the assumption that  $u_{II}/u_I = \Delta K_{II}/\Delta K_I$  is questionable, as it is known that this relationship does not necessarily hold for mode I loading, where it has been shown that  $u_{II}/u_I \neq 0$  even though  $\Delta K_{II}/\Delta K_I = 0$  [39]; moreover, models of shear-induced fracture surface contact indicate that this contact can cause the near-tip mode mixity to differ markedly from the applied value of  $\Delta K_{II}/\Delta K_I$  [31].

Using the measured values of  $K_{cl}$ , an effective, near-tip, mode I, stress-intensity range at threshold,  $\Delta K_{I,TH,eff}$ , can be defined according to Eq. (1).  $\Delta K_{I,TH,eff}$  represents the mode I crack-driving force actually experienced at the crack tip after the effects of crack closure have been “subtracted” from the far-field, applied driving force. When  $K_{cl}$  is less than the minimum applied value of  $K_I$ , closure is not active and  $\Delta K_{I,TH,eff}$  is equal to the applied value of  $\Delta K_{I,TH}$ .

Consideration in this manner of the influence of fatigue-crack closure on the near-tip mode I crack-driving force provides an explanation for the “nose” which is observed in the mixed-mode fatigue-crack growth threshold envelopes (Fig. 2). Recall that this nose is a manifestation of the fact that the mode I stress-intensity range at threshold,  $\Delta K_{I,TH}$ , does not decrease monotonically as the magnitude of shear loading (and hence phase angle,  $\beta$ ) increases. Instead, the value of  $\Delta K_{I,TH}$  increases slightly (for  $R = 0.1$  and 0.5) or remains constant ( $R = 0.8$ ) as  $\beta$  increases from  $0^\circ$  to  $26^\circ$  (Fig. 7). However, when the mode I crack-driving forces are considered in terms of the “closure-corrected” near-tip values,  $\Delta K_{I,TH,eff}$ , the increase in the mode I threshold stress-intensity range as  $\beta$  increases from  $0^\circ$  to  $26^\circ$  is no longer observed (or at least is significantly reduced). This is illustrated in Fig. 7, where  $\Delta K_{I,TH,eff}$  and  $\Delta K_{I,TH}$  are compared as a function of the applied phase angle,  $\beta$ . While it is important to remember that the measured values of  $K_{cl}$  represent only an approximate quantification of crack-tip shielding, these data strongly suggest that the nose which is observed in the mixed-mode fatigue-crack growth threshold envelope is largely a result of a shear-induced enhancement of mode I crack closure.

The measured variation of  $K_{cl}$  with  $R$  for  $\beta = 26^\circ$  also provides some insight regarding the relationship between  $\Delta G_{TH}$  and  $R$  (Fig. 8), which was previously discussed in Part I of this paper. The transition between a region of relatively strong load ratio dependence (for  $R < 0.5$ ) and relatively weak load ratio dependence



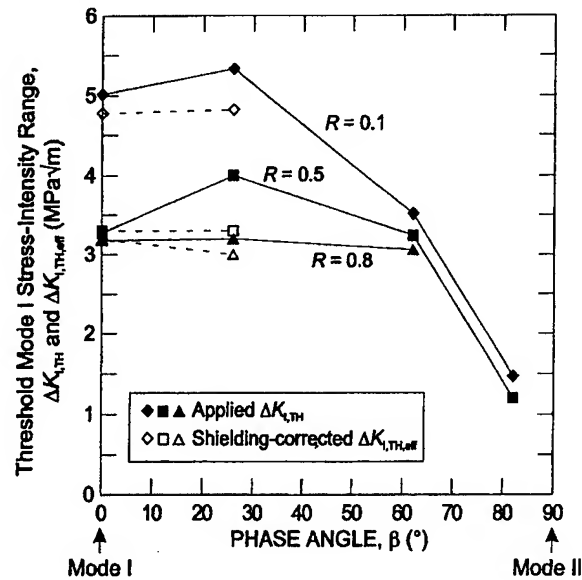


Fig. 7. The mode I stress-intensity range at threshold is plotted as a function of applied phase angle,  $\beta$ , both in terms of the applied  $\Delta K_{I,TH}$  and the near-tip, shielding-corrected  $\Delta K_{I,TH,eff}$ . The slight increase in  $\Delta K_{I,TH}$ , which is observed when  $\beta$  increases from  $0^\circ$  (mode I loading) to  $26^\circ$  ( $\Delta K_{II}/\Delta K_I = 0.5$ ) is essentially eliminated when the effects of crack closure are “subtracted” from the near-tip, crack-driving force, which is characterized by  $\Delta K_{I,TH,eff}$ .

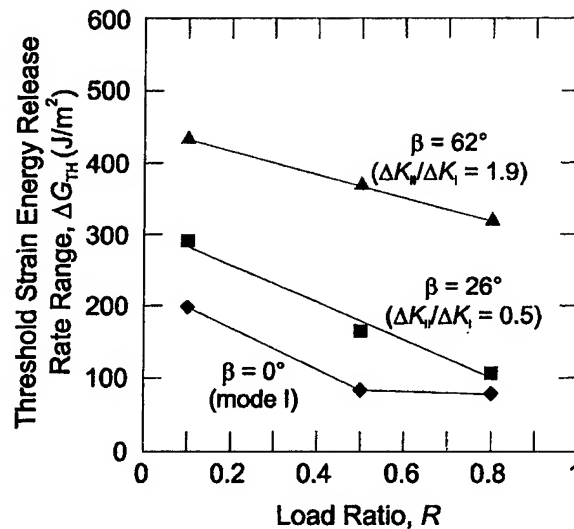


Fig. 8. The threshold range in strain energy release rate,  $\Delta G_{TH}$ , is plotted as a function of load ratio,  $R$ , for  $\beta = 0^\circ$ ,  $26^\circ$  and  $62^\circ$  ( $\Delta K_{II}/\Delta K_I = 0$ ,  $0.5$  and  $1.9$ , respectively). For each value of  $\beta$ , the fatigue-crack growth threshold decreases as load ratio increases.

(for  $R > 0.5$ ), which is exhibited by the pure mode I threshold data ( $\beta = 0^\circ$ ) arises primarily from a suppression of crack closure at higher load ratios [42]. The lack of such a transition for threshold data measured at  $\beta = 26^\circ$  appears to result from the fact that crack closure persists for load ratios up to  $R = 0.8$ .

Moreover, it is speculated that the absence of a transition between regimes of strong and weak load ratio dependence for the shear-dominant threshold data ( $\beta = 62^\circ$ ) is also due to the fact that crack-wake contact mechanisms are operative over the entire range of load ratio investigated. As quantified below, crack-wake contact mechanisms are found to be operative for all load ratios investigated at  $\beta = 62^\circ$  and  $82^\circ$ .

### 3.2.2. Mode II crack-tip shielding

Shielding with respect to the applied mode II loading is believed to arise due to both the development of frictional resistance to a relative shear displacement of the fatigue fracture surfaces, which inhibits but does not preclude relative motion, and mechanical interlock of fracture surface asperities, where any (local) relative motion of the fracture surfaces is severely restricted and must be accompanied by elastic or plastic deformation of the interlocking asperities. Such mode II shielding was quantified for all load ratios at  $\beta = 62^\circ$  and  $82^\circ$  ( $\Delta K_{II}/\Delta K_I = 1.9$  and  $7.1$ ), with the exception of the loading condition  $R = 0.8$  and  $\beta = 82^\circ$ , for which the fatigue-crack growth threshold has not been measured. To measure the magnitude of the effective, near-tip mode II crack-driving force at threshold,  $\Delta K_{II,TH,eff}$ , the following technique, which requires measurement of both the loading and unloading compliance curves, was developed. These compliance curves were determined using a COD gauge mounted approximately 1 mm behind the crack tip (Fig. 1).

The COD gauge employed consisted of a “c-section” of aluminum with strain gauges mounted on both cantilever arms. Likewise, the fixture for measuring mode II crack-wake displacements was machined from aluminum. Both the COD gauge and mode II fixture were adhesively bonded to the measurement surface; the area of contact (both above and below the crack) between the gauge and sample and between the mode II fixture and sample were approximately 1.5 mm (in the direction of displacement measurement) by 4 mm. Prior to attachment, both the COD gauge and mode II fixture were situated using a micrometer-equipped alignment and positioning fixture; this ensured precise placement of the gauge with respect to the crack tip and proper alignment with respect to the desired direction of measurement (mode I or mode II displacements).

An idealization of the general form of the resulting mode II compliance curve (applied load as a function of mode II crack-wake displacement) is shown in Fig. 9a. With respect to quantification of crack-tip shielding, the relevant features of this curve are best illustrated by considering it to be a composite of the following curves. In the absence of any crack-wake contact mechanisms, one would expect the mode II compliance curve to be perfectly linear, as shown in Fig. 9b. However, for a fatigue crack in a polycrystalline material, the crack path is generally somewhat tortuous, such that the fatigue fracture surfaces will come into contact with one another during mixed-mode loading. This fracture surface contact can be manifested as a frictional resistance to the shear displacement of the fracture surfaces with respect to one another. Frictional resistance to mode II crack-wake displacements will give rise to a mode II compliance curve characterized by hysteresis, as shown in Fig. 9c. The “knees” which are observed for the initial portions of both the loading and unloading curves (indicated as points a and b in Fig. 9c) are an indication of frictional locking of the crack wake following a reversal in loading direction. The form of this curve has previously been theorized by Smith and Smith [25].

In addition to developing frictional resistance to mode II shearing of the fracture surfaces, crack-wake contact can also result in asperity interlock, where asperities come into contact and, due to mechanical interlock, are prevented from displacing relative to one another. When such interlock occurs, the contacting asperities will deform elastically or plastically under the influence of the applied shear loading, and may eventually fracture. In Fig. 10, a scanning electron photomicrograph shows the crack-wake profile (imaged at the sample surface) resulting from a fatigue-crack growth threshold measurement at  $R = 0.5$  and  $\beta = 82^\circ$ . Interlocking asperities (indicated by arrows) show evidence of extensive deformation due to the applied shear loading.

The occurrence of asperity interlock will tend to increase the apparent stiffness of the sample as the locked portions of the crack wake will behave like uncracked ligaments. The experimentally observed mode

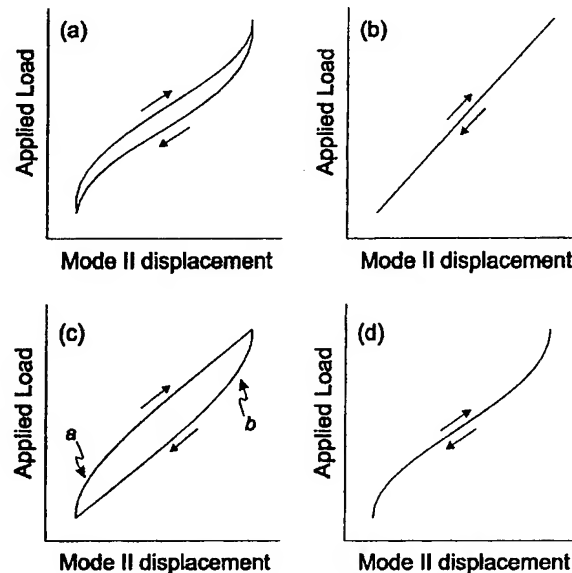


Fig. 9. The disparity between the general form of the mode II compliance curve, shown in (a), and the single linear loading and unloading curve (b), which would be exhibited in the absence of any crack-wake contact mechanisms, can be attributed to the presence of friction and asperity interlock in the fatigue-crack wake during the application of mixed-mode loading. For frictional resistance only to the relative shear displacements in the crack wake, the mode II compliance curve would appear as shown in (c). Here, the “knees” in the loading and unloading curves (indicated as points a and b, respectively) are a result of frictional locking in the crack wake following a reversal in loading direction. With significant asperity interlock present at the extremes of the applied loading cycle (but not friction), the compliance curve will appear as in (d). The observed loading and unloading mode II compliance curve (a) can be viewed as a composite of the curves shown in (b)–(d).

II compliance curves suggest that appreciable asperity interlock is most likely to develop near the maximum and minimum applied load, where the fracture surface asperities are, respectively, most out of registry or being prevented (by contact mechanisms) from returning to registry (Fig. 11). Asperity interlock in the crack wake, in the absence of friction,<sup>2</sup> will produce a compliance curve of the form shown in Fig. 9d. The features of the experimentally measured compliance curve (Fig. 9a) should now be recognizable as the traction-free, linear elastic curve (Fig. 9b), modified by the presence of crack-wake friction and asperity interlock.

Using this rationalization, the effective, near-tip, mode II, crack driving force at threshold,  $\Delta K_{II,TH,eff}$ , can now be estimated by the construction illustrated in Fig. 12. The following assumptions are made: (i) the mode II crack-tip opening displacement ( $CTOD_{II}$ ), measured very near to the crack tip (such that appreciable shielding cannot develop between the point of measurement and the actual crack tip), is characteristic of the actual value of  $K_{II}$  experienced at the crack tip, (ii) the maximum and minimum displacements, measured by the near-tip COD gauge, correspond to the points in the loading cycle where the  $CTOD_{II}$  is, respectively, a maximum and minimum, and (iii) the single, straight-line compliance curve which sample loading and unloading would follow in the absence of friction and asperity interlock (the wake-contact-free compliance) can be approximated as the average of the linear portions of the measured

<sup>2</sup> The condition of interlock in the absence of friction is not likely to occur in a real crack wake, as the asperity contact which gives rise to interlock (a near complete suppression of relative motion of the crack faces) is an extreme case of that which produces friction (inhibition of relative motion). However, consideration of this condition aids in the interpretation of the form of the mode II compliance curve without compromising the validity of the theory being presented here.

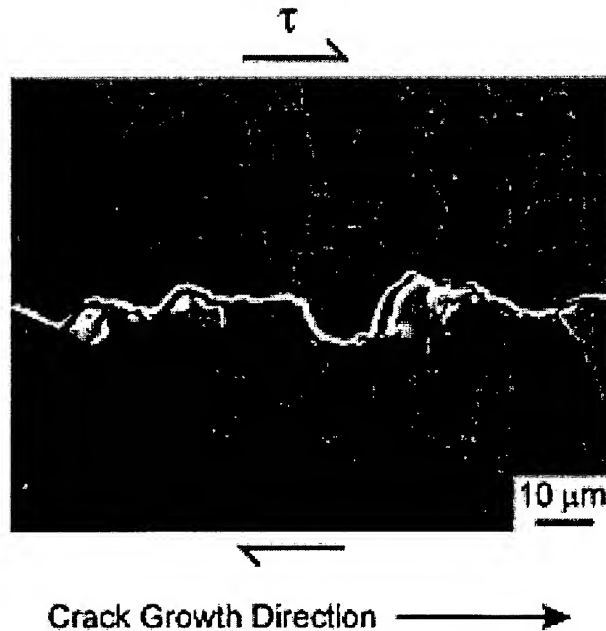


Fig. 10. A scanning electron photomicrograph shows the crack-wake profile (recorded at the sample surface) resulting from a fatigue-crack growth threshold measurement at  $R = 0.5$  and  $\beta = 82^\circ$ . Interlocking asperities (indicated by arrows) show evidence of extensive deformation due to impingement under the applied shear loading.

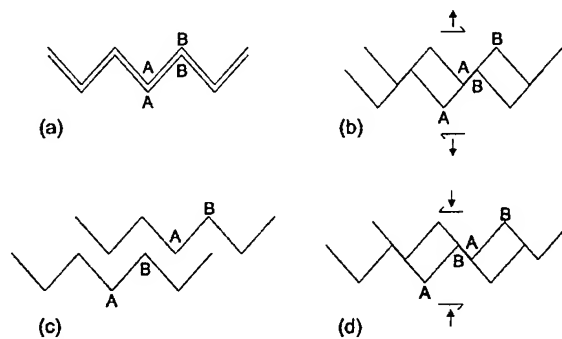


Fig. 11. This schematic illustration provides insight into the mechanistic origin of asperity interlock at the minimum of the applied cyclic loading waveform. In (a), mating fracture surface asperities are shown prior to the first application of mixed-mode loading. In (b), asperity contact is observed during the first loading cycle, as the fracture surfaces are both opened and sheared with respect to one another. At the maximum of the loading cycle (c), the asperities are observed to be out of registry. In (d), it is shown how, upon unloading, the asperities may come into contact in a manner which does not allow the mating fracture surfaces to regain registry at the minimum of the loading cycle, thus giving rise to asperity interlock.

loading and unloading compliance curve (Fig. 12); these linear portions of the measured compliance curves are observed to occur near the mean load.

As shown in Fig. 12, the loads corresponding to the maximum and minimum values of  $K_{II}$  experienced at the crack tip are then determined by the intersections of the maximum and minimum mode II crack-wake displacements,  $u_{II,max}$  and  $u_{II,min}$ , with the wake-contact-free compliance curve (points *a* and *b*). From the

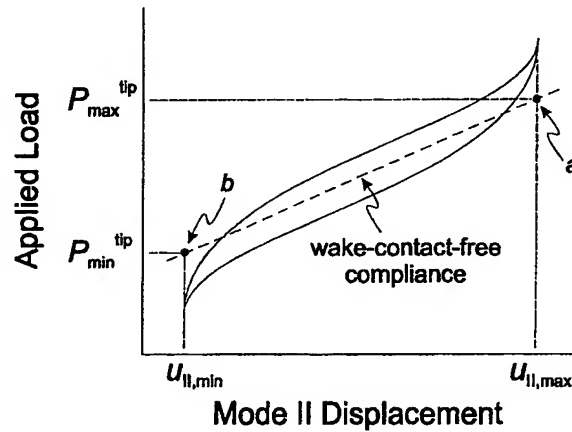


Fig. 12. The effective, near-tip, mode II, crack-driving force at threshold,  $\Delta K_{II,TH,eff}$ , can be estimated by finding the loads,  $P_{max}^{tip}$  and  $P_{min}^{tip}$ , at which the maximum and minimum mode II crack opening displacements intersect the wake-contact-free compliance curve.  $P_{max}^{tip}$  and  $P_{min}^{tip}$  can then be used in conjunction with the known crack length to calculate  $K_{II,max}^{tip}$  and  $K_{II,min}^{tip}$ . The near-tip, mode II, crack-driving force is then estimated as  $\Delta K_{II,TH,eff} = K_{II,max}^{tip} - K_{II,min}^{tip}$ .

second assumption above, these maximum and minimum displacements are representative of the  $CTOD_{II}$  extrema. The points a and b on the wake-contact-free compliance curve indicate the applied loads,  $P_{max}^{tip}$  and  $P_{min}^{tip}$ , which would be necessary to produce these  $CTOD_{II}$  extrema in the absence of any crack-wake shielding mechanisms. Thus,  $P_{max}^{tip}$  and  $P_{min}^{tip}$  can be used with the known crack length and the mode II stress-intensity solution for asymmetric four point bending [18] to calculate the maximum and minimum values of the mode II stress intensity experienced at the crack tip,  $K_{II,max}^{tip}$  and  $K_{II,min}^{tip}$ . An effective, near-tip, threshold, mode II stress-intensity range (from which the effects of crack-tip shielding have been removed) can then be calculated as

$$\Delta K_{II,TH,eff} = K_{II,max}^{tip} - K_{II,min}^{tip}.$$

Table 1 presents a comparison of the applied and effective, near-tip values of the mode II stress-intensity ranges at threshold; also shown is magnitude of the shielding, expressed as the reduction in  $\Delta K_{II}$  ( $= \Delta K_{II,TH} - \Delta K_{II,TH,eff}$ ).

The data presented in Table 1 illustrate that a significant portion of the applied mode II driving force can be absorbed by crack-tip shielding; for example, for  $R = 0.1$  and  $\beta = 82^\circ$ , only 46% of the applied mode II stress-intensity range is transmitted to the crack tip. Inspection of the data indicates that for both  $\beta = 62^\circ$  and  $82^\circ$ , the reduction in  $\Delta K_{II}$  due to crack-tip shielding decreases with increasing load ratio. This trend is consistent with physical intuition; as load ratio increases (for a fixed value of  $\beta$ ), the fatigue crack is more open during the entirety of the loading cycle (due to the elevated magnitudes of  $K_I$ ) and shear-induced,

Table 1

Comparison of applied and shielding-corrected, near-tip, mode II stress-intensity ranges

Load ratio, $R$	Phase angle, $\beta$ ( $^\circ$ )	$\Delta K_{II,TH}$ (MPa $\sqrt{m}$ )	$\Delta K_{II,TH,eff}$ (MPa $\sqrt{m}$ )	Reduction in $\Delta K_{II}$ (MPa $\sqrt{m}$ ) <sup>a</sup>
0.1	62	6.5	3.9	2.6
	82	10.4	4.8	5.6
0.5	62	6.0	4.6	1.4
	82	8.6	5.3	3.3
0.8	62	5.6	5	0.6

<sup>a</sup> The reduction in  $\Delta K_{II}$  is equal to  $\Delta K_{II,TH} - \Delta K_{II,TH,eff}$ .

crack-wake contact will be reduced. Also, consistent with physical intuition is the observation that for both  $R = 0.1$  and  $0.5$ , the reduction in  $\Delta K_{II}$  due to crack-tip shielding increases with mode mixity. An increase in phase angle,  $\beta$ , is accompanied by an increase in the magnitude of the applied shear loading and a decrease in the magnitude of tensile opening of the crack; under these conditions, crack-wake contact would be expected to increase.

### 3.3. Shielding-corrected mixed-mode thresholds

Using the measurements of mode I and mode II crack-tip shielding and the associated definitions of the near-tip mode I and mode II crack-driving forces (Eqs. (1) and (2)), it is now possible to rationalize the measured fatigue threshold data (Figs. 2 and 3) in terms of the driving force actually experienced at the crack tip. Although the meaning of mode I “crack closure” is somewhat altered for shear-dominant loading conditions, where the fatigue fracture surfaces are seemingly in contact during the entirety of the loading cycle (as evidenced by the occurrence of asperity interlock and frictional resistance to mode II crack-wake displacements), the notion of a reduction in the applied  $\Delta K_I$  by a wedging open of the crack continues to apply. As discussed below, consideration of the shielding-corrected fatigue thresholds gives considerable insight into the mechanism for the increase in fatigue-crack growth resistance with increasing mode mixity, observed in Fig. 3.

In Fig. 13, the mixed-mode fatigue-crack growth threshold envelopes for  $R = 0.1$ ,  $0.5$  and  $0.8$  are presented in terms of both the applied and near-tip (shielding-corrected) values of  $\Delta K_I$  and  $\Delta K_{II}$ . For the sake of simplicity, each threshold is presented simply as a single data point which is the average of the measured growth/no growth conditions given in Fig. 2. Applied values of the mode I and mode II driving forces ( $\Delta K_{I,TH}$  and  $\Delta K_{II,TH}$ ) are plotted as filled symbols with a solid line envelope; corresponding values of the

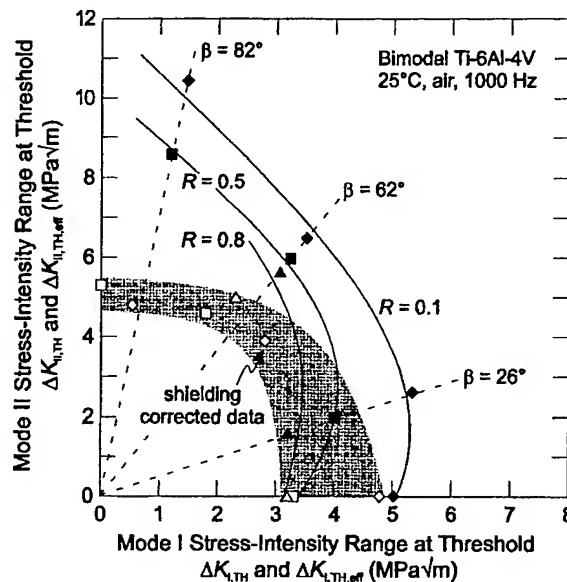


Fig. 13. Mixed-mode, fatigue-crack growth threshold envelopes for  $R = 0.1$ ,  $0.5$  and  $0.8$  are presented in terms of both the applied threshold stress-intensity ranges,  $\Delta K_{I,TH}$  and  $\Delta K_{II,TH}$  ( $\blacktriangle$ ,  $\blacklozenge$ ,  $\blacksquare$ ) and the near-tip, shielding-corrected values,  $\Delta K_{I,TH,eff}$  and  $\Delta K_{II,TH,eff}$  ( $\triangle$ ,  $\lozenge$ ,  $\square$ ). For shear-dominant loading conditions, the shielding-correct fatigue thresholds are considerably lower than those based upon the applied values of crack-driving force.

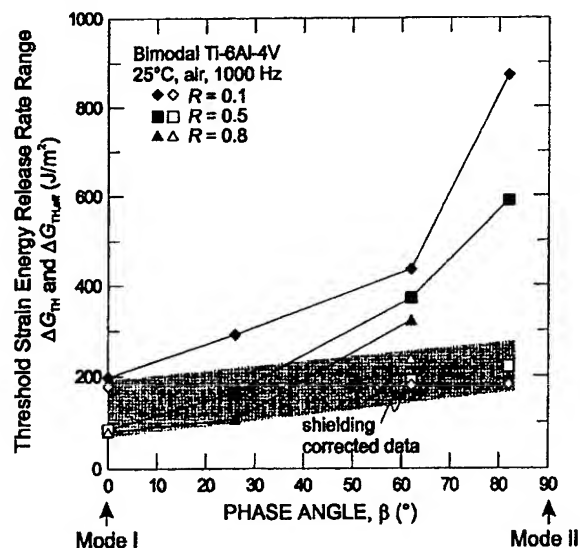


Fig. 14. Mixed-mode, fatigue-crack growth thresholds at  $R = 0.1, 0.5$  and  $0.8$  are presented in terms of both the applied value of  $\Delta G_{TH}$  (represented by  $\blacktriangle, \blacklozenge, \blacksquare$ ) and the shielding-corrected, near-tip driving force,  $\Delta G_{TH,eff}$  ( $\triangle, \diamond, \square$ ) as a function of the applied phase angle,  $\beta$ . From these data, it is apparent that the dramatic rise in fatigue-crack growth resistance (characterized by  $\Delta G_{TH}$ ) with increasing  $\beta$  is largely due to the development of extensive crack-tip shielding.

near-tip (shielding-corrected) driving forces ( $\Delta K_{I,TH,eff}$  and  $\Delta K_{II,TH,eff}$ ) are given by open data symbols bounded by a single scatter band.<sup>3</sup> It is apparent that the fatigue thresholds measured for shear-dominant loading conditions (applied  $\beta$  of  $62^\circ$  and  $82^\circ$ ) are well scaled at all load ratios by plotting the data in terms of the near-tip (shielding-corrected), crack-driving forces; indeed, near-tip threshold data for all load ratios fall within a relatively narrow scatter band.<sup>4</sup> Moreover, it is clear that the magnitude of the mixed-mode threshold is significantly reduced in the absence of crack-tip shielding.

For the tensile-dominant loading conditions, e.g.  $\beta = 0^\circ$  (pure mode I), the threshold data are not as well scaled by the application of crack-tip shielding corrections. However, this finding is consistent with previous reports of mode I fatigue-crack growth behavior in this same bimodal Ti-6Al-4V [38], where it was noted that the degradation of fatigue-crack growth resistance due to increasing load ratio cannot be explained solely by a consideration of crack closure effects.

In Fig. 14, the mixed-mode fatigue-crack growth thresholds are replotted in terms of the range in strain energy release rate as a function of the applied phase angle. Characterization of the thresholds in terms of the applied value of  $\Delta G_{TH}$  is represented by closed data point symbols, while the shielding-corrected, near-tip driving force,  $\Delta G_{TH,eff} (= \{\Delta K_{I,TH,eff}^2 + \Delta K_{II,TH,eff}^2\}/E')$  is represented by open data point symbols. This

<sup>3</sup> Since it was not possible to measure mode I  $K_{cl}$  values at  $\beta = 62^\circ$  and  $82^\circ$ , as noted above, measured values of  $K_{cl}$  at  $\beta = 26^\circ$  for the respective load ratios were used as estimates in order to plot  $\Delta K_{I,TH,eff}$  in Fig. 13. Because  $K_{cl}$  increases with the magnitude of shear offset of the fracture surfaces (Fig. 5), the values of  $K_{cl}$  measured at  $\beta = 26^\circ$  are believed to be conservative estimates of  $K_{cl}$  at  $\beta = 62^\circ$  and  $82^\circ$ . As no measurement was made of  $\Delta K_{II,TH,eff}$  for  $\beta = 26^\circ$ , no attempt is made to plot shielding-corrected threshold data for this phase angle.

<sup>4</sup> It is interesting to note here that the ratio of shear to tension ( $\Delta K_{II}/\Delta K_I$ ) experienced at the crack tip is not equal to the applied value of this parameter; this is indicated in Fig. 13 by the fact that the shielding-corrected thresholds do not lie on the lines of constant  $\beta$ , which intersect the non-shielding-corrected data. This alteration of the near-tip phase angle by crack-wake contact has been predicted by theoretical modeling of the fracture surface interactions [31].

plot suggests that mode I loading may continue to be worst case for mixed-mode thresholds characterized in terms of  $\Delta G_{TH,eff}$ , at least for higher load ratios, e.g.,  $R = 0.5$  and  $0.8$ . However, while the  $\Delta G_{TH}$  thresholds are increased by a factor of  $\sim 4$ – $7$  as  $\beta$  increases from  $0^\circ$  to  $82^\circ$ , in terms of the near-tip (shielding-corrected)  $\Delta G_{TH,eff}$  threshold, the increase is at most a factor of  $\sim 2.5$ . In fact, for  $R = 0.1$ , the  $\Delta G_{TH,eff}$  threshold appears to be essentially independent of mode mixity. Moreover, it is apparent that the threshold values for shear-dominant loading conditions are most significantly reduced when crack-tip shielding is “removed” from the applied crack-driving force; the improvement in fatigue-crack growth resistance associated with crack-tip shielding (i.e., the disparity between the shielding-corrected and uncorrected data) is progressively enhanced with increasing mode mixity.

These results provide strong evidence that the enhancement in fatigue-crack growth resistance, observed with increase in  $\Delta K_{II}/\Delta K_I$ , can be attributed largely to the development of crack-tip shielding due to fracture surface contact mechanisms in the crack wake. However, as noted above, there continues to be a slight increase in crack-growth resistance with increasing applied phase angle, at least for  $R = 0.5$  and  $0.8$  (Fig. 14), even after the effects of shielding have been accounted for (by characterizing in terms of  $\Delta G_{TH,eff}$ ). This suggests that additional mechanisms (aside from crack-tip shielding) may also be operative. It has been shown in Ref. [11] that for equivalent magnitudes of the stress-intensity range (i.e.,  $\Delta K_{II} = \Delta K_I$ ), the cyclic plastic-zone size increases by a factor of  $3.7$  when going from mode I to mode II loading conditions. Moreover, in a related study of interfacial toughness between an elastic–plastic solid and a non-yielding elastic solid, Tvergaard and Hutchinson [43] predict an increasing toughness with increasing applied phase angle due to the development of enhanced crack-tip plasticity in the elastic–plastic material. It is thus possible that the small increase in  $\Delta G_{TH,eff}$  with increasing  $\beta$  is a result of such shear-loading enhanced plastic deformation, and hence, increased shear displacements at the crack tip. Clearly, additional work is needed to make any definitive statements in this regard.

It has been shown that in this Ti–6Al–4V alloy, the pure mode I,  $\Delta G_{TH}$  fatigue-crack growth threshold is lower than that measured for any mixed-mode loading condition. This suggests that for design against HCF, the  $\Delta G_{TH}$  threshold determined in mode I could be used as a conservative estimate of the mixed-mode, fatigue-crack growth threshold. It is pertinent to note, however, that this conclusion is based on a study of cracks large compared to the scale of the microstructure and which have fracture surface dimensions on the order of several millimeters. The marked decrease in mixed-mode, fatigue-crack growth threshold values, when they are “corrected” for the influence of crack-tip shielding, implies that the mode I  $\Delta G_{TH}$  threshold may not be as conservative in the presence of small fatigue flaws with limited crack wake. While the results in Fig. 14 and those for short cracks in Part I [15] indicate that, even in the “absence” of crack-tip shielding, the  $\Delta G_{TH,eff}$  threshold may still increase somewhat with increasing applied phase angle, it is still not known whether such a shielding-corrected, mode I threshold will remain the lower-bound for cracks that are truly small compared to microstructural dimensions or whether the thresholds for such cracks will fall within the scatter band of  $\Delta G_{TH,eff}$  versus  $\beta$  shown in Fig. 14.

### 3.4. Comparison of short-crack and shielding-corrected, large-crack fatigue thresholds

In Fig. 15, mixed-mode, short-crack, fatigue threshold data for bimodal Ti–6Al–4V are compared with the scatterband of shielding-corrected, large-crack threshold data for  $R = 0.1$  to  $0.8$ ; further details regarding the short-crack data are given in Part I [15]. The mixed-mode, short-crack threshold data are generally in good agreement with the shielding-corrected, large-crack data, with two of the three measured short-crack thresholds lying within the shielding-corrected scatterband. However, the short-crack fatigue thresholds are at the lower end of, or even slightly below, the shielding-corrected, large-crack data scatterband.

This comparison between the short-crack and shielding-corrected, large-crack threshold data provides some insight regarding the accuracy of the compliance-based techniques developed for quantifying



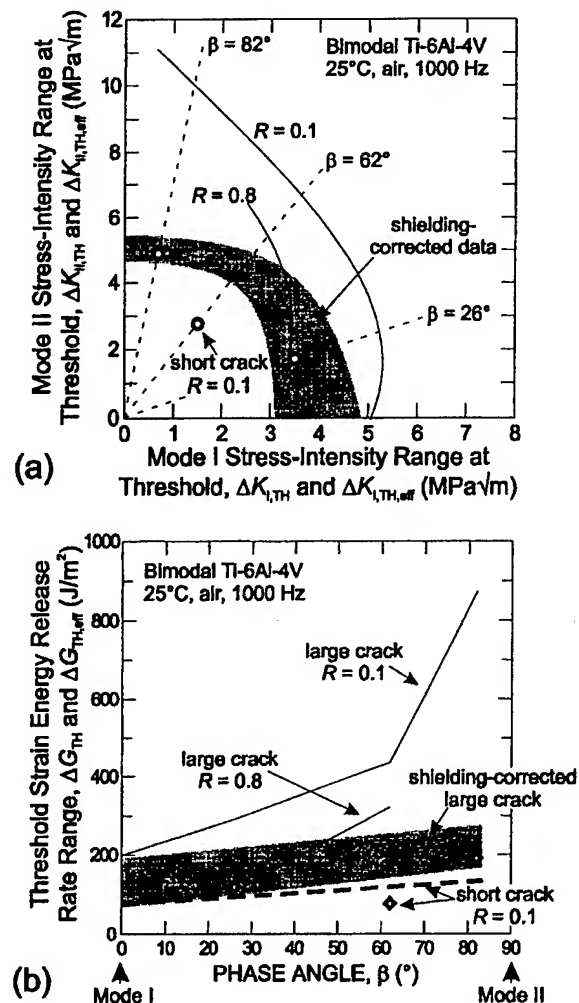


Fig. 15. The short-crack ( $R = 0.1$ , [15]) and large-crack ( $R = 0.1$  and  $0.8$ ) mixed-mode, fatigue-crack growth threshold data in bimodal Ti-6Al-4V are compared with a scatterband representing shielding-corrected, large-crack threshold data for  $R = 0.1$  to  $0.8$  both in terms of (a) the mixed-mode threshold envelope and (b) the threshold range in strain energy release rate,  $\Delta G_{TH}$ , as a function of the applied phase angle,  $\beta (= \tan^{-1}(\Delta K_{II}/\Delta K_I))$ . The short-crack thresholds are observed to be in reasonably good agreement with the shielding-corrected, large-crack data.

crack-tip shielding during mixed-mode cyclic loading. If it is assumed that the primary difference between the crack-growth behavior of large and short fatigue cracks is the disparity in crack-tip shielding, the observed correspondence of the current short-crack and large-crack, shielding-corrected data suggests that the methods employed to estimate crack-tip shielding are reasonably accurate. However, the fact that the scatterband of the shielding-corrected, large-crack thresholds are shifted to slightly higher fatigue-crack growth resistance compared to the short-crack data suggests that these compliance-based techniques for quantification of mixed-mode shielding may yield slightly non-conservative results. Moreover, it is important to remember that the potential influence of crack-wake-contact mechanisms has not been completely eliminated for the short-fatigue cracks due to the  $\sim 200 \mu m$  of crack wake which exists ( $\sim 20$  times the average grain size for bimodal Ti-6Al-4V); the magnitude of shielding which can develop within 200

$\mu\text{m}$  of crack wake is unclear. In the complete absence of crack-tip shielding, it is possible that the mixed-mode, fatigue-crack growth thresholds will be somewhat lower than the shielding-corrected, large-crack threshold reported here; in addition, the dependence of the fatigue-crack growth resistance (in terms of  $\Delta G$ ) on the applied phase angle  $\beta$  may well be further reduced.

#### 4. Conclusions

A study has been made of HCF crack-growth thresholds for large ( $>4$  mm) cracks subjected to high frequency (1000 Hz), combined mode I and mode II loading (mode mixities varying from  $\Delta K_{II}/\Delta K_I = 0$  to  $\sim 7$ ; phase angles from  $0^\circ$  to  $82^\circ$ ) in a Ti-6Al-4V turbine blade alloy with a bimodal (STOA) microstructure. Specifically, sample-compliance-based techniques have been employed to quantify the magnitude of the mixed-mode, crack-tip shielding with respect to both the applied mode I and mode II stress-intensity ranges,  $\Delta K_I$  and  $\Delta K_{II}$ , respectively, for load ratios ranging from  $R = 0.1$  to  $0.8$ . Based on this work, the following conclusions can be made:

(1) The significant increase in the  $\Delta G_{TH}$  fatigue-crack growth threshold with increasing mode mixity can be attributed primarily to a shear-induced enhancement of crack-tip shielding. As the magnitude of applied shear loading increases, the crack closure stress intensity (which shields the crack tip with respect to the applied mode I loading) increases. Furthermore, extensive shear-induced, crack-wake contact develops, which shields the crack tip with respect to the applied mode II loading. Quantitative estimates of the magnitude of this shear-induced, crack-tip shielding have been made by newly developed, experimental, compliance-based techniques.

(2) The mode I threshold stress-intensity range,  $\Delta K_{I,TH}$ , is somewhat insensitive to the superposition of shear loading for  $\Delta K_{II}/\Delta K_I = 0$  to  $1.9$  ( $\beta = 0^\circ$  to  $62^\circ$ ). In fact, for  $R = 0.1$  and  $0.5$ ,  $\Delta K_{I,TH}$  increases slightly as  $\Delta K_{II}/\Delta K_I$  increases from  $0$  to  $0.5$ . This insensitivity of  $\Delta K_{I,TH}$  to the increasing magnitude of superimposed shear loading can be attributed primarily to the above mentioned shear-induced enhancement of mode I fatigue-crack closure. For more strongly shear-dominant loading conditions, e.g.,  $\Delta K_{II}/\Delta K_I = 7.1$  ( $\beta = 82^\circ$ ), the value of  $\Delta K_{I,TH}$  is significantly reduced with respect to its value for pure mode I loading.

(3) When the  $\Delta G_{TH}$  fatigue-crack growth thresholds are characterized in terms of the near-tip (shielding-corrected), crack-driving force, the influence of mode mixity is significantly reduced. Moreover, the influence of load ratio on the fatigue threshold is also reduced for shear-dominant loading conditions (i.e.,  $\Delta K_{II}/\Delta K_I > 1$ ), although for tensile-dominant loading conditions, the thresholds continue to be load ratio dependent.

(4) As the  $\Delta G_{TH}$  fatigue-crack growth threshold for pure mode I is found to be lower than that measured for any other mixed-mode loading condition, this threshold could be considered as a lower-bound estimate of the mixed-mode, fatigue-crack growth threshold under HCF conditions. However, this conclusion has been formulated for cracks of "continuum-size" dimensions; its accuracy in the presence of cracks with microstructural dimensions remains to be tested.

#### Acknowledgements

This work was supported by the US Air Force Office of Scientific Research under Grant no. F49620-96-1-0478 under the auspices of the Multidisciplinary University Research Initiative on *High Cycle Fatigue* to the University of California.

## References

- [1] Cowles BA. High cycle fatigue in aircraft gas turbines – an industry perspective. *Int J Fract* 1996;80:147–63.
- [2] Nicholas T, Zuiker JR. On the use of the Goodman diagram for high cycle fatigue design. *Int J Fract* 1996;80:219–35.
- [3] Waterhouse RB, Lindley TC, editors. *Fretting Fatigue*. European Structural Integrity Society Publication No. 18. Mechanical Engineering Publications, London, 1994.
- [4] Gao H, Brown MW, Miller KJ. Mixed-mode fatigue thresholds. *Fatig Engng Mater Struct* 1982;5:1–17.
- [5] Gao H, Alagok N, Brown MW, Miller KJ. Growth of fatigue cracks under combined mode I and mode II loads. In: Miller KJ, Brown MW, editors. *Multiaxial fatigue*, ASTM STP 853. Philadelphia, PA: ASTM, 1985. p. 184–202.
- [6] Pustejovsky MA. Fatigue crack propagation in titanium under general in-plane loading – I: experiments. *Engng Fract Mech* 1979;11:9–15.
- [7] Pustejovsky MA. Fatigue crack propagation in titanium under general in-plane loading – II: analysis. *Engng Fract Mech* 1979;11:17–31.
- [8] Tanaka K. Fatigue crack propagation from a crack inclined to the cyclic tensile axis. *Engng Fract Mech* 1974;6:493–507.
- [9] Tong J, Yates JR, Brown MW. The influence of precracking techniques on fatigue crack growth thresholds under mixed mode I/II loading conditions. *Fatigue Fract Engng Mater Struct* 1994;17:1261–9.
- [10] Tong J, Yates JR, Brown MW. The significance of mean stress on the fatigue crack growth threshold for mixed mode I + II loading. *Fatigue Fract Engng Mater Struct* 1994;17:829–38.
- [11] Zheng YS, Wang ZG, Ai SH. Mixed-mode I and II fatigue threshold and crack closure in dual-phase steels. *Metall Mater Trans A* 1994;25A:1713–23.
- [12] Iida S, Kobayashi AS. Crack-propagation rate in 7075-T6 plates under cyclic tensile and transverse shear loading. *J Bas Engng* 1969;91:764–9.
- [13] John R, DeLuca D, Nicholas T, Porter J. Near-threshold crack growth behavior of a single crystal Ni-base superalloy subjected to mixed mode loading. In: Miller KJ, McDowell DL, editors. *Mixed-mode crack behavior*, ASTM STP 1359. Philadelphia, PA: ASTM, 1999. p. 312.
- [14] Ritchie RO, Davidson DL, Boyce BL, Campbell JP, Roder O. High-cycle fatigue of Ti–6Al–4V. *Fatigue Fract Engng Mater Struct* 1999;22:621–31.
- [15] Campbell JP, Ritchie RO. Mixed-mode, high-cycle fatigue-crack growth thresholds in Ti–6Al–4V. Part I. A comparison of large- and short-crack behavior. *Engng Fract Mech* 2000;67:209–27.
- [16] Eylon D. Summary of the available information on the processing of the Ti–6Al–4V HCF/LCF program plates. University of Dayton Report, 1998.
- [17] He MY, Cao HC, Evans AG. Mixed-mode fracture: the four-point shear specimen. *Acta Metall Mater* 1990;38:839–46.
- [18] He MY, Hutchinson JW. Asymmetric four-point crack specimen. *J Appl Mech* 2000;67:207–9.
- [19] Suresh S, Shih CF, Morrone A, O'Dowd NP. Mixed-mode fracture toughness of ceramic materials. *J Am Ceram Soc* 1990;73:1257–67.
- [20] Morgan JM, Milligan WW. A 1 kHz servohydraulic fatigue testing system. In: Soboyejo WO, Srivatsan TS, editors. *High Cycle Fatigue of Structural Materials*. Philadelphia, PA: TMS, 1997. p. 305–12.
- [21] Elber W. Fatigue crack closure under cyclic tension. *Engng Fract Mech* 1970;2:37–45.
- [22] Ritchie RO, Yu W. Short crack effects in fatigue: a consequence of crack tip shielding. In: Ritchie RO, Lankford J, editors. *Small Fatigue Cracks*. Philadelphia, PA: TMS-AIME, 1986. p. 167–89.
- [23] Pook LP. A failure mechanism map for mixed mode I and II fatigue crack growth threshold. *Int J Fract* 1985;28:R21–3.
- [24] Liu P, Wang Z. Mixed-mode I and II fatigue threshold and crack deflection angle in SiCp/2024Al composite. *Scripta Mater* 1996;34:1323–30.
- [25] Smith MC, Smith RA. Toward an understanding of mode II fatigue crack growth. In: Fong JT, Fields RJ, editors. *Basic questions in fatigue: vol. I*, ASTM STP 924. Philadelphia, PA: ASTM, 1988. p. 260–80.
- [26] Tong J, Yates JR, Brown MW. The formation and propagation of mode I branch cracks in mixed mode fatigue failure. *Engng Fract Mech* 1997;56:213–31.
- [27] Nayeb-Hashemi H, McClintock FA, Ritchie RO. Effects of friction and high torque on fatigue crack propagation in mode III. *Metall Trans A* 1982;13A:2197–204.
- [28] Tschegg EK. Sliding mode crack closure and mode III fatigue crack growth in mild steel. *Acta Metall* 1983;31:1323–30.
- [29] Tong J, Yates JR, Brown MW. A model for sliding mode crack closure. I. Theory for pure mode II loading. *Engng Fract Mech* 1995;52:599–611.
- [30] Tong J, Yates JR, Brown MW. A model for sliding mode crack closure. II. Mixed mode I and II loading and application. *Engng Fract Mech* 1995;52:613–23.
- [31] Carlson RL, Beevers CJ. A mixed mode fatigue crack closure model. *Engng Fract Mech* 1985;22:651–60.
- [32] Ritchie RO, Yu W, Bucci RJ. Fatigue crack propagation in ARALL laminates: measurement of the effect of crack-tip shielding from crack bridging. *Engng Fract Mech* 1989;32:361–77.

- [33] Campbell JP, Venkateswara Rao KT, Ritchie RO. The effect of microstructure on fracture toughness and fatigue crack growth behavior in  $\gamma$ -titanium aluminide based intermetallics. *Metall Mater Trans A* 1999;30A:563–77.
- [34] Evans AG. Perspective on the development of high-toughness ceramics. *J Am Ceram Soc* 1990;73:187–206.
- [35] Chan KS. Micromechanics of shear ligament toughening. *Metall Trans A* 1991;22A:2021–9.
- [36] Venkateswara Rao KT, Odette GR, Ritchie RO. Ductile-reinforcement toughening in  $\gamma$ -TiAl intermetallic-matrix composites: effects on fracture toughness and fatigue-crack propagation resistance. *Acta Metall Mater* 1994;42:893–911.
- [37] Tada H, Paris PC, Irwin GR. *The Stress Analysis of Cracks Handbook*, 2nd ed. St. Louis, MO: Paris Productions, 1985.
- [38] Ritchie RO, Boyce BL, Campbell JP, Roder O, Thompson AW, Milligan WW. Thresholds for high-cycle fatigue in a turbine engine Ti–6Al–4V alloy. *Int J Fatig* 1999;21:653–62.
- [39] Davidson DL, Lankford J. Fatigue crack growth in metals and alloys: mechanisms and micromechanics. *Int Mater Rev* 1992;37:45–76.
- [40] Abdel-Mageed AM, Pandey RK. Studies on cyclic crack path and the mixed mode crack closure behavior in Al-alloy. *Int J Fatig* 1992;14:21–9.
- [41] Suresh S, Ritchie RO. A geometric model for fatigue crack closure induced by fracture surface morphology. *Metall Trans A* 1982;13A:1627–31.
- [42] Schmidt RA, Paris PC. Threshold for fatigue crack propagation and effects of load ratio and frequency. In: *Progress in flaw growth and fracture toughness testing*, ASTM STP 536. Philadelphia, PA: ASTM, 1973. p. 79–94.
- [43] Tvergaard V, Hutchinson JW. The influence of plasticity on mixed-mode interface toughness. *J Mech Phys Solids* 1993;41: 1119–35.

# Mixed-Mode, High-Cycle Fatigue-Crack-Growth Thresholds in Ti-6Al-4V: Role of Bimodal and Lamellar Microstructures

J.P. CAMPBELL and R.O. RITCHIE

Mixed-mode, high-cycle fatigue-crack growth thresholds are reported for through-thickness cracks (large compared to microstructural dimensions) in a Ti-6Al-4V turbine blade alloy in both lamellar and bimodal microstructural conditions. Specifically, the effect of combined mode I and mode II loading, over a range of phase angles ( $\beta = \tan^{-1} (\Delta K_{II}/\Delta K_I)$ ) from 0 to 62 deg ( $\Delta K_{II}/\Delta K_I \sim 0$  to 1.9), is examined at a load ratio (ratio of minimum to maximum loads) of  $R = 0.1$  and a cyclic loading frequency of 1000 Hz in ambient-temperature air. When the mixed-mode, crack-driving force is characterized in terms of the strain-energy release rate ( $\Delta G$ ), incorporating contributions from both the applied tensile and shear loading, the threshold for fatigue-crack growth is observed to increase significantly with the applied mode-mixity ( $\Delta K_{II}/\Delta K_I$ ) for both microstructures, an effect attributed to enhanced crack-tip shielding. The pure mode I threshold, in terms of  $\Delta G_{TH}$ , is observed to be a lower bound (worst case) with respect to mixed-mode (I + II) behavior. For large crack sizes, the threshold fatigue-crack growth resistance of the lamellar structure is observed to be superior to that of the bimodal material for all phase angles investigated. Consideration of mode I fatigue-crack growth thresholds for small cracks in these same microstructures suggests that this rank ordering of mixed-mode fatigue resistance may not hold for crack lengths that are comparable to microstructural size scales. Examination of the fatigue-crack wake indicates that, for the lamellar microstructure, the path of crack extension is significantly influenced by the local microstructure over length scales on the order of the relatively coarse lamellar colonies ( $\sim 500 \mu\text{m}$ ). Comparatively, the crack path in the bimodal material is more strongly influenced by the applied crack-driving force. This disparity in behavior is attributed primarily to the relatively heterogeneous crack-growth resistance of the coarse lamellar microstructure.

## I. INTRODUCTION

TURBINE engine component failure under high-cycle fatigue (HCF) loading conditions, involving the rapid propagation of fatigue cracks under high-frequency vibratory loading,<sup>[1,2]</sup> is currently a major threat to the safety and readiness of the United States military aircraft fleet. Such failures are extremely costly and can lead to severe engine damage, loss of aircraft, and loss of life. Multiaxial loading conditions are known to exist at specific fatigue-critical locations within the turbine, particularly in association with fretting fatigue in the blade dovetail/disk contact section.<sup>[3]</sup> For fatigue-crack growth in such situations, the resultant crack-driving force may be a combination of the influence of the mode I (tensile opening) stress-intensity range ( $\Delta K_I$ ) as well as the mode II (in-plane shear) and/or mode III (antiplane shear) stress-intensity ranges ( $\Delta K_{II}$  and  $\Delta K_{III}$ , respectively). While the majority of fatigue-crack growth data have been measured in mode I only, it is known that the superposition of cyclic shear ( $\Delta K_{II}$  or  $\Delta K_{III} > 0$ ) to cyclic tension can lower the mode I threshold stress-intensity range,<sup>[4-12]</sup> sometimes significantly.<sup>[13]</sup>

For the HCF of turbine engine alloys, it is critical to

quantify the effect of mixed-mode loading on the fatigue-crack growth threshold, as the extremely high cyclic loading frequencies ( $\sim 1$  to 2 kHz) and correspondingly short times to failure may necessitate a threshold-based design methodology.<sup>[14]</sup> Given this and the fact that such loading conditions exist in fatigue-critical components, the paucity of mixed-mode fatigue-crack-propagation data in aerospace titanium alloys<sup>[5,6,7]</sup> is of some concern.

Accordingly, in the present work, mixed-mode fatigue-crack growth thresholds for combined mode I + II loading are examined in a turbine blade alloy (Ti-6Al-4V) in both the lamellar and bimodal microstructural conditions. The influence of various degrees of mode-mixity on the crack-growth threshold condition (at  $R = 0.1$ ) is investigated for cyclic loading frequencies characteristic of turbine engine HCF. It is found that, provided the crack-driving force is characterized in terms of the strain-energy release rate ( $\Delta G_{TH}$ ), which incorporates both tensile and shear contributions, the fatigue-crack growth threshold for cracks that are large relative to microstructural dimensions actually increases with increasing applied phase angle  $\beta$  (equal to  $\tan^{-1} (\Delta K_{II}/\Delta K_I)$ ) for both microstructures, implying that the mode I threshold, expressed in terms of  $\Delta G_{TH}$ , is the lower bound (at least for continuum-sized cracks). Furthermore, compared to the bimodal microstructure, the lamellar microstructure is seen to be more resistant to (large-crack) mixed-mode fatigue-crack growth for all phase angles investigated, although there are indications that this comparison may be reversed for cracks that are small with respect to microstructural size scales.

J.P. CAMPBELL, formerly with the Department of Materials Science and Mineral Engineering, University of California, is Senior Manufacturing Engineer, Metals Fabrication Division, General Motors, Troy, MI 48084. R.O. RITCHIE, Professor, is with the Department of Materials Science and Engineering, University of California, Berkeley, CA 94720-1760.

Manuscript submitted March 31, 2000.

Table I. Chemical Composition of Ti-6Al-4V Bar Stock (in Weight Percent)<sup>[15]</sup>

Bar Location	Ti	Al	V	Fe	O	N	H
Top	bal	6.27	4.19	0.20	0.18	0.012	0.0041
Bottom	bal	6.32	4.15	0.18	0.19	0.014	0.0041

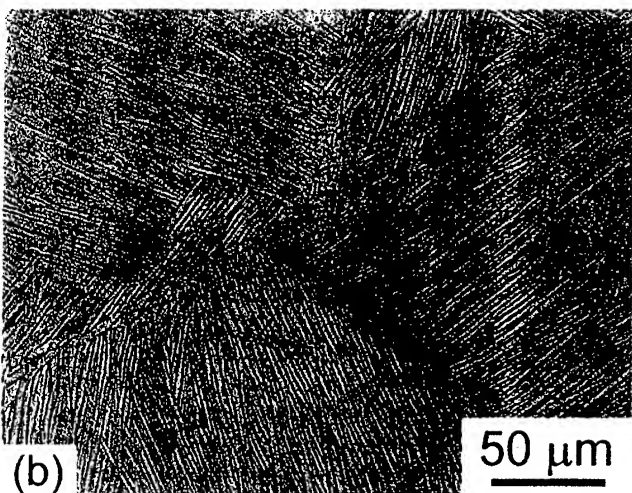
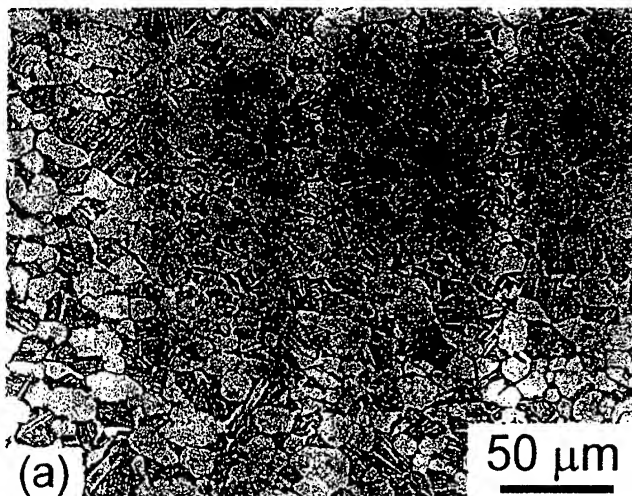


Fig. 1—Optical photomicrographs of the (a) bimodal and (b) lamellar microstructures in Ti-6Al-4V. The bimodal structure consists of nearly equiaxed grains of primary  $\alpha$  phase ( $\sim 20 \mu\text{m}$  in diameter) and regions of lamellar  $\alpha + \beta$ . For the lamellar structure, no equiaxed primary  $\alpha$  phase is present, and the lamellar colony size is considerably larger ( $\sim 500 \mu\text{m}$  average diameter).

## II. MATERIALS AND EXPERIMENTAL METHODS

### A. Material

The material investigated was a forged Ti-6Al-4V turbine engine alloy, of the chemical composition shown in Table I. This alloy was processed as mill-annealed, forging bar stock specifically for the joint military-industry-university HCF program by Teledyne Titanium (Pittsburgh, PA). It was solution treated (1 hour) at  $925^\circ\text{C}$  in air, fan air cooled, and then stabilized (2 hours) at  $700^\circ\text{C}$  *in vacuo*. The resultant bimodal microstructure (Figure 1(a)), which has been

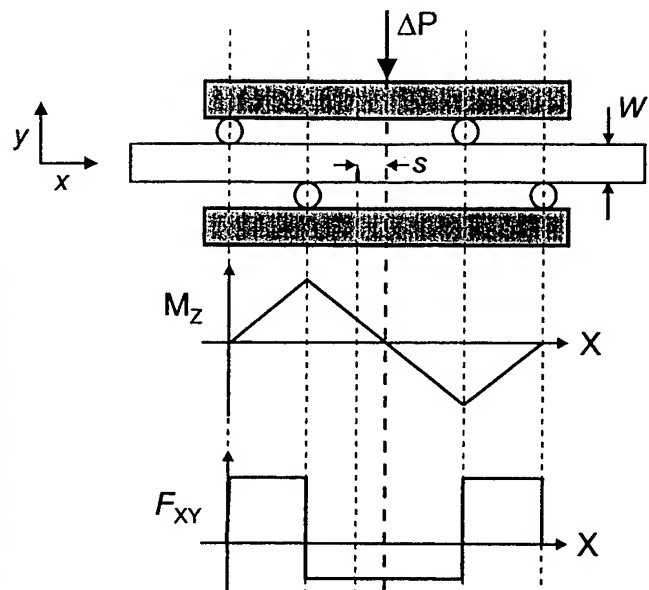


Fig. 2—The asymmetric four-point bend crack growth sample and the associated shear force,  $F_{xy}$ , and bending moment,  $M_z$ , diagrams are shown. A pure mode II loading condition can be applied with the crack located on the load line. When the crack is offset from the load line by an amount  $s$ , the value of  $s/W$  (where  $W$  is the beam height) dictates the ratio of  $\Delta K_{II}$  to  $\Delta K_I$ .

referred to as solution treated and overaged, was composed of 64.1 vol pct nearly equiaxed primary  $\alpha$  (average grain diameter of  $\sim 20 \mu\text{m}$ ) and lamellar  $\alpha + \beta$  colonies (lamellar spacing of  $\sim 1 \mu\text{m}$ ). Full details are given elsewhere.<sup>[14,15,16]</sup>

For comparison, a fully lamellar microstructure (Figure 1(b)) was produced from the bimodal material by solution treating *in vacuo* at  $1005^\circ\text{C}$  for 10 minutes. The material was rapidly quenched from the solution-treatment temperature by filling the chamber with high-purity helium to a small positive pressure; this gave initial cooling rates of  $\sim 100^\circ\text{C}/\text{min}$ , which were chosen to achieve a similar lamellar spacing to the bimodal structure ( $\sim 1 \mu\text{m}$ ). Following cooling, the material was reheated and stabilized *in vacuo* at  $700^\circ\text{C}$  for 2 hours and then slow furnace cooled. This produced a fully lamellar ( $\alpha + \beta$ ) microstructure with average colony and prior- $\beta$  grain sizes of  $\sim 500 \mu\text{m}$  and  $\sim 1000 \mu\text{m}$ , respectively.

Tensile tests, conducted in the longitudinal ( $L$ ) orientation on both microstructures at initial strain rates of  $5 \times 10^{-4} \text{ s}^{-1}$ , gave average yield and tensile strengths of, respectively, 930 and 978 MPa in the bimodal material<sup>[15]</sup> and 975 and 1055 MPa in the lamellar material.

### B. Experimental Methods

Mixed-mode fatigue-crack growth thresholds were measured using asymmetric four-point bend (AFPB) specimens, with a width of 11.3 mm and a thickness of 4.5 mm, which were electrical-discharge machined in the  $L$ - $T$  orientation. Inner and outer loading spans of 12.7 and 25.4 mm, respectively, were utilized. The effect of friction at the loading pins was minimized by the use of a high-pressure  $\text{MoS}_2$  grease. For the AFBP geometry,<sup>[4,17-19]</sup> the bending moment ( $M_z$ ) varies linearly between the inner loading points, while the shear force ( $F_{xy}$ ) is constant in this region (Figure 2), such that a cracked sample may be subjected to loading

conditions ranging from pure mode II to mode I-dominant by varying the distance by which the crack is offset from the load line ( $s$ ). Mixed-mode loading conditions were quantified in terms of the mode-mixity ( $\Delta K_{II}/\Delta K_I$ ), which was varied from 0 (pure mode I) to 1.9, and the corresponding phase angle ( $\beta$ , equal to  $\tan^{-1}(\Delta K_{II}/\Delta K_I)$ ), which varied from 0 to 62 deg\*. Pure mode I tests were conducted in symmetri-

\*Note that although the mode-mixity ( $K_{II}/K_I$ ) varies with crack depth for the AFPB specimens, this was not an issue for the present experiments, as all threshold measurements were made at crack initiation from an identically sized precrack.

cal four-point bend.

Because of the marked influence on mixed-mode behavior of the precracking technique<sup>[9]</sup> and crack-wake shielding effects,<sup>[4,20-23]</sup> a specific fatigue-precracking regimen was employed. Precracks were grown in bending under pure mode I, decreasing- $\Delta K$  conditions using computer-automated stress-intensity control, from a 2-mm-deep electrical discharge machined notch with a load ratio ( $R = K_{min}/K_{max}$ ) of 0.1, a frequency of 125 Hz (sine wave), and a  $K$  gradient\*

\*The  $K$  gradient ( $C$ ) is defined by the equation  $\Delta K_o = \Delta K_i \exp(C(a_o - a_i))$ , where the subscripts  $o$  and  $i$  indicate the current and initial parameter values.

( $C$ ) of  $-0.15 \text{ mm}^{-1}$ . These values of cyclic loading frequency and  $K$  gradient were chosen to allow for rapid, yet easily controlled, load shedding to a near-threshold growth rate. A final precrack length of  $4.50 \pm 0.25 \text{ mm}$  was achieved, corresponding to near-threshold  $\Delta K$  values of  $\sim 4.8$  and  $8.0 \text{ MPa}\sqrt{\text{m}}$  in the bimodal and lamellar microstructures, respectively. In both cases, crack growth rates at the end of precracking were in the range of  $10^{-9}$  to  $10^{-10} \text{ m/cycle}$ . These same loading conditions were used to generate the precracks used to measure mode I thresholds.

It should be noted that the large difference in cyclic loading frequencies between the precracking and fatigue-crack growth threshold measurement is believed to have no effect on the present results. For the same bimodal material investigated here, it has previously been shown that the mode I fatigue-crack growth resistance is independent of loading frequency when tested in ambient-temperature air between 50 and 1700 Hz.<sup>[14]</sup> Here, it is presumed that this frequency independence also holds for mixed-mode loading and for the lamellar microstructure in this same alloy.

Testing was performed on an MTS servohydraulic high-frequency testing machine incorporating a voice-coil servovalve.<sup>[24]</sup> The AFPB samples were loaded with the precrack tip offset from the load line to achieve the desired  $\Delta K_{II}/\Delta K_I$  ratio. The necessary offset and values of  $\Delta K_I$  and  $\Delta K_{II}$  corresponding to the applied-load amplitude were determined using a recently updated stress-intensity solution for the AFPB geometry.<sup>[18]</sup> For the bimodal microstructure, samples were then subjected to 2 million cycles at 1000 Hz (sine wave), with  $R = 0.1$ . If no crack growth was observed by optical microscopy,  $\Delta K_I$  or  $\Delta K_{II}$  was increased by  $\sim 0.25 \text{ MPa}\sqrt{\text{m}}$  and the test was repeated. In this way, the threshold for the onset of crack growth (defined at a growth rate less than  $10^{-11} \text{ m/cycle}$ ) was measured as a "growth/no growth" set of loading conditions bounding the true threshold. Analogous testing procedures were employed to determine the pure mode I fatigue-crack growth threshold, with the exception that a symmetric four-point bend geometry was employed.

Threshold measurements were similar for the lamellar microstructure, except that samples were subjected to 5 million cycles at each load amplitude. As the lamellar microstructure is known to exhibit heterogeneous crack-growth resistance,<sup>[25-30]</sup> a higher number of cycles was used to ensure that a growing crack would sample the relatively stronger barriers present, *e.g.*, colony boundaries and prior  $\beta$  grain boundaries.<sup>[25,26]</sup> In such a way, the measured threshold could be considered representative of the stress intensity above which a fatigue crack would overcome all microstructural barriers and ultimately lead to failure. Utilizing these techniques, fatigue thresholds in the lamellar microstructure were defined at growth rates less than  $10^{-10} \text{ m/cycle}$  ( $\equiv 500 \mu\text{m}$  of crack extension, *i.e.*, the average colony diameter, in 5 million cycles).

### III. RESULTS AND DISCUSSION

#### A. Mixed-Mode Fatigue-Crack Growth Thresholds

Mixed-mode fatigue-crack growth thresholds for large ( $\sim 4.5 \text{ mm}$ ) cracks in lamellar and bimodal Ti-6Al-4V, at a load ratio of  $R = 0.1$  and a frequency of 1000 Hz (sine wave), are compared in Figure 3(a) in terms of threshold envelopes, where the mode II stress-intensity range at the threshold ( $\Delta K_{II,TH}$ ) is plotted as a function of the corresponding mode I value ( $\Delta K_{I,TH}$ ). Data are shown for applied phase angles of  $\beta = 0, 26$ , and  $62 \text{ deg}$  ( $\Delta K_{II}/\Delta K_I = 0, 0.5$ , and  $1.9$ , respectively). For the bimodal microstructure only, results at higher phase angles of up to  $82 \text{ deg}$  ( $\Delta K_{II}/\Delta K_I$  values up to 7) and at load ratios of up to  $R = 0.8$  are presented elsewhere.<sup>[31,32]</sup> In Figure 3(a), the closed and open symbols represent the loading conditions that produced, respectively, no crack growth and crack growth; these loading conditions bound the true threshold for the onset of crack extension. In Figure 3(b), these same data are plotted in terms of the threshold range of the strain-energy release rate ( $\Delta G_{TH}$ ) as a function of  $\beta$ . Here, a single data point represents each threshold, which is the average of the growth/no growth combination of data points in Figure 3(a). The parameter  $\Delta G_{TH}$  incorporates both the applied shear and tensile loading into a single-parameter characterization of the crack-driving force, as  $\Delta G_{TH} = (\Delta K_{I,TH}^2 + \Delta K_{II,TH}^2)/E'$ , where  $\Delta K_{I,TH}$  and  $\Delta K_{II,TH}$  are the applied values of these parameters and  $E' = E/(1 - \nu^2)$  for plane strain where ( $E$  is the elastic modulus and  $\nu$  is the Poisson's ratio).\* The parameter  $\Delta G_{TH}$

\*It should be noted that  $\Delta G$  defined in this way is not exactly equal to  $G_{max} - G_{min}$ , where  $G_{max}$  and  $G_{min}$  are, respectively, the values of  $G$  determined at the maximum and minimum loads of the fatigue cycle.

could also be represented as an equivalent threshold stress-intensity range ( $\Delta K_{eq,TH} = (\Delta K_{I,TH}^2 + \Delta K_{II,TH}^2)^{1/2}$ ), where  $\Delta K_{eq,TH} = (\Delta G_{TH}E')^{1/2}$ . An error analysis has previously been reported<sup>[31]</sup> for the mixed-mode fatigue-crack growth thresholds in the bimodal microstructure.

As reported previously,<sup>[31,32]</sup> the use of this single-parameter characterization of the mixed-mode fatigue-crack growth resistance (Figure 3(b)) indicates that the threshold for fatigue-crack growth in bimodal Ti-6Al-4V, defined in terms of  $\Delta G_{TH}$ , increases monotonically with the applied phase angle. In fact, for phase angles of up to  $82 \text{ deg}$ ,<sup>[31]</sup> the  $\Delta G_{TH}$  threshold for the bimodal material can be up to 7 times the



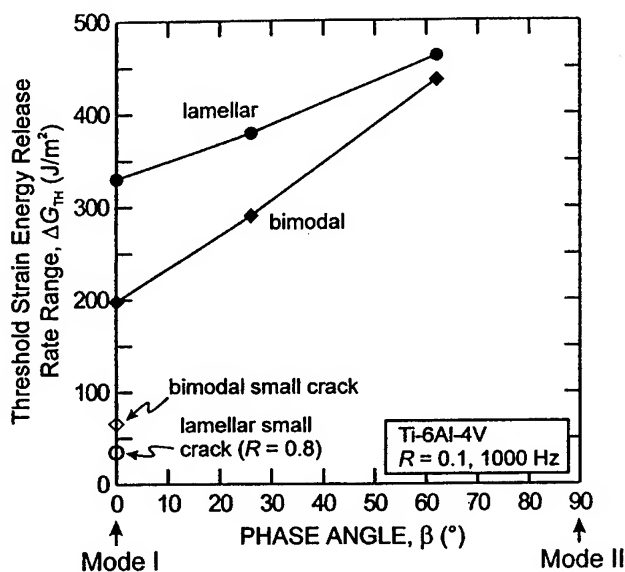


Fig. 5—Mixed-mode fatigue-crack growth thresholds for large crack sizes in lamellar and bimodal Ti-6Al-4V are compared with pure mode I thresholds (in terms of  $\Delta G_{TH}$ ) for small cracks in these same bimodal<sup>[52]</sup> and lamellar<sup>[53]</sup> microstructures.

have been reported for mode I fatigue-crack growth in other titanium alloys.<sup>[39–41,55]</sup> This reversal has been attributed largely to the prominent role of crack-wake shielding on the large-crack fatigue resistance of lamellar microstructures; such effects are necessarily limited for small cracks, due to their restricted wake.<sup>[56,57]</sup> Although mixed-mode small-crack results in Ti-6Al-4V are not currently available, the data in Figure 5 do suggest that the superior mixed-mode fatigue-crack growth resistance of the lamellar microstructure must be considered to be specific to large cracks. This is particularly true given the prominent role that crack-wake shielding has been shown to play during the mixed-mode fatigue-crack growth of large cracks.<sup>[21–23,31,32,58]</sup>

#### IV. SUMMARY AND CONCLUSIONS

Mixed-mode (I + II) fatigue-crack growth behavior has been examined for large cracks in bimodal and lamellar microstructures in a Ti-6Al-4V alloy tested at  $R = 0.1$  and a 1000 Hz frequency in ambient-temperature air. Fatigue-crack growth thresholds were measured for applied phase angles ranging from 0 to 62 deg ( $\Delta K_{II}/\Delta K_I = 0$  to 1.9), and the resultant crack-path trajectories were compared to that predicted by the MTS criterion. Based on these results and a comparison with mode I small-crack fatigue thresholds in the same materials, the following conclusions can be made.

1. Mixed-mode fatigue-crack growth resistance in the presence of large cracks is observed to increase substantially with an increasing applied phase angle, for both the bimodal and lamellar microstructures. Thus, for the continuum-sized cracks (*i.e.*, large when compared to microstructural dimensions) in this alloy, the pure mode I threshold, defined in terms of  $\Delta G_{TH}$ , may be used as a conservative, lower-bound estimate of the mixed-mode fatigue-crack growth threshold. This effect is attributed to enhanced crack-tip shielding in the crack wake with increasing mode-mixity.

2. For all phase angles investigated, the (large-crack) fatigue-crack growth resistance in the lamellar microstructure was found to be superior to that of the bimodal material. However, for shear-dominant loading conditions ( $\Delta K_{II}/\Delta K_I = 1.9$ ), the difference in the crack-growth resistance of the two microstructures is reduced.
3. Whereas the lamellar Ti-6Al-4V alloy displays superior resistance to the bimodal alloy with respect to mixed-mode fatigue-crack growth in the presence of large cracks, comparison with mode I fatigue-crack growth results suggested that this trend may be reversed in the presence of small cracks.
4. The fatigue-crack growth behavior in lamellar Ti-6Al-4V illustrates that the trajectory of crack propagation under mode I and mixed-mode loading is significantly influenced by both the crack-driving force and the near-tip microstructure. For the bimodal microstructure, which is fine-scale and homogeneous, crack extensions over length scales of interest occur along a path governed by the maximum tangential stress ( $\equiv K_{II} = 0$ ). However, due to the heterogeneous crack-growth resistance of the lamellar microstructure, crack paths in this structure are controlled primarily by the microstructure for crack extensions over length scales that are on the order of the characteristic microstructural dimensions. Since these dimensions pertain to the lamellar colony size, which is quite large ( $\sim 500 \mu\text{m}$ ), such behavior is anticipated for crack sizes that are of practical interest for turbine engine high-cycle fatigue.

#### ACKNOWLEDGMENTS

This work was supported by the United States Air Force Office of Scientific Research under Grant No. F49620-96-1-0478 under the auspices of the Multidisciplinary University Research Initiative on *High Cycle Fatigue* to the University of California.

#### REFERENCES

1. B.A. Cowles: *Int. J. Fract.*, 1996, vol. 80, pp. 147-63.
2. T. Nicholas and J.R. Zuiker: *Int. J. Fract.*, 1996, vol. 80, pp. 219-35.
3. *Fretting Fatigue*, R.B. Waterhouse and T.C. Lindley, eds.,ESIS Publication No. 18, European Structural Integrity Society, Mechanical Engineering Publications Ltd., London, 1994.
4. H. Gao, M.W. Brown, and K.J. Miller: *Fatigue Eng. Mater. Struct.*, 1982, vol. 5, pp. 1-17.
5. H. Gao, A. Alagok, M.W. Brown, and K.J. Miller: in *Multiaxial Fatigue*, ASTM STP 853, M.W. Brown and K.J. Miller, eds., ASTM, Philadelphia, PA, 1985, pp. 184-202.
6. M.A. Pustejovsky: *Eng. Fract. Mech.*, 1979, vol. 11, pp. 9-15.
7. M.A. Pustejovsky: *Eng. Fract. Mech.*, 1979, vol. 11, pp. 17-31.
8. K. Tanaka: *Eng. Fract. Mech.*, 1974, vol. 6, pp. 493-507.
9. J. Tong, J.R. Yates, and M.W. Brown: *Fatigue Fract. Eng. Mater. Struct.*, 1994, vol. 17, pp. 1261-69.
10. J. Tong, J.R. Yates, and M.W. Brown: *Fatigue Fract. Eng. Mater. Struct.*, 1994, vol. 17, pp. 829-38.
11. Y.S. Zheng, Z.G. Wang, and S.H. Ai: *Metall. Mater. Trans.*, 1994, vol. 25A, pp. 1713-23.
12. S. Iida and A.S. Kobayashi: *J. Basic Eng.*, 1969, vol. 91, pp. 764-69.
13. R. John, D. DeLuca, T. Nicholas, and J. Porter: in *Mixed-Mode Crack Behavior*, ASTM STP 1359, K.J. Miller and D.L. McDowell, eds., ASTM, West Conshohocken, PA, 1999, p. 312.
14. R.O. Ritchie, D.L. Davidson, B.L. Boyce, J.P. Campbell, and O. Roder: *Fatigue Fract. Eng. Mater. Struct.*, 1999, vol. 22, pp. 621-31.
15. D. Eylon: "Summary of the Available Information on the Processing



- of the Ti-6Al-4V HCF/LCF Program Plates," University of Dayton Report, University of Dayton, Dayton, OH, 1998.
16. B.L. Boyce: Master's Thesis, University of California at Berkeley, Berkeley, CA, 1998.
  17. M.Y. He, H.C. Cao, and A.G. Evans: *Acta Metall. Mater.*, 1990, vol. 38, pp. 839-46.
  18. M.Y. He and J.W. Hutchinson: *J. Appl. Mech.*, 2000, vol. 67, pp. 207-09.
  19. S. Suresh, C.F. Shih, A. Morrone, and N.P. O'Dowd: *J. Am. Cer. Soc.*, 1990, vol. 73, pp. 1257-67.
  20. H. Nayeb-Hashemi, F.A. McClintock, and R.O. Ritchie: *Metall. Trans. A*, 1982, vol. 13A, pp. 2197-2204.
  21. M.C. Smith and R.A. Smith: in *Basic Questions in Fatigue: Volume I*, ASTM STP 924, J.T. Fong and R.J. Fields, eds., ASTM, Philadelphia, PA, 1988, pp. 260-80.
  22. J. Tong, J.R. Yates, and M.W. Brown: *Eng. Fract. Mech.*, 1995, vol. 52, pp. 599-611.
  23. J. Tong, J.R. Yates, and M.W. Brown: *Eng. Fract. Mech.*, 1995, vol. 52, pp. 613-23.
  24. J.M. Morgan and W.W. Milligan: in *High Cycle Fatigue of Structural Materials*, W.O. Soboyejo and T.S. Srivatsan, eds., TMS, Warrendale, PA, 1997, pp. 305-12.
  25. G.R. Yoder, L.A. Cooley, and T.W. Crooker: *Metall. Trans. A*, 1977, vol. 8A, pp. 1737-43.
  26. D. Eylon, J.A. Hall, C.M. Pierce, and D.L. Ruckle: *Metall. Trans. A*, 1976, vol. 7A, pp. 1817-26.
  27. D.L. Davidson and D. Eylon: *Metall. Trans. A*, 1980, vol. 11A, pp. 837-43.
  28. A.W. Bowen: *Acta Metall.*, 1975, vol. 11, pp. 1401-09.
  29. J. Lindigkeit, G. Terlinde, A. Gysler, and G. Lütjering: *Acta Metall.*, 1979, vol. 27, pp. 1717-26.
  30. C.C. Wojcik, K.S. Chan, and D.A. Koss: *Acta Metall.*, 1988, vol. 36, pp. 1261-70.
  31. J.P. Campbell and R.O. Ritchie: *Eng. Fract. Mech.*, 2000, vol. 67, pp. 209-27.
  32. J.P. Campbell and R.O. Ritchie: *Eng. Fract. Mech.*, 2000, vol. 67, pp. 229-49.
  33. M.D. Thouless: *Acta Metall. Mater.*, 1990, vol. 38, pp. 1135-40.
  34. N.P. O'Dowd, M.G. Stout, and C.F. Shih: *Phil. Mag. A*, 1992, vol. 66, pp. 1037-64.
  35. D. Yao and J.K. Shang: *J. Electronic Packaging*, 1997, vol. 119, pp. 114-18.
  36. K.S. Chan, J.E. Hack, and G.R. Leverant: *Metall. Trans. A*, 1986, vol. 17A, pp. 1739-50.
  37. K.S. Chan, J.E. Hack, and G.R. Leverant: *Metall. Trans. A*, 1987, vol. 18A, pp. 581-91.
  38. C.C. Wojcik, K.S. Chan, and D.A. Koss: *Acta Metall.*, 1988, vol. 36, pp. 1261-70.
  39. A.W. Thompson, J.C. Williams, J.D. Frandsen, and J.C. Chesnutt: in *Titanium and Titanium Alloys: Scientific and Technological Aspects*, J.C. Williams and A.F. Belov, eds., Plenum Press, New York, NY, 1982, pp. 691-703.
  40. M.D. Halliday and C.J. Beevers: *Int. J. Fract.*, 1979, vol. 15, pp. R27-R30.
  41. G. Lütjering, J. Albrecht, and A. Gysler: in *Titanium '92: Science and Technology*, F.H. Froes and I. Caplan, eds., TMS, Warrendale, PA, 1993, pp. 1635-46.
  42. G.R. Yoder, L.A. Cooley, and T.W. Crooker: *Eng. Fract. Mech.*, 1983, vol. 17, pp. 185-88.
  43. C.H. Wu: *J. Appl. Mech.*, 1978, vol. 45, pp. 553-58.
  44. K. Palaniswamy and W.G. Knauss: in *Mechanics Today*, S. Nemat-Nasser, ed., Pergamon Press, Oxford, United Kingdom, 1978, vol. 4, pp. 87-148.
  45. M.A. Hussain, S.L. Pu, and J. Underwood: in *Fracture Analysis*, ASTM STP 560, ASTM, Philadelphia, PA, 1974, pp. 2-28.
  46. A.M. Abdel-Mageed and R.K. Pandey: *Int. J. Fract.*, 1990, vol. 44, pp. R39-R42.
  47. A.C. Chambers, T.H. Hyde, and J.J. Webster: *Eng. Fract. Mech.*, 1991, vol. 39, pp. 603-19.
  48. M.W. Brown: in *Advances in Fatigue Science and Technology*, C.M. Branco and L.G. Rosa, eds., Kluwer, Dordrecht, The Netherlands, 1989, pp. 387-402.
  49. L.P. Pook: *Int. J. Fatigue*, 1985, vol. 7, pp. 21-30.
  50. F. Erdogan and G.C. Sih: *J. Basic Eng.*, 1963, vol. 85, pp. 519-25.
  51. R. John, A.H. Rosenberger, D. DeLuca, J.W. Porter, and K. Li: in *Gamma Titanium Aluminides 1999*, Y.-W. Kim, D.M. Dimiduk, and M.H. Loretto, eds., TMS, Warrendale, PA, 1999.
  52. J.O. Peters, O. Roder, B.L. Boyce, A.W. Thompson, and R.O. Ritchie: *Metall. Mater. Trans. A*, 2000, vol. 31A, pp. 1571-83.
  53. J.P. Campbell, D.L. Davidson, and R.O. Ritchie: "MURI on High Cycle Fatigue," University of California, Berkeley, CA, unpublished research, 1998.
  54. A.L. Dowson, A.C. Hollis, and C.J. Beevers: *Int. J. Fatigue*, 1992, vol. 14, pp. 261-70.
  55. G. Lütjering, A. Gysler, and L. Wagner: *6th World Conf. on Titanium*, P. Lacombe, R. Tricot, and G. Béranger, eds., Société Française de Metallurgie, Les Illis, France, 1988, p. 79.
  56. J.P. Campbell, K.T. Venkateswara Rao, and R.O. Ritchie: *Metall. Mater. Trans. A*, 1999, vol. 30A, pp. 563-77.
  57. J.J. Kruzic, J.P. Campbell, and R.O. Ritchie: *Acta Mater.*, 1999, vol. 47, pp. 801-16.
  58. R.L. Carlson and C.J. Beevers: *Eng. Fract. Mech.*, 1985, vol. 22, pp. 651-60.

# Effects of microstructure on mixed-mode, high-cycle fatigue crack-growth thresholds in Ti-6Al-4V alloy

R. K. NALLA<sup>1</sup>, J. P. CAMPBELL<sup>2</sup> and R. O. RITCHIE<sup>1</sup>

<sup>1</sup>Department of Materials Science and Engineering, University of California, Berkeley, California 94720-1760, USA, <sup>2</sup>Metals Fabrication Division, General Motors, Troy, Michigan 48084, USA

Received in final form 10 January 2002

**ABSTRACT** Effect of microstructure on mixed-mode (mode I + II), high-cycle fatigue thresholds in a Ti-6Al-4V alloy is reported over a range of crack sizes from tens of micrometers to in excess of several millimeters. Specifically, two microstructural conditions were examined—a fine-grained equiaxed bimodal structure (grain size  $\sim 20\ \mu\text{m}$ ) and a coarser lamellar structure (colony size  $\sim 500\ \mu\text{m}$ ). Studies were conducted over a range of mode-mixities, from pure mode I ( $\Delta K_{\text{II}}/\Delta K_{\text{I}} = 0$ ) to nearly pure mode II ( $\Delta K_{\text{II}}/\Delta K_{\text{I}} \sim 7.1$ ), at load ratios (minimum load/maximum load) between 0.1 and 0.8, with thresholds characterized in terms of the strain-energy release rate ( $\Delta G$ ) incorporating both tensile and shear-loading components. In the presence of through-thickness cracks—large ( $> 4\text{ mm}$ ) compared to microstructural dimensions—significant effects of mode-mixity and load ratio were observed for both microstructures, with the lamellar alloy generally displaying the better resistance. However, these effects were substantially reduced if allowance was made for crack-tip shielding. Additionally, when thresholds were measured in the presence of cracks comparable to microstructural dimensions, specifically short ( $\sim 200\ \mu\text{m}$ ) through-thickness cracks and microstructurally small ( $< 50\ \mu\text{m}$ ) surface cracks, where the influence of crack-tip shielding would be minimal, such effects were similarly markedly reduced. Moreover, small-crack  $\Delta G_{\text{TH}}$  thresholds were some 50–90 times smaller than corresponding large crack values. Such effects are discussed in terms of the dominant role of mode I behaviour and the effects of microstructure (in relation to crack size) in promoting crack-tip shielding that arises from significant changes in the crack path in the two structures.

**Keywords** crack-tip shielding; fatigue thresholds; high-cycle fatigue; load ratio; microstructure; mixed mode; short cracks; Ti-6Al-4V; titanium.

## INTRODUCTION

The control of failures owing to high-cycle fatigue (HCF) in turbine-engine components has been identified as one of the major challenges facing the readiness of the US Air Force fleet today.<sup>1–3</sup> In order to address this issue, a consortium of industrial, government and academic institutions has been charged with the task of modifying the existing design methodologies for improving the HCF reliability of these components.<sup>4</sup> One critical issue involves the effects of mixed-mode cyclic

loads—that is, the presence of both tensile and shear loading—on the critical states of damage for such HCF failures. Indeed, there are many fatigue-critical locations within the turbine engine where such mixed-mode conditions exist—e.g. in the presence of fretting fatigue cracks in the blade-dovetail contact section.<sup>5</sup> The effective crack-driving force here can be considered to be a combination of the tensile (mode I) stress-intensity range,  $\Delta K_{\text{I}}$ , the in-plane shear (mode II) stress-intensity range,  $\Delta K_{\text{II}}$ , and/or the antiplane shear (mode III) stress-intensity range,  $\Delta K_{\text{III}}$ . From the perspective of preventing HCF failures in turbine engines, it is critical that fatigue crack-growth thresholds are well-characterized for such loading conditions, as the extremely high cyclic frequencies ( $\sim 1\text{--}2\text{ kHz}$ ) involved can lead to very rapid

Correspondence: R. O. Ritchie, Department of Materials Science and Engineering, University of California, Berkeley, California 94720-1760, USA.  
E-mail: RORitchie@LBL.gov

failures, with over three million cycles being accumulated in less than an hour. Moreover, the presence of mixed-mode loading conditions has been reported to reduce the mode I fatigue thresholds (e.g. Ref. [6]).

To date, studies on the HCF performance of engine alloys have largely focused on a bimodal microstructure of Ti-6Al-4V, an  $\alpha + \beta$  alloy typically used in fan disks and compressors in the front, low-temperature stages of the engine. In the context of mixed-mode fatigue crack propagation, in addition to a few earlier reports on titanium (Ti) alloys in the literature,<sup>7-9</sup> Refs [10-12] provide the only results on mixed-mode thresholds in a bimodal Ti-6Al-4V alloy. In the present work, we seek to extend these earlier observations to a fully lamellar microstructure in the same alloy and to compare the relative merits of these two microstructures in mixed-mode fatigue. Specifically, the role of crack size in influencing mixed-mode fatigue thresholds is investigated through a study of large ( $>4$  mm) and short ( $\sim 200$   $\mu\text{m}$ ) through-thickness cracks and microstructurally small ( $<50$   $\mu\text{m}$ ) surface cracks, over a range of mode-mixities, from pure tension ( $\Delta K_{II}/\Delta K_I = 0$ ) to predominantly shear ( $\Delta K_{II}/\Delta K_I \sim 7.1$ ), and load ratios (ratio of minimum to maximum load), from  $R = 0.1$ – $0.8$ .

## BACKGROUND

The selection of a single microstructure in Ti-6Al-4V with optimal resistance to high-cycle fatigue is a complex task in view of the numerous factors influencing HCF failures. For example, coarse lamellar microstructures in many Ti alloys often possess superior toughness and fatigue crack-growth behaviour in the presence of large cracks as compared to the finer equiaxed microstructures; conversely, they can display lower high-cycle fatigue-endurance strengths and inferior small-crack growth behaviour (e.g. Refs [13-15]).

For the purpose of this study, two common microstructural conditions of Ti-6Al-4V are investigated—namely, the coarse-grained lamellar structures consisting of large  $\beta$  grains (diameter  $\sim 1$  mm) and a lamellar matrix of alternating  $\alpha$  and  $\beta$  plates (produced by heat treatment in the high-temperature  $\beta$ -phase field and subsequent slow cooling into the  $\alpha + \beta$  phase field) and the finer bimodal structures (produced by fast cooling from the  $\beta$ -phase field) with individual orientated  $\alpha$  plates (plate width  $\sim 1$   $\mu\text{m}$ ). While lamellar structures are, in general, characterized by large  $\alpha$  colonies (a packet of aligned  $\alpha$  plates with same crystallographic orientation, about 200–400  $\mu\text{m}$  in size), bimodal structures often consist of a low-volume fraction (typically  $\sim 15$ – $30\%$ ) of primary  $\alpha$  grains ( $\sim 20$   $\mu\text{m}$  in size) with colony-type lamellar matrix of alternating  $\alpha$  and  $\beta$  plates within small  $\beta$  grains ( $\sim 20$ – $40$   $\mu\text{m}$ ). For Ti-6Al-4V and other  $\alpha + \beta$  Ti alloys,

fatigue crack-propagation behaviour in such microstructures is well-characterized for pure mode I loading (e.g. Ref. [13-21]). Crack propagation in the  $\alpha$  phase is generally parallel to the (0001) basal plane<sup>21</sup> and hence perpendicular to the orientation of the  $\alpha$  lamellae.<sup>22,23</sup> The superior crack-growth resistance exhibited by lamellar structures has been attributed to this crystallographic nature of the crack trajectory, especially in the near-threshold regime. As the crack path differs from colony to colony, significant crack-path tortuosity results from out-of-plane deflection and secondary cracking, leading to enhanced crack-tip shielding.

Although similar explanations have been proposed for mixed-mode fatigue crack-propagation behaviour in Ti-6Al-4V,<sup>12</sup> there is little information on the role of microstructure in these alloys, or on how crack size may affect this role. The prime objective of the present work is to examine the effect of microstructure on such mixed-mode fatigue thresholds as a function of crack size, specifically through a study of bimodal and fully lamellar microstructures in Ti-6Al-4V.

## EXPERIMENTAL PROCEDURES

### Materials

The material investigated was a turbine-engine Ti-6Al-4V alloy, which originated as bar stock produced by Teledyne Titanium (Pittsburgh, PA, USA) specifically for the joint government-industry-academia HCF program. The composition (in wt.%) is given in Table 1. The original bar stock (63.5 mm in diameter) was sectioned into segments 400 mm long, preheated to 940 °C for 30 min and forged into 400  $\times$  150  $\times$  20 mm plates. These plates were solution-treated at 925 °C for 1 h, fan air-cooled and then stabilized at 700 °C for 2 h.

### Bimodal microstructure

The as-received microstructure of the alloy was in the bimodal condition (sometimes referred to as solution-treated and overaged, STOA), and consisted of colonies of equiaxed primary  $\alpha$  and lamellar  $\alpha + \beta$  (transformed  $\beta$ ) (Fig. 1a). The proportion of primary  $\alpha$  was 64.1% (standard deviation 6.6%), with an average grain size of  $\sim 20$   $\mu\text{m}$ , slightly elongated in the longitudinal (L)

**Table 1** Chemical composition of Ti-6Al-4V bar stock (in wt.%)<sup>23</sup>

Bar location	Ti	Al	V	Fe	O	N	H
Top	Bal.	6.27	4.19	0.20	0.18	0.012	0.0041
Bottom	Bal.	6.32	4.15	0.18	0.19	0.014	0.0041

direction of the forging.<sup>24</sup> Using differential thermal analysis, the  $\beta$ -transus temperature was measured to be 990–1005 °C.

#### Lamellar microstructure

For comparison, a fully lamellar microstructure was obtained by solution treating in a vacuum of  $10^{-5}$ – $10^{-6}$  mbar at 1005 °C (slightly above the  $\beta$ -transus) for 10–30 min (depending on the cross section), followed by a rapid quench ( $\sim 100^\circ\text{C min}^{-1}$ ) in high-purity helium (He); the quench rate was chosen in order to achieve a similar transformed  $\beta$  lath spacing as in the bimodal structure. The alloy was then stabilized at 700 °C for 2 h *in vacuo*, before slowly furnace cooling to ambient temperature. The resulting Widmanstätten

microstructure (Fig. 1b) had an average prior- $\beta$  grain size of  $\sim 1$  mm, a colony size (parallel orientated  $\alpha$ -phase lamellae) of  $\sim 500$   $\mu\text{m}$ , and an average  $\alpha$  lamellae lath width of  $\sim 1$ – $2$   $\mu\text{m}$ , similar to the interlamellar spacing of the transformed  $\beta$  in the bimodal microstructure.

#### Uniaxial tensile and toughness properties

Uniaxial tensile tests were conducted in both microstructures in the L-orientation using a strain rate of  $5 \times 10^{-4} \text{ s}^{-1}$ ; additional data for the bimodal microstructure were taken from Ref. [23]. Results in terms of the strength, ductility and toughness are listed in Table 2, and show that whereas the lamellar structure has somewhat higher strength, the bimodal structure exhibits over a factor of four higher ductility (owing to its smaller grain size that limits the effective slip length). However, despite its lower ductility, the lamellar microstructure has over 50% higher plane-strain fracture toughness.

#### Fatigue testing

##### Large through-thickness cracks

Large ( $> 4$  mm) fatigue-threshold testing was performed in four-point bending, using 6 mm thick samples with inner and outer spans of 12.7 and 25.4 mm, respectively. Pure mode I tests were conducted using symmetric four-point bending. For mixed-mode loading, the mode II component of the loading was introduced using the asymmetric four-point bending (AFPB) configuration<sup>25–28</sup> where the mode-mixity ratio,  $\Delta K_{II}/\Delta K_I$ , can be varied using the offset,  $s$ , from the load line, as shown in Fig. 2. The values of mode I stress-intensity range,  $\Delta K_I$ , and mode II stress-intensity range,  $\Delta K_{II}$ , were determined from linear-elastic stress-intensity solutions for this geometry, recently developed by He and Hutchinson.<sup>28</sup>

Precracking was conducted in room temperature air in a near-identical manner for all large- and short-crack test samples in order to avoid any effect of precracking

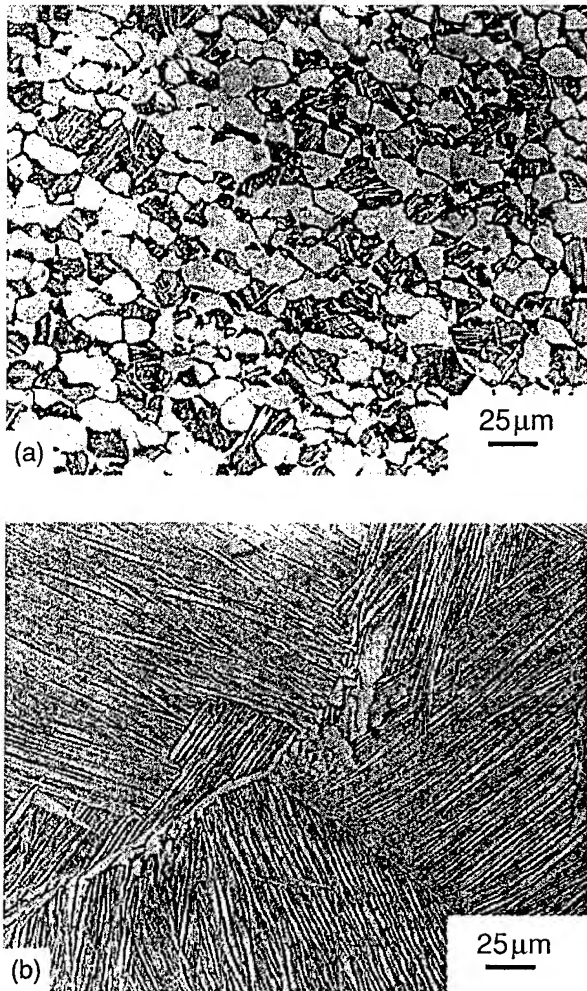


Fig. 1 Optical micrographs of the two microstructures of Ti-6Al-4V investigated: (a) bimodal (solution-treated and overaged, STOA) and (b) lamellar ( $\beta$ -annealed). Etched into  $\sim 10$  sec in 5 parts 70%  $\text{HNO}_3$ , 10 parts 50%  $\text{HF}$ , 85 parts of  $\text{H}_2\text{O}$ .

Table 2 Uniaxial tensile and toughness properties of Ti-6Al-4V

Microstructure	Yield strength (MPa)	Ultimate tensile strength (MPa)	Reduction in area (%)	Fracture toughness $K_{Ic}$ (MPa $\sqrt{\text{m}}$ )
Bimodal	930	978	45	64
Lamellar	975	1055	10	100

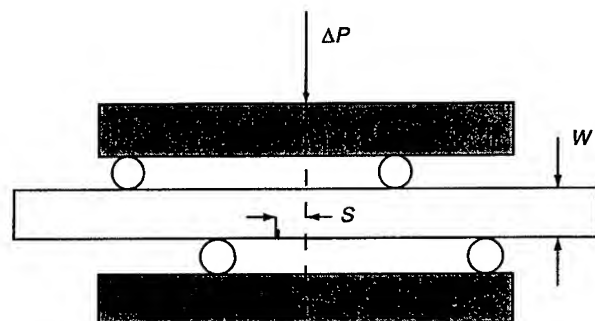


Fig. 2 The asymmetric four-point bend specimen. The offset,  $s$ , from the load line is used in order to control the degree of mode-mixity,  $\Delta K_{II}/\Delta K_I$ , and thereby the phase angle,  $\beta = \tan^{-1}(\Delta K_{II}/\Delta K_I)$ . This geometry is used for the mixed-mode large and short crack testing.

technique on subsequent thresholds obtained. Specifically, fatigue cracks were grown from a 2 mm deep electrodeposition-machined (EDM) through-thickness notch in a symmetric four-point bending sample at a load ratio of 0.1 with a constant loading frequency. (This alloy is known to show little effect of frequency in room air, specifically over the range of 50–20 000 Hz in the bimodal structure<sup>20</sup> and 50–1000 Hz in the lamellar structure<sup>22</sup>). The surfaces of all samples required for crack-length observation were polished to a 0.05  $\mu\text{m}$  finish, whereas the sides to be used to carry the load-bearing pins were ground to a 600 grit finish. As the effect of friction between the specimen and the roller-pin supports can substantially affect the stress-intensity values,<sup>25</sup> frictional effects were minimized at the pin-contact positions through the use of a high-pressure  $\text{MoS}_2$  grease. The final precrack length thus achieved was  $4.50 \pm 0.25$  mm at near-threshold  $\Delta K_I$  values of  $4.8 \pm 0.5$  and  $6.8 \pm 0.5$   $\text{MPa}\sqrt{\text{m}}$ , respectively, for the bimodal and lamellar microstructures.

For large crack ( $>4$  mm) tests, mode-mixities were varied from  $\Delta K_{II}/\Delta K_I = 0$  (pure mode I) to  $\Delta K_{II}/\Delta K_I \sim 7.1$  (nearly pure mode II), representing a change in phase angle,  $\beta = \tan^{-1}(\Delta K_{II}/\Delta K_I)$ , from 0 to  $82^\circ$ . Load ratios were varied from  $R = 0.1$ – $0.8$ . Tests involving cycling precracked specimens at a specified mode-mixity were performed in the following way: if no crack growth was observed (using an optical microscope) after  $2 \times 10^6$  cycles, either  $\Delta K_I$  or  $\Delta K_{II}$  was increased by  $\sim 0.25$   $\text{MPa}\sqrt{\text{m}}$  (with the other being increased accordingly to maintain the mode-mixity) and the procedure repeated. In this way, a 'growth/no growth' condition bounding the actual threshold was obtained. The crack extension defining 'growth' was taken to be of the order of the characteristic microstructural dimension—that is,  $\sim 20$   $\mu\text{m}$  for the bimodal structure and  $\sim 500$   $\mu\text{m}$  for the lamellar structure, yielding threshold growth rates of

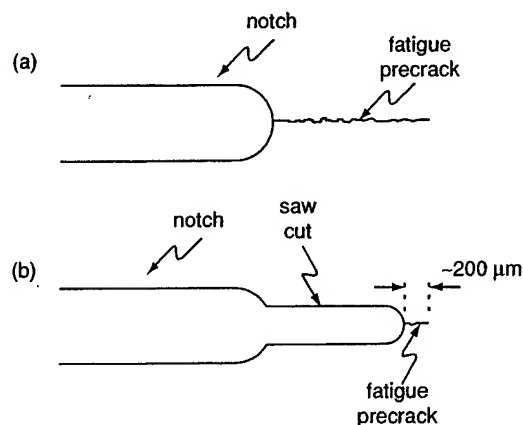


Fig. 3 The procedure used for removing the crack wake of a large crack in order to produce a short crack is illustrated.

$10^{-10}$ – $10^{-11}$   $\text{m cycle}^{-1}$ . The larger 'growth' condition for the lamellar structure also served to ensure adequate sampling of the relatively heterogeneous microstructure.

The magnitude of the crack-tip shielding—used for computing the effective (near-tip) crack-driving force in both modes I and II—was characterized using a recently developed compliance-based technique for both tensile opening and shear-type loading, using two displacement gauges mounted near the crack tip to measure opening and shear displacements. As described, in detail, in Ref. [11], the distinction between the contributions to shielding in modes I and II was achieved by examining separate load-displacement curves using these two crack-tip gauges. Mode I shielding, in the form of crack closure, was determined from the compliance curve for the opening displacements from the first deviation from linearity on unloading, whereas mode II shielding, in the form of crack-surface interference via asperity rubbing and interlock, was determined in an analogous fashion from the compliance curve for shear displacements.

#### Short through-thickness cracks

In order to examine the influence of crack size on mixed-mode fatigue thresholds, the behaviour of large ( $>4$  mm) through-thickness cracks was compared with those of short ( $\sim 200$   $\mu\text{m}$ ) through-thickness cracks and small ( $<50$   $\mu\text{m}$ ) surface cracks. The distinction and relevance of these types of flaws are discussed, in detail, in Appendix A.

Mixed-mode threshold tests on the short cracks were measured on 6–12 mm thick four-point bend bars, using procedures identical to those described above for large cracks, except that the precrack wake was carefully machined away to within  $\sim 200$   $\mu\text{m}$  of the crack tip using a

slow-speed diamond saw (Fig. 3). The rationale for this procedure of removing most of the crack wake was to limit the effect of crack-tip shielding by minimizing the occurrence of any premature contact of the crack faces during unloading. However, as the short cracks were through-thickness, they still 'sampled' the continuum microstructure—that is, typically between 30 and 300 grains. Thresholds were measured in both microstructures at load ratios of  $R = 0.1$ – $0.8$  for mode-mixities of  $\Delta K_{II}/\Delta K_I = 0$  to  $\Delta K_{II}/\Delta K_I \sim 7.1$  (i.e.  $\beta = 0$ – $82^\circ$ ).

#### Small surface cracks

Mixed-mode thresholds for microstructurally small surface cracks were performed using an inclined-crack technique. Wide bend bars (16–25 mm width, 5 mm thickness) were machined in the L–T orientation, with the surfaces required for observation polished to a  $0.05 \mu\text{m}$  finish, and the sides used to carry the load-bearing pins ground to a 600 grit finish. A stress-relief treatment of 2 h at  $695^\circ\text{C}$  *in vacuo* was used in order to minimize any residual stresses from machining and

specimen preparation. A 'precrack' was naturally initiated at the stress of  $\sigma_{\max} = 750 \text{ MPa}$ —that is,  $\sim 80\%$  of yield strength—using standard three-point bending (with a load ratio of 0.1 and a frequency of 50 Hz). In order to enable measurement of the small-crack thresholds, a bend bar was carefully machined out from the original precracked wide bar with the crack inclined at the desired angle (Fig. 4). This sample was subsequently subjected to four-point bending by cycling at a load ratio of 0.1. If no growth (defined as a total crack extension of less than  $20 \mu\text{m}$  per  $2 \times 10^6$  cycles on both ends of the surface crack) was observed, the maximum load (and proportionately the minimum load) was increased by 111 N and the above-mentioned procedure was repeated. Thresholds were thus again determined using a 'growth/no growth' criterion, but for the bimodal microstructure only. The inclined-crack technique could not be usefully employed for the lamellar microstructure as a result of the highly deflected nature of fatigue cracking in this structure.

Linear-elastic solutions for the stress intensities associated with the small, semielliptical surface cracks under mixed-mode loading were taken from two sources. On

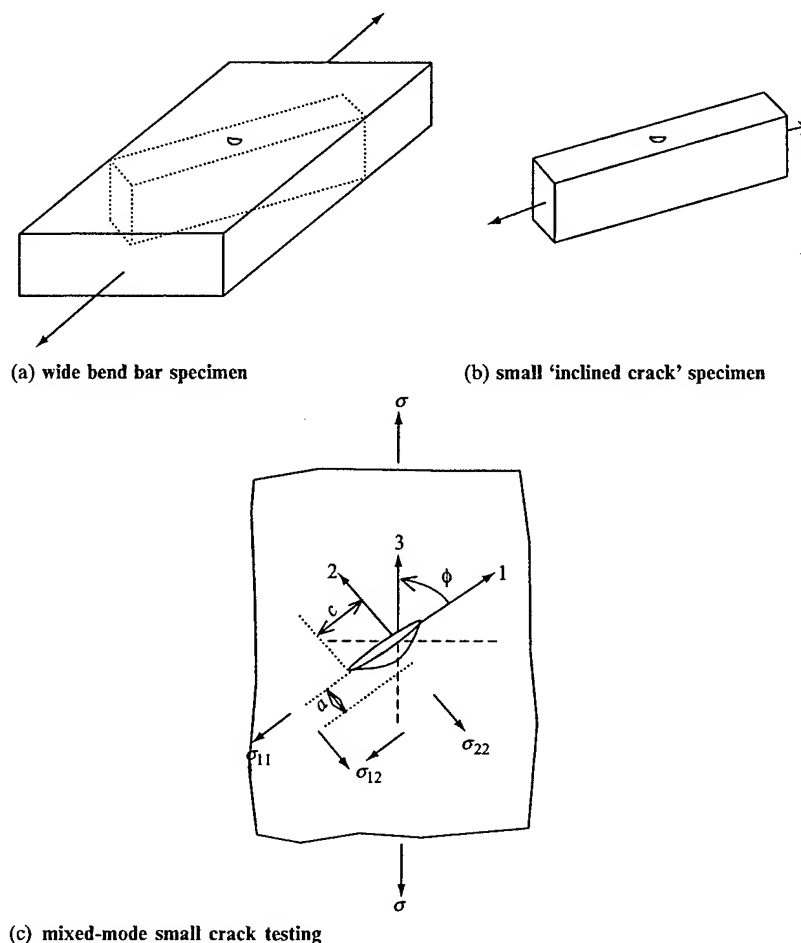


Fig. 4 Schematic showing the procedures utilized for obtaining the small 'inclined crack' specimen. (a) The dotted lines outline the small-crack test sample to be machined at the desired angle of inclination,  $\phi$  from the original wide bend bar. The nominal direction of loading for crack initiation is also shown. (b) The final 'inclined crack' specimen is illustrated. (c) Schematic of the inclined semielliptical surface crack configuration used for the microstructurally small-crack testing. The tensile loading component,  $\sigma_{22}$ , induces the mode I contribution, whereas the shear-loading component,  $\sigma_{12}$ , induces the mode II and mode III components.

the basis that the crack plane was normal to the specimen surface, the mode I component of the stress intensity,  $K_I$ , was computed from the well-known Newman–Raju solution:<sup>29</sup>

$$K_I = (\sigma_t + H\sigma_b) \sqrt{\pi \frac{a}{Q}} F\left(\frac{a}{t}, \frac{a}{c}, \frac{c}{b}, \theta\right) \quad (1)$$

where  $\sigma_t$  is the remote uniform tension stress and  $\sigma_b$  is the remote uniform outer-fibre bending stress. The geometrical factors— $H$ ,  $Q$  and  $F$ —are evaluated from: the crack depth,  $a$ ; the crack half-length,  $c$ ; the specimen thickness,  $t$ ; the specimen half-width,  $b$ ; and the angular position along the crack front,  $\theta$ , as described in detail in Ref. [29].

The mode II component,  $K_{II}$ , conversely, was computed from the newly derived He–Hutchinson solution<sup>30</sup> for elliptical surface cracks under mixed-mode loading:

$$K_{II} = \chi \sigma_{12} \sqrt{\pi a} \quad (2)$$

where  $\chi$  is a numerical factor determined from Ref. [30];  $\sigma_{12}$  is the shear component of the loading and  $a$  is the crack depth. It should be noted here that a three-dimensional corner singularity exists in the solution at the point where the crack intersects with the free surface. However, for the purpose of this study, this is ignored because errors caused by such an assumption are negligible. Moreover, as one moves along the crack front to the interior, the magnitude of the mode II contribution decreases with that of mode III increasing till the point of deepest penetration of the crack is reached.

The applied load/stress on the inclined crack (Fig. 4c) was resolved trigonometrically into tensile and shear components. The tensile component was used for determining  $\Delta K_I$ , using Ref. [29] and the shear component for  $\Delta K_{II}$  and  $\Delta K_{III}$ , using Ref. [30]. As the exact shape of such small surface cracks and the variation in this aspect ratio with crack extension clearly can have an important effect on the crack-driving force and hence the crack-growth behaviour,<sup>31,32</sup> crack shapes (Fig. 4)—in the form of the depth-to-surface length ratio,  $a/2c$ —were determined by postfracture observations; the typical aspect ratio was  $a/2c \sim 0.45$ .

The use of linear-elastic stress-intensity solutions for characterizing the driving forces for the small cracks is justified on the basis of the small cyclic plastic-zone sizes in relation to crack size. For example, for the smallest crack sizes of  $\sim 1 \mu\text{m}$ , where the  $\Delta K_I$  thresholds are  $\sim 1 \text{ MPa m}^{-1/2}$ , plastic-zone size (estimated as  $r_y \sim 1/2\pi (\Delta K_I/\sigma_y)^2$  where  $\sigma_y$  is the yield strength) are on the order of 100 nm. As this is roughly one-tenth of the crack size, it is deemed reasonable to conclude that small-scale yielding conditions prevail.

## RESULTS

### Large-crack behaviour

#### *Effect of load ratio and mode-mixity*

Large crack thresholds for the bimodal and lamellar microstructures under mode I + II loading are shown in Fig. 5 in the form of mixed-mode threshold envelopes, where the mode II threshold stress-intensity range,  $\Delta K_{II,TH}$ , is plotted as a function of the corresponding mode I threshold stress-intensity range,  $\Delta K_{I,TH}$  (note that each threshold is represented by two data points, which indicate the ‘growth’ and ‘no growth’ conditions). The phase angles investigated were 0, 26, 62 and 82° for load ratios of 0.1 and 0.5, and 0, 26 and 62° at a load ratio of 0.8 for both structures. Based on these results, the following observations can be made:

- Akin to behaviour in most metallic alloys (e.g. Refs [8–9,33–35]), a reduction in the fatigue threshold values is clearly evident for both microstructures with increasing load ratio. The slight increase in the mode I threshold,  $\Delta K_{I,TH}$ , with increasing mode-mixity at low phase angles, observed in the present data at phase angles between 0 and 26°, has been attributed to the effect of mode I/mode II crack-tip shielding.<sup>10–12</sup>
- The mode I threshold,  $\Delta K_{I,TH}$ , clearly decreases with increasing mode-mixity. However, if a more appropriate driving force—incorporating both mode I and mode II components—is used in order to characterize the threshold, specifically the range in strain-energy release rate,  $\Delta G = (\Delta K_I^2 + \Delta K_{II}^2)/E$  where  $E' = E$  ( $E$  is Young’s modulus) in plane stress and  $E/(1-\nu^2)$  in plane strain ( $\nu$  is Poisson’s ratio), then there is a progressive increase in the mixed-mode  $\Delta G_{TH}$  fatigue threshold with increasing mode-mixity in both microstructures for all load ratios studied (Fig. 6). This can alternatively be represented in terms of an equivalent stress-intensity factor range,  $\Delta K_{eq,TH} = (\Delta G_{TH} E')^{1/2}$ , which is also plotted in Fig. 6. Note that in this and all subsequent figures, threshold values are represented by a single data point showing the average value of the ‘growth/no growth’ conditions. An alternative means of calculating the mixed-mode thresholds is briefly described in Appendix B.
- From the perspective of thresholds for high-cycle fatigue in Ti-6Al-4V, the results in Fig. 6 strongly imply that despite the presence of mixed-mode loading, the mode I threshold, defined in terms of the strain-energy release rate,  $\Delta G$ , for cracks large compared to microstructural dimensions, represents a *worst-case* condition for the onset of fatigue crack growth under mode I + II loading for both microstructures.
- Though both microstructures showed mixed-mode  $\Delta G_{TH}$  thresholds that increased substantially with

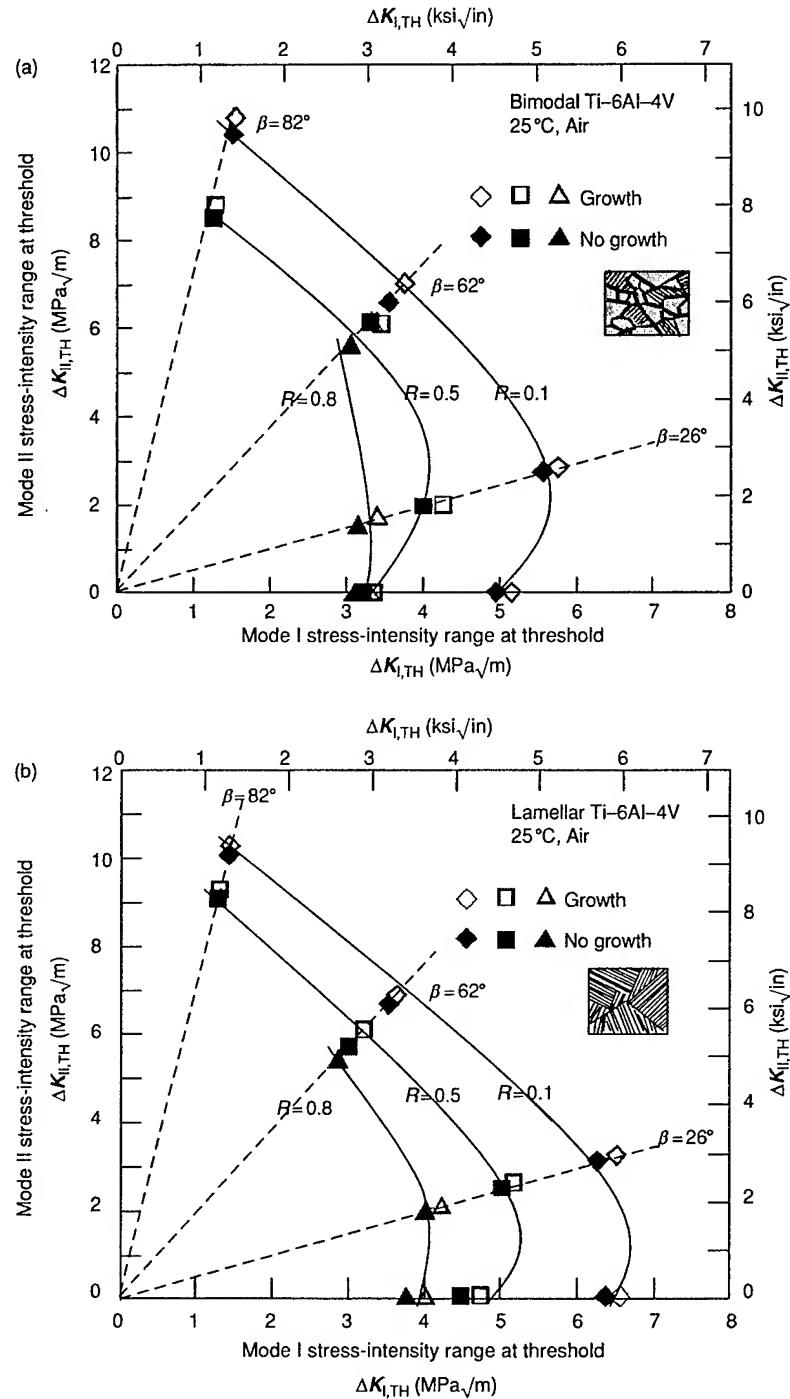


Fig. 5 Mixed-mode threshold envelopes for large (> 4 mm) through-thickness cracks in the (a) bimodal and (b) lamellar microstructures. Note that the lamellar structure shows superior resistance to crack propagation, particularly at the lower phase angles.

increasing mode-mixity, in general the lamellar structure was observed to exhibit the higher threshold values. However, the better fatigue resistance of the lamellar structure was markedly reduced at high mode-mixities, as is evident from the large-crack threshold values listed in Table 3 (the difference between the thresholds for the

two microstructures is included in parentheses for the purpose of comparison). Clearly, the superior fatigue crack-growth properties of the lamellar structure at low mode-mixities ( $\beta = 0$  and  $26^\circ$ ) are nearly eliminated, or in some cases reversed, when significant mode II loading is present ( $\beta = 62$  and  $82^\circ$ ).



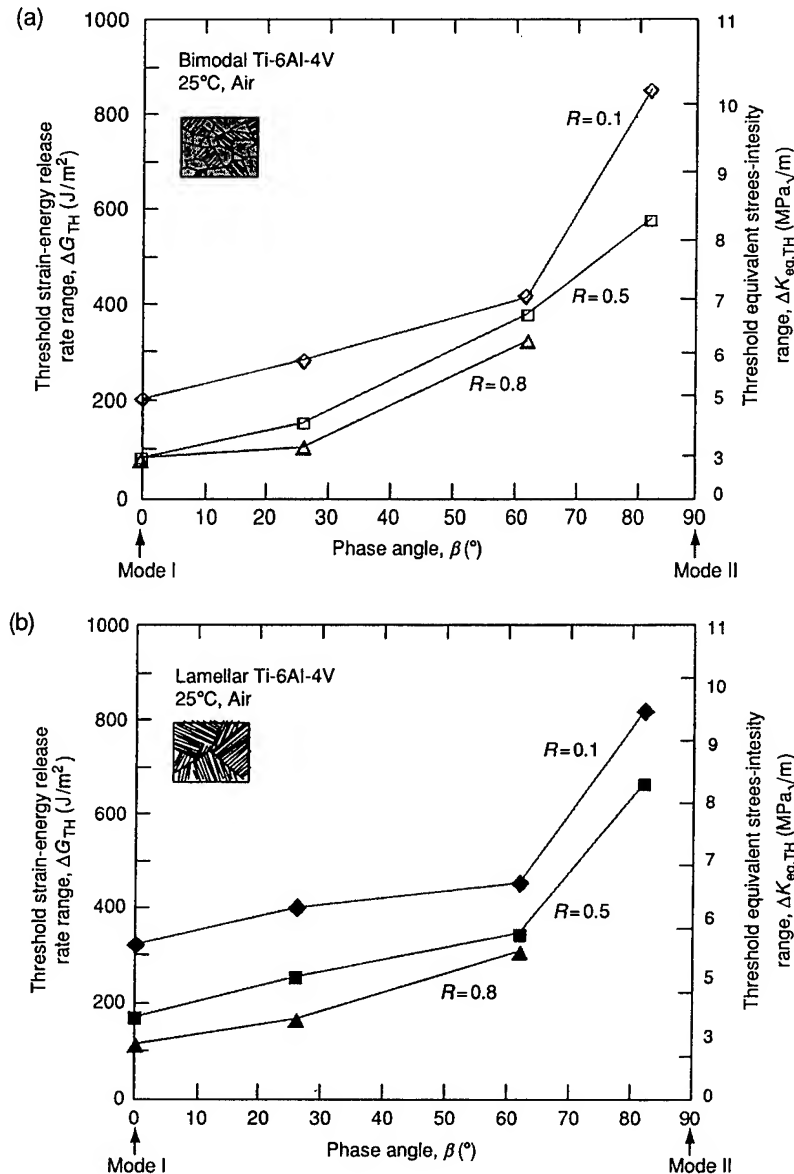


Fig. 6 The threshold strain-energy release rate,  $\Delta G_{TH}$ , is plotted as a function of phase angle,  $\beta$ , for the (a) bimodal and (b) lamellar microstructure for large cracks subjected to mixed-mode loading at  $R = 0.1, 0.5$  and  $0.8$ . Equivalent stress-intensity ranges at threshold,  $\Delta K_{eq,TH}$ , for both microstructures are also shown. The lamellar microstructure, in general, shows superior resistance to fatigue-crack propagation, although the difference is reduced at high mode-mixities.

#### Role of crack-tip shielding

As discussed in Refs. [10,11] for the bimodal structure, the increase in the large-crack mixed-mode thresholds with increasing mode-mixity can be directly related to an increased role of mode I and mode II crack-tip shielding, associated with, respectively, crack closure and sliding crack interference (friction and interlock of crack-surface asperities). This can be appreciated by quantifying the magnitude of such shielding in order to determine a mixed-mode, effective strain-energy release rate,  $\Delta G_{eff}$ , and then 'correcting' the large-crack threshold data in Fig. 6 for such shielding by characterizing in terms of  $\Delta G_{eff}$ .

The effective (near-tip) strain-energy release rate,  $\Delta G_{eff}$ , can be defined as  $(\Delta K_{I,eff}^2 + \Delta K_{II,eff}^2)/E'$ , where  $\Delta K_{I,eff}$  is the effective stress-intensity range in mode I and  $\Delta K_{II,eff}$

is the corresponding effective stress-intensity range in mode II. In the present work,  $\Delta K_{I,eff}$  was determined in the usual fashion used in order to measure crack closure—that is, in terms of  $K_{I,max} - K_{cl}$ , where  $K_{cl}$  is the closure stress intensity defined at the first deviation from linearity of the crack-tip load-displacement curve on unloading. On the other hand,  $\Delta K_{II,eff}$  was measured as the difference between the near-tip maximum and minimum mode II stress intensities in the fatigue cycle. The near-tip mode II stress-intensity range differs from the applied driving force as a result of the presence of shear-induced fracture-surface asperity contact and interlock. Further details on the determination of  $\Delta K_{I,eff}$  and the estimation of  $\Delta K_{II,eff}$  using compliance-based techniques can be found in Ref. [11].

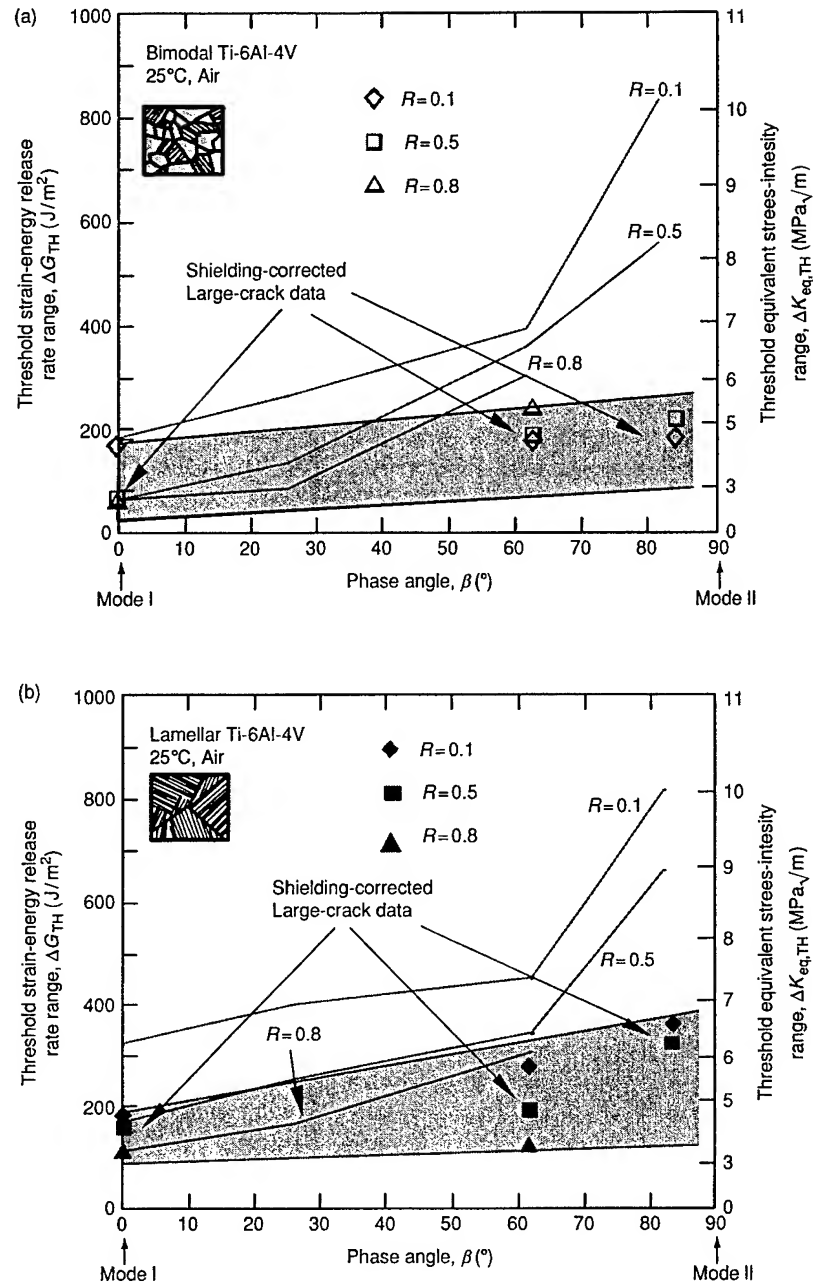


Fig. 7 The threshold strain-energy release rate,  $\Delta G_{TH}$ , is plotted as a function of phase angle,  $\beta$ , for the (a) bimodal and (b) lamellar microstructure for large cracks subjected to mixed-mode loading at  $R = 0.1, 0.5$  and  $0.8$ . Results from Fig. 6 are compared with the  $\Delta G_{TH,eff}$  values which have been corrected for crack-tip shielding. Note the relative absence of any effect of mode-mixity and/or load ratio on the shielding-corrected thresholds.

By so characterizing the driving force in terms of  $\Delta G_{eff}$  by subtracting out the contributions from crack-tip shielding (individual  $\Delta K_I$  and  $\Delta K_{II}$  values are listed in Tables 4 and 5), the effect of mode-mixity on the threshold is found to be greatly reduced for both microstructures. This can be seen in Fig. 7 where the 'shielding-corrected'  $\Delta G_{eff,TH}$  thresholds (plotted as hatched regions) are compared with the 'uncorrected' data of Fig. 6. Several points are worthy of note:

- The shielding-corrected  $\Delta G_{eff,TH}$  threshold values are substantially smaller (by as much as a factor of four)

than the uncorrected  $\Delta G_{TH}$  values, especially at high phase angles.

- Mixed-mode threshold values are essentially independent of both load ratio and mode-mixity. While it is generally appreciated that the effect of load ratio on mode I threshold values is largely associated with crack closure (e.g. Refs [19,20]), these results confirm earlier reports for the bimodal structure<sup>10,11</sup> that the effect of mode-mixity in increasing the  $\Delta G_{TH}$  threshold in Ti-6Al-4V can be principally attributed to an increase in crack-tip shielding (mainly from enhanced crack-surface interference).

**Table 3** Fatigue threshold values for large fatigue cracks in Ti-6Al-4V

Mode-mixity	$\Delta G_{TH}$ (J m <sup>-2</sup> )			$\Delta K_{eq,TH}$ (MPa√m)		
	$R = 0.1$	$R = 0.5$	$R = 0.8$	$R = 0.1$	$R = 0.5$	$R = 0.8$
Bimodal microstructure:						
0°	200	80	80	4.9	3.1	3.1
26°	280	150	100	5.8	4.3	3.5
62°	410	375	320	7.0	6.7	6.2
82°	850	575	—	10.1	8.3	—
Lamellar microstructure*:						
0°	320 (+60%)	170 (+113%)	110 (+38%)	6.2	4.5	3.6
26°	395 (+41%)	255 (+70%)	165 (+65%)	6.9	5.5	4.5
62°	450 (+10%)	345 (-8%)	305 (-5%)	7.4	6.5	6.1
82°	815 (-4%)	660 (+15%)	—	9.9	8.9	—

\*The numbers in parentheses indicate the difference between the magnitudes of the  $\Delta G_{TH}$  threshold of the lamellar structure as compared to the bimodal threshold.

**Table 4** Comparison of the applied and shielding-corrected mode I stress-intensity ranges

Load ratio	Mode-mixity	$\Delta K_{I,TH}$ (MPa√m)	$\Delta K_{I,TH,eff}$ (MPa√m)	Reduction in $\Delta K_I$ (MPa√m)*
Bimodal microstructure:				
0.1	0°	5.0	4.7	0.3 (6%)
	62°	3.6	2.8	0.8 (22%)
	82°	1.5	0.6	0.9 (60%)
0.5	0°	3.3	3.3	0.0 (0%)
	62°	3.3	1.7	1.6 (48%)
	82°	1.2	0.0	1.2 (100%)
0.8	0°	3.2	3.2	0.0 (0%)
	62°	3.1	2.3	0.8 (26%)
Lamellar microstructure:				
0.1	0°	6.5	4.6	1.9 (29%)
	62°	3.6	2.2	1.4 (39%)
	82°	1.4	0.8	0.6 (43%)
0.5	0°	4.6	4.3	0.3 (7%)
	62°	3.1	2.8	0.3 (10%)
	82°	1.3	0.5	0.8 (62%)
0.8	0°	3.9	3.7	0.2 (5%)
	62°	2.9	2.5	0.4 (14%)

\*The numbers in parentheses indicate the percentage reduction in  $\Delta K_I$  owing to correction for crack-tip shielding.

- The superior mixed-mode fatigue threshold properties of the lamellar microstructure are substantially reduced when results are plotted in terms of  $\Delta G_{eff}$ , suggesting that this is also associated with higher levels of crack-tip shielding. This is consistent with the significantly more tortuous crack paths observed in the lamellar structure, which would promote crack-surface interference, as discussed in the following section.

**Table 5** Comparison of the applied and shielding-corrected mode II stress-intensity ranges

Load ratio	Mode-mixity	$\Delta K_{II,TH}$ (MPa√m)	$\Delta K_{II,TH,eff}$ (MPa√m)	Reduction in $\Delta K_{II}$ (MPa√m)*
Bimodal microstructure:				
0.1	62°	6.5	3.9	2.6 (40%)
	82°	10.4	4.8	5.6 (54%)
0.5	62°	6.0	4.6	1.4 (23%)
	82°	8.6	5.3	3.3 (38%)
0.8	62°	5.6	5.0	0.6 (11%)
Lamellar microstructure:				
0.1	62°	6.7	5.2	1.5 (22%)
	82°	10.1	6.6	3.5 (35%)
0.5	62°	5.8	3.8	2.0 (35%)
	82°	9.1	6.2	2.9 (32%)
0.8	62°	5.5	2.9	2.6 (47%)

\*The numbers in parentheses indicate the percentage reduction in  $\Delta K_{II}$  owing to correction for crack-tip shielding.

#### Crack path and fractography

Akin to fatigue crack-growth behaviour in pure mode I in the presence of large cracks,<sup>22</sup> the lamellar microstructure displays superior crack-growth resistance under mixed-mode loading compared to the bimodal structure. This can be attributed to the large degree of crack-path deflection, bifurcation and secondary crack formation associated with crack growth in the lamellar structure. Typical crack paths are illustrated in Fig. 8 for both microstructures, and show the pure mode I precrack (grown at  $R = 0.1$ ) and subsequent crack growth under

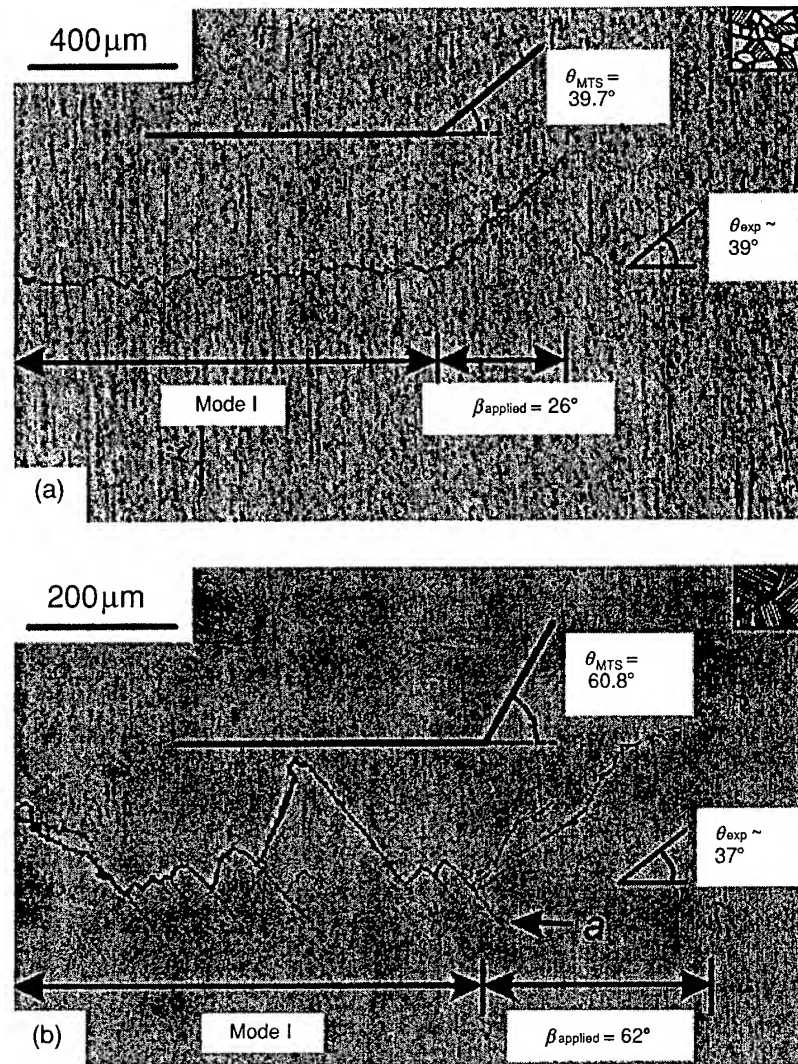


Fig. 8 Typical fatigue crack profiles are compared for the (a) bimodal ( $R = 0.8$ ,  $\beta = 26^\circ$ ,  $\Delta G_{\text{TH}} = 100 \text{ J m}^{-2}$ ) and (b) lamellar ( $R = 0.1$ ,  $\beta = 62^\circ$ ,  $\Delta G_{\text{TH}} = 450 \text{ J m}^{-2}$ ) microstructures. Optical micrographs show both the mode I fatigue precrack and the region of deflected crack growth following the application of cyclic mixed-mode loading. Measured crack deflection angles,  $\theta_{\text{exp}}$ , are compared with those predicted by the path of maximum tangential stress,  $\theta_{\text{MTS}}$  (see Ref. [12]).

mixed-mode loading (at  $R = 0.8$  with  $\Delta K_{\text{II}}/\Delta K_{\text{I}} = 0.5$  for the bimodal structure and at  $R = 0.1$  with  $\Delta K_{\text{II}}/\Delta K_{\text{I}} = 1.9$  for the lamellar structure). There is clearly a substantial difference between the trajectories of cracks in the two structures. This is evident (i) in the crack path especially during mode I crack growth, where the lamellar structure shows substantially higher tortuosity owing to interaction of the crack with the much coarser lamellar microstructure—with characteristic length scales of  $\sim 500 \mu\text{m}$ —and (ii) in the crack direction at the onset of mixed-mode loading, as discussed below.

The crack-path direction is determined through a competition between the maximum crack-driving force and the weakest microstructural path. In fine-scale, homogeneous microstructures, such as the bimodal microstructure (where characteristic length scales are  $\sim 20 \mu\text{m}$ ), the crack-driving force becomes the dominant factor. For nominally elastic conditions, the path of a growing fatigue crack will change in response to a change in the

applied phase angle, so that a pure mode I near-tip condition is maintained—that is, the crack tip follows a path dictated by either a zero mode II stress intensity ( $K_{\text{II}} = 0$ ), maximum tangential stress (MTS), or maximum strain-energy release rate,  $G_{\text{max}}$ <sup>36,37</sup>—all criteria that yield essentially the same crack-path predictions (except at very high phase angles). Accordingly, cracks in the bimodal structure deflect under mixed-mode loading to follow a mode I path, as illustrated in Fig. 8a where the crack deviates almost exactly along the path of maximum tangential stress. For the coarse lamellar structure, conversely, Fig. 8b shows that the crack does not deflect along the maximum tangential stress direction at the onset of the mixed-mode loading; here, the characteristic microstructural dimensions are far larger, so that the crack path *on this scale of observation* cannot be described by continuum notions and is markedly influenced by microstructure. Similar deviations from predicted mode I crack paths under mixed-mode loading have

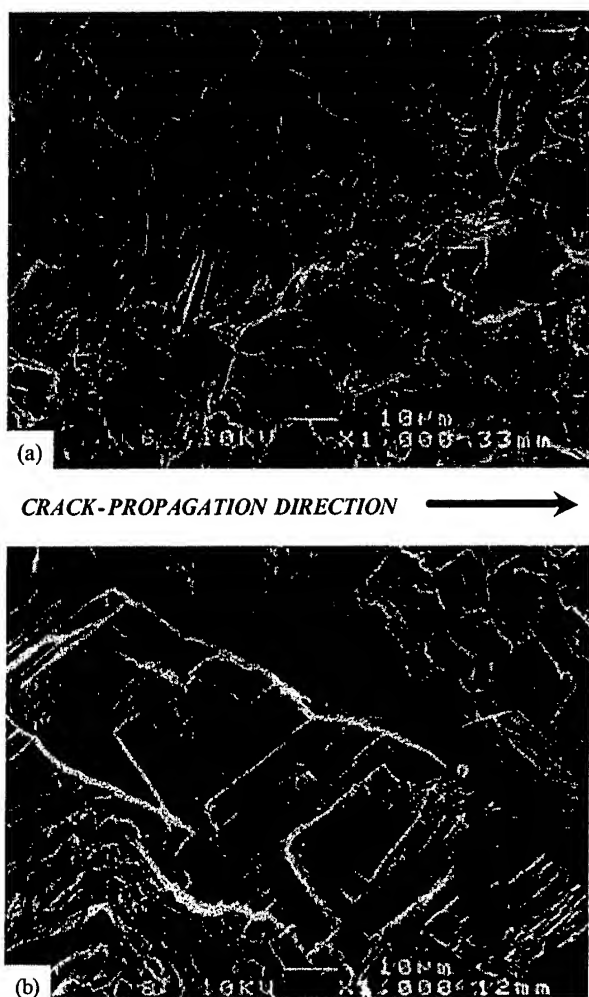


Fig. 9 Typical fractography for mixed-mode fatigue crack growth in the (a) bimodal ( $\Delta G_{TH} = 410 \text{ J m}^{-2}$ ) and (b) lamellar microstructures ( $\Delta G_{TH} = 450 \text{ J m}^{-2}$ ). Both specimens were tested at load ratio,  $R = 0.1$ , and phase angle,  $\beta = 62^\circ$ . The much coarser length scales involved for the lamellar structure are evident.

been observed for coarse-grained lamellar microstructures in titanium aluminide intermetallics, where fatigue cracks can follow a preferential interlamellar path within a single large colony.<sup>38</sup>

All these factors result in substantially rougher fracture surfaces (Fig. 9) in the lamellar microstructure, which *with large cracks* promotes both mode I crack closure, through premature crack-surface asperity contact on unloading, and mode II crack-surface interference, through enhanced asperity rubbing and interlocking within the sliding crack faces. Measurements of the magnitude of such closure and surface interference, listed in Tables 4 and 5, provide experimental confirmation of the more significant role of crack-tip shielding in the coarser lamellar structure; this provides the main reason why this microstructure displays superior resistance to (large

crack) fatigue crack propagation, with higher measured fatigue threshold values under both pure mode I and mixed-mode loading conditions.

### Short-crack behaviour

Corresponding mixed-mode  $\Delta G_{TH}$  thresholds for short ( $\sim 200 \mu\text{m}$ ) through-thickness cracks in the bimodal and lamellar structures (at  $\beta = 0\text{--}82^\circ$  and  $R = 0.1\text{--}0.8$ ) are plotted as a function of the phase angle in Fig. 10; results are compared with the corresponding thresholds (both uncorrected and shielding-corrected) for large cracks from Fig. 7. As noted above, the effect of crack-tip shielding in the crack wake is particularly significant in the presence of shear loading owing to crack-surface friction and interlocking of asperities.<sup>39–41</sup> Consequently, owing to the minimal role of crack-tip shielding associated with cracks of limited wake, measured short crack  $\Delta G_{TH}$  thresholds were:

- substantially lower than the corresponding large-crack values (similar to results for mode I thresholds<sup>22</sup>),
- essentially insensitive to the degree of mode-mixity, in marked contrast to the large crack thresholds, and
- relatively insensitive to the load ratio, again in contrast to large crack results.

Moreover, the short-crack threshold values, which are listed in Table 6, were observed to lie within the scatter-band for shielding-corrected large cracks, again indicating that, similar to observations under pure mode I conditions, the limited effect of shielding for short cracks is responsible for their lower threshold values.

With respect to the role of microstructure, the distinction between the bimodal and lamellar microstructures in terms of the mixed-mode crack-growth resistance is substantially reduced for short cracks compared to that for large cracks. This again implies that the primary effect of microstructure on mixed-mode fatigue thresholds in Ti-6Al-4V arises through the mechanism of crack-tip shielding. Where the role of such shielding is restricted, as in the case of short cracks with limited wake, differences in fatigue resistance between the bimodal and lamellar structures become much less significant. Analogous behaviour can be seen under mode I loading where the superior fatigue crack-growth properties of the lamellar structure are lost at high load ratios, where the effect of crack closure becomes insignificant; once again, the primary role of microstructure occurs through mechanisms of crack-tip shielding.<sup>22</sup>

### Small-crack behaviour

A more realistic flaw—in terms of what is most commonly encountered in real structures—is that of the

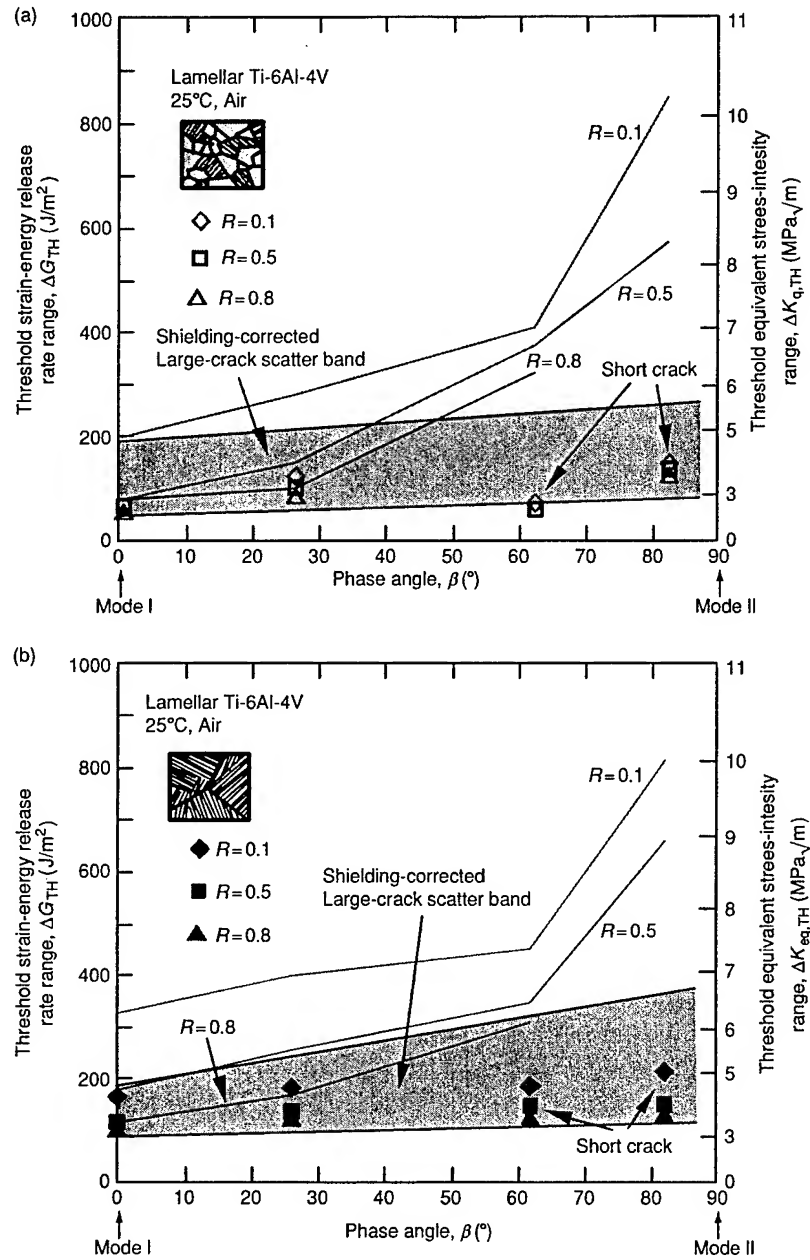


Fig. 10 Variation in mixed-mode thresholds,  $\Delta G_{TH}$ , as a function of phase angle,  $\beta$ , in (a) bimodal and (b) lamellar structures. Shown are results at three load ratios for large ( $> 4$  mm) cracks, before and after 'correcting' for crack-tip shielding, and for short ( $\sim 200 \mu\text{m}$ ) through-thickness cracks. The lamellar microstructure shows somewhat superior resistance to crack propagation in the short crack regime.

small, semielliptical surface crack, which is small in all dimensions. Like short cracks, such cracks experience a minimal effect of crack-tip shielding owing to their limited wake. In the present study on Ti-6Al-4V, mode I  $\Delta G_{TH}$  thresholds for such microstructurally small ( $< 50 \mu\text{m}$ ) cracks in both the bimodal and lamellar structures are compared with corresponding mixed-mode large-crack data in Fig. 11. Threshold values for the small cracks are clearly much smaller than the corresponding values for large cracks. Indeed, small cracks are observed to propagate at threshold levels above  $\Delta G_{TH} = 8.3 \text{ J m}^{-2}$  ( $\Delta K_{I,TH} \sim 1 \text{ MPa}\sqrt{\text{m}}$ ), whereas the

worst-case  $\Delta G$  threshold for large cracks, namely  $\Delta G_{TH} = 29.9 \text{ J m}^{-2}$  ( $\Delta K_{I,TH} \sim 1.9 \text{ MPa}\sqrt{\text{m}}$ ), is a factor of three larger.

Microstructurally, again it is clear that whereas the lamellar structure has superior large-crack threshold properties, this is not apparent in the presence of small cracks where the mode I thresholds are almost identical. Even the subsequent small-crack growth rates, shown as a function of  $\Delta K_I$  in Fig. 12 from a parallel study on the effects of foreign-object damage on high-cycle fatigue in Ti-6Al-4V<sup>42</sup> reveal few differences in the behaviour of the bimodal and lamellar microstructures—observations

which can be related to the minimal role of crack-tip shielding with cracks of limited wake.

However, the behaviour of the small surface crack is different from that of the short (and large) through-thickness crack in the manner in which it statistically 'samples' the microstructure. In the present experiments where the small-crack dimensions were comparable with characteristic microstructural size-scales, their crack fronts cannot sample the 'continuum' microstructure. For example, whereas the average short crack in the bimodal microstructure would 'sample' some 300 grains,

the small crack merely 'samples' one or two grains. Data on the behaviour of such cracks under mixed-mode loading are extremely limited although present results for the bimodal structure, at  $R = 0.1$  only, are shown in Fig. 13 and are compared with the corresponding large- and short-crack mixed-mode threshold values. Clearly, the additional effect of microstructural sampling is evident in these results in which the small-crack thresholds can be seen to be lower than the corresponding values for short cracks and shielding-corrected large cracks. While the marked effect of crack size on the mixed-mode thresholds up to now has been attributed to a difference in the magnitude of the crack-tip shielding, the even lower mixed-mode thresholds for microstructurally small cracks reflect this additional factor of the biased sampling of the 'weak links' in the microstructure by the small flaw. Indeed, quantitatively, large-crack mixed-mode  $\Delta G_{TH}$  thresholds in the bimodal structure at high mode-mixities  $\Delta K_{II}/\Delta K_I = 7.1$  can be some  $\sim 50$ – $90$  times larger than such measured small-crack thresholds.

Table 6 Thresholds obtained for short fatigue cracks in Ti-6Al-4V

	$\Delta G_{TH}$ (J/m <sup>2</sup> )			$\Delta K_{eq,TH}$ (MPa $\sqrt{m}$ )		
Mode-mixity	$R = 0.1$	$R = 0.5$	$R = 0.8$	$R = 0.1$	$R = 0.5$	$R = 0.8$
Bimodal microstructure:						
0°	72	66	59	2.9	2.8	2.7
26°	125	105	85	3.9	3.6	3.2
62°	72	64	52	2.9	2.8	2.5
82°	148	140	130	4.2	4.1	4.0
Lamellar microstructure:						
0°	159	110	96	4.4	3.6	3.4
26°	176	131	119	4.6	4.0	3.8
62°	180	142	121	4.7	4.1	3.8
82°	210	145	125	5.0	4.2	3.9

## DISCUSSION

In the present study, we have examined how varying the microstructure can affect the mixed-mode fatigue crack growth thresholds in a Ti-6Al-4V alloy as a function of load ratio and mode-mixity. What has been found is that microstructure, mode-mixity and load ratio all can have a major influence on the value of the mixed-mode threshold, *but only in the presence of cracks large compared with*

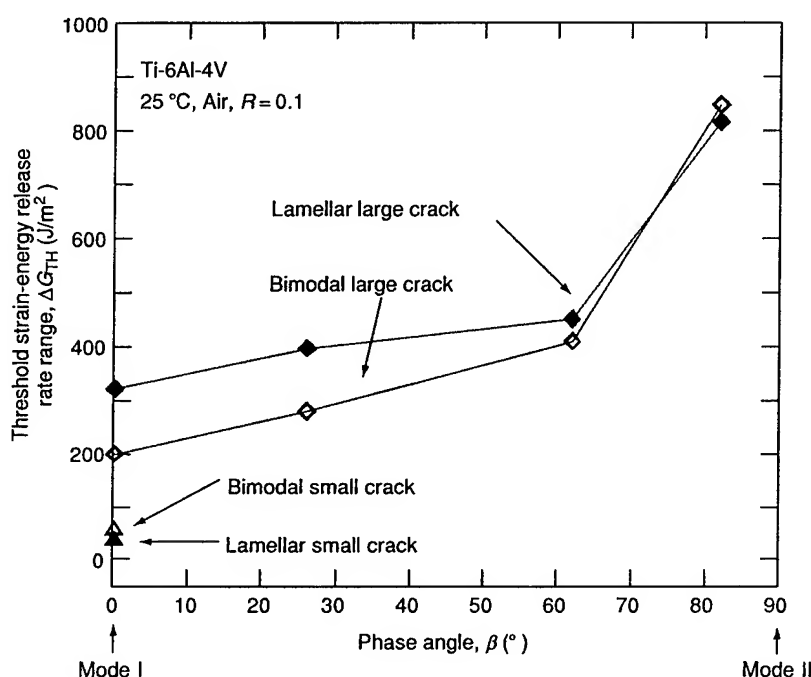


Fig. 11 Mixed-mode thresholds for large (> 4 mm) through-thickness fatigue cracks in bimodal and lamellar Ti-6Al-4V are compared with pure mode I thresholds for microstructurally small cracks. The superior resistance of the lamellar structure observed in the large crack regime is eliminated for small cracks, where the role of microstructural sampling becomes important.

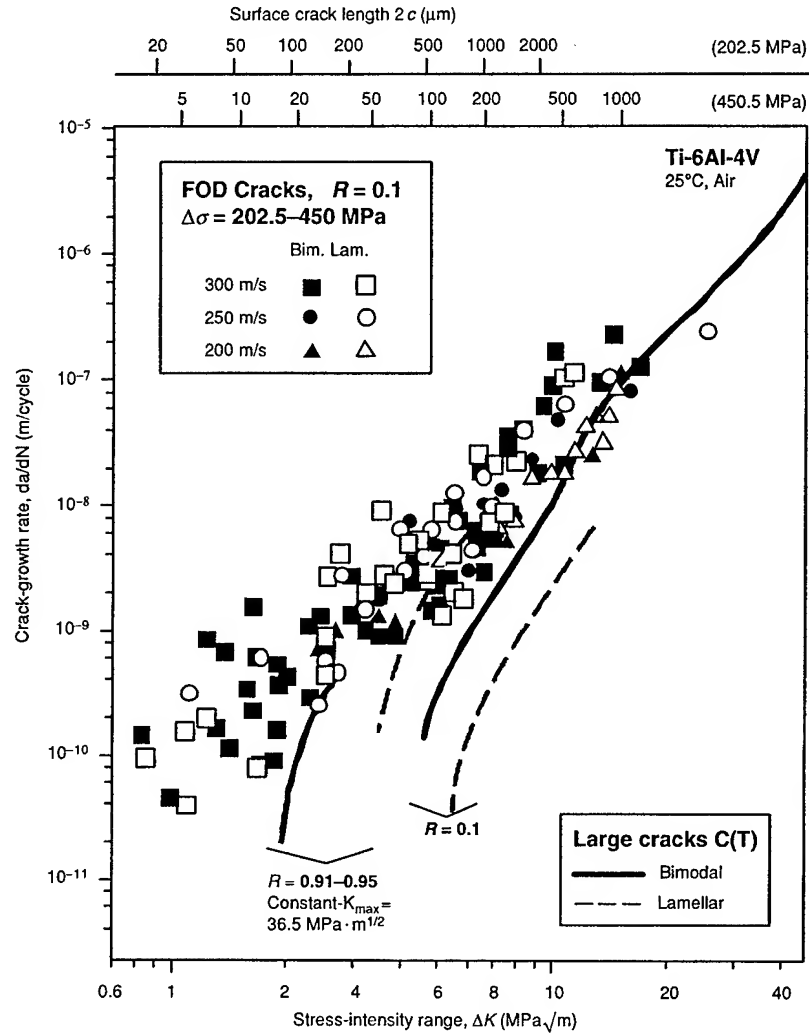


Fig. 12 Fatigue crack growth rates as a function of applied stress-intensity range at  $R = 0.1$  for microstructurally small ( $\sim 2-50 \mu\text{m}$ ) surface cracks in the bimodal and lamellar microstructures. Large-crack growth data at  $R = 0.1$  were obtained from constant load-ratio tests, whereas corresponding data at  $R = 0.91-0.95$  were obtained using constant- $K_{\text{max}}$ /increasing- $K_{\text{min}}$  testing (after Ref. [42]).

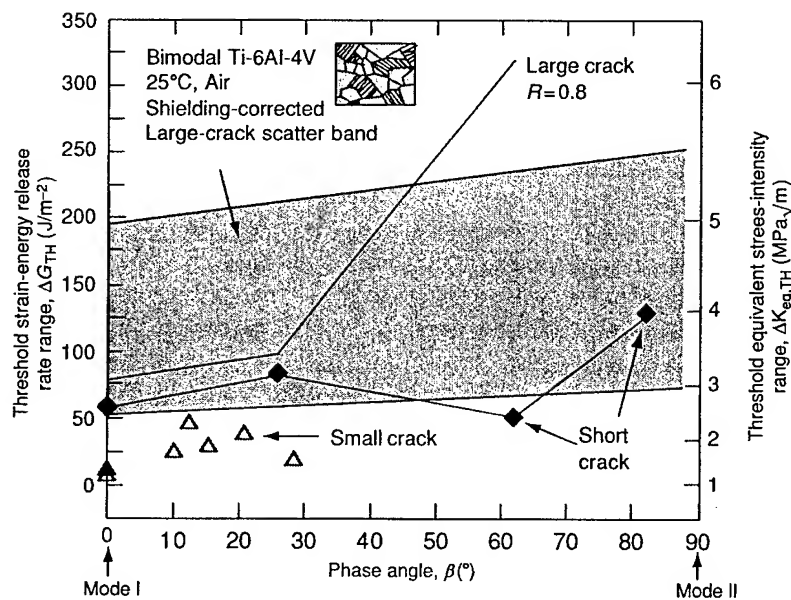


Fig. 13 Variation in mixed-mode thresholds,  $\Delta G_{\text{TH}}$ , as a function of phase angle,  $\beta$ , for microstructurally small ( $< 50 \mu\text{m}$ ) surface cracks in the bimodal microstructure. Shown for comparison are results for short ( $\sim 200 \mu\text{m}$ ) through-thickness cracks and for large ( $> 4 \text{ mm}$ ) through-thickness cracks under *worst-case*, high  $R$  conditions.



*microstructural dimensions.* The fact that microstructure, mode-mixity and load ratio all have a relatively insignificant effect on fatigue thresholds in the presence of short through-thickness cracks and microstructurally small surface cracks strongly implies a dominant role of crack-tip shielding dictated by crack path.

The superior crack-growth resistance, and hence higher large-crack  $\Delta G_{TH}$  thresholds, in the lamellar structure appears to be a consequence of the preferential path taken by the propagating crack, which in turn promotes higher levels of crack-tip shielding. In aligned lamellar structures, the  $\alpha$  phase is orientated perpendicular to the basal plane;<sup>21</sup> crack propagation parallel to the basal plane orientation is thus generally observed perpendicular to the orientation of the  $\alpha$  laths.<sup>22</sup> Because the thin layer of  $\beta$  phase that surrounds the  $\alpha$  laths cannot significantly alter the crack path, crack propagation invariably occurs with almost no change in direction through an entire colony of similarly orientated laths. This strongly crystallographic influence on the fatigue crack path is evident in the significant amount of out-of-plane deflection, secondary cracking and crack-path tortuosity that is characteristic of the coarser lamellar microstructures, as compared to the almost planar crack paths in the finer bimodal structures (Fig. 8).

Such microstructural factors can lead to two effects—one intrinsic and one extrinsic. In the coarser-grained lamellar structure, at the onset of the mixed-mode loading, the crack attempts to deviate along a direction different from that of the preferred path—that is, dictated by the  $G_{max}$ ,  $K_{II} = 0$  or maximum tensile stress (MTS) criteria. Although this clearly requires a higher driving force, its effect on the measured threshold is debatable because the crack is following a weaker *microstructural* path. More important though is the extrinsic effect in which the rougher crack paths give rise to the higher levels of crack closure and crack-surface interference, as shown, respectively, in Tables 4 and 5. The consequences of this are that because these mechanisms act in the crack wake, the prime effect of microstructure on the mixed-mode threshold arises from the presence of the precrack. Thus, as has been observed, it is to be expected that these microstructure effects will be far less apparent if the  $\Delta G_{TH}$  thresholds are measured for short cracks.

A further point of note is that such beneficial effects of microstructure can only be developed where the crack front samples a large enough number of grains, as in the case of the large and short cracks examined in the present study. Indeed, where this is not the case—e.g. for microstructurally small cracks—this may lead to a reversal of the relative ranking of the two structures<sup>21</sup> although the present results do not show this too clearly (Fig. 11). The basis for this reversal involves the density of

microstructural barriers that the crack front encounters. For large and short cracks, a large number of such barriers—e.g. grain boundaries, interfaces between dissimilarly orientated colonies, etc.—are encountered, leading to frequent changes in path, and hence increased tortuosity and higher thresholds for the lamellar structure. However, for small cracks, comparable in size to the characteristic microstructural size-scales, the crack front may encounter as few as one or two grains, or in the case of the lamellar structure be contained within a single grain, resulting in the crack front sampling a much lower density of barriers to crack propagation. Consequently, despite their superior large-crack properties, lamellar structures can show poorer resistance to fatigue crack propagation than bimodal structures in the small-crack regime.<sup>21</sup>

Finally, it is apparent that the near-elimination of the effect of mode-mixity on the large-crack  $\Delta G_{TH}$  thresholds when crack-tip shielding is accounted for (either by measurement or by removal of the crack wake), strongly implies that the threshold behaviour of fatigue cracks under mixed-mode loading is predominantly a mode I phenomenon. The principal influence of the applied shear loading appears to be in dictating the crack-path deflection, in conjunction with the near-tip microstructure in the coarser microstructures; once the crack path is set by the phase angle, the initial crack extension and hence the mixed-mode threshold are dictated by the effective crack-driving force, which is largely independent of mode-mixity. The implications for this are that the mixed-mode fatigue threshold behaviour is essentially identical to mode I behaviour if the additional contributions to the crack-tip shielding that are induced owing to a deflected crack path are carefully accounted for. Moreover, it further implies that the  $\Delta G_{TH}$  threshold, measured under pure mode I loading, can be considered to be a lower bound.

## CONCLUSIONS

Based on an investigation of the mixed-mode high-cycle fatigue behaviour of the fine bimodal microstructure (grain size  $\sim 20 \mu\text{m}$ ) and the coarser lamellar microstructure (colony size  $\sim 500 \mu\text{m}$ ) in a Ti-6Al-4V turbine-engine alloy, the following conclusions can be made:

- 1 Both microstructures displayed a marked effect of mode-mixity and load ratio on the measured mixed-mode fatigue thresholds for through-thickness large ( $> 4 \text{ mm}$ ) cracks. By characterizing the crack-driving force in terms of the strain-energy release rate,  $\Delta G$ , the mode I threshold was found to represent the *worst-case* condition.
- 2 The coarse-grained lamellar microstructure was generally observed to have higher thresholds, and hence superior mixed-mode, near-threshold fatigue crack-growth

resistance, compared to the bimodal structure, in the presence of large through-thickness fatigue cracks. However, this difference was significantly reduced at high phase angles.

- 3 The marked effect of load ratio and mode-mixity was substantially reduced when the large-crack  $\Delta G_{TH}$  thresholds were 'corrected' for crack-tip shielding owing to mode I crack closure and mode II crack-surface interference. As such shielding was promoted in the coarser lamellar microstructure by a higher degree of crack-path tortuosity and fracture-surface roughness, the superior large-crack properties of this structure were significantly reduced by such corrections.
- 4 Mixed-mode  $\Delta G_{TH}$  thresholds for through-thickness short cracks ( $\sim 200 \mu\text{m}$ ) were substantially lower than corresponding large-crack thresholds in both microstructures; moreover, short-crack threshold values were essentially insensitive to load ratio and mode-mixity.
- 5 Compared to large-crack threshold behaviour, the influence of microstructure on such short-crack mixed-mode  $\Delta G_{TH}$  thresholds was substantially reduced. This was attributed to the absence of crack-tip shielding effects with cracks of limited wake.
- 6 Results for naturally initiated microstructurally small ( $< 50 \mu\text{m}$ ) semielliptical surface cracks in the bimodal microstructure indicate that mixed-mode  $\Delta G_{TH}$  thresholds for such cracks are substantially lower than those for large cracks; indeed, large-crack thresholds at high mode-mixities ( $\Delta K_{II}/\Delta K_I \sim 7.1$ ) can be some 50–90 times larger than such measured small-crack thresholds. The substantially lower small-crack thresholds were associated with a limited role of crack-tip shielding and additionally with biased microstructural sampling by cracks of a dimension comparable with the characteristic microstructural size-scales.
- 7 The prime source of the influence of mixed-mode loading in dictating the value of the mixed-mode  $\Delta G_{TH}$  threshold is considered to arise primarily from the trajectory of the precrack. Because microstructure can influence this trajectory, in general microstructural effects on mixed-mode thresholds result mainly from the role of crack-tip shielding that arises from such crack paths. Where crack sizes are small enough so that such shielding cannot fully develop, the influence of microstructure on mixed-mode thresholds becomes minimal.

### Acknowledgements

This work was supported by the US Air Force Office of Scientific Research under Grant No. F49620-96-1-0478 under the auspices of the Multidisciplinary University Research Initiative on *High-Cycle Fatigue* to the University of California at Berkeley. Special thanks are due to Drs B. L. Boyce, I. Altenberger, J. O. Peters and A. W. Thompson for helpful discussions.

### REFERENCES

- 1 Report of the AdHoc Committee on Air Force Aircraft Jet Engine Manufacturing and Production Processes (1992) United States Air Force Scientific Advisory Board, SAF/AQQS: the Pentagon, Washington, D.C., USA.
- 2 Cowles, B. A. (1996) High-cycle fatigue in aircraft gas turbines – an industry perspective. *Int. J. Fract.* **80**, 147–163.
- 3 Chang, J. C. I. (1996) An integrated research approach to attack engine HCF Problems. Air Force Office of Scientific Research, Bolling AFB, Washington, D.C., USA.
- 4 Multidisciplinary University Research Initiative on High-Cycle Fatigue. Grant no. F49620-96-1-0478, U.S. Air Force Office of Scientific Research.
- 5 Waterhouse, R. B. and Lindley, T. C. (1994) *Fretting Fatigue* (Edited by European Structural Integrity Society Publication no. 18). Mechanical Engineering Publications Ltd, London, UK.
- 6 Iida, S. and Kobayashi, A. S. (1969) Crack-propagation rate in 7075-T6 plates under cyclic tensile and transverse shear loadings. *J. Bas. Eng. Trans. ASME* **91**, 764–769.
- 7 Gao, H., Alagok, N., Brown, M. W. and Miller K. J. (1985) Growth of fatigue cracks under combined mode I and mode II loads. In: *Multiaxial Fatigue*, ASTM STP 853 (Edited by K. J. Miller and M. W. Brown). ASTM, Philadelphia, PA, USA, pp. 184–202.
- 8 Pustejovsky, M. A. (1979) Fatigue crack propagation in titanium under general in-plane loading. I. Experiments. *Eng. Fract. Mech.* **11**, 9–15.
- 9 Pustejovsky, M. A. (1979) Fatigue crack propagation in titanium under general in-plane loading. II. Analysis. *Eng. Fract. Mech.* **11**, 17–31.
- 10 Campbell, J. P. and Ritchie, R. O. (2000) Mixed-mode, high-cycle fatigue-crack growth thresholds in Ti-6Al-4V. I. a comparison of large- and short-crack behavior. *Eng. Fract. Mech.* **67**, 209–227.
- 11 Campbell, J. P. and Ritchie, R. O. (2000) Mixed-mode, high-cycle fatigue-crack growth thresholds in Ti-6Al-4V. II. quantification of crack-tip shielding. *Eng. Fract. Mech.* **67**, 229–249.
- 12 Campbell, J. P. and Ritchie, R. O. (2001) Mixed-mode, high-cycle fatigue-crack growth thresholds in Ti-6Al-4V: role of bimodal and lamellar microstructures. *Metall. Mater. Trans. A* **32A**, 497–503.
- 13 Kruzic, J. J., Campbell, J. P. and Ritchie, R. O. (1999) On the fatigue behavior of  $\gamma$ -based titanium aluminides: role of small cracks. *Acta Mater.* **47**, 801–816.
- 14 Thompson A.W. (1999) Relations between microstructure and fatigue properties of alpha-beta titanium alloys. In: *Fatigue Behavior of Titanium Alloys* (Edited by R. R. Boyer, D. Eylon and G. Lütjering). TMS, Warrendale, PA, USA, pp. 23–30.
- 15 Lütjering, G. (1998) Influence of Processing on Microstructure and Mechanical Properties of ( $\alpha+\beta$ ) Titanium Alloys. *Mater. Sci. Eng. A243*, 32–45.
- 16 Irving, P. E. and Beevers, C. J. (1974) Microstructural influences on fatigue crack growth in Ti-6Al-4V. *Mater. Sci. Eng.* **14**, 229–238.
- 17 Bache, M. R., Evans, W. J. and McElhone, M. (1997) The effects of environment and internal oxygen on fatigue crack propagation in Ti-6Al-4V. *Mater. Sci. Eng. A234–236*, 918–922.
- 18 Thomas, J. P. (1998) Subcritical crack growth of Ti-6Al-4V at room temperature under high stress-ratio loading. *Scripta Mater.* **39**, 1647–1652.

- 19 Ravichandran, K. S. (1991) Near threshold fatigue crack growth behavior of a titanium alloy: Ti-6Al-4V. *Acta Metall. Mater.* **39**, 401–410.
- 20 Boyce, B. L. and Ritchie, R. O. (2001) Effect of load ratio and maximum stress intensity on the fatigue threshold in Ti-6Al-4V. *Eng. Fract. Mech.* **68**, 129–147.
- 21 Gregory, J. K. (1994) Fatigue crack propagation in titanium alloys. In: *Handbook of Fatigue Crack Propagation in Metallic Structures* (Edited by A. Carpinteri). Elsevier Science B, V., Amsterdam, The Netherlands, pp.281–321.
- 22 Nalla, R. K., Boyce, B. L., Campbell, J. P., Peters, J. O. and Ritchie, R. O. (2002) Influence of microstructure on high-cycle fatigue of Ti-6Al-4V: bimodal vs. lamellar structures. *Metall. Mater. Trans. A* **33A**, 899–918.
- 23 Eylon, D. (1998) Summary of available information on the processing of the Ti-6Al-4V HCF/LCF program plates. University of Dayton Report, Dayton, OH, USA.
- 24 Boyce, B. L. (1998) High Cycle Fatigue Thresholds in a Turbine Engine Titanium Alloy. *MSc Thesis*, University of California at Berkeley, Berkeley, CA, USA.
- 25 He, M. Y., Cao, H. C. and Evans, A. G. (1990) Mixed-mode fracture: the four-point shear specimen. *Acta Metall. Mater.* **38**, 839–846.
- 26 Suresh, S., Shih, C. F., Morrone, A., O'Dowd, N. P. (1990) Mixed-mode fracture toughness of ceramic materials. *J. Am. Ceram. Soc.* **73**, 1257–1267.
- 27 Slepetz, M., Zagaeski, T. F. and Novello, R. F. (1978) AMMRC-TR-78-30, Army Materials and Mechanics Research Center, Watertown, MA, USA.
- 28 He, M. Y. and Hutchinson, J. W. (2000) Asymmetric four-point crack specimen. *J. Appl. Mech. Trans. ASME* **67**, 207–209.
- 29 Newman, J. C. and Raju, I. S. (1981) An empirical stress-intensity factor equation for the surface crack. *Eng. Fract. Mech.* **15**, 185–192.
- 30 He, M. Y. and Hutchinson, J. W. (2000) Surface crack subject to mixed mode loading. *Eng. Fract. Mech.* **65**, 1–14.
- 31 Ravichandran, K. S. (1997) Effects of crack aspect ratio on the behavior of small surface cracks in fatigue: Part I. simulation. *Metall. Mater. Trans. A* **28A**, 149–156.
- 32 Ravichandran, K. S. and Larsen, J. M. (1997) Effects of crack aspect ratio on the behavior of small surface cracks in fatigue: Part II. experiments on a titanium (Ti-8Al) alloy. *Metall. Mater. Trans. A* **28A**, 157–169.
- 33 Hua, G., Brown, M. W. and Miller, K. J. (1982) Mixed-mode fatigue thresholds. *Fat. Eng. Mater. Struct.* **5**, 1–17.
- 34 Tong, J., Yates, J. R. and Brown, M. W. (1994) The significance of mean stress on the fatigue crack growth threshold for mixed mode I + II loading. *Fat. Eng. Mater. Struct.* **17**, 829–838.
- 35 Qian, J. and Fatemi, A. (1996) Mixed mode fatigue crack growth: a literature survey. *Eng. Fract. Mech.* **55**, 969–990.
- 36 Erdogan, F. and Sih, G. C. (1963) On the crack extension in plates under plane loading and transverse shear. *J. Bas. Eng. Trans. ASME* **85**, 519–525.
- 37 Cotterell, B. (1965) On brittle fracture paths. *Int. J. Fract. Mech.* **1**, 96–103.
- 38 John, R., Rosenberger, A. H., DeLuca, D., Porter J. W. and Li, K. (1999) Mixed mode crack growth in a gamma titanium aluminide alloy. In: *Gamma Titanium Aluminides 1999* (Edited by Y. W. Kim, D. M. Dimiduk and M. H. Loretto ). TMS, Warrendale, PA, USA, pp. 535–540.
- 39 Nayeb-Hashemi, H., McClintock, F. A. and Ritchie, R. O. (1982) Effects of friction and high torque on fatigue crack propagation in mode III. *Metall. Trans. A* **13A**, 2197–2204.
- 40 Tschegg, E. K. (1983) Sliding mode crack closure and mode III fatigue crack growth in mild steel. *Acta Metall.* **31**, 1323–1330.
- 41 Zheng, Y. S., Wang, Z. G. and Ai, S. H. (1994) Mixed-mode I and II fatigue threshold and crack closure in dual-phase steels. *Metall. Mater. Trans. A* **25A**, 1713–1723.
- 42 Peters, J. O. and Ritchie, R. O. (2001) Foreign object damage and high cycle fatigue: Role of microstructure in Ti-6Al-4V. *Int. J. Fatigue* **23**, 1413–1421.
- 43 Suresh, S. and Ritchie, R. O. (1984) Propagation of short cracks. *Int. Metals. Rev.* **29**, 445–476.
- 44 Ritchie, R. O. and Lankford, J. (1986) Small fatigue cracks: a statement of the problem and potential solutions. *Mater. Sci. Eng.* **A84**, 11–16.
- 45 Ritchie R.O. and Wu Y. (1986) Short crack effects in fatigue: a consequence of crack tip shielding. In: *Small Fatigue Cracks* (Edited by R. O. Ritchie and J. Lankford.). TMS-AIME, Warrendale, PA, USA, pp. 167–189.
- 46 Venkateswara Rao, K. T., Yu, W. and Ritchie, R. O. (1988) On the behavior of small fatigue cracks in commercial aluminum–lithium alloys. *Eng. Fract. Mech.* **31**, 623–635.
- 47 Bilby, B. A., Cardew, G. E. and Howard, I. C. (1978) Stress intensity factors at the tips of kinked and forked cracks. In: *Fracture 1977* (Edited by D. M. R. Taplin), Pergamon Press, Oxford. U.K., Vol. 3, pp. 197–200.
- 48 Cotterell, B. and Rice, J. R. (1980) Slightly curved or kinked cracks. *Int. J. Fract.* **16**, 155–169.
- 49 Nalla, R. K., Campbell, J. P. and Ritchie, R. O. (2002) Mixed-mode, high-cycle fatigue-crack growth thresholds in Ti-6Al-4V: role of small cracks. *Int. J. Fatigue*, in press.

## APPENDIX A

### Distinction between large, short and small cracks

A point of note in this work is the distinction between *large*, *short* and *small* cracks. Large fatigue cracks (Fig. A1a) are defined as having dimensions that are large compared to the scale of the microstructure in both directions. Therefore, they generally have a fully developed crack-tip shielding zone and can 'sample' the microstructure in a statistical (continuum) manner.<sup>43</sup> With respect to large cracks, small cracks are generally described as being comparable in size to:<sup>44</sup>

- microstructural dimensions, where biased statistical sampling of the microstructure can lead to accelerated crack advance along 'weak' paths; that is, microstructural features orientated for easy crack growth (a continuum limitation),
- the extent of local inelasticity *ahead* of the crack tip, where the assumption of small-scale yielding implicit in the use of the stress intensity, *K*, is not strictly valid (a linear-elastic fracture mechanics limitation),
- the extent of crack-tip shielding (e.g. crack closure) *behind* the crack tip, where the reduced role of shielding leads to

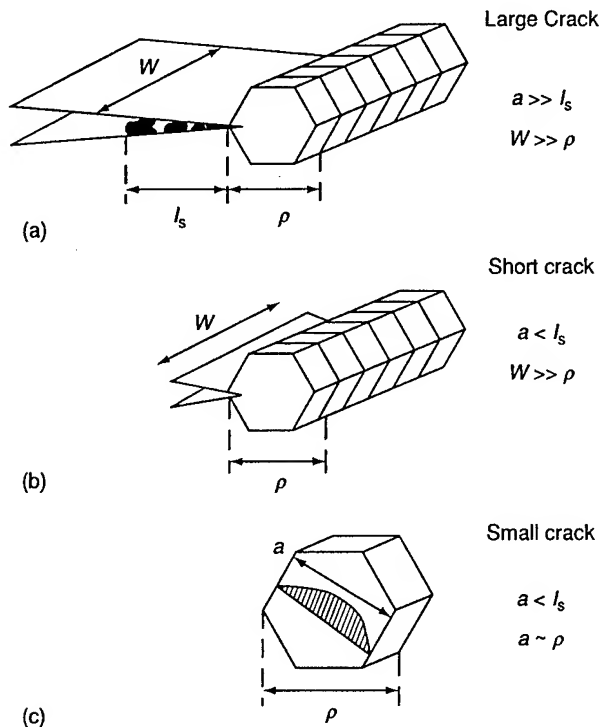


Fig. A1 Schematic illustrations highlighting the key distinctions between large, short and small fatigue cracks. Large cracks (a) have length,  $a$ , and width,  $W$ , which are large both with respect to the equilibrium shielding-zone length,  $l_s$  (indicated here as a region of debris in the crack wake which produces crack closure), and the characteristic microstructural size scale,  $\rho$ , e.g. the grain size. In contrast to this, short fatigue cracks (b) are characterized by  $a < l_s$ , but  $W \gg \rho$ . The reduced crack-wake length results in a lower level of crack-tip shielding. For small cracks (c), the fracture surface is reduced in both dimensions, with  $a$  (and  $W$ ) being small with respect to both  $l_s$  and  $\rho$ . The fact that  $a \sim \rho$  implies that the crack front samples only a few microstructural entities, leading to a biased sampling of the microstructure.

a higher local driving force than the corresponding large crack at the same applied  $K$  level (a similitude limitation).

However, a further important distinction can be made, namely that of a short vs. small crack. This distinction alludes not simply to physical size but the extent to which a fatigue crack is subjected to the first and third factors listed above. Short fatigue cracks (Fig. A1b) are physically short in only one dimension, a condition that is often realized experimentally by machining away the wake of a large crack. This type of fatigue flaw experiences limited crack-tip shielding owing to its reduced length,<sup>45</sup> yet samples the microstructure as a continuum because of its extensive crack front. By contrast, small fatigue cracks (Fig. A1c) are small and comparable to the microstructural size-scale in all dimensions, as typified by the small, semielliptical surface flaw (e.g. Refs [44,46]). With such cracks, crack-tip shielding is significantly reduced (e.g. Ref. [43]), and since the crack front samples only a few microstructural entities, this allows for a biased sampling of microstructurally weak paths. Because of this restriction in shielding and the biased microstructural sampling, fatigue crack growth resistance in the presence of small cracks often tends to be lowest.

## Appendix B

### Calculation of the mixed-mode threshold

In this work, as in prior studies (e.g. Refs [7–12,33,34]) on mixed-mode fatigue thresholds, the threshold values of the mode I and mode II stress intensities required to initiate cracking,  $\Delta K_{I,TH}$  and  $\Delta K_{II,TH}$ , are calculated based on the mode I precrack (which is generated in near-identical fashion for each test); the corresponding mixed-mode threshold,  $\Delta G_{TH}$ , or equivalent stress intensity,  $\Delta K_{eq,TH}$ , are then computed from:

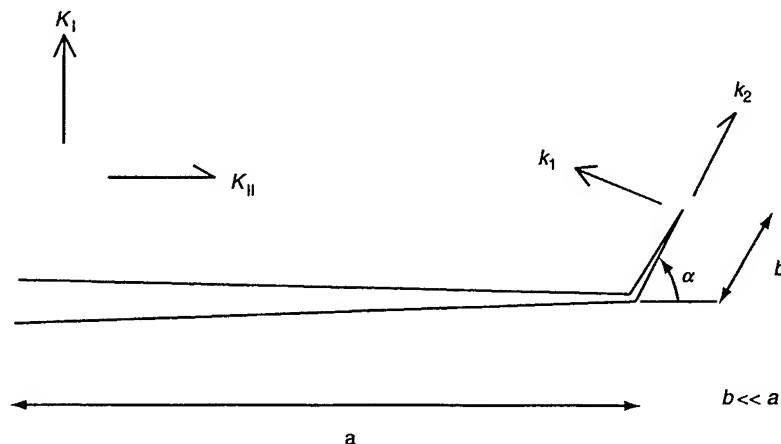


Fig. A2 Schematic illustration of the kinked crack configuration for the alternative calculation of the mixed-mode threshold.

$$\Delta G_{TH} = (\Delta K_{I,TH}^2 + \Delta K_{II,TH}^2)/E' \equiv (\Delta K_{eq,TH}^2)/E' \quad (A1)$$

where  $E'$  is the appropriate elastic modulus.

However, since once the crack starts to grow, it deflects along a different path (corresponding to a local  $K_{II} = 0$  criterion modified by the effect of the microstructure), an alternative calculation of the threshold can be based on the presence of an infinitesimal kink along this direction. Assuming for simplicity that the kink (of length  $b \ll a$ , the crack length) represents an in-plane tilt through angle  $\alpha$  to the precrack plane (Fig. A2), then the local mode I and mode II stress intensities,  $\Delta k_1$  and  $\Delta k_2$ , at the deflected crack tip will be given by:<sup>47,48</sup>

$$\begin{aligned} \Delta k_1(\alpha) &= c_{11}\Delta K_I + c_{12}\Delta K_{II} \\ \Delta k_2(\alpha) &= c_{21}\Delta K_I + c_{22}\Delta K_{II} \end{aligned} \quad (A2)$$

where  $\Delta K_I$  and  $\Delta K_{II}$  are the stress intensities for a main (pre)crack, and the coefficients  $c_{ij}$ , which are a sole function of  $\alpha$ , are given in Refs [47,48]. The mixed-mode thresholds,  $\Delta G'_{TH}$  and  $\Delta K'_{TH}$ , can then be computed from:

$$\Delta G'_{TH} = (\Delta k_{1,TH}^2 + \Delta k_{2,TH}^2)/E' \equiv (\Delta K'_{TH})^2/E' \quad (A3)$$

As discussed elsewhere,<sup>49</sup> the use of Eqn. A3 to calculate the mixed-mode threshold can in fact reduce the computed values of  $\Delta K_{eq,TH}$ , at specific phase angles by as much as 40%. For the bimodal and lamellar Ti-6Al-4V, this translates into a reduction in threshold  $\Delta K_{eq,TH}$  values by typically 1–2 MPa $\sqrt{m}$ .



## Mixed-mode, high-cycle fatigue-crack growth thresholds in Ti-6Al-4V: role of small cracks

R.K. Nalla <sup>a</sup>, J.P. Campbell <sup>b</sup>, R.O. Ritchie <sup>a,\*</sup>

<sup>a</sup> Department of Materials Science and Engineering, University of California, Berkeley, CA 94720-1760, USA

<sup>b</sup> Metals Fabrication Division, General Motors, Troy, MI 48084, USA

Received 7 September 2001; received in revised form 19 December 2001; accepted 25 January 2002

### Abstract

There have been few studies to date describing fatigue-crack propagation thresholds under mixed-mode loading conditions in the presence of cracks, that are small as compared to the characteristic microstructural dimensions. To address this need, the variation in mixed-mode, high-cycle fatigue-crack growth thresholds with crack size is reported for a Ti-6Al-4V turbine blade alloy with a fine-grained bimodal microstructure. Specifically, threshold behavior is examined for large through-thickness cracks (>4 mm in length), short through-thickness cracks (~200  $\mu\text{m}$  in length), and microstructurally-small surface cracks (10–50  $\mu\text{m}$  in diameter) under combined mode I and mode II loading at load ratios (ratio of minimum to maximum load) ranging from 0.1 to 0.8. For mode-mixities ranging from pure mode I to predominantly mode II, large crack, mode I  $\Delta K_{I,TH}$  thresholds were found to decrease substantially with increasing phase angle. However, by characterizing in terms of the range in strain energy release rate,  $\Delta G_{TH}$ , incorporating both mode I and mode II contributions, it was observed that the pure mode I threshold could be regarded as a 'worst case' under mixed-mode loading in this alloy. By estimating the effective crack-driving force actually experienced at the crack tip, the observed increase in the mixed-mode  $\Delta G_{TH}$  threshold with mode-mixity was attributed to an increasing influence of crack-tip shielding due to crack closure and crack-surface interference. Equivalent thresholds for through-thickness short cracks, where the crack wake and hence the effect of such shielding is minimized, were consequently far less sensitive to mode-mixity and corresponded in magnitude to the shielding-corrected large-crack thresholds. This effect was accentuated for the measured thresholds of microstructurally-small surface cracks; such small-crack, mixed-mode  $\Delta G_{TH}$  thresholds not only displayed a minimal influence of mode-mixity but were up to two orders of magnitude smaller than those for corresponding large cracks at the same load ratio and mode-mixity conditions. © 2002 Published by Elsevier Science Ltd.

**Keywords:** High-cycle fatigue; Mixed mode; Fatigue thresholds; Load ratio effects; Small crack effects; Crack-tip shielding; Ti-6Al-4V; Titanium

### 1. Introduction

The occurrence and control of failures due to high-cycle fatigue (HCF) in turbine engine components is currently one of the most critical challenges facing the US military aircraft fleet; in fact, a large fraction of recent engine failures have been attributed to HCF [1–3]. One particular issue involved in this problem is the prediction of the limiting conditions for HCF failures in the presence of multiaxial stresses; this can occur, for example, at sites of fretting fatigue in the turbine blade

dovetail/disk contact section [4]. Although the driving force for cracks in these situations is a combination of tensile (mode I), in-plane shear (mode II) and/or anti-plane shear (mode III) loading, the vast majority of research on fatigue-crack growth behavior in typical turbine blade alloys, such as Ti-6Al-4V, has been limited to pure mode I behavior (e.g. [5–9]). Despite this preponderance of mode I data, there has been an increasing awareness in recent years of the role of mode-mixity in influencing fatigue-crack growth behavior in metallic materials (e.g. [11–18]), with a handful of studies

\* Corresponding author. Tel.: +1-510-486-5798; fax: +1-510-486-4881.

E-mail address: roritchie@lbl.gov (R.O. Ritchie).

<sup>1</sup> It is interesting to note in this regard that although fatigue failure in materials has been documented for over a century, the first investigations on multiaxial fatigue occurred only as recently as 1969 [10].

devoted to Ti-6Al-4V (e.g. [16–18]). However, few investigations have focused on the role of crack size in influencing fatigue-crack growth behavior under multi-axial conditions, and specifically on how the presence of microstructurally-small cracks may affect mixed-mode fatigue thresholds. The present work seeks to address this problem for the high-cycle fatigue of turbine blade materials, specifically for a Ti-6Al-4V alloy with a bimodal microstructure.

## 2. Background

The HCF problem in turbine engine components is associated with a variety of drivers [3], which vary with component and indeed location on that component (Fig. 1). Typically, these components, such as blades and disks, are subjected to high frequency ( $> 1$  kHz) vibrations in the engine (HCF), superimposed on to a low-cycle fatigue component associated with the start-to-stop cycles [2,3]. A critical site for crack initiation is in the attachment section of the blade, where contact between the blade dovetail and disk leads to the formation of fretting fatigue cracks [4]. This problem often involves complex multi-axial loading conditions, surface damage, and associated residual stresses.

At present, most design and 'lifing' methodologies for HCF use traditional stress-life ( $S-N$ ) and Goodman diagram approaches. However, in light of the high frequencies involved, once a fatigue crack starts propagating, final failure can ensue rapidly; consequently, alternative fracture-mechanics based design methodologies utilizing the concept of a threshold stress-intensity, below which no fatigue-crack growth is observed, may offer a preferred approach, provided such thresholds are defined under representative HCF conditions. Unfortunately, as noted above, most available fatigue thresh-

old data (e.g. [19]) have been measured in tension (mode I) on through-thickness cracks, large compared to the microstructural size-scales. These are conditions that may not be relevant to turbine engine HCF, where the loading can be mixed-mode and crack sizes can be of the order of a fraction of a millimeter. In terms of defining a conservative HCF threshold, both these factors are important as small cracks are known to grow (at least in mode I) at apparently anomalously high velocities, well below the established large-crack propagation thresholds [20]; similarly, the superposition of shear loading (resulting in finite mode II or III stress-intensity ranges,  $\Delta K_{II}$  and  $\Delta K_{III}$ , respectively, at the crack tip) has been shown to cause a substantial reduction in the mode I fatigue threshold,  $\Delta K_{I,TH}$ , below which the crack growth is presumed to be dormant (e.g. [10,13,14,16,17]).

Our previous studies [21] on this alloy have shown such a reduction in the  $\Delta K_{I,TH}$  threshold with increasing mode-mixity, although the majority of this work was devoted to large ( $> 4$  mm) through-thickness cracks. Furthermore, the variation in threshold behavior with mode-mixity was found to be related to the degree of crack-tip shielding, by mode I crack closure and mode II crack-surface interference [21,22], which acts locally to reduce the effective driving force at the crack tip [22]. As the potency of such shielding is substantially reduced for cracks with limited wake (e.g. [23–26]), it is important to assess the role of mode-mixity in influencing fatigue threshold behavior for small cracks, where cracks are of a size comparable to the scale of microstructure ahead of the crack tip and/or the extent of shielding behind it. In addition, it is critical to distinguish between these two effects, by comparing the behavior of short cracks that are small only in the length dimension (which limits shielding) with those that are small in all dimensions (which limits both shielding and the ability to 'sample' the continuum microstructure).

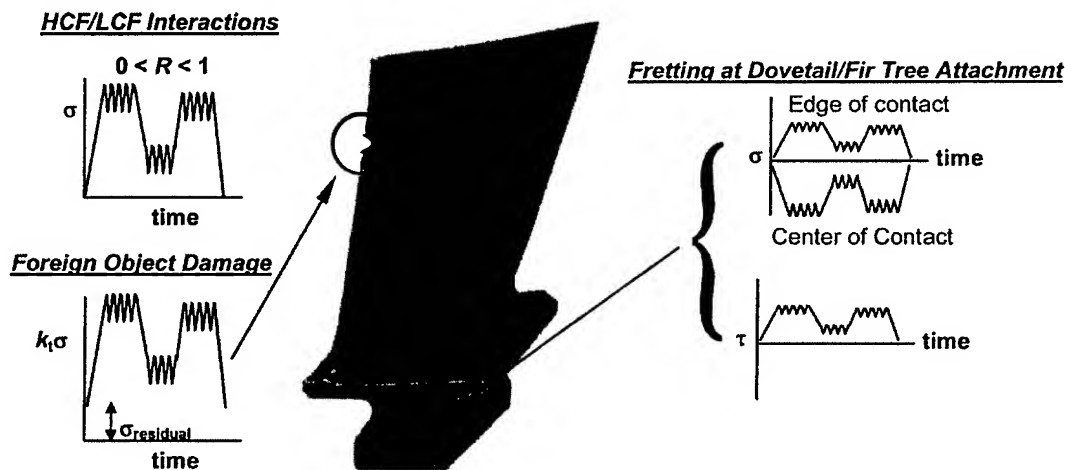


Fig. 1. Diagram illustrating the variety and range of factors involved in HCF failure.

Table 1

Chemical composition of Ti-6Al-4V bar stock (in wt%) [28]

Bar location	Ti	Al	V	Fe	O	N	H
Top	Bal.	6.27	4.19	0.20	0.18	0.012	0.0041
Bottom	Bal.	6.32	4.15	0.18	0.19	0.014	0.0041

Accordingly, in the present work we examine the role of crack size through a study of the mixed-mode, fatigue-crack growth thresholds in Ti-6Al-4V for large ( $>4$  mm), short ( $\sim 200$   $\mu\text{m}$ ) and microstructurally-small ( $<50$   $\mu\text{m}$ ) cracks<sup>2</sup>, over a range of mode-mixities from pure tension ( $\Delta K_{II}/\Delta K_I = 0$ ) to predominantly shear ( $\Delta K_{II}/\Delta K_I \sim 7.1$ ), at positive load ratios (ratio of minimum to maximum load) between  $R = 0.1$ – $0.8$ .

### 3. Experimental procedures

#### 3.1. Materials

The material investigated, a turbine engine Ti-6Al-4V alloy, originated as bar stock produced by Teledyne Titanium specifically for the joint government–industry–academia HCF program; its composition (in wt.%) is given in Table 1. The original bar-stock (63.5 mm in diameter) was sectioned into segments 400 mm long, preheated to 940°C for 30 min and forged into 400  $\times$  150  $\times$  20 mm plates. These plates were solution-treated at 925°C for 1 h, fan air cooled and then stabil-

ized at 700°C for 2 h. The microstructure of this alloy was examined in the as-received, bimodal condition (sometimes referred to as solution treated and overaged—STOA), consisting of colonies of equiaxed primary- $\alpha$  and lamellar  $\alpha$ + $\beta$  (transformed- $\beta$ ) (Fig. 2). A careful investigation of the relative distribution of the two phases indicated an overall primary- $\alpha$  content of  $\sim 64\%$  [27]. The average grain size obtained was  $\sim 20$   $\mu\text{m}$ , with slight grain elongation observed in the longitudinal (L) direction of the forging. Using differential thermal analysis, the  $\beta$ -transus temperature was measured to be 990–1005 °C.

#### 3.2. Uniaxial tensile and toughness properties

Uniaxial tensile tests were conducted in the L-orientation using a strain rate of  $5 \times 10^{-4}$  s<sup>-1</sup>; additional data were taken from [28]. The yield and tensile strengths for this microstructure were found to be 930 and 978 MPa, respectively, with a reduction in area of  $\sim 45\%$ . In addition, the plane-strain fracture toughness,  $K_{Ic}$ , was measured at 64 MPa $\sqrt{\text{m}}$ , using  $\sim 18$ -mm thick, fatigue-precracked, compact-tension samples.

#### 3.3. Large-crack fatigue testing

Fatigue thresholds in pure mode I were conducted using 4.5-mm thick, 11.3-mm wide symmetric four-point bending samples, with inner and outer loading spans of 12.7 and 25.4 mm, respectively. For mixed-mode loading, the mode II component of the loading was introduced using the asymmetric four-point bending (AFPB) configuration, where the  $\Delta K_{II}/\Delta K_I$  ratio can be varied using an offset,  $s$ , from the load-line as shown in Fig. 3(a) (e.g., [13,29]). The values of mode I stress-intensity range,  $\Delta K_I$ , and the mode II stress-intensity range,  $\Delta K_{II}$ , were determined from linear-elastic stress-intensity solutions for this geometry, recently developed by He and Hutchinson [30].

Since mixed-mode thresholds were determined from the initiation, rather than the arrest, of crack growth from a precrack, the process of precracking itself was conducted in a carefully-controlled, near-identical manner for all large-crack test samples to minimize any effects of this procedure on the subsequent threshold determination. Specifically, fatigue cracks were grown in room air from a 2 mm deep electro-deposition machined

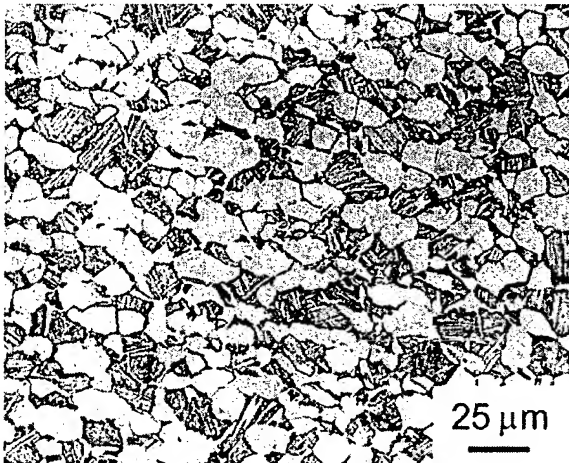


Fig. 2. Optical micrograph of the bimodal (solution treated and overaged, STOA) Ti-6Al-4V microstructure investigated. Etched for  $\sim 10$  s in 5 parts 70% HNO<sub>3</sub>, 10 parts 50% HF, 85 parts of H<sub>2</sub>O.

<sup>2</sup> The distinction between large, short and small cracks is described in Appendix A.



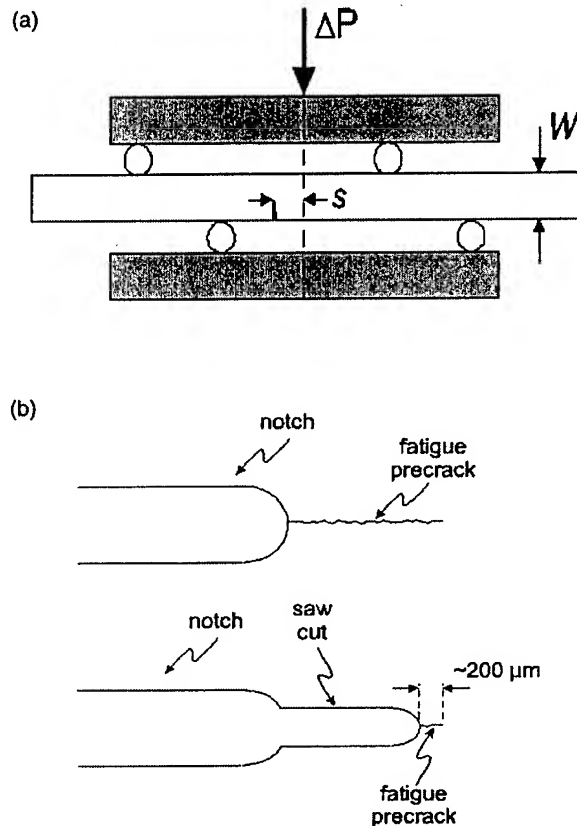


Fig. 3. (a) The asymmetric four-point bend specimen. The offset  $s$ , from the load-line is used to control the degree of mode-mixity,  $\Delta K_{II}/\Delta K_I$ , and thereby the phase angle,  $\beta = \tan^{-1}(\Delta K_{II}/\Delta K_I)$ . (b) The procedure used to remove the crack wake of a large crack, in order to produce a short crack is illustrated.

(EDM) through-thickness notch in a symmetric four-point bending sample at a load ratio,  $R$  of 0.1 with a constant loading frequency (125 Hz, sine wave). This alloy has been known to show little effect of frequency over the range 50–20,000 Hz [8,31]. In all samples, the final precrack length achieved was  $4.50 \pm 0.25$  mm at a near-threshold stress-intensity  $\Delta K$  of  $4.8 \pm 0.5$  MPa $\sqrt{m}$ .

For large crack ( $> 4$  mm) tests, mode-mixities varied from  $\Delta K_{II}/\Delta K_I = 0$  (pure mode I) to  $\sim 7.1$  (nearly pure mode II), representing a change in phase angle,  $\beta = \tan^{-1}(\Delta K_{II}/\Delta K_I)$ , from 0 to  $82^\circ$ . Load ratios were varied from  $R = 0.1$  to 0.8. Tests involving cycling pre-cracked specimens at a specified mode-mixity were performed in the following way: if no crack growth was observed (using an optical microscope) after  $2 \times 10^6$  cycles, either  $\Delta K_I$  or  $\Delta K_{II}$  was increased by  $\sim 0.25$  MPa $\sqrt{m}$  and the procedure repeated. In this way, a 'growth/no growth' condition bounding the actual threshold was obtained. The crack extension defining 'growth' was taken to be of the order of the characteristic microstructural dimen-

sion, i.e.,  $\sim 20$   $\mu m$ , yielding threshold growth rates of  $10^{-11}$  m/cycle.

The magnitude of the crack-tip shielding, used to compute the effective crack-driving force in both modes I and II, was characterized using a recently developed compliance-based technique for both tensile opening and shear type loading, using two displacement gauges mounted near the crack tip to measure opening and shear displacements. As described in detail in [22], the distinction between the contributions to shielding in modes I and II was achieved by examining separate load-displacement curves using these two crack-tip gauges. Mode I shielding, in the form of crack closure, was determined from the compliance curve for the opening displacements from the first deviation from linearity on unloading, whereas mode II shielding, in the form of asperity rubbing and interlock, was determined in an analogous fashion from the compliance curve for shear displacements.

### 3.4. Short-crack fatigue testing

For corresponding tests on short cracks, thresholds were measured using identical procedures on 6–12 mm thick bend bars, except that the precrack wake was the carefully machined to within  $\sim 200$   $\mu m$  of the crack tip using a slow-speed, 0.3-mm thick, diamond saw Fig. 3(b). The rationale here was to limit the shielding (due to premature contact of the crack faces during unloading) by restricting the crack wake, without affecting the degree of sampling of the microstructure along the crack front (as described in the Appendix A). As for large cracks, thresholds were obtained at load ratios ranging from  $R = 0.1$  to 0.8 for mode-mixities of  $\Delta K_{II}/\Delta K_I = 0$  to  $\sim 7.1$ .

The removal of the precrack wake left a machined notch with a measured (semi-circular) root radius of  $\rho \approx 160$   $\mu m$ ,  $\sim 200$   $\mu m$  from the tip of the short crack (Fig. 3b). This, however, was reasoned to not affect the stress and strain field of the short crack. According to Dowling's analysis of the stress intensity for a short crack, of length  $l$ , emanating from a notch [32], the elastic notch field is felt over a distance of  $0.1$ – $0.2$   $l/\rho$  from the notch surface, i.e., over a distance of  $< 40$   $\mu m$ , far less than the length of the short crack. The corresponding plastic field of the notch can be estimated from the Neuber analysis of Hammouda et al. [33], which gives the extent of bulk plasticity as a simple function of the stress level, yield strength and notch size and shape. For the present experiments, this analysis gave a notch plastic field of  $\sim 20$   $\mu m$ , which is again far less than the length of the short crack. Finally, using Rice and Johnson's analysis of a blunted crack tip [34], based on Hill's logarithmic spiral slip-line field solution for a rounded notch [35], the maximum stress of the notch plastic field peaks at a distance of  $0.95\rho$  i.e., in the present case  $\sim 150$   $\mu m$ , from the notch tip, which again implies that the tip

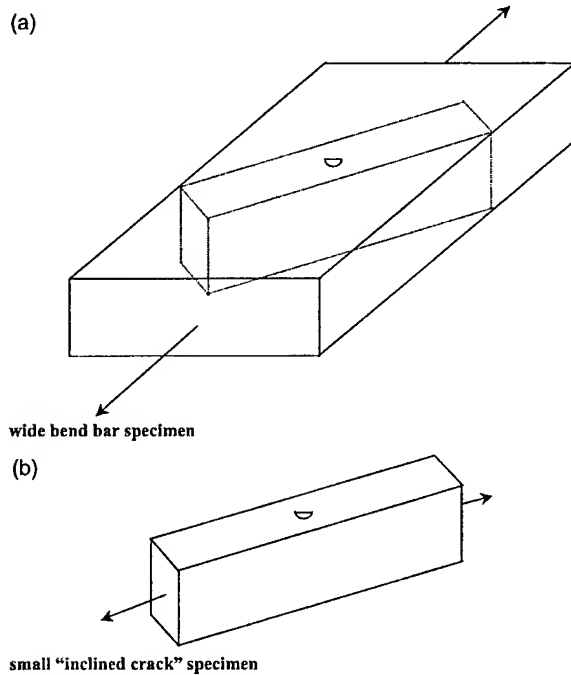


Fig. 4. A schematic illustration showing the procedure utilized for obtaining the small 'inclined crack' specimen. (a) The dotted lines outline the small crack test sample to be machined at the desired angle of inclination,  $\phi$  (see Fig. 5) from the original wide bend bar. The nominal direction of loading for crack initiation is also shown. (b) The final 'inclined crack' specimen is illustrated.

of the short crack is well outside the influence of the notch.

### 3.5. Small-crack fatigue testing

Corresponding mixed-mode testing on microstructurally small cracks was performed using an inclined crack method. Specifically, small, semi-elliptical, surface 'precracks' were naturally initiated on wide, three-point bend samples (5 mm thick, 16–25 mm wide, with a span of 25.4 mm) machined in the L–T orientation (Fig. 4), at a maximum stress of  $\sigma_{\max} \sim 750$  MPa ( $\sim 80\%$  of yield strength) at 50 Hz sinusoidal frequency with  $R = 0.1$ . The surfaces necessary for observation of the crack were polished to a  $0.05 \mu\text{m}$  finish, with the sides to be used to carry the load-bearing pins ground to a 600 grit finish. Following specimen preparation, a stress relief treatment of 2 h at  $\sim 695^\circ\text{C}$  in vacuo was used to minimize residual stresses.

In order to measure a mixed-mode, small-crack thresholds, smaller bend bars were carefully machined out from the original pre-cracked bar with the crack inclined at the desired angle,  $\phi$ , to the length of the sample (Figs. 4–5). The smaller bend bars containing the inclined small surface cracks were then used for threshold determination by cycling in symmetric four-point bending

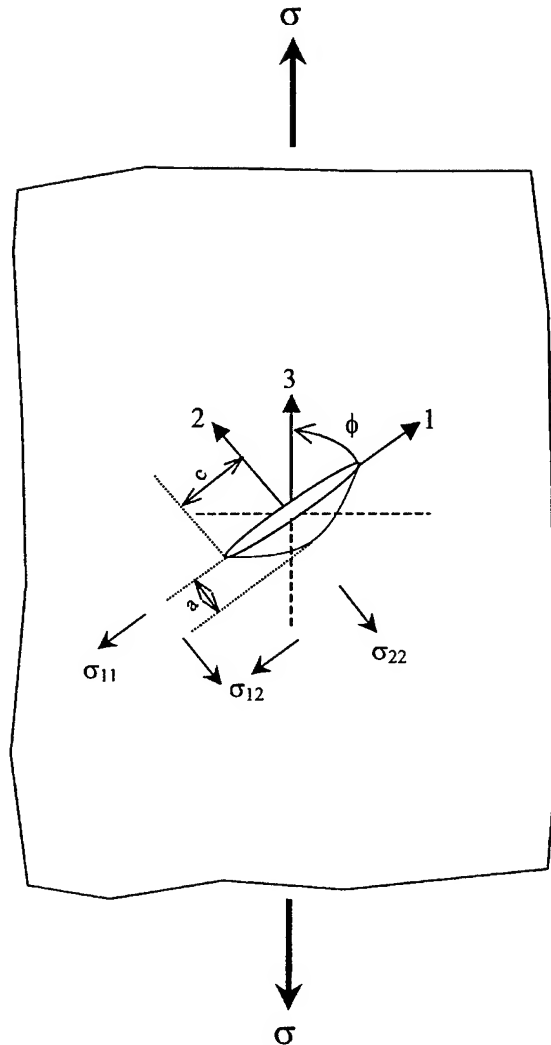


Fig. 5. A schematic of the inclined semi-elliptical surface crack configuration used for the microstructurally-small crack testing. The crack depth,  $a$ , and the crack (half) size,  $c$ , are indicated, as is the angle of inclination,  $\phi$ . The tensile loading component,  $\sigma_{22}$  induces the mode I contribution, while the shear loading component,  $\sigma_{12}$  induces the mode II and mode III components.  $\sigma_{11}$  has no influence.

with a load ratio of 0.1. Similar to large and short-crack testing, thresholds were determined using a 'growth/no growth' criterion. Specifically, if no growth, defined as a total of  $20 \mu\text{m}$  per  $2 \times 10^6$  cycles on both ends of the surface crack was observed, the maximum load (and in proportion the minimum load) was increased by 111 N and the procedure repeated.

Linear-elastic solutions for the stress intensities associated with the small, semi-elliptical surface cracks under mixed-mode loading were taken from two sources. On the basis that the crack plane was normal to the specimen surface, the mode I component of the stress

intensity,  $K_I$ , was computed from the well-known Newman–Raju solution [36]:

$$K_I = (\sigma_t + H\sigma_b) \sqrt{\pi \frac{a}{Q}} F\left(\frac{a}{t}, \frac{a}{c}, \frac{c}{b}, \theta\right)$$

where  $\sigma_t$  is the remote uniform-tension stress and  $\sigma_b$  is the remote uniform outer-fiber bending stress. The geometrical factors  $H$ ,  $Q$  and  $F$  are evaluated from the crack depth,  $a$ , the crack half-length,  $c$ , the specimen thickness,  $t$ , the specimen half-width,  $b$ , and the angular position along the crack front,  $\theta$ , as described in detail in [36].

The mode II component,  $K_{II}$ , conversely, was computed from the newly derived He-Hutchinson solution [37] for elliptical surface cracks under mixed-mode loading:

$$K_{II} = \chi \sigma_{12} \sqrt{\pi a}$$

where  $\chi$  is a numerical factor determined using ref. [37],  $\sigma_{12}$  is the shear component of the loading (see Fig. 5) and  $a$  is the crack depth. It should be noted here that a three-dimensional corner singularity exists in the solution at the point where the crack intersects the free surface; however, for the purpose of this study, this is ignored since errors caused by such an assumption are negligible. Moreover, as one moves along the crack front to the interior, the magnitude of the mode II contribution decreases, with that of mode III increasing till the point of deepest penetration of the crack is reached.

The applied load/stress on the inclined crack (Fig. 5) was resolved trigonometrically into tensile and shear components. The tensile component was used for determining  $\Delta K_I$ , using [36], and the shear component for  $\Delta K_{II}$  and  $\Delta K_{III}$ , using [37]. As the exact shape of such small surface cracks and the variation in the aspect ratio with crack extension clearly can have an important effect on the crack driving force and hence the crack-growth behavior [38,39], crack shapes (Fig. 5), in the form of the depth to surface length ratio,  $a/2c$ , were determined by breaking open the sample after testing; typical aspect ratios were in the range of  $a/2c \sim 0.45$ .

The use of linear-elastic stress-intensity solutions for characterizing the driving forces for the small cracks is justified on the basis of the small cyclic plastic-zones sizes in relation to crack size. For example, for the smallest crack sizes of  $\sim 1 \mu\text{m}$ , where the  $\Delta K_I$  thresholds are  $\sim 1 \text{ MPa}\sqrt{\text{m}}$ , plastic-zone size (estimated as  $r_y \sim 1/2\pi (\Delta K_I/\sigma_y)^2$  where  $\sigma_y$  is the yield strength) are on the order of 100 nm. As this is roughly one tenth of the crack size, it is deemed reasonable to conclude that small-scale yielding conditions prevail.

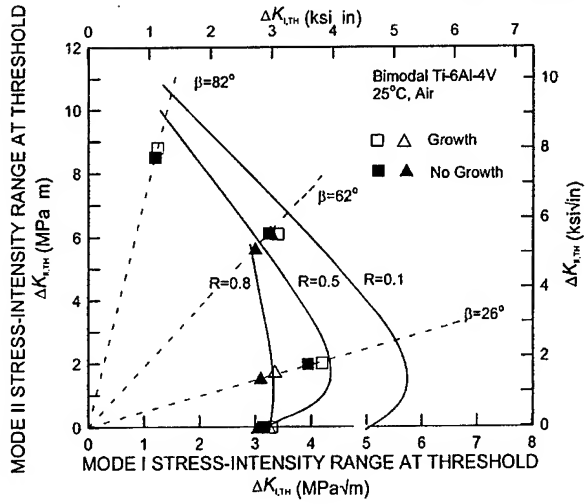


Fig. 6. Mixed-mode threshold envelopes for the bimodal microstructure. Note the deterioration of mixed-mode fatigue resistance with increasing load ratio.

## 4. Results and Discussion

### 4.1. Large-crack behavior

#### 4.1.1. Effect of load ratio and mode-mixity

Results indicating the large-crack threshold behavior under mode I+II loading are shown in Fig. 6 in the form of mixed-mode threshold envelopes, where the mode II threshold stress-intensity range,  $\Delta K_{II,TH}$ , is plotted as a function of the corresponding mode I threshold stress-intensity range,  $\Delta K_{I,TH}$ . The threshold envelope is shown along with the corresponding bounding 'growth' (open symbols) and 'no growth' (closed symbols) conditions for load ratios of 0.1, 0.5 and 0.8 at mode-mixities ranging from pure mode I, i.e.,  $\Delta K_{II}/\Delta K_I = 0$  (phase angle,  $\beta = 0^\circ$ ), to nearly pure mode II, i.e.,  $\Delta K_{II}/\Delta K_I \sim 7.1$  ( $\beta = 82^\circ$ ). Similar to behavior in other materials [13,14], a clear reduction in mode I  $\Delta K_{I,TH}$  threshold values is evident with increasing load ratio. Moreover, the value of  $\Delta K_{I,TH}$  can also be seen to generally decrease with increasing phase angle (except for a slight increase at low phase angles between 0 and  $26^\circ$ , which has been attributed to an effect of mode I/mode II crack-tip shielding [22]).

#### 4.1.2. Single parameter characterization

Although the mode I threshold,  $\Delta K_{I,TH}$ , clearly decreases with increasing mode-mixity, if a more appropriate measure of the mixed-mode driving force is used, specifically the range in strain-energy release rate,  $\Delta G = (\Delta K_I^2 + \Delta K_{II}^2)/E'$ , where  $E' = E$  (Young's modulus) in plane stress and  $E/(1-\nu^2)$  in plane strain ( $\nu$

is Poisson's ratio),<sup>3</sup> then there is a progressive increase in the mixed-mode threshold,  $\Delta G_{TH}$ , with increasing mode-mixity at all load ratios studied (Fig. 7).<sup>4</sup> This marked effect of increasing mode-mixity is such that the  $\Delta G_{TH}$  threshold at  $\beta = 82^\circ$  is some 4–5 times larger than the mode I value ( $\beta = 0^\circ$ ) at  $R = 0.1$ . From the perspective of thresholds for high-cycle fatigue, this implies that in terms of mixed-mode loading, the mode I threshold, defined in terms of  $\Delta G$ , represents a *worst-case* condition; similar observations have been made in other material systems [40,41]. Consequently, the presence of mixed-mode conditions does not preclude the use of a threshold-based design methodology for high-cycle fatigue.

An alternative means of calculating the mixed-mode threshold, which accounts for the deflection of the crack once propagation ensues, is described in Appendix B. This leads to a small change, generally a reduction, in the value of  $\Delta G_{TH}$ .

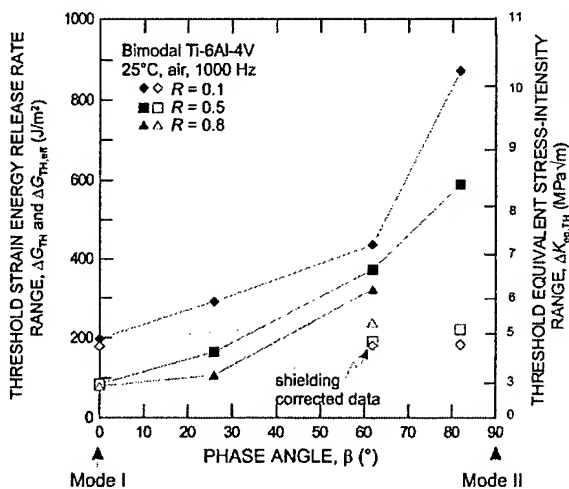
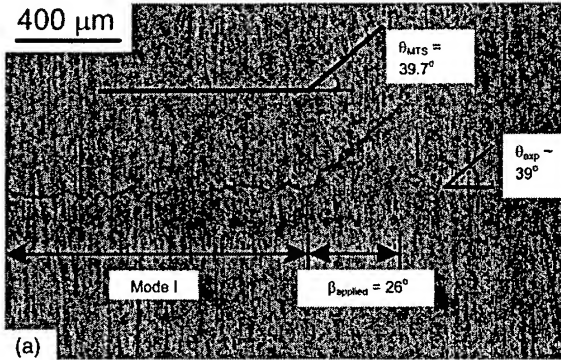


Fig. 7. The threshold strain-energy release rate,  $\Delta G_{TH}$  is given as a function of phase angle,  $\beta$  for large through-thickness cracks. Equivalent stress-intensity factor ranges at threshold,  $\Delta K_{eq,TH}$  are also shown. The mode I threshold clearly represents a *worst-case* condition. Correction for shielding using the recently developed compliance based technique is also shown. Note the relative absence of any effect of mode-mixity and/or load ratio on the shielding-corrected thresholds (after [22]).

<sup>3</sup> Note that with the definition used,  $\Delta$  does not necessarily equal  $G_{max} - G_{min}$  where  $G_{max}$  and  $G_{min}$  are determined from the maximum and minimum loads of the fatigue cycle. Alternatively, mixed-mode crack-growth and threshold data can be represented in terms of an equivalent stress-intensity range, given by  $\Delta K_{eq,TH} = (\Delta G_{TH} E')^{1/2}$ .

<sup>4</sup> Threshold values plotted in Fig. 7 represent the average of the 'growth' and 'no growth' conditions from Fig. 6.



(a) Crack Growth Direction

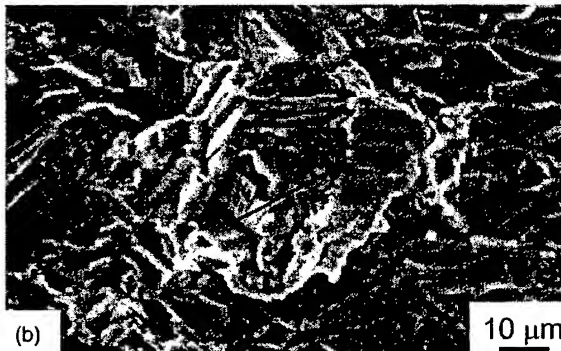


Fig. 8. (a) Fatigue crack profiles are compared for the bimodal ( $R = 0.8$ ,  $\beta = 26^\circ$ ) microstructure. Optical micrographs show both the mode I fatigue pre-crack and the region of deflected crack growth following the application of cyclic mixed-mode loading. Measured crack deflection angles,  $\theta_{exp}$ , are compared with those predicted by the path of maximum tangential stress,  $\theta_{MTS}$ , and (b) Corresponding fractography of the near-tip crack wake showing evidence of fracture surface abrasion (indicated by arrow), presumably due to shear-induced fracture surface contact (from [22]). The  $\Delta G$  levels involved were  $\sim 85$  J/m<sup>2</sup>.

#### 4.1.3. Crack path and fractographic observations

A typical crack path for through-thickness large cracks is illustrated in Fig. 8(a). This profile shows the mode I fatigue pre-crack (at  $R = 0.1$ ) and the crack path following the application of mixed-mode loading conditions at  $R = 0.8$  with  $\beta = 26^\circ$  ( $\Delta K_{II}/\Delta K_I = 0.5$ ). It is apparent that unlike behavior in a coarser lamellar microstructure in this alloy [42], the crack path in the finer-scale bimodal condition is not markedly influenced by microstructure. Specifically, the crack plane (for both mode I and mixed-mode loading) is relatively planar with a degree of tortuosity only on the order of the characteristic microstructural size-scales ( $\sim 20$   $\mu$ m).

Crack paths result from the mutual interaction of the maximum crack-driving force and the weakest microstructural path. In a fine-scale, homogeneous structure such as the bimodal Ti-6Al-4V where the microstructural considerations are of secondary importance, the path of a growing fatigue crack will change primarily in

response to a change in the applied phase angle, the most likely criterion for the crack trajectory being that a purely mode I condition at the crack tip, such that the crack will follow a path dictated by the maximum tangential stress,  $K_{II} = 0$ , or maximum  $G$  [15,42–44]. Except for small differences at very high phase angles, these criteria yield essentially the same crack-path predictions.

In Fig. 8(a), it can be seen that after the application of the mixed-mode loading, the crack proceeds along a direction that is virtually identical to that dictated by a criterion of maximum tangential stress (MTS) [15,43,44]; i.e., it propagates in mode I. More detailed discussion of the effect of mode-mixity on crack path can be found in [21,44].

Fractographically, fatigue fracture surfaces were similar for crack growth under pure mode I and mixed-mode loading. However, there was one distinct difference in that there was evidence of abrasion on the fracture surfaces for growth under mixed-mode loading [Fig. 8(b)]. This is to be expected due to the relative shear displacements of the crack surfaces under mixed-mode loads; moreover, such evidence is an indication of the occurrence of crack-surface interference during mixed-mode crack growth.

#### 4.1.4. Shielding-correction for large-crack thresholds

It is well established that under mixed-mode loading, there is a potential for such interference between the sliding crack surfaces (e.g., [22,45,46]); indeed, the friction and rubbing between the surfaces represents a potent form of crack-tip shielding [45–50], akin to crack closure in mode I (e.g., [51,52]). As discussed in detail elsewhere [21,22], the increase in the large-crack, mixed-mode  $\Delta G_{TH}$  threshold with increasing mode-mixity in this microstructure (shown in Fig. 7) can be related to an increased role in such mode I and mode II shielding, associated, respectively, with crack closure and sliding crack interference from the friction and interlock of crack-surface asperities. Indeed, the magnitude of such shielding can be quantified using compliance-based techniques [22]. This was performed using both mode I opening and mode II side-mounted crack-tip displacement gauges to measure the effective (near-tip) stress intensities in modes I and II. In this manner, the  $\Delta G_{TH}$  threshold data were ‘corrected’ for the presence of shielding by characterizing the driving force in terms of a mixed-mode, effective threshold strain-energy release rate,  $\Delta G_{TH,eff}$ . Results are illustrated in Fig. 7 [22]. It is apparent that once the effect of closure and crack-surface interference are removed, the effects of mode-mixity and load ratio on the fatigue threshold are both greatly reduced. Moreover, ‘correcting’ the driving force for mixed-mode shielding can reduce the value of the large-crack  $\Delta G_{TH}$  thresholds by up to almost an order of magnitude; specifically, whereas the  $\Delta G_{TH}$  threshold in near-

mode II ( $\beta = 82^\circ$ ) is some seven times its value in mode I, the corresponding difference in  $\Delta G_{TH,eff}$  thresholds is less than a factor of 3.

These results strongly imply that the primary effect of increasing mode-mixity in increasing the value of the large-crack, mixed-mode  $\Delta G_{TH}$  threshold can be attributed to an enhanced role of crack-tip shielding in modes I and II, which acts to diminish the effective driving force for crack growth. This is analogous to the well-known effect of decreasing load ratio in increasing the mode I threshold, which has similarly been largely attributed to (mode I) shielding (by crack closure) (e.g., [31,51]). These results also strongly suggest that short fatigue cracks will only show a minimal sensitivity to mode-mixity, as their limited wake acts to restrict such shielding; this question is discussed in detail below.

#### 4.2. Short-crack behavior

Similar studies were performed on short cracks, approximately 200  $\mu\text{m}$  in length, where the crack wake had been largely removed. Although such cracks still have dimensions that are large compared to microstructural size-scales (the crack front ‘samples’ several hundred grains), the limited wake acts to suppress the effect of any crack-tip shielding (e.g. [23,25]). Measured mixed-mode thresholds for such short cracks, expressed in terms of both  $\Delta G_{TH}$  and  $\Delta K_{eq,TH}$ , are plotted in Fig. 9 as a function of the phase angle for load ratios of 0.1–0.8; results are compared with the corresponding thresholds for large cracks.

As alluded to above, the restricted role of wake shielding has a significant effect on the mixed-mode  $\Delta G_{TH}$  thresholds for the short cracks. Specifically, short-crack thresholds can be seen to be:

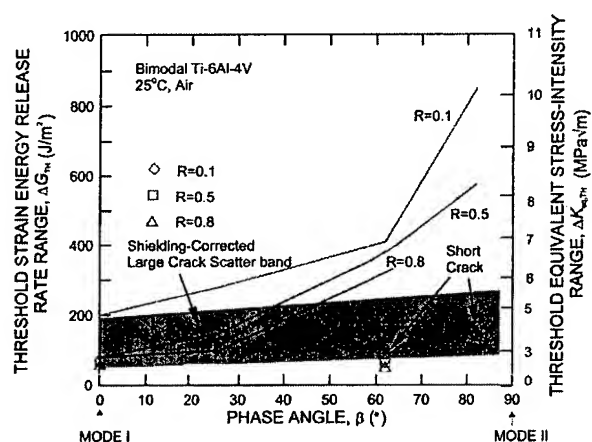


Fig. 9. Variation in mixed-mode thresholds,  $\Delta G_{TH}$ , as a function of phase angle,  $\beta$ , in the bimodal structure. Shown are results at three load ratios for large ( $> 4$  mm) cracks, before and after ‘correcting’ for crack-tip shielding, and for short ( $\sim 200$   $\mu\text{m}$ ) through-thickness cracks.

- far smaller than large-crack values,
- relatively insensitive to mode-mixity,
- essentially insensitive to load ratio,
- comparable in magnitude to the shielding-corrected large-crack values.

Of particular note is that the substantial increase in the large-crack  $\Delta G_{TH}$  thresholds at high mode-mixities ( $\beta = 62^\circ, 82^\circ$ ) is nearly eliminated for short cracks. These results clearly highlight the critical effect of crack size on mixed-mode fatigue-crack propagation behavior, in that when crack-tip shielding is accounted for, either by correcting the 'driving force' or limiting its magnitude by wake removal, the effect of mode-mixity on the  $\Delta G_{TH}$  threshold behavior becomes relatively insignificant.

A typical crack profile ( $R = 0.1, \beta = 26^\circ$ ) and fractography ( $R = 0.1, \beta = 62^\circ, \Delta G \sim 72 \text{ J/m}^2$ ) are included in Fig. 10; the crack deflection angles agree very well with the MTS predictions. Identical to the large-crack results (Fig. 7), the extent of microstructurally-induced

crack-path tortuosity was relatively minor, i.e. in the order of tens of micrometers, and the crack nominally followed a mode I path, as dictated by the MTS criterion following the application of the mixed-mode loading.

It is worth noting that the (through-thickness) short cracks investigated here had crack lengths roughly an order of magnitude larger than the average grain size, and widths over two order of magnitude larger; consequently, their crack fronts were presumed to 'sample' the microstructure adequately, akin to the large, through-thickness cracks discussed above. Such 'continuum sampling' would not be expected for cracks of true microstructural dimensions. Accordingly, we now examine the

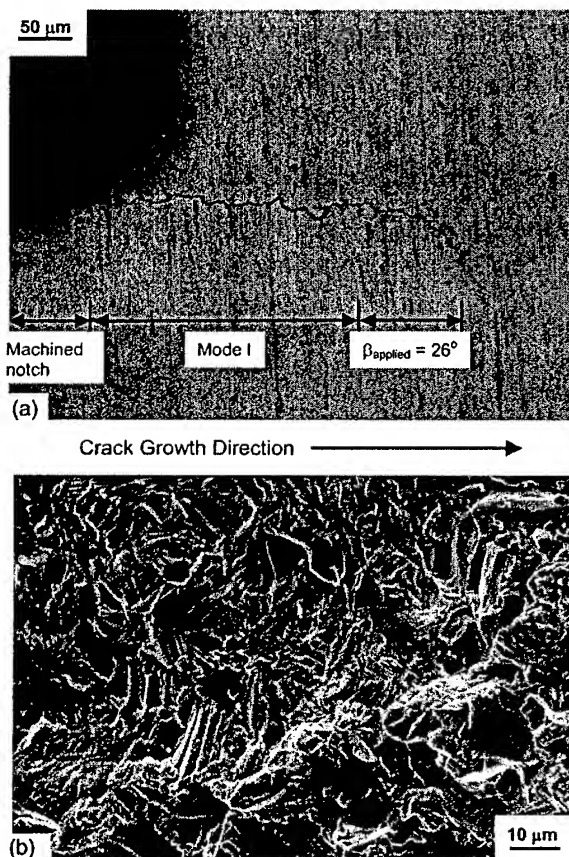


Fig. 10. (a) A typical crack profile ( $R = 0.1, \beta = 26^\circ$ ) obtained for through-thickness short ( $\sim 200 \mu\text{m}$ ) crack mixed-mode thresholds. (b) Near-tip mixed-mode fractography for specimen tested under  $R = 0.1, \beta = 62^\circ$  ( $\Delta G \sim 72 \text{ J/m}^2$ ).

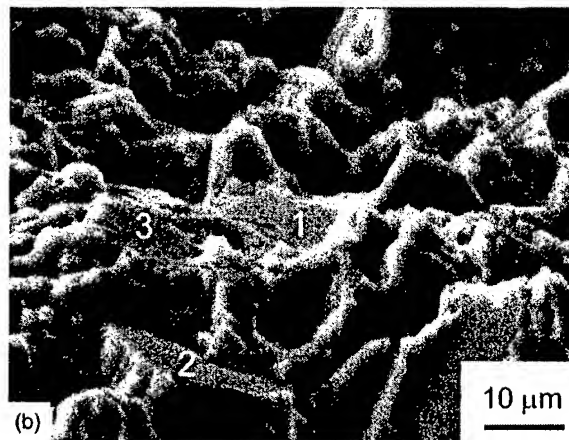
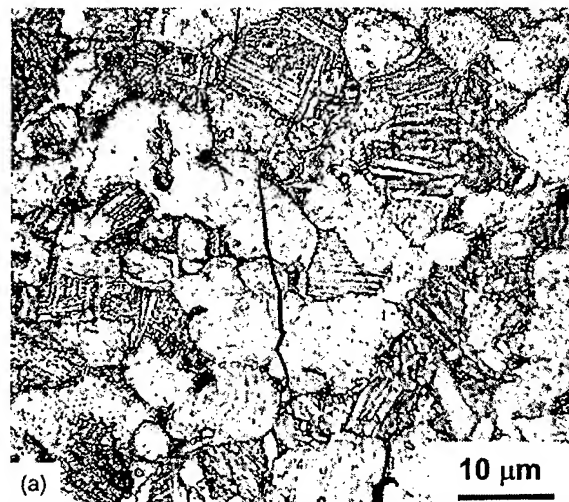


Fig. 11. (a) A typical fatigue-crack initiation site is illustrated for the bimodal microstructure in this optical photomicrograph. Note that initiation predominantly occurs in the primary- $\alpha$  grains, and (b) SEM image of crack initiation and early growth along planar slip bands leading to facet type fracture surface (specimen tilt:  $70^\circ$ ). EBSD analysis of fractured  $\alpha$  grains 1–3 revealed near-basal orientation of the fracture plane. [Fig. 11(b): Courtesy of Dr J.O. Peters].



mixed-mode threshold behavior of small, semi-elliptical surface cracks, where all dimensions are comparable with microstructural size-scales.

#### 4.3. Microstructurally-small crack behavior

##### 4.3.1. Small crack initiation and crack shape considerations

In the present study, small surface precracks were initiated naturally on wide three-point bend specimens. Cracks were found to initiate preferentially within the primary- $\alpha$  grains (Fig. 11(a)). These tend to act as the preferred initiation sites as the longest slip bands can form there, rather than in the secondary- $\alpha$  grains within the transformed  $\beta$ -matrix [53], and furthermore, many of the initiating primary- $\alpha$  grains are aligned with near-basal orientation perpendicular to the stress axis, as has been shown for this microstructure [54] using electron back scattered diffraction (EBSD) analysis (Fig. 11(b)). The shape of these small cracks, which is known to have a profound effect on their behavior [36,38,39], was assessed from observations of the subsequent fracture surfaces; this shape was taken to be semi-elliptical, with  $a/2c \sim 0.45$ , and was assumed to remain constant with crack extension.

##### 4.3.2. Small-crack thresholds

The variation in  $\Delta G_{TH}$  thresholds with increasing mode-mixity for such small flaws is shown in Fig. 12, and compared with corresponding *worst case* data for both large and short fatigue cracks (Table 2). One such flaw, cycled at a phase angle of  $\beta = 28^\circ$ , is shown in Fig. 13, together with the corresponding fracture surface associated with mixed-mode fatigue-crack growth under mixed-mode loading. Crack paths are normally the result

of the interaction between the optimum crack-driving force and the nature of the local microstructure. Whereas for large and short cracks, the former was the dominant factor, it should be noted that the path followed by the small cracks was more strongly influenced by local microstructure.

The data shown in Fig. 12, which are believed to be the first reported results on mixed-mode fatigue thresholds for microstructurally-small cracks, were again determined from the average of the 'growth/no growth' conditions. In general, it can be seen that small-crack  $\Delta G_{TH}$  thresholds vary little with mode-mixity; moreover, their values were lower than those obtained for short through-thickness cracks, and substantially lower than those for large through-thickness cracks. In terms of stress intensities, mixed-mode small crack  $\Delta K_{eq,TH}$  thresholds are generally on the order of 1–2 MPa $\sqrt{m}$ , compared to large-crack values between 3 and 10 MPa $\sqrt{m}$ . Indeed, mixed-mode small-crack growth can be seen at driving forces below the established *worst case* large-crack threshold [8], and even below the 'shielding-corrected' large crack results. This is consistent with previous observations made on small surface cracks in this microstructure under pure mode I conditions, where  $\Delta G_{TH}$  thresholds were found to be as low as 9.5 J/m<sup>2</sup> [54]. The origin of this effect is believed to be two-fold, as discussed below:

**Crack-tip shielding:** As discussed above for short cracks, the highly restricted wake of the small cracks acts to severely limit any crack-tip shielding by crack closure and more importantly crack surface interference. Since the small crack  $\Delta G_{TH}$  thresholds are comparable with the 'shielding-corrected' large crack values, it is reasonable to conclude that the limited effect of wake shielding accounts for the absence of an effect of mode-mixity on the small crack thresholds, and for their very small magnitude compared to corresponding (uncorrected) large-crack results. Similar behavior has been reported for pure mode I tests conducted previously in this bimodal Ti-6Al-4V [55]. However, of note here is the fact that the small crack thresholds are actually somewhat lower than the short crack and shielding-corrected large crack results, indicating that other factors are involved. One such factor involving microstructural sampling, is discussed below.

**Microstructural sampling:** As seen in Fig. 12, the correction for crack-tip shielding for microstructurally-small cracks does reduce the substantial difference between large and small crack thresholds; however, a significant discrepancy remains even after such corrections. This is believed to be the result of biased sampling of microstructural barriers by the crack front and local arrest at such barriers. Indeed, the ratio of crack size (or depth) to the average grain (microstructural unit) size will decide the exact microstructural environment that the crack-front interrogates. In the initial stages of

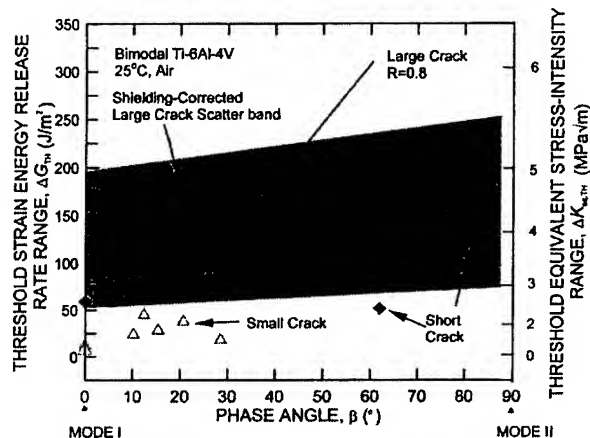


Fig. 12. Variation in mixed-mode thresholds,  $\Delta G_{TH}$ , as a function of phase angle,  $\beta$ , for small ( $< 50 \mu\text{m}$ ) surface cracks in the bimodal microstructure. Shown for comparison are results for short ( $\sim 200 \mu\text{m}$ ) through-thickness cracks and for large ( $> 4 \text{ mm}$ ) through-thickness cracks under *worst-case*, high  $R$  conditions.

Table 2

Approximate thresholds obtained for large, short and small fatigue cracks in Ti-6Al-4V

Mode mixity	$\Delta G_{TH}(J/m^2)$			$\Delta K_{eq,TH}(MPa\sqrt{m})$		
	$R=0.1$	$R=0.5$	$R=0.8$	$R=0.1$	$R=0.5$	$R=0.8$
Large cracks						
0	200	80	80	4.9	3.1	3.1
26	280	150	100	5.8	4.3	3.5
62	410	375	320	7.0	6.7	6.2
82	850	575	-	10.1	8.3	-
Short cracks						
0	72	66	59	2.9	2.8	2.7
26	125	105	85	3.9	3.6	3.2
62	72	64	52	2.9	2.8	2.5
82	148	140	130	4.2	4.1	4.0
Small cracks						
0	10	-	-	1.1	-	-
0	18	-	-	1.5	-	-
10.5	25	-	-	1.8	-	-
12.5	45	-	-	2.3	-	-
15.5	27	-	-	1.8	-	-
21	38	-	-	2.1	-	-
28	20	-	-	1.6	-	-

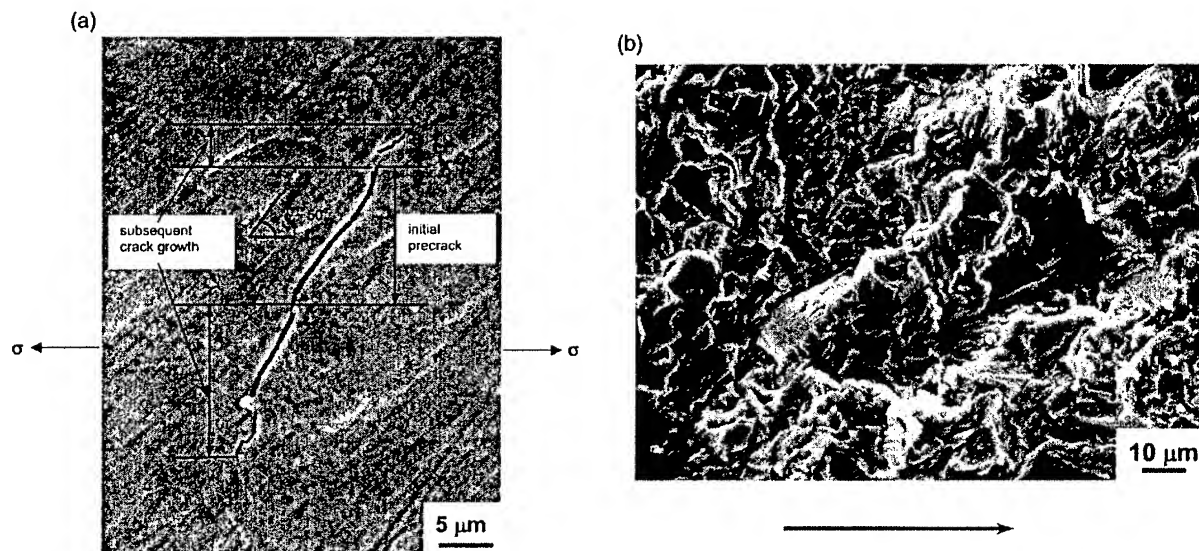


Fig. 13. (a) A typical crack path taken by a microstructurally-small crack under mixed-mode loading ( $R = 0.1$ ,  $\beta \sim 28^\circ$ ,  $\Delta G \sim 20 J/m^2$ , angle of inclination  $\phi \sim 50^\circ$ ) is shown. The precrack was initiated under pure mode I; subsequent growth was under mixed-mode conditions. As is evident, there is a strong influence of local crack-tip microstructure on the crack path. (b) A typical fractograph for mixed-mode small crack growth ( $R = 0.1$ ,  $\beta = 28^\circ$ ,  $\Delta G \sim 20 J/m^2$ ). The arrow indicates the nominal direction of crack propagation.

growth, if the crack is small enough to be contained within a single grain, then the conditions experienced by the crack front are nominally similar to those experienced for growth within a single crystal, resulting in much higher growth rates (e.g. [56]). As the crack extends beyond the grain, the crack front samples more grains, with an increased probability of encountering unfavorably oriented features. However, a crack front with a length on the order of a few grain sizes does not

always sample enough disadvantageously-oriented grains to average out such effects. It has been suggested that this transition from microstructure-sensitive growth (seen for microstructurally-small cracks) to microstructure-insensitive growth (seen for large and short cracks) occurs when the crack size is roughly ten times the average grain size [57]. Since the small cracks investigated here were well below this limit ( $\sim 200 \mu m$ ), the measured crack propagation rates, and fatigue thresholds, were



expected to be affected by microstructure, as was observed (Figs. 12–13). This is considered to be the prime reason for the lower  $\Delta G_{TH}$  thresholds measured for such crack sizes.

## 5. Concluding Remarks

In terms of the computed cyclic plastic-zone size in relation to crack size, all cracks examined in this study can be considered to be linear elastic. Despite this, results clearly indicate a very significant effect of crack size on the mixed-mode fatigue thresholds, as summarized for the bimodal Ti–6Al–4V microstructure structure in Figs. 7, 9 and 12. Specifically, at a load ratio of 0.1, large-crack  $\Delta G_{TH}$  mixed-mode thresholds at a near mode II mixity of  $\Delta K_{II}/\Delta K_I \sim 7$  are some 70–90 times larger than measured short- and small-crack thresholds. Analogous to mode I behavior, this effect can be related to a restricted role of crack-tip shielding for the cracks with a limited wake and, where crack sizes approach microstructural dimensions, to biased sampling of the ‘weak-links’ in the microstructure by the small flaws. However, unlike mode I, the role of the crack-tip shielding, by mode I crack closure and more importantly mode II crack-surface interference, appears to be far more significant. For this reason, the difference in mixed-mode threshold values for cracks large and small compared to microstructural dimensions is far larger than is evident under pure mode I loading [54].

What is also apparent is that where crack sizes remain large with respect to microstructural dimensions, even though the loading is mixed-mode, the crack tends to follow a mode I ( $K_{II} = 0$ ) path, an observation consistent with the fact that the measured  $\Delta G_{TH}$  threshold is worst-case for pure mode I loading. Accordingly, from the perspective of design and ‘lifing’ methodologies for high-cycle fatigue, mode I  $\Delta G_{TH}$  or  $\Delta K_{TH}$  thresholds, (i) measured under extremely high load ratios [31], (ii) corrected for crack-tip shielding [21,22], or (iii) determined for short cracks (all procedures that minimize the effect of ‘shielding’), can be used as a lower-bound for fatigue loading over the complete range of mode-mixities. However, where crack sizes approach microstructural dimensions, it is clear that they are not ‘sampling’ the continuum microstructure; as a consequence, continuum analyses such as deterministic fracture mechanics are only of limited utility and probabilistic methods need to be employed.

## 6. Conclusions

Mixed-mode (mode I+II) fatigue-crack growth thresholds for large ( $> 4$  mm) and short ( $\sim 200$   $\mu$ m) through-thickness cracks and microstructurally-small ( $< 50$   $\mu$ m)

surface cracks have been examined in a fine-grained bimodal (STOA) microstructure (average grain size  $\sim 20$   $\mu$ m) of a Ti–6Al–4V turbine engine alloy over a range of load ratios from 0.1 to 0.8 and a range of mode-mixities from pure mode I, i.e.  $\Delta K_{II}/\Delta K_I = 0$  (phase angle,  $\beta = 0^\circ$ ), to nearly pure mode II, i.e.,  $\Delta K_{II}/\Delta K_I \sim 7.1$  ( $\beta = 82^\circ$ ). Based on this work, the following observations can be made:

1. Fatigue thresholds for through-thickness cracks, large ( $> 4$  mm) compared to microstructural dimensions, were found to be strongly influenced by load ratio and mode-mixity when measured under mixed-mode loading conditions.
2. Using the range of strain energy release rate,  $\Delta G$ , incorporating both mode I and mode II contributions, as a single-parameter characterization of the crack-driving force,  $\Delta G_{TH}$  thresholds values measured under pure mode I loading were found to be *worst case* for the range of mode-mixities studied. This was consistent with the fact that under mixed-mode loading, the initial extension of all cracks followed a mode I, i.e. a  $K_{II} = 0$ , path.
3. By experimentally measuring the magnitude of the crack-tip shielding, in the form of mode I crack closure and mode II crack-surface interference (by asperity rubbing and interlock), in order to estimate the effective (near-tip) mixed-mode driving force,  $\Delta G_{eff}$ , ‘shielding-corrected’ mixed-mode thresholds were determined. Due to the significant influence of shielding under mixed-mode conditions, such  $\Delta G_{TH,eff}$  threshold values were considerably lower than the ‘uncorrected’  $\Delta G_{TH}$  values, and showed minimal sensitivity to either load ratio and mode-mixity.
4. These observations strongly imply that for cracks large compared to microstructural dimensions, fatigue cracking under mixed-mode loading is predominately a mode I phenomenon. The significant influence of mode-mixity (and load ratio) on measured mixed-mode thresholds can be attributed primarily to crack-tip shielding, in particular from crack-surface interference.
5. This is consistent with observations of the corresponding mixed-mode  $\Delta G_{TH}$  thresholds for short ( $\sim 200$   $\mu$ m) through-thickness cracks, obtained by machining off the wake of large cracks. The magnitude of such short-crack thresholds was significantly lower than those measured for large cracks, and was found to be comparable with the crack-tip shielding-corrected large-crack thresholds. Moreover, they were essentially independent of mode-mixity and load ratio, again suggesting a predominant role of shielding on mixed-mode fatigue threshold behavior.
6. Corresponding mixed-mode fatigue threshold results for microstructurally-small ( $< 50$   $\mu$ m) surface cracks indicated that this marked reduction in  $\Delta G_{TH}$  thresh-

olds with diminishing crack dimensions may be even greater when crack sizes approach the scale of microstructure. This was rationalized in terms of the 'biased' sampling the microstructure by such small flaws, in addition to a reduced contribution of crack-tip shielding from their limited crack wake.

## Acknowledgements

This work was supported by the US Air Force Office of Scientific Research under Grant No. F49620-96-1-0478 under the auspices of the Multidisciplinary University Research Initiative on High Cycle Fatigue to the University of California at Berkeley. Special thanks are due to Drs B.L. Boyce, I. Altenberger, J.O. Peters and A.W. Thompson for helpful discussions.

## Appendix A

### Distinction between large, short and small cracks

For the sake of clarity, the salient differences between large, short and small cracks are summarized. Large fatigue cracks [Fig. 14(a)] have fracture surface dimensions that are large compared to the scale of the microstructure in both directions. They therefore generally have a fully developed<sup>5</sup> crack-tip shielding zone and can 'sample' the microstructure in a statistical (continuum) manner [23]. With respect to large cracks, small cracks are generally described as being comparable in size to [24]:

- microstructural dimensions, where biased statistical sampling of the microstructure can lead to accelerated crack advance along 'weak' paths, i.e., microstructural features oriented for easy crack growth (a continuum limitation),
- the extent of local inelasticity ahead of the crack tip, where the assumption of small-scale yielding implicit in the use of the stress intensity,  $K$ , is not strictly valid (a linear-elastic fracture mechanics limitation),
- the extent of crack-tip shielding (e.g., crack closure) behind the crack tip, where the reduced role of shielding leads to a higher local driving force than the corre-

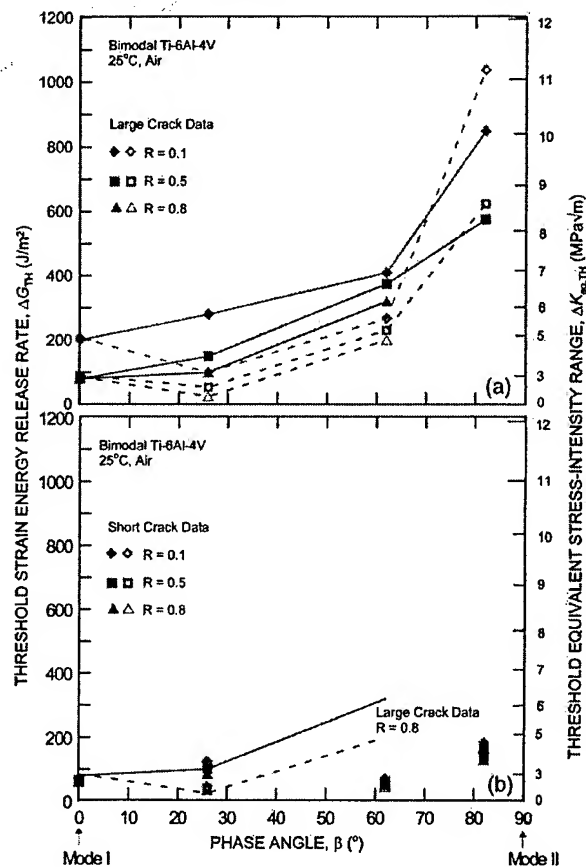


Fig. 14. (a) Mixed mode thresholds for (a) large cracks and (b) short cracks, calculated using the single-parameter characterization [21-22] (solid lines, solid data points) and using the kink-based calculations (dotted lines, hollow data points).

sponding large crack at the same applied  $K$  level (a similitude limitation).

However, a further distinction can be made between short and small cracks (Fig. 14). This distinction alludes not simply to physical size but the extent to which a fatigue crack is subjected to the first and third factors listed above. Short fatigue cracks (Fig. 14(b)) are physically short in only one dimension, a condition that is often realized experimentally by machining away the wake of a large crack. This type of fatigue flaw experiences limited crack-tip shielding due to its reduced length [25], yet still samples the microstructure as a continuum because of its extensive crack front. In contrast, small fatigue cracks (Fig. 14(c)) are small and comparable to the microstructural size scale in all dimensions, as typified by the small, semi-elliptical surface flaw (e.g. [24]). With such cracks, crack-tip shielding is significantly reduced (e.g. [23]), and since the crack front samples only few microstructural entities, this allows for a biased sampling of microstructurally weak paths.

<sup>5</sup> For mixed-mode loading conditions, the shearing of the fracture surfaces with respect to one another can produce crack-wake contact via sliding interference over dimensions which are much larger than for mode I loading, perhaps over the entire wake of a large fatigue crack (e.g. [45-47]). Thus, the notion of a 'fully developed' shielding zone is somewhat unclear for mixed-mode loading conditions. At the least, one would expect the equilibrium shielding-zone length to be a function of the applied ratio of shear to tension.

Because of this restriction in shielding and the biased microstructural sampling, fatigue-crack growth resistance in the presence of small cracks tends to be lowest.

## Appendix B

### Calculation of the mixed-mode threshold

In this work, as in prior studies (e.g., [16-18,21,22,42]) on mixed-mode fatigue thresholds, the threshold values of the mode I and mode II stress intensities required to initiate cracking,  $\Delta K_{I,TH}$  and  $\Delta K_{II,TH}$ , are calculated based on the mode I precrack (which is generated in near-identical fashion for each test); the corresponding mixed-mode threshold,  $\Delta G_{th}$ , or equivalent stress intensity,  $\Delta K_{eq,TH}$ , are then computed from:

$$\Delta G_{TH} = (\Delta K_{I,TH}^2 + \Delta K_{II,TH}^2) / E' \quad (B1)$$

$$\equiv (\Delta K_{eq,TH}^2) / E',$$

where  $E'$  is the appropriate elastic modulus.

However, once the crack starts to grow, it deflects along a different path (generally corresponding to a local  $K_{II} = 0$  criterion modified by the effect of the microstructure). Consequently, an alternative calculation of the threshold can be based on the presence of an infinitesimal kink along this direction. Assuming for simplicity that the kink (of length  $b \ll a$ , the crack length) represents an in-plane tilt through angle  $\alpha$  to the precrack plane (Fig. 15), then the local mode I and mode II stress intensities,  $\Delta k_1$  and  $\Delta k_2$ , at the deflected crack tip will be given by [58,59]:

$$\Delta k_1(\alpha) = c_{11}\Delta K_I + c_{12}\Delta K_{II} \quad (B2)$$

$$\Delta k_2(\alpha) = c_{21}\Delta K_I + c_{22}\Delta K_{II}.$$

where  $\Delta K_I$  and  $\Delta K_{II}$  are the stress intensities for a main (pre)crack, and the coefficients  $c_{ij}$ , which are a sole function of  $\alpha$ , are given in [58,59]. The mixed-mode thresholds,  $\Delta G'_{TH}$  and  $\Delta K'_{eq,TH}$ , can then computed from:

$$\Delta G'_{TH} = (\Delta k_1^2 + \Delta k_2^2) / E' \quad (B3)$$

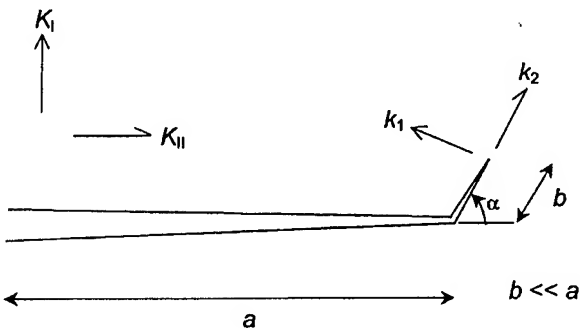


Fig. 15. Schematic illustration of the kinked crack configuration for the alternative calculation of the mixed-mode threshold.

$$+ \Delta k_2^2) / E' \equiv (\Delta K'_{eq,TH})^2 / E'.$$

For the present results, the use of (B3) can either increase or decrease the mixed-mode threshold, as shown for both large and short cracks in Fig. 16. In general though, the trend is to reduce the computed values of  $\Delta K_{eq,TH}$  somewhat, except at very high phase angles. At  $\beta = 26^\circ$ , however, the large crack  $\Delta K_{eq,TH}$  threshold is reduced by as much as 40%; for the bimodal Ti-6Al-4V, this translates into a reduction in threshold  $\Delta K_{eq,TH}$  values by between 1 and 2 MPa $\sqrt{m}$ . Effects are far less significant for the short cracks.

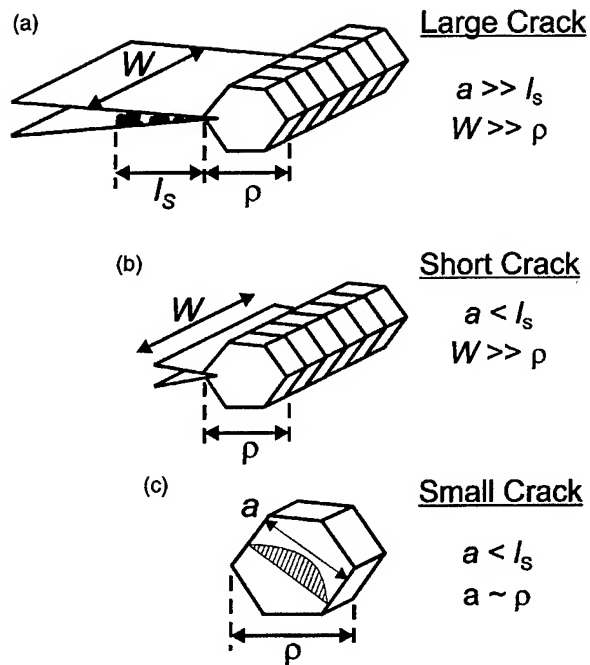


Fig. 16. Schematic illustrations highlighting the key distinctions between large, short and small fatigue cracks. Large cracks (a) have length,  $a$ , and width,  $W$ , which are large both with respect to the equilibrium shielding-zone length,  $l_s$  (indicated here as a region of debris in the crack wake which produces crack closure), and the characteristic microstructural size scale,  $r$ , e.g., the grain size. In contrast to this, short fatigue cracks (b) are characterized by  $a < l_s$ , but  $W \gg \rho$ . The reduced crack-wake length results in a lower level of crack-tip shielding. For small cracks (c), the fracture surface is reduced in both dimensions, with  $a$  (and  $W$ ) being small with respect to both  $l_s$  and  $r$ . The fact that  $a \sim \rho$  implies that the crack front samples only a few microstructural entities, leading to a biased sampling of the microstructure.

## References

- [1] Report of the AdHoc Committee on Air Force Aircraft Jet Engine Manufacturing and Production Processes, United States Air Force Scientific Advisory Board, SAF/AQSS: the Pentagon, Washington, DC, 1992.
- [2] Chang JCI. An integrated research approach to attack engine HCF problems. Air Force Office of Scientific Research, Bolling AFB, Washington, DC; 1996.
- [3] Cowles BA. High cycle fatigue in aircraft gas turbines—an industry perspective. *Int J Fract* 1996;80:147–63.
- [4] Waterhouse RB, Lindley TC, editors. *Fretting fatigue*, European Structural Integrity Society publication no. 18. London: Mechanical Engineering Publications Ltd; 1994.
- [5] Irwing PE, Beevers CJ. The effect of air and vacuum environments on fatigue crack growth rates in Ti-6Al-4V. *Metall Trans* 1974;5:391–8.
- [6] Bache MR, Evans WJ, McElhone MT. The effects of environment and internal oxygen on fatigue crack propagation in Ti-6Al-4V. *Mater Sci Eng A* 1997;234–236:918–22.
- [7] Thomas JP. Subcritical crack growth of Ti-6Al-4V at room temperature under high stress-ratio loading. *Scripta Mater* 1998;39:1647–52.
- [8] Ritchie RO, Boyce BL, Campbell JP, Roder O, Thompson AW, Milligan WW. Thresholds for high-cycle fatigue in a turbine engine Ti-6Al-4V alloy. *Int J Fat* 1999;21:653–62.
- [9] Wanhill RJH. Environmental fatigue crack propagation in Ti-6Al-4V sheet. *Metall Trans A* 1976;7:1365–73.
- [10] Iida S, Kobayashi AS. Crack-propagation rate in 7075-T6 plates under cyclic tensile and transverse shear loadings. *J Basic Eng* 1969;91:764–9.
- [11] Abdel-Mageed AM, Pandey RK. Mixed mode crack growth under static and cyclic loading in Al-alloy sheets. *Eng Fract Mech* 1991;40:371–85.
- [12] Tschegg EK, Stanzl SE, Czegléy M. Crack face interactions and near-threshold fatigue crack growth. *Fat Fract Eng Mater Struct* 1993;16:71–83.
- [13] Hua G, Brown MW, Miller KJ. Mixed-mode fatigue thresholds. *Fat Fract Eng Mater Struct* 1982;51:1–17.
- [14] Tong J, Yates JR, Brown MW. The significance of mean stress on the fatigue crack growth threshold for mixed mode I-II loading. *Fat Fract Eng Mater Struct* 1994;17:829–38.
- [15] Qian J, Fatemi A. Mixed mode fatigue crack growth: a literature survey. *Eng Fract Mech* 1996;55:969–90.
- [16] Pustejovsky MA. Fatigue crack propagation in titanium under general in-plane loading. I. Experiments. *Eng Fract Mech* 1979;11:9–15.
- [17] Pustejovsky MA. Fatigue crack propagation in titanium under general in-plane loading. II. Analysis. *Eng Fract Mech* 1979;11:17–31.
- [18] Gao H, Alagok N, Brown MW, Miller KJ. Growth of fatigue cracks under combined mode I and mode II loads. In: Miller KJ, Brown MW, editors. *Multiaxial fatigue*, ASTM STP 853. Philadelphia, PA: American Society for Testing and Materials; 1985. p. 184–202.
- [19] Taylor D. A compendium of fatigue thresholds and crack growth rates. Warley (UK): EMAS Ltd, 1985.
- [20] Ritchie RO. Small cracks and high-cycle fatigue. In: Chang JCI, Coulter J, Brei D, Martinez D, Hg W, Freidmann PP, editors. *Proceedings of the ASME Aerospace Division, AMD*. New York: ASME; 1996. p. 321–33.
- [21] Campbell JP, Ritchie RO. Mixed-mode, high-cycle fatigue-crack growth thresholds in Ti-6Al-4V. I. A comparison of large- and short-crack behavior. *Eng Fract Mech* 2000;67:209–27.
- [22] Campbell JP, Ritchie RO. Mixed-mode, high-cycle fatigue-crack growth thresholds in Ti-6Al-4V. Quantification of crack-tip shielding. *Eng Fract Mech* 2000;67:229–49.
- [23] Suresh S, Ritchie RO. Propagation of short cracks. *Int Metals Rev* 1984;29:445–76.
- [24] Ritchie RO, Lankford J. Small fatigue cracks: a statement of the problem and potential solutions. *Mater Sci Eng A* 1986;84:11–6.
- [25] Ritchie RO, Wu Y. Short crack effects in fatigue: a consequence of crack tip shielding. In: Ritchie RO, Lankford J, editors. *Small fatigue cracks*. Warrendale, PA: TMS-AIME; 1986. p. 167–89.
- [26] Venkateswara Rao KT, Yu W, Ritchie RO. On the behavior of small fatigue cracks in commercial aluminum-lithium alloys. *Eng Fract Mech* 1988;31:623–35.
- [27] Boyce BL. M.S. thesis, University of California at Berkeley, 1998.
- [28] Eylon D. Summary of available information on the processing of the Ti-6Al-4V HCF/LCF program plates, University of Dayton report, Dayton, OH, 1998.
- [29] Suresh S, Shih CF, Morrone A, O'Dowd NP. Mixed-mode fracture toughness of ceramic materials. *J Am Ceram Soc* 1990;73:1257–67.
- [30] He MY, Hutchinson JW. Asymmetric four-point crack specimen. *J Appl Mech Trans ASME* 2000;67:207–9.
- [31] Boyce BL, Ritchie RO. Effect of load ratio and maximum stress intensity on the fatigue threshold in Ti-6Al-4V. *Eng Fract Mech* 2001;68:129–47.
- [32] Dowling NE. Notched member fatigue life predictions combining crack initiation and propagation. *Fat Eng Mater Struct* 1979;2:129–38.
- [33] Hammouda MM, Smith RA, Miller KJ. Elastic-plastic fracture mechanics for initiation and propagation of notch fatigue cracks. *Fat Eng Mater Struct* 1979;2:139–54.
- [34] Rice JR, Johnson MA. The role of large crack geometry changes in plane strain fracture. In: Kanninen MF, Adler WG, Rosenfield AR, Jaffee RI, editors. *Inelastic behavior of solids*. New York: McGraw-Hill; 1970. p. 641–72.
- [35] Hill R. *The mathematical theory of plasticity*. Oxford: Clarendon Press, 1950.
- [36] Newman JC, Raju IS. An empirical stress-intensity factor equation for the surface crack. *Eng Fract Mech* 1981;15:185–92.
- [37] He MY, Hutchinson JW. Surface crack subject to mixed mode loading. *Eng Fract Mech* 2000;65:1–14.
- [38] Ravichandran KS. Effects of crack aspect ratio on the behavior of small surface cracks in fatigue: Part I. Simulation. *Metall Mater Trans A* 1997;28:149–56.
- [39] Ravichandran KS, Larsen JM. Effects of crack aspect ratio on the behavior of small surface cracks in fatigue: Part II. Experiments on a titanium (Ti-8Al) alloy. *Metall Mater Trans A* 1997;28:157–69.
- [40] Zheng YS, Wang ZG, Ai SH. Mixed-mode I and II fatigue threshold and crack closure in dual-phase steels. *Metall Mater Trans A* 1994;25:1713–23.
- [41] Yao D, Shang JK. Effect of load mix on fatigue crack growth in 63Sn-37Pb solder joints. *J Elect Pack Trans ASME* 1997;119:114–8.
- [42] Campbell JP, Ritchie RO. Mixed-mode, high-cycle fatigue-crack-growth thresholds in Ti-6Al-4V: role of bimodal and lamellar microstructures. *Metall Mater Trans A* 2001;32:497–503.
- [43] Erdogan F, Sih GC. On the crack extension in plates under plane loading and transverse shear. *J Basic Eng Trans ASME* 1963;85:519–25.
- [44] Pook LP. The fatigue crack direction and threshold behavior of mild steel under mixed modes I and III. *Int J Fat* 1985;7:21–30.
- [45] Nayeb-Hashemi H, McClintock FA, Ritchie RO. Effects of friction and high torque on fatigue crack propagation in Mode III. *Metall Trans A* 1982;13:2197–204.
- [46] Tschegg EK, Ritchie RO, McClintock FA. On the influence of rubbing fracture surfaces on fatigue crack propagation in mode III. *Int J Fat* 1983;5:29–35.

- [47] Tscheegg EK. Sliding mode crack closure and mode III fatigue crack growth in mild steel. *Acta Metall* 1983;31:1323–30.
- [48] Gao H, de los Rios ER, Miller KJ. Mixed-mode fracture mechanisms near the fatigue threshold of AISI 316 stainless steel. *Fat Eng Mater Struct* 1983;6:137–47.
- [49] Tong J, Yates JR, Brown MW. A model for sliding mode crack closure. I. Theory for pure mode II loading. *Eng Fract Mech* 1995;52:599–611.
- [50] Tong J, Yates JR, Brown MW. A model for sliding mode crack closure. II. Mixed mode I and II loading and application. *Eng Fract Mech* 1995;52:613–23.
- [51] Ritchie RO. Mechanisms of fatigue crack propagation in metals, ceramics and composites: role of crack-tip shielding. *Mater Sci Eng* 1988;103:15–28.
- [52] Ritchie RO. Mechanisms of fatigue-crack propagation in ductile and brittle solids. *Int J Fract* 1999;100:53–83.
- [53] Thompson AW. Relations between microstructure and fatigue properties of alpha-beta titanium alloys. In: Boyer RR, Eylon D, Lütjering G, editors. *Fatigue behavior of titanium alloys*. Warrendale, PA: TMS; 1999. p. 23–30.
- [54] Peters JO, Boyce BL, Chen X, McNaney JM, Hutchinson JW, Ritchie RO. On the application of the Kitagawa-Takahashi diagram to foreign-object damage and high-cycle fatigue. *Eng Fract Mech* 2002, in press.
- [55] Nalla RK, Boyce BL, Campbell JP, Peters JO, Ritchie RO. Influence of microstructure on high-cycle fatigue of Ti-6Al-4V: bimodal vs. lamellar structures. *Metall Mater Trans A* 2002 33A, in press.
- [56] Lankford J, Davidson DL. The role of metallurgical factors in controlling the growth of small fatigue cracks. In: Ritchie RO, Lankford J, editors. *Small fatigue cracks*. Warrendale, PA: TMS; 1986. p. 51–71.
- [57] Taylor D, Knott JF. Fatigue crack propagation behavior of short cracks: the effect of microstructure. *Fat Eng Mater Struct* 1981;4:147–55.
- [58] Bilby BA, Cardew GE, Howard IC. Stress intensity factors at the tips of kinked and forked cracks. In: Taplin DMR, editor. *Fracture* 1977. Oxford: Pergamon Press; 1977. p. 197–200.
- [59] Cotterell B, Rice JR. Slightly curved or kinked cracks. *Int J Fract* 1980;16:155–69.

## FOREIGN-OBJECT DAMAGE IN Ti-6Al-4V

- J.O. Peters, O. Roder, B.L. Boyce, A.W. Thompson, and R.O. Ritchie, "Role of Foreign Object Damage on Thresholds for High-Cycle Fatigue in Ti-6Al-4V", *Metall. Mater. Trans. A*, vol. 31A, 2000, pp. 1571-83.
- J.O. Peters and R.O. Ritchie, "Influence of Foreign Object Damage on Crack Initiation and Early Fatigue-Crack Growth in Ti-6Al-4V", *Eng. Fract. Mech.*, vol. 67, 2000, pp. 193-207.
- J.O. Peters and R.O. Ritchie, "Foreign Object Damage and High-Cycle Fatigue: Role of Microstructure in Ti-6Al-4V", *Int. J. Fat.*, vol. 23, 2001, pp. S1413-21.
- J.O. Peters and R.O. Ritchie, "Foreign Object Damage and High-Cycle Fatigue in Ti-6Al-4V", *Mater. Sci. Eng.*, vol. 319-21, 2001, pp. 597-601.
- X. Chen and J.W. Hutchinson, "Foreign Object Damage and Fatigue Crack Threshold: Cracking Outside Shallow Indents", *Int. J. Fract.*, vol. 107, 2001, pp. 31-51.
- B.L. Boyce, X. Chen, J.W. Hutchinson, and R.O. Ritchie, "The Residual Stress State due to a Spherical Hard-Body Impact", *Mech. Mater.*, vol. 33, 2001, pp. 441-45.
- B.L. Boyce, X. Chen, J.O. Peters, J.W. Hutchinson, R.O. Ritchie, "Mechanical Relaxation of Localized Residual Stresses Associated with Foreign Object Damage", *Mater. Sci. Eng. A*, 2002, in review.
- J.O. Peters, B.L. Boyce, X. Chen, J.M. McNaney, J.W. Hutchinson, and R.O. Ritchie, "On the Application of the Kitagawa-Takahashi Diagram to Foreign-Object Damage and High-Cycle Fatigue", *Eng. Fract. Mech.*, 2002, in press.

# Role of Foreign-Object Damage on Thresholds for High-Cycle Fatigue in Ti-6Al-4V

J.O. PETERS, O. RODER, B.L. BOYCE, A.W. THOMPSON, and R.O. RITCHIE

The increasing incidence of military aircraft engine failures that can be traced to high-cycle fatigue (HCF) has prompted a reassessment of the design methodologies for HCF-critical components, such as turbine blades and disks. Because of the high-frequency vibratory loading involved, damage-tolerant design methodologies based on a threshold for no crack growth offer a preferred approach. As impact damage from ingested debris is a prime source of HCF-related failures, the current study is focused on the role of such foreign-object damage (FOD) in influencing fatigue crack-growth thresholds and early crack growth of both large and small cracks in a fan blade alloy, Ti-6Al-4V. FOD, which was simulated by the high-velocity (200 to 300 m/s) impact of steel spheres on a flat surface, was found to reduce markedly the fatigue strength, primarily due to earlier crack initiation. This is discussed in terms of four salient factors: (1) the stress concentration associated with the FOD indentation, (2) the presence of small microcracks in the damaged zone, (3) the localized presence of tensile residual hoop stresses at the base and rim of the indent sites, and (4) microstructural damage from FOD-induced plastic deformation. It was found that no crack growth occurred from FOD impact sites in this alloy at  $\Delta K$  values below  $\sim 2.9 \text{ MPa}\sqrt{\text{m}}$ , *i.e.*, over 50 pct higher than the "closure-free", *worst-case* threshold value of  $\Delta K_{TH} = 1.9 \text{ MPa}\sqrt{\text{m}}$ , defined for large cracks in bimodal Ti-6Al-4V alloys at the highest possible load ratio. It is, therefore, concluded that such *worst-case*, large fatigue crack thresholds can, thus, be used as a practical lower-bound to FOD-initiated cracking in this alloy.

## I. INTRODUCTION

THE increasing incidence of high cycle fatigue (HCF)-related failures of gas turbine engines in military aircraft has led to a re-evaluation of the current Goodman design approach for HCF.<sup>[1,2,3]</sup> Larsen *et al.*,<sup>[3]</sup> for example, have reviewed the limitations of the Goodman approach and concluded that it does not account explicitly for such critical factors as interactions of low-cycle fatigue (LCF) and HCF loading, or the microstructural variability and surface damage, *e.g.*, due to fretting or foreign-object damage (FOD), which can act as potential sources for crack initiation under the high-frequency, in-service vibratory loading. Indeed, because of the high frequencies ( $>1$  kHz) involved, any degree of crack growth could potentially result in failure during operation. Consequently, to avoid HCF failures, the design of critical components should involve a damage-tolerant methodology,<sup>[1-4]</sup> specifically based on the concept of a fatigue crack-growth threshold, defined under representative HCF conditions of high frequencies, high load ratios, and small crack sizes.

Foreign-object damage is a prime cause of such HCF failures. The term is used to indicate damage from bird strikes and hard body impacts, such as stones, striking primarily the turbine engine fan blades when ingested with the airflow.<sup>[5,6]</sup> Depending on the impact conditions, FOD can result in the immediate separation of a blade or can cause

sufficient microstructural damage, stress-raising notches, or even cracks, which induce the early initiation of fatigue cracks. Since fan and compressor blades can experience in-service transient airflow dynamics from resonant conditions of the engine, in the form of low-amplitude airfoil excitations in the kHz regime (and, depending on the blade span location, very high mean-stress levels), such premature cracking can result in essentially unpredictable failures due to fatigue crack growth in very short time periods.<sup>[2,3]</sup>

To develop a predictive, mechanism-based model for the role of FOD in inducing HCF failures, a key aspect is to characterize how FOD affects the HCF thresholds. This involves assessing the effect of stress concentration, FOD-induced microcracking, residual stress gradients,<sup>[2,7,8]</sup> and microstructural changes due to the FOD-induced plastic deformation.<sup>[9,10]</sup> It is the objective of the present study to examine this role of FOD, simulated by the normal high-velocity impact of small steel spheres on the flat surfaces of fatigue test specimens, in influencing the fatigue crack-growth thresholds and near-threshold crack growth rates in a Ti-6Al-4V alloy processed for typical turbine blade applications.

## II. BACKGROUND

### A. Stress Concentration

Traditional design approaches for HCF, based on a modified Goodman diagram, assess the role of FOD in terms of the effective fatigue stress-concentration factor ( $k_f$ ), *i.e.*, the ratio of the fatigue limit of a smooth component to that of a FOD-notched component.<sup>[6]</sup> Whereas the HCF life of blunt notches is dominated by crack initiation and can generally be predicted using the elastic stress-concentration factor ( $k_t$ ), for sharp notches, the HCF strength approaches a lower

J.O. PETERS, Postdoctoral Researcher, B.L. BOYCE, Graduate Student, A.W. THOMPSON, Scientist, and R.O. RITCHIE, Professor, are with the Department of Materials Science and Mineral Engineering, University of California, Berkeley, CA 94720-1760. O. RODER, formerly Postdoctoral Researcher, Department of Materials Science and Mineral Engineering, University of California, is Staff Engineer, Daimler Chrysler Aerospace—MTU Munich 80976, Germany.

Manuscript submitted August 5, 1999.



limiting value which can be expressed in terms of  $k_f$ . The existence of a critical notch sharpness in affecting the fatigue limit is attributed to the initiation, growth, and subsequent arrest of short cracks at sharp notches under the influence of a high notch-stress gradient at nominally low stresses.<sup>[11,12,13]</sup> To incorporate these effects into a design for HCF, Hudak *et al.*<sup>[7]</sup> have proposed a "worst-case notch" concept based on a fatigue crack-growth threshold that accounts for the statistical severity of FOD-induced notches.

### B. FOD-Induced Cracking

In brittle alloys, such as gamma titanium aluminides, FOD-like impact damage can result in extensive microcracking within the damaged region, which provides the prime reason for the degradation in fatigue life of these alloys due to FOD.<sup>[14]</sup> However, in more-ductile materials such as Ti-6Al-4V, reports of microcracking in the vicinity of damage sites are rare. The presence of such microcracks, however, is of critical importance, as it provides a very potent site for HCF cracks to initiate.

### C. Residual Stresses

In addition to the geometrical effects of the impact sites, FOD induces residual stresses in the vicinity of these sites, which can have a profound influence on the location and conditions for crack initiation.<sup>[2,8,9,15]</sup> Unfortunately, numerical and experimental analyses of dynamic and quasi-static indentation loading available in the literature,<sup>[9,16-23]</sup> which simulate simple-geometry FOD by indenting a spherical steel indenter often onto a steel target, do not provide consistent residual stress fields with respect to the primary fatigue crack initiation sites at the indent base and rim locations. For example, dynamic indentation simulation, neutron diffraction, and X-ray diffraction analyses are contradictory in predicting both compressive<sup>[16]</sup> and tensile<sup>[18,19]</sup> hoop stresses at the indentation base. Indeed, in general, numerical studies of quasi-static indentation predict either tensile hoop stresses at the base<sup>[20]</sup> and rim<sup>[21]</sup> or compressive hoop stresses at the base<sup>[22]</sup> and rim<sup>[20]</sup> of the indentation sites; experimental studies, conversely, report only tensile hoop stresses at the rim.<sup>[23]</sup> Consequently, in the present work, we attempt to characterize the residual stress field of simulated FOD sites using preliminary X-ray microdiffraction studies, numerical analysis by Chen and Hutchinson,<sup>[21]</sup> and the available literature. At this point, these analyses are largely qualitative, but suggest zones of tensile residual hoop stresses located at the base and rim of the indentation sites, consistent with the location of the preferred sites for crack initiation.

### D. Microstructure

Microstructural variability through thermomechanical treatment is known to have a marked influence on the fatigue properties of titanium alloys, as noted in several recent reviews.<sup>[24,25,26]</sup> Correspondingly, microstructural changes associated with FOD-induced plasticity must be taken into account in any assessment of the role of FOD. This is evident from shot-peening studies on Ti-6Al-4V (*e.g.*, References 27 and 28) where, by separating the influence of microstructure

Table I. Chemical Composition of Ti-6Al-4V Bar Stock Material in Weight Percent<sup>[30]</sup>

Ti	Al	V	Fe	O	N	H
Bal	6.30	4.19	0.19	0.19	0.013	0.0041

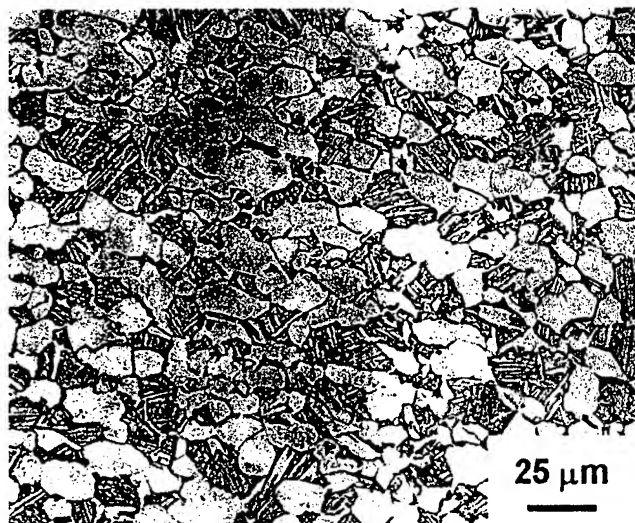


Fig. 1—Optical micrograph of the bimodal (STOA) microstructure of forged Ti-6Al-4V plate material (etched in 3 1/2 pct HNO<sub>3</sub> - 5 pct HF).

from residual stress effects, it was observed that the deformed microstructure exhibited an increased resistance to crack nucleation, yet at the same time a drastically reduced resistance to small-crack growth.<sup>[29]</sup>

## III. EXPERIMENTAL PROCEDURES

### A. Material

The Ti-6Al-4V alloy under study was part of a set of forgings produced specifically for the United States Air Force-sponsored programs on HCF. Its chemical composition is given in Table I. The  $\beta$  transus is at  $\sim 996$  °C. Mill-annealed 63.5-mm-diameter bar stock material, originating from Teledyne Titanium (Pittsburgh, PA), was forged in one stroke at 938 °C on a closed-end channel die to a plate size of 400 × 150 × 20 mm, followed by air cooling. The forging plates were then solution treated in an air furnace at 927 °C for 1 hour, followed by fan air cooling; this resulted in a cooling rate of  $\sim 200$  °C/min. Finally, the plates were stress relieved *in vacuo* for 2 hours at 705 °C. Further material and processing details are given in Reference 30.

After such thermomechanical processing, the plate material showed a bimodal microstructure with a volume fraction of  $\sim 60$  pct primary  $\alpha$  phase (diameter of  $\sim 20$   $\mu$ m) within a lamellar  $\alpha + \beta$  matrix (Figure 1). This microstructure has been termed solution-treated and overaged (STOA). The crystallographic texture of the plate material was measured using Ni-filtered Cu  $K_\alpha$  radiation and is plotted as (0002) and {10 $\bar{1}$ 0} pole figures in Figure 2. In this figure, the numbers represent the ratio of the intensities of the (0002) basal and {10 $\bar{1}$ 0} prismatic planes of the hcp  $\alpha$  phase to that of the random texture of the hot-isostatic-pressed powder standard. The resulting pole figures reveal the preferred



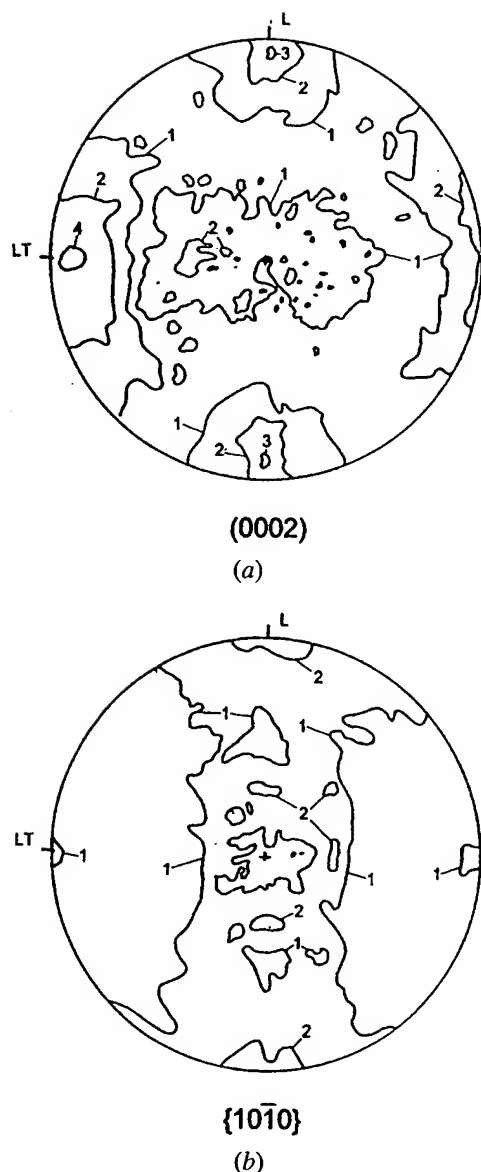


Fig. 2—Crystallographic texture of the forged Ti-6Al-4V shown as pole figures. Numbers represent the ratio of the intensities of the (a) (0002) basal and (b) {10 $\bar{1}$ 0} prismatic planes of the hexagonal closed packed  $\alpha$  phase to that of the random texture of the hot isostatic pressed powder standard.

Table II. Uniaxial Tensile Properties of Bimodal Ti-6Al-4V\*

$E$ (GPa)	$\sigma_{0.2}$ (MPa)	UTS (MPa)	$\sigma_F$ (MPa)	Tens. El. (Pct)	RA (Pct)
110	915	965	1310	19	45

\* $E$ : Young's modulus,  $\sigma_{0.2}$ : yield stress, UTS: ultimate tensile strength,  $\sigma_F$ : true fracture stress, Tens. El.: tensile elongation, RA: reduction of area at fracture; and strain rate  $8 \times 10^{-4} \text{ s}^{-1}$ .

orientation of the basal planes parallel and perpendicular to the length of the forged plate ( $L$  direction).

Uniaxial tensile properties (parallel to the length of the plate,  $L$  orientation) are listed in Table II; the tensile tests were performed at an initial strain rate of  $8 \times 10^{-4} \text{ s}^{-1}$ .

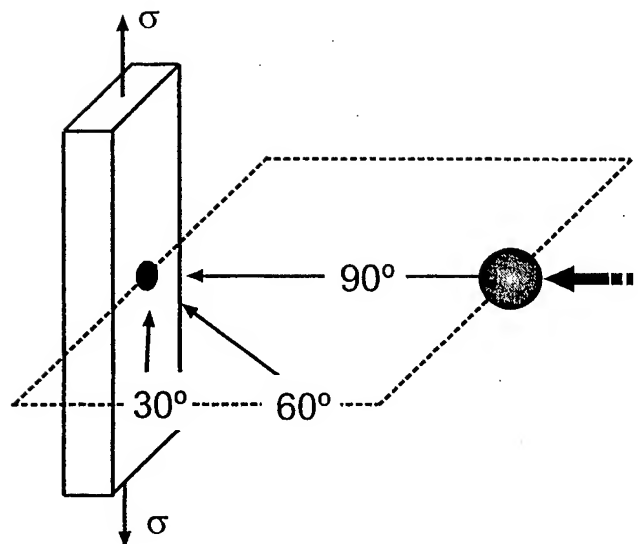


Fig. 3—Schematic illustration showing impact angles with respect to specimen geometry and loading axis for fatigue tests. In this study, a normal (90 deg) impact angle was chosen.

### B. Simulation of FOD

In this study, FOD by hard particles was simulated by shooting steel spheres onto a flat specimen surface to produce a single specific damage site. Chrome-hardened steel spheres, 3.2 mm in diameter and with a Rockwell C hardness of 60, were impacted onto the flat surfaces of the tensile fatigue (so-called  $K_B$ ) specimens at an angle of 90 deg (normal impact, Figure 3) at velocities of 200, 250, and 300 m/s using a compressed-gas gun facility. These velocities represent typical in-service impact velocities on aircraft engine fan blades. The spheres were accelerated by applying gas pressures between 2 and 7 MPa; their velocity was measured photoelectrically prior to impact.

### C. Fatigue Test Methods

#### 1. Smooth-bar and small-crack fatigue tests

For an assessment of FOD on the fatigue behavior, baseline stress-life (S-N) fatigue data of the bimodal Ti-6Al-4V plate material were generated on smooth-bar hourglass specimens. Specimens were machined, with the geometry shown in Figure 4(a), such that the specimen axis was oriented parallel to the length of the plate ( $L$  orientation). They were electrolytically polished to minimize the presence of surface residual stresses and high dislocation densities from the machining. A solution of 59 pct methanol, 35 pct 2-butanol, and 6 pct perchloric acid was used at  $-30^\circ \text{C}$  and 16 V to remove a surface layer of 100  $\mu\text{m}$ . The S-N tests were performed on a Roell Amsler resonant-fatigue testing machine in room-temperature air at a cyclic frequency of 85 Hz.

To investigate small-crack propagation behavior,  $\sim 45$ - to  $60\text{-}\mu\text{m}$ -long surface cracks were naturally initiated at a load ratio ( $R = \sigma_{\min}/\sigma_{\max}$ ) of  $-1$  and an alternating stress of 650 MPa. After initiation, the load ratio was changed to 0.1 and small-crack growth was monitored at a maximum stress of 550 MPa. Tests were periodically interrupted to measure the surface-crack length ( $2c$ ) in a light microscope. The stress-intensity range ( $\Delta K$ ) of the small, semi-elliptical surface

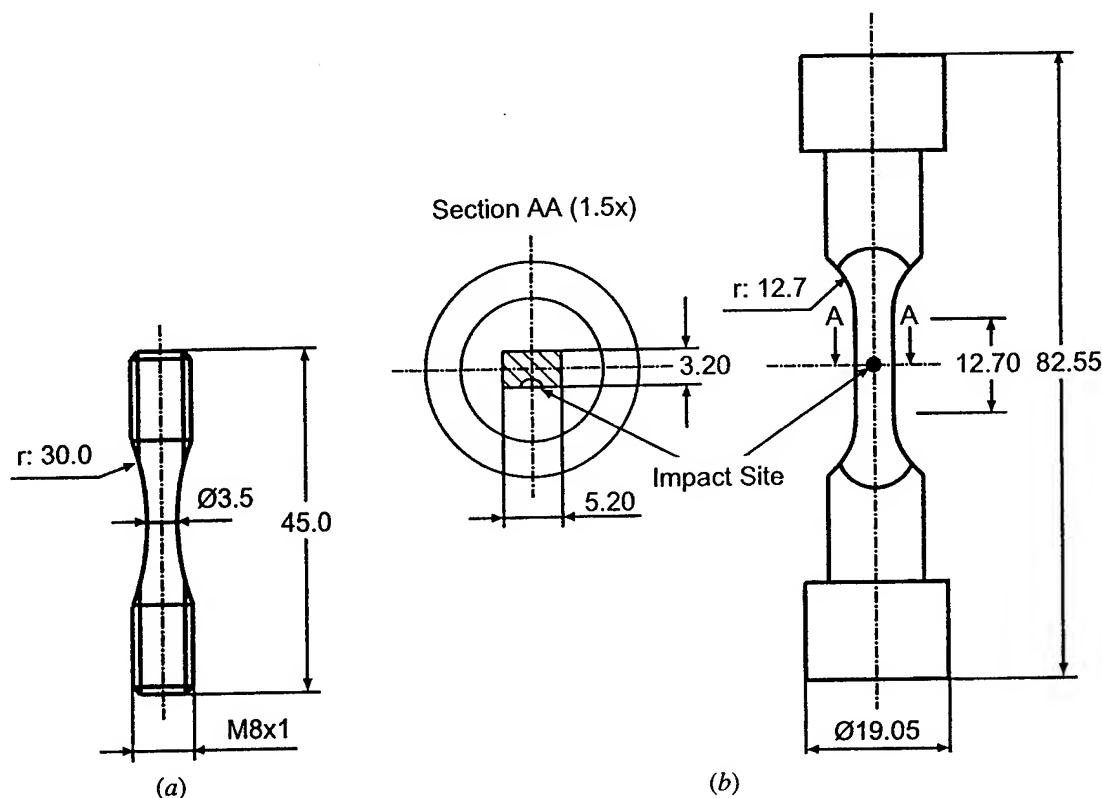


Fig. 4—Drawings of the specimen geometries used, showing (a) smooth-bar specimen for S-N curves and (b) modified  $K_B$  specimen for simulated FOD studies. All dimensions are in millimeters.

cracks was calculated using the Newman-Raju linear-elastic relationship<sup>[31]</sup>

$$\Delta K = \Delta \sigma \sqrt{\pi \frac{a}{Q}} F \quad [1]$$

where  $\Delta \sigma$  is the stress range,  $a$  is the crack depth,  $F$  is the stress-intensity boundary correction factor, and  $Q$  is the crack shape-correction factor. For the present alloy, a crack depth-to-surface crack length ( $a/2c$ ) ratio of 0.45 was assumed, based on fractographic observations.

Fatigue limits were also investigated using the so-called HCF step test. Using modified  $K_B$  specimens, this test consisted of loading in steps of  $10^8$  cycles at 1000 Hz at a constant stress amplitude. If no failure occurred after  $10^8$  cycles, the maximum stress level was successively increased by  $\sim 50$  MPa until specimen failure. This procedure permits an estimation of the HCF fatigue limit with a single specimen.

## 2. Large-crack fatigue tests

The corresponding crack-growth tests on large cracks, typically in excess of  $\sim 5$  mm in length, were performed on compact-tension C(T) specimens in general accordance with ASTM standard E-647. The C(T) specimens were machined in the  $L$ - $T$  orientation, with an 8 mm thickness and 25 mm width. Tests were carried out in room-temperature air at  $R$  ratios varying from 0.1 to 0.95 under automated load or stress-intensity control, at frequencies between 50 and 1000 Hz (sinusoidal wave form). Fatigue crack-growth thresholds ( $\Delta K_{TH}$  and  $K_{max,TH}$ ), defined at a propagation rate of  $10^{-10}$  m/cycle at 50 Hz and  $10^{-11}$  m/cycle at 1000 Hz, respectively,

were determined at load ratios of  $R = 0.1$  to 0.8 using constant  $R$  testing; loads were shed such that  $\Delta K = \Delta K_{initial} \exp(C(a - a_{initial}))$ , with the normalized  $K$  gradient,  $C$ , set to  $-0.08 \text{ mm}^{-1}$  ( $a$  and  $a_{initial}$  are the instantaneous and initial crack lengths, respectively). For load ratios above 0.8, thresholds were approached using variable- $R$ , constant- $K_{max}$ /increasing- $K_{min}$  loading. All testing was performed on automated MTS servohydraulic testing machines; experiments at 1000 Hz were conducted with a newly developed system using a voice-coil servovalve (further details of this instrument are described in Reference 32).

Back-face strain-unloading compliance techniques were used for *in-situ* crack length measurements; crack lengths were periodically verified with optical measurements. Unloading compliance was also used to assess crack closure loads. Specifically, the closure stress intensity ( $K_{cl}$ ) was determined at first contact of the crack surfaces, measured at the point of first deviation from linearity in the elastic compliance curve upon unloading.<sup>[33]</sup>

## 3. The FOD specimen fatigue tests

To investigate the influence of FOD on the fatigue behavior of the bimodal Ti-6Al-4V alloy, modified  $K_B$  specimens were chosen (Figure 4(b)). This specimen geometry, which is essentially identical to that used by General Electric Aircraft Engines for its similarity to the blade-loading configuration,<sup>[34]</sup> was machined with a rectangular gage section ( $3.2 \times 5.2$  mm) with cylindrical buttonhead grip sections. To provide a consistent, nominally stress-free surface, the gage section was prepared using standard stress-relief and chemical-milling procedures. To simulate FOD, steel shot was

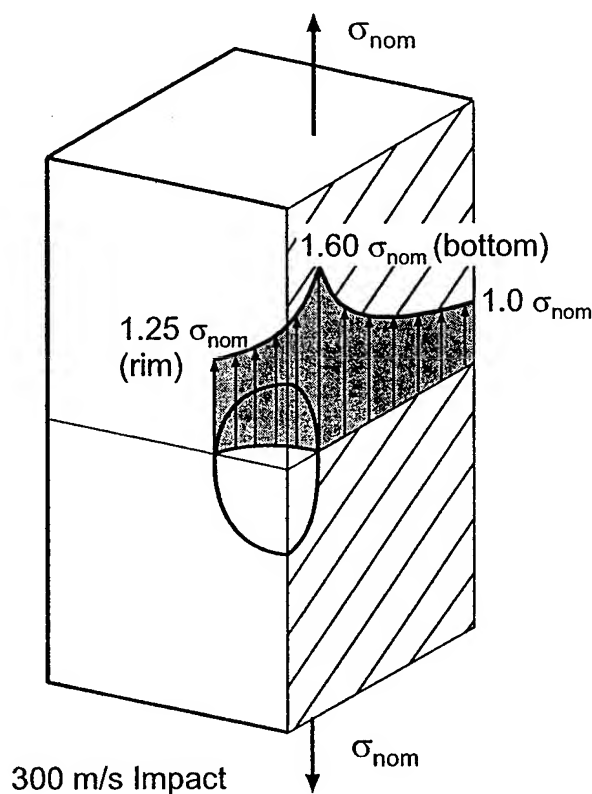


Fig. 5—Schematic illustration showing the stress concentration surrounding a FOD indentation crater (based on Nisida and Kim<sup>[35]</sup>).

fired at 90 deg to the specimen surface at velocities of 200 to 300 m/s, as noted previously. After impacting, specimens were cycled at 20 Hz (sinusoidal waveform) with a maximum stress of 500 MPa, at a load ratio of  $R = 0.1$ . To detect fatigue crack initiation, specimens were removed periodically from the test frame and examined in a scanning electron microscope (SEM); once a crack had initiated, the same procedure was used to monitor subsequent small-crack growth. Stress intensities for the surface cracks were again calculated from Eq. [1], assuming a crack depth-to-surface crack length ratio of 0.45 (determined from fractographic observations).

As an initial assessment of the stress concentration associated with the damage sites, elastic stress-concentration factors surrounding the indentations were determined based on three-dimensional photoelastic experiments performed by Nisida and Kim<sup>[35]</sup> Figure 5 shows schematically the stress distribution surrounding a 300 m/s impact indentation site. Table III lists the impact-site geometry dimensions and the resulting elastic stress-concentration factors, which reach a maximum at the base of the indents, *i.e.*, ranging from  $k_t = 1.6$  (for a 300 m/s impact site) to  $k_t = 1.4$  (for a 200 m/s site). Corresponding values at the crater surface rim range from  $k_r = 1.25$  (300 m/s) to  $k_r = 1.15$  (200 m/s).

To compute local stress-intensity factors for small cracks emanating from such indentations, incorporating both indentation geometry and stress-concentration effects, the relationship of Lukáš<sup>[36]</sup> for small cracks at notches is used, *viz*,

$$\Delta K = \frac{0.7 k_t}{\sqrt{1 + 4.5(a/\rho)}} \Delta \sigma \sqrt{\pi a} \quad [2]$$

Table III. Dimensions of Impact Craters and Stress Concentration Factors\*

Impact Velocity	$\varnothing W$ (mm)	$\delta$ (mm)	$k_t$ (Base)	$k_r$ (Rim)	$k_f$
300 m/s	2.67	0.67	1.60	1.25	1.54
250 m/s	2.38	0.54	1.50	1.20	1.40
200 m/s	2.14	0.43	1.40	1.15	1.40

\* $\varnothing W$ : chord width of impact crater,  $\delta$ : indentation depth (Fig. 6),  $k_t$ : elastic stress concentration factor; [35]  $k_f$ : effective-fatigue stress concentration factor.

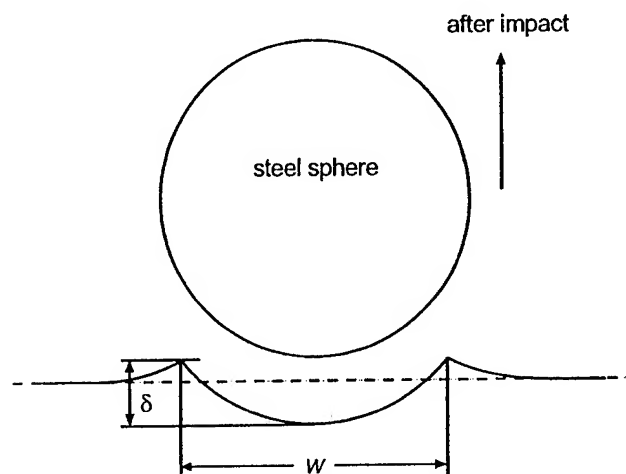


Fig. 6—Schematic illustration of the cross section of simulated FOD crater after impact ( $W$  is the chord width, and  $\delta$  is the depth).

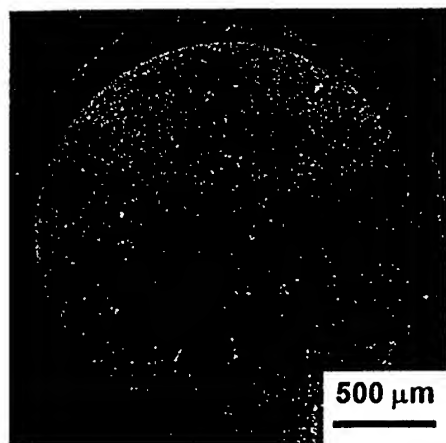
where  $\Delta \sigma$  is the stress range,  $a$  is the crack depth, and  $\rho$  is the indentation radius. However, it should be noted that the contribution to this value from the residual stress field surrounding the indentation has not been taken into account, due to uncertainty in the value of these local stresses. Recent studies have focused on the use of synchrotron X-ray microdiffraction methods, together with numerical analysis,<sup>[21]</sup> to estimate these local stress gradients.

## IV. RESULTS AND DISCUSSION

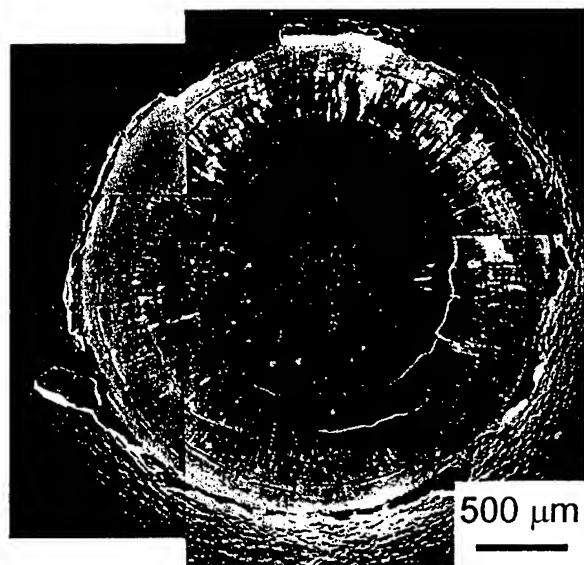
### A. Characterization of FOD

The simulated FOD sites are characterized in terms of size, shape, and possible occurrence of microcracking in Figures 6 through 8 (and Table III) and with respect to induced microstructural changes in Figure 9. Damage clearly can be seen to be a function of impact velocity. Based on these observations, the distribution of the residual stresses surrounding the impact site was deduced, as discussed subsequently, and is shown schematically in Figure 10.

First, with respect to shape, Figure 6 shows a schematic of the cross section of a crater formed by a normal impact. The measured dependence of the crater diameter ( $W$ ) and depth ( $\delta$ ) on the impact velocity are listed in Table III. The SEM micrographs show indentations formed at impact velocities of 200 m/s (Figure 7(a)) and 300 m/s (Figure



(a)

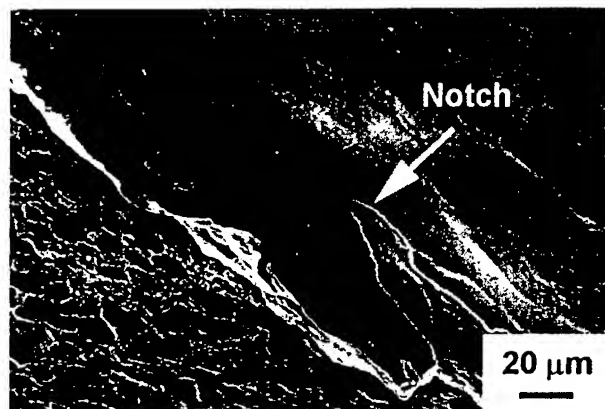


(b)

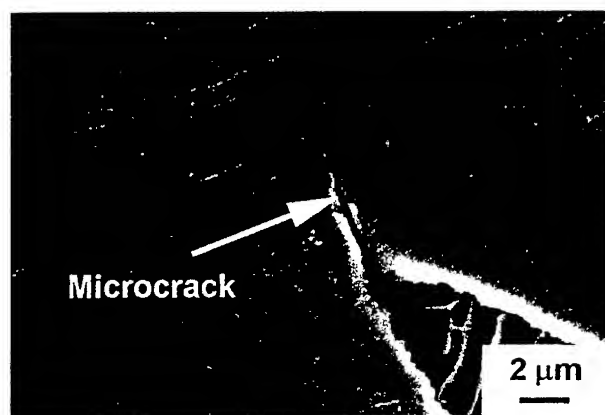
Fig. 7—Scanning electron micrographs of impact damage sites for (a) 200 m/s and (b) 300 m/s impact velocities, indicating increasing damage with increasing velocity with respect to indentation size, lip formation at crater rim, and intense shear band formation emanating at the indent surface.

7(b)). At velocities above 250 m/s, a pronounced pileup at the crater rim, with some detached material (Figure 7(b)), was evident. Of critical importance were the observations, shown in Figure 8, that, for the highest velocity impacts at 300 m/s, plastic flow of material at the crater rim causes local notches (Figure 8(a)) and even microcracking (Figure 8(b)). The microcracks were quite small, *i.e.*, between  $\sim 2$  to  $10\ \mu\text{m}$  in depth, but clearly provided the nucleation sites for subsequent HCF cracking, as shown in Figure 8(c). No such microcracking could be detected in this alloy at lower impact velocities.

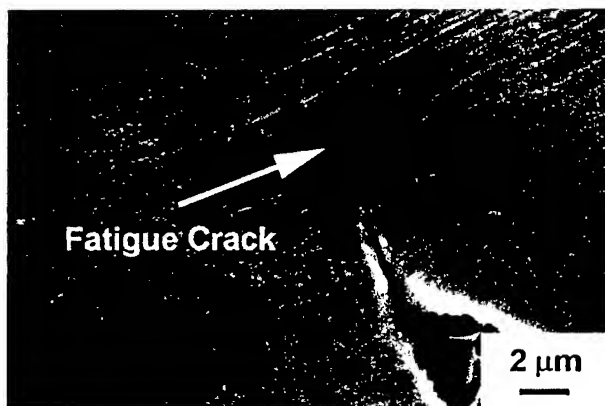
The resulting deformed microstructures, imaged at the center, mid, and rim position of the crater (Figure 9), reveal flattened primary  $\alpha$  grains at the base of the indent (Figure 9(b)), whereas at the mid (Figure 9(c)) and rim locations (Figure 9(d)), the  $\alpha$  grains are deformed in shear, along with the lamellar matrix of the bimodal microstructure. Bulk plastic deformation of the material surrounding the impact crater was found to extend into a region of approximately



(a)



(b)



(c)

Fig. 8—Scanning electron micrographs showing the presence of microcracking at the crater rim of a FOD indent after the highest velocity (300 m/s) impacts. Micrographs show (a) local notches at crater rim caused by plastic flow of material, (b) microcracks emanating from such notches, and (c) subsequent fatigue-crack growth initiated at such microcracks after 5000 cycles at  $\sigma_{\text{max}} = 500\ \text{MPa}$  ( $R = 0.1$ ).

one indentation radius. At the base of the impact crater, strongly localized deformation can be seen in the form of circumferentially oriented intense shear bands emanating from the surface of the impact crater (refer to the arrows in Figures 9(c) and 9(d)). The work of Hutchings<sup>[37]</sup> and Timothy and Hutchings<sup>[38,39,40]</sup> showed that such shear bands form adiabatically during impact in Ti-6Al-4V. For that reason, it is anticipated that localized plasticity due to adiabatic

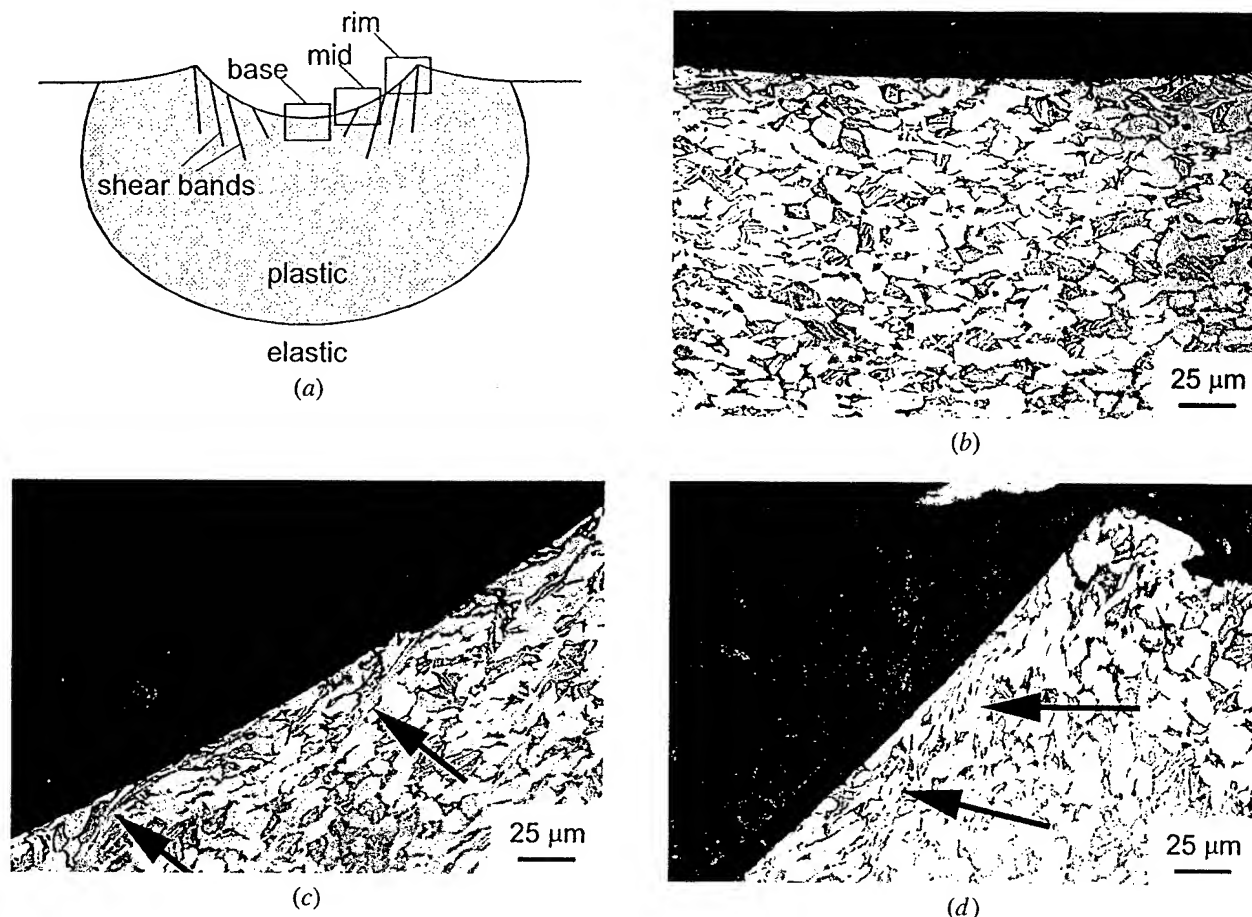


Fig. 9—FOD following 300 m/s impacts, showing (a) schematic of the crater, and optical micrographs of cross sections at the (b) base, (c) mid location, and (d) rim of the crater. Note formation of shear bands emanating from the surface at mid and rim positions (marked by arrows).

heating is the reason for the pronounced pileup formation at the crater rim. This is consistent with the observation that intense shear banding and pileups at the crater rim were only observed for 250 and 300 m/s impacts; neither feature was evident for 200 m/s velocities. This result is consistent with the reported critical velocity of  $214 \pm 16$  m/s for shear banding in a bimodal Ti-6Al-4V alloy with 3.2-mm-diameter steel sphere impacts.<sup>[40]</sup>

Contrary to the shot-peening process, where the surface deformation from multiple impacts imparts compressive residual stresses at the component surface,<sup>[27,28]</sup> with the single impacts typical of FOD, zones of both tensile and compressive residual stresses appear to be generated in the vicinity of the impact site. A proposed residual stress distribution is shown schematically in Figure 10, based on preliminary (qualitative) X-ray microdiffraction and numerical<sup>[21]</sup> studies. Upon impact, the stress state in the target material directly beneath the indenter is subjected to compressive radial stresses ( $\sigma_r$ ) and tensile hoop stresses ( $\sigma_\theta$ ). This is illustrated in Figure 10(a) together with the region of bulk plastic deformation, pile-up formation at the impact-site rim, circumferentially oriented adiabatic shear bands, and an area of localized hydrostatic pressure at the indent base. The corresponding state of residual stresses after unloading is shown in Figure 10(b). The overall constraint of the surrounding elastic material leads to compressive residual hoop stresses,  $\sigma_\theta$ , and tensile residual radial stresses,  $\sigma_r$ , in the

bulk of the plastically deformed material beneath the indentation crater. In addition, three distinct areas of tensile residual hoop stress are generated, namely, (1) surrounding the bulk compressive residual stress zone, due to the balance of tensile and compressive stresses, as in shot-peened components;<sup>[27]</sup> (2) at the crater rim, due to geometrical constraint; and (3) in a shallow surface layer at the base of the indent, due to hydrostatic compressive stresses from contact between the indenter and the target material in this location. As such hydrostatic pressure reduces the magnitude of shear stresses, intense shear bands were only found in regions away from the base of the indent (Figure 9(a)).

## B. Baseline Fatigue Properties

### 1. Fatigue crack initiation

To define baseline conditions, the smooth-bar S-N fatigue properties of the bimodal Ti-6Al-4V material, from tests on unnotched, electrolytically polished hourglass specimens, are shown in Figure 11.<sup>[41]</sup> These data indicate the influence of the maximum stresses ( $\sigma_{\max}$ ) at three different load ratios ( $R = -1, 0.1$ , and  $0.5$ ) on the number of cycles to failure ( $N_f$ ) and show that increasing the load ratio leads to an increase in  $\sigma_{\max}$  at the  $10^7$ -cycle fatigue limit from 375 MPa ( $R = -1$ ) to 500 MPa ( $R = 0.1$ ) and 625 MPa ( $R = 0.5$ ).

Small surface cracks,  $\sim 45$  to  $60 \mu\text{m}$  in size, were observed to nucleate after roughly 10,000 cycles at  $\sigma_{\max} = 650$  MPa

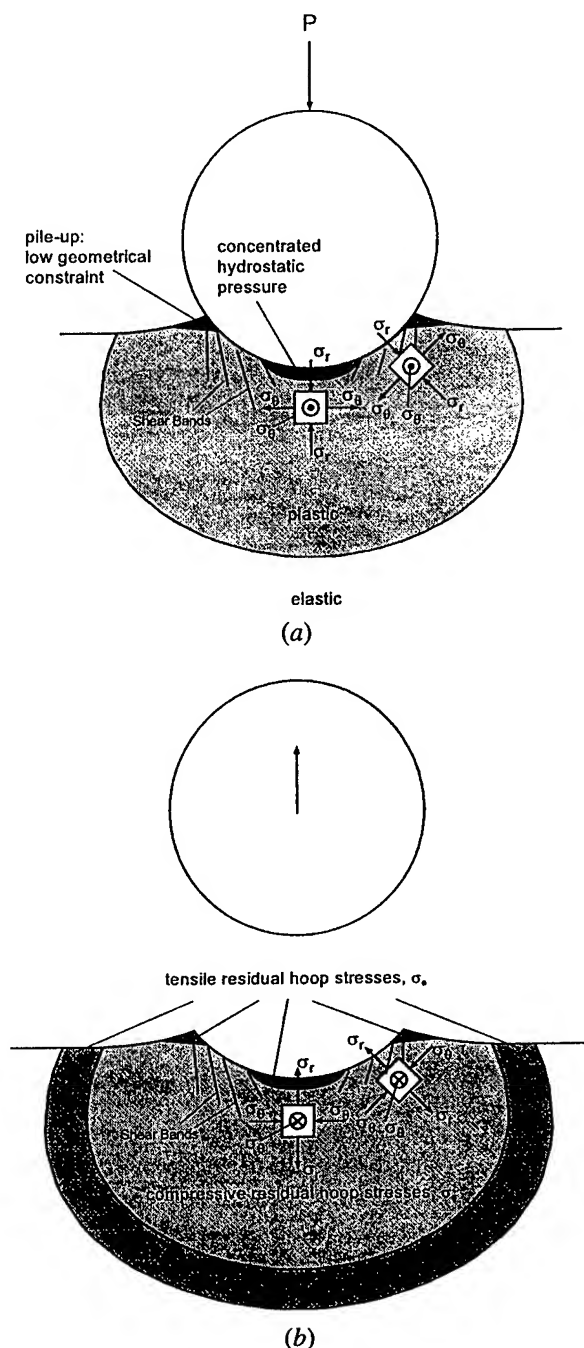


Fig. 10—Model of high-velocity impact loading and resulting residual stress state, showing (a) state of stress at impact loading and (b) state of residual stresses after impact loading ( $\sigma_r$  = radial stress, and  $\sigma_\theta$  = hoop stress).

at  $R = -1$  (Figure 12). Microstructurally, cracks tended to initiate in planar slip bands within the globular  $\alpha$  phase, specifically at the surface at  $R = -1$  (Figure 12) and at the subsurface at  $R = 0.1$  and  $0.5$  (Figure 13). Final failure occurred at a maximum stress of 475 MPa ( $R = 0.1$ ) after  $\sim 5.3 \times 10^7$  cycles.

As noted previously, the current “safe-life” design approach against HCF failure is based on fatigue-limit data generated through S-N tests. To incorporate the influence of load ratio, modified Goodman diagrams were constructed where the limiting alternating stress is plotted against the

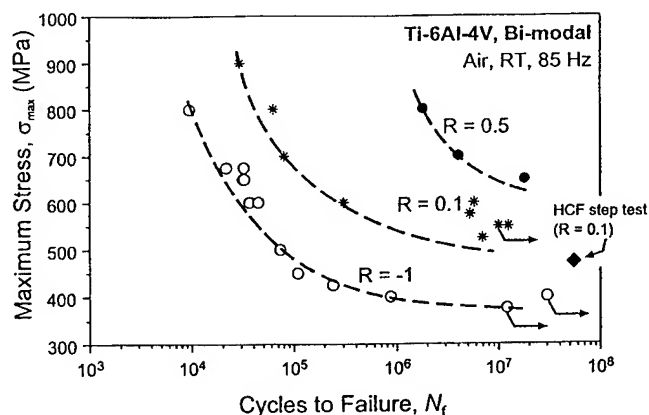


Fig. 11—Stress-life (S-N) curves for bimodal Ti-6Al-4V, determined using smooth-bar specimens.<sup>[41]</sup> Also shown is the result of the HCF step test at  $R = 0.1$ , based on modified  $K_B$  specimen testing.



Fig. 12—Optical micrograph showing surface crack initiation within globular  $\alpha$  phase ( $R = -1$ ,  $\sigma_{\max} = 650$  MPa, and  $N_f = 1 \times 10^4$  cycles).<sup>[41]</sup>

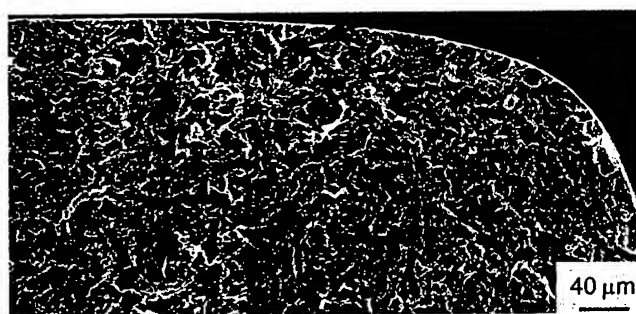


Fig. 13—Scanning electron micrograph showing subsurface crack initiation (see arrow) on a fatigue fracture surface of a modified  $K_B$  specimen (HCF step test at  $R = 0.1$ ,  $\sigma_{\max} = 475$  MPa, and  $N_f = 5.3 \times 10^7$  cycles).

mean stress for, e.g., the  $10^7$ -cycle fatigue limit. Figure 14 shows such a Goodman diagram<sup>[42]</sup> constructed from the  $10^7$ -cycle fatigue limit data for the bimodal Ti-6Al-4V alloy presented in Figure 11. It can be seen that, as the mean stress becomes more tensile, the allowable stress amplitude is reduced and can be plotted as a nearly linear decrease from the fatigue limit at  $R = -1$  to the tensile strength ( $\sigma_a = 0$ ). Furthermore, at very high mean-stress values, the maximum stress level can be seen to approach the yield stress of the material (Figure 14).



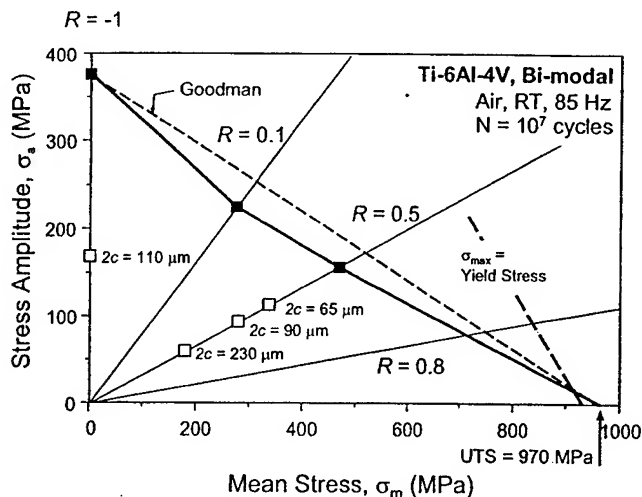


Fig. 14—Modified Goodman diagram showing the mean and alternating stress to give a life of  $N_F = 1 \times 10^7$  cycles in bimodal Ti-6Al-4V, based on smooth-bar specimen tests (closed symbols). Also shown are data for the small-crack HCF threshold testing at  $\Delta K = 1.5 \text{ MPa}\sqrt{\text{m}}$  tests (open symbols).

## 2. Fatigue crack growth of small and large cracks

For the alternative damage-tolerant design approach against HCF, baseline data of near-threshold fatigue crack growth rates and fatigue thresholds are required, ideally for both naturally initiated small cracks and through-thickness large cracks.

Smooth-bar hourglass specimens were precracked at a load ratio of  $R = -1$  (to avoid subsurface crack initiation at positive  $R$  ratios); 10,000 cycles at a stress amplitude of 650 MPa resulted in  $\sim 10$  to 15 surface cracks, with surface lengths ranging from  $\sim 45$  to 60  $\mu\text{m}$ . The subsequent crack-growth behavior of the naturally initiated small cracks was then monitored optically at a maximum stress of 550 MPa at  $R = 0.1$ , i.e., 50 MPa above the  $10^7$ -cycle fatigue limit.<sup>[41]</sup> The resulting growth rates as a function of the applied stress-intensity range are shown in Figure 15 and are compared to corresponding large-crack results based on C(T) testing. Characteristic of the small-crack effect,<sup>[43,44,45]</sup> the growth rates of the small cracks were up to one order of magnitude higher than those of equivalent large cracks at the same applied stress-intensity range.

Since the majority of the small cracks have dimensions larger than the characteristic size-scales of the microstructure, it is reasoned that one of the prime reasons for the small-crack effect is the reduced role of crack-tip shielding (e.g., surface roughness-induced crack closure) due to their limited crack wake (e.g., Reference 46). Based on this consideration, two types of large-crack tests were performed to minimize the extent of closure, in order to simulate the small-crack results on conventional C(T) specimens.<sup>[47]</sup> Specifically, this involved load shedding to approach the threshold using (1) constant- $R$  testing at high load ratios ( $R \sim 0.8$ ) and (2) constant- $K_{\text{max}}$ /increasing  $K_{\text{min}}$  testing, both procedures that tend to minimize crack wedging by ensuring that the crack-tip opening displacements (CTODs) are large enough to limit any premature contact of the crack surfaces upon unloading, i.e., the minimum CTOD in the loading cycle is larger than the dimension of the fracture-surface roughness. Results are compared to the naturally initiated small-crack data in Figure 15.

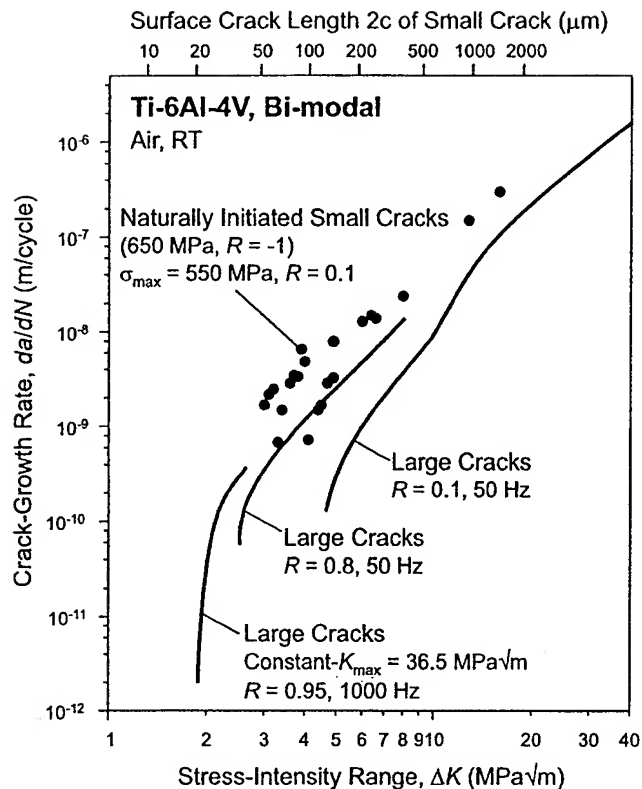


Fig. 15—Variation in crack-growth rates,  $da/dN$ , with the applied stress-intensity range,  $\Delta K$ , for naturally initiated small cracks ( $\sim 45$  to 1000  $\mu\text{m}$ )<sup>[41]</sup> and through-thickness large cracks ( $> 5 \text{ mm}$ ) in bimodal Ti-6Al-4V. Small cracks were initiated at  $\sigma_{\text{max}} = 650 \text{ MPa}$  ( $R = -1$ ). Large-crack growth data for  $R \leq 0.8$  were derived from constant load-ratio tests, whereas for  $R \geq 0.8$ , constant- $K_{\text{max}}$ /increasing- $K_{\text{min}}$  testing was used.

Although the growth rates of the small cracks still exceed those of the "closure-free" large-cracks, the thresholds determined using the constant  $K_{\text{max}}$ /increasing  $K_{\text{min}}$  large-crack tests appear to provide a worst-case for both large- and small-crack results. As discussed elsewhere,<sup>[9]</sup> the threshold value of  $\Delta K_{\text{TH}} = 1.9 \text{ MPa}\sqrt{\text{m}}$  (at  $4 \times 10^{-2} \text{ m/cycle}$ ), at a maximum load ratio of  $R = 0.95$  (above which  $K_{\text{max}} > K_{\text{IC}}$ ), is lower than the stress-intensity range required for the growth of naturally initiated small cracks ( $\sim 2.9 \text{ MPa}\sqrt{\text{m}}$ ) and, as such, is considered as a *practical* lower-bound threshold for this alloy.

Further verification of this worst-case threshold concept was afforded by smooth-bar experiments, where specimens were naturally precracked at  $R = -1$  (stress amplitude of 650 MPa) to different initial surface crack lengths. The stress amplitude was then changed to give a  $\Delta K$  value of  $1.5 \text{ MPa}\sqrt{\text{m}}$  (at  $R = -1$  and 0.5) and the specimens were cycled for  $\sim 4$  to  $5 \times 10^7$  cycles. The test conditions are listed in Table IV. In all cases, no crack growth was detected at  $\Delta K = 1.5 \text{ MPa}\sqrt{\text{m}}$ .

The higher growth rates of the naturally initiated small cracks, compared to the closure-free large cracks, are presumed to be associated with biased statistical sampling of the microstructure. The natural crack initiation process allows for sampling of a very large area of the specimen for more favorable microstructural orientations with respect to crack initiation and growth, compared to that of the large cracks, which essentially samples an average of all microstructural orientations.

Table IV. Small-Crack HCF threshold of  $\Delta K = 1.5 \text{ MPa } \sqrt{\text{m}}$  Test\*

Load Ratio (R)	Initial Surface Crack Length, $2c$ ( $\mu\text{m}$ )	$\sigma_a$ (MPa)	$\sigma_m$ (MPa)	$\sigma_{\max}$ (MPa)	$\Delta N$ (Cycles)
$R = -1$	110	170	0	170	$>5 \times 10^7$
$(\Delta K \text{ based on tensile range})$ $R = 0.5$	65	112.5	337.5	450	$>4 \times 10^7$
	90	93.75	281.25	375	$>4 \times 10^7$
	230	60	180	240	$>4 \times 10^7$

\*(Precracking: 650 MPa,  $R = -1$ , and  $N = 10,000$  to 15,000 cycles);  $\sigma_a$ : stress amplitude,  $\sigma_m$ : mean stress, and  $\sigma_{\max}$ : maximum stress

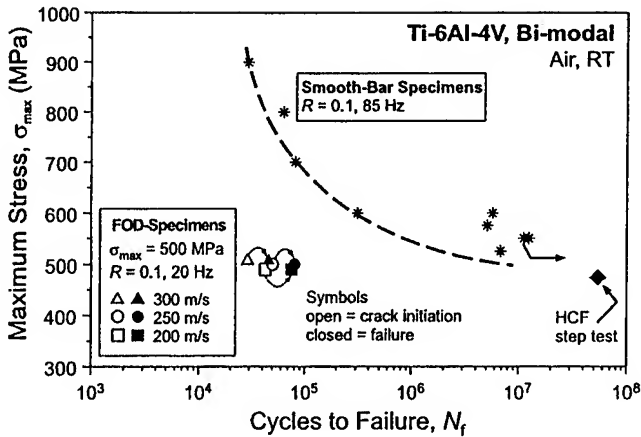


Fig. 16—The effect of FOD on the S-N data for bimodal Ti-6Al-4V, showing sharply reduced lifetimes. In addition, the result of the HCF step test at  $R = 0.1$  is shown for smooth modified  $K_B$  specimen

### C. Effect of FOD

The overall effect of FOD, simulated by impacting fatigue-test specimens with high-velocity steel shot, was to markedly reduce the fatigue life compared to that obtained with undamaged smooth-bar specimens (Figure 16). At a nominal (far-field) maximum stress of 500 MPa ( $R = 0.1$ ), small surface cracks ( $c \sim 50 \mu\text{m}$ ) were initiated at the FOD impact sites within  $\sim 3$  to  $5 \times 10^4$  cycles, with final failure occurring between  $\sim 4$  to  $8 \times 10^4$  cycles. These results show that the fatigue lives were drastically reduced by over two orders of magnitude by FOD, compared to the undamaged smooth-bar properties.

As discussed previously, the reduction in fatigue strength due to FOD can be considered principally in terms of earlier crack initiation due to four salient factors.

- (1) **Stress concentration:** The FOD creates stress-raising notches; their geometry influences the local stress fields in the vicinity of the impact sites.
- (2) **The FOD-initiated microcracking:** At the highest impact velocities (and in brittle alloys<sup>[14]</sup>), microcracks may be formed in the damage zone and provide a potent site for the initiation of HCF cracking.
- (3) **Residual stresses:** The FOD induces a residual stress state, both tensile and compressive, surrounding the impact site due to plastic deformation associated with the impact.
- (4) **Microstructure:** The FOD changes the nature of the microstructure at the damage site, again due to plastic deformation associated with the impact.

### 1. Fatigue crack initiation

Examples of initiation sites of small surface cracks are shown in Figure 17(a) for a 250 m/s impact and in Figure 17(b) for a 300 m/s impact. Based on the results from seven impacted samples, it was found that cracks tended to initiate at the bottom of the indent for the lower-velocity impacts (200 and 250 m/s) and at the crater rim for the higher-velocity impacts (300 m/s). The position of the crack front during crack extension, both depthwise and on the surface, is indicated in these micrographs; this was determined from surface crack-length measurements during the test and subsequent fractography (as the local crack front is oriented perpendicular to the "river markings").

For the 200 and 250 m/s impacts, fatigue crack initiation can be seen on the surface at the base of the indent (Figure 18) and is explained by the stress concentration from the notch geometry. For these impact conditions, the notches are relatively shallow, with  $k_t$  values of  $\sim 1.4$ , close to the corresponding elastic stress-concentration factors of  $k_t \sim 1.4$  to 1.5 (Table III).

For the 300 m/s impacts, initiation conversely occurred at the crater rim. Indeed, impact studies by Gros *et al.*<sup>[16]</sup> also reported fatigue crack initiation both at the base and rim of high-velocity impacts in medium-carbon steel. Similarly, Ruschau *et al.*<sup>[17]</sup> observed crack initiation at the rim location for 60 deg impact angles (glass beads) on simulated fan blade leading-edge specimens of Ti-6Al-4V. For crack initiation at the rim, the stress concentration due to gross indentation geometry is clearly not the only effect, as the location of the maximum stress-concentration factors is still at the base ( $k_t \sim 1.6$  and  $k_f \sim 1.54$  at the base, compared to a value of  $k_t \sim 1.25$  at the crater rim). Here, the tensile residual stresses and highly deformed microstructure play an additional role. The tensile hoop stresses are critical, as they superimpose onto the nominally applied stresses, resulting in higher maximum and mean stresses and, in turn, earlier crack initiation and faster crack growth rates. However, more importantly, at these high impact velocities, small microcracks were detected in the vicinity of the crater rim (Figure 8(b)) and clearly provide the preferred site for fatigue-induced crack propagation (Figure 8(c)). The fact that such microcracks only develop in this alloy at the highest impact velocities strongly implies that the simulation of FOD using lower-velocity impacts will not necessarily involve all the damage processes associated with the phenomenon.

The presence of adiabatic shear bands does not appear to play a significant role in the initiation process of the fatigue cracks. This is thought to be due to the fact that, at the prime locations for crack initiation, *i.e.*, at the base of the indent for the 200 to 250 m/s impacts and at the crater rim for 300



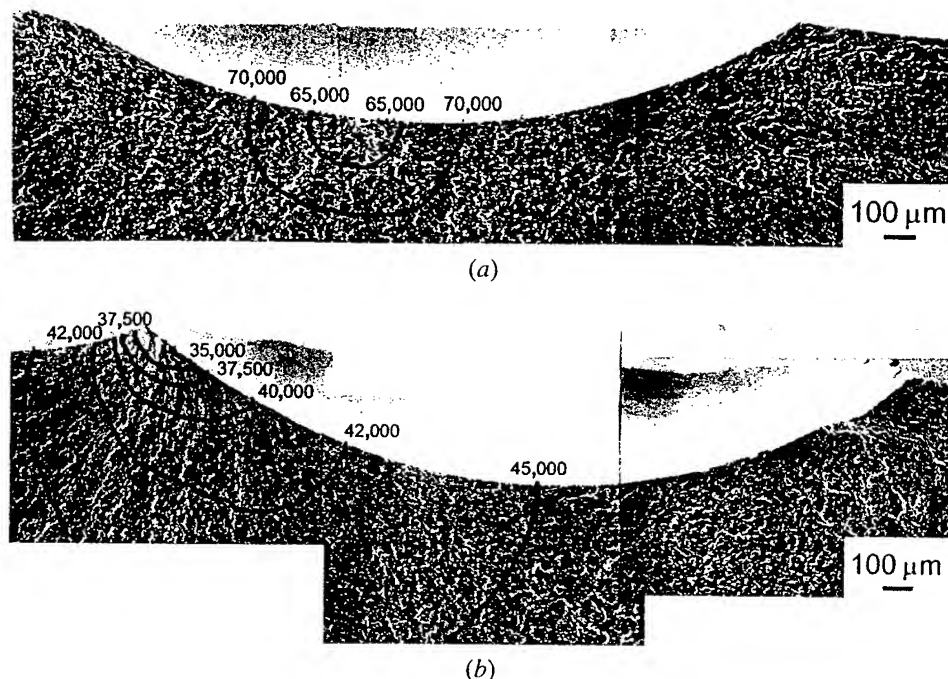


Fig. 17—Scanning electron micrographs showing the growth of fatigue cracks initiated at FOD impact sites. The progressive position of the crack front is marked on the fracture surface to indicate the initiation sites and crack shapes during crack extension for (a) 250 m/s impact and (b) 300 m/s impact.

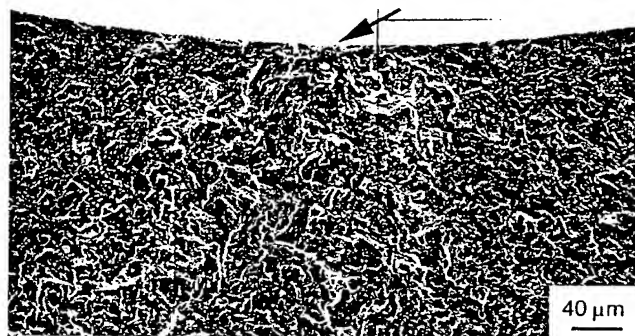


Fig. 18—Scanning electron micrograph of the fracture surface following fatigue of a 250 m/s FOD impacted  $K_B$  specimen, showing surface crack initiation (marked by the arrow) at the base of the indent ( $\sigma_{\max} = 500$  MPa,  $R = 0.1$ , and  $N_F = 7.9 \times 10^4$  cycles).

m/s impacts, the tangentially aligned shear bands are oriented parallel to the applied stress axis.

## 2. Fatigue crack propagation

The growth rates of the small cracks emanating from the 200 to 300 m/s impact sites are compared as a function of the stress-intensity range (ignoring the stress concentration and residual stress effects (open symbols)) in Figure 19 with the baseline growth-rate data for large ( $>5$ -mm long) and naturally initiated small ( $\sim 45$  to  $1000 \mu\text{m}$ ) cracks; also shown are the surface-crack lengths, of the small cracks. It can be seen that both the naturally initiated and FOD-initiated small-crack growth rates are within the same scatter band and are roughly one order of magnitude faster than the corresponding large-crack results. Furthermore, it can be seen that the small-crack data tend to merge with the large-crack results as the crack size increases, specifically above  $\Delta K = 10 \text{ MPa}\sqrt{\text{m}}$ . With respect to the fatigue crack-growth

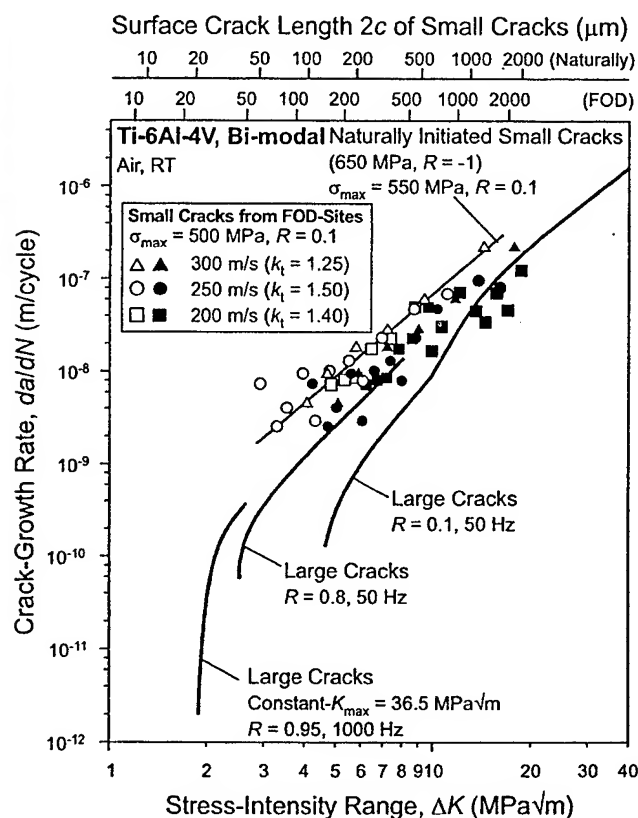


Fig. 19—Comparison of the variation in crack-growth rates,  $da/dN$ , with the applied stress-intensity range,  $\Delta K$ , for FOD-initiated small cracks ( $\sim 45$  to  $1000 \mu\text{m}$ ) with that for naturally initiated small cracks<sup>[41]</sup> and through-thickness large cracks in bimodal Ti-6Al-4V. Stress intensity for FOD initiated crack growth has been corrected for the stress concentration associated with the indent using the  $K$  solution of Lukás<sup>[36]</sup> and stress-concentration factors from Nisida and Kim<sup>[35]</sup> (closed symbols); noncorrected data are shown for comparison (open symbols).

thresholds, however, in the data collected to date, no FOD-initiated cracks have been observed in the studies on Ti-6Al-4V with a bimodal microstructure below a stress-intensity range of  $\Delta K = 2.9 \text{ MPa}\sqrt{\text{m}}$ , which is over 50 pct higher than the worst-case (large-crack) threshold of  $1.9 \text{ MPa}\sqrt{\text{m}}$ . Consequently, we conclude that fatigue crack-propagation thresholds for large cracks, determined under conditions that minimize crack closure, can be used as a practical lower bound for the threshold stress intensities for naturally initiated and FOD-initiated small cracks in this alloy.

Also shown in Figure 19 (by the closed symbols) are the results of the initial assessment to correct for the effect of stress concentration on the calculation of the stress intensities, and, hence, the crack growth rates, of the FOD-initiated small cracks using the Lukáš<sup>[36]</sup> solution (Eq. [2]). The overall effect is that the correction yields a closer correspondence between data from the high-load-ratio large cracks and the FOD-initiated small cracks.

However, at crack sizes above  $2c \sim 100 \mu\text{m}$ , the crack growth rates of the FOD-initiated small cracks are slower than those of the naturally initiated small cracks. Although this effect may be associated with experimental uncertainty, it is reasoned that the effect most probably results from the presence of compressive residual hoop stresses throughout the impact-damaged zone. This implies that, whereas FOD may promote crack initiation and early small-crack growth due to the tensile residual stresses and (at high impact velocities) to microcracking local to the surface at the base and rim of the indent, subsequent crack growth may, indeed, be retarded compared to naturally initiated cracks, due to the presence of the compressive residual stresses.

There is an additional influence of FOD from the presence of the impact-damaged microstructure, which can be seen by comparing the growth mechanisms of small cracks in the smooth-bar (Figure 13) and FOD (Figure 18) specimens. In smooth-bar specimens, naturally initiated small cracks propagate predominantly in slip bands within the primary  $\alpha$  phase; this is attributed to the planar-slip distribution and the relatively large slip length associated with the inherent crystallographic texture (Figure 2) and the high volume fraction of primary  $\alpha$  phase.<sup>[48]</sup> In impacted samples, conversely, the slip distribution is more homogeneous, such that this planar slip-band cracking mechanism is not seen, presumably because the FOD-induced plastic deformation breaks up easy crack paths along single slip bands. The effect of this change in the planarity of slip on the small crack-growth behavior in impact-damaged microstructures is currently under examination. It is known from studies<sup>[49,50]</sup> on high-strength aluminum alloys that crack propagation involving inhomogeneous planar (single) slip is much faster than crack propagation involving homogeneous (multiple) slip ahead of the crack tip.

## V. SUMMARY AND CONCLUSIONS

An increasing proportion of HCF-related failures of military gas-turbine engines has inspired a recent re-examination of the design methodologies for HCF-critical components. In view of the in-service conditions, i.e., small crack sizes, high mean loads, and high-frequency ( $>1 \text{ kHz}$ ) vibratory loading, damage-tolerant design methodologies based on the concept of a threshold for no fatigue crack growth would appear to offer the best approach. As FOD has been identified

as one of the prime sources of HCF-related failures, the current study has focused on the role of (simulated) FOD in influencing fatigue crack growth thresholds and early crack growth of both large and small cracks in an aeroengine fan blade titanium alloy, Ti-6Al-4V, processed with a bimodal microstructure. Based on this work, the following conclusions can be made.

1. The FOD, simulated by the high-velocity (200 to 300 m/s) impact of steel spheres on a flat surface, results in a significant loss in resistance to HCF. At the smooth-bar  $10^7$ -cycle fatigue limit, for example, the crack-initiation lives of FOD samples were less than  $4 \times 10^4$  cycles, three orders of magnitude lower than the lifetimes for undamaged samples.
2. The primary role of FOD is to provide preferred sites for the premature initiation of fatigue cracks. For 200 to 250 m/s impacts on a bimodal Ti-6Al-4V alloy, such cracking initiated at the base of the indentations, whereas, at 300 m/s, initiation occurred at the crater rim.
3. The detrimental effect of FOD results from (1) the stress concentration associated with the FOD indentation, (2) the presence of small microcracks at the crater rim of the damaged zone (seen only at the highest impact velocities), (3) the localized presence of tensile residual hoop stresses at the base and rim of the indent sites, and (4) microstructural damage from FOD-induced plastic deformation.
4. The subsequent propagation of small cracks within the damage zone, however, is somewhat slower than the corresponding propagation rates of naturally initiated small cracks at the same applied stress-intensity levels. This appears to be associated with two effects, namely, (1) the presence of compressive residual stresses throughout most of the damaged zone, and (2) the fact that FOD-induced plastic deformation tends to suppress planar slip-band cracking by making the slip distribution more homogeneous.
5. No crack growth from the FOD impact (or natural-initiation) sites has been observed to date at  $\Delta K$  values below  $\sim 2.9 \text{ MPa}\sqrt{\text{m}}$ . This is over 50 pct higher than the closure-free, worst-case threshold value of  $\Delta K_{TH} = 1.9 \text{ MPa}\sqrt{\text{m}}$ , defined for large cracks in bimodal Ti-6Al-4V at the highest possible load ratio. The worst-case, large-crack threshold can thus be used as a practical lower bound to FOD-initiated cracking in this alloy.

## ACKNOWLEDGMENTS

This work was supported by the Air Force Office of Scientific Research, Grant No. F49620-96-1-0478, under the auspices of the Multidisciplinary University Research Initiative on *High Cycle Fatigue* to the University of California, Berkeley. We acknowledge additional support from the Hertz Foundation for BLB in the form of a graduate fellowship. Tensile test, texture measurements, and smooth-bar testing were conducted at the Technical University of Hamburg-Harburg (Germany), by JOP in collaboration with Dr. J.A. Hines and Professor G. Lütjering. Special thanks are due to Professor Werner Goldsmith (UCB), for providing the compressed-gas gun facility, and to Professor J.W. Hutchinson, J.P. Campbell, and Dr. J.M. McNaney for helpful discussions.

## REFERENCES

1. B.A. Cowles: *Int. J. Fract.*, 1996, vol. 80, pp. 147-63.
2. T. Nicholas and J.R. Zuiker: *Int. J. Fract.*, 1996, vol. 80, pp. 219-35.
3. J.M. Larsen, B.D. Worth, C.G. Annis, Jr., and F.K. Haake: *Int. J. Fract.*, 1996, vol. 80, pp. 237-55.
4. R.O. Ritchie: *Proc. ASME Aerospace Division*, J.C.I. Chang, J. Coulter, D. Brei, W.H.G. Martinez, and P.P. Friedmann, eds., ASME, Fairfield, NJ, 1996, AD-vol. 52, pp. 321-33.
5. *Erosion, Corrosion and Foreign Object Damage Effects in Gas Turbines*, AGARD Conf. Proc. No. 558, North Atlantic Treaty Organization, Advisory Group for Aerospace Research and Development, Propulsion and Energetics Panel, Neuilly-sur-Seine, France, 1994.
6. T. Nicholas, J.P. Barber, and R.S. Bertke: *Exp. Mech.*, 1980, Oct., pp. 357-64.
7. S.J. Hudak, Jr., G.G. Chell, T.S. Rennick, R.C. McClung, and D.L. Davidson: *Proc. 4th Nat. Turbine Engine HCF Conf., CD Rom, Session 10, Materials Damage Tolerance IV*, 1999, pp. 7-17.
8. P. Gravett, R. Bellows, T. Dunyak, D. Herrmann, and S. Hudak, Jr.: *Proc. 4th Nat. Turbine Engine HCF Conf., CD Rom, Session 10, Materials Damage Tolerance IV*, 1999, pp. 1-6.
9. O. Roder, J.O. Peters, B.L. Boyce, A.W. Thompson, and R.O. Ritchie: *Proc. 4th Nat. Turbine Engine HCF Conf., CD Rom, Session 10, Materials Damage Tolerance IV*, 1999, pp. 41-50.
10. R.O. Ritchie, D.L. Davidson, B.L. Boyce, J.P. Campbell, and O. Roder: *Fat. Fract. Eng. Mater. Struct.*, 1999, vol. 22, pp. 621-31.
11. N.E. Frost: *Proc. Inst. Mech. Eng.*, 1959, vol. 173, pp. 811-27.
12. N.E. Dowling: *Fat. Eng. Mat. Struct.*, 1979, vol. 2, pp. 129-39.
13. M.H. El Haddad, T.H. Topper, and K.N. Smith: *Eng. Fract. Mech.*, 1979, vol. 11, pp. 573-84.
14. T.S. Harding, J.W. Jones, P.S. Steiff, and T.M. Pollock: *Scripta Mater.*, 1999, vol. 40, pp. 445-49.
15. J.L. Hamrick II, S. Mall, and T. Nicholas: *Proc. 4th Nat. Turbine Engine HCF Conf., CD Rom, Session 8, Materials Damage Tolerance IV*, 1999, pp. 38-48.
16. V. Gros, B.A. Taweel, M. Ceretti, C. Prioul, and A. Lodini: *Proc. 4th Eur. Conf. on Residual Stresses*, S. Denis, J.-L. Lebrun, B. Bourniquel, M. Barral, and J.-F. Flavenot, eds., SF2M, ENSAM, Cluny en Bourgogne, France, 1996, pp. 567-75.
17. J.J. Ruschau, S.R. Thompson, J.J. Kleck, and T. Nicholas: *Proc. 4th Nat. Turbine Engine HCF Conf., CD Rom, Session 8, Materials Damage Tolerance IV*, 1999, pp. 28-37.
18. K.-P. Hornauer, H.H. Jühc, A. Klinkenberg, and P. Starker: *Härtereitechnische Mitteilungen*, 1981, vol. 36, pp. 322-26.
19. M. Kobayashi, T. Matsui, and Y. Murakami: *Int. J. Fatigue*, 1998, vol. 20, pp. 351-57.
20. G.B. Sinclair, P.S. Follansbee, and K.L. Johnson: *Int. J. Solids Struct.*, 1985, vol. 21, pp. 865-88.
21. X. Chen and J.W. Hutchinson: "Foreign Object Damage and Fatigue Cracking on the Shallow Indentation," Harvard University Report No. ME 358, Cambridge, MA, Nov. 1999.
22. C. Hardy, C.N. Baronet, and G.V. Tordion: *Int. J. Num. Meth. Eng.*, 1971, vol. 3, pp. 451-62.
23. C.J. Studman and J.E. Field: *J. Mater. Sci.*, 1977, vol. 12, pp. 215-18.
24. G. Lütjering: *Mater. Sci. Eng.*, 1998, vol. A243, pp. 32-45.
25. A.W. Thompson: in *Fatigue Behavior of Titanium Alloys*, R.R. Boyer, D. Eylon, and G. Lütjering, eds., TMS, Warrendale, PA, 1999, pp. 23-31.
26. W.J. Evans: *Mater. Sci. Eng.*, 1999, vol. A263, pp. 160-75.
27. L. Wagner and G. Lütjering: *Proc. 2nd Int. Conf. Shot Peening*, H.O. Fuchs, ed., American Shot Peening Society, Paramus, NJ, 1984, pp. 194-200.
28. L. Wagner and G. Lütjering: *Proc. 2nd Int. Conf. Shot Peening*, H.O. Fuchs, ed., American Shot Peening Society, Paramus, NJ, 1984, pp. 201-07.
29. H. Gray, L. Wagner, and G. Lütjering: in *Shot Peening*, H. Wohlfahrt, R. Kopp, and O. Vöhringer, eds., DGM, Oberursel, Germany, 1987, p. 467.
30. D. Eylon: "Summary of the Available Information on the Processing of the Ti-6Al-4V HCF/LCF Program Plates," University of Dayton Report, University of Dayton, Dayton, OH, 1998.
31. J.C. Newman, Jr. and I.S. Raju: *Eng. Fract. Mech.*, 1981, vol. 15, pp. 185-92.
32. J.M. Morgan and W.W. Milligan: in *High Cycle Fatigue of Structural Materials*, W.O. Soboyejo and T.S. Srivatsan, eds., TMS, Warrendale, PA, 1997, pp. 305-12.
33. R.O. Ritchie and W. Yu: in *Small Fatigue Cracks*, R.O. Ritchie and J. Lankford, eds., TMS, Warrendale, PA, 1986, pp. 167-89.
34. A. Coles, R.E. Johnson, and H.G. Popp: *J. Eng. Mater. Technol.*, 1976, pp. 305-15.
35. M. Nisida and P. Kim: *Proc. 12th Nat. Congr. Applied Mechanics*, 1962, pp. 69-74.
36. P. Lukáš: *Eng. Fract. Mech.*, 1987, vol. 26, pp. 471-73.
37. I.M. Hutchings: in *Materials Behavior under High Stress and Ultra High Loading Rates*, J. Mescall and V. Weiss, eds., Plenum Press, New York, NY, 1983, pp. 161-96.
38. S.P. Timothy and I.M. Hutchings: *Acta Metall.*, 1985, vol. 33, pp. 667-76.
39. S.P. Timothy and I.M. Hutchings: *Eng. Fract. Mech.*, 1984, vol. 7, pp. 223-27.
40. S.P. Timothy and I.M. Hutchings: *Proc. of the 3rd Conf. on the Mechanical Properties of Materials at High Rates of Strain*, The Institute of Physics, London, 1984, pp. 397-404.
41. J.A. Hines, J.O. Peters, and G. Lütjering: in *Fatigue Behavior of Titanium Alloys*, R.R. Boyer, D. Eylon, and G. Lütjering, eds., TMS, Warrendale, PA, 1999, pp. 15-22.
42. J. Goodman: *Mechanics Applied to Engineering*, Longmans, Green & Co., Ltd., London, 1899.
43. *Small Fatigue Cracks*, R. O. Ritchie and J. Lankford, eds., TMS-AIME, Warrendale, PA, 1986.
44. *The Behaviour of Short Fatigue Cracks*, K.J. Miller and E.R. de los Rios, eds., The Mechanical Engineering Publishing Ltd., London, 1986.
45. *Short Fatigue Cracks*, K.J. Miller and E.R. de los Rios, eds., The Mechanical Engineering Publishing Ltd., London, 1992.
46. R.O. Ritchie and J. Lankford: *Mater. Sci. Eng.*, 1986, vol. 84, pp. 11-16.
47. R.O. Ritchie, B.L. Boyce, J.P. Campbell, O. Roder, A.W. Thompson, and W.W. Milligan: *Int. J. Fatigue*, 1999, vol. 21, pp. 653-62.
48. J.A. Hines, J.O. Peters, and G. Lütjering: *Proc. 9th World Congr. on Titanium*, I. Gorynin, ed., TMS, Warrendale, PA, 1999, in press.
49. J.O. Peters, A. Gysler, and G. Lütjering: *Proc. ICAA-6, Aluminum Alloys*, T. Sato, S. Kumai, T. Kobayashi, and Y. Murakami, eds., Japan Inst. Light Metals, Tokyo, Japan, 1998, vol. 3, pp. 1427-32.
50. J.O. Peters, A. Gysler, and G. Lütjering: *Fatigue '99*, Proc. 7th Int. Congr. on Fatigue, X.-R. Wu and Z.-G. Wang, eds., Higher Education Press, Beijing/EMAS Ltd., Warley, United Kingdom, 1999, vol. 2, pp. 1009-14.



PERGAMON

Engineering Fracture Mechanics 67 (2000) 193–207

Engineering  
Fracture  
Mechanics

www.elsevier.com/locate/engfracmech

# Influence of foreign-object damage on crack initiation and early crack growth during high-cycle fatigue of Ti-6Al-4V

J.O. Peters, R.O. Ritchie \*

*Department of Materials Science and Mineral Engineering, University of California, 463 Evans Hall 1760, Berkeley, CA 94720-1760, USA*

Received 10 January 2000; received in revised form 4 May 2000; accepted 11 May 2000

## Abstract

The objective of this work is to provide a rationale approach to define the limiting conditions for high-cycle fatigue (HCF) in the presence of foreign-object damage (FOD). This study focused on the role of simulated FOD in affecting the initiation and early growth of small surface fatigue cracks in a Ti-6Al-4V alloy, processed for typical turbine blade applications. Using high-velocity (200–300 m/s) impacts of 3.2 mm diameter steel spheres on the flat surface of fatigue test specimens to simulate FOD, it is found that the resistance to HCF is markedly reduced due to earlier crack initiation. Premature crack initiation and subsequent near-threshold crack growth is primarily affected by the stress concentration associated with the FOD indentation and the presence of small microcracks in the damaged zone (seen only at the higher impact velocities). Furthermore, the effect of residual stresses and microstructural damage from FOD-induced plastic deformation at the indent sites are assessed in terms of fatigue strength degradation. It is shown that FOD-initiated cracks, that are of a size comparable with microstructural dimensions, can propagate at applied stress-intensity ranges on the order of  $\Delta K \sim 1 \text{ MPa}\sqrt{\text{m}}$ , i.e., a factor of roughly two less than the “worst-case” threshold stress-intensity range in Ti-6Al-4V for a crack of a size large compared to microstructural dimensions (a “continuum-sized” crack). Correspondingly, for FOD-initiated failures, where the critical condition for HCF must be defined in the presence of microstructurally small cracks, the Kitagawa-Takahashi diagram, with the limiting conditions of the stress-concentration corrected  $10^7$ -cycle fatigue limit and the “worst-case”  $\Delta K_{\text{TH}}$  fatigue threshold, is proposed as a basis for design against FOD-induced HCF failures. © 2000 Elsevier Science Ltd. All rights reserved.

**Keywords:** Foreign-object damage; High-cycle fatigue; Fatigue-crack growth threshold; Small cracks; Ti-6Al-4V

## 1. Introduction

The high-cycle fatigue (HCF) of aircraft gas-turbine engine components has traditionally been analyzed using a modified Goodman diagram approach; however, because of an increasing incidence of late of HCF-related engine failures, particularly involving titanium alloy fan and compressor blades, this approach is currently being re-evaluated [1–3]. Three major concerns have been identified, namely (i) interactions of low-cycle fatigue (LCF) and HCF loading, (ii) foreign-object damage (FOD) and (iii) fretting. All these

\* Corresponding author. Tel.: +1-510-486-5798; fax: +1-510-486-4995.

E-mail address: roritchie@lbl.gov (R.O. Ritchie).

factors can lead to premature fatigue crack initiation and growth, which can result in seemingly unpredictable *in service* failures, due to the high-frequency vibratory loading ( $>1$  kHz) involved [3]. Consequently, design against HCF based on the damage-tolerant concept of a fatigue-crack growth threshold ( $\Delta K_{TH}$ ) for no crack growth would appear to offer a preferred approach; however, such thresholds must reflect representative HCF conditions of high frequencies, small crack sizes and, depending on the blade span location, very high mean stress levels [1–5].

FOD, from bird strikes or hard body impacts, e.g., stones, primarily on the fan blades, can cause (depending on the impact severity) immediate blade fracture [6] or damage from stress-raising notches [6–8], cracks [8] and deformation of the microstructure. In a recent study on Ti–6Al–4V [9] where FOD was simulated by the high-velocity impact of steel shot on a flat surface, such damage was found to markedly reduce the fatigue strength principally by causing the earlier initiation of fatigue cracks. Limiting conditions for potential HCF-related turbine blade failures were proposed based on the concept of a “worst-case” threshold for no fatigue-crack growth that applies strictly for “continuum-sized” cracks, i.e., large or physically small cracks with dimensions larger than the characteristic microstructural size-scales. The mechanistic effect of FOD on the fatigue-crack growth thresholds was assessed in terms of (i) stress concentration associated with the FOD indentation, (ii) FOD-induced small cracks in the damage zone, (iii) localized presence of impact damage associated residual stresses at locations of the preferred sites for crack initiation, and (iv) microstructural damage from FOD-induced plastic deformation. Of particular note was the observation of the formation of small microcracks in the damaged region of the higher velocity impacts; such microcracks provided preferred sites for premature crack initiation on subsequent fatiguing. However, the quantitative effect of these FOD-induced microcracks on the fatigue-crack growth threshold was not investigated.

The objective of the current study is specifically to examine the role of FOD-induced microcracks ( $\sim 2$ – $25$   $\mu\text{m}$  in surface length) on the earliest stages of FOD-induced fatigue failures in the same Ti–6Al–4V alloy,  $\alpha + \beta$  processed for typical turbine blade applications. This is achieved by defining the limiting conditions for crack initiation and early fatigue-crack growth in the presence of such microcracks, in comparison to the fatigue threshold behavior of naturally initiated small ( $2c \sim 45$ – $1000$   $\mu\text{m}$ ) and large through-thickness ( $>5$  mm) cracks in undamaged material.

## 2. Experimental procedures

### 2.1. Material

The titanium alloy Ti–6Al–4V under study, of chemical composition given in Table 1, was part of a set of forgings produced specifically for the US Air Force sponsored programs on HCF; its  $\beta$ -transus temperature is  $\sim 996^\circ\text{C}$ . Mill annealed 63.5 mm diameter bar stock material was  $\alpha + \beta$  forged in one stroke at  $938^\circ\text{C}$  on a closed-end channel die to a plate size of  $400 \times 150 \times 20$  mm<sup>3</sup>, followed by air-cooling. Subsequently, the forging plates were solution treated in an air furnace at  $927^\circ\text{C}$  for 1 h followed by fan-air cooling; this resulted in a cooling rate of  $\sim 200^\circ\text{C}/\text{min}$ . Finally, the plates were stress relieved in vacuo for 2 h at  $705^\circ\text{C}$ . Additional material and processing details are given in Ref. [10]. The resulting bimodal microstructure of the plate material, consisting of a volume fraction of  $\sim 60\%$  primary  $\alpha$  (diameter  $\sim 20$   $\mu\text{m}$ ) within a lamellar  $\alpha + \beta$  matrix, is shown in Fig. 1; this condition has also been termed “solution treated and overaged” (STOA).

Table 1  
Chemical composition of Ti–6Al–4V bar stock material in wt.% [10]

Ti	Al	V	Fe	O	N	H
Bal.	6.30	4.19	0.19	0.19	0.013	0.0041

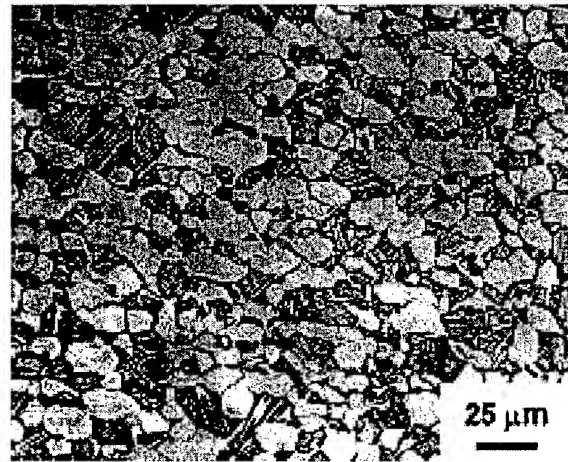


Fig. 1. Optical micrograph of the bimodal (STOA) microstructure of forged Ti-6Al-4V plate material (etched in 3.5% HNO<sub>3</sub>–5% HF).

Table 2  
Uniaxial tensile properties of bimodal Ti-6Al-4V<sup>a</sup>

$E$ (GPa)	$\sigma_{0.2}$ (MPa)	UTS (MPa)	$\sigma_F$ (MPa)	Tens. el. (%)	RA (%)
110	915	965	1310	19	45

<sup>a</sup>  $E$ : Young's modulus,  $\sigma_{0.2}$ : yield stress, UTS: ultimate tensile strength,  $\sigma_F$ : true fracture stress, Tens. el.: tensile elongation, RA: reduction of area at fracture; strain rate  $8 \times 10^{-4} \text{ s}^{-1}$ .

To investigate microstructural changes caused by FOD impacts, transmission electron microscopy (TEM) foils were prepared by mechanical grinding in water and then thinned in a Fischione ion mill at 5 kV. For the impacted condition, the TEM foil location was parallel to the base of the indent (depth below indent is approximately 150  $\mu\text{m}$ ).

Uniaxial tensile properties, based on testing performed in the  $L$ -direction (parallel to the length of the plate) at an initial strain rate of  $8 \times 10^{-4} \text{ s}^{-1}$ , are listed in Table 2.

## 2.2. Simulation of foreign-object damage

Foreign-object damage was simulated by firing 3.2 mm diameter chrome-hardened steel spheres onto a flat specimen surface of tensile fatigue (so-called modified  $K_B$ ) specimens at an angle of  $90^\circ$  (normal impact, Fig. 2) at velocities of 200, 250 and 300 m/s using a compressed-gas gun facility. Impact velocities of 200–300 m/s represent typical *in-service* impact velocities on aircraft engine fan blades. Simulated impact crater dimensions by ballistic shots with 3.2 mm diameter steel spheres were found to generate damage, typical of *in-service* induced FOD notches; indeed, the resulting root radii were seen to correspond closely to surveyed *in-service* FOD root radii. [8] Further details of the 1.2 m-long compressed-gas gun test setup are given in Ref. [9].

## 2.3. Fatigue test methods

For an evaluation of the smooth-bar HCF limit of the bimodal Ti-6Al-4V alloy, in this study 1000 Hz stress-life (S–N) tests were performed on hourglass specimens (diameter: 5.4 mm). To minimize surface residual stresses and high dislocation density from specimen processing, specimens were chemically milled in a solution of 50 ml HF, 500 ml HNO<sub>3</sub> and 1500 ml H<sub>2</sub>O for 30 min at ambient temperature. Specimen axis was parallel oriented to the length of the plate ( $L$ -direction).

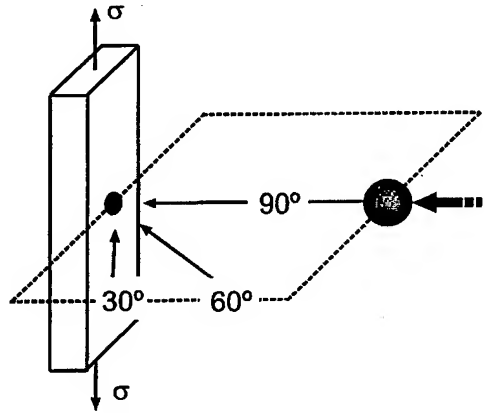


Fig. 2. Schematic illustration showing impact angles with respect to specimen geometry and loading axis for fatigue tests. In this study, a normal (90°) impact angle was chosen.

The effect of FOD on the fatigue behavior of Ti-6Al-4V was examined using modified  $K_B$  specimens. This sample has a rectangular cross-section of  $3.2 \times 7.2 \text{ mm}^2$ , a gauge length of 20 mm and cylindrical buttonhead grips; it was originally developed by GE aircraft engines to assess fatigue performance in blade loading configurations [11]. A nominally stress-free surface in the gauge section was prepared using standard stress relief and chemical-milling procedures. As noted above, steel spheres were fired at high velocity at 90° to this surface to simulate FOD. After impact, specimens were subsequently cycled at 20 Hz (sinusoidal waveform) at a load ratio of  $R = 0.1$  with a nominally maximum stress of 500 MPa. Preliminary tests were performed at nominal maximum stress values of 400 and 350 MPa at 20 Hz and 325 MPa at 1000 Hz. Throughout fatigue testing, specimens were periodically removed from the test frame and the progress of crack initiation and growth examined in a high-resolution LEO 1550 field-emission scanning electron microscope (SEM). To detect the initially small-sized FOD- and fatigue-induced surface cracks, the SEM was operated at a low beam voltage of 3 kV. For the present alloy, fractographic observations [9] revealed an approximate crack depth ( $a$ ) to surface crack length ( $2c$ ) ratio:

$$a/2c \sim 0.45 \quad (2c = 20\text{--}1000 \text{ } \mu\text{m}). \quad (1)$$

After converting the surface crack length ( $2c$ ) into crack depth ( $a$ ) according to Eq. (1), the rate of crack extension caused by the fatigue loading was computed using standard finite difference procedures (with no smoothing routines) and is expressed in terms of average crack extension per cycle ( $da/dN$ ).

Approximate local stress intensities for small cracks at base and crater rim of the indentation were calculated from the relationship of Lukáš [12] for small cracks at notches, which includes both indentation geometry and stress concentration effects:

$$\Delta K = \frac{0.7k_t}{\sqrt{1 + 4.5(a/\rho)}} \Delta\sigma\sqrt{\pi a}, \quad (2)$$

where  $k_t$  is the elastic stress-concentration factor,  $\Delta\sigma$  is the stress range,  $a$  is the crack depth, and  $\rho$  is the indentation radius. The factor of 0.7 is based on the stress-intensity boundary correction and the crack-shape correction factors [12].

Elastic stress-concentration factors,  $k_t$ , surrounding the impact damage sites were determined based on three-dimensional photoelastic experiments performed by Nisida et al. [13]. It is assumed that the pile-up of material at crater rim has no effect on  $k_t$ , because of the relatively small height of the pile-up at the crater rim. The impact crater was treated like hemispherical hollow, with a depth corresponding to the distance



Table 3  
Summary of test conditions<sup>a</sup>

Test no.	Impact velocity (m/s)	$\varnothing W$ (mm)	$\delta$ (mm)	Microcrack initiation	$k_t$ base	$k_t$ rim	$\sigma_{\max}$ (MPa)	$\Delta\sigma$ (MPa)	$N_F$ (cycles)	$k_f$
1	300	2.67	0.67	Rim	1.60	1.25	500	450	$3.4 \times 10^4$	1.65
2	300	2.67	0.67	Rim	1.60	1.25	500	450	$4.6 \times 10^4$	1.55
3	300	2.67	0.67	Base <sup>b</sup> /rim	1.60	1.25	500	450	$6.5 \times 10^4$	1.45
4	300	2.67	0.67	Rim	1.60	1.25	400	360	<sup>c</sup>	
5	300	2.67	0.67	Rim	1.60	1.25	350	315	<sup>c</sup>	
6	300	2.67	0.67	Rim	1.60	1.25	325	292.5	$1.0 \times 10^6$	1.70
7	250	2.38	0.54	Base	1.50	1.20	500	450	$8.0 \times 10^4$	1.40
8	250	2.38	0.54	Base	1.50	1.20	500	450	$7.8 \times 10^4$	1.40
9	250	2.38	0.54	Base	1.50	1.20	500	450	$8.2 \times 10^4$	1.40
10	200	2.14	0.43	Base	1.40	1.15	500	450	$7.5 \times 10^4$	1.40
11	200	2.14	0.43	Base	1.40	1.15	500	450	$1.4 \times 10^5$	1.30

<sup>a</sup>  $\varnothing W$ : chord width of impact crater,  $\delta$ : indentation depth (measured from pile-up at the crater rim to the base of indentation), location of microcrack initiation,  $k_t$ : elastic stress-concentration factor,  $\sigma_{\max}$ : maximum stress,  $\Delta\sigma$ : stress range,  $N_F$ : number of cycles at failure,  $k_f$ : effective-fatigue stress-concentration factor.

<sup>b</sup> Crack initiation at FOD-test-related Si particle at indent base.

<sup>c</sup> Load shedding test.

from the pile-up at the crater rim to the base of the indentation. Indeed, recently performed three-dimensional numerical analysis [14] gave identical  $k_t$ -values at the crater rim, but predicted values  $\sim 10\%$  higher at the base of the indentations. Table 3 lists the impact site geometry dimensions and the resulting elastic stress-concentration factors according to photoelastic experiments [13], which reach a maximum value at the base of the indentation sites, i.e., ranging from  $k_t = 1.6$  (for a 300 m/s impact site) to  $k_t = 1.4$  (for a 200 m/s site). Corresponding values at the pile-up at the crater rim range from  $k_t = 1.25$  (300 m/s) to  $k_t = 1.15$  (200 m/s). Effective stress concentration factors,  $k_f$ , for FOD were estimated from the ratio of the maximum stress (at  $R = 0.1$ ) in an undamaged, smooth-bar sample to the corresponding far-field maximum stress of a sample following simulated FOD damage to give the same life.

It should be noted that contributions to the stress-intensity values (Eq. (2)) from the residual stress field surrounding the indentation have not been taken into account, due to uncertainty in the value of these local residual stresses. Numerical analysis by Chen and Hutchinson [14] and experimental synchronous X-ray micro-diffraction studies at Berkeley [15] are currently focusing on this issue.

### 3. Results and discussion

#### 3.1. Simulation of foreign-object damage

Typical damage sites caused by ballistic impacts of 3.2-mm steel spheres on flat surfaces under normal impact ( $90^\circ$ ) at impact velocities of 200 and 300 m/s are shown, respectively, in the scanning electron micrographs in Fig. 3a and b. The nature of the damage, as characterized by size and shape of the indents and location of microcracking, is a marked function of impact velocity, as listed in Table 3. At velocities above 250 m/s, a pronounced pile-up of material, some of it detached, is evident at the crater rim; in addition, circumferentially oriented intense shear bands are seen, emanating from the surface of the impact crater (Fig. 3b); such effects are not apparent for 200 m/s impacts (Fig. 3a). Moreover, for the high velocity impact at 300 m/s, plastic flow of material at the crater rim results in multiple micro-notches (Fig. 4a) and



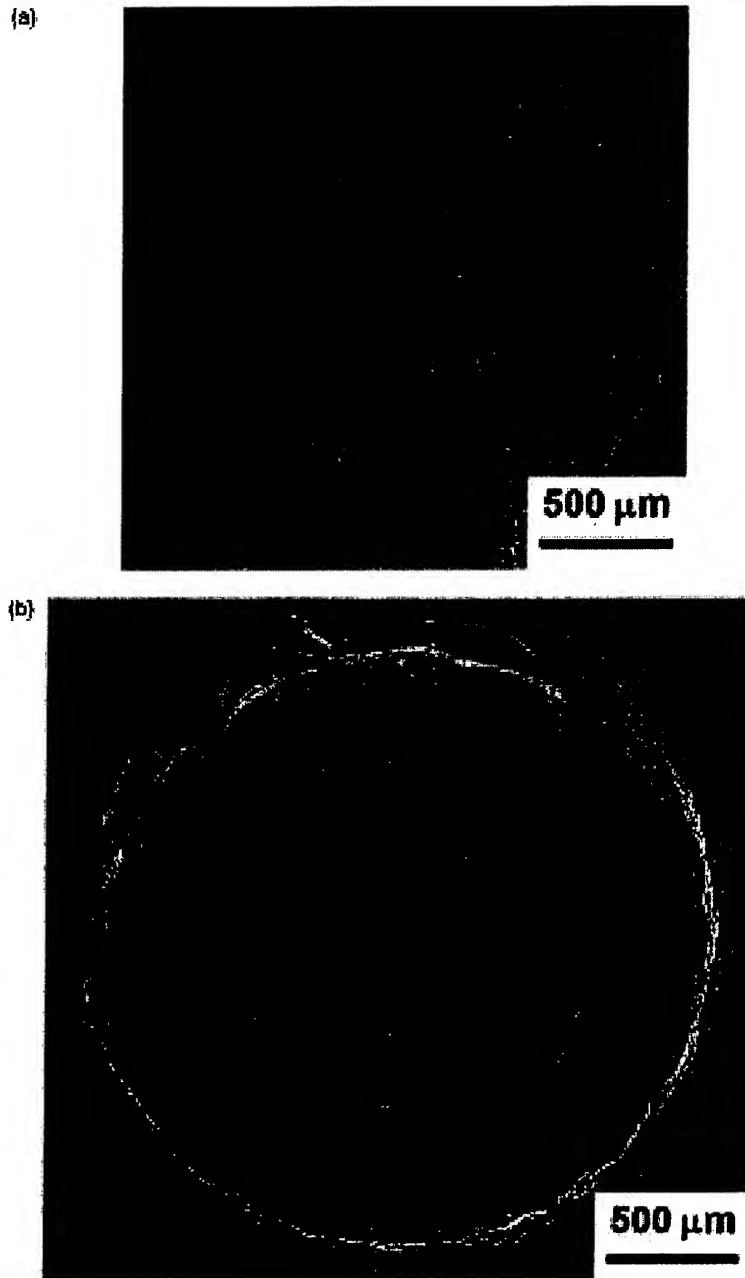


Fig. 3. Scanning electron micrographs of impact damage sites for (a) 200 m/s and (b) 300 m/s impact velocities, indicating increasing damage with increasing velocity with respect to indentation size, pile-up formation at crater rim and intense shear band formation emanating at the indent surface.

microcracking (Fig. 4b). The microcracks are quite small, i.e., between  $\sim 2$  and  $25 \mu\text{m}$  in surface length, but when favorably oriented with respect to the subsequently applied fatigue stress axis, they clearly provided the nucleation sites for high-cycle fatigue-crack growth (Fig. 4c). Such microcracking could not be detected

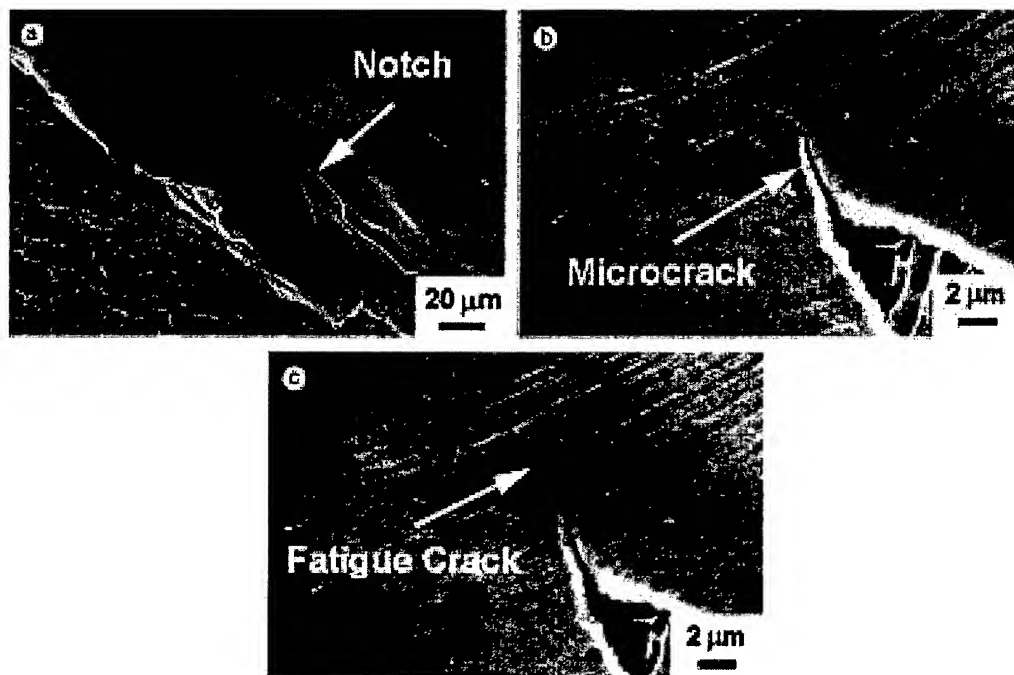


Fig. 4. Scanning electron micrographs showing the presence of microcracking at crater rim of an FOD indent after the highest velocity (300 m/s) impacts. Micrographs show (a) local notches at crater rim caused by plastic flow of material, (b) microcracks emanating from such notches, and (c) subsequent fatigue-crack growth initiated at such microcracks after  $N = 5000$  cycles at nominal  $\sigma_{\max} = 500$  MPa ( $R = 0.1$ ).

in this alloy at impact velocities below 250 m/s. This strongly implies that low velocity or quasi-static indentations do not provide a realistic simulation of FOD, because such lower velocity impacts do not necessarily induce all the damage processes associated with this phenomenon; specifically, FOD-induced microcracking is not seen in this alloy at impact velocities below  $\sim 250$  m/s.

TEM was performed to investigate any microstructural changes caused by FOD impact. The undamaged microstructure (Fig. 5a) revealed in both the globular primary  $\alpha$  phase and the  $\alpha + \beta$  lamellar matrix (alternating  $\alpha$  lamellae and  $\beta$  lamellae) a low dislocation density. The damaged microstructure following a ballistic impact is shown in Fig. 5b (TEM foil prepared from just below base of indentation). Both the primary  $\alpha$  phase and the  $\alpha + \beta$  lamellar matrix exhibit a very high dislocation density. It is evident that the impact loading introduces a very high density of dislocations below the indentation site, with some of the dislocations, specifically within the primary  $\alpha$  phase, arranged in slip bands (see arrows, Fig. 5b).

### 3.2. Fatigue properties

The fatigue life of undamaged smooth-bar specimens was significantly affected by prior high-velocity impact damage, as clearly illustrated by the stress-life (S–N) data in Fig. 6. Previously published fatigue data [16], tested at a frequency of 85 Hz, are shown together with additionally tested 1000 Hz data. At a far-field maximum stress of 500 MPa ( $R = 0.1$ ), which represents the  $10^7$ -cycle fatigue limit<sup>1</sup> for undamaged

<sup>1</sup>  $10^7$  cycles fatigue limit of  $\sigma_{\max} = 500$  MPa was derived from the data shown in Fig. 6. These data have been more recently confirmed by the results of Bellows et al. [17] at the  $10^7$  cycle limit, and by ourselves at the  $10^8$  cycle limit; all these data suggest a fatigue limit of 500 MPa.

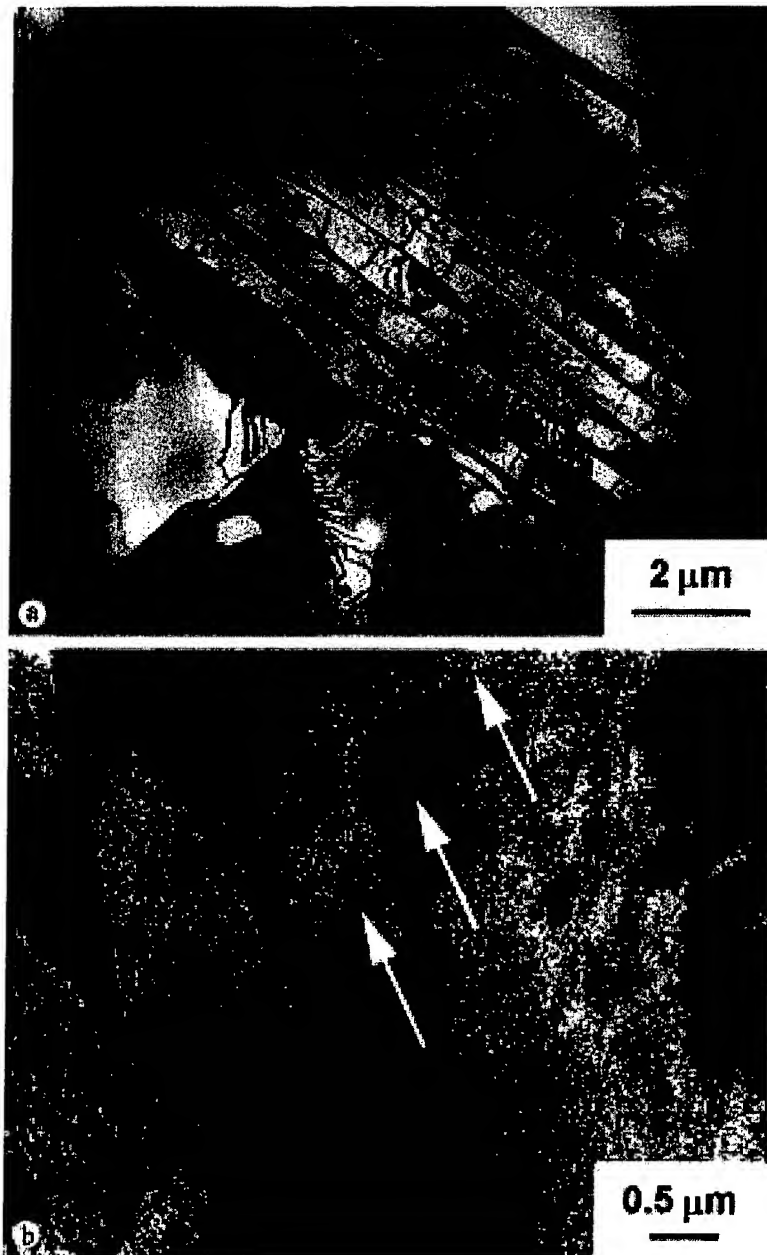


Fig. 5. Transmission electron microscopy bright-field images of (a) undamaged microstructure showing globular primary  $\alpha$  phase within lamellar  $\alpha + \beta$  matrix (alternating  $\alpha$  lamellae (bright contrast) and  $\beta$  lamellae (dark contrast)) and (b) 300 m/s impacted microstructure located close to the base of the indentation site. After high-velocity impact, the microstructure shows very high density of very small dislocations with some dislocations, specifically within the primary  $\alpha$  phase, arranged in preferred microbands (arrows).

material, final failure in the damaged material occurred between  $\sim 4$  and  $10 \times 10^4$  cycles. These results show that FOD severely reduced fatigue lives, by over two orders of magnitude, compared to smooth-bar properties.

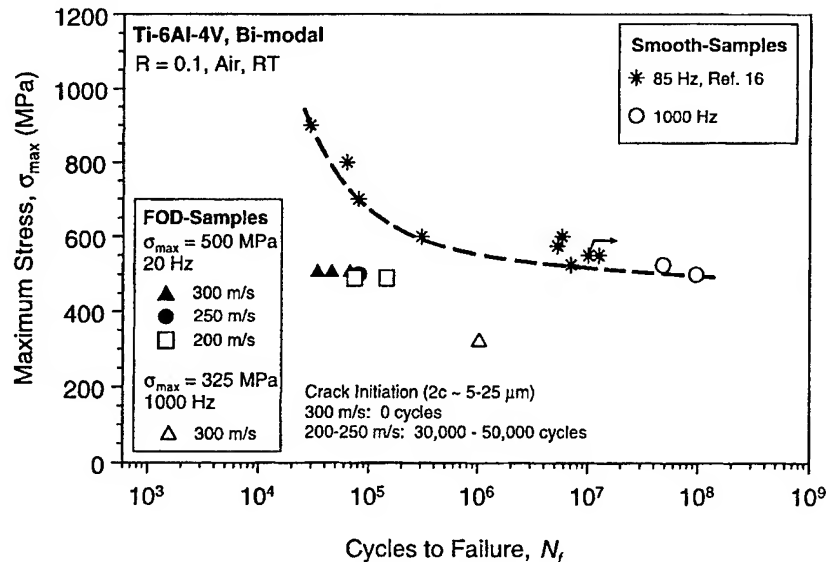


Fig. 6. S-N data show reduced fatigue life due to simulated FOD as compared to smooth-bar specimens in bimodal Ti-6Al-4V. Previously published results shown from Ref. [16] are complemented by 1000 Hz data.

### 3.2.1. FOD-induced crack initiation

With respect to the crack initiation at FOD impact sites (Fig. 7), the location of the initiation sites was found to depend strongly on impact velocity. For 300 m/s impact, fatigue cracks initiated from FOD-induced microcracks at the crater rim (Fig. 7a), whereas for lower velocity impacts (200–250 m/s), surface cracks tended to form at the base of the indentation site, as shown in Fig. 7b.

The change in crack nucleation mechanisms with impact velocity results from the interplay of stress concentration, the presence of microcracking and residual stresses. The crater rim and the base of the FOD indents are regions of high stress concentration [9]. Furthermore, the crater rim is a region of tensile residual stresses, whereas the base of the indent is a region of relatively low compressive residual stresses [14]. The stress concentration at the base of the indent, though, is always larger than that at the crater rim (Table 3); this coupled with the absence of microcracking at the lower impact velocities (200–250 m/s) and low compressive residual stresses leads to premature crack initiation at the indent base. Indeed, for such lower velocity impacts, the damage sites are relatively shallow such that the effective-fatigue stress-concentration factors (measured from the S-N data in Fig. 6) are essentially identical to the computed theoretical elastic values, i.e.,  $k_t \sim 1.4$ ,  $k_i \sim 1.4$ – $1.5$  (Table 3).

For the high velocity impact (300 m/s), conversely, FOD-induced microcracking in the pile-up region of the impact crater rim provides the dominant site for the initiation of fatigue cracks on subsequent cycling. In addition, tensile residual hoop stresses (estimated in Ref. [14]), the highly deformed microstructure in this region (Fig. 5b), and the slightly lower stress-concentration factors ( $k_i \sim 1.25$ , compared to  $k_t \sim 1.6$  at the indent base) are all contributing factors.

A further mode of crack initiation could be detected at the surface of the simulated FOD impact sites. Fig. 7c shows that even smallest dust particles from the test set-up (10 μm Si-containing particles) pressed into the surface by FOD impact resulted in a preferential crack nucleation site.

### 3.2.2. Fatigue thresholds and crack propagation

Thresholds for fatigue-crack growth and the subsequent near-threshold fatigue-crack growth rates were measured on all FOD-damaged samples; results are compared in Fig. 8 with previous results on this alloy

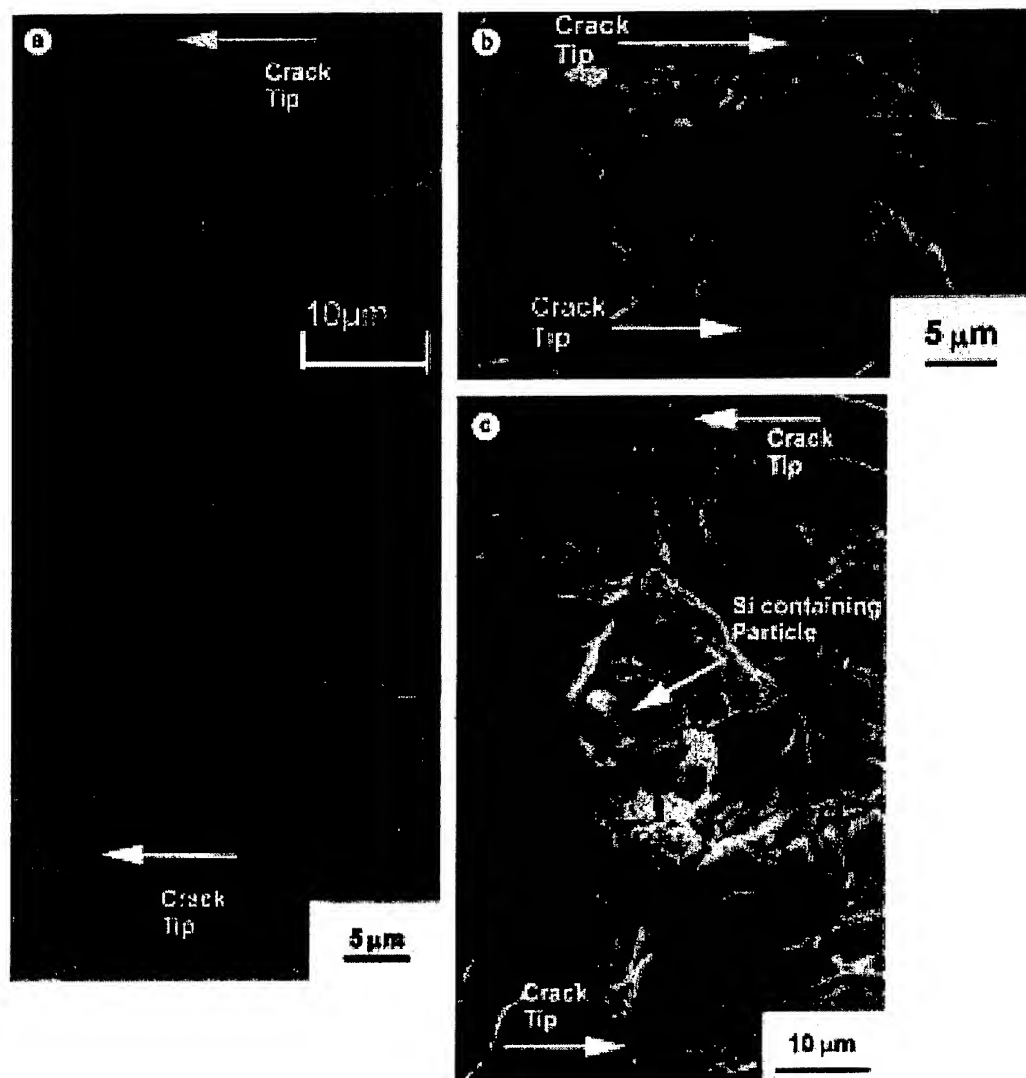


Fig. 7. Scanning electron micrographs of fatigue cracks that formed (a) at the pile-up of a 300 m/s impact velocity indentation crater (nominally applied  $\sigma_{\max} = 500$  MPa,  $R = 0.1$ ,  $N = 29,000$  cycles), (b) at the base of a 200 m/s impact velocity indentation crater (nominally applied  $\sigma_{\max} = 500$  MPa,  $R = 0.1$ ,  $N = 54,000$  cycles), and (c) at a Si containing dust particle that was pressed into the base of a 300 m/s impact velocity indentation crater (nominally applied  $\sigma_{\max} = 500$  MPa,  $R = 0.1$ ,  $N = 24,000$  cycles).

for the behavior of naturally initiated small ( $\sim 45$ – $1000$   $\mu\text{m}$ ) cracks [16] and through thickness large ( $>5$  mm) cracks [18] in undamaged material. The small crack growth-rate data are shown as a function of surface crack length,  $2c$ , and of the applied stress-intensity range (corrected for the stress concentration of the indent using Eq. (2)). For the FOD-induced small cracks, growth rates at  $R = 0.1$  can be described by following best-fit relationship (units: m/cycle, MPa  $\sqrt{\text{m}}$ ):

$$da/dN = 10^{-10}(\Delta K)^{2.8}. \quad (2)$$

It can be seen that FOD-initiated small-crack growth rates are aligned within a scatter band that approximately varies between the large-crack data (as a lower bound) and naturally initiated crack data (as an

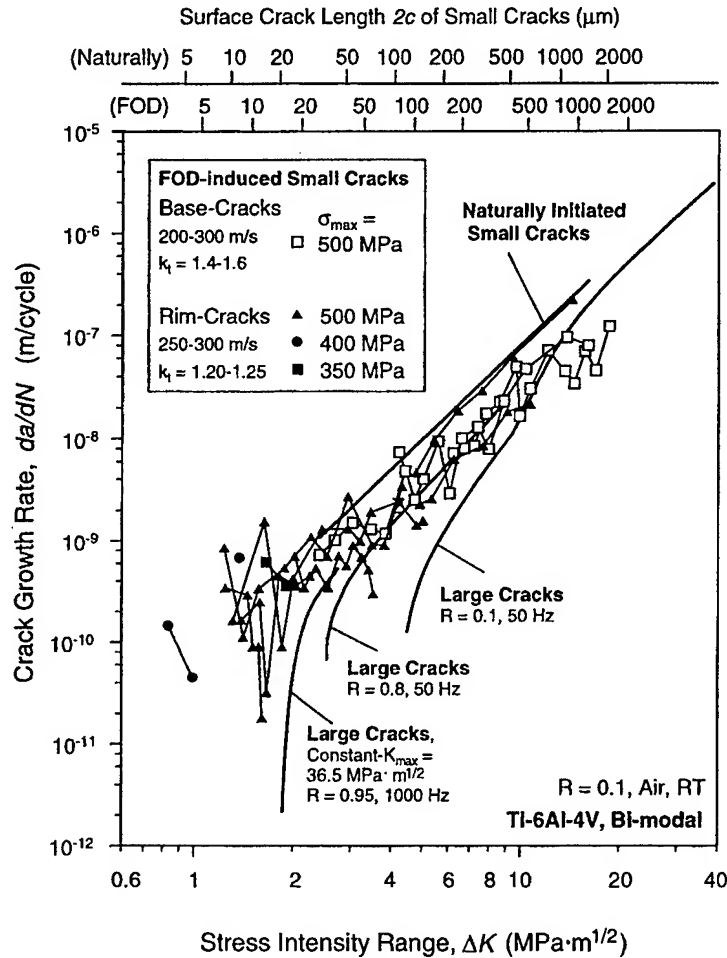


Fig. 8. Comparison of crack-growth rates,  $da/dN$ , as a function of applied stress-intensity range,  $\Delta K$ , of FOD- and naturally-initiated small cracks and through-thickness large cracks in bimodal Ti-6Al-4V. Small cracks were initiated at  $\sigma_{\max} = 650$  MPa ( $R = -1$ ) and the stress-intensity range was based only on the tensile portion of the loading cycle [16]. Large-crack growth data for  $R \leq 0.8$  were derived from constant load-ratio tests, whereas for  $R \geq 0.8$ , constant- $K_{\max}$ /increasing- $K_{\min}$  testing was used [5]. Stress-intensity data for FOD-initiated crack growth has been corrected for the stress concentration associated with the indent using the  $K$  solution of Lukáš [12] and stress-concentration factors from Ref. [13].

upper bound). There is also a tendency for the growth rates of the FOD-initiated cracks formed at the crater rim (rim cracks) to be slightly faster than those that formed at the base (base cracks). In general, the growth rates of the naturally and FOD-initiated small cracks are roughly an order of magnitude faster than corresponding large-crack results at near-threshold levels, i.e., typical for the small-crack effect (see e.g., Ref. [19]). Above a  $\Delta K$  of  $\sim 10$  MPa  $\sqrt{\text{m}}$ , however, the large and small crack results tend to merge, consistent with the increased dimensions of the small cracks.

As discussed in detail elsewhere [5,18], the large-crack results in Fig. 8 were determined up to the highest load ratios ( $R \sim 0.1$ – $0.95$ ) under conditions (constant- $K_{\max}$ /increasing- $K_{\min}$ ) chosen to minimize the effect of crack closure; the threshold of  $\sim 1.9$  MPa  $\sqrt{\text{m}}$  at  $R = 0.95$  is thus considered to be a “worst-case threshold” for cracks of dimensions large compared to the scale of the microstructure, i.e., for “continuum-sized” cracks. Of significance in the present results is that the smallest FOD-initiated cracks, which have

dimensions of  $\sim 2\text{--}25\text{ }\mu\text{m}$ , i.e., comparable with microstructural size scales, can propagate at stress intensities well below this “worst-case” threshold, specifically at applied stress intensities down to a  $\Delta K \sim 1\text{ MPa}\sqrt{\text{m}}$ . The implication of this result is that in the bimodal Ti–6Al–4V alloy, there is a definitive lower-bound  $\Delta K_{\text{TH}}$  threshold ( $\sim 1.9\text{ MPa}\sqrt{\text{m}}$ ) for “continuum-sized” cracks, i.e., large or physically small cracks with dimensions larger than the characteristic microstructural size-scales; however, when crack sizes approach such microstructural size scales, crack growth at applied stress intensities considerably less than this threshold is possible, presumably due to biased sampling of the “weak links” in the microstructure by the microstructurally small crack.

With respect to the possibility of finding a similar well-defined threshold for cracks emanating from regions of impact damage, the present results indicate that FOD-initiated microcracks, with dimensions in the range  $\sim 2\text{--}25\text{ }\mu\text{m}$ , can readily propagate in Ti–6Al–4V at stress-intensity ranges as low as  $\Delta K \sim 1\text{ MPa}\sqrt{\text{m}}$  at nominal maximum stresses from 325 to 500 MPa ( $R = 0.1$ ); moreover, such small cracks show no pronounced threshold behavior. Indeed, it is believed that a  $\Delta K$  of  $1\text{ MPa}\sqrt{\text{m}}$  is the lowest stress-intensity range ever measured for crack growth in Ti–6Al–4V, representing a  $\Delta K$  value roughly a factor of two smaller than the lowest measured fatigue threshold for a “continuum-sized” crack.

It should be noted here that there are still some uncertainties in the calculation of the driving forces for the propagation of the FOD-induced “microstructurally” small cracks, specifically because of their size in relation to the scale of local cyclic plasticity (although maximum plastic-zone sizes are only on the order of  $\sim 0.2\text{--}1\text{ }\mu\text{m}$  for  $1\text{--}10\text{ }\mu\text{m}$  sized cracks at  $\Delta K \sim 1\text{--}2\text{ MPa}\sqrt{\text{m}}$ ), and because of the presence of both tensile and compressive residual stresses. Although residual stresses are not included in the calculation of  $K$  (Eq. (2)), as a first approximation such stresses do not change the stress-intensity range ( $\Delta K$ ); they affect the mean stress and hence alter the local load ratio. Residual stresses are being numerically analyzed using a quasi-static model [14]. Results for the lower velocity impacts (200 m/s) have been experimentally verified by X-ray micro-diffraction methods [15], but numerically results severely overestimate the measured residual stresses for 300 m/s impact, presumably due to rate-sensitive phenomena such as shear-band formation and local heating. The latter effect, the possible relaxation of residual stresses due to fatigue loading, and the appropriate method of superposition of the applied and residual stresses to estimate local driving forces, are currently under study.

It is clear that our previously stated argument [5,9,18] for the notion of a high-cycle fatigue threshold, which was based on the concept of a “worst-case” threshold (determined under  $R \rightarrow 1$  conditions that minimize crack closure), applies strictly for “continuum-sized” cracks; it does not provide a lower-bound threshold stress intensity for cracks on the scale of microstructural dimensions, as in the earliest stages of FOD-induced fatigue failure. However, coupling the notion of the worst-case threshold stress intensity with the fatigue limit, as in the Kitagawa–Takahashi diagram [20], does provide an alternative approach to defining limiting conditions for HCF and FOD-related damage, as discussed below.

### 3.2.3. Threshold conditions based on the Kitagawa–Takahashi diagram

As an alternative HCF-design approach against FOD, which takes into account the presence of microstructurally small cracks, Fig. 9 shows the influence of crack size on the worst-case fatigue thresholds in the form of a modified Kitagawa–Takahashi diagram [20], where the stress range for a corresponding crack-growth threshold condition ( $da/dN = 10^{-11} \text{--} 10^{-10}\text{ m/cycle}$ ) is plotted versus the crack length. According to the Kitagawa–Takahashi approach (solid lines), the stress range  $\Delta\sigma$  for crack arrest is defined by the  $10^7$ -cycle fatigue limit ( $\Delta\sigma_{\text{HCF}} = 450\text{ MPa}$ ) with the fatigue-crack growth threshold ( $\Delta K_{\text{TH}}$ ) measured on “continuum-sized” cracks. El Haddad et al. [21] empirically quantified this approach by introducing a constant (intrinsic) crack length  $2c_0$ , such that the stress intensity is defined as  $Y\Delta\sigma\sqrt{\pi(2c + 2c_0)}$ , where  $Y$  is the geometry factor. The present results, plotted in this format in Fig. 9, show that crack growth from FOD-induced microstructurally small cracks can apparently occur at nominal stress ranges (closed symbols) below the Kitagawa/El Haddad limit, defined by the worst-case  $\Delta K_{\text{TH}}$  threshold and  $10^7$ -cycle fatigue limit;

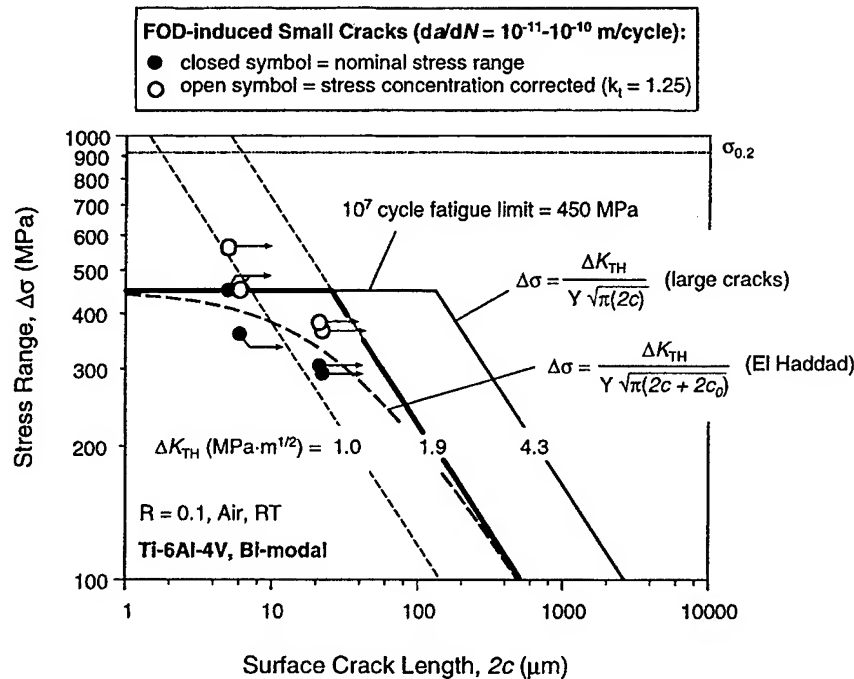


Fig. 9. Crack growth conditions of FOD-induced “microstructurally” small cracks ( $da/dN = 10^{-11} - 10^{-10}$  m/cycle) as a function of cyclic stress range and surface crack length are shown in a modified Kitagawa-Takahashi diagram. Crack growth conditions were calculated for nominal (closed symbols) and stress-concentration corrected stress ranges (open symbols), and compared to smooth-bar  $10^7$ -cycles fatigue limit and “continuum” large-crack growth threshold (solid line) and to a small-crack growth threshold model based on the solution given by El Haddad et al. [21] (dashed curve).

however, if these stresses are corrected for the effect of the stress concentration associated with the FOD indent (open symbols), crack growth occurs above the Kitagawa/El Haddad limit.

#### 4. Summary and conclusions

Based on a study of the role of FOD on thresholds for high-cycle fatigue in a turbine blade Ti-6Al-4V alloy, involving considerations of (i) the stress concentration associated with the FOD indentation, (ii) FOD-induced microcracks, (iii) the localized presence of residual stresses, and (iv) microstructural damage from FOD-induced plasticity, the following conclusions can be made:

(1) Simulated high-velocity (200–300 m/s) FOD impact of steel spheres on a flat surface was found to markedly degrade resistance to high-cycle fatigue. For example, 200–300 m/s impacts on smooth-bar samples reduced the fatigue life by some two orders of magnitude at an applied stress corresponding to the smooth-bar  $10^7$ -cycles fatigue limit ( $R = 0.1$ ), an effect that is related to earlier crack initiation.

(2) The principal effect of FOD in reducing fatigue life was found to induce preferred sites for the premature initiation of fatigue cracks. For lower impact velocities (200–250 m/s), such initiation occurred at the base of the impact sites, where the stress concentration was highest. Conversely, at higher impact velocities (250–300 m/s), initiation occurred at FOD-induced microcracks in the pile-up of material around the impact crater rim.



(3) At nominal maximum stresses from 325 to 500 MPa ( $R = 0.1$ ), FOD-initiated microcracks ( $\sim 2\text{--}25\ \mu\text{m}$  in size) propagated at applied stress intensities as low as  $\Delta K = 1\ \text{MPa}\sqrt{\text{m}}$  and showed no pronounced threshold behavior. This is well below the “worst-case”  $\Delta K_{\text{TH}}$  threshold of  $1.9\ \text{MPa}\sqrt{\text{m}}$  for “continuum-sized” cracks (i.e., cracks larger than the characteristic microstructural size scales) in this alloy. Such FOD-induced fatigue cracks propagated at rates roughly an order of magnitude faster than corresponding large ( $>5\ \text{mm}$ ) cracks at the same applied stress-intensity range. Small cracks initiated at the rim of the indentation sites appeared to grow at rates slightly faster than the cracks that initiated at the base.

(4) Correspondingly, the critical condition for HCF in the bimodal Ti–6Al–4V in the presence of “continuum-sized” cracks (of a size  $>50\text{--}100\ \mu\text{m}$ ) can be defined in terms of the “worst-case” fatigue threshold (determined under  $R \rightarrow 1$  conditions that minimize crack closure). However, this concept alone is inappropriate where microstructurally small cracks (of a size  $\sim 2\text{--}50\ \mu\text{m}$ ) are relevant.

(5) For FOD-initiated failures, where the critical condition for HCF must be defined in the presence of microstructurally small cracks, the Kitagawa–Takahashi diagram is more appropriate, where the limiting conditions are defined in terms of the stress-concentrated corrected  $10^7$ -cycle fatigue limit (at microstructurally small cracks sizes) and the “worst-case”  $\Delta K_{\text{TH}}$  fatigue threshold (at larger, “continuum-sized” crack sizes).

## Acknowledgements

This work was supported by the Air Force Office of Science and Research, grant no. F49620-96-1-0478, under the Multidisciplinary University Research Initiative on “High Cycle Fatigue” to the University of California, Berkeley. Special thanks are due to Prof. Werner Goldsmith (UCB) for providing the compressed-gas gun facility.

## References

- [1] Cowles BA. High cycle fatigue in aircraft gas turbines – an industry perspective. *Int J Fract* 1996;80:147–63.
- [2] Nicholas T, Zuiker JR. On the use of the Goodman diagram for high cycle fatigue design. *Int J Fract* 1996;80:219–35.
- [3] Larsen JR, Worth BD, Annis Jr CG, Haake FK. An assessment of the role of near-threshold crack growth in high cycle fatigue life prediction of aerospace titanium alloys under turbine engine spectra. *Int J Fract* 1996;80:237–55.
- [4] Ritchie RO. Small cracks and high-cycle fatigue. In: Chang JCI, Coulter J, Brei D, Martinez WHG, Friedmann PP, editors. *Proc ASME Aerospace Div, AD-vol. 52*, ASME, Warrendale, PA, 1996. p. 321–333.
- [5] Ritchie RO, Davidson DL, Boyce BL, Campbell JP, Roder O. High-cycle fatigue of Ti–6Al–4V. *Fatigue Fract Engng Mat Struct* 1999;22:621–31.
- [6] Erosion, Corrosion and Foreign Object Damage Effects in Gas Turbines, AGARD Conference Proceedings No. 558, North Atlantic Treaty Organization. Advisory Group for Aerospace Research and Development, Propulsion and Energetics Panel, Neuilly-sur-Seine, France, 1994.
- [7] Nicholas T, Barber JR, Bertke RS. Impact damage on titanium leading edges from small hard objects. *Expt Mech* 1980;20:357–64.
- [8] Hudak SJ, Chan KS, McClung RC, Chell GG, Lee Y-D, Davidson DL. High cycle fatigue of turbine blade materials, Final Technical Report UDRI Subcontract No. RI 40098X SwRI Project No. 18-8653, 1999.
- [9] Peters JO, Roder O, Boyce BL, Thompson AW, Ritchie RO. Role of foreign object damage on thresholds for high-cycle fatigue in Ti–6Al–4V. *Metall Mater Trans A*, 2000;31A, in press.
- [10] Eylon D. Summary of the available information on the processing of the Ti–6Al–4V HCF/LCF program plates. University of Dayton Report, Dayton, OH, 1998.
- [11] Sheldon JW, Bain KR, Donald JK. Investigation of the effects of shed-rate, initial  $K_{\text{max}}$ , and geometric constraint on  $K_{\text{th}}$  in Ti–6Al–4V at room temperature. *Int J Fatigue* 1999;21:733–41.
- [12] Lukáš P. Stress intensity factor for small notch-emanating cracks. *Engng Fract Mech* 1987;26:471–73.
- [13] Nisida M, Kim P. Stress concentration caused by the presence of a spherical cavity or a spherical-surfaced hollow. In: *Proceedings of the Twelfth National Cong Appl Mech*, 1962. p. 69–74.

- [14] Chen X, Hutchinson JW. Foreign object damage and fatigue cracking: on the shallow indentation. *Int J Fract*, Harvard University Report No. ME 358, Nov. 1999, in press.
- [15] Boyce BL, Thompson AW, Roder O, Ritchie RO. Measurement of residual stresses in impact-damaged Ti–6Al–4V. In: Henderson J, editor. *Proceedings of the Fourth National Turbine Engine High Cycle Fatigue (HCF) Conference*, University Technology Corp. Dayton, OH, 1999, CD-Rom, Session 10. p. 28–40.
- [16] Hines JA, Peters JO, Lütjering G. Microcrack propagation in Ti–6Al–4V alloys. In Boyer RR, Eylon D, Lütjering G, editors. *Fatigue behavior of titanium alloys*. Warrendale, PA: TMS, 1999. p. 15–22.
- [17] Bellows RS, Muju S, Nicholas T. Validation of the step test method for generating Haigh diagrams for Ti–6Al–4V. *Int J Fatigue* 1999;21:687–97.
- [18] Ritchie RO, Boyce BL, Campbell JP, Roder O, Thompson AW, Milligan WW. Thresholds for high-cycle fatigue in a turbine engine Ti–6Al–4V alloy. *Int J Fatigue* 1999;21:653–62.
- [19] Ritchie RO, Lankford J. Small fatigue cracks: a statement of the problem and potential solutions. *Mater Sci Engng* 1986;84:11–6.
- [20] Kitagawa H, Takahashi S. Applicability of fracture mechanics to very small cracks or the cracks in the early stage. In *Proceedings of the Second International Conference on Mechanical Behavior of Materials*, ASM, Metals Park, OH, 1976. p. 627–31.
- [21] Haddad MH, Topper TH, Smith KN. Prediction of non propagating cracks. *Engng Fract Mech* 1979;11:573–84.

## Foreign-object damage and high-cycle fatigue: role of microstructure in Ti–6Al–4V

J.O. Peters, R.O. Ritchie \*

Department of Materials Science and Engineering, University of California, Berkeley, CA 94720-1760, USA

### Abstract

The objective of this study was to evaluate the influence of microstructure on the susceptibility to high-cycle fatigue (HCF) failure in Ti–6Al–4V following foreign-object damage (FOD), specifically by comparing a fine-grained bi-modal microstructure with a coarse grained lamellar microstructure. FOD was simulated by high-velocity impacts of steel spheres on a flat surface. This caused a marked reduction in the smooth-bar fatigue strength in both microstructures, primarily because of the premature initiation of fatigue cracking resulting from the stress concentration associated with damage site and FOD-induced microcracking. The FOD-initiated microcracks were found to be of a size comparable with microstructural dimensions, and on subsequent fatigue loading were seen to propagate at applied stress-intensity levels below  $\Delta K \sim 1 \text{ MPa m}^{1/2}$ , i.e. a factor of roughly two less than the ‘worst-case’ threshold stress-intensity range in Ti–6Al–4V for a crack of large size compared to microstructural dimensions (a ‘continuum-sized’ crack). A rational approach against HCF failures from such microcracks is proposed for the fine-grained bi-modal microstructure based on the Kitagawa–Takahashi diagram. For the bi-modal microstructure, the Kitagawa–Takahashi diagram provides a basis for describing the threshold conditions for FOD-induced HCF failures, in terms of the *stress concentration corrected* smooth-bar fatigue limit for small crack sizes and the worst-case threshold for larger continuum-sized cracks. However, this approach was found to be less applicable to the coarse grained lamellar microstructure, primarily because of low small-crack growth resistance relative to its higher smooth-bar fatigue limit. © 2001 Elsevier Science Ltd. All rights reserved.

**Keywords:** Foreign-object damage; High-cycle fatigue; Fatigue-crack growth threshold; Small cracks; Ti–6Al–4V

### 1. Introduction

Because of an increasing number of incidents of high-cycle fatigue (HCF) related jet engine failures of military aircraft, currently used HCF design methodologies, based on stress-life (S–N) curves and the Goodman diagram, are being re-evaluated [1–3]. Both foreign-object damage (FOD) from hard body impacts (e.g. debris ingested from the runway into the inlet of a jet engine, which can primarily damage the leading edge of fan blades) and fretting (e.g. particularly in the blade dovetail/disk sections) are identified as critical problems [1–3], which can lead to premature fatigue crack initiation and subsequent crack growth. This in turn can result in seemingly unpredictable *in service* failures, due to the high-frequency vibratory loading ( $>1 \text{ kHz}$ )

involved [3]. Even cracks growing at slow per-cycle velocities of  $\sim 10^{-10} \text{ m/cycle}$  can propagate to failure in a short time period. In light of this, design against HCF based on the damage-tolerant concept of a fatigue-crack growth threshold ( $\Delta K_{\text{TH}}$ ) for no crack growth would appear to offer a preferred approach; however, such thresholds must reflect representative HCF conditions of small crack sizes, high frequencies and high mean stress levels (depending on the blade span location) [1–5].

As a basis for such an approach, past studies have been focused on the role of FOD in affecting the initiation and early growth of small surface fatigue cracks under HCF conditions in fan blade processed Ti–6Al–4V alloy with fine-grained bi-modal microstructure<sup>1</sup> [6–10]. The prime effect of FOD in markedly lowering resistance to HCF was found to be due to earlier crack initiation. Specifically, premature crack initiation and

\* Corresponding author. Tel.: +1-510-486-5798; fax: +1-510-486-4881.

E-mail address: roritchie@lbl.gov (R.O. Ritchie).

<sup>1</sup> This microstructural condition has also been termed solution treated and overaged (STOA).

subsequent near-threshold crack growth were promoted by the stress concentration associated with the FOD indentation [6–9] and the presence of ('microstructurally') small cracks [7,10] in the damaged zone; in addition, residual stress gradients [6,7,9] and microstructural changes [6,7] due to FOD-induced plastic deformation play an important role. Limiting conditions for potential HCF-related turbine failures were proposed based on the concept of a 'worst-case' threshold for no fatigue crack growth, an approach that strictly applies for 'continuum-sized' cracks, i.e. large or physically small cracks with dimensions larger than the characteristic microstructural size-scales. However, in the presence of *microstructurally* small cracks at FOD indentation site, limiting threshold conditions for crack growth were alternatively defined in terms of *stress concentration corrected* stress ranges in the context of the Kitagawa–Takahashi diagram [11]. To provide limiting criteria for HCF failures using this approach, the threshold conditions were described in terms of the smooth-bar fatigue limit (at microstructurally small crack sizes) and worst-case large-crack fatigue threshold (at larger, continuum-sized, crack sizes) [7].

The purpose of the present study is to examine the influence of microstructural dimensions on the fatigue crack initiation and early fatigue crack growth from FOD-induced microcracks by comparing fine-grained bi-modal microstructure with coarser grained  $\beta$  annealed lamellar microstructure. In contrast to the bi-modal microstructure where FOD-induced microcracks ( $2c \sim 2\text{--}50\text{ }\mu\text{m}$ ) are of comparable dimensions to the fine-grained bi-modal microstructure, in the lamellar microstructure such microcracks are far smaller than the average lamellar colony size ( $\sim 500\text{ }\mu\text{m}$ ).

## 2. Experimental procedures

The Ti–6Al–4V alloy (Ti–6.3Al–4.2V–0.2Fe–0.2O, wt.%) in the bi-modal microstructural condition was part of a set of forgings produced specifically for the U.S. Air Force sponsored programs on HCF. Mill annealed 63.5 mm diameter bar stock material was  $\alpha+\beta$  forged to a plate size of  $400 \times 150 \times 20\text{ mm}^3$ . Subsequently, the forging plates were solution treated (below the  $\beta$ -transus of  $\sim 996^\circ\text{C}$ ) at  $927^\circ\text{C}$  for 1 h followed by fan air cooling. Finally, the plates were stress relieved for 2 h at  $705^\circ\text{C}$ . Additional material and processing details are given in Ref. [12]. The resulting bi-modal microstructure of the plate material, consisting of a volume fraction of  $\sim 60\%$  primary  $\alpha$  (diameter  $\sim 20\text{ }\mu\text{m}$ ) within a lamellar  $\alpha+\beta$  matrix, is shown in Fig. 1(a). To obtain a fully lamellar microstructure for comparison, specimen blanks ( $20 \times 20 \times 90\text{ mm}^3$ ) of bi-modal plate material were  $\beta$  annealed at  $1050^\circ\text{C}$  for 30 min and subsequently cooled by a He-quench (cooling rate of  $\sim 100^\circ\text{C}/\text{min}$ ). Finally,

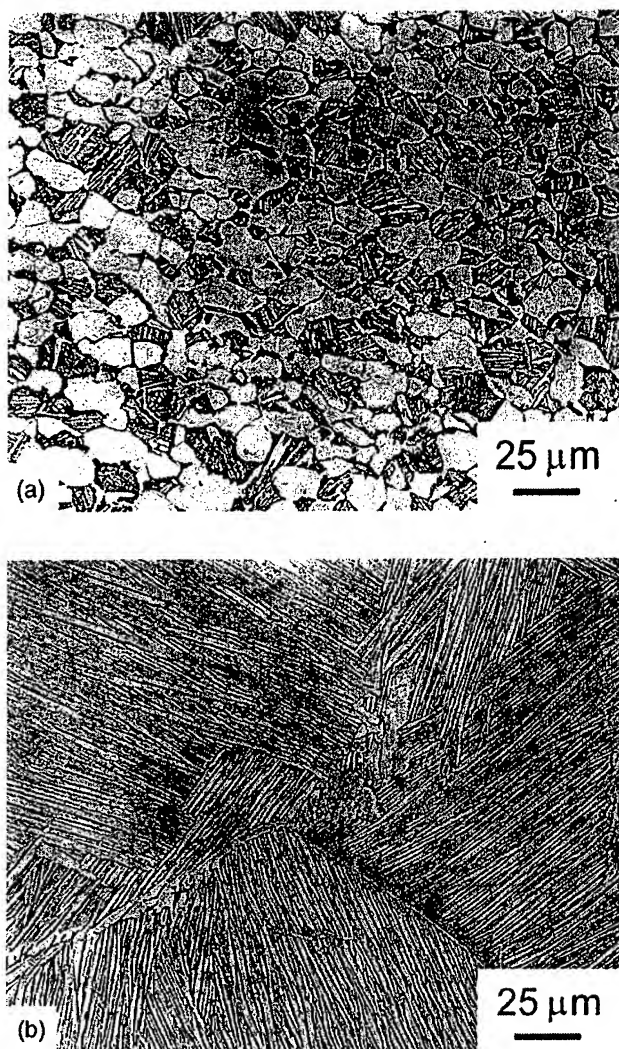


Fig. 1. Microstructures of Ti–6Al–4V: (a) bi-modal (solution treated and overaged, STOA) and lamellar ( $\beta$  annealed).

the blanks received the same stress relief treatment as bi-modal plate material (2 h at  $705^\circ\text{C}$ ). The lamellar microstructure shown in Fig. 1(b) exhibited a  $\beta$  grain size of  $\sim 1000\text{ }\mu\text{m}$ , a colony size (parallel oriented  $\alpha$  phase plates) of  $\sim 500\text{ }\mu\text{m}$  and lamellae thickness of  $\sim 1\text{ }\mu\text{m}$ , corresponding to the lamellae thickness of the bi-modal microstructure. Uniaxial tensile properties (based on testing performed parallel to the length of the plate at an initial strain rate of  $8 \times 10^{-4}\text{ s}^{-1}$ ) are listed in Table 1. The slightly higher yield stress of 975 MPa of

Table 1  
Uniaxial tensile properties of Ti–6Al–4V.  $\sigma_{0.2}$ : yield stress, UTS: ultimate tensile strength, TE: tensile elongation, RA: reduction of area at fracture; strain rate  $8 \times 10^{-4}\text{ s}^{-1}$

Microstructure	$\sigma_{0.2}$ (MPa)	UTS (MPa)	TE (%)	RA (%)
Bi-modal	915	965	19	45
Lamellar	975	1055	12	10

the lamellar microstructure, as compared to 915 MPa of the bi-modal microstructure, is presumably due to higher cooling rate from solution treatment temperature. The markedly higher ductility of the bi-modal condition (reduction in area, RA=45%), compared to the lamellar condition (RA=10%), can be attributed to the much smaller grain size limiting the effective slip length.

In addition to the stress-life ( $S-N$ ) data taken for bi-modal Ti-6Al-4V from Ref. [13] (for  $N_f < 2 \times 10^7$  cycles),  $S-N$  tests were performed on hourglass specimens (diameter: 5.4 mm) at 1000 Hz to provide an evaluation of the smooth-bar HCF limit of the Ti-6Al-4V alloy with bi-modal and lamellar structures. To minimize surface residual stresses and the high-dislocation density from specimen processing, specimen surfaces were chemically milled after machining. The specimen axis was oriented parallel to the length of the plate ( $L$ -direction).

The effect of FOD on the fatigue behavior of Ti-6Al-4V was examined using modified  $K_B$  specimens. This sample has a rectangular cross-section of 3.2 mm by 7.2 mm, a gauge length of 20 mm and cylindrical buttonhead grips. A nominally stress-free surface in the gauge section was prepared using standard stress relief and chemical-milling procedures. FOD was simulated by firing 3.2 mm diameter chrome-hardened steel spheres onto a flat specimen surface of tensile fatigue (modified  $K_B$ ) specimens at an angle of  $90^\circ$  at velocities of 200–300 m/s using a compressed-gas gun facility. Further details of the FOD simulation are given in Ref. [6]. After impact, specimens were cycled (sinusoidal waveform) at load ratios of  $R=0.1$  and  $0.5$ . Throughout fatigue testing, specimens were periodically removed from the test frame and the progress of crack initiation and growth examined in a high-resolution LEO 1550 field-emission scanning electron microscope (SEM).

Approximate local stress intensities for small cracks at base and crater rim of the indentation were calculated from the relationship of Lukáš [14] for small cracks at notches, in terms of elastic stress-concentration factor ( $k_t$ ) surrounding the indentation site [15], stress range ( $\Delta\sigma$ ), crack depth ( $a$ ), and indentation radius ( $\rho$ ). The factor of 0.7 is based on the stress-intensity boundary correction and the crack-shape correction factors [16]

$$\Delta K = \frac{0.7 k_t}{\sqrt{1+4.5(a/\rho)}} \Delta\sigma \sqrt{\pi a} \quad (1)$$

It should be noted here that there are some uncertainties in the calculation of the driving forces for the propagation of FOD-initiated microcracks ( $2c \sim 2\text{--}50 \mu\text{m}$ ), specifically because of their size in relation to the scale of local plasticity (although maximum plastic zone sizes are only roughly  $1/5\text{--}1/10$  of the crack length, i.e. in the order of  $\sim 0.2\text{--}1 \mu\text{m}$  for  $1\text{--}10 \mu\text{m}$  sized cracks at  $\Delta K \sim 1\text{--}$

$2 \text{ MPa m}^{1/2}$ ), and because of the presence of both tensile and compressive residual stresses in the vicinity of the indents. Eq. (1) does not take into account the presence of residual stresses, as to the first approximation such stresses will not change the value of the stress-intensity range ( $\Delta K$ ); they do, however, affect the mean stress and hence alter the local load ratio. The magnitudes of these stresses in the vicinity of the damage site are currently being computed and experimentally measured [17,18], as briefly discussed below. Indeed, the local residual stresses at the base and rim of the FOD indents have been shown in many cases to relax, or redistribute under cyclic loading, specifically at applied stresses comparable with the  $10^7$ -cycle smooth-bar fatigue limit, i.e.  $\sim 500 \text{ MPa}$ , which was used in the present work.

### 3. Results and discussion

#### 3.1. Simulation of FOD

Impact damage sites caused by 300 m/s normal impacts on flat surfaces are shown in Fig. 2(a) and (b) for the bi-modal and lamellar microstructure, respectively. Increasing states of damage have been reported with increasing impact velocity for the bi-modal microstructure [6,7]. In particular, above a 250 m/s impact velocity, pile-up of material occurred at the crater rim with an associated presence of micronotches and microcracks; moreover, circumferentially oriented intense shear bands were formed, emanating from the surface of the impact crater. Such effects were not apparent for 200 m/s impacts. A comparable increase in damage with increasing impact velocity was seen in the lamellar microstructure, although the occurrence of the crater rim pile-up and associated micronotch and microcrack formation were more severe (compare Fig. 2(a) and (b)). However, for the impact velocities of 300 m/s, the sizes of the FOD-induced microcracks were comparable, i.e.  $\sim 2\text{--}50 \mu\text{m}$  in surface length, for both bi-modal and lamellar microstructures. When favorably oriented to the subsequently applied fatigue stress axis, such microcracks provided the preferred nucleation sites for fatigue-crack growth, as shown in Fig. 3(a) and (b) for the bi-modal and lamellar microstructures, respectively. However, as such microcracking was absent for impact velocities below 250 m/s, it is clear that low velocity or quasi-static indentations do not provide a realistic simulation of FOD.

Additionally of importance for crack initiation was the observation of tensile residual stresses ( $\sim 300 \text{ MPa}$  in longitudinal direction) at the side faces of  $K_B$  specimens [17]. These tensile stresses, measured using synchronous X-ray microdiffraction techniques, counterbalance the compressive residual stress field under the indentation,

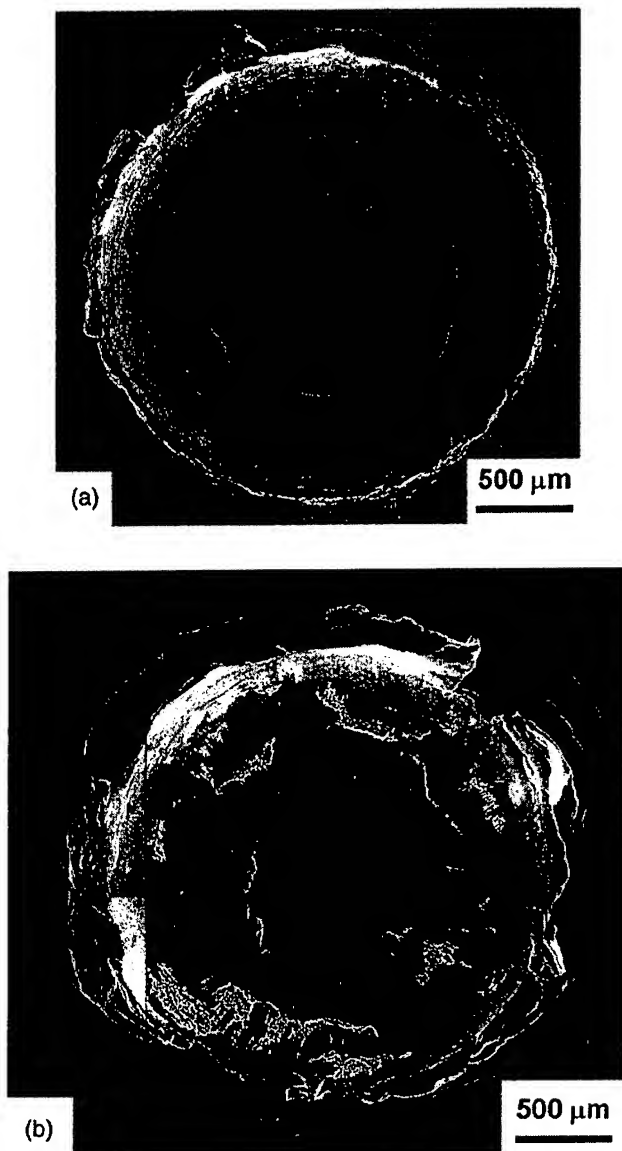


Fig. 2. Scanning electron micrographs of impact damage sites (300 m/s impact velocity) for (a) bi-modal and (b) lamellar microstructure of Ti-6Al-4V. Lamellar microstructure showed increased damage with respect to pile-up formation at crater rim and intense shear band formation emanating at the indent surface.

as numerically analyzed by Chen and Hutchinson [18] and measured by Boyce et al. [17].

### 3.2. Fatigue properties and FOD-induced crack initiation

The fatigue life of undamaged smooth-bar specimens was markedly reduced by prior high-velocity impact damage, as clearly illustrated by the stress-life ( $S-N$ ) data in Fig. 4. This reduction was found at both low- and high-load ratios ( $R=0.1$  and  $0.5$ ) in both microstructures. Basically, two groups of failures could be identified. At high applied stresses (relative to the magnitude of the

tensile residual stresses) and high impact velocities, where large impact-induced microcracks are formed (surface crack lengths are indicated at individual data points), failures initiated from impact-induced cracks at the crater rim. Micrographs of the failed samples are shown in Fig. 5(a) and (b) for the bi-modal and lamellar microstructures, respectively. For lower velocity impacts under these conditions, fatal cracks initiated at the base of the indent site because of the higher stress concentration there compared to that at the crater rim [7]. In contrast, at lower applied stresses and lower impact velocities, where the impact-induced microcracks were absent or much smaller, fatigue cracks were found to initiate in regions of relatively high tensile residual stresses, away from the indent crater, see Fig. 6.

### 3.3. Fatigue thresholds and crack propagation

Thresholds for fatigue-crack growth and the subsequent near-threshold fatigue-crack growth rates were measured on all FOD-impacted samples and are compared in Fig. 7(a) ( $R=0.1$ ) and Fig. 7(b) ( $R=0.5$ ) with results for through-thickness large ( $>5$  mm) cracks in undamaged material [5,19]. The FOD-initiated crack growth rate data are shown as a function of surface crack length,  $2c$ , and the approximate applied stress-intensity range (corrected for the stress concentration of the indent using Eq. (1)). For the FOD-induced microcracks, which are truly microstructurally small cracks, growth-rate data points for both microstructures fall into a single scatter band. Similarly, growth-rate data points for both load ratios ( $R=0.1$  and  $0.5$ ) fall into a single scatter band, indicating the controlling effect of the alternating, rather than the mean, stresses. In general, the growth rates of the FOD-initiated small cracks in both microstructures were at least an order of magnitude faster than the corresponding large-crack results at near-threshold levels; such an effect is typical for microstructurally small cracks [10,20–23]. However, the large and small crack results tend to merge above a  $\Delta K$  of  $\sim 10$  MPa  $m^{1/2}$  for the bi-modal microstructure, consistent with the increased dimensions of the small cracks. This is in contrast to the lamellar microstructure, which exhibits much higher crack-growth resistance than the bi-modal microstructure in the presence of large through-thickness cracks. Because of the larger characteristic microstructural size-scales in this condition, cracks of millimeter dimensions apparently can still display a small crack effect.

One factor associated with the faster growth rates of the FOD-initiated microcracks is the microstructural changes associated with impact-induced plasticity. This is evident from shot-peening experiments on Ti-6Al-4V where, by separating the effect of deformation from residual stresses, it was observed that the deformed microstructure showed drastically reduced resistance to



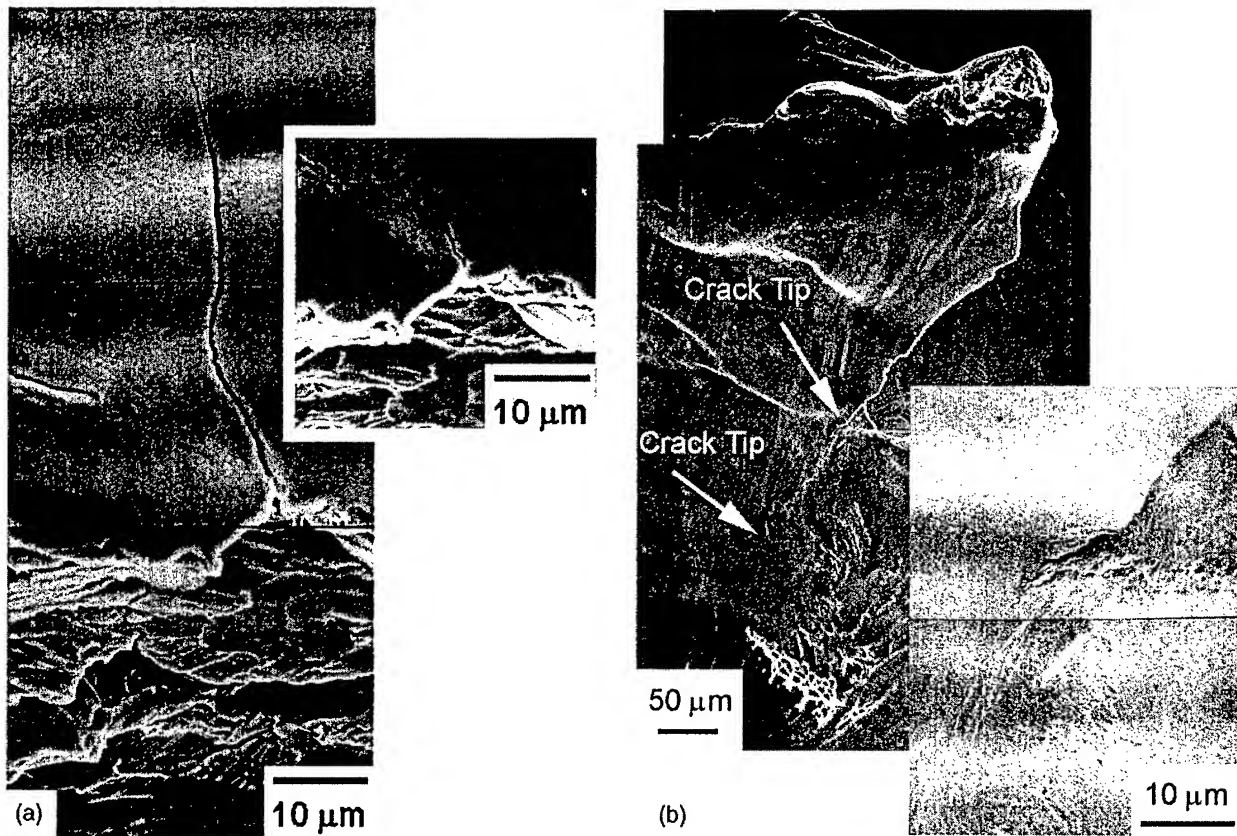


Fig. 3. Examples of fatigue cracks that formed at FOD-induced microcracks (small inserts). (a) Bi-modal microstructure (nominally applied  $\sigma_{\max}=500$  MPa,  $R=0.1$ ,  $N=29,000$  cycles) and (b) lamellar microstructure (nominally applied  $\sigma_{\max}=500$  MPa,  $R=0.1$ ,  $N=3000$  cycles).

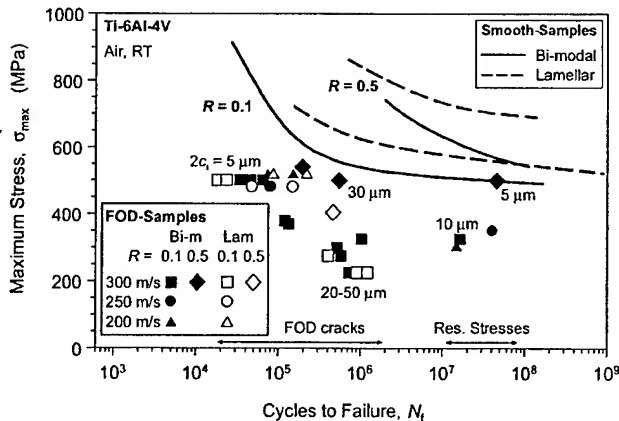


Fig. 4. S–N data ( $R=0.1$  and  $0.5$ ) show reduced fatigue life due to simulated FOD as compared to smooth-bar specimens in bi-modal and lamellar Ti–6Al–4V.  $2c_i$  is the surface crack length of FOD-induced microcracks. Bi-modal smooth-bar data ( $N_f < 2 \times 10^7$  cycles) taken from [13].

crack growth [24,25]. However, the principal factor is associated with the small crack effect.

As discussed elsewhere [5,19], the large-crack thresholds shown in Fig. 7 were determined up to the highest

load ratios ( $R \sim 0.91$ – $0.95$ ) under conditions (constant- $K_{\max}$ /increasing- $K_{\min}$ ) chosen to minimize the effect of crack closure. Accordingly, for the bi-modal microstructure, the threshold of  $\sim 1.9 \text{ MPa m}^{1/2}$  at  $R=0.95$  is considered to be a worst-case threshold for cracks of dimensions that are larger compared to the scale of the bi-modal microstructure, i.e. for continuum-sized cracks. Similarly, a worst-case threshold of  $\sim 3.3 \text{ MPa m}^{1/2}$  at  $R=0.91$  was measured for continuum-sized cracks in the lamellar microstructure [19]. However, observations show that the smallest FOD-initiated cracks, which have dimensions comparable with microstructural size-scales, i.e.  $\sim 2$ – $10 \mu\text{m}$ , can propagate at stress intensities well below these worst-case thresholds, specifically at applied stress intensities as low as  $\Delta K \sim 1 \text{ MPa m}^{1/2}$ , presumably due to biased sampling of the ‘weak links’ in the microstructure.

Based on the results shown in Fig. 7(a) ( $R=0.1$ ) and Fig. 7(b) ( $R=0.5$ ), it is clear that a concept of a worst-case threshold (determined under  $R \rightarrow 1$  conditions that minimize crack closure) applies strictly for continuum-sized cracks. This concept does not provide lower-bound threshold stress intensity for cracks on the scale of microstructural dimensions, as in the earliest stages of FOD-induced fatigue failure in bi-modal microstructure

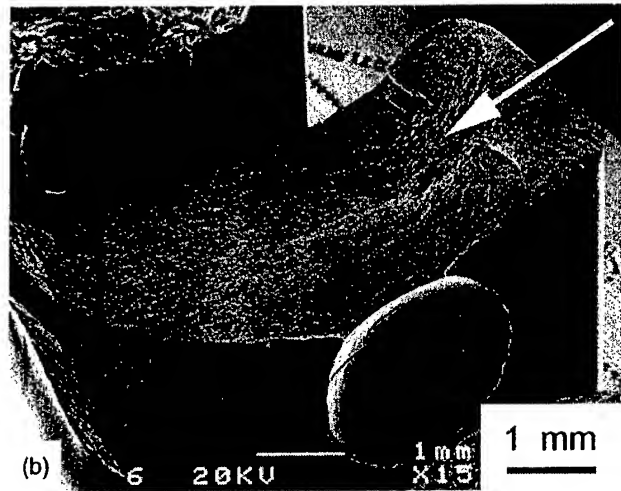
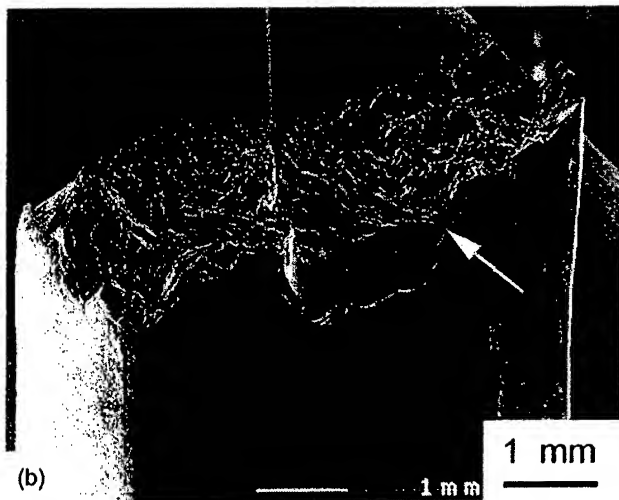
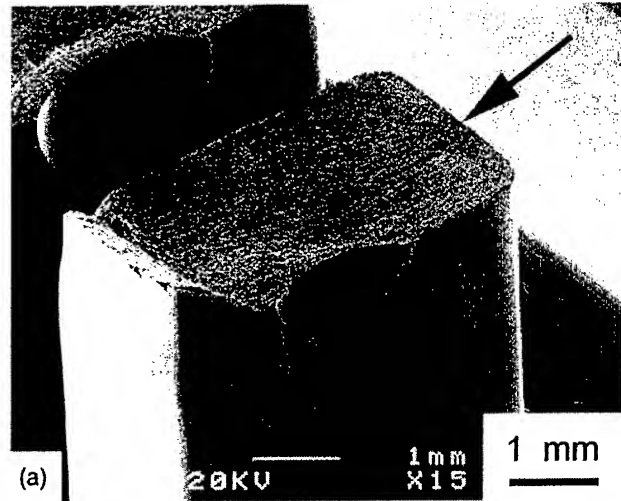
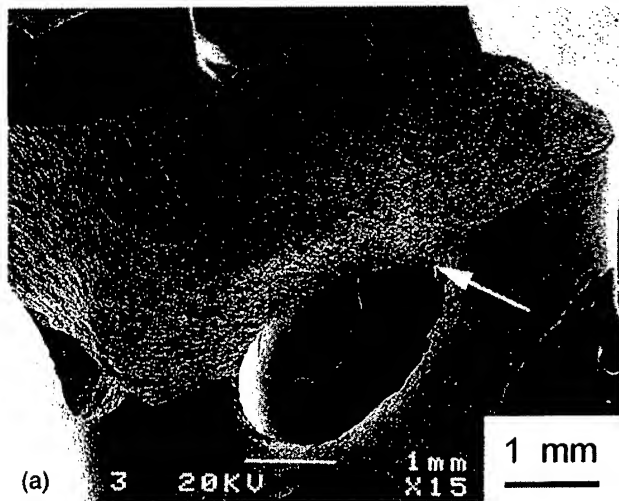


Fig. 5. At high applied stresses relative to the magnitude of the tensile residual stresses and high impact velocities (300 m/s), where large impact-induced microcracks are formed, failures initiated from impact-induced cracks at the crater rim (marked by arrows): (a) bi-modal microstructure (nominally applied  $\sigma_{\max}=500$  MPa,  $R=0.1$ ,  $N_F=65,000$  cycles) and (b) lamellar microstructure (nominally applied  $\sigma_{\max}=500$  MPa,  $R=0.1$ ,  $N_F=23,000$  cycles).

Fig. 6. At lower applied stresses and lower impact velocities, where impact-induced microcracks are much smaller or absent, failures initiated in regions of relatively high tensile residual stresses away from the indents (marked by arrow): (a) fatigue crack initiated close to the surface for 200 m/s impact (bi-modal microstructure, nominally applied  $\sigma_{\max}=325$  MPa,  $R=0.1$ ,  $N_F=1.5 \times 10^7$  cycles) and (b) less common case of fatigue crack initiation in the interior for 300 m/s high velocity impact (bi-modal microstructure, nominally applied  $\sigma_{\max}=325$  MPa,  $R=0.1$ ,  $N_F=1.6 \times 10^7$  cycles).

and even at later stages, e.g. for larger crack sizes, in lamellar microstructure.

#### 3.4. Threshold conditions based on the Kitagawa–Takahashi diagram

For the fine-grained bi-modal microstructure, coupling the concept of the worst-case threshold stress intensity with the  $10^7$ -cycle fatigue limit, as in the Kitagawa–Takahashi diagram [11], has been shown to provide an alternative approach to defining limiting conditions for HCF and FOD-related damage [7,10]. The Kitagawa–Takahashi diagram essentially describes a failure envelope,

given by the smooth-bar fatigue limit and the fatigue crack growth threshold, usually measured on fracture mechanics type specimens. The influence of crack size on the stress range conditions for no crack growth ( $da/dN=10^{-11}$ – $10^{-10}$  m/cycle) in the form of a modified Kitagawa–Takahashi diagram is shown for the bi-modal (closed symbols) and lamellar microstructures (open symbols) in Fig. 8(a) for applied load ratios of  $R=0.1$  and in Fig. 8(b) for  $R=0.5$ .

The results of the bi-modal microstructure (closed symbols and solid lines) show that crack growth at both  $R$ -ratios from FOD-induced microstructurally small



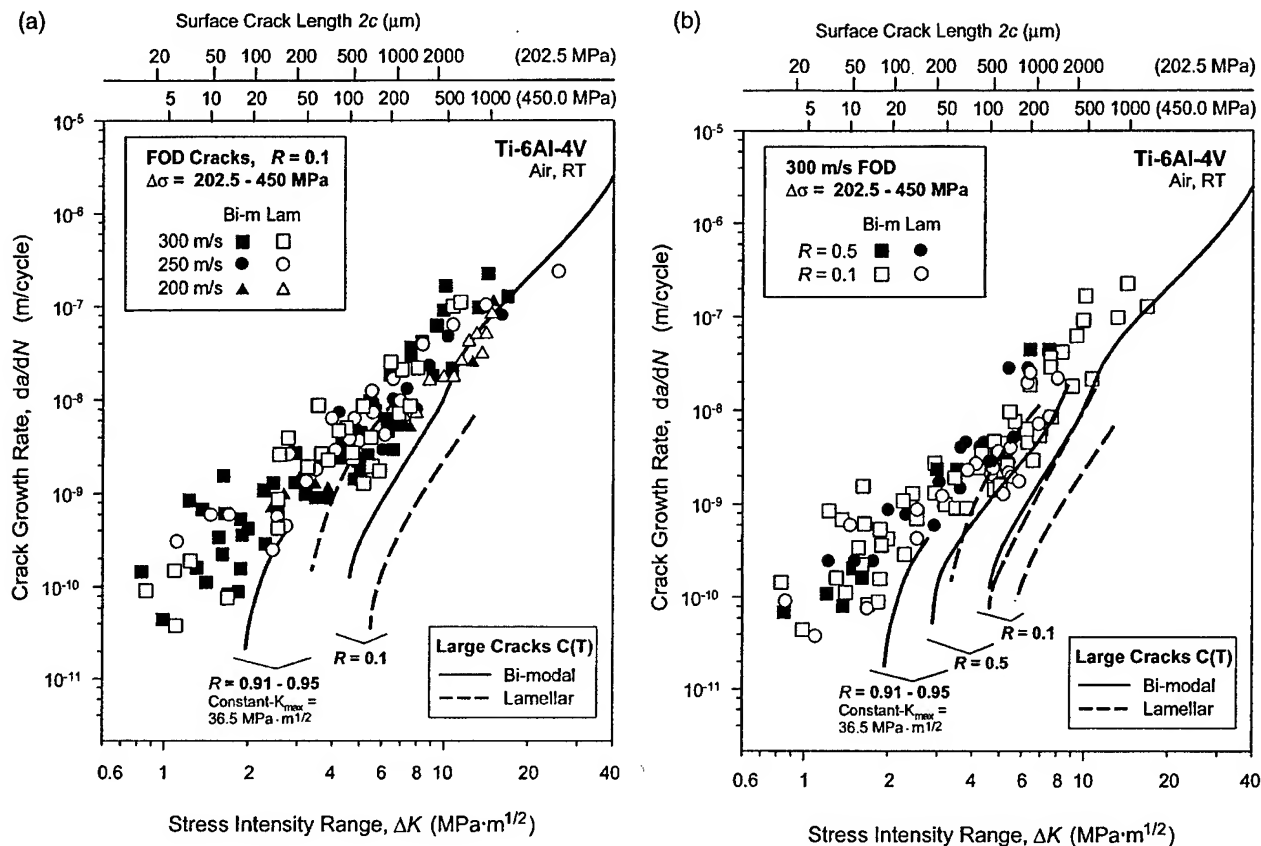


Fig. 7. Crack-growth rates as a function of applied stress-intensity range at load ratios of (a)  $R=0.1$  and (b)  $R=0.1$  and  $0.5$  of FOD small cracks and through-thickness large cracks in bi-modal and lamellar Ti-6Al-4V. Large-crack growth data for  $R=0.1$  were derived from constant load-ratio tests, whereas for  $R=0.91$  (lamellar) and  $0.95$  (bi-modal) constant- $K_{\max}$ /increasing- $K_{\min}$  testing was used [5,19].

cracks can be described by the stress-concentration corrected fatigue limit at relatively high applied stress ranges and by the worst-case threshold for larger continuum-sized cracks at lower stress ranges, Fig. 8(a) ( $R=0.1$ ) and Fig. 8(b) ( $R=0.5$ ). However, for failures in the presence of low applied stresses relative to tensile residual stresses, the effective  $R$ -ratio in the Kitagawa–Takahashi diagram has to be corrected for the presence of these residual stresses, as discussed below.

In the presence of low applied stress ranges relative to the tensile residual stresses in the vicinity of the damage sites, fatigue cracks were seen to be initiated in regions away from the indents (Fig. 6); specifically, they tended to initiate in regions of high tensile residual stress (oriented parallel to applied stresses). Fatigue crack initiation was generally found close to the side faces (Fig. 6(a)) of the rectangular gauge section, where tensile residual stresses of  $\sim 300$  MPa have been measured. A less common case of fatigue crack initiation in the interior for 300 m/s high-velocity impact is shown in Fig. 6(b). Data from these fatigue failures are plotted in Fig. 8(a) and (b) at surface crack lengths of  $2c=1$   $\mu\text{m}$ . Tensile residual stresses of  $\sim 300$  MPa significantly affect the mean stress and hence in this case increase the

$R$ -ratio of  $0.1$  to  $0.5$  (far-field stress range of  $\sim 300$  MPa). However, it can be seen in Fig. 8(c) that provided such residual stresses are accounted for, such failures at both  $R=0.1$  and  $0.5$  can still be described by the proposed Kitagawa–Takahashi approach, provided the limited conditions are given by the residual stress corrected smooth-bar fatigue limit for small crack sizes and worst-case threshold for larger crack sizes.

It should be noted that the failure envelopes in Fig. 8(a)–(c) can be somewhat better represented by the El Haddad et al. [26] empirical quantification of Kitagawa–Takahashi approach. This approach introduces a constant, termed the intrinsic crack length,  $2c_0$ , such that the stress intensity is defined as  $\Delta K = Y\Delta\sigma\sqrt{\pi(2c+2c_0)}$ , where  $Y$  is the geometry factor.

Corresponding threshold conditions for the lamellar microstructure are shown in the context of the Kitagawa–Takahashi approach by the results (open symbols and dashed lines) in Fig. 8(a) ( $R=0.1$ ) and Fig. 8(b) ( $R=0.5$ ). This coarser structure has a significantly better resistance to large-crack growth in the form of a  $\sim 75\%$  higher worst-case threshold, and a greater resistance to crack initiation in the form of a higher smooth-bar fatigue strength. However, the lamellar structure was

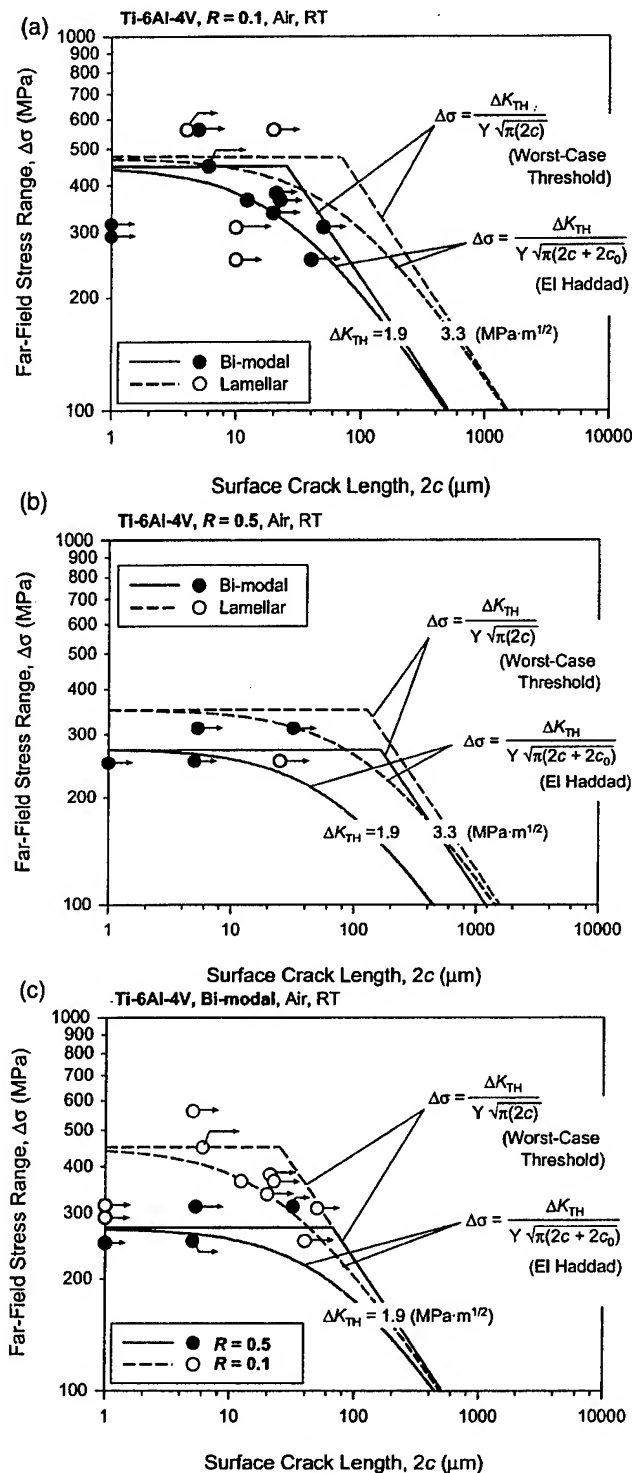


Fig. 8. Modified Kitagawa-Takahashi diagram representing the threshold crack-growth conditions ( $da/dN=10^{-11}$ – $10^{-10}$  m/cycle) at (a)  $R=0.1$  and (b)  $R=0.5$  for FOD-induced small-cracks in bi-modal and lamellar Ti-6Al-4V; (c) shows data for bi-modal microstructure at both  $R=0.1$  and  $0.5$ . Plotted is the threshold stress range as a function of surface crack length. Data points are corrected for the stress concentration of the FOD indents.

more prone to the formation of FOD-induced microcracks, although there was little difference in the HCF properties of the two microstructures in the presence of such microcracks, i.e. small-crack growth rates were essentially identical in the two structures. In general though, as the proposed Kitagawa–Takahashi approach is based on the limiting large-crack threshold and smooth-bar fatigue limit, the approach is somewhat less suited for FOD-induced failures in the lamellar microstructure. This is because the small-crack growth resistance, which controls such failures, is comparatively so much lower than that shown by large cracks in this structure; moreover, measured smooth-bar fatigue limits can be artificially inflated due to the much coarser microstructure which restricts the sampling of microstructural ‘weak links’ in specimens of finite size.

#### 4. Summary and conclusions

Based on a study of the influence of microstructure on FOD and resulting thresholds for HCF in bi-modal and lamellar microstructures in a Ti-6Al-4V alloy, the following conclusions can be made:

1. FOD, simulated by high-velocity (200–300 m/s) impacts of steel spheres on a flat surface, was found to markedly reduce resistance to HCF in both bi-modal and lamellar microstructures. Principally, the effect of FOD was to induce preferred sites for the premature initiation of fatigue cracks on subsequent cycling.
2. Premature crack initiation resulted from (1) the stress concentration due to the FOD indentation, (2) presence of (microstructurally small) microcracks at the crater rim of the damaged zone (seen only at the highest impact velocities), (3) localized presence of tensile residual stresses, and (4) microstructural damage from FOD-induced plastic deformation.
3. For lower velocity impacts (200 m/s), neither such microcracking at the crater rim, nor circumferentially orientated shear bands emanating from the surface of the crater, could be detected. This strongly implies that low velocity or quasi-static indentations do not necessarily provide a realistic simulation of high-velocity FOD.
4. At stress-concentration corrected stress ranges from 250 to 560 MPa, FOD-initiated microcracks ( $\sim 2$ – $10$   $\mu\text{m}$  in size) propagated at applied stress intensities even below  $\Delta K=1$   $\text{MPa m}^{1/2}$  (at both  $R=0.1$  and  $0.5$ ) and showed no pronounced threshold behavior, i.e. small-crack growth occurred at driving forces well below the worst-case  $\Delta K_{TH}$  threshold of  $1.9$   $\text{MPa m}^{1/2}$  (bi-modal) and  $3.3$   $\text{MPa m}^{1/2}$  (lamellar microstructure) for continuum-sized cracks (i.e. cracks larger than the characteristic microstructural

size-scales) in this alloy. Furthermore, such FOD-induced fatigue cracks propagated at rates at least an order of magnitude faster than corresponding large ( $>5$  mm) cracks at the same applied stress-intensity range.

5. The critical condition for HCF in the bi-modal and lamellar Ti-6Al-4V in the presence of continuum-sized cracks could be defined in terms of the worst-case fatigue threshold (determined under  $R \rightarrow 1$  conditions that minimize crack closure). However, this concept alone is inappropriate where microstructurally small cracks are present.
6. For FOD-initiated failures, where the critical condition for HCF must be defined in the presence of microstructurally small cracks, the Kitagawa-Takahashi diagram represents a more appropriate approach, where the limiting conditions are defined in terms of the worst-case  $\Delta K_{TH}$  fatigue threshold (at large continuum-sized crack sizes) and the  $10^7$ -cycle fatigue limit (at small crack sizes), with corrections for the stress concentration of the indent and the presence of residual stresses (which affect the effective load ratio).

## Acknowledgements

This work was supported by the Air Force Office of Science and Research, Grant No. F49620-96-1-0478, under the Multidisciplinary University Research Initiative on 'High Cycle Fatigue' to the University of California, Berkeley. Special thanks are due to Prof. Werner Goldsmith (UCB) for providing the compressed-gas gun facility and to Prof. J.W. Hutchinson, Dr J.M. McNaney and Dr A.W. Thompson for helpful discussions, and to B.L. Boyce, R.K. Nalla, and Xi Chen for providing us with their results prior to publication, and to J.L. Hendricks and C.K. Lau for their help with scanning electron microscopy.

## References

- [1] Cowles BA. High cycle fatigue in aircraft gas turbines — an industry perspective. *Int J Fracture* 1996;80:147–63.
- [2] Nicholas T, Zuiker JR. On the use of the Goodman diagram for high cycle fatigue design. *Int J Fracture* 1996;80:219–35.
- [3] Larsen JR, Worth BD, Annis CG Jr., Haake FK. An assessment of the role of near-threshold crack growth in high cycle fatigue life prediction of aerospace titanium alloys under turbine engine spectra. *Int J Fracture* 1996;80:237–55.
- [4] Ritchie RO. Small cracks and high-cycle fatigue. In: Chang JCI, Coulter J, Brei D, Martinez WHG, Friedmann PP, editors. *Proceedings of the ASME Aerospace Division, AD-Vol. 52*, ASME, Warrendale, PA, 1996:321–33.
- [5] Ritchie RO, Davidson DL, Boyce BL, Campbell JP, Roder O. High-cycle fatigue of Ti-6Al-4V. *Fatigue Fract Eng Mat Struct* 1999;22:621–31.
- [6] Peters JO, Roder O, Boyce BL, Thompson AW, Ritchie RO. Role of foreign-object damage on thresholds for high-cycle fatigue in Ti-6Al-4V. *Metall Mater Trans A* 2000;31A:1571–83.
- [7] Peters JO, Ritchie RO. Influence of foreign-object damage on crack initiation and early crack growth during high-cycle fatigue of Ti-6Al-4V. *Eng Fract Mech* 2000;67A:193–207.
- [8] Nicholas T, Barber JR, Bertke RS. Impact damage on titanium leading edges from small hard objects. *Exp Mech* 1980;October:357–64.
- [9] Hudak SJ, Chan KS, McClung RC, Chell GG, Lee Y-D, Davidson DL. High cycle fatigue of turbine blade materials. Final technical report UDRI Subcontract No. RI 40098X SwRI Project No. 18-8653, 1999.
- [10] Ritchie RO, Peters JO. Small fatigue cracks: mechanics, mechanisms and engineering applications. *Mater Trans* 2001;42:58–67.
- [11] Kitagawa H, Takahashi S. Applicability of fracture mechanics to very small cracks or the cracks in the early stage. In: *Proceedings of the Second International Conference on Mechanical Behavior of Materials*. Metals Park (OH): ASM, 1976:627–31.
- [12] Eylon D. Summary of the available information on the processing of the Ti-6Al-4V HCF/LCF program plates. University of Dayton report, Dayton (OH), 1998.
- [13] Hines JA, Peters JO, Lütjering G. Microcrack propagation in Ti-6Al-4V alloys. In: Boyer RR, Eylon D, Lütjering G, editors. *Fatigue behavior of titanium alloys*. Warrendale (PA): TMS, 1999:15–22.
- [14] Lukáš P. Stress intensity factor for small notch-emanating cracks. *Eng Fract Mech* 1987;26:471–3.
- [15] Nisida M, Kim P. Stress concentration caused by the presence of a spherical cavity or a spherical-surfaced hollow. In: *Proceedings of the Twelfth National Congress Applied Mechanics*, 1962:69–74.
- [16] Newman JC Jr., Raju IS. An empirical stress-intensity factor equation for the surface crack. *Eng Fract Mech* 1981;15:185–92.
- [17] Boyce BL, Chen X, Hutchinson JW, Ritchie RO. The residual stress state due to a spherical hard-body impact. *Mech Mater* 2001;33:441–54.
- [18] Chen X, Hutchinson JW. Foreign object damage and fatigue crack threshold: cracking outside shallow indents. *Int J Fract* 2001;107:31–51.
- [19] Nalla RK, Campbell JP, Ritchie RO. Mixed-mode high-cycle fatigue thresholds in Ti-6Al-4V: a comparison of large and small crack behavior. In: *Proceedings of the Sixth International Conference on Biaxial/Multiaxial Fatigue and Fracture*, Lisbon, Portugal, 2001.
- [20] Suresh S, Ritchie RO. Propagation of short fatigue cracks. *Int Metals Rev* 1984;29:445–76.
- [21] Miller KJ, de los Rios ER. *The behaviour of short fatigue cracks*. Mechanical Engineering Publications, London, UK, 1986.
- [22] Ritchie RO, Lankford J. *Small fatigue cracks*. Warrendale, PA: TMS-AIME, 1986.
- [23] Ravichandran KS, Ritchie RO, Murakami Y. *Small fatigue cracks: mechanics, mechanisms and applications*. Oxford, UK: Elsevier, 1999.
- [24] Wagner L, Lütjering G. Influence of shot peening parameters on the surface layer properties and the fatigue life of Ti-6Al-4V. In: Fuchs HO, editor. *Proceedings of the Second International Conference of Shot Peening*. Paramus (NJ): American Shot Peening Society, 1984:194–200.
- [25] Wagner L, Lütjering G. Influence of a shot peening treatment on the fatigue limit of Ti-6Al-4V. In: Fuchs HO, editor. *Proceedings of the Second International Conference Shot Peening*. Paramus (NJ): American Shot Peening Society, 1984:201–7.
- [26] El Haddad MH, Topper TH, Smith KN. Prediction of non propagating cracks. *Eng Fract Mech* 1979;11:573–84.

# Foreign-object damage and high-cycle fatigue of Ti–6Al–4V

J.O. Peters, R.O. Ritchie \*

*Department of Materials Science and Engineering, University of California, Berkeley, CA 94720-1760, USA*

## Abstract

Recent high-cycle fatigue (HCF) related failures of gas-turbine jet engines have prompted a re-examination of the design methodologies for HCF-critical components, such as titanium alloy turbine blades. As foreign-object damage (FOD) from ingested debris is a key concern for HCF-related failures of such blades, the current study is focused on the role of simulated high velocity FOD in affecting the initiation and early growth of small surface fatigue cracks in a Ti–6Al–4V alloy, processed for typical blade applications. It is found that resistance to HCF is markedly reduced, primarily due to earlier fatigue crack initiation. The mechanistic effect of FOD on such premature fatigue crack initiation and the subsequent crack growth is discussed in terms of four prominent factors: (i) the presence of small microcracks in the damaged zone; (ii) the stress concentration associated with the FOD indentation; (iii) the localized presence of tensile residual hoop stresses at the base and rim of the indent sites; and (iv) microstructural damage from FOD-induced plastic deformation. In view of the in-service conditions, i.e., small crack sizes, high frequency ( $> 1$  kHz) vibratory loading and (depending on the blade span location) high mean stress levels, a damage-tolerant design approach, based on the concept of a threshold for no fatigue-crack growth, appears to offer a preferred solution. It is shown that FOD-initiated cracks that are of a size comparable with microstructural dimensions can propagate at applied stress-intensity ranges on the order of  $\Delta K \sim 1$  MPa $\sqrt{\text{m}}$ . © 2001 Elsevier Science B.V. All rights reserved.

**Keywords:** Foreign-object damage; High-cycle fatigue (HCF); Fatigue-crack growth threshold; Small cracks; Ti–6Al–4V

## 1. Introduction

The increasing incidence of high-cycle fatigue (HCF)-related titanium alloy fan and compressor blade failures in military gas-turbine engines, involving (i) foreign-object damage; (ii) fretting and (iii) interactions of low cycle fatigue (LCF) and HCF loading, has instigated a re-examination of the current Goodman design approach for HCF [1,2]. Indeed, design against HCF, based on a damage-tolerant concept of a fatigue-crack growth threshold for no cracking, would appear to offer a preferred approach. However, such thresholds have to reflect representative HCF conditions of high frequencies, small crack sizes and, depending on the blade span location, very high mean stress levels [1,2].

Foreign-object damage (FOD), from hard body impacts such as stones, which impact primarily on the fan blades, can result in immediate blade fracture or damage from stress-raising notches [3,4] or cracks [5], de-

pending on the severity of impact. In a recent study on Ti–6Al–4V [5], where such damage was simulated by high-velocity impacts of steel shot on a flat surface, FOD was found to markedly reduce the fatigue strength. It was observed that small microcracks formed in the damaged region of the highest velocity impacts ( $300 \text{ m s}^{-1}$ ), and provided preferred sites for premature fatigue crack initiation on subsequent fatigue cycling. In general, these mechanistic effects can be described in terms of (i) FOD-induced microcracks in the damage zone, (ii) stress concentration associated with the FOD-indentation, (iii) localized presence of impact induced tensile residual hoop stresses at locations of the preferred sites for crack initiation, and (iv) microstructural damage from FOD-induced plastic deformation.

In the present study, we further investigate the effect of FOD-induced microcracks ( $\sim 2\text{--}10 \mu\text{m}$ ) at an impact velocity of  $300 \text{ m s}^{-1}$  in a Ti–6Al–4V alloy,  $\alpha + \beta$  processed for turbine blade applications. Specifically, the threshold conditions for fatigue crack initiation and growth of such microcracks are defined and compared

\* Corresponding author. Tel.: +1-510-486-5798; fax: +1-510-486-4995.

E-mail address: roritchie@lbl.gov (R.O. Ritchie).

with the fatigue threshold ( $\Delta K_{TH}$ ) behavior of naturally-initiated small ( $2c \sim 45\text{--}1000\text{ }\mu\text{m}$ ) and large through-thickness ( $> 5\text{ mm}$ ) cracks in undamaged material.

## 2. Experimental procedures

The titanium alloy Ti–6Al–4V under study (chemical composition Ti–6.30Al–4.19V–0.19Fe–0.19O, wt.%), was from the forgings produced for U.S. Air Force sponsored programs on High-Cycle Fatigue. Material and processing details are given in [5]. The bimodal microstructure is shown in Fig. 1. Uniaxial tensile tests (performed parallel to the plate length), gave a yield stress of 915 MPa, UTS of 965 MPa and tensile elongation of 19%. Foreign-object damage was simulated by firing 3.2 mm Cr-hardened steel spheres, normally onto a flat specimen surface of uniaxial fatigue



Fig. 1. Bimodal microstructure of Ti–6Al–4V.

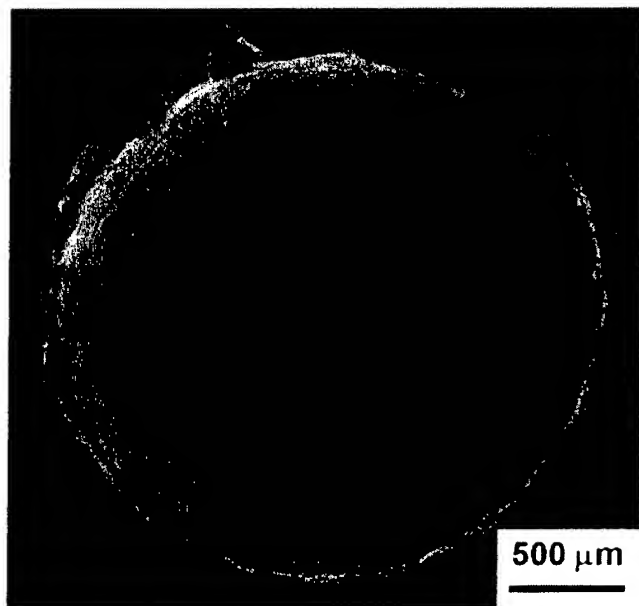


Fig. 2. SEM micrograph of  $300\text{ m s}^{-1}$  impact crater.

(so-called  $K_B$ ) specimens, at a velocity of  $300\text{ m s}^{-1}$  using a compressed-gas gun facility (see [5]).

The effect of foreign-object damage on the fatigue behavior was examined using modified  $K_B$  specimens (cross section  $3.2 \times 5.2\text{ mm}$ , gauge length  $20\text{ mm}$ ). After impact, specimens were subsequently cycled (sinusoidal waveform) at nominally maximum stress levels of  $225\text{--}500\text{ MPa}$  ( $R = \sigma_{\min}/\sigma_{\max} = 0.1$ ). Throughout fatigue testing, specimens were periodically removed from the test frame and the progress of crack initiation and growth examined in a scanning electron microscope (SEM).

Approximate local stress intensities for small cracks at the indentation rim, were calculated from Lukáš' solution [6] for small cracks at notches (which includes indentation geometry and stress concentration effects), in terms of the crack depth  $a$ , indentation radius  $\rho$ , stress range  $\Delta\sigma$ , and elastic stress-concentration factor  $k_t = 1.25$  [7]:

$$\Delta K = \frac{0.7k_t}{\sqrt{1 + 4.5(a/\rho)}} \Delta\sigma \sqrt{\pi a} \quad (1)$$

## 3. Results and discussion

### 3.1. Characterization of foreign-object damage

A typical damage site caused by  $300\text{ m s}^{-1}$  impact is displayed in Fig. 2. Earlier results [5], showed that at velocities above  $250\text{ m s}^{-1}$ , a pronounced pile-up of material (Fig. 2) at the crater rim resulted in multiple micro-notches and microcracking (insert in Fig. 3). When these microcracks ( $\sim 2\text{--}25\text{ }\mu\text{m}$ ) were favorably oriented with respect to applied stress axis on subsequent fatigue cycling, they were found to provide the nucleation sites for high-cycle fatigue-crack growth (Fig. 3).

### 3.2. Fatigue properties

Stress-life (S–N) data in Fig. 4 clearly show the detrimental effect of FOD on the fatigue strength. Specifically, at a far-field maximum stress of  $500\text{ MPa}$  ( $R = 0.1$ ), representing the  $10^7$ -cycle fatigue limit for undamaged material, final failure in the damaged material occurred at approximately  $4\text{--}5 \times 10^4$  cycles. As discussed earlier [5], this reduction in fatigue strength can be considered principally in terms of earlier fatigue crack initiation due to four prominent factors: (i) FOD-induced microcracking, (ii) stress concentration, (iii) residual stresses, and (iv) damaged microstructure.

It was found that the location for crack initiation at impact damaged sites depends strongly on impact velocity. Typically for  $300\text{ m s}^{-1}$  impacts, FOD-induced microcracking in the pile-up region of the impact crater

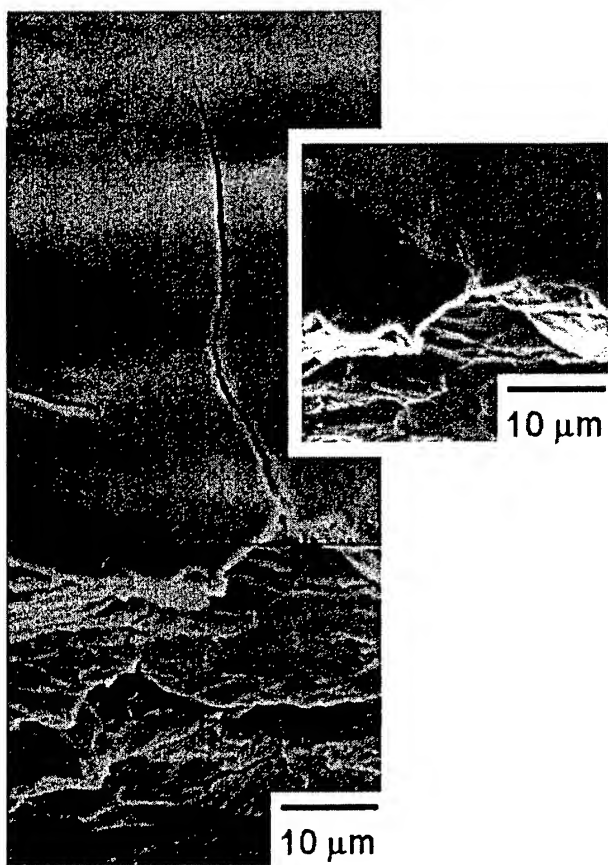


Fig. 3. SEM micrograph of FOD-induced microcracking at the crater rim (insert) and subsequent fatigue-crack growth at such microcrack after 29 000 cycles ( $\sigma_{\max} = 500$  MPa,  $R = 0.1$ ).

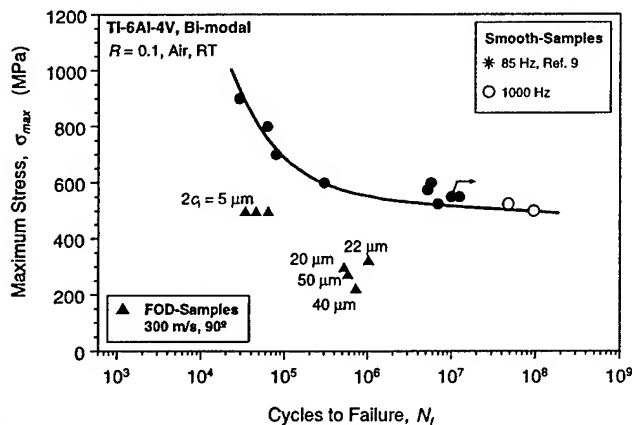


Fig. 4. S–N data show reduced fatigue life due to simulated FOD as compared with smooth-bar specimens [9] in bimodal Ti–6Al–4V.  $2c_i$  is the surface crack length of FOD-induced microcracks.

rim provides the dominant site for the initiation of fatigue cracks on subsequent cycling (Fig. 3). For lower velocity impacts ( $200 \text{ m s}^{-1}$ ), no such microcracking could be detected; in this instance, surface cracks tended to form at the base of the indentation site where the stress concentration was highest [5]. This strongly implies that low velocity or quasi-static indentations do

not necessarily provide a realistic simulation of FOD. In addition, tensile residual hoop stresses (estimated in [8]), the highly deformed microstructure in this region [5], and the stress-concentration factors ( $k_t \sim 1.25$ ) are contributing factors.

Fig. 5 shows the fatigue-crack growth rates of FOD samples as compared with results of naturally-initiated small cracks ( $\sim 45\text{--}1000 \mu\text{m}$ ) [9], and through-thickness large cracks ( $> 5 \text{ mm}$ ) [2] in undamaged material. FOD-initiated small-crack growth rates are aligned approximately between the large-crack data (lower bound) and naturally-initiated crack data (upper bound). Typical for the small-crack effect e.g. [10], the growth rates of the naturally- and FOD-initiated small cracks are roughly in order of a magnitude faster than corresponding large-crack results at near-threshold levels. The large-crack threshold of  $\sim 1.9 \text{ MPa}\sqrt{\text{m}}$  at  $R = 0.95$  (where the effect of crack closure is eliminated) is considered to be a definitive lower bound ‘worst-case’ threshold for cracks of dimensions large compared with the scale of the microstructure, i.e. for ‘continuum-sized’ cracks, as discussed earlier [2]. However, smallest FOD-initiated cracks ( $\sim 2\text{--}25 \mu\text{m}$ ), com-

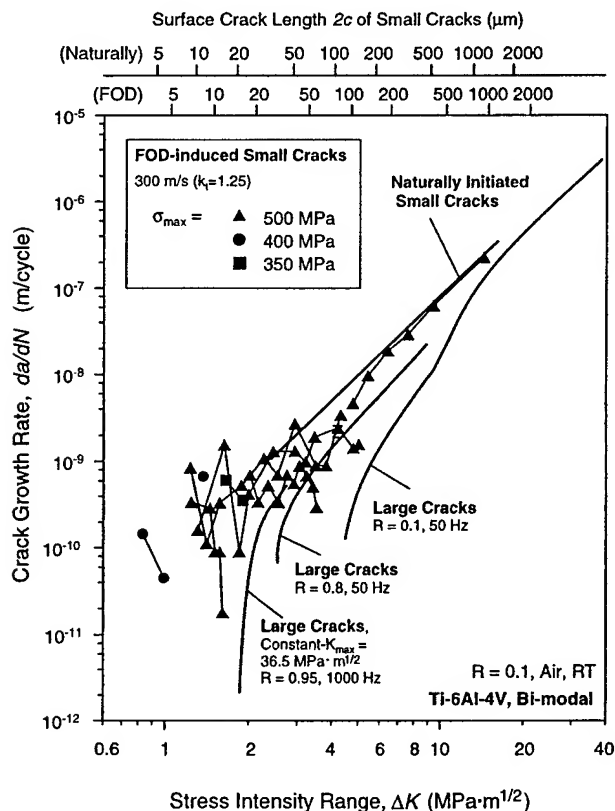


Fig. 5. Crack-growth rates as a function of applied stress-intensity range of FOD- and naturally-initiated small cracks and through-thickness large cracks in bimodal Ti–6Al–4V. Small-cracks were initiated at  $\sigma_{\max} = 650$  MPa ( $R = -1$ ). [9] Large-crack growth data for  $R \leq 0.8$  were derived from constant load-ratio tests, whereas for  $R \geq 0.8$ , constant- $K_{\max}$ /increasing- $K_{\min}$  testing was used [2].

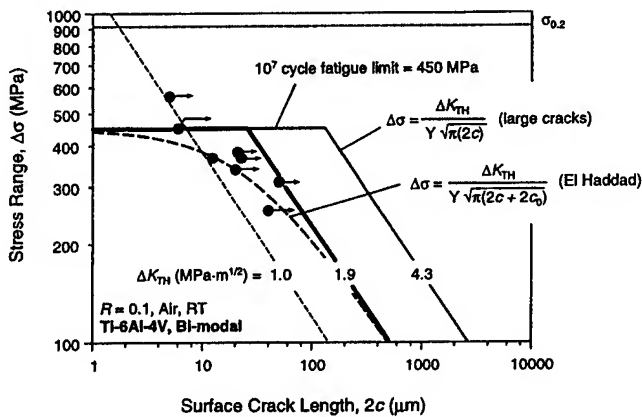


Fig. 6. Crack growth conditions of FOD-induced small-cracks ( $da/dN = 10^{-11}$ – $10^{-10}$  m per cycle) as a function of cyclic stress range and surface crack length are shown in a modified Kitagawa–Takahashi diagram.

parable with microstructural size-scales, can propagate at stress intensities well below this ‘worst-case’ threshold. This is specifically at applied stress intensities as low as  $\Delta K \sim 1 \text{ MPa}\sqrt{\text{m}}$ , at nominal maximum stresses from 325 to 500 MPa ( $R = 0.1$ ), presumably due to biased sampling of the ‘weak links’ in the microstructure. It is believed that a  $\Delta K$  of  $1 \text{ MPa}\sqrt{\text{m}}$  is the lowest stress-intensity range ever measured for crack growth in Ti–6Al–4V. It should be noted here that although the FOD-induced residual stresses are not included in the calculation of  $K$  (Eq. (1)), such stresses do not change the stress-intensity range ( $\Delta K$ ); they affect the mean stress and hence, alter the local load ratio. It is clear that the earlier stated argument [2,5] for the notion of a high-cycle fatigue threshold, which was based on the concept of a ‘worst-case’ threshold (determined under  $R \rightarrow 1$  conditions that minimize crack closure), applies strictly for ‘continuum-sized’ cracks. It does not provide a lower-bound threshold stress intensity for cracks on the scale of microstructural dimensions, as in the earliest stages of FOD-induced fatigue failure.

Coupling the notion of the ‘worst-case’ threshold stress intensity with the fatigue limit, as in the Kitagawa–Takahashi diagram [11], provides an alternative approach to defining limiting conditions for HCF and FOD-related damage. Fig. 6 shows the influence of crack size on the fatigue thresholds in the form of a modified Kitagawa diagram for crack-growth threshold conditions of  $da/dN = 10^{-11}$ – $10^{-10}$  m per cycle. According to this approach (solid line), the stress range  $\Delta\sigma$  for crack arrest is defined by the  $10^7$ -cycle fatigue limit with the fatigue-crack growth threshold ( $\Delta K_{\text{TH}}$ ) measured on ‘continuum-sized’ cracks. El Haddad et al. [12] empirically quantified the threshold conditions by introducing a constant (intrinsic) crack length  $2c_0$ , such that the stress intensity is defined as  $Y\Delta\sigma\sqrt{\pi(2c + 2c_0)}$ , where  $Y$  is the geometry factor.

The present results, plotted in this format in Fig. 6, show that crack growth from FOD-induced microstructurally-small cracks apparently occur at stress concentration corrected stress ranges well predicted by the Kitagawa–El Haddad limit, defined by the ‘worst-case’  $\Delta K_{\text{TH}}$  threshold and  $10^7$ -cycle fatigue limit.

#### 4. Conclusions

Simulated FOD impact ( $300 \text{ m s}^{-1}$ ) of steel spheres on a flat surface markedly degrade fatigue strength of Ti–6Al–4V. Specifically, the fatigue life of smooth-bar samples was reduced by some two orders of magnitude at an applied stress corresponding to the smooth-bar  $10^7$ -cycles fatigue limit ( $R = 0.1$ ).

The detrimental effect of FOD is attributed to (i) FOD-induced precracks at the crater rim of the damaged zone, (ii) stress concentration associated with the FOD indentation, (iii) presence of tensile residual stresses at the crater rim and (iv) microstructural damage due to FOD-impact.

The principal effect of FOD in reducing fatigue life was found to induce microcracks in the pile-up of material around the impact crater rim, i.e. preferred sites for the premature initiation of fatigue cracks.

At far-field maximum stresses from 325 to 500 MPa ( $R = 0.1$ ), FOD-initiated cracks ( $\sim 2$ – $25 \mu\text{m}$ ) grow at applied stress intensities as low as  $\Delta K = 1 \text{ MPa}\sqrt{\text{m}}$ , i.e. well below the ‘worst-case’  $\Delta K_{\text{TH}}$  threshold of  $1.9 \text{ MPa}\sqrt{\text{m}}$  for ‘continuum-sized’ cracks (cracks larger than the characteristic microstructural size-scales) in this alloy.

Correspondingly, the critical condition for HCF in the bimodal Ti–6Al–4V in the presence of ‘continuum-sized’ cracks ( $> 50$ – $100 \mu\text{m}$ ) can be defined in terms of the ‘worst-case’ fatigue threshold (determined under  $R \rightarrow 1$  conditions that minimize crack closure).

However, the preferred approach for FOD-initiated failures in the presence of microstructurally-small cracks is to use the modified Kitagawa–Takahashi diagram, where the limiting conditions for HCF are defined in terms of the stress concentration corrected  $10^7$ -cycle fatigue limit (at microstructurally-small crack sizes) and the ‘worst-case’  $\Delta K_{\text{TH}}$  fatigue threshold (at larger, ‘continuum-sized’ crack sizes).

#### Acknowledgements

This work was supported by the Air Force Office of Science and Research, Grant No. F49620-96-1-0478, under the Multidisciplinary University Research Initiative on ‘High Cycle Fatigue’ to the University of California, Berkeley. Special thanks are due to Professor Werner Goldsmith (UCB) for providing the com-



pressed-gas gun facility, and to Professor J. W. Hutchinson, B. L. Boyce, Dr J. M. McNaney and Dr A. W. Thompson for helpful discussions.

## References

- [1] J.R. Larsen, B.D. Worth, C.G. Annis Jr, F.K. Haake, *Int. J. Fracture* 80 (1996) 237–255.
- [2] R.O. Ritchie, D.L. Davidson, B.L. Boyce, J.P. Campbell, O. Roder, *Fatigue Fract. Eng. Mat. Struct.* 22 (1999) 621–631.
- [3] T. Nicholas, J.R. Barber, R.S. Bertke, *Experiment. Mech.*, (1980), pp. 357–364.
- [4] S.J. Hudak, K.S. Chan, R.C. McClung, G.G. Chell, Y.-D. Lee, D.L. Davidson, *High Cycle Fatigue of Turbine Blade Materials*, Final Technical Report UDRI Subcontract No. RI 40098X SwRI Project No. 18-8653, 1999.
- [5] J.O. Peters, O. Roder, B.L. Boyce, A.W. Thompson, R.O. Ritchie, *Metall. Mater. Trans.* 31A (2000) 1571–1583.
- [6] P. Lukáš, *Eng. Fract. Mech.* 26 (1987) 471–473.
- [7] M. Nisida, P. Kim, *Proceedings of the Twelfth National Congress on Applied Mechanics*, 1962, pp. 69–74.
- [8] X. Chen, J.W. Hutchinson, *Int. J. Fract.*, 2000, in press.
- [9] J.A. Hines, J.O. Peters, G. Lütjering, in: R.R. Boyer, D. Eylon, G. Lütjering (Eds.), *Fatigue Behavior of Titanium Alloys*, TMS, Warrendale, PA, 1999, pp. 15–22.
- [10] R.O. Ritchie, J. Lankford, *Mater. Sci. Eng.* 84 (1986) 11–16.
- [11] H. Kitagawa, S. Takahashi, *Proceedings of Second International Conference on Mechanical Behavior of Materials*, ASM, Metals Park, OH, 1976, pp. 627–631.
- [12] M.H. El Haddad, T.H. Topper, K.N. Smith, *Eng. Fract. Mech.* 11 (1979) 573–584.





## Foreign object damage and fatigue crack threshold: Cracking outside shallow indents

XI CHEN and JOHN W. HUTCHINSON

*Division of engineering and applied sciences, Harvard university, Cambridge, MA 02138, USA*

Received 23 November 1999; accepted in revised form 9 June 2000

**Abstract.** Foreign Object Damage (FOD) usually happens when objects are ingested into jet engines powering military or civil aircraft. Under extreme conditions, FOD can lead to severe structural damage. More commonly it produces local impacted sites of the fan and compressor airfoils, lowering fatigue life of these components. FOD is a prime cause for maintenance and repair in aircraft engines. In this paper, a framework for analyzing FOD and its effect on fatigue cracking is established. A finite element analysis is used to identify three relevant regimes of FOD related to the depth of penetration into the substrate, and to determine the residual stresses. Most of the emphasis in this paper focuses on fatigue cracks emerging from shallow indentations, which are generally expected to be of most practical concern. Full three-dimensional finite element solutions are obtained for semi-circular surface cracks emerging from specific locations at the indentation revealing the influence of the residual stress on the stress intensity factor distribution. For shallow indents, a relatively simple dimensionless formula for the relation between the residual stress intensity factor, the crack size, and the indentation width are developed. These results, together with results for the intensity factor variations due to cyclic loading, have been used to address the question: To what extent do the residual stresses caused by the FOD reduce the critical crack size associated with threshold fatigue crack growth? Formulas for the critical crack size are obtained. Specific results are presented for the blade alloy, Ti-6Al-4V, revealing that FOD can reduce the critical crack size by as much as 60%.

**Key words:** Foreign object damage, contact mechanics, crack mechanics, fatigue analysis, indentation regimes, critical crack size.

### 1. Introduction

Foreign object damage by hard-particles mainly occurs during motion of the aircraft on the airfield, during takeoff and during landing. Typical objects ingested are stones and other debris from the airfield, with sizes in the millimeter regime. Typical impact velocities are in the range of 100 - 350 m/s, depending on the specific engine. Of concern here are impact locations on the blades. Such microstructural damage can promote fatigue-crack growth under high-cycle fatigue loading. This has become a critical issue in the lifetime prediction of turbine-engine components and a prime concern in maintenance and repair (Ritchie et al., 1999; Peters et al., 2000). The unusually high frequencies typical of in-flight vibratory loading necessitate a defect-tolerant approach based on designing below the threshold for fatigue crack propagation. FOD damage must be factored into this approach. Otherwise, the FOD damage can lead to non-conservative life prediction and unexpected high-cycle fatigue failures.

Most FOD occur as damage to the leading edges of turbine blades. To gain insight into the interaction between FOD and fatigue cracking, we have considered a less frequent form of FOD whereas the damage is assumed to occur away from the edge. The research has been coordinated with a parallel experimental study (Peters et al., 2000). The study initiated in

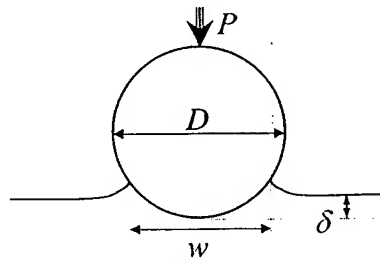


Figure 1. The geometry of spherical indentation.

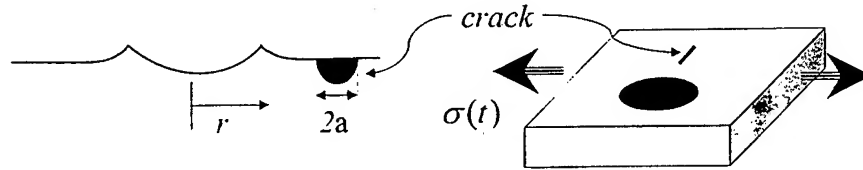


Figure 2. A semi-circular surface crack with radius  $a$  is embedded inside the residual stress field of the indent and subjected to cyclic stress  $\sigma(t)$ .

this paper considers the normal impression of a hard spherical particle into a thick elastic-plastic substrate (Figure 1). The indentation field is axisymmetric. The resulting residual stresses are determined and the locations at the surface where tensile stresses are most likely to promote cracking are identified. The second step in the approach is the three-dimensional finite element analysis of a semi-circular surface crack within the residual stresses field. The final step combines the stationary stress intensity factor due to the indent with the intensity factor variation due to the cyclic loads (Figure 2) to make predictions for critical crack sizes based on threshold fatigue crack growth data.

The parallel experimental study has been conducted by Peters et al. (2000), who investigated the influence of FOD on the high-cycle fatigue properties of Ti-6Al-4V alloy, which is commonly used as gas turbine blades in military aircraft. The material is almost ideally plastic with very little strain hardening and a tensile yield stress of about 950 MPa. In their experiments, they used hardened steel spheres (with diameter 3.175 mm) to normally impact a flat Ti-6Al-4V alloy specimen at 200–300 m s<sup>-1</sup>. After impact, the specimens were cycled at a maximum nominal stress of 500 MPa at a load ratio of 0.1, and the initiation and subsequent growth of the fatigue cracks emerging from the indent were observed. The authors found that FOD provides sites for the initiation of small fatigue cracks, and in some cases crack initiation occurred at cycle lifetimes which were orders of magnitude lower than found for un-impacted specimens. For the 200 m s<sup>-1</sup> impact, crack initiation was observed to occur at the bottom of the indent, while the 300 m/s impact a prominent crater rim was produced and this turned out to be the site of the crack initiation.

The paper is organized by sections to follow the three steps mentioned in connection with the overall approach. Section 2 presents the indentation analysis and results. Here contact is made with recent work on the finite element analysis of indentation. In particular, it will be seen that three separate regimes to the indentation problem can be identified: very shallow, moderately shallow and deep indents. The primary focus in this paper will be on moderately shallow indents for which relatively simple scaling relations exist for the residual stress fields. Some discussion of trends for deep indentations will also be given. The solutions for the stress intensity factor for a semi-circular surface crack within the residual stress field of the

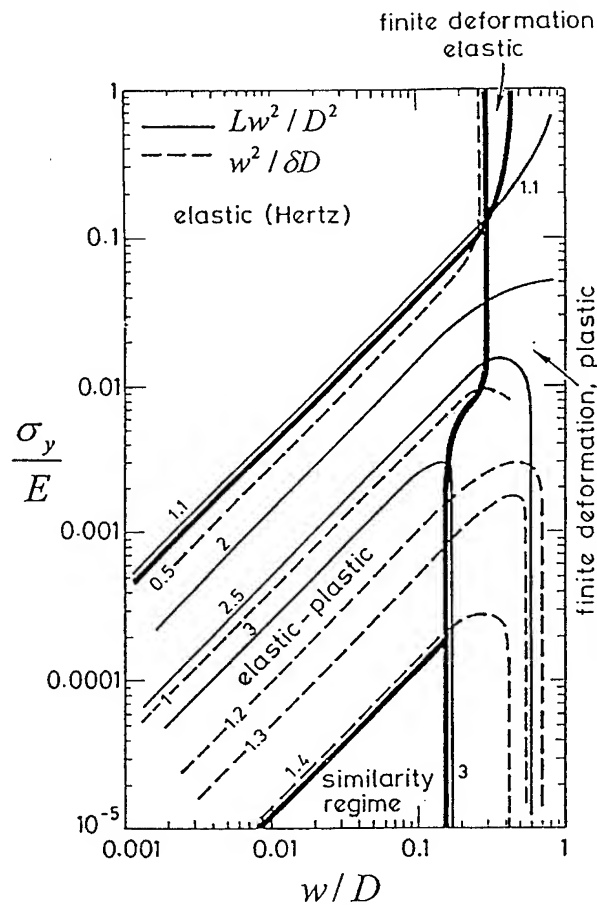


Figure 3. The indentation map from Mesarovic and Fleck (1999a).

indent are presented in Section 3. Finally, in Section 4, the stress intensity factor history accounting for both residual stresses and cyclic loads is assembled and used to predict the largest crack size such that the growth rate is below threshold using data for the Ti-6Al-4V alloy. An analytical method is developed in Section 4 and its accuracy is examined in the next section with full finite element solutions. Some further discussions on the limiting crack radius are also addressed in Section 5. The main findings of this paper are summarized in the last section.

## 2. Residual stresses arising from indentation

As depicted in Figure 1, a rigid sphere of diameter  $D$  is pushed into a half-space to by a load  $P$ . The indentation load is then removed such that the contact diameter is  $w$  and the indent depth is  $\delta$ , both measured after unloading. The material is taken to be elastic-ideally plastic with tensile yield stress  $\sigma_y$ , Young's modulus  $E$  and Poisson's ratio  $\nu$ . This representation is realistic for the titanium alloy Ti-6Al-4V, which has little strain hardening (Ritchie et al., 1999). The half-space is taken to be initially stress-free and infinitely deep, consistent with the assumption that the foreign object is small compared to the substrate thickness. The work

of Mesarovic and Fleck (1999a) reveals that the Poisson's ratio of the substrate material is a minor factor in indentation.

Johnson's classical book (Johnson, 1985) on theoretical contact mechanics contains considerable discussion and modeling of the Brinell's indentation test wherein a stiff elastic sphere is pushed into the surface of an elastic-plastic solid. The load per unit area of impression defines the hardness and is used as a measure of resistance of the material to plastic flow. For the most part, the results in Johnson's book do not reflect the most recent progress in indentation analysis made possible by today's advanced finite element methods. A recent comprehensive finite element study by Mesarovic and Fleck (1999a, 1999b) serves to set the stage for the present problem. Specifically, Mesarovic and Fleck have considered precisely the same indentation problem stated above, but with emphasis on hardness prediction and no determination of residual stresses which are of primary interest here. They show that there are various distinct regimes to the indentation problem. Their indentation regime map is given in Figure 3. Briefly, at sufficiently high and low the response is elastic and characterized by the classical Hertz solution. At a given  $L$ , plasticity becomes increasingly important as  $\mu$  increases. For greater than about 0.16, finite strain effects (large strains and large rotations) begin to become dominant. This corresponds to the regime referred to here as deep indentation. For smaller than 0.16, small strain kinematics pertain. This regime, as it will be seen, sub-divides into two parts, named here as very shallow and moderately shallow indentations, with distinctly different residual stress fields. The regime of primary interest in this paper is that of moderately shallow indentations. Included in the map of Mesarovic and Fleck is a 'similarity regime' characterized by relatively simple functional scaling of the solution as developed by Hill et al. (1989), Bower et al. (1993) and Biwa et al. (1995). This sector of the map lies outside the range of practical concern for the applications in the present study. Mesarovic and Fleck also found that the boundaries of the various indentation regimes are relatively insensitive to the degree of strain hardening and to the level of interfacial friction. However, the level of friction strongly affects the field beneath the indenter. A pre-stress within the half-space parallel to the free surface was shown to have a minor effect on the indentation response.

## 2.1. VERY SHALLOW, MODERATELY SHALLOW AND DEEP INDENTATIONS

From dimensional analysis, the residual stress distribution in the half-space after unloading can be written in the functional form

$$\frac{\sigma_{ij}(r, z)}{\sigma_y} = f_{ij} \left( \frac{P}{\frac{\pi}{4} D^2 \sigma_y}, \frac{\sigma_y}{E}, \mu, \frac{r}{\sqrt{P/\sigma_y}}, \frac{z}{\sqrt{P/\sigma_y}} \right), \quad (1)$$

where  $r$  and  $z$  are the coordinates in the radial and axial direction, respectively, and  $\mu$  is the Coulomb friction coefficient. Throughout, the dimensionless load factor will be denoted by

$$L \equiv \frac{P}{\frac{\pi}{4} D^2 \sigma_y}. \quad (2)$$

The coordinates could be scaled by  $D$ , but the alternative choice in (1) is preferred in the regime of primary interest for moderately shallow indentations, as will be seen.

For given  $L$ ,  $\sigma_y/E$  and  $\mu$  (with  $\nu = 0.3$ ) the stress distributions as functions of the dimensionless coordinates listed above have been computed. Finite element calculations were performed using the commercial code ABAQUS version 5.7 (Hibbit et al., 1998). The rigid

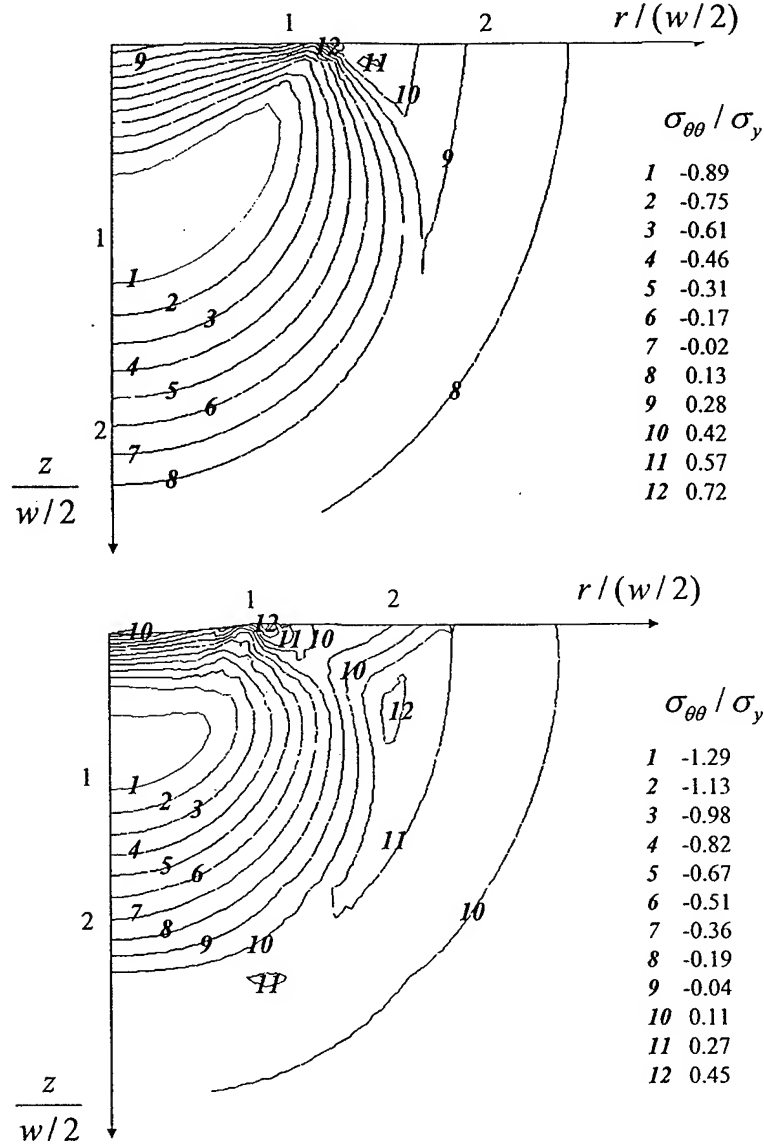


Figure 4. Residual hoop stress field due to indentation. (a)  $L = 0.0013$ , (b)  $L = 0.064$ , (c)  $L = 1.91$ .

contact surface option was used to simulate the rigid indenter, and the option for finite deformation and strain was employed. A typical mesh for the axis-symmetric indentation model comprises more than 2700 8-node elements. As already mentioned, the substrate material is taken to be elastic-perfectly plastic, with a Von Mises surface to specify yielding. Coulomb friction is invoked in the calculations, but it will be shown later that the choice of has only a minor influence on the stresses of interest in the FOD problem.

To make contact with the regime map in Figure 3, consider a representative substrate with  $\sigma_y/E = 0.001$ . If the Mesarovic-Fleck results are expressed in terms of  $L$ , one finds that the indentation is Hertzian for  $L < 10^{-5}$ ; elastic-plastic but shallow if  $10^{-5} < L < 0.08$ , and is deep when  $L > 0.08$ . Figure 4 display the distributions of normalized residual hoop stress,  $\sigma_{\theta\theta}/\sigma_y$ , for three different load levels: very shallow,  $L = 0.0013$ ; moderately shallow,

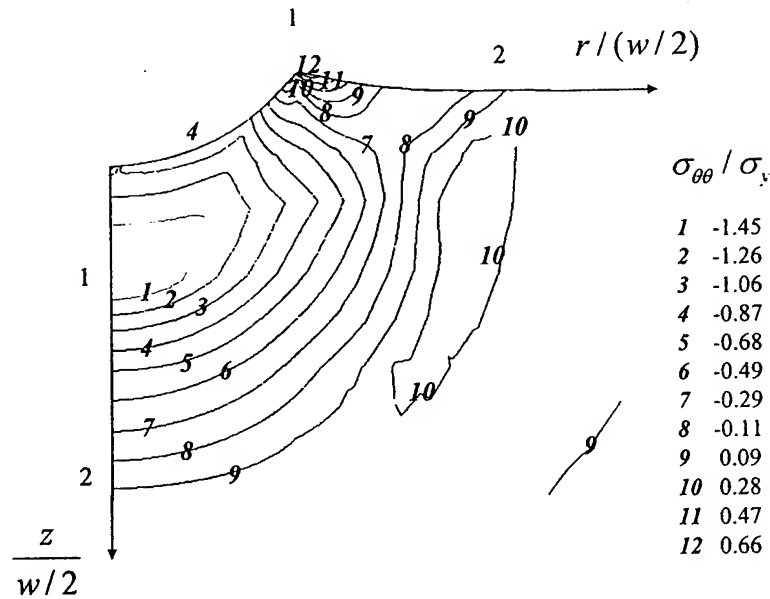


Figure 4. Continued.

$L = 0.064$ ; and deep,  $L = 1.91$ . These results were computed using  $\mu = 0.1$ . In the very shallow regime (Figure 4a), the residual hoop stress within the indent is compressive or nearly so, but becomes tensile just outside the rim and then decays fairly rapidly to zero. For moderately shallow indents (Figure 4b), the surface hoop stress is tensile at the bottom of the indent, but becomes compressive just below the surface. Outside the rim, at a radius about twice that of the indent, the stress is tensile and extends to a considerable distance below the surface. The deep indent in Figure 4c displays compression within the indent and a pronounced tensile region just outside the rim. Then with increasing distance from the rim, the hoop stress becomes compressive and finally tensile again before decaying to zero. These trends are revealed by the plot in Figure 5 of  $\sigma_{\theta\theta} / \sigma_y$  as a function of  $L$  for points at the center of the indent, just outside the rim and a radius that is 2.2 times the rim radius. Figure 5 brings out the fact that the hoop stress outside the rim of the indent is essentially independent of  $L$  in the moderately shallow regime, which for  $\sigma_y/E = 0.001$  corresponds to  $0.006 < L < 0.4$ . In this paper, we will focus on radial surface cracks lying outside the rim in the region of tensile hoop stress, primarily, but not exclusively, for moderately shallow indents. In subsequent work, we will address the problems for cracks at the center of the indent and cracks at the rim.

In experiments on fatigue cracks at FOD sites, radial cracks are observed but circumferential cracks are not. This is consistent with the residual stress calculations for the radial stress component,  $\sigma_{rr}$ , which is found to be weakly tensile only within the indent and then only very near to the surface. Thus, the focus in this paper, as mentioned, will be on radial cracks within regions of tensile hoop stress. A somewhat different cracking pattern is observed in thin brittle, elastic films bonded to metal substrates, which are then impressed by a spherical indenter (Begley et al., 1999). In this case, the predominant tensile stress in the elastic film is the radial component within the indent. Closely spaced cracks in the film are observed to form running circumferentially around the indent.

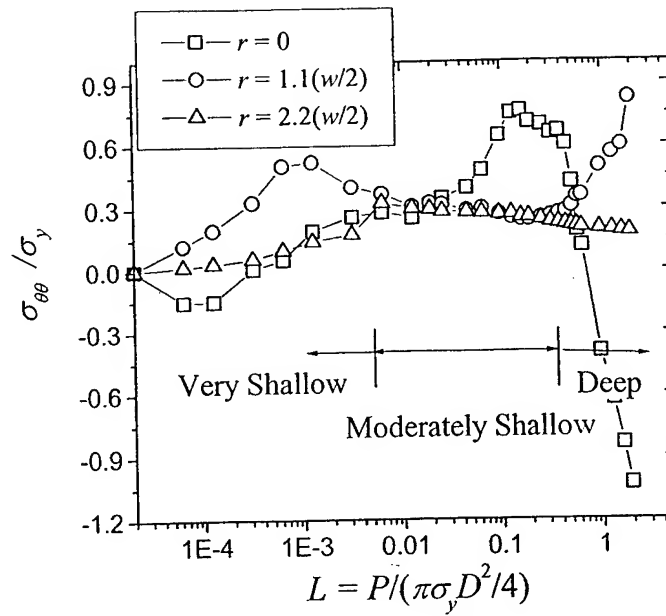


Figure 5. The normalized residual surface hoop stress  $\sigma_{\theta\theta}/\sigma_y$  as a function of  $L$  at three locations. Identification of the three indentation regimes.

## 2.2. SCALING RELATIONSHIPS FOR MODERATELY SHALLOW INDENTS

In order to display the stress behavior in the regime of moderately shallow indentation from another angle, plots of normalized hoop stress at the surface as a function of  $r/w$  are given in Figure 6 for four  $L$  values at the lower end of the regime. The emphasis here is on behavior

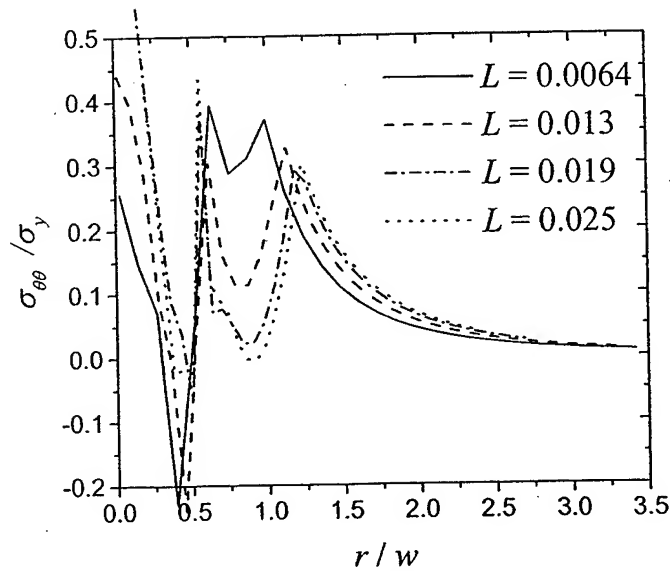


Figure 6. The relation between surface hoop stress  $\sigma_{\theta\theta}/\sigma_y$  and  $r/w$  for loads within the moderately shallow regime.

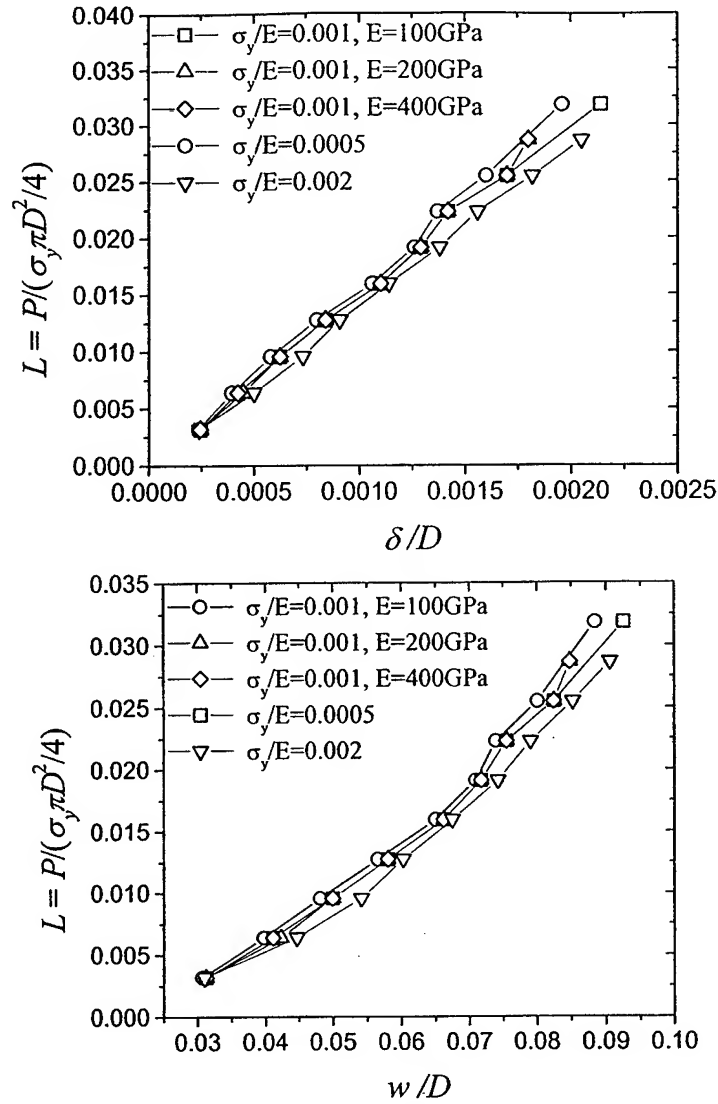


Figure 7. (a)  $L$  as a function of  $\delta/D$  and (b)  $L$  as a function of  $w/D$  for different values of  $\sigma_y/E$ .

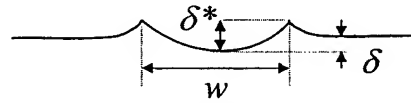


Figure 8. The pile-up that results in  $\delta^* > \delta$ .

outside the rim,  $r > w/2$ . Although there is some spread in the peak stresses just outside the rim, the stress distributions are roughly independent of  $L$  when the radial coordinate is scaled by the indent diameter  $w$ . Moreover, as seen in Figures 7a and 7b, the normalized indent depth  $\delta/D$  and indentation diameter  $w/D$  vary with  $L$  in a manner that is essentially independent of  $\sigma_y/E$ . The fact that  $\sigma_y/E$  has little effect on these relations can be understood by noting that  $L$  in the moderately shallow indentation regime far exceeds the load levels for Hertzian indentation. Thus the elastic modulus plays essentially no role in these relations.



The relation between  $L$  and  $\delta/D$  is nearly linear in Figure 7a, while that between  $L$  and  $w/D$  in Figure 7b is nearly parabolic. Given that both relations are essentially independent of  $\sigma_y/E$  and  $\mu$  (see below), they are well approximated by

$$L \cong 15 \frac{\delta}{D}. \quad (3)$$

$$L \cong 2.9(w/D)^2 \quad \text{or} \quad P \cong 2.3\sigma_y w^2. \quad (4)$$

With reference to Figure 8, note the difference between the two depth quantities,  $\delta$  and the pile-up height  $\delta^*$ . As has been noted elsewhere (Begley et al., 1999),  $\delta^* = \frac{1}{4}w^2/D$  holds in the shallow regime. But from the relations in (3) and (4),  $\delta \cong 0.19 \frac{w^2}{D}$ . As seen in Figure 8, the difference in these two quantities is explained by the pile-up the indenter has caused in the elastic-perfectly plastic substrate.

From (3) and (4), the plastic work,  $PW$ , stored in the substrate is

$$PW = \int P \, d\delta \cong 5.9\sigma_y D \delta^2 \cong 0.23\sigma_y \frac{w^4}{D} \quad (5)$$

This formula will be useful in making connection between the static indentation problem and the dynamic FOD problem discussed in the next section.

The results presented thus far for the stresses and deformation of the substrate have all been computed with the Coulomb friction taken to be  $\mu = 0.1$ . Many of these same computations have been repeated with  $\mu = 1$ . While the stresses within the rim of the indent do depend fairly strongly on the friction coefficient, the stresses outside the rim and the dependencies on  $L$  shown in Figure 7 differ only slightly for these rather extreme choices of the friction coefficient. For practical purposes these relations can be taken to be independent of  $\mu$  for moderately shallow indents. Thus, the normalized hoop stress outside the rim is reasonably well approximated by

$$\frac{\sigma_{\theta\theta}(r, z)}{\sigma_y} = f_{\theta\theta}\left(\frac{r}{w}, \frac{z}{w}\right) \quad \text{when} \quad r > w/2 \quad \text{and} \quad 0.006 < L < 0.4, \quad (6)$$

where from (4)  $w \cong 0.66\sqrt{P/\sigma_y}$  and the contour plot in Figure 4b gives  $\sigma_{\theta\theta}$  for moderately shallow indentation. Most importantly, the indentation diameter  $w$  is the only quantity needed in scaling the stresses in this regime.

### 2.3. PLASTIC WORK OF INDENTATION AND IMPACT KINETIC ENERGY

Equation (5) gives the plastic work of indentation under conditions of quasi-static loading. In order to transfer the quasi-static results to the FOD problem, the fraction of the impact kinetic energy of the particle that is converted to plastic work must be known. To facilitate the transference, a plot of normalized plastic work as a function of normalized contact size  $w/D$  is given in Figure 9. The approximated formula, (5), can be used to determine this relation for moderately shallow indents, but the curve in Figure 9 is based on the finite element results in order to provide maximum accuracy. In addition, these results are extended into the deep indentation regime. Two impact points from the experimental results of Peters et al. (2000) are included in Figure 9 with the kinetic energy of the impacting particle replacing the plastic

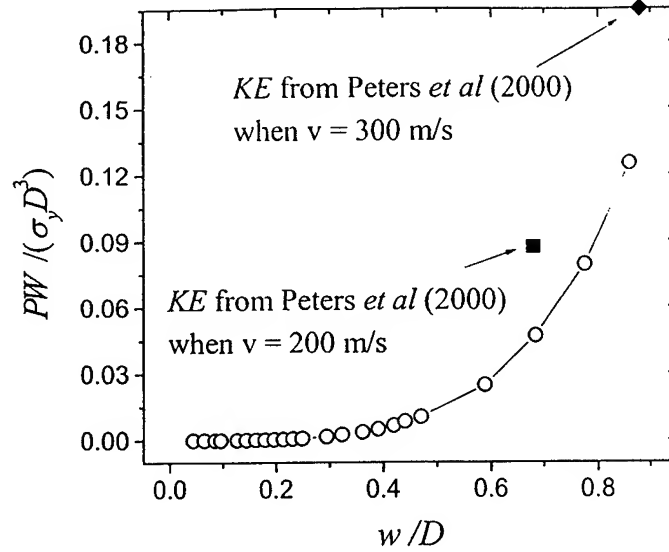


Figure 9. The normalized plastic work as a function of the normalized contact diameter. The total kinetic energy and resulting indent diameter of the impacting sphere for two of the tests of Peters et al. (2000) is also shown.

work in the vertical coordinate. Some of the details of the experiments (Peters et al., 2000) are as follows.

A hardened steel ball was used as the foreign object, with  $D = 3.175 \text{ mm}$ . The density of the steel is  $\rho = 7.9 \text{ Mg m}^{-3}$ . The yield stress of the substrate material (Ti-6Al-4V) is about  $\sigma_y = 950 \text{ MPa}$ . The impact velocity of the foreign object was in the range  $v = 200\text{--}300 \text{ m s}^{-1}$ . The normalized kinetic energy of the foreign object, which was plotted in Figure 9, is:

$$\frac{KE}{\sigma_y D^3} = \frac{1}{12} \frac{\pi \rho D^3 v^2}{\sigma_y D^3} = \frac{\pi \rho v^2}{12 \sigma_y}. \quad (7)$$

For an impact velocity  $v = 200 \text{ m s}^{-1}$ , the experiment has  $KE/\sigma_y D^3 = 0.087$  and  $w/D = 0.68$ , while the quasi-static analysis result at the same  $w/D$  has  $PW/\sigma_y D^3 = 0.047$ . This comparison suggests that 46% of the kinetic energy was dissipated by means other than plastic deformation of the substrate. Similarly, when  $v = 300 \text{ m s}^{-1}$ ,  $KE/\sigma_y D^3 = 0.195$ ,  $w/D = 0.88$ ,  $PW/\sigma_y D^3 = 0.125$ , implying that 36% of the kinetic energy was lost.

The 'lost energy' during impact may take the forms of the kinetic energy of the ricocheting particle, elastic waves in the substrate, and deformation energy in the particle. Assuming that all the lost energy is tied up in rebound kinetic energy, then by simple calculation for the shot with  $v = 200 \text{ m s}^{-1}$  in experiment (Peters et al., 2000), the steel ball should bounce back with a velocity  $v' = 135 \text{ m s}^{-1}$ ; and for  $v = 300 \text{ m s}^{-1}$ ,  $v' = 180 \text{ m s}^{-1}$ . The explicit measured rebound velocities were not obtained.

In conclusion, the relation between normalized plastic work and contact diameter in Figure 9 for the quasi-static indentation, together with the experiments cited above, can be used to estimate the size of the indent and the associated stresses in the FOD problem. Specifically, assume the plastic work is about 60% of the kinetic energy of the FOD particle, and use Figure 9 to obtain  $w/D$ . The other characteristics of the damage then follow. The conversion factor, 60%, for the kinetic energy relies on only two data points, and more data will be required to establish the reliability of this factor.

After unloading, there are

3 most likely crack locations :

$$r = 0, r = w/2 \text{ and } r \cong w.$$

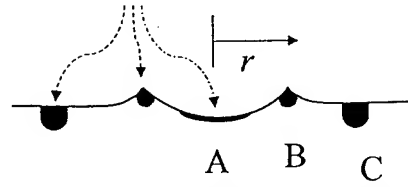


Figure 10. The three most likely crack locations.

### 3. Surface crack in residual stress field of the indent

The theoretical stress distributions indicate three possible regions where the residual stresses may enhance crack growth and lower the threshold of a surface crack. These regions where the hoop stresses are tensile, which have already been identified in Section 2, are designated by A, B, C in Figure 10. For very shallow indentations, from Figure 4a, there are only 2 hoop stress peaks: one at the bottom of the indenter at A and one at the crater ridge at B. The second peak in very shallow indentation is much larger than the first one, and it splits into peak B and peak C when  $L$  passes into the moderately shallow indentation regime. As  $L$  is increased within the moderately shallow indentation regime, the tensile peak at A becomes larger, while the stresses at B and C remain nearly the same, which can also be seen from Figure 5. For deep indentations, however, the peak at A has gone, only peaks B and C remain, with the stress at B being much larger than that at C. This can also be seen in Figure 5.

In this study we have focussed on moderately shallow indents and we will restrict our attention to small surface cracks centered at the peak hoop stress at C, which lies close to the point  $r \cong w$ . The emergence of surface cracks at the other two peaks will be explored in future work, but within this regime, it appears that C should be the critical point. There is a large compressive region directly beneath point A, which would tend to prevent a crack from propagating much below the surface. The peak at B is narrow compared with that of C, so the largest possible residual stress influence is expected for a crack centered at C.

The two tests referred to above (Peters et al., 2000) gave rise to fatigue crack initiation and growth from A for moderately shallow indent lying close to the deep indent transition, and from B for the case of a deep indentation. Thus, it will be important to explore crack growth from points A and B, as well, but the principles are illustrated by cracks placed at C.

Let  $a$  be the radius of a semi-circular surface crack centered at the peak of the hoop stress distribution at C, which roughly corresponds to the point  $r = w$ . Let  $K_{\text{res}}$  be the maximum value of the mode I stress intensity factor around the circumference of the crack. The residual stresses scale with and thus  $K_{\text{res}}$  will scale with  $\sigma_y \sqrt{a}$ . A three-dimensional finite element program (ABAQUS) has been used to compute the distribution of the stress intensity factor around the crack edge for many values of  $a/w$  and a number of values of the load parameter  $L$ . Because the indents were moderately shallow, the slight effect of the non-planarity of the surface was neglected in these computations, i.e., the surface of the substrate was taken to be planar. The calculation was performed by applying the residual hoop stress as computed in Section 2 to the faces of the crack. At each crack size,  $K_{\text{res}}$  was determined. The location along the circumference of the semi-circular crack where the maximum value of the mode I stress

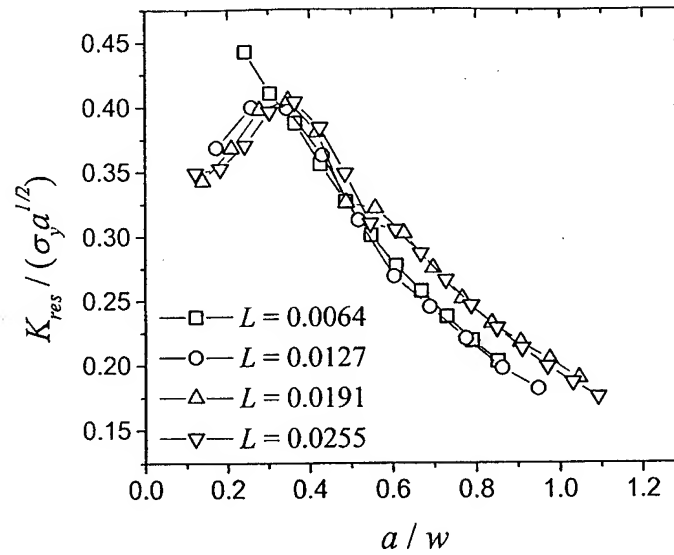


Figure 11. The normalized residual stress intensity factor  $K_{res}/(\sigma_y \sqrt{a})$  as a function of  $a/w$  for moderately shallow indents.

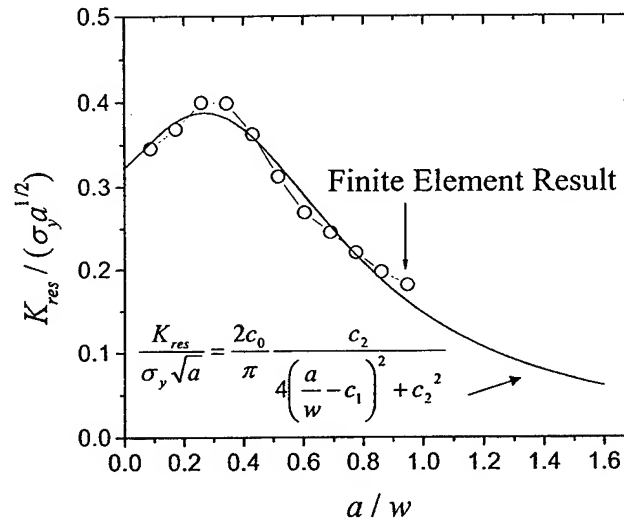


Figure 12. The functional fit between  $K_{res}/(\sigma_y \sqrt{a})$  and  $a/w$ , which is independent of  $L$  in the moderately shallow indentation.

intensity factor (i.e.,  $K_{res}$ ) occurs is somewhere between the surface and depth, where the crack front is opened by the maximum residual hoop stress inside the substrate (cf., Figure 4 (b)). Computed curves of  $K_{res}/(\sigma_y \sqrt{a})$  as a function of  $a/w$  are presented in Figure 11 at four values of the load parameter, all of which lie within the moderately shallow indentation regime. The near-independence of these curves on  $L$  is tied to the fact that that normalized residual stresses discussed in Section 2 are also independent of  $L$  in this regime.

For the purposes of the subsequent fatigue crack analysis, a relatively simple functional form to represent the curves in Figure 11 was found with adjustable parameters chosen to give

the best fit.

$$\frac{K_{\text{res}}}{\sigma_y \sqrt{a}} = \frac{2c_0}{\pi} \frac{c_2}{4\left(\frac{a}{w} - c_1\right)^2 + c_2^2} \quad (8)$$

where  $c_0 = 0.697$ ,  $c_1 = 0.269$ ,  $c_2 = 1.143$ . This function is included in Figure 12. From (8), the maximum value of  $K_{\text{res}}$  (which is attained when  $a \cong 0.4w$ ) is

$$(K_{\text{res}})_{\text{max}} = 0.24\sigma_y \sqrt{w}. \quad (9)$$

The role of the diameter of the indentation,  $w$ , is evident in this formula. Another important specialization of (8) pertains to the limit when the crack is small compared to the diameter of the indent ( $a/w \rightarrow 0$ ). Then,

$$K_{\text{res}}^L = 0.32\sigma_y \sqrt{a}. \quad (10)$$

This result is simply that for a small semi-circular crack in a uniform stress field,  $\sigma_{\theta\theta} = 0.24\sigma_y$ , corresponding to the local stress at point C of the indent.

#### 4. Fatigue crack threshold analysis in the presence of fod

##### 4.1. SPECIFICATION OF THE CYCLIC LOADING AND STRESS INTENSITY HISTORY

The last step in the approach is to consider the combined effect of the residual FOD stresses and cyclic stresses on a pre-existing surface crack of radius  $a$ , as depicted in Figure 2. Specifically, the effect of the FOD damage on threshold growth conditions for the crack will be addressed. Given a cyclic loading history  $\sigma(t)$ , the following notation is used:

$$\begin{aligned} \sigma_{\text{max}} &\equiv \text{Max}[\sigma(t)] \\ \sigma_{\text{min}} &\equiv \text{Min}[\sigma(t)] \end{aligned} \quad ; R_{\text{applied}} = \sigma_{\text{min}}/\sigma_{\text{max}}. \quad (11)$$

By combining the contributions from the residual hoop stress and  $\sigma(t)$ , one obtains the total stress intensity factor on the semi-circular fatigue crack as

$$K(t, a) = K_{\text{res}}(a) + c \cdot \sigma(t) \sqrt{4a/\pi}, \quad (12)$$

where  $c \cdot \sigma(t) \sqrt{4a/\pi}$  is the stress intensity factor of the semi-circular crack due only to  $\sigma(t)$ . For a full circular crack in an infinite body,  $c = 1$ . Based on the present finite element calculations for the semi-circular crack, we take  $c = 1.2$ . The total stress intensity factor range is therefore

$$\Delta K(a) \equiv \text{Max}(K(t, a)) - \text{Min}(K(t, a)) = (\sigma_{\text{max}} - \sigma_{\text{min}}) \cdot c \cdot \sqrt{4a/\pi}. \quad (13)$$

The total R-factor is

$$R(a) \equiv \frac{\text{Min}(K(t, a))}{\text{Max}(K(t, a))} = \frac{K_{\text{res}}(a) + c \cdot \sigma_{\text{min}} \sqrt{4a/\pi}}{K_{\text{res}}(a) + c \cdot \sigma_{\text{max}} \sqrt{4a/\pi}} > R_{\text{applied}}. \quad (14)$$

Thus, as (13) emphasizes,  $\Delta K$  is independent of the residual stress, however, from (14) is seen that the residual stress influences the R-factor in such a way that it is always larger than the

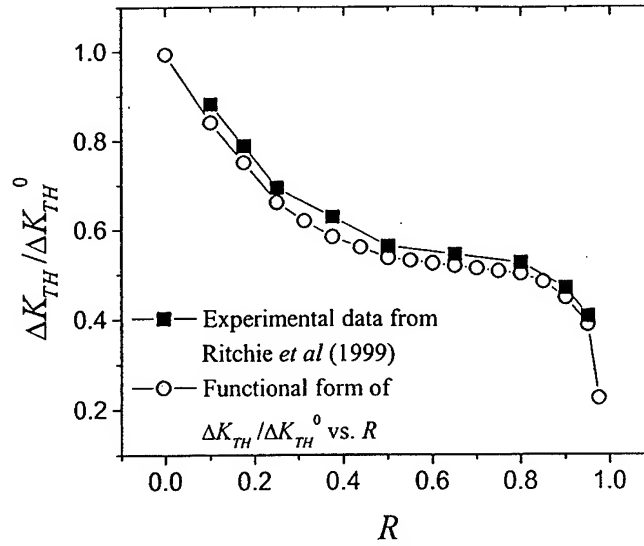


Figure 13. The  $\Delta K_{TH}/\Delta K_{TH}^0$  vs.  $R$  data for Ti-6Al-4V (Ritchie et al., 1999) and a functional fit.

$R$ -factor computed from the cyclic loads alone. To understand how FOD influences the fatigue behavior for a given material, one must consider the interplay between  $\Delta K$  and  $R$ .

#### 4.2. R-DEPENDENCE OF CRACK GROWTH THRESHOLD DATA

As already mentioned, the emphasis here will be on the effect of FOD on fatigue crack growth threshold. To perform the analysis one must have fatigue crack data characterizing the curve of  $\Delta K_{TH}$  versus  $R$  corresponding to threshold growth conditions. A convenient reference value for normalization purposes is

$$\Delta K_{TH}^0 \equiv \Delta K_{TH}(R = 0) \quad (15)$$

Complete threshold data are not available for many materials, but a reasonably complete set is available for the blade alloy of particular interest here, Ti-6Al-4V (Ritchie et al., 1999). These data are shown in Figure 13. For analysis purposes it is convenient to have a functional form for  $\Delta K_{TH}$  vs.  $R$ . The function used here was obtained as a polynomial fit to the data. The cubic form

$$\frac{\Delta K_{TH}}{\Delta K_{TH}^0} = 1 - 2.49R + 4.78R^2 - 3.12R^3 \quad (16)$$

describes the data reasonably well. The limit of  $\Delta K_{TH}$  when  $R \rightarrow 1$  is unimportant, since the total  $R$ -factor will never approach that limit during this study.

#### 4.3. CRITICAL CRACK RADIUS AND AN ILLUSTRATIVE EXAMPLE

A given surface crack (with radius  $a$ ) at the indentation is below threshold for a given cyclic loading if its associated  $\Delta K$  and  $R$  calculated from (13) and (14) lie below the curve of  $\Delta K_{TH}$  versus  $R$ . The critical crack radius at threshold,  $a_c$ , corresponds to

$$\Delta K(a_c) = \Delta K_{TH} \quad \text{at } R(a_c) \quad (17)$$

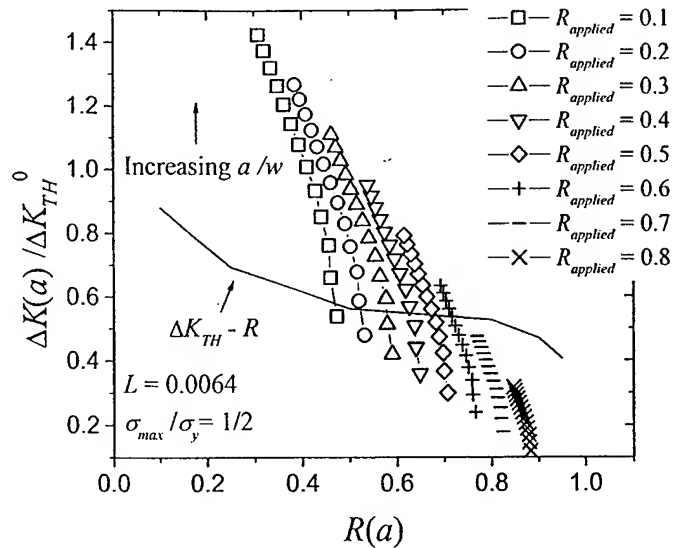


Figure 14.  $\Delta K(a)/\Delta K_{TH}^0$  vs.  $R(a)$  relations for  $L = 0.0064$  and  $\sigma_{max}/\sigma_y = \frac{1}{2}$ , for various values of  $R_{applied}$ . For each of these curves corresponding to a particular  $R_{applied}$ ,  $a/w$  increases from 0.12 at the bottom of the curve to 0.85 at the top. The points shown correspond to twelve equal increments in  $a/w$ . The critical value of  $a/w$  corresponds to the intersection with the curve for the threshold data.

The actual process of determining  $a_c$  is shown in Figure 14 for an indent with  $L = 0.0064$  and  $\sigma_{max}/\sigma_y = \frac{1}{2}$ . Take as an example the loading with  $R_{applied} = 0.5$ . The sequence of points forming the curve of  $\Delta K(a)/\Delta K_{TH}^0$  versus  $R(a)$  correspond to increasing values of  $a/w$  starting from 0.12 at the lower end to 0.85 at the upper end. This curve cuts the crack

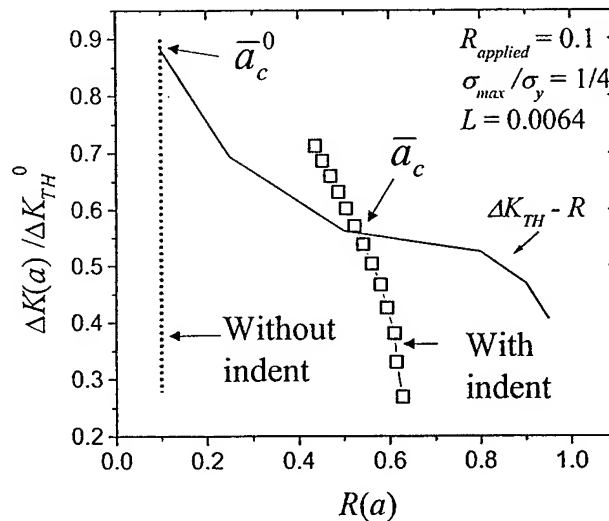


Figure 15. Illustration of the effect of residual stresses on the critical crack radius. In this case  $L = 0.0064$ ,  $\sigma_{max}/\sigma_y = \frac{1}{4}$  and  $R_{applied} = 0.1$ . The dotted vertical line is the relation  $(\Delta K(a), R(a))$  in the absence of an indent with  $a$  increasing from bottom to top. The critical values of  $a$  correspond to the points of intersection with the threshold data.

growth threshold curve at  $a_c/w = 0.39$ . The sequence of points for the other values of  $R_{\text{applied}}$  can be interpreted in the same way. Note that for this example, loadings for which  $R_{\text{applied}}$  is equal to or greater than 0.7 have a critical crack radius lying beyond the range considered. To see the role of the residual stress of the indent more clearly, curves of  $(\Delta K(a), R(a))$  for a particular loading are shown in Figure 15 for the substrate with and without an indent. Define the normalized critical crack radius as

$$\bar{a}_c = \frac{a_c}{(\Delta K_{TH}^0/\sigma_y)^2}. \quad (18)$$

In the absence of an indent,  $R$  is independent of  $a$  and intersects the threshold curve at  $\bar{a}_c^0 = 7.60$ . For the crack at the indent, the residual stress shifts the curve of  $(\Delta K(a), R(a))$  significantly to the right and produces the variation of  $R$  with  $a$  given by (14). The normalized critical crack radius is  $\bar{a}_c = 2.97$  (corresponding to  $a_c/w = 0.52$ ). For this particular example, which has a relatively low value of  $R_{\text{applied}}$ , the critical crack size for the FOD damaged substrate is about 60% smaller than that for the undamaged substrate.

#### 4.4. ANALYTICAL PROCEDURE FOR CRITICAL CRACK SIZE PREDICTION

The equations governing the stress intensity from the residual stress and from the cyclic loading are now put into another dimensionless form well suited to obtaining general results for the dependence of critical crack size on the various parameters of the FOD problem. With the normalized crack radius and indentation diameter defined by

$$\bar{a} = \frac{a}{(\Delta K_{TH}^0/\sigma_y)^2} \quad \text{and} \quad \bar{w} = \frac{w}{(\Delta K_{TH}^0/\sigma_y)^2}. \quad (19)$$

Equation (8) can be rewritten as

$$\frac{K_{\text{res}}}{\Delta K_{TH}^0} = \sqrt{\bar{a}} \frac{2c_0}{\pi} \frac{c_2}{4\left(\frac{\bar{a}}{\bar{w}} - c_1\right)^2 + c_2^2} \equiv \sqrt{\bar{a}} f\left(\frac{\bar{a}}{\bar{w}}\right). \quad (20)$$

Substitution of this equation into (14) gives the total load ratio as a function of  $\bar{a}$ :

$$R(\bar{a}) = \frac{\sqrt{\bar{a}} f\left(\frac{\bar{a}}{\bar{w}}\right) + c \frac{\sigma_{\min}}{\sigma_y} \sqrt{\frac{4\bar{a}}{\pi}}}{\sqrt{\bar{a}} f\left(\frac{\bar{a}}{\bar{w}}\right) + c \frac{\sigma_{\max}}{\sigma_y} \sqrt{\frac{4\bar{a}}{\pi}}}, \quad (21)$$

with  $c = 1.2$ . By (13) and (16), the overall stress intensity factor range  $\Delta K$  and the threshold  $\Delta K_{TH}$  can both be represented as functions of  $\bar{a}$  according to:

$$\frac{\Delta K(\bar{a})}{\Delta K_{TH}^0} = \frac{\sigma_{\max}}{\sigma_y} (1 - R_{\text{apply}}) c \sqrt{\frac{4\bar{a}}{\pi}} \equiv Q(\bar{a}), \quad (22)$$

$$\frac{\Delta K_{TH}}{\Delta K_{TH}^0} = 1 - 2.49R(\bar{a}) + 4.78R^2(\bar{a}) - 3.12R^3(\bar{a}) \equiv T(R(\bar{a})). \quad (23)$$

Therefore, the criterion to determine the critical crack radius at threshold,  $\bar{a} = \bar{a}_c$ , is simply

$$Q(\bar{a}_c) = T(R(\bar{a}_c)). \quad (24)$$



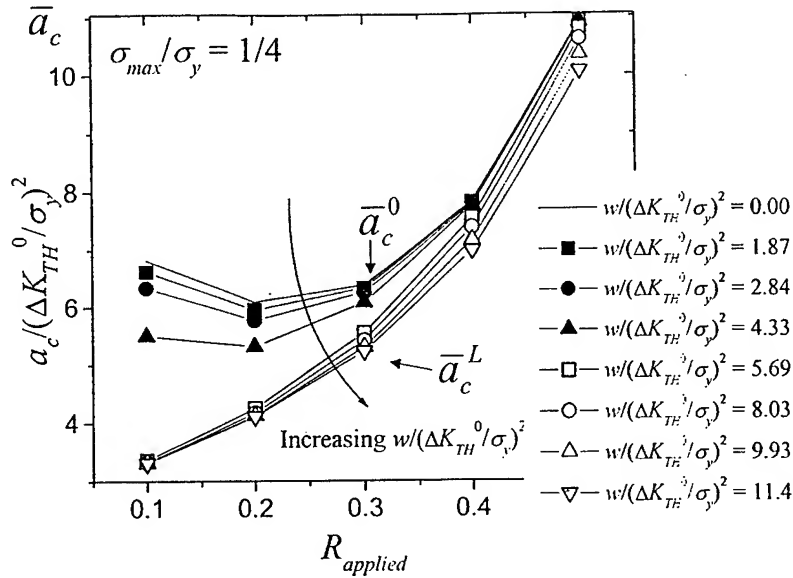


Figure 16. The normalized critical crack threshold  $\bar{a}_c$  predicted from (24) as a function of  $R_{\text{applied}}$ , for a range of indentation sizes  $\bar{w}$  with  $\sigma_{\text{max}}/\sigma_y = \frac{1}{4}$ .

Based on the above equations, curves of normalized critical crack radius,  $\bar{a}_c$ , versus  $R_{\text{applied}}$  for  $\sigma_{\text{max}}/\sigma_y = \frac{1}{4}$  have been plotted in Figure 16 for a sequence of values of the normalized indentation diameter,  $\bar{w}$ . The plot brings out a clear transition from a critical crack radius  $\bar{a}_c^0$  that is independent of  $\bar{w}$  (and is the same as for a substrate with no FOD) to a lower limiting critical radius,  $\bar{a}_c^L$ , which is also essentially independent of  $\bar{w}$ . The range of the indentation diameter over which the transition occurs corresponds roughly for  $\bar{w}$  between 2 to 5. In other words, for this case with  $\sigma_{\text{max}}/\sigma_y = \frac{1}{4}$ , indents smaller than about  $\bar{w} = 2$  will have little influence on the critical crack size, while indents larger than about  $\bar{w} = 5$  will result in a reduced critical crack radius  $\bar{a}_c^L$  which is insensitive to even larger indents, as long as those indents remain in the moderately shallow regime.

The transition in  $\bar{w}$  from essentially no effect due to FOD, to the reduced critical crack size is a strong function of  $\sigma_{\text{max}}/\sigma_y$ . Calculations similar to those described above have been performed for other values of  $\sigma_{\text{max}}/\sigma_y$ , and the transition range is plotted in Figure 17.

#### 4.5. LIMITING CRITICAL CRACK SIZE

The limiting critical crack radius,  $a_c^L$ , corresponds to the limit  $a/w = \bar{a}/\bar{w} = 0$  in (20), such that  $f(a/w) = 0.32$ . The resulting equations for  $a_c$  are independent of  $w$ . In this limit, the indent is sufficient large (but still not deep!) such that the critical crack at C is embedded in a locally uniform residual stress corresponding to  $\sigma_{\theta\theta} = 0.24\sigma_y$ . The effect of the residual stress on the total stress intensity factor comes in solely through the elementary result given in (10). It follows that the prediction for the limiting critical crack radius due to moderately shallow indents can be carried out directly using (10) together with (13) and (14).

Consider the implications for two materials given  $\sigma_{\text{max}}/\sigma_y = \frac{1}{4}$ . For Ti-6Al-4V ( $\sigma_y = 950$  MPa and  $\Delta K_{TH}^0 = 5$  MPa  $\sqrt{m}$  (Ritchie et al., 1999)), the transition indentation diameter

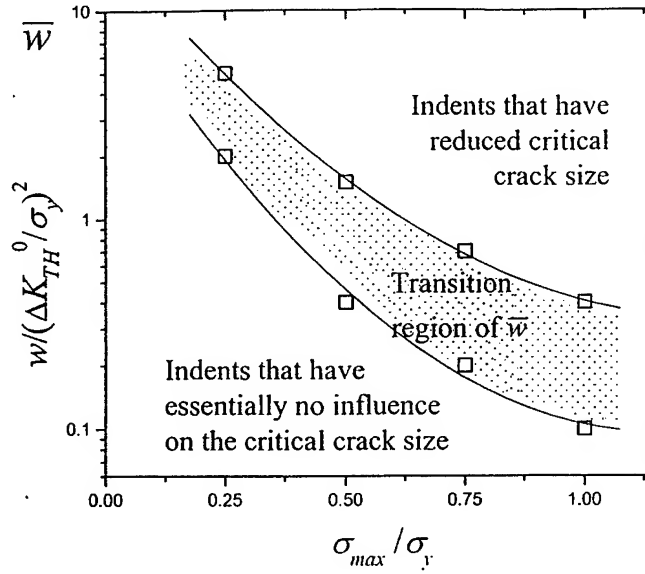


Figure 17. Transition range of normalized indentation size as a function of  $\sigma_{max}/\sigma_y$  for moderately shallow indents. Indents below the transition have essentially no influence on the critical crack size, while indents above have the reduced critical crack size.

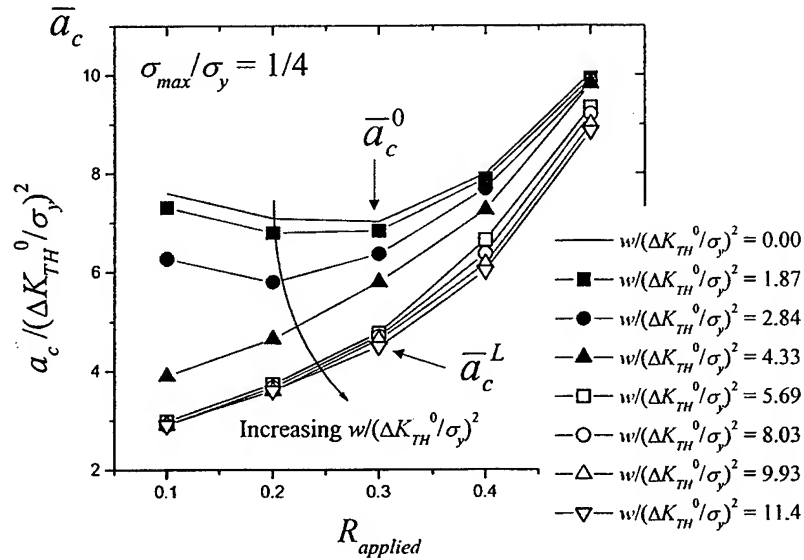


Figure 18. The normalized critical crack threshold  $\bar{a}_c$  computed from full finite element result as a function of  $R_{applied}$ , for a range of indentation sizes  $\bar{w}$  with  $\sigma_{max}/\sigma_y = 1/4$ .

( $\bar{w} = 2$ ) is about  $w = 0.05$  mm. If  $R_{applied}$ , then  $a_c^L = 0.09$  mm, which can be compared with  $a_c^0 = 0.2$  mm for no FOD. Clearly, a very small FOD will have an effect on the critical crack threshold for this particular material. By contrast, for mild steel which has a lower yield stress and a higher threshold, ( $\sigma_y = 200$  MPa and  $\Delta K_{TH}^0 = 15$  MPa  $\sqrt{m}$ ), and the transition occurs at a much larger indent diameter,  $w = 11$  mm. Now, for  $R_{applied} = 0.1$ , one obtains  $a_c^L = 18$  mm, which can be compared with  $a_c^0 = 43$  mm for no foreign object damage.

## 5. Accuracy of the analytical formulation and further results

The analysis underlying the plots in Figure 16 relies on the accuracy of the formula (20) for the effect of the residual stress on the stress intensity factor of the surface crack. Formula (20) has been obtained by fitting the finite element results over a range of the load parameter  $L$  within the moderately shallow regime. Outside this regime (20) loses accuracy. The smallest indents in Figure 16 (those with  $\bar{w} = 2-4$ ) are very shallow such that the accuracy of these curves is suspect. The results of Figure 16 have been recalculated using the full finite element determination of  $K_{\text{res}}$ , without recourse to the approximation (20), and therefore valid for all  $L$ . The plot from the full finite element calculation is shown in Figure 18. These are again for the case  $\sigma_{\text{max}}/\sigma_y = \frac{1}{4}$  and can be compared directly with the previous plots based on the approximate formula (20) in Figure 16. While there is some discrepancy between the two plots for the smaller values of  $\bar{w}$ , the characterization of the transition by  $2 < \bar{w} < 5$  remains robust. Moreover, the limiting value of the reduced critical crack radius,  $a_c^L$ , is unchanged because the indent size associated with this limit is within the regime of moderately shallow indents. The same remarks apply to the results for the other values of  $\sigma_{\text{max}}/\sigma_y$ , for which the transition range of the indentation size has been given in Figure 17. In conclusion, even though (20) loses accuracy for very shallow indents, the consequences for the predictions of the transition from essentially no effect due to FOD to a reduced critical crack size is relatively minor.

A comparison is made in Figure 19 between the normalized critical crack radius in the absence of any indent,  $\bar{a}_c^0$ , and the normalized limiting critical crack radius,  $\bar{a}_c^L$ , for moderately shallow indents is made for a wide range of loadings. The normalized critical crack radius is plotted versus the applied load ratio  $R_{\text{applied}}$ , for four values of  $\sigma_{\text{max}}/\sigma_y$ . The curves in Figure 19a are obtained from full finite element simulations, while those in Figure 19b make use of the analytic approximation (20) for  $K_{\text{res}}$ . As already anticipated, the analytical approximation is highly accurate for determining  $\bar{a}_c^L$ . Over much of the cyclic loading space,  $(\sigma_{\text{max}}/\sigma_y, R_{\text{applied}})$ , the effect of moderately shallow indents is relatively small in that  $\bar{a}_c^L$  is only slightly below the critical crack radius with no indent  $\bar{a}_c^0$ . However, large effects of the indent on reducing the critical crack size occur at high values of  $R_{\text{applied}}$  and also at low values of  $R_{\text{applied}}$  when  $\sigma_{\text{max}}/\sigma_y$  is small.

## 6. Conclusion

Fracture due to foreign object damage is a rather new topic, which brings together contact mechanics, crack mechanics and fatigue analysis. In this paper, finite element methods have been used to investigate the residual stresses due to a spherical indentation and their influence on the stress intensity of a surface crack emerging at a critical location at the indent. A complete framework has been established to analyze the effect of the residual stresses on the crack growth due to subsequent cyclic loading. In particular, the critical crack size associated with threshold fatigue crack growth has been emphasized. While detection of cracks of the critical size may be extremely difficult, or even impossible in high strength materials, the fact that the critical crack size is reduced by FOD is in itself useful knowledge.

The work presented here is just a beginning in that it has primarily focussed on a limited range of indentations, referred to here as being moderately shallow. In addition, attention has been directed to surface cracks emerging from only one location just outside the indent.

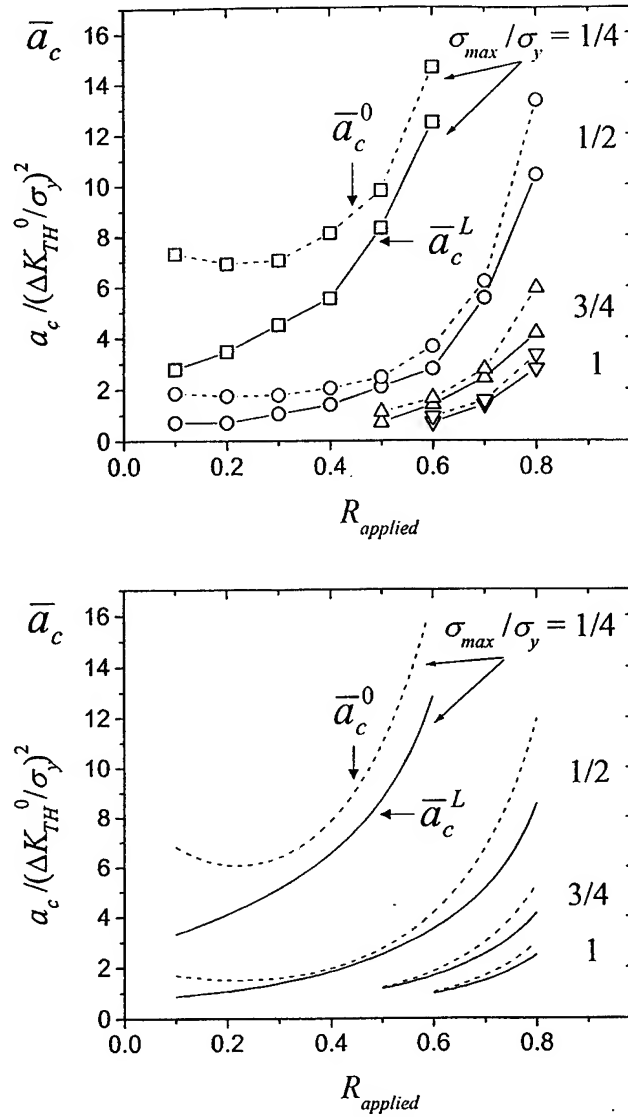


Figure 19. The normalized critical crack radius for shallow indentation,  $\bar{a}_c^0$  for no indents and  $\bar{a}_c^L$  for sufficiently large indents, for a range of  $R_{\text{applied}}$  and  $\sigma_{\text{max}}/\sigma_y$  values. (a) full finite element result, (b) analytical result from (24).

Experimental observations suggest that other locations may be equally, or even more, critical in deeper indentations. Subsequent work will be needed to extend these findings in both directions. We conclude by listing the main findings and implications of the current research:

1. Three indentation regimes were identified with distinct residual stress patterns: very shallow, moderately shallow and deep indents. The present paper focused primarily on the moderately shallow regime corresponding to  $0.006 < L < 0.4$ , where  $L = P / (\frac{1}{4}\pi D^2 \sigma_y)$  is the load parameter. The friction coefficient  $\mu$  and the elastic yield strain,  $\sigma_y/E$ , have minor influence on the residual tensile hoop stress. Estimates for the load factor and the depth of penetration in terms of the kinetic energy of an impacting sphere are given.

2. For moderately shallow indents, the effect the residual stress on a surface crack located just outside the indent (point C in Figure 10) has been determined and an accurate analytic approximation for the stress intensity factor has been presented.
3. The combination of cyclic fatigue loading and the residual stress due to the FOD for fatigue crack growth has been explored, with emphasis on the largest (critical) crack size that remains below the fatigue crack growth threshold. For cracks at moderately shallow indents, FOD can reduce the critical crack size by as much as 60%, depending on the cyclic loading history. The non-dimensional parameter controlling the reduction of the critical crack size is  $\bar{w} = w/(\Delta K_{TH}^0/\sigma_y)^2$ , where  $w$  is the diameter of the indent and  $\Delta K_{TH}^0$  is the stress intensity variation at  $R = 0$  associated with threshold crack growth in the material. When  $\sigma_{\max}/\sigma_y = \frac{1}{4}$ , for values of  $\bar{w}$  less than about 2, the indent has little effect on the crack growth threshold; for values of  $\bar{w}$  greater than about 5, the full reduction in the critical crack size is attained. Similar results have been given for other values of  $\sigma_{\max}/\sigma_y$  (cf., Figure 17).

### Acknowledgements

This work was supported in part by the Multi-University Research Initiative on 'High Cycle Fatigue', which is funded at Harvard by AFSOR under Grant No. SA1542-22500 PG, and in part by the Division of Engineering and Applied Sciences, Harvard University.

### References

- Begley, M., Evans, A.G. and Hutchinson, J.W. (1999). Spherical impression of thin elastic films on elastic-plastic substrates. *International Journal of Solids and Structures*, submitted.
- Biwa, S. and Storakers B. (1995). An analysis of fully plastic Brinell indentation. *J. Mech. Phys. Solids* **43**, 1303–1334.
- Bower, A.F., Fleck, N.A., Needleman, A. and Ogbonna, N. (1993). Indentation of power law creeping solids. *Proceeding Royal Society of London A* **441**, 97–124.
- Hibbit, Karlsson & Sorensen Inc. (1998). *ABAQUS version 5.7 User's Manual*, Hibbit, Karlsson & Sorensen Inc., Pawtucket, RI.
- Hill, R., Storakers, B. and Zdunek, A.B. (1989). A theoretical study of the Brinell hardness test. *Proceedings Royal Society of London A* **423**, 301–330.
- Johnson, K.L. (1985). *Contact Mechanics*, Cambridge University Press, Cambridge.
- Mesarovic, S.D. and Fleck, N.A. (1999a). Spherical indentation of elastic-plastic solids. *Proceeding Royal Society London*, in press.
- Mesarovic, S.D. and Fleck, N.A. (1999b). Frictionless indentation of dissimilar elastic-plastic spheres. *International Journal of Solids and Structures*, in press.
- Peters, J.O., Roder, O., Boyce, B.L., Thompson, A.W. and Ritchie, R.O. (2000). Role of Foreign Object Damage on Thresholds for High-Cycle Fatigue in Ti-6Al-4V. *Metallurgical and Materials Transactions A*, in review.
- Ritchie, R.O., Davidson, D.L., Boyce, B.L., Campbell, J.P. and Roder, O. (1999). High-Cycle Fatigue of Ti-6Al-4V. *Fatigue and Fracture of Engineering Materials and Structures* **22**, 621–631.



## The residual stress state due to a spherical hard-body impact

B.L. Boyce<sup>a</sup>, X. Chen<sup>b</sup>, J.W. Hutchinson<sup>b</sup>, R.O. Ritchie<sup>a,\*</sup>

<sup>a</sup> *Materials Sciences Division, Lawrence Berkeley National Laboratory, and Department of Materials Science and Engineering, University of California, 463 Evans Hall #1760, 1 Cyclotron Road, Berkeley, CA 94720-1760, USA*

<sup>b</sup> *Division of Engineering and Applied Science, Harvard University, Cambridge, MA 02138, USA*

Received 8 May 2001

---

### Abstract

The current study assesses the residual stresses and remnant damage caused by a spherical projectile impacting upon a flat surface. The immediate application of this information is to the problem of foreign object damage (FOD) associated with the ingestion of debris into an aircraft turbine engine and the subsequent reduction in component lifetime. The work is focused on two primary features: (i) the development of numerical models for the evaluation of the deformation and stresses associated with the impact process and (ii) the use of spatially resolved residual stress measurements to verify experimentally the numerical analysis. As a first approximation, a quasi-static numerical model was developed by ignoring time-dependent effects (i.e., strain-rate sensitivity, wave and inertia effects, etc.), where the effects of velocity were approximated by adjusting the depth and diameter of the resulting impact crater to match that of actual impact craters at the corresponding velocity. The computed residual stresses and associated elastic strain gradients were compared to experimentally measured values, obtained using synchrotron X-ray diffraction (XRD) methods. This comparison indicated that the quasi-static numerical analysis was adequate for moderate impact conditions (velocity = 200 m/s, energy = 2.7 J); however, under more aggressive conditions (velocity = 300 m/s, energy = 6.1 J), there was significant discrepancy between the numerical predictions and experimental measurements. Such discrepancy may be attributed to several factors that can occur at higher impact velocities, including strain-rate sensitivity, microcrack formation, and shear-band formation. A dynamic simulation, where the time-dependent effects of strain-rate sensitivity and elastic-wave interactions were approximated, provided results in closer agreement with the experimental diffraction observations. © 2001 Published by Elsevier Science Ltd.

**Keywords:** Titanium; Ti-6Al-4V; Foreign object damage; Impact; Residual stress; X-ray diffraction; Fatigue

---

### 1. Introduction

Foreign objects ingested by turbine engines during operation can cause significant damage to

compressor airfoils. Under the influence of subsequent high-cycle fatigue loading, these damage sites can lead to the premature formation and propagation of incipient cracks, which in turn can result in severe reductions in the lifetime of the component (Aydinmakine, 1994; DiMarco, 1994; Saravanamuttoo, 1994; Larsen et al., 1996; Cowles, 1996). Indeed, the costs associated with such foreign object damage (FOD) have been esti-

---

\* Corresponding author. Tel: +1-510-486-5798; fax: +1-510-486-4881.

E-mail address: roritchie@lbl.gov (R.O. Ritchie).

mated at \$4 billion annually by the Boeing Corporation (Bachtel, 1998). Despite the importance of this problem, current lifetime prediction and design methodologies for turbine engines still rely principally on empirical safety factors to account for FOD, rather than using an approach based on an understanding of the salient mechanisms involved.

To develop an understanding of how FOD degrades the fatigue life of a component, several factors need to be addressed: (i) the stress concentration associated with the geometry of the damage site, (ii) the associated microstructural distortion (i.e. shear bands, local texturing), (iii) the presence and extent of incipient microcracks induced by the impact, (iv) the residual stress field and plastic damage distribution (cold work) resulting from the impact, and (v) the relaxation or redistribution of such residual stresses upon subsequent cycling.

While several investigations are currently underway to address the issues associated with stress concentration, microstructural distortion and the creation of incipient microcracks in order to characterize the influence of FOD on fatigue life

(e.g., Peters and Ritchie, 2000; Ruschau et al., 2001), the issue of the resulting stress and displacement fields created by the FOD impact has not yet been experimentally measured. It is this damage distribution which controls the initiation and early growth of fatigue cracks from FOD sites that eventually lead to the overall failure of the component. Proper characterization should provide critical mechanistic insight into the residual stress state and its influence on fatigue behavior.

The nature of the residual stresses around a surface damage site has been predominantly studied by two communities: (i) those interested in the residual stresses associated with hardness indents for measuring either resistance to cracking or prior residual stress (Salomonson et al., 1996; Suresh and Giannakopoulos, 1998; Zeng et al., 1998) and (ii) those interested in the residual stress field formed from the shot peening process (Johnson, 1968; Studman and Field, 1977; Yokouchi et al., 1983; Al-Obaid, 1990; Li et al., 1991; Kobayashi et al., 1998). The literature related to stresses around hardness indents has almost exclusively focused on the problem of the sharp

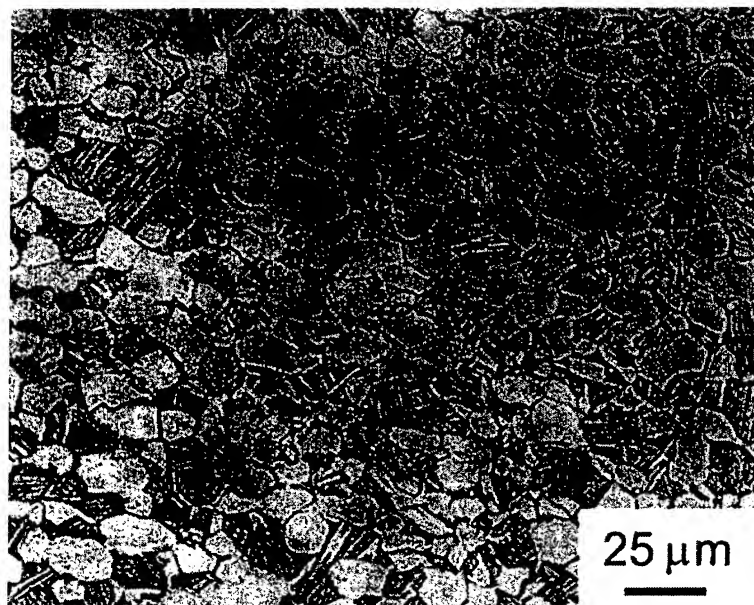


Fig. 1. Two-phase microstructure of the bimodal Ti-6Al-4V alloy under investigation consisting of HCP  $\alpha$  (light gray) and BCC  $\beta$  (dark gray). The  $\alpha$ -phase exists in both the globular primary- $\alpha$  phase and the lamellar colonies of alternating  $\alpha$  and  $\beta$ .



indenter, which is most commonly used for estimates of cracking resistance or prior residual stress. While the analysis of the sharp indenter problem is relevant in its reliance on determining elastic–plastic response, the quasi-static velocities and non-axisymmetric geometry limit its applicability to the FOD case.

The literature on the residual stress state created by shot peening has focused on the spherical impact problem. Here, both the shape and velocity of the impact are similar to the FOD problem, although shot peening involves multiple overlapping impacts whereas FOD is associated with a single impact. In the case of shot peening, the multiple overlapping impacts result in a stress field that is nominally equi-biaxial in the plane of the surface and varies only with depth. However, in the case of a single impact, the resulting stress field is fully three-dimensional and varies in both the depth and along the surface. It is this distinction which limits the applicability of traditional residual stress measurements techniques, such as conventional coarse-spot X-ray diffraction, layer-removal, hole-drilling, etc., to this problem, as these techniques are generally applied to less complex stress states, or stress states that vary in only one direction.

It is the purpose of the current paper to present a numerical model for the distribution of residual stresses resulting from a FOD impact and to verify such stresses using synchrotron X-ray diffraction (XRD) techniques on a Ti–6Al–4V alloy subjected to sub-ballistic impacts by chrome-hardened steel spheres at velocities of 200 and 300 m/s.

## 2. Approach

### 2.1. Material

The material studied was a Ti–6Al–4V alloy with a composition (in wt%) of 6.30 Al, 4.17 V, 0.19 Fe, 0.19 O, 0.013 N, 0.0035 H, bal. Ti. It was received as 20-mm thick forged plates from Tele-dyne Titanium after solution treating 1 h at 925°C and vacuum annealing for 2 h at 700°C. This alloy, which has been chosen as the basis of a compre-

hensive military/industry/university program on *High Cycle Fatigue*, has a microstructure consisting of a bimodal distribution of ~60 vol% primary- $\alpha$  and ~40 vol% lamellar colonies of  $\alpha + \beta$  (Fig. 1).<sup>1</sup> This microstructure displays room temperature yield and tensile strengths of 930 and 970 MPa, respectively, and a Young's modulus of 116 GPa (Eylon, 1998).

Prior to impact,  $35 \times 35 \times 20$  mm<sup>3</sup> rectangular specimens were machined from the as-received plates. Machining damage was minimized by chemical milling (H<sub>2</sub>O, HNO<sub>3</sub>, and HF in a ratio of 30:10:1 at ambient temperature) to remove more than 100  $\mu$ m from each surface of the specimen, followed by a stress-relief anneal at 700°C for 2 h (with a vacuum cool).

### 2.2. Impact method

In this study, foreign object damage was simulated by shooting spherical projectiles onto a flat specimen surface to produce a single hemispherical damage site, as shown in Fig. 2. Chrome-hardened steel spheres, 3.2 mm in diameter with a Rockwell C hardness of 60, were impacted onto the flat surfaces specimens at velocities of 200 and 300 m/s (incident kinetic energies of 2.7 and 6.1 J, respectively) using a compressed-gas gun facility. These velocities represent typical in-service impact velocities on aircraft engine fan blades. The spheres were accelerated by applying gas pressures between 2 and 7 MPa. A more detailed description of the impact process, resulting damage sites, and the associated fatigue behavior can be found in Peters et al. (2000).

### 2.3. Numerical simulation of impact

As an initial simulation of foreign object damage, a quasi-static numerical model was established consisting of a spherical indentation on a flat surface with a static normal indentation load  $P$  (Fig. 2). The indenter was modeled as rigid

<sup>1</sup> In the context of the Air Force *High Cycle Fatigue* program, this microstructure in Ti–6Al–4V has been referred to as “solution treated and overaged” (STOA).

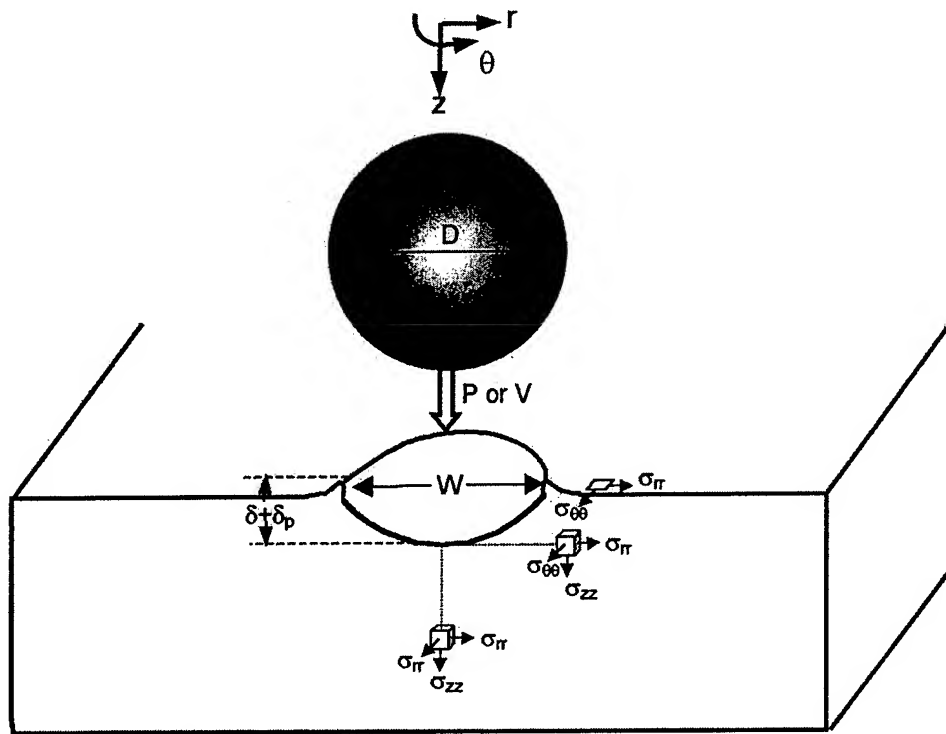


Fig. 2. Illustration of impact of a spherical indenter of diameter,  $D$ , with incident velocity  $V$  (or in the case of quasi-static loading, under normal load,  $P$ ), on a flat surface resulting in a crater of width,  $W$ , depth below the nominal surface,  $\delta$ , and pile-up above the nominal surface,  $\delta_p$ . While the residual stress field throughout the body is of interest, only the near-surface layers can be probed with X-ray diffraction. Traditional layer-removal techniques cannot be applied due to the three-dimensional nature of the stress gradient and geometry.

with a diameter equal to that of the impact experiments,  $D = 3.2$  mm. The indentation load was then removed and a crater formed with depth  $\delta$ , diameter  $w$ , and plastic pile-up height  $\delta_p$ . The size of the crater was adjusted by controlling  $P$  such that the resulting crater dimensions matched with the dimensions measured on the experimental FOD impact. The substrate material was taken to be elastic-perfectly plastic with material properties specified for the bimodal Ti-6Al-4V alloy described in the previous section. Additionally, as a first approximation, impact velocities of 200 and 300 m/s impacts were simulated by quasi-static indentations on a  $35 \times 35 \times 20$  mm rectangular specimen.

Static finite element (FEM) calculations were performed using the commercial code ABAQUS version 5.8 (Hibbit, Karlsson & Sorensen Inc., 1999) based on the implicit integration method.

The rigid contact surface option was used to simulate the rigid indenter, and the option for finite deformation and strain was employed. In order to simplify the model and take advantage of the axis-symmetric approach, the substrate was approximated by a cylindrical block with diameter 35 mm and depth 20 mm. An axis-symmetric mesh was developed for the specimen comprising of 4000 8-node elements. As noted above, the substrate material was taken to be elastic-perfectly plastic, with a Von Mises surface to specify yielding. Coulomb friction was invoked in all calculations, where the friction coefficient  $\mu$  is taken to be 0.1 (nearly frictionless).

At low incident velocities, as indicated in the following section, the quasi-static model yields good agreement with experimental measurements. However, for 300 m/s impact velocities where the

velocity is about 1/10 of the shear wave speed of the substrate material, dynamic effects come into play. In order to account for dynamic effects such as elastic wave, inertia and strain rate effects, dynamic numerical simulations were performed by incorporating the explicit integration method into the finite element program. The rigid spherical projectile was given an initial velocity of 200 or 300 m/s, which then made contact with the substrate and bounced back in about 5  $\mu$ s with a ricocheting speed of about 22% of the incident velocity. After the impact, the residual stresses at the surface were subject to high-frequency vibrations and the steady-state residual stress field was obtained after about 1 ms. In the dynamic numerical simulation, the substrate was given the same material properties as in quasi-static finite element analysis, except that the strain rate sensitivity was included in the approach. This was analytically expressed in a power-law form as

$$\dot{\epsilon} = D \left( \frac{\sigma_y(\dot{\epsilon})}{\sigma_y^0} - 1 \right)^n$$

with  $D = 2 \times 10^4$  and  $n = 3$ , (1)

where  $\dot{\epsilon}$  is the strain rate,  $\sigma_y(\dot{\epsilon})$  is the strain-rate sensitive yield stress, and  $\sigma_y^0$  the yield stress at  $\dot{\epsilon} = 0$ , and  $D$  is a proportionality constant with units of  $s^{-1}$ . This relationship is largely consistent with the experimental data of Meyer (1984) in tension in that it shows a substantial increase in the yield stress at strain rates in excess of  $10^3 s^{-1}$ ; however, it is less linear than the experimental data of Follansbee and Gray (1989) for testing in compression.

#### 2.4. Diffraction analysis of residual stress state

A primary objective in the current study was to compare the numerically predicted residual stress states to experimental observations. To this end, spatially resolved residual stress measurements were performed using synchrotron X-ray diffraction at beamline 2-1 of the Stanford Synchrotron Radiation Laboratory (SSRL). The advantage of the synchrotron source for this particular application was (a) a low divergence ( $< 0.2$  mrad)

source/detector configuration to minimize sample displacement errors associated with the coarse topography of the indent, and (b) a photon flux several orders of magnitude more intense than a conventional sealed-tube source, enabling sub-millimeter spatial resolution without the divergence of capillary optics.

For comparison to numerical predictions, two modes of characterization were utilized. A relatively fast measurement of the  $d$ -spacing normal to the surface yielded an estimate for the residual elastic strain component,  $\epsilon_{zz}$ , normal to the surface. In regions of particular interest, the conventional  $\sin^2 \psi$  method (Prevey, 1977; Noyan and Cohen, 1987) was employed for measuring the in-plane stresses. These two techniques are described in more detail in the following paragraphs. It should be noted that all experimental comparisons to the finite element results were restricted to the specimen surface because traditional layer-removal techniques to observe the subsurface stress gradient cannot be applied here due to the three-dimensional nature of the stress gradient and crater geometry.

*Out-of-plane strain measurement:* The most readily determined component of residual elastic strain is the component normal to the specimen surface,  $\epsilon_{zz}$ . Note that the  $z$ -direction is normal to the specimen surface, as shown in the coordinate axes defined in Fig. 2. Under conditions of symmetric diffraction, where the incident and diffracted X-rays are at equal angles to the specimen surface, the  $d$ -spacing of planes coplanar with the specimen surface are measured. By comparing the  $d$ -spacing of a stressed region to that of an unstressed reference  $d$ -spacing, the  $\epsilon_{zz}$  component can be assessed:

$$\epsilon_{zz} = \frac{d - d_0}{d_0} = \frac{\sin \theta_0}{\sin \theta} - 1. \quad (2)$$

The measured  $\epsilon_{zz}$  values provide a comparison of the relative residual strain distributions formed under various conditions (material, velocity, indenter size, etc.). Conversion of the  $\epsilon_{zz}$  strain value to a stress requires knowledge of the stress state at that location; for example, if the stress state is equi-biaxial ( $\sigma_{rr} = \sigma_{\theta\theta}$ ), as in the case of a shot

peened surface, the stresses can be derived by using the appropriate<sup>2</sup> elastic constants:

$$\sigma_{rr} = \sigma_{\theta\theta} = \frac{E\varepsilon_{zz}}{2\nu}. \quad (3)$$

While this approach is valid when a residual stress state is known or assumed at a particular surface location (e.g. equi-biaxial at the crater floor), it is not possible to convert unambiguously the  $\varepsilon_{zz}$  values measured by this technique into stress components without some knowledge of the stress state elsewhere. Nevertheless, for the purpose of evaluating the validity of a finite element model, it may not be necessary, or beneficial, to convert to stress, but rather to directly compare the numerical and experimental values of the elastic residual strain distribution,  $\varepsilon_{zz}$ .

**Measurement of in-plane stresses:** In the present work, the well-documented  $\sin^2\psi$  technique (Prevey, 1977; Noyan and Cohen, 1987) was used to measure the local stresses in the plane of the specimen. In conventional powder diffraction, as well as the previously described experiment for measuring out-of-plane strain, the diffraction vector is normal to the specimen surface and the interrogated diffraction planes are coplanar with the surface, as shown in Fig. 3. However, the  $\sin^2\psi$  technique interrogates crystallographic planes tilted at multiple angles,  $\psi$ , from the surface-normal. The variation in  $d$ -spacing with tilt-angle,  $\psi$  is uniquely correlated to the stress components in the interrogation volume. In the special case where  $\sigma_{zz} = \sigma_{rz} = \sigma_{\theta z} = 0$ , such as exists at a free surface, the variation in  $d$ -spacing is expected to be linear with respect to  $\sin^2\psi$ . Moreover, the slope of the linear relationship between  $d$ -spacing and  $\sin^2\psi$  is proportional to the stress component,  $\sigma_{\psi=90}$ , in the plane of the specimen, along the direction of the diffraction vector at  $\psi = 90^\circ$ :

<sup>2</sup> For these experiments, “X-ray” elastic constants are generally generated experimentally by in situ loading of a tensile specimen to known levels of stress, and by correlation to the observed change in  $d$ -spacing. In the case of a crystal with anisotropic elastic constants, this calibration must be applied to the same set of planes as used for the interrogation (Prevey, 1977).

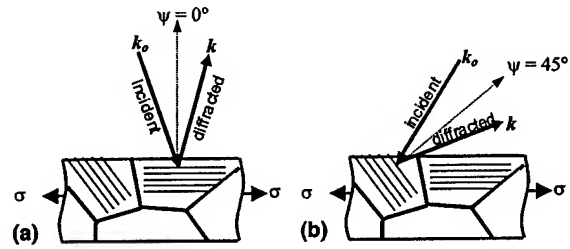


Fig. 3. Illustration of (a) general powder diffraction where the incident and exiting beams make equal angles with the specimen surface and the diffraction vector ( $k - k_0$ , dotted line) is perpendicular to the surface. In this case, the interrogated planes are coplanar with the specimen surface and the observed strain component is normal to the specimen surface along the direction of the diffraction vector. (b) By tilting to non-zero  $\psi$  angles, the planes of interrogation are no longer coplanar with the surface, and again the  $d$ -spacings are measured in the direction of the diffraction vector.

$$\frac{d_\psi - d_0}{d_0} = \frac{1 + \nu}{E} \sigma_{\psi=90} \sin^2 \psi - \frac{\nu}{E} (\sigma_{rr} + \sigma_{\theta\theta}). \quad (4)$$

When this linear relationship between  $d$ -spacing and tilt angle,  $\psi$ , is observed, the corresponding stress in the plane of the specimen can be deduced. A nonlinear relationship may be an indication of non-negligible out-of-plane stresses near the free surface or strong texture and requires a more sophisticated analysis. A more complete description of the assumptions and potential errors associated with the  $\sin^2\psi$  technique is given in Noyan and Cohen (1987).

Independent validation of both the out-of-plane strain measurement technique and the  $\sin^2\psi$  technique was achieved by applying known strain levels to a standard, similar to that used in previous diffraction-based residual stress studies (Prevey, 1977). A strain-gauged Ti-6Al-4V tensile specimen was loaded in an in situ tensile load frame to various levels of strain ranging from 0 to 6000  $\mu\epsilon$  corresponding to uniaxial stresses in the range of 0–700 MPa. The elastic strains measured by the X-ray method were found to be within 300  $\mu\epsilon$  of the observed strain gauge values. It should be noted that in the case where the diffraction vector (the bisector of the incident and diffracted beam) is normal to the specimen surface, the observed strain component is also normal to the specimen surface, and is the Poisson response to the applied strain.

### 3. Results

#### 3.1. Numerical results

In the current study, numerical simulations were performed for two impact velocities (200 and 300 m/s), using two methods: an initial quasi-static analysis and explicit dynamic analysis. There were several general features that were consistent for both velocities and both simulation methods. The results in Fig. 4 focus on the hoop stress component,  $\sigma_{\theta\theta}$ , as the hoop stress component superimposes on the applied load during fatigue crack initiation and growth (Peters et al., 2000; Chen and Hutchinson, 2001). A consistent result from the two methods was the existence at both impact velocities of two primary zones of tension in the immediate vicinity of the indent; these regions of tensile residual stress serve to increase the local mean stress during subsequent fatigue loading, thereby accelerating the initiation and propagation of fatigue cracks. These tensile zones were: (i) a small but intense region at the surface immediately outside the crater rim, and (ii) a broad region approximately one crater radius away from the crater where the maximum stresses in this region are well below the surface. In both tensile zones, the maximum tensile stress was on the order of 40% of the yield stress. The most substantial compressive stresses, conversely, are formed in a large zone directly beneath the crater, and show a maximum value of approximately  $1\frac{1}{2}$  times the yield stress, roughly one crater radius below the crater floor. These observations are consistent for both impact velocities.

While the quasi-static and dynamic finite element analyses predict almost identical residual stress fields away from the surface of the specimen, the results are quite different at the notch surface where the dynamic effects are of most concern. In particular, by ignoring the elastic wave and inertia effects, the quasi-static model predicted a more compressive  $\sigma_{\theta\theta}$  at the crater floor and a more tensile  $\sigma_{\theta\theta}$  at the rim, compared with dynamic simulation. Specific values of  $\sigma_{\theta\theta}$  calculated at surface locations of interest are compared with parallel experimental data in the next section. Indeed, as discussed below, the dy-

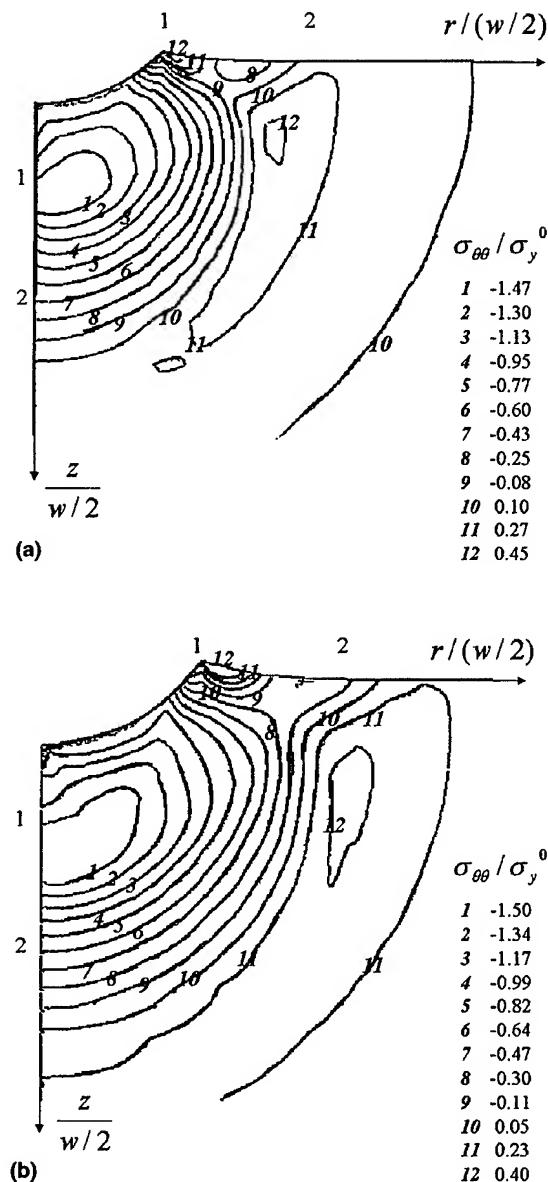


Fig. 4. Contour plots of the residual  $\sigma_{\theta\theta}$  stress field in the vicinity of crater floor predicted from dynamic finite element analysis, showing the stress distribution for (a) 200 m/s and (b) 300 m/s impact velocities. The residual stress fields are normalized by the yield stress at zero strain rate,  $\sigma_y^0$ .

namic finite element simulation based on the explicit integration method is more effective in stimulating the impact process, and hence yields results closer to experimental observations. In

Figs. 4(a) and (b), contour plots of the residual hoop stress field  $\sigma_{\theta\theta}$  around the notch, determined from dynamic finite element approach, are shown for the cases of 200 and 300 m/s impact velocities, respectively.

The prominent residual compressive stress field can also be seen in Fig. 4 beneath the impact crater floor, with the stress gradient being fairly large at the surface. At the 300 m/s impact, for example, the compressive residual  $\sigma_{\theta\theta}$  stress directly below the crater was seen to vary from about  $-0.1\sigma_y^0$  at the surface of the crater floor to  $-0.8\sigma_y^0$  at  $\sim 100$   $\mu\text{m}$  below the surface and continues to decrease to a maximum compressive stress of  $\sim -1.5\sigma_y^0$  at a depth of 1.4 mm, as shown in Fig. 4(b). Two prominent residual tensile regions are developed after impact: one right at the crater rim, and the other located southeast of the crater rim (below the surface), where the maximum value of residual  $\sigma_{\theta\theta}$  stress is about  $0.4\sigma_y^0$ . Both regions are likely to provide fatigue crack initiation sites during subsequent cyclic loading, where the residual tensile  $\sigma_{\theta\theta}$  is proven to be one of the primary driving forces (Peters et al., 2001). The crater floor is another potential fatigue crack formation site due to the higher elastic stress concentration factor compared with the rim, especially at lower impact speeds. At high incident velocity (300 m/s), the microcracks that are formed on impact in the pile-up of material at the crater ridge, plus the residual tensile  $\sigma_{\theta\theta}$  stress field, act in concert to promote fatigue-crack growth; such growth initiates from these microcracks when the applied cyclic stresses are high compared to the magnitude of the maximum tensile residual stresses. Conversely, when the applied cyclic stresses are comparable in magnitude to the residual stress levels, fatigue cracks can initiate below the sample surface away from the impact crater, specifically in the region of high residual tensile stress (Peters et al., 2001).

### 3.2. Experimental results

As a basis for comparison with the numerical results, the gradient in residual strain was measured from the crater rim and emanating away from the crater. To evaluate strain, the (21 $\bar{3}$ 1) diffraction peak at  $\sim 110.5^\circ 2\theta$  (energy = 8048 keV)

was chosen to provide (i) a sufficiently high  $2\theta$  angle to project a small “footprint” on the sample, (ii) a sufficient intensity to allow accurate peak fitting, and (iii) to have similar elastic behavior to that of the overall sample (unlike basal or prism planes which have significantly different elastic behavior due to crystal anisotropy). A spot size was chosen such that the projected X-ray footprint on the sample was  $500 \times 500$   $\mu\text{m}^2$ . This spot size was a compromise between the need for small spatial scale to map out the strain gradient which varies over several millimeters, and the need for a sufficiently large spot size to sample many grains for powder diffraction analysis. During  $\psi$ -tilting experiments, the spot size was adjusted for every  $\psi$ -tilt to keep the sampling area constant. The  $500 \times 500$   $\mu\text{m}^2$  sampling area was estimated to interrogate at least 300 grains simultaneously, whereas at least 100 grains are generally considered sufficient for powder diffraction analysis. To increase the number of grains properly oriented for diffraction, the sample was rocked  $\pm 2^\circ$  on the  $\theta$  axis for each  $2\theta$  position.

The out-of-plane strain measurement, where the diffraction vector was perpendicular to the specimen surface, was useful for mapping out the spatial distribution of the  $\varepsilon_{zz}$  component normal to the surface. An example of a two-dimensional spatial strain map around a 200 m/s impact crater is shown in Fig. 5. This crater map shows a local maximum tensile strain at the crater floor, which corresponds to an equi-biaxial stress of about  $-500$  MPa (assuming that the stress state at the crater is indeed equi-biaxial and the strain normal to the surface is the Poisson response to the equi-biaxial stress).

At specific points of interest, a more thorough  $\sin^2 \psi$  analysis was performed to determine the in-plane stresses,  $\sigma_{\theta\theta}$  and/or  $\sigma_{rr}$ . Because of time constraints, a spatial map of the stresses was not feasible; a two-dimensional map of the in-plane stresses similar to the map presented in Fig. 5 for strain would require more than three weeks of synchrotron time using the current experimental setup. An example of the variation of  $d$ -spacing with  $\sin^2 \psi$  is presented in Fig. 6. As is expected in the case of a negligible out-of-plane stress com-

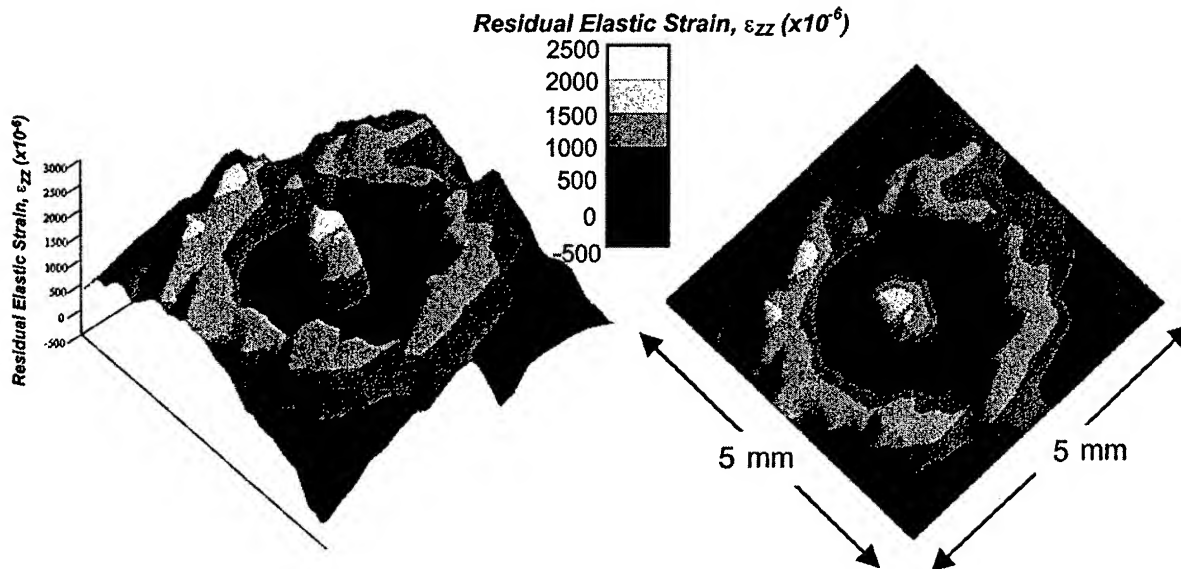


Fig. 5. Two views of a two-dimensional surface-normal strain ( $\epsilon_{zz}$ ) survey around a site of damage formed from a 200 m/s impact. The tensile value of  $\epsilon_{zz}$  at the center of the impact crater is the Poisson strain response to the equi-biaxial compressive stresses that exist at the center of the crater floor.

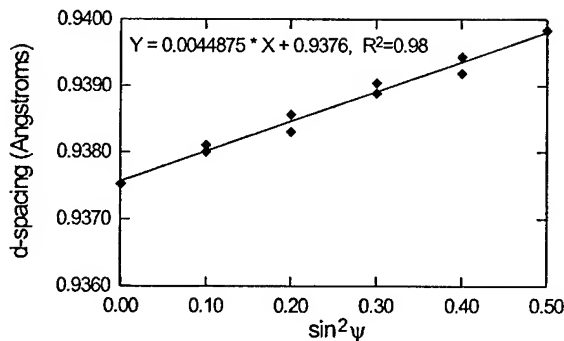


Fig. 6. Variation of  $d$ -spacing with tilt-angle,  $\psi$  as sampled next to the crater rim. This linear behavior is typically observed for both 200 and 300 m/s impact velocities.

ponent and low to moderate texture, the  $d$ -spacing varies linearly with  $\sin^2 \psi$ .

#### 4. Discussion

##### 4.1. Comparison of numerical and experimental results

The primary motivation behind the experimental XRD work was to evaluate the validity of

the numerical models. For this evaluation, there were two primary modes of comparison: (i) a qualitative comparison of the spatial gradient in residual stress (or residual elastic strain) to ensure that the size-scale and nature of the stress state was captured appropriately, and (ii) a quantitative comparison of residual stress values at specific key locations to aid in understanding the driving force for crack formation and propagation.

*Qualitative comparison of gradient shape:* A comparison of the spatial gradient corresponding to three residual elastic strain components is shown in Fig. 7. The relative shape of each of the three gradients is quite similar between the FEM prediction and the diffraction (XRD) analysis. A more direct comparison of the  $\epsilon_{zz}$  strain gradient emanating away from the rim is presented in Fig. 8. Here, the comparison is between the diffraction data and the quasi-static FEM analysis. Again, the shape of the gradient is quite similar between experimental and numerical analysis, although at the higher impact velocity the magnitude of the predicted strains are considerably higher than the observed strains. This discrepancy, which was

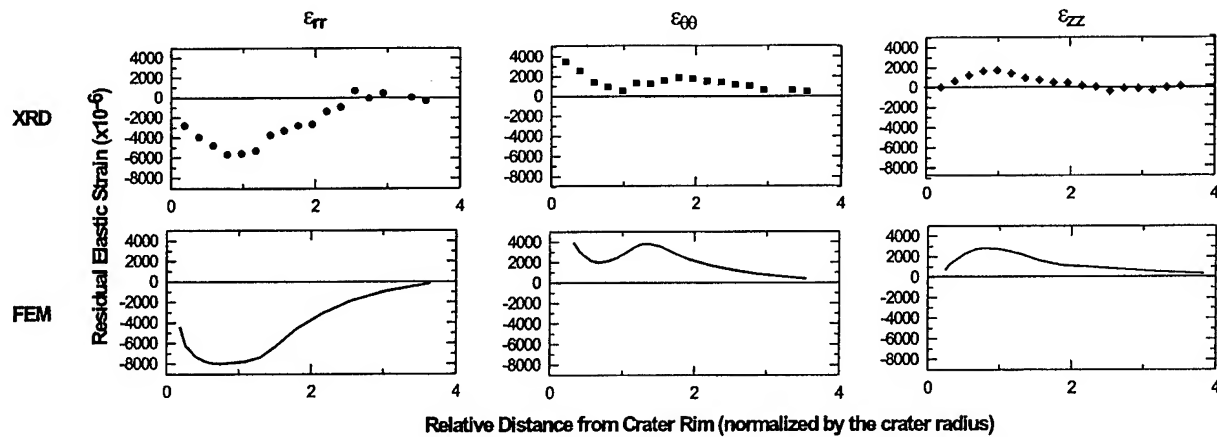


Fig. 7. Spatial gradient in elastic strain components,  $\epsilon_{rr}$ ,  $\epsilon_{\theta\theta}$  and  $\epsilon_{zz}$ , emanating away from the crater rim as predicted by the finite element method, FEM (line), and observed by X-ray diffraction, XRD (points). In the diffraction results,  $\epsilon_{zz}$  was obtained by symmetric diffraction,  $\epsilon_{rr}$  was obtained from the  $\sin^2 \psi$  technique, and  $\epsilon_{\theta\theta}$  was calculated from the other two data sets, assuming that  $\sigma_{zz} = 0$  in the interrogation volume ( $< 10 \mu\text{m}$  from the free surface). For all three components of strain, the shape of the gradient, as well as the relative location of extremes, are consistent between numerical predictions and experimental observations.

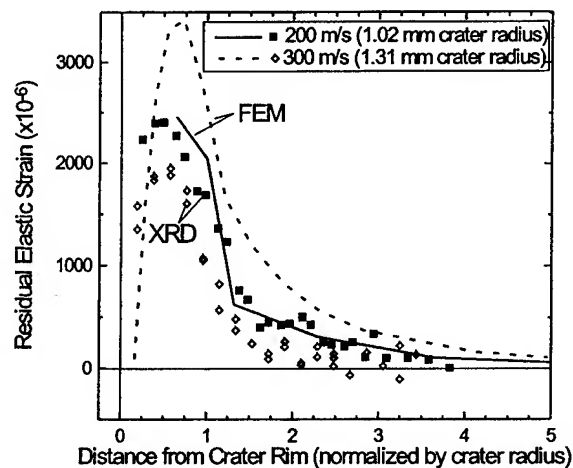


Fig. 8. Comparison of  $\epsilon_{zz}$  strain gradients observed by X-ray diffraction (data points) and predicted by FEM (lines) using a quasi-static analysis. While the gradient associated with the 200 m/s impacts appears to be in agreement between the two methods, the magnitude of the 300 m/s impact gradient is not well captured by the quasi-static analysis.

observed only at the higher impact velocity, is discussed in detail below.

**Quantitative comparison of stresses at key locations** (Table 1): The center of the crater floor and the crater rim were two key locations for the comparison of stresses, based on evidence of crack

formation in these regions during subsequent fatigue loading (Peters and Ritchie, 2000). The role of residual stresses on fatigue crack formation at these locations was discussed in the last section. These locations were also the most challenging for both the FEM model and the XRD experiments due to the high degree of plastic deformation. For purposes of comparison, the stress values from the numerical model were extracted from  $6 \mu\text{m}$  below the surface (the average X-ray penetration depth) and averaged over  $0.5 \text{ mm}^2$  (the X-ray footprint size). The stress component of most importance is the component acting along the  $\theta$  direction,  $\sigma_{\theta\theta}$ , because it is this component which is acting in the same direction as the subsequent fatigue loading, and therefore driving fatigue-crack nucleation (Peters et al., 2000; Chen and Hutchinson, 2001).

The most important observation of the current study is that the quasi-static calculation of the stresses associated with a 200 m/s impact was largely consistent with experimental observation. However, there was a large discrepancy in the stress values predicted for the 300 m/s impact using the quasi-static numerical approximation. This discrepancy was reduced substantially by taking into account three time-dependent effects, specifically the strain rate sensitivity, inertia effect, and elastic-wave interactions. The potential sources for the



Table 1

Comparison of relevant stresses at key locations as predicted by the finite element method (FEM) and measured by X-ray diffraction (XRD)

Method	$\sigma_{rr}$ at center of crater floor (MPa)	$\sigma_{\theta\theta}$ at crater rim (MPa)	Height of crater depth + pile up (mm) ( $\delta + \delta_p$ )
200 m/s			
XRD, dynamic	-523	150	0.43
FEM, quasi-static	-505	267	0.43
FEM, dynamic	-420	150	0.42
300 m/s			
XRD, dynamic	56	0	0.67
FEM, quasi-static	-846	503	0.67
FEM, dynamic	-82	309	0.67

remnant discrepancy are largely non-continuum effects that are not easily captured in a continuum-based model. During the impact process and prior to fatigue loading, two features were observed in the specimens following 300 m/s impact: microcracks (2–50  $\mu\text{m}$ ) which were formed at the crater rim and shear bands that emanated into the interior of the specimen under the indent (Fig. 9). These localized effects would not be readily modeled in the continuum-based FEM calculations and would serve to reduce the intensity of the local stresses, consistent with the observed discrepancy between the FEM model and diffraction measurements. Moreover, the absence of these features for 200 m/s impacts is consistent with the agreement between the two methods at the lower velocity.

#### 4.2. Implications

The residual stresses left by high velocity impacts are thought to play an important role in promoting premature fatigue failure in airfoils and fan components that have suffered foreign object damage due to the ingestion of debris into a turbine engine. Cyclic loading studies on fatigue specimens with simulated foreign object damage, identical to the hemispherical damage sites presented in this work, have shown that in many cases, knowledge of the initial residual stress distribution left by the impacting process is not sufficient to evaluate the driving force for crack formation and propagation (Peters et al., 2001). The elastic stress concentration factor,  $k_t$ , associated with the shape of the indent amplifies the applied stresses most substantially at the crater

floor ( $k_t = 1.6$  from a 300 m/s impact), and at the rim ( $k_t = 1.25$  from a 300 m/s impact). Even more important is the formation of microcracks at the crater rim, which, in the simplest sense, provides a much higher (crack-like) local stress concentration factor.

Recent studies have also shown that the initial residual stress state is substantially reduced by relaxation or redistribution during subsequent fatigue cycling. For example, during fatigue loading at the smooth-bar  $10^7$ -cycle fatigue limit in the bimodal Ti-6Al-4V alloy, i.e., at  $\sigma_{\text{max}} = 500$  MPa, the residual stresses at the rim and crater floor of an indent formed by quasi-static indentation are reduced by 30–50% after the first fatigue cycle. To probe this behavior analytically, the numerical model was modified to take into account the Bauschinger effect (nonlinear cyclic stress-strain relationship with a yield surface similar to kinematic hardening) based on cyclic stress-strain experiments. The numerical model showed a very similar relaxation effect: a reduction of residual stresses on the order of 40% after the first cycle due to the change in yield surface during cycling and the consequential plastic flow leading to stress redistribution. This redistribution or first-cycle relaxation of the residual stresses is important, as it indicates that the initial residual stress state is more aggressive than the residual stress state at the time of crack initiation and propagation.

The current results also have implications to shot peening. There are many similarities (and some notable differences) between the current study, which primarily focused on the impact of a single spherical projectile on a flat surface, and the

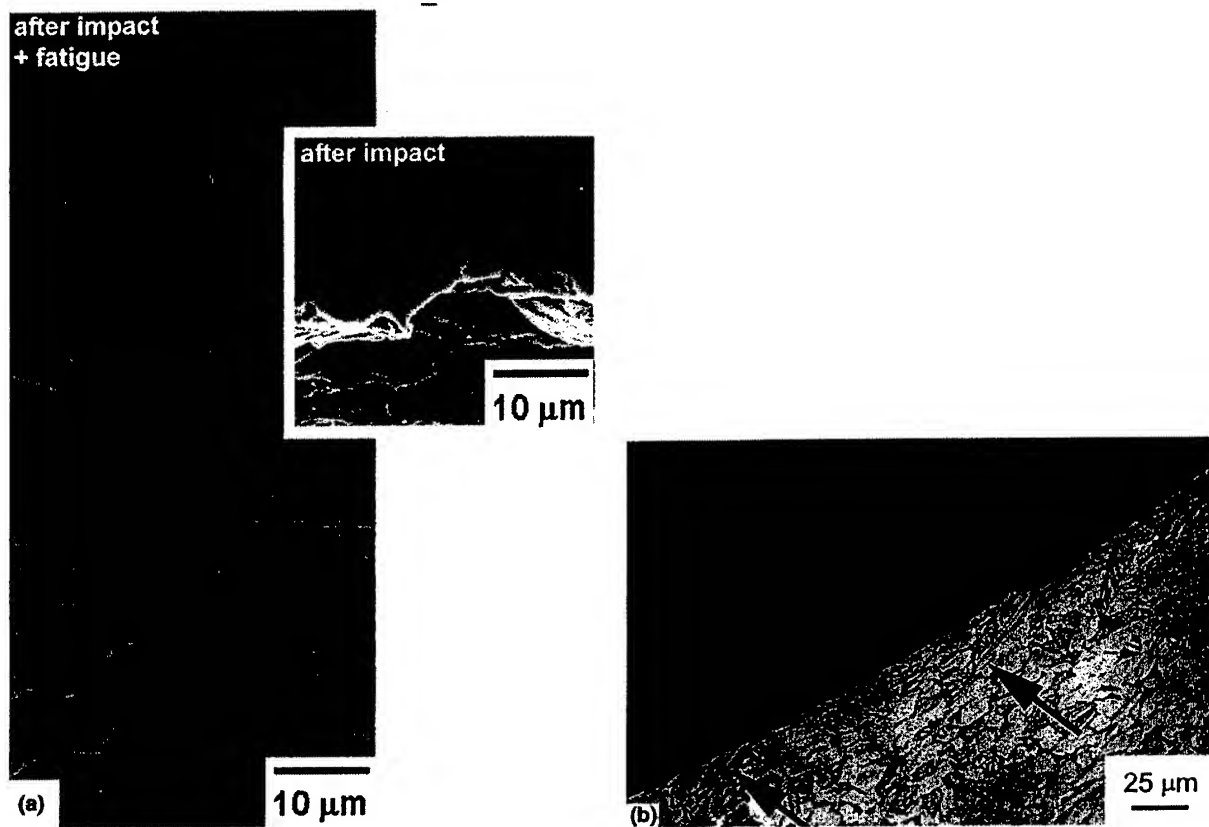


Fig. 9. Features found in 300 m/s impacts but not in 200 m/s impacts, which are not captured in the FEM model. (a) SEM micrograph of a  $\sim 6 \mu\text{m}$  microcrack formed at the crater rim due to the impact process (insert) and the subsequent growth of the microcrack to  $50 \mu\text{m}$  during fatigue loading (nominally applied  $\sigma_{\text{max}} = 500 \text{ MPa}$ ,  $R = 0.1$ ,  $N = 29,000$  cycles). (b) Optical cross-section of the crater floor showing shear band formation along planes of maximum shear (courtesy J.O. Peters).

case of shot peening, where multiple spherical projectiles are impacted on a flat surface in succession. Perhaps the most noteworthy observation is the presence of significant tensile stresses at the crater rim. In the case of multiple overlapping shots, in the simplest sense, the tensile zone at the rim of a single shot is offset when the compressive crater floor of a successive shot is centered on the rim of the first. This is consistent with shot peening observations that indicate that incomplete peening coverage of the surface will leave uncompressed rims, leading to a degradation in the fatigue lifetime. As reported by Wohlfahrt (1982), such incomplete peening coverage results in local zones of tensile residual surface stresses, which can act to promote crack formation.

## 5. Conclusions

Based on the numerical (finite element analysis) and experimental (synchrotron X-ray diffraction) evaluation of a spherical hard-body impact on a flat surface at velocities of 200 and 300 m/s in a Ti-6Al-4V alloy, the following conclusions have been made:

1. The residual stress distribution associated with a spherical hard-body impact has been modeled by quasi-static and dynamic FEM analysis. The hoop stresses, which would superimpose on applied loads along the loading axis, are tensile in two regions: (i) a small but intense region at the surface immediately outside the crater rim, and (ii) a broad region approximately one crater ra-

- dus away from the crater where the maximum stresses in this region are below the surface. Substantial compressive stresses are formed in a large zone directly beneath the crater; the most intense of these are located approximately one-half a crater radius below the crater floor.
2. The maximum values of these residual stresses were found to be approximately 40% of the yield stress in both tensile regions, and  $1\frac{1}{2}$  times the yield stress in the compressive region below the base of the crater. These observations are consistent for both impact velocities.
  3. The shape of the spatial strain gradient predicted by the FEM model is consistent with experimental observations made by spatially resolved XRD.
  4. A 200 m/s impact can be modeled using a quasi-static approach, ignoring time-dependent effects and simply simulating the effect of velocity by matching the relative shape of the crater (depth-to-diameter ratio). The quasi-static model of the 200 m/s indent is quite similar to experimentally observed residual stress values and strain gradients. There is a small discrepancy ( $\sim 150$  MPa) in predicted versus measured residual stresses at the rim, which can be reduced by incorporating dynamic effects into the numerical model.
  5. There are substantial errors arising from the application of a quasi-static analysis to the simulation of a 300 m/s impact. These errors are in part attributable to time-dependent effects (strain-rate sensitivity, elastic-wave interactions); indeed, they are substantially reduced by incorporating such time-dependence into the numerical model. Remnant discrepancy between the numerical model and diffraction-based results may be associated with observed non-continuum effects, such as microcracking and shear-band formation.

### Acknowledgements

This work was supported by the US Air Force Office of Scientific Research under Grant No. F49620-96-1-0478 under the auspices of the Multidisciplinary University Research Initiative on

*High Cycle Fatigue* to the University of California (for numerical modeling and fatigue analysis), the Office of Science, US Department of Energy under contract #DE-AC03-76SF00098 (for experimental diffraction results), and the Stanford Synchrotron Radiation Laboratory, operated by the Department of Energy, Office of Basic Energy Sciences (for X-ray beamtime). BLB acknowledges the financial support of the Hertz Foundation in the form of a fellowship. Thanks are due to Dr. J.O. Peters for performing the ballistic impacts, to Dr. J.M. McNaney for assisting with the in situ straining experiments, and to R.K. Nalla for helpful discussions.

### References

- Al-Obaid, Y.F., 1990. A rudimentary analysis of improving fatigue life of metals by shot peening. *J. Appl. Mech.* 57, 307–312.
- Aydinmakine, F., 1994. Understanding and preventing failures and their causes in gas turbine engines. Technical Evaluator's Report, AGARD-CP-558, p. K.1.
- Bachtel, B., 1998. Foreign object debris and damage prevention. *Aeromagazine* 1, Article S.
- Chen, X., Hutchinson, J.W., 2001. Foreign object damage and fatigue crack threshold: cracking outside shallow indents. *Int. J. Fract.* 107, 31–51.
- Cowles, B.A., 1996. High cycle fatigue in gas turbines – an industry perspective. *Int. J. Fract.* 80, 147–163.
- DiMarco, C., 1994. Navy foreign object damage and its impact on future gas turbine low pressure compression system. Technical Evaluator's Report, AGARD-CP-558, p. G.1.
- Eylon, D., 1998. Summary of the available information on the processing of the Ti-6Al-4V HCF/LCF program plates. University of Dayton Report, Dayton, OH.
- Follansbee, P.S., Gray, G.T., 1989. An analysis of the low temperature, low and high strain-rate deformation of Ti-6Al-4V. *Metall. Trans. A* 20, 863–874.
- Hibbit, Karlsson & Sorensen Inc., 1999. ABAQUS version 5.8 User's Manual. Hibbit, Karlsson & Sorensen Inc., Pawtucket, RI.
- Johnson, K.L., 1968. In: Heyman, J., Leckie, F.A. (Eds.), *Engineering Plasticity*. Cambridge University Press, Cambridge, p. 341.
- Kobayashi, M., Matsui, T., Murakami, Y., 1998. Mechanism of creation of compressive residual stress by shot peening. *Int. J. Fatigue* 20, 351–357.
- Larsen, J.M., Worth, B.D., Annis, C.G., Haake, F.K., 1996. An assessment of the role of near-threshold crack growth in high-cycle-fatigue life prediction of aerospace titanium alloys under turbine engine spectra. *Int. J. Fract.* 80, 237–255.

- Li, Y.K., Mei, Y., Duo, W., Renzhi, W., 1991. Mechanical approach to the residual stress field induced by shot peening. *Mater. Sci. Eng. A* 147, 167–173.
- Meyer, L.W., 1984. In: Lütjering, G., Zwick, U., Bunk, W. (Eds.), *Titanium, Science and Technology*. Deutsche Gesellschaft für Metallkunde, pp. 1851–1858.
- Noyan, I.C., Cohen, J.B., 1987. *Residual Stress: Measurement by Diffraction and Interpretation*. Springer, New York.
- Peters, J.O., Roder, O., Boyce, B.L., Thompson, A.W., Ritchie, R.O., 2000. Role of foreign-object damage on thresholds for high-cycle fatigue in Ti–6Al–4V. *Metall. Mater. Trans. A* 31, 1571–1583.
- Peters, J.O., Ritchie, R.O., 2000. Influence of foreign-object damage on crack initiation and early crack growth during high-cycle fatigue of Ti–6Al–4V. *Eng. Fract. Mech.* 67, 193–207.
- Peters, J.O., Boyce, B.L., Chen, X., McNaney, J.M., Hutchinson, J.W., Ritchie, R.O., 2001. Role of residual stresses on high-cycle fatigue of impact-damaged Ti–6Al–4V: surface vs. subsurface crack initiation. In: Tscheegg, S. (Ed.), *Proceedings of the International Conference on Fatigue in the Very High Cycle Regime*.
- Prevey, P.S., 1977. A method of determining the elastic properties of alloys in selected crystallographic directions for X-ray diffraction residual stress measurement. *Adv. X-ray Anal.* 20, 345–354.
- Ruschau, J.J., Nicholas, T., Thompson, S.R., 2001. Influence of foreign object damage (FOD) on the fatigue life of simulated Ti–6Al–4V airfoils. *Eng. Fract. Mech.* 25, 233–250.
- Salomonson, J., Zeng, K., Rowcliffe, D., 1996. Decay of residual stress at indentation cracks during slow crack growth in soda-lime glass. *Acta Mater.* 44, 543–546.
- Saravanamutto, H.I.H., 1994. Erosion, corrosion and foreign object damage in gas turbines. Technical Evaluator's Report, AGARD-CP-558, p. T.1.
- Studman, C.J., Field, J.E., 1977. The indentation of hard metals: the role of residual stresses. *J. Mater. Sci.* 12, 215–218.
- Suresh, S., Giannakopoulos, A.E., 1998. A new method for estimating residual stress by instrumented sharp indentation. *Acta Mater.* 46, 5755–5767.
- Wohlfahrt, H., 1982. Shot peening and residual stress. In: Kula, E., Weiss, V. (Eds.), *Residual Stress and Stress Relaxation*, Sagamore Army Materials Research Conference Proceedings. Plenum Press, New York, pp. 1–18.
- Yokouchi, Y., Chou, T.W., Greenfield, I.G., 1983. Elastic-plastic analysis of indentation damages in copper: work hardening and residual stress. *Metall. Trans. A* 14, 2415–2421.
- Zeng, K., Giannakopoulos, A.E., Rowcliffe, D., Meier, P., 1998. Residual stress fields at the surface of sharp pyramid indentations. *J. Am. Ceram. Soc.* 81, 689–694.

**Materials Sciences Division, Lawrence Berkeley National Laboratory, and  
Department of Materials Science and Engineering  
University of California at Berkeley**

**MECHANICAL RELAXATION OF LOCALIZED RESIDUAL STRESSES  
ASSOCIATED WITH FOREIGN OBJECT DAMAGE**

***B. L. Boyce<sup>1\*</sup>, X. Chen<sup>2</sup>, J. O. Peters<sup>1\*\*</sup>, J. W. Hutchinson<sup>2</sup>, and R. O. Ritchie<sup>1</sup>***

<sup>1</sup>Materials Sciences Division, Lawrence Berkeley National Laboratory,  
and Department of Materials Science and Engineering,  
University of California, Berkeley, CA 94720, USA

<sup>2</sup>Division of Engineering and Applied Science,  
Harvard University, Cambridge, MA 02138, USA

\* present address: Sandia National Laboratories, P.O. Box 5800, MS 0889, Albuquerque, NM 87185-0889

\*\* present address: Technical University Hamburg-Harburg, 21071 Hamburg, Germany

May 2002

submitted to *Materials Science and Engineering - A*

Work supported by the U.S. Air Force Office of Scientific Research under Grant No. F49620-96-1-0478 under the auspices of the Multidisciplinary University Research Initiative on *High Cycle Fatigue* to the University of California (for numerical modeling and fatigue analysis), the Office of Science of the U. S. Department of Energy under contract #DE-AC03-76SF00098 (for experimental diffraction results), and the Stanford Synchrotron Radiation Laboratory, operated by the Department of Energy, Office of Basic Energy Sciences (for beamtime).

# MECHANICAL RELAXATION OF LOCALIZED RESIDUAL STRESSES ASSOCIATED WITH FOREIGN-OBJECT DAMAGE

B. L. Boyce<sup>1\*</sup>, X. Chen<sup>2</sup>, J. O. Peters<sup>1\*\*</sup>, J. W. Hutchinson<sup>2</sup> and R. O. Ritchie<sup>1\*\*\*</sup>

<sup>1</sup>Materials Sciences Division, Lawrence Berkeley National Laboratory, and  
Department of Materials Science & Engineering, University of California, Berkeley, CA 94720

<sup>2</sup>Division of Engineering and Applied Science, Harvard University, Cambridge, MA 02138

**Abstract:** - Foreign-object damage associated with the ingestion of debris into aircraft turbine engines can lead to a marked degradation in the high-cycle fatigue life of turbine components. This degradation is generally considered to be associated with the premature initiation of fatigue cracks at or near the damage sites; this is suspected to be due to, at least in part, the impact-induced residual stress state, which can be strongly tensile in these locations. However, recent experimental studies have shown the unexpected propensity for impact-induced fatigue crack formation at locations of *compressive* residual stress in the vicinity of the impact site. To address this issue, *in situ* and *ex situ* spatially-resolved X-ray diffraction and numerical modeling are utilized to show that the initial residual stress state can be strongly relaxed during the fatigue loading process. The magnitude and rate of relaxation is strongly dependent on the applied loads. For a Ti-6Al-4V turbine blade alloy, little relaxation was observed for an applied maximum stress of 325 MPa ( $0.35\sigma_y$ , where  $\sigma_y$  is the yield stress), and cracks tended to form in subsurface zones of tensile residual stress *away* from the damage sites. In contrast, at an applied maximum stress of 500 MPa ( $0.54\sigma_y$ ), equal to the smooth-bar  $10^7$ -cycle endurance strength, cracks tended to form *at* the damage sites in zones of high stress concentration that had initially been in strong compression, but had relaxed during the fatigue loading.

**Keywords:** Titanium, Ti-6Al-4V, Foreign-object damage, Impact, Residual stress, X-ray diffraction, Fatigue

---

\* present address: Sandia National Laboratories, P.O. Box 5800, MS 0889, Albuquerque, NM 87185-0889

\*\* present address: Technical University Hamburg-Harburg, 21071 Hamburg, Germany

\*\*\* Corresponding author. Tel: +1-510-486-5798; fax: +1-510-486-4881.

E-mail address: [roritchie@lbl.gov](mailto:roritchie@lbl.gov) (R. O. Ritchie)

## 1. Introduction

The ingestion of airborne objects or debris into aircraft turbine engines can lead to severe reductions in the expected high-cycle fatigue (HCF) life of impact-damaged components [1,2]. In a simplified simulation of such damage using high-velocity impacts of hard spherical objects onto a Ti-6Al-4V blade alloy, studies [3,4] have shown that the endurance strength can be reduced by as much as 50% and the number of cycles to failure at a given stress amplitude decreased by several orders of magnitude. The reduction in fatigue life due to such foreign-object damage (FOD) was reasoned to be associated with four main factors: (i) impact-induced residual stresses, (ii) microcracks formed upon impact, (iii) the stress-concentrating effects of the impact site, and (iv) distortion of the microstructure.

In an effort to specifically quantify the contribution of residual stresses, spatially-resolved synchrotron X-ray diffraction experiments were carried out to measure local residual stress values in the vicinity of the impact sites [5]. While the presence of such local stresses was thought to influence the premature initiation of fatigue cracks and their subsequent early growth during subsequent fatigue cycling, these preliminary studies [4-7] indicated the potential relaxation of the impact-induced residual stresses during fatigue loading, implying that in this relaxed state, the residual stresses might not be a significant driving force (or mitigating force) in crack formation and propagation.

It is the purpose of the current paper to evaluate the redistribution and/or relaxation of impact-induced residual stresses during mechanical fatigue loading using *in situ* and *ex situ* synchrotron X-ray diffraction, to compare the observed behavior with numerical

modeling of the damage and subsequent relaxation processes, and to use this information to develop a better understanding of the driving force for the initiation and subsequent propagation of cracks at sites of impact damage during high-cycle fatigue loading.

## 2. Background

The residual stress state left by the impact of a projectile onto a metallic surface can be significantly altered during subsequent fatigue loading. Such mechanical cycle-dependent redistribution of residual stresses is often termed “cyclic relaxation” or “fading”, and has been studied predominantly with respect to shot peening and welding induced residual stresses.<sup>1</sup> Although there is little information on single impact damage, multiple impact shot peening studies in steels have identified four regimes of relaxation of the residual compressive stresses under fully reversed loading [8,9] (Fig. 1): (I) the compressive portion of the first cycle, (II) the tensile portion of the first cycle, (III) the subsequent cycles up to crack initiation, and (IV) cycles after crack initiation. During the first cycle, i.e., in regimes I and II, stress relaxation occurs when the superposition of the applied and residual stresses exceeds the yield stress<sup>2</sup>. Thereafter, the residual stresses are often observed to decay at a rate proportional to the logarithm of the number of loading cycles [8,9]. This decay is typically associated with the reordering of the dislocation substructure and is thought to be related to the occurrence of cyclic softening,

---

<sup>1</sup> It should be noted that the term “relaxation” can also be used to refer to thermally-driven redistribution of residual stresses. This is a separate driving force from the purely mechanical relaxation discussed herein.

<sup>2</sup> The yield stress referred to in stage II (where the applied and residual stresses are of an opposite sense) is the reverse yield stress; its magnitude is often smaller than the monotonic yield stress due to the Bauschinger effect.



i.e., the reduction in the flow stress during cyclic loading. Upon the formation of a fatigue crack, however, the relaxation rate can increase, presumably due to the stress-concentrating effect and plasticity associated with the crack. For each of the four regimes, there is a material-dependent threshold stress amplitude below which no relaxation is seen.

In addition to relaxing the residual stresses, fatigue cycling can also cause a decay in the dislocation density or cold work associated with the residual stresses, as shown by a reduction in the Bragg peak width (FWHM). Again, results on steels (AISI 4140) show the Bragg peak width to decay linearly with the logarithm of the number of cycles after shot peening at room temperature [9]. There is a threshold stress amplitude below which the peak-widths are unaltered by cycling. In this steel, the threshold is several hundred MPa higher than the threshold for (type-I) residual stress relaxation, indicating that at intermediate stress amplitudes, the macroscopic residual stress state can decay with cycling while the degree of plastic damage remains constant. Similar observations have been reported for AISI 304 steel and AZ31 magnesium alloys, where residual stresses relaxed substantially during fatigue loading, whereas the peak-widths remained essentially constant [10].

Corresponding results on peening-induced residual stresses in titanium alloys, specifically a comparison of “near- $\alpha$ ” IMI-685 (in a  $\beta$  annealed condition) and “ $\alpha+\beta$ ” Ti-6Al-4V (in a condition similar to that of the present study), show the marked effect of cyclic deformation properties on relaxation [11]. In IMI-685, which undergoes very little cyclic softening, cycling at a maximum stress of  $0.75\sigma_y$  (where  $\sigma_y$  is the yield stress) led

to a small ( $\sim 10\%$ ) reduction in the peak longitudinal stress. In contrast, cycling IMI-318 at  $0.83\sigma_y$  caused a much larger ( $\sim 60\%$ ) reduction, consistent [12] with the fact that this alloy experiences substantial cyclic softening. It is thought that this difference in softening behavior is more related to the differences in the microstructure and not as much due to differences in chemical composition.

### 3. Approach

#### 3.1 Material

The material studied in this investigation was a Ti-6Al-4V alloy with composition (in wt.%) of 6.30 Al, 4.17 V, 0.19 Fe, 0.19 O, 0.013 N, 0.0035 H, bal. Ti. It was received as 20-mm thick forged plates from Teledyne Titanium after solution treating 1 hr at  $925^\circ\text{C}$  and vacuum annealing for 2 hr at  $700^\circ\text{C}$ . This alloy, which has been chosen as the basis of a comprehensive military/industry/university program on *High Cycle Fatigue*, has a microstructure consisting of a bimodal distribution of  $\sim 60$  vol.% primary- $\alpha$  and  $\sim 40$  vol.% lamellar colonies of  $\alpha + \beta$  (Fig 2).<sup>3</sup> At ambient temperatures, this structure displays yield and tensile strengths of, respectively, 930 and 970 MPa, and a Young's modulus of 116 GPa [13].

Prior to impact or quasi-static indentation, specimens were machined from the as-received plates into a threaded tensile dogbone geometry (similar to the so-called  $K_b$  bar geometry), as shown in Fig. 3. After machining, surface damage was minimized by a

---

<sup>3</sup> In the context of the Air Force *High Cycle Fatigue* program, this microstructure in Ti-6Al-4V has been referred to as "solution treated and overaged" (STOA).

standard chemical milling procedure ( $\text{H}_2\text{O}$ ,  $\text{HNO}_3$ , and  $\text{HF}$  in a ratio of 30:10:1 at ambient temperature), followed by a stress-relief anneal at  $700^\circ\text{C}$  for 2 hr (with a helium cool).

### 3.2 *Simulation of foreign object damage*

As in our previous studies [4-7], foreign-object damage was simulated by firing Cr-hardened steel spheres of diameter 1 or 3.2 mm at the flat, nominally stress-free surface of the dogbone specimens at velocities of 200 to 300 m/s using a compressed-gas gun. For comparison, similar states of damage were also induced using quasi-static indentation. A 3.2 mm diameter sphere was indented into the surface to a maximum load of 9 or 22 kN to produce a residual indent with dimensions equivalent to those produced by dynamic 200 or 300 m/s impacts, respectively. Interestingly, the residual stresses for the quasi-static indentations were larger than for the dynamic impacts, especially at the key locations of the crater floor and rim; however, no microcracking was observed around the rim of the indents, as is seen during dynamic impact in this alloy [4]. Because the quasi-static indentations generated the higher compressive and tensile residual stresses, this method, rather than dynamic impacting, was principally used in the present study of the relaxation of the residual stresses during subsequent fatigue cycling.

### 3.3 *Fatigue loading*

**3.3.1 *Ex situ residual stress measurements:*** Following indentation, specimens were subjected to a fatigue loading at a fixed stress ratio  $R = \sigma_{\min}/\sigma_{\max} = 0.1$  with a constant applied maximum stress,  $\sigma_{\max}$ , of 500 MPa ( $0.54\sigma_y$ ) or 325 MPa ( $0.35\sigma_y$ ). 500 MPa represents the smooth-bar  $10^7$ -cycle endurance strength (or fatigue limit) at this load ratio

in this alloy [4-7]. Specimens were cycled on an automated MTS servo-hydraulic testing machine, and periodically removed for residual stress measurements after 1, 10, 100, and 1000 cycles. Stresses were measured at two specific locations at the damage sites, namely the crater floor and rim; both locations represent potential initiation sites for fatigue failure [4-7]. The crater floor was of particular interest because moderately high compressive stresses were found for the initial residual stress state; such stresses are seemingly inconsistent with observations that fatigue cracks generally initiated at this location following lower velocity (200 m/s) impact damage.

*3.3.2 In situ residual strain measurements during cyclic loading:* In a separate set of experiments, the first several cycles were applied in an *in situ* tensile loading frame that permitted the X-ray diffraction experiments to be performed on the specimen under loads up to 12 kN. In this way, the response of the residual stresses to cyclic loading could be monitored at several steps along the fatigue cycle, specifically at  $N = 0, 0.2, 0.5, 1, 1.5, 10$ , and 5000 cycles. (The latter 5000 cycles were not applied *in situ*). In this experiment the mode of characterization focused on establishing a spatial map of the surface normal strains ( $\epsilon_{zz}$ ) and the Bragg peak widths as they evolved during fatigue loading.

#### *3.4 Experimental evaluation of residual stress and strain gradients*

Spatially resolved residual stress measurements were performed using synchrotron X-ray diffraction at beamline 2-1 of the Stanford Synchrotron Radiation Laboratory. The advantage of the synchrotron source for this particular application was the low divergence ( $<0.2$  mrad) source/detector configuration to minimize sample displacement errors associated with the coarse topography of the indent, and a photon flux several orders of

magnitude more intense than a conventional sealed-tube source, enabling spatial resolution on the order of a few hundred micrometers without the divergence of capillary optics.

Two modes of characterization were utilized. A relatively fast measurement of the lattice-plane  $d$ -spacings normal to the surface,  $d_{\perp}$ , yielded an estimate for the residual elastic strain component,  $\varepsilon_{zz}$ , normal to the surface, when compared to the unstressed lattice constant,  $d_0$ . Application of Bragg's law indicates that this surface normal strain is related to the ratio of the sines of the unstressed and stressed Bragg angles,  $\theta_0$  and  $\theta$ , respectively:

$$\varepsilon_{zz} = \frac{d_{\perp} - d_0}{d_0} = \frac{\sin \theta_0}{\sin \theta} - 1 . \quad (1)$$

As these measurements do not yield values for any of the stress components (without additional restrictions on the stress state), the conventional  $\sin^2\psi$  method [14,15] was used to interrogate specific locations at the damage sites, namely, the crater rim and floor. This method permits measurement of the individual stress components with a precision that is much less sensitive to the exact value of the  $d$ -spacing. In this technique, the diffraction vector is tilted away from the surface normal at various angles  $\psi$ . In many cases, the  $d$ -spacing varies linearly with  $\sin^2\psi$  (hence the name of the technique); in these instances, the slope of this variation can be related to the stress component along the direction of the diffraction vector at  $\psi = 90^\circ$  via the X-ray elastic constants (typically characterized experimentally for a particular Bragg reflection):

$$\frac{d_{\psi} - d_0}{d_0} = \frac{1 + \nu}{E} \sigma_{\psi=90} \sin^2 \psi - \frac{\nu}{E} (\sigma_{rr} + \sigma_{\theta\theta}) . \quad (2)$$

Independent validation of both the out-of-plane strain measurement technique and the  $\sin^2 \psi$  technique was achieved by applying known strain levels to a standard, similar to that used in previous diffraction-based residual stress studies [15]. A strain-gauged Ti-6Al-4V tensile specimen was loaded in an *in situ* tensile load frame to various levels of strain ranging from 0 to 6000  $\mu\epsilon$  corresponding to uniaxial stresses in the range of 0 to 700 MPa. The elastic strains measured by the X-ray method were found to be within 300  $\mu\epsilon$  of the observed strain gauge values.

### 3.5 Numerical methods for estimating residual stress states

The numerical simulation was performed with the finite element method (FEM) using the commercial ABAQUS code [16]. To make connection with experiments, the exact specimen geometries were used. A typical mesh for the three-dimensional indentation model comprised more than 54,000 27-node three-dimensional brick elements (with reduced integration). The rigid contact surface option was used to simulate the rigid indenter, and the option for finite deformation and strain employed. Coulomb friction was invoked in the calculations, with the friction coefficient taken to be 0.1.

The hardening law used for the Ti-6Al-4V alloy was defined taking into account the Bauschinger effect. In continuum mechanics, this effect is conveniently regarded as a nonlinear isotropic/kinematic (mixed) hardening material feature in a constitutive model. With the reduction in flow stress after a reversal in strain direction, additional plastic deformation can occur at relatively low applied cyclic load. Consequently, both

compressive and tensile residual stresses are relaxed. In the present work, the flow rule of the mixed hardening model consisted of two components: a purely kinematic hardening term, which describes the translation of the yield surface in stress space through the backstress tensor,  $\alpha$ , and an isotropic hardening term, which relates the size of the yield surface with the accumulated plastic deformation. Throughout, the kinematic hardening law was taken as [16]:

$$\dot{\alpha}_{ij} = C \frac{\sigma_{ij} - \alpha_{ij}}{\sigma_0} \dot{\bar{\varepsilon}}^p - \gamma \alpha_{ij} \dot{\bar{\varepsilon}}^p \quad (3)$$

where  $\dot{\bar{\varepsilon}}^p = \sqrt{\frac{2}{3} \dot{\varepsilon}_{ij}^p \dot{\varepsilon}_{ij}^p}$  is the equivalent plastic strain rate and  $\sigma_0$  is the equivalent stress defining the yield surface.  $C$  and  $\gamma$  are material parameters; both equal zero for isotropic hardening. The size of the yield surface,  $\sigma_0$ , is a function of  $\bar{\varepsilon}^p$  through isotropic hardening.

Experimentally, the Bauschinger effect was characterized by conducting a symmetric strain-controlled cyclic experiment at a strain range  $\Delta\varepsilon = \pm 3\%$ . The resulting uniaxial stress-strain relationship taken over five load cycles is shown in Fig. 4. A functional fit to these data yielded kinematic hardening parameters of  $C = 1.38 \cdot 10^{11}$  Pa and  $\gamma = 635$ . It is apparent that the Bauschinger effect in this alloy is fairly large, i.e., the reversed yield stress is small (0.2% offset yield of -600 MPa compared to 930 MPa for monotonic loading), such that the non-linearity of the cyclic stress-strain behavior is fairly strong. The stabilized constitutive relationship was thus obtained after just two load cycles and behaved essentially the same as kinematic hardening.

To perform the calculation, after the initial indentation, a number of loading cycles at an applied maximum stress of  $\sigma_{\max} = 325$  MPa (or 500 MPa) at  $R = 0.1$  was applied to the specimen, with the cyclic stress acting in the longitudinal direction. The calibrated Bauschinger effect was incorporated into the three-dimensional finite element program by using the empirical data from Fig. 4. The predictions from numerical simulations are compared below with the corresponding experimental measurements in section 4.3.

## **4. Results and Discussion**

### ***4.1 Initial residual stress state***

The initial residual stress state, prior to fatigue loading, due to the impact or quasi-static indentations has been determined previously by a combination of experimental X-ray diffraction and finite element analysis [5,17]; however, it is worthwhile to emphasize some key features of this residual stress distribution here. An overview of the general shape of the residual stress field, illustrated in Fig. 5, reveals two primary zones of tension in the immediate vicinity of the indent, namely (i) a small but intense region at the surface immediately outside the crater rim, and (ii) a broader region approximately one crater radius away from the impact site where the maximum stresses are well below the surface. The most substantial compressive stresses, which counterbalance the regions of residual tension, are formed in a large zone directly beneath the crater, and show a maximum of approximately  $1\frac{1}{2}$  times the yield stress at roughly one crater radius below



the crater floor. The residual stresses remain compressive at the surface of the crater floor, although they are substantially smaller.

While the absolute magnitudes of the stresses are affected by whether the indentation is achieved quasi-statically or dynamically, the general features of the residual stress field are the same in both cases. In the present study where the quasi-static indentation of a  $K_b$  tensile specimen was examined, the resulting indent had a diameter of 2.05 mm and a depth of 300  $\mu\text{m}$ , i.e., similar to the size of an indent produced dynamically at an impact velocity of 200 m/s. With this configuration, quantitatively the initial residual stress state before fatigue cycling consisted of compressive residual stresses at the crater floor of magnitude  $-0.50\sigma_y$ , tensile hoop stresses at the crater rim of magnitude  $0.45\sigma_y$  and compressive radial stresses at the rim of  $-0.40\sigma_y$ .

#### *4.2 Baseline response of undamaged surface state*

It is known from studies in both high-strength aluminum alloys [18,19] and SAE 1040 steel [20] that fatigue loading by itself can induce surface residual stresses due to inhomogeneous flow of the material. To evaluate the evolution (if any) of such fatigue-induced residual stresses, a nominally stress-free surface was cycled under identical conditions as used for the mechanically damaged samples in this study, i.e., at  $\sigma_{\text{max}} = 325$  or 500 MPa ( $\sim 0.3$  or  $0.5 \sigma_y$ ) at  $R = 0.1$ . However, over the range of cycles of interest, i.e., over the first 1000 cycles, no alteration in the surface residual stress state induced by the

applied load levels could be detected. Consequently, this effect was not considered further in this study.

#### *4.3 Evolution of residual stress state during fatigue loading*

For the quasi-static indents, of a size matched to that of a 200 m/s impact, the numerically predicted and experimentally measured change in residual stress levels due to fatigue loading at applied maximum stresses of  $\sigma_{\max} = 325$  MPa ( $\sim 0.3\sigma_y$ ) and 500 MPa ( $\sim 0.5\sigma_y$ ) is shown in Fig. 6. It is apparent that due to the additional plastic deformation induced by the applied cyclic loads:

- the residual stresses, both at the crater floor and crater rim, were reduced, i.e., the rim stresses became less tensile and the crater floor stresses less compressive,
- the effect was most significant for the higher applied stress level ( $\sigma_{\max} = 500$  MPa),
- the longitudinal residual stresses (along the direction of loading) were subject to the most relaxation,
- the vast majority of the effect occurred in the first cycle, with little evidence of a continuous decay over subsequent cycles.

Indeed, by cycling at a  $\sigma_{\max}$  of 500 MPa, the longitudinal residual stresses were reduced by as much as 50% within the first cycle; the transverse stresses were also reduced, but only by  $\sim 20\%$ . With further cycling out to 1000 cycles, there was little, if any, additional change in the residual stress state at the floor or the rim of the damage sites. Here, an improved stress resolution may have revealed a very slight decay, although the current

observations show almost no change in residual stress levels over three decades in life. Moreover, the numerical and experimental results in Fig. 6 give an identical result in this regard.

It should be noted that the maximum applied stress is small compared to the yield stress ( $\sigma_{\max}/\sigma_y < 0.6$ ) and the stress-concentration factors associated with the indent are typically in the range 1.15 to 1.5. Consequently, in the absence of the Bauschinger effect, the plastic deformation and ensuing relaxation of the residual compressive stress would not have occurred. We therefore conclude that the Bauschinger effect and nonlinear cyclic stress-strain behavior of Ti-6Al-4V represent the primary reason behind the fatigue-induced relaxation of the residual stresses in the vicinity of the damage sites. The Bauschinger effect is especially significant in this particular alloy, where the reverse yield stress is quite small compared to the forward yield stress. Specifically, the reverse yield stress is  $\sim 600$  MPa estimated using the 0.2% offset method and first deviation from linearity occurs almost immediately upon compression at values  $\sim 20$  MPa compared to the forward yield stress of  $\sim 930$  MPa. The first-cycle relaxation occurs when the superposition of applied and residual stresses exceed the appropriate yield condition, leading to some plastic accommodation of pre-existing elastic strains associated with the initial residual stress state. The impact-induced residual stresses can be thought of simply as an elastic clamp bearing down on a plastically oversized region, i.e., a plastic clamp contained in an elastic region, with the relaxation attributed to plastic accommodation of initial incompatibility between the elastic and plastic regions.

These observations are consistent with the existing literature on mechanical relaxation [8,9,11]. Specifically, at sufficiently low applied stresses, relaxation is either minimal or completely absent, as shown by behavior at  $\sigma_{\max} = 325$  MPa ( $\sim 0.3\sigma_y$ ). In contrast, at intermediate applied stresses, relaxation is almost entirely associated with the first cycle of loading, again as shown by the present study at 500 MPa ( $\sim 0.5\sigma_y$ ). Although not captured in finite element model which does not take into account the localized reordering of the dislocation substructure, the observed relaxation of stresses did not progress, with logarithmic decay, much beyond this first cycle; such behavior is generally associated with much higher applied cyclic stresses closer to the yield stress, and with the development of significant cyclic softening with continued cycling [8,9]. This apparent lack of any decay in residual stress after the first cycle may have been due to the fact that residual stresses were only characterized in the present during the first  $\sim 1\%$  of the total fatigue life.

#### *4.4 Spatial maps of evolving surface-normal strain and peak widths*

To further probe the spatial redistribution of the stress state caused by relaxation, a specimen of the same nominal starting conditions (a quasi-static indent with dimensions identical to those caused by a 200 m/s impact) was loaded using the *in situ* loading rig. The surface-normal strain distribution was mapped in a quadrant around the indent at several load levels during the first cycle and subsequent cycles up to 5000 cycles, as shown in Fig. 7. From this figure, it is apparent that at a low initial applied stress ( $\sigma_{\text{applied}}$ ) of 200 MPa ( $\sim 0.2\sigma_y$ ), the residual strain distribution has merely been amplified by the

applied stresses. However, at higher loads, there appears to be a distortion in the residual stress state most notably in the reduction in elastic strain at the center of the crater. When the applied stress reaches 500 MPa ( $\sim 0.5\sigma_y$ ), the crater floor undergoes local yielding due to the superposition of the residual stresses and the applied stress multiplied by the stress-concentration factor in this location ( $\sim 1.5$ ). A von Mises estimate for the required applied stress to exceed local yielding at the surface is indeed in the vicinity of 500 MPa. At the lower applied stress of 200 MPa, stress relaxation did not occur as the local stresses were not sufficient to cause yielding in this location.

During unloading of the first cycle there is a further slight decay or redistribution in the strain map, albeit much less pronounced than during the loading portion of the cycle. The strain maps at 1 and 10 cycles look very similar, supporting the notion that the redistribution occurs almost entirely in the first cycle. However, there does appear to be some small degree of further redistribution between 10 and 5000 cycles.

Also of interest are the spatial maps of the Bragg peak widths (FWHM) that give an indication of the degree of plasticity; these are plotted along side the strain maps in Fig. 7. During loading in the first cycle, some broadening of the Bragg peak can be seen, which is most pronounced in the center of the crater where the stress-concentration factor is the highest. Nevertheless, by the end of 10 cycles, the peak widths return to their initial values (or even slightly below), and are essentially stabilized with little evidence of further evolution out to 5000 cycles. This indicates that the nature of the plasticity, e.g., dislocation substructure, is not significantly altered by the fatigue cycles under these loading conditions. Therefore, one can conclude that the fatigue initiation and growth

characteristics are only altered by the relaxing residual stresses, and not by a relaxation of the plastic damage due to fatigue loading. Here again, under higher applied stresses (not considered in this study), this relaxation of plastic damage would likely ensue and its evolving role on the fatigue behavior should be considered.

## **5. Implications for foreign object damage**

Recent studies [4-7] on the effects of simulated foreign object damage on the high-cycle fatigue behavior of Ti-6Al-4V have shown that for applied cyclic stresses of  $\sigma_{\max} = 500$  MPa ( $\sim 0.5\sigma_y$ ), fatigue cracking tends to initiate at the damage crater rim for the highest velocity (300 m/s) impacts and at the crater floor for the lower velocity (200 m/s) impacts. Although the stress concentration associated with the crater is smaller at the rim compared to the floor ( $k_{t,\text{floor}} \sim 1.5$ ,  $k_{t,\text{rim}} \sim 1.15$ ), fatigue cracks initiate there after higher impact velocities due to the presence of impact-induced microcracking. At lower velocities (and for quasi-statically loaded indents), such microcracking is absent and the higher stress-concentration factor at the floor of the crater promotes fatigue crack initiation there instead. When considering the presence of the residual stresses, this latter conclusion is at first sight somewhat surprising because of the relatively high compressive residual stresses of -400 MPa ( $-0.4\sigma_y$ ) initially present at the crater floor, compared to the substantial tensile stresses of 500 MPa ( $0.5\sigma_y$ ) at the crater rim. However, the current observations provide a feasible explanation why crack initiation can occur in this location by revealing an immediate relaxation of these compressive residual stresses on fatigue cycling at 500 MPa.

At lower applied stresses ( $\sigma_{\max} = 325$  MPa) where relaxation is far less pronounced, cracks no longer form at the crater floor of lower velocity and quasi-static impact sites, presumably due to the presence of unrelaxed compressive stresses there. In these instances, fatigue cracks tend to initiate at subsurface regions of residual tension at the side of the crater (see Fig. 5) [4]. Numerical calculations, confirmed by X-ray diffraction experiments, suggest that the residual tensile stresses present in this subsurface zone are on the order of 370 MPa ( $\sim 0.4\sigma_y$ ). By considering the sum of the (marginally relaxed) residual stresses and stress-concentration corrected applied stresses along the direction of loading, the resultant stresses in this region are comparable with those at the crater rim; however, as the rim tensile zone is considerably smaller and surrounded by a zone of compression, this may promote crack formation in the much broader subsurface zone of tensile residual stresses at the side of the indent.

It should be noted here that the presence of such unrelaxed residual stresses does not necessarily change the *primary* driving force for fatigue crack initiation or growth, i.e., the *amplitude* of the local stress and strain; however, it does change the local mean stress and strain, and hence the local load ratio  $R$ , which can still have a significant effect on the limiting conditions for crack initiation and growth.

From a perspective of how this information can be used to develop design rules for the onset of FOD-induced high-cycle fatigue failures in blade alloys such as Ti-6Al-4V, our previous work [4] has demonstrated the utility of the Kitigawa-Takahashi approach [21] in evaluating the limiting conditions for such failures. Where applied stresses are high and comparable to the magnitude of the residual stress, such that significant stress

relaxation occurs and fatigue cracks are initiated directly at the impact site, the limiting threshold conditions for HCF failures can be defined in terms of the stress-concentration corrected (smooth-bar) fatigue limit at microstructurally-small crack sizes and a “worst-case” (large-crack) fatigue-crack growth threshold at crack sizes larger than the scale of microstructure. For smaller applied stresses where significant stress relaxation does not occur and fatigue cracks are initiated away from the impact site, an additional correction must be made to the local load ratio to allow for the presence of the stable residual stresses. Using this approach, described in more detail in ref. [4], “threshold” stresses for the likelihood of high-cycle fatigue failure can be defined in the aftermath of foreign-object damage.

## **6. Conclusions**

Based on a numerical (finite element analysis) and experimental (synchrotron X-ray diffraction) evaluation of the fatigue loading-induced relaxation of localized residual stresses formed around a site of simulated foreign-object damage in a forged Ti-6Al-4V alloy, the following conclusions can be drawn:

1. The initial residual stress state associated with foreign-object damage can decay during subsequent mechanical loading, e.g., by fatigue, and therefore may only have a limited bearing on the driving forces for crack initiation and growth. The degree and rate of this relaxation of residual stresses is dependent on the magnitude of the applied stresses (in relation to the yield stress) during the fatigue cycling.



2. At a low applied maximum stress of 325 MPa (equivalent to 35% of the yield strength  $\sigma_y$ ), where the *local* stresses at the impact crater floor and rim were computed to be  $0.50\sigma_y$  and  $0.42\sigma_y$ , respectively, only a slight mechanical relaxation in the damage-related residual stresses was observed.
3. At a higher applied stress of 500 MPa ( $0.54\sigma_y$ ), the smooth-bar fatigue limit, where the *local* stresses at the floor and rim were, respectively,  $0.78\sigma_y$  and  $0.64\sigma_y$ , significant relaxation was seen, with the longitudinal residual stresses, i.e., along the loading direction, decaying by as much as 50% from their initial values. This decay was observed only during the first cycle; subsequent cycles showed little, if any, further relaxation. The lack of a logarithmic decay in residual stresses with number of cycles, as has been reported for shot-peened steels, was reasoned to be associated with the lower applied stresses (compared to the yield stress) utilized in the current study.
4. Numerical modeling which incorporated the experimentally-determined cyclic yield surface, i.e., Bauschinger reversed yield stress, was found to predict this first-cycle relaxation phenomenon with reasonable accuracy, and to yield residual stress values close to those measured using synchrotron X-ray diffraction. This lends credence to the notion that the mechanism for this relaxation is associated with localized yielding in the vicinity of the damage site, based on the monotonic or (where appropriate) reversed yield strength.
5. Spatial surface-normal strain maps, derived from *in situ* synchrotron X-ray diffraction measurements during loading, were consistent with a mechanism of first-cycle

relaxation involving local plastic yielding caused by the superposition of the applied and residual stresses.

6. The relaxed residual stress state, combined with the product of the applied stress and appropriate stress-concentration factor at the damage site, provides a means to estimate the driving force for crack nucleation during subsequent high-cycle fatigue loading. This approach explains in large part the propensity for crack formation at the floor of the impact crater at high applied stresses ( $\sigma_{\max} \sim 0.5\sigma_y$ ) and at subsurface locations at lower applied stresses ( $\sigma_{\max} \sim 0.3\sigma_y$ ).

### **Acknowledgements**

This work was supported by the U.S. Air Force Office of Scientific Research under Grant No. F49620-96-1-0478 under the auspices of the Multidisciplinary University Research Initiative on *High Cycle Fatigue* to the University of California (for numerical modeling and fatigue analysis), the Office of Science, U. S. Department of Energy under contract #DE-AC03-76SF00098 (for experimental diffraction results), and the Stanford Synchrotron Radiation Laboratory, operated by the Department of Energy, Office of Basic Energy Sciences (for X-ray beamtime). BLB would like to thank the Hertz Foundation for their generous support in the form of a Hertz fellowship. Thanks are due to Dr. J. M. McNaney for many helpful discussions.

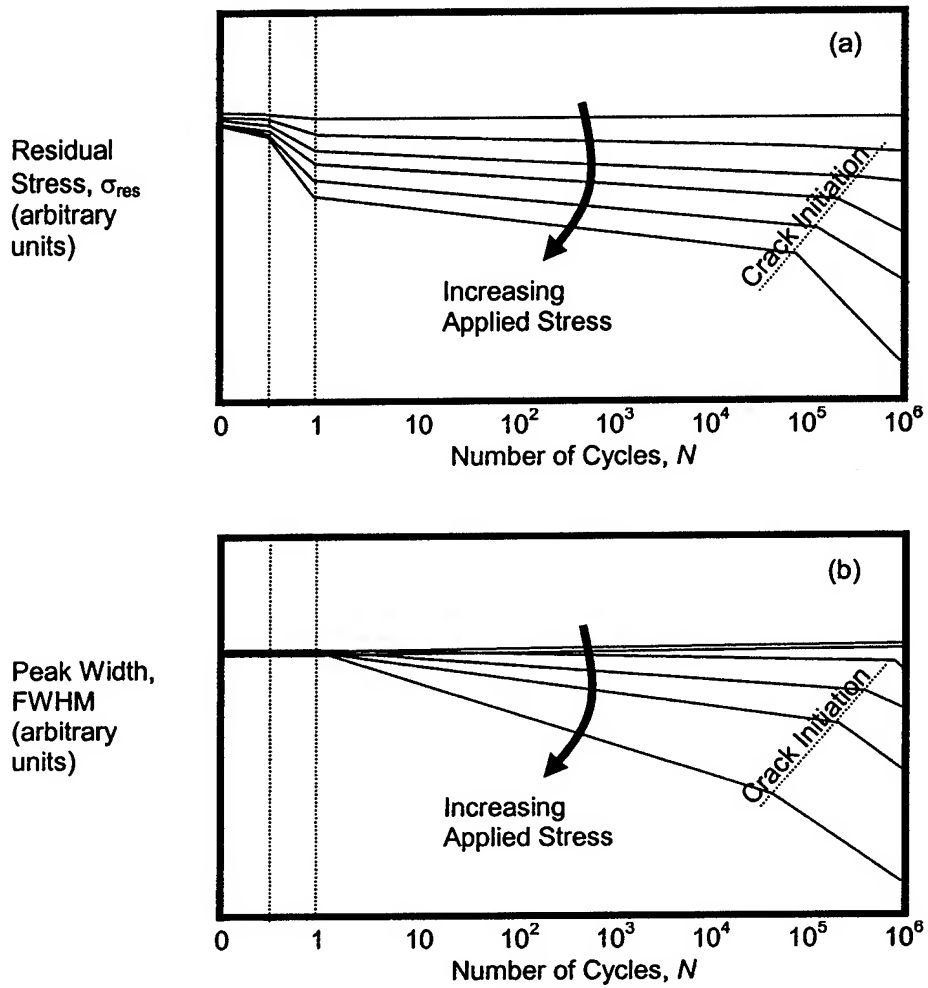
## References

1. T. Nicholas, *Int. J. Fatigue*, 21 (1999), S221.
2. S.J. Hudak, Jr., K.S. Chan, R.C. McClung, G.G. Chell, Y.-D. Lee, and D.L. Davidson, High cycle fatigue of turbine engine materials, Final Technical Report, Southwest Research Institute, August 31, 1999.
3. J. J. Ruschau, T. Nicholas, and S. R. Thompson, *Int. J. Impact Eng.*, 25 (2001) 233.
4. J. O. Peters, B. L. Boyce, X. Chen, J. M. McNaney, J. W. Hutchinson and R. O. Ritchie, *Eng. Fract. Mech.*, (2002) in press.
5. B. L. Boyce, X. Chen, J. W. Hutchinson, and R. O. Ritchie, *Mech. of Mater.*, 33 (2001) 441.
6. J.O. Peters and R.O. Ritchie, *Eng. Fract. Mech.*, 67 (2000) 193.
7. J.O. Peters and R.O. Ritchie, *Int. J. Fatigue*, 23 (2001) S413.
8. H. Holzapfel, V. Schulze, O. Vöhringer, and E. Macherauch, *Mater. Sci. Eng.*, A248 (1998), 9.
9. A. Wick, V. Schulze, and O. Vöhringer, *Mater. Sci. Eng.*, A293, (2000), 191.
10. I. Altenberger, B. Scholtes, in: J. Kenny and A. Brebbia (Eds.), *Surface Treatment IV*, Southampton, UK, 1999.
11. B.R. Sridhar, K. Ramachandra, and K.A. Padmanabhan, *J. Mater. Sci.*, 31 (1996) 4381.
12. L. Wagner and G. Lütjering, in: H. O. Fuchs (Ed.), *Proceedings of the Second International Conference on Shot Peening (ICSP-1)*, American Shot Peening Society, Paramus, New Jersey, 1984, p.306.
13. D. Eylon, Summary of the available information on the processing of the Ti-6Al-4V HCF/LCF program plates, University of Dayton Report, Dayton, OH, 1998.
14. I.C. Noyan and J.B. Cohen, *Residual Stress: Measurement by Diffraction and Interpretation*. Springer-Verlag, New York, 1987.
15. P.S. Prevey, *Advances in X-ray Analysis*, 20 (1977) 345.
16. Hibbit, Karlsson & Sorensen Inc. ABAQUS version 5.7 User's Manual, Hibbit, Karlsson & Sorensen Inc., Pawtucket, RI, 1998.
17. X. Chen and J.W. Hutchinson, *Int. J. Fract.*, 107 (2001) 31.
18. M.R. James and W.L. Morris, *Scripta Metall.*, 17 (1983) 1101.
19. W.L. Morris, R.V. Inman, and M.R. James, *J. Mater. Sci.*, 17 (1982) 1413.
20. M. McClinton and J.B. Cohen, *Mater. Sci. Eng.*, 56 (1982) 259.

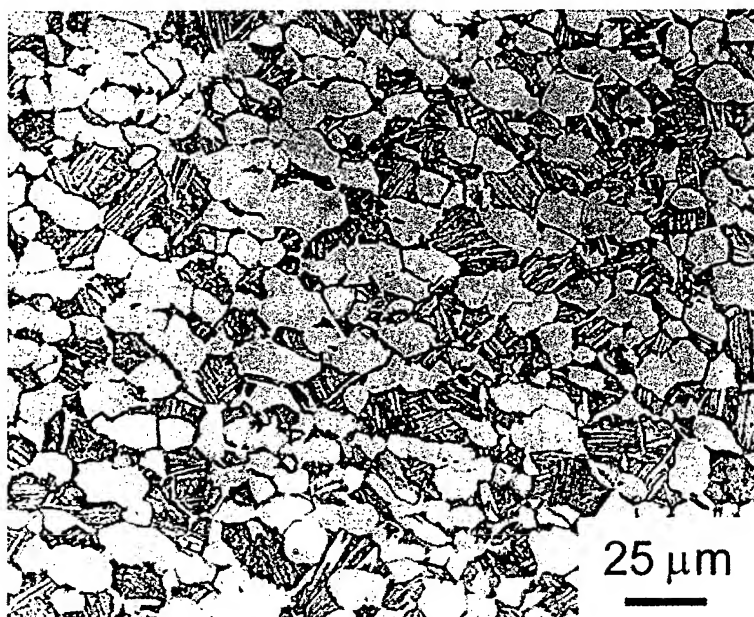
21. H. Kitagawa and S. Takahashi, Applicability of fracture mechanics to very small cracks or cracks in the early stage, in: Proceedings of the Second International Conference on Mechanical Behavior of Materials, ASM, Metals Park, OH, 1976, pp. 627-631.

## List of Figure Captions

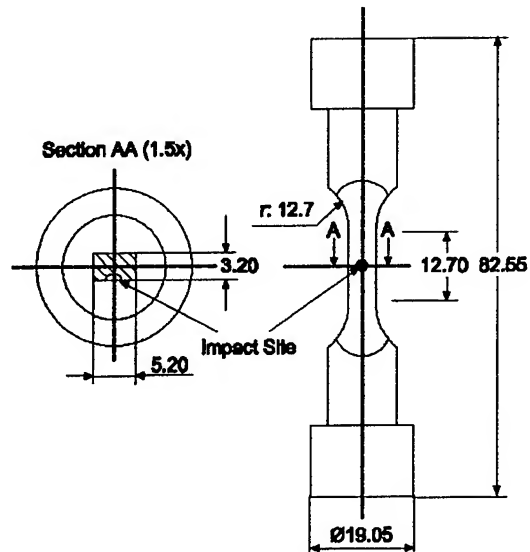
- Figure 1.** Schematic illustrations of the relaxation behavior as a function of applied stress observed in shot peened AISI 4140 steel subjected to fully reversed ( $R = -1$ ) fatigue loading, showing (a) relaxation of residual stresses and (b) relaxation of plastic damage as described by the Bragg peak width [9].
- Figure 2.** Optical micrograph of the two-phase microstructure of the bimodal Ti-6Al-4V forged plate alloy, consisting of the hexagonal closed-packed  $\alpha$ -phase and body-centered cubic  $\beta$ -phase. Kroll's etchant preferably attacks the phase boundaries of globular and lamellar alpha phase giving contrast to optical microscopy. The  $\alpha$ -phase exists in both the globular primary- $\alpha$  phase and in the lamellar colonies of alternating  $\alpha$  and  $\beta$ . (etched in 3.5%  $\text{HNO}_3$ -5% HF).
- Figure 3.** Tensile dogbone specimens in the so-called  $K_b$  geometry typically used to mimic the purely tensile fatigue loading condition of centrifugally-loaded rotating blades. All dimensions are in millimeters.
- Figure 4.** Experimentally measured cyclic uniaxial stress-strain behavior of the Ti-6Al-4V alloy loaded under strain control to a total strain  $\pm 3\%$  for 5 cycles. Strain was measured axially in the gage section using an extensometer.
- Figure 5.** General shape of the residual  $\sigma_{\theta\theta}$  stress field associated with a hemispherical damage site. This hoop stress component is the component that acts in the direction of the subsequent applied fatigue loading (and thus to first approximation would superimpose on the applied fatigue stresses). Both quasi-static and dynamic impacts produces similar stress fields, although the magnitudes of the stresses are different. Stress field is based on the FEM analysis of Chen and Hutchinson [17] and consistent with spatially-resolved residual stress measurements on the surface [9].
- Figure 6.** Cyclic response of the residual stresses at the floor and rim of the damaged crater, following fatigue loading at two maximum stress levels of 325 and 500 MPa at  $R = 0.1$ . Results are represented both by the FEM predictions (lines) and the spatially-resolved X-ray diffraction measurements (points). It is apparent that the most significant relaxation occurred during the first cycle, and for the highest applied stress level.
- Figure 7.** *In situ* X-ray diffraction measurements showing the surface-normal strain (left column) and Bragg peak width (FWHM) maps (right column) for a quasi-static loaded indent (equivalent in dimension to a 200 m/s impact) during the process of subsequent fatigue cycling out to  $N = 5000$  cycles.



**Figure 1.** Schematic illustrations of the relaxation behavior as a function of applied stress observed in shot peened AISI 4140 steel subjected to fully reversed ( $R = -1$ ) fatigue loading, showing (a) relaxation of residual stresses and (b) relaxation of plastic damage as described by the Bragg peak width [9].

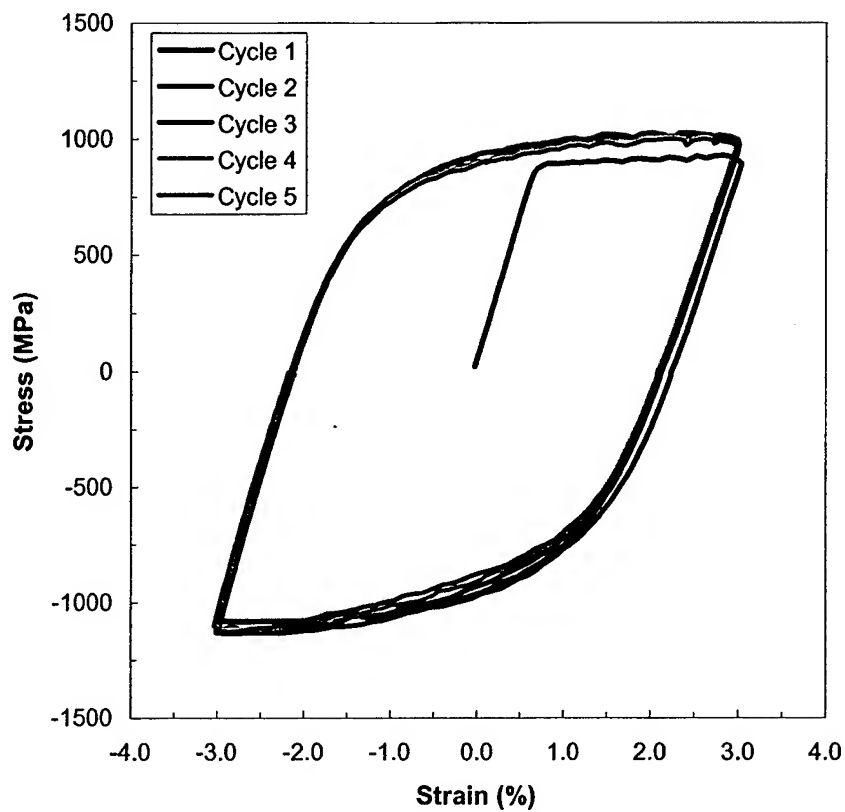


**Figure 2.** Optical micrograph of the two-phase microstructure of the bimodal Ti-6Al-4V forged plate alloy, consisting of the hexagonal closed-packed  $\alpha$ -phase and body-centered cubic  $\beta$ -phase. Kroll's etchant preferably attacks the phase boundaries of globular and lamellar alpha phase giving contrast to optical microscopy. The  $\alpha$ -phase exists in both the globular primary- $\alpha$  phase and in the lamellar colonies of alternating  $\alpha$  and  $\beta$ . (etched in 3.5%  $\text{HNO}_3$ -5% HF).

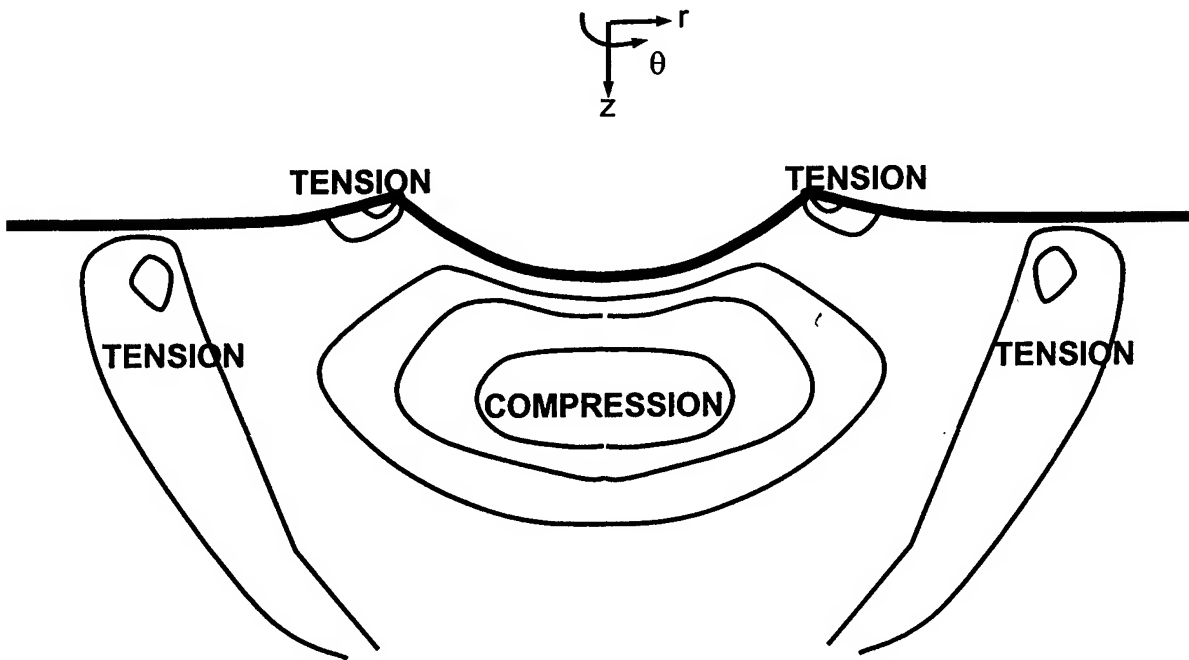


**Figure 3.** Tensile dogbone specimens in the so-called  $K_b$  geometry typically used to mimic the purely tensile fatigue loading condition of centrifugally-loaded rotating blades. All dimensions are in millimeters.

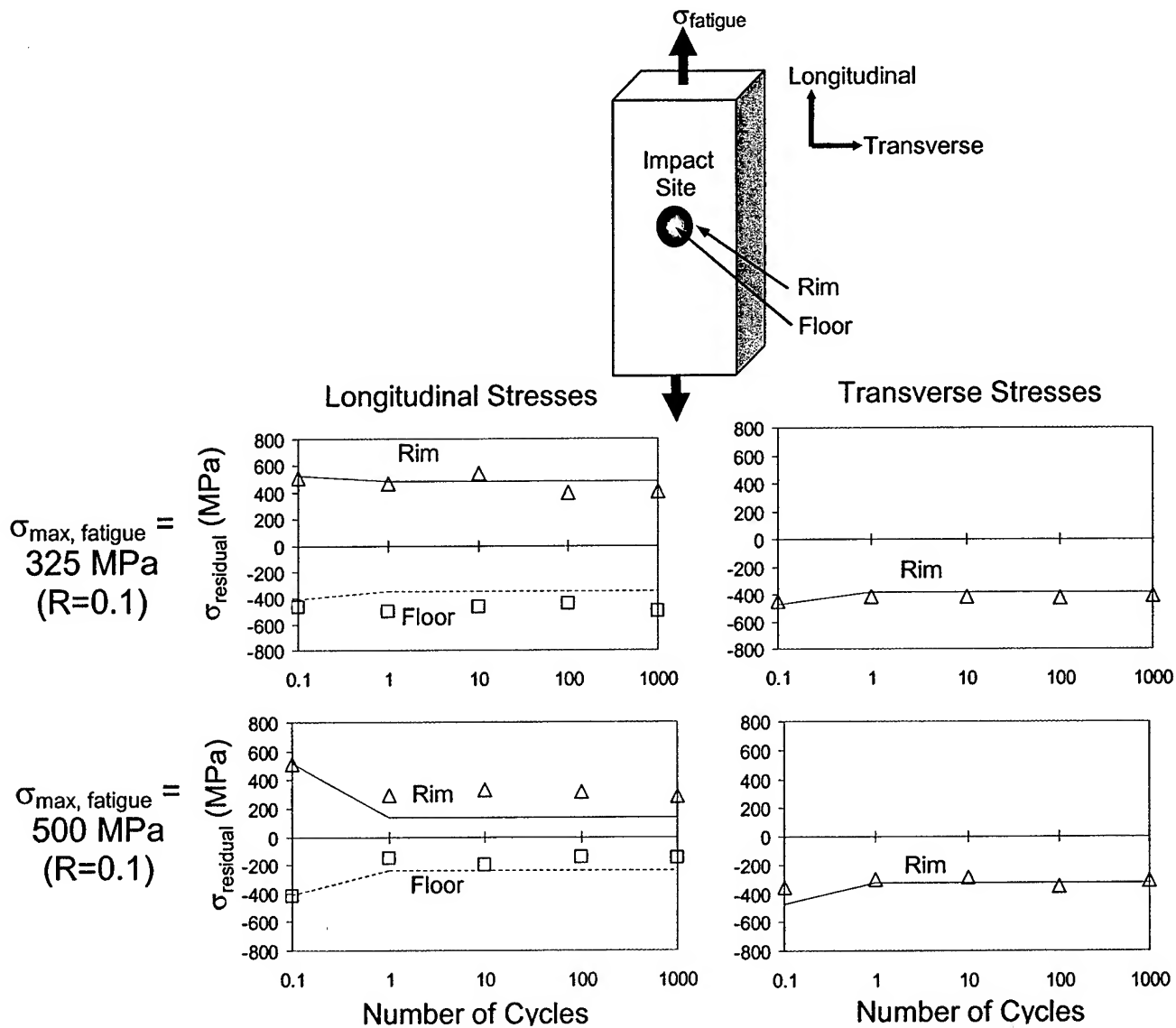




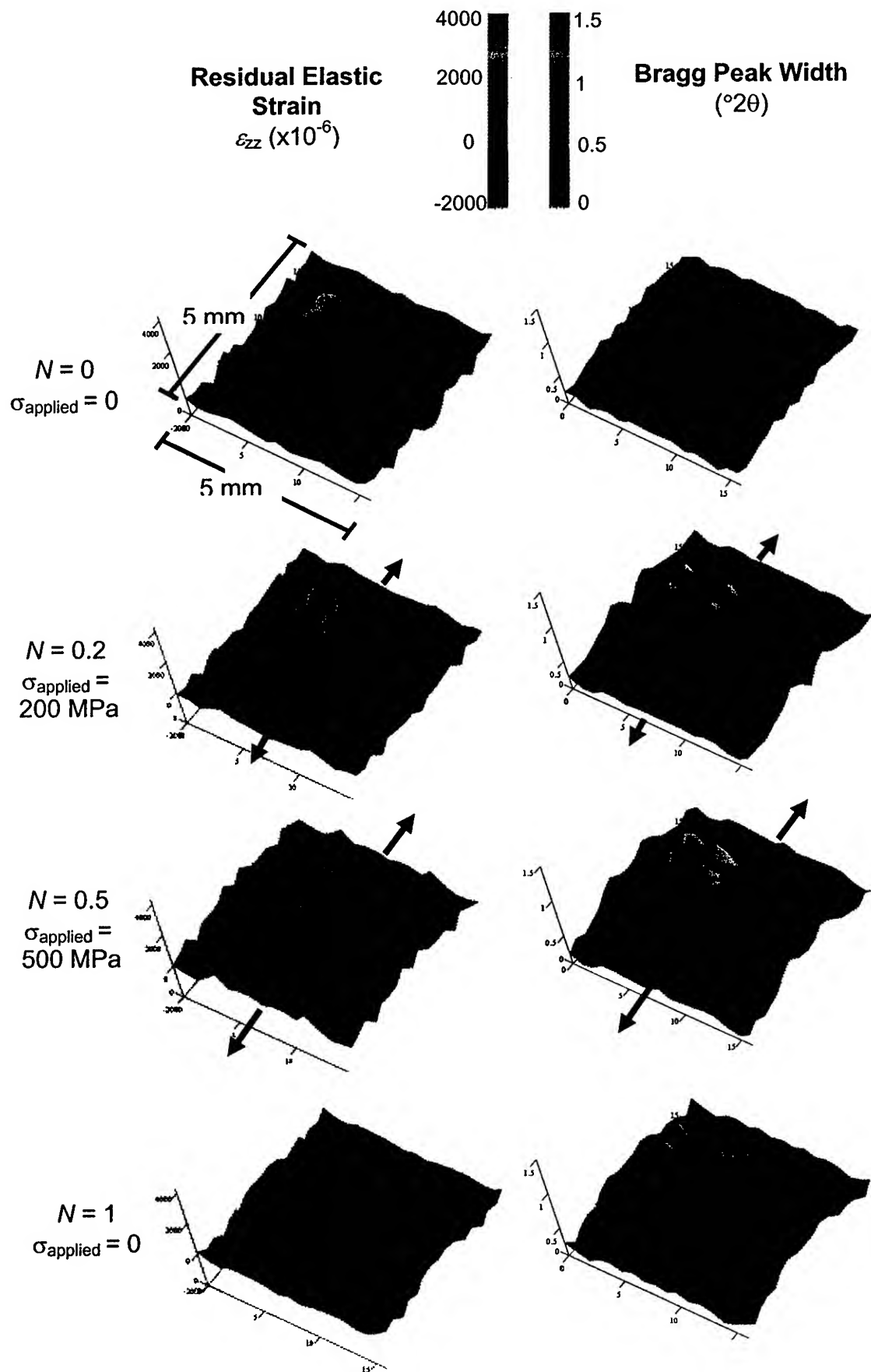
**Figure 4.** Experimentally measured cyclic uniaxial stress-strain behavior of the Ti-6Al-4V alloy loaded under strain control to a total strain  $\pm 3\%$  for 5 cycles. Strain was measured axially in the gage section using an extensometer.



**Figure 5.** General shape of the residual  $\sigma_{\theta\theta}$  stress field associated with a hemispherical damage site. This hoop stress component is the component that acts in the direction of the subsequent applied fatigue loading (and thus to first approximation would superimpose on the applied fatigue stresses). Both quasi-static and dynamic impacts produces similar stress fields, although the magnitudes of the stresses are different. Stress field is based on the FEM analysis of Chen and Hutchinson [17] and consistent with spatially-resolved residual stress measurements on the surface [5].



**Figure 6.** Cyclic response of the residual stresses at the floor and rim of the damaged crater, following fatigue loading at two maximum stress levels of 325 and 500 MPa at  $R = 0.1$ . Results are represented both by the FEM predictions (lines) and the spatially-resolved X-ray diffraction measurements (points). It is apparent that the most significant relaxation occurred during the first cycle, and for the highest applied stress level.



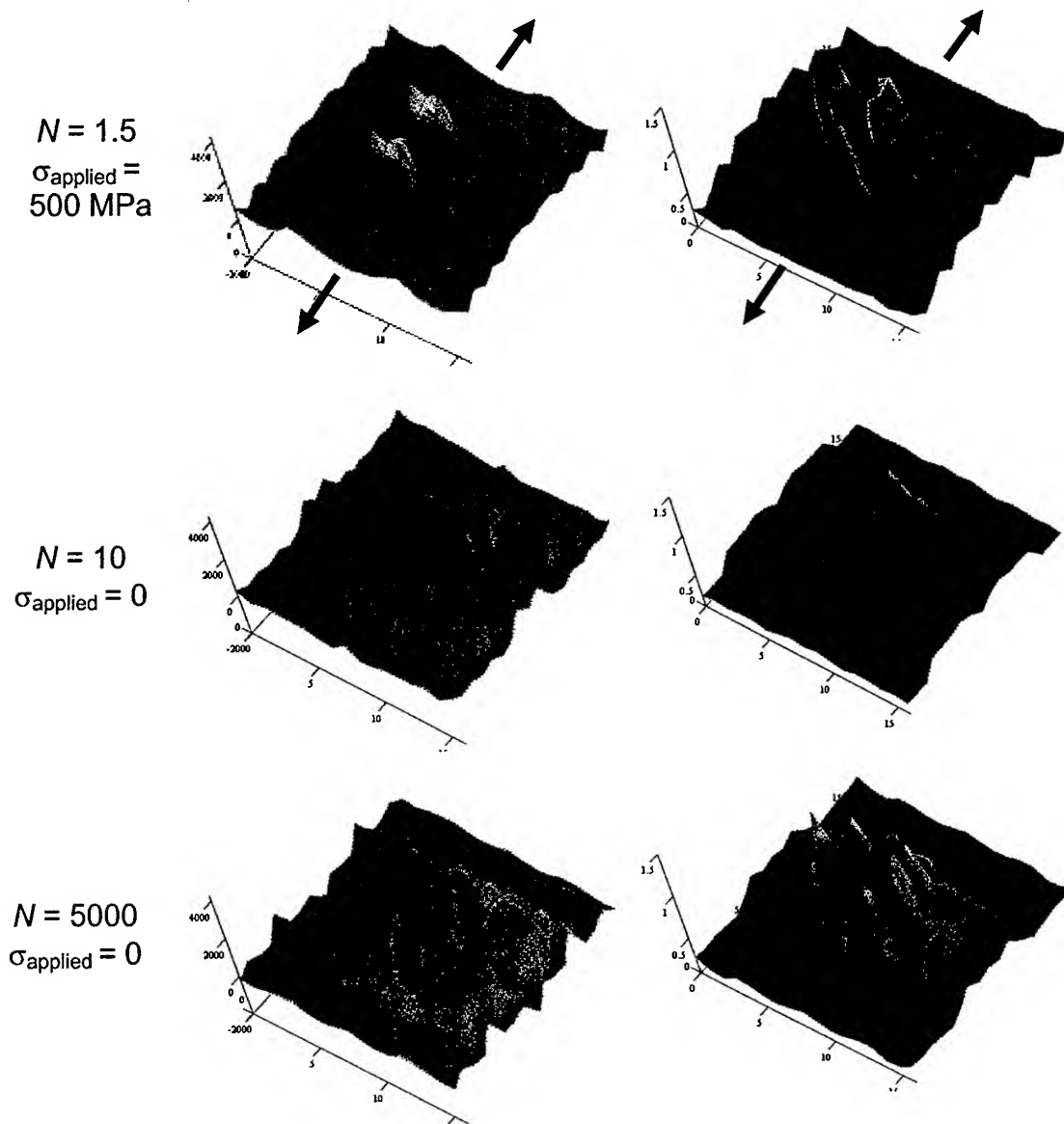


**Figure 7.** *In situ* X-ray diffraction measurements showing the surface-normal strain (left column) and Bragg peak width (FWHM) maps (right column) for a quasi-static loaded indent (equivalent in dimension to a 200 m/s impact) during the process of subsequent fatigue cycling out to  $N = 5000$  cycles.



PERGAMON

Engineering Fracture Mechanics xxx (2002) xxx-xxx

Engineering  
Fracture  
Mechanics

www.elsevier.com/locate/engfractmech

## On the application of the Kitagawa-Takahashi diagram to foreign-object damage and high-cycle fatigue

J.O. Peters <sup>a,1</sup>, B.L. Boyce <sup>a,2</sup>, X. Chen <sup>b</sup>, J.M. McNaney <sup>a</sup>, J.W. Hutchinson <sup>b</sup>,  
R.O. Ritchie <sup>a,\*</sup>

<sup>a</sup> Lawrence Berkely National Laboratory, Department of Materials Science and Engineering, University of California, 463 Evans Hall, Berkeley, CA 94720-1760, USA

<sup>b</sup> Division of Applied Sciences, Harvard University, Cambridge, MA 02138, USA

Received 20 August 2001; received in revised form 22 November 2001; accepted 28 November 2001

### Abstract

The role of foreign-object damage (FOD) and its effect on high-cycle fatigue (HCF) failures in a turbine engine Ti-6Al-4V alloy is examined in the context of the use of the Kitagawa-Takahashi diagram to describe the limiting conditions for such failures. Experimentally, FOD is simulated by firing 1 and 3.2 mm diameter steel spheres onto the flat specimen surface of tensile fatigue specimens at velocities of 200 and 300 m/s. Such damage was found to markedly reduce the fatigue strength of the alloy, primarily due to four factors: stress concentration, microcrack formation, impact-induced plasticity and tensile residual stresses associated with the impact damage. Two groups of fatigue failures could be identified. The first group initiated directly at the impact site, and can be readily described through the use of a fatigue-crack growth threshold concept. Specifically, a Kitagawa-Takahashi approach is presented where the limiting threshold conditions are defined by the stress-concentration corrected smooth-bar fatigue limit (at microstructurally small crack sizes) and a "worst-case" fatigue-crack growth threshold (at larger crack sizes). The second group of failures was caused by fatigue cracks that initiated at locations far from the impact site in regions of high tensile residual stresses, the magnitude of which was computed numerically and measured experimentally using synchrotron X-ray diffraction. Specifically, these failures could be rationalized due to the superposition of the residual stresses on the far-field applied mean stress, leading to a locally elevated load ratio (ratio of minimum to maximum loads). The effects of residual stress, stress concentration, and microstructurally small cracks are combined in a modified Kitagawa-Takahashi approach to provide a mechanistic basis for evaluating the detrimental effect of FOD on HCF failures in Ti-6Al-4V blade alloys. © 2002 Published by Elsevier Science Ltd.

**Keywords:** Ti-6Al-4V; Foreign-object damage; High-cycle fatigue; Residual stress; Fatigue-crack initiation; Fatigue-crack growth threshold

\* Corresponding author. Tel.: +1-510-486-5798; fax: +1-510-486-4881.

E-mail address: roritchie@lbl.gov (R.O. Ritchie).

<sup>1</sup> Now with Department of Physical Metallurgy and Materials Technology, Technical University Hamburg-Harburg, 21071 Hamburg, Germany.

<sup>2</sup> Now with Sandia National Laboratories, P.O. Box 5800, MS 0899, Albuquerque, NM 87185-0899, USA.

## 1. Introduction

High-cycle fatigue (HCF) of turbine engine disk and blade components represents one of the major concerns limiting the readiness and safety of military aircraft. Since *in-flight* HCF conditions invariably involve high cyclic frequencies, small crack sizes and (in some airfoil locations) very high mean stress levels, a preferred fracture-mechanics based approach for design against HCF can be based on the concept of a limiting threshold for no fatigue-crack growth [1–7]. Foreign-object damage (FOD) by hard particles, such as stones ingested into the compressor, has been identified as one of the key factors associated with such HCF related failures in titanium alloy blades [1–4]. Specifically, FOD has been found to reduce the fatigue strength of fan and compressor blades, principally by causing stress-raising notches [5,6] and microcracks [6] at impact sites; this, in association with the plastic deformation [4] and tensile residual stresses [4] resulting from such impacts, can lead to the early nucleation and growth of fatigue cracks.

Recent studies [8–10] on the HCF properties of an  $\alpha + \beta$  processed Ti–6Al–4V blade alloy, where FOD was simulated using high-velocity impacts of steel shot on a flat surface, have focused primarily on the definition of threshold conditions for crack initiation and growth during subsequent fatigue cycling. The mechanistic effect of FOD was considered in terms of (i) the possibility of microcrack formation in the damage zone, (ii) the stress concentration associated with the shape of the impact crater, (iii) microstructural damage from FOD-induced plastic deformation, and (iv) the presence of localized tensile residual hoop stresses in the vicinity of the impact site. Although all of these factors play an important role under certain conditions, in the case of high impact velocities (300 m/s) the formation of damage-induced microcracks appears to be the primary contributor to lifetime reduction. During subsequent cycling after impact, these microcracks, which are formed in the pile-up of material around the rim, can act as preferred sites for propagating fatigue cracks. When applied stresses are large compared to the impact-induced tensile residual stresses, and in the presence of relatively large ( $\sim 30$ – $50\ \mu\text{m}$ ) impact-induced microcracks, HCF failures (within  $10^5$ – $10^6$  cycles) initiate directly at the impact site and lead to short fatigue lives. In contrast, at low-applied stresses relative to the residual stresses, HCF failures (after  $10^7$ – $10^8$  cycles) initiate in locations away from the impact site at regions of peak tensile residual stress, and the necessity for crack nucleation leads to longer fatigue lives.

In analyzing the high stress failures, it was found that FOD-initiated microcracks, together with the stress concentration of the indent, were the prime reasons that the HCF failures initiated at the FOD sites. The microcracks (some as small as  $1\ \mu\text{m}$ ) grew at applied stress intensities as low as  $\Delta K = 1\ \text{MPa}\sqrt{\text{m}}$ , which is well below the “worst-case”  $\Delta K_{\text{TH}}$  threshold in this material [11] of  $1.9\ \text{MPa}\sqrt{\text{m}}$  based on the propagation of large cracks (macroscopic “homogeneous continuum-sized” cracks which are considerably larger than the scale of the microstructure). This worst-case threshold had previously been defined at elevated mean loads (or load ratios, i.e., the ratio of minimum to maximum loads, in excess of  $R = 0.9$ ) in an attempt to eliminate effects of crack closure and to provide a lower-bound threshold for propagation [11]. However, it is clear that this threshold is only relevant to cracks larger than the scale of the microstructure, i.e.,  $\sim 50$ – $100\ \mu\text{m}$  length in the current microstructure. Since the microcracks associated with impact damage are more than an order-of-magnitude smaller than this, an alternative approach was proposed [9,10] to describe the threshold HCF conditions in the presence of FOD. This approach was based on a Kitagawa–Takahashi diagram where the limiting conditions for failure in this case were defined in terms of the stress-concentration corrected smooth-bar fatigue limit (at microstructurally small cracks sizes) and the worst-case threshold (at larger, homogeneous continuum-sized crack sizes).

In contrast to HCF failures under such high-applied stresses, at low-applied stress ranges failures were caused by fatigue cracks that initiated at locations far from the impact site, specifically in regions of high tensile residual stresses. Accordingly, it is the primary purpose of this study to further examine the utility of the Kitagawa–Takahashi approach to provide a general description of HCF failures in impact damaged Ti–6Al–4V. Specifically, we investigate the role of the relative magnitudes of the applied and residual stresses in

dictating the sites for the initiation of HCF failures, in order to provide a methodology to describe the limiting threshold conditions for such failures at both low- and high-applied cyclic stresses. To achieve this objective, the magnitudes of the residual stresses in the vicinity of various damage sites are computed numerically [12] and measured experimentally using spatially resolved synchrotron X-ray diffraction (with spot sizes on the order of  $300 \times 300 \mu\text{m}^2$ ) [13]. Such stresses are thought to alter the local mean stress (or load ratio) for subsequent fatigue cracking. The role of load ratio on fatigue life is evaluated by determining smooth-bar stress-life ( $S-N$ ) curves over a wide range of load ratios from  $R = -1$  to 0.8. Using such results, a modified Kitagawa-Takahashi approach is presented to provide a phenomenological understanding of the effect of FOD on HCF failures in Ti-6Al-4V.

## 2. Experimental procedures

### 2.1. Material

The Ti-6Al-4V alloy under investigation was part of a set of forgings produced specifically for the U.S. Air Force sponsored National High-Cycle Fatigue Program, and is representative of material typically used in the front compressor stages of the turbine engine. The chemical composition is given in Table 1. The bimodal microstructure of the plate material, consisting of  $\sim 60\%$  primary  $\alpha$  (grain size  $\sim 20 \mu\text{m}$ ) within a lamellar  $\alpha + \beta$  matrix, is shown in Fig. 1; this condition has also been termed "solution treated and overaged" (STOA). Material and processing details are given in Refs. [8,14]. Uniaxial tensile properties, based on tests parallel to the length of the plate, are listed in Table 2.

Table 1  
Chemical composition of Ti-6Al-4V bar stock material in wt.% [14]

Ti	Al	V	Fe	O	N	H
Bal.	6.30	4.19	0.19	0.19	0.013	0.0041

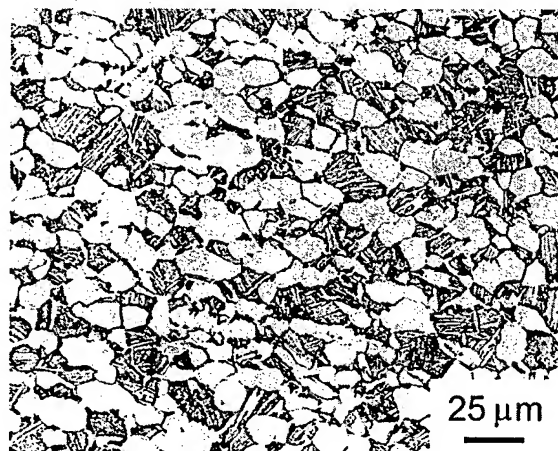


Fig. 1. Optical micrograph of the bimodal (STOA) microstructure of forged Ti-6Al-4V plate material.



Table 2  
Uniaxial tensile properties of bimodal Ti-6Al-4V

$E$ (GPa)	$\sigma_{0.2}$ (MPa)	UTS (MPa)	$\sigma_f$ (MPa)	Elong. (%)	RA (%)
110	915	965	1310	19	45

$E$ : Young's modulus,  $\sigma_{0.2}$ : yield stress, UTS: ultimate tensile strength,  $\sigma_f$ : true fracture stress, Elong.: tensile elongation, RA: reduction of area at fracture; strain rate  $8 \times 10^{-4} \text{ s}^{-1}$ .

## 95 2.2. Simulation of foreign-object damage

96 FOD was simulated by firing 1 or 3.2 mm diameter chrome-hardened steel spheres onto a flat specimen  
97 surface of tensile fatigue (so-called " $K_B$ ") specimens at angles of  $60^\circ$  and  $90^\circ$  (see Fig. 2), and at velocities of  
98 200 and 300 m/s using a compressed-gas gun facility. Such impact velocities represent typical in-service  
99 impact velocities on aircraft engine fan blades, with the 300 m/s velocities representing a worst-case. The  
100 impact damage craters are also of a size typical of those seen in service, with root radii similar to those of  
101 actual damage sites [6].

## 102 2.3. Fatigue test methods

103 To evaluate the smooth-bar fatigue limit of the bimodal Ti-6Al-4V alloy, previous  $S-N$  data [15] have  
104 been complemented by 25 Hz tests (for shorter lives  $<10^6$  cycles) and 1000 Hz tests (for longer lives  $>10^6$   
105 cycles) on hourglass specimens with minimum diameters of 3.0 mm (25 Hz) and 5.4 mm (1000 Hz). (No  
106 effect of frequency on near-threshold fatigue-crack propagation is apparent in this alloy between 50 and  
107 20,000 Hz for tests in ambient air environments [11].) Specifically, 1000 Hz tests were conducted on an  
108 automated MTS servo-hydraulic testing machine, with a newly developed system using a voice-coil ser-  
109 vovalve (further details are described in Ref. [16]). To obtain a nominally stress-free surface, specimens were  
110 stress relieved in vacuo for 2 h at  $705^\circ\text{C}$  prior to chemically milling in a solution of 50 ml HF, 500 ml  $\text{HNO}_3$   
111 and 1500 ml  $\text{H}_2\text{O}$ . For all tests, the loading direction of the specimen was parallel to the long axis of the  
112 forged plate.

113  $K_B$  specimens were used to study the effect of FOD on the fatigue strength of Ti-6Al-4V. These samples  
114 have a rectangular cross-section of  $3.2 \times 7.2 \text{ mm}^2$ , a gauge length of 20 mm and cylindrical buttonhead  
115 ends. As with the hourglass samples, they were prepared with a "stress-free" surface (in the gauge length)  
116 using stress relief and chemical-milling procedures. After impacting with the steel spheres to simulate FOD,  
117 the damaged regions were examined for the presence of potential crack initiation sites or microcracks in a

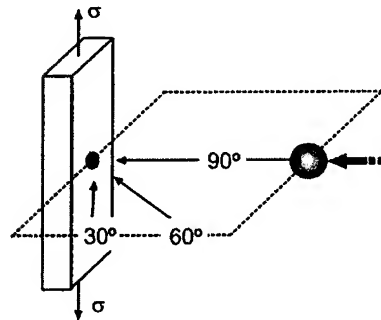


Fig. 2. Schematic illustration showing impact angles with respect to specimen geometry and loading axis for fatigue tests. In this study, normal ( $90^\circ$ ) and inclined ( $60^\circ$ ) impact angles were chosen.

high-resolution LEO 1550 field-emission scanning electron microscope (SEM), prior to cycling at maximum stress values between 225 and 500 MPa at  $R = 0.1$  and  $0.5$  (with a sinusoidal waveform). Throughout fatigue testing, specimens were periodically removed from the test frame and the progress of crack initiation and growth at the surface of the impact site was examined in the SEM. The position of the crack front during crack extension, both on the surface and depthwise, was determined from two sets of measurements. The surface crack length was measured periodically during the fatigue test in the SEM; the crack depth was estimated by subsequent fractography as the local crack front is oriented perpendicular to the "river markings". For the bimodal Ti-6Al-4V alloy, growing fatigue cracks had an approximate crack depth,  $a$ , to surface crack length,  $2c$ , ratio of  $a/2c \sim 0.45$  [8]. After converting the surface crack length into crack depth, the rate of crack extension caused by the fatigue loading was computed using standard finite-difference procedures (with no smoothing routines) and expressed in terms of average crack extension per cycle ( $da/dN$ ).

To define stress-intensity values for the thresholds and early fatigue-crack growth conditions associated with microcracks at the impact site, the relationship of Lukáš [17] for small cracks at notches was utilized, which includes both indentation geometry and stress-concentration effects:

$$\Delta K = \frac{0.7k_t}{\sqrt{1 + 4.5(a/\rho)}} \Delta \sigma \sqrt{\pi a}. \quad (1)$$

In Eq. (1),  $k_t$  is the elastic stress-concentration factor,  $\Delta \sigma$  is the stress range,  $a$  is the crack depth, and  $\rho$  is the indentation radius. The factor of 0.7 is based on the stress-intensity boundary correction and the crack-shape correction factors for semi-elliptical surface cracks ( $a/2c \sim 0.45$ ) [18].

Table 3 lists the impact site dimensions and the resulting elastic stress-concentration factors according to photoelastic experiments [19]. The stress concentration is at a maximum at the base of the impact indentation sites, with values ranging from  $k_t = 1.8$  (for 1 mm shot at 300 m/s) to  $k_t = 1.4$  (for 3.2 mm shot at 200 m/s). Corresponding values at the crater rim range from  $k_t = 1.3$  (1 mm shot, 300 m/s) to  $k_t = 1.15$  (3.2 mm shots, 200 m/s). These  $k_t$ -values for the crater rim are identical to those computed recently by three-dimensional numerical analysis [12]; however, values for the indent base are  $\sim 10\%$  higher. Corresponding elastic stress-concentration factors for inclined impacts are also listed in Table 3.

It should be noted, that there might be some concern over the application of linear-elastic fracture mechanics to such microcracks where crack sizes may be comparable to the scale of the microstructure and crack-tip plasticity. With respect to the scale of microstructure, it is known that misorientations between individual  $\alpha$  grains and the high density of grain boundaries in globular or bimodal titanium alloys sig-

Table 3  
Ti-6Al-4V, summary of impact conditions, fatigue loading and crack initiation sites

Impact condition	Velocity (m/s)	Crater width (mm)	Crater depth (mm)	$k_t$ (base)	$k_t$ (rim)	$\sigma_{max}$ , $R = 0.1$ (MPa)	Crack initiation	Cycles at failure
1 mm, 90°	300	0.93	0.26	1.8	1.30	500	Rim	$3.2 \times 10^5$
1 mm, 90°	300	0.93	0.26	1.8	1.30	325	Interior	$1.3 \times 10^8$
3.2 mm, 90°	300	2.67	0.67	1.6	1.25	500	Rim	$3-6 \times 10^4$
3.2 mm, 90°	300	2.67	0.67	1.6	1.25	325	Rim, interior, side*	$5 \times 10^5-1.7 \times 10^7$
3.2 mm, 90°	200	2.14	0.43	1.4	1.15	500	Base	$8 \times 10^4-1.4 \times 10^5$
3.2 mm, 90°	200	2.14	0.43	1.4	1.15	325	Side*	$1.5 \times 10^7$
3.2 mm, 60°	300	2.58	0.67	1.6	1.25	500	Rim	$5 \times 10^4$
3.2 mm, 60°	300	2.58	0.67	1.6	1.25	325	Rim	$5 \times 10^5$
3.2 mm, 60°	200	1.93	0.34	1.3	1.10	500	Rim	$1.2 \times 10^5$
3.2 mm, 60°	200	1.93	0.34	1.3	1.10	325	Interior	$1.5 \times 10^8$

\* Side face of  $K_B$  sample.

nificantly affect *local* driving forces and hence the crack-growth rates of microstructurally small cracks [15,20,21]. However, in case of FOD impacts, the resulting highly plastically deformed microstructure with its inherently high dislocation density [9] effectively tends to lessen this influence of the local orientation of microstructural features. With respect to the corresponding scale of the plastic zone ahead of the crack tip, in the near-threshold regime of  $\Delta K \sim 1\text{--}2 \text{ MPa } \sqrt{\text{m}}$ , computed maximum plastic zone sizes are only  $\sim 0.2\text{--}1 \text{ } \mu\text{m}$  for  $1\text{--}10 \text{ } \mu\text{m}$  sized cracks, and therefore such conditions are close to those of small-scale yielding. Furthermore, the contribution of the residual stresses is not included in the  $\Delta K$  calculation in Eq. (1), since to the first approximation these stresses will not change the value of the stress-intensity range. They do, however, affect the mean stress and hence alter the local load ratio, as is specifically addressed in this paper.

### 3. Results and discussion

#### 3.1. Smooth-bar fatigue: surface vs. subsurface initiation

To investigate the role of impact-induced tensile residual stresses acting as a mean stress superimposed on the applied fatigue stress range, smooth-bar  $S\text{--}N$  fatigue tests were performed over a wide range of mean stress values, i.e., over a range of load ratios from  $R = -1$  to  $0.8$ . Resulting smooth-bar  $S\text{--}N$  fatigue properties of the bimodal Ti-6Al-4V material are shown in Fig. 3(a) and (b) in terms of the cyclic maxi-

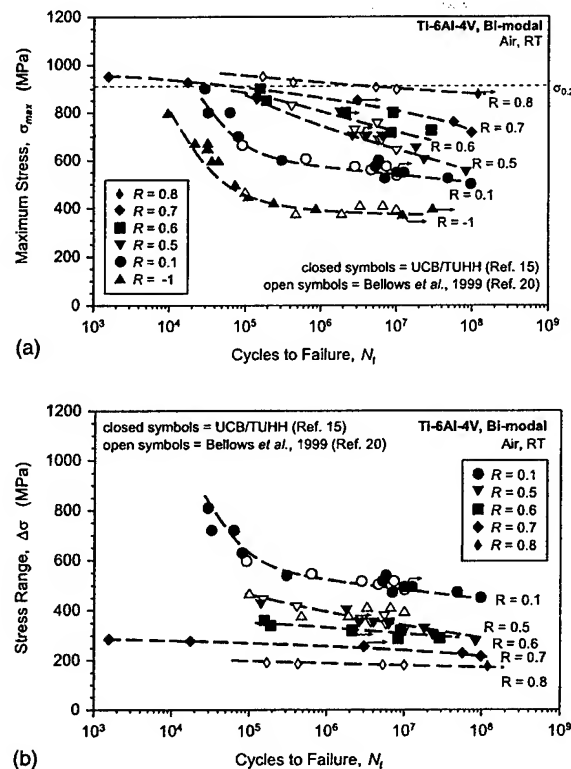


Fig. 3. Stress-life ( $S\text{--}N$ ) curves for bimodal Ti-6Al-4V, determined using smooth-bar specimens at load ratios from  $R = -1$  to  $0.8$  in terms of (a) maximum stress,  $\sigma_{max}$ , and (b) stress range,  $\Delta\sigma$ . Previously published results from Ref. [15] are complemented by 20 and 1000 Hz data. Also shown are  $S\text{--}N$  data (open symbols) of the same material published by Bellows et al. [22].

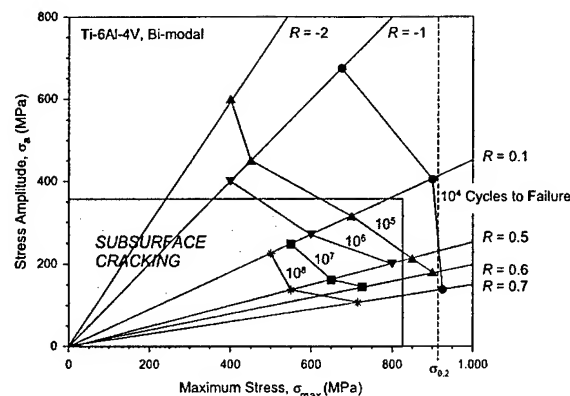


Fig. 4. Subsurface failure envelope for smooth-bar bimodal Ti-6Al-4V specimens, determined at load ratios ranging from  $R = -2$  to  $0.7$ . The failure envelope indicates the occurrence of subsurface crack initiation with both decreasing stress amplitude,  $\sigma_a$ , and maximum stress values,  $\sigma_{max}$ .

163 mum stress and cyclic stress range, together with previously published fatigue results [15,22]. These data  
164 indicate that an increase in mean stress, and hence load ratio, leads to an increase in the limiting value of  
165 maximum applied stress necessary to cause HCF failure (Fig. 3(a)); however, the corresponding limiting  
166 applied stress range  $\Delta\sigma$  is markedly decreased (Fig. 3(b)).

167 Crack initiation sites were examined as a function of the maximum and alternating stresses. Under fully  
168 reversed loading ( $R = -1$ ), fatigue cracks were found to initiate at the specimen surface [15], whereas at  
169 positive load ratios ( $R = 0.1$ – $0.8$ ), initiation was generally subsurface. The occurrence of subsurface crack  
170 initiation in smooth-bar test specimens can be best described in a plot of stress amplitude vs. maximum  
171 stress (Fig. 4). The resulting subsurface failure envelope displayed in Fig. 4 clearly shows that interplay of  
172 both relatively low stress amplitude and maximum stress level results in subsurface cracking in smooth-bar  
173 samples. In addition, it was found that the crack initiation site moved from regions close to the surface  
174 ( $\sim 40$ – $100 \mu\text{m}$ ) to farther into the interior ( $\sim 250$ – $450 \mu\text{m}$ ) with decreasing stress amplitude; this led to a  
175 corresponding increase in fatigue life at a given load ratio. Specifically, at fatigue lives greater than  
176  $\sim 5 \times 10^7$  cycles, cracks initiated in regions  $250$ – $450 \mu\text{m}$  below the surface (cf. Fig. 5(a) and (b) for  $R = 0.1$ ).  
177 An example of such a high- $R$  ( $= 0.7$ ) fatigue-crack initiation farther in the interior is shown in Fig. 6(a). As  
178 reported previously for Ti-6Al-4V [22,23], at even higher maximum applied stresses exceeding the yield  
179 stress, fatigue failures occur entirely by ductile rupture, as shown for high- $R$  loading in Fig. 6(b).

180 Subsurface crack initiation is not common in fatigue, but has become increasingly reported of late for  
181 fatigue failures under very long life conditions, particularly in titanium alloys and steels [24–27]. Most  
182 traditional explanations for this phenomenon rely on the presence of processing-induced surface com-  
183 pressive residual stresses, i.e., due to heat treatment, case-hardening, or shot-peening procedures. Other  
184 explanations include the formation of compressive residual stresses due to preferential plastic deformation  
185 at the surface under tension–tension loading [28], or the larger volume of material contained in the interior  
186 compared to the surface and hence the higher probability of finding a stress-raising defect (e.g., inclusions  
187 in steels) or a weak microstructural orientation (e.g., in titanium alloys). In the present experiments, the as-  
188 tested surfaces were nominally stress free (verified by X-ray diffraction), and therefore it is believed that the  
189 subsurface initiation is the result of the latter effect. Indeed, Evans and Bache [29] have recently pointed out  
190 the significance of such weak microstructural orientations, and the related stress redistribution between  
191 individual grains to the cause of premature crack initiation in titanium alloys.

192 A typical subsurface HCF crack initiation site in the bimodal Ti-6Al-4V alloy is shown in Fig. 7(a).  
193 Higher magnification imaging (Fig. 7(b)) revealed a facet-type fracture surface, involving crack initiation

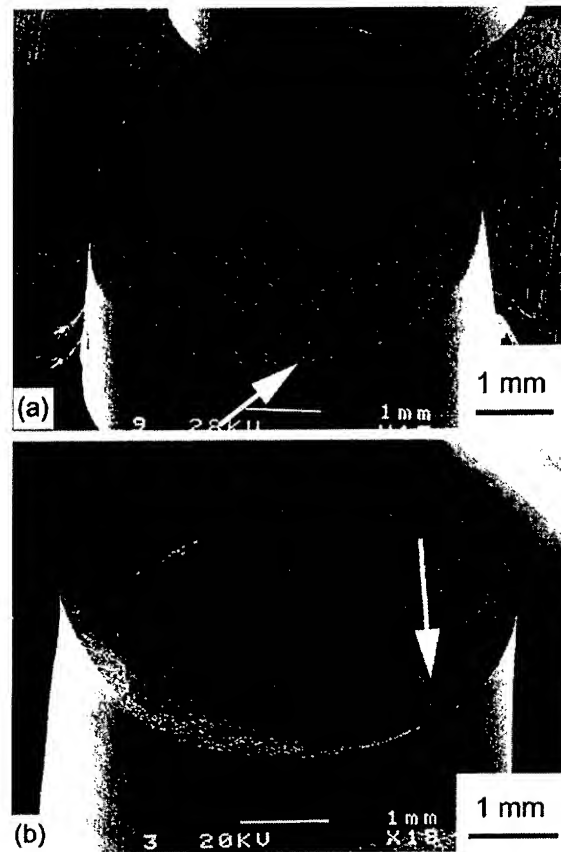


Fig. 5. At low load ratio of  $R = 0.1$ , fatigue cracks initiated (a) close to the surface ( $\sigma_{\max} = 525$  MPa,  $N_f = 4.8 \times 10^7$  cycles), and (b) in the interior away from the surface ( $\sigma_{\max} = 500$  MPa,  $N_f = 9.6 \times 10^7$  cycles).

194 and early growth along planar slip bands. The facets of fractured  $\alpha$  grains, which were aligned perpen-  
195 dicular to stress axis, were of near-basal orientation, based on electron backscattered diffraction (EBSD)  
196 analysis.

### 197 3.2. Impact-induced damage state

198 A wide variety of impact conditions was investigated in this study. The flat surface of the rectangular  
199 gauge section of  $K_B$  specimens was impacted at angles of  $90^\circ$  (normal impact) and  $60^\circ$  (Fig. 2) using impact  
200 velocities of 200–300 m/s. Steel shot of 3.2 mm diameter was used for normal and inclined impacts; ad-  
201 ditionally, 1 mm steel shot was also used for 300 m/s normal impact experiments. All impact conditions and  
202 consequent impact geometries used in this study are listed in Table 3. Examples of damage sites on the flat  
203 surface of  $K_B$  specimens, resulting from 300 m/s normal impacts ( $90^\circ$ ) with 1 and 3.2 mm steel shot, show  
204 similar features. From dimensional analysis, the indentation depth, crater diameter and plastic pile-up scale  
205 with the size of the foreign object, and only depend on the impact velocity. Therefore, the resulting geo-  
206 metric features of the impact craters are virtually the same for 300 m/s normal impacts ( $90^\circ$ ) with either size  
207 of projectile, despite the order-of-magnitude difference in kinetic energy involved [30].

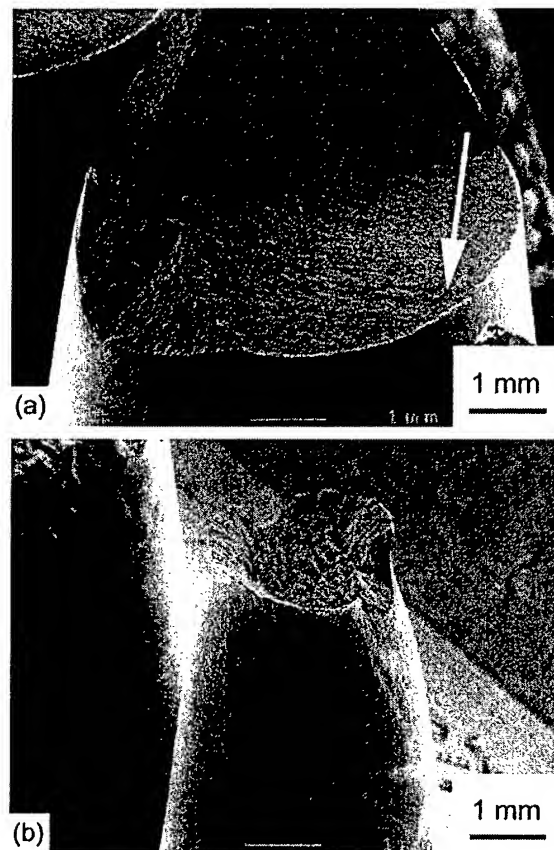


Fig. 6. At a high load ratio of  $R = 0.7$  and (a) maximum stress values below yield stress, the fatigue-crack initiation mechanism is the same as low  $R = 0.1$  failures ( $\sigma_{\max} = 725$  MPa,  $N_f = 9.8 \times 10^7$  cycles); however, (b) maximum applied stress values exceeding the yield stress resulted in gross plasticity and ductile tensile fracture ( $\sigma_{\max} = 925$  MPa,  $N_f = 1.7 \times 10^4$  cycles).

208 Increasing impact velocity has previously been associated with increasingly severe damage states in the  
209 present material [8–10]. For impact velocities in excess of  $\sim 250$  m/s, pile-up of material at the crater rim  
210 (Fig. 8) resulted in the formation of multiple micronotches and microcracks (inset in Fig. 9). Moreover,  
211 rings of circumferentially oriented shear bands were formed within the impact crater, emanating from the  
212 surface into the material beneath the damaged site. For both the 3.2 and 1 mm diameter steel shot, the  
213 microcracks ( $\sim 2$ – $50$   $\mu\text{m}$  in length) formed in 300 m/s impacts provided the nucleation sites for crack growth  
214 on subsequent cycling (Fig. 9). Such microcracking was not apparent at slower 200 m/s impacts. For this  
215 reason, we believe that low-velocity or quasi-static indentations do not provide a worst-case simulation of FOD  
216 conditions [8–10].

217 Scanning electron micrographs and cross-sections of 300 m/s impacts using 3.2 mm steel spheres for  $90^\circ$   
218 and  $60^\circ$  impact angles are shown in Figs. 10 and 11, respectively. Whereas the  $90^\circ$  impact angle resulted in  
219 symmetrical impact site, the  $60^\circ$  impact angle created a significantly larger plastic pile-up at the exit side of  
220 the crater rim as compared to the entry side. However, the depth of the impact site, the maximum size of  
221 pile-up and the associated micronotch/microcrack formation at crater rim were similar for both  $60^\circ$  and  $90^\circ$   
222 impact angles (Table 3).

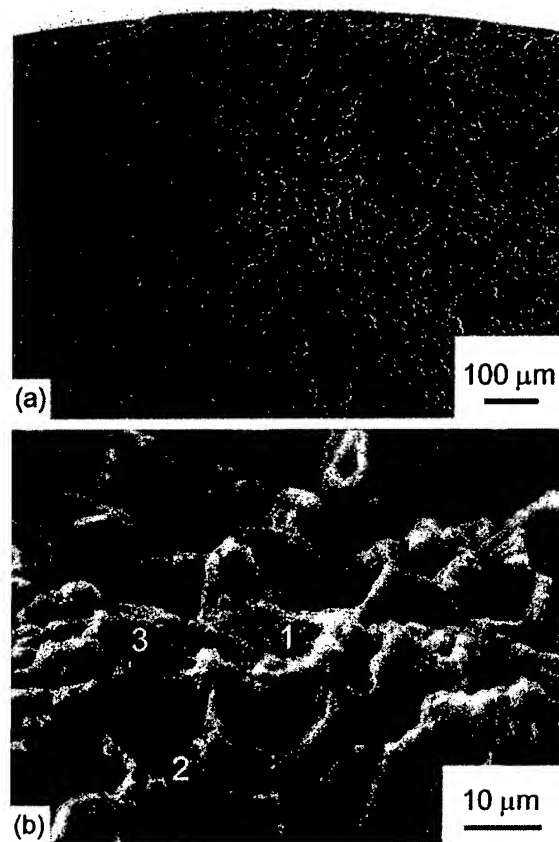


Fig. 7. Fracture surfaces of an  $S-N$  sample tested at a high load ratio of  $R = 0.7$ ,  $\sigma_{\max} = 725$  MPa ( $N_f = 9.8 \times 10^7$  cycles), showing (a) subsurface crack initiation site (350  $\mu\text{m}$  below surface) and (b) crack initiation and early growth along planar slip bands leading to facet-type fracture surface (specimen tilt:  $70^\circ$ ). EBSD analysis of fractured  $\alpha$  grains (numbered 1–3) revealed a near-basal orientation of fracture plane.

In addition to the formation of FOD-induced microcracks, the distribution of tensile residual stresses in the  $K_B$  specimens was also of importance for crack initiation. X-ray diffraction [13] revealed tensile residual stresses on the side surface of the rectangular gauge section. These tensile stresses, which are formed on the side faces of the tensile specimen due to the proximity of the side surface to the impact crater, proved to be important in the case of low stress, high-cycle behavior in the  $10^7$ – $10^8$  cycles regime. Confirmed by numerical analysis [12,13], these tensile stresses counterbalance the compressive residual stress field directly beneath the indentation. The numerically estimated distribution of these FOD-induced stresses in the  $K_B$  specimen are shown in Fig. 12(a) and (b) for 300 m/s normal impacts ( $90^\circ$ ) using 1 and 3.2 mm steel shot, respectively. The residual stress fields are calculated with the finite element method using the ABAQUS/Explicit code, which is based on the explicit time integration method [12]. The dynamic effects, such as inertia, strain rate sensitivity, and stress wave interactions, are included in the simulation. To make connection with experiments, the exact  $K_B$  geometries are used, with a clamped–clamped boundary condition prescribed. The substrate is assumed to be elastic-perfectly plastic with a Von Mises surface to specify yield. The yield stress does not vary with strain, but is a function of the strain rate [30]. The rigid contact surface option is used to simulate the rigid projectile, and the option for finite deformation and strain is employed. Full details are given in Refs. [12,13,30].

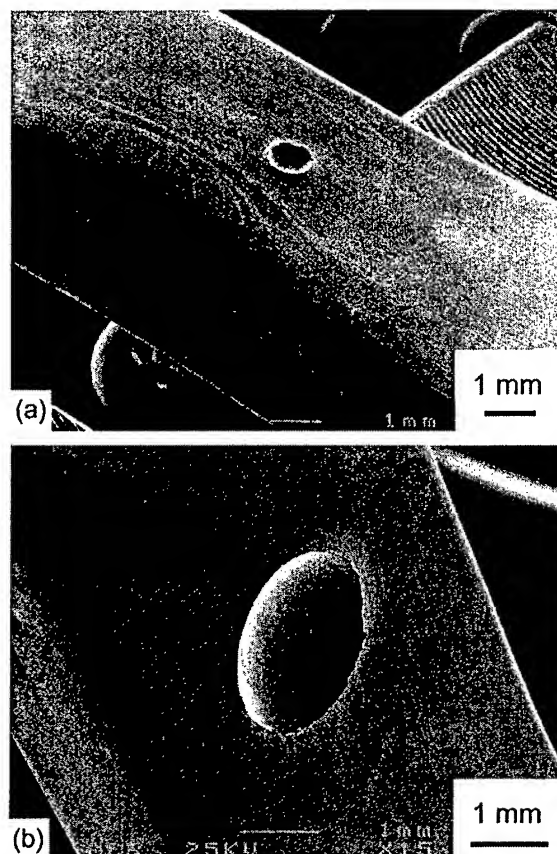


Fig. 8. Gauge section of modified  $K_B$  specimens for simulated FOD studies after high-velocity impacts using (a) 1 mm diameter steel sphere and (b) 3.2 mm diameter steel sphere (normal impact angle).

239 The residual stress distributions for normal impacts display an axis-symmetric stress field with tensile  
 240 residual stresses (in longitudinal direction) as high as  $\sim 220$  MPa ( $\sigma_{33}/\sigma_y = 0.24$ ) to 385 MPa  
 241 ( $\sigma_{33}/\sigma_y = 0.42$ ), where  $\sigma_y$  is the yield stress, and  $\sigma_{33}$  the residual stress in longitudinal direction. The  
 242 magnitude of these tensile stresses was verified by X-ray diffraction. The corresponding residual stress  
 243 distribution for an inclined ( $60^\circ$ ) impact is illustrated in Fig. 12(c) for the case of a 200 m/s, 3.2 mm  
 244 projectile and shows a highly asymmetric stress field, although the peak residual stresses are similar to those  
 245 of normal impacts. In particular, the residual stress field on the exit side of the  $K_B$  specimen is of same  
 246 magnitude as the normal impact at the same impact velocity, whereas residual stress field on the entry side  
 247 corresponds to that of lower speed normal impacts [30]. Furthermore, the residual stresses at the base of the  
 248 indents are also of similar magnitude for both  $90^\circ$  and  $60^\circ$  impacts [30]. Such residual stresses can have a  
 249 significant effect on the initiation sites of fatigue cracks and on the value of the fatigue-crack growth  
 250 thresholds, as discussed below.

### 251 3.3. FOD-affected fatigue properties

252 Stress-life ( $S-N$ ) data in Fig. 13 clearly show the detrimental effect of FOD on fatigue strength. The  
 253 reduced lifetimes following impact damage were seen for both projectile sizes, at both low and moderate



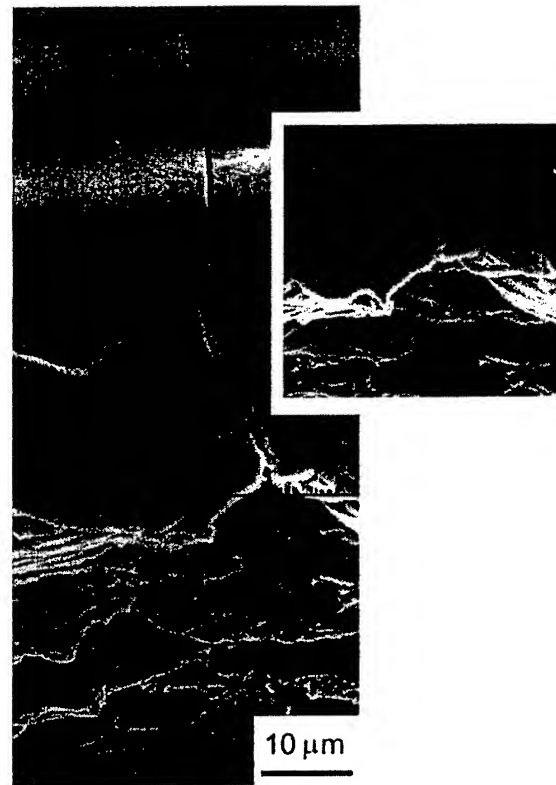


Fig. 9. SEM micrograph of a fatigue crack that formed at a FOD-induced microcrack (small inserts). 3.2 mm steel shot, 300 m/s impact velocity. Nominally applied  $\sigma_{\max} = 500$  MPa,  $R = 0.1$ ,  $N = 29,000$  cycles.

load ratios ( $R = 0.1$  and  $0.5$ ), and both impact angles (although only normal impact data are displayed). As discussed previously [8–10], this detrimental effect of FOD can be considered in terms of premature fatigue-crack initiation resulting from four major factors: (i) the stress concentration of the indent, (ii) FOD-induced microcracking, (iii) plastically deformed microstructure and (iv) residual stresses associated with the impact damage.

Two distinct groups of failures can be identified in Fig. 13, depending upon the magnitude of the applied stresses relative to the tensile residual stresses. At high-applied stresses, HCF failures initiate directly at the impact crater, either at the rim or the base of the crater. Under these conditions, the initiation of a growing fatigue crack is observed at the crater rim at 300 m/s due to the presence of microcracks; conversely, such initiation is observed at the base of the indent at 200 m/s due to the high local stress concentration and the absence of microcracks elsewhere. In contrast, at low-applied stresses (and lower impact velocities), where FOD-induced microcracks were not formed or were much smaller, fatigue cracks were found to initiate away from the indent crater, in regions of substantial tensile residual stresses.

An example of fatigue-crack initiation at low-applied cyclic stresses ( $\sigma_{\max} = 325$  MPa,  $R = 0.1$ ) in regions away from the damage site in the interior of the specimen is shown in Fig. 14(a) and (b) for 300 m/s impacts by 1 and 3.2 mm diameter shot, respectively. A further example (at  $\sigma_{\max} = 300$  MPa,  $R = 0.1$ ), where initiation occurred close to surface at the side face of the specimen, is shown in Fig. 14(c). Similarly, fatigue-crack initiation remote from the damage site was observed to occur in the interior of a 60° inclined impacted specimen, as shown in Fig. 14(d) ( $\sigma_{\max} = 325$  MPa,  $R = 0.1$ ). In all cases, fatigue cracking initiated

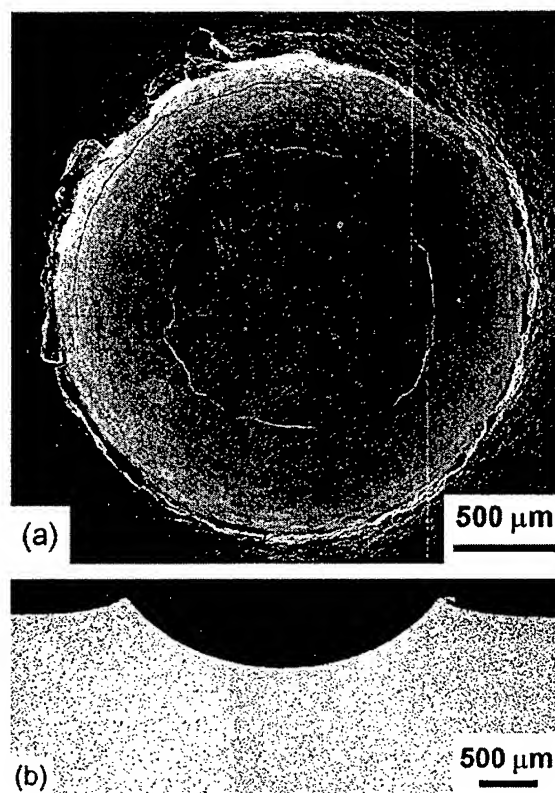


Fig. 10. (a) Scanning electron micrograph and (b) cross-section of impact site after 300 m/s normal (90°) impact using 3.2 mm steel shot.

in regions of the high tensile residual stresses away from the indent; specifically, these residual stresses were on the order of 300 MPa, based on synchrotron X-ray diffraction measurements [13] and numerical computations [12,13] (Fig. 12).

As noted previously, such tensile residual stresses act to elevate the local mean stress (or load ratio), when simply superimposed on the applied far-field fatigue stresses. Based on FOD-related failures at applied cyclic stresses of  $\Delta\sigma = 270\text{--}300$  MPa at  $R = 0.1$  and 250 MPa at  $R = 0.5$ , superimposing a tensile residual stress of  $\sim 300$  MPa increases these  $R$ -ratios from 0.1 to  $\sim 0.5$  and from 0.5 to  $\sim 0.7$ , assuming no relaxation (Table 4). The corresponding increase in the maximum stress by this superposition is marked by arrows in the  $S$ - $N$  diagram shown in Fig. 13. From these  $S$ - $N$  results, it is clear that simple superposition of initial tensile residual stress onto applied far-field stresses provides a significant contribution to the reduction in fatigue life due to FOD.

### 3.4. FOD-affected fatigue thresholds and fatigue-crack propagation

Thresholds for fatigue-crack growth and the subsequent near-threshold fatigue-crack growth rates of all impacted samples are compared to results for naturally initiated small cracks ( $\sim 45\text{--}1000$   $\mu\text{m}$ ) [15] and through-thickness large ( $>5$  mm) [11,31] cracks in undamaged material in Fig. 15(a) (for  $R$ -ratios of 0.1 and 0.5), in Fig. 15(b) (for projectile sizes of 1 and 3.2 mm), and in Fig. 15(c) (for impact angles of 90° and 60°). The FOD-initiated crack-growth rate data are shown as a function of surface crack length,  $2c$ , and the

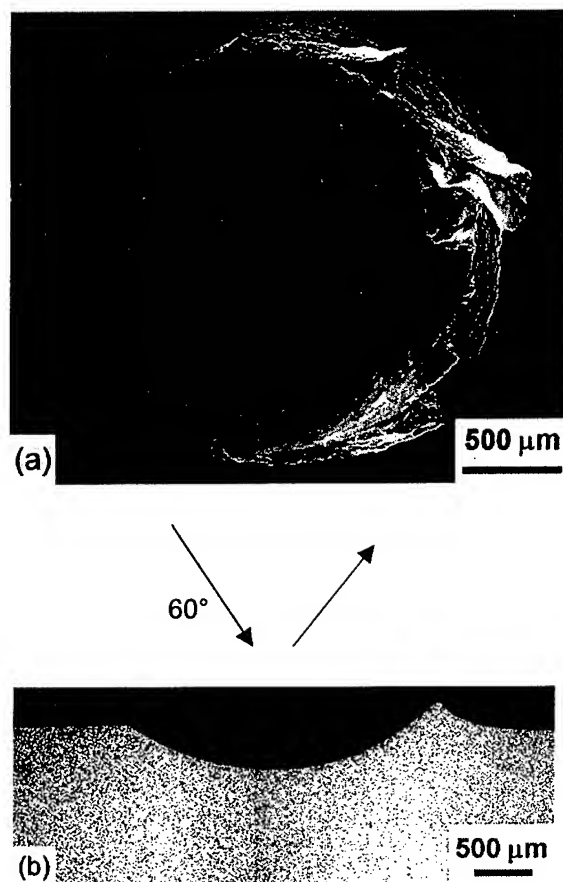


Fig. 11. (a) Scanning electron micrograph and (b) cross-section of impact site after 300 m/s inclined ( $60^\circ$ ) impact using 3.2 mm steel shot.

approximate applied stress-intensity range (corrected for the stress concentration of the indenter using Eq. (1)). Crack-growth rate data of the FOD-induced microcracks ( $2c \sim 5\text{--}100\text{ }\mu\text{m}$ ), which are truly microstructurally small cracks, fall into a single scatter band for all impact conditions under study (Fig. 15(a)–(c)). Specifically, comparable growth-rate data of microcracks at low ( $R = 0.1$ ) and moderate ( $R = 0.5$ ) load ratios indicate that mean stresses play little role in small-crack propagation (Fig. 15(a)). In general, the growth rates of the FOD-initiated small cracks were at least an order-of-magnitude faster than the corresponding large-crack results at near-threshold levels. Such an effect is typical for cracks with dimensions comparable to microstructural size-scales [32–35]. However, the large and small-crack results tend to merge above a  $\Delta K$  of  $\sim 10\text{ MPa}\sqrt{\text{m}}$ , as the small cracks grow to dimensions substantially larger than the microstructure, consistent with the development of crack closure associated with the progressively increasing wake of the small cracks. In addition, at these higher  $\Delta K$  levels, the progressively increasing length of the crack front experiences a statistical sampling of a representative average of all microstructural barriers, similar to the large cracks.

An additional factor associated with the faster growth rates of the FOD-initiated microcracks is the microstructural changes associated with impact-induced plasticity. This is evident from shot-peening experiments on Ti-6Al-4V where, by separating the effect of deformation from residual stresses, it has been

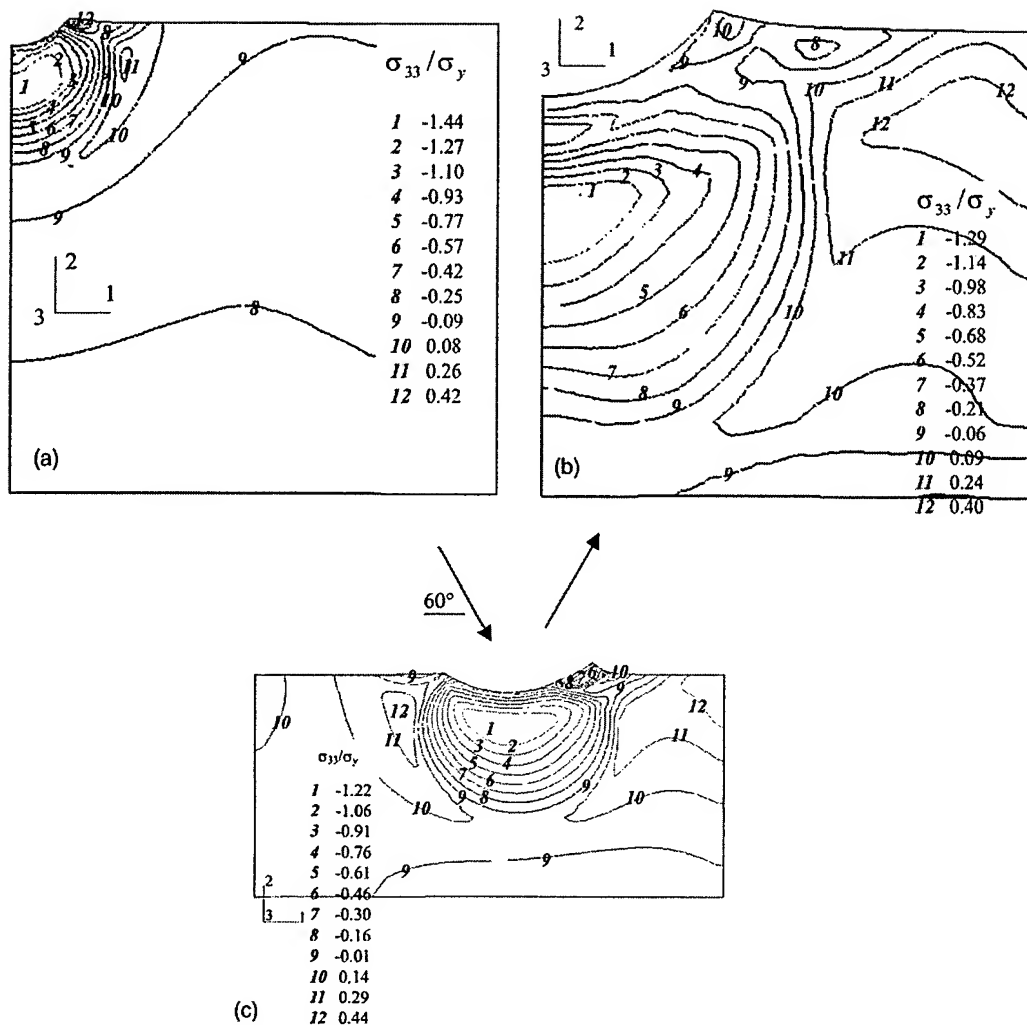


Fig. 12. Residual stress distribution in plane perpendicular to longitudinal axis of  $K_B$  specimen, after 300 m/s normal ( $90^\circ$ ) impact using (a) 1 mm and (b) 3.2 mm diameter steel shot, or (c) 200 m/s inclined ( $60^\circ$ ) impact using 3.2 mm steel shot. After Chen and Hutchinson [12].  $\sigma_{ii}$  = normal residual stress,  $\sigma_y$  = yield stress (915 MPa).

observed that the deformed microstructure, with its inherently high dislocation density, showed a reduced resistance to crack growth [26,27].

As discussed elsewhere [11,31], the large-crack thresholds shown in Fig. 15 were determined up to the highest load ratios ( $R \sim 0.91$ – $0.95$ ) under constant- $K_{\max}$ /increasing- $K_{\min}$  loading conditions chosen to minimize the effect of crack closure. Accordingly, for the bimodal Ti-6Al-4V microstructure, the measured threshold of  $\sim 1.9 \text{ MPa } \sqrt{\text{m}}$  at  $R = 0.95$  is considered to be a worst-case threshold for cracks of dimensions large compared to the scale of the microstructure. However, observations show that the smallest FOD-initiated cracks, which have dimensions comparable with microstructural size-scales ( $\sim 2$ – $10 \text{ } \mu\text{m}$ ), can propagate at stress intensities well below these worst-case thresholds, specifically at applied stress intensities as low as  $\Delta K \sim 1 \text{ MPa } \sqrt{\text{m}}$ , presumably due to biased sampling of the “weak links” in the microstructure. Based on the results shown in Fig. 15, it is clear that a concept of a worst-case threshold (determined under

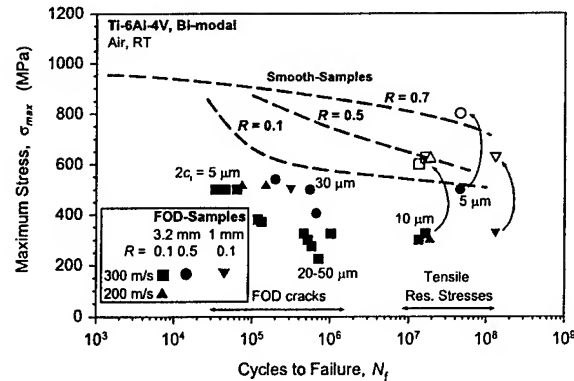


Fig. 13.  $S$ - $N$  data showing reduced fatigue life due to simulated FOD, as compared to smooth-bar specimens in bimodal Ti-6Al-4V.  $2c_i$  is the surface crack length of FOD-induced microcracks. For failures at  $10^7$ - $10^8$  cycles, the effect of local tensile residual stress ( $\sim 300$  MPa) in increasing the local maximum stress (and hence the local load ratio) is illustrated by arrows and open symbols.

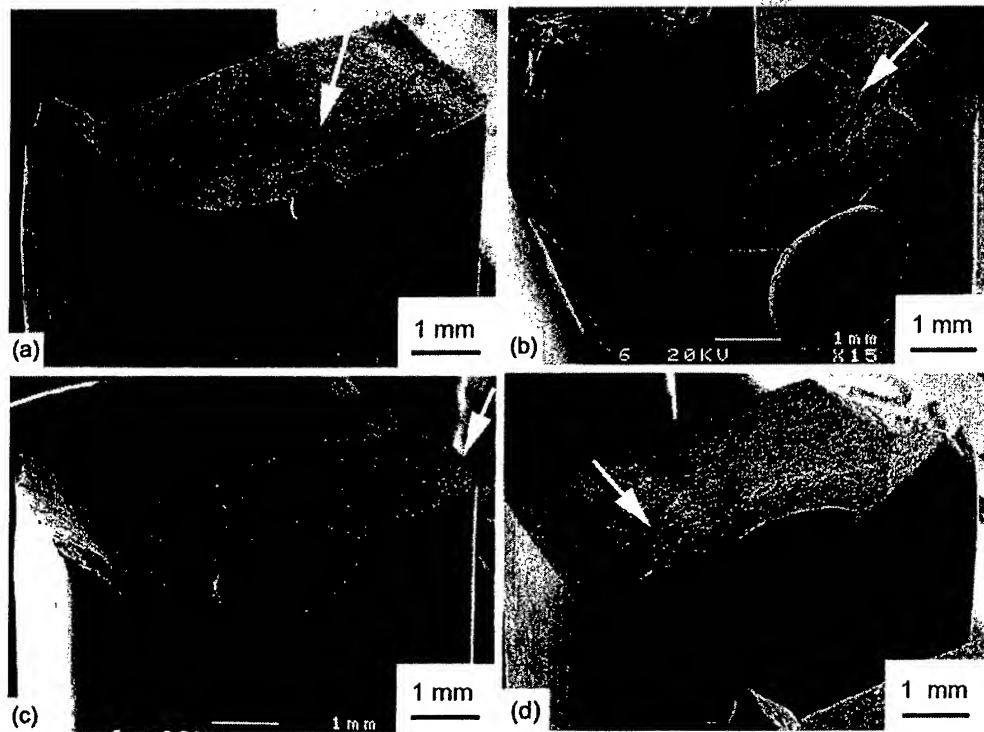


Fig. 14. Lower stress fatigue loading after 300 m/s impact ( $90^\circ$ ) using 1 or 3.2 mm diameter steel shot caused crack initiation away from the indent site (marked by arrows): (a) 1 mm steel shot, nominally applied  $\sigma_{\max} = 325$  MPa,  $R = 0.1$ ,  $N_f = 1.3 \times 10^8$  cycles, (b) 3.2 mm steel shot ( $90^\circ$ ), nominally applied  $\sigma_{\max} = 325$  MPa,  $R = 0.1$ ,  $N_f = 1.6 \times 10^7$  cycles, and (c) nominally applied  $\sigma_{\max} = 300$  MPa,  $R = 0.1$ ,  $N_f = 1.3 \times 10^7$  cycles. (d) 200 m/s inclined impact ( $60^\circ$ ) using 3.2 mm steel shot, nominally applied  $\sigma_{\max} = 325$  MPa,  $R = 0.1$ ,  $N_f = 1.5 \times 10^8$  cycles.

317  $R \rightarrow 1$  conditions that minimize crack closure) applies strictly for homogeneous continuum-sized cracks  
318 larger than microstructural size-scales. This concept does not provide a lower-bound threshold stress in-

Table 4  
Superposition of initial tensile residual stress on nominally applied cyclic stress

Load ratio, $R$ ( $\sigma_{\min}/\sigma_{\max}$ )	$\sigma_{\min}$	$\sigma_{\max}$	$\sigma_{\text{res}}$	$\sigma_{\min,\text{eff}}$ ( $\sigma_{\min} + \sigma_{\text{res}}$ )	$\sigma_{\max,\text{eff}}$ ( $\sigma_{\max} + \sigma_{\text{res}}$ )	Effective load ratio, $R_{\text{eff}}$ ( $\sigma_{\min,\text{eff}}/\sigma_{\max,\text{eff}}$ )
0.1	30	300	300	330	600	0.55
0.1	33	325	300	333	633	0.53
0.5	250	500	300	550	850	0.69

$\sigma_{\min}$ : applied minimum stress,  $\sigma_{\max}$ : applied maximum stress,  $\sigma_{\text{res}}$ : residual stress,  $\sigma_{\min,\text{eff}}$ : effective minimum stress,  $\sigma_{\max,\text{eff}}$ : effective maximum stress. All stresses are in MPa.

tensity for cracks on the scale of microstructural dimensions, as can be the case in the earliest stages of FOD-induced fatigue failure.

The full *quantitative* effect of the FOD-induced residual stresses on fatigue failures at  $10^5$ – $10^6$  cycles where fatigue cracks initiated directly at the impact site is still under study. Although simple superposition of the residual and applied stresses was considered above for low-applied stresses ( $\sigma_{\max} = 325$  MPa,  $R = 0.1$ ), recent numerical modelling and in situ synchrotron X-ray diffraction results have indicated that at high-applied stresses ( $\sigma_{\max} = 500$  MPa,  $R = 0.1$ ) during the first few fatigue cycles, significant relaxation of both the tensile and compressive residual stresses (by typically  $\sim 30\%$ ), can occur [13].

What is interesting here is that due to plastic deformation (aided by the Bauschinger effect) at the FOD indentation site when the high stresses (relative to the level of residual stresses) are applied, the compressive stresses at the base of the crater are partially relaxed, permitting crack initiation to occur there for low impact velocities due to the higher stress concentration [8,9]. The tensile residual stresses at the crater rim are also relaxed, but due to the presence of microcracks following 300 m/s impacts this still is the preferred site for crack initiation at higher impact velocities. Thus, for subsequent fatigue cycling at high-applied stresses, the FOD-induced residual stresses do not play a major role on the initial crack growth of FOD-induced microcracks ( $2c \sim 5$ – $100$   $\mu\text{m}$ ) due to their relaxation on cyclic loading.

There are conditions, however, where relaxation does not occur or substantial residual stresses are stable during cycling. Most specifically, the rate and extent of relaxation is a function of the applied stresses. When the applied stresses are low enough, the residual stresses are stable and relaxation is not observed. Therefore, the regions closest to the indent exhibit the greatest degree of relaxation, due to the stress concentrating effects of the indent on the applied stresses. It is thought that this explains the stability (and hence importance) of the tensile residual stresses far from the indent even under conditions where the residual stresses near the indent show substantial relaxation.

Moreover, the stress field ahead of a propagating crack can potentially serve to further relax the residual stresses. This crack-driven relaxation becomes increasingly important as the crack grows to larger crack sizes under a fixed load amplitude, due to the increase in the  $\Delta K$  field ahead of the tip. This may explain the factor-of-six longer life exhibited by an indent formed by a 1 mm projectile compared to a 3.2 mm projectile (both formed at 300 m/s). In spite of the similar features (pile-up, microcracking, shear bands), and similar aspect ratio of the craters, the absolute proximity of the retarding compressive zone beneath the crater base is different. As illustrated in Fig. 16, the rim-crack formed in the smaller indent is still quite small ( $2c \sim 0.7$  mm) by the time it reaches any mitigating residual compressive stresses beneath the base, whereas the rim-crack formed in the large indent has grown to a substantial size ( $2c \sim 2.5$  mm) by the time it has reached the compressive zone beneath the base. It is thought that the larger crack size results in more substantial relaxation of any mitigating compressive residual stresses, thereby leading to a shorter propagation time. Moreover, larger impact indentation sites also lower the overall fatigue life due to initial crack size effects. Once a growing fatigue crack initiates, the effective initial crack size is larger in the case with larger indentation site, and hence it propagates initially faster.

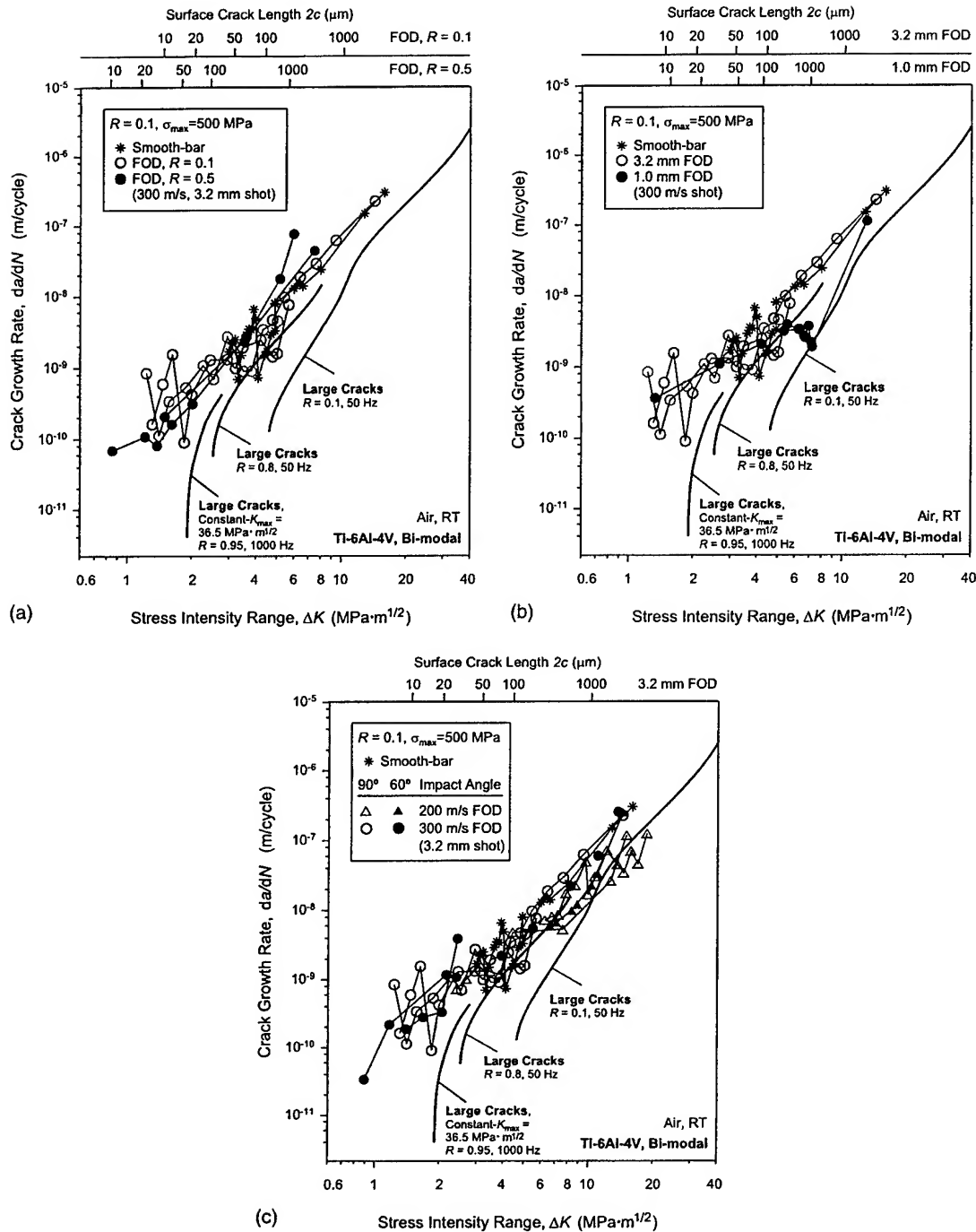


Fig. 15. Fatigue crack-growth rate data of FOD-induced small cracks emanating directly from FOD impacts as a function of (a) load ratio ( $R = 0.1$  and  $0.5$ ), (b) projectile size ( $1$  and  $3.2$  mm), and (c) impact angle ( $60^\circ$  and  $90^\circ$ ). FOD-initiated small-crack growth-rate data are compared to naturally initiated small-crack [15] and through-thickness large-crack results in undamaged bimodal Ti-6Al-4V. Large-crack growth rates for  $R = 0.1$  and  $0.8$  were derived from constant load-ratio tests, whereas for  $R = 0.95$  constant- $K_{max}$ /increasing- $K_{min}$  testing was used [11,31].

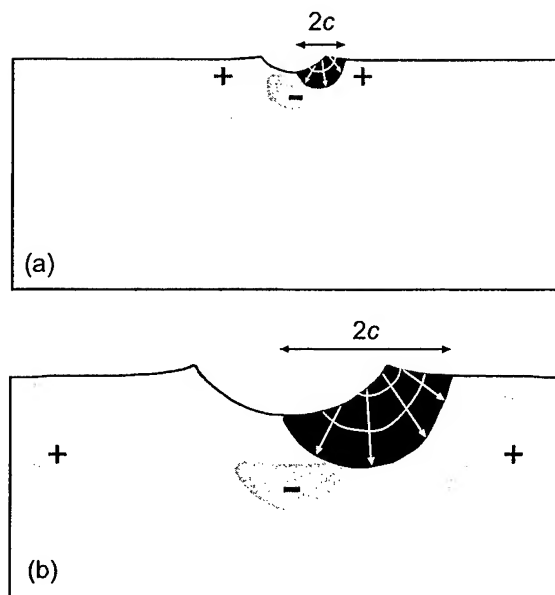


Fig. 16. Schematic display of progressive positions of crack fronts and relative sizes of cracks at the point when the cracks encounter the prominent compressive residual stress region beneath indentation site of (a) 1 mm and (b) 3.2 mm steel shot impacts.

### 3.5. Threshold conditions based on the Kitagawa-Takahashi diagram

Previous work [9,10] has illustrated the utility of the Kitagawa-Takahashi diagram [36] in evaluating the limiting conditions for FOD-induced HCF failures when the applied stress ranges are high (relative to the magnitude of the residual stress) and cracks are formed directly at the impact site. Here, the limiting threshold conditions were defined by the stress-concentration corrected smooth-bar fatigue limit (at microstructurally small crack sizes) and a worst-case fatigue-crack growth threshold (at larger homogeneous continuum-sized crack sizes). A more favorable representation of the failure envelopes for the two load ratios of 0.1 and 0.5 in Fig. 17 can be made using the El Haddad et al. [37] empirical quantification of Kitagawa-Takahashi approach; this approach introduces a constant, termed the intrinsic crack length,  $2c_0$ , such that the stress intensity is defined as  $\Delta K = Y\Delta\sigma\sqrt{\pi(2c + 2c_0)}$ , where  $Y$  is the geometry factor.

It is now possible to extend the application of the Kitagawa-Takahashi diagram to include cracks formed far from the indent by evaluating the effective  $R$ -ratio induced by the superposition of stable residual stresses. Using the fatigue failures plotted in Fig. 17 as data points at surface crack lengths of  $2c = 1 \mu\text{m}$ , and superimposing the measured tensile residual stress of  $\sim 300 \text{ MPa}$ , the  $R$ -ratios are increased from 0.1 to  $\sim 0.5$  and from 0.5 to  $\sim 0.7$  at far-field stress range of  $\sim 300 \text{ MPa}$  (Table 4). Accordingly, such failures at both load ratios can still be described by the proposed Kitagawa-Takahashi approach, provided the limiting conditions are given by the stress concentration and residual stress corrected smooth-bar fatigue limit at small crack sizes and the "worst-case threshold" for larger crack sizes.

## 4. Conclusions

Based on a study of the role of FOD in affecting HCF failures in a turbine engine Ti-6Al-4V alloy with a bimodal (STOA) microstructure, the following conclusions can be made:



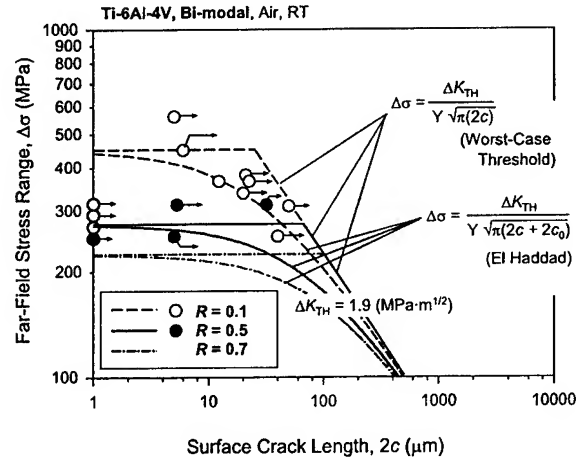


Fig. 17. Modified Kitagawa–Takahashi diagram representing the limiting threshold crack-growth conditions ( $da/dN = 10^{-11}$ – $10^{-10}$  m/cycle) at  $R = 0.1$  and  $0.5$  for FOD-induced small cracks in bimodal Ti–6Al–4V. Plotted is the threshold stress range as a function of surface crack length. The limiting conditions are defined by the worst-case  $\Delta K_{TH}$  threshold for homogeneous continuum-sized cracks (at large crack sizes) and the smooth-bar fatigue limited, corrected for stress concentration and residual stresses (at smaller crack sizes). Accordingly, data points are corrected for the stress concentration of the FOD indents.

1. FOD, simulated by the high-velocity (200–300 m/s) impact of steel spheres (1 and 3.2 mm diameter) at impact angles of  $60^\circ$  and  $90^\circ$  on a flat specimen surface, markedly reduced the fatigue performance. The principal effect of FOD was to induce preferred sites for the premature initiation of fatigue cracks.
2. Premature crack initiation was caused by the interplay of a number of factors, specifically (i) the stress concentration due to the FOD indentation, (ii) the creation (at highest impact velocities only) of microcracks at the crater rim of the damaged zone, (iii) microstructural damage from FOD-induced plastic deformation, and (iv) the localized presence of tensile residual stresses around the indent.
3. Since such microcracking at the crater rim (and indeed the shear band formation) could only be detected at the sites of the higher velocity impacts, it is concluded that low-velocity or quasi-static indentations cannot provide a worst-case simulation of FOD.
4. The magnitudes of the residual stresses in the vicinity of the damage sites have been computed numerically and measured experimentally using synchrotron X-ray diffraction. Prior to fatigue cycling, peak tensile values of these residual stresses are on the order of 300 MPa and are located in the interior adjacent to the highly deformed region beneath the indentations.
5. Two groups of FOD-induced HCF failures could be identified. The first group involved the initiation of growing fatigue cracks directly at the impact site and caused failures within  $10^5$ – $10^6$  cycles. At stress-concentration corrected stress ranges from 250 to 560 MPa, FOD-initiated microcracks ( $\sim 2$ – $10$   $\mu\text{m}$  in size) propagated from both  $60^\circ$  and  $90^\circ$  impact sites at applied stress intensities below a  $\Delta K$  of 1 MPa  $\sqrt{\text{m}}$  (at both  $R = 0.1$  and  $0.5$ ) and showed no pronounced threshold behavior, i.e., small-crack growth occurred at driving forces well below the worst-case  $\Delta K_{TH}$  threshold of 1.9 MPa  $\sqrt{\text{m}}$  for cracks larger than the characteristic microstructural size-scales in this alloy. The proposed criterion for such failures has been described by a modified Kitagawa–Takahashi approach, where the limiting threshold conditions are defined by the stress-concentration corrected smooth-bar fatigue limit (at microstructurally small crack sizes) and the worst-case  $\Delta K_{TH}$  threshold (at larger homogeneous continuum-sized crack sizes).
6. The second group of failures at  $10^7$ – $10^8$  cycles initiated at locations remote from impact damage in regions of high tensile residual stresses. It was found that simple superposition of the initial tensile residual stresses onto the applied stresses provided a significant contribution to the reduction in fatigue strength

by affecting the local mean stress and load ratio. Accordingly, the modified Kitagawa-Takahashi approach proposed above must be additionally corrected for the presence of tensile residual stresses to account for such failures. With this correction, this approach provides a rational basis for the effect of FOD on HCF failures in Ti-6Al-4V.

## Acknowledgements

This work was supported by the Air Force Office of Science and Research, grant no. F49620-96-1-0478, under the auspices of the Multidisciplinary University Research Initiative on "High Cycle Fatigue" to the University of California, Berkeley. Special thanks are due to Prof. W. Goldsmith (UCB) for providing the compressed-gas gun facility, to J.D. Donovan, Y. Yanxia and H.-R. Wenk (UCB) for help with the EBSD analysis, and to A.W. Thompson for helpful discussions. BLB would also like to thank the Hertz Foundation for financial support in the form of a fellowship for graduate study.

## References

- [1] Cowles BA. High cycle fatigue in aircraft gas turbines—an industry perspective. *Int J Fract* 1996;80:147–63.
- [2] Nicholas T, Zuiker JR. On the use of the Goodman diagram for high cycle fatigue design. *Int J Fract* 1996;80:219–35.
- [3] Larsen JR, Worth BD, Annis Jr CG, Haake FK. An assessment of the role of near-threshold crack growth in high cycle fatigue life prediction of aerospace titanium alloys under turbine engine spectra. *Int J Fract* 1996;80:237–55.
- [4] Nicholas T. Critical issues in high cycle fatigue. *Int J Fatigue* 1999;21:S221–31.
- [5] Nicholas T, Barber JR, Bertke RS. Impact damage on titanium leading edges from small hard objects. *Exp Mech* 1980;October:357–64.
- [6] Hudak SJ, Chan KS, McClung RC, Chell GG, Lee Y-D, Davidson DL. High Cycle Fatigue of Turbine Blade Materials, Final technical report UDRI subcontract no. RI 40098X SwRI project no. 18-8653, 1999.
- [7] Ritchie RO. Small cracks and high-cycle fatigue. In: Chang JCI, Coulter J, Brei D, Martinez WHG, Friedmann PP, editors. *Proceedings of the ASME Aerospace Division, AD-vol. 52*. Warrendale, PA: ASME; 1996. p. 321–33.
- [8] Peters JO, Roder O, Boyce BL, Thompson AW, Ritchie RO. Role of foreign-object damage on thresholds for high-cycle fatigue in Ti-6Al-4V. *Metall Mater Trans A* 2000;31A:1571–83.
- [9] Peters JO, Ritchie RO. Influence of foreign-object damage on crack initiation and early crack growth during high-cycle fatigue of Ti-6Al-4V. *Eng Fract Mech* 2000;67:193–207.
- [10] Peters JO, Ritchie RO. Foreign-object damage and high-cycle fatigue: role of microstructure in Ti-6Al-4V. *Int J Fatigue*, in press.
- [11] Ritchie RO, Davidson DL, Boyce BL, Campbell JP, Roder O. High-cycle fatigue of Ti-6Al-4V. *Fatigue Fract Eng Mater Struct* 1999;22:621–31.
- [12] Chen X, Hutchinson JW. Foreign object damage and fatigue crack threshold: cracking outside shallow indents. *Int J Fract* 2001;107:31–51.
- [13] Boyce BL, Chen X, Hutchinson JW, Ritchie RO. The residual stress state due to a spherical hard-body impact. *Mech Mater* 2001;33:441–54.
- [14] Eylon D. Summary of the Available Information on the Processing of the Ti-6Al-4V HCF/LCF Program Plates, University of Dayton Report, Dayton, OH, 1998.
- [15] Hines JA, Peters JO, Lütjering G. Microcrack propagation in Ti-6Al-4V alloys. In: Boyer RR, Eylon D, Lütjering G, editors. *Fatigue behavior of titanium alloys*. Warrendale, PA: TMS; 1999. p. 15–22.
- [16] Morgan JM, Milligan WW. A 1 kHz servohydraulic fatigue testing system. In: Soboyejo WO, Srivatsan TS, editors. *High cycle fatigue of structural materials*. Warrendale, PA: TMS; 1997. p. 305–12.
- [17] Lukáš P. Stress intensity factor for small notch-emanating cracks. *Eng Fract Mech* 1987;26:471–3.
- [18] Newman Jr JC, Raju IS. An empirical stress-intensity factor equation for the surface crack. *Eng Fract Mech* 1981;15:185–92.
- [19] Nisida M, Kim P. Stress concentration caused by the presence of a spherical cavity or a spherical-surfaced hollow. In: *Proceedings of the Twelfth National Congress on Applied Mechanics*, 1962. p. 69–74.
- [20] Ravichandran KS, Li X-D. Fracture mechanical character of small cracks in polycrystalline materials: concept and numerical *K* calculations. *Acta Mater* 2000;48:525–40.
- [21] Ravichandran KS. Three-dimensional crack-shape effects during the growth of small surface fatigue cracks in a titanium-base alloy. *Fatigue Fract Eng Mater Struct* 1997;20:1423–42.

- [22] Bellows RS, Muju S, Nicholas T. Validation of the step test method for generating Haigh diagrams for Ti-6Al-4V. *Int J Fatigue* 1999;21:687-97.
- [23] Morrissey RJ, McDowell DL, Nicholas T. Frequency and stress ratio effects in high cycle fatigue of Ti-6Al-4V. *Int J Fatigue* 1999;21:679-85.
- [24] Murakami Y, Nomoto T, Ueda T. Factors influencing the mechanism of superlong fatigue failure in steels. *Fatigue Fract Eng Mater Struct* 1999;22:581-90.
- [25] Murakami Y, Takada M, Toriyama T. Super-long life tension-compression fatigue properties of quenched and tempered 0.46% carbon steel. *Int J Fatigue* 1998;16:661-7.
- [26] Wagner L, Lütjering G. Influence of shot peening parameters on the surface layer properties and the fatigue life of Ti-6Al-4V. In: Fuchs HO, editor. *Proceedings of the 2nd International Conference on Shot Peening*. Paramus, NJ: American Shot Peening Society; 1984. p. 194-200.
- [27] Wagner L, Lütjering G. Influence of a shot peening treatment on the fatigue limit of Ti-6Al-4V. In: Fuchs HO, editor. *Proceedings of the 2nd International Conference on Shot Peening*. Paramus, NJ: American Shot Peening Society; 1984. p. 201-7.
- [28] Adachi S, Wagner L, Lütjering G. Influence of microstructure and mean stress on fatigue strength of Ti-6Al-4V. In: Lütjering G, Zwicker V, Bunk W, editors. *Titanium science and technology. Proceedings of the 5th International Conference on Titanium*. Oberursel, Germany: DGM; 1985. p. 21-39.
- [29] Evans WJ, Bache MR. Dwell-sensitive fatigue under biaxial loads in the near-alpha titanium alloy IMI685. *Int J Fatigue* 1994;16:443-52.
- [30] Chen X. Foreign-object damage and fatigue cracking. PhD thesis. Harvard University, Cambridge, 2001.
- [31] Boyce BL, Ritchie RO. Effect of load ratio and maximum stress intensity on the fatigue threshold in Ti-6Al-4V. *Eng Fract Mech* 2001;68:129-47.
- [32] Ritchie RO, Peters JO. Small fatigue cracks: mechanics, mechanisms and engineering applications. *Mater Trans* 2001;42:58-67.
- [33] Suresh S, Ritchie RO. Propagation of short fatigue cracks. *Int Metals Rev* 1984;29:445-76.
- [34] Miller KJ, de los Rios ER, editors. *The behaviour of short fatigue cracks*. London, UK: Mechanical Engineering Publication; 1986.
- [35] Ritchie RO, Lankford J, editors. *Small fatigue cracks*. Warrendale, PA: TMS-AIME; 1986.
- [36] Kitagawa H, Takahashi S. Applicability of fracture mechanics to very small cracks or the cracks in the early stage. In: *Proceedings of the Second International Conference on Mechanical Behavior of Materials*. Metals Park, OH: ASM; 1976. p. 627-31.
- [37] El Haddad MH, Topper TH, Smith KN. Prediction of non propagating cracks. *Eng Fract Mech* 1979;11:573-84.

## HIGH-TEMPERATURE HIGH-CYCLE FATIGUE THRESHOLDS IN NICKEL-BASE SUPERALLOYS

- J. M. Morgan and W.W. Milligan: "A 1 kHz Servohydraulic Fatigue Testing System", in *High Cycle Fatigue of Structural Materials*, W. O. Soboyejo and T. S. Srivatsan, eds, TMS, 1997, pp. 305-12.
- S.A. Padula II, A. Shyam, R.O. Ritchie, and W.W. Milligan, "High Frequency Fatigue Crack Propagation Behavior of a Nickel-Base Turbine Disk Alloy", *Int. J. Fat.*, vol. 21, 1999, pp. 725-31.
- S. Sinharoy, P. Virro-Nic and W. W. Milligan, "Deformation and Strength Behavior of Two Nickel-Base Turbine Disk Alloys at 650°C", *Metall. Mater. Trans. A*, vol. 32A, 2001, pp. 2021-32.
- S.A. Padula II, A. Shyam, D.L. Davidson and W.W. Milligan, "In Situ Study of High Frequency Fatigue Crack Propagation in a Single Crystal Superalloy", in *The David L. Davidson Symposium on Fatigue*, K.S. Chan, P.K. Liaw, R.S. Bellows, T Zogas, and W.O. Soboyejo, TMS, Warrendale, PA, 2002, pp. 183-89
- Shyam, S.A. Padula II, S. Marras, and W.W. Milligan, "Fatigue Crack Propagation Thresholds in Nickel-Base Superalloys at High Frequencies and Temperatures", *Metall. Mater. Trans. A*, vol. 33A, 2002, in press.

## A 1 kHz SERVOHYDRAULIC FATIGUE TESTING SYSTEM

Jill M. Morgan<sup>1</sup> and Walter W. Milligan<sup>2</sup>

1) MTS Systems Corporation  
14000 Technology Drive, Eden Prairie, MN 55344

2) Department of Metallurgical and Materials Engineering  
Michigan Technological University, Houghton, MI 49931

### Abstract

High cycle fatigue testing to long lives requires high frequency equipment. For example, a  $10^9$  cycle test takes over seven months in a traditional 50 Hz servohydraulic testing machine, but only 11 days at 1,000 Hz. In response to these needs, and in order to study frequency and temperature effects in the vibrational loading regime, a servohydraulic system capable of load-controlled testing at 1,000 Hz and high temperature has been developed. This paper describes modifications which are necessary to the load frame and servovalve design, the control algorithms, and the calibration procedures. It also describes an approach to measuring crack opening displacement at high temperature and 1,000 Hz, and some preliminary results.

## Introduction

Significant interest has developed recently in high cycle fatigue testing of aircraft engine structural materials. This has been driven by the US Air Force, which is in search of new methodologies for life prediction and design against high cycle fatigue failure. Typically, fatigue problems emanate from a damage site, such as a compressor blade airfoil which has been damaged by a bird strike or an ingested hard particle, or a dovetail face which has been damaged by fretting. Fatigue failure occurs when these damaged sites lead to crack propagation, driven by vibrational stresses, and usually at high mean stresses but low stress amplitudes. Since the vibrational frequencies are high and the stress amplitudes are low, real data is scarce. Lifetimes of up to  $10^9$  cycles are of interest. These lifetimes are difficult to come by in standard testing machines. As an example, a fatigue test conducted to  $10^9$  cycles at 50 Hz in a traditional servohydraulic testing machine would take over 7 months (231 days) to complete. Few laboratories can afford to tie up a servohydraulic machine for 7 months in order to obtain just one data point, and the likelihood of completing a 7 month test without a mechanical failure or power outage is very low.

In response to these needs, and in order to study frequency effects at high frequencies, new types of machines are being developed. Several different design philosophies are being explored, but documentation is lacking since the efforts are all recently initiated. One approach being developed at Southwest Research Institute is to set up a resonance condition using piezoelectric drivers [1]. Frequencies near 2 kHz can be achieved, but frequency is limited to the resonance point and is a function of the specimen and grips. At Wright Patterson Air Force Base, two approaches are being pursued [2]: in the first approach, electrodynamic "shakers" are used in conjunction with pneumatic chambers (which apply the mean stress); in the second approach, prototypes are being developed which utilize a magnetostrictive material as an actuator. The "shakers" run at 350 - 600 Hz, depending on the size of the machine, the grips and specimen. The magnetostrictive actuator machine runs at about 2 kHz. Finally, in the approach described in this paper, servohydraulic machines are being modified to run at frequencies up to 1 kHz. Each of these design approaches has advantages and disadvantages when compared to the alternatives. For each design, the durability remains to be established.

This paper describes a servohydraulic machine, capable of 1 kHz, which has been developed by MTS Systems Corporation. The system will be integrated for high temperature fatigue testing and crack growth testing at Michigan Technological University. Crack opening displacement will be measured by a capacitive displacement probe which is capable of measuring displacement in the kHz frequency range and at temperatures up to 1000°C. At the time of this paper, the machine had been constructed and had successfully accomplished several demanding room-temperature test sequences.

## High Frequency Servohydraulic Fatigue Testing

### Evolution of the Present System

MTS developed expertise in high frequency testing due to a market need in the elastomeric materials community. Elastomers utilized for vibration damping materials (such as automobile engine mounting fixtures) must be characterized for damping behavior over a range of frequencies. Typically, these "elastomer systems" perform short duration bursts of varying load levels, while sweeping through a wide range of frequencies, from 20 to 1,000 Hz. These systems are designed to keep load frame resonance frequencies out of the full range of

frequency sweeping. To avoid resonance, a large seismic-mass base and short columns are used. These frames are clearly different in physical appearance from the more traditional MTS 250 kN (50 kip) systems which are generally used for metals testing.

The first kHz-regime machine designed by MTS specifically for high cycle fatigue testing was based on the elastomer system. The changes to the system were subtle. Dual, as opposed to single, high frequency servovalves were used to achieve higher flow rates resulting in actuator displacements of  $\pm 0.065$  mm at 1,000 Hz. Although the frequencies utilized by the elastomer researchers are high, the duration of each test is generally short, so little information is currently available about the expected durability of these systems in an HCF environment.

More recently, the traditional 250 kN frame was fitted with a high performance, high flow "voice coil" servovalve. (Servovalve issues are discussed in the next section.) The goal behind this new combination of servovalve and frame type was to design a low cost, high frequency system capable of achieving higher actuator displacements in the vicinity of 1,000 Hz. To meet these requirements, the traditional 250 kN frame was redesigned. The height of the base plate was reduced to limit deflection and increase the stiffness of the frame, thus minimizing vibration effects. The column height was also reduced to eliminate any high frequency "tuning fork" effects. A tie bar across the top of the columns was added for stability. The crosshead was modified to tighten tolerances, increase stiffness and achieve better alignment. The actuator was coated with a wear resistant ceramic coating, to prevent potential wear of the actuator (rod banding). With these changes, the system is capable of approximately  $\pm 0.1$  mm of displacement and dynamic loads of around  $\pm 20$  kN at 1,000 Hz.

A note regarding the resonance frequencies of the system: the design intention of the present system was to develop a discrete high frequency system for metals applications. Unlike the elastomer rigs, the modified 250 kN system was not designed for resonance-free operation over a full range of testing frequencies. Frame resonant frequencies do exist. They are variable and are dependent upon the particular system configuration, in particular crosshead height and grip mass. Once the test configuration is determined, a frequency sweep can be performed to determine the resonance-free areas of operation. In the MTU system, with the axial grips installed, resonance points exist at approximately 630 and 930 Hz.

#### Servovalve Issues

The most critical design decision in the present system was the choice of the appropriate servovalve. Two goals were agreed upon: first, to increase the flow rate and response speed to obtain large deflections at 1,000 Hz; and second, to prevent possible premature fatigue failure of the servovalve. In machines that can run  $10^9$  cycles in 11 days, fatigue failure of the testing machine is a real concern.

A cross section of a traditional servovalve is shown in Figure 1. In the first stage, a torque motor is used to bend the so-called "flexure tube" and move the "nozzle flapper." The subsequent pressure change due to the movement of the flapper controls spool position and ultimately actuator displacement. The expected life of traditional servovalves is "greater than a billion cycles", but the concern was that the flexure tube might fail after only one or two long-term HCF tests. Further, the flow capacity of the nozzle flapper valve is limited. Therefore, it was decided that an alternative approach would be pursued.

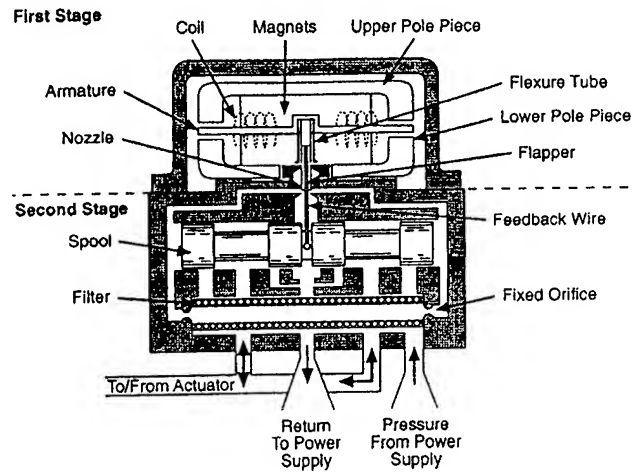


Figure 1. Cross section of a traditional servovalve (MTS model 252). The flapper and flexure tube may be subject to fatigue failure.

The approach used in the current system was a "voice coil" servovalve, shown schematically in Figure 2. The voice coil valve uses an electrodynamic pilot stage, driven in the same way as an audio speaker. The voice coil moves a spool in the pilot stage back and forth, and this spool acts exactly like the spool in a traditional servovalve. Hydraulic fluid from the pilot stage is used to drive the spool in the main stage servovalve. Essentially, the main stage acts as a hydraulic amplifier of the pilot stage. There is no torque tube or flapper, and the only parts which are mechanically stressed are the coil springs in the pilot stage.

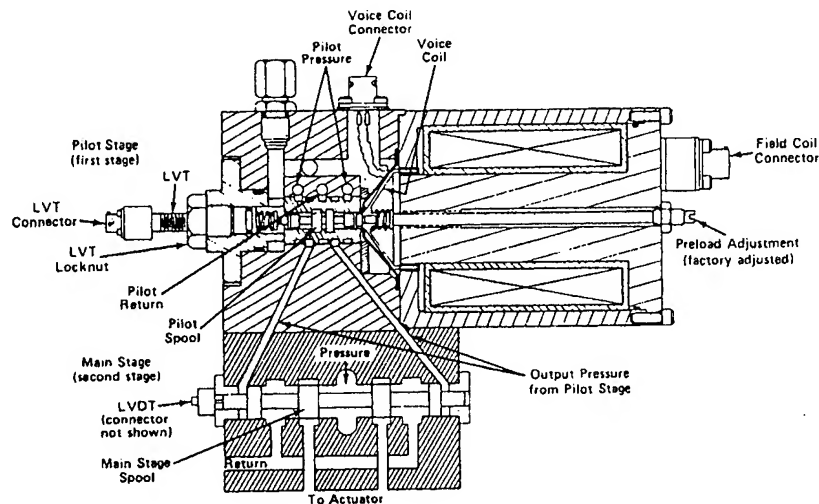


Figure 2. Cross section of a voice coil servovalve (MTS model 257). The only mechanically-stressed parts are the coil springs in the pilot stage.



In addition to the expected increase in durability, the voice coil valve has superior high frequency response and higher flow rates, characteristics which are both crucial to achieving larger actuator displacements at very high frequencies. Yet further consideration was given to the expected modes of failure. Failure of the flapper valve is likely to occur by rupturing of the internal flexure, the aftermath being a high pressure fine spray of oil in the test area. When the voice coil valve fails, however, there is no external rupturing; the oil is self-contained. The failure would most likely be observed as an error detected in the outer-loop control circuit, as the programmed load end levels would not be maintained.

#### Acceleration Compensation of the Load Cell

Acceleration effects due to moving mass of the load train are significant at high frequencies and must be compensated for in the control loop. Actual acceleration measurements are discussed in the "preliminary results" section of this paper. The inaccuracy in the load signal, if the load cell is not compensated for acceleration effects, has been determined to be approximately 25% at 1,000 Hz with the axial grips. There are two methods of compensating for acceleration, each of which utilizes an accelerometer positioned on the active elements of the load cell.

The first method is quick and simple. The system is run at frequency in displacement control with only the grip masses attached. With no specimen inserted and the load train open, the acceleration effects can be seen as load output from the system load cell. The affiliated load cell acceleration signal is then conditioned and inverted. The user then gradually sums this inverted signal into the system load cell feedback signal via potentiometer adjustment or a digital slide bar, depending on the controller being used. This is done until no further load output is monitored. This method brings the load values to within 8% of actual values.

The second and preferred method is essentially a dynamic load verification test with a strain gaged specimen closing the load train. The specimen strains are first statically calibrated as a function of load using the system load cell. An initial test is then performed at actual test conditions. The difference between the system load cell signal and that from the measured specimen strain is monitored. Via the same procedure as in the first method, the acceleration compensation circuit is then adjusted until the difference between the two load signals is nulled.

#### The Controller

The digital "TestStar" controller which runs traditional servohydraulic systems also runs the 1 kHz system; the only modifications are the acceleration compensation boards, and the use of an adaptive control scheme which yields steady-state load control at 1,000 Hz. The digital controller utilizes a patented phase amplitude compensator (PAC) to detect and correct amplitude roll-off and phase lag in sinusoidal command waveforms. An analog controller version, based on the MTS 458 system, is also under development.

## HCF and FCP Testing at Ambient and Elevated Temperatures

### Grips, Fixtures, and Loading Strategies

One advantage of the servohydraulic approach to high frequency fatigue testing is that very few modifications to standard fatigue lab procedures are necessary. The MTU system has axial grips that are capable of fully reversed loading and high temperature testing with induction heating. Traditional pin-and-clevis grips for compact tension specimens should work as well. There are only two constraints on grips and fixtures: first, the mass of the grips should be minimized for optimum system response; and second, the length of the load train should be short, to minimize load frame motion and potential resonance. The axial grips add about one kilogram of mass to the actuator, and it would not be advisable to use grips that are much bulkier than these.

Much of the FCP research in this program will be accomplished in 4-point bending. The reasons for this are: the experimental setup is simple and easy to align; the grips and fixtures weigh less than 400 grams; and it is possible to conduct Mode II and Mixed Mode I/II testing by using an asymmetric 4-point bending geometry [3].

### Measurement of Crack Length in FCP Testing at 1,000 Hz and High Temperature

A major experimental challenge at high temperatures and high frequencies is measurement of crack length. Because of the high temperatures, techniques like back-face strain gage and surface-mounted metal foils that measure remaining ligament length are not possible. Because of the high frequencies and temperatures, traditional crack opening displacement (COD) gages will not work. Measuring compliance from actuator displacement and load may be possible, but this technique may lack the necessary sensitivity, and it may be necessary to slow the test down (or stop it completely) to accurately measure the compliance. This is not desirable in high temperature testing, because slowing down or stopping the test will influence time-dependent and rate-dependent processes, and therefore the crack growth rates.

It is highly desirable to measure crack length dynamically and with as little lag time as possible. Two techniques appear to be promising. The first is the potential drop technique [4,5], and the second is the use of a capacitive COD probe. Neither of these have been demonstrated at 1,000 Hz, and the technological challenges associated with developing them are not trivial. Both will require significant development and testing, and it is not known at this time what degree of success will be attainable. In this research program, the use of the non-contact capacitive COD probe will be explored first. The system is described below.

Capacitec, Inc [6] manufactures non-contact displacement probes capable of temperatures up to 1,000°C and frequencies up to 5 kHz. Depending on the probe diameter, the absolute accuracy can be as small as 0.25  $\mu\text{m}$ . The probes measure the gap between the tip of the probe and any metal plate which is connected to ground. The unit provides a 0-10 V DC signal that can be calibrated to displacement. It is important to note that a "wide-band" amplifier must be specially ordered from the manufacturer to apply the capacitive approach to 1 kHz frequencies [6]. A schematic of the intended configuration in 4-point bending is shown in Figure 3. The probes can also be used with compact tension specimens, or as simple axial extensometers. A major challenge will be developing mounting procedures for the probes that do not shake off during 1,000 Hz loading.

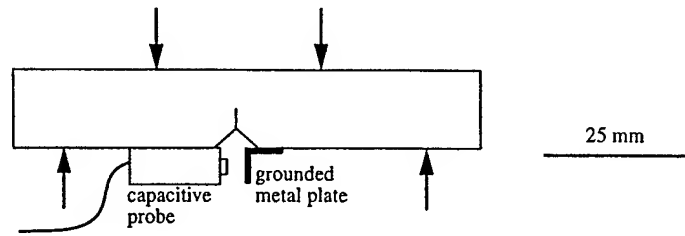


Figure 3. Schematic diagram of the 4-point bend geometry and the capacitive COD probe.

During fatigue testing, a dedicated PC with a 200 kHz, 16 bit data acquisition card will be used to acquire the DC waveform corresponding to COD. Analysis software and calibration data will be used to calculate crack length from COD and provide a 0-10 V DC "crack length" signal to the digital controller which is running the fatigue test. In this way, K-controlled fatigue testing at 1,000 Hz and 1,000°C should be possible.

#### Preliminary Results

A 1020 steel specimen with the geometry shown in Figure 3 was cycled in 4-point bending at 1,000 Hz for 4 minutes. The test was designed and conducted only as a demonstration of the 4-point bend geometry at 1,000 Hz, and so ASTM procedures for pre-cracking and testing were not followed. The specimen was notched with a 250  $\mu\text{m}$  thick water-cooled abrasive wheel, and then loaded at  $\Delta K \approx 10 \text{ MPa}\sqrt{\text{m}}$  and  $R = 0.1$ . The test ran well, with no apparent fretting under the loading pins. About 2 mm of crack growth was observed in 4 minutes, which is in the expected range for this steel and stress intensity factor [7]. From this test, it appears that bend testing at 1,000 Hz should be achievable. Crack length was not monitored by the capacitive probe, and the development of this technique is currently underway.

A 4140 steel smooth-bar specimen was cycled in the axial grips, between 5 and 55 MPa (100 to 1,000 lbs). This test was intended to demonstrate the feasibility of testing to  $10^9$  cycles with stable long-term control and durability. The test ran flawlessly for over 8 days, to 840 million cycles. The load waveform at the end of the test was identical to that at the beginning of the test. At 840 million cycles, the machine shut itself down due to a hydraulic system interlock, apparently related to an irregularity in the incoming cooling water pressure. The test was successfully re-started after the interlock was reset, and continued until 970 million cycles, at which time the test room was no longer available and the test was manually aborted.

During this test, accelerometers were mounted in various places on the load frame. The acceleration output on the crosshead and base plate measured 10.5 g's. Those on the upper grip attached directly to the load cell showed 25 g's of acceleration. The largest accelerations were measured on the lower grip mass attached directly to the moving actuator rod. These were found to be as high as 121 g's. As per the earlier discussion regarding acceleration compensation of the load cell, the effect due to the moving mass of the load train are

significant. The uncompensated vs compensated load comparisons are very dependent on the specimen spring rate, load and frequency test conditions, and grip mass. For the conditions of this particular test, the difference between uncompensated and compensated values was found to be up to 25%.

After the completion of the long-term test, various components of the load frame were inspected. The actuator rod was examined with a profilometer and microscope. There were no indications of rod banding. The servovalve was taken off and the various step responses and valve specifications were re-verified on the test bench. The springs were also inspected. All conditions were normal. The load cell was disassembled for inspection as well and was found to be fine. This test leads to some confidence that long-term 1,000 Hz testing will be feasible.

#### Summary

HCF testing to  $10^9$  cycles at room temperature and 1,000 Hz has been achieved in the current system, with no apparent deterioration. FCP testing in 4-point bending has been demonstrated. Current efforts are aimed at developing a capacitive COD probe which will be capable of measuring crack length at 1,000°C and 1,000 Hz.

#### Acknowledgments

This work was supported by the MURI on "High Cycle Fatigue", funded at Michigan Technological University by the Air Force Office of Scientific Research, Grant No. F49620-96-1-0478, through a subcontract from the University of California at Berkeley.

#### References

1. D.L. Davidson, Southwest Research Institute, San Antonio, TX, private communication, 1997.
2. T. Nicholas, Air Force Research Laboratory, Wright-Patterson AFB, OH, private communication, 1997.
3. S. Suresh, C.F. Shih, A. Morrone, and N.P. O'Dowd, "Mixed-Mode Fracture Toughness of Ceramic Materials," J. Am. Ceram. Soc., 73 (1990), 1257-1267.
4. J.K. Donald, "Direct Current Potential Difference Fatigue Crack Measurement Techniques", in Fatigue Crack Measurements: Techniques and Applications, K.J. Marsh, R.O. Ritchie and R.A. Smith, eds., EMAS, West Midlands UK, (1990).
5. R.H. Van Stone and T.L. Richardson, "Potential Drop Monitoring of Cracks in Surface Flawed Specimens", in Automated Test Methods for Fracture and Fatigue Crack Growth, ASTM STP 877, W.H. Cullen, R.W. Landgraf, L.R. Kalsand and J.H. Underwood, eds., American Society for Testing and Materials, Philadelphia, PA, (1985), 148-166.
6. Jeffrey R. Peduzzi, Capacitec Inc, Ayer, MA, 01432, Phone (508) 772-6033, private communication, 1997.
7. R.W. Hertzberg, Deformation and Fracture Mechanics of Engineering Materials, 3rd Ed., Wiley, New York (1989), 555.

# High frequency fatigue crack propagation behavior of a nickel-base turbine disk alloy

S.A. Padula II <sup>a</sup>, A. Shyam <sup>a</sup>, R.O. Ritchie <sup>b</sup>, W.W. Milligan <sup>a,\*</sup>

<sup>a</sup> Department of Metallurgical and Materials Engineering, Michigan Technological University, Houghton, MI 49931, USA

<sup>b</sup> Department of Materials Science and Mineral Engineering, University of California, Berkeley, CA 94720, USA

Received 12 July 1998; received in revised form 1 August 1998

## Abstract

Fatigue crack propagation tests were conducted on the powder metallurgy nickel-base superalloy KM4 at room temperature. Two different heat treatments were investigated, one which produced a relatively coarse grain size around 55  $\mu\text{m}$ , and another which produced a very fine grain size around 6  $\mu\text{m}$ . Tests were conducted at 50 Hz and 1000 Hz in an advanced servohydraulic testing machine at  $R$ -ratios between 0.4 and 0.7. There was no effect of frequency on the fatigue behavior at room temperature, which is expected in this type of alloy, and this result yields confidence in the reliability of the servohydraulic fatigue testing system. The threshold stress intensity for fatigue crack propagation decreased with decreasing grain size and with increasing  $R$ -ratio, again as expected. With increasing grain size, the crack path tortuosity and the crystallographic facet size on the fracture surface both increased substantially, leading to increases in roughness-induced closure and a higher apparent threshold. The threshold  $\Delta K$  values measured at  $10^{-10}$  m/cycle corresponded to essentially infinite lifetimes, as very small decreases in  $\Delta K$  from the threshold values resulted in complete crack arrest, and led to difficulty in restarting the crack growth at higher  $\Delta K$  levels. Finally, comparisons of the observed thresholds with existing models revealed significant discrepancies between the predicted and measured values. © 1999 Elsevier Science Ltd. All rights reserved.

**Keywords:** Fatigue; High cycle fatigue; Fatigue crack propagation; Fatigue thresholds; Nickel-base alloys; Superalloys

## 1. Introduction

Nickel-base superalloys are high performance materials subject to severe operating conditions in the high temperature turbine section of gas turbine engines. Turbine blades in modern engines are fabricated from Ni-base alloy single crystals which are strengthened by ordered  $\gamma'$  precipitates. Turbine discs are made from polycrystalline Ni-base alloys because these components have less stringent creep resistance requirements (due to lower temperatures) but higher strength requirements (due to higher stresses).

Damage-tolerant design philosophies have allowed the calculation of residual life in turbine disks, by assuming a flaw exists in a critical location which is as large as can be reliably detected by non-destructive inspection

techniques. The predicted lifetime is then calculated by integrating the  $da/dN$  vs  $\Delta K$  curve from this assumed flaw size to some critical size [1, pp. 13–14]. This approach works well for low cycle fatigue (LCF) loading, and has been an unqualified success at reducing LCF failures while at the same time extending the useful lives of critical components. With these advances, the most common cause of military engine component failures is now high cycle fatigue (HCF) [2]. These incidents are related to engine vibrations, and are therefore typically found at very high frequencies (in the kHz range), as well as low stress amplitudes and high  $R$ -ratios. No design methodology exists for these types of failures, since they often initiate from a damage site such as a manufacturing defect, fretting defect, or foreign object damage, and involve small fatigue crack propagation at very high frequency [2]. This results in very short lives, in terms of time to failure, even at crack propagation velocities near the typical threshold rates of  $10^{-10}$  m/cycle [3]. Therefore, a design philosophy which would be useful in this regime should be based on

\* Corresponding author. Tel.: +1-906-487-2015; fax: +1-906-487-2934.

E-mail address: milligan@mtu.edu (W.W. Milligan)

fatigue crack propagation thresholds. This study, which is part of the Air Force Multi-University Research Initiative (MURI) on High Cycle Fatigue, is aimed at studies of onset of fatigue crack propagation in the nickel-base turbine components of military engines. In another paper [3], similar threshold studies of a titanium compressor alloy are reported. Some of the important issues in high cycle fatigue, including the interaction of small or short cracks with microstructure, are discussed in this report [3]. This paper gives results on a turbine disk alloy at room temperature, while future research will focus on high temperature behavior in both disk alloys and single crystal blade alloys. Effects of temperature, frequency, microstructure, and damage state will be evaluated.

## 2. Material

The turbine disk material studied in this program was the alloy designated KM4 [4], developed by GE Aircraft Engines and Pratt and Whitney. It is a powder metallurgy alloy, which is consolidated by hot extrusion and then forged. Like all nickel-base superalloys, KM4 is strengthened by the formation of  $\gamma'$  precipitates based on  $\text{Ni}_3\text{Al}$ . The nominal composition of the alloy is given in Table 1, and a detailed report of its microstructure and deformation behavior is given elsewhere [5]. All specimens studied in this program were cut from a turbine disk forging that was heat treated by GE Aircraft Engines.

The material is typically heat treated in two different ways [6]. If it is solution treated below the  $\gamma'$  solvus temperature, some of the  $\gamma'$  remains undissolved, and this pins the grain boundaries. After quenching and ageing, the grain size is only 6  $\mu\text{m}$ , as shown in Fig. 1(a). This will be referred to as the 'sub-solvus' material in this paper. The large particles seen in Fig. 1(a) are the undissolved  $\gamma'$ , which are not present in Fig. 1(b). If, however, the alloy is solution treated above the  $\gamma'$  solvus temperature, all the  $\gamma'$  is dissolved, which allows the

grains to grow during the solutionizing treatment. It is then forced-air quenched and aged. The result is a material with a grain size of about 55  $\mu\text{m}$ , as shown in Fig. 1(b). This microstructure will be referred to as the 'super-solvus' material in the remainder of this paper. At a finer size scale, both materials contain a bi-modal distribution of  $\gamma'$  particles, with coarse particles on the order of 300 nm and fine particles on the order of 50 nm in size [5]. The super-solvus material contains a slightly higher fraction of  $\gamma'$  within the grains (55% vs 45%) because of the lack of grain boundary  $\gamma'$ . At 650°C, the super-solvus alloy has a yield strength of about 1050 MPa, while the sub-solvus material has a yield strength of about 1150 MPa [5]. The difference in strength between room temperature and 650°C is negligible in these types of alloys [7], and so the room temperature values should be about the same.

## 3. Procedures for high frequency FCP testing

Fatigue crack propagation tests were conducted on an MTS servohydraulic testing machine which was specifically designed for testing at frequencies from 0 to 1000 Hz. The details of the machine are described elsewhere [8], but it is noted here that the machine is quite flexible, with dynamic load capacities to 25 kN. Fatigue crack propagation tests were conducted largely in compliance with ASTM E647, on four-point bend bars with the dimensions shown in Fig. 2. Four-point bending was chosen because effects of mode-mixity will be examined later in asymmetric four-point bending, and it was desirable to keep the geometry constant. Increasing/decreasing  $K$  tests were conducted several times to verify the observed threshold behavior, but only the increasing part of the tests have been given in the figures. The  $K$ -solution of Tada [9] for pure bending, corrected for finite width, was utilized to calculate stress intensity factors. Plots of  $da/dN$  vs  $\Delta K$  were obtained using the secant method, per ASTM E647.

In an earlier paper [8], a capacitive crack opening displacement (COD) gage was described which is capable of measuring COD at 1000 Hz. The intention was to use this gage to measure crack length in the current project. However, while the gage was capable of measuring COD quite well at 1000 Hz, it was not possible to use this measurement to reproducibly measure crack length, since the crack length function was highly sensitive to very small changes in measured COD, zero position, and temperature. It was not possible to measure the dynamic compliance due to slight noise in the signals at 1000 Hz. Therefore, crack lengths were measured by using a Questar telescope with a 2  $\mu\text{m}$  resolution. The entire test was videotaped, and the crack length was measured manually from the videotape. Post-test fractographic measurements verified the Questar crack lengths to a high degree of confidence.

Table 1  
Composition of KM4

Element	wt%
Co	18
Cr	12
Mo	4
Al	4
Ti	4
Nb	2
B	0.03
C	0.03
Zr	0.03
Ni	balance

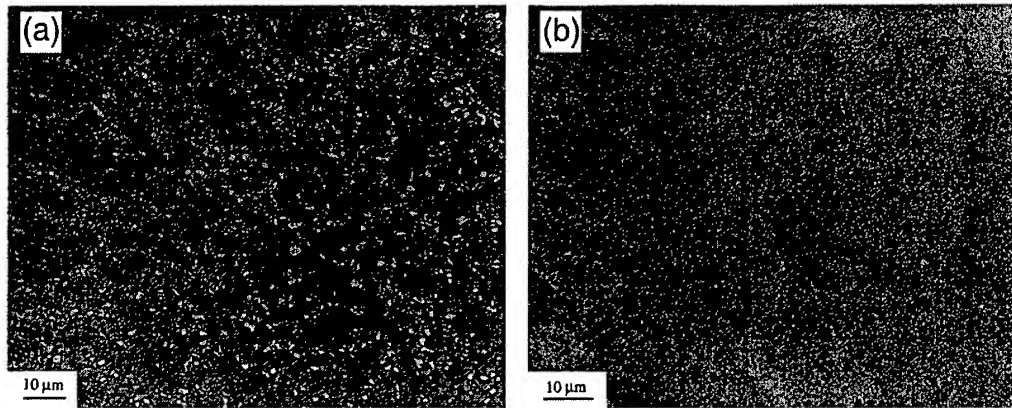


Fig. 1. Optical microstructures of KM4 after heat treatment. (a) Sub-solvus heat treatment, showing large  $\gamma'$  particles which did not dissolve during solution treatment. Grain boundaries are not resolved, but are decorated by the large  $\gamma'$  particles. (b) Super-solvus heat treatment, showing larger grain size and lack of undissolved  $\gamma'$  precipitates. In both cases, finer  $\gamma'$  which is responsible for strengthening is too small to be resolved at this magnification.

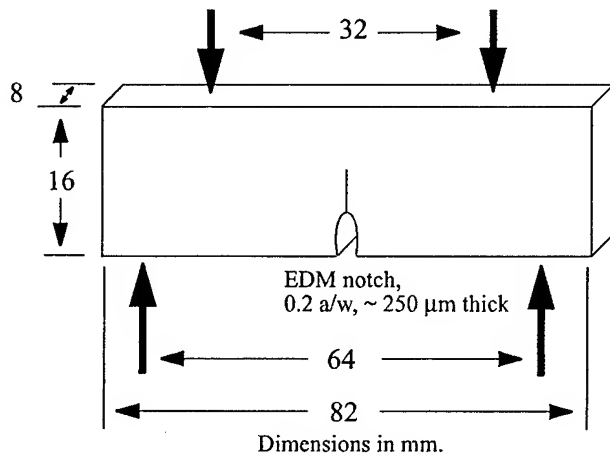


Fig. 2. Dimensions of the four-point bend specimens, with loading points indicated by heavy arrows.

## 4. Results and discussion

### 4.1. Effects of frequency

Sub-solvus KM4 specimens were tested in the Paris regime at 50 and 1000 Hz at an  $R$ -ratio of 0.5. The curves are shown in Fig. 3. Within experimental error, the curves are indistinguishable, indicating no effect of frequency at room temperature. This was expected, since nickel-base superalloys do not become highly rate sensitive until temperatures in excess of 700°C [7], and previous research by our group found almost no frequency effect on the yield strength of KM4 at 650°C [5]. The major implication of this result is that the newly-developed servohydraulic testing machine gives reliable results at frequencies of 1000 Hz. Similar results have been found for the titanium alloy [3].

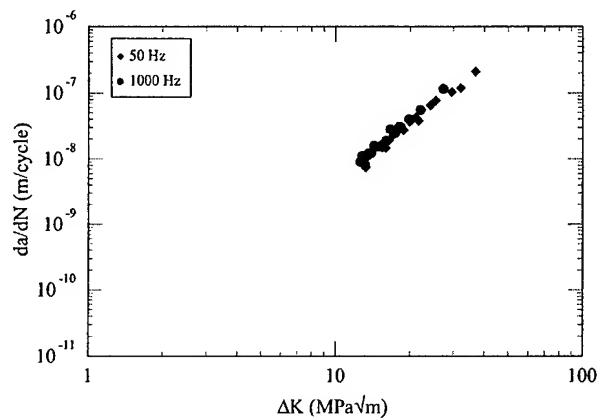


Fig. 3. Fatigue crack propagation curves for sub-solvus KM4 in the Paris regime at frequencies of 50 and 1000 Hz at  $R=0.5$ .

### 4.2. Effects of microstructure

Fig. 4 shows FCP curves for sub-solvus and super-solvus materials at a frequency of 1000 Hz and  $R=0.7$ . It is evident that the Paris slopes were similar ( $\sim 4$ ), but the sub-solvus material had a consistently higher fatigue crack propagation rate (at equivalent  $\Delta K$ ) as well as a lower threshold. The measured threshold values ( $10^{-10}$  m/cycle growth rates) at this  $R$ -ratio were 6.8 MPa $\sqrt{m}$  (sub-solvus) and 9.9 MPa $\sqrt{m}$  (super-solvus). Decreasing the  $\Delta K$  level by only 0.1 MPa $\sqrt{m}$  led essentially to crack arrest; no propagation was detected even after 200 million cycles. When this was allowed to occur, it became very difficult to restart the crack, suggesting an oxide-induced 'coaxing' phenomenon [10]. This behavior suggests that the measured threshold at  $10^{-10}$  m/cycle is truly a 'no growth'  $\Delta K$  value, and that essentially infinite life would result at constant  $\Delta K$  levels below the measured values.

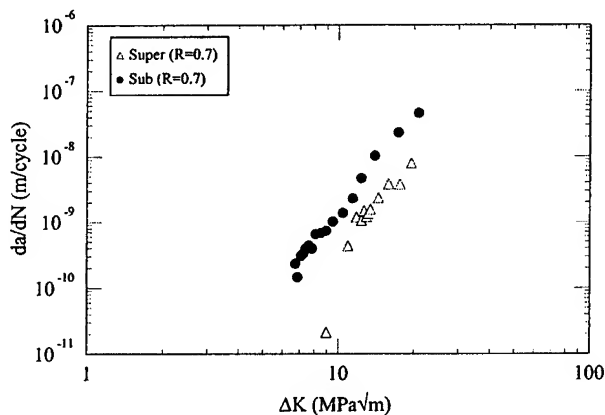


Fig. 4. Fatigue crack propagation curves for sub-solvus and super-solvus KM4 in the threshold and early Paris regimes at 1000 Hz and  $R=0.7$ .

The lower threshold and higher FCP rates were observed in the sub-solvus material, which had a grain size an order of magnitude finer than the super-solvus material, as discussed earlier and shown in Fig. 1. Optical micrographs of the crack paths seen at the surface in sub-solvus and super-solvus materials are shown in Fig. 5. It is evident that there was substantially more crack path tortuosity in the coarse-grained super-solvus material which exhibited a higher threshold and a lower FCP rate. Measurements of the actual crack length divided by the projected crack length in the Mode I plane resulted in ratios of 1.6 for the super-solvus and 1.2 for the sub-solvus, confirming quantitatively that the crack path tortuosity did increase with grain size. Numerous previous investigators [11–20] have found similar effects of grain size on FCP rates in similar nickel-base superalloys tested at low temperatures. The difference in the FCP behavior with grain size has been attributed to intrinsic factors such as slip reversibility and extrinsic factors such as increases in roughness-induced closure;

however, these factors are often interrelated [18]. The large grain size leads to increases in heterogeneity of deformations and this heterogeneity leads to better slip reversibility [12,17–19] as well as larger crystallographic facets on the fracture surfaces which leads to more roughness-induced closure [18]. Further, the crack paths become more tortuous and deviate from the Mode I plane [18]. All of these effects combine to reduce the crack growth rates and increase the thresholds as the grain size is increased. Evidence supporting these phenomena in KM4 at 1000 Hz is clearly present in Figs. 5 and 6. Fig. 5 shows the increase in crack path tortuosity and the deviation from the Mode I plane, while Fig. 6 shows the substantial increase in crystallographic facet size for the larger-grained material. Finally, the super-solvus material exhibited faceted growth up to a high transition  $\Delta K$  level of 35  $\text{MPa}\sqrt{\text{m}}$ , compared to only 13  $\text{MPa}\sqrt{\text{m}}$  for the sub-solvus, indicating that non-continuum microstructural effects are playing a larger role in the large-grained material, as would be expected. This high transition  $\Delta K$  level for super-solvus leading to greater crack path tortuosity results in bursts in crack growth and hence more scatter in data.

#### 4.3. Effects of load-ratio

The effect of load ratio ( $R=0.4$  and  $0.7$ ) on the fatigue crack propagation behavior at 1000 Hz is illustrated in Figs. 7 and 8, and threshold values are summarized in Table 2. The figures and tables show that the effect of  $R$ -ratio is higher in the near-threshold regime of crack growth. The sub-solvus curves show expected behavior, such that an increase in  $R$ -ratio gives higher crack growth rates and a lower threshold, which can generally be explained by attendant crack closure effects. The super-solvus material also exhibited a slightly reduced threshold at the higher  $R$ -ratio. However, the super-solvus material displayed anomalous behavior in the  $\Delta K$

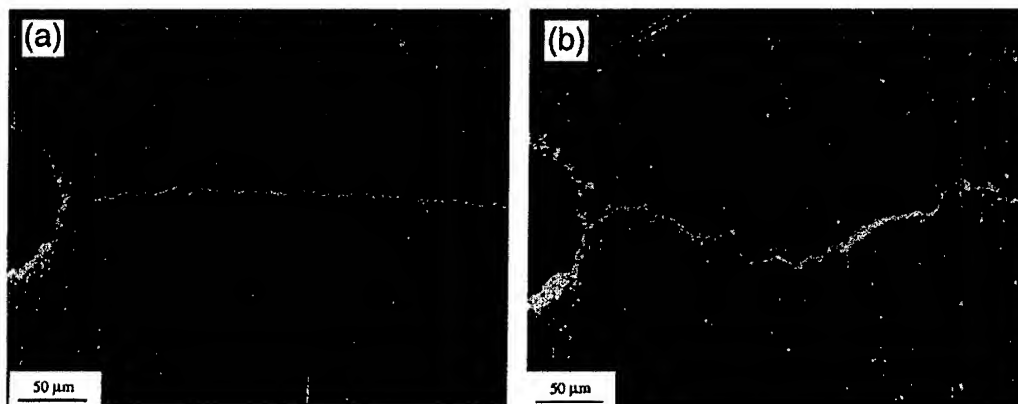


Fig. 5. Optical micrographs of the crack paths in KM4 tested at 1000 Hz. EDM notches are visible at the left. (a) Sub-solvus material (6  $\mu\text{m}$  grain size), showing relatively planar crack. (b) Super-solvus material (55  $\mu\text{m}$  grain size), showing substantial crack path tortuosity. Crack branching was also observed in the super-solvus material.



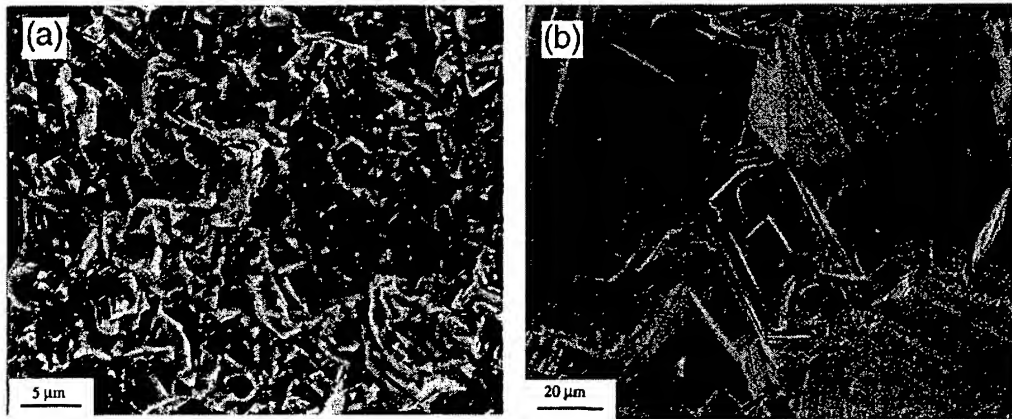


Fig. 6. Scanning Electron Micrographs of the fracture surfaces in the near-threshold regime. KM4 at 1000 Hz and  $R=0.7$ . (a) Sub-solvus, showing very fine facets. (b) Super-solvus, showing significantly larger crystallographic facets related to the larger grain size. Note magnification in (a) is 4× higher than in (b), so the differences in facet size are even greater than apparent on first glance.

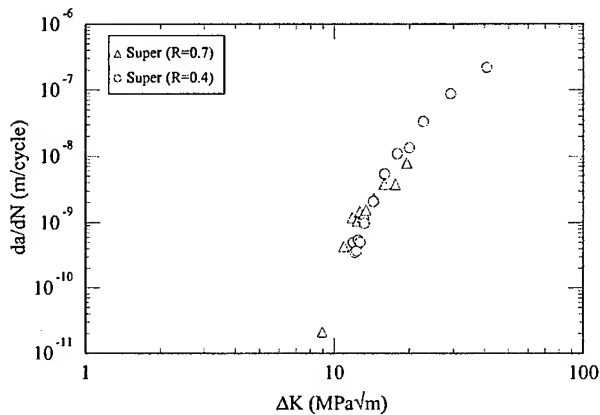


Fig. 7. Fatigue crack propagation curves for super-solvus KM4 at 1000 Hz and two different  $R$ -ratios.

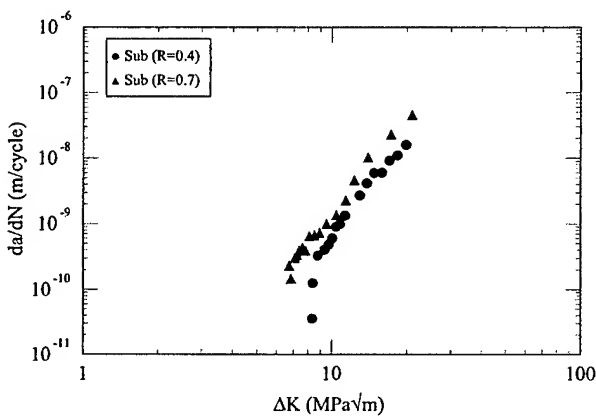


Fig. 8. Fatigue crack propagation curves for sub-solvus KM4 at 1000 Hz and two different  $R$ -ratios.

Table 2

Measured threshold stress intensity values ( $10^{-10}$  m/cycle)

Heat treatment	Grain size, $\mu\text{m}$	$\sigma_y$ , MPa <sup>a</sup>	$\Delta K_{th}$ , MPa $\sqrt{\text{m}}$	
			$R=0.4$	$R=0.7$
Sub-solvus	6	1150	8.4	6.8
Super-solvus	55	1050	10.3	9.9

<sup>a</sup> Estimated from value measured in [5] at 650°C.

region above threshold, since the crack growth rates at the two different  $R$ -ratios are basically indistinguishable. Anomalous crack growth behavior in the Paris regime for super-solvus specimen with increasing  $R$  could be a stochastic phenomenon (since there was much more scatter in the data in the supersolvus specimens) or it could be due to the fact that monotonic modes of fracture superimpose on cyclic modes of fracture at higher  $R$ -ratios [21]. Crack path tortuosity showed a slight increase as  $R$  was increased. The ratio of the actual crack length to projected crack length was 1.45 for  $R=0.4$  and 1.59 for  $R=0.7$ . This implies that there might be a  $K_{max}$  effect on threshold. The  $K_{max}$  values increase rapidly as the crack length increases. Since faceted growth is observed well into the regime where Paris–Law is obeyed, higher  $R$ -ratios (and hence higher  $K_{max}$  values) lead to facilitation of mode-I fracture which in turn shows up as better defined facets in the crack path. This may explain the increase in crack path tortuosity and slightly slower crack growth rates as  $R$  increases in the super-solvus specimen.

#### 4.4. Intrinsic thresholds

It is desirable for the development of a HCF design method to obtain the intrinsic threshold  $\Delta K$  value below

which cracks will not propagate, in the absence of extrinsic effects such as crack closure. In our earlier paper [3] it was found that this value could be reliably obtained for a Ti-6-4 alloy by conducting long crack FCP tests at  $R=0.9$ . The threshold only increased by about 10% when going from  $R=0.92$  to  $R=0.8$ , and based on this it is reasonable to assume that the thresholds measured here at  $R=0.7$  are within 20% or better of the actual intrinsic thresholds. These measured values can be compared to existing theoretical models, as discussed below.

Sadananda and Shahinian [22] gave an expression for threshold stress intensity based on dislocation emission from the crack tip as

$$K_{th} = \frac{\sqrt{2\pi b}}{A} \left[ \frac{\mu}{4\pi(1-\nu)} \ln \frac{\alpha \rho}{b} + \frac{\mu b}{4\pi(1-\nu)\rho} + \frac{\gamma}{\sqrt{2b}} + \frac{\sigma_{ys}}{2} \right]. \quad (1)$$

where the four terms on the right hand side are, respectively, contributions from self energy of the dislocation, image force, surface energy of the ledge formed and the friction stress which is taken to be the 0.2% yield stress of the material divided by two. Here  $\mu$  is the shear modulus,  $\gamma$  is the surface energy,  $\rho$  is the dislocation distance from the crack tip,  $\alpha$  is the dislocation core constant,  $b$  is the Burgers vector,  $\nu$  is Poisson's ratio and  $A$  is the orientation factor of the slip plane given by  $\cos(\theta/2) \cdot \sin(\theta/2) \cdot \cos(3\theta/2)$ , where  $\theta$  is the angle between the actual crack propagation direction and the pure Mode-I direction. The threshold stress intensity range,  $\Delta K$ , can be represented in terms of  $K_{th}$  as

$$\Delta K_{th} = K_{th} \cdot (1-R) \quad (2)$$

Substituting,  $\theta=45^\circ$ ,  $\rho=b=2.54 \times 10^{-10}$  m,  $\alpha=4$ ,  $\mu=77$  GPa,  $\nu=0.3$ ,  $\gamma=1.7$  J/m<sup>2</sup> and  $\sigma_{ys}=1100$  Mpa for the superalloy into Eqs. (1) and (2) gives a predicted threshold  $\Delta K$  value of 2.3 MPa $\sqrt{m}$  at  $R=0.7$ , which is clearly too low.

Weertman's analysis [23] of intrinsic thresholds consisted of modifying limiting conditions for emission of a dislocation from an atomically sharp Griffith crack. The Weertman intrinsic threshold is given by

$$\Delta K_{th} = 2g \left[ \frac{2\gamma E}{1-\nu^2} \right]^{1/2}, \quad (3)$$

where  $E$  is the Young's modulus,  $\gamma$  is the true surface energy of the solid and  $\nu$  is Poisson's ratio. The modifying parameter  $g$  describes the degree of ductility (and varies from 0.6 to 1.0, with the latter representing the perfectly brittle case) and is a function of the ratio of the theoretical tensile strength to the theoretical shear strength. Using this approach with reasonable values for the material parameters, the intrinsic threshold for KM4 was predicted to be around 1.7 MPa $\sqrt{m}$ . Again, this value is too low.

Finally, Lin and Fine [24] suggested a relation for intrinsic threshold, which involved activation of a source

identified by dislocation cell wall at a distance from the crack tip, given by

$$\Delta K_{th} = m\mu b \sqrt{\frac{2\pi}{d}}, \quad (4)$$

where  $\mu$  is the shear modulus,  $m$  is the average orientation factor which varies between 2 and 3 for random polycrystals,  $d$  is the dislocation cell size and  $b$  is the Burgers vector. This model predicts an intrinsic threshold value of  $\sim 1$  MPa $\sqrt{m}$  for KM4 and is again an underestimate.

The predicted intrinsic thresholds are given for all three models in comparison with the data in Table 3. It is clearly seen that the models under-predict the actual fatigue threshold. Further, the same trend was found in the other report on the Ti-6-4 alloy [3] and potential reasons for the discrepancies between measured and predicted values are discussed in that paper. It is clear that this is a fruitful area for further research.

## 5. Summary

KM4, a new generation powder metallurgy turbine disk alloy, behaved in a similar fashion to other alloys in its class. It exhibited a grain size effect on FCP rates and thresholds, such that finer grain sizes led to lower thresholds and higher FCP rates. Further, increasing  $R$ -ratios resulted in decreasing thresholds. Fractographic observations were consistent with similar alloys, in that faceted fracture associated with crystallographic slip planes was observed at low  $\Delta K$  levels, and facet size scaled with grain size. The measured thresholds at  $10^{-10}$  m/cycle corresponded to essentially infinite lifetimes, as very small decreases in  $\Delta K$  from the threshold values resulted in complete crack arrest, and led to difficulty in re-starting the crack growth at higher  $\Delta K$  levels. Existing threshold models predicted threshold  $\Delta K$  values that were substantially different from those observed experimentally.

The two main contributions of this research are demonstrating that:

- The trends in thresholds, grain size effects, and  $R$ -ratio effects in this polycrystalline nickel-base superalloy at room temperature were the same at 1000 Hz

Table 3  
Predicted intrinsic threshold values

Model	$\Delta K_{th}$ , MPa $\sqrt{m}$
Sadananda and Shahinian [20]	2.3 ( $R=0.7$ )
Weertman [21]	1.7
Lin and Fine [22]	1

as they were in studies by previous investigators conducted on similar alloys, mainly at 50 Hz;

- Crack growth rates as a function of  $\Delta K$  for the alloy studied here were the same at 50 Hz and at 1000 Hz in the Paris regime.

These two results, taken with the results on the titanium alloy in the parallel study, make it clear that there is no effect of frequency on fatigue crack propagation behavior of polycrystalline nickel-base superalloys between 50 and 1000 Hz at room temperature.

### Acknowledgements

This work was supported by the MURI on "High Cycle Fatigue", funded at Michigan Technological University by the Air Force Office of Scientific Research, Grant No. F49620-96-1-0478, through a subcontract from the University of California at Berkeley.

### References

- [1] Suresh S. Fatigue of materials. 2nd ed. Cambridge: Cambridge University Press, 1998.
- [2] Cowles BA. *Int J Fracture* 1996;80:147–63.
- [3] Boyce BL, Campbell JP, Roder O, Thompson AW, Milligan WW, Ritchie RO. Thresholds for high-cycle fatigue in a turbine engine Ti–6Al–4V alloy. *Int J Fatigue*, this issue.
- [4] Krueger DD et al. US Patent 5143563, September 1, 1992.
- [5] Sinharoy S, Virro-Nic P, Oja EA, Milligan WW. Deformation behavior of two nickel-base turbine disk alloys at 650°C. *Metall Mater Trans A*, in review.
- [6] Huron ES, Casey RL, Henry MF, Mourer DP. In: Kissinger RD et al., editor. *Superalloys 1996*. Warrendale, PA: TMS, 1996:667–76.
- [7] Leverant GR, Gell M, Hopkins SW. *Mater Sci Eng* 1971;8:125–33.
- [8] Morgan JM, Milligan WW. In: Soboyejo WO, Srivatsan TS, editors. *High cycle fatigue of structural materials*. Warrendale, PA: The Minerals, Metals and Materials Society, 1997:305–12.
- [9] Tada H, Paris PC, Irwin GR. *The stress analysis of cracks handbook*. Hellertown, PA: Del Research Corporation, 1973.
- [10] Suresh S, Zamiski GF, Ritchie RO. *Metall Trans A* 1981;12A:1435–43.
- [11] Bartos J, Antolovich SD. In: Taplin DMR, editor. *Fracture 1977*. NY: Pergamon Press, 1977:995–1005.
- [12] Antolovich SD, Jayaraman N. In: Burke JJ, Weiss V, editors. *Fatigue: environment and temperature effects*. NY: Plenum Press, 1983:119–44.
- [13] James LA, Mills WJ. *Engr Fract Mech* 1985;22:797–817.
- [14] King JE. *Metal Sci* 1982;16:345–55.
- [15] Venables RA, Hicks MA, King JE. In: Davidson DL, Suresh S, editors. *Fatigue crack growth threshold concepts*. Warrendale (PA): The Minerals, Metals and Materials Society, 1984:341–55.
- [16] Yuen JL, Roy P. *Scripta Metall* 1985;19:17–22.
- [17] Lerch BA, Jayaraman N, Antolovich SD. *Mater Sci Eng* 1984;66:151–66.
- [18] King JE. *Mater Sci Tech* 1987;3:750–64.
- [19] Krueger DD, Antolovich SD, Van Stone RH. *Metall Trans A* 1987;18A:1431–49.
- [20] Denda T, Britz PL, Tien JK. *Metall Trans A* 1992;23A:519–26.
- [21] Sadananda K, Vasudevan AK. In: Soboyejo WO, Srivatsan TS, Ritchie RO, editors. *Fatigue and fracture of ordered intermetallic materials II*. Warrendale, PA: The Minerals, Metals and Materials Society, 1995:273–86.
- [22] Sadananda K, Shahinian P. *Int J Fracture* 1977;13:585–94.
- [23] Weertman J. In: Mura T, editor. *Mechanics of fatigue*. NY: ASME, 1981:11–9.
- [24] Lin GM, Fine ME. *Scripta Metall* 1982;16:1249–54.

# Deformation and Strength Behavior of Two Nickel-Base Turbine Disk Alloys at 650 °C

SHUBHAYU SINHARROY, PAULINE VIRRO-NIC, and WALTER W. MILLIGAN

Two powder metallurgy nickel-base turbine disk alloys, RENE'95\* and KM4, were studied for

---

\*RENE'95 is a trademark of General Electric Company, Fairfield, CT.

---

strength and deformation behavior at 650 °C. Two classes of microstructures were investigated: unimodal size distributions of  $\gamma'$  precipitates with particle sizes ranging from 0.1 to 0.7  $\mu\text{m}$  and commercially heat-treated structures with bimodal or trimodal size distributions of  $\gamma'$  precipitates. The strength and deformation mechanisms were heavily influenced by the microstructure. In both alloys, deformation during compression tests consisted of a combination of  $a/2\langle 110 \rangle$  antiphase boundary (APB)-connected dislocation pairs and  $a/3\langle 112 \rangle$  partials creating superlattice intrinsic stacking faults (SISFs). In unimodal alloys, the fault density increased with decreasing particle size and decreasing strain rate. These trends, observed in compression testing, are consistent with earlier studies of similar alloys, which were tested in creep. As the  $\gamma'$  size was reduced, the nature of the faults changed from being isolated within single precipitates to being extended across entire grains. Commercially heat-treated alloys, containing a bimodal distribution of  $\gamma'$  particles, exhibited significantly more faulting than unimodal alloys at the same cooling  $\gamma'$  size. This augmentation of the faulting in commercial alloys was apparently due to the presence of the fine, aging  $\gamma'$  particles. The two typical commercial heat treatments (supersolvus and subsolvus) resulted in different deformation structures: the subsolvus behavior was similar to that of unimodal alloys with  $\gamma'$  sizes between 0.2 and 0.35  $\mu\text{m}$ , while the supersolvus deformation was similar to that of unimodal alloys with the 0.1  $\mu\text{m}$   $\gamma'$  size. These differences were attributed to differences in the size of the fine, aging  $\gamma'$  particles. Creep deformation in a commercially heat-treated material at 650 °C occurred solely by SISF-related mechanisms, resulting in a macroscopic slip vector of  $\langle 112 \rangle$ . The effects of alloy chemistry, APB energy, and microstructure on the deformation and mechanical behavior are discussed in detail, and possible effects of the faulting mechanisms on the mechanical behavior are explored. Finally, models for yield strength as a function of microstructure for bimodal alloys with large volume fractions of precipitates are found to be in need of development.

## I. INTRODUCTION

NICKEL-BASE alloys are subjected to severe operating conditions in commercial and military gas turbine engine disks. In recent years, a damage-tolerant design philosophy has emerged, which uses fracture-mechanics concepts to predict crack growth rates and guide engine inspection schedules. Crack propagation due to creep fatigue, accentuated by environmental embrittlement due to oxygen, has been identified as a major concern in turbine disks. KM4, an alloy which was patented by General Electric (GE) in 1992,<sup>[1]</sup> is a material which was specifically designed to optimize hold-time crack growth rates in turbine disk applications. In this article, fundamental deformation mechanisms which occur at 650 °C in KM4 and RENE'95 (a first-generation powder metallurgy disk alloy) are presented and discussed. (RENE'95 will be abbreviated as R95 in the

remainder of this article.) Both alloys are prepared by powder processing, followed by extrusion and forging, and both contain approximately 55 pct of the strengthening  $\gamma'$  precipitates.<sup>[2]</sup> Typical alloy compositions for the two materials are given in Table I.

The microstructures that develop during commercial heat treatments in large components, such as turbine disks, typically contain a bimodal  $\gamma'$  size distribution. Large  $\gamma'$  particles, varying in diameter from 0.2 to 0.5  $\mu\text{m}$ , form on cooling from the solutionizing temperature; finer  $\gamma'$  particles, typically less than 0.1  $\mu\text{m}$  in diameter, form upon aging or cooling from the aging treatment. In order to determine fundamental deformation mechanisms in these alloys as a function of  $\gamma'$  size via transmission electron microscopy (TEM), heat-treatment schedules were designed to produce a monosized (unimodal)  $\gamma'$  particle distribution in KM4 and R95. The heat treatments produced an equilibrium volume fraction of  $\gamma'$  particles with a unimodal size distribution, with average sizes ranging from 0.1 to 0.7  $\mu\text{m}$ . Commercial heat treatments were also studied for KM4. In addition to microstructural effects, two strain rates were investigated, to better understand the deformation obtained in the plastic zone ahead of a crack under creep conditions. Finally, a specimen that had been subjected to creep testing at 650 °C was studied.

---

SHUBHAYU SINHARROY, formerly Graduate Student, Department of Materials Science and Engineering, Michigan Technological University, is with the Engine Components Division, Eaton Corporation, Marshall, MI 49068. PAULINE VIRRO-NIC, formerly Graduate Student, Department of Materials Science and Engineering, Michigan Technological University, is a Consultant. WALTER W. MILLIGAN, Professor, is with the Department of Materials Science and Engineering, Michigan Technological University, Houghton, MI 49931.

Manuscript submitted September 28, 2000.

Table I. Typical Alloy Compositions (Weight Percent)

Element	KM4	R95
Co	18	8
Cr	12	13
Mo	4	3.5
Al	4	3.5
Ti	4	2.5
Nb	2	3.5
W	0	3.5
B	0.03	0.01
C	0.03	0.06
Zr	0.03	0.05
Ni	balance	balance

## II. EXPERIMENTAL PROCEDURES

The R95 and KM4 slabs were received from GE Aircraft Engines (Evendale, Ohio). The slabs had been fabricated by a combination of powder processing and hot working, by proprietary processes. One of the KM4 slabs received a solutionizing treatment at 1140 °C (referred to as the subsolvus treatment), which is below the  $\gamma'$  solvus temperature of 1170 °C. The other KM4 slab and the R95 slab were solutionized at 1180 °C (referred to as the supersolvus treatment). The KM4 slab that was creep tested received a supersolvus treatment.

In order to study the deformation behavior of unimodal alloys, cylindrical rods approximately 15 mm in diameter were machined from the slabs. The specimens were solutionized in air at 1180 °C for 30 minutes, followed by quenching in air, water, oil, or a high-temperature salt bath at temperatures between 500 °C and 850 °C. The quenched specimens were aged at 870 °C or 980 °C for times from 15 minutes to 500 hours. Commercial microstructures in KM4 were produced by GE using proprietary processes. These consist of a partial or complete solutionizing step, followed by rapid controlled cooling and a double aging treatment.

Cylindrical tension specimens were machined from the heat-treated cylinders and the as-received slabs. It was found that quench cracks were present in some heat-treated specimens (especially the R95), and so specimens broke either in machining or during initial loading in tension tests. Therefore, mechanical testing was conducted under compression on cylindrical specimens which were 6 mm in diameter and approximately 10 mm in height. Identical specimens were also made from the heat-treated KM4 slabs. Specimens were induction heated to 650 °C, using nickel-base superalloy loading platens which were also heated by the induction coil. The temperature was measured and controlled with a thermocouple which was welded directly on the surface of the compression specimen, at the midpoint of the specimen height. Temperature gradients were measured by scanning the surface with a radiation pyrometer, and the induction coil was adjusted until the temperature was within 10 °C of 650 °C along the entire length of the specimen. Strain was measured by a high-temperature extensometer, with quartz rods attached to the superalloy loading platens, in close proximity to the platen/specimen interface. Loading was accomplished in a servohydraulic testing machine, in displacement control, at displacement rates that corresponded to strain rates of approximately  $10^{-3}$  and  $10^{-5}$  s<sup>-1</sup>. The

"fast" tests lasted approximately 1 minute, while the "slow" tests were completed after approximately 90 minutes and, therefore, contained a component of "creep" loading. Tests were interrupted for deformation studies after between 2 and 5 pct plastic strain. For the unimodal alloys, one test was conducted for each combination of  $\gamma'$  size and strain rate for R95, and two to four tests were conducted for KM4. One test was also conducted for each combination of commercial heat treatment (sub/supersolvus) and strain rate on the KM4 slab.

The grain size was characterized by optical and scanning electron microscopy, after etching in a solution of 33 pct acetic acid, 33 pct nitric acid, 33 pct water, and 1 pct hydrofluoric acid. Disks of 3 mm in diameter for TEM studies were obtained by electrical discharge machining of rods from the middle of the compression specimens and then slicing them into disks of 400  $\mu$ m in thickness with a water-cooled wafering saw. The disks were obtained from the mid-height positions of the compression and creep-tested specimens, where the loading was uniaxial and the temperature was very close to 650 °C. Thin foils were prepared for TEM by twin-jet electropolishing in a solution of 10 pct perchloric acid and 35 pct butyl cellosolve in ethanol, at -20 °C and 30 to 40 V. Precipitate sizes were measured by TEM and also by scanning electron microscopy (SEM) at the larger particle sizes. Several hundred precipitates were measured at each heat-treatment condition to determine average  $\gamma'$  sizes. In the case of cuboidal precipitates (which are oriented along  $\langle 001 \rangle$  directions and which have sizes above about 0.2  $\mu$ m), sizes were measured with TEM micrographs using  $\langle 001 \rangle$  beam directions, so the sizes measured have little error. In the case of spherical precipitates, the particle diameter was measured. No correction was made for finite foil thickness. Because the matrix always thins at a higher rate than the precipitate in these alloys, the fine  $\gamma'$  (less than 0.07  $\mu$ m) which is contained in the matrix is rarely truncated, and, therefore, the measurements of average particle diameter should be quite precise. Precipitate sizes around 0.1  $\mu$ m, which is close to the foil thickness, might have some error due to the assumption of a planar section.

Deformation structures were characterized by standard two-beam and weak-beam TEM techniques. One KM4 creep specimen (with a commercial microstructure), which was tested by GE Aircraft Engines at 650 °C and 800 MPa, was also studied *via* TEM.

## III. RESULTS: MICROSTRUCTURES

### A. KM4 and R95 with Unimodal Size Distributions of $\gamma'$ Particles

The goal of the heat treatment was to develop monosized  $\gamma'$  particles, with sizes varying between 0.1 and 0.7  $\mu$ m. These structures would encompass the  $\gamma'$  sizes found in commercial heat treatments, in which bimodal distributions are typically encountered, with primary  $\gamma'$  particles between 0.1 and 0.5  $\mu$ m and fine  $\gamma'$  particles below 0.1  $\mu$ m.

Rods, 15 mm in diameter, were solutionized at 1180 °C and quenched in several quenching media. Air cooling, a forced air quench, oil quenching, water quenching, and high-temperature salt bath quenching were all investigated. For R95, only water quenching was successful; the salt bath resulted in catastrophic quench cracks, while the air, forced

gas, and oil resulted in bimodal  $\gamma'$  distributions. For KM4, both water and oil were successful. The as-quenched  $\gamma'$  sizes for both alloys were between 0.08 and 0.10  $\mu\text{m}$ . The  $\gamma'$  particle sizes reported in this article correspond to diameters of spherical particles, or cube-edge lengths for cuboidal particles. Grain sizes for the unimodal alloys were approximately 55  $\mu\text{m}$ .

Aging was conducted at 980 °C, for times up to 500 hours. Particle sizes of  $\gamma'$  ranging from 0.1 to 0.7  $\mu\text{m}$  were obtained, and both alloys coarsened at similar rates. A reasonably unimodal size distribution was maintained during aging. Particle shapes were cuboidal at particle sizes of 0.2  $\mu\text{m}$  and up and were spherical at particle sizes of 0.1  $\mu\text{m}$  and below. This was the case for both alloys, in the unimodal condition and in the commercially heat-treated condition.

Average particle sizes that develop during diffusion-controlled coarsening are expected to follow a relationship of the form

$$r^n - r_0^n = \alpha t \quad [1]$$

where  $r$  is the particle size,  $r_0$  is the initial size,  $t$  is the time,  $\alpha$  is a constant, and the exponent,  $n$ , is equal to 3 if classical Lifshitz-Slyozov-Wagner coarsening kinetics<sup>[3,4,5]</sup> are obeyed. Previous studies<sup>[5,6,7]</sup> of coarsening in nickel-base alloys with large  $\gamma'$  volume fractions have demonstrated that Eq. [1], with an exponent of 3, describes the behavior quite well, as long as coherency is maintained and the particles do not adopt a plate shape during aging.<sup>[6]</sup> A least-squares analysis of the 980 °C aging data using Eq. [1] resulted in a good fit, with an exponent of 3.7, which is reasonably close to the classical value and that of earlier studies.

The mechanical properties of unimodal alloys were studied at four nominal, average precipitate sizes: 0.1, 0.2, 0.35, and 0.7  $\mu\text{m}$ . Standard deviations were measured on average particle sizes and were found to be as follows: 0.02, 0.05, 0.06, and 0.16  $\mu\text{m}$ , in order of increasing  $\gamma'$  size from 0.1 to 0.7  $\mu\text{m}$ .

#### B. KM4 with Commercial Heat Treatment

Commercial heat treatments of turbine disk materials result in bimodal or trimodal particle-size distributions. A subsolvus heat treatment is typically used if the designer desires a fine grain size and the maximum strength. In this case, the material is partially solutionized just below the  $\gamma'$  solvus temperature, resulting in some undissolved  $\gamma'$  particles that coarsen, remain on the grain boundaries, and limit grain growth. This "primary"  $\gamma'$  is visible in the optical micrograph of Figure 1. The subsolvus treatment resulted in a grain size of about 6  $\mu\text{m}$ , and the primary  $\gamma'$  particles are seen as the large white precipitates which form a necklace structure and delineate the grain boundaries. If the material is subjected to a supersolvus heat treatment, which is a complete solutionizing treatment above the  $\gamma'$  solvus, the primary  $\gamma'$  dissolves, and the grains coarsen substantially. Figure 2 shows optical microstructures of the supersolvus heat treatment, including the lack of primary  $\gamma'$  particles and the larger grain size of about 55  $\mu\text{m}$ . At a finer length scale, both subsolvus and supersolvus heat treatments result in a bimodal particle-size distribution inside the grains, as shown in the TEM micrograph in Figure 3. The larger particles are referred to as "cooling"  $\gamma'$  and form upon cooling

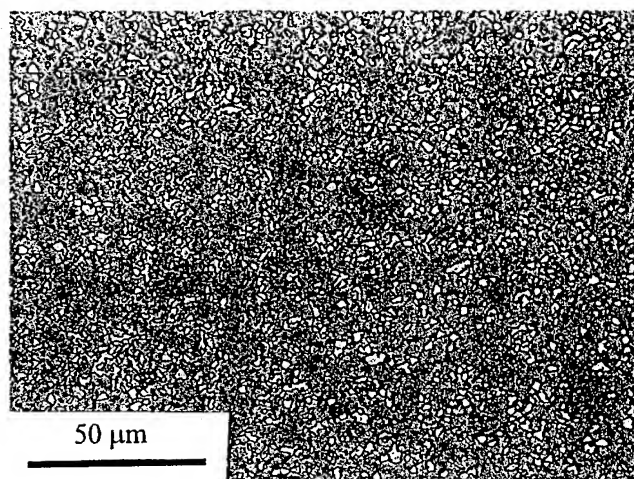


Fig. 1—Optical micrograph of subsolvus treated KM4, showing fine grain size and large, primary  $\gamma'$  precipitates, which did not dissolve during incomplete solution treatment.

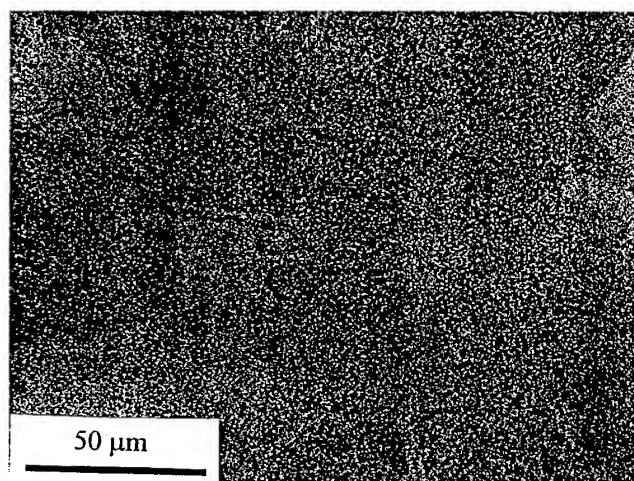


Fig. 2—Optical micrograph of supersolvus treated KM4, showing coarser grain size and lack of primary  $\gamma'$  precipitates.

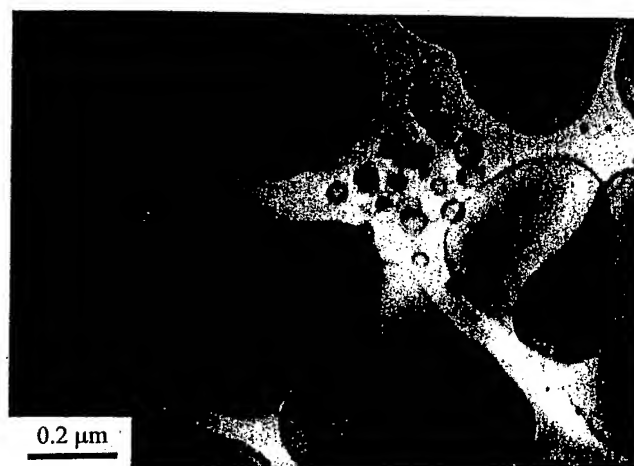


Fig. 3—Bright-field TEM micrograph of precipitate structure inside the grains, supersolvus heat treatment, showing bimodal  $\gamma'$  size distribution.  $g = \langle 111 \rangle$ .



Table II. Microstructures in KM4 (Commercial Heat Treatment)

	Primary $\gamma'$		Cooling $\gamma'$			Aging $\gamma'$			Total $f$
	Size ( $\mu\text{m}$ )	$f$	Size ( $\mu\text{m}$ )	Standard Deviation ( $\mu\text{m}$ )	$f$	Size ( $\mu\text{m}$ )	Standard Deviation ( $\mu\text{m}$ )	$f$	
Supersolvus	—	—	0.36	0.19	0.45*	0.04	0.03	0.10**	0.55
Subsolvus	~2	0.11*	0.29	0.14	0.35*	0.07	0.05	0.09**	0.55

\*Measured by quantitative stereology.

\*\*Obtained by subtracting measured  $f$ 's from total  $f$ . Total  $f$  of 0.55 was determined to a high degree of precision by another group.<sup>[2]</sup>

from the solutionizing treatment. The smaller particles are referred to as "aging"  $\gamma'$  and form either during the aging treatment or upon cooling from one of the aging steps. Therefore, subsolvus materials have a trimodal size distribution (primary  $\gamma'$  on the grain boundaries, and cooling and aging  $\gamma'$  inside the grains), while supersolvus materials have a bimodal size distribution (cooling and aging  $\gamma'$  throughout).

Quantitative analysis of the different  $\gamma'$  particle distributions was performed via TEM and SEM, and the results for average particle sizes and volume fractions, as well as standard deviations of average particle sizes, are given in Table II. Aging  $\gamma'$  volume fractions are approximately constant at about 0.10 for both treatments, although the size of the aging  $\gamma'$  particles was larger for the subsolvus material. Conversely, the supersolvus material had substantially more cooling  $\gamma'$  (45 vs 35 pct), and the size of the cooling  $\gamma'$  particles was larger for the supersolvus material (0.36 vs 0.29  $\mu\text{m}$ ). Finally, as already discussed, only the subsolvus heat treatment results in primary  $\gamma'$ , at a size of about 2  $\mu\text{m}$  and a volume fraction of 0.11. Fine carbides were observed occasionally in both microstructures, as well as in the unimodal heat treatments.

#### IV. RESULTS: YIELD STRENGTHS

Compression tests were conducted to between 2 and 5 pct plastic strain at 650 °C on R95 specimens that had been water quenched and aged, on KM4 specimens that had been oil quenched and aged, and on the commercially treated KM4 specimens. The unimodal R95 and KM4 specimens aged for 8 hours or longer at 980 °C had virtually identical average  $\gamma'$  sizes of approximately 0.2, 0.35, and 0.70  $\mu\text{m}$ . For the smallest  $\gamma'$  size of 0.1  $\mu\text{m}$ , the R95 was aged at 870 °C for 8 hours, while the KM4 specimen was aged for 15 minutes at 980 °C. Tests were conducted in displacement control. Average strain rates calculated from the displacement rates and the specimen heights were approximately  $10^{-3} \text{ s}^{-1}$  (designated *fast* in the remainder of this article) and  $10^{-5} \text{ s}^{-1}$  (designated *slow*).

The yield strengths (0.2 pct offset) are reported in Tables III (unimodal distributions) and IV (commercial heat treatments.) Average values are plotted as a function of cooling  $\gamma'$  size in Figure 4. The following conclusions can be drawn from these tables and figures.

- (1) For unimodal  $\gamma'$  microstructures, the R95 was stronger than the KM4 at all conditions tested, and both alloys were stronger at finer  $\gamma'$  sizes.
- (2) The commercial KM4 alloys were, however, substantially stronger than unimodal R95 at equivalent cooling

Table III. Yield Strengths of Unimodal R95 and KM4 at 650 °C

$\gamma'$ Size, $\mu\text{m}$	Yield Strength (0.2 Pct Offset), MPa			
	$10^{-3} \text{ s}^{-1}$		$10^{-5} \text{ s}^{-1}$	
	KM4	R95	KM4	R95
0.1	970*	1250**	1040*	1290**
0.22 (R95)				
0.20 (KM4)	840†	970**	850*	1020**
0.33 (R95)				
0.36 (KM4)	740†	880**	750*	870**
0.7 (R95)				
0.68 (KM4)	610**	790**	650*	890**

\*Average of two tests.

\*\*One test result.

†Average of three tests.

Table IV. Yield Strengths of KM4 at 650 °C (Commercial Heat Treatments)

$\gamma'$ Size, $\mu\text{m}$	Yield Strength (0.2 Pct Offset), MPa	
	$10^{-3} \text{ s}^{-1}$	$10^{-5} \text{ s}^{-1}$
Supersolvus		
0.36 (cooling $\gamma'$ )		
0.04 (aging $\gamma'$ )	960*	1050**
Subsolvus		
0.29 (cooling $\gamma'$ )		
0.07 (aging $\gamma'$ )	1080*	1160**

\*Average of two tests.

\*\*One test result.

$\gamma'$  sizes. Among the commercial alloys, the subsolvus treatment resulted in the highest strength.

- (3) Finally, it is also evident that the strength exhibited a negative strain-rate sensitivity, as the slower strain rates resulted in slightly higher strengths for nine out of the ten cases listed in Tables III and IV.

While the general trends in strength are self-consistent and consistent with literature results on similar alloys, and while there was not a large amount of scatter in the duplicate and triplicate tests that were conducted, it should be mentioned that small numbers of tests were generally conducted (one to three at each condition). Because of this, the degree of statistical confidence in the average strengths reported here could be better.

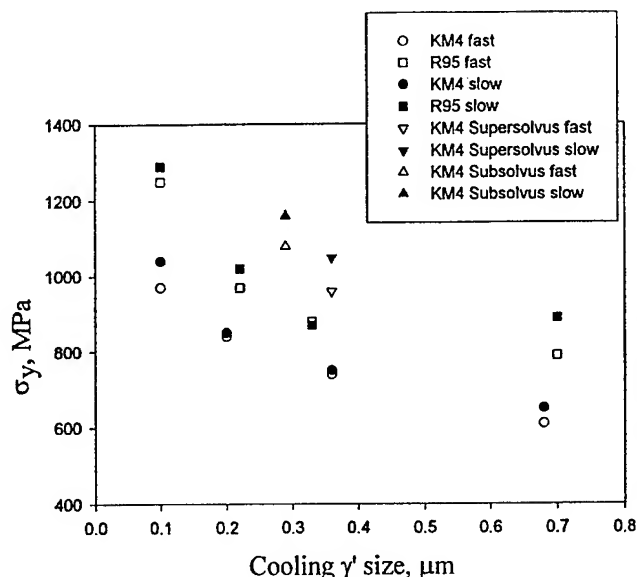


Fig. 4—Average yield strengths (0.2 pct offset) at various cooling  $\gamma'$  sizes and strain rates.

## V. RESULTS: DEFORMATION BEHAVIOR

### A. General Observations

The TEM foils were prepared and studied from compression specimens at each  $\gamma'$  size and strain-rate tested, for both the unimodal alloys and commercially treated alloys. The TEM foils from the creep-tested commercial KM4 specimen were also studied. The compression specimens which were examined had been subjected to 2 to 5 pct plastic strain at 650 °C. This section outlines the major trends that were observed, and details are provided in subsequent sections. In general, the following trends were observed in the unimodal KM4 and R95 alloys deformed in compression:

- (1) The initial defect density was extremely low. While it was not quantified, less than ten dislocations (and an occasional isolated stacking fault) were typically observed in an entire foil of an as-heat-treated material.
- (2) At the largest  $\gamma'$  size of 0.7  $\mu\text{m}$ ,  $\gamma'$  shearing by  $a/2\langle 110 \rangle$  dislocation pairs was the only deformation mechanism observed.
- (3) At smaller  $\gamma'$  sizes, an increasing number of superlattice intrinsic stacking faults (SISFs) were present after deformation. The density of faults increased as the  $\gamma'$  size decreased and as the strain rate decreased. These faults coexisted with  $a/2\langle 110 \rangle$  pairs.
- (4) The SISFs observed at the 0.2 and 0.35  $\mu\text{m}$   $\gamma'$  sizes were generally confined to individual cooling  $\gamma'$  precipitates, while those observed at the 0.1  $\mu\text{m}$   $\gamma'$  size extended long distances through both the matrix and the precipitates and often across entire grains.
- (5) The density of SISFs was significantly higher in R95 than in KM4 at equivalent particle sizes.

The following observations were made in the case of the commercially heat treated KM4:

- (1) All commercially treated compression specimens exhibited both  $a/2\langle 110 \rangle$  pairs and SISF deformation.
- (2) Subsolvus compression specimens generally had a lower

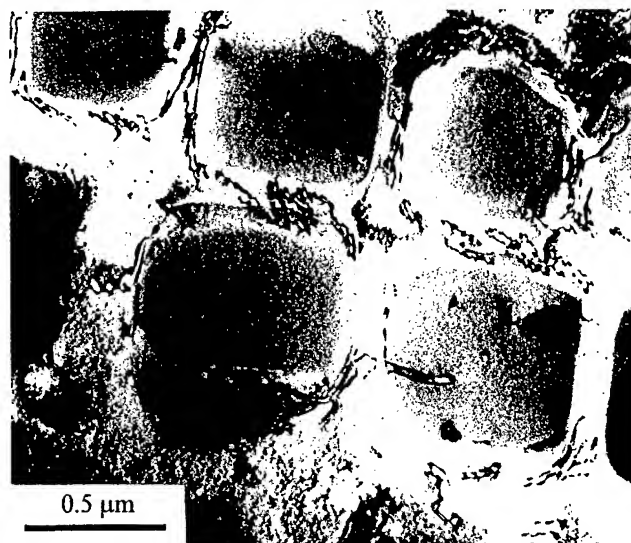


Fig. 5—Bright-field TEM micrograph of compression deformation in unimodal R95 with 0.7  $\mu\text{m}$   $\gamma'$  size. Deformation is solely by  $a/2\langle 110 \rangle$  pairs, seen most often pressed into precipitate interface. Fast test,  $\epsilon_p = 3.8$  pct, and  $g = \langle 200 \rangle$ .

density of SISFs than supersolvus specimens, and the SISFs in the subsolvus specimens were confined to the larger  $\gamma'$  precipitates; conversely, supersolvus compression specimens (which contained a higher density of SISFs) also contained many faults, which extended long distances across the matrix and precipitates.

- (3) In both microstructures, the slower strain rate qualitatively contained a higher density of SISFs.
- (4) For the creep-tested supersolvus specimen, extended stacking faults were found to exist in the matrix, as well as to extend over several  $\gamma'$  particles. No evidence of  $a/2\langle 110 \rangle$  pair shearing was found.

These observations are now discussed and supported in detail. Section V-B discusses unimodal microstructure deformation behavior, while Section V-C presents commercial microstructure deformation mechanisms. Finally, Section V-D includes a complete analysis of the stacking faults (which were found to be SISFs, as discussed in Section V-D) and the partial dislocations responsible for creating them.

### B. Unimodal Microstructures

Figure 5 shows a TEM micrograph of an R95 specimen with 0.7  $\mu\text{m}$   $\gamma'$  particles. Visible are a large number of dislocation pairs in the matrix, near the  $\gamma/\gamma'$  interfaces. There are also a few dislocations trapped inside  $\gamma'$  particles. Weak-beam analysis of several of these  $\gamma'$ -trapped dislocations indicated that they were antiphase boundary (APB) pairs. Other areas in the foils exhibited planar slip bands with dislocation pairs cutting the precipitates, and the structures observed in R95 and KM4 were similar. Therefore, it may be concluded that at the coarsest  $\gamma'$  sizes, both R95 and KM4 deform by the classical mechanism involving planar slip bands and APB-coupled  $a/2\langle 110 \rangle$  dislocation pairs.

Figure 6 is a micrograph of a KM4 specimen with 0.35  $\mu\text{m}$   $\gamma'$  deformed at the fast strain rate. In addition to interfacially trapped dislocations and dislocations within the  $\gamma'$ , there are a number of stacking faults (analyzed in the next section)



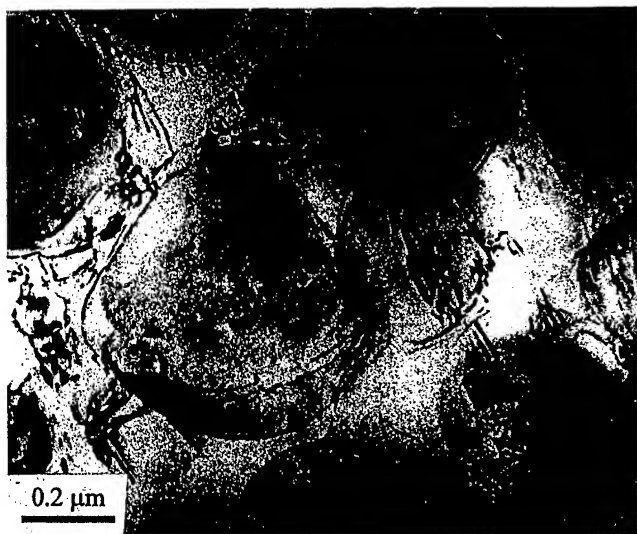


Fig. 6—Bright-field TEM micrograph of compressive deformation in unimodal KM4 with  $0.35\ \mu\text{m}$   $\gamma'$  size. Deformation debris consists of  $a/2\langle 110 \rangle$  pairs as well as isolated SISFs in the matrix and precipitates. Fast test,  $\epsilon_p = 2$  pct, and  $g = \langle 200 \rangle$ .



Fig. 7—Bright-field TEM micrograph of compressive deformation in unimodal R95 with  $0.2\ \mu\text{m}$   $\gamma'$  size.  $a/2\langle 110 \rangle$  pairs are present, but SISFs (still mostly confined to individual precipitates) are much more numerous. Slow test,  $\epsilon_p = 3.4$  pct, and  $g = \langle 200 \rangle$ .

visible in both the  $\gamma'$  and the matrix. Figures 7 and 8 show R95 specimens at  $0.2$  and  $0.1\ \mu\text{m}$   $\gamma'$  sizes, respectively, which contain an increasing density of stacking faults. It is clear from Figures 5 through 8 that the fault density increased substantially from the  $0.7$  to  $0.1\ \mu\text{m}$   $\gamma'$  size range. Another change which is visible in the micrographs is that the faults are generally confined to individual  $\gamma'$  particles or matrix channels in the  $0.2$  to  $0.35\ \mu\text{m}$   $\gamma'$  size range, while the faults extend across many  $\gamma'$  particles (and through the intervening matrix channels) at the smallest  $\gamma'$  size of  $0.1\ \mu\text{m}$ . Qualitative studies of a relatively large number of foils (two to three foils, for most conditions) indicated that the fault densities were noticeably higher at the slower strain rate.

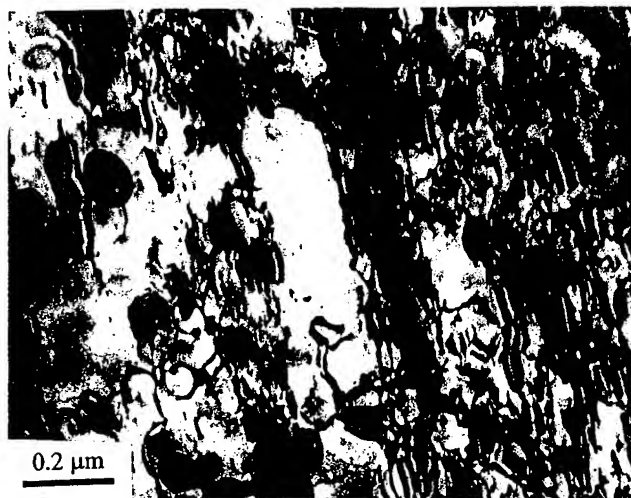


Fig. 8—Bright-field TEM micrograph of compression deformation in unimodal R95 with  $0.1\ \mu\text{m}$   $\gamma'$  size. High density of SISFs are present, which are no longer confined to individual precipitates. Slow test,  $\epsilon_p = 2.5$  pct, and  $g = \langle 200 \rangle$ .



Fig. 9—Bright-field TEM micrograph of compressive deformation in KM4 subsolvus material, showing unresolved APB pairs as well as SISFs, which are mostly confined to individual precipitates. Slow test,  $\epsilon_p = 2.1$  pct, and  $g = \langle 200 \rangle$ .

### C. KM4—Commercial Microstructures

Figure 9 shows a bright-field micrograph of a deformed bimodal subsolvus KM4 specimen tested at the slow strain rate. The faults were confined mainly within the particles, and dislocation pairs were present at the  $\gamma'/\gamma'$  interfaces. Few extended faults were observed in this case, but the SISF density was qualitatively higher than that observed in the unimodal alloys at the same primary  $\gamma'$  size. Weak-beam microscopy (not shown) also revealed the presence of APB-coupled dislocation pairs inside the  $\gamma'$  precipitates.

Figure 10 shows a bright-field micrograph of a deformed bimodal supersolvus KM4 specimen. While the photo is not ideal due to the rapidly changing thickness in this foil, it does illustrate a major difference in deformation modes between the subsolvus and supersolvus material. Figure 10

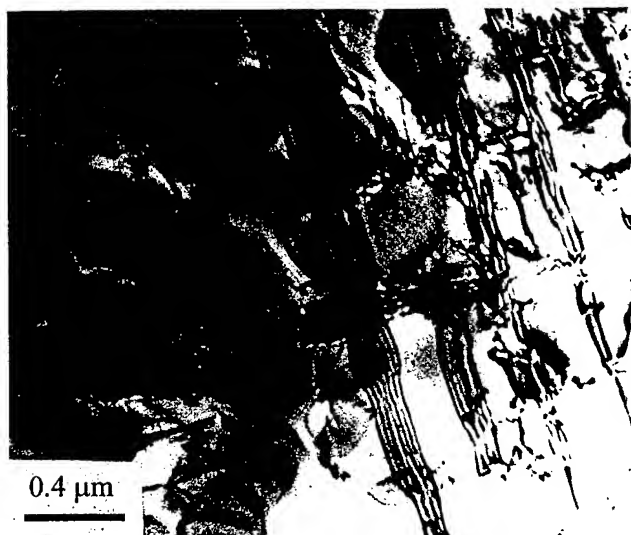


Fig. 10—Bright-field TEM micrograph of compression deformation in KM4 supersolvus material, showing SISFs, which are extended across multiple precipitates and the matrix. Fast test,  $\epsilon_p = 2.8$  pct, and  $g = \langle 200 \rangle$ .

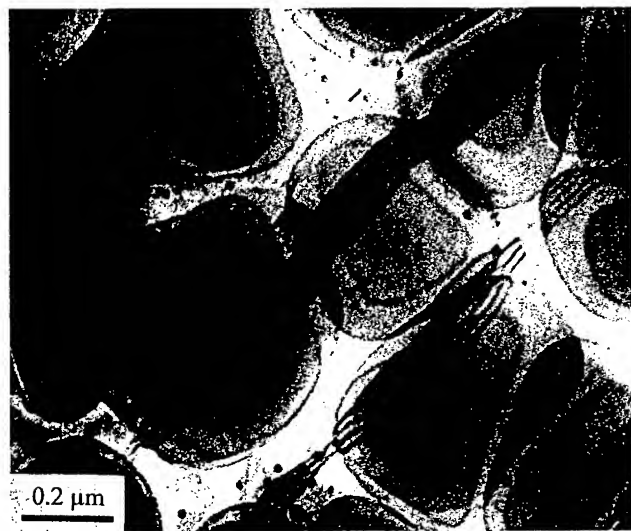


Fig. 11—Bright-field TEM micrograph of deformation in a supersolvus creep specimen (800 MPa, 650 °C, and  $\epsilon_p < 1$  pct). The only deformation debris observed was highly extended SISFs, and no  $a/2\langle 110 \rangle$  dislocations were present anywhere in the foils.  $g = \langle 111 \rangle$ .

shows that the SISFs observed in the supersolvus material were extended, traversing many precipitates and the intervening matrix. This mode was verified in another supersolvus foil, but was not observed in subsolvus foils. Therefore, the subsolvus material deformed in a similar manner to the unimodal microstructures with  $\gamma'$  sizes of 0.2 to 0.35  $\mu\text{m}$ , while the supersolvus material behaved like the unimodal microstructures with a  $\gamma'$  size of 0.1  $\mu\text{m}$ . This is explored further in Section VI-C.

A supersolvus creep specimen, which had been crept by GE at 800 MPa and 650 °C to a strain of less than 1 pct, was also studied by TEM. Figure 11 shows a typical deformation structure. The only deformation debris found in this specimen was SISFs, and no  $a/2\langle 110 \rangle$  dislocations were present in these foils. The SISFs are extended across many precipitates and the intervening matrix, similar to the faults seen



Fig. 12—Bright-field TEM micrograph showing heavy faulting mostly confined to individual particles, R95 with 0.2  $\mu\text{m}$   $\gamma'$  size. Slow test,  $\epsilon_p = 3.4\%$ , and  $g = [111]$ . The fault labeled "A" was analyzed in detail (Fig. 13).

in the supersolvus compression tests. The only difference is that the compression tests also contained a substantial number of  $a/2\langle 110 \rangle$  dislocations, in addition to the SISFs.

Finally, in the subsolvus specimens, the large, primary  $\gamma'$  particles observed in the grain boundaries did contain substantial dislocation debris after testing. The deformation substructures in the primary  $\gamma'$  were always APB-coupled pairs in planar bands, and no SISFs were observed.

#### D. Analysis of the Stacking Faults

As discussed previously, there were two different classes of stacking faults observed in this study. Faults that *extended* across multiple precipitates and the intervening matrix were found after compression testing in unimodal alloys with a  $\gamma'$  size of 0.1  $\mu\text{m}$  and after creep testing and compression testing of the supersolvus KM4. *Isolated* faults, confined to individual precipitates for the most part, were found in all other conditions except at the largest  $\gamma'$  size (which contained no faults). It was not possible to analyze the partial dislocations which created the extended faults, since the faults were so large, and since the leading and trailing partials were never both within the usable thin area of a foil. Standard dark-field imaging was used on the extended faults, however, and they were found to be always intrinsic in nature, confirming that they were SISFs.

It was possible to analyze the isolated faults. A detailed study was conducted on an unimodal R95 specimen with a 0.2  $\mu\text{m}$   $\gamma'$  size strained at the slow strain rate, which contained many isolated faults. Figure 12 shows the area of interest, which contained a number of faulted  $\gamma'$  particles. The marked fault, whose associated leading partial only traversed part of a  $\gamma'$  particle before the mechanical test was interrupted, was studied by standard bright-field, dark-field, and weak-beam techniques. The stereographic projection was determined, and ten different two-beam  $g$ -vectors were utilized, not all of which are presented here. Figures 13(a) and 14 show the fault in dark-field mode with the deviation parameter ( $w$ ) equal to 0. The  $[111]$   $g$ -vector points away from the light fringe in this imaging mode, consistent with a SISF.<sup>[8]</sup> The intrinsic nature of the fault was confirmed

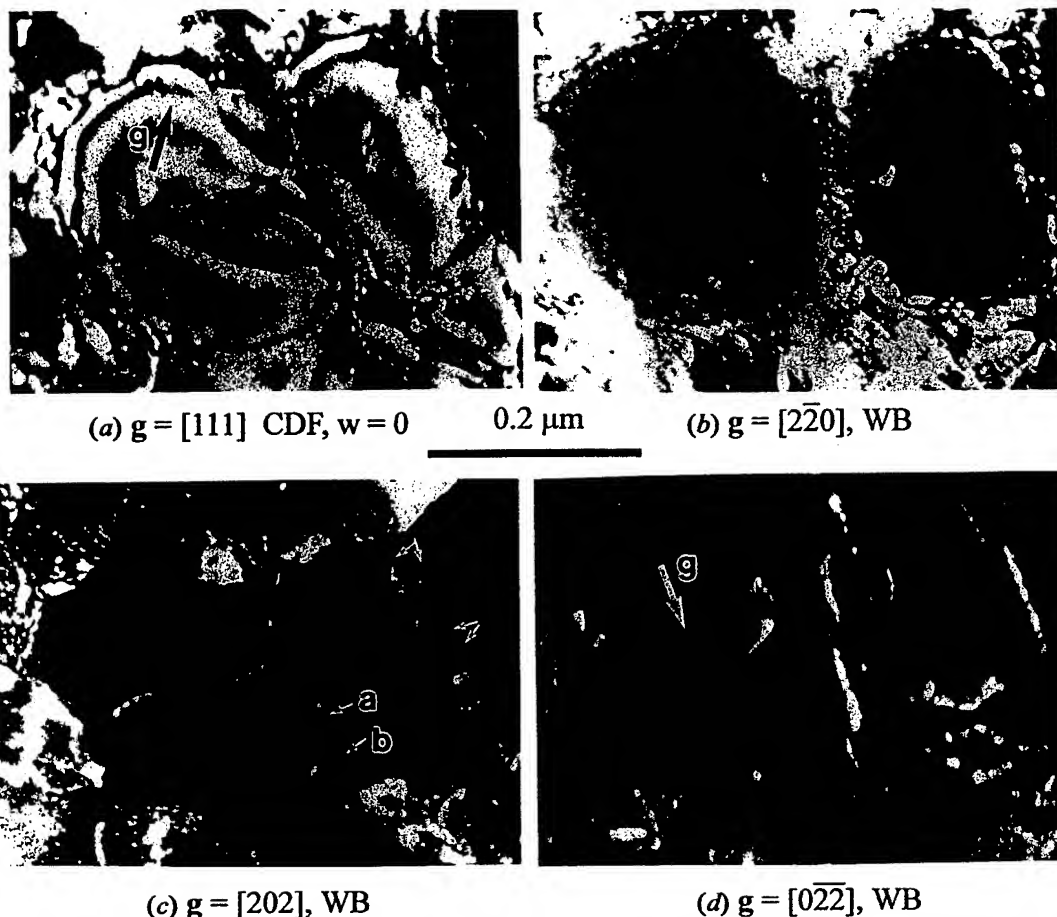


Fig. 13—(a) through (d) Selected TEM photos from an analysis involving ten unique  $g$  vectors in the area of Fig. 12. The fault marked “A” in Fig. 12 is contained in the precipitate on the left. CDF = centered dark field, and WB = weak beam micrograph. Refer to the text for discussion. In (c), pairs are indicated by double-arrows.

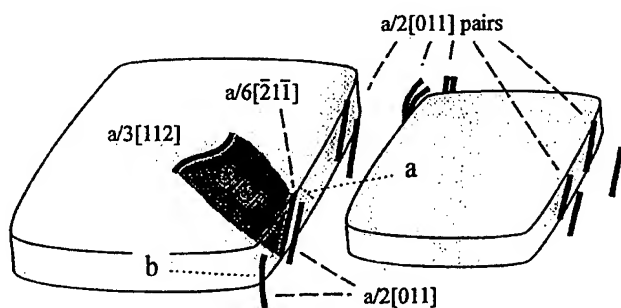


Fig. 14—Schematic diagram illustrating the dislocation and fault arrangement present in Figs. 12 and 13. Dislocations labeled “a” and “b” are also labeled in Fig. 13(c), but dislocation “a” actually consists of a superpartial and a Shockley.

with dark-field imaging under the  $\bar{2}00$  reflection as well. Figures 13(b) through (d) show three weak-beam micrographs in which the fault is invisible, satisfying  $g \cdot R_f = 0$  and indicating consistently that the fault lies on the  $(\bar{1}\bar{1}1)$  plane. The plane of the fault was confirmed by tilting experiments. These three reflections are included here because the lack of fault-fringe contrast aids in the identification of bounding partial dislocations.

A single SISF is created on  $(\bar{1}\bar{1}1)$  when the  $\gamma'$  is sheared by an  $a/3\langle 112 \rangle$  partial, formed by one of the following families of dislocation reactions:

$$\frac{a}{2} [101] \rightarrow \frac{a}{6} [12\bar{1}] + \frac{a}{3} [112] \quad [2]$$

$$a[101] \rightarrow \frac{a}{3} [2\bar{1}1] + \frac{a}{3} [112] \quad [3]$$

Four more similar reactions are possible on this plane, two each from the  $(\bar{1}\bar{1}1)[011]$  slip system and the  $(\bar{1}\bar{1}1)[\bar{1}10]$  slip system. The leading partial is invisible in Figure 13(b), for which  $g = [220]$ . Since  $g \cdot b = 0$  for this condition, and the fault created by the dislocation lies on  $(\bar{1}\bar{1}1)$ , the leading partial is unambiguously identified as  $(\bar{1}\bar{1}1)a/3[112]$ . Dislocation contrast under all other reflections verified this. This indicates that the fault was formed either by one of the two reactions given in Eqs. [2] and [3] or by one of the following two reactions, each of which can yield an  $a/3[112]$  partial and an SISF on  $(\bar{1}\bar{1}1)$ :

$$\frac{a}{2} [011] \rightarrow \frac{a}{6} [\bar{2}1\bar{1}] + \frac{a}{3} [112] \quad [4]$$

$$a[011] \rightarrow \frac{a}{3} [\bar{1}21] + \frac{a}{3} [112] \quad [5]$$

Identification of the trailing partial (and, therefore, the reaction) is not as straightforward as identifying the leading partial and the fault plane. Difficulties arise from the “pillow-shaped”  $\gamma'$  particles which result from electropolishing the matrix at a slightly higher rate than the  $\gamma'$  particles, as well

as the interfacial elastic strain and the possibility that more than one dislocation is in close proximity to the interface. For example, if the  $\gamma'$  is being sheared mainly by pairs of APB-coupled  $a/2[101]$  dislocations, and dissociation of a leading  $a/2[101]$  superpartial occurs suddenly at an interface by the reaction given in Eq. [2], then two dislocations will remain at the interface: the  $a/6[12\bar{1}]$ , which is in the interface and anchored to the fault, and the trailing  $a/2[101]$  superpartial, which is in the matrix close to the interface. A further complication is the presence of fault fringes under most two-beam imaging conditions.

Despite these difficulties, the analysis was able to identify the reaction with a good degree of certainty. Close inspection of Figure 13 reveals several features which clarify the analysis. First, there were a number of dislocation pairs in the matrix, some of which are marked in Figure 13(c).  $g \cdot b$  analysis revealed that these were  $a/2[011]$  dislocation pairs lying on  $(\bar{1}\bar{1}1)$ , the same plane as the SISF. Trace analysis revealed that the majority of these were nearly pure screw. Figure 13(d) shows that the projected line directions of these pairs are nearly parallel to the  $[022]$  vector corresponding to both  $g$  and  $b$ , and tilting analysis showed that the projected lengths were maximized under this reflection (as seen in Figure 13(d)), both consistent with the screw nature of the pairs. Second, the dislocation arrangements at the interface where the fault was formed are slightly complicated, but consistent with the rest of the structure, and with a decomposition of a leading  $a/2[011]$  superpartial by the reaction given in Eq. [4]. The dislocation marked "a" in Figure 13(c) is actually two dislocations, as can be seen by close inspection; the dislocation marked "b" in Figure 10(c), which was identified as an  $a/2[011]$  superpartial, is on a parallel slip plane (as can be seen in the tilting from Figure 13(c) to (d)) and had nothing to do with the interface reaction. This arrangement occurred as follows: a pair of  $a/2[011]$  partials, similar to those in close proximity to the fault (marked in Figure 13(c)), encountered a  $\gamma'$  particle; the leading partial decomposed by Eq. [4] to an  $a/3[112]$ , which sheared the  $\gamma'$  and created the SISF, as well as an  $a/6[12\bar{1}]$ , which remained trapped at the interface due to the APB energy (APBE); the  $a/6[12\bar{1}]$  (in the interface) and the trailing  $a/2[011]$  (in the matrix) did not shear the precipitate and were left behind in close proximity to each other. Figure 14 shows a schematic diagram of the dislocation arrangement in Figures 12 and 13 and helps to visualize the development of the substructure. The  $g \cdot b$  analyses using the micrographs in Figure 13, as well as seven other unique weak-beam  $g$ -vectors, verified the dislocation arrangement sketched in Figure 14 to a high degree of confidence. This arrangement is consistent with many recent analyses conducted on similar alloys which had been subjected to creep at 650 °C to 850 °C.<sup>[9-16]</sup>

It should be pointed out that while pairs of  $a/2\langle 110 \rangle$  dislocations were often observed in association with faults, SISF formation only requires a single dislocation to decompose at the interface. Pairs are naturally present because the dominant slip mode is APB-coupled  $a/2\langle 110 \rangle$  pairs, even when a substantial number of faults are present.

## VI. DISCUSSION

### A. Effects of Faulting on Mechanical Behavior

In all cases, during compression testing,  $\gamma'$  shearing by  $a/2\langle 110 \rangle$  pairs was observed. This was the only deformation

mechanism observed at the largest unimodal  $\gamma'$  size of 0.7  $\mu\text{m}$  and occurred even in the finest unimodal  $\gamma'$  size of 0.1  $\mu\text{m}$ . However, as the  $\gamma'$  size was reduced, an increasing density of SISFs was observed. The presence of a large number of SISFs in a thin foil can be misleading, however, in that an extended fault is left behind by the passage of a single partial dislocation with a slip offset of only 0.2 nm. If the fault is extended, as in the case of the creep specimen, the supersolvus KM4 compression specimens, and the 0.1  $\mu\text{m}$  unimodal  $\gamma'$  sizes, then the slip vector will be  $\langle 112 \rangle$  for the partials causing the faults and  $\langle 110 \rangle$  for the APB pairs. This is the case because the  $a/2\langle 110 \rangle$  superpartial that decomposed at the interface recombined on exiting the  $\gamma'$  particle and left behind a faulted loop as debris.<sup>[9-12,14]</sup> If the faults are confined to the  $\gamma'$  particles, as in the case of the subsolvus alloy and the 0.2 to 0.35  $\mu\text{m}$  unimodal alloys, then the slip vector will be  $\langle 110 \rangle$ .

The effects of the faulting mechanism on the mechanical properties of high-volume-fraction superalloys are generally unknown, with the exception of the primary creep of blade alloys at about 750 °C. In that case, it is well established that the macroscopic slip vector is  $\langle 112 \rangle$ , as observed by lattice rotations of single crystals.<sup>[17,18]</sup> This is consistent with the present study at 650 °C, where the deformation mode after creep was found to be solely one that leaves extended stacking faults behind (Figure 11). However, the dislocation reaction responsible for the  $\langle 112 \rangle$  slip is still uncertain; Leverant and Kear<sup>[17]</sup> proposed a mechanism involving SISF/superlattice extrinsic stacking-fault pairs and a combination of different  $a/2\langle 110 \rangle$  dislocations at the interface, but, to our knowledge, this mechanism has never been validated by more-recent researchers. The most likely reaction, based on this study and others,<sup>[9-16]</sup> seems to be the decomposition of an  $a/2\langle 110 \rangle$  dislocation (via Eq. [2]), which does not recombine on exiting the particles. In this case, the net slip vector is  $\langle 112 \rangle$  (consistent with the lattice rotation studies), and large extended faults similar to those shown in Figures 8, 10 and 11 should be found.

Additional effects of the presence of the fault and the partial dislocations which cause them are likely to exist, even when the faulting mechanisms coexist with APB-pair deformation. For example, Milligan and Antolovich<sup>[14,19]</sup> proposed that the unique behavior of PWA1480 single crystals, which exhibit a 20 pct reduction in strength from room temperature to 400 °C, correlated exactly with the temperature dependence of an SISF-based mechanism. Even if the faults do not have a large effect on yield strength, it seems reasonable that the deformation debris seen in Figures 6 through 10 would have some effect on strain hardening and, particularly, on cyclic strain hardening and slip reversibility during fatigue deformation. Such effects might explain some of the large differences in the fatigue behavior of superalloys with similar microstructures and yield strengths. This is a complex problem that deserves further attention.

### B. Influence of Microstructure and Strain Rate on Deformation

It has been demonstrated here that there were an increasing number of SISFs in the deformation substructures (1) as the  $\gamma'$  size was reduced; (2) as the strain rate was reduced; and (3) in bimodal alloys, which contained very fine, aging  $\gamma'$  particles. As discussed subsequently, these observations are

consistent with those found for similar alloys in earlier studies. However, generally, these earlier studies were conducted on creep specimens; it was somewhat surprising to find such a high density of SISF debris in these alloys after testing at conventional strain rates.

Concerning particle size, Caron *et al.*'s study<sup>[11]</sup> of particle shearing during creep in CMSX-2 (a blade alloy with a high volume fraction of  $\gamma'$ ) at 760 °C suggested that, for a given SISF energy, shearing of particles by SISFs became more common as the particle size decreased and as the particle shape became more spherical. This is accordance with the observations in this study. Mukherji *et al.*<sup>[15]</sup> studied stacking-fault formation in an IN738LC alloy, which had been heat treated to give unimodal  $\gamma'$  sizes of about 0.09 and 0.4  $\mu\text{m}$ , then subjected to mechanical testing at elevated temperatures. At large particle sizes during creep, deformation consisted of APB pairs and SISFs which were confined to individual particles. However, for small particle sizes, deformation primarily consisted of extended stacking faults which spread through the matrix. These results are quite similar to those reported in the current study. Bhowal *et al.*<sup>[13]</sup> observed similar deformation in R95 at 650 °C, during creep and stress-rupture testing. They observed that specimens having small cooling  $\gamma'$  sizes exhibited planar slip and extended stacking faults, while specimens with a large  $\gamma'$  size deformed by bowing and looping of  $a/2\langle 110 \rangle$  partials.

In the bimodal alloys studies here, there was a propensity to form extended stacking faults, which is likely due to the presence of the fine  $\gamma'$  in these structures. Quantitative data from this study shows an interesting effect of  $\gamma'$  size in the bimodal alloys, which were commercially heat treated: the supersolvus specimens contained substantially finer aging  $\gamma'$  than the subsolvus specimens (40 nm for supersolvus vs 70 nm for subsolvus, Table II), and this corresponded to a change in SISF structure from extended faults (40 nm for supersolvus, Figure 10) to faults which were contained inside  $\gamma'$  precipitates (70 nm for subsolvus, Figure 9). This is completely consistent with the unimodal alloys, which underwent a transition from isolated faults inside precipitates to extended faults as the  $\gamma'$  decreased. However, it should be noted that the cooling  $\gamma'$  is actually *larger* in the supersolvus material than in the subsolvus. Therefore, in the commercial alloys at least, it appears that the fine, aging  $\gamma'$  is more important to the nature of the SISFs produced than the cooling  $\gamma'$ . As the aging  $\gamma'$  size decreases, the propensity for the  $a/2\langle 110 \rangle$  partials to recombine after exiting the precipitates is reduced, leading to macroscopic  $\langle 112 \rangle$  slip and extended faults. This effect of the fine  $\gamma'$  particles on deformation mechanisms merits further research.

Concerning strain-rate effects, the fault density was found to increase in specimens tested at lower strain rates, and this was more pronounced for the unimodal alloys than for the bimodal alloys. Mukherji *et al.*<sup>[15]</sup> reported similar behavior for unimodal IN738, and most of the studies in the literature of SISFs were produced by creep loading. The occurrence of such high densities of SISFs in this study was, therefore, surprising, because of the relatively modest temperatures and tensile test-type strain rates. It is possible that the dissociation reaction in Eq. [2] is thermally activated, thus facilitating a higher density of faults at slower strain rates.

### C. Strength of Commercial Disk Alloys

Due to processing constraints (section size and quenching limitations), commercial disk alloys have bimodal  $\gamma'$  sizes, with cooling  $\gamma'$  sizes between 0.1 and 0.5  $\mu\text{m}$ . It is of interest to develop accurate, predictive models of mechanical behavior as a function of heat treatment and microstructure in this critical range of cooling  $\gamma'$  sizes. These models can be input into computational design schemes to accelerate new-material introduction and to facilitate the development of new alloys. This section presents a preliminary analysis of these two alloys in the cooling  $\gamma'$  size range of interest.

Inspection of Figure 4 and Tables III and IV in the cooling  $\gamma'$  size range from 0.1 to 0.5  $\mu\text{m}$  reveals the following trends: (1) unimodal R95 is about 15 pct stronger than unimodal KM4; (2) subsolvus and supersolvus KM4 are both about 25 pct stronger than unimodal KM4 at an equivalent cooling  $\gamma'$  size; and (3) it appears that the increase in strength (at equivalent cooling  $\gamma'$  sizes) due to the commercial heat treatments is larger for the subsolvus heat treatment than the supersolvus, but further testing is necessary to validate this statistically. Any useful model of the yield strength will have to be consistent with these trends. An excellent review of the pertinent issues is contained in the monograph of Nembach.<sup>[20]</sup> Several groups have proposed strength models for high-volume-fraction superalloys,<sup>[21–28]</sup> and two have attempted to model bimodal microstructures.<sup>[29,30]</sup> However, the combination of large volume fractions and bimodal distributions appears to remain a significant, unsolved challenge. This is complicated further by a Hall–Petch effect, as the subsolvus and supersolvus materials have grain sizes which are approximately one order of magnitude different. This is a subject of current research and will not be discussed further here. Still, models developed for large volume fractions with unimodal distributions lent some insight into the differences between R95 and KM4 and are briefly discussed subsequently.

In this article, it was demonstrated that although SISFs are present in alloys with cooling  $\gamma'$  sizes in the range of interest, they were always accompanied by APB pairs (except in the case of creep in commercial alloys). Therefore, let us assume for the case of strength modeling that the SISFs might affect strain hardening and slip reversibility in fatigue, but that the yield strength at 650 °C is controlled by APB-coupled  $a/2\langle 110 \rangle$  dislocation pairs. This is consistent with our observation that  $a/2\langle 110 \rangle$  dislocations are necessary at the  $\gamma/\gamma'$  interface to form SISFs; their presence requires that the operation of an  $a/2\langle 110 \rangle$  dislocation source (*i.e.*, yielding) must precede SISF formation. With this assumption, existing models of strength can be applied to unimodal KM4 and R95 at 650 °C.

It has been proposed<sup>[20,22–30]</sup> that a generalized, empirical superposition law is required to accurately model superalloy strength, such that

$$\tau_y^k = \tau_m^k + \Delta\tau_p^k \quad [6]$$

where  $\tau_y$  is the shear strength of the alloy,  $\tau_m$  is the shear strength of the matrix,  $\Delta\tau_p$  is the increase in shear strength due to the precipitates, and  $k$  is an empirical exponent that varies between 1 and 2. At the peak strength in unimodal alloys containing large volume fractions of  $\gamma'$  precipitates, these types of models postulate that



$$\Delta\tau_p^{\text{peak}} = \frac{\Gamma}{b} \frac{\omega_r}{(\pi\omega_q)^{1/2}} f^{1/2} \psi \quad [7]$$

where  $\Gamma$  is the APB energy,  $f$  is the volume fraction of precipitates,  $\omega_r$  and  $\omega_q$  are statistical parameters related to the particle-size distributions, and  $\psi$  is the Schwarz-Labusch correction factor for large volume fractions.<sup>[20,22]</sup> When comparing similar alloys at equilibrium volume fractions and with similar statistical distributions of precipitates, most of the terms in Eq. [7] can be grouped into one constant,  $c$ , and Eq. [6] becomes

$$\tau_y^k = \tau_m^k + (c\Gamma)^k \quad [8]$$

Nitz and Nembach<sup>[27]</sup> determined that  $\tau_m = 40$  MPa and  $k = 1.1$  at 650 °C for NIMONIC 105,\* which has a similar

\*NIMONIC 105 is a trademark of INCO Alloys International, INCO, Huntington, WV.

alloy composition and  $\gamma'$  volume fraction as R95 and KM4. NIMONIC 105 has a yield strength in shear in excess of 300 MPa, indicating that  $\Delta\tau_p$  accounts for approximately 90 pct of the alloy strength. Therefore, the only parameter that can have a substantial effect on strength, keeping equivalent volume fractions and particle size distributions, is the APBE ( $\Gamma$ ). A similar conclusion can be drawn based on the classical Copley-Kear static model of strength for high-volume-fraction nickel-base superalloys,<sup>[21]</sup> which proposed that

$$\tau_y = \frac{\Gamma}{2b} - \frac{T}{br} + \frac{(\tau_m + \tau_p)}{2} \quad [9]$$

where  $T$  is the line tension,  $r$  is the average particle radius in the slip plane, and  $\tau_m$  and  $\tau_p$  are the friction stresses of the matrix and precipitates. The term in  $\Gamma$  accounts for over 80 pct of the strength,<sup>[21]</sup> again implying that a change in the APBE from one alloy to another with similar microstructures is the only parameter that is able to account for substantial changes in yield strength.

Unimodal R95 at 650 °C is approximately 15 to 20 pct stronger than that of unimodal KM4 at equivalent precipitate size and strain rate. Assuming that the exponent  $k$  is in the range of 1.1 for both KM4 and R95 (as was the case for NIMONIC 105, a similar alloy),<sup>[27]</sup> this implies that the APBE of R95 is approximately 20 pct higher than that of KM4. Inspection of Table I shows that the significant differences between the alloys are that KM4 has more cobalt and titanium, but less niobium and tungsten, while the remaining elements are similar. Cobalt partitions to the matrix and has little effect on the APBE.<sup>[31]</sup> Tungsten, niobium, and titanium all increase the APBE.<sup>[32,33,34]</sup> The sum of W + Nb + Ti in R95 is 9.5 pct, while it is only 6 pct for KM4. Further, R95 contains almost twice as much Nb as KM4, and Nb is the most potent APBE booster in the alloys.<sup>[33,34]</sup>

The increase in APBE from KM4 to R95 is apparent not only in the higher strength, but also in the deformation substructures. As discussed in Section V, R95 contained a significantly higher number of SISFs after deformation than KM4 at the same particle size. The SISFs become more energetically favorable as the ratio of SISF energy to APB energy decreases,<sup>[14,35]</sup> so it is not surprising that an increase in APBE of 20 pct would result in a higher density of SISFs, as was observed.

## VII. CONCLUSIONS

Deformation mechanisms and strengths in powder metallurgy turbine disk alloys are influenced significantly by microstructure. The main conclusions from this study of RENE'95 and KM4, deformed at 650 °C, are as follows:

In both alloys, unimodal microstructures tested in compression at tensile-test strain rates deformed solely by APB pairs at the largest  $\gamma'$  size of 0.7  $\mu\text{m}$ . As the precipitate size was reduced, the materials tended to deform by both APB pairs and SISFs, which formed by the decomposition of an  $a/2\langle 110 \rangle$  superpartial in the precipitate/matrix interface. At  $\gamma'$  sizes of 0.2 to 0.35  $\mu\text{m}$ , the SISFs were isolated within single particles, while at 0.1  $\mu\text{m}$ , the faults were widely extended across entire grains. The fault density increased with decreasing particle size and strain rate. These trends, observed in compression testing, are consistent with earlier studies of similar alloys which were tested in creep.

Commercially heat-treated alloys, containing a bimodal distribution of  $\gamma'$  particles, exhibited significantly more faulting than unimodal alloys at the same cooling  $\gamma'$  size. This augmentation of the faulting is due to the presence of the fine  $\gamma'$  particles. The supersolvus heat-treated material, which contained the finest aging  $\gamma'$  particles, contained a higher density of faults than either the subsolvus or unimodal material. Further, faults were typically extended in the supersolvus material and were confined to single particles in the subsolvus material, implying that the aging  $\gamma'$  precipitates had an influence on the partials as they exited the precipitates.

The presence of these faults on mechanical behavior is unknown. They probably do not have a large effect on yield strength, but it seems reasonable that they would affect strain hardening, cyclic strain hardening, slip planarity, slip reversibility, and, therefore, fatigue performance.

R95 was stronger than KM4 in all conditions tested, and this corresponded to a higher APBE in the case of R95. This increase in APBE was accompanied by an increase in SISF density after deformation, compared to KM4 at equivalent precipitate sizes. Commercial heat treatments, which resulted in bimodal  $\gamma'$  size distributions, were substantially stronger than unimodal alloys at an equivalent  $\gamma'$  size. No model of strength in bimodal particle distributions at high volume fractions was found to be suitable for these materials.

Supersolvus KM4, tested in creep at 650 °C to less than 1 pct strain, did not contain any evidence of APB-pair shearing. Only extended SISFs were observed, implying a macroscopic  $\langle 112 \rangle$  slip vector.

## ACKNOWLEDGMENTS

We gratefully acknowledge the financial support of the National Science Foundation, under Grant No. DMR-92-57465, which was monitored by Dr. Bruce MacDonald, as well as the financial and laboratory support of GE Aircraft Engines, under the direction of Dr. Ken Bain. Latter stages of the work were supported by the Air Force Office of Scientific Research under the "MURI on High Cycle Fatigue," Grant No. F49620-96-1-0478, through a subcontract from the University of California at Berkeley.

## REFERENCES

1. D.D. Krueger, J.F. Wessels, and K-M. Chang: U.S. Patent 5,143,563, Sept. 1, 1992.
2. E.S. Huron: GE Aircraft Engines, Evendale OH, private communication, 1996.
3. I.M. Lifshitz and V.V. Slyozov: *J. Phys. Chem. Solids*, 1961, vol. 19, pp. 35-50.
4. C. Wagner: *Z. Elektrochem.*, 1961, vol. 65, pp. 581-91.
5. A.J. Ardell: *Proc. Int. Symp. on Mechanisms of Phase Transformations in Crystalline Solids*, Institute of Metals Monograph and Report Series, 1968, pp. 111-16.
6. R.A. MacKay and M.V. Nathal: *Acta Metall. Mater.*, 1990, vol. 38, pp. 993-1005.
7. H.A. Calderon, P.W. Voorhees, J.L. Murray, and G. Kostorz: *Acta Metall. Mater.*, 1993, vol. 42, pp. 991-1000.
8. D.B. Williams and C.B. Carter: *Transmission Electron Microscopy*, Plenum Press, New York, NY, 1996, pp. 385-87.
9. A.J. Huis in't Veld, G. Boom, P.M. Bronsveld, and J.T.M. de Hosson: *Scripta Metall.*, 1985, vol. 19, pp. 1123-28.
10. M. Condat and B. Décamps: *Scripta Metall.*, 1987, vol. 21, pp. 607-12.
11. P. Caron, T. Khan, and P. Veyssière: *Phil. Mag. A*, 1988, vol. 57, pp. 859-75.
12. R. Bonnet and A. Ati: *Acta Metall.*, 1989, vol. 37, pp. 2153-69.
13. P.R. Bhowal, E.F. Wright, and E.L. Raymond: *Metall. Trans. A*, 1990, vol. 21A, pp. 1709-17.
14. W.W. Milligan and S.D. Antolovich: *Metall. Trans. A*, 1991, vol. 22A, pp. 2309-18.
15. D. Mukherji, F. Jiao, W. Chen, and R.P. Wahi: *Acta Metall.*, 1991, vol. 39, pp. 1515-24.
16. T. Link and M. Feller-Kniepmeier: *Metall. Trans. A*, 1992, vol. 23A, pp. 99-105.
17. G.R. Leverant and B.H. Kear: *Metall. Trans.*, 1970, vol. 1, pp. 491-98.
18. R.A. MacKay and R.D. Maier: *Metall. Trans. A*, 1982, vol. 13A, pp. 1747-54.
19. W.W. Milligan and S.D. Antolovich: *Metall. Trans. A*, 1989, vol. 20A, pp. 1888-89.
20. E. Nembach: *Particle Strengthening of Metals and Alloys*, Wiley and Sons, New York, NY, 1997.
21. S.M. Copley and B.H. Kear: *Trans. TMS-AIME*, 1967, vol. 239, pp. 984-92.
22. A.J. Ardell, V. Munjal, and D.J. Chellman: *Metall. Trans. A*, 1976, vol. 7A, pp. 1263-68.
23. B. Reppich: *Acta Metall.*, 1982, vol. 30, pp. 87-94.
24. B. Reppich, P. Schepp, and G. Wehner: *Acta Metall.*, 1982, vol. 30, pp. 95-104.
25. E. Nembach, S. Schänzer, W. Schröer, and K. Trinckauf: *Acta Metall.*, 1988, vol. 36, pp. 1471-79.
26. S. Schänzer and E. Nembach: *Acta Metall. Mater.*, 1992, vol. 40, pp. 803-13.
27. A. Nitz and E. Nembach: *Metall. Mater. Trans. A*, 1998, vol. 29A, pp. 799-807.
28. A. Nitz and E. Nembach: *Mater. Sci. Eng.*, 1999, vol. A263, pp. 15-22.
29. B. Reppich, W. Kuhlein, G. Meyer, D. Puppel, M. Schulz, and G. Schumann: *Mater. Sci. Eng.*, 1986, vol. 83, pp. 45-63.
30. D.J. Chellman, A.J. Luévano, and A.J. Ardell: *Proc. 9th Int. Conf. on the Strength of Metals and Alloys*, D.G. Brandon, R. Chaim, and A. Rosen, eds., Freund Publishing House, London, 1991, vol. 1, p. 537.
31. R.N. Jarrett and J.K. Tien: *Metall. Trans. A*, 1982, vol. 13A, pp. 1021-32.
32. J.P. Collier, P.W. Keefe, and J.K. Tien: *Metall. Trans. A*, 1986, vol. 17A, pp. 651-61.
33. B.H. Kear and D.P. Pope: *Refractory Alloying Elements in Superalloys*, J.K. Tien and S. Reichman, eds., ASM, Metals Park, OH, 1984, pp. 135-51.
34. L.R. Curwick: Ph.D. Thesis, University of Minnesota, Minneapolis, MN, 1972.
35. K. Suzuki, M. Ichihara, and S. Takeuchi: *Acta Metall.*, 1979, vol. 27, pp. 193-200.

## **In Situ Study of High Frequency Fatigue Crack Propagation in a Single Crystal Superalloy**

Santo A. Padula II,<sup>1</sup> Amit Shyam,<sup>2</sup> David L. Davidson,<sup>3</sup> and Walter W. Milligan<sup>2</sup>

1) NASA Glenn Research Center  
Cleveland, Ohio 44135

2) Department of Materials Science and Engineering  
Michigan Technological University, Houghton, MI 49931

3) Southwest Research Institute  
San Antonio, TX 78228

### **Abstract**

High frequency fatigue crack propagation tests were conducted in situ, in a scanning electron microscope, on single crystals of the nickel-base superalloy Rene N5. The threshold was found to be around 2 MPa $\sqrt{m}$ , and the FCP curve appeared to be consistent with that of a similar polycrystalline alloy but with a lower threshold. Crack propagation was observed to occur on {111} as well as {001} planes at low  $\Delta K$ . Strain maps were measured ahead of the crack tip with the DISMAP stereo-imaging technique. SEM images of plasticity associated with the crack tip indicated plastic zone sizes mainly consistent with isotropic linear elastic fracture mechanics estimates, but the plasticity was concentrated in highly planar slip bands parallel to the crack, and the shape of the plastic zone and strain distribution were not isotropic. It is suggested that the threshold behavior may be related to the fracture surface roughness, since the threshold increased in from single crystal to fine-grain polycrystal to coarse-grain polycrystal, in the same order as the fracture surface roughness.

Fatigue – David L. Davidson Symposium  
Edited by K.S. Chan, P.K. Liaw,  
R.S. Bellows, T.C. Zogas and W.O. Soboyejo  
TMS (The Minerals, Metals & Materials Society), 2002



## Introduction

High cycle fatigue has emerged as one of the most common failure mechanisms in military turbine engines [1]. Because the operating frequencies under vibratory high cycle fatigue are so high, a design philosophy has emerged which is based on the concept of fatigue crack propagation thresholds [2, 3]. For this reason, threshold behavior of nickel-base superalloys used in turbine engines has been studied in this research.

In related research, fatigue crack propagation thresholds were determined for a polycrystalline nickel-base turbine disk alloy at ambient and elevated temperatures, and frequencies up to 1,000 Hz [3,4]. Those experiments were conducted with a servohydraulic testing machine, on bulk specimens. In this study, tests were conducted in situ, in a scanning electron microscope equipped with a resonant loading stage capable of frequencies up to 2,000 Hz. Experiments were conducted on the nickel-base superalloy single crystal Rene N5 [5], in order to examine micromechanisms of fatigue crack propagation for this material.

The polycrystalline alloy has about the same volume fraction of strengthening  $\gamma'$  as the single crystal; its microstructure and mechanical properties are fully described in [6].

## Experimental Procedures

A specially designed and built resonant loading stage was fitted inside a scanning electron microscope (SEM) at Southwest Research Institute (SwRI). This instrument, described in [7], is capable of loading specimens at frequencies up to 2 kHz, depending on the specimen geometry and associated resonant frequency. The specimens cannot be imaged while they are vibrating, but can be imaged intermittently by stopping the vibration and holding the mean load.

Single crystals of Rene N5 were cycled along  $\langle 001 \rangle$  at a load ratio of 0.8 and a frequency of 1,800 Hz. The specimens had been pre-cracked with a semi-elliptical surface crack, by EDM and high frequency loading, with a total crack length of approximately 1 mm. The samples had a hourglass shape with a rectangular cross section approximately 15 mm wide by 8 mm thick.

Fatigue crack propagation rates and thresholds were determined by intermittently interrupting the loading and measuring the crack length in the SEM, and using a standard secant method. Thresholds were determined by load shedding, and were compared to those for the polycrystalline alloy.

Strain maps were generated by the DISMAP SEM stereo-imaging technique developed at SwRI [8]. The procedure is as follows: Images are taken at maximum load and minimum load; following this, a feature recognition algorithm is used to discern locations that appear in both images. The displacement vectors between features are then determined, and through numeric differentiation, the strains are calculated. The strain maps were compared to surface slip traces and linear elastic fracture mechanics theory to study the plastic zone geometry in these single crystals.

## Results

Figure 1 shows the near-threshold fatigue crack propagation curve determined by load shedding for the single crystal material, in comparison with two different microstructures of the polycrystalline alloy which had been cycled in a servohydraulic machine under similar conditions. The single crystal was cycled at 1,800 Hz and  $R = 0.8$ , while the polycrystals were cycled at 1,000 Hz and  $R = 0.7$ , all at room temperature. The curves for the polycrystal were obtained in increasing K tests, and therefore more of the Paris regime is presented for those tests.

One may observe that the FCP curve for the single crystal material appears to be consistent with the curves for the polycrystalline material. That is, had the polycrystal not reached a threshold value of  $\Delta K$  on load shedding, its FCP curve for both microstructures would have joined the single crystal curve. This indicates that the FCP rates and mechanisms in the Paris regime are similar for the single crystal and both the fine-grain and coarse-grain polycrystal, but that the threshold behavior is a strong function of microstructure.

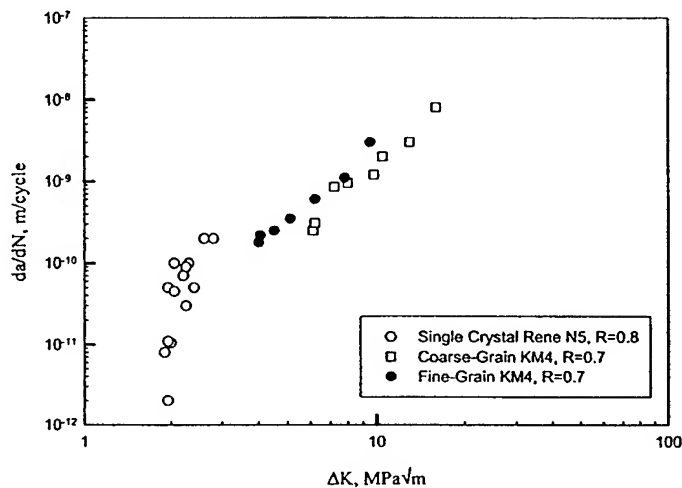


**Figure 1:** Crack growth rate data for polycrystalline KM4 and single crystalline Rene N5. Grain size for coarse-grain KM4 was 55  $\mu\text{m}$ , while that for fine-grain KM4 was 6  $\mu\text{m}$ .

SEM photomicrographs obtained during growth in the single crystal specimen indicate growth along slip bands which extend some 20-30  $\mu\text{m}$  ahead of the crack tip, Figure 2. Such slip band extension is unlikely in the polycrystalline material due to the existence of the grain boundaries. Other growth behavior of interest is the apparent crack growth occurring on  $\{100\}$  at low  $\Delta K$ , rather than on  $\{111\}$ , as shown in Figure 3. This phenomena coincides with growth behavior observed by Telesman and Ghosn [9] in similar alloys.

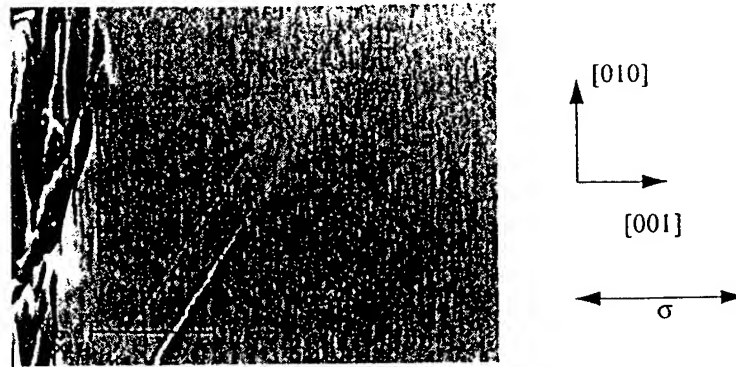


**Figure 2:** Planar slip bands ahead of the crack tip. The feature to the left is an etched eutectic region. Loading direction corresponds to  $\langle 001 \rangle$ , and is horizontal in all images in this paper.

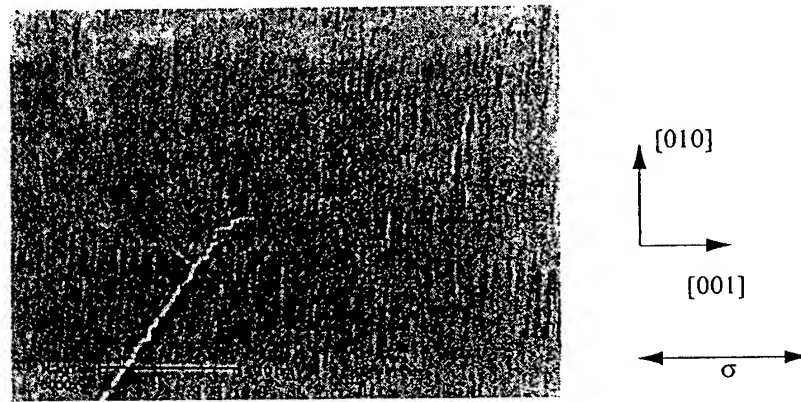


**Figure 3:** Crack growth on  $\{100\}$  (stepwise fashion) occurring at low  $\Delta K$ .

Strain maps were obtained using DISMAP, and a typical result is shown in Figure 4. The strain map is clearly not isotropic, as would be expected for a single crystal and for the deformation pattern seen in Figure 4(a). Further research would be useful to correlate the strain maps with the observed deformation behavior and crack propagation behavior.

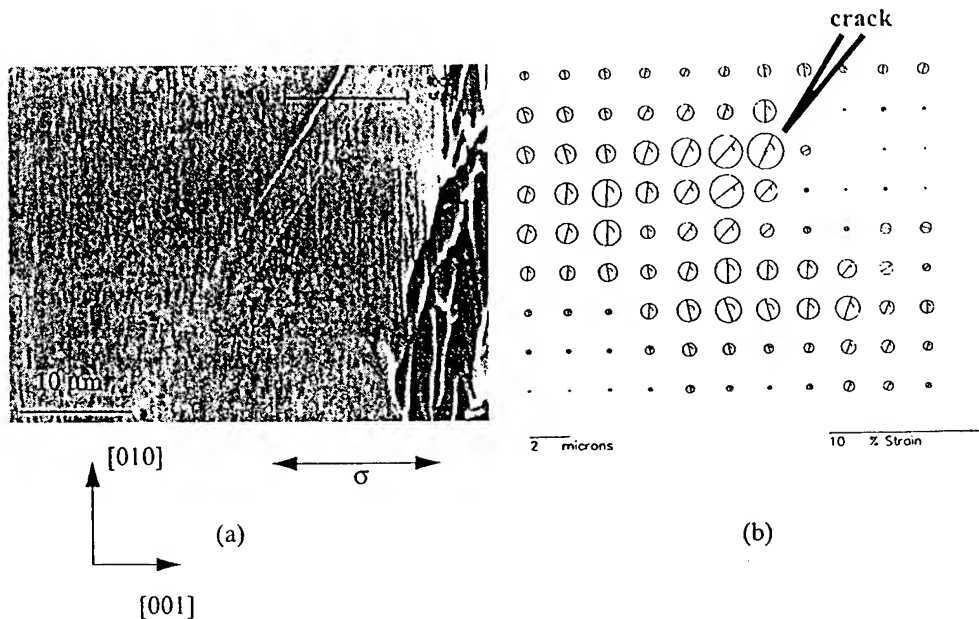


Figure 4: (a) SEM micrograph and (b) strain map measured by DISMAP in the same region, with the crack orientation drawn in. Note that magnifications are slightly different, and image is shifted between the strain map and the photo.

An estimate of the plastic zone size using the standard linear elastic fracture mechanics calculation for plane stress can be obtained from:

$$2r_p = \frac{1}{\pi} \left[ \frac{K}{\sigma_y} \right]^2$$

where  $K$  is the maximum stress intensity factor and  $\sigma_y$  is the yield strength, about 1 GPa. The isotropic LEFM plastic zone size is predicted to be 43 μm for the experimental conditions associated with Figure 4. Experimental observations showed slip band extension at the surface some 30-40 μm ahead of the crack tip, which is in reasonable agreement with the LEFM prediction. However, the shape of the plastic zone and the strain map is clearly anisotropic, as seen in Figure 4, and as would be expected in a single crystal.

### Discussion

Figure 1 is a demonstration that, at least at room temperature, the FCP curves of single crystalline and polycrystalline superalloys with similar microstructures are similar except with regards to threshold. The natural question is why the single crystal has such a low threshold compared to the polycrystals. The conventional explanation is that the grain boundaries act as obstacles to crack propagation and arrest cracks. An alternative explanation might be based on the relative near-threshold fracture surface roughness of the different microstructures. Figure 5 shows optical micrographs of the polycrystalline material crack propagation, at a magnification

about 10X lower than that in Figures 2-4 for the single crystal. It is clear from these figures that the roughness increases from the single crystal to the fine-grain polycrystal to the coarse-grain polycrystal. This is the same order as the threshold increases.

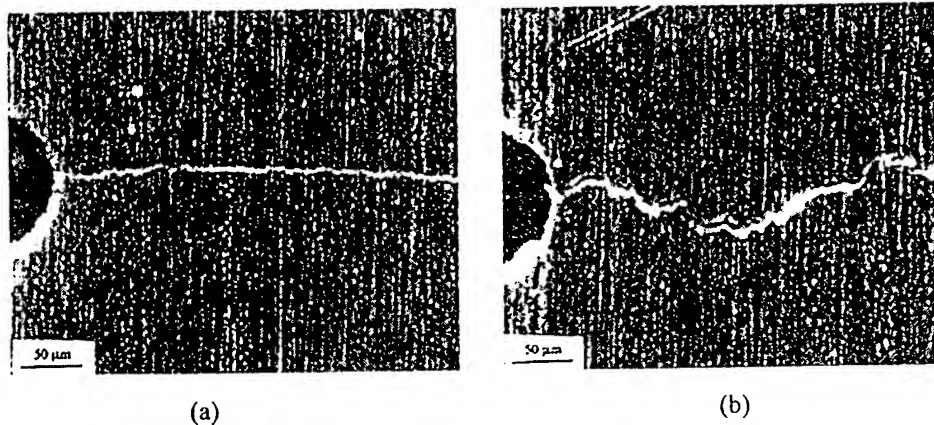


Figure 5: Optical micrographs of room temperature crack propagation in (a) fine-grain KM4, and (b) coarse-grain KM4. From [3]

In related research [4], a quantitative relationship was found to exist between fracture surface roughness and threshold for the coarse-grain polycrystal. Further research is necessary to elucidate the mechanisms and likelihood that fracture surface roughness is actually the controlling mechanism in threshold of these alloys at room temperature.

#### Acknowledgement

This work was supported by the MURI on "High Cycle Fatigue", funded at Michigan Technological University by the Air Force Office of Scientific Research, Grant No. F49620-96-1-0478, through a subcontract from the University of California at Berkeley.

#### References

1. B.A. Cowles: *Int. J. Fract.*, 1996, vol. 80, pp. 147-163.
2. R.O. Ritchie, B.L. Boyce, J.P. Campbell, O. Roder, A.W. Thompson and W.W. Milligan: *Int. J. Fatigue*, 1999, vol. 21, pp. 653-662.
3. S.A. Padula II, A. Shyam, R.O. Ritchie and W.W. Milligan: *Int. J. Fatigue*, 1999, vol. 21, pp. 725-731.
4. A. Shyam, S.A. Padula II, S. Marras and W.W. Milligan: *Metall. Trans. A*, in press.

5. W.S. Walston, K.S. O'Hara, E.W. Ross, T.M. Pollock and W.H. Murphy: in *Superalloys 1996*, R. D. Kissinger, D. J. Deye, D. L. Anton, A. D. Cetel, M. V. Nathal, T. M. Pollock, and D.A. Woodford, eds., The Minerals, Metals and Materials Society, Warrendale, PA, 1996, pp. 27-34.
6. S. Sinharoy, P. Virro-Nic and W.W. Milligan: *Metall. Mater. Trans. A*, vol. 32A, 2001, pp. 2021-2032.
7. D.L. Davidson, A. Nagy and T.S. Owen: in *High Cycle Fatigue of Structural Materials*, W.O. Soboyejo and T.S. Srivatsan, eds., The Minerals, Metals and Materials Society, Warrendale, PA, 1997, pp. 263-268.
8. D.L. Davidson: in *Experimental Techniques for Fracture*, J. S. Epstein, Ed., VCH Publishers, New York, 1993, pp. 41-59.
9. J. Telesman and L.J. Ghosn; *Engineering Fracture Mechanics*, vol. 34, 1989, pp. 1183-1196.

# Fatigue-Crack-Propagation Thresholds in a Nickel-Base Superalloy at High Frequencies and Temperatures

A. SHYAM, S.A. PADULA II, S.I. MARRAS, and W.W. MILLIGAN

Fatigue-crack-propagation (FCP) tests were conducted on the powder metallurgy nickel-based superalloy KM4 at temperatures of 20 °C, 550 °C, and 650 °C. Two different heat treatments were investigated, one yielding a relatively coarse grain size of 55  $\mu\text{m}$  and another yielding a fine grain size of 6  $\mu\text{m}$ . Tests were conducted at 100 Hz and 1000 Hz and at load ratios between 0.3 and 0.7. In the Paris regime, trends observed at high frequencies for KM4 were identical to those observed by earlier investigators at lower frequencies: coarse grains, low load ratios, low temperatures, and higher frequencies generally resulted in lower crack-propagation rates. However, in contrast to the Paris-regime behavior, thresholds were a complicated function of microstructure, load ratio, temperature, and frequency, and the only variable that resulted in a consistent trend in threshold was the load ratio. For example, thresholds increased from 100 to 1000 Hz for the fine-grained material at 550 °C, but decreased with the same frequency variation at 650 °C. One reason for this complexity was a change to intergranular fracture in the fine-grained microstructure at 650 °C, which was beneficial for high-frequency thresholds. Higher load ratios and lower frequencies promoted intergranular fracture. However, not all of the complexity could be explained by changing fracture mechanisms. Scanning electron microscope (SEM) stereofractography was utilized to determine quantitative measures of fracture-surface roughness. The most useful quantitative measure was found to be the standard deviation of the fracture-surface height, which is a physically meaningful length parameter and which corresponded to about half the grain size during room-temperature fatigue at near-threshold  $\Delta K$  levels. The roughness of the fracture surface was found to increase as the load ratio was increased for both microstructures. For the coarse-grained microstructure, there was a direct correlation between fracture-surface roughness and FCP threshold over the entire range of temperatures, frequencies, and load ratios. However, measurements of closure loads indicated that roughness-induced closure was not the sole reason for the varying FCP thresholds.

## I. INTRODUCTION

NICKEL-BASED superalloys are used in gas turbines because of their superior elevated-temperature mechanical properties. By using threshold data and fatigue-crack-propagation (FCP) curves to predict fatigue lives, failures in turbine engines under low-cycle fatigue (LCF) conditions have been minimized in recent years. Because of this success, the single largest cause of failure in military aircraft gas turbines is now high-cycle fatigue (HCF).<sup>[1]</sup> The reason that this remains a pervasive problem may be related to the highly empirical approach, based on Goodman diagrams, which is currently employed to estimate HCF capability. A fracture-mechanics, threshold-based HCF approach would be, therefore, highly desirable. Mechanisms of crack arrest associated with FCP thresholds are very complex, and there is a large discrepancy between results predicted from theoretical threshold models and experimentally determined values.<sup>[2]</sup> These models deal exclusively with either intrinsic

or extrinsic factors affecting the threshold, without taking into account their synergistic interactions. To address these problems, data under engine HCF conditions (very high frequencies in the Kilohertz range and high  $R$  values) is necessary. In this work, elevated-temperature long-crack FCP tests were performed at high frequencies (up to 1 kHz) in a Ni-based turbine disk alloy under a variety of experimental conditions. Four important factors affecting threshold (temperature, frequency, microstructure, and load ratio) were systematically varied in order to understand the relative importance of individual factors and the level of interaction between them. Similar work at room temperature for the same alloy has been reported earlier.<sup>[3]</sup>

## II. MATERIALS

A polycrystalline Ni-based superalloy designated KM4<sup>[4]</sup> was studied in this program. It was developed by General Electric (GE) Aircraft Engines specifically to resist creep FCP and is similar to the commercial alloys Rene95 and IN100 in its microstructure and basic mechanical properties.<sup>[5]</sup> This disk alloy was produced by a process route involving the consolidation of atomized powders by hot extrusion, followed by forging. The nominal composition of the alloy is given in Table I, and the details of its microstructure and deformation characteristics have been reported elsewhere.<sup>[5]</sup> The specimens studied in this work were obtained from a single forging of KM4, which was heat treated by GE Aircraft Engines.

A. SHYAM, Graduate Student, and W.W. MILLIGAN, Professor, are with the Department of Materials Science and Engineering, Michigan Technological University, Houghton, MI 49931. Contact e-mail: milligan@mtu.edu S.A. PADULA II, formerly Graduate Student, Department of Materials Science and Engineering, Michigan Technological University, is with NASA-Glenn Research Center, Cleveland, OH 44135. S.I. MARRAS, formerly Graduate Student, Department of Materials Science and Engineering, Michigan Technological University, is serving in the Greek military.

Manuscript submitted March 6, 2001.

Table I. KM4 Alloy Composition

Element	KM4 Wt Pct <sup>(4)</sup>
Co	18
Cr	12
Mo	4
Al	4
Ti	4
Nb	2
B	0.03
C	0.03
Zr	0.03
Ni	balance

Two different heat treatments were performed on slabs cut from the forging. One of the slabs received a solutionizing treatment at 1140 °C (below the  $\gamma'$  solvus temperature, henceforth referred to as the "fine-grained" material in this article). After quenching and aging, a relatively small grain size of 6  $\mu\text{m}$  was obtained. An optical micrograph of this heat treatment is presented in Figure 1(a). The particles shown in this figure are the undissolved "primary"  $\gamma'$  particles, which remain as a result of the incomplete solutionizing treatment. These particles limit grain growth by pinning the grain boundaries. The other slab, however, received a solutionizing treatment at 1180 °C (above the  $\gamma'$  solvus temperature, and, henceforth, referred to as the "coarse-grained" material in this article). No primary  $\gamma'$  particles remain during this heat treatment, allowing grain growth during solutionizing. A much coarser microstructure with an average grain size of about 55  $\mu\text{m}$  developed, as shown in Figure 1(b). On a finer scale, both microstructures contained a bimodal distribution of  $\gamma'$  particles.<sup>[5]</sup> Both microstructures contained about 55 pct by volume of the coherent  $\gamma'$  precipitates, and the size distribution of these particles is discussed in Reference 5. The monotonic mechanical properties of the heat treatments for both the coarse-grained and fine-grained materials are summarized in Table II.<sup>[6]</sup>

### III. EXPERIMENTAL PROCEDURES

The FCP tests were conducted on an MTS servohydraulic testing system at 100 and 1000 Hz in an ambient environment. This instrument is described elsewhere.<sup>[7]</sup> The FCP tests were accomplished largely in compliance with the ASTM E647 standard, using a four-point-bend geometry with the dimensions shown in Figure 2. This setup made it convenient to wrap an induction coil around the midspecimen area containing the crack. Thermocouple wires were welded on both faces of the specimen in order to control the temperature and also to ensure that no significant thermal gradients were present through the thickness. Using this technique, the temperature variation through the thickness and in the zone of crack propagation (from the notch to final failure) was  $\pm 5$  °C. One of the faces of the specimen was coated with a thin layer of gold to improve optical contrast of the crack at high temperatures. Using a Questar telescope, crack lengths could be measured on the coated face with a resolution of 10  $\mu\text{m}$ . The entire test was videotaped, and the crack lengths were calculated manually from the tape.

A stepwise load-shedding procedure was used to obtain

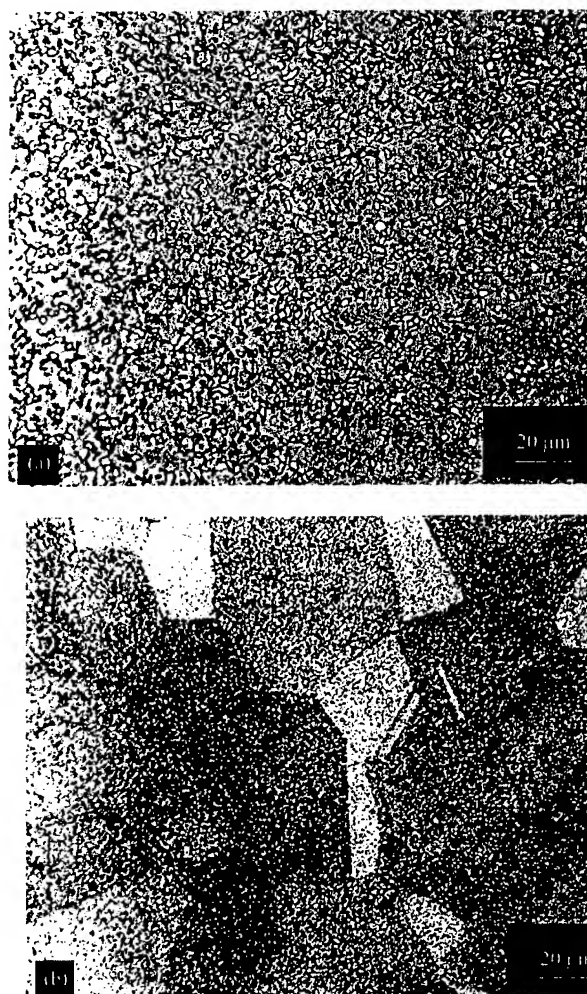


Fig. 1—Optical microstructures of KM4 after heat treatment: (a) fine-grain microstructure, with large primary  $\gamma'$  particles and a 6- $\mu\text{m}$  grain size. (b) Coarse-grain microstructure, with no primary  $\gamma'$  particles and a 55- $\mu\text{m}$  grain size.

the fatigue threshold values. The load-shedding rates were substantially lower than the maximum allowed in ASTM E647. The threshold condition was defined to be the stress-intensity range corresponding to a crack growth rate of  $10^{-10}$  m/cycle for the room-temperature tests and no detectable growth for the high-temperature tests (corresponding to  $<10^{-11}$  m/cycle). After a threshold was obtained and duplicated, the load was slightly increased, and an increasing- $\Delta K$  test was then performed. The fatigue-crack-growth data presented in this article are only from this increasing- $\Delta K$  portion of the test. The FCP curves were constructed by utilizing the secant method, as described in ASTM E647. Some of the samples were broken after the completion of the test, and the fracture surfaces were studied using stereo imaging in a scanning electron microscope (SEM). The three-dimensional (3-D) fracture surfaces were reconstructed and quantitatively measured from stereo pairs using the commercially available MeX software package.<sup>[8,9]</sup> Details of the procedure used to analyze the fracture surfaces are given in Section V.



Table II. Basic Mechanical Properties of KM4

Temperature (°C)	Coarse Grain			Fine Grain		
	E (GPa)	YS (MPa)	UTS (MPa)	E (GPa)	YS (MPa)	UTS (MPa)
RT	230	1069	1448	230	1151	1551
550	202	965	1344	202	1069	1448
650	193	945	1317	193	1041	1420

Data from Ref. 6; strain rate of  $\sim 10^{-4} \text{ s}^{-1}$ .

E = elongation, YS = yield strength, and UTS = ultimate tensile strength.

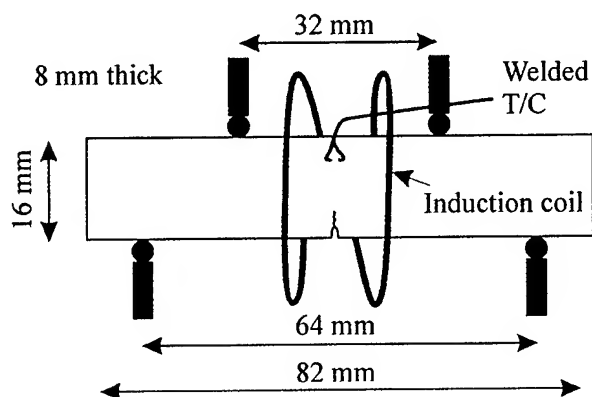


Fig. 2—Dimensions of the induction-heated four-point bend specimen, with loading points represented by pins and the location of the induction coil indicated.

Crack-closure load levels were measured at room temperature, for both microstructures, on specimens cycled at 1000 Hz and load ratios of 0.3, 0.4, 0.55, and 0.7. Closure loads were measured by using a high-resolution Capacitance COD gage, which was fixed to the specimen during cycling. The procedure was as follows. The FCP threshold was reached by the load-shedding techniques described previously, and then the load amplitude was slowly reduced to zero while the mean load was maintained. (The specimen was not unloaded between cycling and closure measurements.) The load was then statically increased from the mean load to a level corresponding to  $K_{max}$  at threshold during the previous cycling. At that point, unloading compliance was measured by monitoring the COD vs the load. The closure load was defined as the point where the curve deviated from linearity. The system was calibrated on specimens with electrodischarge-machined notches, and it was verified that the unloading compliance of the notched specimens was completely linear down to zero load.

In order to explore the possibility of oxide-induced closure at elevated temperatures, similar closure measurements were made on specimens that had been cycled at 550 °C and 650 °C,  $R = 0.4$ , and a frequency of 1000 Hz. In these tests, the threshold condition was obtained by load shedding at elevated temperature, as described previously. The specimen was then rapidly cooled (recall that the heating method was induction), while the mean load was held. After reaching room temperature, the COD gage was fixed to the specimen, and unloading compliance was determined.

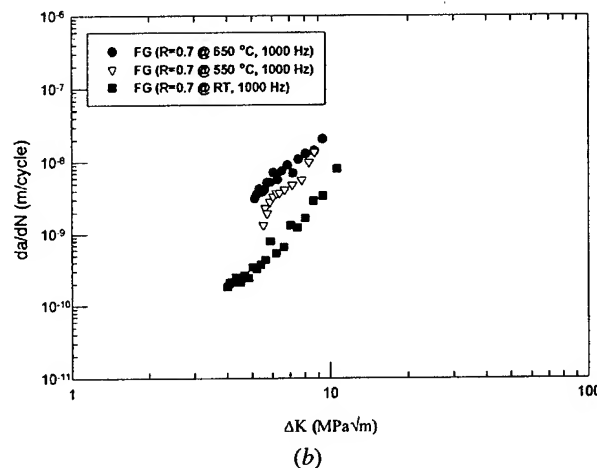
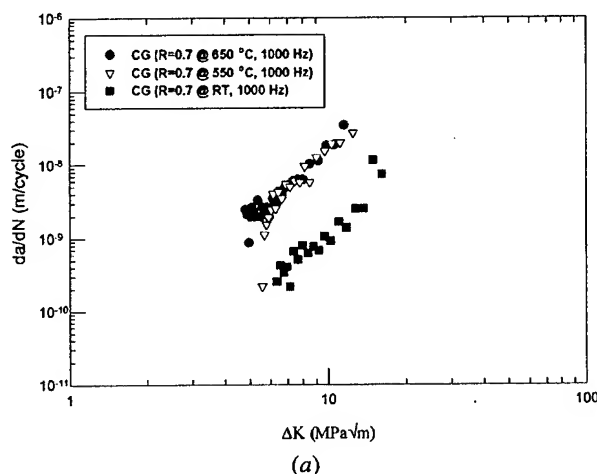


Fig. 3—Fatigue crack propagation curves for (a) coarse-grain (CG) and (b) fine-grain (FG) microstructures at three different temperatures.

#### IV. CRACK-PROPAGATION RATES AND FATIGUE THRESHOLDS

##### A. Effects of Temperature

Typical FCP curves for both microstructures at room temperature, 550 °C, and 650 °C under identical conditions ( $R = 0.7$  and  $\nu = 1000 \text{ Hz}$ ) are presented in Figure 3. It is evident that the crack growth rates increased significantly as the temperature increased.

It should be noted that the FCP curves presented in this

Table III. FCP Thresholds (MPa $\sqrt{m}$ )

T, °C	Frequency, Hz	Fine Grain				Coarse Grain			
		R = 0.30	R = 0.40	R = 0.55	R = 0.70	R = 0.30	R = 0.40	R = 0.55	R = 0.70
20	1,000	5.9	5.2	4.7	4.0	7.9	7.3	6.7	6.0
550	100	—	5.1	—	4.4	—	6.2	—	5.6
	1,000	—	5.9	—	5.0	—	6.2	—	5.4
650	100	—	5.2	—	4.7	—	4.6	—	4.0
	1,000	—	4.3	—	3.9	—	5.6	—	4.6

article do not always extend down to threshold values, for the following reasons. At elevated temperatures, there was no detectable crack growth at the threshold value, and the high-frequency controller required a complete stop in cycling followed by a manual change and a restart in order to increase the  $\Delta K$  level and start the crack growth again. At elevated temperatures, this process sometimes led to difficulty in restarting the crack growth without a fairly substantial increase in  $\Delta K$  level above the threshold. Therefore, on the increasing- $\Delta K$  curves, there is often a " $\Delta K$  gap" of up to 1 MPa $\sqrt{m}$  between the first data point and the measured threshold. When this phenomenon was first noticed, multiple experiments were conducted to verify that the lower value was, indeed, the threshold. This turned out to be true, as repetitive load-shedding procedures always resulted in the lower, originally measured threshold value. There are many possible explanations for the apparent crack retardation on initiating the increasing- $\Delta K$  portion of the test, including oxidation, closure, and crack blunting due to creep.

Table III gives a summary of the average threshold values determined in this study by the load-shedding technique, and the values at load ratios of 0.4 and 0.7 are plotted as a function of temperature in Figure 4. The threshold values reported in Table III are the averages of the measured values. These values were verified at least once, and in most cases, three to four times on two different specimens. In every case, individually measured threshold values were within  $\pm 0.15$  MPa $\sqrt{m}$  of the reported mean values. It is evident from Figure 4(a) and Table III that threshold values dropped between room temperature and 650 °C for the coarse-grained material. However, the threshold behavior for the fine-grained material was more complicated: at 1000 Hz, the fine-grained material's threshold increased between 20 °C and 550 °C, then decreased between 550 °C and 650 °C, however, at 100 Hz, the 650 °C threshold was slightly higher than the 550 °C threshold. As discussed later, the increase in threshold from 550 °C to 650 °C for the fine-grained material was accompanied by a change in crack-propagation mode from transgranular to intergranular, while there was no obvious reason for the increase in the threshold between room temperature and 550 °C.

It should be pointed out that the 1000 Hz room-temperature data presented in this article are not consistent with those published by our group earlier.<sup>[3]</sup> In the earlier experiments, FCP thresholds were reported at values significantly higher than those reported here. It was found that the digital controller of the first-generation MTS 1000 Hz servohydraulic machines was actually overloading the specimens when the cycling was stopped during manual load shedding. These overloads led to apparent threshold behavior, which was

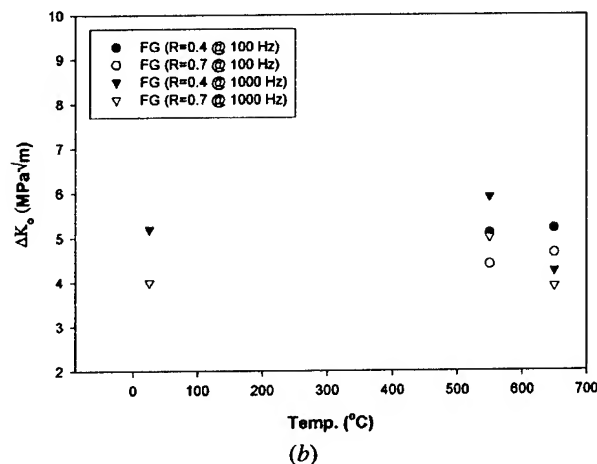
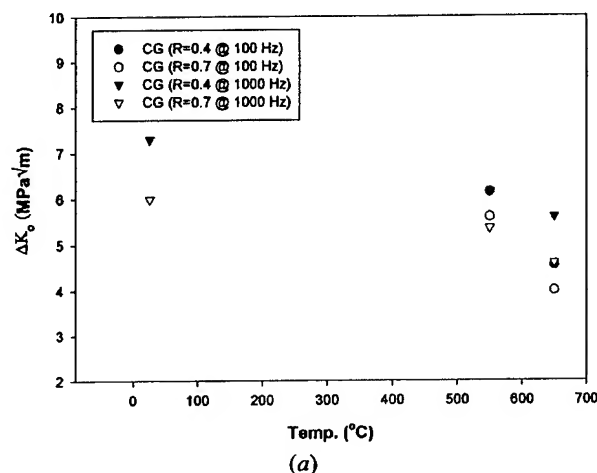
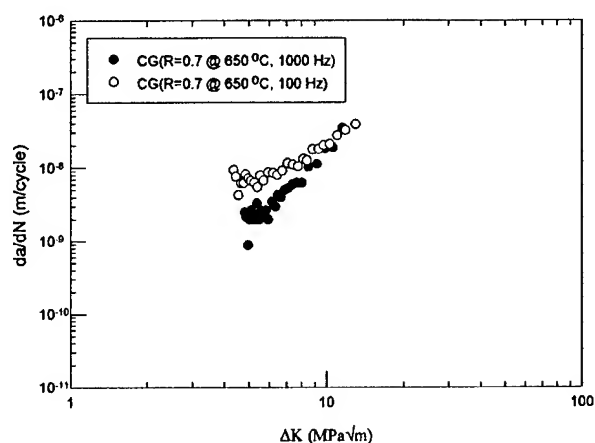


Fig. 4—Threshold variation with temperature for (a) coarse-grain and (b) fine-grain material.

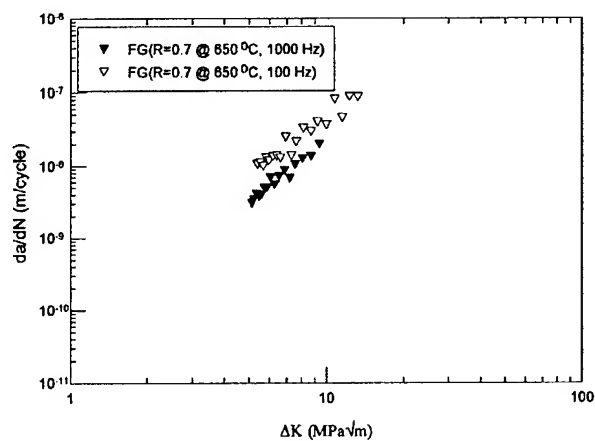
actually crack arrest due to overload. After this was discovered, the digital controller was upgraded so the load amplitude could be gradually decreased to zero to stop cycling. With this upgrade, thresholds at 1000 Hz could be reproduced to a high degree of accuracy on multiple specimens, and these thresholds were as much as a factor of 2 lower than those observed in the initial research.

#### B. Effects of Frequency and Microstructure

As reported earlier,<sup>[3]</sup> no effect of frequency exists between 50 and 1000 Hz at room temperature. This was not



(a)

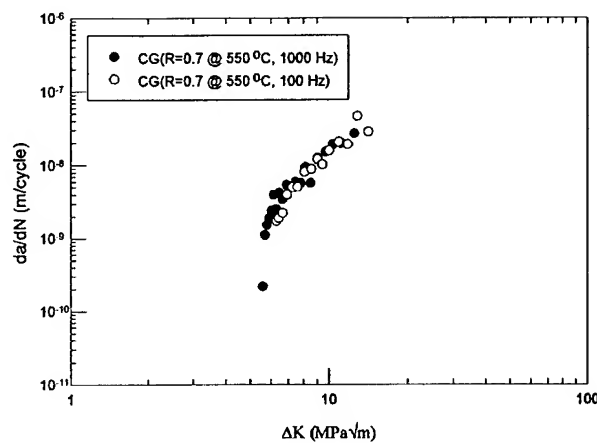


(b)

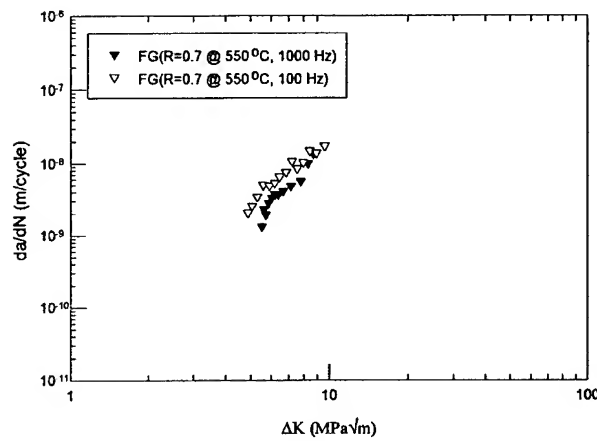
Fig. 5—Fatigue crack propagation curves for (a) coarse-grain and (b) fine-grain microstructures, showing the effect of changing the frequency by an order of magnitude at 650 °C.

generally the case at elevated temperatures, and one can observe in Figure 5 an increase in fatigue-crack growth rates at the lower frequency of 100 Hz for both microstructures at 650 °C. Figure 6 shows similar results for the fine-grained microstructure at 550 °C; however, the FCP curves for the coarse-grained material are indistinguishable for frequencies of 100 and 1,000 Hz at 550 °C. The FCP curves from both the coarse- and fine-grained microstructures at 650 °C for frequencies of 100 and 1000 Hz are compared in Figure 7. Both figures indicate slightly enhanced FCP resistance in the Paris regime for the coarse-grained material. These elevated-temperature results in microstructural effects on FCP behavior are consistent with trends reported earlier for KM4 at room temperature<sup>[3]</sup> and for similar superalloys at lower frequencies.<sup>[10–19]</sup> It should be noted from our results that the beneficial effects of the coarse-grained microstructure on Paris FCP rates diminished as the temperature increased.

The FCP thresholds were more complicated than the Paris-regime FCP curves. Inspection of Table III shows that the thresholds were a complex function of frequency, temperature, and microstructure. At 650 °C, thresholds were higher at 1000 Hz (compared to 100 Hz) for the coarse-grained material (by 10 to 25 pct, depending on  $R$  value), while they



(a)



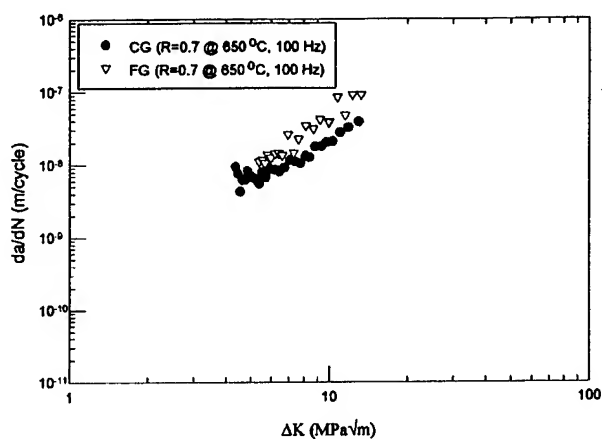
(b)

Fig. 6—Fatigue crack propagation curves for (a) coarse-grain and (b) fine-grain microstructures, showing the effect of changing the frequency by an order of magnitude at 550 °C.

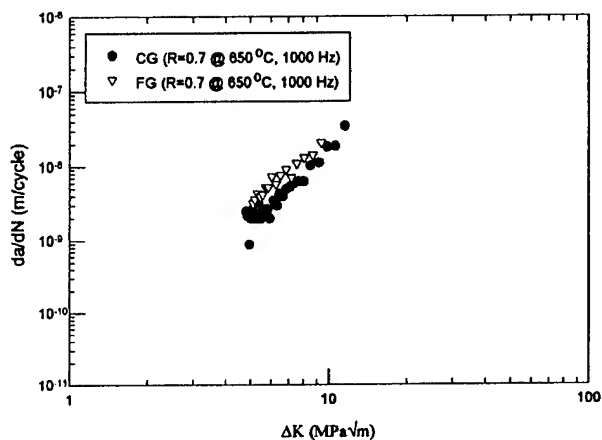
were lower at 1000 Hz (compared to 100 Hz) for the fine-grained material (again, by 10 to 25 pct). At 550 °C, the trends reversed. The fine-grained material had a higher threshold at higher frequency (the opposite of that observed at 650 °C), while the thresholds were relatively insensitive to frequency for the coarse-grained material at 550 °C. This complicated threshold behavior is discussed in detail later.

### C. Effects of Load Ratio

The FCP curves for both microstructures, at two different load ratios of 0.4 and 0.7 at 650 °C and 100 Hz, are shown in Figure 8. As can be observed, the load ratio has a larger effect in the near-threshold crack-growth regime. As expected, an increase in load ratio in both microstructures resulted in higher growth rates and lower thresholds in every case. The decrease in the threshold value as the load ratio is increased has been illustrated in Figure 9 for both the coarse- and fine-grained materials at room temperature. It should be noted that the variation of the threshold value with load ratio is approximately linear and remarkably similar for both microstructures. The coarse-grained material exhibited



(a)



(b)

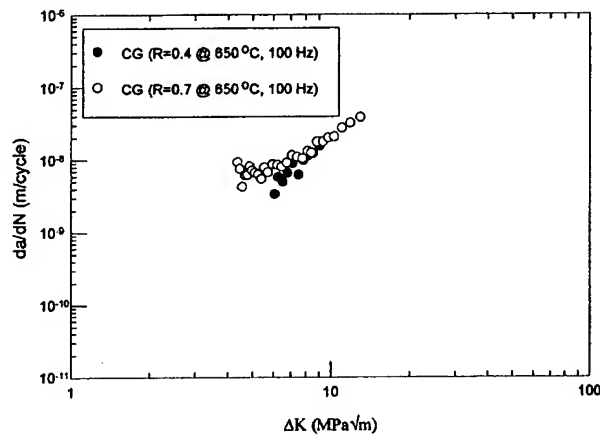
Fig. 7—Fatigue crack propagation curves showing the effect of microstructure at 650 °C and (a) 100 Hz and (b) 1000 Hz. In both cases, the coarse-grain microstructure exhibits superior crack propagation resistance in the Paris regime.

a higher threshold value by around  $2 \text{ MPa}\sqrt{\text{m}}$  for every load ratio at room temperature.

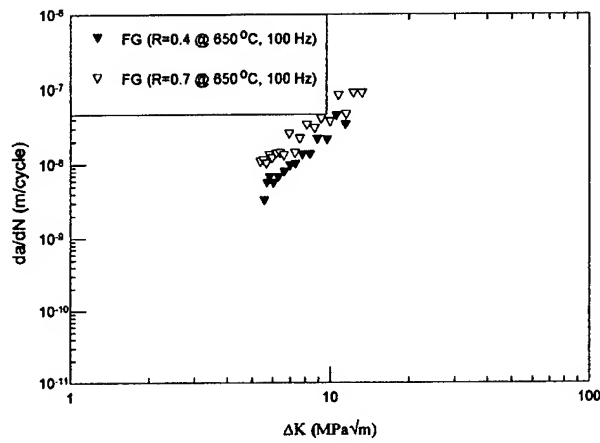
#### D. Summary and Interpretation

After examining all the FCP curves, it can be concluded that FCP behavior in the Paris regime at frequencies up to 1000 Hz is similar to what has been observed by previous investigators<sup>[10–19]</sup> for most superalloys at traditional testing frequencies. Lower temperatures, higher frequencies, coarse-grained microstructures, and lower load ratios impede fatigue-crack growth in the Paris regime. However, as discussed subsequently, the variation of fatigue thresholds was not as straightforward as the variation of FCP behavior in the Paris regime, except for the consistent observation of reducing thresholds with increasing load ratios.

Elevated-temperature FCP thresholds are plotted as a function of frequency at different temperatures, microstructures, and load ratios in Figure 10. A straight line has been drawn between the two frequency points in this figure for



(a)



(b)

Fig. 8—Effects of load ratio on the FCP behavior at 650 °C for (a) coarse-grain and (b) fine-grain materials.

illustration purposes only and does not imply a linear relationship. Several conclusions can be drawn from this figure.

- (1) The basic shapes of the curves are not a function of load ratio. Changing the load ratio simply shifts the curves up or down. Further, the reproducible shape of the curves at different load ratios lends confidence (supported by duplicate and triplicate testing) that the relatively small variations in measured thresholds were real, and not statistical scatter, since different load ratios were always done on different specimens.
- (2) The coarse-grained microstructure is insensitive to frequency (in the range from 100 to 1000 Hz) at 550 °C and below.

Besides these two conclusions, nothing about the thresholds is straightforward. The fine-grained material's threshold increased with frequency at 550 °C, but decreased with frequency at 650 °C. At 650 °C, the curves for the fine- and coarse-grained materials intersect, such that the fine-grained material had a better threshold at 100 Hz, but a worse threshold at 1000 Hz. Quantitative fractographic studies have

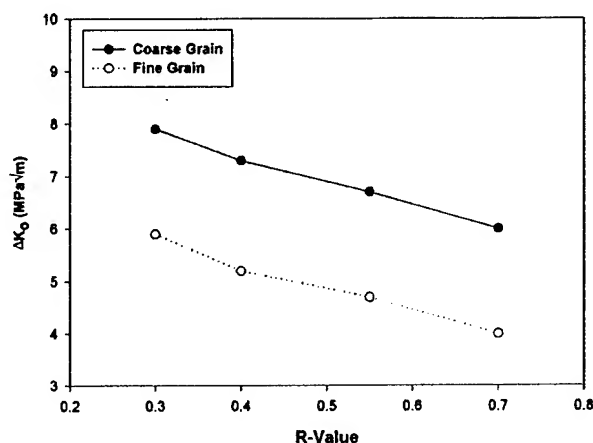


Fig. 9—Effect of load ratio on the fatigue threshold value for both microstructures at room temperature.

revealed some correlations between the threshold and near-threshold fracture-surface morphology, and results from these studies are presented subsequently.

## V. QUANTITATIVE STEREOFRACTOGRAPHY

It has now been well established that the roughness of the fatigue-fracture surface can be an important extrinsic factor in reducing the driving force for FCP. For example, our previous room-temperature results<sup>[3]</sup> showed that, consistent with many earlier studies, the fracture-surface roughness correlated qualitatively with threshold values at different grain sizes. That is, the coarser-grained material consistently had a rougher, more faceted fracture surface with a higher degree of crack-path tortuosity and also a higher threshold value.

Various profile and surface-area parameters have been used in previous studies to represent the roughness of fracture surfaces. These parameters include three quantitative measures of roughness, which are based on cross-sectional line profiles of traced fracture surfaces or on 3-D reconstructions of fracture surfaces made by serial sectioning or stereofractography: the ratio of the total length of a line profile to its projected length ( $R_L$ ),<sup>[20]</sup> the ratio of the actual fracture-surface area to its projected area ( $R_S$ ),<sup>[21]</sup> and the standard deviation of the height distribution obtained from multiple line profiles ( $\sigma_H$ ).<sup>[22]</sup> The term  $\sigma_H$  represents the deviations of the individual asperity height about the mean of the values.

In this study, all the specimens were quantitatively characterized by SEM stereofractography. The 3-D images of the fracture surfaces were reconstructed *via* the MeX software, and the average quantitative values of the roughness parameters were determined by taking 80 to 200 line profiles through each reconstructed 3-D surface fractograph. Eighty horizontal lines were used to calculate  $\sigma_H$ , while 100 horizontal and 100 vertical lines were used to calculate  $R_S$  and  $R_L$ . Determining 80 horizontal line profiles on the fractographs is the equivalent of conducting serial sectioning with a removal rate of 4  $\mu\text{m}$  per pass (coarse-grained-specimen micrographs) or 0.8  $\mu\text{m}$  per pass (fine-grained-specimen micrographs) and is much less tedious. To obtain good statistical data, at least eight different stereo pairs were analyzed

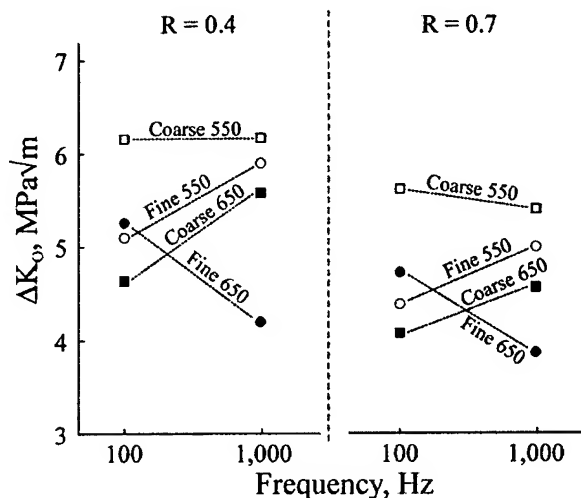


Fig. 10—Summary of elevated temperature fatigue thresholds. Coarse and fine refer to the grain sizes. Increasing the load ratio simply shifts the curves up, but there are no other obvious trends in threshold values as a function of temperature, microstructure, or frequency. Lines are drawn to aid in identifying trends only and are not meant to imply a linear relationship.

for each condition, corresponding to eight different near-threshold locations on the fracture surface. The mean values of  $R_L$ ,  $R_S$ , and  $\sigma_H$ , which were measured in this manner, are reported in Table IV. While each of the roughness parameters gives some information about roughness, it was determined that the standard deviation of the fracture-surface height ( $\sigma_H$ ) was the most useful, for two reasons. First, the value of  $\sigma_H$  is a physically meaningful length parameter; that is, the standard deviation of the fracture-surface height is directly related to the average asperity height on a fracture surface. Second,  $\sigma_H$  was found to be a very weak function of magnification, unlike the other two parameters. For these reasons,  $\sigma_H$  will be used as the quantitative measurement of fracture-surface roughness in the remainder of this article. Quoted values of "roughness" correspond to measured average values of  $\sigma_H$ .

Figures 11 and 12 show typical near-threshold fracture surfaces at room temperature and 550 °C in the coarse-grained and fine-grained materials, respectively, at a load ratio of 0.7. The roughness and threshold values are also indicated. It is quite clear from these images and quantitative measurements that the fracture surfaces were substantially smoother at higher temperatures. It is interesting to note that the room-temperature roughness values are around half the grain size for both the coarse- and fine-grained materials. Slip is highly planar and crystallographic in superalloys at room temperature, and inspection of the fractographs revealed that fracture-surface facets generally spanned entire grains at room temperature. Since the roughness value indicates the deviation from the mean fracture-surface height, and since most crack facets spanned entire grains at room temperature, it is reasonable that there was a direct relationship between the grain size and the roughness parameter. At elevated temperature, as seen in Figures 11(b) and 12(b), fracture was much less crystallographic, and facets generally did not span entire grains. Accordingly, the roughness parameters are substantially smaller than half the grain size. This

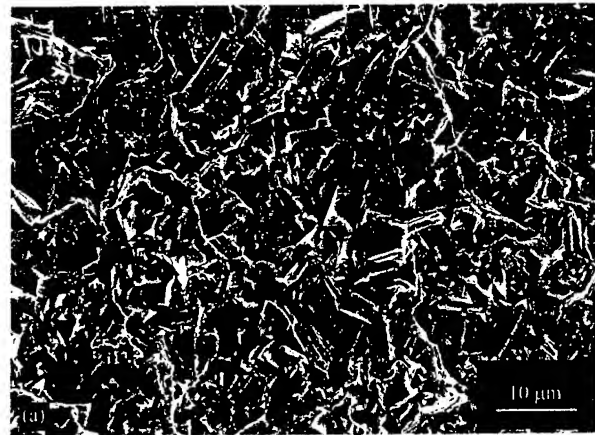
Table IV. Quantitative Fracture Surface Roughness Parameters at Threshold

	Fine Grain $R = 0.4$					Fine Grain $R = 0.7$				
	20 °C	550 °C		650 °C		20 °C	550 °C		650 °C	
	1000 Hz	100 Hz	1000 Hz	100 Hz	1000 Hz	1000 Hz	100 Hz	1000 Hz	100 Hz	1000 Hz
$R_S$	1.61	1.14	1.15	1.31	1.17	1.68	1.17	1.20	1.41	1.29
$R_L$	1.30	1.07	1.08	1.17	1.08	1.38	1.08	1.11	1.25	1.16
$\sigma_H$ ( $\mu\text{m}$ )	2.5	0.8	1.1	1.6	0.8	2.7	1.0	1.1	2.7	1.3
$\Delta K_{th}$ (MPa $\sqrt{\text{m}}$ )	5.2	5.1	5.9	5.2	4.3	4.0	4.4	5.0	4.7	3.9
	Coarse Grain $R = 0.4$					Coarse Grain $R = 0.7$				
	20 °C	550 °C		650 °C		20 °C	550 °C		650 °C	
	1000 Hz	100 Hz	1000 Hz	100 Hz	1000 Hz	1000 Hz	100 Hz	1000 Hz	100 Hz	1000 Hz
$R_S$	2.18	1.19	1.19	1.07	1.15	2.38	1.23	1.22	1.14	1.19
$R_L$	1.68	1.10	1.10	1.04	1.08	1.79	1.14	1.12	1.07	1.11
$\sigma_H$ ( $\mu\text{m}$ )	24.1	9.8	9.4	3.6	8.0	31.0	12.8	12.5	7.2	10.5
$\Delta K_{th}$ (MPa $\sqrt{\text{m}}$ )	7.3	6.2	6.2	4.6	5.6	6.0	5.6	5.4	4.0	4.6



$\Delta K_0 = 6.0 \text{ MPa}/\text{m}$ , Roughness =  $31.0 \mu\text{m}$

(a)



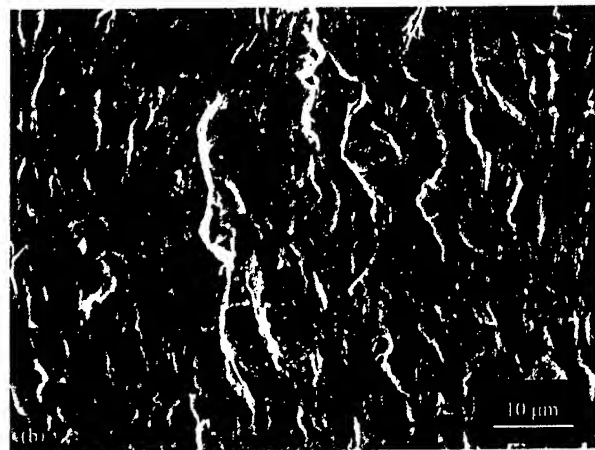
$\Delta K_0 = 4.0 \text{ MPa}/\text{m}$ , Roughness =  $2.7 \mu\text{m}$

(a)



$\Delta K_0 = 5.3 \text{ MPa}/\text{m}$ , Roughness =  $12.5 \mu\text{m}$

(b)

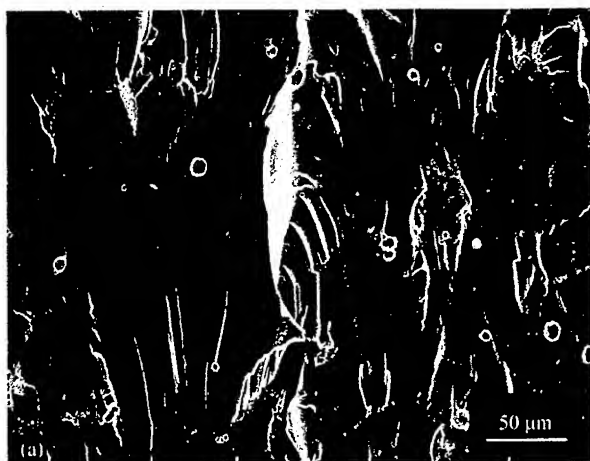


$\Delta K_0 = 5.0 \text{ MPa}/\text{m}$ , Roughness =  $1.14 \mu\text{m}$

(b)

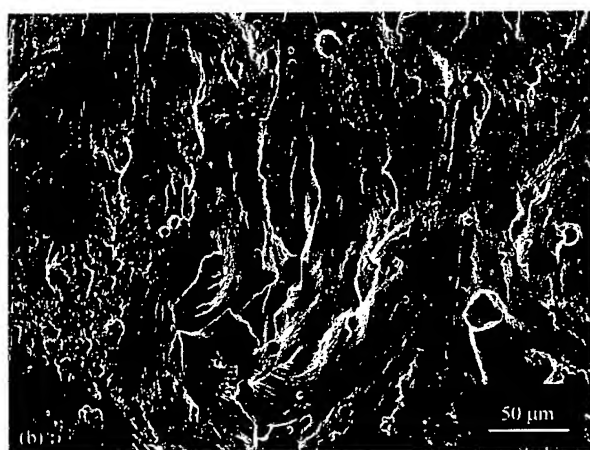
Fig. 11—SEM micrographs of coarse-grain material showing the near-threshold fracture surfaces at 1000 Hz and  $R = 0.7$  at (a) room temperature and (b) 550 °C. Roughness values correspond to the standard deviation of the fracture surface height, determined by quantitative SEM stereofractography.

Fig. 12—SEM micrographs of fine-grain material showing the near threshold fracture surfaces at 1000 Hz and  $R = 0.7$  at (a) room temperature, and (b) 550 °C.



$\Delta K_0 = 4.0 \text{ MPa}/\text{m}$ , Roughness =  $7.2 \text{ } \mu\text{m}$

(a)



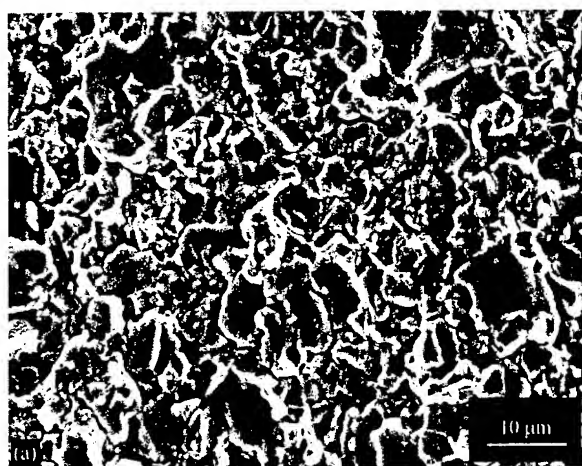
$\Delta K_0 = 4.6 \text{ MPa}/\text{m}$ , Roughness =  $10.5 \text{ } \mu\text{m}$

(b)

Fig. 13—Near-threshold fracture surfaces of the coarse-grain material at  $R = 0.7$  and  $T = 650 \text{ } ^\circ\text{C}$ : (a) 100 Hz and (b) 1000 Hz.

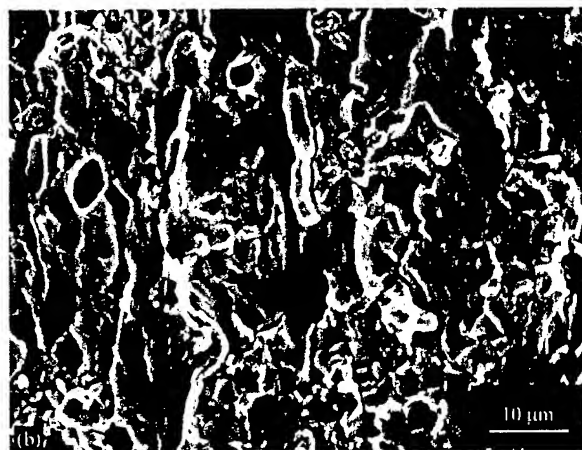
observation illustrates the advantage of using  $\sigma_H$ , which contains a physically relevant length scale, as the roughness parameter: the quantitative value of  $\sigma_H$  can be used to gain insight into microstructural effects on fracture processes. This is not the case when using the traditional roughness parameters  $R_L$  and  $R_S$ .

Figure 13 shows typical near-threshold fracture surfaces in the coarse-grained material at  $650 \text{ } ^\circ\text{C}$  and two different frequencies of 100 and 1000 Hz at a load ratio of 0.7. The lower frequency created a smoother fracture surface and also had a lower threshold. Figure 14 shows typical fracture surfaces for the fine-grained material in the near-threshold regime under the same two frequencies. In this case, opposite to the behavior of the coarse-grained material, the lower frequency created a rougher surface, but again, the rougher surface corresponded to a higher threshold. Figure 15 shows another typical fracture surface in the coarse-grained material at  $650 \text{ } ^\circ\text{C}$  and 100 Hz at a lower load ratio of 0.4. When compared to Figure 13(a), it can be seen that the roughness of the fracture surface was reduced by a factor of 2 with a



$\Delta K_0 = 4.65 \text{ MPa}/\text{m}$ , Roughness =  $2.7 \text{ } \mu\text{m}$

(a)



$\Delta K_0 = 3.9 \text{ MPa}/\text{m}$ , Roughness =  $1.3 \text{ } \mu\text{m}$

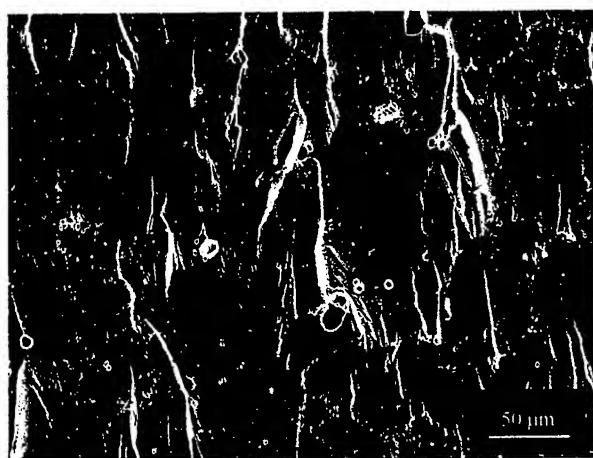
(b)

Fig. 14—Near-threshold fracture surfaces of the fine-grain material at  $R = 0.7$  and  $T = 650 \text{ } ^\circ\text{C}$ : (a) 100 Hz and (b) 1000 Hz, showing intergranular propagation at 100 Hz and partially intergranular propagation at 1000 Hz. The SEM stereopairs (not shown) clearly revealed the intergranular propagation mode.

decrease in the load ratio. Table IV demonstrates that the fracture surfaces became rougher with increasing load ratio (with all other variables held constant) *in every case*.

The average roughness values under all the conditions for which the threshold tests were done at elevated temperature are plotted as a function of frequency in Figure 16. It should be once again mentioned that a line has been drawn between the two frequency points in this figure only to clarify the trends, not to imply a linear relationship. Two conclusions can easily be drawn from this figure.

- (1) There is some similarity in the shapes of Figures 10 (threshold) and 16 (roughness).
- (2) As the load ratio increased, the slopes of the curves remained similar, but the curves shifted up. In other words, if all other factors are equal, increasing the load ratio increases the fracture-surface roughness.



$\Delta K_0 = 4.6 \text{ MPa}/\sqrt{\text{m}}$ , Roughness =  $3.6 \mu\text{m}$

Fig. 15—Near-threshold fracture surface of the coarse-grain material at  $R = 0.4$  and  $T = 650^\circ\text{C}$  at 100 Hz. This should be compared to Fig. 13(a), which shows a similar fracture surface for the  $R = 0.7$  case.

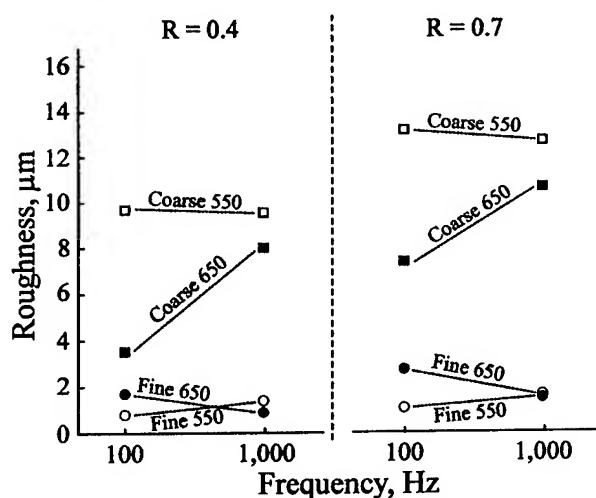
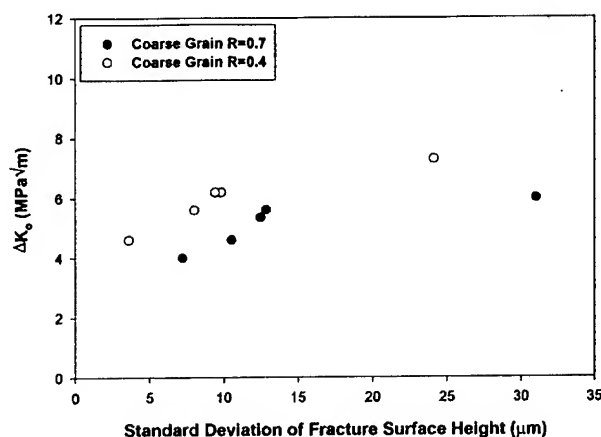


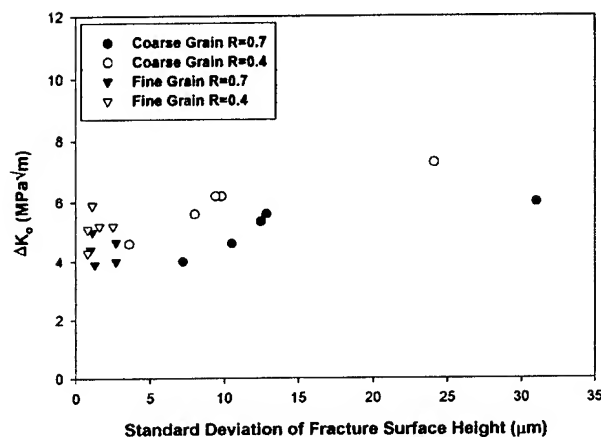
Fig. 16—Summary of the average of the elevated temperature near-threshold fracture surface roughness values. Increasing the load ratio simply shifts the curves up without an appreciable change in the slope. Lines are drawn to aid in identifying trends only and are not meant to imply a linear relationship.

In summary, while there was no consistent trend in threshold behavior as a function of microstructure, frequency, or temperature, there was an apparent correlation between fracture-surface roughness and threshold. To explore this further, Figure 17 is a plot of the roughness parameter vs the measured threshold for every test conducted in this study at load ratios of 0.4 and 0.7, including data based on fine and coarse grain sizes and temperatures of  $20^\circ\text{C}$ ,  $550^\circ\text{C}$ , and  $650^\circ\text{C}$ . It is clear that the relationship between fracture-surface roughness and threshold is dependent upon microstructure, as noted subsequently.

- (1) For the coarse-grained material, the threshold value increased as the near-threshold fracture-surface roughness increased; that is, there was a direct relationship between the near-threshold fracture-surface roughness and the



(a)



(b)

Fig. 17—Relationship between fracture surface roughness (standard deviation of fracture surface height) and FCP threshold for three temperatures and two frequencies for load ratios of 0.4 and 0.7 for the (a) coarse-grain material and (b) both microstructures.

threshold value. This increase, however, appears to plateau at higher values of roughness.

- (2) On the other hand, there does not seem to be a clear relationship between the threshold value and this roughness parameter for the fine-grained material. The roughness *decreased* by a factor of around 2.5 between room temperature and  $550^\circ\text{C}$  at 1000 Hz, but the threshold value *increased* by 15 to 25 pct in the same temperature range for this microstructure. Additionally, for the fine-grained material loaded at 1000 Hz at a load-ratio of 0.7, comparing between  $550^\circ\text{C}$  and  $650^\circ\text{C}$ , the smoother fracture surface had a higher threshold.

## VI. DISCUSSION

### A. General Observations

The research presented here represents some of the first results of FCP thresholds in superalloys at elevated temperatures and frequencies around 1000 Hz. An important conclusion from this study is that the trends observed at 1000 Hz in the Paris regime are completely consistent with those



observed at lower frequencies by many other investigators: in general, high load ratios, fine grain sizes, and low frequencies lead to higher FCP rates. Of course, at 1000 Hz, the strain rates are high, so thermally activated processes such as diffusion and intergranular fracture may be shifted in temperature space, as would be expected.

However, it is clear from Figures 10 and 17 that the benefits of the coarse-grained microstructure do not always extend to the measured threshold values. The coarse-grained microstructure does result in a higher threshold at temperatures of 550 °C and lower. However, at 650 °C, the fine-grain material actually has a higher threshold at 100 Hz than the coarse-grained material. The reason for the improved threshold behavior at 650 °C in the fine-grained material is related to a change in fracture behavior from transgranular to intergranular. Intergranular fracture was only observed in the fine-grained material at 650 °C. Fracture near the threshold was completely intergranular at  $R = 0.7$  and 100 Hz (Figure 14(a)) and was a combination of intergranular and transgranular fracture for the other test conditions at 650 °C (for example, Figure 14(b)). This transition from transgranular to intergranular fracture at fine grain sizes has been observed in similar alloy systems at lower frequencies.<sup>[14,17]</sup> Another interesting result is that the higher load ratio promoted intergranular crack growth, since the 100 Hz fracture surface was completely intergranular at  $R = 0.7$  but only partially intergranular at  $R = 0.4$ . Further, the roughness parameter at the condition showing completely intergranular crack propagation increased to about half the grain size, similar to the room-temperature value but much higher than the 550 °C value. This value of roughness is consistent with cracks propagating through grain boundaries and being deflected, on average, by an amount equal to half the grain size.

A general conclusion which may be reached by examining Table III and Figures 10 and 17 is that there is remarkably little variation in threshold values over wide changes in microstructure, temperature, and frequency. At a constant load ratio, the threshold  $\Delta K$  values all fall within a range of  $3 \text{ MPa}\sqrt{\text{m}}$  of each other, even though the grain size and frequency both varied by one order of magnitude and the temperature varied from 20 °C to 650 °C. This conclusion may change at lower frequencies, or after introducing a hold time.

## B. Mechanisms of Threshold

Fundamental intrinsic models of FCP thresholds predict a threshold value of around 1 to  $2 \text{ MPa}\sqrt{\text{m}}$  for KM4 at  $R = 0.4$ .<sup>[3]</sup> Since the thresholds are always higher than this, and since there is significant variation in the threshold with microstructure, temperature, and frequency, other factors besides dislocation nucleation at the crack tip must be important in governing the FCP threshold over the range of experimental conditions studied here. These factors are discussed subsequently.

### 1. Crack closure

A natural suspect for the variation seen in the threshold value is roughness-induced crack closure,<sup>[23]</sup> since Figure 17(a) is a clear demonstration that there is a direct relationship between roughness and threshold for the coarse-grained microstructure. Wasen and Heier<sup>[22]</sup> have shown that, for a

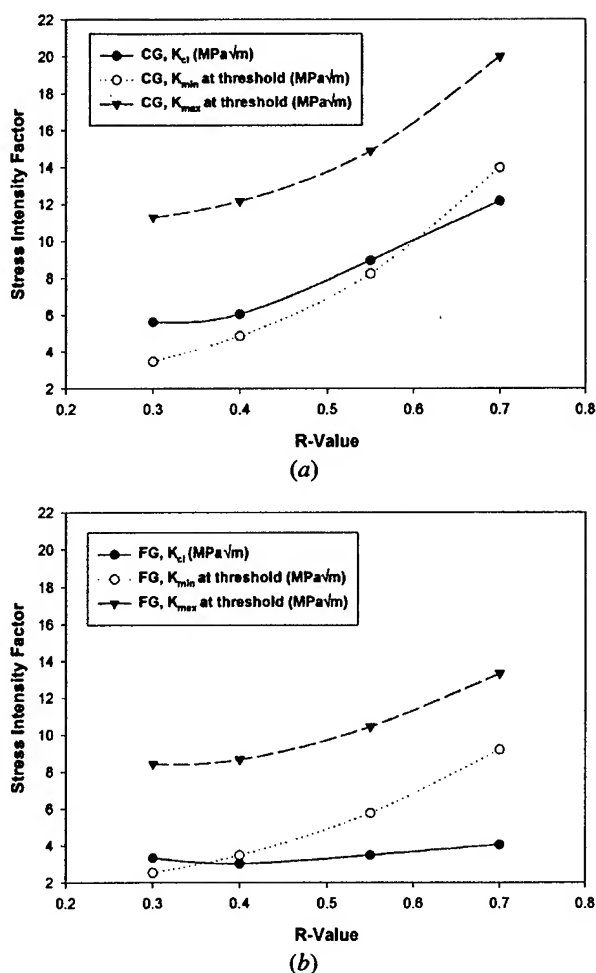


Fig. 18— $K_{max}$ ,  $K_{min}$ , and  $K_{closure}$  at room temperature for (a) coarse-grain and (b) fine-grain materials. The tests were done at room temperature. Above the load ratio at which the  $K_{min}$  and  $K_{cl}$  lines intersect, the crack remains completely open during cycling, and closure effects are expected to be minimal.

variety of steels (with grain sizes varying by roughly two orders of magnitude between 1 and  $100 \mu\text{m}$ ), the experimentally measured roughness-induced crack-closure levels are uniquely determined by the standard deviation of the height-distribution roughness parameter. In order to explore the relative importance of these effects in the present study, closure was measured in selected cases, by the procedures described earlier.

Figure 18 is a plot of  $K_{cl}$ ,  $K_{min}$ , and  $K_{max}$  at threshold vs the load ratio for both the coarse- and the fine-grained materials at room temperature. This figure shows that the load ratio above which the crack remains completely open during cycling is around 0.60 (coarse-grained material) and 0.35 (fine-grained material). Above these load ratios, the threshold value should remain constant as the load ratio is increased, if crack closure is controlling the threshold value. This is clearly not the case, as seen in Figure 9, which shows that the threshold values keep decreasing, for both microstructures, in a linear fashion with increasing load ratios, at least up to  $R = 0.7$ . Table V reveals that the closure behavior at elevated temperature was almost identical to that

Table V. Closure Results

Microstructure	T, °C	R	$\Delta K_0$ MPa $\sqrt{m}$	$\Delta K_{cl}$ MPa $\sqrt{m}$	$\Delta K_{eff}$ MPa $\sqrt{m}$
Fine grain	20 °C	0.30	5.9	0.9	5.0
		0.40	5.2	0	5.2
		0.55	4.7	0	4.7
		0.70	4.0	0	4.0
		0.40	5.9	0	5.9
Coarse grain	550 °C	0.40	4.3	0	4.3
	20 °C	0.30	7.9	2.2	5.7
		0.40	7.3	1.2	6.1
		0.55	6.7	0.8	5.9
		0.70	6.0	0	6.0
	550 °C	0.40	6.3	1.0	5.3
	650 °C	0.40	5.6	0	5.6

All tests conducted at 1000 Hz.

at room temperature: closure was not observed in tests at  $R = 0.4$  and  $0.7$ , except under one condition (the coarse-grained material,  $R = 0.4$ , and  $550^\circ\text{C}$ ), and the  $\Delta K_{cl}$  value of  $1 \text{ MPa}\sqrt{m}$  is almost identical to the value of  $1.2 \text{ MPa}\sqrt{m}$  observed at room temperature. Since the room-temperature tests were closure-free at  $R = 0.7$ , it is reasonable to assume that the crack remained completely open for all elevated-temperature tests at this load ratio. Figure 10 shows that the observed threshold properties are similar for both load ratios at elevated temperatures, even though, once again, the crack-closure contributions are expectedly different, as discussed previously. Based on all these factors, it can be concluded that roughness-induced closure is not the underlying mechanism by which roughness is related to thresholds in the conditions studied here.

## 2. Crack deflection

Another potential factor contributing extrinsically to the threshold is crack deflection. The quantitative fracture-surface roughness values which were measured in this study are not only a measure of roughness, but also a measure of the deflection of the crack from the pure mode I plane. Suresh has shown<sup>[24,25]</sup> that microstructures that promote crack deflection lead to improved crack-propagation resistance and increased apparent threshold values. In a dual-phase steel, a heat treatment which promoted large deviations from the mode I fracture plane yielded a higher threshold than a heat treatment which promoted more planar growth. The mechanism of increasing threshold was proposed to be due more to mixed-mode-mechanics mechanisms than closure, although it was postulated that both occur and that there may be some interaction between them. This is consistent with the current study, in that the coarse-grained microstructure promoted more crack deflection and generally had a higher threshold. Suresh used linear-elastic analysis to calculate a corrected  $\Delta K$  value in the presence of kinked cracks:

$$\Delta K_{\text{corr}} = \Delta K_i \cdot \cos^2(\theta_0/2) \quad [1]$$

where  $\theta_0$  is the angle between the local crack-growth direction and the plane perpendicular to the loading axis, and  $\Delta K_{\text{corr}}$  is the corrected stress-intensity factor due to kinking. The term  $\theta_0$  can be imagined to be an equivalent orientation angle and can be estimated by the following relation:<sup>[26]</sup>

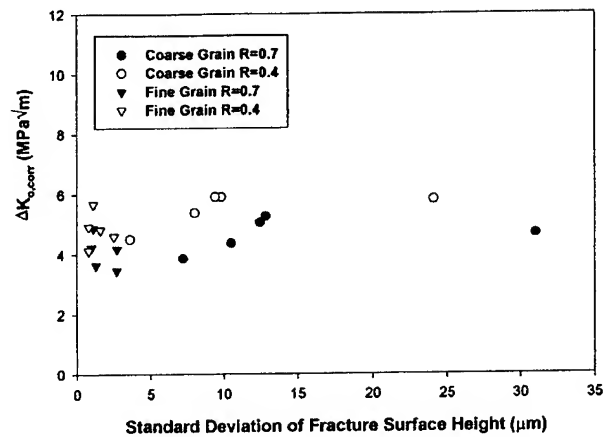


Fig. 19—Replot of Fig. 17(b), using threshold values corrected for crack deflection.

$$\theta_0 = \cos^{-1}\left(\frac{1}{R_L}\right) \quad [2]$$

where  $R_L$  values may be obtained from Table IV. This methodology of estimating  $\theta_0$  based on the roughness parameter  $R_L$  can be done based on the example of Reference 26. The line profile can be assumed to be made up of individual chords of an equal length of  $L_i$  (on the projecting plane) and having an angle of  $\theta_i$  with the plane perpendicular to the loading direction. In this way, the parameter  $R_L$ , which is the ratio of the total length of the line making the profile to its projected length, can be demonstrated to be

$$R_L = \frac{\sum_{i=1}^n (L_i / \cos \theta_i)}{\sum_{i=1}^n L_i} = \frac{\sum_{i=1}^n (1 / \cos \theta_i)}{n} \quad [3]$$

It was found from the line-profile data that  $R_L$  can be calculated to a good degree of precision using Eq. [3]. Since  $R_L$  is directly related to the orientation of the individual chords, which make up the line profile, it is reasonable to assume that it gives an indication of the equivalent orientation angle by Eq. [2]. Figure 19 is a replot of Figure 17(b), correcting  $\Delta K$  for deflection via the aforementioned approach. If crack deflection was the sole cause of threshold increases, one would predict that the slope should be zero, i.e., that correcting  $\Delta K$  for deflection would eliminate the extrinsic contribution. This approach may have some merit, as Figure 19 shows that the deflection-corrected  $\Delta K$  levels observed at threshold are fairly insensitive to the roughness changes in the fracture surface. However, the scatter observed in Figure 19 may lead to some doubt about this approach.

## 3. Intrinsic mechanisms

Vasudevan and co-workers<sup>[27,28,29]</sup> have argued that load-ratio effects on the threshold are not generally due to extrinsic effects such as crack closure or branching, but due to intrinsic FCP mechanisms which change with microstructure, environment, or loading conditions. They proposed a model for FCP thresholds which depends on both  $\Delta K$  and  $K_{\text{max}}$ . For example, aluminum alloys subjected to different aging treatments exhibit different threshold maps, with the basic shapes

of the  $\Delta K_{\text{threshold}}$  vs  $K_{\text{max}}$  maps being constant, but with their values shifting around at different microstructures, environments, or loading schemes. It is plausible that this approach may be able to explain the data. Fracture-surface roughness certainly is a result of intrinsic deformation mechanisms that change with temperature, microstructure and frequency. It is possible that intrinsic factors such as slip homogeneity, reversibility, and crack-tip environmental interactions cause both changes in threshold and changes in fracture-surface roughness. This argument would imply that the fracture-surface roughness variation is simply an indication of changing mechanisms leading to a changing threshold and not the cause of it. Figure 16 lends further support to this argument; it shows a consistent decrease in roughness values as the load ratio is decreased at elevated temperatures, and the same behavior has been observed at room temperature in other work done by this group. This change in fracture-surface roughness can also be suspected to be due to a change in crack-tip deformation mechanisms.

There is fractographic evidence for a substantial change in intrinsic deformation and crack-propagation modes with grain size. Figures 11(b) and 12(b) show coarse-grained and fine-grained fracture surfaces under identical conditions (550 °C,  $R = 0.7$ , and 1000 Hz). The magnification difference is about a factor of 5, while the grain-size difference is about a factor of 9. Therefore, if Figure 12(b) were magnified by approximately 2 times more, both micrographs would span an equal number of grains and should have a similar appearance if the fracture mechanism does not change. It is evident by inspecting these figures that this is not the case; that is, the fracture morphology scaled for grain size is different between the two microstructures, presumably due to differences in deformation mechanisms. Transmission electron microscope (TEM) studies of deformation are in progress.

As already mentioned, the relationship between roughness and threshold is different for the two microstructures. For the same microstructure, this relationship depends, among other things, on the mode of fatigue-crack growth, namely, transgranular, intergranular, or mixed. Intergranular fracture was observed in the fine-grained material at 650 °C, but nowhere else. Intergranular fracture is mechanistically quite different from transgranular fracture and should be analyzed by different models. If one removes the 650 °C, fine-grained-material data points out of Figure 10, because they were intergranular, the high-temperature threshold picture becomes much more clear. First, increasing the load ratio reduces the threshold. Second, the coarse-grained microstructure is insensitive to frequency at 550 °C. Third, coarse grains are always better than fine grains. Finally, where there is a frequency effect without intergranular fracture (the fine-grained material at 550 °C and coarse-grained material at temperatures up to 650 °C), increasing the frequency increases the threshold. The latter point is consistent with both thermally activated deformation and thermally activated environmental interactions, which are discussed subsequently. It is interesting to note that the onset of intergranular fracture results in an increase in both the roughness and threshold value. In the fine-grained material fatigued at 100 Hz at 650 °C, which was almost completely intergranular at  $R = 0.7$  and partially intergranular at  $R = 0.4$ , the surface-roughness and threshold values were both higher than at

1000 Hz (where fracture was, in both cases, less intergranular). This was the only case where the threshold was measurably higher at the lower frequency.

#### 4. Environmental effects

It was mentioned earlier that after the crack arrested at threshold, the stress intensity was increased slightly to make the crack grow again at high temperatures. When this was done, the resulting minimum crack growth rate just above threshold (shown in Figure 3) increased substantially as the temperature increased. This suggests, consistent with many previous studies, that oxidation kinetics plays an important role in elevated-temperature near-threshold FCP.<sup>[30]</sup>

For more oxide to form on the crack faces, oxygen should diffuse to the crack tip and through the already existing oxide layer to the metal-oxide interface. Since all these processes should occur in series, the activation energy of the entire process would be determined by the process having the highest activation enthalpy.<sup>[31]</sup> In this case, that process is diffusion of the oxygen atoms through the oxide layer. In all four cases (two different microstructures between 550 °C and 650 °C at 100/1000 Hz), this activation energy was calculated from the crack growth rate near arrest by an Arrhenius-type rate equation and was found to be  $60 \pm 20$  kJ/mol. This result is comparable to the similar activation energies found for Alloy 718 of  $56 \pm 21$  kJ/mol by Yuen *et al.*<sup>[30]</sup> and for Rene' 80 of 41 kJ/mol by Antolovich *et al.*<sup>[32]</sup> This indicates that environmental interactions at the crack tip are important at high temperatures. Vasudevan *et al.*<sup>[27]</sup> have proposed that this might also be the case at room temperature, and this is worthy of further research.

#### 5. Sources of the roughness variation

The natural question resulting from this work is as follows: what changes in the plastic-zone deformation mechanisms affect threshold values and crack-wake roughness? Preliminary results indicate that the most important factor may be heterogeneity of deformation. Consider the coarse-grained microstructure. Figure 11(a) shows that at near-threshold  $\Delta K$  values at room temperature, huge facets span the fracture surface, while almost none are observed at 550 °C (Figure 11(b)). It is well known that high-volume-fraction superalloys continue to deform by planar deformation mechanisms up to temperatures of 750 °C,<sup>[33]</sup> so the change in fracture morphology from large facets to smoother surfaces cannot be ascribed to the onset of wavy slip, which occurs only above about 800 °C.<sup>[33]</sup> A possible explanation for the change observed between Figures 11(a) and (b) is that deformation is much more homogeneous at 550 °C, so that fracture along heavily damaged planar slip bands separated by wider terraces of virgin material is less likely than at room temperature. Support for this notion was found by fractography of the room-temperature specimen in the higher- $\Delta K$  regime: the roughness was reduced from 25  $\mu\text{m}$  (at threshold) to 10  $\mu\text{m}$  (at 20 MPa $\sqrt{\text{m}}$ ), and the large crystallographic facets were no longer observed. It would be expected that higher  $\Delta K$  values would lead to more intense plastic-zone deformation and, likely, to more even distributions of slip bands. At the moment, this is speculative, and studies of slip traces as a function of strain (along with quantitative TEM studies) are necessary to prove this postulate. These studies are in progress.

## VII. CONCLUSIONS

The general behavior of KM4 at frequencies up to 1000 Hz is identical to similar alloys tested at more traditional testing frequencies (10 to 100 Hz). In the Paris regime, coarse grains, low load ratios, low temperatures, and high frequencies generally resulted in lower crack-propagation rates. Thresholds followed similar general trends, with the exception of the fine-grained microstructure at 650 °C, which had a superior threshold to the coarse-grained microstructure at 100 Hz but not at 1000 Hz and which exhibited a change to intergranular crack propagation at 650 °C. Intergranular crack propagation in the fine-grained material became more pronounced both with decreasing frequency and increasing load ratio, and the onset of intergranular crack propagation was beneficial for high-frequency thresholds.

Quantitative SEM stereofractography revealed a good correlation between fracture-surface roughness (defined as the standard deviation of the fracture-surface height) and the threshold for the coarse-grained material, but not for the fine-grained material. This correlation was valid over the entire range of temperatures, load ratios, and frequencies studied. Further, as the load ratio was increased, the near-threshold fracture-surface roughness also increased. It appears that quantifying the microscopic fracture-surface roughness can lend insight into the changing deformation and fracture mechanisms that control threshold.

Closure-load measurements showed that roughness-induced crack closure alone cannot explain the threshold variations, even though there was a direct correlation between roughness and threshold for the coarse-grained material. It appears that the variation in the crack-propagation threshold with load ratio, microstructure, temperature, and frequency is controlled by a combination of both intrinsic and extrinsic mechanisms, but further research is necessary to establish the relative importance of the mechanisms.

## ACKNOWLEDGMENTS

This work was supported by the MURI on "High Cycle Fatigue," funded at Michigan Technological University by the Air Force Office of Scientific Research, Grant No. F49620-96-1-0478, through a subcontract from the University of California at Berkeley. We thank Dr. David L. Davidson, retired from Southwest Research Institute, for helpful comments on this manuscript.

## REFERENCES

1. B.A. Cowles: *Int. J. Fract.*, 1996, vol. 80, pp. 147-63.

2. R.O. Ritchie, B.L. Boyce, J.P. Campbell, O. Roder, A.W. Thompson, and W.W. Milligan: *Int. J. Fatigue*, 1999, vol. 21, pp. 653-62.
3. S.A. Padula II, A. Shyam, R.O. Ritchie and W.W. Milligan: *Int. J. Fatigue*, 1999, vol. 21, pp. 725-31.
4. D.D. Krueger, J.F. Wessels, and K.M. Chang: U.S. Patent 5,143,563, Sept. 1, 1992.
5. S. Sinharoy, P. Virro-Nic, and W.W. Milligan: *Metall. Mater. Trans. A*, 2001, vol. 32A, pp. 2021-32.
6. K.R. Bain: General Electric Aircraft Engines, Evendale, OH, private communication, May 31, 2000.
7. J.M. Morgan and W.W. Milligan: in *High Cycle Fatigue of Structural Materials*, W.O. Soboyejo and T.S. Srivatsan, eds., TMS, Warrendale, PA, 1997, pp. 305-12.
8. MeX Software, Alicona GmbH, Berchtesgaden, Germany, [www.alicon.com](http://www.alicon.com).
9. O. Kolednik, S. Scherer, P. Schwarzbock, and P. Werth: in *Fracture Mechanics: Applications and Challenges*, Proc. ECF13, M. Fuentes, M. Ellices, A. Martin-Meizoso, and J.M. Martinez-Esnaola, eds., Elsevier, Amsterdam, 2000, paper no. 1U.60 (CD-ROM).
10. S.D. Antolovich and N. Jayaraman: in *Fatigue: Environmental and Temperature Effects*, J.J. Burke and V. Weiss, eds., Plenum Press, New York, NY, 1983, pp. 119-44.
11. B. Lerch, N. Jayaraman, and S.D. Antolovich: *Mater. Sci. Eng.*, 1984, vol. 66, pp. 151-66.
12. L.A. James and W.J. Mills: *Eng. Fract. Mech.*, vol. 22, 1985, pp. 797-817.
13. R.V. Miner and J. Gayda: *Int. J. Fatigue*, 1984, vol. 6, pp. 189-93.
14. J. Bartos and S.D. Antolovich: in *Fracture 1977*, D.M.R. Taplin, ed., University of Waterloo Press, Waterloo, 1977, vol. 2, pp. 996-1006.
15. S. Floreen and R.H. Kane: in *Superalloys 1980*, J.K. Tien et al., eds., ASM, Metals Park, OH, 1980, pp. 595-664.
16. H.F. Merrick and S. Floreen: *Metall. Trans. A*, 1978, vol. 9A, pp. 231-36.
17. J. Gayda and R.V. Miner: *Metall. Trans. A*, 1983, vol. 14A, pp. 2301-08.
18. B.A. Cowles, D.L. Sims, J.R. Warren, and R.V. Miner: *J. Eng. Mater. Tech. (Trans. ASME)*, 1980, vol. 102, pp. 356-63.
19. J.E. King: *Mater. Sci. Technol.*, 1987, vol. 3, pp. 750-64.
20. E.E. Underwood and K. Banerji: *Mater. Sci. Eng.*, 1986, vol. 80, pp. 1-14.
21. T. Ogawa, K. Tokaji, and K. Ohya: *Fatigue Fract. Eng. Mater. Struct.*, 1993, vol. 16, pp. 973-82.
22. J. Wasen and E. Heier: *Int. J. Fatigue*, 1998, vol. 20, pp. 737-42.
23. R.O. Ritchie and S. Suresh: *Metall. Trans. A*, 1981, vol. 13A, pp. 937-40.
24. S. Suresh: *Metall. Trans. A*, 1983, vol. 14A, pp. 2375-85.
25. S. Suresh: *Metall. Trans. A*, 1985, vol. 16A, pp. 249-60.
26. J. Wasen, B. Karlsson, and K. Hamberg: *Acta Stereol.*, 1987, vol. 6, pp. 199-204.
27. A.K. Vasudevan, K. Sadananda, and N. Louat: *Mater. Sci. Eng.*, 1994, vol. A188, pp. 1-22.
28. K. Sadananda and A.K. Vasudevan: *Int. J. Fatigue*, 1997, vol. 19 (1), pp. S193-S189.
29. A.K. Vasudevan, K. Sadananda, and K. Rajan: *Int. J. Fatigue*, 1997, vol. 19 (1), pp. S151-S159.
30. J.L. Yuen, P. Roy, and W.D. Nix: *Metall. Trans. A*, 1984, vol. 15A, pp. 1769-75.
31. A.K. Jena and M.C. Chaturvedi: *Phase Transformations in Materials*, 1st ed, Prentice Hall, Englewood Cliffs, NJ, 1992, p. 115.
32. S.D. Antolovich, R. Baur, and S. Liu: in *Superalloys 1980*, J.K. Tien et al., eds., ASM, Metals Park, OH, 1980, pp. 605-13.
33. W.W. Milligan and S.D. Antolovich: *Metall. Trans. A*, 1987, vol. 18A, pp. 85-96.

## FRETTING

- A.E. Giannakopoulos and S. Suresh, "A Three-Dimensional Analysis of Fretting Fatigue", *Acta Mater.*, vol. 46, 1997, pp. 177-92.
- A.E. Giannakopoulos, T.C. Lindley, and S. Suresh, "Aspects of Equivalence between Contact Mechanics and Fracture Mechanics: Theoretical Connections and a Life-Prediction Methodology for Fretting-Fatigue", *Acta Mater.*, vol. 46, 1998, pp. 2955-68.
- A.E. Giannakopoulos, T.A. Venkatesh, T.C. Lindley, and S. Suresh, "The Role of Adhesion in Contact Fatigue", *Acta Mater.*, vol. 47, 1999, pp. 4653-64.
- J.W. Hutchinson and M.R. Begley, "Plasticity in Fretting of Coated Surfaces", *Eng. Fract. Mech.*, vol. 62, 1999, pp. 145-64.
- A.E. Giannakopoulos, T.C. Lindley, S. Suresh, and C. Chenut, "Similarities of Stress Concentration in Contact at Round Punches and Fatigue at Notches: Implication to Fretting Fatigue Crack Initiation", *Fatigue Fract. Engin. Mater. Struct.*, vol. 23, 2001, pp. 561-71.
- T.A. Venkatesh, B.P. Conner, C.S. Lee, A.E. Giannakopoulos, T.C. Lindley, and S. Suresh, "An Experimental Investigation of Fretting Fatigue in Ti-6Al-4V: The Role of Contact Conditions and Microstructure", *Metall. Mater. Trans. A*, vol. 32A, 2001, pp. 1131-46.
- E. W. Andrews, A. E. Giannakopoulos, E. Plisson and S. Suresh, "Analysis of the Impact of a Sharp Indenter", *Int. J. Solids Struct.*, vol. 39, 2002, pp. 281-95.



## A THREE-DIMENSIONAL ANALYSIS OF FRETTING FATIGUE

A. E. GIANNAKOPOULOS and S. SURESH

Department of Materials Science and Engineering, Massachusetts Institute of Technology, Cambridge, MA, 02139, U.S.A.

(Received 20 February 1997; accepted 26 June 1997)

**Abstract**—Three-dimensional finite element analyses of fretting contact fatigue between a sphere and a flat surface of the same material are presented. A radial expansion of the displacement fields around the contact center is used to map the entire three-dimensional fields into a radial-axial plane of reference which contains the slip direction. The computational results for the limiting case of the onset of rigid body sliding are first shown to be in agreement with known theoretical results. The present computations are then used to capture the evolution of surface and sub-surface fields for different levels of partial slip, interfacial friction and externally imposed mean stress values. It is shown that the magnitude as well as distribution of the fields change markedly by the sign of the superimposed mean stress; this result has significant implications for fretting fatigue in the presence of a residual surface stress induced by shot peening or coating. The computational model is also used to simulate the evolution of fretting damage in prior experiments conducted on a bearing steel and an aluminum alloy with the sphere on flat surface fretting arrangement. It is shown that the model captures many of the salient features of fretting damage and failure documented in the experiments. Conditions governing the occurrence of elastic shakedown and the onset of surface plasticity are also briefly examined to illustrate the capability of the present computational approach. © 1997 Acta Metallurgica Inc.

### 1. INTRODUCTION

Fretting fatigue commonly refers to the degradation in the fatigue properties of a material due to repeated sliding of two contacting surfaces over small relative displacements, with amplitudes typically in the range 10–50  $\mu\text{m}$ . Examples of practical situations where fretting wear and fretting fatigue influence mechanical integrity include such diverse applications as bolted and riveted joints, key-way-shaft couplings, shrink-fitted couplings, metallic coil ropes and suspension cables, coil wedges of generator rotors, and blade-dovetail contact sections of turbine engines (e.g. Ref. [1]).

The reduction in the fatigue strength of a material due to fretting can be influenced in a complex manner by such factors as (i) the elastic and plastic mismatch in properties between the contacting materials, (ii) the normal contact pressure, (iii) the roughnesses of the mating surface asperities and the ensuing frictional forces, (iv) the amplitude of sliding displacement, (v) cyclic frequency and waveform, (vi) environment, (vii) test temperature, (viii) microstructural changes and phase transformations, if any, induced by local heating during fretting, and (ix) residual stresses and mechanical loads imposed on the specimen. Experimental, analytical and computational studies of fretting fatigue have sought to quantify the role of many of these factors in influencing cyclic damage and fatigue cracking. Detailed summaries of these various developments can be

found in conference proceedings [1], review articles [2, 3] and research monographs [4, 5].

The theoretical basis for many of the fretting fatigue analyses stems from the works of Mindlin [6], Mindlin and Deresiewicz [7], Deresiewicz [8], Hamilton and Goodman [9] and Hamilton [10]. These studies collectively led to analytical elastic solutions for the axisymmetric case involving incipient full slip from complete stick, and partial slip and steady-state global sliding of a sphere on a planar surface. Analytical and numerical extensions of this problem to other fretting contact situations involving planar or axisymmetric geometries have been reported (for reviews, see [4, 5]). Such two-dimensional idealizations are necessary to contain the scope of the analysis to within reasonable computational resource requirements. To our knowledge, essentially all numerical modeling of the micromechanics of fretting fatigue reported in the open literature pertains to planar and axisymmetric analyses. Indeed, the directionality of the field quantities produced during alternating sliding in fretting inevitably calls for three-dimensional models.

This paper reports three-dimensional finite element computations of repeated fretting contact between a metallic sphere and a flat surface of an identical material. The present analyses introduce several novel approaches to the study of fretting fatigue:

- A radial expansion of the displacement fields around the contact center is used to map the entire field into a radial-axial ( $r, z$ ) plane of reference that includes the direction of sliding, thereby capturing the three-dimensional aspects of the problem.
- Prior numerical studies (see, for example, Ref. [5]) have analyzed the two-dimensional cylindrical contact wherein the surface tractions were generally prescribed, thus circumventing the analysis of the actual sliding contact problem. The present work, to our knowledge, attempts for the first time to model the full three-dimensional sliding and cyclic fretting contact of a sphere on a flat surface including the elastic-plastic material response.
- An outcome of the present numerical formulation is that the stress and strain fields around the fretting contact area can be captured for any partial slip situation including conditions where plastic yielding occurs. Available theories, however, are applicable only for the limited case of incipient global elastic sliding wherein asymptotic analyses are needed to retrieve the field values at the surface and full numerical analysis is needed to locate the maximum field variables.
- The present approach easily permits the superposition of an external cyclic load as well as an internal stress field (such as that arising from shot peening and other surface modifications) on the fretted specimen.

The paper is arranged in the following manner. A brief summary of relevant theories of fretting fatigue is first given, followed by details of the present numerical approach. The fields in the vicinity of the contact area are then shown to be in good agreement with the classical analytical results for monotonic incipient sliding. The effective stress distribution at the periphery of the contact zone is then captured numerically during the imposition of a small relative cyclic displacement between the sphere and the flat surface. The computational results are then compared with the experimental observations of Kuno *et al.* [11, 12] and Lamacq *et al.* [13] for two model systems where a sphere was repeatedly fretted against a flat surface of the same material: a bearing steel and an aluminum alloy. These direct experimental observations were found to be in reasonable accord with the three-dimensional numerical predictions of the size and shape of the fretting damage annulus under comparable test conditions. Systematic and parametric analyses of the effects of the following key fretting parameters on the evolution of cyclic deformation fields and damage evolution were then performed: the ratio of the normal to the shear tractions at the contact surface, the friction coefficient, the relative cyclic displacement amplitude of the mating surfaces, and the mechanical load imposed on the

fretted material. Possible criteria for the inception of a fretting fatigue crack are also examined.

## 2. THEORETICAL BACKGROUND

A full description of the implications of the present finite element simulations requires a comparison with known analytical formulations for monotonic incipient sliding. For this purpose and to introduce the necessary nomenclature, we briefly examine in this section the relevant theoretical models for fretting and sliding.

A normal force,  $P$ , pressing a sphere and a half-space together, gives rise to a well characterized circular contact area which has dimensions given by the classical Hertz solution [14], Fig. 1. Any tendency for relative slip to occur between the two contacting bodies introduces a tangential force of friction,  $T$ , acting on each surface in a direction which opposes the motion. The force  $T$  arises from static friction, which does not exceed the limiting friction force corresponding to the onset of slipping.

If the sphere and the fretted substrate have the same elastic constants, their surfaces conform exactly with each other and the resultant deformations do not mutually affect the distribution of normal pressure [4]. Under these conditions, the shape and size of the contact area are independent of the tangential force  $T$ . When the coefficient of limiting friction is less than unity, the tangential

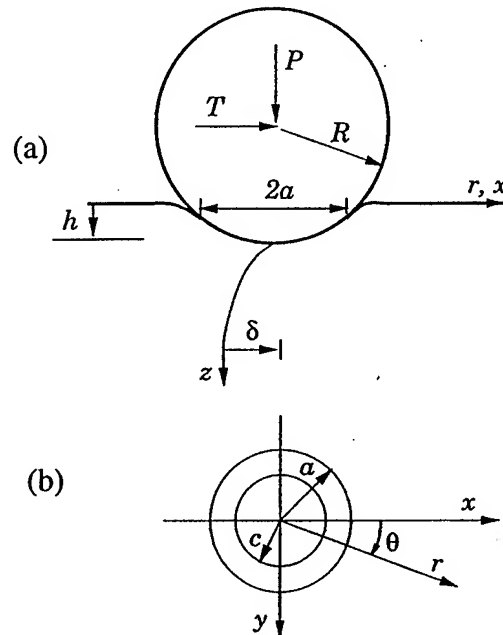


Fig. 1. (a) Schematic and nomenclature for fretting contact between a sphere and a flat surface. (b) The view from the top showing the circular contact region and the cylindrical coordinate system.

tractions do not significantly influence the normal pressure and the contact area. We neglect this influence throughout the analysis, and assume that the stresses and deformations due to normal pressure and tangential traction are independent of each other, and that in the case of elasticity, they can be linearly superposed.

### 2.1. Sliding elastic sphere on a flat surface

The tangential tractions,  $q$ , and the normal pressure,  $p$ , in sliding contact are related by the Amonton/Coulomb law:

$$\frac{|q|}{p} = \frac{|T|}{P} = \mu, \quad (1)$$

where  $\mu > 0$  is a constant coefficient of kinetic friction (see, for example, Refs [15, 16]). For a sphere which slides over a plane surface in a constant direction, as shown in Fig. 1, the radius,  $a$ , of the circular contact area and the pressure distribution,  $p(r)$ , are given by [14]

$$a = \left( \frac{3PR}{4E^*} \right)^{1/3}, \quad \frac{1}{E^*} = \left\{ \frac{1-\nu_1^2}{E_1} + \frac{1-\nu_2^2}{E_2} \right\}, \quad (2)$$

$$p(r) = \frac{3P}{2\pi a^2} \sqrt{1 - \left( \frac{r^2}{a^2} \right)}; \quad 0 \leq r \leq a, \quad (3)$$

where the indices 1 and 2 refer to the sphere and the half-space, respectively, for elastic modulus ( $E$ ) and Poisson ratio ( $\nu$ ), and  $R$  is the radius of the sphere. If the sphere and the planar half space have the same elastic properties, as in the present case,  $E_1 = E_2 = E$ , and  $\nu_1 = \nu_2 = \nu$ . The tangential traction at incipient sliding is [4, 5]

$$q(r) = \frac{3\mu P}{2\pi a^2} \sqrt{1 - \left( \frac{r^2}{a^2} \right)}; \quad 0 \leq r \leq a, \quad (4)$$

acting parallel to the sliding direction within the contact area. Using the Cerruti solution [17] for a concentrated tangential force, explicit equations for calculating the stress components have been given by Hamilton and Goodman [9] and Hamilton [10].

The maximum value of the von Mises effective stress, which is an indicator of incipient plasticity, can also be extracted from the foregoing analyses. When there exists only a normal force between the sphere and the planar substrate, the maximum Mises stress occurs below the surface (for example, for  $\nu = 0.3$ , it is on the loading axis at a depth  $z \approx 0.5a$  beneath the reference planar surface). Friction increases the magnitude of the Mises stress and moves it closer to the surface and towards the back edge of the sliding contact. For  $\mu > 0.3$ , the maximum Mises stress appears on the surface and the second invariant of the deviatoric stresses,  $J_2$ , is given by [10]

$$\frac{\sqrt{J_2}}{p_{\max}} = \frac{1}{\sqrt{3}} \left\{ \frac{(1-2\nu)^2}{3} + \frac{(1-2\nu)(2-\nu)\mu\pi}{4} + \frac{(16-4\nu+7\nu^2)\mu^2\pi^2}{64} \right\}^{1/2}, \quad (5)$$

with  $p_{\max} = 3P/(2\pi a^2)$  and the yield criterion in shear,  $J_2 = \tau_y^2$ , where  $\tau_y$  is the shear yield strength of the substrate. Tangential friction also enhances the compressive stress at the front edge of the sliding contact and intensifies the tensile stress at the trailing edge. The maximum principal tensile stress occurs at the surface [10].

### 2.2. Partial sliding

A tangential force,  $T$ , which is smaller than the limiting friction force,  $\mu P$ , does not cause global sliding, but induces frictional traction at the contact interface leading to a small relative motion, referred to as *micro-slip*, over part of the interface. The remainder of the interface deforms without relative motion and such regions are said to *stick*. All surface points within the "stick" region undergo the same tangential displacements.

The analyses of Cattaneo [18], Mindlin [6] and Deresiewicz [8] show that stick conditions exist over a circular region that is concentric with the contact area. The outer boundary  $c$  of the stick zone has a radius

$$\frac{c}{a} = \left[ 1 - \frac{T}{\mu P} \right]^{1/3}; \quad 0 \leq c/a \leq 1. \quad (6)$$

The resultant tangential tractions,  $q(r)$ , act parallel to the slip direction. In the region where the surfaces slip, Fig. 2(a),

$$q(r) = \frac{3\mu P}{2\pi a^2} \left( 1 - \frac{r^2}{a^2} \right)^{1/2}; \quad c \leq r \leq a. \quad (7a)$$

In the stick region, the resultant tangential tractions are

$$q(r) = \frac{3\mu P}{2\pi a^2} \left\{ \left( 1 - \frac{r^2}{a^2} \right)^{1/2} - \frac{c}{a} \left( 1 - \frac{r^2}{a^2} \right)^{1/2} \right\}; \quad c \leq r \leq a. \quad (7b)$$

Neglecting terms of order  $\nu/(4-2\nu)$ , the relative tangential displacement (in the direction of  $T$ ) is, as shown in Fig. 2(b),

$$\delta = \frac{3\mu P}{16a} \left\{ \frac{2-\nu_1}{G_1} + \frac{2-\nu_2}{G_2} \right\} \times \left\{ 1 - \left( 1 - \frac{T}{\mu P} \right)^{2/3} \right\}. \quad (8a)$$

The initial slope of the  $T$ - $\delta$  curve is:

$$\left. \frac{dT}{d\delta} \right|_{T=0} = 8a \left\{ \frac{2-\nu_1}{G_1} + \frac{2-\nu_2}{G_2} \right\}^{-1}. \quad (8b)$$

Here,  $G_i = E_i/[2(1+\nu_i)]$ ,  $i = 1, 2$ , are the shear



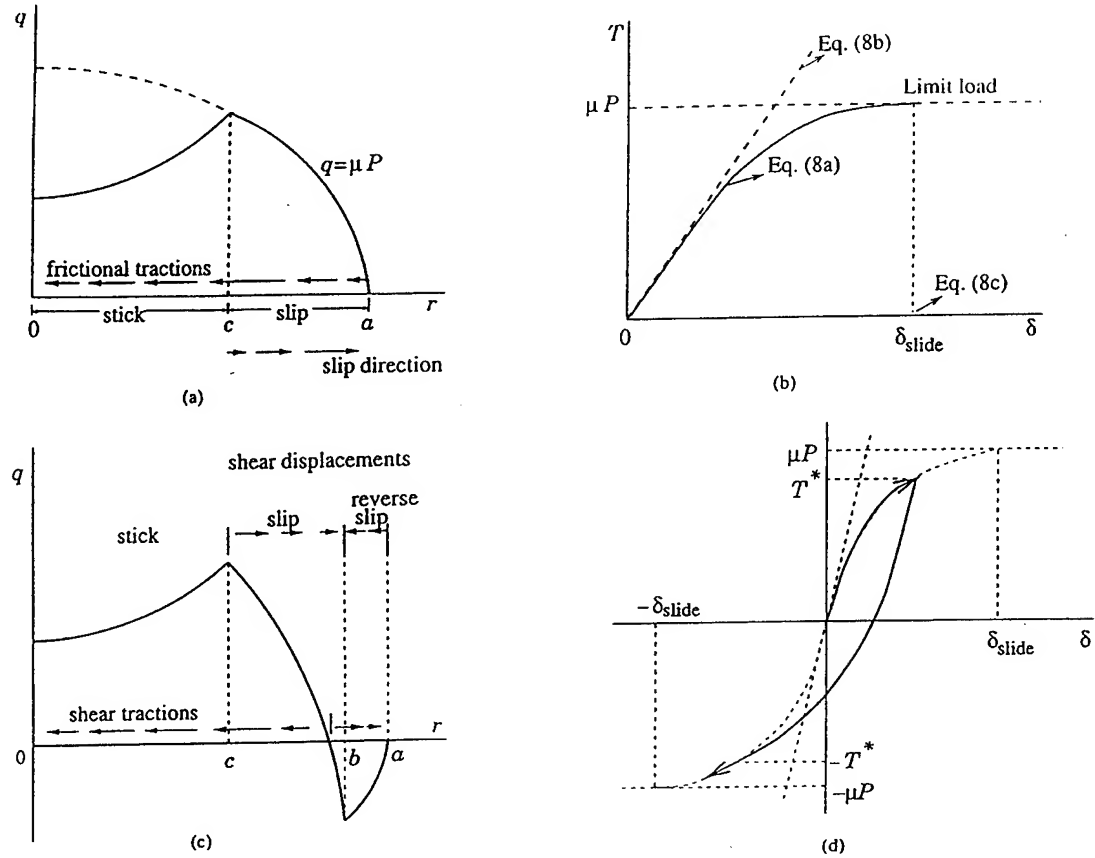


Fig. 2. (a) Tangential traction ( $q$ ) on the contact surface under fixed normal load and monotonically increasing tangential load. (b) Tangential load ( $T$ ) vs tangential displacement ( $\delta$ ) during the loading process in (a). (c) Tangential traction ( $q$ ) distribution on the contact surface under fixed normal load and decreasing tangential load. (d)  $T$  vs  $\delta$  during the loading process in (a) and the unloading process in (c).

moduli of the sphere and the half-space. For the present case of fretting between identical materials,  $G_1 = G_2 = G$  and  $\nu_1 = \nu_2 = \nu$ . For  $T = 0$ ,  $\delta = 0$ , and for  $T = \mu P$ ,  $\delta$  is a maximum and the limiting condition occurs when  $dT/d\delta = 0$ ; at this point, the tangential stiffness of the spherical contact is lost and the sphere can slide with only displacement control. This situation is termed *sliding* (whereas the term *slip* is reserved for relative tangential displacement over only a portion of the contiguous surfaces). In Fig. 2(b), the onset of full sliding occurs at a displacement,

$$\delta_{slide} = \frac{3\mu P(2-\nu)}{16aG}. \quad (8c)$$

Experimental measurements of the tangential displacements by Johnson [19] support the validity of equation (9).

### 2.3. Reversed sliding

Upon releasing the tangential load from  $T^*$  ( $0 < T^* < \mu P$ ), slip of opposite sign develops from  $r = a$  to  $r = b$ , Fig. 2(c), with

$$\frac{b}{a} = \left\{ 1 - \frac{(T^* - T)}{2\mu P} \right\}^{1/3}; \quad \frac{c}{a} \leq \frac{b}{a} \leq 1. \quad (9)$$

The relation between the cyclic tangential tractions and the tangential displacement in the adhered region are plotted in Fig. 2(d). (The analytical expressions can be found in Refs [4, 5].) For  $-T^* \leq T \leq T^*$ ,  $c \leq b \leq a$ . For  $-\mu P < T \leq -T^*$ , the tractions follow the previous case of increasing  $T$ , but with the signs reversed.

### 3. NUMERICAL FORMULATION

As noted earlier, the nature of the fretting fatigue problem clearly requires a three-dimensional (3D) simulation. The only symmetry is about the principal plane that contains the direction of sliding. In view of this symmetry, only half of the planar surface and half of the sphere need to be discretized. If a straightforward 3D finite element model is employed, it can be estimated that a 3D mesh with approximately 100 000 eight-noded, trilinear elements would be needed in order to capture a satisfactory degree of resolution of the local fields in the

vicinity of the contact region. Such a high number of elements will render the calculations too complex, slow and unmanageable. An alternative, more efficient means to capture the three-dimensional nature of the fields is predicated upon the trigonometric expansion of the displacement fields around the contact center. This leads to the use of the so-called ring-elements which were employed by Jørgensen [20] who studied, using a specially written numerical code, indentation problems involving monotonic normal contact in polymeric composites. This method was extended to include full 3D variations of the field variables in the large spherical indentation of graded organic composites [21]. In this paper, we extend this method of radial expansion of displacement fields to the study of fretting fatigue using the general purpose finite element program, ABAQUS [22]. For the present problem, however, a modification of the contact conditions in ABAQUS was coded as described in the following.

The displacement field variables are expressed with reference to a cylindrical coordinate system  $(r, z, \theta)$ , whose origin is taken to be the centroid of the contact area. Here,  $z$  is the vertical depth coordinate,  $r$  is the radial position from the vertical axis, and  $\theta$  is the circumferential angle measured from the sliding direction (Fig. 1). Denoting by  $u$ ,  $v$  and  $w$  the radial, circumferential and axial components of the displacements, and using the symmetry conditions,

$$\begin{aligned} u(r, z, \theta) &= \sum_{n=0}^M u_n^c(r, z) \cos(2n\theta), \\ v(r, z, \theta) &= \sum_{n=0}^M v_n^c(r, z) \cos(2n\theta), \\ w(r, z, \theta) &= \sum_{n=0}^M w_n^s(r, z) \sin(2n\theta). \end{aligned} \quad (10)$$

The superscripts  $c$  and  $s$  denote the corresponding amplitudes in the cosine and sinusoidal terms of the above Fourier expansions of the displacements. In the present problem, the absence of any stress singularity makes the above expansion complete.

The advantage of equation (10) is that they map the entire field into a radial-axial  $(r, z)$  plane of reference that includes the direction of sliding. The strength of this approach lies in the high rate of convergence of the above series.  $M = 0$  corresponds to the two-dimensional analysis involving axisymmetric deformation. On the basis of prior experience (e.g. Refs [20, 21]), it can be shown that a series expansion up to  $M = 2$  is sufficient to produce very good convergence. Linear kinematics and small strains were assumed. Within the principal plane of reference, the field variables were resolved in terms of four-noded isoparametric elements. The number of degrees of freedom per node depends on

the choice of  $M$ . For a given  $M$ , the stiffness of each ring-element is integrated. The integration in the circumferential direction involves products of harmonic functions of  $\theta$  and uses the trapezoidal rule with six integration points. The integration on the radial-axial (symmetry) plane uses full Gaussian integration.

The material model employed here involves an isotropic, linear elastic formulation, with an option to introduce the associative flow rule with isotropic or kinematic strain hardening. The spherical indenter is modeled as a rigid paraboloid of revolution with radius  $R(z = r^2/(2R))$ . Coulomb-type friction was assumed with a friction coefficient (which could also vary with the number of fretting fatigue cycles  $N$  in a predetermined manner) between  $\mu \rightarrow 0$  (frictionless case) and  $\mu \rightarrow \infty$  (perfect stick case). The friction coefficient was taken to be isotropic on the plane of sliding.

Nodal contact was considered for at least 13 nodes on the topmost surfaces of about 12 elements. Contact is made successively over an area comprising nodes with an outwardly expanding radius; this dictates the radius of the contact perimeter. Contact conditions with friction were found by recourse to an iterative predictor-corrector solution method, which invoked the penalty method to enforce them. In this procedure, the friction force is gradually applied, with the equilibrium conditions and the stick-slip kinematics satisfied at all times. This is a well known numerical method of implementing unilateral conditions such as the present one, by accepting initial gross slip of the contacting surfaces and subsequently correcting the slip by enforcing the correct tractions as per Coulomb's friction law. The procedure terminates when a pre-defined degree of allowable error in slip displacement is reached. In the present analysis, the numerically allowed error in the slip displacement was less than 1/1000 of the instantaneous value of the slip displacement.

The contact boundary conditions have to be in conformity with the general displacement angular expansion, equation (10). Then the contact conditions have to be described in all  $(M + 1)$  planes that form the basis of the expansion. These planes cut the initially free surface of the substrate along radial lines that are confocal to the center of the contact circular region and make an angle of  $\pi/M$  in-between them. A local coordinate system is attached at the tangent to the surface plane, centered at the tip of the spherical punch. The contact conditions are considered with respect to a moving substrate that has equal magnitudes (but opposite in sign) contact displacements.

To achieve well-posed contact conditions, the normal and radial displacements along the aforementioned surface lines have to be assigned using the following procedure. The normal contact displacements are constrained to be identically the same

for all nodes of the surface lines, thus enforcing the substrate to deform in the axisymmetric shape of the punch. The tangential sticking conditions are implemented by constraining the radial displacements of all nodes of the surface lines so that the tangential displacements  $\delta$  have the same magnitudes and directions with the stick zone. This enforces an antisymmetric shear traction distribution.

Initial stresses in the fretting specimen (i.e. the substrate half space in this case) can be prescribed, as well as any variation of elastic or plastic property with depth. This is particularly useful, as shown later, for studying fretting damage in loaded specimens and to simulate different surface treatments, such as shot-peening. The loading can be applied as displacement-controlled or load-controlled. The normal loading is applied first and then a sequence of cyclic oscillations is applied, one at a time.\* Quasi-static equilibrium is satisfied during all loading sequences. A mesh of about 5000 elements is found to be sufficient to give convergent results, with  $M = 2$ . The foregoing method is some eighty times faster than the time required for a complete 3D simulation, just for the elastic case.

#### 4. NUMERICAL PREDICTIONS VS ANALYTICAL RESULTS

In this section, we compare the computational predictions with known analytical results for some limiting cases of sliding, in an attempt to evaluate the accuracy of the computations. (More involved computational results dealing with a parametric study of fretting fatigue will be addressed in Section 5.) For this purpose, the sphere is taken to be rigid. The normal load,  $P$ , is applied first, after which the tangential force,  $T$ , is increased monotonically from zero. The material response for the planar substrate is first chosen to be primarily elastic with  $\nu = 0.3$  and a range of constant friction coefficients,  $\mu$ . As expected from the theory, the distribution of normal tractions is insignificantly altered during the application of  $T$ . Therefore, equation (8) holds with better than 99.5% accuracy.

##### 4.1. Fixed normal force, monotonically increasing tangential force

For this situation, slip commences at the edge of the contact region and progresses radially inward, as expected from the theory [4, 5]. For  $T < \mu P$ , slip inside the center of the contact is absent and the tangential tractions are radially symmetric. Slip occurs in an annular zone, whose outer radius is  $a$ , given by equation (2), and whose inner radius is  $c$ ,

given by equation (6). The size of the annular zone is predicted by the simulations to an accuracy of better than 95%. The distribution of tangential tractions,  $q$ , on the contact surface follow equation (7) with better than 98.5% accuracy. The tangential displacement,  $\delta$ , relates to  $T$  as per equation (8) with a comparable precision.

As  $T \rightarrow \mu P$ ,  $c \rightarrow 0$ , and the stick region of the contact surface shrinks to zero. Then,  $\delta \rightarrow \delta_{\text{slide}}$ , at which point the displacement becomes indeterminate (under no other constraint) as rigid-body sliding takes place over the entire contact surface. Around that limiting point,  $dT/d\delta \rightarrow 0$ , the computations with load control become unstable, and the numerical analysis has to be continued with tangential displacement control.

##### 4.2. Fixed normal force, decreasing tangential force

Once the tangential force attains a value  $T^*$  ( $0 < T^* < \mu P$ ), a reversal is initiated with  $T$  in the range  $-T^* \leq T \leq T^*$ . This induces slip of opposite sign at the contact perimeter. The reverse slip region penetrates to a radius  $b$  according to equation (9). Here, the unloading must be of sufficient resolution (i.e.  $(b - c)$  should be resolved by at least two elements) to capture accurately the reverse slip. For  $T = -T^*$ ,  $b = c$  and reverse sliding extends as much as the initial slip, as expected from the theory. When  $T = 0$ , permanent deformation is comparable to that estimated from theory, and the accompanying traction is a self-equilibrated distribution with  $b/a = (1 - T^*/(2\mu P))^{1/3}$ . The tractions and displacements depend on the entire loading history and the instantaneous relative rates of change of the tangential forces.

##### 4.3. Fixed normal force constant, alternating tangential force

As expected from the theory, the trends corresponding to  $T = -T^*$  are the same as those at

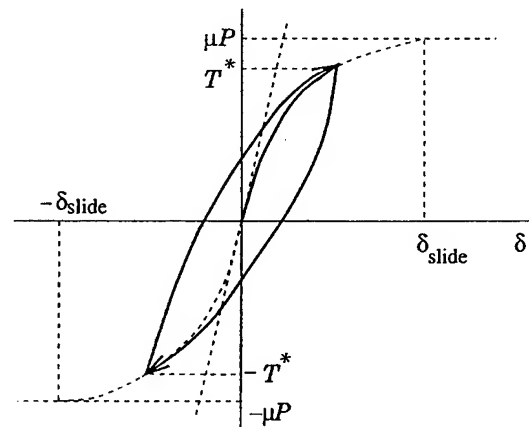


Fig. 3.  $T$  vs  $\delta$  cyclic hysteresis loop for fretting fatigue with partial slip.

\*With the present formulation, it is feasible to model any smooth axisymmetric indenter fretting against a planar surface, for any combination of normal and tangential loading.

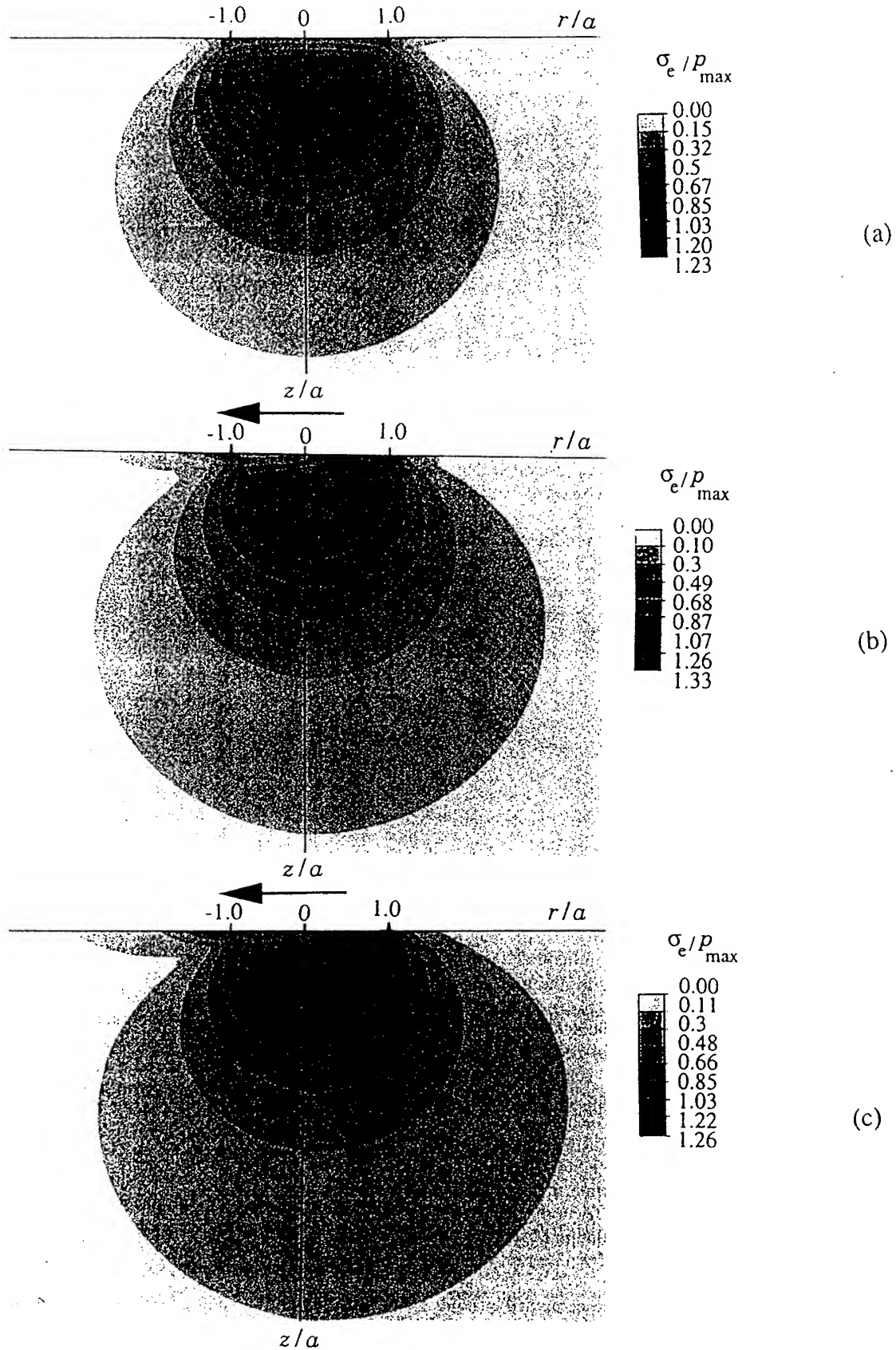


Fig. 4. Contours of von Mises effective stress for (a)  $\mu = 0.0$  (normal Hertzian contact), (b)  $\mu = 0.25$ , and (c)  $\mu = 0.50$ . The arrow indicates the direction of sliding in (b) and (c). The stresses are normalized by the maximum normal pressure,  $p_{\max} = 3P/(2\pi a^2) = 1200$  MPa, and the distances by the contact radius,  $a$ . Poisson ratio,  $\nu = 0.3$  in all cases. The axes  $r/a$  and  $z/a$  are drawn to the same scale.

$T = T^*$ , except for the reversal of sign. A subsequent increase of  $T$  from  $-T^*$  to  $T^*$  is accompanied by events that are similar to those occurring during  $T^*$  to  $-T^*$ , except for the appropriate reversal of sign. The area enclosed in the predicted  $t$ - $\delta$  loop, shown in Fig. 3, gives the frictional energy loss per cycle,  $\Delta W$ . Theory [7] shows that the work,  $\Delta W$ , done by the tangential force in a complete fretting cycle is dissipated during the reversal of micro-slip in the annular area  $c \leq r \leq a$ :

$$\Delta W = \frac{9(\mu P)^2}{10a} \left\{ \frac{2 - \nu_1}{G_1} + \frac{2 - \nu_2}{G_2} \right\} \times \left\{ \left[ 1 - \left( 1 - \frac{T^*}{\mu P} \right) \right]^{5/3} - \frac{5T^*}{6\mu P} \left[ 1 - \left( 1 - \frac{T^*}{\mu P} \right)^{2/3} \right] \right\}. \quad (11)$$

The value of  $\Delta W$  extracted from the computational results of Fig. 3 match the predictions of equation (11) to an accuracy of 99% (provided that each branch of the  $T$ - $\delta$  curve is reached with at least 10 equal steps).

A subsequent reduction in  $T$  produces a repetition of the events accompanying the first unloading. During several oscillations of  $T$  between  $\pm T^*$ , with constant  $P$ , the  $T$ - $\delta$  loop is essentially the same. However, numerical round-off errors are expected to become significant for more than  $10^5$  cycles.

#### 4.4. Elastic sliding

The numerically determined stress fields were tested for nearly full sliding conditions,  $T \approx \mu P$ . Figures 4(a), (b) and (c) show contours of constant von Mises effective stress for three different friction coefficients:  $\mu = 0$  (i.e. normal contact only),  $\mu = 0.25$  and  $\mu = 0.50$ , respectively. All length dimensions in these figures are normalized by the contact radius,  $a$ , and all stresses by the maximum normal Hertzian contact pressure,  $p_{\max} = 3P/(2\pi a^2)$ .

Figure 4(a) simply reproduces the normal Hertzian contact solution with no friction, to provide a basis for subsequent comparisons. In Fig. 4(b), note the leading edge of the contact region with high stress values (which is on the left side of the contact area in Fig. 4(b) with the sphere sliding on the substrate from right to left as indicated by the arrow; the substrate half-space is stationary). An increase in the friction coefficient moves the location of the maximum Mises stress (denoted by the "+" sign) from beneath the fretted surface for  $\mu = 0.25$ , Fig. 4(b), to the surface for  $\mu = 0.50$ , Fig. 4(c). The computed maximum Mises stress differs at most by 1.6% from the analytical predictions [10] predicated on equation (5).

### 5. FURTHER NUMERICAL PREDICTIONS AND COMPARISONS WITH EXPERIMENTS

#### 5.1. Stress fields under partial slip

Figures 5(a) and (b) are contours of normalized von Mises effective stress for  $\mu = 0.25$  and  $0.50$ , respectively, predicted by the 3D computations for the partial slip condition characterized by  $\delta = 0.5\delta_{\text{slide}}$  (see Fig. 3 and equation (8c)). The effects of partial slip on the distortion of the Mises stress fields can be understood from a comparison of Figs 4(a)-(c) and Figs 5(a) and (b). For the normal Hertzian contact with no tangential force, the maximum pressure resides directly beneath the spherical indenter on the  $z$ -axis, at a depth  $z \approx 0.5a$  below the contact surface (for  $\nu = 0.3$ ). As a partial relative displacement  $\delta = 0.5\delta_{\text{slide}}$  is introduced, the maximum Mises stress is displaced behind (with respect to the direction of sliding of the sphere on the stationary substrate) the line of application of the normal load, Fig. 5(a). The elevation in the Mises stress behind the line of application of the normal load is evident in Fig. 5(a), even at the surface. The position of the maximum Mises stress is marked by the symbol "+". As the friction coefficient  $\mu$  is raised from 0.25 to 0.50, the site of maximum Mises stress moves up, closer to the free surface. When these contours of partial slip are compared with the corresponding ones for the onset of complete sliding (Fig. 4) at the appropriate values of  $\mu$ , it is evident that increasing the radius of the zone in which partial slip occurs or introducing rigid-body sliding causes the Mises stress maximum to be displaced further behind the line of the application of the normal load, and to be displaced closer to the free surface. This effect is more pronounced for  $\mu > 0.3$ , where the site of maximum Mises stress occurs at the free surface, Fig. 4(c). Such effects of friction and the extent of partial slip influence significantly the location of onset of plastic flow as well as cracking. Note that all these conclusions pertain to the situation where no residual stresses exist at the fretted surface.

Since the present three-dimensional computational models are capable of determining the cyclic fields under conditions of partial slip that are typical of fretting fatigue, they can be applied to interpret a variety of available experimental data on the fretting fatigue of a sphere on a flat surface. The conditions governing the occurrence of fretting damage and the onset of fatigue cracking can also be identified from the numerical results by invoking a variety of failure criteria. In the following, two specific examples are considered.

#### 5.2. Fretting analysis for an AISI 52100 steel

We first present a comparison of our computational results with the experiments conducted by Kuno *et al.* [11, 12] for an AISI 52100 bearing steel. The fretting contact analyzed here comprises a

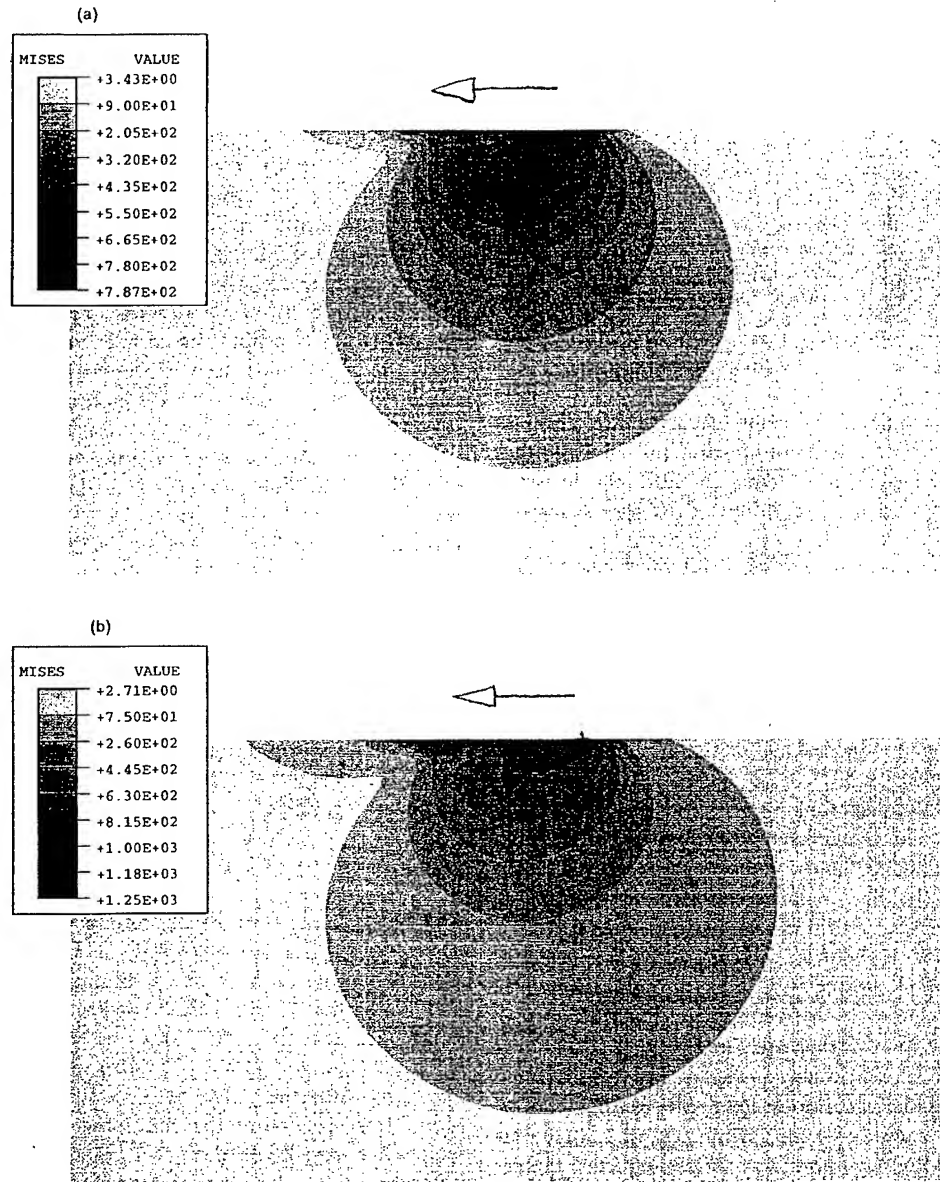


Fig. 5. Contours of von Mises effective stress for (a)  $\mu = 0.25$  and (b)  $\mu = 0.50$  for  $\delta = 0.5\delta_{\text{slide}}$ . The arrow indicates the direction of sliding. The stresses are normalized by the maximum normal pressure,  $p_{\text{max}} = 3P/(2\pi a^2) = 1200$  MPa, and the distances by the contact radius,  $a$ . Poisson ratio,  $\nu = 0.3$  in both cases. The axes  $r/a$  and  $z/a$  are drawn to the same scale.

sphere-on-plate arrangement, with the sphere and the plate made from the same steel. The material

properties for the steel are listed in Table 1. The specimen dimensions and other experimental par-

Table 1. Properties of AISI 52100 [11]

Young's modulus ( $E$ )	206 GPa
Poisson ratio ( $\nu$ )	0.3
Monotonic yield stress ( $\sigma_y$ )	1730 MPa
Tensile strength ( $\sigma_{TS}$ )	2015 MPa
Fatigue strength coefficient ( $\sigma'_f$ )	2585 MPa
Fatigue strength exponent ( $b$ )	-0.09
Fatigue ductility coefficient ( $\epsilon'_f$ )	0.18
Fatigue ductility exponent ( $c$ )	-0.56
Thermal expansion coefficient ( $\alpha$ )	$10 \times 10^{-6}/^\circ\text{C}$
Thermal conductivity ( $k$ )	23 W/(m $^\circ\text{C}$ )

Table 2. Experimental geometry and test conditions for the AISI 52100 steel studied in Ref. [11]

Normal load ( $P$ )	180 N
Diameter of the sphere ( $2R$ )	25.4 mm
Average friction coefficient ( $\mu$ )	0.3 (Max 0.7, Min 0.0)
Cyclic frequency	60 Hz
Contact radius ( $a$ )	247 $\mu\text{m}$
Slip fretting scar ( $c/a$ )	0.80-1.00
Transverse load ( $T/(\mu P)$ )	0.89
Initial tensile stress	600 MPa
Macroscopic slip amplitude	5-45 $\mu\text{m}$
Fretting cycles ( $N_f$ )	$10^6$ - $3.5 \times 10^5$
Specimen temperature	20-200 $^\circ\text{C}$

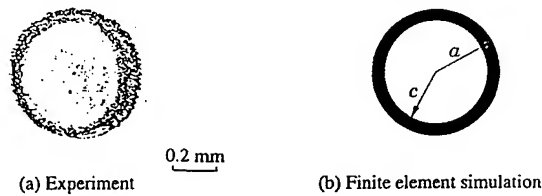


Fig. 6. A plan view of the fretting scar produced in the AISI 52100 steel for the conditions listed in Table 2. (a) Experimental observations of Kuno *et al.* [11]. Normal load,  $P = 180$  N, average friction coefficient,  $\mu = 0.3$ , number of reversals to failure,  $2N_f = 10^6$ , uniform mean tensile stress, 600 MPa. (b) Finite element predictions (this study).

ameters simulated by finite elements are given in Table 2. It was determined from the analyses that the fatigue conditions remained fully elastic (on a macroscopic scale), for values of friction coefficient,  $\mu \leq 0.7$ .

For the experiments described in Table 2, note that a uniform static tensile stress of 600 MPa was externally applied to the specimen as repeated fretting contact was simultaneously imposed on the specimen surface. Figure 6(a), taken from Kuno *et al.* [11] shows a plan view of the fretting scar on the surface of the specimen after the application of  $10^6$  fatigue cycles with a fixed normal load of 180 N and a cyclic displacement amplitude of  $5 \mu\text{m}$ . The average friction coefficient measured for this experiment was 0.3.\* Fig. 6(b) shows the same plan view predicted by the present finite element simulations for the same conditions as in the experiments of Kuno *et al.* [11]. In the absence of macroplasticity, Johnson [19] showed that the slip annular region is directly related to the fretting scar. The fretting scar appearing as a darker area in Fig. 6 is a manifestation of surface microplasticity. The macroscopic tangential deformation seen in the fretting scar of Fig. 6(a) exceeds, in an asymmetric way, that predicted in Fig. 6(b) possibly as a consequence of surface oxidation and of the compliance of the testing system.

Figures 7(a) and (b) show the computed von Mises effective stress contours for  $\mu = 0$  and 0.3, respectively, for the partial slip fretting conditions listed in Table 2; here, the uniform tensile normal stress of 600 MPa imposed on the fretted specimen is included in the simulation (with the tensile stress axis parallel to the direction of slip). A comparison of Fig. 7(a) with Fig. 4(a) shows that superimposed tensile stress causes no reduction in the size of the contact region and confines the high stresses to a

region immediately beneath the contact region. It also elevates the value of the maximum Mises stress (indicated by the “+” symbol) within the fretted specimen. The superposed uniform tensile stress also leaves the location of the maximum Mises stress unaltered for  $\mu = 0$ . Figure 7(b) shows that when  $\mu = 0.3$ , the Mises stress decreases directly beneath the contact region and increases at the contact surface behind the normal loading axis, as compared to the normal indentation with no friction. The residual tensile stresses amplify the effective Mises stress behind the contact area. They also draw the stress fields deeper into the material compared to when there is no superimposed tensile stress.

From the information available on the fretting scar, the tangential force  $T$  was estimated analytically, using equation (6), to be 54 N. For this tangential load and for an average friction coefficient,  $\mu = 0.3$ , the maximum Mises effective strain increment during a fretting cycle,  $\epsilon_{\text{eff}}$ , was estimated from the finite element simulations to be  $\epsilon_{\text{eff}} = 6.6 \times 10^{-3}$ . With this effective strain from the computations, a simple criterion for fatigue failure for the primarily elastic, multiaxial loading prevailing under fretting fatigue can be formulated by using the effective (elastic) strain in the Basquin equation (e.g. [23]):

$$\frac{\epsilon_{\text{eff}}}{2} = \frac{\sigma'_f}{E} (2N_f)^b, \quad (12)$$

where  $2N_f$  is the number of fretting reversals (two per fretting cycle) to form a fatigue crack under the aforementioned experimental conditions, and  $\sigma'_f$ ,  $E$ , and  $b$  are the experimentally determined material parameters for the steel listed in Table 1. From equation (12),  $N_f = 1.4 \times 10^5$  cycles. This compares favorably with the value of  $3.5 \times 10^5$  reported by Kuno *et al.* [11]. (For the conditions of the experiments, we have determined from our detailed computations that the temperature increase in the vicinity of the contact region was not sufficient to affect the present results appreciably.)

A number of commonly employed manufacturing processes (e.g. [12]) as well as shot peening introduce compressive surface stresses in fretted specimens. We now illustrate how the existence of a local compressive stress not only influences the magnitude of the fields in the vicinity of the contact area, but also changes the very structure of the evolution of the fields. For this purpose and for comparisons with the results presented in Figs 4 and 7, consider the fretting conditions and materials that are identical to those simulated in Fig. 7, with the exception that the uniform uniaxial tensile stress of 600 MPa is replaced by a uniform uniaxial compressive normal stress of  $-600$  MPa. The Mises effective stresses computed for this partial slip case are shown in Fig. 8(a) and (b) for  $\mu = 0.0$  and 0.3, respectively. Here the stresses are spread out more

\*The variation of friction coefficient  $\mu$ , estimated as ratio of the measured tangential force to the normal load, as reported in [11] as a function of the number of fatigue cycles. Since the actual tangential compliance of the fretting set-up can influence the real value of  $\mu$ , we choose an average value of  $\mu$  for our analysis. With this choice, the partial slip radius  $c$  was computed from the simulations.



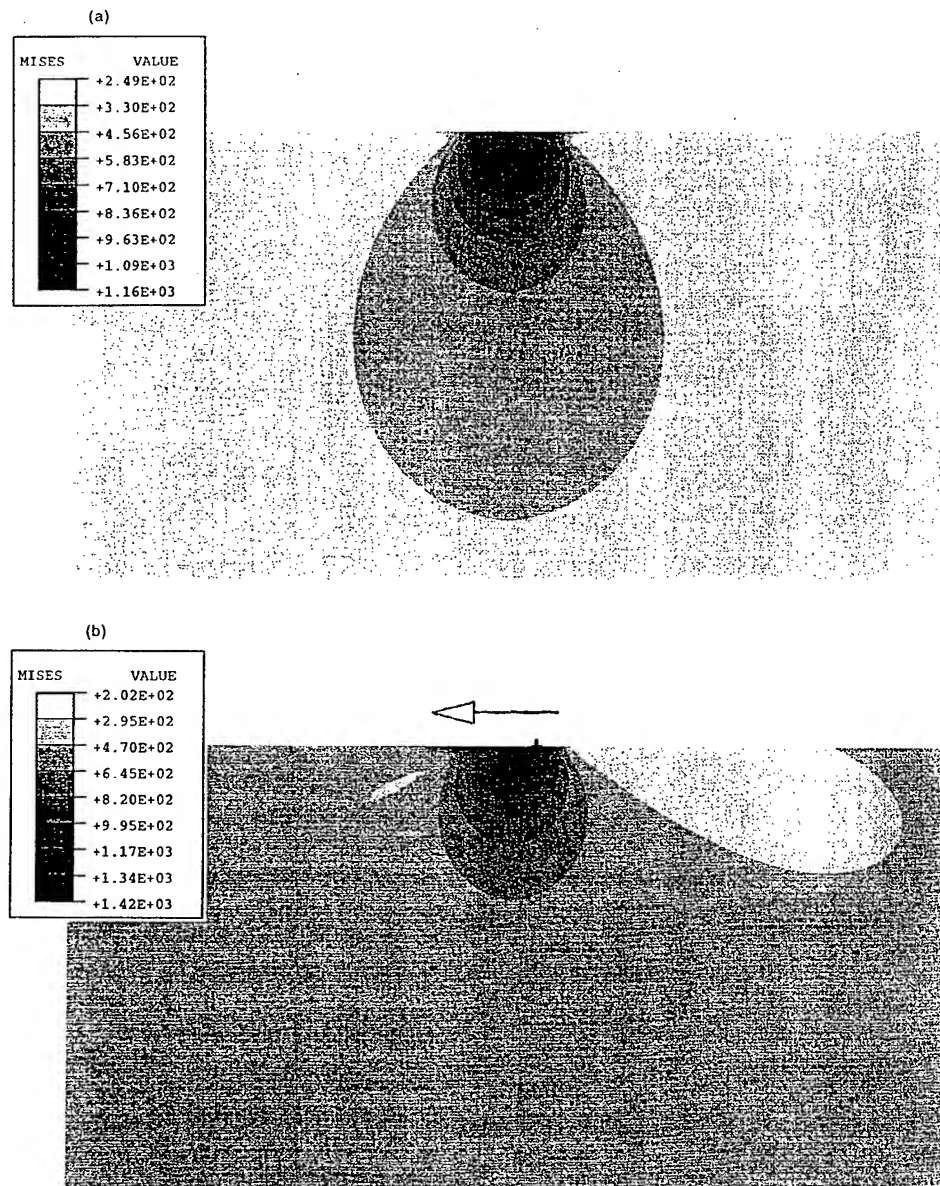


Fig. 7. Contours of constant effective von Mises stress for (a)  $\mu = 0.0$  (normal contact) and (b)  $\mu = 0.30$ . The stresses are normalized by the maximum normal pressure,  $p_{\max} = 3P/(2\pi a^2)$ , and the lengths by the contact radius,  $a$ . Poisson ratio,  $\nu = 0.3$ . The data of Kuno *et al.* [11], Table 2, are simulated, with the fretted specimen subjected to a uniform, externally imposed tensile stress of 600 MPa. The maximum contact pressure  $p_{\max} = 1400$  MPa. Partial sliding of the sphere occurs in the direction indicated by the arrow. The axes  $r/a$  and  $z/a$  are drawn to the same scale.

along the slip direction, and they do not penetrate as deeply into the substrate as in the tensile stress case. Because of the uniform compressive stress, the magnitude of the Mises stresses is reduced. The trailing portion of lower stresses seen in Fig. 7(b) at the surface is erased by the application of a compressive mean stress. Instead, it moves directly below the contact region.

Figure 9 shows the contours of constant principal tensile stress for partial sliding with a compressive mean stress of 600 MPa. In the situation involving no mean stress or a tensile mean stress, the maxi-

mum in the local principal tensile stress occurs in the wake of the contact region. However, the compressive mean stress moves the location of the local principal tensile stress to the front of the contact region. This has the effect of moving the location of possible cracking to the leading edge of fretting contact in surfaces with compressive residual stresses, a phenomenon seen in many fretting experiments (e.g. [12]).

It is important to note here that the information about the fretting scar size was used in the above analysis in order to assess the tangential load,  $T$ .



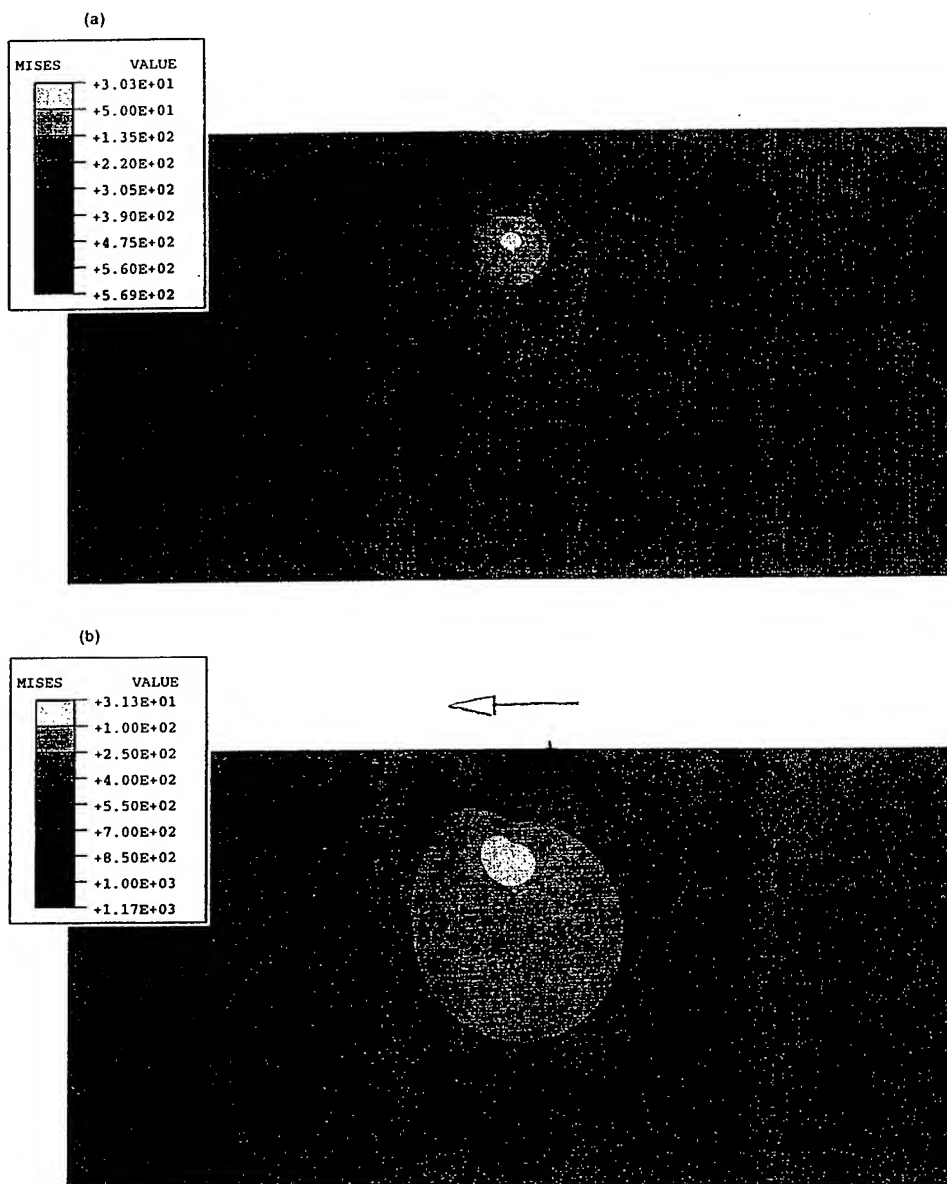


Fig. 8. Same as in Fig. 7 with the exception that the fretted specimen is subjected to a uniform, externally imposed (compressive) stress of  $-600$  MPa. (a)  $\mu = 0.0$  (normal contact) and (b)  $\mu = 0.30$ . The axes  $r/a$  and  $z/a$  are drawn to the same scale.

Predictions can also be made in a different manner: the fretting scar annulus,  $c$ , can be determined from the tangential load in the computational model since the finite element analysis gives the slip conditions in the contact regime. In the same way, one can find the applied normal load,  $P$ , from the contact radius,  $a$ . This is important in fretting experiments because the tangential displacement (or the tangential load) may not be accurately measured due to experimental difficulties arising from the compliance of the specimen and the fretting-fixture. In fact, the limited control of the tangential load con-

stitutes a major problem in performing fretting experiments. With the present analyses, this experimental problem may be circumvented by actually assessing the tangential load (or displacement) from the observations of the fretting scar damage annulus dimensions, for any fretting situation from partial slip to global sliding. Thus the present approach provides a significantly more powerful tool to interpret fretting experiments, such as the ones reported by Kuno *et al.* [11,12], than the simple fretting failure criteria (e.g. [24]). In addition, the three-dimensional finite element analyses

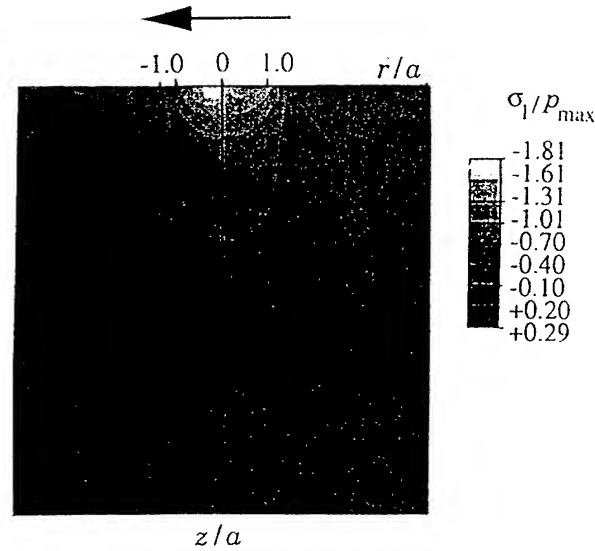


Fig. 9. Contours of constant maximum principal tensile stress for  $\mu = 0.30$ . Conditions and normalization same as in Fig. 8.

provide the complete fields for partial slipping, even in the presence of initial residual stresses and externally imposed loads.

### 5.3. Fretting analysis for a 7075-T6 aluminium alloy

Lamacq *et al.* [13] have reported fretting experiments on a 7075 aluminum alloy with a sphere-on-plate arrangement. The material of both the sphere and the plate was Al 7075-T6. The material properties and experimental conditions from Ref. [13] are summarized in Tables 3 and 4, respectively.

Our computations show that, when using the nominal input values of friction coefficients and the mean values of normal load reported for the experiments of Lamacq *et al.* [13], there was evidence that a small amount of bulk plasticity was possibly present. Due to the uncertainty in their nominal input values (e.g. the actual tangential load may be smaller), we analyzed their results using only elasticity. From Tables 3 and 4, we implemented in our computations the elastic properties of Al 7075-T6, contact pad geometry (which had a rounded tip radius,  $D/2 = 300$  mm, instead of being a complete sphere), the reported friction coefficient ( $\mu = 1.2$ ), the contact radius ( $a = 1.8$  mm), an initial tensile stress ( $\sigma_D = 230$  MPa) and a shear

force ( $T = 755$  N). The calculations gave a normal force  $P = 1112$  N, a stick radius  $c/a \approx 0.76$ , and a slip amplitude  $\delta = 9.5$   $\mu$ m. These results compare very well with the experimental values [13], Table 4.

The maximum effective strain increment was computed  $\epsilon_{\text{eff}} = 6.96 \times 10^{-3}$ . Note that this is somewhat above the elastic strain of  $5.78 \times 10^{-3}$ . Inserting the computed effective strain together with the material constants of Table 3 into the Basquin equation (12), we found an estimate of failure cycles  $N_f = 2.6 \times 10^5$ , which compares reasonably well with the range of cycles reported by Lamacq *et al.* ( $5 \times 10^4 - 1 \times 10^6$ ).

### 5.4. Plastic yielding during fretting fatigue

We conclude our discussions by a brief examination of plastic flow during the fretting fatigue contact between a sphere and a planar surface. This section is intended to merely illustrate some of the capabilities of the computational model, and is not

Table 3. Properties of 7075-T6 aluminium alloy [13]

Young's modulus ( $E$ )	72 GPa
Poisson ratio ( $\nu$ )	0.3
Monotonic yield stress ( $\sigma_y$ )	416 MPa
Tensile strength ( $\sigma_{TS}$ )	670 MPa
Fatigue limit stress ( $\sigma_D$ )	230 MPa
Fatigue strength coefficient ( $\sigma'_f$ )	1317 MPa
Fatigue strength exponent ( $b$ )	-0.126
Fatigue ductility coefficient ( $\epsilon'_f$ )	0.19
Fatigue ductility exponent ( $c$ )	-0.56

Table 4. Experimental geometry and test conditions for the 7075-T6 aluminium alloy, studied in Ref. [13]

Normal load ( $P$ )	1000-900 N
Diameter of the sphere ( $2R$ )	600 mm (Al 7075 T6)
(rounded tip contact pad with tip radius of 300 mm)	
Average friction coefficient ( $\mu$ )	1.2
Cyclic frequency	5 Hz
Contact radius ( $a$ )	1.8-1.85 mm
Slip fretting scar ( $c$ )	1.1-1.25 mm
Transverse load ( $T$ )	930 N
Initial tensile stress	230 MPa
Macroscopic slip amplitude	35 $\mu$ m
Fretting cycles ( $N_f$ )	$5 \times 10^4 - 10^6$
Initial crack position and direction	emanates from stick perimeter, $55^\circ - 65^\circ$ towards the vertical line

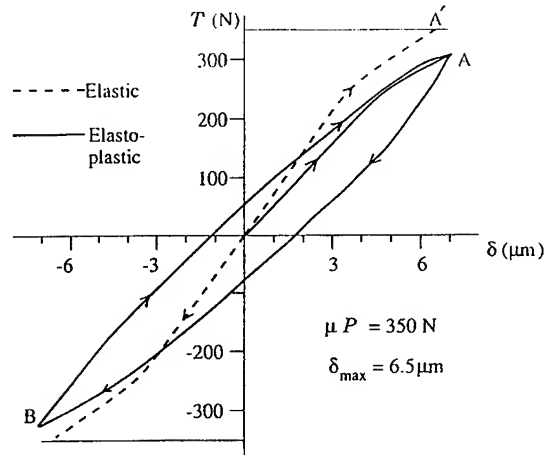


Fig. 10. The effect of plasticity on the evolution of  $T$  vs  $\delta$  during reversed sliding. See text for details.

deemed to be a complete parametric analysis of plastic deformation.

In order to investigate the evolution of inelastic deformation, the indenter was modelled as rigid and the substrate as elastic-perfectly plastic. The yield response of the substrate was characterized by the von Mises criterion ( $J_2 = \tau_y^2 = \sigma_y^2/3$ , where  $J_2$  is the second invariant of the deviatoric stress tensor, and  $\tau_y$  and  $\sigma_y$  are the yield strength values in shear and uniaxial tension, respectively). Increments of plastic strain were assumed to satisfy the associative flow rule.

We consider the following case for an illustration of the predictive capabilities of the analysis throughout this section: same material properties for the sliding spherical indenter and the planar fretted surface ( $E = 103$  GPa,  $\nu = 0.3$ ,  $\sigma_y/E = 1.46 \times 10^{-3}$ , which represent the properties of a titanium alloy). The indenter geometry and loading conditions were:  $D = 50.8$  mm, fixed normal load,  $P = 500$  N, normalized indenter penetration depth,  $h/D = 1.48 \times 10^{-4}$ , normalized contact radius,  $a/D = 8.5 \times 10^{-3}$ , and maximum contact pressure,  $p_{\max} = 1.22 \times 10^{-2} E$ .

For frictionless normal indentation loading and unloading ( $\mu = 0$ ), the computations showed that the elastic shakedown limit was:

$$\frac{3P}{2\pi a^2 \tau_y} = \frac{p_{\max}}{\tau_y} = 4.5. \quad (13)$$

This value compares quite well with the elastic shakedown limit against alternating plasticity,  $p_{\max}/\tau_y = 4.675$ , which was proposed by Ponter *et al.* [25]. If a high friction coefficient of  $\mu = 0.7$  is introduced in our numerical simulations of sliding, the elastic limit for shakedown was found to be  $p_{\max}/\tau_y = 1.4$ , and the shakedown limit against the incremental growth (ratchetting) of surface strain was found to be  $p_{\max}/\tau_y = 1.5$ . These results are also in accord with the theoretical upper bound value of  $p_{\max}/\tau_y = 1/\mu$ , predicted by Ponter *et al.* for  $\mu > 0.3$ .

Figure 10 is a plot of  $T$  vs  $\delta$  plot (similar to Fig. 2(b) and (d)) which compares the elastic and plastic deformation response during fretting fatigue. For the elastic case, nearly full sliding conditions are simulated, with  $T \approx \mu P = 350$  N, with  $\mu = 0.7$  and a displacement limit of  $\delta_{\max} = 6.5$   $\mu\text{m}$  (point A'). When plastic yielding is permitted, the tangential compliance,  $dT/d\delta$ , becomes considerably softer than the elastic case, as anticipated. Reversal of sliding, commencing at point A, and extending all the way to  $\delta_{\max} = -6.5$   $\mu\text{m}$  (point B) and back to  $+6.5$   $\mu\text{m}$  (point A) causes a hysteresis response as shown in Fig. 10. After the third reversal, the  $T$ - $\delta$  hysteresis loop attains a stable configuration between points A and B.

For the same material properties and loading and friction conditions in Fig. 10, we now consider the evolution of plastic strains. Figure 11(a) shows contours of constant von Mises equivalent plastic strains,  $\epsilon_{\text{pl}}^{\text{eq}}$ , on the plane of sliding (i.e. the  $x$ - $y$  plane). Plotted in this figure is the evolution of non-axisymmetric yielding for the partial slip displacement  $\delta$  (of the sphere on the stationary substrate) of 4  $\mu\text{m}$  ( $T = 217$  N) in the direction indicated by the arrow. Note the occurrence of an enlarged plastic zone in the substrate in the wake of the slipping sphere. The enlargement of the plastic zone at  $\delta = 7$   $\mu\text{m}$  ( $T = 313$  N) is shown in Fig. 11(b). This corresponds to the point of first sliding displacement reversal, point A, shown in Fig. 10. When the slip direction is reversed with  $\delta = 7$   $\mu\text{m}$  ( $T = -315$  N), which corresponds to the extreme slip displacement in the opposite direction (point B in Fig. 10), the plastic strain contours evolve as shown in Fig. 11(c). It is evident from Fig. 11(a)-(c) that for typical fretting displacements commonly encountered in a Ti alloy, a high friction coefficient between the fretted surfaces (which may arise from trapped debris or oxide particles and rough surface asperities) may be sufficient to cause plastic yielding at the surface. If such plastic strains accumulate during cyclic displacements (i.e. when the appropri-

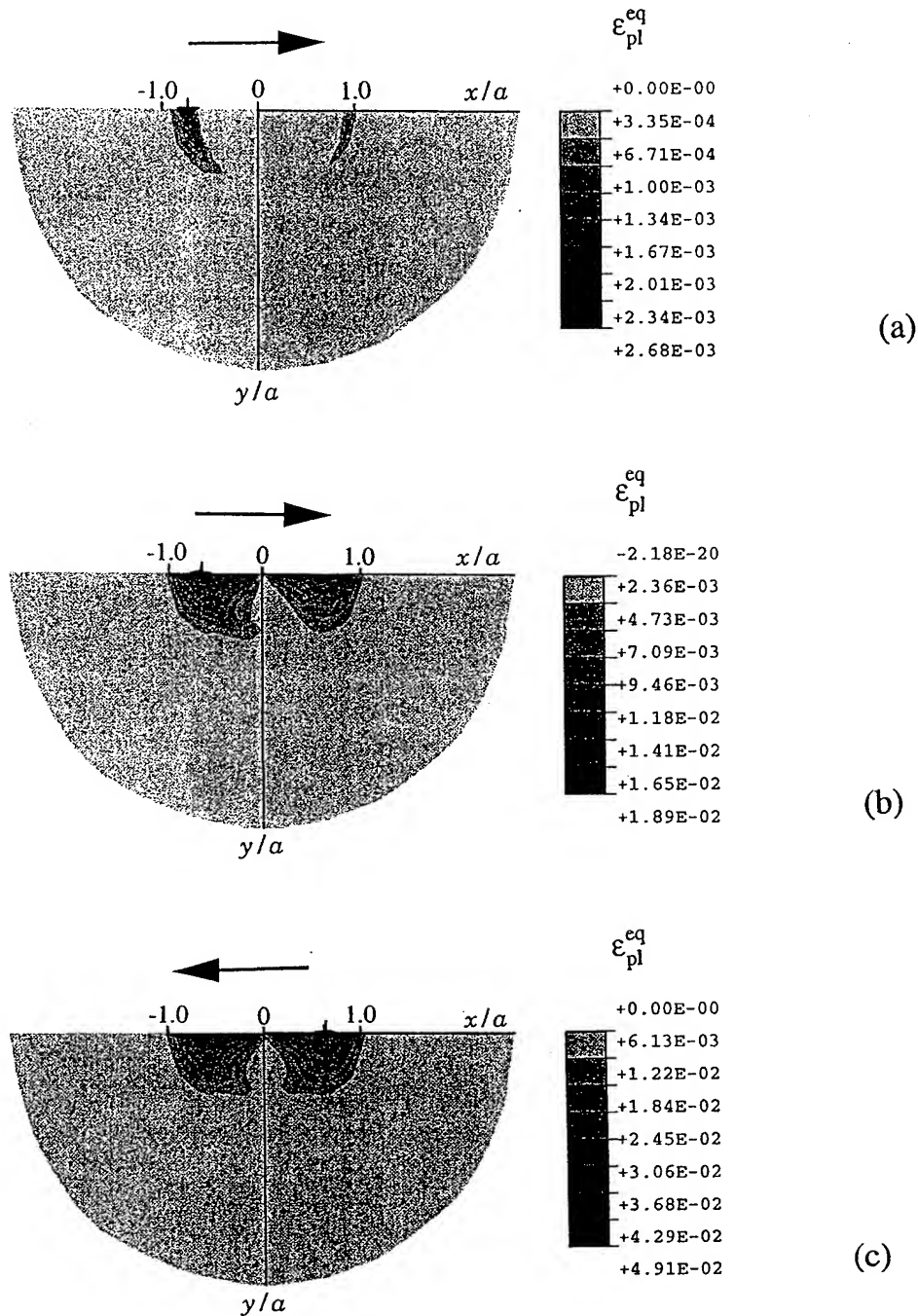


Fig. 11. Contours of constant equivalent plastic strain on the sliding plane (x-y plane) during forward sliding ((a)  $\delta = 4 \mu\text{m}$  and (b)  $\delta = 7 \mu\text{m}$ ) and reverse sliding ((c)  $\delta = -7 \mu\text{m}$ ). The axes  $r/a$  and  $z/a$  are drawn to the same scale.

ate shakedown limit is exceeded), crack initiation can be facilitated by a ductile failure process.

## 6. CONCLUSION

A three-dimensional finite element model for fretting contact fatigue, which is predicated upon the radial expansion of the displacement fields around the contact center, has been developed. The model

provides a capability for elastic and elastoplastic analyses of fretting fatigue between a sphere and a planar surface. The computational predictions were first checked with known analytical solutions for the limiting case of full sliding under elastic conditions. Surface and sub-surface fields evolving under conditions of partial slip were then simulated where the pronounced effects of interfacial friction and externally imposed tensile or compressive mean

stresses were investigated. The computational model was then used to simulate the fretting scar dimensions and the number of cycles to fretting crack initiation in two previously reported experiments, where simple criteria predicated upon high-cycle fatigue data for the materials were employed. The shakedown limits predicted by the simulation were then shown to be in reasonable agreement with known bounds. It was also shown that high friction values at the contact interface can promote surface plastic flow. The evolution of plastic strains was simulated for several repeated oscillations of the sphere on the substrate, to illustrate the capabilities of the model. The spherical contact modeled here can also be viewed, from a microscopic point of view, as the contact between an asperity tip and a planar surface.

The present computations could be extended to include a number of additional cases and more complex situations. These include: fretting contact fatigue between elastically dissimilar solids, more detailed parametric analyses of plastic deformation at the surface including kinematic hardening, the evolution of stress and deformation fields in the presence of a spatially non-uniform mean stress or internal stress, different axisymmetric fretting contact (indenter) geometries, and the deformation response of the fretted substrate whose elastic and/or plastic properties discretely or gradually change as a function of depth beneath the contact interface as, for example, in coated or case-hardened alloys.

**Acknowledgements**—This work was supported by the MURI on "High Cycle Fatigue", funded at MIT by the Air Force Office of Scientific Research, Grant No. F49620-96-1-0478, through a subcontract from the University of California at Berkeley. The authors are grateful to J. Dominguez and M. Olsson for helpful comments on the manuscript.

#### REFERENCES

1. Waterhouse, R. B. and Lindley, T. C., *Fretting Fatigue*.ESIS Publication No. 18, European Structural Integrity Society, Mechanical Engineering Publications Limited, London, 1994.
2. Waterhouse, R. B., *Int. Metal. Rev.*, 1992, **37**, 77.
3. Lindley, T. C., Fretting Fatigue in Engineering Alloys. in *Fretting Fatigue of Metallic Materials*, ed. A. K. Vasudevan and T. Nicholas. Proc. Engineering Foundation Conference, Hyannis, MA, U.S.A., to be published.
4. Johnson, K. L., *Contact Mechanics*. Cambridge University Press, Cambridge, 1985.
5. Hills, D. A. and Nowell, D., *Mechanics of Fretting Fatigue*. Kluwer Academic Publishers, Dordrecht, The Netherlands, 1994.
6. Mindlin, R. D., *J. Appl. Mech.*, 1949, **16**, 259.
7. Mindlin, R. D. and Deresiewicz, H., *J. Appl. Mech.*, 1953, **20**, 327.
8. Deresiewicz, H., *J. Appl. Mech.*, 1957, **24**, 623.
9. Hamilton, G. M. and Goodman, L. E., *J. Appl. Mech.*, 1966, **33**, 371.
10. Hamilton, G. M., *Proc. Inst. Mech. Engng.*, 1983.
11. Kuno, M., Dinsdale, K., Pearson, B. R., Ottewill, B., Waterhouse, R. B., *J. Phys. E: Sci. Instrum.*, 1988, **21**, 929.
12. Kuno, M., Waterhouse, R. B., Nowell, D. and Hills, D. A., *Fatigue and Fracture Engng. Mater. Struct.*, 1989, **12**, 387.
13. Lamacq, V., Dubourg, M. C. and Vincent, L., *J. Tribology*, 1996, **118**, 711.
14. Hertz, H., *J. Reine und Angewandte Mathematik*, 1882, **92**, 156.
15. Bowden, F. P. and Tabor, D., *Friction and Lubrication of Solids*, Vol. I. Oxford University Press, London, 1951.
16. Bowden, F. P. and Tabor, D., *Friction and Lubrication of Solids*, Vol. II. Oxford University Press, London, 1964.
17. Cerruti, V., *Acc. Lincei, Me. fis. mat.*, 1882.
18. Cattaneo, C., *Rendiconti dell' Accademia Nazionale dei Lincei*, 1938, **27**, 342-434474.
19. Johnson, K. L., *Proc. Royal Society*, 1955, **A230**, 531.
20. Jørgensen, O., *Comp. Meth. Appl. Mech. Engng.*, 1993, **2**, 319.
21. Jørgensen, O., Giannakopoulos, A. E. and Suresh, S., *Int. J. Solids and Structures*, 1997, in press.
22. ABAQUS, *User's Manual, Version 5.5*, Hibbit, Karlson and Sorensen, Inc., Pautacket, R. I., 1996.
23. Suresh, S., *Fatigue of Materials*. Cambridge University Press, Cambridge, U.K., 1991.
24. Ruiz, C., Boddington, P. H. B. and Chen, K. C., *Exp. Mech.*, 1984, **24**, 208.
25. Ponter, A. R. S., Hearle, A. D. and Johnson, K. L., *J. Mech. Phys. Solids*, 1985, **33**, 339.



## OVERVIEW NO. 129

# ASPECTS OF EQUIVALENCE BETWEEN CONTACT MECHANICS AND FRACTURE MECHANICS: THEORETICAL CONNECTIONS AND A LIFE-PREDICTION METHODOLOGY FOR FRETTING-FATIGUE

A. E. GIANNAKOPOULOS, T. C. LINDLEY† and S. SURESH

Department of Materials Science and Engineering, Massachusetts Institute of Technology, Cambridge, MA 02139, U.S.A.

(Received 12 November 1997; accepted in revised form 18 December 1997)

**Abstract**—We identify aspects of quantitative equivalence between contact mechanics and fracture mechanics via asymptotic matching. An analogy is invoked between the geometry of the near-tip regions of cracked specimens and that of the sharp-edged contact region between two contacting surfaces. We then demonstrate that the asymptotic elastic stress and strain fields around the rim of the contact region, as derived from classical contact mechanics analyses, are identical to those extracted from linear-elastic fracture mechanics solutions for analogous geometries. Conditions of validity of this model for contact mechanics are established by recourse to the singular fields and small-scale-yielding concepts of fracture mechanics. With this method, the geometry of the contact-pad/substrate system naturally introduces a fictitious crack length, thereby providing a physical basis to analyze contact-fatigue fracture initiation and growth. Possible extensions of this crack analogue model are then suggested, for situations where static or cyclic mechanical loads are superimposed parallel to the direction of interfacial friction, using the two-parameter fracture characterization that involves the stress intensity factor  $K$  and the non-singular  $T$ -stress, or alternatively, the  $J$  integral and the triaxiality parameter,  $Q$ . The predictions of the crack analogue model are then compared with fretting-fatigue experiments and are shown to be in agreement with a variety of independent experimental observations. A new life-prediction methodology for fretting fatigue is also proposed on the basis of the present approach. © 1998 Acta Metallurgica Inc.

## 1. INTRODUCTION

The elastic singular fields at the sharp edges of a two-dimensional contact between a rigid flat punch and a planar surface were derived by Sadowski [1]. Subsequently, Nadai [2] analyzed the asymptotic stresses within the elastic substrate in the vicinity of the corners of the punch for both normal and shear loading. Nadai's results confirmed the contact surface stresses predicted by Sadowski for a flat punch, and in addition, the contact stresses derived earlier by Hertz [3] for normal loading of a cylindrical punch. These developments preceded the evolution of the concepts of linear elastic and elastic-plastic fracture mechanics based on the stress intensity factor,  $K$  (e.g. [4]) and the  $J$  integral [5], respectively. Substantial progress has been made in the past five decades in the analysis of crack-tip fields on the basis of fracture mechanics principles. Although the singular fields for sharp-edged con-

tacts (e.g. [6–8]) and for cracked bodies (e.g. [9, 10]) suggest similarities (e.g. [11, 12]), it is somewhat surprising that no quantitative connection has been explored in sufficient detail, to our knowledge, between the vast literature of contact mechanics and fracture mechanics. Such possible connections have not been employed, to our knowledge, to interpret various experimental observations of damage and cracking in contact failures.

We demonstrate in this paper a quantitative equivalence as well a broad connection between the asymptotic stress and strain fields derived by classical analysis for sharp-edged contacts (e.g. [7]) and the crack-tip fields predicted from fracture mechanics methods (e.g. [13]). *This equivalence is established by identifying geometries of cracked bodies which facilitate an analogy with contact geometries.* In an attempt to validate this “crack analogue”, the following cases are considered:

(1) A two-dimensional rectangular rigid punch pressed normally against a frictionless flat surface (which is analogous to the compression loading of a double-edge-cracked plate).

†Present address: Department of Materials, Imperial College of Science, Technology and Medicine, London SW7 2BP, U.K.

(2) The axisymmetric geometry of a rigid circular cylinder pressed edge-on against a flat surface (which is analogous to a circumferentially cracked cylindrical specimen subjected to normal compressive loading along the cylinder axis).

The conditions governing the validity of the "crack analogue" model to contact mechanics are established by employing the small-scale yielding concepts routinely used in linear elastic fracture mechanics. It is suggested that the "crack analogue" model could be developed further for cases where static and cyclic loads are imposed parallel to the friction interface, by using the two-parameter fracture concepts based on the stress intensity factor  $K$  and the  $T$ -stress. Because contact between the rigid punch and the substrate implicitly introduces a "fictitious crack length scale", the problems frequently associated with the identification of an initial crack size can be circumvented. Available experimental studies of fretting fatigue and, in particular, the quantitative data on the initial crack growth direction and transition crack size for a change in the crack growth direction allow us to compare predictions from the crack analogue model with experimental observations. Combinations of elastic properties of the two contacting bodies, which lead to square-root singular fields at the contact rim and which facilitate the crack analogue approach, are also identified.

The paper is arranged in the following sequence. Section 2 demonstrates the theoretical equivalence between the asymptotic solutions of fracture mechanics with the fields around sharp-edges of contact regions for analogous geometries. (The validity of this analogue for different combinations of the elastic properties of the punch and the substrate, for different interface friction conditions is addressed separately in Appendix A.) In Section 2, we consider a two-dimensional planar analogy as well as a three-dimensional axisymmetric analogy, and both normal and shear loading. This is followed by discussions of the range of validity of the crack analogue in Section 3, which exploit known concepts of small-scale yielding in linear elastic fracture mechanics. Possible extensions of the crack analogue model for contact mechanics are then suggested using the two-parameter approach to fracture mechanics. Section 4 deals with a variety of quantitative comparisons of the crack analogue model with experimental observations derived from fretting fatigue. The paper concludes in Section 5 with a summary of the salient features as well as limitations of the present approach.

## 2. THEORETICAL VALIDATION

The equivalence between the asymptotic fields for sharp-edged contacts derived from classical contact mechanics analyses and the fields at stationary cracks, as determined from fracture mechanics, is

demonstrated in this section for a two-dimensional and a three-dimensional contact geometry. The steps involved in this exercise are as follows for the case of frictionless normal loading.

(1) Identify the cracked specimen configuration which provides a geometric equivalence for the contact region under a sharp-edged punch which is normally pressed against a planar surface of the same material. A direct geometric correlation is established between the radius of the contact zone (which is a function of the normal load  $P$  and the punch width or diameter,  $2a$ ) and the cracked specimen, through appropriate coordinate transformation.

(2) Find the asymptotic solutions to the stress and strain fields at the edges of sharp contacts, from classical contact analyses.

(3) Determine the corresponding stress and strain field solutions for the analogous cracked body, from linear elastic fracture mechanics analysis. Here, invoke the assumption that the cracked body is subjected to a normal compressive load whose magnitude  $P$  is the same as that of the load pressing the punch against the planar surface. The scalar amplitude of the singular fields at the crack tip is the stress intensity factor  $K_I$ .

(4) Equate the different components of the stress fields determined from steps 2 and 3, and solve for  $K_I$ , which is obtained as a function of  $P$ , the overall geometry of the cracked body, and the characteristic punch dimension.

(5) Consult any standard text or handbook of fracture mechanics (e.g. [14–16]) and determine the stress intensity factor  $K_I$  as a function of  $P$  and the geometry of the cracked body.

(6) Show that steps 4 and 5 lead to identical results. This proves the quantitative equivalence between the contact mechanics and fracture mechanics solutions.

An identical result can also be obtained in a slightly different manner. Perform steps 1 and 2 as shown above. Perform the above step 4 next, and

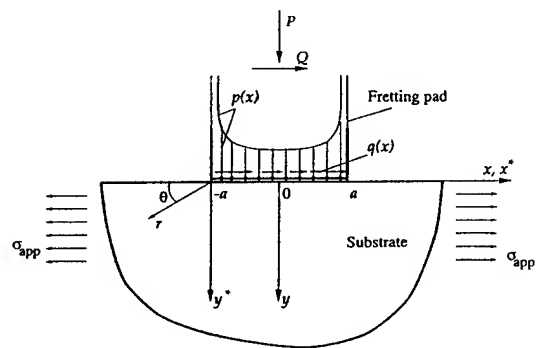


Fig. 1. A schematic representation of the contact between a two-dimensional rectangular punch and a substrate. The normal and shear loading at the contact interface and the external loading of the substrate are also indicated.

from the stress intensity factor so determined, find the mode I crack-tip fields. Show that these fields are identical to those found in step 2.

### 2.1. Two-dimensional "crack analogue"

Figure 1 schematically shows the two-dimensional contact between a rectangular punch and a flat-surfaced substrate. The width of the punch is  $2a$ . Consider the most general loading situation where the contact interface transmits a compressive normal force  $P$  and a shear force  $Q$  per unit thickness of the contact area (i.e.  $P$  and  $Q$  have units of force per unit length). In many practical situations, such as those involving sliding-contact or fretting fatigue, typical loading conditions are represented by fixed  $P$  and fluctuating  $Q$ . The uniform traction,  $\sigma_{xx}$ , acts along the slip direction (i.e., the  $x$  direction in Fig. 1) and may include residual stresses or oscillatory mechanical loads. Given the symmetry of the contact geometry about the  $y$ - $z$  plane, we focus attention at the corner,  $(x, y) = (-a, 0)$  in Fig. 1, without any loss of generality.

The following assumptions are invoked in the static analysis. (1) The substrate, whose depth and width are at least  $6a$  (it is assumed to be semi-infinite), is taken to be linear elastic and isotropic with small-strain deformation at all times. (2) Small-scale yield conditions are assumed such that the size of the plastic zone or damage zone,  $r_p$ , at the sharp edges of the contact region is small compared to the width of the contact area, i.e.  $r_p \leq a/20$ . (3) Gross sliding does not occur between the punch and the substrate, and any partial slip occurring at the outer edges of the contact area does not significantly alter the asymptotic solutions, which is strictly true for rigid pads on incompressible (i.e. the Poisson ratio,  $\nu = 0.5$ ) or frictionless (i.e. the coefficient of friction,  $\mu = 0$ ) surfaces. A more detailed examination of the pad-substrate elastic mismatch and its implications on the present analyses is provided in Appendix A and Table 3.

Figure 2 illustrates the geometry of a two-dimensional cracked specimen, which finds an analogy with the punch/substrate contact system shown in Fig. 1. This cracked plate is infinitely wide and contains double-edge (semi-infinite) cracks whose tips are separated by a distance  $2a$ . The plate is remotely subjected to tensile and shear loads,  $P$  and  $Q$ , respectively, such that they induce mode I and mode II stress intensity factors,  $K_I$  and  $K_{II}$ , re-

spectively, at the crack-tips. The  $x^*-y^*$  coordinate axes centered at the contact edge or the crack tip are shown in Figs 1 and 2. The cracked plate of Fig. 2 may additionally be subjected to a uniform normal stress  $\sigma_{xx} = \sigma_{app}$  (known as the  $T$  stress†) along the  $x$  direction to simulate conditions which represent superimposed mechanical loads during sliding or fretting contact, and/or residual stresses which arise from surface treatments such as coating, shot peening, etc.

It is evident that in the contact situation shown in Fig. 1, a crack is likely to initiate at an angle  $\theta$  below the contact surface and outside the contact area. In the crack analogue of this contact geometry shown in Fig. 2, it is expected that normal and/or shear loading would lead to the initiation of a kinked crack at the tip of one or both mode I cracks (which are modelled here as non-closing under the applied compressive normal load). This initial kink angle is denoted as  $\phi$  in Fig. 2. Thus, the cracking conditions in Figs 1 and 2 can be made equivalent by introducing a coordinate transformation whereby  $\theta$  in Fig. 1 is made to equal  $\pi - \theta = \phi$  in Fig. 2 for  $0 \leq \theta \leq \pi$ .

Note that the stress boundary conditions for the rectangular punch outside the contact area are:  $\sigma_{\theta\theta} = \sigma_{r\theta} = 0$ . Within the contact area,  $\epsilon_{\theta\theta} = 0$ . The former conditions are identical to those of a traction-free crack surface of a mode I flaw in the crack analogue, and the latter condition is identical to that ahead of the crack tip which preserves symmetric mode I deformation. Note also that whereas a constant displacement  $u_z$  occurs throughout the contact area for the rectangular punch; this, however, does not affect the crack-tip stress and strain fields.

2.1.1. Normal loading, plane strain (mode I "crack analogue"). The singular stress fields at the sharp edges of the contact between the rectangular rigid punch and the incompressible substrate are known from the asymptotic contact analyses of Sadowski [1] and Nadai [2]. Using the polar coordinates  $(r, \theta)$ , Fig. 1, the stresses at the left edge  $(-a, 0)$  are found to vary as:

$$\begin{pmatrix} \sigma_{rr} \\ \sigma_{\theta\theta} \\ \sigma_{r\theta} \end{pmatrix} \propto -\frac{3}{4\sqrt{r}} \begin{pmatrix} \sin \frac{3\theta}{2} + 5 \sin \frac{\theta}{2} \\ -\sin \frac{3\theta}{2} + 3 \sin \frac{\theta}{2} \\ \cos \frac{3\theta}{2} - \cos \frac{\theta}{2} \end{pmatrix}. \quad (1)$$

Using the "crack analogue" transformation (Fig. 2), we note that

$$\theta \longrightarrow \pi - \theta = \phi; \quad 0 \leq \theta \leq \pi. \quad (2)$$

Expanding the trigonometric terms in equation (1), the angular ( $\phi$  in Fig. 2) variation of stresses‡ are written as:

†The  $T$ -stress considered here for the case of an infinite substrate should be modified if the substrate were to be on finite dimensions.

‡The strains ( $\epsilon_{rr}$ ,  $\epsilon_{\phi\phi}$ ,  $\epsilon_{r\phi}$ ) can be found from the stresses and the elastic constitutive equations. The displacement vector components, however, are not the same for the two cases and differ by a constant value which is the uniform indentation penetration depth for the rectangular punch.



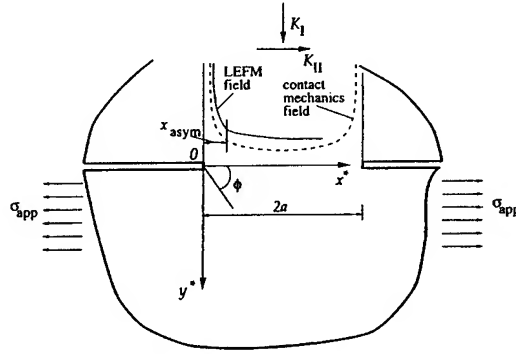


Fig. 2. Crack analogue of Fig. 1 showing the double-edge cracked plate specimen which is subjected to mode I and mode II stress intensity factors,  $K_I$  and  $K_{II}$ .

$$\begin{pmatrix} \sigma_{rr} \\ \sigma_{\phi\phi} \\ \sigma_{r\phi} \end{pmatrix} \propto \frac{1}{\sqrt{r}} \begin{pmatrix} \cos \frac{\phi}{2} \left( 1 + \sin^2 \frac{\phi}{2} \right) \\ \cos^3 \frac{\phi}{2} \\ \sin \frac{\phi}{2} \cos^2 \frac{\phi}{2} \end{pmatrix}. \quad (3)$$

Note that their stress fields are identical to those derived by Williams [13] for a Mode I crack.

For the calculation of the Mode I stress intensity factor in the crack analogue, we note that the contact pressure gives the only non-zero component of stress at the contact surface [1]:

$$\sigma_{yy} = -\frac{P}{\pi\sqrt{a^2 - x^2}}. \quad (4)$$

Taking the asymptote of equation (4) for the left crack in Fig. 2,  $x \rightarrow -a$ , we find that

$$\sigma_{yy} \rightarrow -\frac{P}{\pi\sqrt{2ar}}, \quad a + x = r \rightarrow 0. \quad (5)$$

The opening stress at the crack tip is related to the stress intensity factor by

$$\sigma_{yy} \rightarrow \frac{K_I}{\sqrt{2\pi r}}, \quad r \rightarrow 0. \quad (6)$$

Comparing equations (5) and (6), it is clear that

$$K_I = -\frac{P}{\sqrt{\pi a}}. \quad (7)$$

This  $K_I$  calibration result agrees with that given in standard fracture mechanics handbooks (e.g. [14–16]) for a double-edge-cracked infinite plate (containing two semi-infinite cracks whose tips separated by a distance of  $2a$ ) loaded remotely with a concentrated symmetric normal load  $P$ .

†The boundary conditions outside the contact area in this case are the same as those for the mode II situation. However, the stress and strain fields are anti-symmetric in plane for the mode II analogue.

2.1.2. *Tangent loading, plane strain (mode II “crack analogue”)*. Now consider the contact problem shown in Fig. 1 where the interface between the rigid rectangular punch and the incompressible substrate is subjected to a tangential force  $Q$  per unit depth; the normal force  $P$  is now taken to be zero. The local asymptotes of the stresses at the sharp corner of the contact region are also given by Nadai [2]. Using the polar coordinates  $(r, \theta)$ , Fig. 1, the stresses at the left edge of the contact,  $(-a, 0)$ , are seen to vary as

$$\begin{pmatrix} \sigma_{rr} \\ \sigma_{\theta\theta} \\ \sigma_{r\theta} \end{pmatrix} \propto \frac{1}{4\sqrt{r}} \begin{pmatrix} 3 \cos \frac{3\theta}{2} + 5 \cos \frac{\theta}{2} \\ 3 \cos \frac{3\theta}{2} - 3 \sin \frac{\theta}{2} \\ 3 \sin \frac{3\theta}{2} - \sin \frac{\theta}{2} \end{pmatrix}. \quad (8)$$

Now introduce the coordinate transformation, equation (2), for the critical orientation for crack initiation, from angle  $\theta$  in Fig. 1 to angle  $\phi$  in the crack analogue of Fig. 2, to obtain the crack-tip stresses as:†

$$\begin{pmatrix} \sigma_{rr} \\ \sigma_{\phi\phi} \\ \sigma_{r\phi} \end{pmatrix} \propto \frac{1}{\sqrt{r}} \begin{pmatrix} \sin \frac{\phi}{2} \left( 1 - 3 \sin^2 \frac{\phi}{2} \right) \\ -3 \sin \frac{\phi}{2} \cos^2 \frac{\phi}{2} \\ \cos \frac{\phi}{2} \left( 1 - 3 \sin^2 \frac{\phi}{2} \right) \end{pmatrix}, \quad r \rightarrow 0. \quad (9)$$

These fields are identical to the standard stress fields at the tip of a Mode II crack, as derived from linear elastic fracture mechanics methods (e.g. [9, 10, 13]). Classical contact mechanics analyses (e.g. [6–8]) identify the only non-zero component of stress at the surface to be

$$\sigma_{xy} = \frac{Q}{\pi\sqrt{a^2 - x^2}}. \quad (10)$$

Taking the asymptote of equation (10),  $x \rightarrow -a$ ,

$$\sigma_{xy} \rightarrow \frac{Q}{\pi\sqrt{2ar}}, \quad a + x = r \rightarrow 0. \quad (11)$$

But, with the Mode II stress intensity factor  $K_{II}$  in the “crack analogue” of Fig. 2,

$$\sigma_{xy} = \frac{K_{II}}{\sqrt{2\pi r}}, \quad r \rightarrow 0. \quad (12)$$

Comparing equations (11) and (12), it is clear that

$$K_{II} = \frac{Q}{\sqrt{\pi a}}. \quad (13)$$

This  $K$ -calibration equation matches the result for the double-edge-cracked plate subjected to in-plane-shear loading, where the crack-tips are separated by a distance of  $2a$  and loaded at infinity with shear

stresses corresponding to a concentrated shear force  $Q$ .

*Complete stick:* The discussions up to this point dealt with frictionless normal or shear loading of a punch on a planar surface which may be compressible. We now consider a limiting case where the rigid punch adheres completely to the surface. Here, in addition to the normal load  $P$  pressing the punch to the surface, a tangential force arises because of interfacial friction; the ratio  $Q/P$  signifies an effective friction coefficient. For this case, the shear stress at the surface is (e.g. [7])

$$\sigma_{xy} = -\frac{(1-2\nu)}{2\pi^2(1-\nu)} \frac{P}{\sqrt{a^2-x^2}} \ln\left(\frac{a+x}{a-x}\right) + \frac{Q}{\pi\sqrt{a^2-x^2}}. \quad (14)$$

Here  $P$  and  $Q$  are line loads defined earlier and  $\nu$  is Poisson's ratio of the contacting substrate. The corresponding  $K_{II}$  calibration for the complete stick case becomes

$$K_{II} = \frac{Q}{\sqrt{\pi a}} - \frac{P}{\sqrt{\pi a}} \frac{(1-2\nu)}{2\pi(1-\nu)} \cdot \ln\left\{\frac{r}{2a}\right\}, \quad (15)$$

where  $\nu$  is Poisson's ratio of the substrate.

*2.1.3. Mechanical loads superimposed on the substrate.* The superposition of a static or a cyclic mechanical load,  $\sigma_{app}$ , applied parallel to the direction of interfacial friction, can also be modelled with the crack analogue of contact mechanics. This superposition becomes necessary for applications involving sliding contact fatigue or fretting fatigue. For this purpose, we invoke the classical  $T$ -stress concept of linear elastic fracture mechanics. It is noted that the in-plane stresses at the tip of a mode I, linear elastic crack vary as

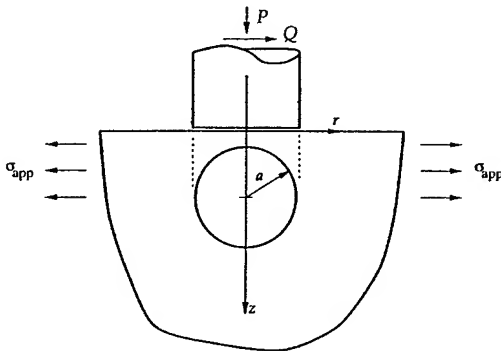


Fig. 3. A schematic representation of the contact between the end of a right-circular cylindrical punch and a substrate. The normal and shear loading at the contact interface and the external loading of the substrate are also indicated.

$$\begin{pmatrix} \sigma_{xx} & \sigma_{xy} \\ \sigma_{yx} & \sigma_{yy} \end{pmatrix} = \frac{K_I}{\sqrt{2\pi r}} \begin{pmatrix} \tilde{\sigma}_{xx}^I(\theta) & \tilde{\sigma}_{xy}^I(\theta) \\ \tilde{\sigma}_{yx}^I(\theta) & \tilde{\sigma}_{yy}^I(\theta) \end{pmatrix} + \begin{pmatrix} T & 0 \\ 0 & 0 \end{pmatrix} + (\text{terms which vanish at crack tip});$$

$$T = \sigma_{app}, \text{ static or oscillating.} \quad (16)$$

The superimposed stress  $\sigma_{app}$  in the contact mechanics problem of Fig. 2 plays the role of the  $T$ -stress in the crack analogue. The fracture mechanics solutions that include the  $T$ -stress term can then be applied to the contact problems with the appropriate geometrical analogy.

## 2.2. Three-dimensional "crack analogue"

Sneddon [12] found the elastic solution for a normally loaded axisymmetric rigid punch of circular contact radius  $a$ , shown in Fig. 3. It is shown in this section that the stress fields of the contact problem are the same as those of the semi-infinite circumferential crack in a right circular, cylindrical rod, Fig. 4.

*2.2.1. Normal loading, axisymmetric (Mode I crack analogue).* Using the cylindrical coordinates,  $r, z, \theta$ , in Fig. 3, the non-zero stresses are

$$\begin{pmatrix} \sigma_{zz} \\ \sigma_{rz} \\ \sigma_{\theta\theta} \\ \sigma_{rr} + \sigma_{\theta\theta} \end{pmatrix} = -\frac{4\mu(\lambda+\mu)}{(\lambda+2\mu)} \frac{h}{\pi a} \times \begin{pmatrix} J_1^0 + \zeta J_2^0 \\ \zeta J_2^1 \\ \lambda J_0^1 + \left(J_0^0 - \frac{(\lambda+\mu)}{\mu} \zeta J_2^1\right)/\rho \\ (2\lambda+\mu)J_1^0 - (\lambda+\mu)\zeta J_2^0 \end{pmatrix} \quad (17)$$

where  $\lambda$  and  $\mu$  are Lamé's elastic constants,  $\rho = r/a$ ,  $\zeta = z/a$  are normalized coordinates,  $h$  is the indentation depth that is related to the applied normal force,  $P$ , according to

$$P = \frac{8\mu(\lambda+\mu)}{(\lambda+2\mu)} ah. \quad (18)$$

Finally, the functions  $J_1^0, J_2^1, J_2^0, J_0^1$  are given by

$$\begin{aligned} J_1^0 &= R^{-1/2} \sin \frac{\omega}{2}, & J_2^1 &= \rho R^{-3/2} \sin \frac{3\omega}{2}, \\ J_2^0 &= r^* R^{-3/2} \sin \left( \frac{3\omega}{2} - \Omega \right), \\ J_0^1 &= \frac{1}{\rho} \left( 1 - R^{1/2} \sin \frac{\omega}{2} \right), \end{aligned} \quad (19)$$

where the transformed coordinates are

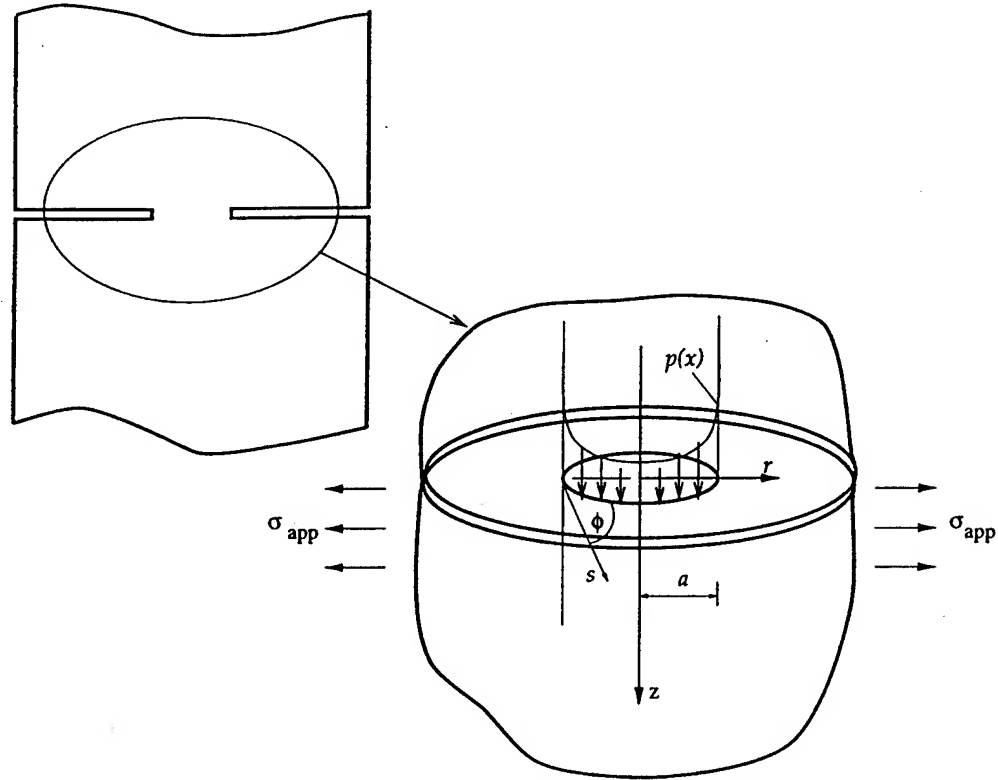


Fig. 4. Crack analogue of Fig. 3 showing the circumferentially cracked cylindrical rod specimen, and the associated nomenclature.

$$r^{*2} = 1 + \zeta^2, \quad R^2 = (\rho^2 + \zeta^2 - 1)^2 + 4\zeta^2, \\ \tan \Omega = 1/\zeta, \quad \tan \omega = 2\zeta/(\rho^2 + \zeta^2 - 1). \quad (20)$$

Taking the asymptotes (see Fig. 4,  $s \rightarrow 0$ ) of the stresses at the surface ( $\zeta \rightarrow (s/a)\sin \phi$ ) and close to the contact perimeter  $\rho \rightarrow 1 + (s/a)\cos \phi$ , we obtain  $\Omega \rightarrow \pi/2 - (s/a)\sin \phi$ ,  $\omega \rightarrow \phi - (s/(2a))\sin \phi$ ,  $r^* \rightarrow 1 +$ ,  $R \rightarrow 2(s/a)(1 + (s/a)\cos \phi)$ . Then,

$$\begin{pmatrix} \sigma_{zz} \\ \sigma_{rz} \\ \sigma_{rr} \\ \sigma_{\phi\phi} \end{pmatrix} \rightarrow -\frac{P}{2\pi a^2 \sqrt{2s}} \cos \frac{\phi}{2} \begin{pmatrix} 1 + \sin \frac{\phi}{2} \sin \frac{3\phi}{2} \\ \sin \frac{\phi}{2} \cos \frac{3\phi}{2} \\ 1 - \sin \frac{\phi}{2} \sin \frac{3\phi}{2} \\ 2\nu \end{pmatrix}. \quad (21)$$

Therefore, all stresses are square root singular with respect to  $s$ , the local radial coordinate of the "crack analogue", Fig. 4.

For the calculation of Mode I stress intensity factor, we note that the contact pressure gives the only non-zero stress at the surface, e.g. [7],

$$\sigma_{zz} = -\frac{P}{2\pi a} (a^2 - r^2)^{-1/2}. \quad (22)$$

The first of equation (21) is the correct asymptote of equation (22) as  $r \rightarrow a -$ . From

$$\sigma_{zz} = -\frac{K_I}{\sqrt{2\pi(a-r)}}, \quad (23)$$

we readily conclude

$$K_I = -\frac{P}{2a\sqrt{\pi a}}. \quad (24)$$

This result is the same as that in [14–16] for a circular semi-infinite crack located along the circumference of a cylindrical rod (with an uncracked ligament of radius  $a$ ) loaded remotely with a concentrated normal load  $P$ , Fig. 4. Equation (21) also provide stress distributions which are identical to those for the fields ahead of a circumferentially located crack in a cylindrical rod (where the crack depth  $\gg$  uncracked ligament radius).

**2.2.2. Tangent loading, axisymmetric (Mode II crack analogue).** Using the standard analysis for the shear loading of a circular punch [7], it is seen that

$$\sigma_{rz} = \frac{Q}{2\pi a} (a^2 - r^2)^{-1/2}. \quad (25)$$

Taking the asymptote of equation (25) as  $r \rightarrow a -$ , we obtain

$$K_{II} = \frac{Q}{2a\sqrt{\pi a}}. \quad (26)$$

This result is the same as that in fracture handbooks [14-16] for a circular semi-infinite crack located along the circumference of a cylindrical rod (with an uncracked ligament of radius  $a$ ) loaded remotely with a concentrated shear load  $Q$ .

### 3. RANGE OF APPLICABILITY OF THE CRACK ANALOGUE

#### 3.1. Limits of the linear elastic "crack analogue"

The elastic solutions predict that stress singularities develop at the contact perimeter and that such stresses would inevitably lead to plasticity or damage at this location. It should be emphasized that the asymptotic forms presented in the preceding section are valid only in the region around the contact edges. The asymptotic stresses along the contact region, equation (11), away from the contact edges, overestimate the full solution, equation (10), as shown in Fig. 2.

In order to assess quantitatively the difference between the contact mechanics and the asymptotically matched fracture mechanics fields, consider the tensile opening stresses given by equations (4) and (5), respectively. Dividing  $\sigma_{yy}$ , as given by equation (5), by that from equation (4) yields:

$$\begin{aligned} \frac{P/(\pi\sqrt{2ar})}{P/(\pi\sqrt{a^2-x^2})} &= \frac{P/(\pi\sqrt{2a}\sqrt{a-x})}{P/(\pi\sqrt{a+x}\sqrt{a-x})} \\ &= \frac{\sqrt{a+x}}{\sqrt{2a}} = \epsilon. \end{aligned} \quad (27a)$$

This ratio equals one when the contact mechanics and the asymptotic fracture mechanics solutions match exactly. The distance over which they asymptotically match for various levels of accuracy,  $x_{\text{asym}}$ , can be quantitatively assessed by letting the ratio in equation (27a) equal the parameter  $\epsilon$ . From equation (27a).

$$x_{\text{asym}} = |2\epsilon^2 - 1| a. \quad (27b)$$

In other words, when the contact mechanics and the asymptotically matched fracture mechanics solutions are at least 95% of each other, i.e. when  $\epsilon = 0.95$ , equation (27b) shows that  $x_{\text{asym}} = 0.8a$ . This implies that the two solutions match to an accuracy of better than 95% over 20% of the contact radius measured from the rim of the contact.

#### 3.2. Limits of small-scale yielding

In order to obtain estimates of the extent of the plastic zone on the surface, we use the elastic solutions as derived above. We confine the analysis to two-dimensional plane strain. Let  $\sigma_y$  be the yield strength of the surface region of the substrate. The onset of yielding, as per the von Mises criterion, occurs when

$$\begin{aligned} 2\sigma_y^2 &= (\sigma_{xx} - \sigma_{yy})^2 + (\sigma_{yy} - \sigma_{zz})^2 \\ &+ (\sigma_{zz} - \sigma_{xx})^2 + 6\sigma_{xy}^2. \end{aligned} \quad (28)$$

Under plane strain conditions

$$\sigma_{zz} = \nu(\sigma_{xx} + \sigma_{yy}), \quad (29)$$

where  $\nu$  is the Poisson ratio of the surface.

If  $\sigma_{\text{app}} = \sigma_{xx} = 0$  (absence of  $T$ -stress), then equation (28) becomes

$$2\sigma_y^2 = \sigma_{yy}^2[1 + \nu^2 + (1 - \nu)^2] + 6\sigma_{xy}^2. \quad (30)$$

Using the results for the rigid punch solution, equations (4) and (10), it can be shown that for  $-a \leq x \leq a$ ,

$$\sigma_y^2 = \frac{1}{\pi^2 |a^2 - x^2|} \left\{ \frac{P^2}{2} [1 + \nu^2 + (1 - \nu)^2] + 3Q^2 \right\}. \quad (31)$$

Therefore, for small-scale plastic conditions

$$2\epsilon | \epsilon^2 - \frac{1}{2} | a \gg \frac{1}{\pi\sigma_y} \left\{ \frac{P^2}{2} [1 + \nu^2 + (1 - \nu)^2] + 3Q^2 \right\}^{1/2}. \quad (32)$$

If  $\sigma_{\text{app}} = T$ ,  $|T| \ll \sigma_y$ , and  $\nu = 0.5$ , then equation (30) becomes

$$4\sigma_y^2 = 3(T - \sigma_{xy})^2 + 12\sigma_{xy}^2. \quad (33)$$

After some straightforward algebraic manipulation, the condition for small-scale plasticity becomes

$$\begin{aligned} \{2\pi\epsilon | \epsilon^2 - \frac{1}{2} |^{-1} a\}^{-1} &\gg \\ \frac{-B + \sqrt{B^2 - 4(T^2 - 4\sigma_y^2/3)A}}{2A}, \end{aligned} \quad (34)$$

where

$$\begin{aligned} A &= (P^2 + 4Q^2), \quad B = 2TP, \\ B^2 - 4\left(T^2 - \frac{4\sigma_y^2}{3}\right)A &\geq 0. \end{aligned} \quad (35)$$

Note that if the uniform residual stress or applied stress is compressive ( $T < 0$ ), the plastic range is considerably reduced whereas the opposite is true if it is tensile ( $T > 0$ ).

The present approach can be extended, in some cases, to situations beyond small-scale yielding by employing the known results of non-linear fracture mechanics. This could entail use of the two-parameter approach involving the  $J$ -integral and the triaxiality parameter,  $Q$  (e.g. [17]). Cyclic plastic zones could also be evaluated in the context of fretting contact fatigue using fracture mechanics concepts.

### 4. APPLICATIONS TO FRETING FATIGUE

While the basic features of the asymptotic equivalence between contact mechanics and fracture

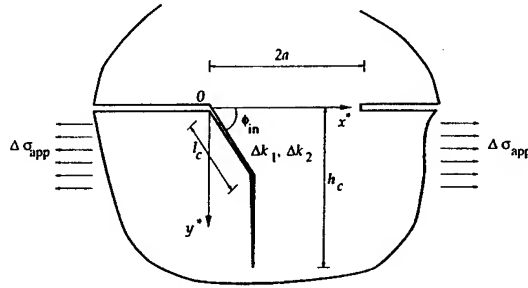


Fig. 5. Analysis of cracking patterns in fretting fatigue using the crack analogue model. A small surface crack initiates at an angle  $\phi_{in}$  to the contact surface and advances into the substrate over a distance  $l_c$ . It then reorients itself normal to the external cyclic stresses  $\Delta\sigma_{app}$  and penetrates the substrate over a distance  $h_c$  at which point catastrophic failure initiates.

mechanics have many broad applications, we take up here a particular case of the present approach which offers newer insights into the cracking phenomena under fretting fatigue conditions. Fretting fatigue refers to the contact between two surfaces where small, oscillatory sliding displacements (typically in the range 2–50  $\mu\text{m}$ ) occur between the surfaces. Given the presence of a corrosive environment, considerable oxidation leading to wear and material removal can occur at the fretted surface. Usually, one or both surfaces in contact is/are also subjected to fluctuating stresses as a consequence of such factors as vibration. It is known that repeated fretting of surfaces can cause a drastic reduction (by a factor of two or more) in the fatigue endurance limit, and orders of magnitude decrease in fatigue life from that seen under pure mechanical cyclic loading alone (e.g. [18–20]). Fretting fatigue failures are known to occur in such diverse situations as: the seating of the turbine disk on drive shaft in land-based turbines, the dovetail or fir-tree sections of aircraft jet engines, interwire contacts of cables and ropes in electric power transmission lines, riveted joints, spline joints, keyways and shrink-fits.

The implications of the crack analogue model are examined here for the particular case of high-cycle, fretting fatigue because of the following considerations:

(a) Fretting fatigue represents a complex contact problem in which repeated tractive (partial) sliding between surfaces occurs in conjunction with superimposed cyclic loading (*T*-stress in the present analogy).

†The conditions governing the inception of a fatigue crack at a fretted surface are dictated by such complex processes as surface oxidation and debris formation, fretting wear, multiple cracking, and possibly local changes in near-surface microstructure. We confine attention here only to the mechanical cracking processes which are influenced solely by the macroscopic contact conditions and the applied loads.

(b) Detailed experimental observations of the onset and progression of cracks near the contact region as well as their continued advance into the substrate under the influence of superimposed cyclic loads have been reported in a number of independent studies on fretting fatigue. This makes it possible to quantitatively evaluate the predictions and capabilities of the crack analogue approach directly with experiments.

(c) In many fretting fatigue situations, global sliding and large-scale plasticity do not occur between the contacting surfaces, thereby making the asymptotic matching of the crack-tip and contact-edge fields justifiable.

#### 4.1. General loading

Consider the two-dimensional contact problem, schematically shown in Fig. 1, for which the equivalent crack geometry is schematically sketched in Figs 2 and 5. We begin with a consideration of loading conditions which are representative of typical fretting fatigue. The normal load  $P$  in Fig. 1 is taken to be constant, while the tangential load  $Q$  cyclically varies in the range  $-Q_{\max} \leq Q \leq Q_{\max}$ . Let the fretted substrate (at least in the regions close to the contact surface) be additionally subjected to a normal stress,  $\sigma_{app}$ , as shown in Figs 1 and 2. Such a stress can arise from residual stresses due to surface treatments (e.g. shot-peening, laser shock peening or coating), or from externally imposed loads. We consider a general case of a cyclically varying uniform normal stress of amplitude  $\Delta\sigma_{app}$  and load ratio,  $R_{app}$ .

From Sections 2.1.1 and 2.1.2, it is readily seen that the remote stress intensity factors,  $K_I$  and  $K_{II}$ , in Fig. 2 are

$$K_I = -\frac{P}{\sqrt{\pi a}}, \quad \Delta K_I = 0, \\ K_{II}|_{\max} = \frac{Q_{\max}}{\sqrt{\pi a}}, \quad \Delta K_{II} = \pm \frac{Q_{\max}}{\sqrt{\pi a}}, \quad (36)$$

with  $-K_{II}|_{\max} \leq K_{II} \leq K_{II}|_{\max}$ . Here  $\Delta K_I$  and  $\Delta K_{II}$  are the cyclic amplitudes of  $K_I$  and  $K_{II}$ , respectively.

#### 4.2. Surface crack initiation under fretting fatigue

Once a fatigue crack initiates in the contact region, at some angle to the contact surface, under the influence of the contact loads, the conditions for its continued advance are dictated by the amplitudes of the local mode I and mode II stress intensity factors,  $\Delta k_I$  and  $\Delta k_{II}$ , respectively. The estimation of the angle,  $\phi_{in}$ , at which a fatigue crack initiates at the fretted surface (see Fig. 5) and the direction along which continued crack growth occurs requires a fracture criterion†.

It is postulated here that the crack initiates and advances in a direction along which the local mode II stress intensity factor amplitude,  $\Delta k_{II}$ , vanishes. For the incipient small crack, oriented at an angle,

$\phi$ , to the free surface, the local  $k_1$  and  $k_2$  are related to the remote  $K_I$  and  $K_{II}$  by (e.g. Cotterell and Rice [21]):

$$\begin{aligned} k_1 &= a_{11}(\phi)K_I + a_{12}(\phi)K_{II}, \\ k_2 &= a_{21}(\phi)K_I + a_{22}(\phi)K_{II}. \end{aligned} \quad (37a)$$

To a first order approximation in  $\phi$ , the dimensionless factors for the infinitesimal kink are [21]

$$\begin{aligned} a_{11}(\phi) &= \frac{1}{4} \left( 3 \cos \frac{\phi}{2} + \cos \frac{3\phi}{2} \right), \\ a_{12}(\phi) &= -\frac{3}{4} \left( \sin \frac{\phi}{2} + \sin \frac{3\phi}{2} \right), \\ a_{21}(\phi) &= \frac{1}{4} \left( \sin \frac{\phi}{2} + \sin \frac{3\phi}{2} \right), \\ a_{22}(\phi) &= \frac{1}{4} \left( \cos \frac{\phi}{2} + 3 \cos \frac{3\phi}{2} \right). \end{aligned} \quad (37b)$$

The fretting fatigue crack can initiate at either or both crack-tips. Without any loss of generality, we choose the left crack tip in the double-edge crack analogue in Fig. 5. Note that this corresponds to contact fatigue crack initiation at the left edge of the two-dimensional contact region in Fig. 1.

In order to determine the initiation angle of the surface crack,  $\phi_{in}$ , use the expression for  $k_2$  in equations (37a–b) in conjunction with equation (36). Then solve for  $\phi_{in}$  by invoking the condition that  $k_2 = 0$ . This result gives the contact-fatigue crack initiation angle at the surface which is determined by solving the following equation for  $\phi_{in}$ :

$$\begin{aligned} \left( \sin \frac{\phi_{in}}{2} + \sin \frac{3\phi_{in}}{2} \right) \times \left| \cos \frac{\phi_{in}}{2} + 3 \cos \frac{3\phi_{in}}{2} \right|^{-1} \\ = \frac{Q_{max}}{P} = \mu. \end{aligned} \quad (38)$$

#### 4.3. Small crack growth from the surface

It is seen from equations (37a–b) that although  $P$  (and hence  $K_I$ ) is fixed,  $k_1$  oscillates because  $K_{II}$  oscillates. A fatigue crack initiating at  $\phi_{in}$  is then subjected to an effective opening stress intensity factor (arising from both  $P$  and  $Q$ ) whose amplitude is:

$$\Delta k_1 = \pm \frac{3}{4} K_{II} |_{max} \left( \sin \frac{\phi_{in}}{2} + \sin \frac{3\phi_{in}}{2} \right). \quad (39)$$

As the small surface crack begins to advance into the substrate, the effects of the contact loads  $P$  and

$\Delta Q$  in providing a sufficiently large  $\Delta k_1$  to advance the crack rapidly diminish, and there arises a competition between the applied uniform cyclic stress  $\Delta \sigma_{app}$  and the contact loads†. After some initial growth over a distance  $l_c$  from the contact periphery, the small surface crack would, therefore, try to reorient itself normal to the applied tensile cyclic stress  $\Delta \sigma_{app}$ . This is schematically sketched in Fig. 5. If at the critical distance  $l_c$ , the tensile opening stress intensity factor due to the applied loads is larger than the effective mode I threshold stress intensity factor range,  $\Delta K_{th}$ , the crack would reorient itself normal to the uniform applied stress and would continue to advance into the substrate in mode I. Otherwise, the crack would arrest completely. The condition for the reorientation of the crack normal to  $\Delta \sigma_{app}$  can then be phrased by linking the mode I driving force to  $\Delta K_{th}$  in the following manner:

$$\begin{aligned} \Delta K_{th} &= \frac{\Delta \sigma_{app} \sqrt{\pi l_c}}{4} \times F(\phi_{in}) \\ l_c &= \left( \frac{4 \Delta K_{th}}{\Delta \sigma_{app} \sqrt{\pi}} \right)^2 \cdot \{F(\phi_{in})\}^{-2}. \end{aligned} \quad (40a)$$

Here  $F(\phi_{in})$  is the function which provides the stress intensity factor calibration (see, for example, Ref. [22]) for the doubly-kinked crack after the appropriate coordinate transformation described in Section 2.1:

$$\begin{aligned} F(\phi_{in}) &= F_1(\phi_{in}) \left( 3 \cos \frac{(\pi - 2\phi_{in})}{4} + \cos \frac{3(\pi - 2\phi_{in})}{4} \right) \\ &+ 3F_2(\phi_{in}) \left( \sin \frac{(\pi - 2\phi_{in})}{2} + \sin \frac{3(\pi - 2\phi_{in})}{2} \right). \end{aligned} \quad (40b)$$

Tables of  $F_1$  and  $F_2$  are listed in Isida [22], from where it is found that

$$\begin{aligned} F_1(\phi) &\approx 1.058 \sin \phi - 0.065 \sin(3\phi), \quad \text{and} \\ F_2(\phi) &\approx 0.374 \sin(2\phi) + 0.023 \sin(4\phi). \end{aligned} \quad (40c)$$

#### 4.4. Extent of subsurface crack growth due to applied loads

The fatigue crack would continue to advance in mode I under the influence of  $\Delta \sigma_{app}$  until a critical crack length,  $h_c$ , at which catastrophic failure occurs. The critical crack length is reached when the maximum stress intensity factor of the fatigue cycle reaches the fracture toughness of the material,  $K_c$ , for a very deep substrate:

$$\begin{aligned} K_{max} &= 1.12 [\sigma_{app}]_{max} \sqrt{\pi h_c} \\ &= 1.12 \left\{ \frac{\Delta \sigma_{app}}{1 - R_{app}} \right\} \sqrt{\pi h_c} \rightarrow K_c. \end{aligned} \quad (41)$$

Since  $K_c$ ,  $\Delta \sigma_{app}$  and  $R_{app}$  are known quantities (with  $R_{app}$  being the load ratio of the applied cyclic load  $\Delta \sigma_{app}$ ),  $h_c$  is readily determined from this equation.

†The initial growth of the stage I small crack is postulated here to occur along a constant path which is at an angle  $\phi_{in}$  to the surface. In reality, however, the small crack, once initiated at an angle  $\phi_{in}$ , would be expected to gradually reorient itself until it becomes a mode I crack with respect to  $\Delta \sigma_{app}$ ; see, for example, the discussion in Section 4.6.

#### 4.5. Life-prediction methodology for fretting fatigue fracture

We have thus far reasoned how the fretting fatigue crack growth process can be divided into two stages:

(1) Stage I crack growth: A surface crack initiates under the influence of contact loads at an angle  $\phi_{in}$  to the contact surface. The growth of this small crack occurs (along a direction where  $\Delta k_2 = 0$ ) until a critical distance,  $l_c$ .

(2) Stage II crack growth: Here Mode I crack growth is primarily governed by the uniform cyclic stress,  $\Delta\sigma_{app}$ , imposed on the substrate.

The inception and the early growth of the small surface crack are dictated by a number of complex factors which include surface oxidation, initial surface roughness, fretting wear debris formation, surface treatments (involving peening, coating or lubrication), and local multiaxial stress states. Here we consider only the mechanical effects and invoke the notion that crack initiation occurs solely as a result of contact loads in a direction along which the local Mode II stress intensity factor vanishes.

Let the crack growth rate per contact cycle, as determined experimentally for the small surface flaw, be approximated by the Paris-law:

$$\frac{dl}{dN} = C_I(\Delta k_I)^{m_I}, \quad (42)$$

$$N_2 = \int_{l_c \sin \phi_{in}}^{h_c} \frac{dl}{C_{II}(1.12\Delta\sigma_{app}\sqrt{\pi l})^{m_{II}}} = \begin{cases} \frac{1}{C_{II}(1.12\Delta\sigma_{app}\sqrt{\pi})^{m_{II}}} \cdot \left(\frac{2}{m_{II}-2}\right) \cdot \{(l_c \sin \phi_{in})^{(2-m_{II})/2} - h_c^{(2-m_{II})/2}\}, & m_{II} \neq 2 \\ \frac{1}{C_{II}(1.12\Delta\sigma_{app}\sqrt{\pi})^2} \cdot \ln \frac{h_c}{l_c \sin \phi_{in}}, & m_{II} = 2 \end{cases} \quad (45)$$

where  $C_I$  and  $m_I$  are material constants representative of the growth of small surface flaw (until it reaches a length  $l_c$ ) and of the local mixed-mode loading condition;  $\Delta k_I$  is the amplitude of the near-tip opening stress intensity factor defined in equation (39), and  $l$  is the instantaneous crack length measured along the initial growth plane located at the angle  $\phi_{in}$  to the surface. Note that the load ratio  $R$  for stage I crack growth is essentially zero, since  $Q$  is fully reversed while  $P$  is fixed.

Similarly, let the growth of the stage II crack be characterized by the equation,

$$\frac{dl}{dN} = C_{II}(\Delta k_I)^{m_{II}} = C_{II}(1.12\Delta\sigma_{app}\sqrt{\pi l})^{m_{II}}, \quad (43)$$

where  $C_{II}$  and  $m_{II}$  are experimentally determined material constants representative of the growth of a long edge crack in the substrate material, from an initial crack length  $l = l_c \sin \phi_{in}$  to a final crack length  $h_c$ .

The total time or number of cycles to failure under fretting fatigue can then be estimated in the following manner. The total life consists of two parts:

(1) The number of cycles,  $N_1$ , for near-surface fatigue crack growth in stage I, and

(2) The number of cycles,  $N_2$ , for mode I fatigue crack growth in stage II due to the applied stresses  $\Delta\sigma_{app}$ .

The total number of cycles to failure is:  $N = N_1 + N_2$ .

Integrating equation (42) for stage I crack growth, it is seen that

$$N_1 = \int_0^{l_c} \frac{dl}{C_I(\Delta k_I)^{m_I}} \approx \frac{l_c}{C_I(\Delta k_I)^{m_I}}. \quad (44)$$

Note that  $N_1$  refers to the number of oscillations of the pad on the substrate and not the number of cycles of the applied stress  $\Delta\sigma_{app}$ . If  $\nu_{I,c}$  is the cyclic frequency of oscillations of the pad, the time to failure in stage I is:  $t_{r,I} = N_1/\nu_{I,c}$ .

Similarly, integrating equation (43),

Here  $N_2$  refers to the number of cycles of the applied stress  $\Delta\sigma_{app}$ . If  $\nu_{II,c}$  is the cyclic frequency of applied stress, the time to failure in stage II is:  $t_{r,II} = N_2/\nu_{II,c}$ .

The total time to failure in fretting fatigue, with the given phenomenology of cracking, is

$$t_r = t_{r,I} + t_{r,II} = \frac{N_1}{\nu_{I,c}} + \frac{N_2}{\nu_{II,c}}. \quad (46)$$

It should be recalled here that no incubation period is assumed for the initiation of a surface crack at the contact rim. Should such a period be known to exist, the time to incubation should be added to the total time to failure. (A worked-out example which illustrates the life prediction methodology developed here can be found in Ref. [20].)

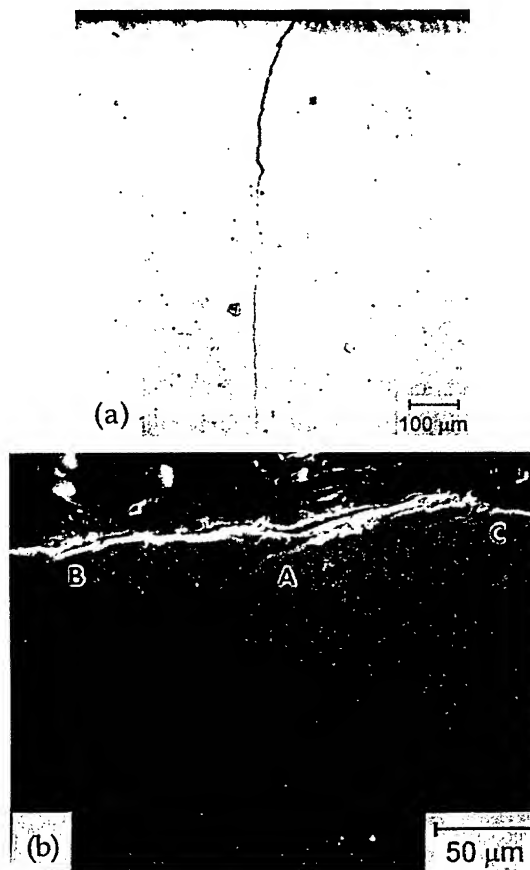


Fig. 6. (a) An overall view of the initial inclination of a stage I fretting fatigue crack at the surface at the edge of the rectangular contact pad, and the gradual reorientation of the crack to advance perpendicularly to the applied cyclic stress on the substrate. (b) An enlarged view of multiple cracking and of the evolution of a dominant fretting fatigue crack for the same system, but with a higher cyclic load on the substrate. After Ref. [23]. Photographs reprinted from *Mater. Sci. Eng. A*, 1997, A237, 229, by Antoniou and Radtke, with permission of Elsevier Science S.A., Amsterdam, The Netherlands.

#### 4.6. Comparisons with a variety of experimental observations

**4.6.1. Qualitative observations of crack initiation and growth.** The models of crack initiation and growth considered in the preceding subsections find experimental support in a variety of independent in-

vestigations of fretting fatigue. For example, Fig. 6(a) shows the initiation of a fatigue crack in a Ti alloy (with 5 Al, 4 Mo, 4 Cr, 2 Zr and 2 Sn, all in wt%) substrated fretted with a Ti-6Al-4V rectangular pad at room temperature at a cyclic frequency of 20 Hz with the substrate subjected to an alternating tensile stress of 400 MPa at  $R = 0.1$  (after Ref. [23]). With the static and dynamic friction coefficients determined to be approximately 0.85 and 0.70, respectively, for the conditions of the experiments, it is found from this figure that a stage I fatigue crack initiates at the contact rim at an angle  $\phi_{in} \approx 55^\circ$ . After advancing in stage I over a distance of approximately 100–200  $\mu\text{m}$ , the crack gradually curves around to become a mode I fatigue crack normally oriented to the applied alternating stress. Figure 6(b) shows a higher magnification view of the inception of multiple fatigue cracks (marked A, B and C) at the fretted surface from another experiment with the same conditions with the exception that the applied cyclic stress amplitude is 1000 MPa instead of 400 MPa; out of these multiple stage I cracks, one of them (marked A) becomes a dominant flaw. The two micrographs in Fig. 6(a) and (b) thus lend support to the basic process of crack initiation, orientation and subsequent advance which is modelled in the present study.

**4.6.2. Quantitative comparisons of crack path.** The methodology described in Sections 4.1–4.4 can be applied to interpret quantitatively a variety of experimental observations on contact fatigue already available in the literature. In view of the availability of quantitative information on the crack initiation angle and on failure modes, we choose to compare the predictions of the crack analogue model with fretting fatigue experimental results. Table 1 gives the background information on the materials studied in these experiments along with the relevant references to sources where full details on the experiments can be found. A direct comparison of the present predictions of the crack initiation angle,  $\phi_{in}$ , the extent of stage I crack growth,  $l_c$ , and the occurrence of catastrophic fretting-fatigue failure with experimental observations is provided in Table 2. It is seen that the predictions are in agreement with experiments for 15 different fretting fatigue experiments from several different research studies.

Table 1. Background information on materials and their basic properties for the fretting fatigue experiments conducted in the cited references

Material	Heat treatment	Microstructure	Yield stress (MPa)	Tensile strength (MPa)	Vickers hardness (Hv)	Reference
Ti alloy (with 5 Al, 2 Zr, 2 Sn, 4 Mo and 4 Cr, in wt%)	$\alpha + \beta$ alloy	Widmanstätten	1080	1130	—	[23]
JIS SUP9 steel	austenitised 850°C + temper 400°C	tempered martensite	1538	1677	498	[24]
S45C Steel	—	ferrite/pearlite	461	718	190	[24]
SVS 304L stainless steel	—	austenite	225	570	206	[25]
2014 aluminum alloy	—	—	458	504	155	[26]
3.5NiCrMoV steel	—	bainite	600	733	222	[27]



Table 2. A comparison of the predictions of the crack initiation angle ( $\phi_{in}$ ), the extent of stage I crack growth ( $l_c$ ), and the occurrence of catastrophic fretting-fatigue failure with experimental observations

Material	Crack angle $\phi_{in}$ (deg.)		Crack angle $\phi_{in}$ (deg.)	$l_c$ ( $\mu m$ )		$\Delta\sigma_{app}$ (MPa)	$\Delta K_1$ (MPa $\sqrt{m}$ )		$\Delta K_{th}$ (MPa $\sqrt{m}$ )	Catastrophic failure predicted? (observed experimentally?)		Reference
	Predicted	Measured		Predicted	Measured		calculated	measured		yes/no		
Ti alloy (with 5 Al, 2 Zr, 2 Sn, 4 Mo and 4 Cr, in wt%) SUP9 steel	47–50	55	150	140	400	—	—	—	—	yes (yes)	—	[23]
	21	19	—	2	300	—	—	—	—	—	—	[24]
	26	24	—	2	400	—	—	—	—	—	—	
	34	27	—	—	—	—	—	—	—	—	—	
	30	32	—	—	—	—	—	—	—	—	—	
S45C steel	43	40	—	—	—	—	—	—	—	—	—	
	45	48	—	—	—	—	—	—	—	—	—	
	39	36	4.6	4	170	—	—	—	—	—	—	[24]
	41	46	7.7	6	220	—	—	—	—	—	—	
	45	45	8.6	10	300	—	—	—	—	—	—	
SUS 304L steel	—	65	5500	2800	—	—	17.6	7.0	7.0	yes (yes)	—	[25]
	—	65	1400	2100	—	—	8.8	7.0	7.0	yes (yes)	—	
	—	60	3700	1900	—	—	13.0	7.0	7.0	yes (yes)	—	
2014 aluminum alloy 3.5NiCrMoV steel	36	30	12.8	40	—	—	0.4	1.17	1.17	no (no)	—	[26]
	90	80	—	—	—	—	19.8	13	13	yes (yes)	—	[27]

## 5. CONCLUDING REMARKS

In this paper, we have demonstrated some broad connections between the asymptotic fields of sharp-ended contacts between two materials and the crack-tip fields for equivalent geometries. It is also shown how such connections could be used to identify the conditions governing the onset and growth of contact fatigue cracks. A simplified life prediction methodology for contact fatigue is developed from this "crack analogue" model. The predictions of this approach have been compared with a number of independent experimental observations on fretting in different alloy systems. The main feature of this life prediction method is that it provides quantitative estimates of the fatigue lives for different stages of contact fatigue, and provides tractable results for a highly complex phenomenon of considerable engineering significance. Another noteworthy feature of this approach is that the crack analogue model naturally introduces a length scale to the problem whereby the classical fracture mechanics solutions can be applied to contact mechanics, and whereby contact fatigue lives can be estimated from a knowledge of the crack growth behavior known from laboratory specimens. It is to be noted that initial surface roughnesses of the contacting bodies, possible changes in surface microstructure due to severe tribological contact, surface treatments and lubrication are factors which could markedly alter the total fatigue lives. These complexities have not been incorporated into the present analysis.

*Acknowledgements*—This work was supported by the Multi-University Research Initiative on "High Cycle Fatigue", which is funded at MIT by the Air Force Office of Scientific Research, Grant No. F49620-96-1-0478, through a subcontract from the University of California at Berkeley. The authors thank T. Nicholas, M. Olsson and C. F. Shih for helpful discussions on this work. Thanks are also due to J. W. Hutchinson for his review of this paper and for his suggestions.

## REFERENCES

1. Sadowski, M., *Z. Angew. Math. Mech.*, 1928, **8**, 107.
2. Nadai, A. I., *Theory of Flow and Fracture of Solids*, Vol. II, McGraw-Hill, NY, 1963.
3. Hertz, H., *J. Reine Angew. Math.*, 1882, **92**, 156.
4. Irwin, G. R., *J. Appl. Mech.*, 1957, **24**, 361.
5. Rice, J. R., *J. Appl. Mech.*, 1968, **35**, 379.
6. Gladwell, G. M. L., *Contact Problems in the Classical Theory of Elasticity*, Sijthoff and Noordhoff, Alphen aan den Rijn, 1980.
7. Johnson, K. L., *Contact Mechanics*, Cambridge University Press, Cambridge, 1985.
8. Hills, D. A., Nowell, D. and Sackfield, A., *Mechanics of Elastic Contacts*, Butterworth Heinemann, Oxford, 1993.
9. Kanninen, M. F. and Popelar, C. H., *Advanced Fracture Mechanics*, Oxford Engineering Science Series, Oxford University Press, 1985.

Table 3. Conditions for strict validity of square root singular fields.  $\alpha$  and  $\beta$  are the Dundurs parameters defined by equation (A.1)

Case	Pad or punch stiffness	Substrate stiffness	Friction coefficient, $\mu$	Angle of the pad $\gamma$	Remarks
1	rigid ( $\alpha = -1$ )	elastic incompressible ( $\beta = 0$ )	$\infty$ (adherence)	$0 < \gamma \leq \pi/2$	—
2	elastic	elastic	$\infty$ (adherence)	$\gamma = \pi/2$	$2\beta = 1 - \alpha$
3	rigid ( $\alpha = -1$ )	elastic	0 (frictionless)	$0 < \gamma \leq \pi/2$	displacement controlled loading
4	rigid ( $\alpha = -1$ )	elastic incompressible ( $\beta = 0$ )	finite	$0 < \gamma \leq \pi/2$	—
5	elastic	elastic	$\pm(2/3)[(\alpha + 1)/((\alpha + 1) + \beta)]$	$\gamma = \pi/2$	+ for slipping in +x direction, - for slipping in -x direction
6	elastic	elastic	$\pm[(\alpha + 1)\cot(\gamma/2)[1 + \cos \gamma]] / \{3(\alpha + 1)\cos^2(\gamma/2) + \beta[1 + \sin^2(\gamma/2)]\}$	$0 < \gamma \leq \pi/2$	+ for slipping in +x direction, - for slipping in -x direction

10. Anderson, T. L., *Fracture Mechanics: Fundamentals and Applications*, 2nd Edn., CRC Press, Boca Raton, FL, 1995.
11. Westergaard, H. M., *J. Appl. Mech.*, 1939, 6, 49.
12. Sneddon, I. N., *Proc. Cambridge Philos. Soc.*, 1946, 42, 29.
13. Williams, M. L., *J. Appl. Mech.*, 1957, 24, 109.
14. Tada, H., Paris, P. C. and Irwin, G. R., *Stress Analysis of Cracks Handbook*, Del Research Corporation, Hellertown, 1973.
15. Rooke, D. P. H. and Cartwright, D. J., *Compendium of Stress Intensity Factors*, Her Majesty's Stationary Office, London, 1976.
16. Murakami, Y., *Stress Intensity Factors Handbook*, Pergamon Press, New York, 1987.
17. O'Dowd, N. P. and Shih, C. F., *J. Mech. Phys. Solids*, 1991, 39, 989.
18. Waterhouse, R. B. and Lindley, T. C. (Eds), *Fretting Fatigue*,ESIS Publication No. 18, European Structural Integrity Society, Mechanical Engineering Publications Limited, London, 1994.
19. Hills, D. A. and Nowell, D., *Mechanics of Fretting Fatigue*, Kluwer Academic Publishers, Dordrecht, The Netherlands, 1994.
20. Suresh, S., *Fatigue of Materials*, Cambridge University Press, Cambridge, UK, 1st Edn., 1991; 2nd Edn., 1998, in press.
21. Cotterell, B. and Rice, J. R., *Int. J. Fract.*, 1980, 16, 155.
22. Isida, M., *Trans. Jpn Soc. Mech. Eng. A*, 1979, 45, 306.
23. Antoniou, R. A. and Radtke, T. C., *Mater. Sci. Eng. A*, 1997, 237, 229.
24. Tanaka, K., Mutoh, Y., Sakoda, S. and Leadbeater, G., *Fat. Fract. Eng. Mater. Struct.*, 1985, 8, 129.
25. Sato, K., Fujii, H. and Kodama, S., *Wear*, 1986, 107, 245.
26. Nix, K. J. and Lindley, T. C., *Fat. Fract. Eng. Mater. Struct.*, 1985, 8, 143.
27. Lindley, T. C. and Nix, K. J., in *Standardization of Fretting Fatigue Test Methods and Equipment*, ed. H. A. Attia and R. B. Waterhouse, Special Technical Publication 1159, American Society for Testing and Materials, Philadelphia, 1992, pp. 153–169.
28. Spence, D. A., *Proc. Cambridge Philos. Soc.*, 1973, 73, 249.
29. Dundurs, J., *J. Appl. Mech.*, 1969, 36, 650.
30. Dundurs, J. and Lee, M.-S., *J. Elasticity*, 1972, 2, 109.
31. Bogy, D. B., *J. Appl. Mech.*, 1971, 38, 377.
32. Gdoutos, E. E. and Theocaris, P. S., *J. Appl. Mech.*, 1975, 42, 688.
33. Comninou, M., *J. Appl. Math. Phys.*, 1976, 27, 493.

## APPENDIX A

The crack analogue of contact mechanics presented in this work strictly holds for rigid orthogonal (straight-sided) pads on incompressible elastic substrates, or for rigid orthogonal pads on elastic substrates with frictionless interfaces. This analogy is expected to be adequate also for situations where the substrate undergoes limited plastic yielding in the highly stressed region of the contact edge, or where the friction coefficient is very small. Local partial slip could be present in the case of strong elastic mismatch between the surface and the pad, which could result in a reduction in the intensity of the stress singularity. Such corrections, however, are not expected to be very significant (e.g. [28]). Therefore, in the proximity of the contact perimeter, the present approach could be adequate for a wide variety of practical applications.

The problem becomes more complicated, however, if the punch is also elastically deformable and the angle at the corner ( $\gamma$ ) is other than  $90^\circ$ . (Throughout this paper, however, we have considered only a straight-sided punch for which  $\gamma = 90^\circ$ .) In Fig. A.1, a two-dimensional elastic wedge (body 2 in Fig. 7) of angle  $\gamma$  is pressed into contact with an elastic half-space (body 1 in Fig. 7), where a constant friction coefficient,  $\mu$ , is assumed at their interface. The influence of the elastic constants is governed by the Dundurs' parameters [29]  $\alpha$ ,  $\beta$ :

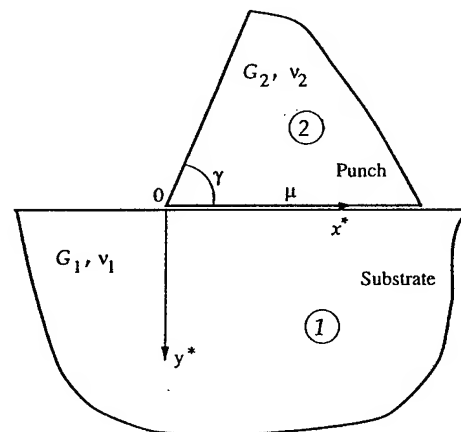


Fig. A.1. The general two-dimensional case of a wedge-shaped elastic punch in contact with an elastic half space.

$$\alpha = \frac{(1 - \nu_1)/G_1 - (1 - \nu_2)/G_2}{(1 - \nu_1)/G_1 + (1 - \nu_2)/G_2},$$

$$\beta = \frac{1(1 - 2\nu_1)/G_1 - (1 - 2\nu_2)/G_2}{2(1 - \nu_1)/G_1 + (1 - \nu_2)/G_2}, \quad (\text{A.1})$$

where  $\nu_1$  and  $\nu_2$  are the Poisson ratios of materials 1 and 2, respectively, and  $G_1$  and  $G_2$  are their corresponding shear moduli.

The variation of the stress components are not always square-root singular. Depending on  $\alpha$ ,  $\beta$ ,  $\gamma$  and  $\mu$ , power, logarithmic, or more complex singularities may arise. In some cases, there could be no singularity at all. The gen-

eral problem has been addressed by Dundurs and Lee [30] for the frictionless case, by Bogy [31] for the perfect adherence case, and by Gdoutos and Theoccharis [32] and Comninou [33] for the friction case. However, there are some material combinations,  $\alpha$ ,  $\beta$ , as well as pad angles  $\gamma$  and friction coefficients  $\mu$ , which rigorously give the square-root singular solutions discussed in Section 2 of the present paper. These cases are summarized in Table 3. Thus, the square-root singular solutions are expected to be either rigorously or approximately valid for a large variety of material combinations and pad geometries.



PERGAMON

*Acta mater.* Vol. 47, No. 18, pp. 4653–4664, 1999  
© 1999 Acta Metallurgica Inc.  
Published by Elsevier Science Ltd. All rights reserved.  
Printed in Great Britain  
1359-6454/99 \$20.00 + 0.00

PII: S1359-6454(99)00312-2

## THE ROLE OF ADHESION IN CONTACT FATIGUE

A. E. GIANNAKOPOULOS, T. A. VENKATESH, T. C. LINDLEY† and S. SURESH‡

Department of Materials Science and Engineering, Massachusetts Institute of Technology, Cambridge, MA 02139, U.S.A.

(Received 26 May 1999; accepted in revised form 12 August 1999)

**Abstract**—By incorporating the effects of interfacial adhesion in the mechanics of rounded contact between two bodies, a new approach is proposed for the quantitative analysis of a wide variety of contact fatigue situations involving cyclic normal, tangential or torsional loading. In this method, conditions of “strong” and “weak” adhesion are identified by relating contact mechanics and fracture mechanics theories. Invoking the notion that for strong and weak adhesive contact, a square-root stress singularity exists at the rounded contact edge or at the stick–slip boundary, respectively, mode I, II or III stress intensity factors are obtained for normal, sliding and torsional contact loading, accordingly. A comparison of the cyclic variations in local stress intensity factors with the threshold stress intensity factor range for the onset of fatigue crack growth then provides critical conditions for crack initiation in contact fatigue. It is shown that the location of crack initiation within the contact area and the initial direction of crack growth from the contact surface into the substrate can be quantitatively determined by this approach. This method obviates the need for the assumption of an artificial length scale, i.e. the initial crack size, in the use of known fracture mechanics concepts for the analyses of complex contact fatigue situations involving rounded contact edges. Predictions of the present approach are compared with a wide variety of experimental observations. © 1999 Acta Metallurgica Inc. Published by Elsevier Science Ltd. All rights reserved.

**Keywords:** Adhesion; Fracture; Fatigue; Wear; Surfaces and interfaces

### 1. INTRODUCTION

Functional structures, at macro or micro size-scales, by design or default, involve contact between similar or dissimilar materials, under static or cyclic loading conditions, in a passive or aggressive, thermo-chemical environment. Consequently, in the most general case, different aspects of contact such as material properties, interface chemistry and contact mechanics can independently or interdependently influence the overall mechanical behavior of the contacting system.

In most cases, the bulk mechanical behavior of the contacting system is characterized by a macroscopic continuum level analysis that evaluates the uncoupled mechanics response [1]. However, a more complete analysis requires a consideration of the microscopic or atomic structure where coupled interactions at the contact interface become significant. These are typically analyzed within the framework of surface thermodynamics by recognizing that contacting surfaces are subject to short-range interatomic forces such as the van der Waals forces. Consequently, spontaneous adhesion leading to the formation of a low energy interface reduces

the total energy of the system, while elastic deformation across the interface that accommodates adhesion leads to an increase in the potential energy of the system. The resulting thermodynamic equilibrium and extent of adhesion is then determined by the relative dominance of these competing phenomena.

For monotonic contact loading, adhesion has been well documented analytically and experimentally under normal loads [1–5], and to a lesser extent under tangential loads [6]. For cyclic loading, a number of experimental studies have investigated adhesion in a variety of materials — metals [7, 8], glasses [9], and polymers [10], for different surface and environmental conditions [11, 12], temperatures [13], hardness [8], and fatigue cycles [14].

Theoretical work has demonstrated that under monotonic compressive loading of the contact interface, adhesion induces tensile square-root singular stress fields at the contact edges [2, 3]. However, connections to contact fatigue experiments specifically aimed at correlations between adhesion and fatigue crack initiation have not been established.

The objectives of the present work are, therefore, to develop and experimentally validate a general continuum level mechanics model that incorporates work of adhesion, material elastic properties, and contact loads, for predicting key features of contact fatigue crack initiation (thresholds for the onset of

†Permanent address: Department of Materials, Imperial College of Science, Technology and Medicine, Prince Consort Road, London SW7 2BP, U.K.

‡To whom all correspondence should be addressed.

cracking, location of cracking, and initial orientation of the crack plane with respect to the contact surface) for a variety of loading conditions (cyclic mode I or steady mode I with cyclic mode II or cyclic mode III) and contact geometry (sphere or cylinder on a planar substrate).

This paper addresses the following key issues of contact mechanics and contact fatigue.

First, the present work extends the crack analogue methodology developed earlier [15] for the contact between a sharp-edged pad and a planar substrate, where stress singularities are introduced by the sharp cornered geometry. We now investigate the more general case of rounded contacts where stress singularities are induced by adhesion† and thus present a universal methodology that enables analysis of a variety of contact problems from those due to fretting fatigue in large-scale structures to contact fatigue in micro-scale devices, with adhesive or non-adhesive, sharp or rounded geometries.

Second, as the adhesion-induced, square-root singular stress fields are amenable for analysis within the framework of a "crack analogue" [15], the pre-existing long crack introduced by the contact circumvents "length scale" problems inherent in the modeling of crack initiation based on conventional fracture mechanics [16], or small crack growth based on initial dislocation distributions [17].

Third, under conditions of small-scale yielding, the effects of static and/or oscillatory bulk stresses (i.e. residual stresses induced by surface treatments such as shot-peening or laser shock-peening, or far-field applied stresses acting parallel to the contact surface) on contact fatigue crack initiation can also be analyzed by recognizing that these are analogous to the  $T$ -stresses present in a simple linear elastic fatigue-fracture formulation.

Fourth, all previous analyses which are based on stress-based approaches to fatigue at critical points (such as those using elastic stress fields of a sphere on a flat plane [18] in combination with a variety of fatigue strain-based, multiaxial criteria for endurance limits [19–22], predict contact fatigue cracking to initiate at the contact perimeter. This prediction is contrary to many experimental results which clearly indicate that cracking could initiate at either the contact perimeter or the stick-slip boundary. The present analysis, though an examination of the work of adhesion *via-à-vis* the crack driving force

arising from the contact loads, leads to a novel classification whereby cases of strong and weak adhesion are recognized unambiguously‡. Thus, the crack initiation location (contact perimeter for strong adhesion and the stick-slip boundary for weak adhesion) can be predicted without uncertainty.

Fifth, the present methodology conceptually facilitates the incorporation of known effects of surface conditions, environment, hardness, and temperature on adhesion, through a simple modification of the work of adhesion.

The paper is arranged in the following sequence. The mechanics of adhesive contacts for a variety of monotonic loading conditions are reviewed in Section 2. The contact mechanics of cyclic loading for three-dimensional, spherical, adhesive contacts are analyzed in Section 3. The results of the adhesion model for cyclic loading for two-dimensional, cylindrical contacts are presented in Section 4. The range of applicability of the adhesion model as well as its significance and limitations are discussed in Section 5. Available experimental results for different material systems and loading configurations are compared to model predictions in Section 6. Finally, the paper concludes with a summary of results and potential palliatives for contact fatigue from the perspective of the adhesion model in Section 7.

## 2. MECHANICS OF STATIC ADHESIVE CONTACT

Consider a sphere of diameter,  $D$ , elastic modulus,  $E$ , and Poisson ratio,  $\nu$ , contacting the planar surface of a large substrate of similar material, Fig. 1(a), with  $r$  and  $z$  being the global radial and depth coordinates attached to the center of the contact circle. Three loading conditions are considered as follows.

### 2.1. Normal loading

For elastic, monotonic loading from zero to  $P_{\max}$  ( $>0$ ), under non-adhesive conditions, the contact stress field is non-singular [Fig. 1(b)] and the maximum contact radius,  $a_0$ , is given as [1]

$$a_0 = \left[ \frac{3D(1-\nu^2)}{4E} P_{\max} \right]^{1/3}. \quad (1)$$

Under adhesive conditions, when two surfaces with surface energies  $\gamma_1$  and  $\gamma_2$  adhere to form a new interface of lower energy,  $\gamma_{12}$ , the corresponding work of adhesion is defined as,  $w = (\gamma_1 + \gamma_2 - \gamma_{12}) \geq 0$ . For two contacting solids with the same elastic properties, which are presently considered,  $w = 2\gamma_1$ . For metals,  $w \approx 1$  N/m [23].

The short-range forces of attraction that promote adhesion effectively increase the contact load across the interface and thus increase the contact radius,  $a_{\max}$  [Fig. 1(c)], to the one given as

†The adhesion induced stress singularities are not expected to modify the geometry induced stress singularities in the case of sharp edged contacts.

‡The conditions of strong and weak adhesion can conceptually be visualized as being analogous, respectively, to the concepts of "static" and "dynamic" friction when the interfacial slip behavior across two contacting surfaces is considered.

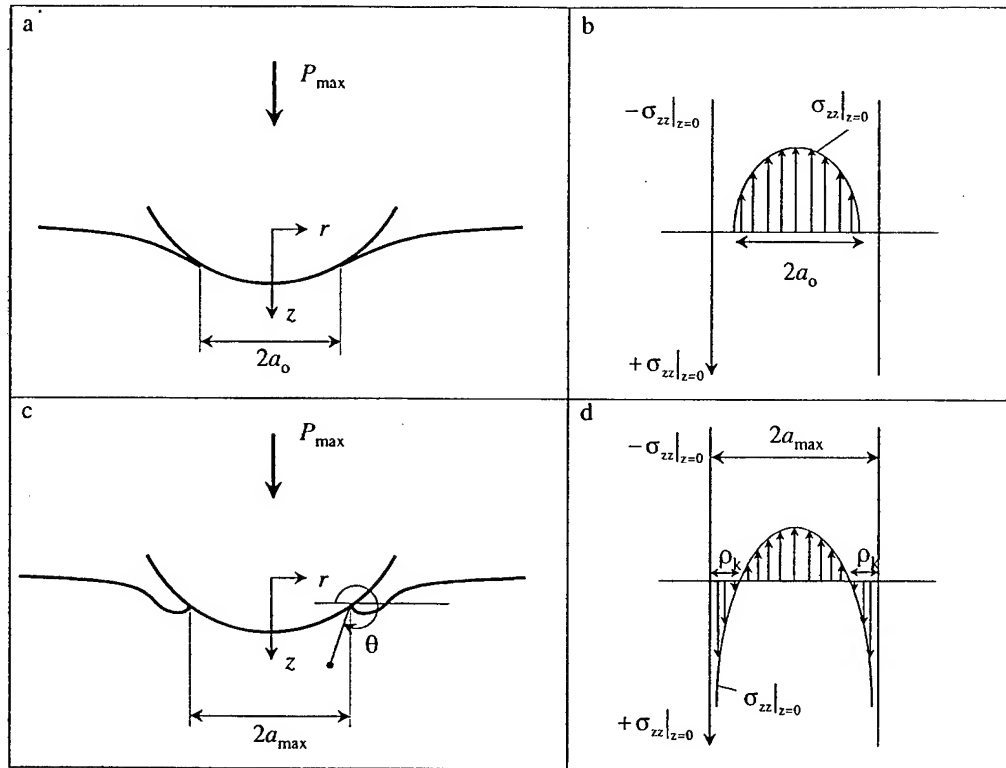


Fig. 1. Schematics illustrating: (a) non-adhesive contacts and (b) the corresponding non-singular contact stress field; (c) adhesive contacts and (d) the corresponding stress field exhibiting tensile square-root singularity.

$$a_{\max} = \left[ \frac{3D(1-\nu^2)}{4E} \left( P_{\max} + \frac{3\pi Dw}{2} \right) + \sqrt{3\pi Dw P_{\max} + \left( \frac{3\pi Dw}{2} \right)^2} \right]^{1/3} \quad (2)$$

$$P_{\max}^* = \frac{4Ea_{\max}^3}{3(1-\nu^2)D} \quad (3)$$

The apparent load,  $P_{\max}^*$ , required to maintain the same contact radius,  $a_{\max}$ , without adhesion is given by Hertzian analysis [1]

Unlike the non-adhesive case (Fig. 2), the adhesive contact produces a tensile, square-root singular stress field [24] which is asymptotically equal to the mode I crack field at the contact perimeter (Fig. 1(d)). With  $\rho$  and  $\theta$  as the local polar coordinates at the contact perimeter,  $\phi$  the angular circumferential coordinate, and  $T_{rr}$  and  $T_{\phi\phi}$  as the non-singular stress terms in the radial and circumferential directions, the asymptotic stress field is given by [24]

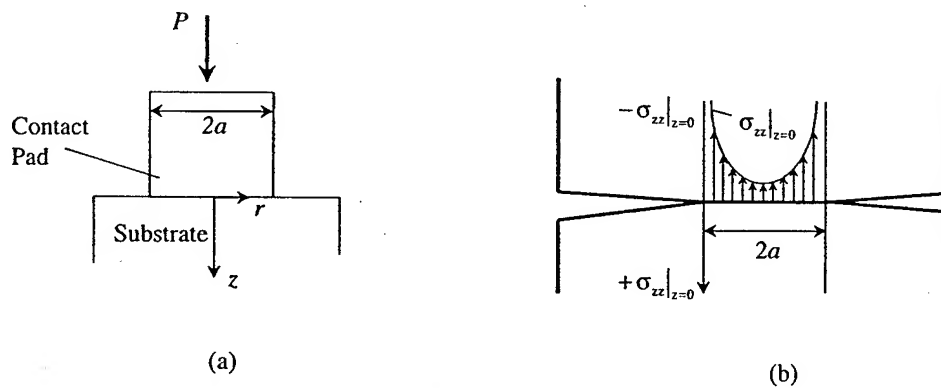


Fig. 2. Schematics illustrating: (a) sharp-edged, non-adhesive contact and (b) the corresponding crack analogue exhibiting compressive stress singularity.

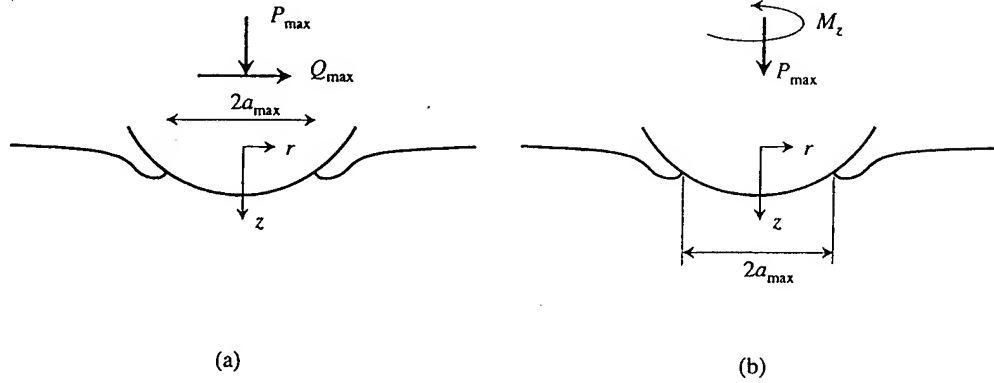


Fig. 3. Schematics illustrating: (a) tangential loading and (b) torsional loading of adhesive, spherical contacts.

$$\sigma_{rr}^{\text{nor}} = \frac{K_I}{\sqrt{2\pi\rho}} \cos \frac{\theta}{2} \left( 1 - \sin \frac{\theta}{2} \sin \frac{3\theta}{2} \right) + T_{rr} \quad (4a)$$

$$\sigma_{zz}^{\text{nor}} = \frac{K_I}{\sqrt{2\pi\rho}} \cos \frac{\theta}{2} \left( 1 + \sin \frac{\theta}{2} \sin \frac{3\theta}{2} \right) \quad (4b)$$

$$\sigma_{rz}^{\text{nor}} = \frac{K_I}{\sqrt{2\pi\rho}} \cos \frac{\theta}{2} \left( \sin \frac{\theta}{2} \cos \frac{3\theta}{2} \right) \quad (4c)$$

$$\sigma_{\phi\phi}^{\text{nor}} = \nu(\sigma_{rr}^{\text{nor}} - T_{rr} + \sigma_{zz}^{\text{nor}}) + T_{\phi\phi}. \quad (4d)$$

The corresponding tensile stress intensity factor,  $K_I$ , is given as [25, 26]

$$K_I = \frac{P^* - P_{\max}}{2a_{\max} \sqrt{\pi a_{\max}}}. \quad (5)$$

The size of the  $K$ -dominance around the contact perimeter,  $\rho_k$ , is identified by the nodal positions in the stress field [Fig. 1(d)] and is given by

†(a) For contacting surfaces of different diameters,  $D$  can be replaced by  $D_1 D_2 / (D_1 + D_2)$ , where the indices 1 and 2 refer to the contacting bodies 1 and 2. (b) For contact involving elastically dissimilar materials,  $(1-\nu^2)/E$  can be replaced by  $\{[(1-\nu_1^2)/E_1 + (1-\nu_2^2)/E_2]/2\}$  and the energy release rate relations are preserved. However, the form of the stress intensity factor remains invariant only if the stress fields are square-root singular for which the second Dundurs' parameter,  $\beta = 0$  [27], i.e.

$$\frac{E_2(1+\nu_1)(1-2\nu_1) - E_1(1+\nu_2)(1-2\nu_2)}{E_2(1-\nu_1^2) + E_1(1-\nu_2^2)} = 0.$$

‡In general, a mixed mode II/III field is obtained along the contact perimeter with the corresponding stress intensity factors being:

$$K_{II} = \frac{Q_{\max} \cos \phi}{2a_{\max} \sqrt{\pi a_{\max}}}, \quad K_{III} = \frac{Q_{\max} \sin \phi}{2a_{\max} \sqrt{\pi a_{\max}}}$$

where  $\phi$  is the angle between the radius vector at the peripheral point and the direction of  $Q_{\max}$  [29].

$$\rho_k = \frac{D}{4} \sqrt{\frac{2(1-\nu^2)\pi w}{Ea_{\max}}}. \quad (6)$$

The associated energy release rate can be identified as  $(1-\nu^2)K_I^2/E$ . The maximum non-singular stresses in the radial and circumferential directions due to contact at maximum load are given by

$$\max T_{rr} = -\max T_{\phi\phi} = \max T = \frac{(1-2\nu)P_{\max}^*}{2\pi a_{\max}^2}. \quad (7)$$

## 2.2. Combined normal and tangential loading

For elastic, monotonic, tangential loading from zero to  $Q_{\max}$  ( $>0$ ), under a constant normal load,  $P_{\max}$ , an adhesion-induced, square-root singular stress field [6] is obtained at the contact perimeter (Fig. 3(a)). The mode II field, at the leading and the trailing edges‡, can be expressed as [15]

$$\sigma_{rr}^{\text{tan}} = \frac{K_{II}}{\sqrt{2\pi\rho}} \left( -\sin \frac{\theta}{2} \right) \left( 2 + \cos \frac{\theta}{2} \cos \frac{3\theta}{2} \right) \quad (8a)$$

$$\sigma_{zz}^{\text{tan}} = \frac{K_{II}}{\sqrt{2\pi\rho}} \sin \frac{\theta}{2} \cos \frac{\theta}{2} \sin \frac{3\theta}{2} \quad (8b)$$

$$\sigma_{rz}^{\text{tan}} = \frac{K_{II}}{\sqrt{2\pi\rho}} \cos \frac{\theta}{2} \left( 1 - \sin \frac{\theta}{2} \sin \frac{3\theta}{2} \right) \quad (8c)$$

$$\sigma_{\theta\theta}^{\text{tan}} = \nu(\sigma_{rr}^{\text{tan}} + \sigma_{zz}^{\text{tan}}) \quad (8d)$$

where the mode II stress intensity factor,  $K_{II}$ , is given as

$$K_{II} = \frac{Q_{\max}}{2a_{\max} \sqrt{\pi a_{\max}}}. \quad (9)$$

The maximum  $T$ -stresses due to contact are obtained at the maximum tangential load and are given as

$$\max T_{rr} = \frac{P_{\max}^*}{2\pi a_{\max}^2} \left[ (1-2\nu) + \frac{3\mu\pi(4+\nu)}{8} \right] \quad (10a)$$

$$\max T_{\phi\phi} = -\frac{P_{\max}^*}{2\pi a_{\max}^2} \left[ (1-2\nu) - \frac{9\mu\pi\nu}{8} \right]. \quad (10b)$$

### 2.3. Combined normal and torsional loading

For elastic, monotonic, torsional loading from zero to  $M_z$  ( $>0$ ) (Fig. 3(b)), under a constant normal load,  $P_{\max}$ , the adhesive asymptotic stress field due to torsional loading†, is square-root singular at the contact perimeter [28]:

$$\sigma_{rz}^{\text{tor}} = \frac{K_{\text{III}}}{\sqrt{2\pi\rho}} \sin \frac{\theta}{2}, \quad \sigma_{\theta z}^{\text{tor}} = \frac{K_{\text{III}}}{\sqrt{2\pi\rho}} \cos \frac{\theta}{2} \quad (11)$$

with the mode III stress intensity factor,  $K_{\text{III}}$ , given as

$$K_{\text{III}} = \sigma_{rz}^{\text{tor}} \sqrt{2\pi(a_{\max} - r)} = \frac{3M_z}{4a_{\max}^2 \sqrt{\pi a_{\max}}}. \quad (12)$$

The maximum energy release rate,  $\max G$ , is related to the mode I and III stress intensity factors as

$$\max G = \frac{K_{\text{III}}^2(1+\nu)}{E} + \frac{K_I^2(1-\nu^2)}{E} \quad (13)$$

where  $K_{\text{III}}$  is given by equation (24) and  $K_I$  is given by equation (26). The mode III fields do not produce any  $T$ -stresses.

## 3. MECHANICS OF CYCLIC ADHESIVE CONTACT

### 3.1. Model assumptions

In modeling adhesive contacts under cyclic loading conditions, we invoke the following assumptions.

1. Materials are homogeneous, isotropic and linear elastic.
2. In order to keep the analysis simple and to avoid complications from elastic mismatch of the contacting bodies and from the strong nonlinear effects of contact geometry, only the sphere or cylinder on flat surface of similar materials is analyzed. To avoid microstructural scale effects, the contact area is assumed to cover at least several grains of the material.
3. For ideal contact conditions characterized by clean, smooth surfaces under inert atmospheres, a direct relationship between adhesion and friction can be obtained [30–32]. However, under real, ambient, atmospheric conditions, where the

contacting surfaces are not perfectly clean or smooth, a direct correlation between friction and adhesion has not been established. Hence, in order to maintain generality, an a priori relationship between friction and adhesion is not assumed [33]. Therefore, work of adhesion and coefficient of friction are introduced in the analysis in an independent way. However, for particular cases where an explicit relationship between friction and adhesion can be identified, the analysis can be modified as indicated in the Appendix.

4. Strong adhesion is defined as that for which the work needed to debond the two contacting surfaces,  $G_d$ , is high enough to resist local debonding at the contact perimeter. The work of adhesion for receding (separating or opening) contact,  $G_d$ , is greater than the work of adhesion for advancing (approaching or closing) contact,  $w$ , i.e.  $G_d > w$ . Such adhesion hysteresis is due to mechanical and/or chemical effects, e.g. microplasticity of asperities [34, 35].
5. The effect of bulk and/or residual stresses in the substrate, on fatigue crack initiation, can be incorporated by superposition with the contact-induced  $T$ -stresses.
6. Finally, when certain fatigue threshold conditions are met (as described below), contact fatigue cracks are expected to initiate both in the contact pad and the flat substrate. As cracks in the contact pad are expected to be mirror images of those in the substrate across the plane of contact (i.e. they initiate at the same contact location), we discuss the stress state of the substrate only.

### 3.2. Three-dimensional spherical contacts

**3.2.1. Normal contact fatigue.** Consider a spherical pad in oscillatory normal contact with a flat substrate (Fig. 1), with the applied load,  $P$ , in the range  $P_{\max} \geq P_{\min} \geq 0$ . As the load decreases from its maximum,  $P_{\max}$ , to its minimum value,  $P_{\min}$ , the strain energy release rate,  $G$ , at the contact perimeter increases monotonically.

When  $\max G < G_d$  or  $(P_{\max} - P_{\min}) \leq 3\pi G_d D/4$ , strong adhesion is obtained with the contact radius remaining unchanged at  $a_{\max}$ . The mode I cyclic stress intensity factor at the contact perimeter is given as

$$\Delta K_I = K_{\max} - K_{\min} = \frac{P_{\max} - P_{\min}}{2a_{\max} \sqrt{\pi a_{\max}}} \quad (14)$$

with the corresponding load ratio,  $R = (\min K_I / \max K_I) = (P_{\min} / P_{\max})$ .

When  $\max G > G_d$  or  $(P_{\max} - P_{\min}) \geq 3\pi G_d D/4$ , weak adhesion is obtained as the work of adhesion is insufficient to sustain the singularity at the maximum contact radius,  $a_{\max}$ †. Consequently, the con-

†The normal load creates a mode I stress field, as described by equations (4).

‡It is implicitly assumed in this work that debonding always occurs in a brittle and axisymmetric manner along the contact perimeter. Hence, the maximum value of  $G_d$  cannot be higher than the critical energy release rate for fracture of the bulk contacting materials under monotonic loading.



tact debonds at the contact perimeter and the contact radius decreases. The oscillatory mode I stress intensity factor at the contact edge,  $a_{\max}$ , is given as

$$\Delta K_I = \frac{3\pi G_d D}{8a_{\max} \sqrt{\pi a_{\max}}} \quad (15)$$

with the corresponding load ratio,  $R$ , being

$$R = \frac{P_{\max} - (3\pi G_d D/4)}{P_{\max}} \quad (16)$$

As the contact conditions effectively imply a virtual circumferential crack with a circular crack front coincident with the contact perimeter [15], the initiation of a fatigue crack at the contact edge is conceptually equivalent to the onset of propagation of this pre-existing virtual crack. Hence, a fatigue crack is expected to initiate at the contact edge,  $a_{\max}$ , for strong or weak adhesion, if  $\Delta K_I \geq \Delta K_{th}$ , where  $\Delta K_{th}$  is the mode I long crack initiation fatigue threshold stress intensity range for the corresponding values of  $R$  and max  $T$ .

**3.2.2. Tangential fretting fatigue.** Consider a sphere in contact with a planar substrate under an applied normal load  $P_{\max}$  (Fig. 4). The maximum tangential load,  $\bar{Q}_{\max}$ , that can sustain adhesion at maximum contact radius is

$$\bar{Q}_{\max} = 2 \times \sqrt{\frac{(2-2\nu)}{(2-\nu)} \pi a_{\max}^3 \left[ G_d^{II} \frac{E}{(1-\nu^2)} - \left( \frac{3G_d^I \pi D}{4a_{\max}^{3/2}} \right)^2 \right]} \quad (17)$$

where  $G_d^I$  and  $G_d^{II}$  are the critical debonding energies under pure normal and tangential loads, respectively.

If the amplitude of the applied tangential load  $Q_{\max} \leq \bar{Q}_{\max}$  or equivalently the maximum energy release rate at the contact edge upon load reversal,  $\max G < G_d$ , then strong adhesion (stick) is obtained†.

The stress intensity factor that corresponds to the mixed mode I (steady) crack field is given by equation (5) and that which corresponds to mode II (oscillatory) crack fields at the leading and the trailing contact edges is given by

$$\Delta K_{II} = \frac{Q_{\max}}{a_{\max} \sqrt{\pi a_{\max}}} \quad (18)$$

with the local effective load ratio,  $R = -1$ .

If the amplitude of the applied tangential load  $Q_{\max} \geq \bar{Q}_{\max}$  or equivalently the maximum energy release rate at the contact edge upon load reversal,  $\max G > G_d$ , then weak adhesion (stick-slip) is

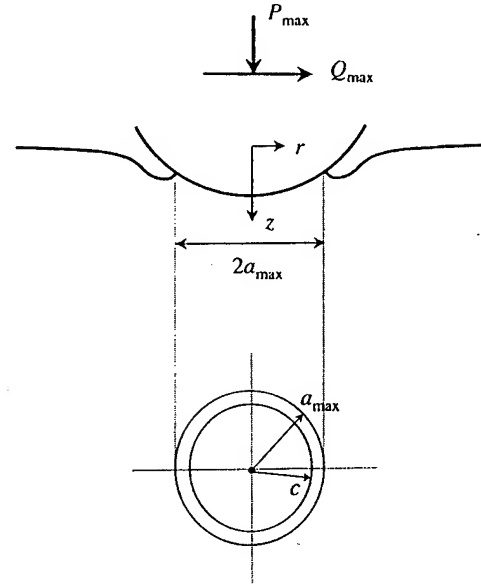


Fig. 4. Schematic illustrating tangential loading of the spherical contact.

obtained resulting in a partial slip annulus,  $c \leq r \leq a_{\max}$  (Fig. 4). From global equilibrium [28]

$$Q_{\max} = \mu P_{\max} \left[ 1 - \left( \frac{c}{a_{\max}} \right)^3 \right]; \quad (19)$$

$$\bar{Q}_{\max} < Q_{\max} \leq \mu P_{\max}.$$

The tangential load that is balanced in the stick zone of radius,  $c$ , is

$$Q_{\max}^{\text{in}} = Q_{\max} - \mu \frac{P_{\max}}{a_{\max}^3} (a_{\max}^2 - c^2)^{3/2}. \quad (20)$$

In this case,  $K_I = 0$ , as the crack analogue predicts a closed crack-tip.

The mode II stress intensity factor at the leading and trailing edge of the stick-slip interface is given by

$$\Delta K_{II} = 2 \times \min \left( \frac{Q_{\max}^{\text{in}}}{2c\sqrt{\pi c}}, \sqrt{\frac{G_d^{II} E}{1-\nu^2}} \right) \quad (21)$$

with the local load ratio  $R = -1$ .

A fatigue crack is expected to initiate, at the contact perimeter or the stick-slip boundary, for strong or weak adhesion, respectively, if the corresponding  $\Delta K_{II} \geq \Delta K_{th}$  where  $\Delta K_{th}$  is the threshold stress intensity range that corresponds to  $R = -1$ , and under mixed constant mode I and oscillatory mode II fatigue. This situation holds both for strong adhesion and under pure oscillatory mode II fatigue for weak adhesion.

Upon initiation, the continued propagation of the crack-tip depends on the local mode I and mode II

†The critical energy release rate,  $G_d$ , may depend on the mode mixity,  $K_I/K_{II}$ , and this could introduce a contact size effect for elastically dissimilar surfaces.

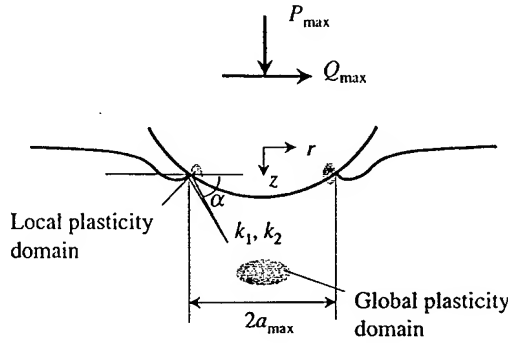


Fig. 5. Schematic illustrating crack initiation from the edge of the contact perimeter with the local crack-tip mode I and II stress intensity factors being  $k_1$ ,  $k_2$  and domains of local and global plasticity.

stress intensity factors,  $k_1$  and  $k_2$ , respectively (Fig. 5). Following Cotterell and Rice [36], it is postulated that the crack advances in a direction along which the local mode II stress intensity factor,  $k_2$ , vanishes [or equivalently, the strain-energy release rate is maximized ( $\partial/\partial\theta(k_1^2 + k_2^2) = 0$ , ( $\partial^2/\partial\theta^2(k_1^2 + k_2^2) < 0$ )). The initial angle of crack propagation,  $\alpha$ , is then readily obtained from

$$k_2 = \frac{1}{4} \left( \sin \frac{\alpha}{2} + \sin \frac{3\alpha}{2} \right) K_I + \frac{1}{4} \left( \cos \frac{\alpha}{2} + 3 \cos \frac{3\alpha}{2} \right) K_{II} = 0 \quad (22)$$

at maximum load.

**3.2.3. Torsional fretting fatigue.** Consider a sphere in contact with a planar substrate under an applied normal load  $P_{\max}$  (Fig. 3). The maximum torsional load,  $\bar{M}_z$ , that can sustain adhesion at maximum contact radius is

$$\bar{M}_z = \frac{4a_{\max}}{3} \sqrt{\pi a_{\max}^3 \left[ G_d^{III} \frac{E}{(1+\nu)} - \left( \frac{3G_d^I \pi D}{4a_{\max}^{3/2}} \right)^2 \right]} \quad (23)$$

where  $G_d^I$  and  $G_d^{III}$  are the critical debonding energies under pure normal and torsional loads, respectively.

If the amplitude of the applied torsional load  $M_z \leq \bar{M}_z$ , or equivalently, the maximum energy release rate at the contact edge upon load reversal,  $\max G < G_d$ , then strong adhesion (stick) is obtained†.

The stress intensity factor that corresponds to the mixed mode I (steady) [equation (5)] and III (oscillatory) crack fields at the leading and the trailing

contact edges is given by

$$\Delta K_{III} = 2\sigma_{rz}^{\text{lor}} \sqrt{2\pi(a_{\max} - r)} = \frac{3M_z}{2a_{\max}^2 \sqrt{\pi a_{\max}}} \quad (24)$$

with the local effective load ratio,  $R = -1$ .

If the amplitude of the applied tangential load,  $M_z \geq \bar{M}_z$ , or equivalently, the maximum energy release rate at the contact edge upon load reversal,  $\max G > G_d$ , then weak adhesion (stick-slip) is obtained resulting in a partial slip annulus,  $c \leq r \leq a_{\max}$ . A power series approximation for the relation between  $c/a_{\max}$  and  $M_z/P_{\max}$ , that is accurate within  $-3.4\%$  error of the exact solution is given by [37]

$$\frac{M_z}{\mu P_{\max} a_{\max}} \approx k^2 \left( 1 - \frac{3}{8} k^2 - \frac{1}{64} k^4 \right); \quad (25)$$

$$k = \sqrt{1 - (c/a_{\max})^2}.$$

The torsional load that is balanced in the stick zone is

$$M_z^{\text{in}} = M_z - \frac{3\mu P_{\max} a_{\max}}{8} \left( \frac{\pi}{2} - \arcsin \frac{c}{a_{\max}} - \frac{c}{a_{\max}} \left( 2 \frac{c^2}{a_{\max}^2} - 1 \right) \sqrt{1 - \frac{c^2}{a_{\max}^2}} \right) \quad (26)$$

and the mode III cyclic stress intensity factor is given by

$$\Delta K_{III} = 2 \times \min \left( \frac{3M_z^{\text{in}}}{4c^2 \sqrt{\pi c}}, \sqrt{\frac{G_d E}{1+\nu}} \right). \quad (27)$$

In this case,  $K_I = 0$ , as the crack analogue predicts a closed crack-tip.

A fatigue crack is expected to initiate, at the contact perimeter or the stick-slip boundary, for strong or weak adhesion, respectively, if the corresponding  $\Delta K_{III} \geq \Delta K_{\text{th}}$  where  $\Delta K_{\text{th}}$  is the threshold stress intensity range that corresponds to  $R = -1$  and  $T = 0$ . This is valid both under mixed constant mode I and oscillatory mode III fatigue for strong adhesion, and under pure oscillatory mode III fatigue for weak adhesion.

### 3.3. Two-dimensional cylindrical contacts

**3.3.1. Normal contact fatigue.** For a cylinder of diameter,  $D$ , in adhesive contact with a flat substrate (Fig. 6) under a normal load,  $P_{\max}$ , the contact width,  $a_{\max}$ , is given as [5]

$$P_{\max} = \frac{\pi E}{4(1-\nu^2)} \left\{ \frac{a_{\max}^2}{D} - 2 \left[ \frac{4a_{\max} w(1-\nu^2)}{\pi E} \right] \right\}. \quad (28)$$

Under an oscillatory normal load in the range  $P_{\max} \geq P_{\min} \geq 0$ , conditions for strong or weak adhesion are obtained when

†The critical energy release rate,  $G_d$ , may depend on the mode mixity,  $K_I/K_{III}$ , and this could introduce a contact size effect for elastically dissimilar surfaces.

Table 1. Adhesion-induced stress intensity factors for the case of a cylinder in oscillatory contact with a planar substrate

Loading Adhesion Mode	Normal		In-plane		Out-of-plane
	Strong-I	Weak-I	Strong-II	Weak-II	Strong-III
$\Delta K$	$\frac{P_{\max} - P_{\min}}{\sqrt{\pi a_{\max}}}$	$\frac{3}{\sqrt{2\pi a_{\max}}} \left( \frac{G_d^2 \pi E D}{8(1-\nu^2)} \right)^{1/3}$	$\frac{2Q_{\max}}{\sqrt{\pi a_{\max}}}$	$2 \min \left( \frac{Q_{\max}^{\text{in}}}{\sqrt{\pi c}}, \sqrt{\frac{G_d E}{1-\nu^2}} \right)$	$\frac{S_{\max} - S_{\min}}{\sqrt{\pi a_{\max}}}$
$R$	$\frac{P_{\max}}{P_{\min}}$	$1 - \frac{3}{2P_{\max}} \left( \frac{G_d^2 \pi E D}{8(1-\nu^2)} \right)^{1/3}$	-1	-1	-1
$T$ -stress	$\max T_{xx}, \max T_{yy} = 0$		$\max T_{xx} = \nu \max T_{yy} = (2\mu P_{\max}^* / \pi a_{\max})$		$\max T_{xx}, \max T_{yy} = 0$

$$(P_{\max} - P_{\min}) \leq \text{ or } > \frac{3}{2} G_d^{2/3} \left[ \frac{\pi E D}{8(1-\nu^2)} \right]^{1/3} \quad (29)$$

respectively. The corresponding stress intensity factors are summarized in Table 1.

**3.3.2. In-plane fretting fatigue.** When a cylindrical pad in contact with a much larger, flat substrate (Fig. 6) is subjected to an oscillatory tangential line load  $Q_{\max}$  ( $0 \leq Q_{\max} \leq \mu P_{\max}$ ), under a constant normal load  $P_{\max}$ , the elastic energy of the cylinder becomes unbounded and the displacements are indeterminate. The solution to this problem depends critically on the overall dimensions of the fretting

specimen and the applied far-field boundary conditions. Hence the precise definition for strong and weak adhesion cannot be made by the contact analysis alone.

For weak adhesion, however, the stick-zone width,  $c$ , is given from global equilibrium as

$$Q_{\max} = \mu P_{\max} \left[ 1 - \left( \frac{c}{a_{\max}} \right)^2 \right]; \quad (30)$$

$$0 < Q_{\max} \leq \mu P_{\max}.$$

Assuming adhesion is re-established at the stick zone, the tangential line load that is balanced in the stick zone is given as

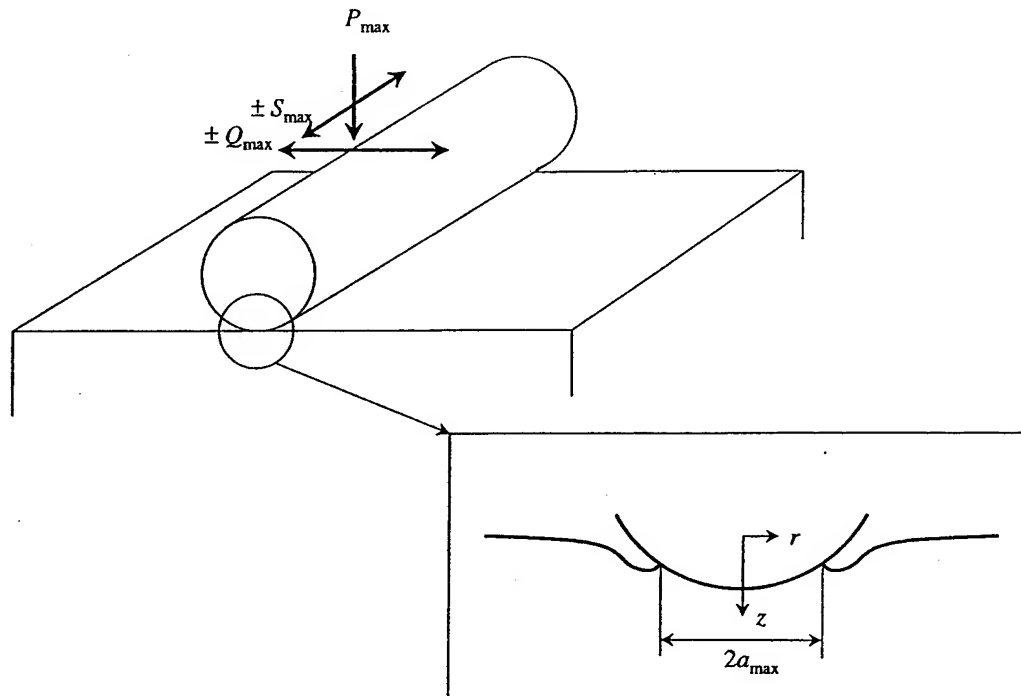


Fig. 6. Schematic illustrating loading configurations for the two-dimensional cylindrical contact geometry.

$$Q_{\max}^{\text{in}} = Q_{\max} - \frac{\mu P_{\max}}{\pi} \times \left[ \frac{\pi}{2} + \arctan \frac{c\sqrt{a_{\max}^2 - c^2}}{c^2 - a_{\max}^2} - \frac{c}{a_{\max}} \left( 1 - \frac{c^2}{a_{\max}^2} \right) \right] \quad (31)$$

The corresponding stress intensity ranges for strong and weak adhesion cases are summarized in Table 1. Crack initiation is expected at the contact edge or the stick-slip boundary for strong or weak adhesion cases, respectively, when the corresponding stress intensity ranges exceed the fatigue thresholds for the corresponding  $R$ -ratios and  $T$ -stresses.

**3.3.3. Out-of-plane fretting fatigue.** The case of a cylinder of diameter,  $D$ , under a constant normal load,  $P_{\max}$ , subjected to an oscillatory line load with amplitude,  $S_{\max}$ , and in adhesive contact with a flat substrate (Fig. 6), can also be analyzed along similar lines and a mode III cyclic stress intensity factor range can be identified at the contact edge for strong adhesion as summarized in Table 1.

#### 4. RANGE OF APPLICABILITY OF THE ADHESION MODEL

The preceding analysis is strictly valid under linear elastic conditions, the limits of which are defined by several criteria that predict the onset of local or global plasticity (Fig. 5). Noting that adhesion increases the effective stress under the contact area, global indentation induced plasticity can be avoided [38], provided that

$$\frac{a_{\max} E}{D\sigma_y(1-\nu^2)} < 3.675, \quad \frac{G_d E^2}{D\sigma_y^3(1-\nu^2)^2} < 7.031 \quad (32)$$

where  $\sigma_y$  is the yield strength of the softer of the two contacting bodies. Also, macroscopic plasticity is suppressed for  $\mu > 0.25$ , if [18, 24]

$$\sigma_y^3 > \frac{3P_{\max}}{2\pi a_{\max}^2} \left[ \frac{(1-2\nu)^2}{3} + \frac{(1-2\nu)(2-\nu)\mu\pi}{4} + \frac{(16-4\nu+7\nu^2)\mu^2\pi^2}{64} \right]^{1/2} \quad (33)$$

An alternative, self-consistent, Dugdale-Barenblatt model [39] for adhesive normal contact, that assumes the maximum adhesive force intensity,  $\sigma_0$ , to be constant until debonding is reached, whereupon it falls to zero, predicts the elastic (local, small-scale plasticity) conditions for adhesion to be preserved for

$$\sigma_0^3 \frac{D(1-\nu^2)^2}{\pi G_d E^2} > \frac{250}{9} \quad (34)$$

The maximum adhesive stress,  $\sigma_0$ , could be related to the uniaxial yield strength of the cohesively

weaker of the two contacting bodies,  $\sigma_0 \approx 3\sigma_y$ , when small-scale plasticity conditions are valid at the contact perimeter [40]. Alternately,  $\sigma_0$  could be an effective stress that combines the maximum normal and the frictional shear stress [40].

Metals show appreciable adhesion at elevated temperatures and prolonged contact loading times. Under high-frequency fretting conditions, friction produces heat that raises the surface temperature and could promote creep. Therefore, for the preceding analysis to be valid, the maximum surface temperature due to tangential load oscillations must be less than a third of the homologous temperature,  $T_H$

$$\frac{9(3\pi-4)(2-\nu)(1+\nu)}{64\pi^2 EK} \left[ \frac{\mu P_{\max}}{a_{\max}} \right]^2 \Omega < \frac{T_H}{3} \quad (35)$$

where  $\Omega$  is the fretting frequency and  $K$  is the thermal conductivity coefficient [41].

Another limitation of the present analysis comes from the surface morphology. Surface roughness diminishes the influence of adhesion if [42]

$$\left[ \frac{3(1-\nu^2)}{2E} \right]^2 \geq 100 \frac{G_d^2 \rho_0}{\Sigma^3} \quad (36)$$

where  $\Sigma$  is the standard deviation of the micro-asperity heights and  $\rho_0$  is the average radius of curvature of the asperity tips.

#### 5. EXPERIMENTAL VALIDATION OF THE ANALYSES

In comparing various experiments to model predictions, only reasonable estimates are chosen from the empirical relationship [equation (A1)] that relates the friction coefficient to the debond energy, since experimentally measured values for the debond energy are not available.

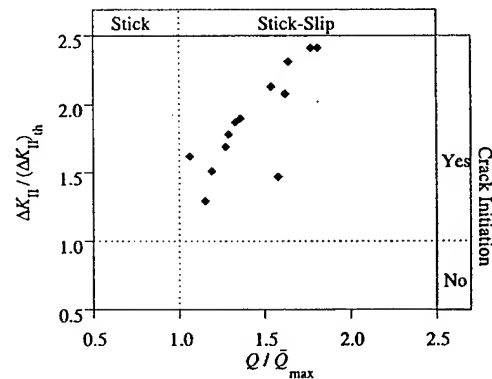


Fig. 7. Room temperature fretting fatigue experiments on Al-7075 T6 (with in 2 in. diameter sphere on flat geometry) (see Ref. [22] and current work), evaluated using the present adhesion model where in the mode II threshold stress intensity factor for an  $R$ -ratio of  $-1$  was estimated to be  $\approx 1 \text{ MPa m}^{1/2}$  and the work of adhesion for advancing and receding contacts ( $w$ ,  $G_d$ ) being  $\approx 1$  and  $\approx 19 \text{ N/m}$ , respectively.

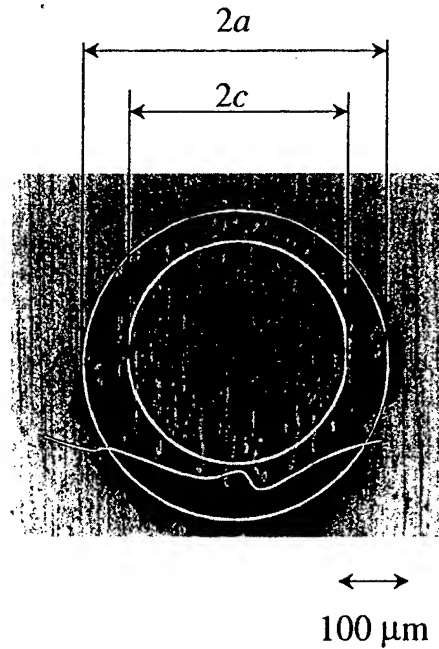


Fig. 8. Fretting scar produced on the flat Al-7075 T6 substrate [22] when fretted with a spherical pad of the same material and diameter 2 in., for  $P_{\max}=20$  N,  $Q_{\max}=15$  N and an axial stress of 59 NPa with an  $R$ -ratio = -1 indicating that cracks initiate near the stick-slip boundary.

### 5.1. Three-dimensional spherical contacts

Room temperature tangential fretting fatigue experiments, using a set-up described in detail in Ref. [43], were performed by Wittkowsky *et al.* [22] on 7075 T6 aluminum alloy, with mechanical properties,  $E=71.5$  GPa,  $\nu=0.33$ ,  $\sigma_y=483$  MPa, and threshold  $\Delta K_{II}=1$  MPa  $m^{1/2}$ , and the experimentally determined friction coefficient,  $\mu=1.2$ . Using reasonable values for the work of adhesion for advancing and receding contacts,  $w=1$  N/m and  $G_d=19$  N/m [from equation (A1)], the adhesion

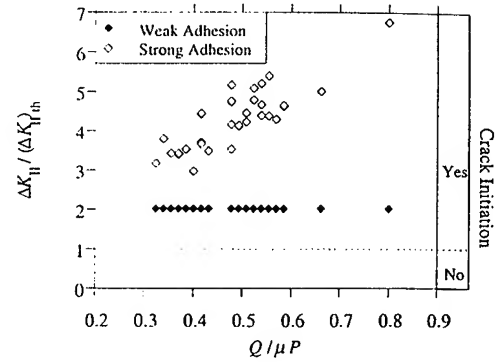


Fig. 9. Room temperature fretting fatigue experiments on Al-2024 T351 (with a 0.5 in. diameter cylinder on flat geometry [50]) evaluated using the present adhesion model where in the mode II threshold stress intensity factor for an  $R$ -ratio of -1 was estimated to be  $\approx 1$  MPa  $m^{1/2}$  and the work of adhesion for advancing and receding contacts ( $w$ ,  $G_d$ ) being  $\approx 1$  and  $\approx 12$  N/m, respectively.

model predicts weak adhesion, in agreement with experiments where in all cases, stick-slip behavior was observed. The conditions (Fig. 7) and location of crack initiation (stick-slip boundary, Fig. 8) are also predicted well by the model. While the model predicts an initial crack angle of  $70.5^\circ$ , crack initiation angles ranging between  $61^\circ$  and  $80^\circ$  were observed experimentally. Some deviations from model predictions are expected as the material grain size of  $60\mu m$  was comparable to the stick-slip zone size in many cases, while the model is strictly valid under conditions of complete material homogeneity and isotropy.

Also, as summarized in Table 2, fretting fatigue experiments on a variety of other material systems can be interpreted within the context of adhesion. Conditions of strong and weak adhesion can be identified and, in a number of cases, the observed location of crack initiation agrees with the model predictions, as shown in Table 2.

Table 2. Experimental observations on contact fatigue crack initiation\*

Material	$D_{\text{eff}}$ (mm)	$P_{\max}$ (N)	$P_{\min}$ (N)	$Q$ (N)	$M$ (Nm)	$\mu$	$\bar{P}_{\max}$ (N), $\bar{Q}_{\max}$ (N), $\bar{M}_z$ (Nm)	Adhesion	$\Delta K_{\text{model}}$ (MPa $m^{1/2}$ )	$\Delta K_{\text{th}}$ (MPa $m^{1/2}$ )	Cracking predicted (observed)	Location		Ref.
												Predicted	Observed	
En31 steel	10.16	1537	170	0	0	0.8	0.9	Weak	0.02	2-5	No (Yes)	-	Surface	[44]
Hard steel	63.5	127,400	4900	0	0	0.8	6.0	Weak	0.004	2-5	No (Yes)	-	Edge	[45]
SAE 52100 steel	12.7	88	88	0	0.009	0.8	0.001	Weak	2.5	2-5	Yes (Yes)	Stick-slip	Surface	[46]
Al-7075	600	1000	1000	930	0	1.2	296	Weak	2.4	1	Yes (Yes)	Stick-slip	Edge, stick-slip	[20, 21]
Al-7075 T7351	1000	500	500	525	0	1.2	252	Weak	2.4	1	Yes (Yes)	Stick-slip	Edge, stick-slip	[47]
Ti-6Al-4V	300	700	700	525	0	0.8	152	Weak	2.1	2	Yes (Yes)	Stick-slip	Edge	[47]
Ti-6Al-4V	8	100	100	70	0	0.8	9	Weak	2.1	2	Yes (Yes)	Stick-slip	Edge	[13]
Nb	6.25	10.9	10.9	10	0	1.0	2.8	Weak	2.3	-	- (Yes)	-	Stick-slip	[49]

\* In all cases, sphere on flat geometry was used, except for Nb where a cylinder on cylinder point contact was established.  $D_{\text{eff}}$ : the effective diameter of the contacting sphere;  $P_{\max}$ : maximum normal load;  $P_{\min}$ : minimum normal load;  $Q$ : tangential load amplitude;  $M$ : torsional load amplitude;  $\bar{P}_{\max}$ ,  $\bar{Q}_{\max}$ ,  $\bar{M}_z$ : critical normal, tangential or torsional loads above which weak adhesion is obtained;  $\Delta K_{\text{model}}$ : stress intensity factor range predicted by the adhesion model;  $\Delta K_{\text{th}}$ : material fatigue threshold stress intensity factor range for load ratio  $R=-1$  (estimated from Ref. [48]); Surface: contact surface; Edge: edge of the contact; Stick-slip: stick-slip boundary.

### 5.2. Two-dimensional cylindrical contacts

For the tangential fretting fatigue studies on 2024-T351 aluminum reported in Ref. [50], with material properties,  $E=74.1$  GPa,  $\nu=0.33$ ,  $\mu=0.65$ , and using threshold  $\Delta K_{II}=1$  MPa m<sup>1/2</sup>,  $w=1$  N/m and  $G_d=12$  N/m, the cyclic mode II stress intensity factors predicted by the model are greater than the fatigue threshold for  $R=-1$ , in agreement with the observation of crack initiation in all the reported experiments (Fig. 9). While dominant fatigue cracks were located at the contact edge, cracks were also observed at the stick-slip boundary. This indicates a possible transition from an initial strong adhesion stage to a final weak adhesion stage.

In fretting fatigue studies on 0.34% carbon steel [51], adhesion was identified as a precursor to the contact edge cracks that initiated under very low tangential load amplitude. This indicates strong adhesion in the context of the present analysis.

When a cylinder on cylinder line contact system was subjected to oscillatory oblique force loading, two type of cracks, one at the contact edge and the second at the stick-slip boundary were observed [52]. The adhesion model can explain this phenomenology by recognizing that the equivalent normal and tangential load oscillations can initiate cracks at the contact edge and the stick-slip boundary, respectively.

In addition, the adhesion model can qualitatively predict the observed cracking pattern reported by Dawson [45] for normal load contact fatigue tests with cylindrical pads while conventional contact mechanics analysis cannot do so as it predicts a fully compressive stress field. However, a rigorous quantitative comparison is not attempted here as substantial plasticity was observed in these experiments.

## 6. CONCLUSIONS

The present work examined the role of adhesion in contact mechanics with a particular emphasis on fatigue crack initiation for a variety of contact geometries (sphere or cylinder on a flat substrate) and loading conditions (constant or oscillatory normal, tangential or torsional).

It was demonstrated that:

- The adhesion-induced, square-root singular stress fields could be analyzed within the framework of a "crack analogue" and hence the pre-existing, virtual long crack introduced by the contact circumvents "length scale" problems inherent in the modeling of crack initiation based on conventional fracture mechanics;
- Under adhesive normal, tangential or torsional contact loading conditions, mode I, II or III stress intensity factors could be identified at the contact perimeter or at the stick-slip boundary for strong or weak adhesion, respectively;

- By comparing to the material fatigue thresholds, contact conditions required for crack initiation could be predicted. Additionally, the location and initial crack propagation directions could also be predicted, in reasonable agreement with experimental results.

Under conditions of small-scale yielding, the effects of static and/or oscillatory bulk stresses acting parallel to the contact surface (such as the far-field applied or residual stresses arising from surface modification treatments due to shot-peening or laser shock-peening) can be analyzed by recognizing that these are analogous to the  $T$ -stresses present in a linear elastic fatigue-fracture formulation. The propensity for contact fatigue crack initiation could be suppressed by selecting material or environmental combinations that effectively reduce adhesion in a contact system.

*Acknowledgements*—This work was supported by the Multi-University Research Initiative on "High Cycle Fatigue", which is funded at MIT by the Air Force Office of Scientific Research, Grant No. F49620-96-1-0278, through a subcontract from the University of California at Berkeley.

## REFERENCES

1. Johnson, K. L., *Contact Mechanics*. Cambridge University Press, Cambridge, 1985.
2. Johnson, K. L., *Proc. R. Soc. Lond.*, 1954, A230, 531.
3. Johnson, K. L., Kendall, K. and Roberts, A. D., *Proc. R. Soc. Lond.*, 1971, A324, 301.
4. Pollock, H. M., Maugis, D. and Barquins, M., *App. Phys. Lett.*, 1978, 33, 798.
5. Kalker, J. J., *Wear*, 1987, 119, 63.
6. Savkoor, A. R. and Briggs, G. A. D., *Proc. R. Soc. Lond.*, 1977, A356, 103.
7. Bethune, B. and Waterhouse, R. B., *Wear*, 1965, 8, 22.
8. Bethune, B. and Waterhouse, R. B., *Wear*, 1968, 12, 289, 369.
9. Sato, J., Shima, M. and Sugawara, T., *Wear*, 1985, 106, 53.
10. Higham, P. A., Bethune, B. and Stott, F. H., *J. Mater. Sci.*, 1977, 12, 2503.
11. Burton, R. A. and Russell, J. A., *J. Basic Engng.*, 1966, 88, 573.
12. Malkin, S., Majors, D. P. and Courtney, T. H., *Wear*, 1972, 22, 235.
13. Koenen, A., Vermoux, Ph., Gras, R., Blouet, J., Dewulf, J. M. and De Monicault, J. M., *Wear*, 1996, 197, 192.
14. Waterhouse, R. B., *Wear*, 1977, 45, 355.
15. Giannakopoulos, A. E., Lindley, T. C. and Suresh, S., *Acta mater.*, 1998, 46, 2955.
16. Cheng, W., Cheng, H. S., Mura, T. and Keer, L. M., *ASME Trans. J. Tribology*, 1994, 116, 2.
17. Hills, D. A., *Wear*, 1994, 173, 107.
18. Hamilton, G. M., *Proc. Inst. Mech. Engrs*, 1983, 197C, 53.
19. Fouvry, S., Kapsa, Ph., Vincent, L. and Dang Van, K., *Wear*, 1996, 195, 21.
20. Lamacq, V., Dubourg, M.-C. and Vincent, L., *J. Tribology*, 1996, 118, 711.
21. Lamacq, V., Dubourg, M.-C. and Vincent, L., *Tribology Int.*, 1997, 30, 391.

22. Wittkowsky, B. U., Birch, P. R., Dominguez, J. and Suresh, S., in *Fretting Fatigue: Current Technology and Practices*, ed. D. W. Hoepfner, Chandrasekaran and C. B. Elliot. American Society for Testing and Materials, 1999, ASTM STP 1367.
23. Semchenko, V. K., *Surface Phenomena in Metals and Alloys*. Addison-Wesley, Reading, MA, 1962.
24. Barquins, M. and Maugis, D., *J. Mec. Theor. Appl.*, 1982, 1, 331.
25. Maugis, D. and Barquins, M., *J. Phys. D: Appl. Phys.*, 1978, 11, 1989.
26. Greenwood, J. A. and Johnson, K. L., *Phil. Mag.*, 1981, 43, 697.
27. Williams, M. L., *Bull. Seismol. Soc. Am.*, 1959, 49, 199.
28. Mindlin, R. D., *J. Appl. Mech.*, 1949, 16, 259.
29. Westmann, R. A., *J. Appl. Mech.*, 1965, 87, 411.
30. Bowden, F. P. and Tabor, D., *Friction and Lubrication of Solids, Part I*. Oxford University Press, London, 1950.
31. Bowden, F. P. and Tabor, D., *Friction and Lubrication of Solids, Part II*. Oxford University Press, London, 1964.
32. McFarlane, J. S. and Tabor, D., *Proc. R. Soc. Lond.*, 1950, A202, 244.
33. Bickerman, J. J., *Wear*, 1976, 39, 1.
34. Chowdhury, S. K. R., Hartley, N. E. W., Pollock, H. M. and Wilkins, M. A., *J. Phys. D: Appl. Phys.*, 1980, 13, 1761.
35. Chowdhury, S. K. R. and Pollock, H. M., *Wear*, 1981, 66, 307.
36. Cottrell, B. and Rice, J. R., *Int. J. Fract.*, 1980, 16, 155.
37. Deresiewicz, H., *J. Appl. Mech.*, 1954, 76, 52.
38. Maugis, D. and Pollock, H. M., *Acta Metall.*, 1984, 32, 1323.
39. Maugis, D., *J. Colloid Interface Sci.*, 1992, 150, 243.
40. Johnson, K. L., *Langmuir*, 1996, 12, 4510.
41. Greenwood, J. A. and Alliston-Greiner, A. F., *Wear*, 1992, 155, 269.
42. Fuller, K. N. G. and Tabor, D., *Proc. R. Soc. Lond.*, A345, 327.
43. Wittkowsky, B. U., Birch, P. R., Dominguez, J. and Suresh, S., *Fatigue Fract. Engng Mat. Str.*, 1999, 22(4), 307.
44. Kennedy, N. G., *Proc. Int. Conf. Fatigue of Metals*, London. I. Mech. E., ASME, 1956, p. 282.
45. Dawson, P. H., *J. Mech. Engng Sci.*, 1967, 9, 67.
46. Kennedy, P. J., Stallings, L. and Peterson, M. B., *ASLE Trans.*, 1983, 27, 305.
47. Blanchard, P., Colombie, Ch, Pellerin, V., Fayeulle, S. and Vincent, L., *Metal. Trans.*, 1991, 22A, 1535.
48. Suresh, S., *Fatigue of Materials*, 2nd ed. Cambridge University Press, Cambridge, 1998.
49. Bryggman, U. and Soderberg, S., *Wear*, 1988, 125, 39.
50. Szolwinski, M. P. and Farris, T. N., *Wear*, 1998, 221, 24.
51. Endo, K. and Goto, H., *Wear*, 1976, 38, 311.
52. Yashamita, N. and Mura, T., *Wear*, 1983, 91, 235.

## APPENDIX

An empirical relation between adhesion and friction of metal surfaces and a spherical indenter based on micro-plasticity of the asperities under shear and normal loading was derived in Ref. [32]. Using the smallest normal load and the sphere diameter used in their experiments, their empirical equation can be stated in terms of critical debonding energy release rate,  $G_d$ , as

$$G_d = 14.3651\sqrt{0.3 + \mu^2} \text{ (N/m)}. \quad (\text{A1})$$

As an example, for  $\mu = 1$ ,  $G_d = 16 \text{ N/m}$ .



## Plasticity in fretting of coated substrates

Matthew R. Begley<sup>a</sup>, John W. Hutchinson<sup>b,\*</sup>

<sup>a</sup>*Department of Mechanical Engineering, University of Connecticut, Storrs, CT 06269-3139, USA*

<sup>b</sup>*Division of Engineering and Applied Sciences, Harvard University, Cambridge, MA 02138, USA*

Received 27 July 1998; received in revised form 28 October 1998; accepted 20 December 1998

---

### Abstract

A detailed analysis is performed of the plastic deformation in a metal substrate fretted by a flat-bottomed circular peg under steady normal load and cyclic tangential load. The substrate is coated with a thin layer of soft metal. Two limiting asymptotic problems are identified which characterize small scale yielding behavior in the substrate in the vicinity of the corners of the peg. Deformation within the plastic zone is characterized, including regions of elastic shakedown, steady reversed cyclic plastic straining, and strain ratchetting. Implications for nucleation of fretting cracks are discussed. © 1998 Elsevier Science Ltd. All rights reserved.

*Keywords:* Fretting; Coated substrates; Plasticity

---

### 1. Introduction

Fretting and fretting fatigue are long-standing problems which continue to require attention in a variety of important applications [1,2]. The mechanics for coping with fretting is based almost entirely on elastic analysis (see, for example [3,4]). Measures of certain combinations of stresses and displacements local to the point of contact between a fretting peg and a substrate calculated from an elastic analysis have been proposed for correlating the onset of crack nucleation [5,6]. To date, the approach to life prediction using these measures has been largely empirical. However, a recent attack has been launched on the behavior of cracks emerging from the most highly stressed region at the edge of a fretting peg [7], and a preliminary study of the plasticity taking place in the contact zone has been published [8].

As a step towards the development of a mechanics of fretting damage, the present paper

---

\* Corresponding author

*E-mail address:* Hutchinson@husm.harvard.edu (J.W. Hutchinson)



focuses on the local plastic deformation accompanying fretting contact. Specifically, the paper investigates plastic deformation in substrates which have been coated with a thin, soft metal layer for the purpose of reducing their fretting susceptibility. The substrate is fretted by a circular, flat bottomed peg subject to a constant normal load and a fully reversed cyclic tangential load. The tangential load is assumed to be sufficiently large to cause the coating to undergo reversed yielding in shear in each cycle. Bulk cyclic stressing of the substrate is not considered. The role of the coating in the redistribution of the contact tractions is modeled. Two limiting boundary conditions for the peg–substrate interaction, as modified by the coating, are proposed and analyzed. Generally, plasticity in the substrate is limited to the immediate vicinity of the edge of the peg. This makes possible the formulation of a small-scale yielding problem wherein the relevant load factors become amplitudes characterizing the elastic solution at the peg corner. The approach closely parallels the small scale yielding analysis of crack tip plasticity, where the plastic zone is embedded within the elastic field whose amplitude is the stress intensity factor.

## 2. Asymptotic Formulations for Small Scale Yielding in Fretting

The geometry of the flat-bottom cylindrical peg in contact with the semi-infinite coated

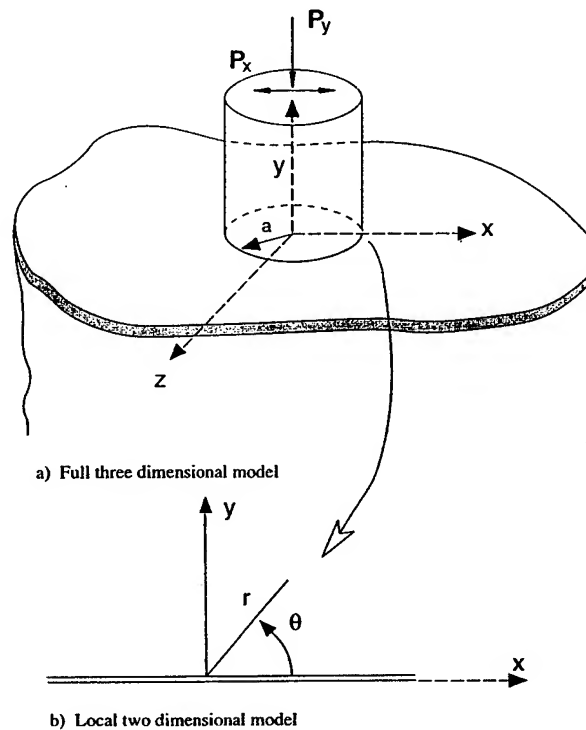


Fig. 1. (a) Three-dimensional fretting geometry. (b) Local two-dimensional geometry at right corner of fretting peg.

substrate is shown in Fig. 1. The radius of the peg,  $a$ , is assumed to be very large compared to the coating thickness. The ratio of the shear yield stress of the thin film coating,  $\tau_y^f$ , to that of the substrate,  $\tau_y^s$ , is one of the important parameters in the model. The metals comprising the coating and the substrate are each taken to be elastic–perfectly plastic and characterized by von Mises yield surfaces. The Young's modulus and Poisson's ratio of the substrate are  $E$  and  $\nu$  (Poisson's ratio is taken to be 0.3 for all the calculations reported here). A constant downward vertical force  $P_Y$  is exerted by the peg on the substrate. The peg is displaced back and forth tangential to the substrate under nonslip conditions. The amplitude of the tangential cyclic displacement is assumed to be large enough such that the shear stress of the coating is reached everywhere under the peg (i.e. the peak tangential force attains  $P_X = \pm \pi a^2 \tau_y^f$  in each cycle). This assumption reflects the function of the soft coating and controls the maximum stresses exerted by the peg on the substrate, as will be detailed subsequently.

For realistic levels of loading, plastic deformation in the substrate is confined to a small annulus about the rim of the peg. The maximum extent of the cyclic plastic zone from the rim will be found to be less than several percent of the radius of the peg radius  $a$ . The smallness of the zone permits a small scale yielding formulation to be developed where the plastic zone is embedded within the elastic field local to the edge. Thus, to analyze and present results for plastic behavior, one need not consider the full geometry in Fig. 1. Instead, one can focus on portions of the edge of most concern and introduce amplitude factors characterizing the local elastic fields. The approach closely parallels that employed extensively and effectively in the small-scale yielding approach to crack tip plasticity. In the present study, attention is focused on the leading (and, by symmetry, trailing) edge of the peg in the vicinity of ( $X = a$ ,  $Y = 0$ ,  $Z = 0$ ) in Fig. 1a. The coordinate system local to the edge of interest is defined in Fig. 1b.

The choice of boundary conditions to model the interaction of the peg and the coated substrate is not straightforward. Two sets of boundary conditions are introduced here which are expected to bracket the range of cyclic plastic behavior at the leading edge of the peg. The first set is termed the *uniform normal traction formulation*, and the second will be referred to as the *uniform normal displacement formulation*. In each, the tangential traction exerted on the substrate at the peak of the cycle is the shear yield stress in the coating. The two sets are taken in turn with discussion of the elastic amplitude factors and associated near-edge fields used to characterize the respective small scale yielding problems.

### 2.1. The uniform normal traction formulation

As remarked above, the cyclic tangential displacement of the peg relative to the substrate is assumed to be sufficiently large such that at the peak of the cycle in either direction the coating is yielded in shear at all points under the peg. Thus at the peak of the cycle the magnitude of the shear stress  $\sigma_{XY}$  acting on the substrate in the region  $X^2 + Z^2 \leq a^2$  is  $\tau_y^f$ . A second implication which follows from the fact that the thin coating beneath the peg is at yield in shear is that the coating can only support an additional hydrostatic pressure  $p$ . The nonzero components of stress in the coating at the loading peak are

$$\sigma_{ij} = -p\delta_{ij} \quad \text{with} \quad \sigma_{XY} = \pm \tau_y^f \quad (1)$$

An elementary application of equilibrium of the coating reveals that  $p$  must be independent of  $X$  and  $Y$  beneath the peg. The pressure beneath the peg becomes uniform when the elastic–perfectly plastic coating is fully yielded in shear. This argument ignores a small region at the edge of the peg on the order of the coating thickness, consistent with the underlying assumption that the film thickness is very small compared to all other length scales of interest. Thus, Eq. (1) implies that the tractions acting on the surface of the substrate in the region  $X^2 + Z^2 \leq a^2$  at the peak of the cycle are

$$\begin{aligned}\sigma_{YY} &= -P_Y/\pi a^2 \\ \sigma_{XY} &= P_X/\pi a^2 \\ \sigma_{YZ} &= 0 \quad \text{with} \quad P_X = \pm \pi a^2 \tau_y^f\end{aligned}\tag{2}$$

where the sign of the shear traction depends on the direction of the peg displacement.

The construction of the elastic solution for a half-space subject to Eq. (2) is well known. It makes use of solutions for concentrated loads acting on the surface of the half-space [9,10]. Integral representations for the stresses can be obtained by a straightforward superposition of the concentrated load solutions over the circular portion of the surface,  $X^2 + Z^2 \leq a^2$ . The stresses at any point in the substrate off the edge of the circle can be evaluated with high accuracy using numerical integration techniques widely available in numerical analysis software packages. The stresses at the edge of the peg are logarithmically singular at the edge of the peg in the elastic solution. Specifically, in the plane  $Z=0$  in the vicinity of the leading edge (Fig. 1b), the local stress distribution is

$$\begin{aligned}\sigma_{xx} &= \frac{P_X}{\pi a^2} \left\{ \frac{2}{\pi} \ln \left( \frac{r}{a} \right) + \frac{1}{\pi} (\sin \theta)^2 + c_{xx} \right\} + \frac{P_Y}{\pi a^2} \left\{ \frac{1}{\pi} \theta + \frac{1}{2\pi} \sin 2\theta + c_{xy} \right\} \\ \sigma_{yy} &= \frac{P_X}{\pi a^2} \left\{ -\frac{1}{\pi} (\sin \theta)^2 \right\} + \frac{P_Y}{\pi a^2} \left\{ \frac{1}{\pi} \theta - \frac{1}{2\pi} \sin 2\theta \right\} \\ \sigma_{zz} &= \frac{P_X}{\pi a^2} \left\{ \frac{2\nu}{\pi} \ln \left( \frac{r}{a} \right) + \nu c_{xx} + c_{zx} \right\} + \frac{P_Y}{\pi a^2} \left\{ \frac{2\nu}{\pi} \theta + \nu c_{xy} + c_{zy} \right\} \\ \sigma_{xy} &= \frac{P_X}{\pi a^2} \left\{ -\frac{1}{\pi} \theta - \frac{1}{2\pi} \sin 2\theta \right\} + \frac{P_Y}{\pi a^2} \left\{ \frac{1}{\pi} (\sin \theta)^2 \right\}\end{aligned}\tag{3}$$

Note that for the convention used here, positive  $P_Y$  acts downward. This representation of the stresses near the leading edge of the peg contains both the logarithmically singular contributions and all contributions which do not vanish as  $r$  approaches zero. The local field is a state of generalized plane strain because the strain component  $\epsilon_{zz}$  is bounded but nonzero at  $r=0$ :

$$\varepsilon_{zz} = \frac{1}{\pi a^2 E} \{P_x c_{zx} + P_y c_{zy}\} \quad (4a)$$

The four coefficients in Eq. (3) have been obtained numerically such that Eq. (3) reproduces the full three-dimensional solution as  $r$  approaches zero:

$$c_{xx} = -0.190$$

$$c_{xy} = -0.165$$

$$c_{zx} = -0.220$$

$$c_{zy} = 0.190 \quad (4b)$$

The domain of accuracy of the asymptotic distribution Eq. (3), has been checked by a comparison with numerical results for the full three-dimensional solution. Comparisons indicate that the field Eq. (3), provides a good approximation (e.g. better than 5% accuracy) in the plane  $Z=0$  for  $r \leq a/10$ .

In small scale yielding, the plastic zone must be sufficiently small compared to the peg radius  $a$  such that the stress field in an annular region outside the zone is accurately given by Eq. (3). Effectively, this means the plastic zone must be small compared to  $a/10$ . The concept is very similar to that used in crack tip plasticity studies. In the numerical approach used in the next section, the distribution, Eq. (3), is used to generate tractions on a circular boundary 'remote' from the origin at  $r=0$ .

## 2.2. The uniform normal displacement formulation

The formulation just described relies on the soft metal coating to redistribute the normal traction beneath the peg such that it becomes uniform at the peak of the cycle when the coating yields in shear. This process requires that the coating be thick enough to flow and redistribute the normal traction. Redistribution would be somewhat thwarted by strain hardening in the coating, the more so the thinner the coating. An alternative formulation of the substrate loading is proposed which ignores the tendency of the coating to redistribute the normal traction, while continuing to account for yielding of the coating in shear. A uniform displacement  $u_y$ , together with a uniform shear traction  $\sigma_{xy} = \pm \tau_y^f$ , is imposed on the substrate over the circular region under the peg. The displacement  $u_y$  is chosen such that the average normal compressive stress under the peg is  $\bar{\sigma} = P_y/\pi a^2$ . This formulation is consistent with a rigid peg and no normal traction redistribution by the coating. It is expected to overestimate the stresses in the vicinity of the peg edge.

The two-dimensional plane strain version of this alternative formulation is studied in this paper. The elastic version of this problem has uniform displacement  $u_y$  and uniform shear traction,  $\sigma_{xy} = \pm \tau_y^f$ , prescribed on the surface for  $|x| \leq a$  and zero tractions for  $|x| \geq a$ , where the uniform displacement is chosen such that under the peg the average normal compressive stress is  $\bar{\sigma}$ . The elastic solution to this problem can be obtained using complex function methods. The stresses in the vicinity of the peg edge (i.e. near the origin in Fig. 1b) are

$$\begin{aligned}
\sigma_{xx} &= \frac{\bar{\sigma}}{2\pi} \sqrt{\frac{a}{2r}} \left\{ 3 \sin \frac{\theta}{2} + \sin \frac{5\theta}{2} \right\} + \frac{\bar{\tau}}{2} \left\{ \frac{1}{\pi} \left[ 4 \ln \frac{r}{2a} - \cos 2\theta + 1 \right] - \frac{1}{2} \left( \frac{\kappa-1}{\kappa+1} \right) \sqrt{\frac{a}{2r}} \left[ 3 \sin \frac{\theta}{2} + \right. \right. \\
&\quad \left. \left. \sin \frac{5\theta}{2} \right] \right\} \\
\sigma_{yy} &= \frac{\bar{\sigma}}{2\pi} \sqrt{\frac{a}{2r}} \left\{ 5 \sin \frac{\theta}{2} - \sin \frac{5\theta}{2} \right\} + \frac{\bar{\tau}}{2} \left\{ \frac{1}{\pi} [\cos 2\theta - 1] - \frac{1}{2} \left( \frac{\kappa-1}{\kappa+1} \right) \sqrt{\frac{a}{2r}} \left[ 5 \sin \frac{\theta}{2} - \sin \frac{5\theta}{2} \right] \right\} \\
\sigma_{xy} &= \frac{\bar{\sigma}}{2\pi} \sqrt{\frac{a}{2r}} \left\{ \cos \frac{\theta}{2} - \cos \frac{5\theta}{2} \right\} - \frac{\bar{\tau}}{2} \left\{ \frac{1}{\pi} [\sin 2\theta + 2\theta] + \frac{1}{2} \left( \frac{\kappa-1}{\kappa+1} \right) \sqrt{\frac{a}{2r}} \left[ \cos \frac{\theta}{2} - \right. \right. \\
&\quad \left. \left. \cos \frac{5\theta}{2} \right] \right\}
\end{aligned} \tag{5}$$

with  $\sigma_{zz} = \nu(\sigma_{xx} + \sigma_{yy})$  and where  $\kappa = 3 - 4\nu$  in plane strain. Once again, the sign convention is such that positive  $\bar{\sigma}$  implies an average compressive stress acting downward. The elastic solution has an inverse square root singularity in the stresses, in addition to the weaker logarithmic singularity produced by the tangential shear load  $\bar{\tau}$ . The contribution associated with the normal load  $\bar{\sigma}$  is identical to the mode I distribution at the tip of a plane strain crack. An additional mode I contribution is induced by the shear load  $\bar{\tau}$ , due to the fact that the surface under the peg is constrained against rotation. The domain of accuracy of Eq. (5) relative to the full plane strain solution is similar to that discussed for the other formulation.

### 2.3. Numerical model

Finite element formulations of the two small scale yielding problems have been used to generate behavior in the plastic zone in the substrate under cyclic fretting loads. The two primary dimensionless system parameters are: (i) the ratio of the steady normal load to the cyclic shear load; and (ii) the ratio of the coating yield stress to that of the substrate. Traction consistent with either Eqs. (3) or (5) are applied on a circular boundary remote from (and centered on) the origin  $r=0$  in Fig. 1b. The choice of remote boundary is arbitrary as long as it is sufficiently large compared to the plastic zone;  $r = a/5$  was used. As remarked at the beginning of this section, the materials comprising the coating and the substrate are each taken to be elastic-perfectly plastic with von Mises yield surfaces. The behavior of the coating is incorporated through the tractions applied to the surface of the substrate directly under the pin.

The boundary conditions were imposed by prescribing nodal forces or displacements that are consistent with either Eq. (3) or Eq. (5). Displacement fields associated with the asymptotic stress fields in Eqs. (3) and (5) were derived. For the outer radius, the choice of whether to prescribe tractions or displacements is somewhat arbitrary, but prescribing displacements is

generally favored as they did not involve elemental integration to determine nodal forces. Under the pin, the constant shear traction boundary condition was imposed by prescribing nodal forces in the  $x$ -direction which resulted in a constant shear stress. For the uniform normal pressure case, nodal forces in the vertical direction were used consistent with this loading. The generalized plane strain cases involved the additional requirement of specifying the strain in the direction normal to the plane of the model according to the prescription (4a).

The finite element solutions were generated using the commercial code ABAQUS with eight-noded quadrilateral plane strain elements. (Generalized plane strain elements were used for the case of uniform normal tractions by specifying the out-of-plane strain component.) It is assumed that behavior closer to the origin than about  $r = a/100$  from the model need not be resolved, both because the fidelity of the model becomes questionable (e.g. the finite thickness of the coating is not taken into account) and because the length scale relevant to fatigue crack nucleation will usually be larger than this. The mesh consisted of 1000 elements in a radial fan focusing on the origin. Results from a coarser mesh with approximately 1000 elements in a radial fan focusing on the origin. Results from a coarser mesh with approximately 600 elements revealed negligible differences in plastic strain values outside  $r = a/100$ . Since run times were not significantly different for the two meshes, the finer mesh was used for all the calculations.

A cycle is defined as going from maximum shear load in one direction to an equivalent

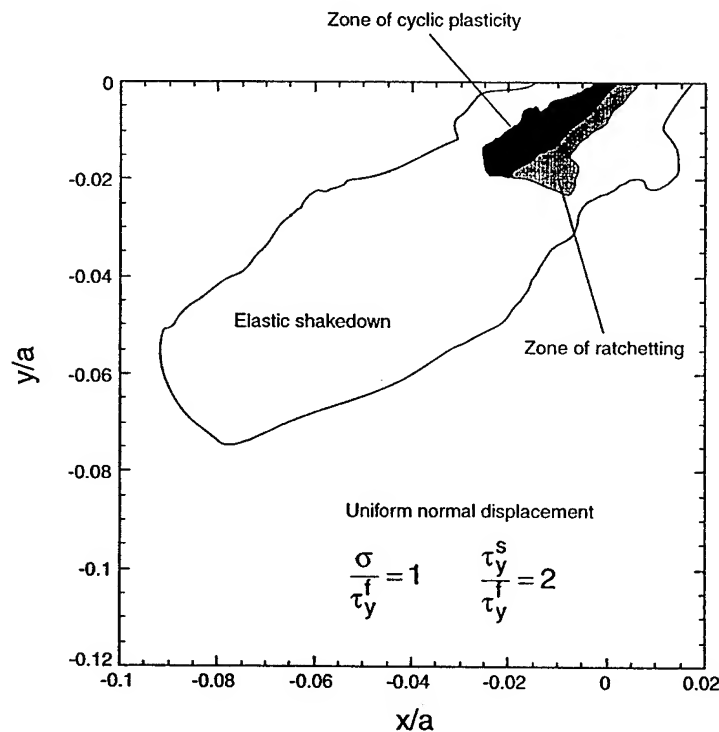


Fig. 2. Plastic zones in the vicinity of the right corner of the peg for the formulation of uniform normal displacement.

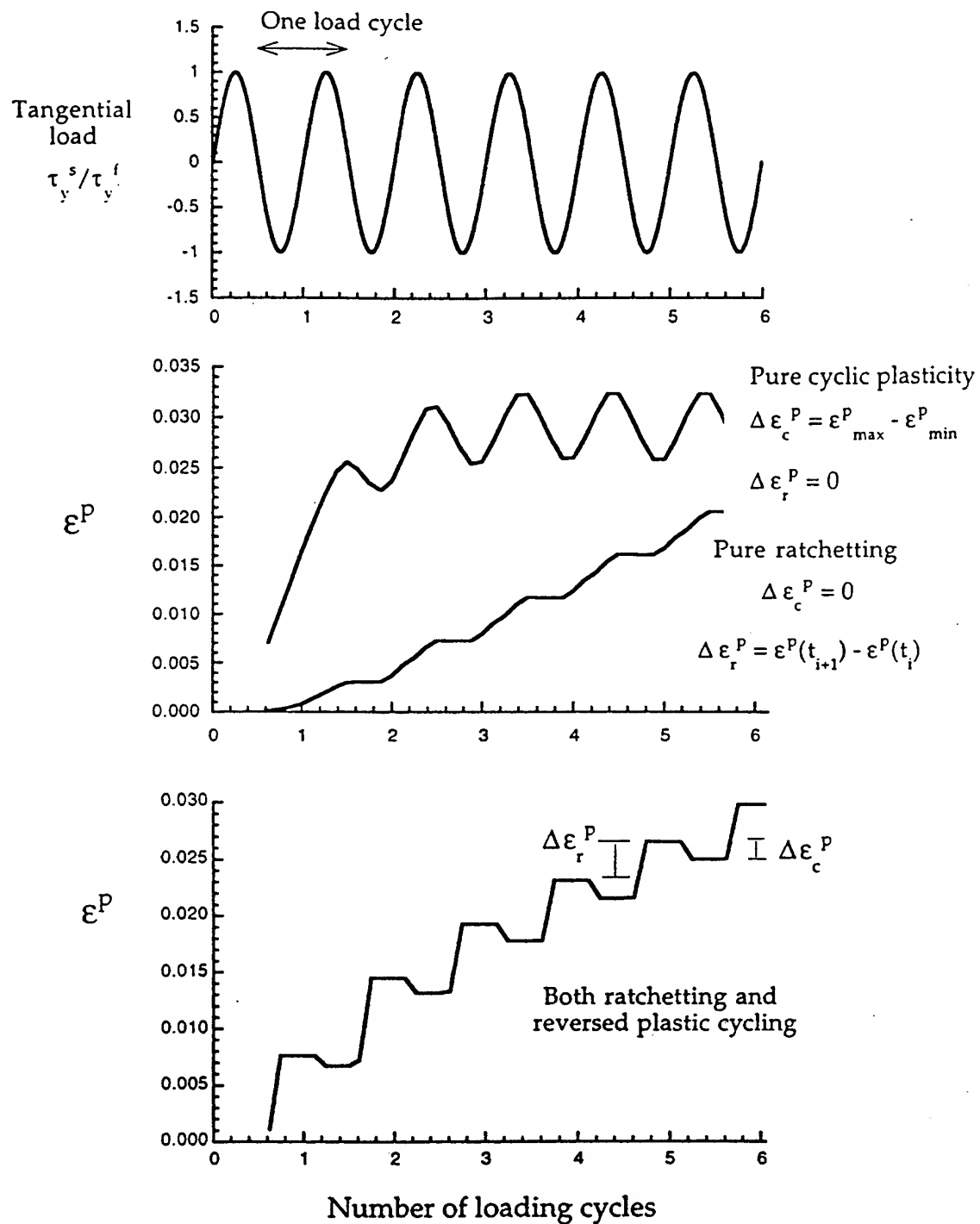


Fig. 3. Schematic of the different types of cyclic plastic strain responses.

magnitude in the opposite direction, and returning again to the first maximum shear load. By this definition, a quarter cycle is needed to increase the applied loads from zero to the first maximum. Both shear and normal loads were first increased from zero to their maximum values in direct proportion; then, the normal load was held fixed, while the tangential load was cycled. Six full cycles were simulated after the loads were brought to their initial maxima. Care was taken to ensure that the imposed boundary conditions (displacements or nodal forces) properly account for the cyclic component from the shear traction and the constant component from the normal displacement or pressure. This is achieved by computing the individual contributions from each type of loading and superimposing them at each time in the cycle.

### 3. Plasticity in the substrate

Behavior in the plastic zone is fairly complex. To aid the discussion, a detailed plastic zone map is given in Fig. 2 for a specific set of parameters. The example is for the uniform normal displacement formulation, but details for the other formulation are qualitatively similar. The outer boundary, extending out to just over  $a/20$  from the peg edge, is the zone of plastic deformation occurring in the first loading cycle when the normal load is brought up to its maximum value along with the shear load. From the peak of the first cycle, the normal load is held constant and the shear load is cycled. The outer portion of the initial plastic zone experiences no further plastic strain increments after the first or second cycle. (At some points, no further plastic increments occur after the time corresponding to maximum negative shear.) The outer portion of the zone experiences elastic shakedown. Plastic strain increments continue to occur in subsequent cycles in the inner portion of the plastic zone, extending to a distance of approximately  $0.03a$  from the origin for this example. The zone of active incremental plasticity can be divided into two sub-zones, one dominated by ratchetting behavior and the other by cyclic plastic strains. Precise definitions of these terms within the present context will now be given.

#### 3.1. Elastic shakedown, cyclic plastic straining and ratchetting

Four types of response at points within the initial plastic zone are indicated in Fig. 3 for a representative component of plastic strain,  $\varepsilon^p$ . At the top of the figure, the cyclic tangential loading history is indicated with integer values of time coinciding with the beginning of one cycle and the end of the one before. The initial load application in which the normal load is brought up to its constant maximum occurs between  $t=0$  and  $1/4$ . In the portion of the initial plastic zone where elastic shakedown occurs, elastic unloading occurs following the peak of the first or second cycle and the yield condition is never again reached. To distinguish between cyclic plastic straining and ratchetting, consider first pure limits of these behaviors shown in Fig. 3. In pure cyclic straining each plastic strain component oscillates between minimum and maximum values which do not change after the first few cycles. Repeatable reversed plasticity occurs with yielding necessarily taking place under both positive and negative shearing of the peg. Such behavior has been termed 'plastic shakedown' by some authors. Pure ratchetting involves an increment of the plastic strain component in each cycle associated with shearing in



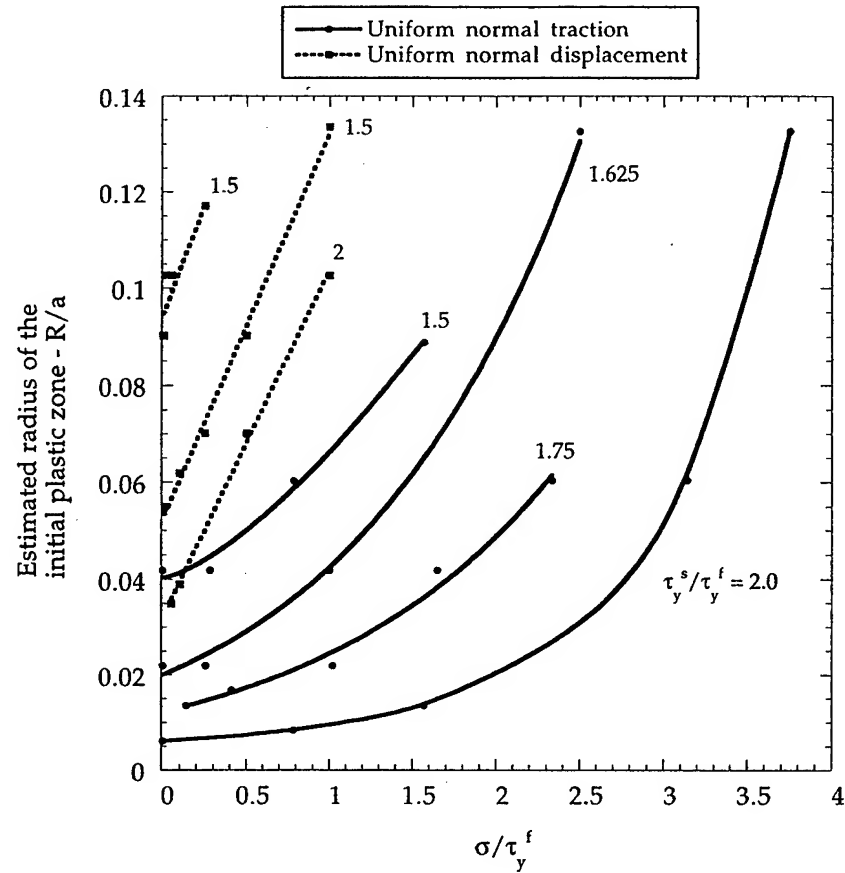


Fig. 4. Size of the plastic zone at the peak of the first load cycle as dependent on the two dimensionless system parameters,  $\sigma/\tau_y^f$  and  $\tau_y^s/\tau_y^f$ , and the model formulation.

one direction but not the other. Reversed plastic straining does not occur. The increment per cycle,  $\Delta\epsilon_f^P$ , is constant after the first few cycles. Generally, neither pure cyclic plastic straining nor pure ratchetting occur in the fretting problem, although this behavior may occur at localized regions in the plastic zone. At a typical point within the zone of active plasticity a combination of these two responses are observed to take place, as depicted in the bottom sketch in Fig. 3. Here again, after the first one or two cycles, the behavior settles down to a repeatable pattern in which a fixed amplitude of reversed cyclic plastic straining,  $\Delta\epsilon_c^P$ , occurs simultaneously with a fixed amplitude of ratchetting,  $\Delta\epsilon_f^P$ . The two sub-zones referred to in connection with Fig. 2 are defined consistent with which class of deformation is dominant. Further definitions needed to ascertain the cyclic and ratchetting amplitudes in terms of all the component of strain are given below.

For the case depicted at the bottom of Fig. 3 involving combined cyclic plasticity and ratchetting, define the plastic ratchetting strain once the deformation has settled down as the difference in plastic strains at any two comparable times in the loading history (such as the points of maximum tangential shear) of two subsequent cycles according to:

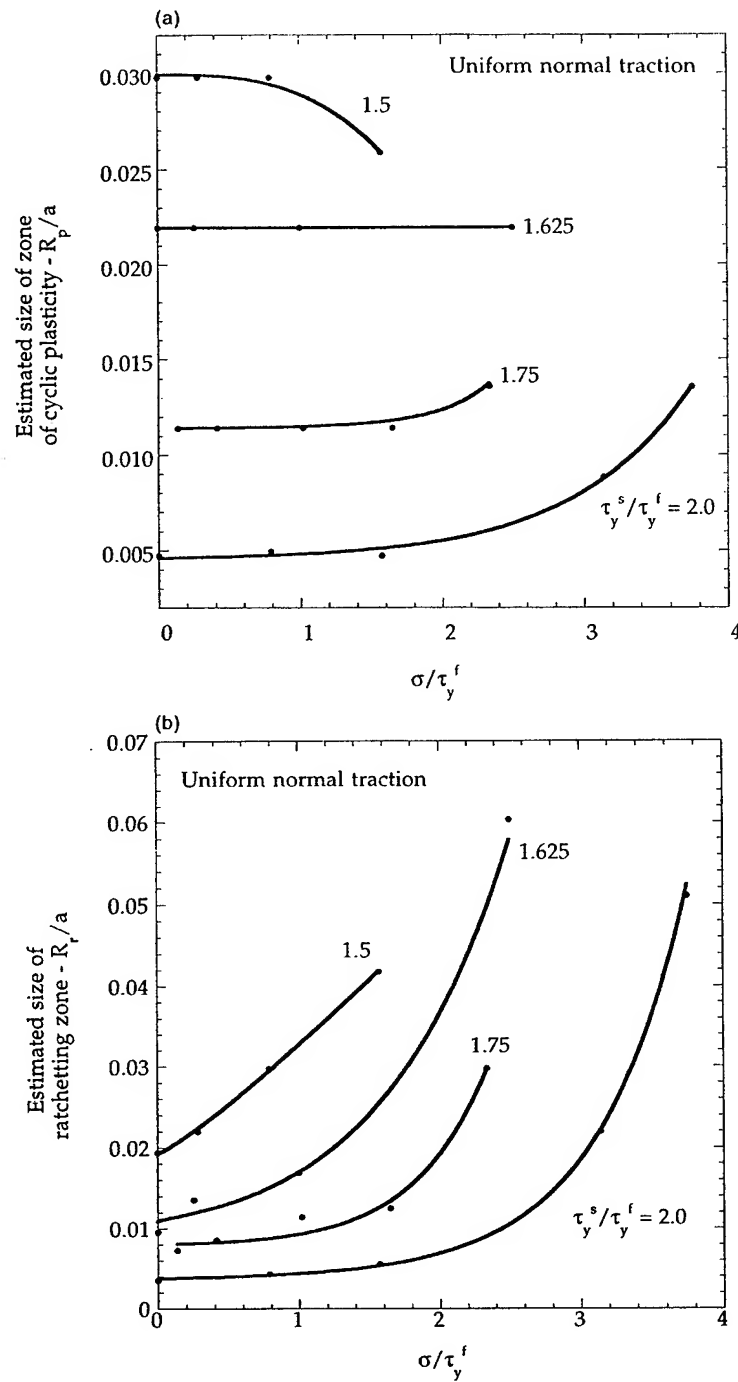


Fig. 5. Size of the active plastic zones for the uniform normal traction model. (a) Zone of cyclic plasticity. (b) Zone of ratchetting plasticity.

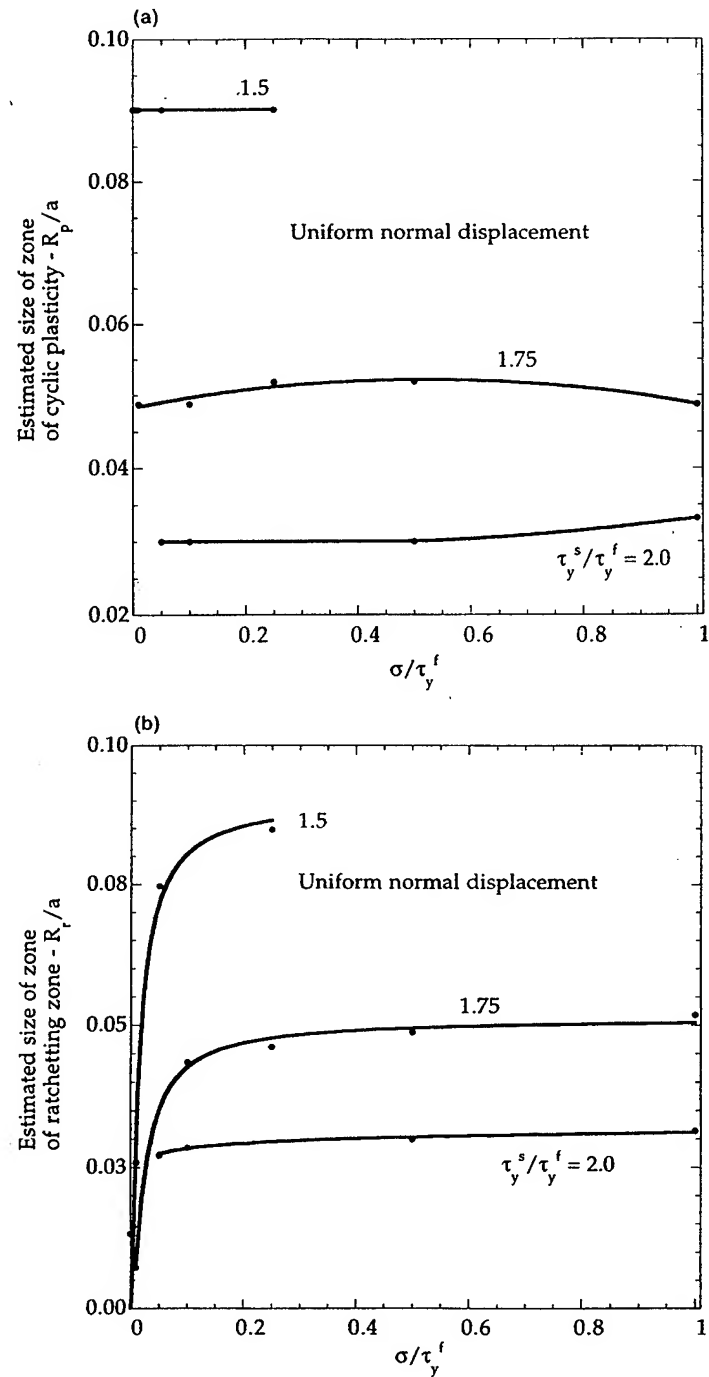


Fig. 6. Size of the active plastic zones for the uniform normal displacement model. (a) Zone of cyclic plasticity. (b) Zone of ratchetting plasticity.

$$(\Delta \epsilon_{ij}^p)_r = \epsilon_{ij}^p(t_{i+1}) - \epsilon_{ij}^p(t_i) \quad (6)$$

The cyclic plastic strain can then be defined as (see Fig. 3):

$$(\Delta \epsilon_{ij}^p)_c = (\epsilon_{ij}^p)_{\max} - (\epsilon_{ij}^p)_{\min} - (\Delta \epsilon_{ij}^p)_r \quad (7)$$

where the first two values represent the maximum and minimum values of the components in a given cycle. These values are almost always attained at points where the shear load undergoes reversal in direction. Effective measures of the amplitudes are used. The effective cyclic plastic strain is defined as<sup>1</sup>

$$\Delta \epsilon_c^p = \sqrt{\frac{2}{3}(\Delta \epsilon_{ij}^p)_c(\Delta \epsilon_{ij}^p)_c} \quad (8)$$

and the ratchetting strain amplitude is

$$\Delta \epsilon_r^p = \sqrt{\frac{2}{3}(\Delta \epsilon_{ij}^p)_r(\Delta \epsilon_{ij}^p)_r} \quad (9)$$

With reference to the sub-zones in Fig. 2, the zone of cyclic plastic straining has  $\Delta \epsilon_c^p > \Delta \epsilon_r^p$ , while the ratchetting zone has  $\Delta \epsilon_r^p > \Delta \epsilon_c^p$ .

### 3.2. Size of initial plastic zone and zones of cyclic plasticity and ratchetting

It is already evident from Fig. 2 that a soft coating cannot fully isolate the substrate from plastic deformation. The size of the initial plastic zone at the end of the first full load cycle when the normal load attains its maximum value is shown in Fig. 4 as a function of the two primary parameters,  $\tau_y^s/\tau_y^f$  and  $\sigma/\tau_y^f$ , where  $\sigma$  is the average normal compressive stress exerted by the peg. After the first cycle, subsequent loading does not change the size of the plastic zone. The zone associated with the uniform normal displacement conditions is substantially larger than that associated with uniform normal traction. Otherwise, the trends are in accord with intuition: the initial zone size increases with harder coatings and with larger normal peg force.

The roles of  $\tau_y^s/\tau_y^f$  and  $\sigma/\tau_y^f$  in determining the size of the zones of cyclic plasticity and ratchetting are shown in Figs. 5 and 6. The size of the zone of cyclic plastic straining is specified by the requirement that  $\Delta \epsilon_c^p$  must be greater than 1% of the uniaxial strain at yield ( $\epsilon_y = \sqrt{3}\tau_y^f/E$ ).<sup>2</sup> Analogous requirements are made on the effective ratchetting strains in the definition of the ratchetting zone. Ratchetting generally occurs at locations dominated by cyclic plastic straining, and vice versa. As such, the delineation between zones of ratchetting and cyclic plasticity is qualitative.

The average normal compressive traction  $\sigma$  has little influence on the size of the zone of cyclic plastic straining for either of the two sets of boundary conditions. On the other hand, the yield stress ratio,  $\tau_y^s/\tau_y^f$ , has a strong effect on the zone size. Decreasing the flow stress of

<sup>1</sup> The summation convention is implied for all repeated indices.

<sup>2</sup> The additional requirement that  $\Delta \epsilon_c^p$  must be larger than  $\Delta \epsilon_r^p$  does not significantly alter the figures; this additional requirement was used to delineate between ratchetting and cyclic plasticity 'zones' in Fig. 2.

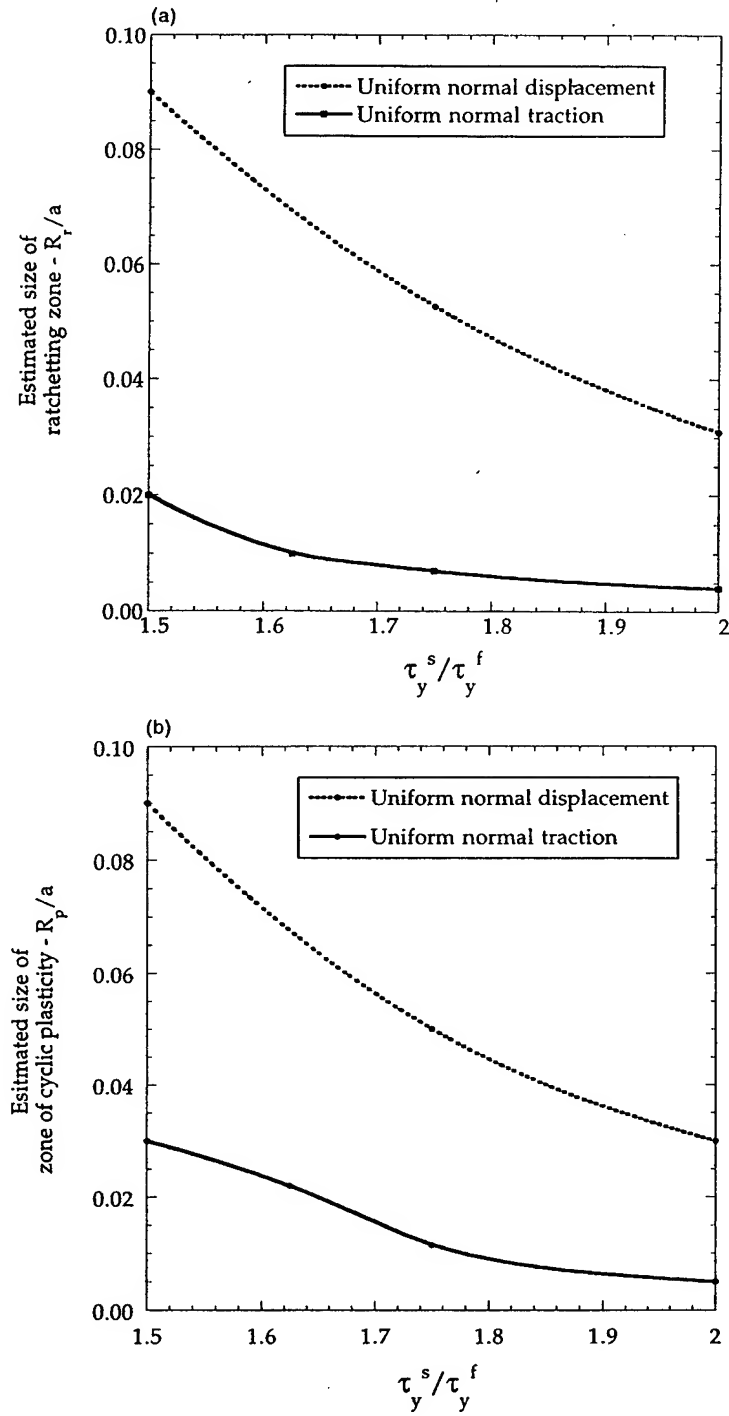


Fig. 7. Approximate size of the active plastic zones as a function of  $\tau_y^s / \tau_y^f$ . The results for most of the range for which  $\sigma / \tau_y^f$  does not exceed unity. (a) Zone of cyclic plasticity. (b) Zone of ratchetting plasticity.

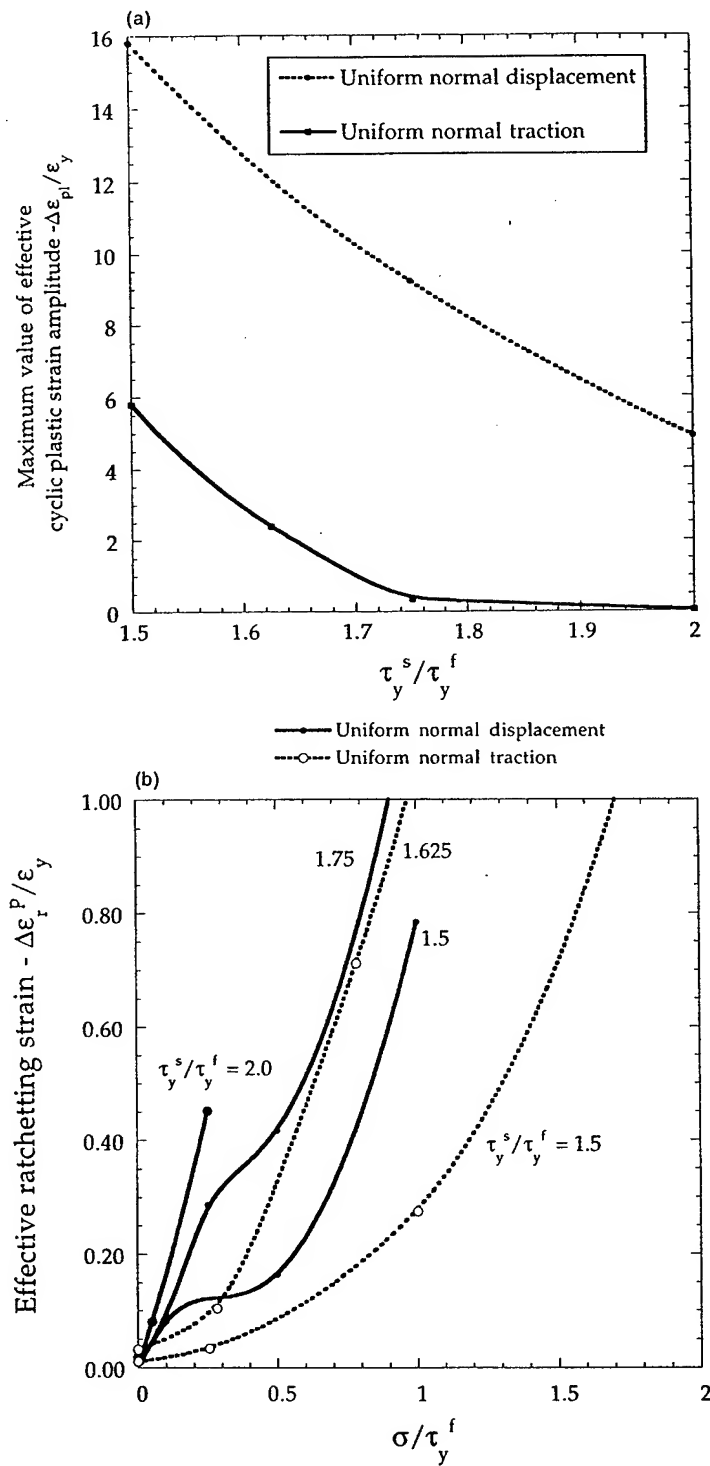


Fig. 8. Maximum value of the effective plastic strain amplitudes occurring each cycle outside the circle  $r/a=0.01$  centered at the peg corner ( $\sigma/\tau_y^f=1$ ). (a) Maximum cyclic plastic strain amplitude (for all values of  $\sigma/\tau_y^f$  considered). (b) Ratchetting strain amplitudes as a function of normal loading.

the coating from  $2/3$  to  $1/2$  of the flow stress of the substrate results in a dramatic reduction in the size of both the zone of cyclic plastic straining and the ratchetting zone. The average normal traction has a fairly large effect on the ratchetting zone size, especially for the case of uniform normal tractions. At low  $\sigma/\tau_y^f$  the cyclic plastic zone is larger than the ratchetting zone, but the ratchetting zone becomes the larger of the two as the normal pressure from the peg increases.

The same results are presented in a different manner in Fig. 7, where the estimated size of the respective zones are shown as a function of  $\tau_y^s/\tau_y^f$ . The size of the zone of cyclic plastic straining has been plotted using data in the range where it is relatively independent of  $\sigma/\tau_y^f$ . Only at the highest values of  $\sigma/\tau_y^f$  do the lower curves in Fig. 7a, b significantly underestimate the zone size for the uniform normal traction model. The upper curves in Fig. 7a, b, which apply to the uniform normal displacement model, have been plotted using values at the high end of the range of  $\sigma/\tau_y^f$ , and thus these curves represent the upper limit for this model.

The two sets of results taken together should bound the zone sizes, because the uniform normal traction model undoubtedly exaggerates the ability of the coating to redistribute the normal traction near the peg corner while the uniform normal displacement model almost certainly underestimates the effect. The trends of Fig. 7 further emphasize the important role played by the coating hardness in determining the size of the cyclic and ratchetting plastic zones in the substrate.

### 3.3. Plastic strains

The trends in plastic zone size are complemented by the curves of Fig. 8 showing the maximum of the effective cyclic plastic strain outside the circle  $r/a=0.01$  surrounding the peg corner as a function of the yield stress ratio. Here,  $\Delta\epsilon_c^p$  is the amplitude of the effective cyclic plastic strain, where any ratchetting contribution has been removed via Eq. (7). As suggested by the fact the cyclic plastic zone size is insensitive to the average normal traction (Figs. 5a and 6a), the magnitude of the effective cyclic plastic strain is insensitive as well. Indeed, increasing the average normal traction will generally *decrease* the maximum of the effective cyclic plastic strain; as such the curves in Fig. 8 represent upper bounds on the cyclic plastic strain. The amplitude decreases strongly with decreasing coating flow stress. The uniform normal traction model predicts the cyclic plastic strain amplitude falls to almost zero for  $r/a>0.01$  if  $\tau_y^s/\tau_y^f \geq 1.75$ . By contrast, the other model indicates that significant cyclic plastic straining will still occur, although the amplitude decreases sharply with increasing  $\tau_y^s/\tau_y^f$ .

The magnitude of the effective ratchetting strain amplitude has a much stronger dependence on the average normal traction and increases sharply with increasing normal loading. This phenomena is illustrated in Fig. 8b. As such, it is impossible to place upper bounds on the magnitude of ratchetting strain amplitude for a given  $\tau_y^s/\tau_y^f$ , as was done in Fig. 8a. It is interesting to note that for the uniform normal displacement case, the ratchetting strain amplitude will increase significantly with increasing normal pressure, despite the fact that the ratchetting zone *size* does not increase (see Fig. 6b). For all uniform normal displacement cases, the effective ratchetting amplitude is an order of magnitude smaller than the effective cyclic plastic strain. For the uniform normal traction cases where  $\tau_y^s/\tau_y^f > 1.6$ , the ratchetting strain amplitudes are comparable with effective cyclic plastic strains.

The two plastic sub-zones extend under the peg at roughly a 135–150° angle to the surface (Fig. 2). At higher values of the normal pressure in the uniform normal traction case, there is an additional ‘lobe’ of the plastic zone which extends at roughly 60° (at a right angle to the primary plastic zone). Ratchetting zones dominate this portion of the plastic zone. The deformation in the cyclic zone comprises significant reversed plastic shearing parallel to the zone. Plastic straining in the ratchetting zone is consistent with material being squeezed out from under the peg emerging at the surface just to the right of the peg corner. Ratchetting is

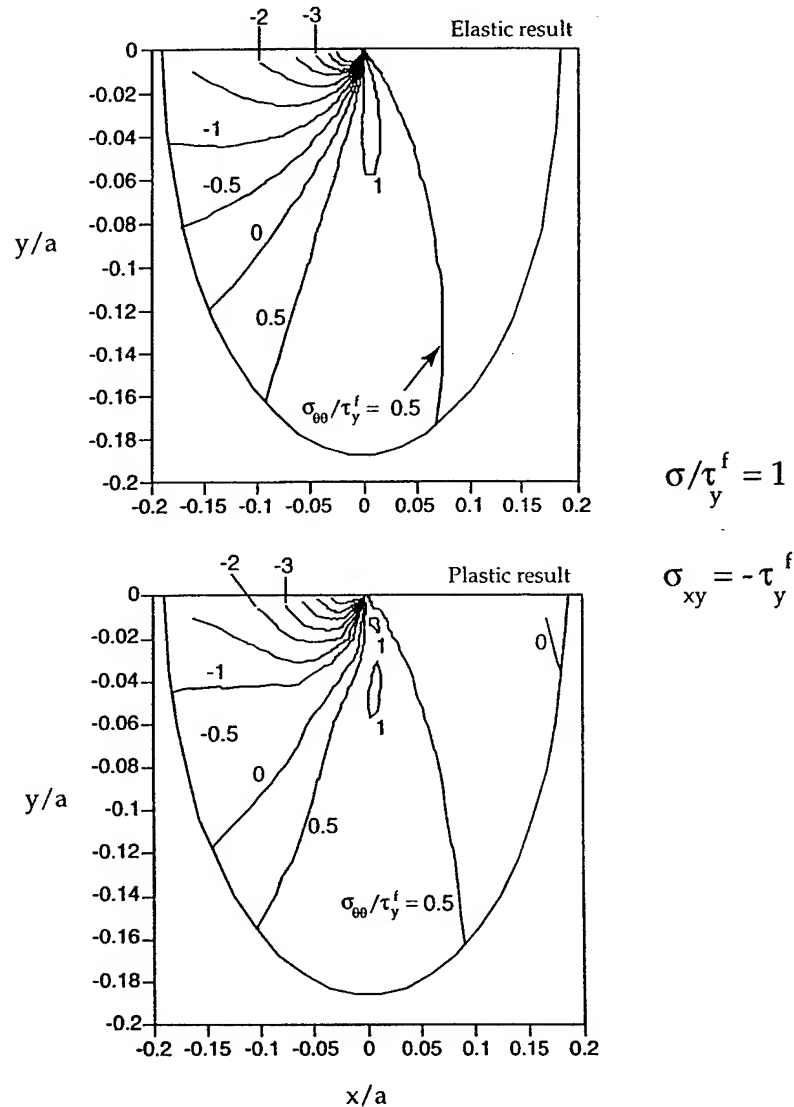


Fig. 9. Contours of constant values of  $\sigma_{\theta\theta}/\tau_y^f$  near the peg corner at the point in the loading cycle when  $\sigma_{xy} = -\tau_y^f$  for the uniform normal displacement formulation with  $\sigma/\tau_y^f = 1$  and  $\tau_y^s/\tau_y^f = 2$ . The horizontal and vertical axes are  $x/a$  and  $y/a$ .



expected to cause a redistribution of normal traction under the corner of the indenter. The local traction distribution will vary slowly from cycle to cycle as material is squeezed out from the immediate vicinity of the corner. It is not evident how this process saturates.

Fig. 9 displays the distribution of the circumferential component of stress,  $\sigma_{\theta\theta}$ , at every point in the vicinity of the peg corner in the sixth cycle at the point where the peg is at the peak negative tangential displacement (i.e.  $\sigma_{xy} = -\tau_y^f$  under the peg). These distributions are for the uniform normal displacement model with system parameters identical to those for the plastic zones in Fig. 2. A plot for the corresponding elastic solution is also shown in Fig. 9, indicating there is no significant qualitative difference between the two fields and, in particular, in the predicted regions of tensile hoop stress. Tensile circumferential stresses occur in a fan of approximately  $40^\circ$  centered on  $\theta \cong -80^\circ$  under the peg corner. The combination of active plastic straining and tensile stress is expected to promote the formation of fatigue cracks. Note that the tensile stresses at the right corner of the peg only occur during the portion of the cycle when the shearing force exerted by the peg is directed to the left.

#### 4. Summary of findings and implications for fretting

The zones of cyclic and ratchetting plasticity in the substrate extend beneath the peg at an angle of approximately  $35^\circ$  to the peg–substrate interface ( $\theta = -145^\circ$ ). It is suggestive that the plastic zones (as depicted in Fig. 2) are aligned with the direction of crack nucleation in experiments (e.g. [1,11,12]). The size of these active plastic zones diminish sharply with softer substrate coatings (i.e. with diminishing  $\tau_y^f/\tau_y^s$ ). As long as the integrity of a soft coating is preserved, it is highly effective at lowering stresses in the most highly stressed region under a fretting peg. Tensile circumferential stresses occur below the peg during the portion of the cycle when the peg is sheared away from the respective corner. These stresses are also lowered by lowering the coating yield stress. The zone of active plasticity and the region experiencing tensile circumferential stress overlap only in a small region at the peg corner, but their proximity suggests that the substrate is likely to be susceptible to fatigue cracks emerging from the corner downward at an angle somewhere in the range  $-135^\circ < \theta < -45^\circ$ . The direction of the emerging fatigue crack at the corner of a peg fretting an uncoated substrate has been studied using an elastic analysis in [4].

The role of ratchetting strains in fretting failure is not clearly understood, probably due in large part to the fact that predictive approaches have been based almost exclusively on elastic analyses (a typical approach is to use elastic effective strain amplitudes in a Coffin–Manson relationship [1]). However, there has been some work done to investigate the role of ratchetting strains on cyclic failure [13,14]. Johnson suggests two modes of failure: low cycle fatigue (LCF) (dominated by cyclic plastic strains) and ratchetting fatigue (RF) (dominated by ratchetting strains). Johnson and Kapoor summarize experimental evidence that supports the notion that the number of cycles to failure will show a different dependence on cyclic strain amplitude and ratchetting strain amplitude.

In other words, different Coffin–Manson relationships would be needed for LCF and RF, and failure will be governed by whichever predicts a shorter lifetime [13]. In this context, the implication of the results presented here is that increasing the average normal traction may

switch failure mechanisms from LCF to RF, and significantly alter the crack nucleation time scale. Furthermore, the transition point from LCF to RF would depend on the ratio  $\tau_y^f/\tau_y^s$ . As far as ratchetting failure is concerned, it remains to be resolved whether increasing  $\tau_y^f/\tau_y^s$  would have as strong an effect of lifetimes as implied in Fig. 8a and b. It would depend strongly on the magnitude of the average normal traction, unlike failure governed by cyclic plasticity.

The quantitative difference between the predictions from the two asymptotic formulations, uniform normal tractions and uniform normal displacements, is appreciable. The uniform normal displacements formulation predicts significantly more plasticity activity than the other formulation. Further modeling will be required before it is clear which of the two formulations is the more accurate. It is expected that the thickness of the coating will play a role in determining the plasticity activity in the substrate, as will any tendency of the coating to display cyclic strain hardening or softening.

### Acknowledgements

The authors are indebted to helpful discussions with A. G. Evans and to D. N. Hutchinson who carried out the comparisons of the asymptotic elastic stress fields with the full three-dimensional elastic fields. This work is supported in part by the Multi-University Research Initiative on 'High Cycle Fatigue', which is funded at Harvard by AFSOR under grant no. SA1542-22500 PG, and in part by the Division of Engineering and Applied Sciences, Harvard University.

### References

- [1] Waterhouse RB. Fretting fatigue. *Int Mater Rev* 1992;37:77–97.
- [2] Cowles BA. High cycle fatigue in aircraft gas turbines—an industrial perspective. *Int J Fracture* 1996;80:147–63.
- [3] Helmi Attia M, Waterhouse RB, editors. Standardization of fretting fatigue test methods and equipment STP 1159. Philadelphia, PA: ASTM.
- [4] Hills DA, Nowell D. *Mechanics of fretting fatigue*. Dordrecht: Kluwer Academic, 1994.
- [5] Ruiz C, Boddington PHB, Chen KC. An investigation of fatigue and fretting in a dovetail joint. *Exp Mech* 1984;24:208–17.
- [6] Szolwinski MP, Farris TN. Mechanics of fretting fatigue crack initiation. *Wear* 1996;198:193–207.
- [7] Giannakopoulos AE, Lindley TC, Suresh S. Aspects of equivalence between contact mechanics and fretting mechanics: theoretical connections and life prediction methodology for fretting fatigue. *Acta Materialia* (in press).
- [8] Giannakopoulos AE, Suresh S. A three-dimensional analysis of fretting fatigue. *Acta Materialia* 1997;46:177–92.
- [9] Timoshenko SP, Goodier JN. *Theory of elasticity*, 3rd ed. New York: McGraw-Hill, 1970.
- [10] Johnson KL. *Contact mechanics*. Cambridge: Cambridge University Press, 1985.
- [11] Anton DL, Guillemette R, Reynolds J, Lutian M. Fretting fatigue damage analysis in Ti-6Al-4 V. In: Gregory JK, Rack HJ, Eylon D, editors. *Surface performance of titanium*. The Mineral, Metals and Materials Society, 1997.
- [12] Sato K, Fujii H, Kodama S. Crack propagation behavior in fretting fatigue. *Wear* 1986;107:245–62.
- [13] Johnson KL. Contact mechanics and the wear of metals. *Wear* 1995;190:162–70.

- [14] Kapoor A. A re-evaluation of the life to rupture of ductile materials by cyclic plastic strain. *Fatigue Fract Engng Mater Struct* 1994;17:201–19.

# Similarities of stress concentrations in contact at round punches and fatigue at notches: implications to fretting fatigue crack initiation

A. E. GIANNAKOPOULOS, T. C. LINDLEY,<sup>1</sup> S. SURESH and C. CHENUT<sup>2</sup>

*Department of Materials Science and Engineering, Massachusetts Institute of Technology, Cambridge, MA 02139, USA, <sup>1</sup>Department of Materials, Imperial College of Science, Technology and Medicine, London SW7 2BP, UK, <sup>2</sup>Ecole Polytechnique, 91128 Palaiseau Cedex, France*

*Received in final form 18 March 2000*

**ABSTRACT** A linear elastic model of the stress concentration due to contact between a rounded flat punch and a homogeneous substrate is presented, with the aim of investigating fretting fatigue crack initiation in contacting parts of vibrating structures including turbine engines. The asymptotic forms for the stress fields in the vicinity of a rounded punch-on-flat substrate are derived for both normal and tangential loading, using both analytical and finite element methods. Under the action of the normal load,  $P$ , the ensuing contact is of width  $2b$  which includes an initial flat part of width  $2a$ . The asymptotic stress fields for the sharply rounded flat punch contact have certain similarities with the asymptotic stress fields around the tip of a blunt crack. The analysis showed that the maximum tensile stress, which occurs at the contact boundary due to tangential load  $Q$ , is proportional to a mode II stress intensity factor of a sharp punch divided by the square root of the additional contact length due to the roundness of the punch,  $Q/(\sqrt{(b-a)}\sqrt{\pi b})$ . The fretting fatigue crack initiation can then be investigated by relating the maximum tensile stress with the fatigue endurance stress. The result is analogous to that of Barsom and McNicol where the notched fatigue endurance stress was correlated with the stress intensity factor and the square root of the notch-tip radius. The proposed methodology establishes a 'notch analogue' by making a connection between fretting fatigue at a rounded punch/flat contact and crack initiation at a notch tip and uses fracture mechanics concepts. Conditions of validity of the present model are established both to avoid yielding and to account for the finite thickness of the substrate. The predictions of the model are compared with fretting fatigue experiments on Ti-6Al-4V and shown to be in good agreement.

**Keywords** contact mechanics; round punches; notch fatigue; fretting fatigue; crack initiation.

## NOMENCLATURE

- $a$  = initially flat part of a half contact
- $A$  = constant used in the limit of elastic analysis
- $A^*, \rho_0$  = constants used in the asymptotic analysis
- $b$  = width of half contact
- $c$  = half stick zone
- $D/2$  = curvature radius of the parabolically rounded pads
- $E^*$  = composite contact stiffness
- $E_p, E_s$  = Young's moduli of the punch and the substrate, respectively
- $K_I, K_{II}$  = mode I and II stress intensity factors
- $p(x)$  = normal contact pressure
- $\tilde{p}(\alpha)$  = Fourier cosine transform of the contact pressure
- $P$  = normal line load
- $q(x)$  = shear contact pressure
- $Q$  = tangential line load
- $r, \theta$  = polar coordinates
- $R$  = stress ratio

- $t$  = specimen half-thickness  
 $w$  = specimen width  
 $x, y$  = Cartesian coordinates  
 $x^*, y^*$  = transformed Cartesian coordinates  
 $\mu$  = kinetic friction coefficient of the contacting surface  
 $\nu_p, \nu_s$  = Poisson's ratios of the punch and the substrate, respectively  
 $\sigma_{xx}^Q$  = stress in the  $x$ -direction due to shear force  
 $\sigma_{ij}^P$  = asymptotic stresses due to normal load  
 $\sigma_{ij}^Q$  = asymptotic stresses due to tangential load  
 $\sigma_b$  = bulk stress  
 $\sigma_e$  = Mises effective stress  
 $\sigma_{end}$  = fatigue endurance stress  
 $\sigma_1$  = maximum tensile stress  
 $\phi, \phi_0$  = coordinate transformation variables

## INTRODUCTION

The useful fatigue life of mechanical components is determined by the sum of the elapsed load cycles required to initiate a fatigue crack and to propagate the crack from subcritical size to critical dimensions. Understanding fatigue crack initiation and fatigue crack propagation is important from a scientific as well as a practical point of view. Barsom and McNicol<sup>1</sup> studied the issue of fatigue crack initiation life by testing HY-130 steel specimens having widely varying notch acuities. They obtained endurance data in the range of  $10^3$ – $10^6$  cycles and analysed them using both linear elastic fracture mechanics and the theory of stress concentrations in notched specimens. Their results showed that the number of elapsed load cycles required to initiate a fatigue crack in a notched specimen is related to the ratio of the stress intensity factor range to the square root of the notch-tip radius. Barsom and McNicol<sup>1</sup> subsequently found that fatigue crack initiation can be expressed in terms of the maximum endurance stress of the unnotched specimen using the stress-field characteristics that were determined by Creager and Paris<sup>2</sup> for a blunt crack. Later, other investigators confirmed the above findings with other types of steel, e.g. Barsom and Rolfe,<sup>3</sup> while Yoder *et al.*<sup>4</sup> examined the resistance to the fatigue crack initiation in Ti-6Al-4V, using blunt key-hole-notched and sharp V-notched compact specimens.

Fretting fatigue refers to damage caused by localized relative motion between contact surfaces on adjacent components, of which at least one component is under oscillatory tangential load and may produce premature surface cracking and failure. Of particular interest at the present time is the fretting fatigue failure of turbine engine disks and blades in the dovetail attachment region. Turbine engine blade roots experience fretting in a flat-on-flat contact region which can be modelled as a rounded punch-on-flat configuration. In the limit case

of a sharp cornered punch, a quantitative equivalence between the asymptotic stress and strain fields derived by classical analysis of sharp-edged contacts and crack-tip fields predicted from fracture mechanics methods was demonstrated by Giannakopoulos *et al.*<sup>5</sup> and termed 'crack analogue'. The conditions governing the validity of the 'crack analogue' model were established by employing the small-scale yielding concepts routinely used in linear elastic fracture mechanics. Because contact between the punch and the substrate implicitly introduces a fictitious crack length scale, the problems associated with 'small fatigue cracks' can be circumvented.

In this work, it is shown that the analysis of a flat-ended contact with rounded edges leads to the extension of the 'crack analogue' to the 'notch analogue'. In this approach, the maximum tensile stress is related to the ratio of the stress intensity factor of the sharp punch divided by the square root of a characteristic length. The important question that arises is:

- How can the maximum tensile stress be used to obtain critical loading conditions for fretting fatigue crack initiation?

We addressed this question in this work by examining the following issues.

- Evaluation of the stress fields close to the contact edges of a rounded flat punch on a substrate.
- Identification of the similarities and differences between fracture mechanics and contact mechanics regarding the 'notch analogue'.
- Derivation of the characteristic length necessary to establish the notch analogue and its relation to the roundness of the edges.
- Connection between the punch fretting fatigue test and the plain fatigue test of a smooth specimen of the same material.

- Evaluation of the ratio of fretted and unfretted fatigue strength, also called 'knockdown factor'.

This paper is arranged as follows. In the next section, we address the theoretical questions of the stress fields due to normal and tangential loading of a two-dimensional flat punch with equally rounded corners. The maximum tensile stress in the substrate is derived together with the asymptotic stress fields around the edges. Next, we discuss the limits of the notch analogue theory and in particular the applicability of the linear elastic assumption and the influence of the finite thickness of the substrate. The validation of the theoretical predictions is given in a later section, where the similarities and differences between the rounded punch and the blunt crack asymptotic solutions are discussed. We continue with the verification of the model using available experimental data for fretting fatigue initiation in Ti-6Al-4V, an alloy widely used for aircraft engine and airframe components. Finally, we conclude with the summary of the proposed methodology and its limitations.

## MECHANICS OF THE LINEAR ELASTIC ROUNDED PUNCH-ON-FLAT CONTACT

The similarity between the asymptotic stress fields around the contact edges of a flat punch with rounded corners and the asymptotic stress fields around a stationary crack with a blunt tip is demonstrated in this section for the cases of two-dimensional plane stress or plane strain.

The geometry of the indenter is shown schematically in Fig. 1. The punch consists of a flat part ( $y=0$ ,  $-a \leq x \leq a$ ) and two equal parabolic parts of curvature radius  $D/2$ . The parabolically rounded pads connect continuously with the flat part. The pad is loaded first with a normal line load  $P$  and subsequently with a tangential line load  $Q$ .

Under the influence of the normal load, the contact expands outside the initially flat part  $2a$  to a width of  $2b$

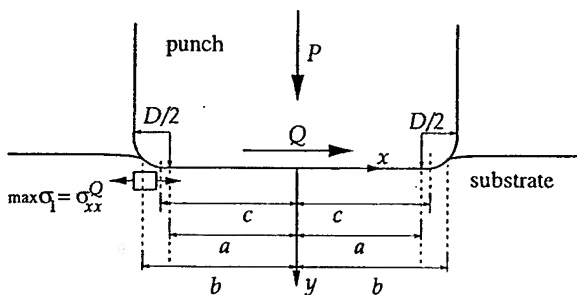


Fig. 1 Geometry of the indenter, coordinates, loading and important geometric lengths. The location of the maximum tensile stress due to tangential load is also indicated

with  $b > a$ . Because this type of contact is incomplete, the contact pressure falls continuously to zero, and the square root stress singularity, characteristic of the sharp edge punch, disappears.

Assuming that the punch and the substrate are isotropic and linear elastic, the measure of the composite contact stiffness is given by

$$E^* = \left( \frac{1 - \nu_p^2}{E_p} + \frac{1 - \nu_s^2}{E_s} \right)^{-1} \quad (1)$$

where  $E_p$ ,  $E_s$  are the Young's moduli, and  $\nu_p$ ,  $\nu_s$  are the Poisson's ratios of the punch and substrate, respectively. In the following, the elastic mismatch of the contacting bodies will be accounted for in Eq. (1). Such an approach is adequate provided that the second Dundurs' parameter is approximately zero.

## Basic contact mechanics results

### Normal contact

The normal line load,  $P$ , results in a contact pressure distribution,  $p(x)$ ,  $-b \leq x \leq b$ . At one extreme,  $a \rightarrow 0$ , the contact pressure is given by the cylinder-on-flat solution

$$p(x) = \frac{2P}{\pi b} \sqrt{1 - (x/b)^2}; \quad |x| \leq b \quad (2)$$

For the other extreme, if  $D \rightarrow 0$  and therefore  $b \rightarrow a$ , the contact pressure is given by the flat-on-flat solution

$$p(x) = \frac{P}{\pi \sqrt{1 - (x/b)^2}}; \quad |x| \leq b \quad (3)$$

The contact pressure of a rounded flat punch on a semi-infinite substrate was given in closed form by Ciavarella *et al.*<sup>6</sup>

$$\begin{aligned} \frac{\pi b}{2P} p(\phi) &= \frac{1}{\pi - 2\phi_0 - \sin(2\phi_0)} \\ &\times \left[ (\pi - 2\phi_0) \cos \phi + \ln \left( \left| \frac{\sin(\phi + \phi_0)}{\sin(\phi - \phi_0)} \right| \right)^{\sin \phi} \right. \\ &\times \left. \left| \tan \frac{\phi + \phi_0}{2} \tan \frac{\phi - \phi_0}{2} \right|^{\sin \phi_0} \right]; \quad |x| \leq b \end{aligned} \quad (4)$$

where

$$\sin \phi = x/b; \quad \sin \phi_0 = a/b \quad (5)$$

The relation between the contact half-width  $b$  and the normal line load  $P$  is<sup>6</sup>

$$\frac{PD}{a^2 E^*} = \frac{\pi - 2\phi_0}{2 \sin^2 \phi_0} - \cot \phi_0 \quad (6)$$

### Tangential loading

It is now assumed that after the application of the normal line load  $P$ , a monotonically increasing tangential line force  $Q$  is applied to the punch, keeping the normal load constant, and  $Q < \mu P$ , where  $\mu$  is the kinetic friction coefficient of the contacting surfaces. Global sliding of the punch is expected, if  $Q = \mu P$ , and stick-slip conditions, if  $Q < \mu P$ . The analysis for elastically similar punch and substrate has been performed by Ciavarella *et al.*<sup>7</sup> and is summarized below. For elastically dissimilar punch and substrate, the following results would be approximate.

Upon applying the tangential line load  $Q$ , the initial stick zone extends along the entire contact width ( $|x| \leq b$ ). Further increase of  $Q$  results in a slipping region that starts at the contact boundary,  $x = \pm b$ , and spreads inwards up to  $x = \pm c$ , where  $c < b$ .

In the limit of a sharp flat punch ( $D \rightarrow 0$ ,  $b \rightarrow a$ ), no partial slip solution is possible when the stick zone ( $y = 0$ ,  $|x| \leq c$ ) is contained entirely within the initial flat part of the punch. Therefore, the stick zone cannot be smaller than the initial flat part of the contact, i.e.  $c \geq a$ . The shear contact traction is

$$q(x) = \mu p(x); \quad c \leq |x| \leq b \quad (7a)$$

$$q(x) = \mu[p(x) + q^*(x)]; \quad |x| \leq c \quad (7b)$$

where  $q^*(x)$  has a similar form to  $p$  in Eq. (2), provided that Eq. (3) is replaced by  $\sin \phi = x/c$  and  $\sin \phi_0 = a/c$ .

The relation between the applied tangential line force,  $Q$ , and the stick zone,  $c$ , is<sup>7</sup>

$$\frac{Q}{\mu P} = 1 - \left(\frac{c}{b}\right)^2 \frac{\pi - 2\theta_0 - \sin(2\theta_0)}{\pi - 2\phi_0 - \sin(2\phi_0)}; \quad c > a \quad (8a)$$

$$\frac{Q}{\mu P} = 1; \quad c \leq a \quad (\sin \theta_0 = a/c, \sin \phi_0 = a/b) \quad (8b)$$

Note that in the limit,  $a \rightarrow 0$ , the classic result of cylinder-on-flat case is recovered

$$\frac{Q}{\mu P} = 1 - \left(\frac{c}{b}\right)^2 \quad (9)$$

The above results can be extended to the case of a cyclic tangential loading where the normal load is kept constant.

In the present analysis, adhesion between the contacting bodies is assumed to be weak. Therefore, slip at the rounded parts of the punch is possible, as described by Eq. (8). If strong adhesion is present, then the stresses will be square-root singular throughout the contact region and slip will be prevented in the rounded parts of the punch.

### Maximum tensile stress in the substrate

The strength of the contact may be quantified by the maximum tensile stress that develops at maximum tangential load. In this respect, the following observations can be made. First, the maximum tensile stress develops always at the contact boundary ( $x = \pm b$ ,  $y = 0$ ). Second, the two-dimensional normal contact of a semi-infinite substrate does not produce any tensile stress anywhere in the substrate. Third, only the tangential load produces tensile stress in the substrate, as indicated in Fig. 1.

If  $q(x)$  is the distribution of shear tractions at the contact region due to tangential line load, then the maximum tension is given by<sup>8</sup>

$$\max \sigma_{xx} = \sigma_{xx}^Q = \frac{2}{\pi} \int_{-b}^b \frac{q(s)}{b-s} ds \quad (10a)$$

In the sharp punch limit, we use the coordinate transformation, Eq. (5), into Eq. (10a) to obtain

$$\sigma_{xx}^Q = \frac{2Q}{\pi P} \int_{-\pi/2}^{\pi/2} \frac{p(\phi)}{1 - \sin(\phi)} \cos \phi d\phi \quad (10b)$$

Inserting Eq. (4) into Eq. (10b), we calculated  $\sigma_{xx}^Q$  as a function of  $a/b$  and the results are shown in Table 1. In the limit of  $b \rightarrow a$ , we find

$$\sigma_{xx}^Q = \frac{1.926}{\sqrt{b-a}} \frac{Q}{\sqrt{\pi b}} \quad (11)$$

### Asymptotic contact pressure for the sharp cornered punch

Of particular importance is the limit case of the sharp cornered punch on flat substrate ( $D \rightarrow 0$ ,  $b \rightarrow a$ ). Goodier and Loutzenheiser<sup>9</sup> have shown that in this limit case

Table 1 Normalized tensile stress due to tangential line load  $Q$  as a function of  $a/b$

$a/b$	$\sigma_{xx}^Q b/Q$	$a/b$	$\sigma_{xx}^Q b/Q$
0.0	4/π	0.91	3.586
0.1	1.313	0.92	3.796
0.2	1.364	0.93	4.053
0.3	1.462	0.94	4.365
0.4	1.514	0.91	4.775
0.5	1.628	0.96	5.335
0.6	1.789	0.97	6.133
0.7	2.031	0.98	7.550
0.8	2.447	0.99	10.87
0.9	3.407	0.9975	21.15
		0.9995	76.55

The results are valid for  $Q \rightarrow \mu P$  and/or  $b \rightarrow a$ .

the contact pressure has two maxima which are given by

$$\max p(x) = \frac{7.182\sqrt{2}}{8\pi} \frac{P}{\sqrt{b(b-a)}} \quad \text{at } x = \pm [b - 0.695(b-a)] \quad (12)$$

as indicated in Fig. 2. The contact pressure is zero at  $x = \pm b$  and has a relative minimum at  $x = 0$

$$\min p(x=0) = \frac{P}{\pi b} \quad (13)$$

Using the Goodier and Loutzenheiser approximation, we obtain the asymptotic shear contact traction

$$q(x) = \frac{Q}{P} p(x); \quad |x| \leq b \quad (14)$$

### Asymptotic stress field around the edges of a sharp cornered punch

In the limiting case of a sharp flat punch ( $D \rightarrow 0$ ,  $b \rightarrow a$ ), the stress field can be approximated as follows. Very close to the rounded edge, the punch behaves as a parabolic punch, therefore the stresses should vary as  $\sqrt{b-x}$ , whereas further away, they should vary as  $1/\sqrt{b-x}$ . A new coordinate system  $(x^*, y^*)$  is positioned at the edge of the contact, as shown in Fig. 3. Without loss of generality, the coordinates  $(x, y)$  and  $(x^*, y^*)$  are related as

$$y^* = y; \quad x^* = -x + b \quad (15)$$

Let  $r$  and  $\theta$  be the polar coordinates attached to the new system, as shown in Fig. 3, so that

$$x^* = r \cos \theta; \quad y^* = r \sin \theta \quad (16)$$

Regarding normal loading only, we performed a formal expansion of the stress fields in the region  $0 < r < (b-a)$

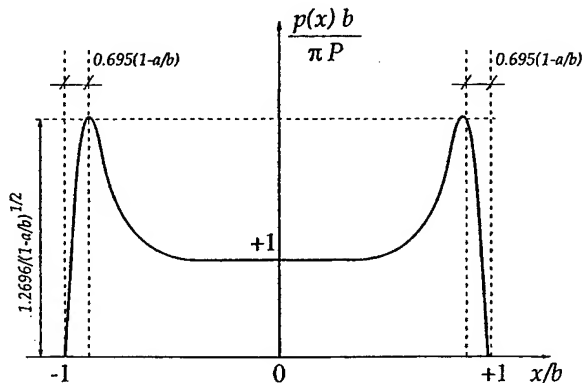


Fig. 2 Contact pressure distribution for a round cornered punch in the limiting case  $b \rightarrow a$ .<sup>9</sup>

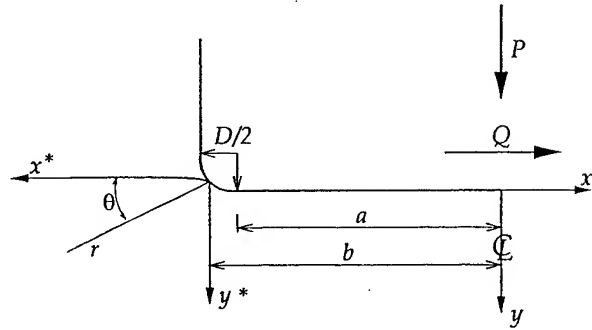


Fig. 3 The new coordinates  $(x^*, y^*)$  used in the asymptotic expansion of the stress fields close to the contact edges.

and  $0 \leq \theta \leq \pi$ , and obtained

$$\begin{pmatrix} \sigma_{rr}^P(r, \theta) \\ \sigma_{\theta\theta}^P(r, \theta) \\ \sigma_{r\theta}^P(r, \theta) \end{pmatrix} = -\frac{P}{\sqrt{\pi b}} \frac{r^2}{(r^2 + r_0^2)} \frac{A^*}{\sqrt{r}} \begin{pmatrix} \sin \frac{3\theta}{2} + 5 \sin \frac{\theta}{2} \\ -\sin \frac{3\theta}{2} + 3 \sin \frac{\theta}{2} \\ \cos \frac{3\theta}{2} - \cos \frac{\theta}{2} \end{pmatrix} - \frac{P}{\sqrt{\pi b}} \frac{r^2}{(r^2 + r_0^2)} \frac{A^* r_0}{r \sqrt{r}} \begin{pmatrix} \sin \frac{5\theta}{2} + 3 \sin \frac{\theta}{2} \\ -\sin \frac{5\theta}{2} + 5 \sin \frac{\theta}{2} \\ \cos \frac{5\theta}{2} - \cos \frac{\theta}{2} \end{pmatrix} \quad (17)$$

where  $r_0$  is a length and  $A^*$  is a free parameter that must be chosen to optimize the asymptotic amplitudes. The length  $r_0$  is introduced so that for  $r_0 \rightarrow 0$ , the sharp punch asymptotic solution is retrieved, in accord with the crack analogue model.<sup>5</sup> On the other hand, for large values of  $r_0$ , Eq. (17) gives the smooth punch solution asymptote. To optimize the expansion, we fitted the above result to the actual maximum contact pressure given by Eq. (12) and obtained the values

$$A^* = 0.1482; \quad r_0 = 0.695 (b-a) \quad (18)$$

Assuming tangential loading only, with the tangential load being positive as indicated in Fig. 3, a formal expansion of the stress fields in the region  $0 < r < (b-a)$



and  $0 \leq \theta \leq \pi$ , gives

$$\begin{pmatrix} \sigma_{rr}^Q(r, \theta) \\ \sigma_{\theta\theta}^Q(r, \theta) \\ \sigma_{r\theta}^Q(r, \theta) \end{pmatrix} = -\frac{Q}{\sqrt{\pi b}} \frac{r^2}{(r^2 + r_0^2)} \frac{A^*}{\sqrt{r}} \begin{pmatrix} -3 \cos \frac{3\theta}{2} - 5 \cos \frac{\theta}{2} \\ 3 \cos \frac{3\theta}{2} - 3 \cos \frac{\theta}{2} \\ 3 \sin \frac{3\theta}{2} - \sin \frac{\theta}{2} \end{pmatrix} - \frac{Q}{\sqrt{\pi b}} \frac{r^2}{(r^2 + r_0^2)} \frac{A^* r_0}{r\sqrt{r}} \begin{pmatrix} 5 \cos \frac{5\theta}{2} + 3 \cos \frac{\theta}{2} \\ -5 \cos \frac{5\theta}{2} + 5 \cos \frac{\theta}{2} \\ -5 \sin \frac{5\theta}{2} + \sin \frac{\theta}{2} \end{pmatrix} \quad (19)$$

Full finite element analysis showed that the stress expansions described by Eqs (17) and (19) are within less than 11% inside a region of  $0 < r < b/5$  and  $0.9 < a/b < 1.0$ .<sup>10</sup> For  $b \rightarrow a$ , the singular part of the stresses, associated with the crack analogue structure of the sharp punch solution,<sup>5</sup> extends beyond the region of validity of the non-singular part of the stresses associated with the rounded part of the punch.

The asymptotic Eqs (17) and (19) ignore a possible constant stress that runs parallel to the surface (the T-stress in the fracture mechanics terminology). Such stress can be found from the general two-dimensional contact analysis<sup>8</sup> from

$$\sigma_{xx}^Q = \frac{2}{\pi} \int_0^b \frac{\sigma_{x\theta}^Q(s, \pi)}{s} ds \quad (20)$$

Inserting the shear traction  $\sigma_{x\theta}^Q(s, \pi)$  from Eq. (19) into Eq. (20), we obtain

$$\sigma_{xx}^Q = \frac{8QA^*\sqrt{2}}{\pi\sqrt{\pi b r_0}} [\arctan(\sqrt{2b/r_0} + 1) + \arctan(\sqrt{2b/r_0} - 1)] \quad (21a)$$

and for  $b \gg r_0$ ,

$$\sigma_{xx}^Q = \frac{2.011}{\sqrt{b-a}} \frac{Q}{\sqrt{\pi b}} \quad (21b)$$

which is 4.4% higher than the exact result given by Eq. (11). Therefore, it can be concluded that the asymptotic expansions given by Eqs (17) and (19) are fairly good.

## RANGE OF APPLICABILITY OF THE LINEAR ELASTIC ROUNDED PUNCH-ON-FLAT CONTACT ANALYSIS

### Limits of the linear elastic analysis

The previous analysis was based on linear elasticity, therefore it is important to investigate the limit of elastic behaviour which can be achieved under combined normal and tangential load and which is influenced by the friction coefficient  $\mu$  and the geometric ratio  $a/b$ . The most general case is complex. However, for  $a/b > 0.3$ ,  $\mu > 0.25$  and  $Q \rightarrow \mu P$ , a simple solution for the maximum Mises effective stress can be found. Under the above conditions, the maximum effective stress,  $\max \sigma_e$ , occurs at the contact boundary ( $y=0$ ,  $x=\pm b$ ) and is given by

$$\max \sigma_e = A \sigma_{xx}^Q \quad (22a)$$

$$A = 1 \text{ (plane stress)}$$

$$A = \sqrt{[1 + \nu_s^2 + (1 - \nu_s)^2]/2} \text{ (plane strain)} \quad (22b)$$

where  $\sigma_{xx}^Q$  can be found from Eq. (11) or, equivalently, from Table 1. Obviously, yielding of the substrate is avoided if  $\max \sigma_e \leq \sigma_y$ , where  $\sigma_y$  is the yield strength of the substrate. Here it is implicitly assumed that the punch will withstand plastic yielding.

In the limit of a cylinder-on-flat case,  $a \rightarrow 0$ , the regime of elasticity is given in terms of the loading as

$$\frac{P}{b\sigma_y} \leq \frac{\pi}{4\mu A}; \quad Q \rightarrow \mu P \quad (23)$$

In the limit of a sharp punch-on-flat case,  $b \rightarrow a$ , the regime of elasticity is given in terms of the loading as

$$\frac{P}{b\sigma_y} \leq \frac{1.926}{\mu A \sqrt{1 - a/b}}; \quad Q \rightarrow \mu P \quad (24)$$

### Influence of the finite thickness of the substrate

Most fretting fatigue experiments employ a pair of identical fretting pads loaded symmetrically against a specimen of finite thickness by a normal force and an oscillatory bulk stress. The contact pressure is close to that predicted by the half-plane solution, if the specimen thickness is more than about five times the contact zone, whereas for substrate thickness that is less than  $5b$ , the contact pressure become uniform,  $p(x) \approx P/(2b)$ .<sup>8</sup> In contrast to the contact pressure, the axial stresses in the substrate of finite thickness undergo more drastic changes, the most important of which is that they become tensile at the surface, outside the contact zone ( $y=0$ ,  $|x| > b$ ). This deviation from the semi-infinite substrate is due only to the normal loading, the tangential

loading produces stresses that are close to those found from the solution of the semi-infinite substrate.<sup>11</sup> It can be concluded that the maximum tensile stress needs to be corrected by taking into account the finite thickness of the substrate. The correction stress is due to the normal load,  $\sigma_{xx}^P$ , at  $(x = \pm b, y = 0)$ . In the elastic regime, superposition gives the maximum tensile stress as

$$\max \sigma_1 = \rho_{xx}^Q + \sigma_{xx}^P \quad (25)$$

where  $\sigma_{xx}^P$  depends on the thickness of the substrate and the normal load, and is given in Appendix A, Table A1.

## APPLICATIONS TO FRETTING FATIGUE CRACK INITIATION

### Similarity of rounded punch and blunt crack asymptotic solutions

The asymptotic stress solution around the tip of a circularly rounded crack-tip of radius  $\rho$  was found by Creager and Paris.<sup>2</sup> It contains the regular (singular) sharp crack solution and an additional (non-singular) part that depends upon the ratio  $\rho/r$ . The radial variation of the stresses of the rounded punch-on-flat contact [Eqs (17), (19)] is similar to that of the blunt crack for mode I and II crack opening. However, the angular variation of the non-singular stress fields of the rounded punch-on-flat contact differ from that of the blunt crack.

For a blunt crack under mode I loading, the maximum tensile stress is<sup>2</sup>

$$\max \sigma_1 = \sigma_{yy}(r = \rho/2, \theta = 0) = 2 \frac{K_I}{\sqrt{\pi\rho}} \quad (26)$$

This form was used by Barsom and McNicol<sup>1</sup> to examine the effect of the stress concentration on the fatigue crack initiation at the notch-tip. In the contact problem at hand, the maximum tensile stress for a sharp-edged punch is given by Eq. (11). Previous analysis<sup>5</sup> has shown that for a perfectly sharp punch, a mode II stress intensity factor,  $K_{II} = Q/\sqrt{\pi b}$ , can characterize the strength of the singularity close to the contact boundary. Then, for the sharply rounded punch Eq. (11) becomes

$$\max \sigma_1 = \sigma_{xx}^Q = 3.414 \frac{K_{II}}{\sqrt{\pi(b-a)}} \quad (27)$$

The similarity of Eqs (26) and (27) is obvious, provided the 'notch radius' is recognized to be  $(b-a)$ . It should be emphasized that the link between the contact mechanics of a rounded corner and fatigue at a notch is based here on fracture mechanics concepts rather than stress-based criteria.

In the most general case, the total maximum tensile stress,  $\max \sigma_1^{\text{tot}}$ , can be found by superposition of the

maximum tensile stresses due to the tangential load,  $\sigma_{xx}^Q$ , due to the normal load,  $\sigma_{xx}^P$ , and due to the bulk stress,  $\max \sigma_b$ . Superposition of the uniform bulk stress,  $\max \sigma_b$ , to the contact stress is a good approximation for the actual tangential stresses at the edge of the contact.<sup>12</sup> We propose that the condition for fretting fatigue crack initiation is when the total maximum tensile stress which develops at the extremity of the contact pad corner becomes equal to the endurance stress,  $\sigma_{\text{end}}$ , of the unfretted specimen for the same material and load ratio,  $R$ .

$$\sigma_{\text{end}}(R) = \max \sigma_1^{\text{tot}} = \sigma_{xx}^Q + \sigma_{xx}^P + \max \sigma_b \quad (28)$$

In this work we present fracture mechanics methodology to predict crack initiation at a rounded punch corner. A life prediction methodology for the subsequent development of the slant crack and the normal crack can be found using the concepts developed previously for the crack analogue.<sup>5</sup> Detailed expressions describing the subsequent stages of the crack development (i.e. direction and size of the slant crack and number of cycles spent propagating the crack up to complete failure) were addressed and can be found in Ref. [5]. This type of analysis is possible because the range of the singular stress fields (crack analogue) extends further than the range of the non-singular stress fields (notch analogue), as discussed in a previous section.

### Experimental verification

We have found few fretting experiments that examine systematically the roundness of sharp punch-on-flat contact. Recently, Hutson and co-workers<sup>13,14</sup> developed a fretting fatigue test to simulate the fretting fatigue crack initiation that occurs in turbine engine blade attachments. Their test system, shown schematically in Fig. 4, employs a flat-on-flat contact with blending radii which

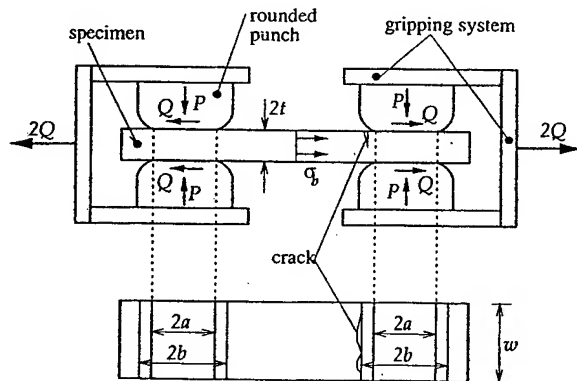


Fig. 4 Schematic of the loading and gripping system of the fretting fatigue test. The apparatus produces two nominally identical regions of fretting for each test specimen.<sup>13</sup>

reproduce the nominal levels of normal and bulk stresses present in dovetail joints. A gripping system was used to allow control and measurement of critical fretting parameters through instrumented clamping of the punches. Each of the two grips was fitted with removable fretting pads to facilitate control of the contact conditions. The axial fretting fatigue specimen was sandwiched in the grips and both ends were given identical contact conditions. Tests were conducted at 300 and 400 Hz in laboratory air environment. The bulk stress,  $\sigma_b$ , and the tangential line load,  $Q$ , were oscillatory, whereas the clamping (normal) line load,  $P$ , remained constant. Symmetry in the apparatus provided a specimen which failed on one end, leaving the other end with a surface scar. Testing was conducted using the stepped loading approach developed by Maxwell and Nicholas,<sup>15</sup> where the axial bulk stress was set below the anticipated endurance stress and was raised gradually by 2–5%, each resulting intermediate loading run up to  $10^7$  cycles and the process repeated until specimen failure. A fatigue endurance stress (noted as Goodman stress in Hutson *et al.*<sup>13</sup>) was defined as the maximum bulk stress corresponding to a survival life of  $10^7$  cycles.

Both the axial specimens and the contacting part of the fretting pads used by Hutson *et al.*<sup>13</sup> were machined from vacuum-annealed and hot-rolled Ti-6Al-4V bar stock. The material was stress relieved by vacuum heat treatment at 705 °C for 2 h, static argon cooled to below 149 °C, vacuum-annealed at 549 °C for 2 h and static argon cooled to less than 549 °C. This treatment produced a microstructure of 90%  $\alpha$ -phase with 10% intergranular  $\beta$ -phase. The balance of the fretting pads was machined from AMS 4928 Ti-6Al-4V with TE01 heat treatment. All specimens and fretting pads were low stress ground to a RMS 16 surface finish.

The geometry of the specimens and the pads, as well as the loading condition for the tests performed by Hutson and co-workers<sup>13,14</sup> are given in Table 2a and b for  $R = 0.1$  and  $0.5$ , respectively. For the purpose of our analysis, typical material properties of Ti-6Al-4V were selected:  $E_s = 115$  GPa,  $\nu_s = 0.3$ ,  $\sigma_y = 960$  MPa and  $\mu = 0.7$ . The line loads  $P$  and  $Q$  were calculated from the total clamping force and the width of the specimen,  $w$ . In the test configuration shown in Fig. 4, overall equilibrium relates the tangential line load  $Q$  and the bulk stress  $\sigma_b$  as

$$Q = t\sigma_b \quad (29)$$

In this case the tangential load  $Q$  and bulk stress  $\sigma_b$  are in phase, therefore the load ratio is

$$R = \min \sigma_b / \max \sigma_b = \min Q / \max Q \quad (30)$$

We used the experimental input of Table 2a and b with Eq. (6) to compute the contact width  $2b$ . The

contact width was used with Table 1 to compute  $\sigma_{xx}^Q$ . The additional tension due to finite thickness,  $\sigma_{xx}^P$ , was obtained from Table 1. The total maximum tensile stress was found from superposition,

$$\max \sigma_1^{\text{tot}} = \sigma_{xx}^Q + \sigma_{xx}^P + \max \sigma_b$$

The results of our analysis are presented in Table 3a and b for  $R = 0.1$  and  $0.5$ , respectively. The average value for the total maximum tensile stress is  $\langle \max \sigma_1^{\text{tot}} \rangle = 539$  and  $792$  MPa for  $R = 0.1$  and  $0.5$  MPa, respectively. These values compare well with the corresponding experimental values of the endurance stress,  $\sigma_{\text{end}} = 600$  and  $825$  MPa for  $R = 0.1$  and  $0.5$ , respectively. Therefore, the maximum tensile stress which develops at the extremity of the contact punch corner can predict quite well the endurance stress of the unfretted specimen (for the same material and load ratio) and can be used as an indicator of fretting fatigue crack initiation for the punch-on-flat geometry.

The analysis supports a fretting fatigue crack initiation methodology similar to the one proposed by Barsom and McNicol<sup>1</sup> for fatigue crack initiation at notches. Equation (28) suggests a reduction factor due to fretting by rounded punches

$$\text{Reduction factor} = 1 + (\sigma_{xx}^Q + \sigma_{xx}^P)t / \max Q \quad (31)$$

Furthermore, it can be noted that because  $\sigma_{xx}^Q$  and  $\sigma_b$  are proportional to  $Q$  (but not to  $P$ ) and  $\sigma_{xx}^P$  is proportional to  $P$ , it is expected that for low normal loads, high bulk stress (thus, high tangential loads) and thicker specimens, the endurance stress (also called Goodman stress in this case) will be unaffected by  $P$ . This theoretical result was clearly observed and noted in the experimental work of Hutson *et al.*<sup>13</sup>

## CONCLUSIONS

In the present work, we developed an analytical model for fretting fatigue at a rounded corner punch contacting a substrate and an analogy made with fatigue crack initiation at a notch tip. We examined the similarities and differences between stress concentrations at the edge of sharply rounded punch-on-flat contact and the tip of a blunt crack. The asymptotic stress fields and the maximum tensile stress were found explicitly as functions of the applied loads and punch geometry. The maximum tensile stress was used to develop a 'notch analogue' approach aimed at predicting fretting fatigue crack initiation. The notch analogue methodology provides a direct connection between the round cornered flat punch fretting fatigue and the plain fatigue crack initiation of a smooth specimen of the same material. The ratio of the fatigue strength of the fretted and unfretted specimen

Table 2 Geometry and loading used in the fretting fatigue experiments

(a)

Case	$a$ (mm)	$D/2$ (mm)	$t$ (mm)	$w$ (mm)	$P$ (kN/mm)	$Q$ (kN/mm)	$\sigma_b$ (MPa)	$R$
1	5.853	0.508	0.943	9.910	3.532	0.156	165	0.1
2	12.17	0.508	1.005	10.15	3.448	0.218	216	0.1
3	3.150	3.175	0.980	9.990	3.504	0.156	159	0.1
4	5.840	0.508	0.925	9.990	3.707	0.185	200	0.1
10	12.44	0.508	0.920	9.930	2.115	0.172	187	0.1
11	3.169	3.175	0.945	9.940	2.113	0.136	143	0.1
12	9.528	3.175	1.005	10.18	2.063	0.183	182	0.1
19	12.46	0.508	0.945	9.910	3.532	0.256	272	0.1
20	11.09	0.508	0.950	9.920	2.117	0.122	128	0.1
24	3.153	3.175	1.065	10.15	3.448	0.198	186	0.1
25	3.152	3.175	1.035	10.31	3.395	0.202	195	0.1

(b)

Case	$a$ (mm)	$D/2$ (mm)	$t$ (mm)	$w$ (mm)	$P$ (kN/mm)	$Q$ (kN/mm)	$\sigma_b$ (MPa)	$R$
5	5.841	0.508	0.945	9.930	3.525	0.265	280	0.5
6	12.17	0.508	0.995	10.15	3.448	0.328	330	0.5
7	3.199	3.175	1.005	10.16	3.449	0.251	250	0.5
8	5.840	0.508	0.920	9.910	5.520	0.276	300	0.5
13	9.525	3.175	0.930	9.960	3.705	0.185	200	0.5
14	12.17	0.508	0.910	9.940	2.113	0.287	315	0.5
15	3.175	3.175	0.890	9.920	2.117	0.232	260	0.5
16	11.10	3.175	0.940	9.910	2.119	0.320	340	0.5
17	3.197	3.175	1.015	10.01	2.597	0.267	263	0.5
18	9.507	3.175	1.000	10.15	2.069	0.350	350	0.5
21	12.46	0.508	0.870	9.950	3.518	0.313	359	0.5
22	12.46	0.508	0.943	9.910	2.119	0.358	380	0.5
23	3.175	3.175	0.950	9.920	3.528	0.253	266	0.5
26	3.200	3.175	1.015	10.00	2.600	0.292	288	0.5
30	3.197	3.175	0.990	10.01	2.297	0.238	240	0.5

Reference: Hutson *et al.*<sup>13,14</sup>

Configuration: Fig. 4.

Material: Ti-6Al-4V (both pad and substrate).

Properties:  $E^* = 64.8$  GPa,  $\mu = 0.7$ ,  $\sigma_{\text{end}} = 600$  MPa ( $R = 0.1$ ) and 825 MPa ( $R = 0.5$ ).

(the reduction factor) can be predicted from the derived analytic results.

Two important limits of applicability of the rounded corner punch analysis were considered: the onset of plasticity and the influence of the finite thickness of the substrate. Other possible effects, e.g. the contact surface asperities, geometric imperfectness of the punch, load waveform and frequency, as well as material inhomogeneity and anisotropy, were not examined in this work. Subsequently, the similarity of the rounded flat punch and the crack-notch asymptotic solutions was discussed. The experimental results quoted in the literature have been used to experimentally verify the proposed methodology.

The basic formula that relates the stress concentration with the stress intensity factor is similar in both contact

mechanics and fracture mechanics contexts. It is then concluded that crack initiation in fretting fatigue at a sharp punch-on-flat contact can be modelled with the 'notch analogue' method, by testing punch configurations of different radii and evaluating the corresponding stress concentration using the present analysis. The proposed methodology establishes the endurance limit in fretting at a rounded punch corner, analogous to the fatigue crack initiation stress proposed by Barsom and McNicol.<sup>1</sup>

#### Acknowledgements

The authors would like to thank Ms A. Hutson and Dr T. Nicholas for constructive discussions and access to some of their unpublished work. This work was sup-

Table 3 Results from the contact analysis and the maximum tensile stress in the fretting fatigue experiments

(a)

Case	$b$ (mm) Eq. (6)	$b-a$ (mm)	$t/b$	$\sigma_{xx}^Q$ (MPa) Table 1	$\sigma_{xx}^P$ (MPa) Table 1A	$\sigma_{xx}^Q + \sigma_{xx}^P + \max \sigma_b$ (MPa)	$R$
1	5.905	0.0521	0.160	292	73	530	0.2
2	12.21	0.0402	0.082	269	22	507	0.1
3	3.352	0.1986	0.292	230	204	593	0.4
4	5.894	0.0540	0.157	382	75	657	0.2
10	12.47	0.0298	0.074	293	12	492	0.1
11	3.116	0.1426	0.285	227	119	489	0.3
12	9.995	0.4669	0.101	96	19	297	0.2
19	12.503	0.0411	0.076	309	21	602	0.1
20	11.12	0.0288	0.085	233	15	376	0.1
24	3.352	0.1986	0.318	293	208	687	0.4
25	3.351	0.1986	0.309	299	203	697	0.4

(b)

Case	$b$ (mm) Eq. (6)	$b-a$ (mm)	$t/b$	$\sigma_{xx}^Q$ (MPa) Table 1	$\sigma_{xx}^P$ (MPa) Table 1A	$\sigma_{xx}^Q + \sigma_{xx}^P + \max \sigma_b$ (MPa)	$R$
5	5.894	0.0526	0.160	497	74	851	0.5
6	12.21	0.0402	0.082	405	22	757	0.5
7	3.405	0.2057	0.295	361	200	810	0.6
8	5.914	0.0739	0.156	215	110	625	0.6
13	9.680	0.1549	0.096	464	32	696	0.5
14	12.20	0.0292	0.075	500	13	828	0.5
15	3.318	0.1429	0.268	387	115	762	0.6
16	11.20	0.1021	0.084	316	15	671	0.5
17	3.366	0.1694	0.302	421	150	834	0.6
18	9.612	0.1046	0.104	404	19	773	0.5
21	12.50	0.0411	0.070	403	20	789	0.5
22	12.49	0.0299	0.075	609	12	1001	0.5
23	3.380	0.2057	0.281	359	201	826	0.6
26	3.370	0.1696	0.301	460	150	898	0.6
30	3.366	0.1694	0.294	375	148	763	0.6

Reference: Hutson *et al.*<sup>13,14</sup>

Configuration: Fig. 4.

Material: Ti-6Al-4V (both pad and substrate).

Properties:  $E^* = 64.8$  GPa,  $\mu = 0.7$ ,  $\sigma_{\text{end}} = 600$  MPa ( $R = 0.1$ ) and 825 MPa ( $R = 0.5$ ).

ported by the Multi University Research Initiative on High Cycle Fatigue which is funded at MIT by the Airforce Office of Scientific Research Grant No. F49620-96-1-0278 through a subcontract from the University of California at Berkeley.

## APPENDIX A

### Calculation of the maximum tensile stress in a strip of finite thickness under normal contact load

The geometry shown in Fig. A1 is examined, where an elastic strip of thickness  $2t$  is loaded by symmetric distributions of normal pressure on the opposite faces of

the specimen. The stresses in the strip are evaluated using Fourier transform theory.<sup>16</sup> The maximum tensile stress develops at the contact boundary ( $x = \pm b$ ,  $y = \pm t$ ) and is given by

$$\sigma_{xx}^P = \frac{2}{\pi} \int_0^\infty \tilde{p}(\alpha) \{ \cosh(\alpha t) A_P - 2 \cosh(\alpha t) + (\alpha t) \sinh(\alpha t) D_P \} \cos(\alpha b) d\alpha \quad (\text{A1})$$

$$A_P = \frac{(\alpha t) \cosh(\alpha t) + \sinh(\alpha t)}{(\alpha t) + \sinh(\alpha t) \cosh(\alpha t)} \quad (\text{A2})$$

$$D_P = \frac{\sinh(\alpha t)}{(\alpha t) + \sinh(\alpha t) \cosh(\alpha t)} \quad (\text{A3})$$

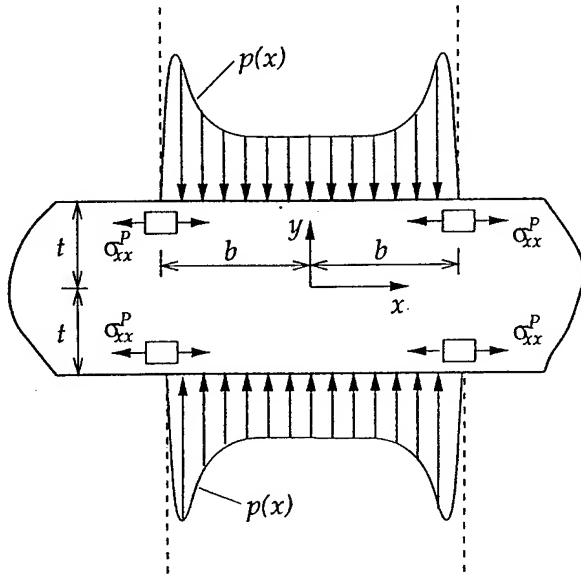


Fig. A1 Geometry of an elastic strip of thickness  $2t$ , loaded symmetrically by similar rounded punches.

and  $\bar{p}(\alpha)$  is the Fourier cosine transform of the contact pressure  $p(x)$

$$\bar{p}(\alpha) = \int_0^\infty p(x) \cos(\alpha x) dx \quad (\text{A4})$$

The Fourier transform of constant contact pressure distribution,  $p(x) = P/(2b)$ , is  $\bar{p}(\alpha) = P \sin(\alpha b)/(2\alpha b)$  and the Fourier transform of the Hertzian contact pressure distribution,  $p(x) = p_0 \sqrt{1 - (x/b)^2}$ ,  $p_0 = 2P/(\pi b)$ , is  $\bar{p}(\alpha) = \pi p_0 J_1(\alpha b)/(2\alpha)$ , where  $J_1$  is the Bessel function of order one. For the case of Hertzian contact pressure, the resulting maximum tensile stress  $\sigma_{xx}^P/p_0$  is given in Table A1 as a function of the thickness ratio  $t/b$ .

Table A1 Variation of normalized maximum tensile stress,  $\sigma_{xx}^P/(\pi b)/(2P)$ , for different normalized strip thickness,  $t/b$

$t/b$	$\sigma_{xx}^P(\pi b)/(2P)$	$t/b$	$\sigma_{xx}^P(\pi b)/(2P)$
$\infty$	0.000	0.1	0.132
10	0.083	0.09	0.125
5	0.154	0.08	0.118
3	0.237	0.07	0.110
1	0.389	0.06	0.103
0.9	0.387	0.05	0.096
0.8	0.382	0.04	0.076
0.7	0.372	0.03	0.063
0.6	0.357	0.02	0.049
0.5	0.336	0.01	0.039
0.4	0.309	0.00	0.000
0.3	0.274		
0.2	0.228		

## REFERENCES

- 1 J. M. Barsom and R. C. McNicol (1974) Effect of stress concentration on fatigue crack initiation in HY-130 steel. In: *Fracture Toughness and Slow-Stable Cracking*, ASTM STP 559, Am. Soc. for Testing and Materials, pp. 183–204.
- 2 M. Creager and P. C. Paris (1967) Elastic field equations for blunt cracks with reference to stress corrosion cracking. *Int. J. Fracture Mech.* 3, 247–252.
- 3 J. M. Barsom and S. T. Rolfe (1987) *Fracture and Fatigue Control in Structures: Application of Fracture Mechanics*, Prentice Hall, Englewood Cliffs, NJ, USA.
- 4 G. R. Yoder, L. A. Cooley and T. W. Crooker (1985) Observations on a fracture mechanics approach to fatigue crack initiation in Ti-6Al-4V. In: *Fracture Mechanics: 16th Symposium*, ASTM STP 868 (Edited by M. F. Kanninen and A. T. Hopper), Am. Soc. for Testing and Materials, pp. 392–405.
- 5 A. E. Giannakopoulos, T. C. Lindley and S. Suresh (1998) Aspects of equivalence between contact mechanics and fracture mechanics: theoretical connections and a life-prediction methodology for fretting-fatigue. *Acta Mater.* 46, 2955–2968.
- 6 M. Ciavarella, D. A. Hills and G. Monno (1998) The influence of rounded edges on indentation by a flat punch. *Proc. Inst. Mech. Engrs.* 212C, 319–328.
- 7 M. Ciavarella, G. Demelio and D. A. Hills (1999) The use of almost complete contacts for fretting fatigue tests. In: *Fatigue and Fracture Mechanics*, 29th volume, ASTM STP 1332 (Edited by T. L. Panontin and S. D. Sheppard), Am. Soc. Testing Materials, West Conshohocken, PA, USA, pp. 696–709.
- 8 K. L. Johnson (1985) *Contact Mechanics*, Cambridge University Press, UK.
- 9 J. N. Goodier and C. B. Loutzenheiser (1965) Pressure peaks at the ends of plane strain rigid die contacts (elastic). *J. Appl. Mech.* 32, 462–463.
- 10 C. Chenut (1998) The influence of the roundness on the fretting flat punch. Diploma thesis, Ecole Polytechnique and MIT.
- 11 L. J. Fellows, D. Nowell and D. A. Hills (1995) Contact stresses in a moderately thin strip (with particular reference to fretting experiments). *Wear* 185, 235–238.
- 12 P. A. McVeigh and T. N. Farris (1997) Finite element analysis of fretting stresses. *ASME, J. Tribol.* 119, 797–801.
- 13 A. L. Hutson, T. Nicholas and R. Goodman (1999) Fretting fatigue of Ti-6Al-4V under a flat-on-flat contact. *Int. J. Fatigue* 21, 663–670.
- 14 A. L. Hutson and T. Nicholas (2000) Fretting fatigue behavior of Ti-6Al-4V against Ti-6Al-4V under flat-on-flat contact with blending radii. In: *Fretting Fatigue: Current Technology and Practices*, ASTM STP 1367 (Edited by D. W. Hoepfner, V. Chandrasekaran and C. B. Elliot), Am. Soc. for Testing and Materials, West Conshohocken, PA, USA, pp. 308–321.
- 15 D. C. Maxwell and T. Nicholas (1999) A rapid method for generation of a Haigh diagram for high cycle fatigue. In: *Fatigue and Fracture Mechanics: 29th volume*, ASTM STP 1332 (Edited by T. L. Panontin and S. D. Sheppard), Am. Soc. for Testing Materials, pp. 626–641.
- 16 I. N. Sneddon (1951) *Fourier Transforms*, McGraw-Hill, NY, USA.

# An Experimental Investigation of Fretting Fatigue in Ti-6Al-4V: the Role of Contact Conditions and Microstructure

T.A. VENKATESH, B.P. CONNER, C.S. LEE, A.E. GIANNAKOPOULOS, T.C. LINDLEY, and S. SURESH

A systematic investigation of the fretting fatigue behavior of the titanium alloy Ti-6Al-4V in both the mill-annealed (MA) and the solution-treated and overaged (STOA) conditions was carried out. A sphere-on-flat fretting fatigue device was used that facilitated real-time control and monitoring of all the relevant parameters such as the contact geometry, contact (normal and tangential) loads, and bulk alternating stress. While different sets of experiments were conducted to examine the influence of the bulk stress, the tangential load, and the normal load, respectively, on fretting fatigue response, the effect of microstructure on fretting fatigue was explored with experiments on the acicular, Widmannstätten, and martensitic microstructures as well. In experiments where the contact loads were maintained constant and the bulk stress was varied, fretting reduced the fatigue strength of Ti-6Al-4V. For this case, the "strength reduction factor" was higher for the experiments with higher tangential loads. For cases where the bulk stress and the normal or the tangential loads were maintained constant, lower fretting fatigue lives were obtained at larger tangential loads and at smaller normal loads. Of all the microstructures studied, preliminary results on the martensitic structure suggest an enhanced fretting fatigue resistance, compared to the basic STOA or the MA microstructure. Using the measured maximum static friction coefficient for Ti-6Al-4V, the experimentally observed contact and stick-zone radii were found to exhibit good agreement with analytical predictions. Furthermore, conditions for crack initiation were determined through the application of the recently developed adhesion model for fretting fatigue. The model predictions of weak adhesion and crack initiation were validated with experimental observations of stick-slip behavior and fretting fatigue failures, respectively.

## I. INTRODUCTION

FRETTING fatigue refers to the contact between two surfaces, where small, oscillatory sliding displacements, typically in the range of 2 to 50  $\mu\text{m}$ , occur between the surfaces, while one or both of the contacting surfaces could be subjected to fluctuating stresses. In the presence of aggressive environments, considerable oxidation leading to wear and material removal can occur at the fretted surface. In addition to surface damage, repeated fretting of surfaces can cause a drastic reduction (by a factor of 2 or more) in the fatigue endurance limit and orders of magnitude decrease in fatigue life from that seen under pure axial cyclic loading alone.<sup>[1-4]</sup> Consequently, fretting fatigue has been recognized as a complex multistage, multiaxial, fatigue-fracture phenomenon involving fatigue crack initiation, early (small) crack propagation, and sometimes either crack arrest or continued growth, ultimately leading to catastrophic failure.

From a theoretical/analytical perspective, approaches to predict fretting fatigue cracking can broadly be classified as one of two types: stress based or fracture mechanics based. The stress-based approach typically involves formulation of

multiaxial criteria such as those due to Crossland, Findley, Sines, Smith-Watson-Topper, McDiarmid, Papadopoulos, *etc.* (as reviewed in Reference 5) by considering a combination of stresses at a particular/critical location in the contact zone. One of the appealing features of such a "stress at a point" approach is its relative simplicity. However, because it does not incorporate a length scale in the analysis, this approach has its limitations and it does not capture essential features of fretting fatigue damage such as prediction of crack initiation, location of crack initiation, or crack propagation direction, in all fretting situations. For example, in the cases of various fretting contact geometries,<sup>[3]</sup> cracks have been observed to initiate in the slip zone or the stick-slip boundary, while the stress-based approaches always predict the fretting cracks to initiate at the edge of the contact.

By incorporating an appropriate lengthscale in the analysis for fretting crack initiation and propagation, the fracture mechanics approach addresses a principal limitation of the stress-based approaches. However, most of the fracture mechanics approaches do not provide a framework for identifying/deriving this lengthscale unambiguously and hence the initial crack length has to be assumed *a priori*.

Recently, a new model for fretting fatigue crack initiation has been developed<sup>[6]</sup> wherein the effects of interfacial adhesion between the contacting bodies were incorporated in the analysis of the mechanics of contact fatigue. By recognizing that adhesion induces square-root singular stress fields in the contact zone, a fracture mechanics methodology was applied to derive a natural lengthscale for the fretting fatigue problem. A comparison of the cyclic variations in local stress intensity factors with the threshold stress intensity factor range for the onset of fatigue crack growth then provided

T.A. VENKATESH, Postdoctoral Associate, B.P. CONNER, Graduate Student, and S. SURESH, R.P. Simmons Professor, and A.E. GIANNAKOPOULOS, Research Scientist, are with the Department of Materials Science and Engineering, Massachusetts Institute of Technology, Cambridge, MA 02139. T.C. LINDLEY, Lecturer, is with the Department of Materials Science and Engineering, Imperial College of Science, Technology and Medicine, London SW7 2BP, United Kingdom. C.S. LEE, formerly Visiting Scientist at the Massachusetts Institute of Technology, is Professor at the Pohang University of Science and Technology, South Korea.

Manuscript submitted August 23, 2000.

critical conditions for crack initiation. It was also shown that the location of crack initiation within the contact area and the initial direction of crack growth from the contact surface into the substrate could be quantitatively determined by this approach.

The experimental investigation of fretting fatigue on various materials (metals, ceramics, and polymers), using different methods/contact geometry (with bridge-type, cylindrical, or spherical fretting pads), indicates that the different stages in fretting fatigue depend to varying extent on a number of material, mechanical, and environmental variables; these include the microstructure, geometry, stresses, temperature, frequency, surface modification, residual stresses, surface roughness, *etc.*<sup>[1-4]</sup> Given the complexity of the phenomenon, there exists a critical need for developing methods to characterize the fretting behavior of materials in a manner that allows for easy control of all the major variables that influence fretting. Hence, a novel fretting fatigue device that allowed for the real-time control and monitoring of all the pertinent variables in a fretting fatigue experiment was developed<sup>[7]</sup> and validated with experiments on 7075 T6 aluminum alloy.<sup>[8]</sup>

Several aspects of the fretting fatigue behavior of the titanium alloy Ti-6Al-4V have been investigated, mostly using a flat-on-flat or a cylinder-on-flat geometry (*e.g.*, References 9 and 10) and to a lesser extent on the sphere-on-flat geometry.<sup>[11,12]</sup>

The objectives of the current work are as follows. Through a systematic experimental study of the sphere-on-flat fretting fatigue of the titanium alloy Ti-6Al-4V, we

- (1) characterize the fretting fatigue response of Ti-6Al-4V and its dependence on the various mechanical and geometrical factors such as the contact (normal and tangential) loads, bulk loads, and fretting pad geometry;
- (2) investigate the role of microstructure in the fretting fatigue response of Ti-6Al-4V through experiments on Ti-6Al-4V subjected to different heat treatment schedules;
- (3) quantify damage such as the fretting scar size, crack initiation locations, crack propagation angles, and their dependence on the experimental conditions;
- (4) identify the different regions of fretting fatigue crack growth from initiation through specimen failure and the fraction of life spent in each of those regions; and
- (5) assess the results within the context of the new fretting fatigue adhesion model.

This article is arranged in the following sequence. Section II presents details of the materials and microstructures used, experimental methods employed, and conditions investigated in this study. Section III presents fretting fatigue results from experiments where each of the following variables, normal contact load, tangential load, bulk load, and material microstructure, was varied systematically. In Section IV, the observed microstructural details such as the fretting scars, crack initiation locations, and crack propagation angles are discussed by recourse to classical analysis of the fretting contact as well as through the adhesion model of fretting fatigue. Principal conclusions from this study are presented in Section V.

Table I. Ti-6Al-4V Subjected to Various Heat Treatments to Obtain Different Microstructures

Microstructure	Heat Treatment
STOA	1.25 h at 932 °C in air and air cooled to room temperature; followed by 2 h at 704 °C and fan cooled in argon atmosphere to room temperature
MA	2 h at 704 °C followed by air cooling
Martensitic	0.5 h at 1050 °C followed by water quench
Coarse-grained STOA	48 h at 930 °C followed by air cooling; 12 h at 700 °C followed by air cooling
Acicular	0.5 h at 1050 °C followed by air cooling
Widmanstätten	0.5 h at 1050 °C followed by furnace cooling to 700 °C (1 h) and air cooled to room temperature

## II. EXPERIMENTS

### A. Material System

Two variants of Ti-6Al-4V, with nominal compositions of 6.08 pct Al, 4.01 pct V, 0.19 pct Fe, 0.18 pct O, 0.02 pct C, 0.01 pct N, 0.0004 pct H, <0.001 pct Y and the balance Ti, and 6.30 pct Al, 4.17 pct V, 0.19 pct Fe, 0.19 pct O, 0.13 pct N, and the balance Ti (by weight), respectively, in the mill-annealed (MA) and solution-treated and overaged (STOA) conditions, were selected for the fretting fatigue study. Through appropriate heat treatment schedules (Table I), the basic STOA microstructure was modified further to obtain coarse-grained STOA, martensitic, acicular, and lamellar/Widmanstätten microstructures (Figures 1 through 3).

Optical metallography samples, prepared by polishing with SiC paper, 3  $\mu\text{m}$  diamond solution, 0.3  $\mu\text{m}$  alumina solution, and 0.05  $\mu\text{m}$  Mastermet solution and subsequently etched with a reagent consisting of 5 pct HF, 10 pct HNO<sub>3</sub>, and 85 pct distilled water, revealed the microstructural details of the different materials, as described subsequently.

The MA material exhibited a duplex microstructure, with elongated primary alpha grains (10  $\mu\text{m}$  in width by 50 to 80  $\mu\text{m}$  in length) along the longitudinal direction and an equiaxed structure, with an average primary alpha grain size about 5 to 10  $\mu\text{m}$ , in the transverse cross section. The basic STOA material displayed a duplex/bimodal microstructure with primary alpha grains (10 to 20  $\mu\text{m}$ ) surrounded by a lamellar matrix with a minor elongation of grains in the longitudinal direction, while the coarse STOA material had a primary alpha grain size between 20 and 25  $\mu\text{m}$ . The martensitic material was characterized by a needlelike microstructure. The acicular microstructure consisted of colonies of coarse lamellar grains with an average colony diameter of approximately 300  $\mu\text{m}$ . The Widmanstätten microstructure had lamellae with a width of about 15 to 20  $\mu\text{m}$ .

Fretting fatigue test samples had rectangular gage cross sections (Figure 4) for all six microstructures. The fretting pads with spherical contact surfaces (Figure 4) were machined from the MA material for the fretting tests on the MA material, while they were machined from the basic STOA material for all other fretting tests. The test samples and the fretting pads were polished with 0.3  $\mu\text{m}$  alumina solution. The pertinent mechanical properties of the test samples and pads are listed in Table II.



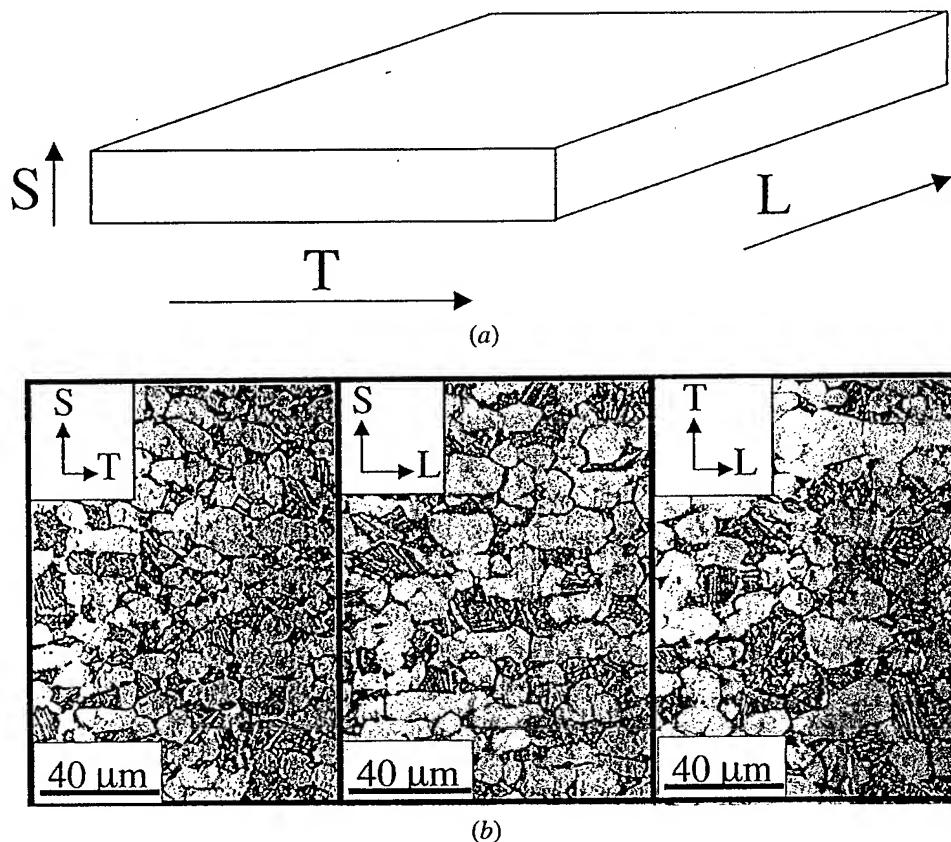


Fig. 1—(a) and (b) Microstructure of Ti-6Al-4V in the STOA condition. (The various cross sections are illustrated with reference to the as-received ingot (a)).

### B. Fretting Fatigue Experiments

A fretting fatigue test apparatus (Figure 5) was designed for independent control and accurate, real-time monitoring of all the pertinent experimental variables such as the specimen bulk load,  $P$ , the normal,  $N$ , and tangential,  $Q$ , loads, at the specimen/fretting pad interface, and the relative displacement between the contacting surfaces,  $\delta$ , as described in more detail in Reference 7.

Briefly, the specimen is subjected to a variable axial load through the actuator of a servohydraulic testing machine, and the normal load is transmitted to the specimen through spring-loaded spherical pads. The supports of the spherical pads are mounted on a compliant system and attached to the structure of the testing machine. Upon the application of the bulk/axial load,  $P$ , the resulting strain in the test specimen translates, due to friction at the contact, to a tangential load,  $Q = -(C_p/C_q)P$ , where  $C_p$  and  $C_q$ , respectively, are the compliances of the load train and the pad-support system. Experimentally, this tangential load is determined as a sum of the load values measured by the two load cells mounted below the linear bearings. The coupling of  $Q$  and  $P$  through friction results in the same load ratio,  $R'$ , between  $Q$  and the bulk stress  $\sigma_b$ .

With its many points of adjustment for alignment and compliance, the fretting fatigue device allows for the system compliance to be changed such that the tangential load, or the relative displacement between the specimen and the pads, can be varied systematically while maintaining the normal

and bulk loads constant for each test. As discussed in Appendix A, this device also allows for the measurement of the average friction coefficient.

The experimental conditions investigated in this work are summarized in Table III. All tests were conducted in air with 60 to 70 pct relative humidity at 25 °C. The axial load varied from fully tensile to fully compressive (load ratio,  $R' = -1$ ), and the maximum bulk stress never exceeded the endurance limit for this material. The test frequency was 10 Hz. Each side of the specimen was longer than  $6a$ , where  $a$  was the contact radius. Such a constraint on dimensions was necessary to prevent edge effects from interfering with the test.

As the fretting fatigue device allowed for the fretting of two opposite sides of the specimens under identical loading conditions (Figure 5), each fretting test effectively constituted two tests performed under identical conditions. As expected, major fretting fatigue cracks initiated on either of the two contacts.

### III. RESULTS

The following sections present results of the fretting fatigue experiments, where the influence of the various factors such as the bulk, normal, and tangential loads, fretting pad geometry, and the material microstructure on fretting damage (*i.e.*, fretting scars and cracks) and total fretting fatigue life was examined systematically.

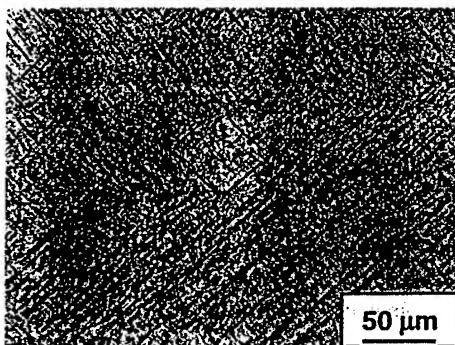
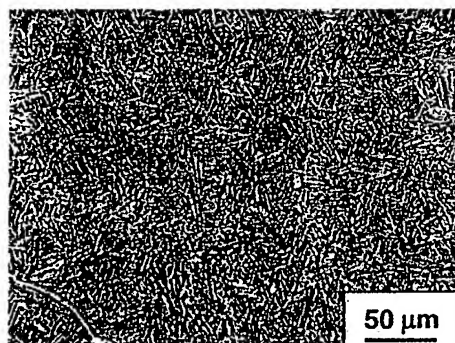
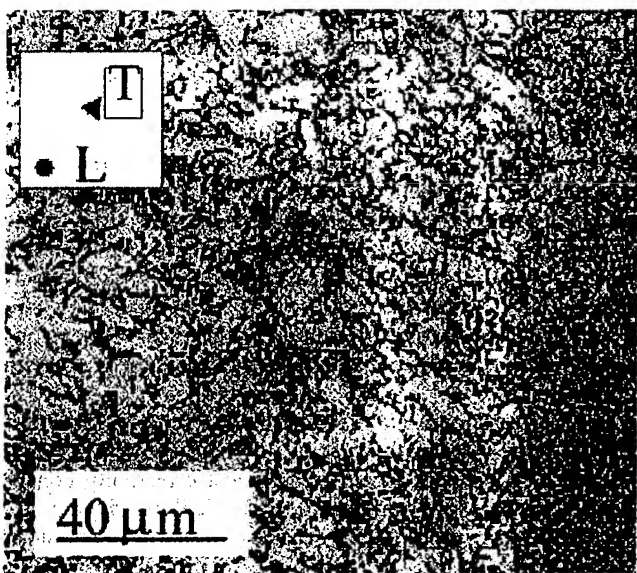
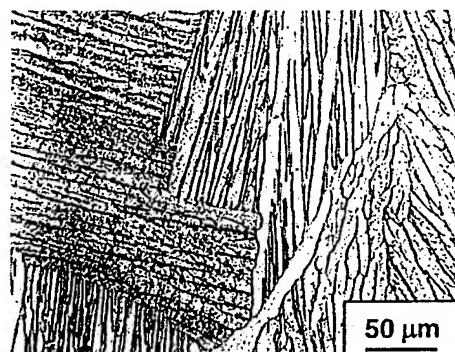
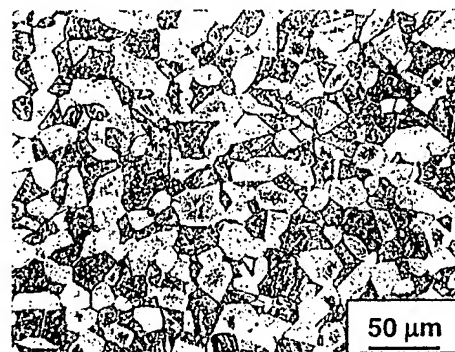
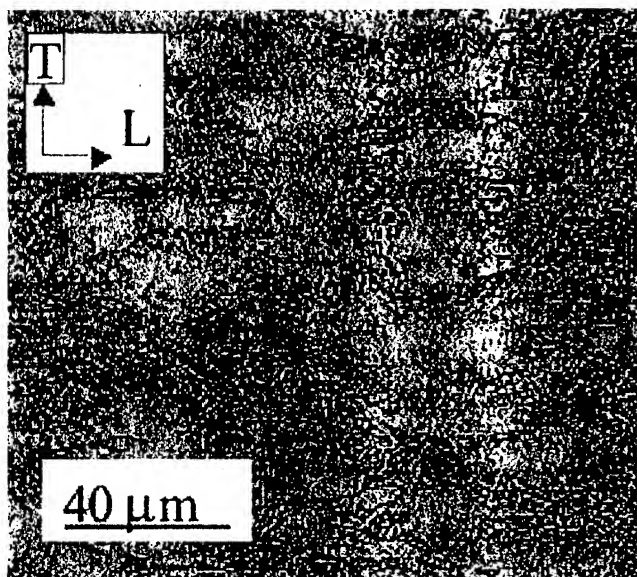
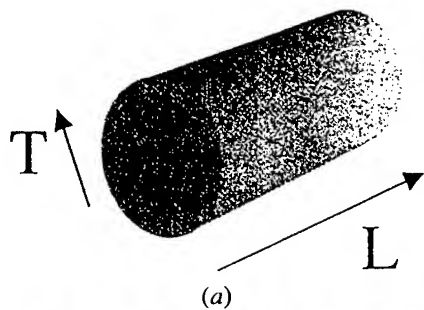


Fig. 2—(b) and (c) Microstructure of Ti-6Al-4V in the MA condition. (The different cross sections are illustrated with respect to the (a) as-received rod).

Fig. 3—Various microstructures of Ti-6Al-4V: (a) coarse-grained STOA, (b) Widmanstätten structure, (c) acicular structure, and (d) martensitic structure.

#### A. Fretting Scars and Cracks

In all the experiments, the fretted area of the samples displayed scars that were typically characterized by a central

stick zone surrounded by an annulus of slip zone, with a slight eccentricity (Figure 6). A significant amount of oxide

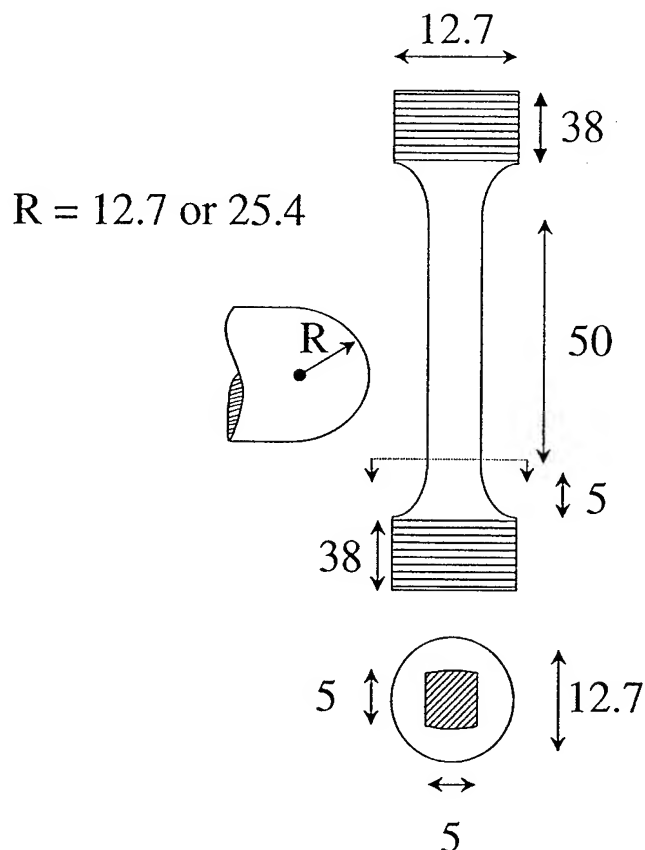


Fig. 4—Schematic of fretting fatigue sample and pad geometry (all dimensions in millimeters, not to scale).

debris was also produced by the fretting action at the trailing edge of the contact,\* as seen in Figure 6. In each case the

\*It is believed that gravity in combination with the higher contact stresses present at the trailing edge (Appendix B) may have contributed toward creating this asymmetry in debris accumulation. The effects of this asymmetry on the adhesion debond energies (Section IV) have not been incorporated in the current analysis.

scar on the fretting pad was a mirror image of that on the sample surface. Indirect evidence for adhesion between contacting surfaces could be discerned from the fact that some brightly reflecting regions, possibly created by the rupture of microwelds, were also observed in several fretting scars.

Because the sliding of the samples upon failure typically damaged the scars, the fretting scars were studied in detail in those experiments where sample failure did not occur. The contact zone radius,  $a$ , stick-zone radius,  $c$ , and the eccentricity,  $e$ , observed in the experiments where samples did not fail are presented in Table IV.

Fretting cracks typically initiated near the trailing edge

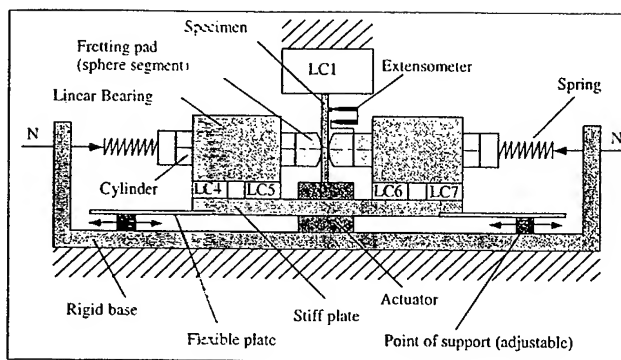


Fig. 5—Fretting fatigue test apparatus.<sup>17)</sup> LC = load cell.

of the contact or in the slip zone close to the trailing edge of the contact (Figure 7, Table III). (For the definition of the trailing edge of the contact, see Appendix B). In some cases, multiple crack initiation sites were also noted.

Upon initiation at the specimen contact surface, the fretting fatigue cracks propagated along the specimen surface in a direction perpendicular to the direction of the bulk load as well as into the interior of the specimen. The crack propagation angle was determined optically by inspecting the fractured surface (details of which are presented in Appendix C).

#### B. Effect of the Bulk Stress

Four sets of experiments (tests 1 through 21, Table III) were performed on the MA material, where for each set, the normal load, the tangential load, and the fretting pad radius were maintained constant while the sample bulk load was varied (Figure 8). In general, the life of the fretted samples increased as the bulk stress decreased with an endurance limit being reached at lower bulk stresses. In all cases, fretting reduced the fatigue strength of Ti-6Al-4V, with the "strength reduction factor" being higher for the experiments with the higher tangential load,  $Q = 30$  N, compared to those with the lower tangential load,  $Q = 15$  N.

Among all the experiments with a tangential load of 30 N, those experiments with the larger pad radius of 25.4 mm typically exhibited longer lives and a higher fatigue strength. A similar trend was also observed for the experiments with a tangential load of 15 N, where the fatigue for those experiments with the larger pad radius was marginally higher than for the experiments with the lower pad radius.

#### C. Effect of the Tangential Load

Two sets of experiments were performed on the MA (tests 22 through 28, Table III) and STOA material (tests 37 through 46, Table III), where for each set, the normal load,

Table II. The Mechanical Properties of Ti-6Al-4V Used in the Fretting Fatigue Experiments

Properties	MA	STOA	Acicular	Widmanstätten	Martensitic
Elastic Modulus (GPa)	116	116	116	116	116
Poisson's ratio	0.34	0.34	0.34	0.34	0.34
Yield strength (MPa)	963	935	935	855	1137
Tensile strength (MPa)	1016	970	995	890	1243

Table III. List of Experimental Conditions and Results of All the Fretting Fatigue Experiments on Ti-6Al-4V

Experiment	Experimental Input Parameters				$N_f$	$N_{(III)}$	$b_0$ ( $\mu\text{m}$ )	$d_0$ ( $\mu\text{m}$ )	$\alpha$ (Deg)	Fracture Location	$l_c$ ( $\mu\text{m}$ )
	$N$ (N)	$Q$ (N)	$\sigma_b$ (MPa)	$2R$ (m)							
Effect of bulk stress (MA Ti-6Al-4V)											
1	50	14.5	394	0.0254	107,899	53,232	280	300	80.7	unclear	283.7
2	50	13	357	0.0254	31,540	—	—	—	—	—	—
3	50	15	341	0.0254	266,176	65,575	180	310	—	eoc	—
4	50	14.5	300	0.0254	474,656	177,275	200	250	—	eoc	—
5	50	15	280	0.0254	2,055,856	147,124	180	310	68.7	eoc	193.2
6	50	15	341	0.0508	192,000	73,473	120	275	—	eoc	—
8	50	15	338	0.0508	1,609,238	84,474	130	255	72.9	oc	136.0
7	50	15	325	0.0508	872,863	104,417	250	300	—	eoc	—
9	50	17	300	0.0508	8,596,572*	—	—	—	—	—	—
10	50	15	292	0.0508	3,962,688	137,493	200	300	—	eoc	—
11	50	15	276	0.0508	4,273,718*	—	—	—	—	—	—
12	50	16	254	0.0508	2,288,839*	—	—	—	—	—	—
13	50	30	315	0.0254	117,183	104,030	150	275	56.3	eoc	180.3
14	50	30	300	0.0254	142,746	132,074	180	280	—	unclear	—
15	50	30	250	0.0254	278,238	247,080	160	210	58.0	eoc	188.7
16	50	33	225	0.0254	691,612	374,035	231	256	68.9	eoc	247.6
17	50	30	375	0.0508	85,957	77,427	180	230	67.4	eoc	194.9
18	50	30	320	0.0508	212,491	179,662	100	170	—	eoc	—
19	50	30	265	0.0508	245,637	178,088	260	350	71.9	eoc	273.5
20	50	30	260	0.0508	253,700	—	150	255	—	eoc	—
21	50	30	225	0.0508	3,295,860	390,790	320	360	73.5	eoc	333.7
Effect of tangential load (MA Ti-6Al-4V)											
22	50	30	300	0.0254	142,746	132,074	180	280	57.3	unclear	213.9
23	50	23	300	0.0254	307,653	153,745	70	260	75.3	eoc	72.3
24	50	14.5	300	0.0254	474,656	177,275	200	250	75.7	eoc	206.3
25	50	11	300	0.0254	3,057,892	152,907	138	240	82.9	slip zone	138.5
26	50	10	300	0.0254	2,163,277	399,807	360	250	72.8	slip zone	376.8
27	50	32	300	0.0508	207,258	120,466	—	—	—	—	—
28	50	21	300	0.0508	598,191	140,926	150	210	71.6	oc	158.0
Effect of normal load (MA Ti-6Al-4V)											
29	70	16.5	300	0.0254	2,969,846	144,293	150	250	75.1	slip zone	155.2
30	60	16.3	300	0.0254	1,235,575	147,827	140	250	60.2	slip zone	161.3
31	50	14.5	300	0.0254	474,656	177,275	200	250	75.3	eoc	206.7
32	40	16	300	0.0254	401,153	183,118	90	200	60.9	eoc	103.0
33	30	16	300	0.0254	499,291	258,959	75	150	61.9	eoc	85.0
34	22	15	300	0.0254	284,670	184,700	100	200	—	eoc	—
35	30	17	300	0.0508	5,342,499	199,458	100	250	65.8	eoc	109.6
36	25	17	300	0.0508	12,000,000*	—	—	—	—	—	—
Effect of tangential load (STOA Ti-6Al-4V)											
37	50	37.5	300	0.0254	182,617	163,544	222	272	65.3	eoc	244.3
38	50	23	300	0.0254	227,972	124,413	222	309	77.2	slip zone	227.6
39	50	21	300	0.0254	317,073	241,400	185	210	70.9	eoc	195.7
40	50	20	300	0.0254	260,894	179,285	160	228	79.0	eoc	162.9
41	50	18	300	0.0254	433,195	281,618	185	198	70.1	slip zone	196.7
42	50	17	300	0.0254	605,023	162,264	197	259	72.0	slip zone	207.1
43	50	14	300	0.0254	745,000	257,406	148	185	78.4	slip zone	151.0
44	50	13	300	0.0254	1,955,612	147,613	123	241	59.3	eoc	143.0
45	50	20.5	300	0.0508	244,054	162,583	173	241	68.3	eoc	186.2
46	50	18.3	300	0.0508	4,708,273	142,253	148	253	55.4	eoc	179.8
Effect of microstructure											
47	50	30.5	300	0.0254	194,260	—	—	—	—	—	—
48	50	24	300	0.0254	4,720,061*	—	—	—	—	—	—
49	50	24	300	0.0254	227,100	—	—	—	—	—	—

Table III. Continued. List of Experimental Conditions and Results of All the Fretting Fatigue Experiments on Ti-6Al-4V

Experiment	Experimental Input Parameters				$N_f$	$N_{(III)}$	$b_0$ ( $\mu\text{m}$ )	$d_0$ ( $\mu\text{m}$ )	$\alpha$ (Deg)	Fracture Location	$l_c$ ( $\mu\text{m}$ )
	$N$ (N)	$Q$ (N)	$\sigma_b$ (MPa)	$2R$ (m)							
50	50	20	300	0.0254	369,920	—	—	—	—	—	—
51	50	16	300	0.0254	1,100,649*	—	—	—	—	—	—
52	50	14	300	0.0254	1,501,900*	—	—	—	—	—	—
53	50	20.5	300	0.0254	240,501	—	114	235	52.1	eoc	144.4
54	50	15.5	300	0.0254	378,782	—	102	248	57.9	eoc	120.4
55	50	26	300	0.0254	271,576	—	—	—	—	eoc	—
56	50	19.5	300	0.0254	290,286	—	190	337	—	slip zone	—
57	50	14	300	0.0254	936,000	—	—	—	—	eoc	—

Key:  $N$  = normal contact load;  $Q$  = tangential contact load;  $\sigma_b$  = maximum bulk stress;  $2R$  = diameter of fretting pad;  $N_f$  = total number of fatigue cycles to failure;  $N_{(III)}$  = number of cycles spent in region III;  $N_{(I+II)}$  = number of cycles spent in regions I and II = [ $N_f - N_{(III)}$ ];  $b_0$  and  $d_0$  = crack geometry at the beginning of region III;  $\alpha$  = average angle of crack initiation into the specimen; eoc = edge of contact; oc = outside the contact zone;  $l_c$  = length of crack in region II; and \* = samples did not fail. Tests 1 through 36 were performed on MA Ti-6Al-4V (with MA fretting pads); tests 37 through 46 were performed on the Ti-6Al-4V in the STOA structure (with STOA fretting pads); tests 47 through 54, 55 through 56, and 57 corresponded, respectively, to martensitic, coarse STOA, Widmanstätten, and acicular microstructures (with STOA fretting pads).

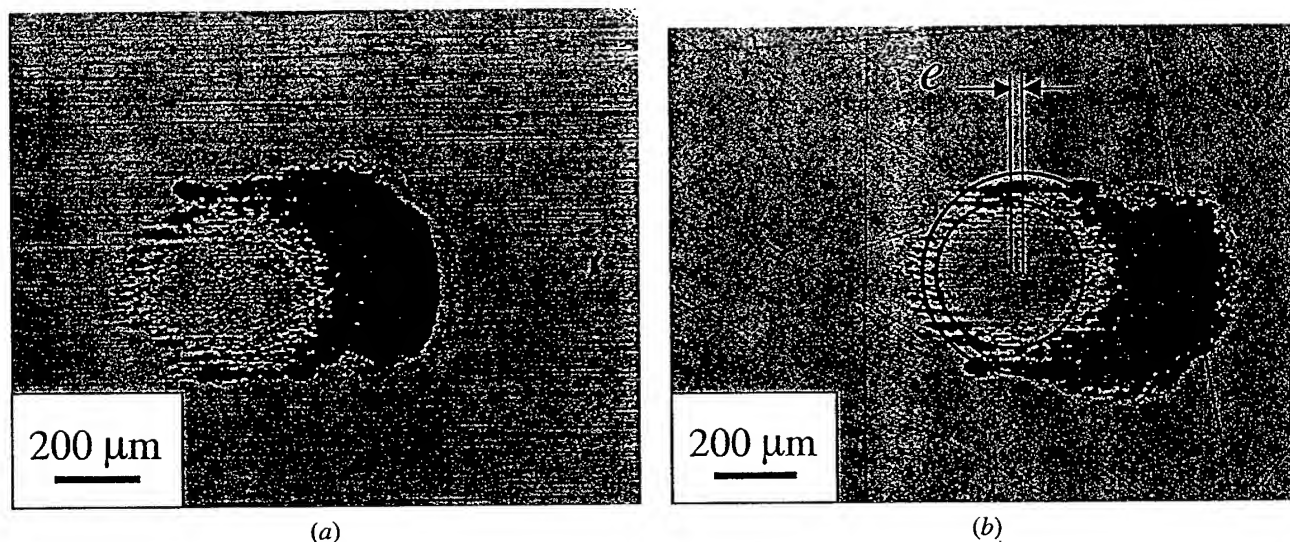


Fig. 6—Fretting fatigue scars on (a) the fretting pad and (b) the sample surface, for an experiment with the normal, tangential, and bulk loads being 50 N, 36 N, and 300 MPa, respectively (the pad radius was 12.7 mm). The circles are obtained theoretically (Eq. 1) and the eccentricity,  $e$  (Eq. 3) is fitted to the observed stick zone.

Table IV. List of Experiments Where the Observed Fretting Scar Dimensions (Contact Radius  $a$ , Stick-Zone Radius  $c$ , and Eccentricity  $e$ ) Are Compared to Theoretical Predictions (Subscripts  $p$  and  $m$  Refer to Predicted and Measured Quantities; and MA and STOA Refer to MA and Solution Treated and Overaged Ti-6Al-4V). For a discussion on eccentricity  $e$ , see Section IV—A

Test	Material	$\sigma_b$	$Q$ (N)	$N$ (N)	$R$ (mm)	$a_p$ ( $\mu\text{m}$ )	$a_m$ ( $\mu\text{m}$ )	$c_p$ ( $\mu\text{m}$ )	$c_m$ ( $\mu\text{m}$ )	$e_p$ ( $\mu\text{m}$ )	$e_m$ ( $\mu\text{m}$ )
1	MA	300	36	50	25.4	244	238	152	179	54.2	31
2	MA	300	36	50	25.4	244	253	152	167	54.2	13.3
3	MA	300	22.5	50	25.4	244	253	197	206	54.2	26.7
4	MA	300	22.5	50	25.4	244	273	197	193	54.2	26.7
5	STOA	300	17	50	12.7	194	200	167	143	27.1	20
6	MA	300	17	50	12.7	194	220	167	200	27.1	23.3
7	STOA	300	19.5	50	12.7	194	185	172	125	27.1	23.8
8	STOA	300	17	50	12.7	194	200	167	133	27.1	66.7
9	MA	300	17	25	25.4	194	200	127	173	54.2	26.7



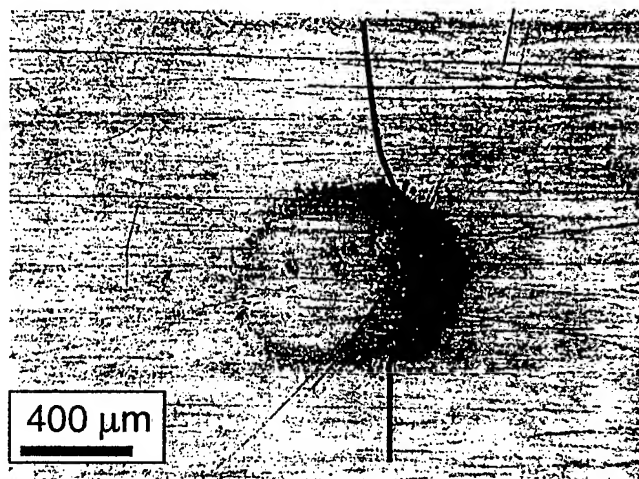


Fig. 7—Fretting fatigue crack observed in the MA Ti-6Al-4V tested under the following conditions:  $R = 12.7$  mm,  $N = 50$  N,  $Q_{\max} = 21$  N, and  $\sigma_b = 300$  MPa; test stopped after 290,000 cycles.

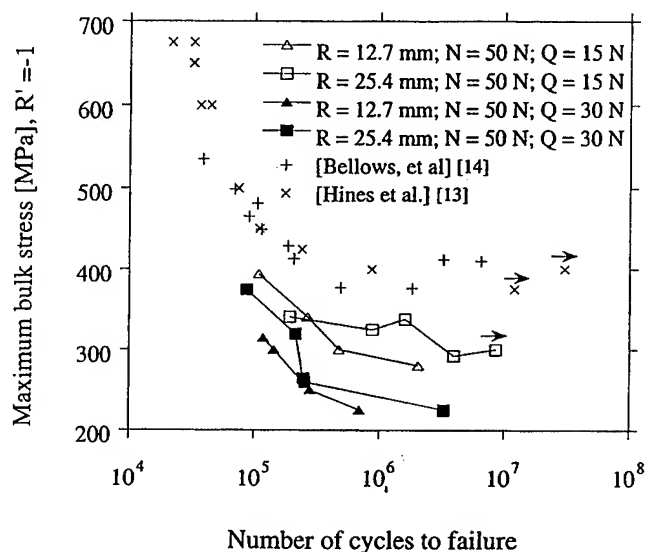


Fig. 8—Fretting fatigue results from experiments on the MA Ti-6Al-4V illustrating variation of total life with changes in the bulk stress applied to the specimen, for a variety of contact geometry and loading conditions. Uniaxial fatigue results from ref. [13] and [14].

the bulk stress, and the fretting pad radius were maintained constant while the tangential load was varied by changing the compliance of the system (Figure 9). In general, the total life to failure of the fretted materials was reduced as the tangential load increased, the reduction in life being larger for the experiments with the lower pad radius of 12.7 mm.

#### D. Effect of the Normal Load

Two sets of experiments were conducted on the MA material (tests 29–36, Table III), where for each set, the tangential load, the bulk stress, and the fretting pad radius were maintained constant while the normal load was varied (Figure 10). The total life to failure of the fretted materials increased as the normal load increased, the increase in life being larger for the experiments with the larger pad radius of 25.4 mm.

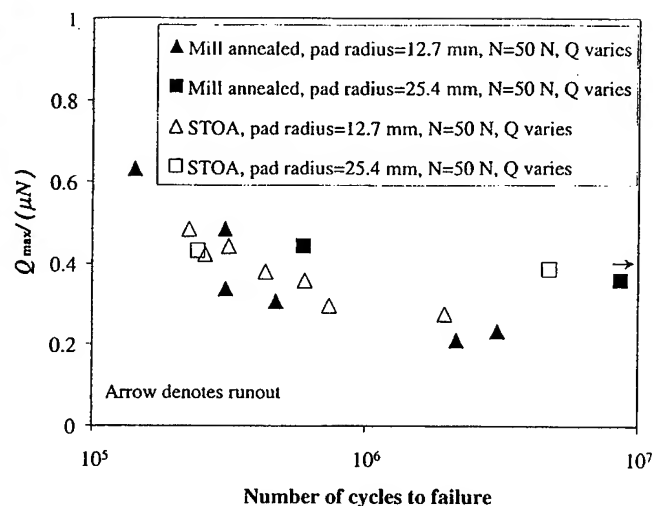


Fig. 9—Fretting fatigue results from experiments on the MA and STOA Ti-6Al-4V illustrating variation of total life with changes in the tangential loads applied to the fretting contact, for a variety of contact geometry ( $\sigma_b = 300$  MPa, and  $\mu = 0.95$ ).

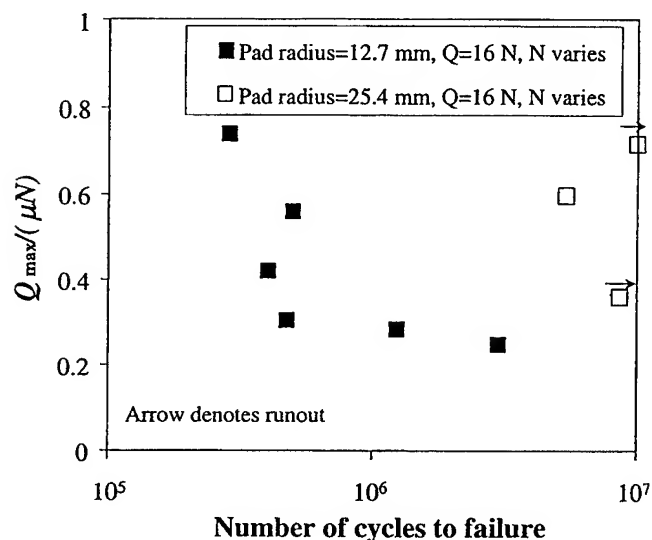


Fig. 10—Fretting fatigue results from experiments on the MA Ti-6Al-4V illustrating variation of total life with changes in the normal loads applied to the fretting contact, for a variety of contact geometry ( $\sigma_b = 300$  MPa, and  $\mu = 0.95$ ).

#### E. Effect of the Microstructure

One set of experiments was conducted on the materials with different microstructures: martensitic (tests 47 through 52, Table III), coarse STOA (tests 53 and 54, Table III), Widmanstätten (tests 55 and 56, Table III), and acicular (test 57, Table III), where the bulk and the normal loads were maintained constant while the tangential load was varied. With the exception of the martensitic structure, where preliminary results suggested an enhanced fretting fatigue resistance (Figure 11), the other microstructures did not exhibit a significant improvement in fretting fatigue resistance, compared to the basic STOA or the MA microstructure. The martensitic material also exhibited higher Vicker's hardness as compared to other microstructures (Figure 12).

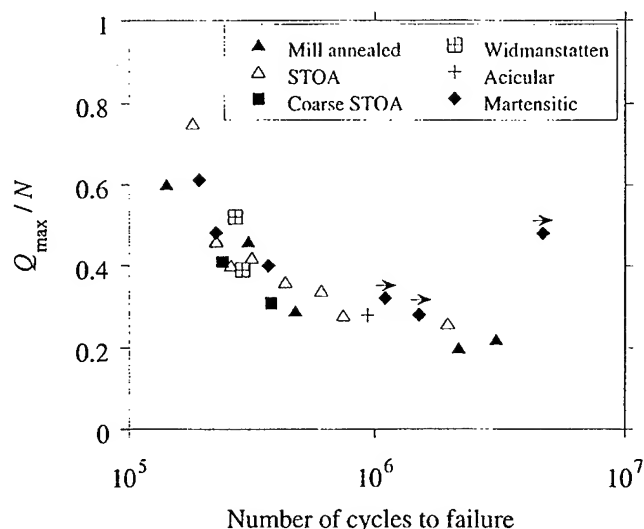


Fig. 11—Fretting fatigue results from experiments on Ti-6Al-4V with different microstructures illustrating variation of total life with changes in the tangential loads applied to the fretting contact ( $\sigma_b = 300$  MPa,  $R = 12.7$  mm, and  $N = 50$  N).

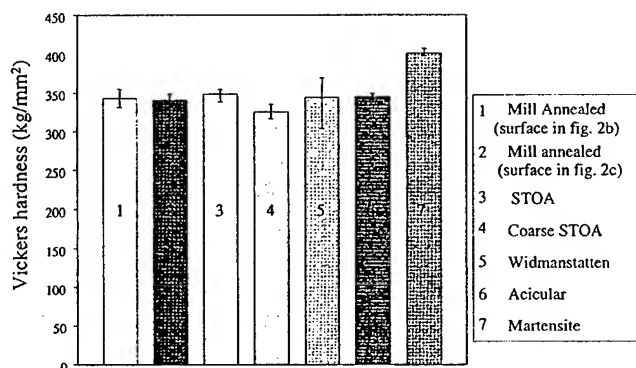


Fig. 12—The average Vickers hardness of different Ti-6Al-4V microstructures.

## IV. DISCUSSION

### A. Fretting Scars and Friction

A sphere of diameter,  $D$ , elastic modulus,  $E$ , and Poisson ratio,  $\nu$ , contacting the planar surface of a large substrate of similar material, under an elastic load,  $N$ , results in a contact radius,  $a$ , given as<sup>[15]</sup>

$$a = \left[ \frac{3D(1 - \nu^2)}{4E} N \right]^{1/3} \quad [1]$$

From Table IV, it is evident that the observed contact radii correlate well with theoretical predictions of Eq. [1].

Upon the application of an oscillatory tangential load,  $-Q_{\max} \leq Q \leq Q_{\max}$ , to the contact via the fretting pad, under stick-slip conditions (i.e.,  $(Q/N) < \mu$ , where  $\mu$  is the coefficient of friction), the radius of the stick zone,  $c$ , is given as<sup>[16]</sup>

$$c = a \left[ 1 - \frac{Q_{\max}}{\mu N} \right]^{1/3} \quad [2]$$

For the case where the oscillatory tangential load, at the

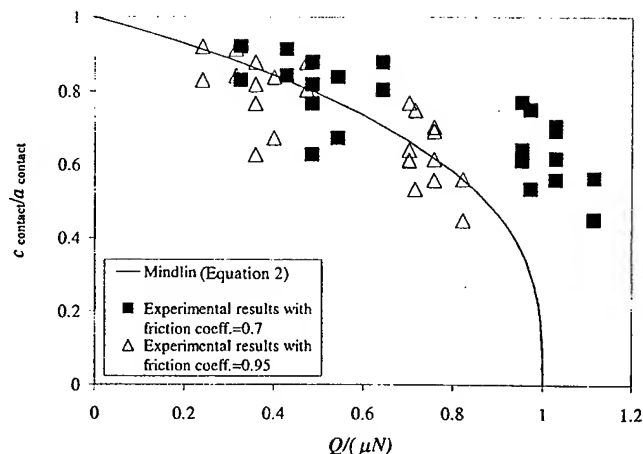


Fig. 13—The experimentally determined fretting scar sizes compared to theoretical predictions for two different values for the coefficient of friction, illustrating a better fit for  $\mu = 0.95$ .

contact interface, is generated through the application of an oscillatory bulk stress,  $-\sigma_b \leq \sigma \leq \sigma_b$ , to the substrate, the radius of the stick zone remains unchanged at  $c$ . But the center of the stick zone is displaced from the center of the contact area by  $e$ , defined as the eccentricity of the contact, given approximately as<sup>[8]</sup>

$$e \approx \frac{(1 - \nu)}{(4 - 3\nu)} \frac{4\sigma_b a}{\pi \mu p_{\max}} = \frac{(1 - \nu)(1 - \nu^2)}{(4 - 3\nu)} \frac{2\sigma_b D}{\mu E} \quad [3]$$

$$\text{where } p_{\max} = \frac{3N}{2\pi a^2}$$

As seen in Eq. [2] and [3], the theoretical predictions for the stick-zone radius,  $c$ , and the eccentricity,  $e$ , depend on the friction coefficient. Using the measured maximum static (or breakaway) friction coefficient of 0.95 for Ti-6Al-4V (Appendix A), there is good agreement between the theoretical prediction of Eq. [2] and the experimentally observed values for the stick-zone radius (Table IV). From Figure 13, it is evident that compared to using the sliding friction coefficient of 0.7, the use of the maximum static friction coefficient of 0.95 results in a better match between the experimental observations and predictions from Eqs. [1] and [2] for the contact and stick-zone radii, respectively.

The observed eccentricities compare reasonably well with those predicted by Eq. [3] for experiments with a fretting pad radius of 12.7 mm. However, for those experiments with a fretting pad radius of 25.4 mm, the observed values are a factor of 2 less than the predicted ones. This observation is consistent with the general expectation that for combinations of conditions where the expected eccentricities are low, i.e., low bulk stress and/or pad diameter, or high friction coefficient and/or modulus, Eq. [3] provides good estimates for eccentricities.

### B. Fretting Fatigue Crack Initiation and Propagation

In general, the fretting fatigue phenomenon can be envisioned as encompassing four regions (Figure 14):

- (I) crack initiation,
- (II) crack propagation under the combined influence of contact and bulk loads,

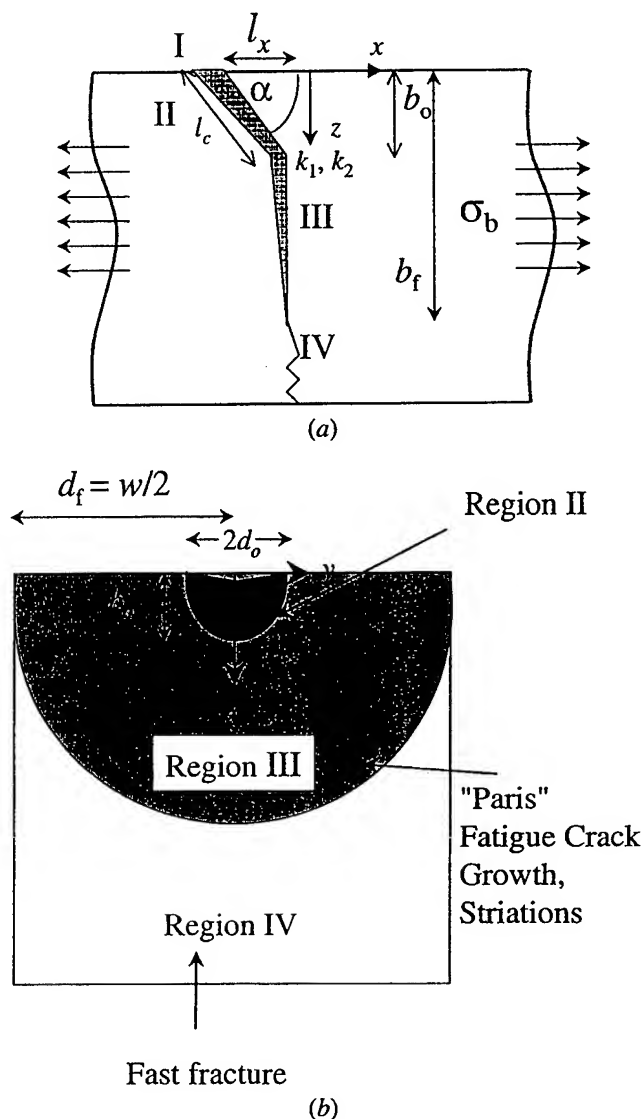


Fig. 14—Schematic illustrating different regions of fretting fatigue cracking in (a) the longitudinal section and (b) the lateral cross section of the specimen.

- (III) crack propagation under the influence of the bulk load only, and
- (IV) catastrophic component failure.

#### 1. Crack initiation

Traditionally, several criteria such as Crossland, max shear stress, Findley, Sines, Smith-Watson-Topper, McDiarmid, and Papadopoulos (as reviewed in Reference 5), which are based on different combinations of stresses at a critical location in the contact zone, have been invoked to predict crack initiation. These methods are typically applied to loading scenarios where the stresses in the contact zone are finite. It has been recently demonstrated<sup>[6]</sup> that under conditions where the contacting surfaces adhere to each other, tensile stress singularities could develop, either at the edge of the contact or at the stick-slip boundary, depending on the strength of adhesion. Hence, the direct application of any stress-based criterion to adhesive contact scenarios (where infinite stresses are predicted) would lead to the prediction that cracks initiate regardless of the magnitudes of the

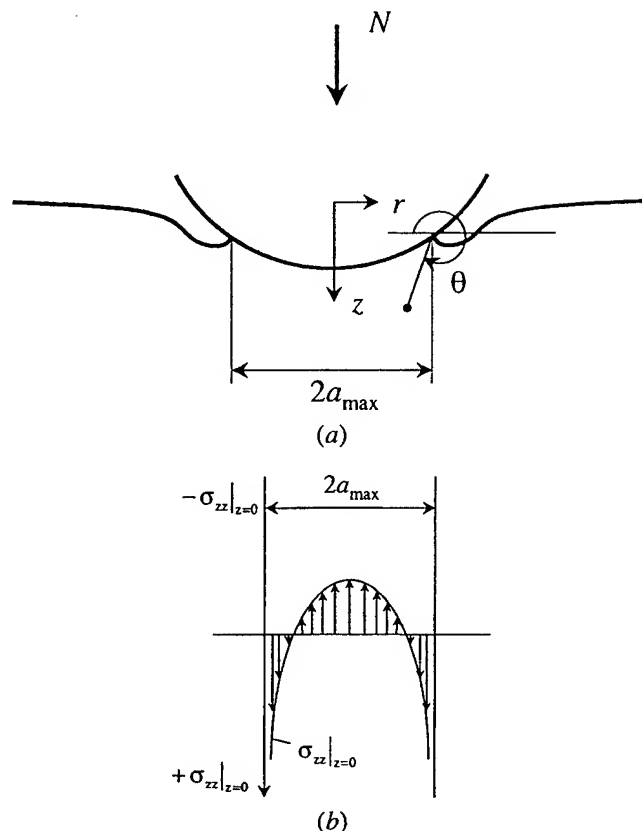


Fig. 15—Schematics illustrating (a) adhesive contacts and (b) the corresponding stress field exhibiting tensile square-root singularity.<sup>[6]</sup>

applied contact loads, contrary to experimental observations. Hence, we invoke a fracture mechanics based approach, which provides a framework to deal with such stress singularities.

By noting that the adhesion induces square-root singular stress fields in the asymptotic limit, an analogy can be made between the (real) sphere-on-flat substrate adhesive contact and a (virtual) circumferential cracked body with an uncracked ligament equal to the contact zone (Figure 15). The procedure for deriving the corresponding cyclic stress intensity factors as a function of the work of adhesion, loading, conditions, and geometry, for the case of the contact fatigue scenario, has been described in detail in Reference 6 and is summarized in brief below.

Under adhesive conditions, when two surfaces with surface energies  $\gamma_1$  and  $\gamma_2$  adhere to form a new interface of lower energy,  $\gamma_{12}$ , the corresponding work of adhesion is defined as  $w' = (\gamma_1 + \gamma_2 - \gamma_{12}) \geq 0$ . For two contacting solids with the same elastic properties, which are presently considered,  $w' = 2\gamma_1$ . For metals,  $w' \approx 1 \text{ N/m}$ .<sup>[17]</sup>

For a sphere of diameter,  $D$ , elastic modulus,  $E$ , and Poisson ratio,  $\nu$ , contacting the planar surface of a large substrate of similar material, under an applied normal load  $N_{\max}$ , the short-range forces of attraction that promote adhesion effectively increase the contact load across the interface and thus increase the contact radius,  $a_{\max}$  (Figure 15), given as

$$a_{\max} = \left[ \frac{3D(1-\nu^2)}{4E} \left( N_{\max} + \frac{3\pi Dw'}{2} \right) \right]^{1/3} \quad [4]$$



$$+ \sqrt{3\pi Dw'N_{\max} + \left(\frac{3\pi Dw'^2}{2}\right)} \Bigg]^{1/3}$$

and the maximum tangential load,  $\bar{Q}_{\max}$ , that can sustain adhesion at maximum contact radius is

$$\bar{Q}_{\max} = 2 \sqrt{\frac{(2-2\nu)}{(2-\nu)}} \pi a_{\max}^3 \left[ G_d^{\text{II}} \frac{E}{(1-\nu^2)} - \left( \frac{3G_d^{\text{I}} \pi D}{4a_{\max}^{3/2}} \right)^2 \right] \quad [5]$$

where  $G_d^{\text{I}}$  and  $G_d^{\text{II}}$  are the critical debonding energies under pure normal and tangential loads, respectively. The debonding energy,  $G_d$  (N/m), can be empirically related to the friction coefficient as<sup>[6,18]</sup>

$$G_d = 14.4 (0.3 + \mu^2)^{1/2} \quad [6]$$

If the amplitude of the applied tangential load  $Q_{\max} \leq \bar{Q}_{\max}$ , strong adhesion (stick) is obtained.

The stress-intensity factor,  $K_{\text{I}}$ , that corresponds to the mode I (steady) crack field is given by<sup>[6]</sup>

$$K_{\text{I}} = \frac{N_{\max}^* - N_{\max}}{2a_{\max} \sqrt{\pi a_{\max}}} \quad [7]$$

where the apparent load,  $N_{\max}^*$ , required to maintain the same contact radius,  $a_{\max}$ , without adhesion is given by Hertzian analysis:

$$N_{\max}^* = \frac{4Ea_{\max}^3}{3(1-\nu^2)D} \quad [8]$$

The stress-intensity factor that corresponds to mode II (oscillatory) crack fields at the leading and the trailing contact edges is given by

$$\Delta K_{\text{II}} = \frac{Q_{\max}}{a_{\max} \sqrt{\pi a_{\max}}} \quad [9]$$

with the local effective load ratio  $R' = -1$ .

If the amplitude of the applied tangential load  $Q_{\max} \geq \bar{Q}_{\max}$ , then weak adhesion (stick slip) is obtained resulting in a partial slip annulus,  $c \leq r \leq a_{\max}$ .

From global equilibrium,

$$Q_{\max} = \mu N_{\max} \left[ 1 - \left( \frac{c}{a_{\max}} \right)^3 \right]; \quad \bar{Q}_{\max} < Q_{\max} \leq \mu N_{\max} \quad [10]$$

The tangential load that is balanced in the stick zone of radius  $c$  is

$$Q_{\max}^{\text{in}} = Q_{\max} - \mu \frac{N_{\max}}{a_{\max}^3} (a_{\max}^2 - c^2)^{3/2} \quad [11]$$

In this case,  $K_{\text{I}} = 0$ , as the model predicts a closed crack tip.<sup>[6]</sup>

The mode II stress intensity factor at the leading and trailing edge of the stick-slip interface is given by

$$\Delta K_{\text{II}} = 2 \times \min \left( \frac{Q_{\max}^{\text{in}}}{2c\sqrt{\pi c}}, \sqrt{\frac{G_d^{\text{II}} E}{1-\nu^2}} \right) \quad [12]$$

with the local load ratio  $R' = -1$ .

A fatigue crack is expected to initiate at the contact perimeter or the stick-slip boundary, for strong or weak adhesion,

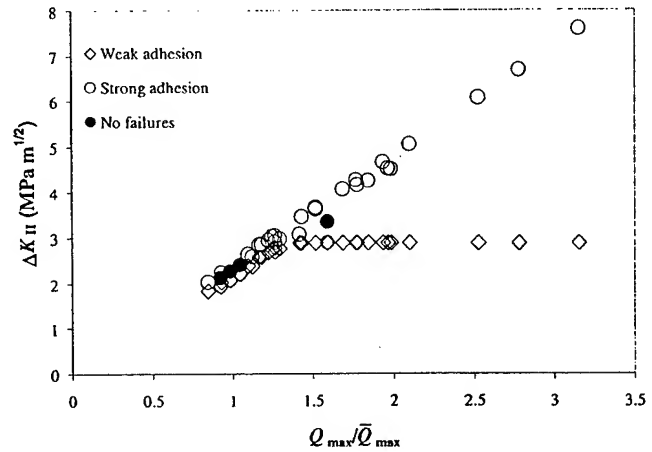


Fig. 16—Room-temperature fretting fatigue experiments on Ti-6Al-4V evaluated using the adhesion model, where the mode II threshold stress-intensity factor for an  $R'$  ratio of  $-1$  was estimated to be  $\approx 2$  MPa $\sqrt{\text{m}}$  and the work of adhesion for advancing and receding contacts ( $w$ ,  $G_d$ ) to be  $\approx 1$  and  $\approx 15.8$  N/m, respectively.

respectively, if the corresponding  $\Delta K_{\text{II}} \geq \Delta K_{\text{th}}$ , where  $\Delta K_{\text{th}}$  is the threshold stress intensity range that corresponds to  $R' = -1$ , and under mixed constant mode I and oscillatory mode II fatigue. This situation holds both for strong adhesion and under pure oscillatory mode II fatigue for weak adhesion.

The fretting fatigue experiments on Ti-6Al-4V can be analyzed within the context of the adhesion model, using the material parameters (Table II), threshold  $\Delta K_{\text{II}} \approx 2$  MPa $\sqrt{\text{m}}$  (estimated from<sup>[19]</sup>), and the experimentally determined friction coefficient,  $\mu = 0.95$ . Using reasonable values for the work of adhesion for advancing and receding contacts,  $w' = 1$  N/m and  $G_d = 15.8$  N/m (Eq. [6]), the adhesion model predicts weak adhesion, in agreement with experiments where in all cases stick-slip behavior was observed (Figure 16).

However, while the model predicts cracks to initiate at the stick-slip boundary, in many cases, the cracks were found to have initiated in the slip zone and sometimes closer to the edge of the contact. This might indicate that conditions of strong adhesion may have existed prior to the development of the partial slip during which time the cracks could have initiated at the edge of the contact.

## II. Crack propagation under the combined influence contact and bulk loads

Upon initiation, the continued propagation of the crack tip depends on the local mode I and mode II stress intensity factors,  $k_1$  and  $k_2$ , respectively (Figure 14). Following Cottrell and Rice,<sup>[20]</sup> it is postulated that the crack advances in a direction along which the local mode II stress intensity factor  $k_2$  vanishes. The initial angle of crack propagation,  $\alpha$ , is then obtained from

$$k_2 = \frac{1}{4} \left( \sin \frac{\alpha}{2} + \sin \frac{3\alpha}{2} \right) K_{\text{I}} + \frac{1}{4} \left( \cos \frac{\alpha}{2} + 3 \cos \frac{3\alpha}{2} \right) K_{\text{II}} = 0 \quad [13]$$

While the model predicts an initial crack angle of 70.5 deg, the observed crack initiation angles (computed as  $\alpha = \arctan(b_0/l_x)$ , where  $b_0$  and  $l_x$  are as illustrated in Figures

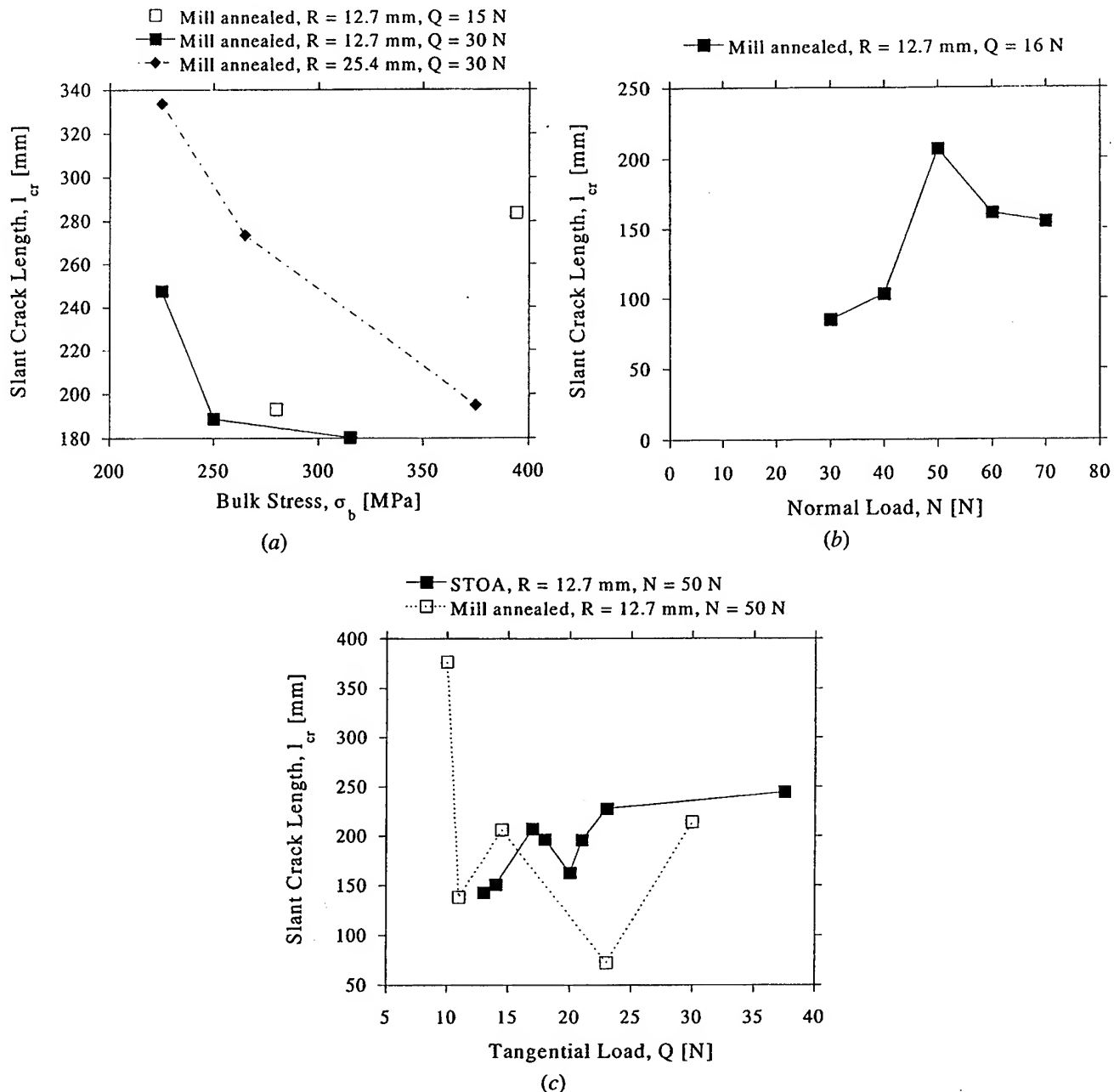


Fig. 17—The effects of the (a) bulk stress, (b) the normal load, and (c) the tangential load on the slant crack length.

14(b) and Ca), had a mean of 68 deg with a standard deviation of 8 deg (Table III).

As the small surface crack grows further into the substrate, the effects of the contact loads,  $N$ , and  $\Delta Q$ , in providing a sufficiently large  $\Delta k_I$  to advance the crack tip, rapidly diminish, leading to a competition between the applied uniform cyclic bulk stress,  $\Delta\sigma_b$  and the contact loads. After some initial growth over a distance  $l_c$  into the substrate, the crack is expected to reorient itself normal to the applied tensile cyclic stress  $\Delta\sigma_b$ . If at the critical distance  $l_c$ , the tensile opening stress intensity factor due to the applied loads is larger than the effective mode I threshold stress intensity factor range,  $\Delta K_{th}$ , the crack would reorient itself normal to the uniform applied stress and would continue to advance

into the substrate in mode I. Otherwise, the crack is expected to arrest completely.

From an inspection of results from tests 13, 15, and 16 as well as 17, 19, and 21 (Table III), it is apparent that with an increase in the bulk stress (while the contact loads and fretting pad radius were maintained constant), the critical slant crack length,  $l_c$ , decreases, as expected (Figure 17(a)). An exception to the general trend is noted in tests 1 and 5, where  $l_c$  is found to be higher in test 1 compared to test 5.

From tests 29 through 34 (Table III), it is evident that at higher normal loads ( $>50$  N), an increase in the normal loads (while the bulk stress and the tangential loads are maintained constant) results in a decrease in the critical slant

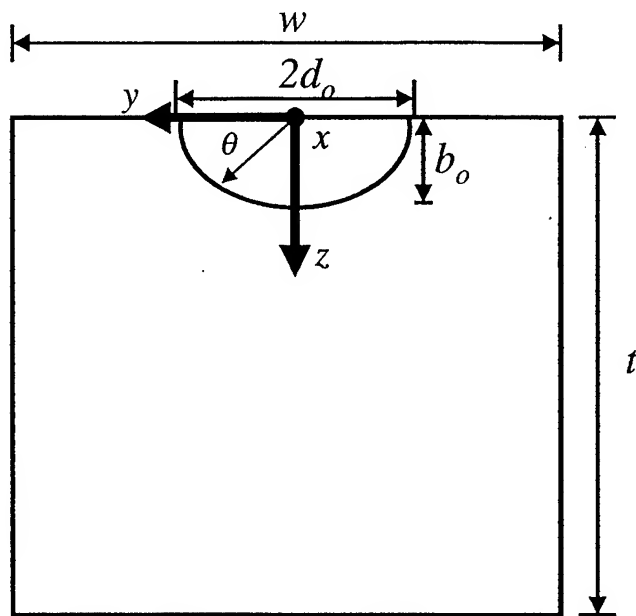


Fig. 18—Schematic illustrating the various input geometric parameters for the calculation of the stress-intensity factors for the fretting fatigue crack in region III.

crack length,  $l_c$  (Figure 17(b)). This observation is consistent with the expectation that an increase in the normal loads would tend to decrease the mode I stress intensity factor at the tip of the slant crack,  $\Delta K_I$ , thus reducing  $l_c$ . In the limiting case, where the normal loads tend to zero, the contact fields are expected to be very weak and fatigue cracking is expected to be dominated by the bulk stress. Consequently, the slant crack lengths are expected to be small, thus explaining the smaller slant crack lengths observed at lower normal loads ( $< 50$  N).

It is expected that an increase in the tangential loads would tend to promote slant crack growth in region II and thus increase  $l_c$ . This general trend is observed in tests 37 through 44 (Table III), while considerable scatter exists in the results of tests 22 through 26 (Table III, Figure 17(c)).

### III. Crack propagation under the influence of bulk load only

An inspection of the fractured surfaces of the specimens indicates that the crack shape at the end of region II could be approximated as being semielliptical (Figure 18). The subsequent propagation of the crack in region III, under the influence of the bulk loads,  $\Delta\sigma_b$ , in a plane perpendicular to the applied bulk load, can be modeled as being driven by the crack-tip stress intensity factor.<sup>[21]</sup>

$$K_I = \sigma_b \sqrt{\frac{\pi b}{Q'}} \times F\left(\frac{b}{t}, \frac{b}{c}, \frac{d}{w}, \theta\right) \quad [14]$$

where

$$Q' = 1 + 1.464 \left(\frac{b}{d}\right)^{1.65},$$

$$F = \left[ M_1 + M_2 \left(\frac{b}{t}\right)^2 + M_3 \left(\frac{b}{t}\right)^4 \right] f_\theta f_w$$

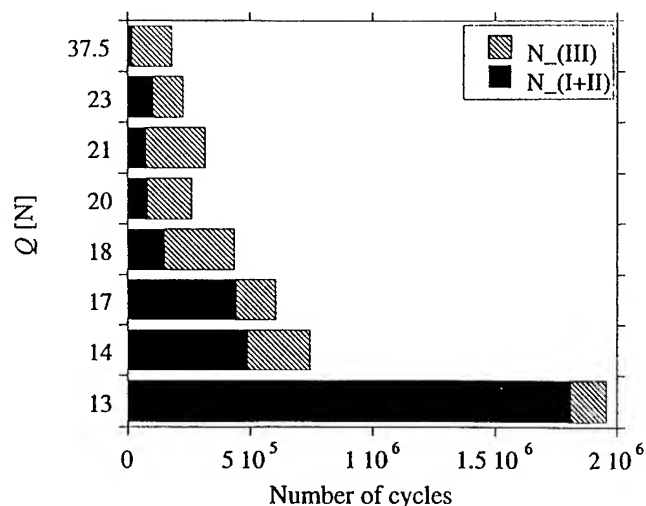


Fig. 19—Analysis of fretting experiments (37 through 44, Table III), illustrating fretting life in the different regions. (In all these cases,  $N = 50$  N,  $R = 12.7$  mm, and  $\sigma_b = 300$  MPa).

$$M_1 = 1.13 - 0.09 \left(\frac{b}{d}\right), \quad M_2 = -0.54 + \frac{0.89}{0.2 + b/d},$$

$$M_3 = 0.5 - \frac{1.0}{0.65 + b/d} + 14 \left(1.0 - \frac{b}{d}\right)^{24} \quad [15]$$

$$g = 1 + \left[ 0.1 + 0.35 \left(\frac{b}{t}\right)^2 \right] (1 - \sin \theta)^2,$$

$$f_\theta = \left[ \left(\frac{b}{d}\right)^2 \cos^2 \theta + \sin^2 \theta \right]^{1/4}$$

$$f_w = \left[ \sec \left( \frac{\pi d}{2w} \sqrt{\frac{b}{t}} \right) \right]^{1/2}$$

The rate of crack propagation, in region III, is taken as following a Paris-type power law:

$$\frac{db}{dN} = C (\Delta K_I)^m \quad [16]$$

where  $C$  and  $m$  are material constants. For mill-annealed Ti-6Al-4V,  $C$  and  $m$  were determined from low load ratio experiments (accounting for crack closure), respectively, as  $7.5 \times 10^{-13}$  and 4.1 (where  $db/dN_{III}$  and  $\Delta K_I$  were in the units of m/cycle and  $\text{MPa}\sqrt{\text{m}}$ , respectively).<sup>[22]</sup>

The mode I stress intensity factor range,  $\Delta K_I$ , is given as  $\Delta K_I = (1 - R')K_{\max}$ , where  $K_{\max}$  is the stress intensity factor that corresponds to monotonic loading. For fully reversed fatigue loading with  $R' = -1$ ,  $\Delta K_I = 2K_I$ . The life of the specimen in region III can be obtained through the integration of the Paris law (Eq. [16]) between the limits ( $b_o, d_o$ ) and ( $b_f, d_f$ ), where  $d_f = (w/2)$ . Assuming the specimen fractures catastrophically in the final cycle, the total life spent by the specimen in the several regions is presented in Table III.

As illustrated in Figure 19, for experiments where the bulk stress and the normal contact loads were maintained constant, the life spent in regions I and II scales with the tangential load, while the life spent in region III remains almost constant, as expected. From an inspection of results

from tests 1 and 5, 13, 15, and 16 as well as 17, 19, and 21 (Table III), it is apparent that with an increase in the bulk stress (while the contact loads and fretting pad radius were maintained constant), the fraction of fretting fatigue life spent by the specimen in the third region,  $N_{III}$ , decreases, as expected.

#### IV. Catastrophic component failure

While the mode I fracture toughness,  $K_{IC}$ , of Ti-6Al-4V can range between 33 and 110  $\text{MPa}\sqrt{\text{m}}$  depending on the oxygen content and the heat treatment, the mill-annealed and STOA microstructures studied in this work exhibit a fracture toughness of 65  $\text{MPa}\sqrt{\text{m}}$ .<sup>[23]</sup> As the critical crack length,  $b_c$ , that corresponds to this  $K_{IC}$  is between 7 and 22 mm, which is much greater than the sample size (5 mm), the sample failure was attributed to mechanical overload.

#### F. Effect of Contact Conditions and Microstructure—Overall Analysis

The observed trends in the variation of the fretting fatigue lives for the different sets of controlled experiments could be examined within the framework presented in Sections IV–A through D (Table V).

- (1) An increase in the bulk load (while keeping all other parameters constant) effectively reduces the critical slant crack length,  $l_c$ , and thus reduces the life spent in region II. Additionally, the life in stage III is reduced as well, resulting in a decrease in the total fretting fatigue life.
- (2) An increase in the tangential load,  $Q$ , increases the effective cyclic mode I stress intensity factor,  $\Delta k_I$ , ahead of the slant crack and thus reduces the life spent in region II. Assuming the life in region III to remain unchanged with changes in  $Q$  (to a first order), this analysis predicts the total fretting fatigue life to decrease with an increase in  $Q$ .
- (3) An increase in the normal load,  $N$ , increases the maximum contact pressure,  $p_{\max}$ . Consequently,  $\Delta k_I$  decreases as the slant crack tip is effectively shielded. Thus, the life spent in region II increases. Assuming, the life in region III to be invariant with changes in  $N$ , the total fretting fatigue life is expected to increase with an increase in  $N$ .
- (4) An increase in the fretting pad radius,  $R$ , decreases the

maximum contact pressure and leads to the prediction that the total fretting fatigue life should decrease. However, the experiments indicate that the total fretting fatigue life actually increases with an increase in  $R$ . This increase in total life may be attributed to an increase in the life spent in region I (i.e., the crack initiation stage) that is not accounted for in this analysis.

- (5) The preliminary study of the effect of microstructure on fretting fatigue in Ti-6Al-4V indicated that the martensitic microstructure might have enhanced fretting resistance. It is possible that this enhanced fretting resistance may be related to the higher yield strength and hardness observed in the martensitic microstructure (Figure 12). The effect of the different microstructures on the crack growth rates in regions II and III needs to be assessed and further work is planned.

#### V. CONCLUSIONS

From a systematic experimental study of the fretting fatigue response of the titanium alloy Ti-6Al-4V, the following conclusions are drawn.

1. In the experiments where the contact loads were maintained constant while the bulk stress was varied, fretting reduced the fatigue strength of Ti-6Al-4V. Because the slant crack propagation rates in region II are directly and strongly correlated to the tangential load, the strength reduction factor was higher for those experiments with a constant but higher tangential load compared to those with a constant but lower tangential load.
2. For cases where the bulk stress and the normal loads were maintained constant, the total life to failure of the fretted materials was reduced as the tangential load increased. This is consistent with the expectation that higher tangential loads promote faster fretting fatigue crack growth in region II.
3. In the experiments where the bulk stress and the tangential loads were maintained constant, the total life to failure of the fretted materials increased as the normal load increased. This was due to the fact that higher normal loads tend to reduce the slant crack propagation rate in region II.
4. In general, the increase in pad radius tended to increase

**Table V. An Overall Summary of the Comparison between the Predicted Trends and the Experimental Observations for the Different Sets of Fretting Experiments (with a Load Ratio  $R' = -1$ ) Where the Test Parameters Such as the Bulk Stress ( $\sigma_b$ ), the Tangential Load ( $Q$ ), the Normal Load ( $N$ ), and the Pad Radius ( $R$ ) Were Varied Systematically**

$\sigma_b$	$Q$	$N$	$R$	$p_{\max}$	$a$		$c$		$cla$		$\Delta k_I$	$N_{(I+II)}$	$N_{(III)}$	$N_f$	
					Predicted	Observed	Predicted	Observed	Predicted	Observed				Predicted	Observed
Increases	Constant	Constant	Constant	Constant	Constant	Constant	Constant	Constant	Constant	Constant	Constant	Decreases	Decreases	Decreases	Decreases
Constant	Increases	Constant	Constant	Constant	Constant	Constant	Decreases	Decreases	Decreases	Decreases	Increases	Decreases	Constant	Decreases	Decreases
Constant	Constant	Increases	Constant	Increases	Increases	Increases	Increases	Increases	Increases	Increases	Decreases	Increases	Constant	Increases	Increases
Constant	Constant	Constant	Increases	Decreases	Increases	Increases	Increases	Increases	Constant	Constant	—	—	Constant	—	Increases

Key: Predictions for the different output parameters were obtained as follows.

$a$  = contact radius, Eq. [1].

$c$  = stick-zone radius, Eq. [2].

$N_{III}$  = number of cycles spent in region III, Section IV–C.

$N_{I+II}$  = number of cycles spent in region I + II.

$N_f$  = total fretting fatigue life.

$p_{\max}$  = Maximum contact pressure.

$\Delta k_I$  = cyclic mode I stress intensity factor at the tip of the slant crack in region II.

the total fretting fatigue life. This effect can be attributed to an increase in the crack initiation life (region I).

5. Limited results for the martensitic structure, which had a higher yield stress and hardness compared to the other Ti-6Al-4V microstructures, suggest an enhanced fretting fatigue resistance. However, a more comprehensive study is required to fully assess the fretting response of the martensitic structure.
6. Using the measured maximum static friction coefficient of 0.95 for Ti-6Al-4V, the experimentally observed contact and stick-zone radii exhibited good agreement with analytical predictions.
7. The adhesion model predictions concerning strength of adhesion (i.e., weak adhesion) and conditions for crack initiation and initial crack propagation angles were validated with experimental observations.

## ACKNOWLEDGMENTS

This work was supported by the Multi-University Research Initiative on "High Cycle Fatigue," which is funded at MIT by the Air Force Office of Scientific Research, Grant No. F49620-96-1-0478, through a subcontract from the University of California at Berkeley. Assistance from Laurent Chambon with some of the fretting experiments is gratefully acknowledged.

## APPENDIX A

Given the important role that friction plays in the fretting fatigue problem, the following experiment was designed to evaluate the average friction coefficient.

At a constant normal contact load (of 10 or 14 or 15 N), conditions of stick slip were first established at a tangential load of 1.0 N, by suitable choice of the bulk stress, at a test frequency, initially at 1 Hz and finally at 10 Hz. The tangential load was then increased (by increasing the bulk stress) until full sliding occurred. The transition from stick slip to full sliding was recognized by following the change in the hysteresis behavior of tangential load with bulk stress, from a closed loop (during stick slip) to an open loop (during full sliding). The ratio of the tangential load to the normal load at this transition is taken as the breakaway (or maximum static) coefficient of friction,  $\mu_b = Q/N$ .

Immediately following this breakaway, the maximum tangential load decreased to a new steady state,  $Q_{\text{slip}}$ , and the corresponding dynamic coefficient of friction,  $\mu_d$ , was taken as  $\mu_d = (Q_{\text{slip}}/N)$ .

After a few thousand cycles of full sliding behavior, conditions of stick slip were re-established, possibly due to an increase in the friction at the contact interface caused by roughening and oxide debris buildup. By increasing the bulk stress, full sliding could be established, albeit at tangential loads greater than that corresponding to the first breakaway point (Figure A1).

For specimens with well-developed fretting scars, the measured breakaway and dynamic friction coefficients, 0.95 and 0.70, respectively, which were independent of the normal contact loads, were slightly larger than those reported in the literature ( $\mu_b = 0.85$ ,<sup>[24]</sup>  $\mu_d = 0.70$ ,<sup>[24]</sup> or  $0.60$ <sup>[23]</sup>).

The upper limit on the maximum static friction coefficient can be estimated by setting  $\max(G_d) = G_c = (K_{IC}^2/E)$  and

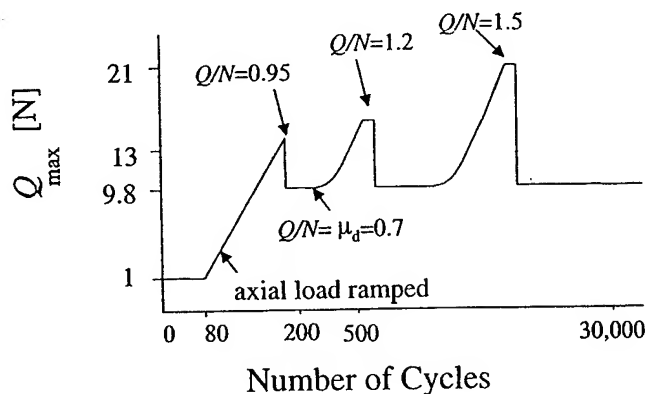


Fig. A1—Schematic illustrating the variation with the number of fatigue cycles of the tangential load as the bulk load on the specimen is increased, indicating onset of full sliding at several values of the tangential loads (under a constant normal load of 14 N).

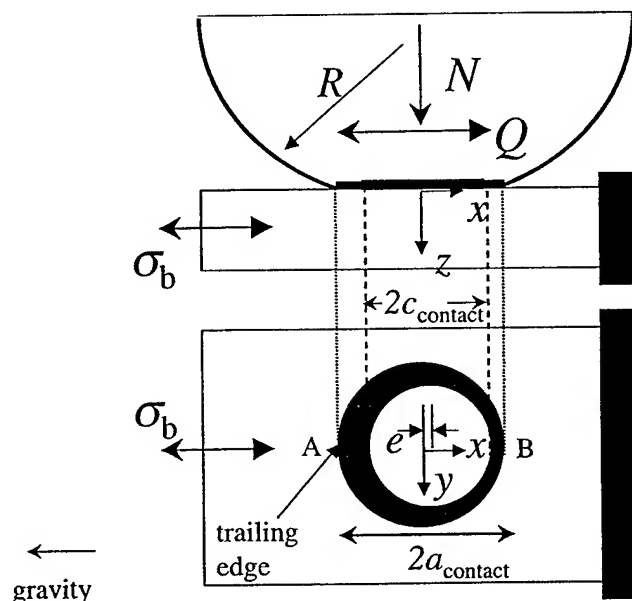


Fig. B1—Schematic illustrating the location of the trailing edge of the contact.

using  $K_{IC} = 65 \text{ MPa}\sqrt{\text{m}}$  for Ti-6Al-4V in Eq. [6] to yield max ( $\mu$ ) = 2.55.

It is believed that the maximum static friction coefficient measured in the fretting tests may depend on the velocity of slip (i.e., the test frequency) across the contacting interfaces. Hence, in order to be consistent with the fretting experiments (Table III), where the frequency was 10 Hz, the friction measurements were conducted at a test frequency of 10 Hz as well.

## APPENDIX B

During one-half of the fatigue cycle, when the sample is fully loaded in tension, the maximum tensile stress created by the tangential loading occurs at location A in the sample. Upon load reversal, the maximum tensile stress due to the tangential load occurs at location B. However, since the sample is under compression, the effective tensile stress at B is much smaller than at A. Thus, location A, which is the

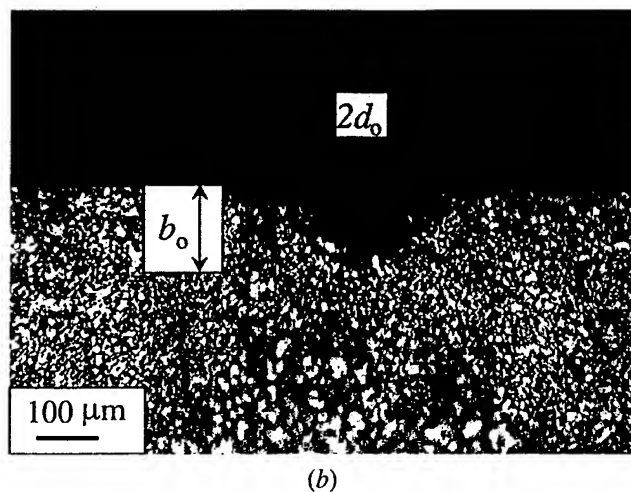
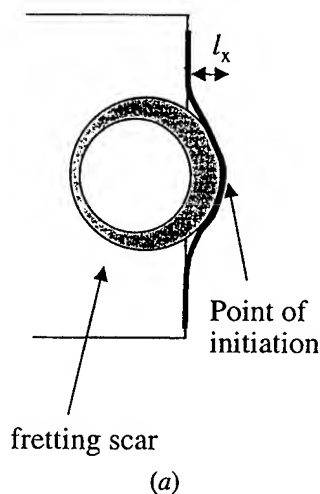


Fig. C1—(a) Schematic illustrating the location of crack initiation and geometric parameter,  $l_x$ . (b) Fractured surface indicating the parameter,  $b_0$ .

perimeter of the contact closest to the actuator, is designated as the trailing edge of the contact (Figure B1).

### APPENDIX C

For the samples that failed, the average angle at which the fretting fatigue cracks initiated in the substrate is obtained through an inspection of two different sections of the specimens, as illustrated in Figure C1. The geometry of the crack as seen from the surfaces gives  $\alpha = \arctan(b_0/l_x)$ .

### REFERENCES

1. R.B. Waterhouse: *Fretting Fatigue*, Applied Science Publishers, London, 1981.
2. R.B. Waterhouse and T.C. Lindley: *Fretting Fatigue*, European Structural Integrity Society Publication 18, London, 1994.
3. R.B. Waterhouse: *Int. Mater. Rev.*, 1992, vol. 37, pp. 77-97.
4. T.C. Lindley: *Int. J. Fatigue*, 1997, vol. 19, pp. S39-S49.
5. I.V. Papadopoulos, P. Davoli, C. Gorla, M. Filippini, and A. Bernasconi: *Int. J. Fatigue*, 1997, vol. 19, pp. 219-35.
6. A.E. Giannakopoulos, T.A. Venkatesh, T.C. Lindley, and S. Suresh: *Acta Mater.*, 1999, vol. 47, pp. 4653-64.
7. B.U. Wittkowsky, P.R. Birch, J. Dominguez, and S. Suresh: *Fatigue Fracture Eng. Mater. Structures*, 1999, vol. 22, pp. 307-20.
8. B.U. Wittkowsky, P.R. Birch, J. Dominguez, and S. Suresh: in *Fretting Fatigue: Current Technology and Practices*, ASTM STP 1367, D.W. Hoepfner, V. Chandrasekaran, and C.B. Elliot, eds., ASTM, Philadelphia, PA, 1999, pp. 213-27.
9. A.L. Hutson, T. Nicholas, and R. Goodman: *Int. J. Fatigue*, 1999, vol. 21, pp. 663-69.
10. R. Cortez, S. Mall, and J.R. Calcaterra: *Int. J. Fatigue*, 1999, vol. 21, pp. 709-17.
11. S. Goto and R.B. Waterhouse: in *Titanium '80: Science and Technology*, H. Kimura and O. Izumi, eds., TMS, Warrendale, PA, 1980, vol. 3, pp. 1837-44.
12. P. Blanchard, C. Colombie, V. Pellerin, S. Fayeulle, and L. Vincent: *Metall. Trans. A*, 1991, vol. 22A, pp. 1535-44.
13. J.A. Hines and G. Lütjering: *Fatigue Fract. Eng. Mater. Structures*, 1999, vol. 22, pp. 657-665.
14. R.S. Bellows, S. Muju, and T. Nicholas: *Int. J. Fatigue*, 1999, vol. 21, pp. 687-697.
15. H. Hertz: *J. Reine. Angewandte Mathematik*, 1882, vol. 92, pp. 156-71.
16. R.D. Mindlin: *J. Appl. Mech.*, 1949, vol. 16, pp. 259-68.
17. V.K. Semchenko: *Surface Phenomena in Metals and Alloys*, Addison-Wesley, Reading, MA, 1962.
18. J.S. McFarlane and D. Tabor: *Proc. R. Soc., London*, 1950, vol. A202, pp. 244-53.
19. R.O. Ritchie, B.L. Boyce, J.P. Campbell, O. Roder, A.W. Thompson, and W.W. Milligan: *Int. J. Fatigue*, 1999, vol. 21, pp. 653-62.
20. B. Cottrell and J.R. Rice: *Int. J. Fracture*, 1980, vol. 16, pp. 155-69.
21. J.C. Newman and I.S. Raju: *Eng. Fracture Mech.*, 1981, vol. 15, pp. 185-92.
22. G.R. Yoder, L.A. Cooley, and T.W. Crooker: in *Fracture Mechanics: 16th Symp.*, ASTM STP 868, M.F. Kanninen and A.T. Hopper, eds., ASTM, Philadelphia, PA, pp. 392-405.
23. G. Welsch, R. Boyer, and E.W. Collings: *Materials Properties Handbook: Titanium Alloys*, ASM International, Materials Park, OH, 1995.
24. R.A. Antoniou and T.C. Radtke: *Mater. Sci. Eng. A*, 1997, vol. 237, p. 229.



PERGAMON

International Journal of Solids and Structures 39 (2002) 281–295

INTERNATIONAL JOURNAL OF  
**SOLIDS and  
STRUCTURES**

www.elsevier.com/locate/ijssolstr

## Analysis of the impact of a sharp indenter

E.W. Andrews<sup>a</sup>, A.E. Giannakopoulos<sup>a</sup>, E. Plisson<sup>b</sup>, S. Suresh<sup>a,\*</sup>

<sup>a</sup> *Department of Materials Science and Engineering, Massachusetts Institute of Technology, RM 8-309, 77 Massachusetts Avenue, Cambridge, MA 02139, USA*

<sup>b</sup> *Ecole Polytechnique, 91128 Palaiseau Cedex, France*

Received 11 August 2001; in revised form 20 August 2001

### Abstract

The present work investigates the impact of a sharp indenter at low impact velocities. A one-dimensional model is developed by assuming that the variation of indentation load as a function of depth under dynamic conditions has the same parabolic form (Kick's Law) as under static conditions. The motion of the indenter as it indents and rebounds from the target is described. Predictions are made of the peak indentation depth, residual indentation depth, contact time, and rebound velocity as functions of the impact velocity, indenter mass and target properties. Finite element simulations were carried out to assess the validity of the model for elastoplastic materials. For rate-independent materials agreement with the model was good provided the impact velocity did not exceed certain critical values. For rate-dependent materials the relationship between load and depth in the impact problem is no longer parabolic and the model predictions cannot be applied to this case. The rate-dependent case can be solved by incorporating the relationship between the motion of the indenter and the dynamic flow properties of the material into the equation of motion for the indenter. © 2001 Elsevier Science Ltd. All rights reserved.

**Keywords:** Indentation; Impact; Dynamic plasticity

### 1. Introduction

We consider here the impact of a sharp indenter. Indentation problems are difficult to analyze: the problem is generally three-dimensional, a complicated contact problem must be solved at the interface of the indenter and the target, and material nonlinearities due to plasticity, friction, phase transformations and microcracking are often involved. For the case of an impact problem, target inertia and rate-dependent material behavior add to the complexity of the problem. The impact of a sharp indenter is a problem of considerable technological interest, both as a means of assessing dynamic material behavior and for evaluating the damage caused by the impact of small, sharp particles on various types of structures. Impacts of this kind on aircraft bodies and engine components, termed foreign object damage (FOD), is a significant concern to airframe and aircraft engine manufacturers.

\* Corresponding author. Tel.: +1-617-253-3320; fax: +1-617-253-0868.

E-mail address: ssuresh@mit.edu (S. Suresh).

Indentation tests provide a nondestructive method for extracting several basic material properties, at various size scales. Nearly all standard instrumented indentation tests are carried out under quasi-static conditions. Results have been reported for dynamic indentation tests using sharp (Graham, 1973; Marshall et al., 1983; Koepfel and Subhash, 1999) and spherical indenters (Tirupataiah and Sundararajan, 1991). A dynamic indentation test offers the possibility of determining the dynamic hardness and rate-dependent response of the material.

In this paper, we analyze the impact of a sharp indenter in the context of dynamic elastoplasticity. In Sections 2 and 3 we analyze theoretically and computationally the case of rate-independent response of the target. In Section 4, we analyze computationally the case of rate-dependent response of the target and provide a general methodology to relate the impact response with the rate-dependent plastic properties of the target.

## 2. Analytical one-dimensional model

The indenter is assumed to be sharp, such as a pyramid or circular cone indenter. The indenter is assumed to be rigid. It has a mass  $m$  and contacts the target at an initial velocity  $V_0$  normal to the surface. The target is assumed to be a rate-independent, elastoplastic, homogeneous, isotropic body whose dimensions are large compared to the contact diameter. The contact is assumed to be frictionless. Prior to the impact, the target is stress-free and at rest.

For sharp indentation under quasi-static conditions, if  $P$  is the force exerted by the indenter on the target and  $h$  is the depth of indentation, the  $P$ – $h$  curve follows a parabolic relation during loading, i.e.  $P = Ch^2$ , known as Kick's law. The unloading curve is assumed to be linear. The slope of the unloading curve reflects the elastic properties of the indenter and the target, as well as the area of contact at the instant of unloading. Note that as the load approaches zero, typically the unloading curve becomes nonlinear. However, a linear unloading curve is employed in this analysis. We define a new constant  $C_e$  in terms of the unloading slope  $dP/dh$  and the peak indentation depth  $h_{\max}$  as  $dP/dh = C_e h_{\max}$ . The constant  $C_e$  has the same units as  $C$ . By asserting that the contact area corresponding to elastic response at the maximum load should be less than or equal to the actual contact area it can be shown that the slope of the unloading curve must be greater than or equal to the instantaneous slope of the loading curve at the point of unloading. This requires that  $C/C_e$  must be less than or equal to 0.5. Fig. 1 shows the loading and unloading curves for various allowable

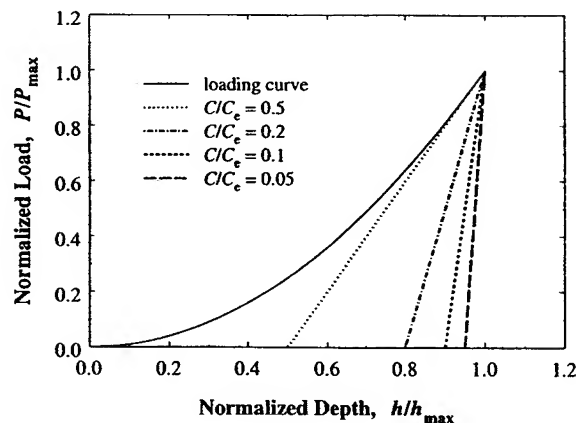


Fig. 1. Force–depth curves showing allowable values of the unloading slope.



values of the dimensionless parameter  $C/C_e$ . Expressions for  $C$  and the unloading slope for various sharp indenter geometries under static conditions are available (e.g. Giannakopoulos and Suresh, 1999).

During the impact, the motion  $h(t)$  of the indenter is governed by Newton's second law:

$$m\ddot{h} + P = 0. \quad (1)$$

The velocity and acceleration of the indenter will be denoted by  $\dot{h}$  and  $\ddot{h}$ , respectively. Time  $t = 0$  is taken to be the instant when the indenter touches the target. The motion of the indenter has three phases: an indentation phase, a rebound phase and a free-flight phase. During the indentation phase, the velocity of the indenter decreases as the initial kinetic energy is converted to energy associated with deformation of the target. Part of the initial energy is stored as elastic energy which is recovered in the rebound phase, while the rest is dissipated as plastic work.

To analyze the impact problem it is assumed that the shape of the  $P$ - $h$  curve is unchanged under dynamic conditions. If the impact velocity is high enough the kinetic energy of the target becomes significant. Furthermore, adiabatic heating and thermal softening, localization of the deformation, phase transformations or even melting of the material can occur under dynamic conditions. Under these conditions, the dynamic  $P$ - $h$  curve will not follow the quasi-static curve and this analysis will not be valid. Assuming that the quasi-static curve is followed during the indentation phase  $P$  increases with  $h$  as  $P = Ch^2$  so we have that

$$m\ddot{h} + Ch^2 = 0; \quad t \geq 0 \quad (2)$$

with initial conditions  $h = 0$  and  $\dot{h} = V_0$  at  $t = 0$ . Integration of Eq. (2) leads to the energy balance expression:

$$\frac{1}{2}m\dot{h}^2 - \frac{1}{2}mV_0^2 = -\frac{1}{3}Ch^3. \quad (3)$$

The maximum penetration depth  $h_{\max}$  can be determined from Eq. (3) by setting  $\dot{h} = 0$  and solving for  $h$ :

$$h_{\max} = \left( \frac{3mV_0^2}{2C} \right)^{1/3}. \quad (4)$$

Eq. (3) can be integrated with respect to time to obtain the duration of the penetration phase  $t_1$ , i.e. the time taken to reach  $h_{\max}$ :

$$t_1 = \int_0^{h_{\max}} \left( V_0^2 - \frac{2}{3} \frac{Ch^3}{m} \right)^{-1/2} dh = \left( \frac{3m}{2CV_0} \right)^{1/3} \left[ \frac{1}{3} \beta \left( \frac{1}{3}, \frac{1}{2} \right) \right] = 1.402 \left( \frac{3m}{2CV_0} \right)^{1/3}, \quad (5)$$

where  $\beta$  is the beta function (Euler's integral of the first kind) defined as

$$\beta(x, y) = \int_0^1 t^{x-1} (1-t)^{y-1} dt. \quad (6)$$

More generally, if  $t(h)$  is the time taken by the indenter to penetrate to a depth  $h$  of the target, a similar calculation gives:

$$t(h) = \int_0^h \left( V_0^2 - \frac{2}{3} \frac{Cu^3}{m} \right)^{-1/2} du = \left( \frac{3m}{2CV_0} \right)^{1/3} \int_0^{h/h_{\max}} \frac{dx}{\sqrt{1-x^3}}. \quad (7)$$

During the rebound phase, the load follows the linear unloading curve shown in Fig. 1. During unloading the load may be expressed as  $P = C_e h_{\max} h + (C - C_e) h_{\max}^2$ . This expression comes from the definition of the unloading slope, and using the condition that the load  $P$  is equal to  $Ch_{\max}^2$  at  $h = h_{\max}$ . The motion of the indenter is governed by

$$m\ddot{h} + C_e h_{\max} h + (C - C_e) h_{\max}^2 = 0, \quad t \geq t_1 \quad (8)$$

with initial conditions  $h = h_{\max}$  and  $\dot{h} = 0$  at  $t = t_1$ . The solution of this differential equation is

$$h(t) = h_{\max}(1 - \bar{C} + \bar{C} \cos(\omega t - \omega t_1)), \quad (9)$$

where  $\omega = (C_c h_{\max}/m)^{1/2}$  and  $\bar{C} = C/C_c$ . The indenter accelerates away from the target until the force  $P$  decreases to 0. From the expression for the unloading curve the depth  $h_2$  when  $P = 0$  can be found to be

$$h_2 = h_{\max}(1 - \bar{C}). \quad (10)$$

The depth  $h_2$  represents the final or residual indentation depth; the difference between  $h_{\max}$  and  $h_2$  corresponds to the elastic recovery of the target. By setting  $h(t) = h_2$  in Eq. (9) the time  $t_2$  when  $P = 0$  can be found to be

$$t_2 = t_1 + \frac{\pi}{2} \left( \frac{m}{C_c h_{\max}} \right)^{1/2}. \quad (11)$$

During the final (free-flight) phase the indenter and the target are no longer in contact. No forces act on the indenter; it moves away from the target at constant velocity. In this phase the velocity,  $\dot{h}$ , is equal to its value at  $t = t_2$ . This rebound velocity can be determined by differentiation of Eq. (9) and setting  $t = t_2$ :

$$V_{\text{rebound}} = -V_0 \left( \frac{3\bar{C}}{2} \right)^{1/2}. \quad (12)$$

The position during the free-flight phase is given as

$$h(t) = h_2 - (t - t_2) \left( \frac{3\bar{C}V_0^2}{2} \right)^{1/2}. \quad (13)$$

The absolute value of the ratio of the rebound velocity to the impact velocity, the coefficient of restitution  $e$ , is evaluated using Eq. (12) to be

$$e = \left| \frac{V_{\text{rebound}}}{V_0} \right| = \left( \frac{3\bar{C}}{2} \right)^{1/2}. \quad (14)$$

The coefficient of restitution is independent of the impact velocity. In terms of a normalized time  $\bar{t} = t/t_1$  and a normalized indentation depth  $\bar{h} = h/h_{\max}$ , the motion of the indenter may be written as

$$\bar{t}(\bar{h}) = 0.713 \int_0^{\bar{h}} \frac{dx}{\sqrt{1-x^3}} = 0.713 \bar{h} F(1/3, 1/2; 4/3; \bar{h}^3), \quad 0 \leq t \leq t_1 \quad (15)$$

$$\bar{h}(\bar{t}) = \bar{C} \left( \cos \left( \frac{\bar{t} - 1}{0.582 \bar{C}^{1/2}} \right) - 1 \right) + 1, \quad t_1 < t \leq t_2 \quad (16)$$

$$\bar{h}(\bar{t}) = \bar{h}_2 - (\bar{t} - \bar{t}_2)(2.948 \bar{C})^{1/2}, \quad t > t_2. \quad (17)$$

In the above expressions,  $F$  is the hypergeometric function,  $\bar{h}_2 = 1 - \bar{C}$ , and  $\bar{t}_2 = 1 + 0.915(\bar{C})^{1/2}$ . The complete motion of the indenter is shown in Fig. 2 which plots the function  $\bar{h}(\bar{t})$  for various values of the dimensionless ratio  $C/C_c$ . Marshall et al. (1983) considered the impact of a sharp indenter and provided expressions for the peak depth  $h_{\max}$  and loading time  $t_1$  analogous to Eqs. (4) and (5). The present study extends their analysis by considering the rebound phase, and providing expressions for the complete motion of the indenter. The rebound phase can be important if elastic deformation of the target is significant (e.g. brittle materials).

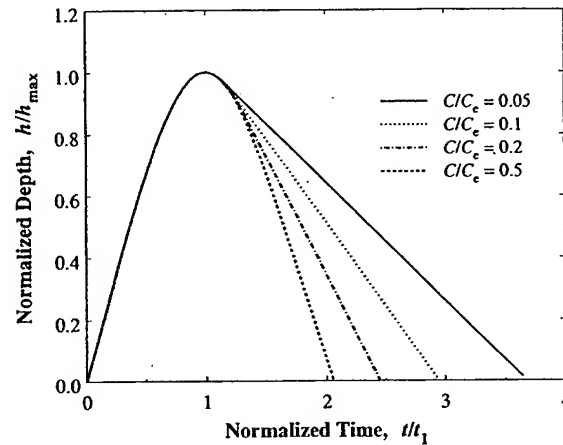


Fig. 2. Analytical prediction of normalized indentation depth vs. normalized time for various values of  $C/C_e$ .

### 3. Finite element simulations for rate-independent materials

In this section the results of a finite element study are presented. The objective is to assess the range of validity of the analytical results presented in Section 2. The commercial finite element package ABAQUS/Explicit (HKS, Pawtucket, RI) was used to simulate the impact. The mesh used is shown in Fig. 3(a). A typical deformed mesh at the peak depth of indentation is shown in Fig. 3(b). The simulation uses infinite elements away from the contact area to simulate a semi-infinite region. The mesh has a total of 19,200 axisymmetric, 4-noded, reduced integration, continuum elements, and 160 infinite elements at the boundary. Although the analytical results in Section 2 apply for any sharp indenter, in these simulations the indenter is considered to be a cone with a  $70.3^\circ$  included half angle. This gives approximately the same ratio of indentation depth to contact area as the common Vickers and Berkovich indenters. At the peak depth of indentation approximately 14–18 elements spanned the contact radius. Large deformation analysis and the adaptive meshing option were employed. The indenter was represented as a rigid surface with an associated mass element. To study the role of indenter mass two different values were used:  $m = 10$  mg and 10 g. The impact velocity  $V_0$  varied from 0.5 to 1800 m/s. The simulations were isothermal; heating of the material and the associated thermal softening were not included.

To consider a variety of materials, the stress–strain response of the target was represented by four different elastoplastic materials: 6061 Aluminum (Giannakopoulos et al., 1994), annealed commercial brass (ASM, 1979), mild steel and 4340 steel (ASM, 1987). Classical Mises elastoplastic behavior was assumed, i.e. isotropic linear hypoelasticity and incremental plastic strains calculated using an associated Mises flow rule. Fig. 4 shows the uniaxial tensile true stress–logarithmic plastic strain curves for these materials. These curves are from quasi-static tests. In some cases the uniaxial data did not extend out to the large strains necessary to carry out the indentation simulations; in these cases the data were extended assuming constant strain hardening. Values of  $C$  and  $C_e$  for each material were determined from quasi-static simulations and are reported in Table 1.

In order to compare the finite element analysis (FEA) results with the analytical results, we will first compare with the predicted maximum indentation depth  $h_{\max}$ . The expression for  $h_{\max}$  in Eq. (4) can be rewritten as follows:

$$h_{\max} = h_i \left( \frac{V_0}{V_i} \right)^{2/3}. \quad (18)$$

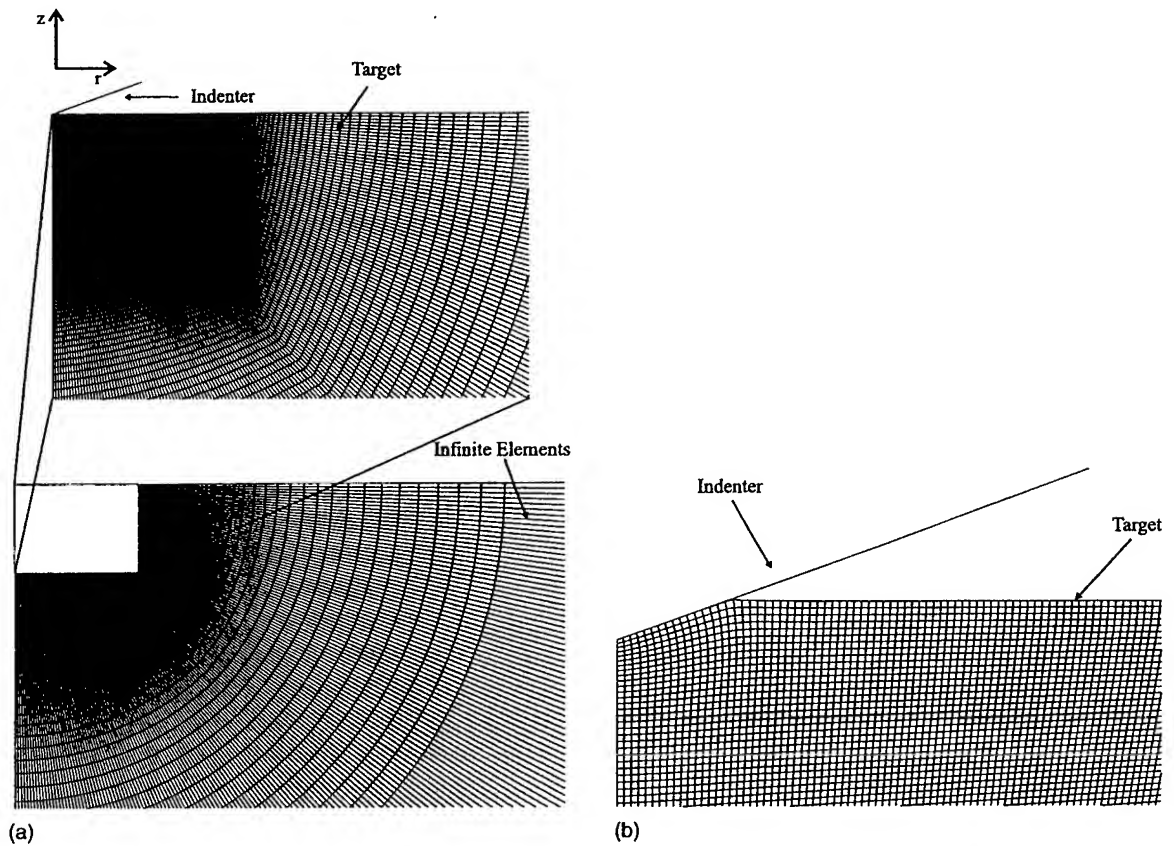


Fig. 3. (a) Finite element mesh used for dynamic indentation simulations. (b) Typical deformed mesh at peak indentation depth.

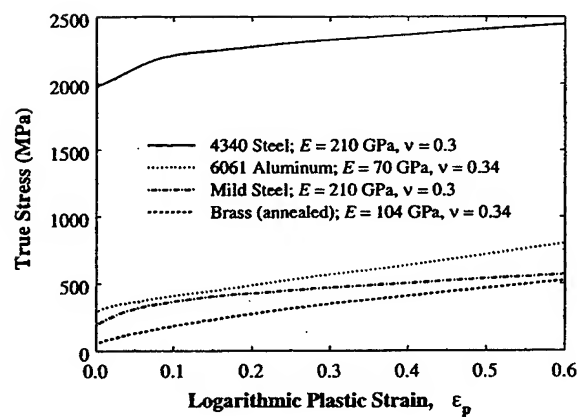


Fig. 4. True stress–logarithmic plastic strain curves for the materials considered in the finite element simulations.

Table 1  
Indentation characteristics of the different alloys considered in this study

	Al 6061	Mild steel	4340 steel	Brass
$C$ (GPa)	30.07	28.32	139.20	12.50
$C_e$ (GPa)	516.4	1564.4	1334.6	701.7
$C/C_e$	0.059	0.018	0.104	0.018
$\rho_{\text{target}}$ (g/cm <sup>3</sup> )	2.7	7.9	7.9	8.5
$V_l$ (m/s)	3337	1905	4224	1220

The quantities  $h_l$  and  $V_l$  are defined as

$$h_l = \left( \frac{3m}{2\rho_{\text{target}}} \right)^{1/3}, \quad (19)$$

$$V_l = \left( \frac{C}{\rho_{\text{target}}} \right)^{1/2}, \quad (20)$$

where  $\rho_{\text{target}}$  is the mass density of the target material. The velocity  $V_l$  is a characteristic velocity for the dynamic sharp indentation problem. As  $V_0$  approaches  $V_l$  the kinetic energy absorbed by the target becomes significant and results in discrepancies between the simulations and the analytical results. The values of  $V_l$  are reported in Table 1. The peak depth (FEA results) as a function of impact velocity is shown in Fig. 5. Eq. (18) suggests that if the normalized depth  $h_{\text{max}}/h_l$  is plotted versus the normalized impact velocity  $V_0/V_l$ , the results for the different materials and indenter kinetic energies should fall on the same curve. Fig. 6 shows this plot. It can be seen that up to a velocity of approximately  $0.1V_l$  good agreement holds between the theory and the FEA results, above that velocity the depths seen in the simulations are less than those predicted by the theory.

An additional way to assess the range of validity of the analysis is to examine the coefficient of restitution  $e$ . Recall from Eq. (14) that  $e$  should be independent of the impact velocity and depends only on the ratio  $C/C_e$ . Fig. 7 shows  $e$  (FEA results) plotted as a function of impact velocity. Fig. 8 plots the normalized coefficient of restitution (FEA result divided by theoretical prediction) vs. the normalized impact velocity ( $V_0/V_l$ ). It can be seen that for all four materials the FEA results deviate from the analytical prediction

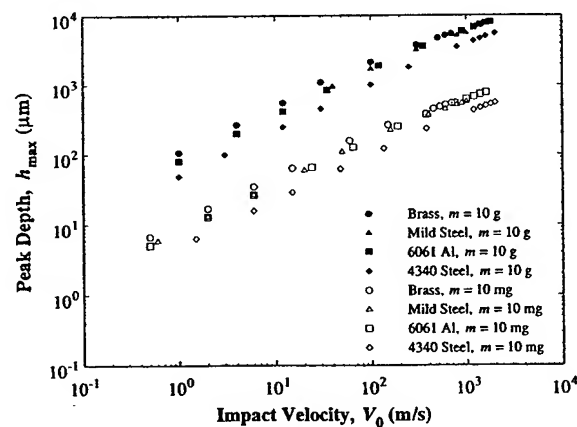


Fig. 5. Peak depth vs. impact velocity (FEA results).

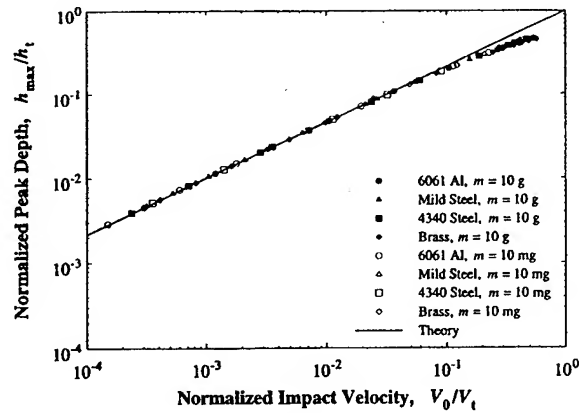


Fig. 6. Normalized peak depth vs. normalized impact velocity, along with the analytical result, Eq. (4).

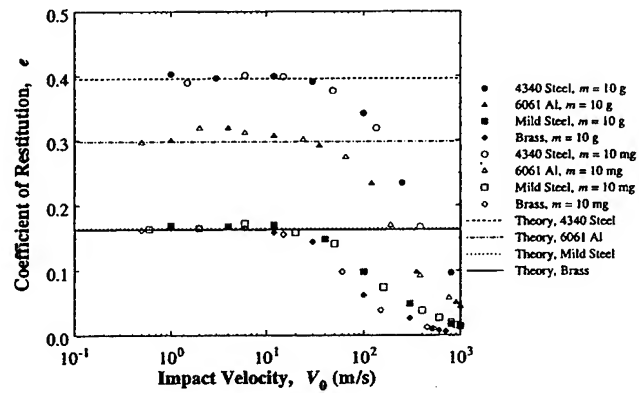


Fig. 7. Coefficient of restitution vs. impact velocity (FEA results). The analytical result, Eq. (14), is also shown.

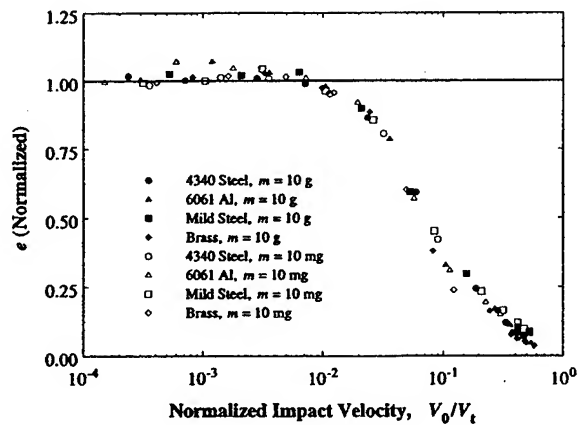


Fig. 8. Normalized coefficient of restitution vs. normalized impact velocity.

when the impact velocity exceeds approximately  $0.01V_t$ . Below this velocity, the coefficient of restitution is approximately constant and in reasonable agreement with the theory.

As a final means of assessing the range of validity of the analysis, we compare the contact time in the finite element simulations with the theoretical prediction, Eq. (11). The contact time  $t_2$  can be expressed as

$$t_2 = t_1 \left( \frac{V_0}{V_t} \right)^{-1/3}, \quad (21)$$

where we have introduced the quantity  $t_1$  defined as

$$t_1 = \left( \frac{m^2 \rho_{\text{target}}}{C^3} \right)^{1/6} [1.605 + 1.468(\bar{C})^{1/2}]. \quad (22)$$

Fig. 9 shows the contact time  $t_2$  (FEA results) plotted as a function of impact velocity. Eq. (21) suggests that if a normalized contact time, defined as  $t_2/t_1$ , is plotted versus the normalized impact velocity,  $V_0/V_t$ , the results for the different materials and indenter kinetic energies should fall on the same curve. Fig. 10 plots

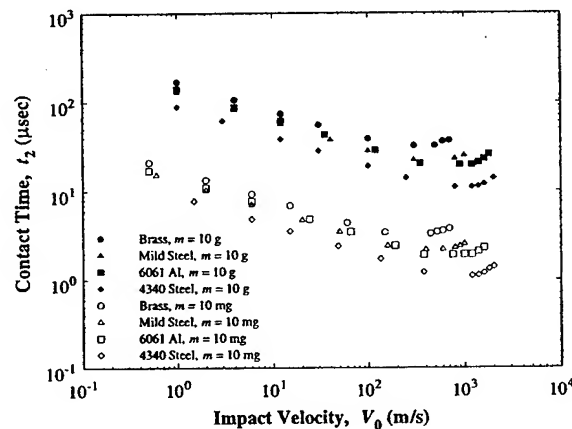


Fig. 9. Contact time vs. impact velocity (FEA results).

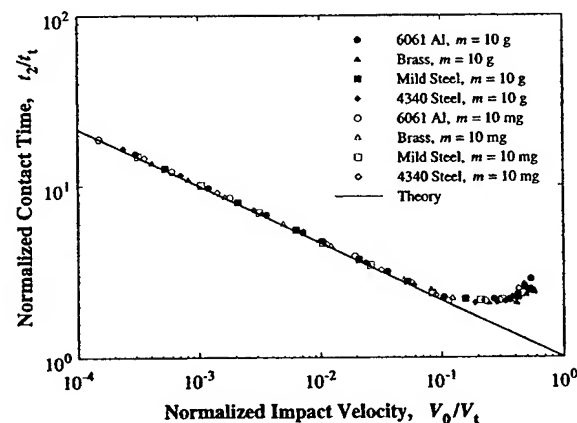


Fig. 10. Normalized contact time vs. normalized impact velocity, along with the analytical result, Eq. (11).

these results; it can be seen that good agreement is obtained up to impact velocities of  $\approx 0.1V_t$ , above that value the contact time observed in the simulations does not continue to decrease as predicted by the theory and instead begins to increase slightly with increasing impact velocity.

The finite element simulations demonstrate the existence of a characteristic velocity  $V_t$  which defines the range of validity of the analytical results. As the impact velocity approaches the  $V_t$  the role of target inertia, neglected in the analytical model, becomes significant and results in discrepancies between the analytical model and the FEA results seen in Figs. 6, 8 and 10. Comparing the analytical results with the finite element simulations, it appears that quantities associated with the loading phase (e.g. peak depth) show good agreement with the analytical results at impact velocities up to  $\approx 0.1V_t$ , while quantities associated with the rebound phase (e.g. rebound velocity) show good agreement up to lower velocities,  $\approx 0.01V_t$ . The contact time has a contribution from both the loading phase and the rebound phase. The contribution from the loading phase is significantly larger than that from the rebound phase, hence the contact time shows good agreement with the analytical results at impact velocities up to  $\approx 0.1V_t$ .

#### 4. Rate-dependent material response

The simulations in the previous section assumed rate-independent material behavior. In this section we consider the influence of rate-dependent plasticity on the impact of a sharp indenter. It is well known that for some materials the yield stress can vary with the imposed strain rate (e.g. Clifton, 2000; Frantz and Duffy, 1972; Huang and Clifton, 1985; Klopp, 1984; Lee et al., 2000; Li, 1982; Nicholas, 1980; Senseny et al., 1978). Fig. 11 shows the variation in yield stress with strain rate for a variety of metals, showing the increase in flow stress with strain rate. Some of this data is for dynamic shear tests, and the shear quantities have been converted to equivalent uniaxial values. Fig. 12 shows this same data plotted with the dynamic yield stress normalized by the quasi-static yield stress. One way to include the strain rate effect is the power law form

$$\sigma_y(\epsilon, \dot{\epsilon}) = \sigma_y^0(\epsilon) \left( 1 + \left( \frac{\dot{\epsilon}}{\dot{\epsilon}_0} \right)^b \right), \quad (23)$$

where  $b$  and  $\dot{\epsilon}_0$  are material constants. To assess the role of rate-dependent material behavior on the impact of a sharp indenter, finite element simulations using ABAQUS/Explicit were carried out in which the yield

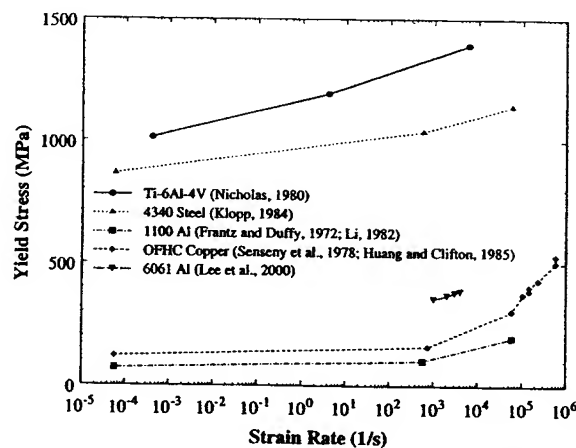


Fig. 11. Yield stress vs. strain rate for a variety of metals showing the increase in yield stress with strain rate.



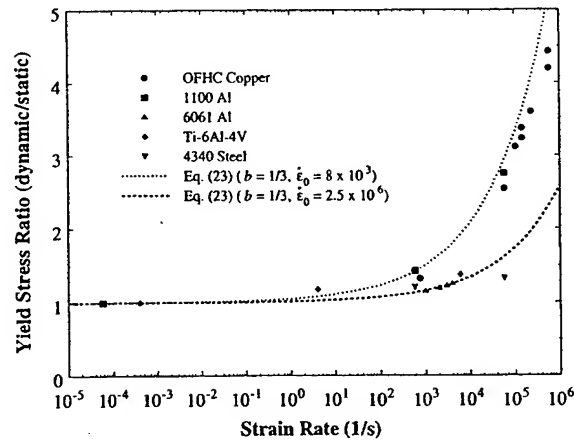


Fig. 12. Yield stress ratio vs. strain rate for the experimental data shown in Fig. 12.

stress varied with strain rate. The mesh used in these simulations was the same as that described in Section 3. A strongly rate sensitive material (with properties corresponding to 1100-O aluminum) and a weakly rate sensitive material (with properties corresponding to 6061 aluminum) were simulated. Values of  $b = 1/3$ ,  $\dot{\epsilon}_0 = 8000 \text{ s}^{-1}$  and  $b = 1/3$ ,  $\dot{\epsilon}_0 = 250,000 \text{ s}^{-1}$  were used for the strongly rate sensitive and weakly rate sensitive materials, respectively. The cases  $b = 1/2$  and  $\dot{\epsilon}_0 = 8000 \text{ s}^{-1}$  and  $b = 1/6$  and  $\dot{\epsilon}_0 = 250,000 \text{ s}^{-1}$  were also examined. For these materials the variation in flow stress with strain rate is shown in Fig. 12. Material data was defined in such a way that the strain hardening was not rate sensitive.

The effect of rate-dependent material response in dynamic indentation is to increase the resistance to indentation. This effect is illustrated in Fig. 13 which shows the dynamic  $P$ - $h$  curve for a simulation in which the rate-dependent response was included for the case of 1100 Aluminum. The indenter mass and impact velocity are 10 mg and 3 m/s, respectively. Even at this low impact velocity, the inclusion of rate-dependent plasticity has the effect of decreasing the peak depth compared to the rate-independent case. The reduction in peak depth, and thus in the final indent size, demonstrates how elevated hardness values are observed under dynamic conditions.

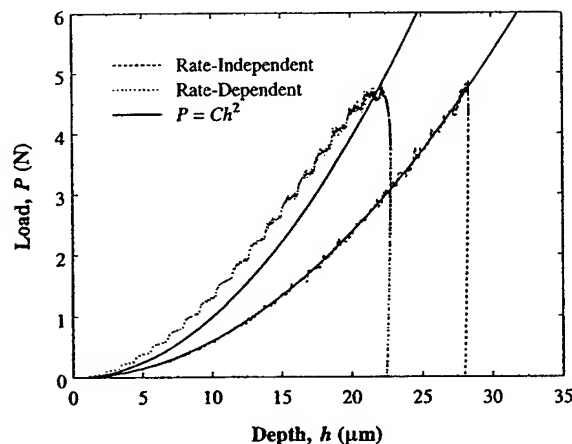


Fig. 13. Load vs. depth in dynamic indentation simulations, rate-dependent and rate-independent, for 1100 Al,  $m = 10 \text{ mg}$ ,  $V_0 = 3 \text{ m/s}$ .

To assess the validity of Kick's law for the rate-dependent case we attempted to fit curves of the form  $P = Ch^2$  to the loading portion of the load–depth curves. A typical result shown in Fig. 13 shows a poor fit. In fact, at the final stages of the loading curve the load becomes constant and then actually decreases slightly. For rate-dependent materials Kick's law is not valid for the impact problem, and therefore the analytical results derived in Section 2 cannot be applied.

Kick's Law is not valid for the rate-dependent case as the loading rates, and thus the material strength, vary during the impact. When the material response is rate-sensitive,  $C$  is not constant and instead varies with the loading rate. The strain rates in the material scale with the rate quantity  $\dot{h}/h$  (e.g. Lucas and Oliver, 1999; Woodcock and Bahr, 2000) and thus  $C$  depends on material properties and  $\dot{h}/h$ . For a flow stress variation that follows Eq. (23),  $C$  can be approximated as

$$C = C_0 f(\dot{h}/h), \quad (24)$$

where  $C_0$  is the quasi-static value of  $C$ , i.e. the value of  $C$  as  $\dot{h}/h \rightarrow 0$ . Therefore the function  $f(\dot{h}/h)$  is positive with  $f(0) = 1$ . This suggests that if the motion of the indenter  $h(t)$  were such that  $\dot{h}/h$  were held constant, rate-dependent materials will follow Kick's law, with the constant  $C$  elevated above its quasi-static value.

We now apply these results to analyze the impact problem. In the following we will suppress the argument  $\dot{h}/h$  and denote the function  $f(\dot{h}/h)$  simply as  $f$ . During impact the velocity will decrease as the indenter advances into the material. The rate quantity  $\dot{h}/h$  is not constant; it will decrease as indentation proceeds, eventually becoming equal to 0. During the loading phase the governing equation for the motion of the indenter is

$$m\ddot{h} + Ch^2 = m\dot{h} + C_0 f \dot{h}^2 = 0; \quad t \geq 0 \quad (25)$$

with initial conditions  $h = 0$  and  $\dot{h} = V_0$  at  $t = 0$ . If the values of  $m$  and  $V_0$  are provided, and  $C_0$  and  $f$  are known, Eq. (25) can be solved numerically to find the motion  $h(t)$ . As was done for the rate-independent case, Eq. (25) can be integrated to yield the instantaneous energy balance equation

$$\frac{1}{2} m \dot{h}^2 + \frac{1}{3} C_0 f h^3 - \frac{C_0}{3} \int_0^t (h^2 \ddot{h} - h \dot{h}^2) f' dt = \frac{1}{2} m V_0^2, \quad (26)$$

where  $f'$  represents the derivative of  $f$  with respect to its argument  $\dot{h}/h$ . Using the condition that at the peak indentation depth,  $h = h_{\max}$ , the velocity  $\dot{h} = 0$  and  $f(0) = 1$ , the peak indentation depth can be determined to be:

$$h_{\max}^3 = \frac{3}{2} \frac{m V_0^2}{C_0} - \int_0^{t_1} (h \dot{h}^2 - h^2 \ddot{h}) f' dt, \quad (27)$$

where  $t_1$  is the time at which the peak depth is reached and  $\dot{h} = 0$ . Comparing with the rate-independent result, Eq. (4), it can be seen that for the rate-dependent case the peak depth is reduced.

To assess this analysis, finite element simulations were carried out in which the motion  $h(t)$  was such that  $\dot{h}/h$  was a constant whose value was varied over the range 2500–500,000  $s^{-1}$ . The motion was of the form  $h(t) = h_0 \exp(rt)$  where  $r$  is the value of  $\dot{h}/h$ . As the exponential curve does not satisfy  $h(0) = 0$ , a short period of constant velocity motion is imposed to connect the zero point with the exponential curve. The constant velocity takes place over a depth less than 2% of the total depth, so the influence of this region is expected to be small. Fig. 14(a) shows the form of the motion imposed for the case  $r = 5000 s^{-1}$ , while Fig. 14(b) shows a detail of the initial stages of the motion and the constant velocity segment that connects to the exponential curve.

Fig. 15 shows the load vs. depth curves for 1100 Al at various values of the rate parameter  $\dot{h}/h$ , along with the quasi-static result. It can be seen that in all cases the  $P$ – $h$  curve is well represented by Kick's law, and from these results the constant  $C$  may be determined for each case. Good agreement with Kick's law

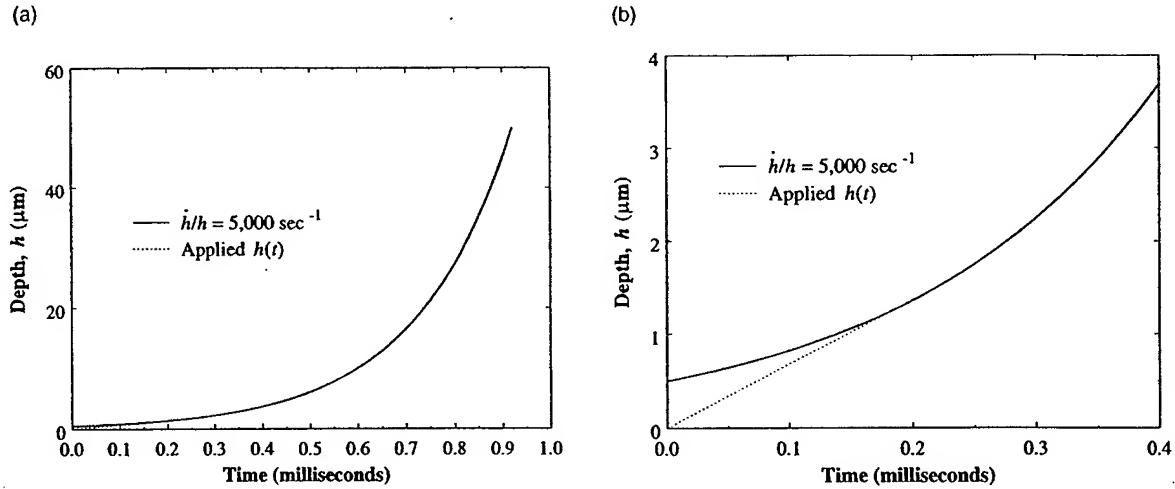


Fig. 14. (a) Applied  $h(t)$  for rate-dependent indentation simulations. (b) Applied  $h(t)$  showing constant velocity region.

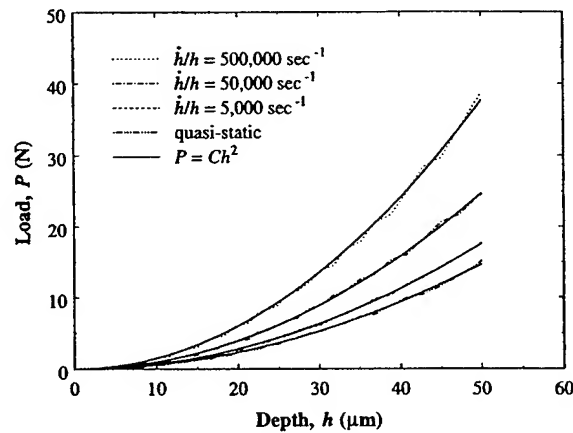


Fig. 15. Load vs. depth in dynamic indentation simulations at constant indentation loading rate  $\dot{h}/h$  for 1100 Al, along with the quasi-static result.

was also found for 6061 Al. The variation of  $C$  as a function of  $\dot{h}/h$  for the two different materials is plotted in Fig. 16. As expected, the strongly rate sensitive material shows greater sensitivity to the rate parameter  $\dot{h}/h$ . These results allow one to assess the form of  $f(\dot{h}/h)$ .

For the case where the strain rate influences the flow stress according to Eq. (23), we fit the variation of  $C$  as a function of  $\dot{h}/h$  using the following function which involves two unknown parameters  $c$  and  $r_0$

$$f(\dot{h}/h) \approx \left[ 1 + \left( \frac{\dot{h}/h}{r_0} \right)^c \right]. \quad (28)$$

Within the range of parameters examined, we found that  $c \approx b$  and  $r_0 \approx 40\dot{\epsilon}_0 c$ . Using the expression in Eq. (28) for  $f(\dot{h}/h)$  the integral in Eq. (27) converges and was evaluated numerically for a range of impact velocities and masses using the values of  $h(t)$ ,  $\dot{h}(t)$  and  $\ddot{h}(t)$  obtained from FEA. The peak depth was

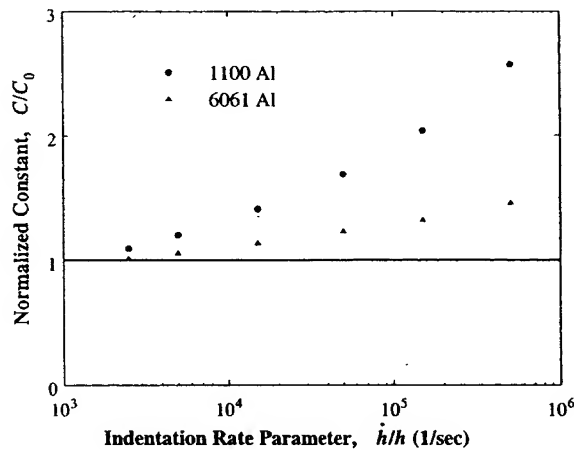


Fig. 16. Normalized constant  $C/C_0$  vs. the indentation rate parameter  $\dot{h}/h$ .

predicted to within 5% in all cases examined, which implies that Eq. (24) is a valid representation of the variation of  $C$  under impact conditions. For the case of dynamic spherical indentation, Tirupataiah and Sundararajan (1991) define an average strain rate in the plastically deforming region, using expressions for the average strain and the contact time of the indenter. Koeppel and Subhash (1999) have suggested an average or effective strain rate equal to the velocity of the indenter divided by the final size of the indentation. The results presented here suggest an alternative approach in which the average variation in strain rate is followed during the impact through the function  $f(\dot{h}/h)$ . The present formulation suggests a way to obtain the dynamic material constants  $b$  and  $\epsilon_0$ . The least information is either the displacement or velocity history for at least three dynamic indentation tests at different indenter kinetic energies  $mV_0^2/2$ . Equally well, one can use at least two dynamic indentation tests at different kinetic energies and one static test which provides  $C_0$  directly.

## 5. Conclusions

An analysis of the impact of a sharp indenter has been presented. A solution describing the motion of the indenter has been given. The maximum depth of indentation, the residual depth of indentation, the time the indenter is in contact with the target and the rebound velocity have been provided.

The analytical results have been compared with dynamic rate-independent elastoplastic finite element simulations. The peak indentation depth, contact time and rebound velocity from the simulations were compared with the analytical predictions. The quantity  $(C/\rho_{\text{target}})^{1/2}$  was found to be a characteristic velocity  $V_t$  for the dynamic sharp indentation problem and indicates the point at which the kinetic energy lost to the target becomes significant. It was found that the peak indentation depth and the contact time showed good agreement with the theoretical results up to impact velocities  $\approx 0.1V_t$ , while the rebound velocity deviated from the analytical prediction when the impact velocity exceeded  $\approx 0.01V_t$ . It appears that quantities associated with the loading phase (e.g. peak depth) show good agreement up to  $\approx 0.1V_t$ , while quantities associated with the rebound (e.g. rebound velocity) show good agreement only up to  $\approx 0.01V_t$ .

Rate-dependent plasticity has the effect of increasing the average contact pressure required for indentation, and increases the resistance to indentation. For the case of rate-dependent response in the impact problem the relationship between load and depth is no longer parabolic, and thus Kick's law is not valid

under these conditions. The problem can be solved by incorporating the relationship between the motion of the indenter and the dynamic flow properties of the material into the equation of motion for the indenter.

### Acknowledgements

AEG and SS gratefully acknowledge support from the Multi-University Research Initiative on “High Cycle Fatigue”, which was funded at MIT by the Air Force Office of Scientific Research, Grant no. F49620-96-1-0478.

### References

- ASM, Source Book on Copper and Copper Alloys, 1979.
- ASM, Atlas of Stress–Strain Curves, 1987.
- Clifton, R.J., 2000. Response of materials under dynamic loading. *Int. J. Solids Struct.* 37, 105–113.
- Frantz, R.A., Duffy, J., 1972. The dynamic stress–strain behavior in torsion of 1100-O aluminum subjected to a sharp increase in strain rate. *J. Appl. Mech.* 39, 939–945.
- Giannakopoulos, A.E., Larsson, P.L., Vestergaard, R., 1994. Analysis of vickers indentation. *Int. J. Solids Struct.* 31, 2679–2708.
- Giannakopoulos, A.E., Suresh, S., 1999. Determination of elastoplastic properties by instrumented sharp indentation. *Scripta Mater.* 40, 1191–1198.
- Graham, G.A.C., 1973. Contribution to Hertz’s theory of elastic impact. *Int. J. Engng. Sci.* 11, 409–413.
- Huang, S., Clifton, R.J., 1985. Dynamic plastic response of OFHC Copper at high shear strain rates. In: Kawata, K., Shioiri, J. (Eds.), *Macro and Micromechanics of High Velocity Deformation and Fracture*, IUTAM, Tokyo, 63–73.
- Klopp, R.W., 1984. Pressure-shear deformation of 4340 steel at strain rates of  $10^5 \text{ s}^{-1}$ . In: M.Sc. Thesis. Brown University, Providence, RI.
- Koeppel, G.J., Subhash, G., 1999. Characteristics of residual plastic zones under static and dynamic Vickers indentations. *Wear* 224, 56–67.
- Lee, W.-S., Shyu, J.-C., Chiou, S.-T., 2000. Effect of strain rate on impact response and dislocation substructure of 6061-T6 aluminum alloy. *Scripta Mater.* 42, 51–56.
- Li, C.H., 1982. A pressure-shear experiment for studying the dynamic plastic response of metals at shear strain rates of  $10^5 \text{ s}^{-1}$ . In: Ph.D. Thesis. Brown University, Providence, RI.
- Lucas, B.N., Oliver, W.C., 1999. Indentation power-law creep of high-purity indium. *Metall. Mater. Trans. A* 30, 601–610.
- Marshall, D.B., Evans, A.G., Nisenholz, Z., 1983. Measurement of dynamic hardness by controlled sharp-projectile impact. *J. Am. Cer. Soc.* 66, 580–585.
- Nicholas, T., 1980. Tensile testing of materials at high rates of strain. *Exp. Mech.* 21, 177–185.
- Senseny, P.E., Duffy, J., Hawley, R.H., 1978. Experiments on strain rate history and temperature effects during plastic deformation of close-packed metals. *J. Appl. Mech.* 45, 60–66.
- Tirupataiah, Y., Sundararajan, G., 1991. A dynamic indentation technique for the characterization of the high-strain rate plastic flow behavior of ductile metals and alloys. *J. Mech. Phys. Solids* 39, 243–271.
- Woodcock, C.L., Bahr, D.F., 2000. Plastic zone evolution around small scale indentations. *Scripta Mater.* 43, 783–788.

## MISCELLANEOUS STRESS-INTENSITY SOLUTIONS

- M.Y. He and J.W. Hutchinson, "Asymmetric Four-Point Crack Specimen", *J. Appl. Mech.*, vol. 67, 2000, pp. 207-09.
- M.Y. He and J.W. Hutchinson, "Surface Crack Subject to Mixed Mode Loading", *Eng. Fract. Mech.*, vol. 65, 2000, pp. 1-14.

# Brief Notes

A Brief Note is a short paper that presents a specific solution of technical interest in mechanics but which does not necessarily contain new general methods or results. A Brief Note should not exceed 1500 words or equivalent (a typical one-column figure or table is equivalent to 250 words; a one line equation to 30 words). Brief Notes will be subject to the usual review procedures prior to publication. After approval such Notes will be published as soon as possible. The Notes should be submitted to the Technical Editor of the JOURNAL OF APPLIED MECHANICS. Discussions on the Brief Notes should be addressed to the Editorial Department, ASME, United Engineering Center, Three Park Avenue, New York, NY 10016-5990, or to the Technical Editor of the JOURNAL OF APPLIED MECHANICS. Discussions on Brief Notes appearing in this issue will be accepted until two months after publication. Readers who need more time to prepare a Discussion should request an extension of the deadline from the Editorial Department.

## Asymmetric Four-Point Crack Specimen

M. Y. He

Materials Engineering Department, University of California, Santa Barbara, CA 93106

J. W. Hutchinson

Fellow ASME, Division of Engineering and Applied Sciences, Harvard University, Cambridge, MA 02138

*Accurate results for the stress intensity factors for the asymmetric four-point bend specimen with an edge crack are presented. A basic solution for an infinitely long specimen loaded by a constant shear force and a linear moment distribution provides the reference on which the finite geometry solution is based.*  
[S0021-8936(00)03601-1]

This note was prompted by a comparison ([1]) of existing numerical solutions ([2-4]) for the crack specimen known as the asymmetric four-point specimen shown in Fig. 1. Discrepancies among the solutions are as large as 25 percent within the parameter range of interest. Moreover, in some instances the full set of nondimensional parameters specifying the geometry (there are four) have not been reported. The specimen has distinct advantages for mixed mode testing, including the determination of mixed mode fatigue crack thresholds. Here a new fundamental reference solution is given for a infinitely long cracked specimen subject to a constant shear force and associated bending moment distribution. The small corrections needed to apply this solution to the finite four-point loading geometry are included.

By static equilibrium (the configuration in Fig. 1 is statically determinant), the shear force,  $Q$ , between the inner loading points and the bending moment,  $M$ , at the crack are related to the force,  $P$ , by (all three quantities are defined per unit thickness):

$$Q = P(b_2 - b_1)/(b_2 + b_1) \quad \text{and} \quad M = cQ. \quad (1)$$

Consider first the reference problem of an infinite specimen with crack of length  $a$  subject to a constant shear force  $Q$  and associated linearly varying bending moment  $M$ . In the absence of

the crack, the exact solution for the cross section has a parabolic distribution of shear stress proportional to  $Q$  and a linear variation of normal stress proportional to  $M$  ([5]). By superposition of these two contributions, the solution for the intensity factors in the presence of the crack can be written exactly in the form

$$K_I^R = \frac{6cQ}{W^2} \sqrt{\pi a} F_I(a/W) \quad (2a)$$

$$K_{II}^R = \frac{Q}{W^{1/2}} \frac{(a/W)^{3/2}}{(1-a/W)^{1/2}} F_{II}(a/W) \quad (2b)$$

where, anticipating the application, we have taken  $M = cQ$  at the crack. The solution (2a) is the same as that for a pure moment. It has been obtained numerically to considerable accuracy. Tada et al. [6] give

$$F_I\left(\frac{a}{W}\right) = \sqrt{\frac{2W}{\pi a} \tan \frac{\pi a}{2W}} \frac{0.923 + 0.199 \left(1 - \sin \frac{\pi a}{2W}\right)^4}{\cos \frac{\pi a}{2W}} \quad (3a)$$

for  $0 \leq \frac{a}{W} \leq 1$

while Murakami [7] gives

$$F_I\left(\frac{a}{W}\right) = 1.122 - 1.121 \left(\frac{a}{W}\right) + 3.740 \left(\frac{a}{W}\right)^2 + 3.873 \left(\frac{a}{W}\right)^3 - 19.05 \left(\frac{a}{W}\right)^4 + 22.55 \left(\frac{a}{W}\right)^5 \quad \text{for } \frac{a}{W} \leq 0.7. \quad (3b)$$

The second solution (2b) is not in the literature.

Finite element analyses of the reference problem have been carried out to obtain both  $F_I$  (as a check) and  $F_{II}$ . Our results for  $F_I$  agree with (3b) to four significant figures over the entire range

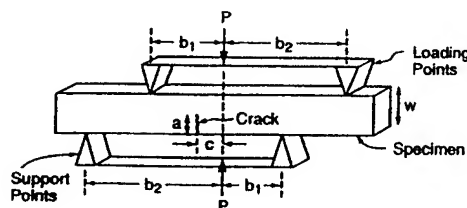


Fig. 1 Geometry of the asymmetric bending and shear specimen

Contributed by the Applied Mechanics Division of THE AMERICAN SOCIETY OF MECHANICAL ENGINEERS for publication in the ASME JOURNAL OF APPLIED MECHANICS. Manuscript received and accepted by the ASME Applied Mechanics Division, Feb. 22, 1999. Associate Technical Editor: A. Needleman.

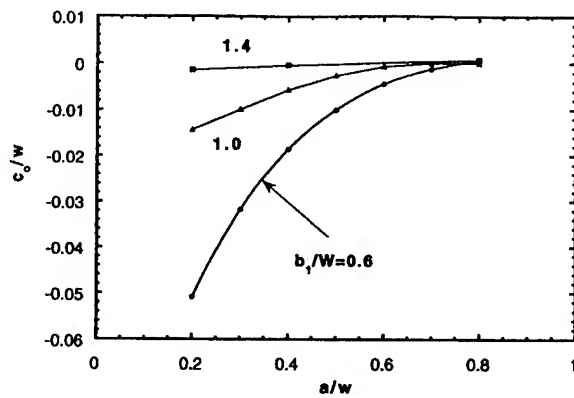


Fig. 2 Location of the crack for pure mode II at its tip ( $\alpha=1$ )

of  $a/W$  indicated. Equation (3a) appears to be less accurate over this same range (with error less than two percent), but it can be used for  $a/W > 0.7$ . The same finite element meshes were used to compute  $F_{II}$ . The following polynomial representation was obtained by fitting the numerical results:

$$F_{II}\left(\frac{a}{W}\right) = 7.264 - 9.37\left(\frac{a}{W}\right) + 2.74\left(\frac{a}{W}\right)^2 + 1.87\left(\frac{a}{W}\right)^3 - 1.04\left(\frac{a}{W}\right)^4 \quad \text{for } 0 \leq \frac{a}{W} \leq 1. \quad (4)$$

This result is believed to be accurate to within one percent over the entire range of  $a/W$ . The results of Suresh et al. [4] determined for a specific choice of the other dimensional parameters of the finite geometry are in good agreement with (4).

Without loss of generality, the solution for the asymmetrically loaded specimen in Fig. 1 can be written as

$$K_I = \frac{6(c-c_0)Q}{W^2} \sqrt{\pi a} F_I(a/W) \quad (5a)$$

$$K_{II} = \frac{\eta Q}{W^{1/2}} \frac{(a/W)^{3/2}}{(1-a/W)^{1/2}} F_{II}(a/W) \quad (5b)$$

where, in general,  $c_0/W$  and  $\eta$  are functions of  $a/W$ ,  $c/W$ ,  $b_1/W$ , and  $b_2/W$ . The mode I stress intensity factor is not precisely zero where  $M=0$ , motivating the introduction of  $c_0$ . The representation (5) is chosen because it reduces to the reference solution ( $c_0/W=0, \eta=1$ ) when the loading points are sufficiently far from the crack. The finite element results presented below indicate the reference solution is accurate to within about two percent as long as the distance of nearest loading point to the crack is greater than  $1.4W$ .

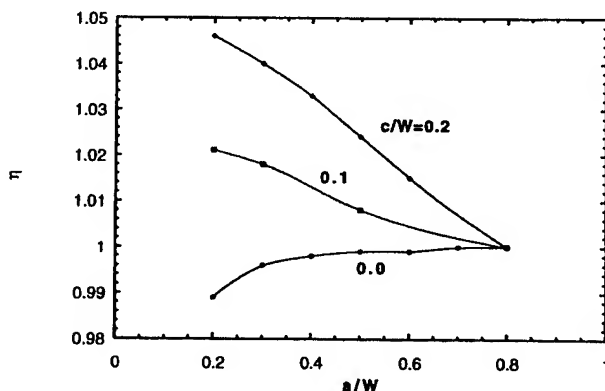


Fig. 3 Correction factor for mode II intensity factor ( $\alpha=1$ )

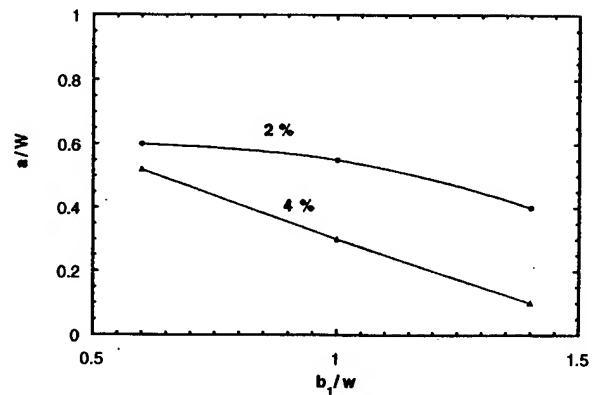


Fig. 4 Error boundaries for mode II stress intensity factor of two percent and four percent for the reference solution (2). Combinations ( $a/W, b_1/W$ ) lying above a boundary have smaller error.

Figure 2 displays the dependence of  $c_0/W$  on  $a/W$  for three values of  $b_1/W$  and  $\alpha \equiv (b_2 - b_1)/W = 1$ . This was computed as the  $c/W$  at which  $K_I=0$ . If the moment at the crack vanishes (i.e.,  $c=0$ ), the mode I factor can be significant when the loading points are near the crack. For example, for the extreme, but not entirely unrealistic case, where  $b_1/W=0.6$ ,  $\alpha=1$ ,  $a/W=0.2$ , and  $c=0$ , the mode mixity,  $\psi = \tan^{-1}(K_{II}/K_I)$ , is 65 deg instead of 90 deg.

Variations of the mode II correction factor  $\eta$  with  $a/W$  for several  $c/W$  are shown in Fig. 3 for  $b_1/W=1.0$  and  $\alpha=1$ . The error is largest for short cracks and for cracks on the order of a distance  $W$  from the closest loading point. Curves corresponding to constant values of the correction factor are plotted in Fig. 4, with  $c/W=0.2$  and  $\alpha=1$ . If the combination ( $b_1/W, a/W$ ) lies above the curve, the correction factor will be smaller than the corresponding  $\eta$ .

Finally, the effect of the parameter  $\alpha = (b_2 - b_1)/W$  is displayed in Fig. 5 by normalizing each of the respective stress intensity factors by the reference value from (2). These results have been computed with  $b_1/W=1.4$  and  $c/W=0.2$ . The error in the reference values is less than roughly 2 percent when  $\alpha > 0.5$ .

The plots in Figs. 2–5 provide guidance for either: (i) ensuring the test parameters are such that the reference solution (2) can be used with confidence, or (ii) estimating the corrections to the reference solution using (5). As long as the distance between the crack and the nearest loading point is greater than about  $1.4W$

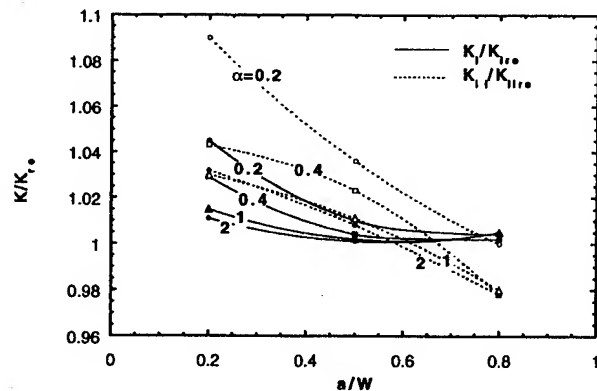


Fig. 5 Role of  $\alpha = (b_2 - b_1)/W$  in error of the reference solution (2) for  $b_1/W=1.4$  and  $c/W=0.2$



(i.e.,  $(b_1 - c)/W > 1.4$  with  $b_2 > b_1$ ) the reference solution is accurate to within a few percent. The errors in the reference solution are the smallest for deep cracks, i.e.,  $a/W \geq 0.5$ .

## Acknowledgment

This work was supported in part by the Multi-University Research Initiative on "High Cycle Fatigue," which is funded at Harvard by AFSOR under Grant No. SA1542-22500 PG, and in part by the Division of Engineering and Applied Sciences, Harvard University.

## References

- [1] Campbell, J. P., 1998, private communication, University of California, Berkeley.
- [2] Wang, K. J., Hsu, C. L., and Kao, H., 1977, "Calculation of Stress Intensity Factors for Combined Mode Bend Specimens," *Advances in Research on the Strength and Fracture of Materials*, Vol. 4, D. M. R. Taplin, ed., ICF4, Waterloo, Canada, Pergamon Press, New York, pp. 123-133.
- [3] He, M. Y., Cao, H. C., and Evans, A. G., 1990, "Mixed-Mode Fracture: The Four-Point Shear Specimen," *Acta Metall. Mater.*, **38**, pp. 839-846.
- [4] Suresh, S., Shih, C. F., Morrone, A., and O'Dowd, N. P., 1990, "Mixed-Mode Fracture Toughness of Ceramic Materials," *J. Am. Ceram. Soc.*, **73**, pp. 1257-1267.
- [5] Timoshenko, S. P., and Goodier, J. N., 1970, *Theory of Elasticity*, 3rd Ed. McGraw-Hill, New York.
- [6] Tada, H., Paris, P. C., and Irwin, G. R., 1985, *The Stress Analysis of Cracks Handbook*, Del Research Corp., St. Louis, MO.
- [7] Murakami, Y., 1987, *Stress Intensity Factors Handbook*, Pergamon Press, New York.

## Large Shearing of a Prestressed Tube

### M. Zidi

Université Paris 12 Val de Marne, Faculté des Sciences et Technologie, CNRS ESA 7052, Laboratoire de Mécanique Physique, 61, avenue du Général De Gaulle, 94010 Creteil Cedex, France  
e-mail: zidi@univ-paris.12.fr

*This study is devoted to a prestressed and hyperelastic tube representing a vascular graft subjected to combined deformations. The analysis is carried out for a neo-Hookean response augmented with unidirectional reinforcing that is characterized by a single additional constitutive parameter for strength of reinforcement. It is shown that the stress gradients can be reduced in presence of prestress. [S0021-8936(00)00101-X]*

## 1 Introduction

Mechanical properties are of major importance when selecting a material for the fabrication of small vascular prostheses. The operation and the handling of prostheses vessel by surgeons, on the one part, the design of such grafts, on the other, induce specific loading and particularly boundary or initial conditions. Consequently, the interest in developing a theoretical model to describe the behavior of the prostheses vessel is proved ([1]). In this paper, we consider a thick-walled prestressed tube, hyperelastic, transversely isotropic, and incompressible assimilated to a vessel graft. We give an exact solution of the stress distributions when the tube is subjected to the simultaneous extension, inflation, torsion, azimuthal, and telescopic shears ([2-10]). The first theoretical re-

sults, in the case of a silicone tube, indicate that the increase of prestress minimizes the stress gradients due to the effects of the shear.

## 2 Model Formulation

Consider a nonlinearly elastic opened tube defined by the angle  $\omega_0$  (Fig. 1). Let us suppose that the tube undergoes two successive deformations; first, including the closure of the tube which induced residual strains ([11]) and second, including inflation, extension, torsion, azimuthal and telescopic shears. The mapping is described by

$$r = r(R) \quad \theta = \left( \frac{\pi}{\omega_0} \right) \omega + \phi \alpha Z + \Theta(r) \quad z = \lambda \alpha Z + \Delta(r) \quad (1)$$

where  $(R, \omega, Z)$  and  $(r, \theta, z)$  are, respectively, the reference and the deformed positions of a material particle in a cylindrical system.  $\phi$  is a twist angle per unloaded length,  $\alpha$  and  $\lambda$  are stretch ratios (respectively, for the first and the second deformation),  $\Theta$  is an angle which defined the azimuthal shear, and  $\Delta$  is an axial displacement which defined the telescopic shear.

It follows from (1) that the physical components of the deformation gradient  $\mathbf{F}$  has the following representation in a cylindrical system:

$$\mathbf{F} = \begin{bmatrix} \dot{r}(R) & 0 & 0 \\ r(R)\dot{\Theta}(r)\dot{r}(R) & \frac{r(R)}{R} \frac{\pi}{\omega_0} & r\phi\alpha \\ \Delta(r)\dot{r}(R) & 0 & \alpha\lambda \end{bmatrix} \quad (2)$$

where the dot denotes the differentiation with respect to the argument.

Incompressibility then requires that  $J \equiv \det \mathbf{F} = 1$ , which upon integration yields

$$r^2 = r_i^2 + \frac{\omega_0}{\pi\alpha\lambda} (R^2 - R_i^2) \quad (3)$$

where  $R_i$  and  $r_i$  are, respectively, the inner surfaces of the tube in the free and in the loaded configurations ( $R_e$  and  $r_e$  are the outer surfaces).

The strain energy density per unit undeformed volume for an elastic material, which is locally and transversely isotropic about the  $\mathbf{t}(R)$  direction, is given by

$$W = W(I_1, I_2, I_3, I_4, I_5) \quad (4)$$

where

$$I_1 = \text{Tr} \mathbf{C}, \quad I_2 = \frac{1}{2} [(\text{Tr} \mathbf{C})^2 - \text{Tr} \mathbf{C}^2], \quad I_3 = 1, \\ I_4 = \mathbf{t} \mathbf{C} \mathbf{t}, \quad I_5 = \mathbf{t} \mathbf{C}^2 \mathbf{t} \quad (5)$$

are the principal invariants of  $\mathbf{C} = \bar{\mathbf{F}} \mathbf{F}$  which is the right Cauchy-Green deformation tensor ( $\bar{\mathbf{F}}$  is the transpose of  $\mathbf{F}$ ).

The corresponding response equation for the Cauchy stress  $\boldsymbol{\sigma}$  for transversely isotropic incompressible is (see [12])

$$\boldsymbol{\sigma} = -p \mathbf{1} + 2[W_1 \mathbf{B} - W_2 \mathbf{B}^{-1} + I_4 W_4 \mathbf{T} \otimes \mathbf{T} \\ + I_4 W_5 (\mathbf{T} \otimes \mathbf{B} \cdot \mathbf{T} + \mathbf{T} \cdot \mathbf{B} \otimes \mathbf{T})] \quad (6)$$

where  $\mathbf{B} = \bar{\mathbf{F}} \mathbf{F}$  is the left Cauchy-Green tensor,  $\mathbf{1}$  the unit tensor, and  $p$  the unknown hydrostatic pressure associated with the incompressibility constraint,  $W_i = (\partial W / \partial I_i)$  ( $i = 1, 2, 4, 5$ ) and  $\mathbf{T} = (1/\sqrt{I_4}) \mathbf{F} \mathbf{t}$ .

From (6), the equilibrium equations in the absence of body forces are reduced to

$$\frac{d\sigma_{rr}}{dr} + \frac{\sigma_{rr} - \sigma_{\theta\theta}}{r} = 0 \quad (7a)$$

Contributed by the Applied Mechanics Division of THE AMERICAN SOCIETY OF MECHANICAL ENGINEERS for publication in the ASME JOURNAL OF APPLIED MECHANICS. Manuscript received by the ASME Applied Mechanics Division, Mar. 24, 1998; final revision, Oct. 12, 1999. Associate Technical Editor: M. M. Carroll.



PERGAMON

Engineering Fracture Mechanics 65 (2000) 1–14

[www.elsevier.com/locate/engfracmech](http://www.elsevier.com/locate/engfracmech)

## Engineering Fracture Mechanics

# Surface crack subject to mixed mode loading

M.Y. He<sup>a</sup>, J.W. Hutchinson<sup>b,\*</sup>

<sup>a</sup>*Materials Engineering Department, University of California, Santa Barbara, CA 93106, USA*

<sup>b</sup>*Division of Engineering and Applied Sciences, Applied Sciences, 315 Pierce Hall, 29 Oxford Street, Harvard University, Cambridge, MA 02138, USA*

Received 19 April 1999; received in revised form 2 November 1999; accepted 10 November 1999

### Abstract

Stress intensity factor distributions at the edge of semi-circular and semi-elliptical surface cracks are obtained for cracks aligned perpendicular to the surface of a semi-infinite solid subject to remote shear parallel to the plane of the crack. Mixed mode conditions along the crack edge are characterized. Application to fatigue crack thresholds in mixed mode is discussed. © 2000 Elsevier Science Ltd. All rights reserved.

**Keywords:** Surface crack; Modes II and III; Fatigue crack growth; Fatigue threshold

### 1. Introduction

Surface crack solutions are widely used in applications of fracture mechanics to fatigue and monotonic loadings. A semi-elliptical surface crack lying perpendicular to the surface and subject to applied stresses with no shear component parallel to the crack experiences mode I conditions around its edge. It is usually tacitly assumed that this orientation is the critical one. Whether this orientation is critical for designs based on fatigue crack thresholds has been called into question by some recent experimental data [1–3] which indicate that long crack threshold conditions may be lower under mixed mode than under mode I. It is this observation which motivates the present study of the mixed mode stress intensity factors for cracks at surfaces under general remote uniform stressing. Attention is directed to cracks which are perpendicular to the surface. The results presented below supplement the mode I stress intensity factors of Raju and Newman [4,5] for cracks perpendicular to the surface and by Noda and Miyoshi [6] and Noda et al. [7] for cracks inclined to the surface. The only other results in

\* Corresponding author. Tel.: +1-617-495-2848; fax: +1-617-495-9837.

E-mail address: [hutchinson@husm.harvard.edu](mailto:hutchinson@husm.harvard.edu) (J.W. Hutchinson).

the literature on the mixed mode crack problem analysed in this paper appears to be preliminary results in a paper by Murikami [8] which will be discussed later.

The problem addressed here is depicted in Fig. 1(a). An isotropic elastic half-space with a semi-circular or semi-elliptical crack in the  $(x_1, x_3)$  plane is subject to a remote uniform stress specified by the components  $(\sigma_{11}^0, \sigma_{22}^0, \sigma_{12}^0)$ . The crack is not influenced by the component  $\sigma_{11}^0$  since this component produces no traction on the crack plane. The component  $\sigma_{22}^0$  induces a mode I stress intensity factor distribution along the crack edge which is available in Ref. [5]. The component  $\sigma_{12}^0$  induces both mode II and mode III intensity factor distributions. It is these distributions which will be computed and characterized in this paper. The solution for arbitrary uniform remote stressing is obtained by superposition of the distributions due to  $\sigma_{22}^0$  and  $\sigma_{12}^0$ . A crack inclined to a remote tensile field, as shown in Fig. 1(b), is a special case of this solution. This case will be used to illustrate potential mixed mode effects later in the paper.

## 2. Solution for shear stress applied parallel to the crack

Consider semi-elliptical cracks in the  $(x_1, x_3)$  plane with depth  $a$  and half-length  $c$  at the surface (Fig. 1(a)). The only nonzero remote stress component is  $\sigma_{12}^0$ . The Young's modulus of the elastic material is  $E$  and the Poisson's ratio is  $\nu$ . The symmetry of the geometry and anti-symmetry of the loading dictates that the mode I stress intensity factor,  $K_I$ , vanishes along the crack edge. The mode II and mode III intensity factors,  $K_{II}$  and  $K_{III}$ , vary along the crack edge and will be regarded as functions of the angle  $\varphi$  defined in Fig. 1(a). These factors are odd and even functions, respectively, with respect to the deepest point of the crack,  $\varphi = \pi/2$ . It will be seen that  $K_{II}$  is largest in magnitude near the surface, while  $K_{III}$  is largest where the crack penetrates most deeply into the body.

### 2.1. A reference solution

A useful reference solution is that for the similarly aligned and loaded elliptical crack in an infinite

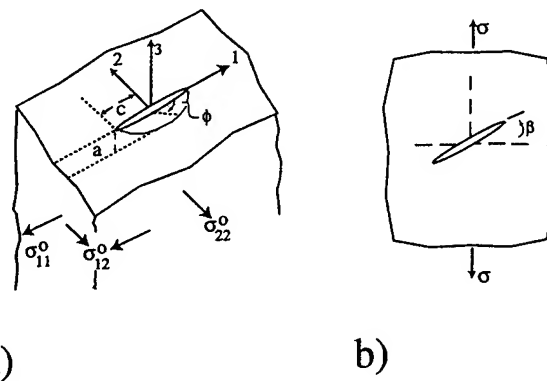


Fig. 1. (a) Semi-elliptical surface crack in a semi-infinite isotropic elastic solid subject to uniform remote stresses  $(\sigma_{11}^0, \sigma_{22}^0, \sigma_{12}^0)$ . The present paper considers the shear loading  $\sigma_{12}^0$  which induces mode II and III stress intensities along the crack front. Solutions for the mode I problem due to  $\sigma_{22}^0$  exist in the literature. The stress component  $\sigma_{11}^0$  has no influence on the stress intensity factors. (b) Surface crack aligned obliquely to the remote tensile field.

solid [9-11]. This is an exact solution given by

$$K_{II}^0 = \frac{\sigma_{12}^0 \sqrt{\pi a} k^2 (a/c) \cos \varphi}{B [\sin^2 \varphi + (a/c)^2 \cos^2 \varphi]^{1/4}}$$

$$K_{III}^0 = \frac{\sigma_{12}^0 \sqrt{\pi a} k^2 (1 - \nu) \sin \varphi}{B [\sin^2 \varphi + (a/c)^2 \cos^2 \varphi]^{1/4}} \quad (1)$$

where

$$k^2 = 1 - (a/c)^2, \quad B = (k^2 - \nu)E(k) + \nu(a/c)^2 K(k)$$

with elliptic integrals defined by

$$E(k) = \int_0^{\pi/2} \sqrt{1 - k^2 \sin^2 \varphi} \, d\varphi, \quad K(k) = \int_0^{\pi/2} \frac{d\varphi}{\sqrt{1 - k^2 \sin^2 \varphi}}$$

The maximum values of the reference intensity factors will be used for scaling the surface crack solutions:

$$(K_{II}^0)_{\varphi=0} = \sigma_{12}^0 \sqrt{\pi a} k^2 (a/c)^{1/2} / B$$

$$(K_{III}^0)_{\varphi=\pi/2} = \sigma_{12}^0 \sqrt{\pi a} k^2 (1 - \nu) / B \quad (2)$$

Numerical values for these factors are given in Table 1 for a range of  $c/a$  and  $\nu$ .

Table 1  
Maximum values of the reference intensity factors from Eq. (2)

$\nu$	$c/a$	$(K_{II}^0)_{\varphi=0} / \sigma_{12}^0 \sqrt{\pi a}$	$(K_{III}^0)_{\varphi=\pi/2} / \sigma_{12}^0 \sqrt{\pi a}$
0	1	0.637	0.637
0	1.5	0.618	0.756
0	2	0.584	0.826
0	3	0.518	0.898
0.2	1	0.707	0.566
0.2	1.5	0.710	0.695
0.2	2	0.685	0.775
0.2	3	0.623	0.863
0.3	1	0.749	0.525
0.3	1.5	0.767	0.657
0.3	2	0.750	0.743
0.3	3	0.693	0.841
0.5	1	0.849	0.425
0.5	1.5	0.913	0.559
0.5	2	0.927	0.655
0.5	3	0.895	0.775

## 2.2. Behavior at the corner of the crack at the free surface ( $\varphi = 0$ )

Under general stressing, the stress field along interior points of the crack edge is the superposition of the conventional mode I, II and III fields, which are characterized by an inverse square root dependence on the distance from the tip. At the point where the crack edge intersects the free surface, a three-dimensional corner singularity exists [12–14]. With  $R$  as the distance from the corner point, the singular stresses associated with the symmetric field (mode I) become unbounded as  $R$  diminishes according to

$$\sigma \propto R^{-S_s} \quad (3a)$$

while the stresses in the anti-symmetric fields (modes II and III) satisfy

$$\sigma \propto R^{-S_a} \quad (3b)$$

Plots of  $S_s$  and  $S_a$  as a function of  $\nu$  are given in Fig. 2. Except for  $\nu = 0$ , the corner singularity of the mode I field is weaker, and that of the anti-symmetric modes is stronger, than inverse square root behavior. The relationship between the corner and interior singularity strengths and the character of the full solution has been examined for a specific three-dimensional, mode I problem [15] (e.g. the through-crack in a finite thickness plate). The effective zone of dominance of the corner singularity comprises a very small fraction of the crack edge. Over most of the crack edge, the stress intensity factor associated with the inverse square root behavior governs the stresses and strains, although the distance from the crack tip for which local plane strain conditions are achieved is a small fraction of the plate thickness.

The effect of the strong corner singularity (3b) on the mode II and III stress intensity factor distributions for the problem considered here will be apparent. However, no attempt has been made to incorporate the corner singularity (3b) in the representation of the numerical results for the distributions. High resolution accuracy at the corner may not be worth pursuing, in any case, because the geometry where the crack intersects the surface is expected to adjust under loading so as to ameliorate the stronger singularity.

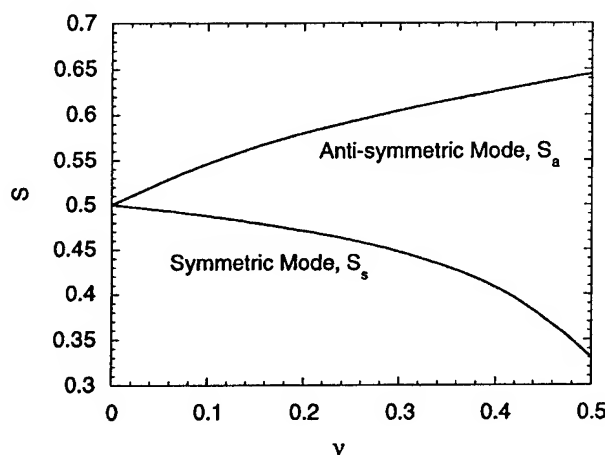


Fig. 2. Dependence of the singularity exponents (3) for stress fields at the corner where the crack intersects the surface of the half space,  $S_s$  for the mode I and  $S_a$ , for mode II and III, respectively [14].

### 2.3. Finite element meshes

A three-dimensional finite-element analysis has been used to calculate the strain energy release rate and the mode II and III stress-intensity factor distributions along the surface crack front. The finite-element mesh for a semi-elliptical crack can be obtained from that for a semi-circular crack by an elliptical transformation. This transformation is convenient for generating the mesh, and it has advantages for the evaluation of the energy release rate because of its orthogonal nature. The element sides along the crack front are perpendicular to the front. This increases the accuracy of strain energy release rate (for crack advance in the plane of the crack) when it is evaluated numerically using the  $J$ -integral with the domain integral method [16]. Specifically, the  $(x, y, z)$  Cartesian coordinates of a node in the semi-circular case become the  $(x', y', z')$  coordinates of the same node in the semi-elliptical case when

$$x = a\eta \cos \varphi \quad (4a)$$

$$y = a\eta \sin \varphi \quad (4b)$$

such that

$$\begin{aligned} x' &= \cos \varphi (c^2 + (\eta^2 - 1)a^2)^{1/2} \\ y' &= y \\ z' &= z \end{aligned} \quad (5)$$

for  $c/a > 1$ . The relation between circular arcs and radial lines in the  $(x, y)$  plane of the semi-circular crack and ellipses and hyperbolas, respectively, in the  $(x', y')$  plane of the semi-elliptical crack is illustrated in Fig. 3(a). While the total energy release rate,  $G$ , was evaluated using  $J$ -integral method, the individual stress intensity factors were determined by fitting the near-tip displacement fields for mode II and III to the crack face displacement components from the numerical solution.

A general purpose finite element code, ABAQUS was used for the analysis. Twenty-node quadratic isoparametric brick elements were employed to model the problem. Symmetry and anti-symmetry conditions were exploited such that only one quarter of the half space was meshed. Several meshes were used to gauge accuracy (see Fig. 3(b) for a representative mesh). The coarse mesh used in the convergence study had 864 element and 4698 nodes. A finer mesh, which had 1728 elements and 9002 nodes, was used to generate the main results in the paper.

To evaluate the quality of the mesh, the energy release rate was calculated for an embedded elliptical crack in the full space under uniform remote shear stress using the same mesh employed to produce solutions for the surface crack problems. The results were within 0.5% of the exact solution from Eq. (1).

Examples of the numerical solution for the stress intensity distributions are presented in Fig. 4 for the semi-circular crack ( $c/a = 1$ ). Complications at the corner at  $\varphi = 0$  do not appear in Fig. 4(a) when Poisson's ratio vanishes. A fine mesh has been employed in the vicinity of the corner, as revealed by the points in the figure where the stress intensity factors have been evaluated. The solution to the semi-circular surface crack is very close to that for the penny-shaped crack in the infinite body (I) when  $\nu = 0$ . The effect of the corner singularity is evident in Fig. 4(b) for  $\nu = 0.3$ . In the vicinity of the corner,  $K_{III}$  does not go smoothly to zero, and  $K_{II}$  displays distinctly non-uniform behavior for  $\varphi < 0.1 (\cong 5^\circ)$ ,

consistent with the existence of a corner singularity Eq. (3) stronger than the square root dependence in the interior. The effect of the finite element mesh is also evident in Fig. 4(b). The coarse mesh provides accuracy almost equal to that of the moderately fine mesh for  $\varphi > 0.35 (\cong 20^\circ)$ , but provides inadequate resolution nearer to the corner.

Another exploration of meshing is presented in Fig. 5, which shows the energy release rate along the front of a semi-circular surface crack normalized by the corresponding distribution,  $G_0(\varphi)$ , from Eq. (1) for the penny-shaped crack in the infinite body. The rates are for crack advance in the plane of the crack. The two meshes used have the same number of elements. One is the fine mesh described above, and the other employs smaller elements near the free surface and larger elements along the edge in the interior. The  $J$ -integral has been used to compute the energy release rate at points along the front. For  $\nu = 0.3$ , the evaluation points for the mesh with the finest resolution at the corner are indicated by solid diamonds in Fig. 5, while a curve has been drawn for the results from the other mesh. The role of the strong corner singularity for  $\varphi < 0.1 (\cong 5^\circ)$  is brought out clearly by the trend near the corner. (The results for  $\nu = 0$ , which have not been plotted, are virtually identical to those for the penny-shaped crack in the infinite solid with  $G$  going smoothly to the limit at the corner.) For  $\nu = 0.3$ , both meshes capture the upturn in the energy release at the corner for  $\varphi < 0.1 (\cong 5^\circ)$ . Apart from the behavior very near the corner, the distribution for the penny-shaped crack is within 5% of that of the surface crack. Whether the highly localized behavior at the corner has important physical implications will have to await comparison with observations. In this paper, no attempt has been made to provide accurate

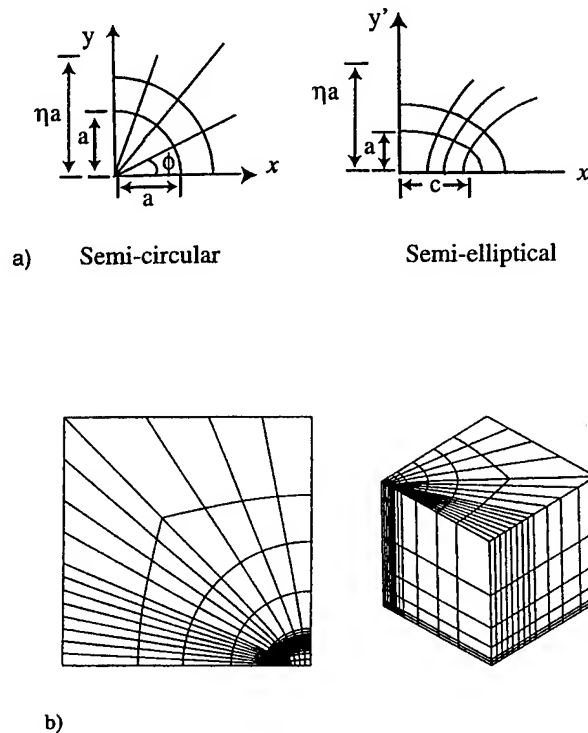


Fig. 3. (a) Coordinates used to generate the mesh. (b) Representative finite element mesh for  $c/a = 1.5$ .

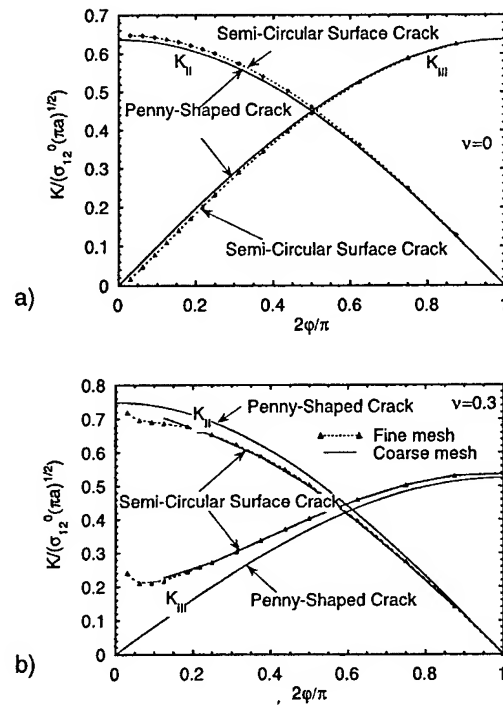


Fig. 4. Distributions of the stress intensity factors for (a)  $\nu = 0$  and (b)  $\nu = 0.3$  for the semi-circular surface crack and the penny-shaped crack in the infinite solid, both subject to nonzero  $\sigma_{12}^0$ . Comparison between predictions of coarse and fine meshes are shown in (b).

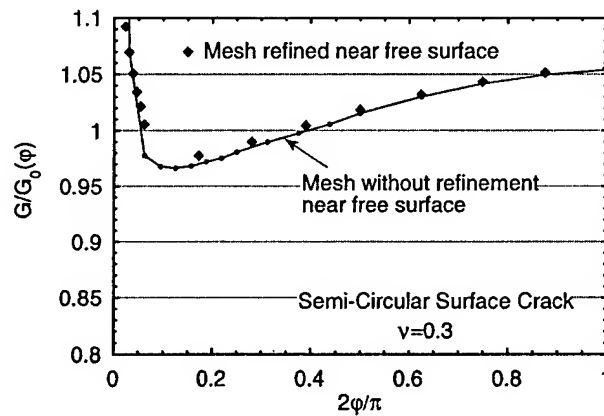


Fig. 5. Energy release rate of semi-circular surface crack normalized by energy release rate of penny-shaped crack in an infinite body at same  $\phi$  for  $\nu = 0.3$ . The applied stress is  $\sigma_{12}^0$ . A comparison is shown between the predictions of two meshes with the same number of elements but differing refinement near the corner where the crack meets the free surface at  $\phi = 0$ .



resolution of the intensity factors within about  $\varphi = 0.05 (\cong 2.5^\circ)$  of the corner. The fine mesh with the more uniformly distributed spacing around the crack front was used in the following.

#### 2.4. Stress intensity distributions

The main results for semi-elliptical surface cracks are given in Fig. 6 and Fig. 8. Stress intensity factor distributions for  $c/a = 1, 1.5$  and  $2$  are plotted in Fig. 6(a) for  $\nu = 0.2$  and in Fig. 6(b) for  $\nu = 0.3$ . The intensity factors,  $K_{II}$  and  $K_{III}$ , have been normalized by the corresponding maximum values for the full elliptical crack with the same  $c/a$  and  $\nu$  defined in Eq. (2) and provided in Table 1. The corresponding normalized distributions for elliptical cracks in the infinite body are plotted for comparison purposes in Fig. 7. Inspection of the reference solution (1) for the full elliptical crack, normalized by the respective maxima in Eq. (2), reveals that the normalized distributions are independent of  $\nu$  (i.e. all the dependence on  $\nu$  is contained in the normalizing factors,  $(K_{II}^0)_{\varphi=0}$  and  $(K_{III}^0)_{\varphi=\pi/2}$ ). The dependence on  $\nu$  of the normalized distributions for the surface crack is displayed in the three plots of Fig. 8 for  $c/a = 1, 1.5$  and  $2$ . Now the role of Poisson's ratio shows up as a fairly strong influence on the stress intensity distribution near the corner at  $\varphi = 0$ , which is related to the effect of  $\nu$  on the corner singularity discussed in Section 2.2. The influence on  $K_{III}$  is by far the largest, but this occurs in a range of  $\varphi$  in which  $K_{III}$  is relatively small.

Away from the corner, the role of  $\nu$  on the normalized distributions is relatively small. The main

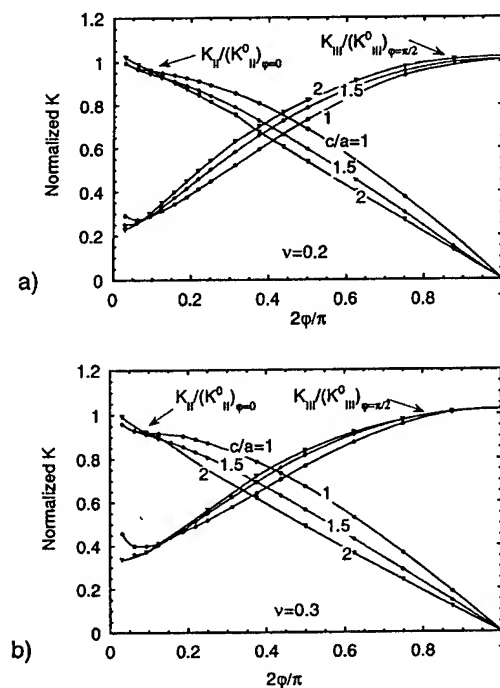


Fig. 6. Normalized distributions of the stress intensity factors for the semi-elliptical surface crack subject to nonzero  $\sigma_{12}^0$ : (a)  $\nu = 0.2$  and (b)  $\nu = 0.3$ .

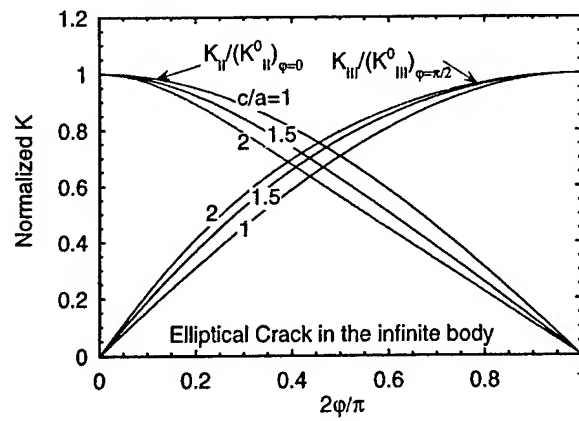


Fig. 7. Normalized distributions of the stress intensity factors for the elliptical crack in the infinite body subject to nonzero  $\sigma_{12}^0$ . The normalized distributions are independent of Poisson's ratio.

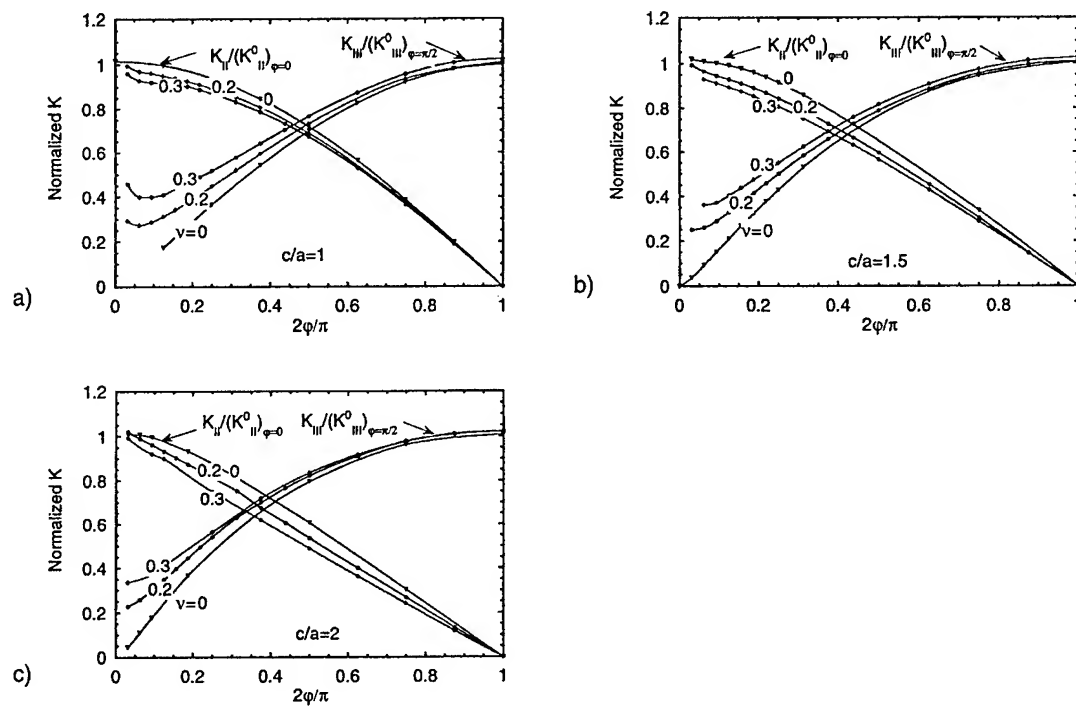


Fig. 8. Normalized distributions of the stress intensity factors for the semi-elliptical surface crack subject to nonzero  $\sigma_{12}^0$  for  $\nu = 0, 0.2$  and  $0.3$ : (a)  $c/a = 1$ , (b)  $c/a = 1.5$  and (c)  $c/a = 2$ .

dependence of the intensity factors on  $v$  is contained in the normalizing factors (2). Indeed, comparison of the distributions in Figs. 6 and 8 with those in Fig. 7 for the full elliptical crack in the infinite body indicates that, away from the corner, the full elliptical crack solution (1) provides a reasonably accurate approximation to problem for the semi-elliptical surface crack. The error in this approximation can be displayed by expressing the intensity factors of the surface crack as the sum of the reference intensity factors (1) and the corrections:

$$K_{II} = K_{II}^0 + \delta K_{II} \quad \text{and} \quad K_{III} = K_{III}^0 + \delta K_{III} \quad (6)$$

Values of  $\delta K_{II}/(K_{II}^0)_{\varphi=0}$  and  $\delta K_{III}/(K_{III}^0)_{\varphi=\pi/2}$  are presented as solid points in Fig. 9 for  $c/a = 1.5$ . The error in using Eq. (1) for the surface crack is less than 10% for the distributions in almost the entire range of  $\varphi$ , except for  $K_{III}$  near the corner. The error in the vicinity of the maxima of the respective

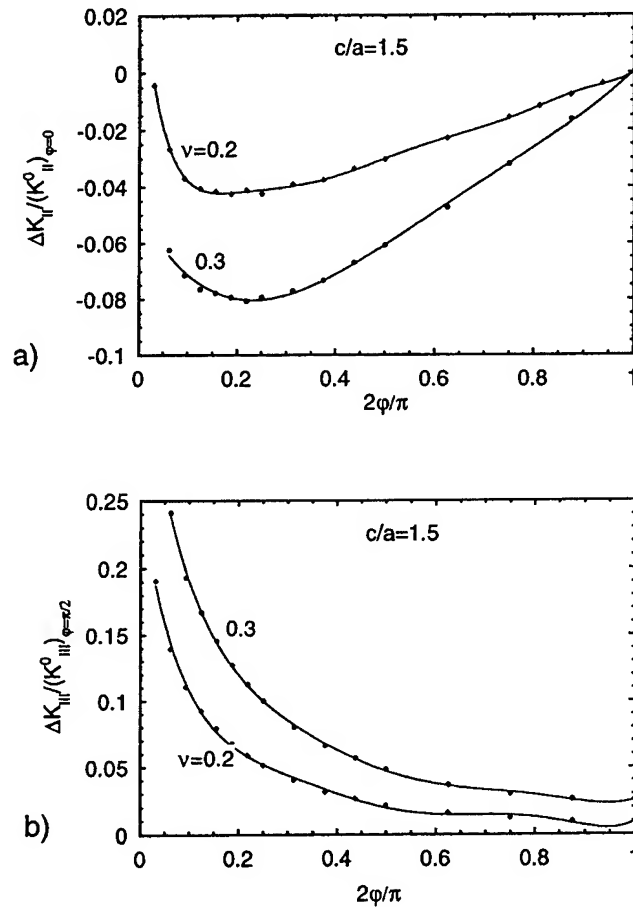


Fig. 9. Normalized distributions of the corrections to Eq. (1), defined in Eq. (6), for the semi-elliptical crack in the infinite body for the case  $c/a = 1.5$ . The solid points are the computed values, and the curves are the polynomial fits given in Table 2.

intensity factors is well below 5%. The trends for  $\delta K_{II}/(K_{II}^0)_{\varphi=0}$  and  $\delta K_{III}/(K_{III}^0)_{\varphi=\pi/2}$  for the other two values of  $c/a$  are similar and will not be shown. Accurate polynomial fits to the normalized corrections over the range  $0.1 < \varphi \leq \pi/2$  are presented in Table 2, and these are shown for the case  $c/a = 1.5$  as the curves in Fig. 9. The numerical results for the cases in this study can be reproduced using Eq. (6) with the polynomial representations in Table 2.

Murikami's [8] estimates of the stress intensity factors for the mixed mode surface crack employs what is essentially an approximation of the full elliptical crack solution. The error in this estimate can be somewhat larger than that in using the full elliptical crack solution itself.

### 3. Trends under mixed mode

The results presented in the previous section presenting the response of the surface crack to the applied stress component  $\sigma_{12}^0$  can be combined by superposition with the results of Newman and Raju [5] for the mode I contribution due to  $\sigma_{22}^0$ , giving the distribution of each of the three stress intensity factors along the crack front. (Recall that  $\sigma_{11}^0$  has no effect on the intensity factors.) Thus, for example, the energy release rate distribution associated with crack advance in the extended crack plane can be computed using the well known relation

$$G = (1 - \nu^2)(K_I^2 + K_{II}^2)/E + (1 + \nu)K_{III}^2/E \quad (7)$$

The general solution for the combined modes also permits one to compute energy release rates for local crack advance in directions other than in the original crack plane. In principle, the mixed mode solution contains the information required to implement any criterion for a brittle material based on local conditions in the immediate vicinity of the crack front. Several such mixed mode criteria have been widely studied and employed for cracking under monotonic loading. None are well established when the mode III component is significant.

The situation with respect to fatigue cracking is less certain under mixed mode. There seems to be general agreement, a few exceptional cases aside, that the local crack front advances under mode I conditions once it has begun to propagate. However, criteria governing threshold conditions for

Table 2  
Polynomial approximations for the stress intensity factor corrections in Eq. (6)<sup>a</sup>

$K$	$\nu$	$c/a$	$c_0$	$c_1$	$c_2$	$c_3$	$c_4$	$c_5$	$c_6$	$c_7$	$c_8$
$\gamma_{II}$	0.2	1	0.0134	-0.7898	4.893	-13.94	20.63	-15.25	4.436		
$\gamma_{III}$	0.2	1	0.3141	-2.851	14.08	-38.12	55.28	-40.23	11.53		
$\gamma_{II}$	0.2	1.5	0.03585	-1.706	15.22	-72.67	203.8	-342.6	338.9	-181.7	40.66
$\gamma_{III}$	0.2	1.5	0.2476	-2.258	11.35	-31.53	47.34	-35.81	10.67		
$\gamma_{II}$	0.2	2	0.0542	-1.214	6.921	-19.95	30.58	-23.44	7.041		
$\gamma_{III}$	0.2	2	0.1949	-1.452	5.474	-10.36	9.411	-3.250			
$\gamma_{II}$	0.3	1	0.0153	-2.494	27.32	-143.5	421.1	-723.8	723.8	-389.7	87.34
$\gamma_{III}$	0.3	1	0.5177	-4.421	22.59	-63.87	96.07	-71.99	21.13		
$\gamma_{II}$	0.3	1.5	-0.0475	-0.3309	1.041	-1.063	0.4011				
$\gamma_{III}$	0.3	1.5	0.3608	-2.528	10.62	-26.41	36.99	-26.72	7.715		
$\gamma_{II}$	0.3	2	0.02388	-1.019	3.102	-3.975	2.401	-0.5322			
$\gamma_{III}$	0.3	2	0.3341	-2.406	8.369	-14.63	12.35	-3.991			

<sup>a</sup> where  $y = c_0 + c_1x + c_2x^2 + c_3x^3 + c_4x^4 + c_5x^5 + c_6x^6 + c_7x^7 + c_8x^8$ ,  $x = 2\varphi/\pi$ , and  $y \equiv \gamma_{II} = \delta K_{II}/(K_{II}^0)_{\varphi=0}$  or  $y \equiv \gamma_{III} = \delta K_{III}/(K_{III}^0)_{\varphi=\pi/2}$ .

initiating fatigue crack growth under mixed mode cyclic loading are not established. It seems reasonable to expect that the threshold stress intensity factor,  $(\Delta K_I)_{TH}$ , determined in a mode I test might be greater than the  $\Delta K_I$  component at threshold under mixed mode cyclic loading. However, there is little data on which to base such a criterion. For example, it is not known whether the decidedly more conservative criterion based on a threshold energy release rate provides a bound. That is, does a threshold value of the cyclic variation of the energy release rate determined in a mode I test,  $(\Delta G_I)_{TH}$ , provide an lower bound to  $\Delta G$  at threshold under mixed mode? Some recent experiments under combined mode I and II on an alloy with a very fine and relatively isotropic micro-structure [3] have suggested that  $(\Delta G_I)_{TH}$  may provide a lower bound, although that conclusion must be regarded as tentative until more data is available.

As remarked above, the present results for the shear loading, when combined with those for the tensile loading [5], can be used to generate distributions along the surface crack front relevant to any potential fracture criterion. As an illustration, consider the surface crack oriented at an angle  $\beta$  to the applied tensile stress  $\sigma$  in Fig. 1(b). The applied stress components in axes aligned with the crack are

$$(\sigma_{11}^0, \sigma_{22}^0, \sigma_{12}^0) = \sigma(\sin^2 \beta, \cos^2 \beta, \sin \beta \cos \beta) \quad (8)$$

An issue, for example, is whether the crack orientation perpendicular to the tensile stress ( $\beta = 0$ ) is critical for threshold fatigue crack growth when  $\sigma$  is cycled, or whether a mixed mode orientation gives rise to fatigue crack growth at the lowest  $\sigma$ . It is not possible to answer this question in the absence of a

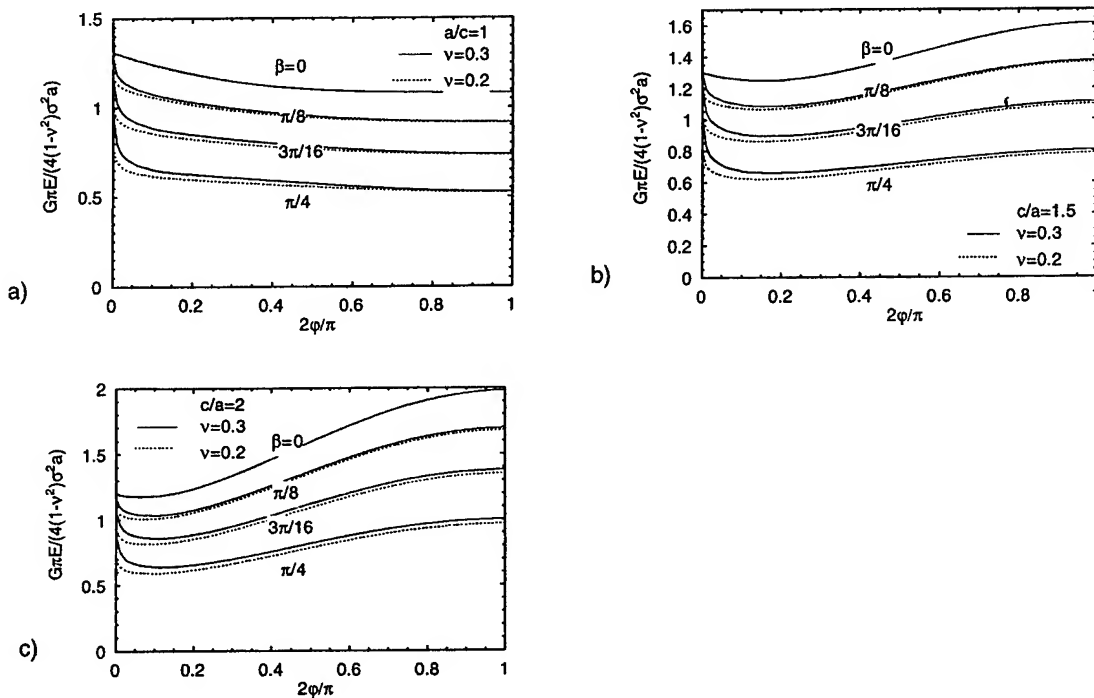


Fig. 10. Distributions of the energy release rate along the crack front for a surface crack oriented at angle  $\beta$  to an applied tensile stress  $\sigma$ : (a)  $c/a = 1$ , (b)  $c/a = 1.5$  and (c)  $c/a = 2$ .

criterion for threshold under mixed mode conditions. However, examination of the energy release rate (7) distribution at various orientations can provide insight. Both  $K_{II}$  and  $K_{III}$  contribute significantly to this measure in addition to  $K_I$ , and it is plausible that  $(\Delta G_I)_{TH}$  might provide a conservative threshold criterion under mixed mode. The energy release rate  $G$  has been computed using Eqs. (7) and (8) together with the distributions of  $K_I$  due to  $\sigma_{22}^0$  from [5] and with those for  $K_{II}$  and  $K_{III}$  due to  $\sigma_{12}^0$  from the data in Figs. 6 and 8 (or, equivalently, using Eq. (6) and the polynomial expressions in Table 2).

Plots of  $G/[4(1-\nu^2)\sigma^2a/(\pi E)]$  as a function of  $\varphi$  are shown in Fig. 10 for four orientations of the surface crack and three crack shapes. As already emphasized, values within about  $\varphi = 0.05 (\cong 2.5^\circ)$  from the corner at  $\varphi = 0$  are not reliable. In any case, it is only the semi-circular crack for which the largest values of  $G$  occur within an appreciable vicinity of the corner. For  $c/a = 1.5$  and 2, the largest values of the energy release rate occur at the point of deepest penetration of the crack at  $\varphi = \pi/2$ . The most notable feature for each of the three crack shapes shown in Fig. 10 is that the energy release rate distribution for the crack oriented perpendicularly to the tensile stress lies well above those for the other orientations. At a given point along the crack front, the energy release monotonically decreases as  $\beta$  increases. Quantitatively, similar behavior occurs for the full elliptical crack in the infinite body. If fatigue crack threshold under mixed mode were governed by  $(\Delta G_I)_{TH}$ , the critical orientation would be  $\beta = 0$ . Based on the seemingly conservative nature of the criterion based on  $(\Delta G_I)_{TH}$ , it would be most surprising if a surface crack at an orientation other than  $\beta = 0$  were critical for threshold growth.

#### 4. Summary

Mode II and III stress intensity factor distributions for semi-elliptical surface cracks subject to remote shear stress have been obtained for a limited range of crack ellipticity. When combined with existing results for the mode I distributions due to remote tensile stress, these results make it possible to compute critical conditions for brittle fracture initiation or fatigue crack growth threshold for any criterion requiring stresses and strains at localities near the crack front. The mode III stress intensity factor distribution, in particular, is strongly affected by a corner singularity in stresses which differs from the conventional inverse square root singularity at interior points along the front. In the vicinity of the corner, the mode III factor does not go smoothly to zero unless Poisson's ratio is zero. Apart from behavior in the vicinity of the corner, the solution (1) for the intensity factor distributions for the full elliptical crack in an infinite body provides a reasonably good approximation to the surface crack distributions for shear loading parallel to the crack. Corrections to Eq. (1) for the surface crack problem are defined in Eq. (6) and provided by polynomials given in Table 2.

#### Acknowledgements

This work was supported in part by the Multi-University Research Initiative on 'High Cycle Fatigue', which is funded at Harvard by AFSOR under Grant No. SA1542-22500 PG, and in part by the Division of Engineering and Applied Sciences, Harvard University.

#### References

- [1] John B, Nicholas A, Lackey F, Porter WJ. Mixed-mode crack growth in a single crystal Ni-based superalloy. In: Lutjering G, Nowack H, editors. Fatigue '96, Proceedings of the Sixth International Fatigue Congress. Oxford: Pergamon Press, 1996. p. 399–404.

- [2] John B, DeLuca D, Nicholas T, Porter J, Near-threshold crack growth behavior of a single crystal Ni-based superalloy subject to mixed mode loading. In: Miller KJ, McDowell DL, editors. Mixed mode behavior, ASTM STP 1359, ASTM, Philadelphia, PA, to be published.
- [3] J. P. Campbell, A. W. Thompson and R. O. Ritchie, Mixed-mode crack growth thresholds in Ti-6Al-4V under turbine-engine high cycle fatigue loading conditions. Proceedings of the 4th National Turbine Engine High Cycle Fatigue Conference, Monterey, CA, February 1999.
- [4] Raju IS, Newman Jr. JC. Stress-intensity factors for a wide range of semi-elliptical surface cracks in finite-thickness plates. *Engng Fracture Mech* 1979;11:817–29.
- [5] Newman Jr. JC, Raju IS. An empirical stress-intensity factor equation for the surface crack. *Engng Fracture Mech* 1981;15:185–92.
- [6] Noda N-A, Miyoshi S. Variation of stress intensity factor and crack opening displacement of semi-elliptical surface crack. *Int J Fracture* 1996;75:19–48.
- [7] Noda N-A, Kobayashi K, Yagishita M. Variation of mixed modes stress intensity factors of an inclined surface crack. *Int J Fracture*, in press.
- [8] Murikami Y. Analysis of stress intensity factors of mode I, II, III of inclined surface crack of arbitrary shape. *Engr Fracture Mech* 1985;22:101–14.
- [9] Kassir MK, Sih GC. Three dimensional stress distributions around an elliptical crack under arbitrary loadings. *J Appl Mech* 1966;33:601–11.
- [10] Sih GC, Liebowitz H. Mathematical theories of brittle fracture. In: *Treatise on fracture*, vol. 2. New York: Academic Press, 1998.
- [11] Tada H, Paris PC, Irwin GR. The stress analysis of cracks handbook, 3rd ed., to be published by ASME.
- [12] Benthem JP. State of stress at the vertex of a quarter-infinite crack in a half-space. *Int J Solids Structures* 1977;13:479.
- [13] Bazant ZP, Estenssoro LF. Surface singularity and crack propagation. *Int J Solids Structures* 1979;16:661.
- [14] Ghahremani F. Numerical variational method for extracting 3D singularities. *Int J Solids Structures* 1991;27:1371–86.
- [15] Nakamura T, Parks DM. Three-dimensional elastic stress field near the crack front of a thin elastic plate. *J Appl Mech* 1988;55:805.
- [16] Shih CF, Moran B, Nakamura T. Energy release rate along a three-dimensional crack front in a thermally stressed body. *Int J of Fracture* 1986;30:79–102.